People's Democratic Republic of Algeria
Algerian Journal of Engineering, Architecture and Urbanism
https://www.aneau.org/ajeau/
ISSN : 2588-1760

Vol. 5 S.I. Nr. 3 2021

Summary

1. **Kherifi Wahida, Hecini Linda, Bekiri Fedia,** Physico-chemical characterization of the waters of the Foum El-Kharza dam for agricultural use, 1-12
2. **Samir DAHDOUH, Abdelhamid SADEDDINE, Hakim AIT-AMOKHTAR**, Temporal aspects of the Portevin-Le Chatelier effect in the Al-2.5%Mg alloy, 13-20
3. **Samira Boumous, Zouhir Boumous, Fatima Zohra kebab**, modeling soil effects on the insulation of hvdc underground cable against lightning strikes, 21-29
4. **Ibtissem. Bousnoubra , Soumia.Fassi, K. Djebbar ,** DECOLORIZATION AND MINERALIZATION OF AN ORGANIC POLLUTANT (BROMOCRESOL PURPLE) BY ADVANCED OXIDATION PROCESSES IN AN AQUEOUS MEDIUM, 30-38
5. **H. MAKRI , D.H.MESSAOUDI,** ETUDE DU DÉLAMINAGE DANS LES TUBES EN MATERIAUX COMPOSITES., 39-48
6. **Abdelhakim Begar, M.E. DJEGHLAL, M. OULD HAMOU,** Optimisation de la récupération du zinc et de l'argent dans les résidus de lixiviation , 49-58
7. **Zakarya AMARA, Latefa GHOMRI, Ali RIMOUCHE,** Machine Learning for Optimization of Flow-Rack AS/RS Performances, 59-73
8. **Adel MOKRANE, Abdellatif ZERGA, Ismael JUMARE,** Modelling and Optimization of a Stand-Alone PV-Diesel Hybrid System with Hydrogen Storage: Case of Algeria.74-85
9. **Salima BORSALI ,** Set INVERSION FOR THE CALIBRATION OF A 3-AXIS ROBOT, 86-96
10. **Fedia BEKIRI, Hanane RAHALI,** MODELLING OF POLYMER SOLUTION USED IN MEMBRANE ELABORATION, 97-102
11. **Attaouia BENTAHAR, Malika KANDOUCI, Samir GHOUALI, Radia MADJIDI,** Impact of DFB laser parameters on FTTH-GPON System , 103-109
12. **Lyes BORDJA , Yassine DEMAGH, El Wardi BITAM, Redjem HADEF,** Dimensional analysis of a parabolic trough collector with a sinusoidal absorber tube, 110-120
13. **Asma BOUDAOUD, Mebrouk DJEDID, Chifaa AD**, Chemical recovery of cadmium ions from charged biosorbent, 121-124
14. **Youcef CHEIKHAOUI, Hamza CHENITI, Salim BENSEHAMDI, Souhib LORABI,** the scale and the shape effects using the udec modeling of an underground mining pillar , 125-135
15. **Mohamed Amine Cherier , Mohammed Bennekrouf, Sidi Mohammed Meliani,** Optimisation of transportation, production, storage and distribution in agrifood supply chain: an Algerian case study, 136-144
16. **Dekhili Nourelhouda, Dekhili Mariem,** How to detect and treat the bacterial corrosion resulting of water separated from petroleum?, 145-151

17. **Chahrazed DJILANI, Rachida ZAGHDOUDI, Fayçal DJAZI,** ELABORATION DE MATERIAUX COMPOSITES BIFONCTIONNELS , 152-165
18. **Farid BELOUAHCHI, Elkheir MERABET,** Design of a New Direct Torque Control Using Sliding mode Theory for Double Star Induction Motor, 166-176
19. **GHALIFodil, DRIZ Samia , FASSI Benattou,** High Speed Transmissions over RoF-OCDMA Networks using ZCZ Spreading Code, 177-186
20. **Sarah GOUDJIL, Saadia GUERGAZI, Toufik MASSMOUDI,** Effeciency of coagulants aid for the removal of a Cationic dye From synthetic solutions, 187-194
21. **Lynda HECINI, Wahida KHERIFI , Khadidja BOUZID**, Groundwater quality of Mih-Ouensa, El Oued (SOUTHEAST of ALGERIA), 195-207
22. **Abdelhek IDIR, Francesco DELLORO, Mohand Amokrane BRADAI, Rassim YOUNES, Abdelhamid SADEDDINE,,** Experimental study on the effect of spraying distance on microstructural and tribological behavior of flame sprayed Ni alloy coatings. 208-220
23. **Younès MENAIL** , IMPACT OF DRILLING ON A CARBON-ORTHOCRYL COMPOSITE MATERIAL FOR THE PRODUCTION OF AN ORTHOPAEDIC PROSTHESIS, 221-227
24. **Younès MENAIL , Abderahim EL MAHI , Bachir REDJEL,** CHOICE BETWEEN TWO GLASS-EPOXY COMPOSITES WITH SERGE AND UD TEXTURE FOR THE REALISATION OF A BOAT HULL, 228-233
25. **Lynda BENBAHOUCHE , Billal BISBIS** , Numerical study investigating the performance of hvigbt-npt under functional and thermal stress, 134-138
26. **Khellaf BELKHIRI,** COMPUTER SIMULATIONS OF BLOOD FLOW IN HUMAN ARTERIAL BIFURCATION, 139-142
27. **Abdelhak Roubi, Abderrazak Allali** , EXPERIMENTAL AND THEORETICAL CONTRIBUTION OF FRICTION WELDING, 143-151
28. **Sakina AOUN, Aziz BOUKADOUM, Laatra YOUSFI,** INDIRECT VECTOR CONTROL OF A DFIG BASED IN AWIND ENERGY CONVERSION SYSTEM, 152-161
29. **Asma MESMOUDI, Samira MESMOUDI, Chaima MADAOUI,** Optimization of Wireless Sensor Network Coverage based on a New Optimal Sensor Placement Strategy, 162-169
30. THE PERFORMANCE OF THE DESALINATION PLANT CHATT EL-HILLAL-BENI-SAF
31. **ZIREG Hanane, MANSOUR Mohamed , HEBBAR Chafika ,** LA PERFORMANCE DE LA STATION DE DESSALEMENT CHATT EL-HILLAL-BÉNI-SAF, 170-178
32. **Salah-Eddine HOUICHER, Rabah Djekidel,** Distribution of the Magnetic Fields Intensity around Overhead Power Transmission Lines, 179-193
33. **Sara BOUDJIT, Rassim YOUNES, Issam BOUKLOUCHE, Mohand Amokrane BRADAI,** Comparative study between two hyperelastic models of an elastomeric specimen), 194-205
34. **Tablit bassima, chellil ahmed, lecheb Samir, Brihmat chahira,** Numerical study of the use of composite piston and estimation of the lifetime. 206-213
35. **Bendadi Mohammed El Khalil, Merouane Habib**, STUDY OF A NON-PREMIXED METHANE/AIR PILOT FLAME, 214-220
36. **Soufiane BOUDJEMAA, Hamoudi MEKHALFI, Ammar BENAMRANI,** Etudes structurales et optiques de nanoparticules Zn1-xFexO préparées par la méthode Sol-Gel: Applications à la photodégradation du colorant Rhodamine B (RhB) sur la lumière solaire, 221-233

37. **Lalaoui Lahouaoui , djaalab abdelhak, Dib Fouad,** Unsupervised segmentation of images by Markov segmentation into regions, 234-247
38. **Oussama Mezouar, Fatiha MESKINE, I. Boukerch,** Co-Evolution Binary Particle Swarm for RFM Optimization of Satellite Images Ortho-rectification, 248-257
39. **Brahim ROSTANE , Abdelkrim BENMANSOUR , Said ABBOUDI, Rima LAZZOUNI , Asma BOUZZIZA** , STUDY AND CONTROL OF AERODYNAMIC FLOW IN AUTOMOTIVE VEHICLES, 258-264
40. **Leila KERDJA, Yazid FIZI, BOUALEM KESKES,** Identification of the parameters of the dynamic behavior law of an Al6061-T6 aluminum using the Taylor impact test, 265-274
41. **Ismail BOUYAKOUB , Rachid TALEB , Maamar SOUAIHIA, Izzeddine CHERCHAR , Wissam NABED ,** DIGITAL IMPLEMENTATION OF MULTICELL SERIAL CONVERTER, 275-282
42. **Soumia Fassi, Ibtissem Bousnoubra and K.Djebbar,** APPLICATION OF THE HETEROGENEOUS PHOTOCATALYSIS TO THE DEGRADATION OF DYE (Purple Ethyl) IN AQUEOUS MEDIUM, 283-288
43. **Ilhem DJAGHOUT , Rabah KSOURI,** OPTIMISATION PAR LE PLAN DE BOX-BENKHEN DE L'ÉLECTROCOAGULA- TION DES POLLUANTS DES EAUX USÉES DE LA VILLE DE GUELMA, 289-295
44. **Brahim ROSTANE , Khaled ALIANE , Said ABBOUDI, Abdelhakim TAZOUTA , Abdelhakim BOUGHRARA ,** Numerical Study of the Cavitant Flow in the Venturi Tube, 296-304
45. **Saadia YSBAA, Omar HADDOUCHE, Abdelhak BOUTALEB, Madjid CHEMAM,** CARBONATE-HOSTED PB-ZN-FE (CU, F, BA) DEPOSITS OF THE NORTHERN EAST ALGERIA: METALLOGENY, STRUCTURAL AND GRAVIMETRIC /AEROMAGNETIC LINEAMENTS CONTROLS, 305-322
46. **Imene HARRATE, Sofiane FATMI, Nacera CHIBANI ,** Comparative study of the physicochemical and organoleptic characteristics of two similar creams, 323-337
47. **M'hamed BERIACHE, Moustefa HADJ HENNI, Leila MOKHTAR SAIDIA,** Évaluation expérimentale des performances d'un moteur diesel alimenté en éthanol/Diesel et méthanol/Diesel,338- 352
48. **Mohamed Khemissi BABOURI, Nouredine OUELAA, Abderrazek DJEBALA,** Diagnosis of mechanical faults in rotating machines based on vibration monitoring in an industrial environment, 353-362
49. **Toufik BOUDIAR, Eric VERNEY**, Asymmetrical and symmetrical coplanar isolator based on ferrite films, 363-371
50. **Hakima MOULAY, Ahmed Bouzidi DJEBBAR, Brahim DEHRI,** Blind Classification of Digital Modulation for D-STBC Cooperative Relaying Networks, 372-382
51. **Rachid TALEB, Taieb BESSAAD, Mohamed MOSTEFAOUI , Maamar SOUAIHIA,** CONTROL OF ASYMMETRICAL MULTILEVEL INVERTER BY PWM WITH SELECTIVE HARMONIC ELIMINATION FOR PV APPLICATIONS, 383-395
52. **Mekki Mounira,** Etude de l'impact du raccordement d'une production décentralisée dans un réseau de distribution, 396-400
53. **Djezouli MOULAI-KHATIR**, Presentation of a three-dimensional metrology software - Application To flatness, 401-407
54. **Zohra BENHARKAT**, Fluide rotatif soumis a la mhd avec effet hall autour une plaque verticale en mouvement, 408-417

55. **Younes BENNACER, Mounia GUERGOURI,** 4,4"-bis(pyrrylideneimino)-3,3"-dimethylbiphnyle: Synthesis and application in organic photovoltaic cell , 418-422
56. **Boualamallah Djamal, Ghazi Abdelkader, Miloudi Abdelkader**, IMPROVEMENT OF THE MANUFACTURING PROCESS. 423-432
57. **Saber ZIARI, Rassim BELAKROUM**, Simulation numérique des instabilités aéroélastiques des plaques minces sous l'effet d'un écoulement supersonique, 433-442
58. **Fatma REZGANE, Rassim BELAKROUM**, Youcef MOUADJI, Modélisation théorique de la production d'énergie par cyclone solaire : cas d'étude l'Algérie, 443-449
59. **Amina DJIR, Fatiha MESKINE, Mohammed Larbi TAYEBI**, Study and performance analysis of a hybrid FSO/FO system with spatial diversity under different weather conditions, 450-458
60. **Moufida SAADI , Djalel DIB, Billel MEGHNI ,** Effect MPPT control on Wind Energy Convention System based in DFIG controlled by vector control (IFOC), 459-472
61. **Bilal SOLTANI, Nedjem-Eddine BENCHOUIA,** Vehicle Embedded by a Fuel Cell System: a review 473-502
62. **ALLEM Mohamed Nazim , HEBBAR Chafika , KHEMSINE Yanis ,** TREATMENT OF OILY WATER FROM THE API-CINA HMD UNIT, 503-511
63. **Nour el houda Herarsi, Ahmed Hassam, Mohammed el amin Mkedder,** TECHNICAL STUDY AND SIMULATION OF THE WASTE WATER TREATMENT, 512-521
64. **Nour el houda Herarsi, Ahmed Hassam, Mohammed el amin Mkedder,** STUDY AND SUPERVISION OF A MPS SYSTEM VIA WINCC FLEXIBLE SOFTWARE, 522-530
65. **Karima SMILI, Lazhar HEROUS, Azzedine DEKHANE,** The Flow Analysis of Electrical Charges deposited by Corona Discharge on Polyethylene Terephthalate (PET) Plates, 531-539
66. **Rayane Nadjet Fassi , Chahrazed Boukhalfa –Djebbar,** Direct determination of Iron(III) in water by UV-Visible Spetrophotometry Application to waters loaded with metallic cations, 540-546
67. **Mohammed Larbi TAYEBI, Amina DJIR**, Performance evaluation of FSO-OF-VLC , 547-558
68. **Lalaoui Lahouaoui , djaalab abdelhak, Dib Fouad**, Segmentation for different image modality , 559-566
69. **Aziz Boukadoum, Tahar Bahi, Abla Bouguerne,** Power quality improvement using fuzzy logic control for pwm rectifier , 567-573
70. **INES Righi,** Conception d'observateur proportionnel intégral à entrée inconnue (PI-UIO) pour l'estimation simultanée d'état et de défaut, 574-593
71. **INES Righi** , Conception d'observateur proportionnel à entrée inconnue (P-UIO) pour les systèmes singuliers de type T-S, 594-608
72. **Nor-el-houda BERRAMDAN, Samia LEMBOUB, Said BOUDEBANE,** Elaboration and characterization of Cu-W obtained by sintering and cold rolling.609-617
73. **Sihem BOURICHE, Farouk REZGUI,** Preparation and physical state characterization of metformin in PLA microparticles, 618-625
74. **Ilhem DJAGHOUT , Rabah KSOURI, Fatima KESRI, Abed Mohamed AFFOUNE**, ELECTROCHEMICAL NUCLEATION AND GROWTH OF NICKEL IN THE PRESENCE OF SURFACTANTS, 626-637

75. **Billel LOUNICI, Mohammed OUALI, El Hadi OSMANI**, MODELING AND DYNAMIC SIMULATION OF A ROBOT USING THE SOLIDWORKS MOTION TOOL, 638-647
76. **Ilyas BENSALEM, Abdennour BENHIZIA,** FINITE ELEMENT ANALYSIS OF HIERARCHICAL HONEYCOMB STRUCTURES UNDER IMPACT LOADING , 648-655
77. **Abdelghafour HERIZI, Riyadh ROUABHI, Kaisse TOUMIAT , Abdelmonim ZANAT**, Hybrid Fuzzy-Vector Control of a Doubly Fed Induction Machine, 656-666
78. **Messaoud HAMDI, Bachir MEZIANI, Aimad KOULALI, Djamel SADAOUI,** Natural and mixed convection heat transfer in 't' lid-driven cavity , 667-681
79. **Abderrahmane HALIS,** Study of the magnetic induction of an electromagnetic solenoid applied to plasma arc torches.682-692
80. **Djamila BENYOUCEF, Afaf DJARAOUI, Samira NOUI,** Numerical Analysis of Convection Heat Transfer of Nanofluids , 693-701
81. **Afaf DJARAOUI, Djamila BENYOUCEF, Samira NOUI,** Numerical Investigation of Heat Transfer with Phase Change in Al- 7wt% Si , 702-710
82. **Fatima Zohra Kebbab, Louarem sabah , Djamel eddine chouaib belkhiat** , SPEED CONTROL OF ULTRASONIC MOTOR USING FUZZY PI CONTROLLER, 703-716
83. **Tarek Bentahar, Atef Bentahar, Riad Saidi,** Une nouvelle mappe de qualité pour le déroulement de phase de l'InSAR, 717-724
84. **NEZLIOUI FERROUDJA, BENSLIMANE ABDELHAKIM, HAMTACHE BRAHIM,** Analyze performances energetic of a diesel engine overfed by water injection in the channel of admission.725-733
85. **GUERFI ROQIYA, BOUDCHICHA Mohamed Redda, HEBHOUB Houria,** incorporation des cendres de biomasse dans un bétons auto-plaçants , 734-739
86. **W.Benosman, N.Mehtougui,** Structural, electronic and magnetic properties of double perovskite LaFeO3 using GGA and GGA+U, 740-746
87. **Mohamed Tahar HANNACHI, Mohamed BRADJI**, Evolution of radius of plastic zone with Crack Tip-OPENING DISPLACEMENT , 747-749

Algerian Journal of Engineering Architecture and Urbanism Vol. 5 Nr. 3 2021
ISSN: 2588-1760

Physico-chemical characterization of the waters of the Foum El-Kharza dam for agricultural use

Kherifi Wahida[1]
1. PhD, CRSTRA Scientific and Technical Research Center on Arid Regions, Biskra, Algeria.
e-mail: e-mail address: wahidakherifi@yahoo.fr
Hecini Linda[2]
2. PhD, CRSTRA Scientific and Technical Research Center on Arid Regions, Biskra, Algeria.
e-mail: e-mail address :lindahecini@yahoo.fr
Bekiri Fedia[3]
3. PhD, CRSTRA Scientific and Technical Research Center on Arid Regions,
Biskra, Algeria, e-mail address sandi_elamel@yahoo.fr

Abstract

The pollution of the waters of the Biskra region has a cumulative toxic impact in agriculture and therefore dangerous for health. This study aims to assess and monitor the level of pollution of the Foum El Gherza dam and the waters of the Oued Al Abeid which feeds the dam and also at the level of the canal by measuring the physicochemical parameters and heavy metals. Two specific surface water observation and monitoring campaigns were launched in January to April 2019. These campaigns, which continue during this period, notably included analyzes of the main physicochemical parameters (T °, pH , Ca, Mg, TAC, Cl, Na and K) and heavy metals (Pb, Fe, Cu and Zn).

The study is being carried out with the aim of estimating the quality of water in three environments of the study region by the spatial-temporal evolution of the parameters of salts and heavy metals and to find the correlations that may exist between certain parameters. Processing the results will also allow us to classify the sites and determine their chemical facies as well as assess the state of water quality for agricultural use.

Key words: Water pollution, water quality, dam water, agricultural use, Foum El Gherza dam.

Introduction:

L'eau ressource naturelle autour de laquelle se maintient et se développe la vie doit faire l'objet d'une surveillance attentive et d'un contrôle rigoureux. En Algérie, comme partout dans le monde, les activités domestiques, agricoles, et industrielles rejettent dans l'environnement et rendent les eaux superficielles très vulnérables au phénomène de la pollution. (FRIOUA, 2014). Une eau polluée pourrait être à l'origine de graves maladies à l'exemple des dysenteries, la fièvre typhoïde, l'hépatite du type A …etc. (Kherifi w , 2017). Dans la wilaya de Biskra, les eaux superficie constituent la première source pour l'alimentation en eau potable et pour l'irrigation et ces ressources sont parfois exploitées d'une manière irrationnelle (Fattoum, 2017). En contrepartie, la demande en eau est sans cesse croissante. Les contraintes importantes liées à la ressource en eau proviennent surtout d'une gestion actuelle avec diverses lacunes.

Problématique:

Nos travaux s'instaure dans le cadre global de l'appréciation de la qualité physico-chimique des eaux de surface naturellesde la region de Biskra. Ils ont surtout pour objectif de mettre en

Creative Commons Attribution-NonCommercial-NoDerivatives 4.0 International License (CC BY-NC-ND)

exergue les problèmes de qualité des eaux souterraines spécifique à la région du Sahara.Les eaux de la zone d'étude (Oued Al Abiod, Le Barrage de Foum El Gherza et le canal) sont utilisées pour l'irrigation, ce qui se traduit par un déplacement du polluant d'un milieu à un autre. De ce fait il devient impératif de déterminer la qualité de ces eaux selon des critères quantitatifs et qualitatifs, connaitre le facies chimique des eaux de la zone d'étude afin d'estimer et d'apprécier la nature de ces eaux et de classifier les eaux qui sont utilisées en irrigation.

Matériel et méthode:

1.Matériel

Sept (07) points de prélèvement ont été échantillonnés, choisis en fonction de l'urbanisation du bassin versant. Les échantillons d'eau ont été pris dans les eaux du barrage de Foum El Gherza ainsi que au niveau de l'eau de l'Oued Al Abeid qui alimente le barrage et aussi au niveau du canal (La sortie du Barrage) (Figure 01). Deux campagnes spécifiques d'observation et de surveillance des eaux de surface ont été lancées au Janvier 2019 à Avril 2019. Ces campagnes, qui se poursuivent dans cette période, ont notamment comporté des analyses in situ et au laboratoire du CRSTRA sur les principaux paramètres physico-chimiques (T°, pH, Ca, Mg, TAC ,Cl, SO_4 , Na and K) et des métaux lourds (Pb, Fe, Cu et Zn) susceptibles de caractériser la qualité des eaux de Barrage de Foum El Gherza et ses affluants.

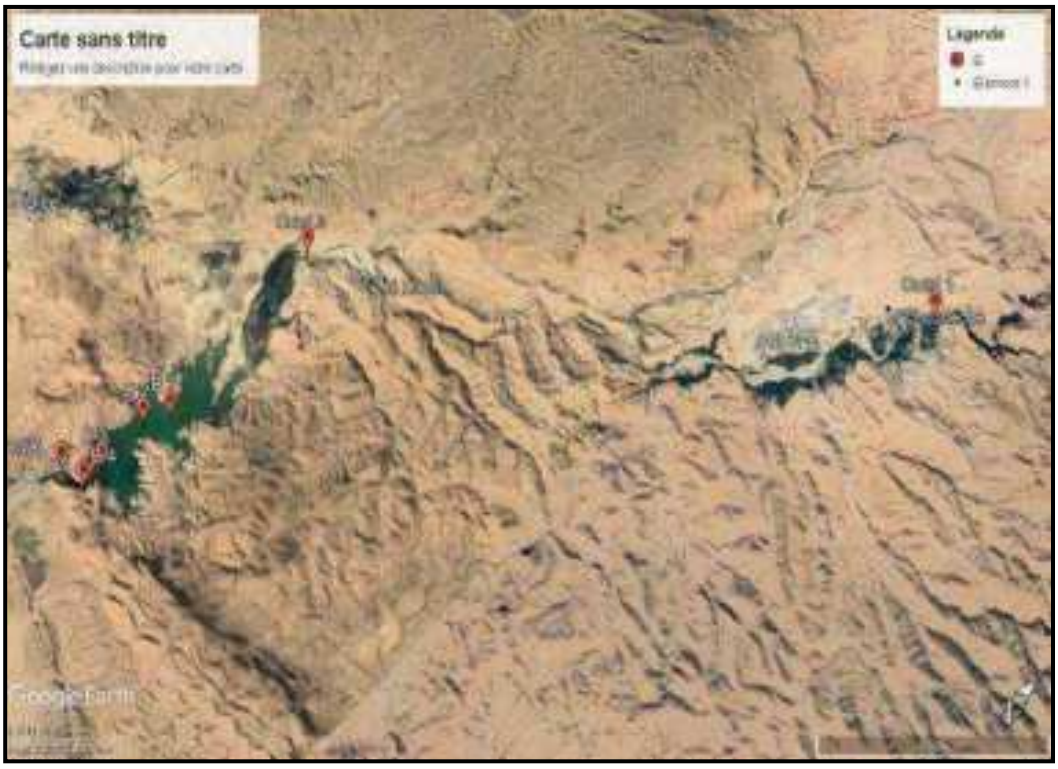

Figure 1. Vue satellitaire de sites ciblés pour l'échantillonnage (2019)

Creative Commons Attribution-NonCommercial-NoDerivatives 4.0 International License (CC BY-NC-ND)

2. Méthode

Le traitement des données des eaux superficielles de la région d'étude nous à permis d'apprécier leur qualité chimique. L'évaluation de la qualité des eaux et de l'évolution des paramètres physico-chimiques nous a obligé à utilisé des méthodes de traitement classiques et d'application adéquats représentés par les logiciels d'hydrochimie et statistique «Excel, DIAGRAM, XL Stat».

Résultats et discussion:

1. Caractérisations physico-chimiques et métaux lourd des eaux de la région d'étude

Les eaux de la zone d'étude (Oued Al Abiod, Le Barrage de Foum El Gherza, le canal) sont utilisées pour l'irrigation, ce qui se traduit par un déplacement du polluant d'un milieu à un autre. De ce fait il devient impératif de déterminer la qualité de ces eaux selon des critères quantitatifs et qualitatifs.

1.1. Volume d'eau de barrage

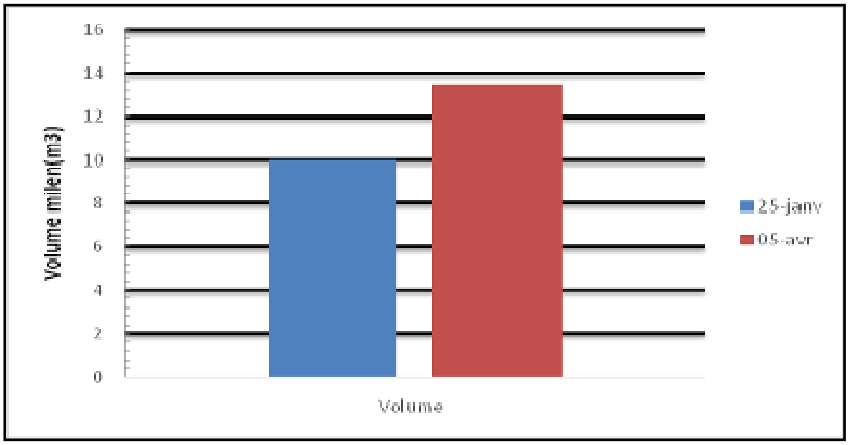

Figure 2. Volume d'eau dans le barrage de Foum El Gherza de la région d'étude (2019)

La figure 2 présente le volume d'eau dans le barrage de Foum El Gherza durant la période hivernale. Cependant au début de la période hivernal, le volume d'eau atteint 10 mille m^3qui présente la période des basses eaux. De la même façon que la pluviométrie relativement importante dans cette saison a certainement influencé les valeurs du volume et donc le débit. Donc cette valeur augmente immédiatement à la fin de période jusqu' à 13.5 mille m^3 qui présente la période des hautes eaux.

1.2.Etude la variation spatio-temporelle des paramètres physico-chimique des eaux de la zone d'étude durant l'année 2019

Creative Commons Attribution-NonCommercial-NoDerivatives 4.0 International License (CC BY-NC-ND)

Algerian Journal of Engineering Architecture and Urbanism Vol. 5 Nr. 3 2021
ISSN: 2588-1760

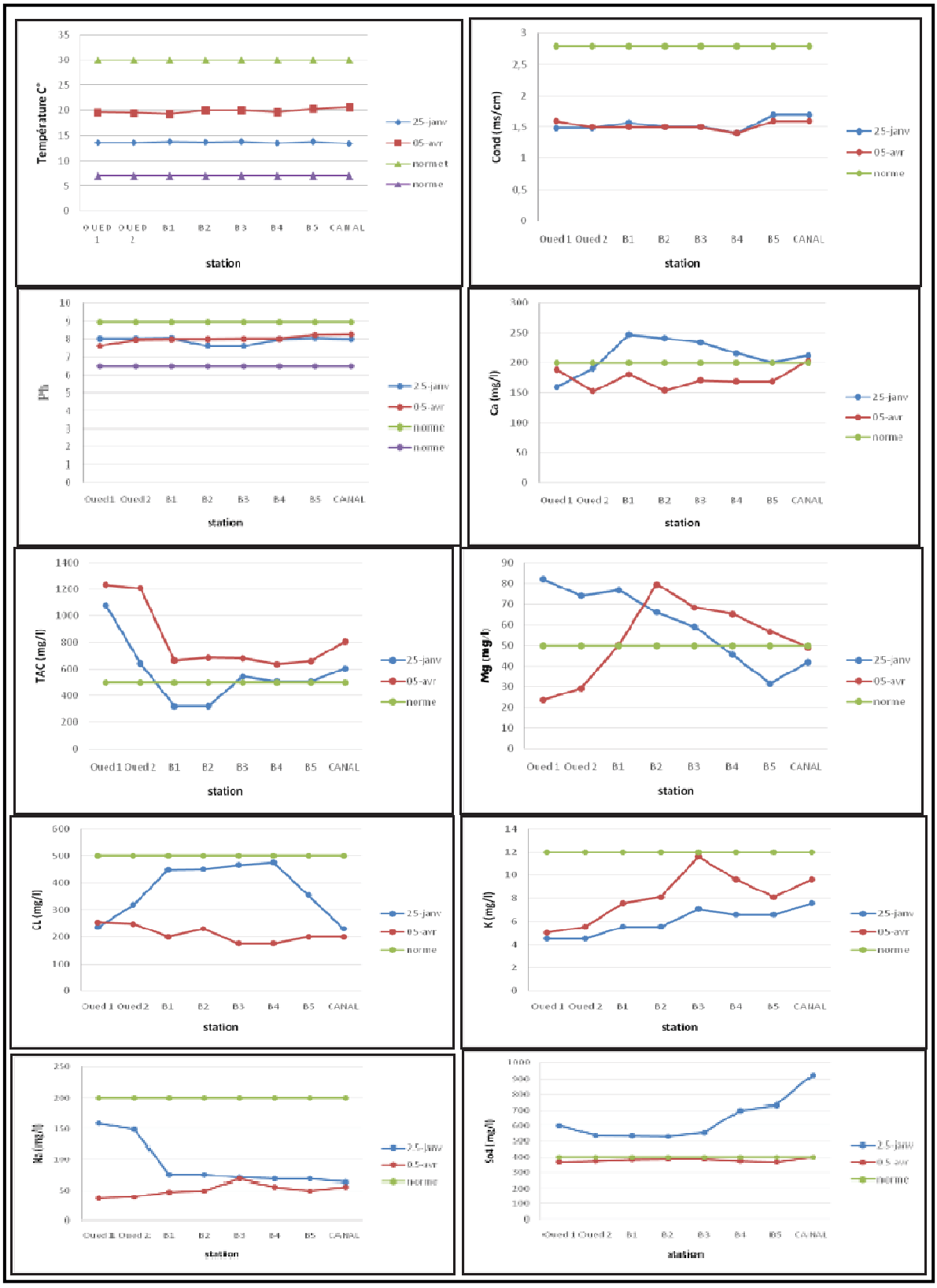

Figure 3. Evolution spatio-temporelle des paramètres physico-chimique des eaux de la zone d'étude durant l'année 2019

Creative Commons Attribution-NonCommercial-NoDerivatives 4.0 International License (CC BY-NC-ND)

Algerian Journal of Engineering Architecture and Urbanism Vol. 5 Nr. 3 2021
ISSN: 2588-1760

L'évolution des densités moyennes des paramètres physico-chimiques et les sels (Figure 3) ont montré également une variabilité spatio-temporelle dans la majorité des paramètres. Cette variabilité a était remarquée dans les trois milieux différents (Oued, Barrage et Canal) et ces valeurs dans les deux périodes ne dépassent pas la norme de l'OMS de l'eau (2006). Sauf certains paramètres des sels (Bicarbonate, magnésium, calcium et le sulfate) dans les eaux du Barrage durant la période des basses dépassent la norme.

1.3. Etude la variation spatiale des métaux lourds des eaux de la zone d'étude durant l'année 2019

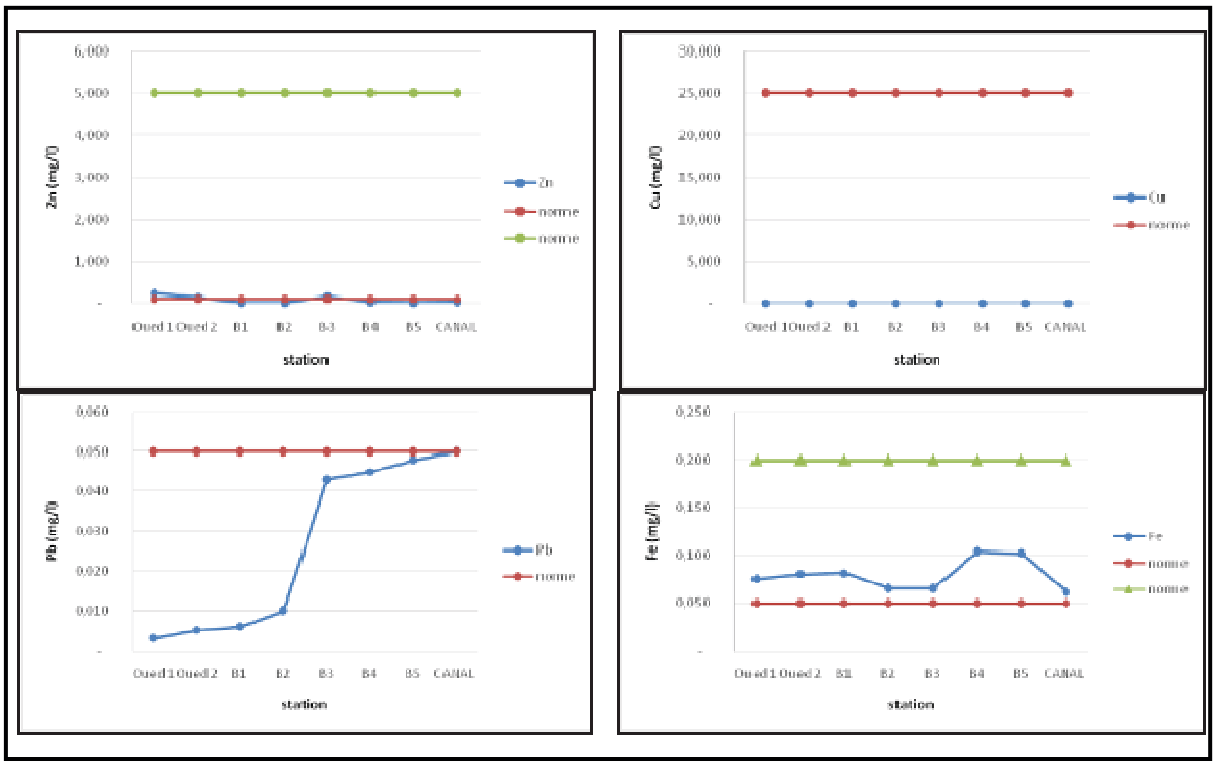

Figure 4. L'évolution spatiale des métaux lourds des eaux de la zone d'étude durant l'année 2019

L'évolution des densités moyennes des traces des métaux lourds (Figure 4) ont montré également une variabilité spatiale dans la majorité des paramètres. Cette variabilité a était remarquée dans les trois milieux différents (Oued, Barrage et Canal) et ces valeurs dans cette période ne dépassent pas la norme de l'OMS de l'eau (2006).

2. Représentation graphique des facies chimique des eaux de la zone d'étude :

La représentation des données physico-chimiques des eaux de surface de la zone d'étude sur le diagramme Piper permet de préciser le faciès de l'eau et de déterminer leur origine naturelle ou anthropique (Drever, 1997 ; Debieche, 2002 ; Rouabhia, 2006 ; Maoui, 2007).

2.2. Représentation graphique des facies chimique des eaux par le diagramme de Piper :

Le traitement des données durant la période des basses eaux et hautes eaux sur le logiciel DIAGRAMME à retiré les diagrammes suivants :

Creative Commons Attribution-NonCommercial-NoDerivatives 4.0 International License (CC BY-NC-ND)

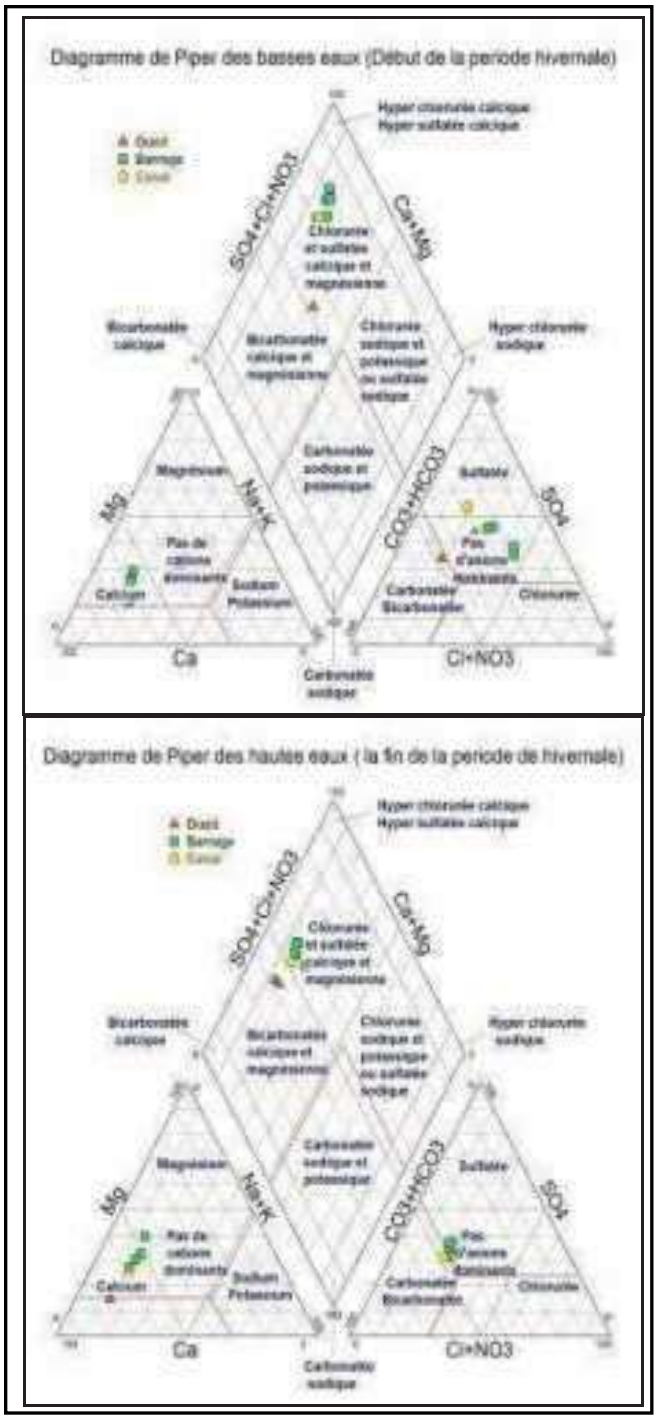

Figure 5. Représentation graphique des facies chimique des eaux par le diagramme de Piper

Selon les diagrammes dans les figures (5) on peut déduire que les eaux de surface dans différentes stations étudiées ne présentent pas les mêmes aspects dans l'espace et dans le temps au niveau des caractéristiques hydro-chimiques des eaux de la région d'étude .

Les résultats d'analyses sur les diagrammes de Piper dans les deux périodes montrent que:

Creative Commons Attribution-NonCommercial-NoDerivatives 4.0 International License (CC BY-NC-ND)

- Les eaux des Oueds sont bicarbonatées et calciques et magnésiennes pendant les deux périodes d'étude (Hautes eaux, Basses eaux). Les bicarbonatée pourrait être attribué aux rejets anthropiques et des effluents d'élevages, qui entraînent le phénomène de photosynthèse intense qui provoque l'augmentation des concentrations en ions HCO_3, ou ceci est expliqué peut être par la nature de terrain et le lessivage du sol par le fait du ruissellement. Ainsi que le calcium provient du lessivage des formations salifères gypseuse, alors que le magnésium et calciques en partie provient des argiles.

$$HCO_3^- + H_2O \rightleftharpoons CO_2 + H_2O$$

Les eaux de barrage et canal sont Chlorurées et sulfatées calciques magnésiennes pendant les deux périodes d'étude (Hautes et Basses eaux). L'origine des chlorures est liée principalement à la dissolution des formations salifères et à l'effet de la salinité du sol. La présence des ions de sulfate dans l'eau est liée toujours aux formations gypseuses ($CaSO_4$, $2H_2O$) et pourrait être attribué aux rejets des effluents d'élevages ces resultats confirment les resultats de (kherifi wahida,2016).

2.2.Représentation graphique des facies chimique des eaux par le diagramme de scholler:

Le diagramme de Schoeller Berkalov permet de représenter le facies chimique des eaux. Chaque échantillon est représenté par une ligne brisée. Le traitement des données durant la période des basses eaux et hautes eaux sur le logiciel Scholler à retiré les diagrammes suivants :

Creative Commons Attribution-NonCommercial-NoDerivatives 4.0 International License (CC BY-NC-ND)

Algerian Journal of Engineering Architecture and Urbanism Vol. 5 Nr. 3 2021
ISSN: 2588-1760

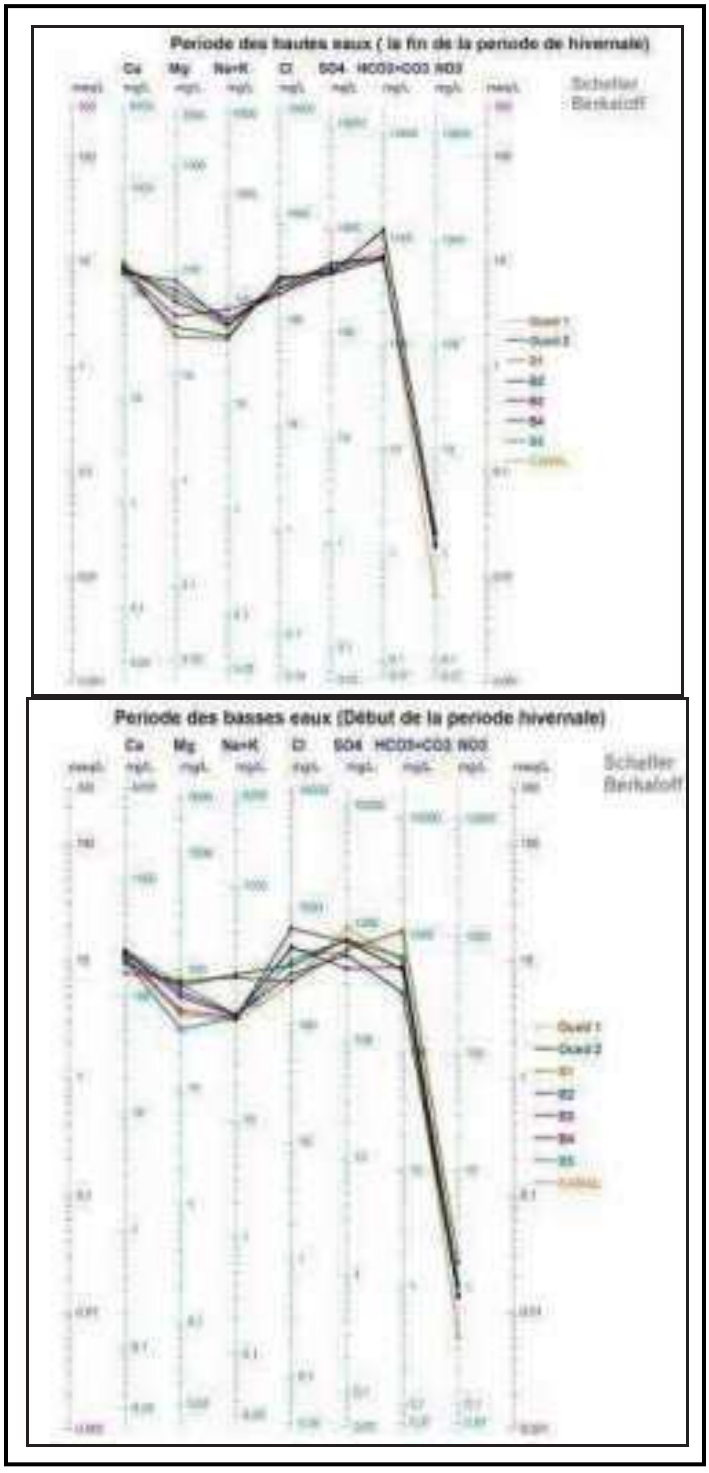

Figure6. Diagramme de Schoeller Berkaloff des eaux de la région d'étude

Le graphe de Schoeller tracés (Figure 6) dans différentes périodes montrent que les éléments dominants dans les eaux de surface de la région (Oued ,Barrage et Canal) dans différentes stations étudiées présentent une grande dissemblance dans l'espace et dans le temps au niveau des caractéristiques hydro chimiques des eaux . Sur ce dernier les courbes ont la même allure et montrent deux familles distinctes, confirmant les résultats observés sur le diagramme Piper.

Creative Commons Attribution-NonCommercial-NoDerivatives 4.0 International License (CC BY-NC-ND)

Algerian Journal of Engineering Architecture and Urbanism Vol. 5 Nr. 3 2021
ISSN: 2588-1760

3. Classification des eaux d'irrigation selon la méthode de Riverside :

D'après les valeurs concernant le SAR, on constate que la proportion du sodium adsorbée est inferieure à 4méq/l pendant les deux périodes d'étude, ce qui affirme un très faible apport du sodium à solution du sol selon la classification du SAR .

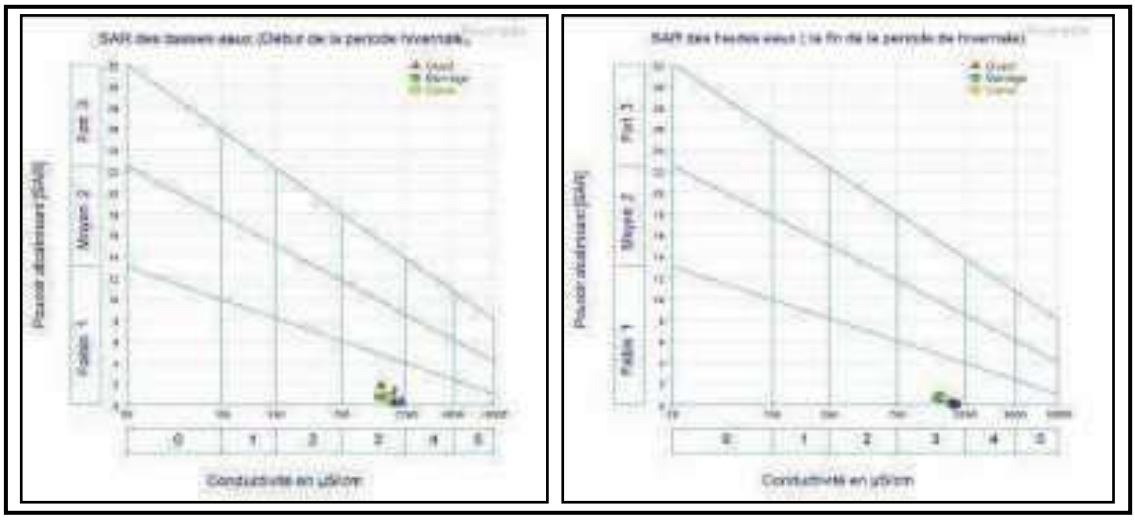

Figure 7. Diagramme de Riverside des eaux la région d'étude (Oued , Barrage , canal)

Tous les points d'eau sont reportés sur le diagramme de Riverside (Richards, 1954), selon la conductivité électrique et la valeur de SAR (Figures 7), montre que dans les deux périodes d'étude (Basses et hautes eaux) présente la classe (3-1) qui désigne les eaux admissibles pour l'irrigation des cultures.

On constate que la qualité des eaux de la région d'étude, selon la méthode de Riverside présente un faible danger d'alcalinisation et pourraient être utilisées en irrigation. La comparaison des deux périodes de répartition du SAR a montré une distribution semblable des classes d'aptitude à l'irrigation**.**

4. Analyse en composant principal des eaux de la région d'étude

Dans le but d'établir une relation entre les différents paramètres étudiés et pour mieux évaluer l'effet des différents activités sur la qualité des eaux superficielles ,une analyse en composante principale (ACP) (Abdoulaye Demba N'diaye ,2011), a été réalisée sur des variables centrées réduites à l'aide du logiciel XLSTAT. Cette méthode est largement utilisée pour interpréter les données hydro-chimiques **(El Blidi et al, 2006 ; El Morhit et al, 2008).**

Les données portent sur l'ensemble des huit (08) stations des eaux de la zone d'étude (Oueds, Barrage et Canal) durant la période de hautes eaux (05 Avril 2019). Sept (07) variables ont été traité, à savoir les paramètres ions et cations dominants (Cl^-, Ca^{2+}, HCO_3^-) et les métaux lourds (Cu^{2+} ,Pb^{2+} ,Fe^{2+} ,Zn^{2+}).

Creative Commons Attribution-NonCommercial-NoDerivatives 4.0 International License (CC BY-NC-ND)

Algerian Journal of Engineering Architecture and Urbanism Vol. 5 Nr. 3 2021
ISSN: 2588-1760

4.1. Projection des variables sur le plan factoriel (F1, F2)

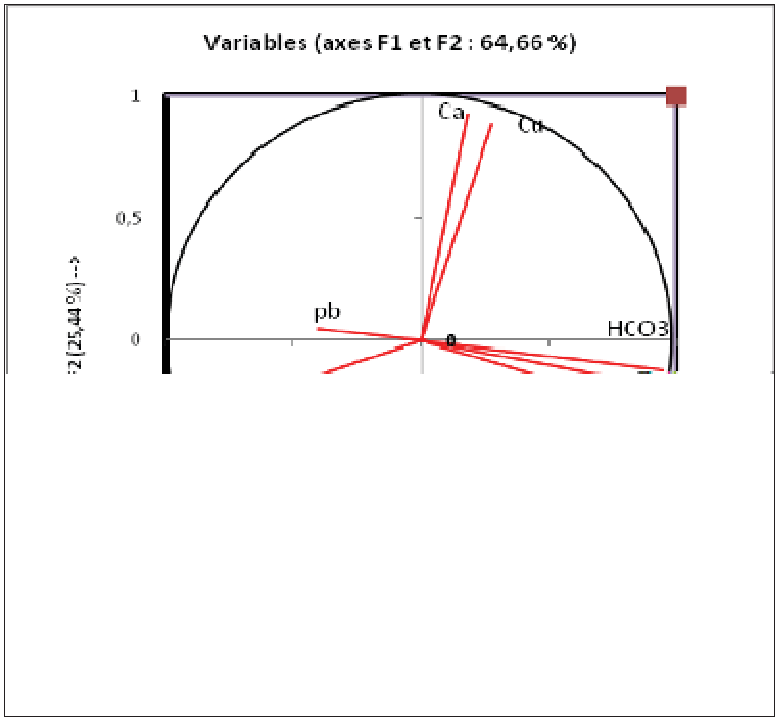

Creative Commons Attribution-NonCommercial-NoDerivatives 4.0 International License (CC BY-NC-ND)

4.2. Projection des individus sur le plan factoriel (F1, F2)

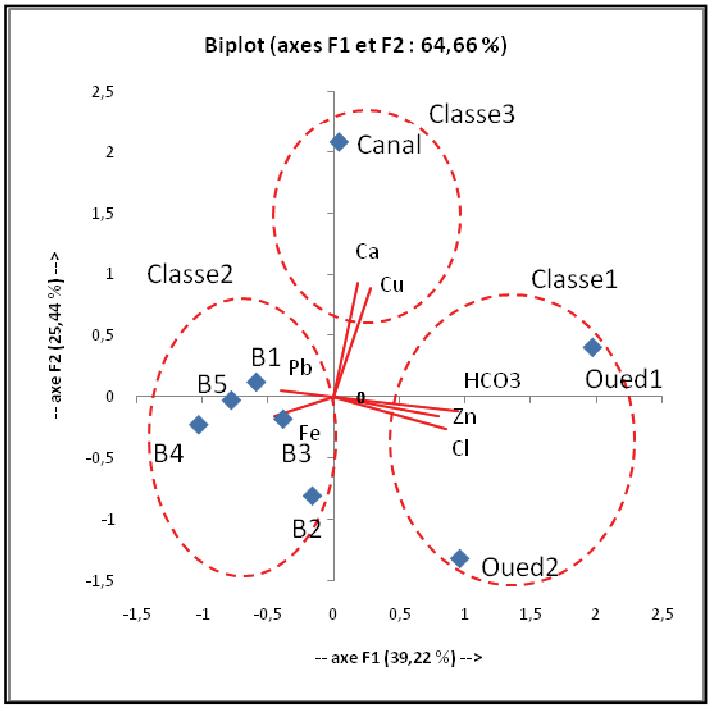

Figure 8. La représentation graphique des stations sur le plan factoriel (F1, F2)

La représentation graphique des individus (Figure 8) permet de distinguer également trois groupes :

- Le premier groupe formé par les variables prend en compte les deux stations Oued 1 et 2 qui représentent les point dont la qualité de l'eau est chargée en (Cl, HCO_3^- et Zn) est faiblement par le Pb et Fe. Les hautes teneurs en sels minéraux, montre la concentration des paramètres et le lessivage du sol par le fait du ruissellement dans l'Oued durant la période des hautes eaux.

- La deuxième classe contient uniquement les eaux de Barrage (les stations B1 jusqu'a B5) qui représentent les points dont la qualité de l'eau est chargée en (Pb et Fe) est faiblement minéralisée par le (Ca et HCO_3^-). Ceci est expliqué par la dilution des eaux dans le barrage qui est alimente par les eaux d'Oued El Abiod et les eaux de pluie.

- La troisième classe contient les eaux du canal qui présentent les points dont la qualité de l'eau est exprimée par (Ca^{2+}, Cu). Les hautes teneurs en sels minéraux, montre la concentration dans le canal durant la période des hautes eaux.

Conclusion:

L'évolution spatio-temporelle des densités moyennes des paramètres physico-chimiques et les traces des métaux lourds ont montré également une variabilité spatio-temporelle dans la majorité des paramètres.

Creative Commons Attribution-NonCommercial-NoDerivatives 4.0 International License (CC BY-NC-ND)

Les résultats d'analyses sur les diagrammes de Piper dans les deux périodes d'étude (basses et hautes eaux) montrent que les eaux des Oueds sont bicarbonatées et calciques et magnésiennes et les eaux de barrage et canal sont chlorurées et sulfatées calciques magnésiennes.

L évaluations de l'état de la qualité des eaux de la région d'étude en vue d'un usage agricole a révélé que les eaux représentent une qualité admissible et faible danger d'alcalinisation, d'où la possibilité de leur utilisation pour l'irrigation.

L'ananlyse composante principal des données montre que les différentes variables (sels et métaux lourd) dans les trois milieux étudiés ont été corrélées entre elle. On constate aussi que les eaux des deux stations des Oueds (1 et 2) représentent les point dont la qualité de l'eau est chargée en (Cl^-, HCO_3^- et Zn^{2+}) est faiblement par le Pb et Fe et les eaux de Barrage (les stations B1 jusqu'a B5) représentent les points dont la qualité de l'eau est chargée en (Pb^{2+},Fe^{2+}) est faiblement minéralisée par le (Ca^+ et HCO_3^-) ainsi que les eaux du canal présentent les points dont la qualité de l'eau est exprimée par (Ca^{2+}, Cu^{2+}).

Référence:

Abdoulaye Demba N'diaye et al (2011), *Evaluation des teneurs en coliformes fécaux par couplage avec des paramètres physicochimiques en ACP : Cas des effluents de la Périmètre STEP du Maraicher de Sebkha, Nouakchott Cameroon. Journal Of Experimental Biology Vol. 07 N°01, (35-40)PP.*

Debieche .(2002) **;** *Evolution de la qualité des eaux (salinité, azote et métaux lourds) sous l'effet de la pollution saline, agricole et industrielle Application à la basse plaine de la Seybouse - Nord-Est Algérien ; Thèse de doctorat en Hydrogéologie et Environnement. université de Franche-Comté,235 P.*

Drever.(1997) ;*The geochimisty of natural water3rdED.Upper Saddle River,NJ;Prentice hall Inc,436P.*

El Blidi et al.(2006); *Contamination des rizières de la plaine du Gharb (Maroc) par des métaux traces. VECTEUR Environnement,* 39, 1, 47-53.

El Morhit et al (2008). *Impact de l'aménagement hydraulique sur la qualité des eaux et des sédiments de l'estuaire du Loukkos (côte atlantique, Maroc), Bulletin de l'Institut Scientifique, Rabat, section Sciences de la Terre 30.*

Fattoum.(2017) , *Diagnostic de la qualité des eaux souterraines et superficielles de la région de Biskra, Thèse présentée en vue de l'obtention, Hydraulique urbaine et aménagement, , Université Mohamed Khider – Biskra*

Frioua .(2014). *Localisation et caractéristiques des zones sources de pollution des ressources en eau de la ville de Biskra à l'aide de S.I.G. Mémoire de Master en Sciences de l'Eau et de l'Environnement. Université Mohamed Khider Biskra, Algérie, 79P.*

OMS (2006). *Directives de qualité pour l'eau de boisson, troisième édition. Recommandations. Organisation mondiale de la Santé, Genève, 78 p.*

Kherifi wahida .(2016), *Pollution et protection des eaux du lac Mellah (N-E Algérien) au droit des rejets urbains: proposition d'un collecteur principal, these de doctorat , université d'Annaba, 2016.*

Kherifi .w , Kherici Bousnoubra H., (*2017).évolution saisonnière de la qualité microbiologique des eaux du LAC mellah (nord –est algérien) , Larhyss Journal, ISSN 1112-3680, n° 11, Novembre 2012, pp. 109-118.*

Maoui.(2007). *Evolution et origine du chimisme des eaux de l'aquifère superficiel de Zaâfrane : région de la steppe Sud Algéroise .Etude de la variation spatiale de la salinité et ses risques sur les sols et la végétation. These de doctorat en Hydrogéologie. Université d'Annaba, Algerie,279P.*

Rouabhia.(2006); *Vulnérabilité et risques de pollution des eaux souterraines de la nappe des sables miocenes de la plaine d'el ma el abiod nord-est Algérien .Thèse de doctorat en Hydrogéologie. Université d'Annaba ,Algerie,152P.*

Creative Commons Attribution-NonCommercial-NoDerivatives 4.0 International License (CC BY-NC-ND)

Algerian Journal of Engineering Architecture and Urbanism Vol. 5 Nr. 3 2021
ISSN: 2588-1760

TEMPORAL ASPECTS OF THE PORTEVIN-LE CHATELIER EFFECT IN THE AL-2.5%MG ALLOY

Samir DAHDOUH
PhD student, Laboratory of Mechanics, Materials and Energetic (L2ME),
Faculty of Technology, University of Bejaia, 06000 Bejaia, Algeria,
e-mail: dahdouh.samir.gm@gmail.com

Abdelhamid SADEDDINE
Professor, Laboratory of Mechanics, Materials and Energetic (L2ME),
Faculty of Technology, University of Bejaia, 06000 Bejaia, Algeria,
e-mail: hsadeddine@yahoo.fr

Hakim AIT-AMOKHTAR
Professor, Laboratory of Physical Chemistry of Materials and Catalysis (LPCMC)
Faculty of Exact Sciences, University of Bejaia, 06000 Bejaia, Algeria,
e-mail: hakim.aitmokhtar@gmail.com

Abstract:
Jerky flow due to the Portevin-Le Chatelier (PLC) effect is investigated in the Al-2.5% Mg alloy at room temperature in simple tension at imposed strain rate ranging from 10^{-6} to 10^{-3} s^{-1}. The study highlights the effect of strain and applied strain rate on the characteristic parameters of the PLC effect, such as the type of instability (A, B and C), the magnitude of the stress drops and the critical plastic strain for the onset of unstable plastic flow. Transitions from one type of instability to another were also observed as a function of strain and strain rate. The analysis shows that the dynamic strain aging becomes less and less significant and, consequently, the heterogeneous plastic flow less and less accentuated when the imposed strain rate is increased. An inverse effect is observed when the strain is increased for an imposed strain rate. The results are discussed and interpreted in accordance with the dynamic strain aging mechanisms of mobile dislocations.

Key words: Portevin-Le Chatelier effect; Dynamic strain aging; Critical plastic strain, Strain localisation.

Introduction:

Le phénomène Portevin-Le Chatelier (PLC) est l'une des formes de la déformation plastique hétérogène. Il est observé dans certains matériaux métalliques, particulièrement dans les alliages Al-Mg (Ait-Amokhtar et al., 2006; Ait-Amokhtar et al., 2008; Chihab et al., 1987). Ce phénomène est une conséquence directe du vieillissement dynamique des dislocations mobiles (DSA: Dynamic Strain Aging), c'est à dire de l'interaction dynamique entre les atomes du soluté et les dislocations mobiles. Les atomes de soluté diffusent et épinglent davantage les dislocations mobiles pendant leurs arrêts temporaires aux obstacles de la foret (dislocations de la forêt, précipités… etc.) (Kubin et al., 1991; McCormick, 1972; Van den Beukel, 1975). Ce phénomène anti-thermiquement activé conduit à l'augmentation de la contrainte d'écoulement des dislocations mobiles. Ainsi, le DSA réduit la sensibilité de la contrainte d'écoulement à la vitesse de déformation (SRS: strain rate sensitivity) qui peut

Creative Commons Attribution-NonCommercial-NoDerivatives 4.0 International License (CC BY-NC-ND)

devenir négative dans certaines conditions de déformation, de température et de vitesse de déformation. Dans une telle situation, l'écoulement plastique devient hétérogène et instable. La déformation se localise sous forme de bandes de déformation en produisant des chutes de contrainte sur la courbe contrainte-déformation (Ait-Amokhtar et al., 2008; Chihab et al., 1987).

Selon la vitesse de déformation et la température imposées, trois types d'instabilité PLC peuvent être observées lors d'un essai de traction sur machine dure (Chihab et al., 1987; Pink et al., 1982). Aux faibles vitesses de déformation (ou aux températures élevées), des bandes de type C apparaissent de manière aléatoire sur la surface du matériau déformé. Elles sont associées à de grandes chutes de contrainte sur la courbe de déformation. Aux vitesses de déformation élevées (ou aux basses températures), les bandes sont de type A, elles produisent de faibles ondulations sur la courbe contrainte-déformation et sont caractérisées par une propagation continue. Les bandes de type B, observées à des vitesses de déformation et des températures intermédiaires, se déplacent par sauts successifs le long de l'éprouvette (hopping band). Les chutes de contrainte associées sont régulières et plus petites que celles associées aux instabilités de type C (Ait-Amokhtar et al., 2006; Chibane et al., 2013).

Pour une vitesse de déformation donnée, l'effet PLC apparait au-delà d'une déformation plastique critique ε_c. En fonction de la vitesse de déformation imposée, ε_c présente une branche descendante aux faibles vitesses de déformation (comportement dit inverse) et une branche ascendante aux vitesses de déformation élevées (comportement dit normal) (Ait-Amokhtar et al., 2008; Ziani et al., 2012).

Le présent travail est consacré à la caractérisation de l'effet PLC dans l'alliage Al-2.5%Mg à température ambiante et à différentes vitesses de déformation imposée. Nous analysons l'influence de la déformation et de la vitesse de déformation sur les paramètres caractéristiques de l'effet PLC. Nous nous intéressons en particulier à l'effet de la vitesse de déformation imposée sur la déformation plastique critique nécessaire pour l'apparition des instabilités.

Problématique:

L'une des problématiques de la mécanique des matériaux est la localisation de la déformation plastique, lors de la fabrication de pièces mécaniques par exemple. Le phénomène Portevin-Le Chatelier (PLC) est l'une des formes de la déformation plastique hétérogène et instable.

Cet article est consacré à la caractérisation de l'effet PLC dans l'alliage Al-2.5%Mg à température ambiante et à différentes vitesses de déformation imposée. Nous analysons l'influence de la déformation et de la vitesse de déformation sur les paramètres caractéristiques de l'instabilité plastique.

Matériau étudié et procédure expérimentale:

Le matériau utilisé dans cette étude est un alliage d'aluminium-magnésium, sa composition chimique (% en poids) est donnée dans le tableau 1. Les éprouvettes de traction

Creative Commons Attribution-NonCommercial-NoDerivatives 4.0 International License (CC BY-NC-ND)

(longueur 80 mm, largeur 10 mm et épaisseur 1.4 mm) ont été découpées de tôle polycristallines laminées puis déformées à température ambiante à l'aide d'une machine dure avec des vitesses de déformation comprises entre 10^{-6} et 10^{-3} s^{-1}. Tous les essais de traction ont été réalisés dans les mêmes conditions.

Alliage	Éléments d'addition (% en poids)						
Al-2.5%Mg	Mg	Cr	Si	Fe	Cu	Mn	Ti
	2.52	0.23	0.09	0.35	0.02	0.10	0.01

Tableau 1. Composition chimique de l'alliage étudié.

.

Résultats et discussion:

La figure 1 montre une courbe contrainte-déformation de l'alliage Al-2.5%Mg déformé à température ambiante avec une vitesse de déformation imposée de $1.04\times10^{-5}s^{-1}$. Les chutes de contrainte associées à l'effet PLC apparaissent sur la courbe de déformation après une certaine déformation critique caractéristique (voir le zoom sur la figure 1). Au-delà de cette déformation, l''écoulement plastique devient instable et l'amplitude moyenne des chutes de contrainte augmente avec la déformation.

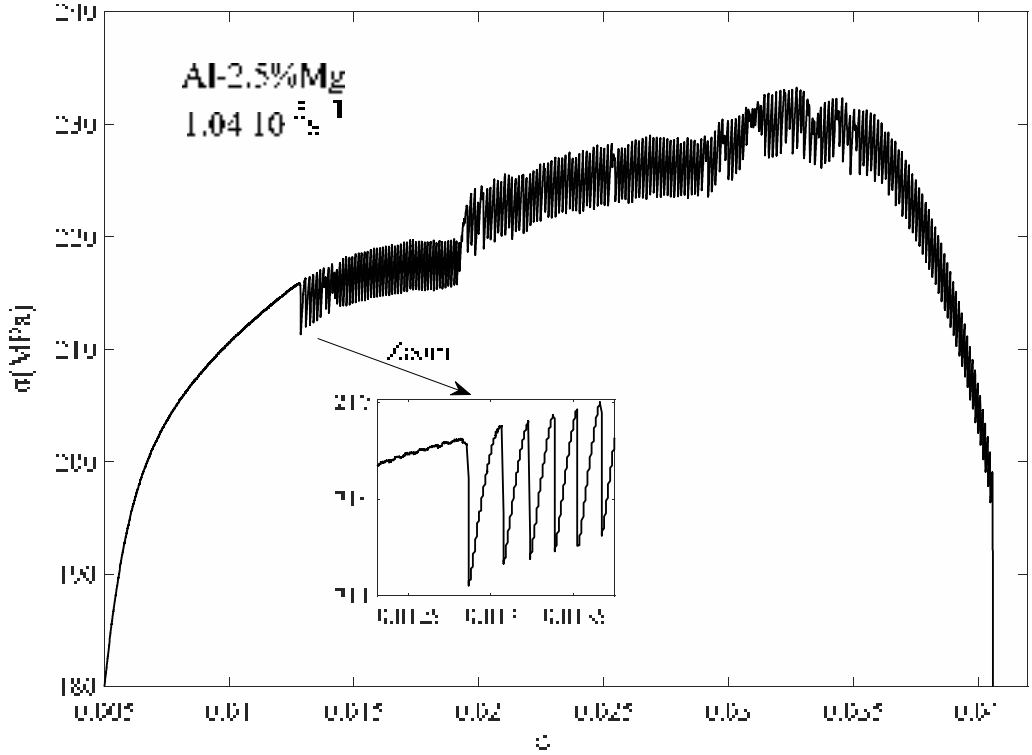

Fig1. Courbe de déformation de l'alliage Al-2.5%Mg à température ambiante et à vitesse de déformation imposée de $1.04\times10^{-5}s^{-1}$.

En fonction de la vitesse de déformation imposée, trois types d'instabilités PLC ont été observées sur les courbes de déformation (figure 2).

Creative Commons Attribution-NonCommercial-NoDerivatives 4.0 International License (CC BY-NC-ND)

Algerian Journal of Engineering Architecture and Urbanism Vol. 5 Nr. 3 2021
ISSN: 2588-1760

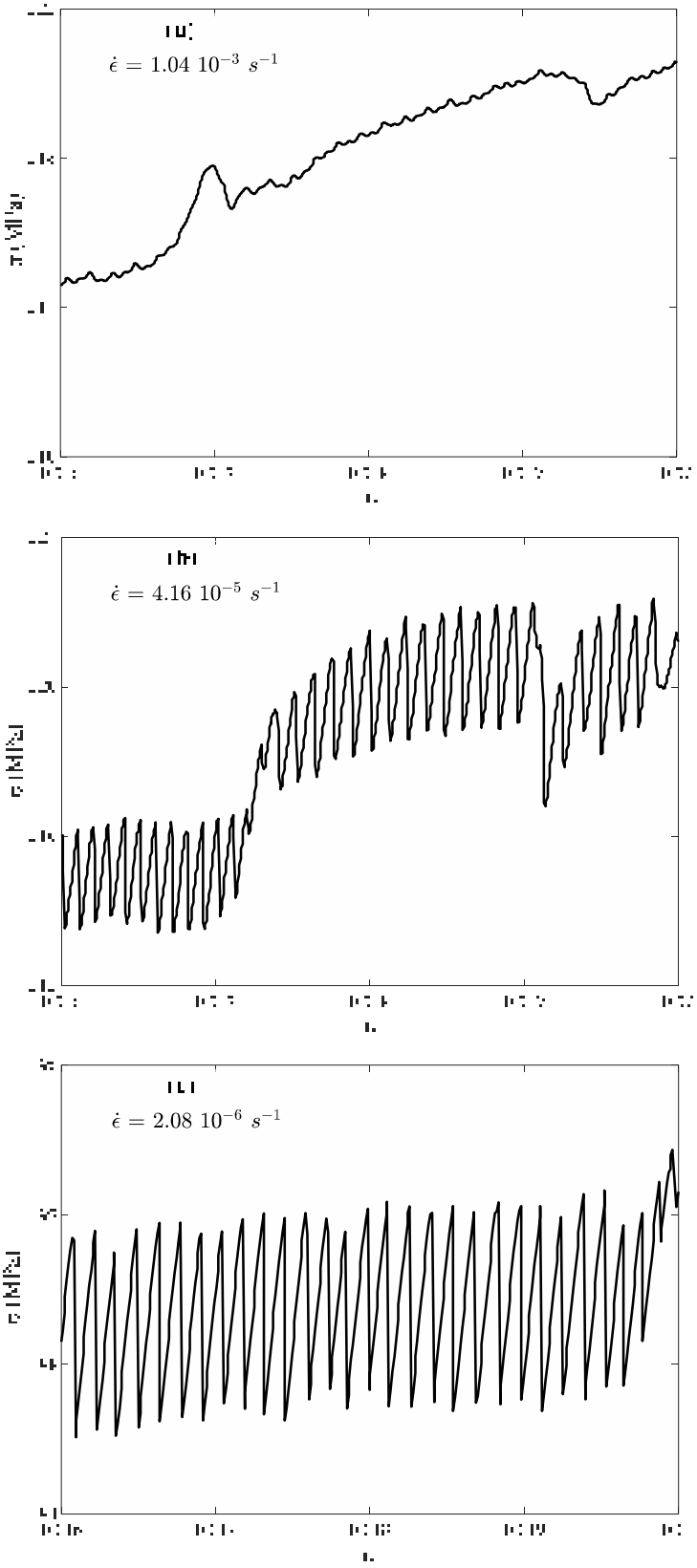

Fig 2. Courbes "contrainte-déformation" de l'alliage Al-2.5%Mg, à température ambiante, présentant les instabilités PLC : (a) type C, (b) type B, (c) type A.

Creative Commons Attribution-NonCommercial-NoDerivatives 4.0 International License (CC BY-NC-ND)

Algerian Journal of Engineering Architecture and Urbanism Vol. 5 Nr. 3 2021
ISSN: 2588-1760

Aux vitesses de déformation élevées (1.04×10^{-3} s^{-1}), les instabilités sont de type A (figure 2.a), elles se présentent sous forme de faibles ondulations. Aux faibles vitesses de déformation (2.08×10^{-6} s^{-1}), les instabilités observées sont de type C (figure 2.c). Elles sont caractérisées par des grandes amplitudes et des recharges partiellement plastiques entre deux chutes successives. Aux vitesses de déformation intermédiaires (4.16×10^{-5} s^{-1}), les instabilités sont de type B (figure 2.b). Elles se manifestent par des chutes de contrainte régulières et sont caractérisées par des recharges élastiques entre instabilités consécutives.

L'amplitude des chutes de contrainte sur les courbes de déformation, $\Delta\sigma$, est l'un des paramètres caractéristiques des instabilités PLC. Elle est reliée à l'intensité du DSA et, par conséquent, au degré d'hétérogénéité de la déformation plastique. Une grande amplitude implique que la déformation plastique est fortement localisée (Chihab et al., 1987; Pink et al., 1982).

La figure 3 représente l'évolution de l'amplitude des chutes de contrainte en fonction de la déformation pour différentes vitesses de déformation imposée dans l'alliage Al-2.5%Mg. Pour une vitesse de déformation donnée, la valeur moyenne de $\Delta\sigma$ augmente en fonction de la déformation pour atteindre une valeur de saturation aux déformations élevées. Pour une déformation donnée, $\Delta\sigma$ diminue en fonction de la vitesse de déformation. Ce résultat est en accord avec les résultats expérimentaux rapportés dans la littérature (Ait-Amokhtar et al., 2006; Chihab et al., 1987).

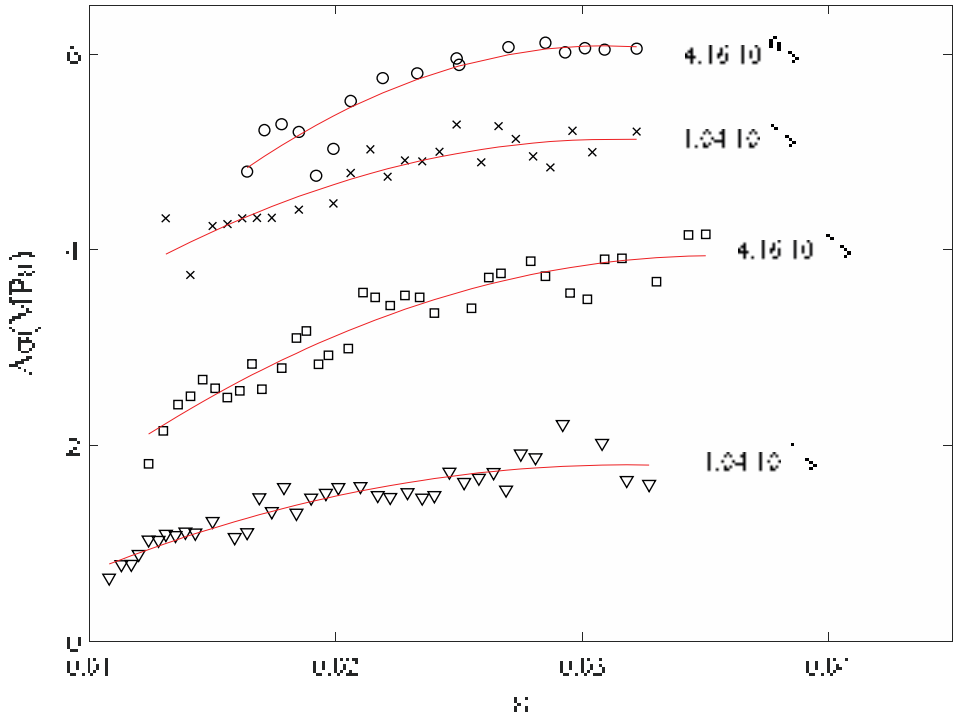

Fig 3. Effet de la déformation et de la vitesse de déformation imposée sur l'amplitude des chutes de contrainte dans l'alliage Al-2.5%Mg déformé à température ambiante.

Creative Commons Attribution-NonCommercial-NoDerivatives 4.0 International License (CC BY-NC-ND)

L'augmentation de $\Delta\sigma$ avec la déformation ε s'explique par l'augmentation de la densité des dislocations au cours de la déformation, ce qui rend le mouvement de celles-ci de plus en plus difficile et qui augmente le temps d'attente t_w des dislocations mobiles aux obstacles de la forêt. En conséquence, le vieillissement dynamique devient de plus en plus intense et l'amplitude des chutes de contrainte de plus en plus importante (Ait-Amokhtar et al., 2006; Ziani et al., 2012). Pour une déformation donnée, $\Delta\sigma$ diminue avec la vitesse de déformation imposée. En effet, lorsqu'on augmente la vitesse de déformation le temps d'attente des dislocations t_w diminue et par conséquent, la concentration en soluté sur les lignes de dislocations diminue. Le vieillissement dynamique devient moins important, ce qui se traduit sur la courbe de déformation par la diminution de l'amplitude des chutes de contrainte.

Après chaque chute de contrainte (entre deux instabilités successives), une période de rechargement Δt est nécessaire pour poursuivre la déformation plastique. Le rechargement entre instabilités successives peut être élastique (type B) ou partiellement plastique (type C). La figure 4 représente l'évolution de Δt en fonction de la déformation et de la vitesse de déformation imposée. Pour une vitesse de déformation donnée, Δt augmente avec la déformation et tend vers une saturation aux déformations élevées. L'augmentation de la densité de dislocations rend le mouvement de celles-ci de plus en plus difficile à cause des différents enchevêtrements, ce qui augmente t_w et, par conséquent, l'intensité du vieillissement dynamique. Pour une déformation donnée, l'augmentation de la vitesse de déformation réduit le temps de vieillissement et, par conséquent, le temps de recharge Δt.

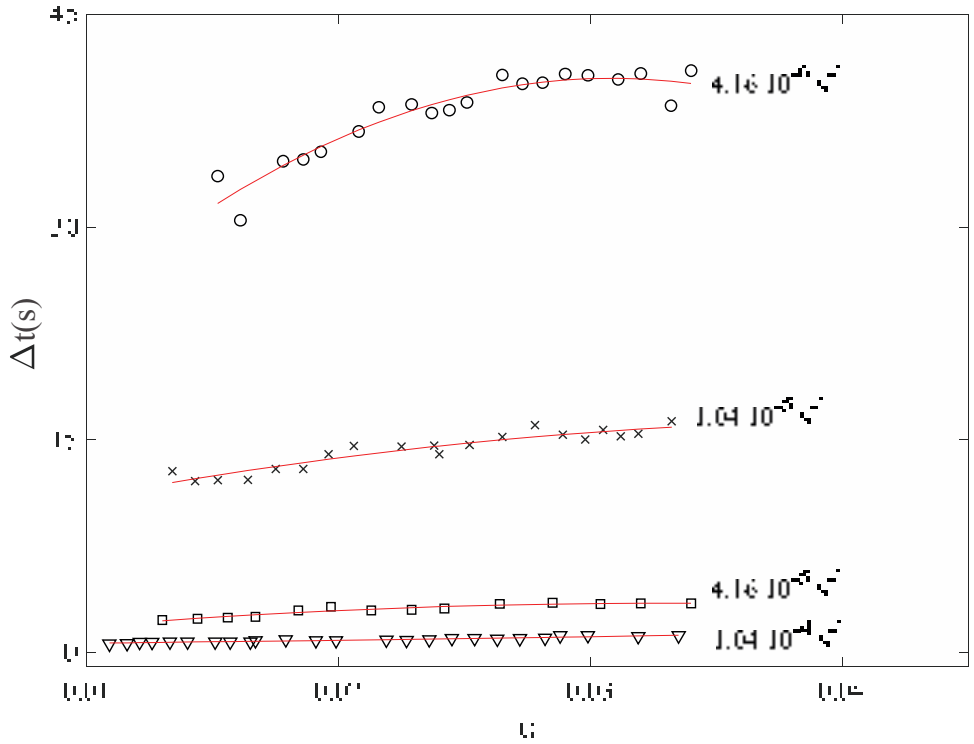

Fig 4. Evolution du temps de recharge entre deux instabilités successives en fonction de la déformation et de la vitesse de déformation imposée.

Creative Commons Attribution-NonCommercial-NoDerivatives 4.0 International License (CC BY-NC-ND)

Algerian Journal of Engineering Architecture and Urbanism Vol. 5 Nr. 3 2021
ISSN: 2588-1760

Les instabilités PLC apparaissent sur la courbe de déformation à partir d'une certaine déformation plastique critique ε_c (figure 1) qui dépend de plusieurs paramètres (vitesse de déformation, microstructure du matériau, concentration en soluté...etc.) (Ait-Amokhtar et al., 2006; McCormick, 1972; Ziani et al., 2012). L'évolution de ε_c en fonction de la vitesse de déformation dans l'alliage Al-2.5%Mg est illustrée sur la figure 5. ε_c présente deux comportements : Aux faibles vitesses de déformation, où les instabilités sont de type C où B, ε_c décroît en fonction de la vitesse de déformation $\dot{\varepsilon}$ (comportement dit inverse). Aux vitesses de déformation élevées, où les instabilités sont de type A, ε_c croît en fonction $\dot{\varepsilon}$ (comportement dit normal). Dans le sous-domaine des vitesses de déformation correspondant au minimum de la courbe $\varepsilon_c = \varepsilon_c(\dot{\varepsilon})$, les instabilités passent progressivement du type A vers le type B au cours de la déformation.

Le comportement normal de ε_c peut être expliqué par les modèles de vieillissement dynamique (Kubin et al., 1991; McCormick, 1972). Pour une déformation donnée, l'augmentation de la vitesse de déformation réduit le temps d'attente des dislocations aux obstacles de la forêt et par conséquent l'intensité du DSA. La concentration critique en soluté autour des dislocations, qui rend la SRS négative et l'écoulement plastique instable, n'est atteinte qu'on augmentant la déformation. Ce qui retarde de plus en plus l'apparition des instabilités quand on augmente la vitesse de déformation. Le comportement inverse de ε_c reste toujours en l'objet de controverses de nombreux modèles. (Bréchet et al., 1995) associent ce comportement à un mécanisme de précipitation, alors que (Hahner, 1997) affirme qu'il est dû au DSA et non pas au changement de mécanisme de déformation.

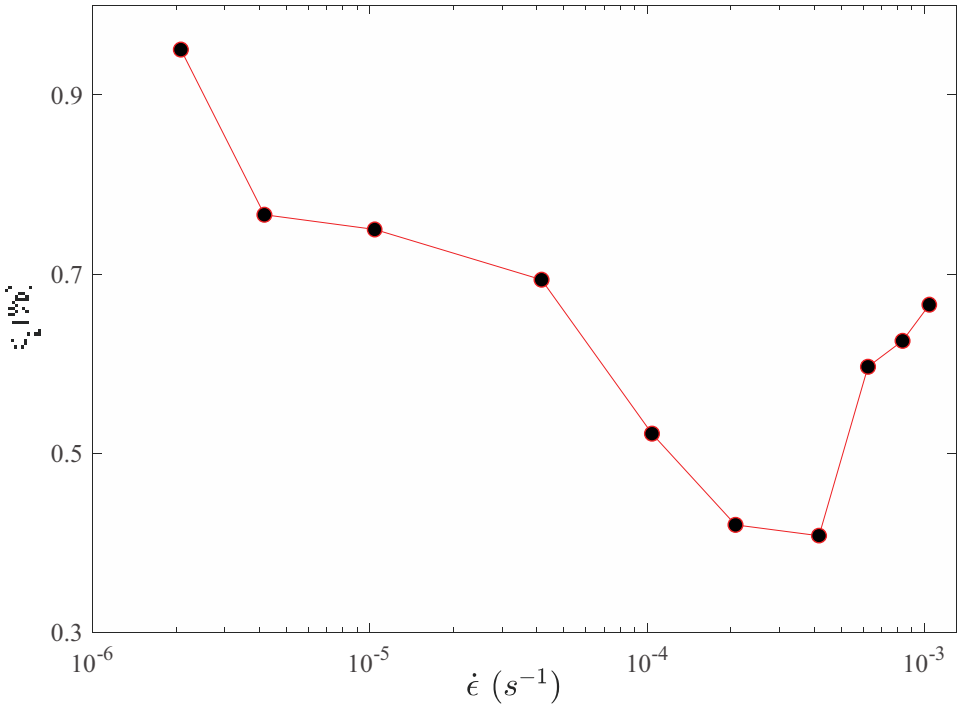

Fig 5. Evolution de la déformation critique en fonction de la vitesse de déformation dans l'alliage Al-2.5%Mg.

Creative Commons Attribution-NonCommercial-NoDerivatives 4.0 International License (CC BY-NC-ND)

Conclusion:

L'effet Portevin-Le Chatelier (PLC) a été étudié en traction uniaxile et à température ambiante dans l'alliage Al-2.5%Mg. L'analyse des courbes de déformation a montré l'effet de la vitesse de déformation imposée et de la déformation sur l'aspect et les paramètres caractéristiques des instabilités PLC. Pour une déformation donnée, les instabilités passent de type C au type B ensuite au type A quand on augmente la vitesse de déformation imposée.

L'amplitude des instabilités PLC et le temps de recharge entre deux instabilités successives augmentent en fonction de la déformation et diminuent avec la vitesse de déformation pour une déformation donnée. La variation de la déformation critique ε_c nécessaire pour l'apparition de l'effet PLC en fonction de la vitesse de déformation présente deux types de comportements. Un comportement normal aux vitesses de déformation élevées (où les instabilités sont de type A) et un comportement inverse aux faibles vitesses de déformation (où les instabilités sont de type C ou B). Ces résultats ont été interprétés à la lumière du mécanisme de vieillissement dynamique des dislocations mobiles.

Références:

Ait-Amokhtar H., Boudrahem S., Fressengeas C. (2006), Spatiotemporal aspects of jerky flow in Al–Mg alloys, in relation with the Mg content, Scripta Mater. **54(12):** 2113-2118.

Ait-Amokhtar H., Fressengeas C., Boudrahem S. (2008), The dynamics of Portevin-Le Chatelier bands in an Al-Mg alloy from infrared thermography Mater. Sci. Eng:A. **488(1-2):** 540-546.

Ait-Amokhtar H., Vacher P., Boudrahem S. (2006), Kinematics fields and spatial activity of Portevin-Le Chatelier bands using the digital image correlation method, Acta Mater. **54(16):** 4365-4371.

Brechet Y., Estrin Y. (1995), On the influence of precipitation on the Portevin-Le Chatelier effect. Acta Metall. Mater. **43(3):** 955-963.

Chibane N., Ait-Amokhtar H. (2013), On the Portevin-Le Chatelier instabilities in the industrial Al-2.5%Mg alloy, 21ème Congrès Français de Mécanique, Bordeaux, France.

Chihab K., Estrin Y., Kubin L.P. (1987), Vergnol The kinetics of the Portevin-Le Chatelier bands in an A1-5at%Mg alloy, Scripta Metall **21(2)**: 203-208.

Hahner P. (1997), On the critical conditions of the Portevin-Le Châtelier effect, Acta Mater. **45(9):** 3695-3707.

Kubin L.P., Estrin Y. (1991), Dynamic strain ageing and the mechanical response of alloys, J. Phys. III. **1(6):** 929-943.

McCormick P.G. (1972), A model for the Portevin-Le Chatelier effect in substitutional alloys, Acta Metall. **20(3):** 0351-354.

Mehenni M., Ait-Amokhtar H., Fressengeas C. (2019), Spatiotemporal correlations in the Portevin-Le Chatelier band dynamics during the type B - type C transition, Mater. Sci. Eng:A. **756(22):** 313-318.

Pink E., Grinberg A. (1982), Stress Drops In Serrated Flow Curves Of A15Mg, Acta Metall. **30(12):** 2153–2160.

Van den Beukel A. (1975), Theory of the effect of dynamic strain aging on mechanical properties, Phys. Stat. Sol. **30(1):** 197-206.

Ziani L., Boudrahem S., Ait-Amokhtar H., Mehenni M., Kedjar B. (2012), Unstable plastic flow in the Al-2%Mg alloy, effect of annealing process,Mater. Sci. Eng:A. **536:** 239-243.

Creative Commons Attribution-NonCommercial-NoDerivatives 4.0 International License (CC BY-NC-ND)

Algerian Journal of Engineering Architecture and Urbanism Vol. 5 Nr. 3 2021
ISSN: 2588-1760

MODELING SOIL EFFECTS ON THE INSULATION OF HVDC UNDERGROUND CABLE AGAINST LIGHTNING STRIKES

Samira Boumous
Laboratory of Electrical engineering and renewable energies
Mohamed Cherif Messaidia University, Souk Ahras, Algeria

Zouhir Boumous
Laboratory of Electrical engineering and renewable energies
Mohamed Cherif Messaidia University, Souk Ahras, Algeria

Fatima Zohra kebbab
Laboratory DACHR
Ferhat Abbas University, Setif, Algeria

Abstract:
High voltage direct current power transmission HVDC is now in full expansion in the world. Two main factors are behind this craze. The first is linked to the difficulty of building new overhead lines to ensure the development of the high-voltage network which means that the use of underground cables is more and more frequent. The performance of a high voltage underground cable due to a lightning discharge has always been the objective of several studies. The location of the lightning strike, the soil resistance and the types of cables have major effects on the performances and the level of insulation in these types of configurations of electrical networks. The simulation was performed using Alternative Transient Program version of the Electromagnetic Transients Program (ATP-EMTP) software to the simulation of HVDC underground cables. the results were represented and discussed.

Key words: HVDC, Strike lightning, ATP/EMTP, underground cable, soil resistance

Introduction:

La transmission d'énergie en courant continu et haute tension (HVDC) se développe actuellement dans le monde entier. Deux facteurs principaux expliquent cet engouement.
Le premier facteur est lié aux difficultés de construction de nouvelles lignes aériennes pour assurer le développement du réseau haute tension et donc l'utilisation de câbles souterrains est de plus en plus fréquente, He Peiyu (2020).

Cependant, l'utilisation de ces câbles est limitée en longueur à quelques dizaines de km en raison du courant capacitif généré par le câble lui-même. Au-delà de cette longueur limite, la solution consiste généralement à transporter du courant continu (DC). Le deuxième facteur est lié au développement de l'éolien offshore, qui nécessite de connecter des puissances de plusieurs centaines de MW au réseau continental au moyen de câbles dont les longueurs peuvent atteindre quelques centaines de km et nécessitent donc un transport en HVDC. Lekai Zou(2020).

Un système de mise à la terre avec une résistance à la terre élevée fournit un chemin dangereux pour le courant de défaut, ce qui augmente le risque de défaillance de l'équipement

Creative Commons Attribution-NonCommercial-NoDerivatives 4.0 International License (CC BY-NC-ND)

ainsi que la probabilité de blessures graves pour l'être humain. Dans ce cas, si un courant de défaut ne trouve aucun chemin pour traverser le sol à travers un système de mise à la terre conçu, il trouve un chemin alternatif soit via un équipement sophistiqué, soit, dans le pire des cas, à travers le corps humain.

De plus, une mauvaise mise à la terre du système entraîne des erreurs d'instrumentation et des distorsions harmoniques dans tout système électrique. Par conséquent, un bon système de mise à la terre est très important non seulement pour des raisons de sécurité, mais aussi pour éviter d'endommager les installations et équipements industriels. La conception d'un bon système de mise à la terre dépend de nombreux facteurs tels que les conditions météorologiques, les caractéristiques du sol, l'environnement de l'installation électrique, la disposition des électrodes de mise à la terre, etc. S.N.M. Arshad(2018), Md. Abdus SALAM(2015).

Le phénomène de la foudre ne peut être contrôlé et difficile à prévoir puisqu'il s'agit d'un phénomène naturel. Lorsqu'un éclair se propage et atteint la surface de la terre, les surtensions induites qui se forment dans le sol peuvent provoquer une panne des câbles souterrains XLPE de 90 kV qui ont été enterrés à proximité du point d'impact. M.A.Omidiora (2011).

Les systèmes de câbles souterrains qui sont installés pour la ligne de transmission et la ligne de distribution peuvent être endommagés ou avoir des pannes causées par le courant de foudre et la tension induite. Avec le support de nombreux logiciels de simulation informatique, l'analyse de la surtension transitoire devient plus précise, efficace et facile. Les études de surtension transitoire sur un câble souterrain dues à un coup de foudre sont très importantes pour déterminer toute possibilité de défaillance ou de panne d'isolation. La sélection du logiciel de simulation adapté en fonction du modal support et l'analyse du projet faciliteront le travail de conception du modèle, l'exécution de la simulation et l'analyse du résultat.

Le programme alternatif transitoire (ATP) et le programme électromagnétique transitoire (EMTP) sont des logiciels les plus largement utilisés par l'industrie de l'énergie électrique pour la simulation numérique des phénomènes transitoires de système électrique de nature électromagnétique et électromécanique dans les systèmes d'alimentation électrique. Le programme ATP est un outil puissant pour modéliser les transitoires du système d'alimentation. Predrag Maric(2009).

Modèles de simulation :

Le système étudié est composé d'un câble souterrain « HVDC », le sol et l'air, il est donné sur la figure 1.

Creative Commons Attribution-NonCommercial-NoDerivatives 4.0 International License (CC BY-NC-ND)

Algerian Journal of Engineering Architecture and Urbanism Vol. 5 Nr. 3 2021
ISSN: 2588-1760

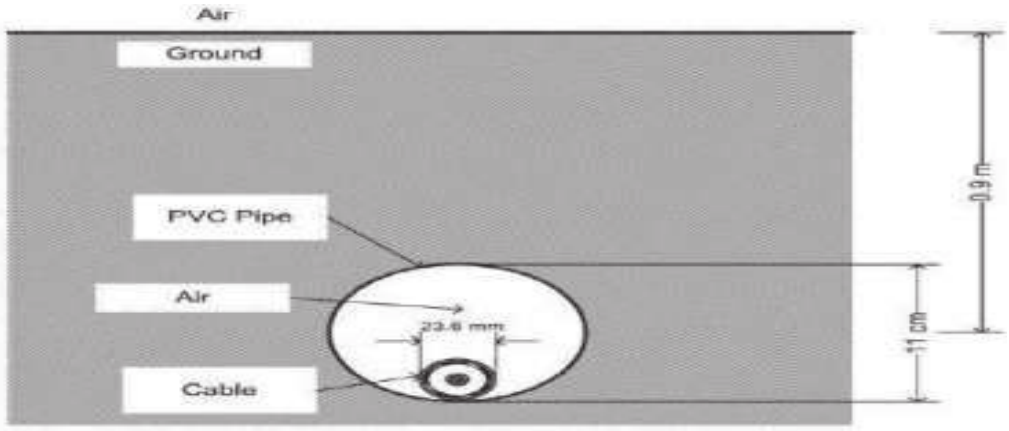

Fig1. Système complet à modélisé.

Simulation du câble « HVDC »:

Fig2. Coupe transversale du cable

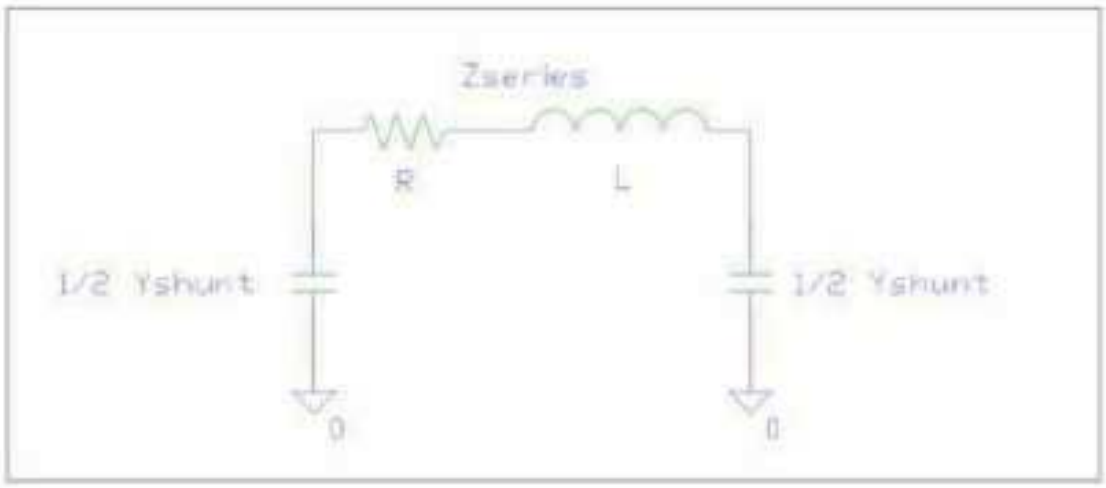

Fig3. Schéma électrique de simulation

Creative Commons Attribution-NonCommercial-NoDerivatives 4.0 International License (CC BY-NC-ND)

Modélisation du sol:

Le sol recouvre une grande partie des terres sur Terre. Tous les sols sont composés de sable, de limon ou d'argile. Cela décrit la taille des particules et non le type de matériau parent dont elles sont constituées. Les matériaux sont les types de roches et de minéraux dont il est dérivé. Les sols ont d'autres composants : l'air, l'eau et la matière organique (plantes et animaux en décomposition). Il existe de nombreux types de sols, et chacun a des couleurs, des textures, une structure et une teneur en minéraux différentes. M. Ali Anadol(2011), M.A Omidiora(2009).

La profondeur du sol varie également. Chaque type de sol à une résistivité, une perméabilité et une permittivité qui affectent le câble souterrain.
On suppose qu'un câble souterrain de système de 90 kV est installé à une profondeur de 2 mètre et la résistivité du sol varie selon le type de terrain. Le point de coup de foudre est considéré à 12 m du point de départ de la ligne.

Outre la résistivité du sol, la résistance au claquage électrique du sol était l'une des valeurs importantes à considérer. La rigidité diélectrique des sols est considérée comme la valeur de l'intensité du champ électrique, qui provoque un claquage dans une configuration de champ homogène. La figure 4 montre la représentation du modèle de sol utilisée pour cette simulation.

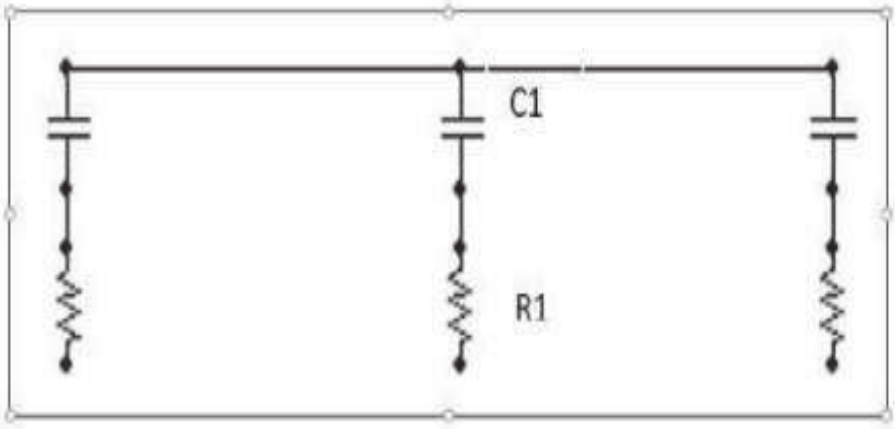

Fig4. Modéle du sol.

La résisivité électrique des differents solest donné dans le tableau 1.

Creative Commons Attribution-NonCommercial-NoDerivatives 4.0 International License (CC BY-NC-ND)

Soil Type	Resistivity (Ω-cm)		
	Minimum	Average	Maximum
Ashes, brine or cinders	590	2,370	7,000
Concrete (below ground)	-	3,000	-
Clay, gumbo, loam or shale	340	4,060	16,300
Clay, gumbo, Loam or shale with varying portions of sand and gravel	1,020	15,800	135,000
Gravel, sand or stone with little clay or loam	59,000	94,000	458,000

Tableau 1. Résistivités des differnts type de sol.

Modélisation du coup de foudre :

La foudre est une contrainte électrique très sévère, avec une amplitude atteignant 200 kA en quelques microsecondes, ayant des fréquences très élevées. Elle est donc plus contraignante que celle due à la manœuvre. Expressions analytiques, le plus souvent utilisées dans la littérature pour représenter le courant à la base du canal, Dans la bibliothèque ATP-EMTP, il existe un certain nombre de modèles qui peuvent être utilisés pour représenter le coup de foudre.

Il peut être représenté par une source de courant de forme exponentielle en parallèle avec une résistance représentant le canal de foudre (d'environ 400 Ω) ou encore une source de tension ayant toujours une forme exponentielle. Z. Anane (2018),

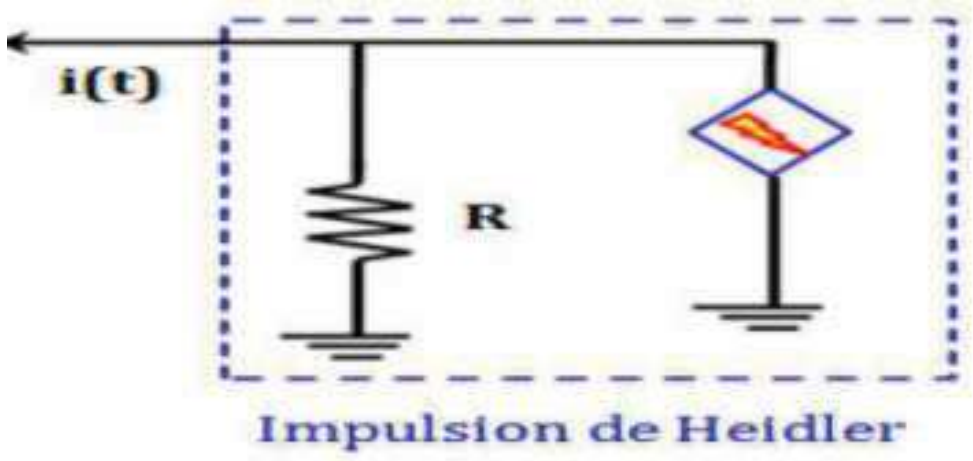

.

Fig5. Modèle de la foudre utilisé.

Dans le logiciel AtpDraw, le coup de foudre est représenté par fonction de surtension des formes Heidler de type 15. Le type de source peut être défini sur courant ou tension. L'ampli est le nombre multiplicatif en Ampère ou Volt et il ne représente pas la valeur de crête du monter. T_f est la durée du front en secondes qui est l'intervalle entre t = 0 et le pic de fonction.

Description du système :

Creative Commons Attribution-NonCommercial-NoDerivatives 4.0 International License (CC BY-NC-ND)

Algerian Journal of Engineering Architecture and Urbanism Vol. 5 Nr. 3 2021
ISSN: 2588-1760

Le système se compose d'un câble souterrain d'une longueur de 100 mètres enterré à une profondeur de 2 mètre: 90kV Cu / XLPE / CWS / PVC / HDPE, le câble sous gaine en polychlorure de vinyle (PVC). Dans cette recherche, on a étudié l'effet de trois types du sol, Argile humide, seche et sable sec sur l'intensité de la tension induite dans un cable HVDC suite à une onde de choc transmise par un coup de foudre prés du sol.

Lors de la simulation , on a appliqué un coup de foudre d'intensité 50KA, T_f=1µs et τ=0.5µs, le modèle de simulation par AtpDraw est donné sur la figure 6.

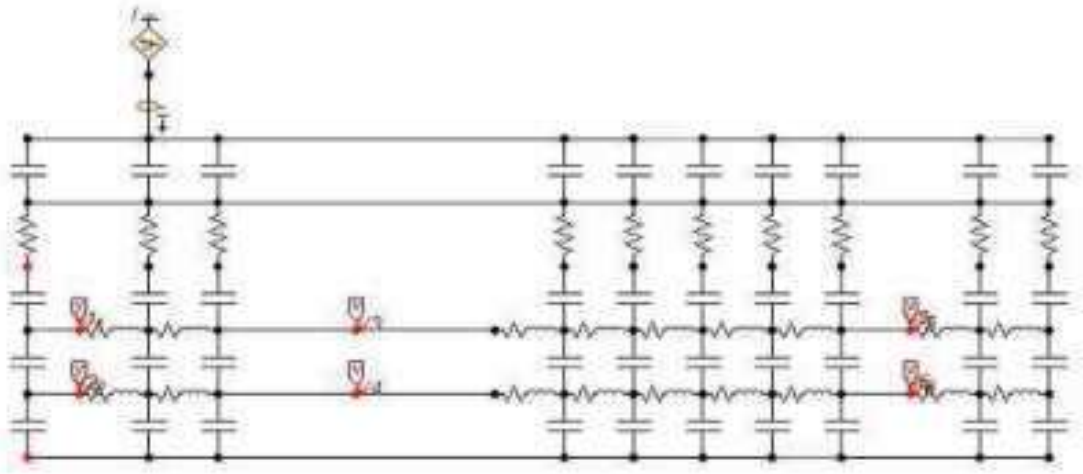

Fig 6. Schema électrique réalisé par AtpDraw

Résultas et discussion:

Sur la figure 7, on montre la forme d'onde du courant de surtension injectée au sol au-dessus du câble.

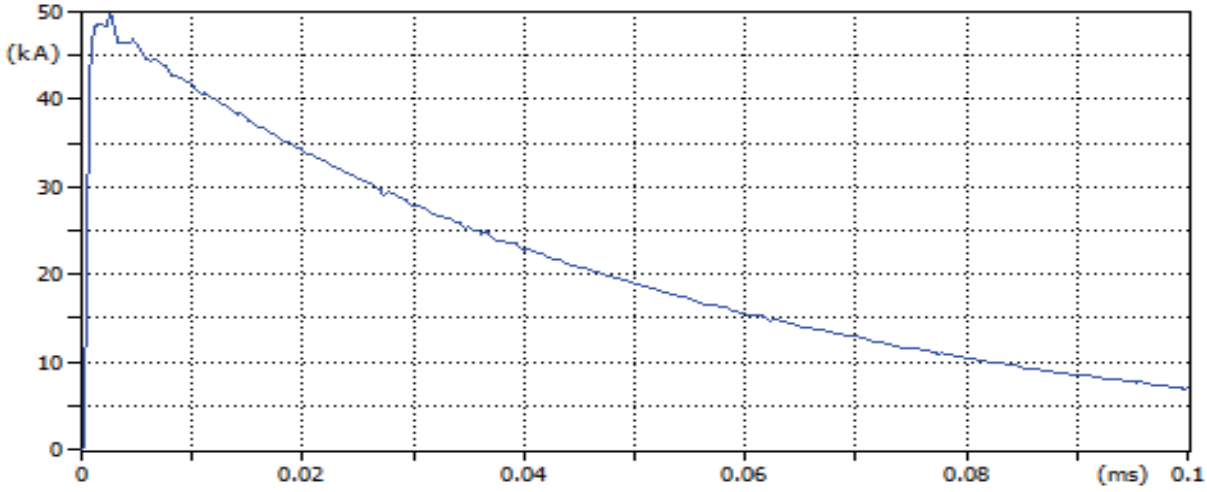

Creative Commons Attribution-NonCommercial-NoDerivatives 4.0 International License (CC BY-NC-ND)

Fig 7. Evolution de la fonction de la foudre injectée.

Les figures suivantes montrent les résultats de simulation d'un coup de foudre injecté prés du sol à une distance de 12m du début du cable enterré à 2 m du sol, l'étude menée dans ce papier est réalisée sur trois types du sol à differentes résistivités électriques.

Tension induites pour un Sol en Argile humide:

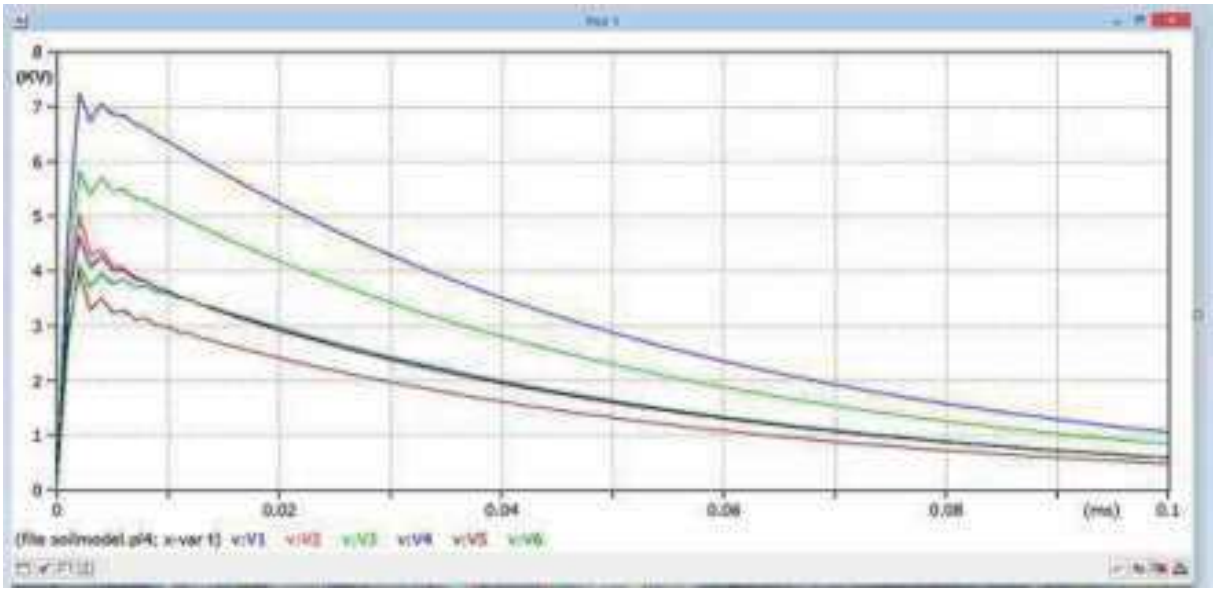

Fig 8. Tension induite pour l'argile humide.

Tension induites pour un Sol en sable sec:

Creative Commons Attribution-NonCommercial-NoDerivatives 4.0 International License (CC BY-NC-ND)

Algerian Journal of Engineering Architecture and Urbanism Vol. 5 Nr. 3 2021
ISSN: 2588-1760

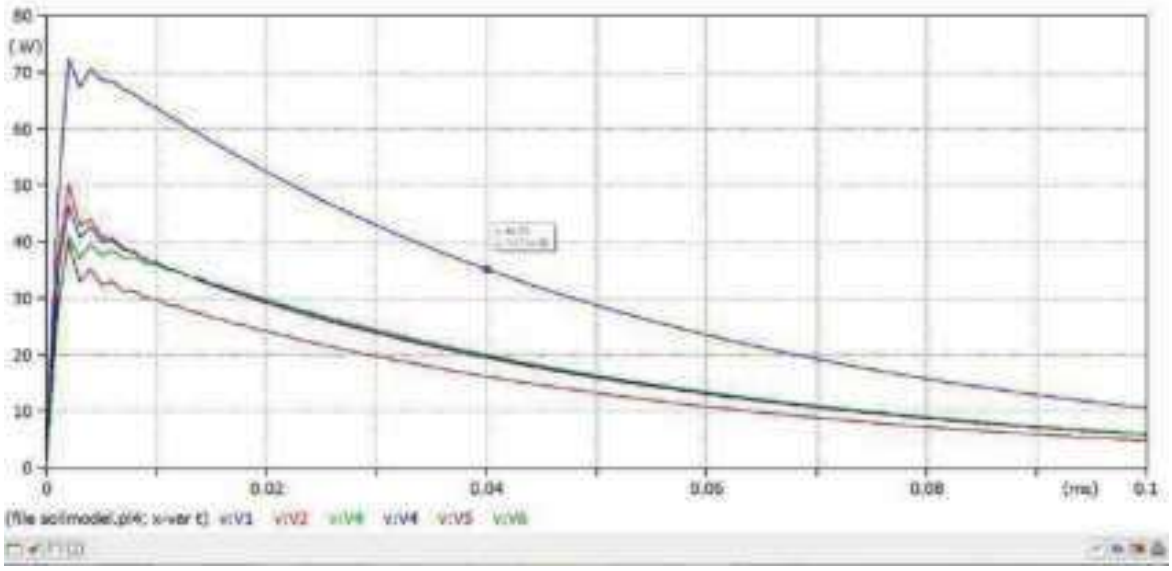

Fig 9. Tension induite pour sable sec.

Tension induites pour un Sol en Argile séche:

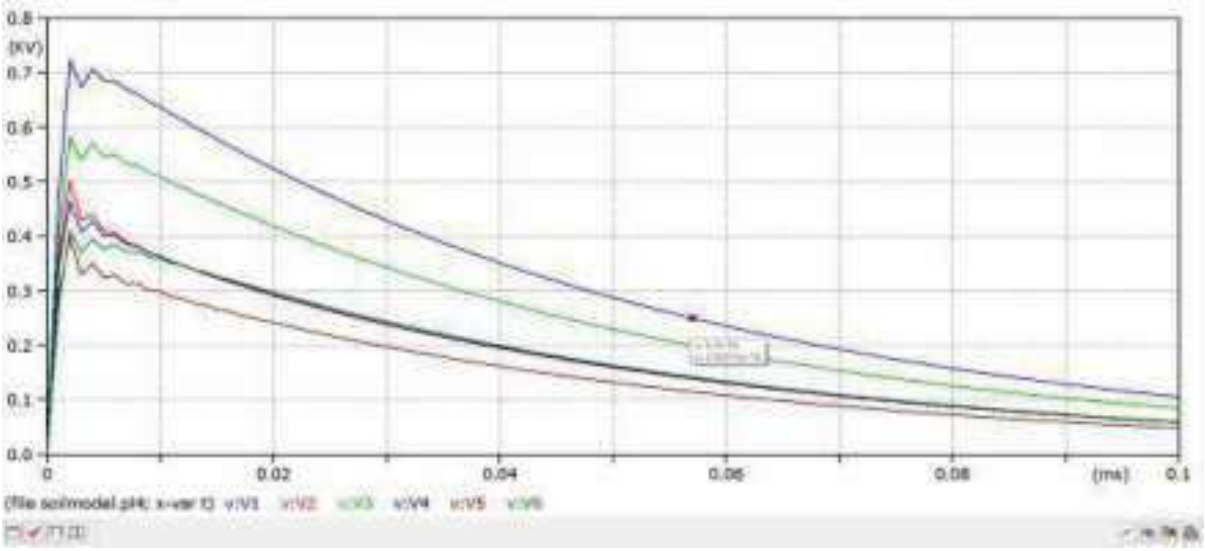

Fig 10. Tension induite pour l'argile sèche.

Les résultats de simulation montrés sur les Fig.8, Fig.9 et Fig.10 indique une tension plus élevée déchargée dans le sol milieu qui a une résistivité plus élevée. Le sable sec a une tension induite plus élevés que les tensions se comparent à l'argile humide et au milieu d'argile sèche. De l'ordre de dix fois par rapport à l'argile humide et 100 fois par rapport à l'argile sèche.

Par conséquent, ceux-ci ont prouvé que lorsque le courant généré par la foudre pénètre dans le sol, d'une plus grande résistivité qui est dans cette étude le sable sec. Un champ généré par la foudre est supérieur à la valeur seuil que le sol peut résister, il y aura donc un

Creative Commons Attribution-NonCommercial-NoDerivatives 4.0 International License (CC BY-NC-ND)

risque major d'une décharge dans le sol et créé un canal de claquage à l'intérieur du milieu au sol.

Conclusion :

Dans cette étude, pour un coup de foudre d'un courant de crête de 50 kA d'amplitude prés du sol, nous avons constaté des résultats de simulation par le logiciel AtpDraw que :
une tension plus élevée induite est enregistrée à l'extérieur couche d'isolation du câble sous un milieu de sable sec, suivi par l'argile humide et le milieu d'argile sèche.

Références:

He Peiyu, Li Peng, Peng Qingjun, Cao Min, Yi Hu and Li Bo (2020), *Calculation model for the earth potential of HVDC ground electrode based on image recognition of surface-layer soil moisture,* Measurement and Control 2020, Vol. 53(9-10) 1682–1693

S.N.M. Arshad, N.S. Tajudin, N.H. Halim, A.Z. Abdullah, C.L. Wooi, Nuriziani Hussin (2018), *Simulation on Lightning Effects to 132 kV Underground Cable by using Alternative Transients Program / Electromagnetic Transients Program (ATP/EMTP)*, IEEE 7th International Conference on Power and Energy (PECon)

Md. Abdus SALAM, Quazi Mehbubar RAHMAN, Swee Peng ANG, Fushuan WEN (2015), *Soil resistivity and ground resistance for dry and wet soil,* J. Mod. Power Syst. Clean Energy, DOI 10.1007/s40565-015-0153-8

Lekai Zou, Fan Yang, Bing Gao, Hanwu Luo Ligang Ye, and Wenzhen Li. (2020), *Grounding Current Dispersion of HVDC Grounding System under Dynamic Seasonal Frozen Soil* Progress In Electromagnetics Research C, Vol. 103, 211–223.

Abdullah Hoshmeh , Uwe Schmidt (2017), *A Full Frequency-Dependent Cable Model for the Calculation of Fast Transients*, Energies 2017, 10, 1158; doi:10.3390/en10081158.

Michael Adebayo Omidiora, (2011) *Modeling and Experimental Investigation of Lightning Arcs and Overvoltages for Medium Voltage Distribution Lines, thesis in Technology , School of Electrical Engineering Espoo, Finland).*

M. Ali Anadol, M. Aydin, T. Yalcinoz (2011), *Design and Implementation of a Laboratory Scale Underground Cable Model*, International Review on Modelling and Simulations (I.RE.MO.S.), Vol. 4, N. 4.

Predrag Maric, Srete Nikolovski, Laszlo Prikler(2009), *Simulation of Short Circuit and Lightning Transients on 110 kV Overhead and Cable Transmission Lines Using ATP-EMTP, Conference:* EEUG User group meeting 2009.

M.A Omidiora, M. Lehtonen (2009), *Simulation Performance of Induced Voltages on Power Lines due to Lightning Discharge to nearby Tree,* European EMTP-ATP Conference, Delft, The Netherlands.

Z. Anane, A. Bayadi, K. Huang, (2018), *Distortion phenomena on transmission lines using corona modeling ATP/EMTP* , IEEE Transactions on Dielectrics and Electrical Insulation, Vol. 25, Issue. 2, pp 383 - 389.

Z. Anane, A. Bayadi, N. Harid (2018), *A dynamic corona model for EMTP computation of multiple and non-standard impulses on transmission lines using a type-94 circuit component* , Electric Power Systems Research, Vol. 163, pp. 133–139..

Creative Commons Attribution-NonCommercial-NoDerivatives 4.0 International License (CC BY-NC-ND)

Algerian Journal of Engineering Architecture and Urbanism Vol. 5 Nr. 3 2021
ISSN: 2588-1760

DECOLORIZATION AND MINERALIZATION OF AN ORGANIC POLLUTANT (BROMOCRESOL PURPLE) BY ADVANCED OXIDATION PROCESSES IN AN AQUEOUS MEDIUM

Ibtissem. Bousnoubra [1], Soumia.Fassi[1], K. Djebbar [1*].

1. Laboratory science and technology environment. Department of Chemistry. Faculty of Sciences. University of Constantine 25000 Algeria.

E-mail : ibtissem.bousnoubra@gmail.com.

Abstract:
New treatment processes have emerged in recent years, among which advanced oxidation processes (P.O.As) are very interesting for the degradation of the recalcitrant organic molecule.
In this work we focused on the effectiveness of photochemical techniques on the process of discolouration and mineralization of an anionic dye (bromocresol violet BCP) in aqueous medium. These are Like Fenton (H_2O_2/Fe^{+3}) and Like Fenton (H_2O_2/Fe^{+3}/UV) at 254 and 365nm). For Like Fenton, the results obtained show that the fastest discolouration was obtained for the ratio $[H_2O_2]_0/ [Fe^{+3}]_0 = 10$, at pH=3 and for a concentration of 25 ppm of the dye, where it is of the order of 85% and for a reaction time of 120 minutes. The association of UV radiation (254 nm) with the Like Fenton process, for the same concentration and for the same ratio, led to a better efficiency of this process with a percentage of the order of 100% after 120 minutes. This performance seems to be linked to the production of radicals by multiple reactions: the photoreduction of Iron (III) at 254 nm which leads directly to the release of •OH and the formation of Iron (II); the photolysis of H_2O_2 at the same wavelength which generates radicals •OH; the reaction between H_2O_2 and Iron (II), The evolution of the COD as a function of the irradiation time was followed for the same conditions where the measured values show that this dye mineralizes more slowly than their decolorization rate.

Key words: BCP, Like- Fenton (H_2O_2 /Fe^{+3}), Photo Like - Fenton (H_2O_2 /Fe^{+3}/ UV), Mineralization, irradiation UV.

Introduction:

Les effluents industriels issus des activités de textile présentent souvent une charge polluante colorante importante. L'utilisation intensive des colorants dans la vie courante a engendré des problèmes aussi bien dans l'environnement que dans l'alimentation (T. Sauer G et al, 2002].

L'élimination de cette pollution représente un des principaux problèmes dans le processus de traitement, parce qu'ils sont généralement des composés toxiques difficilement biodégradables. Plusieurs méthodes de décontaminations ont été développées on cite comme exemple : les échanges ioniques (Dusart O et al , 1999 ; Perineau F et al, 1983), les procédés de floculation/ coagulation (Linsheng Z et al, 1992), les procédés d'adsorption sue les différents supports (MC Kay G et al,1988; Specchiar V et al, 1988; Sethraman v , 1975; McKay G et al,1985), les procédés biologiques (Paprowicz J et al, 1988; Porter J et al,1976 ; Ogawa Tet al, 1986). De nouveaux procédés de traitement ont émergé au cours des dernières années parmi lesquels les procédés d'oxydation avancés (P.O.As). Ces procédés reposent sur

Creative Commons Attribution-NonCommercial-NoDerivatives 4.0 International License (CC BY-NC-ND)

la formation *in situ* des radicaux hydroxyles $HO^{\cdot}$ qui possèdent un pouvoir oxydant supérieur à celui des oxydants traditionnels tels que Cl_2, ClO_2 ou O_3 et qui sont des espèces très réactifs en quantité suffisante pour oxyder la majorité des produits organiques (Milano J et al, 1994; Al-Quaradawi S, 2002 ; Daneshvar Net al,2003 ; Gomes Da Silva Cet al,2003). Cette étude a été entreprise pour évaluer Le procédé (H_2O_2 /Fe^{+3}) appelé ‹ like-Fenton›, qui est largement utilisé dans la décomposition des polluants. Il est basé sur la décomposition du peroxyde d'hydrogène en présence d'ions ferriques à pH acide pour produire les radicaux $^{\bullet}OH$ (Gallard, 1998) .Sa combinaison avec les rayonnements UV(H_2O_2 /Fe^{+3}/ UV) appelé ‹Photo- like-Fenton› donne des taux de dégradation très élevés**.**

Materials and methods:

Les solutions mères en Bromocrésol Pourpre de concentration de 100 ppm, ont été préparées par dissolution respective de leur sel dans l'eau bidistillé à l'obscurité et sous agitation magnétique pour faciliter la dissolution. La structure du Bromocrésol Pourpre est représentée en (Fig. 1).

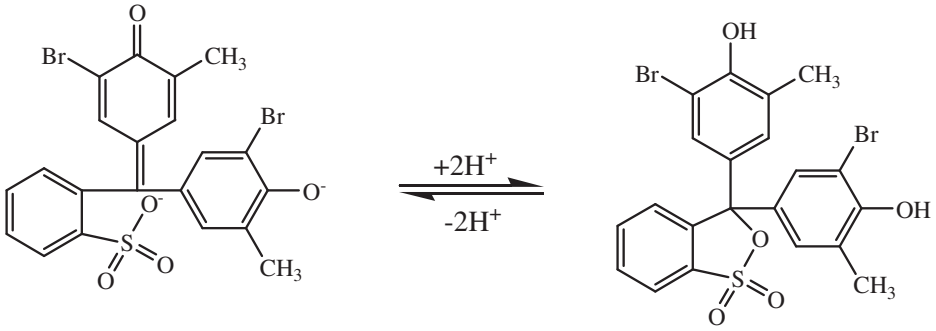

Fig.1. Structure du Bromocrésol pourpre.

Les solutions mères de H_2O_2 (Labosi, 30%) ont été préparées à partir de la solution commerciale.

Les solutions mères Fe (III) ont été préparées à partir de Perchlorate de Fe(III) hydraté ($Fe(ClO_4)_3H_2O$), Prolabo (99 %).

Les expériences d'irradiation à 254 nm, ont été réalisées dans une enceinte cylindrique, comprenant un réacteur tubulaire de 2,5 cm de diamètre et de 3 lampes UV « germicides » à vapeur de mercure basse pression et entourant ce réacteur dans une symétrie parfaite, le refroidissement est assuré par un ventilateur.

Les expériences d'irradiation à 254 nm, ont été réalisées dans une enceinte cylindrique, comprenant un réacteur tubulaire de 2,5 cm de diamètre et de 3 lampes UV « germicides » à vapeur de mercure basse pression et entourant ce réacteur dans une symétrie parfaite, le refroidissement est assuré par un ventilateur.

Les irradiations à 365 nm, ont été réalisées dans une enceinte réfléchissante cylindrique munie de trois lampes à Vapeurs de mercure haute pression 125 W. La surface de

Creative Commons Attribution-NonCommercial-NoDerivatives 4.0 International License (CC BY-NC-ND)

la suspension est à 10 cm approximativement des lampes. L'émission est filtrée par un globe noir se situant principalement à 365 nm. Le réacteur est en pyrex, équipé d'une jaquette permettant la circulation d'eau afin de maintenir la température 20± 2 °C.

La détermination de la DCO se fait essentiellement par oxydation avec le dichromate de potassium($K_2Cr_2O_7$) dans une solution d'acide sulfurique portée à ébullition, à reflux pendant 2 heures (T =148°C), en présence d'ions Ag^+ comme catalyseurs d'oxydation et d'ions Hg+ permettant de complexer les ions chlorures.

L'évolution spectrale et les mesures de la D.O des Solutions du colorant, à différents temps de réaction ont été suivies par spectromètre UV de type " Helios α- Unicam spectronic".

Results and discussions:

1- Oxydation de BCP par le procédé like-Fenton ($[H_2O_2]/ [Fe^{3+}]$)

Le procédé (H_2O_2 /Fe^{+3}) appelé ‹ like-Fenton› est largement utilisé dans la décomposition des polluants. Il est basé sur la décomposition du peroxyde d'hydrogène en présence d'ions ferriques à pH acide pour produire les radicaux $^{\bullet}OH$ selon le mécanisme suivant (Gallard, 1998) :

$Fe^{+3} + H_2O_2 \longrightarrow Fe\text{-}OOH^{+2} + H^+$ $\quad k=10^{-3}\ mol^{-1}s^{-1}$ (I)

$Fe\text{-}OOH^{+2} \longrightarrow HO^{\cdot}_2 + Fe^{+2}$ $\quad k=2,7\ 10^{-3}\ mol^{-1}s^{-1}$ (II)

$Fe^{+2} + H_2O_2 \longrightarrow Fe^{+3} + OH^- + {}^{\cdot}OH$ $\quad k=63\ mol^{-1}s^{-1}$ (III)

1-1- Influence du rapport $[H_2O_2]_o$ / $[Fe^{3+}]_o$ sur la décoloration du BCP par le système like-Fenton

Dans le but de déterminer la stœchiométrie convenable pour la dégradation du colorant, nous avons étudié l'oxydation du BCP (25 ppm) à l'obscurité, pour une concentration de 10^{-4}M en Fe(III) et pour des concentrations variables en H_2O_2 et selon les rapports suivants : $[H_2O_2]_o$ / $[Fe^{+3}]_o$ = 0.5, 1,2,5 et 10. L'ajout des réactifs (H_2O_2, Fe^{+3}) à la solution contenant le polluant se fait immédiatement l'un après l'autre. Ainsi, l'addition du deuxième réactif (Fe^{+3}) détermine le temps t=0 de la réaction. Le pH initial des solutions est dans tous les cas égal à 3. Les cinétiques de disparition du BCP sont représentées sur la (Fig.2).

Creative Commons Attribution-NonCommercial-NoDerivatives 4.0 International License (CC BY-NC-ND)

Algerian Journal of Engineering Architecture and Urbanism Vol. 5 Nr. 3 2021
ISSN: 2588-1760

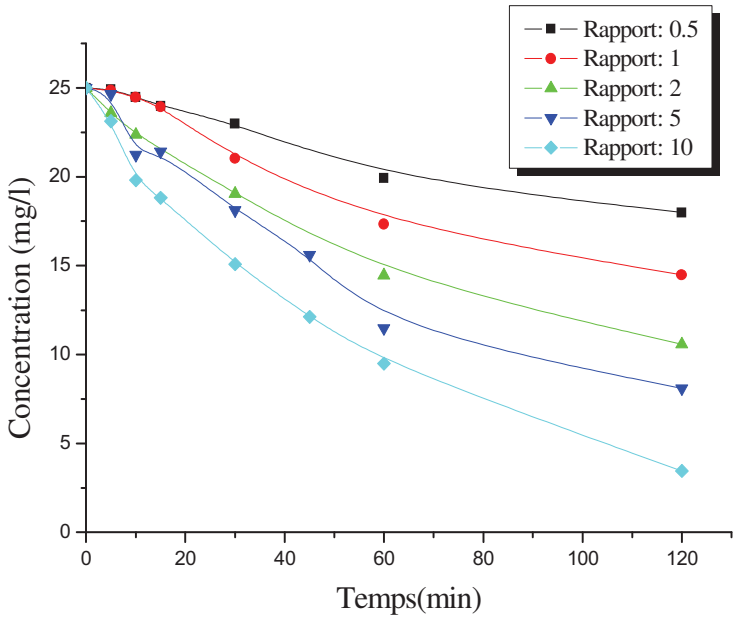

Fig.2. Influence du rapport sur la décoloration du BCP par le système like-Fenton, [BCP] =25 mg. L^{-1}. [Fe^{3+}]= 10^{-4} M

La (Fig2) montre que la vitesse d'oxydation du BCP est lente, particulièrement pour les rapports égaux à 0.5, 1 et 2. Celle-ci augmente pour devenir performante pour la valeur 10 de ce rapport, où le taux de décoloration obtenu est de l'ordre de 85% pour un temps de réaction égale à 120 minutes.

1-2-Minéralisation du BCP par le procédé Like- Fenton

L'évolution de la DCO en fonction du temps d'irradiation a été suivie pour notre colorant pour une concentration initiale de 25 mg. L^{-1}, à pH égal à 3, en présence de H_2O_2 à/ 10^{-3} M et à l'obscurité. Les valeurs de la DCO mesurées en fonction du temps et la courbe représentant la variation de celle-ci en fonction du temps, est reportée en (Fig.3). Il apparait clairement que ce colorant se minéralise plus lentement que leur décoloration. Dans ces conditions le processus de minéralisation est atteint au bout de 240 minutes où le taux d'élimination est de l'ordre de 79.34% .

Creative Commons Attribution-NonCommercial-NoDerivatives 4.0 International License (CC BY-NC-ND)

Algerian Journal of Engineering Architecture and Urbanism Vol. 5 Nr. 3 2021
ISSN: 2588-1760

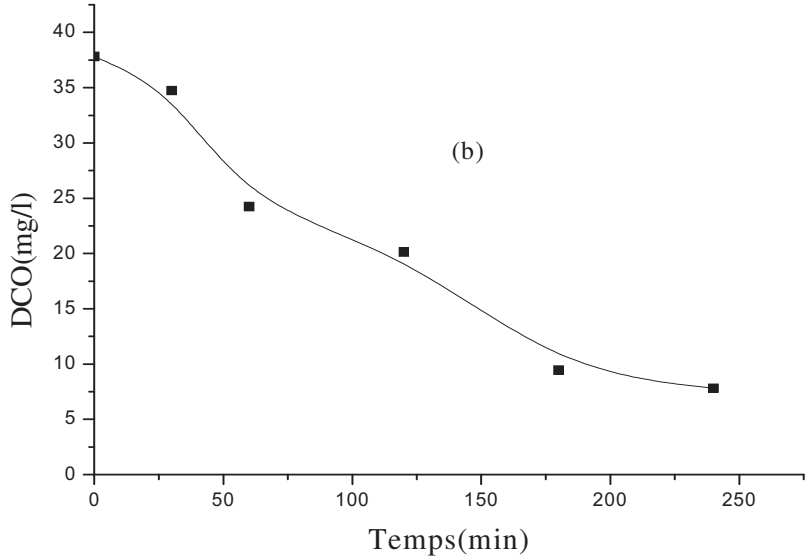

Fig.3. Evolution de la DCO en fonction du temps lors du traitement par le procédé Like-Fenton.;$[H_2O_2]$ = 10^{-3} mol. L^{-1} F(III)=10^{-4} mol.L^{-1},

2-Oxydation de BCP par le procédé Photo-like-Fenton ($[H_2O_2]$/ $[Fe^{3+}]$/UV)

2-1-Influence du rapport $[H_2O_2]_o/[Fe^{3+}]_o$ sur la photo-oxydation de BCP à 254 nm.

L'association du rayonnement UV (254 nm) au processus like-Fenton dans la dégradation du BCP, pour la même concentration du colorant et pour les mêmes rapports $[H_2O_2]_o/[Fe^{+3}]_o$ à pH acide, a conduit à une meilleure efficacité de ce processus (Fig.4).

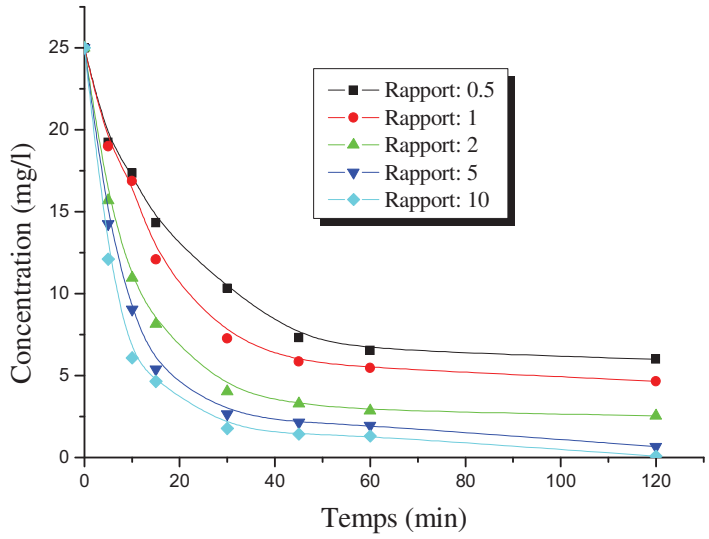

Fig.4 . Influence de la concentration initiale de H_2O_2 sur la décoloration du BCP par le procédé photo-like-Fenton,$[BCP]_o$= 25 mg. L^{-1}, $[Fe^{3+}]$=10^{-4} M, pH=3 et λ_{irr}=254nm

Creative Commons Attribution-NonCommercial-NoDerivatives 4.0 International License (CC BY-NC-ND)

En effet, nous observons que la disparition du BCP est plus rapide lorsque le système like-Fenton est couplé à la lumière. Cette performance parait liée à une production des radicaux par des réactions multiples (Djebbar, 2002) :

- la photoréduction de Fer (III) à 254 nm qui conduit directement à la libération des $^{\bullet}OH$ et à la formation de Fer (II).
- la photolyse de H_2O_2 à cette même longueur d'onde qui génère des radicaux $^{\bullet}OH$
- la réaction entre le H_2O_2 et Fer (II) qui, en plus de la production des radicaux $^{\bullet}OH$ régénère le Fer (III) assurant par la même la production cyclique de ces entités très actives.

On note par ailleurs, que le meilleur taux d'abattement est obtenu pour le rapport 10 avec un ordre de 94.76% au bout de 60 minutes.

2-2-Influence de la longueur d'onde d'irradiation sur la photo-oxydation du BCP par le procédé photo-like-Fenton à 365 nm

Il est clair que la longueur d'onde d'irradiation affecte sur le procédé photo-Like-Fenton. Pour cela nous avons irradié le BCP (25mg.L^{-1}) à 365 nm à pH=3, en présence de Fe^{+3}(10^{-4}M) et à des concentrations variables en H_2O_2 et en fonction des mêmes rapports que ceux utilisés à 254 nm. La (Fig.5) montre clairement que la vitesse de décoloration de colorant est un peu plus faible que celle obtenue à 254 nm. Ce qui pourrait être attribué à une production insuffisante de radicaux $^{\bullet}OH$ à cette longueur d'onde. (Cette production insuffisante, n'est que légère au regard de taux de décoloration obtenus à 254 nm).

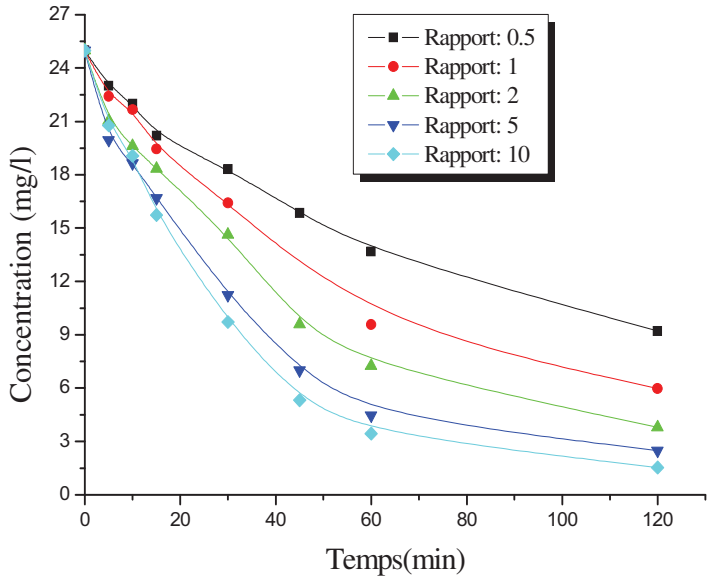

Fig.5 . Influence de la de la longueur d'onde d'irradiation sur la décoloration du BCP par le procédé photo- like-Fenton, $[VM]_o=[BCP]_o$= 25 mg. L^{-1}, $[Fe^{3+}]=10^{-4}$ M, pH=3 et λ_{irr}=365 nm

2-3- Minéralisation du BCP par le procédé photo-Like-Fenton

L'évolution de la DCO en fonction du temps d'irradiation a été suivie pour le BCP pour une

Creative Commons Attribution-NonCommercial-NoDerivatives 4.0 International License (CC BY-NC-ND)

concentration initiale de 25 mg L^{-1}, à pH égale à 3, en présence de 10^{-3} M de H_2O_2 et sous irradiation UV à 254 nm. Les valeurs de la DCO mesurées également en fonction du temps et les courbes représentant la variation de celle-ci en fonction du temps, sont reportées en (Fig.6). Il apparait clairement que le colorant se minéralise plus lentement que leur vitesse de décoloration et que ce processus de minéralisation, est obtenu pour un taux d'élimination (100%) pour un temps de réaction (240 minutes).

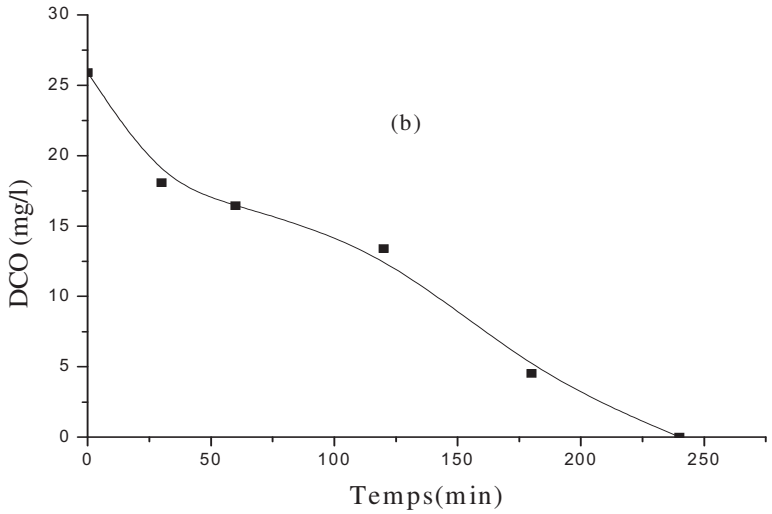

Fig.6. Evolution de la DCO du BCP en fonction du temps lors du traitement par le procédé Photo Like-Fenton à 254 nm. F(II)=10^{-4} mol. L^{-1}, [H_2O_2] = 10^{-3} M

3- Comparaison des efficacités des systèmes Like-Fenton et Photo-Like-Fenton

La (Fig.7) permet de comparer les cinétiques de dégradation de BCP par les deux procédés Like-Fenton et photo-Like-Fenton (à 254 nm et 365 nm). Pour comparer ces deux procédés, nous avons conservé les mêmes conditions expérimentales à savoir :

- un rapport $[H_2O_2]_o/[Fe^{+3}]_o=10$ (où $[Fe^{+3}]=10^{-4}$ M).
- une même concentration en BCP (25mg.L^{-1}).
- un pH acide du milieu (pH=3).

Creative Commons Attribution-NonCommercial-NoDerivatives 4.0 International License (CC BY-NC-ND)

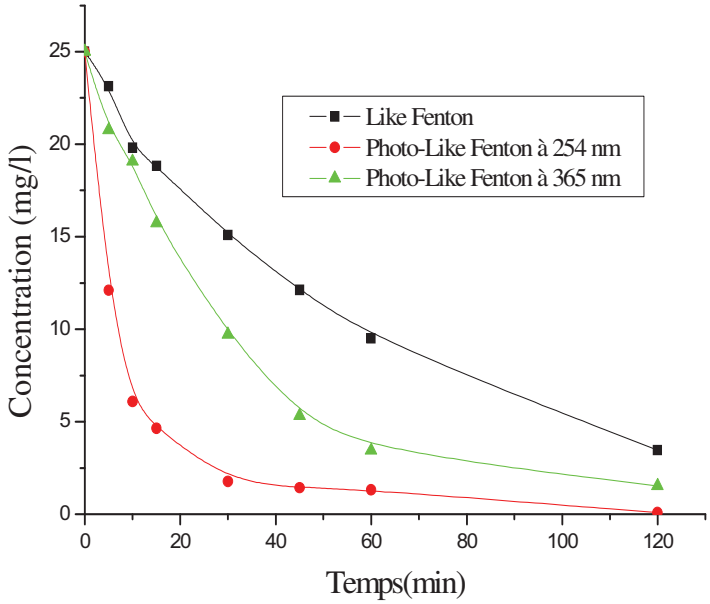

Fig.7. Comparaison des procédés Like-Fenton et Photo-Like Fenton au dégradation du BCP, $[BCP]_o$ =25 mg. L^{-1}, $[H_2O_2]$ = 10^{-3}mol. L^{-1}, F(III)=10^{-4}mol. L^{-1}, pH=3.

On observe que le processus de dégradation de BCP par le procédé photo-Like-Fenton à 254 nm est plus rapide que celui obtenu à 365 nm et par le réactif de Like-Fenton. Ceci est dû à la production supplémentaire des radicaux $^{\bullet}OH$ obtenus par la photolyse de H_2O_2 à cette même longueur d'onde. De plus, le nombre des radicaux $^{\bullet}OH$ issus de la photolyse du peroxyde d'hydrogène est plus élevé que celui obtenu par la photoréduction des ions ferriques à 365 nm via l'espèce monomère $Fe(OH)^{2+}$. Pour ces raisons, le procédé Photo-like-Fenton à 254nm est plus efficace pour la dégradation de BCP comparativement au procédé like-Fenton.

Conclusion:

Nous pouvons conclure que :

- La vitesse et le taux d'élimination de Bromocrésol pourpre par les procédés like-Fenton et photo-like-Fenton, dépendent du rapport $[H_2O_2]_o$/ $[Fe^{3+}]_o$. Ainsi plus le rapport est élevé plus le taux d'abattement est grand.
- La disparition de BCP est plus rapide par le procédé H_2O_2/Fe^{+3}/UV que par le procédé H_2O_2/Fe^{+3}.
- Le procédé H_2O_2/Fe^{+3}/ UV (254 nm) est un peu plus efficace que celui utilisé à 365nm.
- une minéralisation un peu lente pour le BCP en utilisant les procédés Like- Fenton et Photo-Like-Fenton

Creative Commons Attribution-NonCommercial-NoDerivatives 4.0 International License (CC BY-NC-ND)

References:

Al-Quaradawi S., Salman RS. (2002), *Journal of Photochem. Photobiol. A Chemistry* **148(1-3)** :161-168.
Daneshvar N., Salari D.,Khataee A.R. (2003), *Journal of Photochem. Photobiol. A/ Chemistry* **157 (1) :**111-116.
Djebbar K. E. (2002), Thèse doctorat d'état en chimie. Université Mentouri-Constantine.
Dusart O., Serpaud B. (1991), *La tribune de l'eau* **44(554)**: 15-22.
Gallard H. (1998), *Thèse de l'Université de Poitiers***.**
Gomes Da Silva C., Luis Faria J. (2003), *Journal of Photochem. Photobiol. A : Chemistry* **155(1-3) :**133-143.
Linsheng Z ., Dobias B. (1992), *Water Treatment* **7**: 221-232.
MC Kay G., Al Duri B A. A. (1988), Colourage. **35(20):** 24-28.
McKay G., Otterburn M.C. (1985), *Water, Air and Soil pollution* **24:** 307- 322.
Milano J.C., Loste- Berdot P., Vernet J.L. (1994), *Environ. Techn*. **16 :**329-341.
Ogawa T., Yatom C., Idaka E., Kamiya H. (1986), *Journal S.D.C*. **102:** 12-14.
Paprowicz J., Slodezyk S. (1988), *Env. Tech . Let* **9:** 271- 280
Perineau F., Moliner J ., Gazet A. (1983), *Wat. Res* **17(5)** :559- 567
Porter J.J., Snider E.H. (1976), *Journal W.P.C.F*. **5 :** 926-935.
Sethraman v.v., Raymahashay B. C.(1975), *Env. Sci. Tech* **9 :** 1139-1140.
Specchiar V ., Ruggeri B., Gianetto.(1988), *Chem. Eng. Comm* **68:** 99-117.
T. Sauer G., Gesconeto HJ. J ., Moreita. (2002), R. F. P.M **149:** 147-154.

Creative Commons Attribution-NonCommercial-NoDerivatives 4.0 International License (CC BY-NC-ND)

Algerian Journal of Engineering Architecture and Urbanism Vol. 5 Nr. 3 2021
ISSN: 2588-1760
.

ETUDE DU DÉLAMINAGE DANS LES TUBES EN MATERIAUX COMPOSITES.

H. MAKRI [1, 2],
1 Département de Génie Mécanique, Faculté de Technologie,
Université de Msila, Algérie.
2 LMSM, Laboratoire des Matériaux et Structures Mécaniques,
Université of Msila, Algérie.
hocine.makri@univ-msila.dz

D.H.MESSAOUDI[1,2]
1 Département de Génie Mécanique, Faculté de Technologie,
Université de Msila, Algérie.
2 LMSM, Laboratoire des Matériaux et Structures Mécaniques, Université
mohameddiaelhak.messaoudi@univ-msila.dz

Résumé:
Les composites multicouches en polymères renforcés de fibre de verre ont remplacé beaucoup de matériaux conventionnels dans les applications de transport de liquides à cause de certains avantages qu'elles offrent. Mais, lorsqu'ils sont chargés, ces matériaux sont vulnérables aux dommages menant à la séparation des couches. Ce mode de dégradation est connu sous le nom de délaminage. L'objectif principal de ce travail expérimental est d'étudier le comportement vis-à-vis du délaminage en Mode-I pour des éléments en matériaux composites présentant un rayon de courbure et qui sont prélevés de tubes. Focalisant l'influence de l'angle d'enroulement et la fissure initiale sur la ténacité interlaminaire GIC. Pour atteindre cet objectif, des échantillons DCB présentant a courbure sont réalisés à partir de tubes composites de 500mm de rayon fabriqués à partir de résine de vinyle ester et renforcé en fibre de verre élaborés par enroulement filamentaire selon différents angles d'enroulement (±45°, ±55° et ±65°) et comportant fissure initiale a_0 de longueur différentes 50, et 100mm. Les pré-fissures sont réalisés par interposions d'un film mince de PTFE dans la couche médiane lors de l'élaboration des tubes. Des dispositifs de chargement spéciaux conformes aux normes ASTM D5528-94a ont été préparés et utilisés pour mener les essais mécaniques de rupture en mode-I. Les essais ont été réalisés sur une machine INSTRON-5969. Les résultats obtenus ont montré une relation inverse entre les valeurs de ténacité de la rupture interlaminaire et la longueur de la fissure c'est à dire, moins long sont les longueurs des pré-fissures plus grands sont les valeurs de la ténacité de la rupture interlaminaire et que l'angle d'enroulement ± 65° confère au matériau un bon comportement vis-à-vis du délaminage que les angles ± 55° et ± 45°.

Mots clés*:* Délaminage en Mode I - Eprouvettes a courbure - Composites vinyle ester /fibre de verre - Rupture interlaminaire.

Introduction:

Les composites en polymères renforcés de fibres ont prouvé leur efficacité pour le stockage des liquides; actuellement leurs domaines d'applications sont en permanente extension, Cela est dû au rapport résistance / poids élevé, au coût de fabrication faible [1], isolation électrique,

Creative Commons Attribution-NonCommercial-NoDerivatives 4.0 International License (CC BY-NC-ND)

excellente durabilité et absence de revêtement, de protection cathodique ou de toute autre forme de prévention de la corrosion. [2, 3],

Les Tuyaux en composites polymères renforcés de fibre de verre sont fabriqués par un processus d'enroulement filamentaire. Ce processus de fabrication permet d'atteindre un taux de fibre important d'environ 65% ou plus. [4] Ce ci procure aux pipes de bonnes caractéristiques d'usage et de résistance. Malgré cela, sous contraintes ces matériaux sont vulnérables aux dommages qui se manifestent sous forme de séparation des couches communément appelé délaminage. [5,18]

La résistance à la rupture par délaminage des matériaux est exprimée en termes d'énergie par le taux critique de libération d'énergie de déformation (Gc). Chaque mode de chargement conduit à un mode de délaminage différent auquel on fait correspondre une énergie Gc différente. Pour mesurer les énergies Gc sous différents modes de délaminage des méthodes d'essais ont été développées. Parmi les modes d'essais, Le mode-I correspond au cas de chargement en écartement des brins d'éprouvette est le mieux indiqué pour caractériser la rupture interlaminaire. [6] Pour caractériser la ténacité des matériaux composites au délaminage en mode I, les normes ASTM D5528-94a. Ont proposé l'essai normalisé utilisant des éprouvettes en poutres cantilevers doubles en anglais : Double-Cantilever Beam (DCB). [7, 8 et 9].

Dans la littérature scientifique la plus part des travaux relatifs au délaminage utilisent des éprouvettes DCB droites, rare sont ceux qui se rapportent aux éprouvettes DCB obtenus par enroulement filamentaire et qui présentent une courbure. [10].

Plusieurs facteurs peuvent intervenir dans le phénomène du délaminage certaines sont relatifs à l'élaboration du matériau comme le taux de fibre contenu, l'angle d'inclinaison des fibres, le nombre de plis ou l'épaisseur du pli. D'autres sont relatifs à l'échantillon comme la rectitude ou la courbure, la pré-fissure et d'autres encore sont relatifs au mode expérimental comme l'application des charges, la répartition des appuis et la fixation. Ozdil et al. [11, 12] En examinant l'influence de la courbure de l'éprouvette, ont utilisé l'énergie d'initiation du délaminage GIC et la complaisance C pour comparer les échantillons plats aux échantillons courbés (80 mm de rayon interne) vis-à-vis du délaminage. Ils ont conclu qu'il y a une faible influence de la courbure sur le GIc et la complaisance C, mais qui diminue par rapport à l'augmentation de l'épaisseur du stratifié.

Davies et Benzeggagh, [13] ont etudié expérimentalement l'influence du taux de fibre contenu dans le composite vis-à-vis de la rupture interlaminaire. Ils ont enregistré des valeurs élevées d'énergie de rupture interlaminaire en mode-I pour des composites époxy renforcés de fibre de carbone dont la fraction volumique de fibres de 61%. Ils ont attribué ces valeurs au pontage de fibres formé dans le voisinage du fond de fissure qui enjambent la fissure et augmentent la résistance au délaminage.

Davies et al. [2] ont examiné l'effet de l'angle d'inclinaison, utilisant des échantillons découpés parallèlement à l'axe de tubes fabriqués par enroulement filamentaire, ils ont comparé le GIC relatif aux échantillons unidirectionnels et droits avec ceux avec trois angles d'enroulement différents. Aucune variation de GIc n'a été enregistrée pour les deux types d'échantillons. Nicholls et Gallagher. [14] ont trouvé pour des échantillons DCB en stratifiés de graphite époxy pour une large gamme d'angles, que l'augmentation de GIc est lié à l'augmentation l'angle d'orientation la fibre peut être attribuée à la déformation de la matrice dans les couches et à la bifurcation du fond de fissure, et que ces deux faits sont à l'origine de la propagation des fissures le long des interfaces des couches. Shetty et al. [15] ont étudié la resistance à la rupture interlaminaire dans 14couches bidirectionnelles de composites époxy renforcé de fibre de verre type E, ils ont obtenu une augmentation de la ténacité à la rupture

Creative Commons Attribution-NonCommercial-NoDerivatives 4.0 International License (CC BY-NC-ND)

interlaminaire comme conséquence a la variation de l'angle d'orientation des fibres allant de 0° à 90° par rapport à la direction de propagation de la fissure. Ils ont conclu que les composites présentent une résistance à la rupture et une durabilité élevées lorsque les fibres sont orientés transversalement par rapport à la ligne de propagation des fissures. Ce travail expérimental a pour objectif de vérifier la tenue vis-à-vis du délaminage en mode-I d'un produit de Maghreb pipe fabriqué et commercialisé en Algérie.

La Rupture interlaminaire en mode-I :

Le taux de libération d'énergie critique en mode-I est déterminé par la méthode de calibration de la complaisance (CC méthode) exprimée par l'équation:

$$GIc = \frac{nP\delta}{2ba} \quad (1)$$

Où, P et δ sont la charge et le déplacement de la charge, a et b sont la longueur de la fissure et la largeur de la poutre, respectivement, n représentent la pente du tracé log-log de la longueur de la fissure et de la complaisance, il peut être calculé à partir de la pente du tracé log-log en utilisant les valeurs d'amorçage de délamination (initiation de la fissure) observées visuellement et toutes les valeurs de propagation.

La complaisance, C = δ/P est calculée à partir des données expérimentales et peut être exprimé par :

$$C = m.a^n \quad (2)$$

Où; (a) est la longueur de délaminage et (m) et (n) sont des paramètres de loi de puissance représentant les constantes intrinsèques du matériau, n représentent la pente du tracé log-log de la longueur de la fissure et de la complaisance et peuvent être déterminés à partir de la formule ci-dessous:

$$LogC = n.Loga + Logm \quad (3)$$

Matériaux et Techniques expérimentales :

Matériaux :

Les matériaux de base utilises pour la fabrication des tubes en composites utilisés dans l'expérimental sont les fibres de verre continues type-E6 avec 2400Tex de type EDR24-2400-38 utilisés en tant que renfort et le vinylester, une résine thermodurcissable liquide, utilisé comme agent d'imprégnation. Les caractéristiques des fibres de renfort sont les suivantes: diamètre de fibre ~24 µm, densité 2,54 g/cm3, résistance à la traction 2741MPa, module de Young 81 232GPa, coefficient de Poisson 0,22 et allongement 4%. L'agent d'imprégnation est obtenu par mélange d'une résine et d'un durcisseur, qui réagissent pour se solidifier après réaction. L'ajout du durcisseur à la résine se fait progressivement en mélangeant dans un malaxeur et en contrôlant la viscosité de manière à maintenir une certaine fluidité et pour garantir un aspect acceptable après durcissement. Les propriétés mécaniques de la résine thermodurcissable ont été déterminées par des essais de traction et de flexion comme suit: résistance limite à la flexion ~150 Mpa, module de flexion 3,8Gpa, résistance à la traction limite ~ 85MPa, module de Young 3,3GPa.

Préparation des tubes :

Les tubes ont été élaborés par un processus d'enroulement filamentaire (Figure.1) par une entreprise locale MAGHREB PIPE COMPANY. Le principe d'élaboration consiste à imprégner des fibres de verre de renfort dans le vinylester liquide. Une fois imprégnées, Les fibres de verre sont enroulées sur un mandrin rotatif selon l'angle désiré et avec une tension de manière à assurer la forme tubulaire régulière et une rigidité du tube. Le tube en composite

Creative Commons Attribution-NonCommercial-NoDerivatives 4.0 International License (CC BY-NC-ND)

Algerian Journal of Engineering Architecture and Urbanism Vol. 5 Nr. 3 2021
ISSN: 2588-1760
.

polymère renforcé de fibre de verre est ainsi obtenu par l'ajustement de deux mouvements respectivement, la rotation du mandrin avec le mouvement alternatif du guide de bande de verre. Après mise en forme par enroulement filamentaire, une cure thermique à 150° C pendant 30 à 40minutes est nécessaire tout en maintenant sa rotation. Trois angles d'enroulement ont été considérés lors de la fabrication des tubes; (± 45°, ± 55° et ± 65°), avec 8 et pour chaque angle d'enroulement. Un film de polytétrafluoroéthylène (PTFE) d'épaisseur 13mm a été inséré dans la couche moyenne pendant la fabrication, pour initier une fissure lors du chargement. (Figure. 2).

Figure. 1. PRESENTATION DU PROCESSUS D'ENROULEMENT FILAMENTAIRE.

Figure.2. INTERPOSITION D'UN FILM POLYTETRAFLUOROETHYLENE (PTFE) A MI-EPAISSEUR DU TUBE.

Préparation des échantillons :

Des échantillons ont été découpés dans des tuyaux GFR (500 mm de diamètre interne), à l'aide d'une scie à disque diamantée. Selon les normes D5528-94a, [7, 16] les dimensions des éprouvettes sont de (200x25x5) mm avec des fissures initiales de longueur a_0= 55 et 100 ± 0,2mm. Les surfaces des éprouvettes ont été frottés avec du papier de verre et, les bords ont été nettoyés et polis à plat avant de coller des blocs de chargement avec un adhésif sur les deux côtés de l'échantillon (Figure.3).

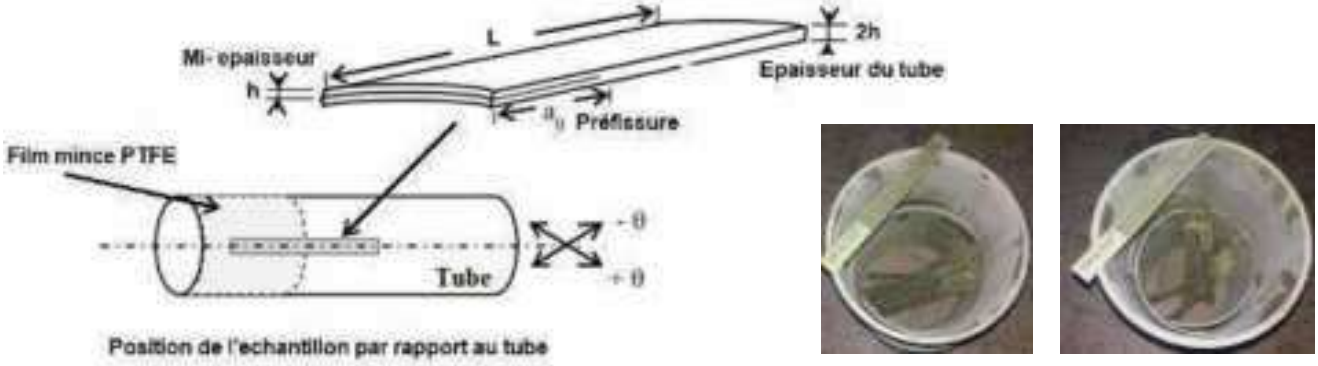

Figure. 3. DECOUPAGE DES ECHANTILLONS

Essais mécaniques:

Une paire de blocs métalliques a été collée à l'extrémité de chargement de l'éprouvette (Figure.4) afin de permettre l'application de la charge de manière à ce que les forces restent

Creative Commons Attribution-NonCommercial-NoDerivatives 4.0 International License (CC BY-NC-ND)

perpendiculaires aux faces de l'éprouvette réalisant une fissure ouvrant des charges pendant les essais et d'éviter moment au point de chargement. Des essais mécaniques d'ouverture en mode I ont été effectués à 20 °C conformément à la norme ISO 15024, en utilisant une machine d'essai universelle INSTRON-5969 équipée d'un capteur de force d'une capacité de 50KN pour enregistrer les charges. Le mors mobile de la machine d'essais se déplace à une vitesse de 1mm/min et des données de force-déplacement (P–δ) ont été obtenues. L'observation de la propagation de la fissure lors des essais a été facilitée en traçant des repères le long des bords par intervalles de 1mm. Une caméra LCD connectée à un ordinateur placé devant le dispositif permettant la capture, le stockage des images et le suivi du chemin de fissure lors des essais de rupture. Des parties des échantillons ont été coupés et ses bords ont été observés et analysés à l'aide d'un microscope équipé d'une caméra et d'un logiciel de traitement d'image.

Figure.4. DISPOSITIF EXPERIMENTAL UTILISE SUR LA MACHINE D'ESSAI.

Résultats et discussions

La fraction de verre dans les tubes utilisés pour la préparation des échantillons a été déterminée par des essais de perte au feu et est d'environ 67,52% pour des tubes à 8 plis. Ces valeurs sont supérieures aux valeurs nominales qui ont été fixées théoriquement fixées à 55%; qui confirment le fait que l'enroulement filamentaire procure aux matériaux élabores selon ce procédé des valeurs de taux de fibres élevées ce qui s'accorde avec certains travaux d'auteurs comme Davies R, Ranneau [2]. Les courbes charge-déplacement ont été tracées et présentées sur les figures de 5 à 6 respectivement, afin d'étudier et de comparer leur comportement.

Les traces ont la même allure et toutes les courbes comportent trois des parties distinctes d'après le changement de leur allure. Elles présentent une tranche linéaire au début perturbé par des petits pics. La linéarité traduit un comportement élastique du matériau tandis que la présence des petits pics est attribuée à la différence des comportements élastiques entre les fibres et la matrice lors de l'application des charges. Le délaminage des composites est formé par une croissance de la fissure stable et instable combinés.

Creative Commons Attribution-NonCommercial-NoDerivatives 4.0 International License (CC BY-NC-ND)

Algerian Journal of Engineering Architecture and Urbanism Vol. 5 Nr. 3 2021
ISSN: 2588-1760

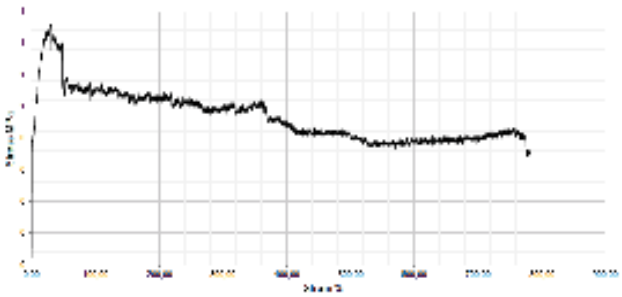

ANGLE D'INCLINAISON 45° ET FISSURE INITIALE DE 50 mm.

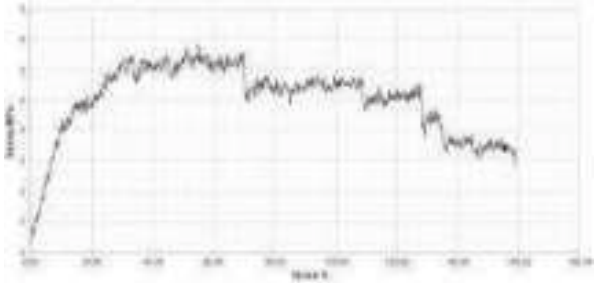

ANGLE D'INCLINAISON 55° ET FISSURE INITIALE DE 50 mm.

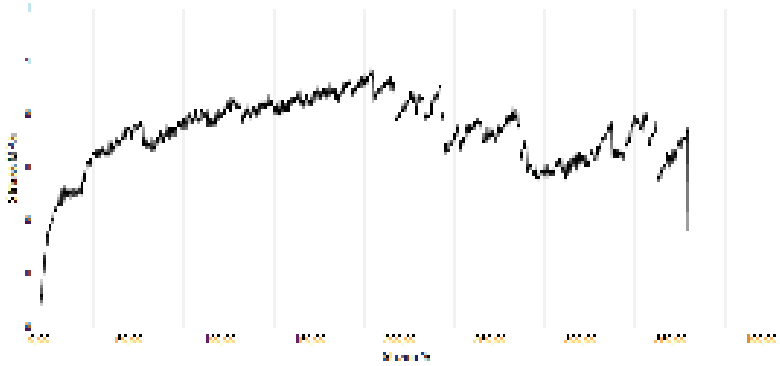

ANGLE D'INCLINAISON 65° ET FISSURE INITIALE DE 50mm.

Figure.5. COURBES CHARGE-DEPLACEMENT POUR DES EPROUVETTES 45, 55 ET 65° D'ANGLE D'INCLINAISON ET 50 mm DE FISSURE INITIALE.

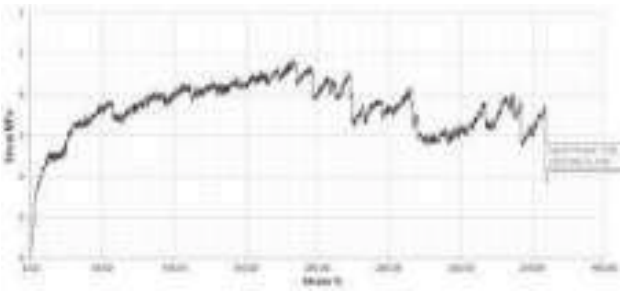

ANGLE D'INCLINAISON 65° ET FISSURE INITIALE DE 100mm.

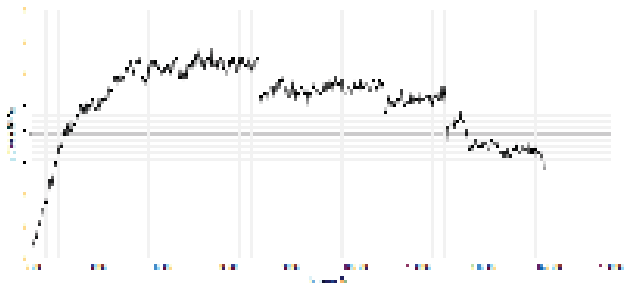

ANGLE D'INCLINAISON 55° ET FISSURE INITIALE DE 100mm.

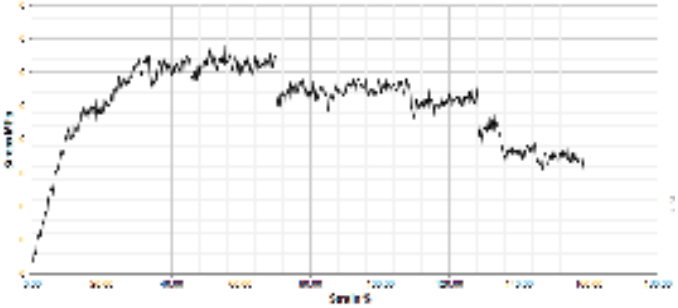

ANGLE D'INCLINAISON 65° ET FISSURE INITIALE DE 100mm.

Figure.6. COURBE CHARGE-DEPLACEMENT POUR LES EPROUVETTES 45, 55 ET 65 ° D'ANGLE D'INCLINAISON ET 100 mm DE FISSURE INITIALE.

Creative Commons Attribution-NonCommercial-NoDerivatives 4.0 International License (CC BY-NC-ND)

Algerian Journal of Engineering Architecture and Urbanism Vol. 5 Nr. 3 2021
ISSN: 2588-1760

A La fin de la partie linéaire de la courbe, s'amorcent les fissures, on constate une augmentation de la charge après la phase d'amorçage qui est attribuée au phénomène de pontage des fibres qui contribue significativement à l'augmentation les valeurs de GIc. Ce constat s'accord avec les observations de Davallo [17] et avec Davies et Benzeggagh. [13] Le relâchement continu jusqu'à la rupture en fonction de la croissance des fissures est attribué à la propagation stable de la fissure ou aussi propagation stable du délaminage.
Les pics constituent la réponse du matériau au mode de propagation de la fissure qui est caractérisée par des augmentations et des réductions de charge soudaines qu'on peut expliquer par le saut de la fissure entre les interfaces adjacentes (fissuration translaminaire). Des explications similaires ont été trouvées dans les travaux de Shokrieh et al. [6]. La chute remarquable de la charge est attribuée à une propagation instable de la fissure qui est probablement causée par la rupture des ponts de fibres évoqués précédemment.

3.1. Determination des parametres intrinseques du materiau et le GIc.

Afin de déterminer les paramètres intrinsèques du matériau n et m, les courbes de la complaisance en fonction de la croissance du délaminage ont été traces conformément à l'équation ci-dessous

$$\text{Log } C = n \log a + \log m.$$

Ou n représente la pente des courbes linéaires. Comme montré sur les figures.7 les courbes présentent une pente linéaire, Le paramètre n peut être obtenu par les données relatives à ces figures.

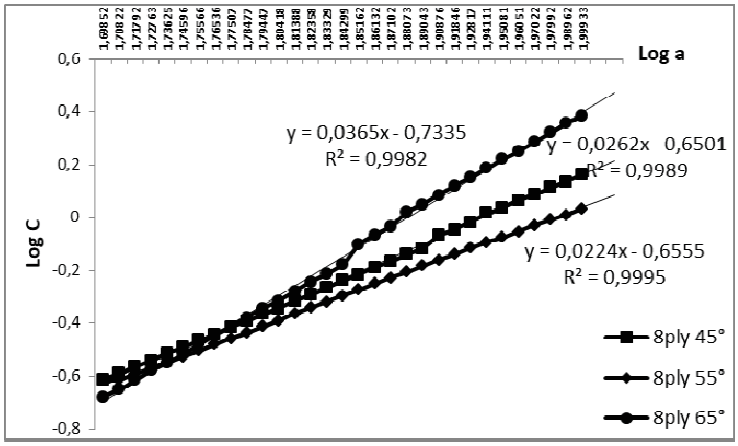

Figure.7. COURBES DE LOG C EN FONCTION DE LOG A, POUR DIFFERENTS ANGLES D'ORIENTATION.

Sur la base des résultats des figures 5 à 6, les valeurs des paramètres intrinsèques du matériau n et m déduites sont présentées dans le tableau. 1.

	n	m
[±45°]	1,559	1,97
[±55°]	2,594	3,17
[±65°]	3,641	4,86

Table.1. VALEURS DES PARAMETRES INTRINSEQUES N ET M DU MATERIAU.

Les valeurs des GIc obtenus sont présentées dans le tableau. 2 et sont présentés sous forme d'histogrammes des taux d'énergie GIc en fonction des angles d'enroulement selon les différentes valeurs des fissures initiales (figure 8).

Creative Commons Attribution-NonCommercial-NoDerivatives 4.0 International License (CC BY-NC-ND)

	a0 (mm)	Pc (N)	δ (mm)	C (mm/N)	GIC (J/m²)	GICmoyen (J/m²)
[±45°]	50	28,66	21,93	0,76517795	390,379687	300,392033
	100	26,96	25,13	0,93212166	210,404379	
[±55°]	50	32,01	15,58	0,4867229	515,405891	468,913039
	100	36,89	22,16	0,6007048	422,420188	
[±65°]	50	34,79	14,68	0,42196033	740,845149	765,685038
	100	15,46	70,5	4,56015524	790,524926	

Table.2. TAUX DE RESTITUTION D'ENERGIE GIC POUR 8PLIS ET ANGLES D'ENROULEMENT [± 45°], [± 55°] ET [± 65°].

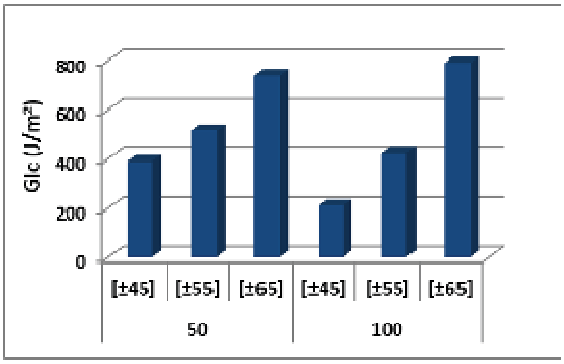

Figure.8. GI_C EN FONCTION DES ANGLES D'ENROULEMENT ET DES LONGUEURS DES FISSURES INITIALES.

On constate que les composites ayant les angles d'enroulement de [±65°] ont des valeurs de GIC supérieure que celles de [±55°] et [±45°]. Ce qui permet d'établir que le taux de restitution d'énergie GIC augmente en fonction de l'augmentation des angles d'enroulement. Ce constat s'accorde un certain nombre de travaux cités précédemment.

Compte tenu de l'influence de la fissure initiale sur le GIc, on constate que les éprouvettes avec une fissure initiale de 50mm présentent des valeurs de GIC légèrement élevé par rapport à celles avec des fissures initiales de 100mm. Ce qui semble paradoxal. Ces ci peut être expliqué par à la flexion des brins des éprouvettes survenant lors des essais de délaminage en raison du manque de rigidité suivant le sens de la longueur pour les éprouvettes moins épaisses. Cette flexion perturbe les résultats par consommation d'une partie de l'énergie en flexion plutôt qu'en délaminage.

3.3. Observation Microscopique:

Un examen microscopique des plans fracturés a été effectuées et quelques micrographies ont été prises près des extrémités des fissures et ont été présentées à la figure.9.

Figure.9. EXAMEN MICROSCOPIQUE DES FACIES DE RUPTURE (x500FOIS).

Des micro-fissures se sont formées situées dans la matrice entre les fibres, probablement provoquées par la flexion de différents plis lors du chargement. Cela suggère une présence de

Creative Commons Attribution-NonCommercial-NoDerivatives 4.0 International License (CC BY-NC-ND)

fracture intra-laminaire. Une déformation plastique de la matrice autour des fibres a été observée au fort grocissement; ceci est attribué à la concentration d'une phase ductile au niveau de la région de la fibre/matrice contribuant à l'amélioration de la liaison interfaciale par transfert de contraintes de la matrice vers les fibres de renforcement. La décohésion des fibres mises en évidence de part et d'autre des éprouvettes conduit à la formation de ponts contribuant au renforcement du matériau contre le délaminage. De cette analyse, il apparaît que le composite traité dans cette étude a une résistance assez élevée des fibres de renforcement par rapport à la matrice qui subit une fissuration interfaciale ce comportement est attribué à la teneur élevée en rapport de fibres.

4. Conclusion

Dans cet article, le comportement de délaminage a été étudié; l'effet de l'angle d'orientation des fibres et la pre-fissure sur le délaminage a été focalisé. Des essais de chargement en mode I ont été réalisés sur des éprouvettes DCB courbées obtenues par découpage dans des tubes composites en polymère renforcé de fibres de verre fabriqués par un procédé d'enroulement filamentaire. Les conclusions sont faites et sont les suivantes:

- L'association des fibres de verre E6 et du polymère d'ester vinylique ont permis de produire un matériau composite aux bonnes propriétés.
- Le procédé de production a fourni une teneur en verre d'environ 67,52%. Ces valeurs sont suffisamment élevées pour qu'il soit nécessaire de penser à réduire pour réduire les coûts de production
- Le délaminage diminue avec l'augmentation de l'angle d'orientation des fibres par rapport à la direction de propagation de la fissure indépendamment du nombre de plis et les angles d'orientation des fibres de 55° et 65° confèrent aux tubes composites une meilleure comportement par rapport au délaminage que les angles de 45°.
- Au cours des essais de délaminage, deux phénomènes ont affecté les résultats: la flexion des lèvres d'éprouvette et le pontage des fibres. La flexion des lèvres qui se produisant sur les brins de l'échantillon est responsable de la dissipation d'une grande partie de l'énergie en flexion plutôt qu'en délaminage et son effet augmente avec l'augmentation de l'angle d'orientation. Cette flexion peut être évitée par l'augmentation de l'épaisseur des échantillons à travers l'augmentant le nombre de plis. Quant au pontage des fibres entre les brins des échantillons, il contribue au renforcement du matériau composite contre le délaminage en retardant la progression de la fissure par absorption de l'énergie de propagation. cependant pour évaluer correctement l'effet de ce phénomène sur le délaminage, il est nécessaire de déterminer le nombre de fibres engagées dans le pontage et mesurez la force de pontage.
- Les composites étudiés montrent une bonne résistance des fibres de renfort par rapport à la matrice pour autant que les fissures soient davantage liées à cette dernière; ils sont sujets à des fissures interfaciales provoquées par la flexion des brins de l'éprouvette lors de l'application des charges.

References:

1. **Pop Metodieva B., MSc. Zhezhova S., Srebrenkoska S., Naseva S., Prof. Dr Srebrenkoska**. (2015), *Design of polymer composite pipes produced by filament winding technology*, Scientific proceedings XII international congress "machines, technologies, materials". ISSN 1310-39461.

Creative Commons Attribution-NonCommercial-NoDerivatives 4.0 International License (CC BY-NC-ND)

2. **R. Davies and F. Rannou. (**1995), *The Effect of Defects in Tubes: Part 1. Mode I Delamination Resistance*. Applied Composite Materials 1: 333-349.
3. **D.Srinkanth Rao, P.Ravinder Reddy, Sriram Venkatesh**. (2017), *Determination of mode-I fracture toughness of epoxy-glass fibre composite laminate*, Procedia Engineering 173: 1678-1683.
4. **Fatih Daricik, Züleyha Aslan**. (2017), *Characterization of Delamination Crack in Multidirectional E-glass/epoxy Composite under Mode I Loading*, European Mechanical Science, Vol. 1(4): 117-128.
5. **Habib Achache, Abdelouahab Benzerdjeb**. (2017), *Delamination of a Composite Laminated under Monotonic Loading*, International Journal of Theoretical and Applied Mechanics, Volume 2: 119-128.
6. **M.M. Shokrieh, M. Heidari-Rarani, M.R. Ayatollahi.** (2012), *Delamination R-curve as a material property of unidirectional glass/epoxy composites*. Materials and Design 34: 211–218.
7. *Standard Test Method for Mode I Interlaminar Fracture Toughness of Unidirectional Fiber-Reinforced Polymer Matrix Composites* Designation: D 5528 – 01 (Reapproved 2007)
8. **A.J.Smiley and R.B.Pipes**. (1987), *Rate Sensitivity of Mode II Interlaminar Fracture Toughness in Graphite/Epoxy and Graphite/PEEK Composite Materials*,Composites Science and Technology 29: 1-15.
9. **Panuwat Suppakul, Sri Bandyopadhyay.** (2002), *The e□ect of weave pattern on the mode-I interlaminar fracture energy of E-glass/vinyl ester composites*. Composites Science and Technology 62: 709–717.
10. **W. Beckert, B. Lauke and K. Friedrich**. (1995), *Delamination Toughness Computation for Curved Thermoplastic Composites* .Applied Composite Materials 1: 395--400.
11. F**. Ozdil and L. A. Carlsson**. (2000), *Characterization of Mode I Delamination Growth in Glass/Epoxy Composite Cylinders*, Journal of Composite Materials, 34: 398.
12. **F. Ozdil and L. A. Carlsson**. (2000), *Characterization of Mixed Mode Delamination Growth in Glass/Epoxy Composite Cylinders*, Journal of Composite Materials, vol.34 N°5.
13. **P. Davies and M.L. Benzeggagh**, (1989), *PART IIA. Interlaminar Fracture Studies, Chapter 3: Interlaminar Mode-I Fracture Testing, in: Application of Fracture Mechanics to Composite Materials* edited by K. Friedrich 81-112
14. **D.J. Nicholls and J. P. Gallagher.** (1983), *Determination of GIC in Angle Ply Composites Using a Cantilever Beam Test Method*, Journal of reinforced plastics and composites, Vol 2.
15. **M.R. Setty, K.R. Vijay S. Sudir, P. Raghu and D. Madhuranath R.M.V.G. K. Rao.** (2000), *Eeffect of fibre orientation on mode I interlaminar fracture toughness of glassy epoxy composites*, Journal of Reinforced Plastics and Composites. Vol. 19, N°08.
16. **P. Mertiny, F.Ellyin, A. Hothan.** (2004), *An experimental investigation on the effect of multi angle filament winding on the strength of tubular composite structures*, Composites Science and Technology 64 (1) .
17. **M. Davallo**, (2010), *Factors Affecting Fracture Behaviour of Composite Materials*, International Journal of Chem Tech Research. Vol.2, No.4, pp 2125-2130.
18.R. **Davies and F. Rannou.** (1994), *The Effect of Defects in Tubes: Part 1. Mode I Delamination Resistance*. Applied Composite Materials 1: 333-349.

Creative Commons Attribution-NonCommercial-NoDerivatives 4.0 International License (CC BY-NC-ND)

Algerian Journal of Engineering Architecture and Urbanism Vol. 5 Nr. 3 2021
ISSN: 2588-1760

OPTIMISATION DE LA RECUPERATION DU ZINC ET DE L'ARGENT DANS LES RESIDUS DE LIXIVIATION

Abdelhakim Begar
Dr. Génie minier, Département de Génie Mécanique, Université de Biskra,
B.P.145 Biskra, Algérie a.begar@univ-biskra.dz

M.E. DJEGHLAL
Prof. Métallurgie, Laboratoire L.S.G.M , Département de Métallurgie, ENP , 10 Avenue Pasteur
B.P182, El-Harrach, Alger, Algérie. dmlamine2015@gmail.com

M. OULD HAMOU
Prof., Génie minier, Laboratoire L.G.M , Département de Génie Minier, ENP , 10 Avenue Pasteur
B.P182, El-Harrach, Alger, Algérie. ould_hamou@g.enp.edu.dz

Résumé :
La présente étude a été réalisée dans le but de récupérer du zinc et de l'argent à partir des résidus de lixiviation acide. Nous avons employé dans cette étude un procédé de lixiviation en milieu acide à chaud avec neutralisation et précipitation de fer sous forme de jarosite. Nous avons finalement obtenu un résultat satisfaisant car la majorité du zinc passe en solution d'où l'obtention d'un bon rendement d'extraction en zinc. Contrairement à l'argent qui malgré sa précipitation restait toujours sous forme complexe et ne nous permet pas une bonne récupération.

Mots-clés : Jarosite, Zinc, Argent, Lixiviation.

Introduction :

Les matières utiles sont généralement dispersées dans des roches sans valeur. Dans le cas où un traitement de valorisation est économiquement envisageable, on se trouve en présence d'un minerai.

Pour des raisons techniques et économiques, la valorisation des minerais nécessite une concentration préalable des phases minérales valorisables.

Une fois réalisée, la concentration des phases minérales intéressantes, le rôle de la métallurgie consiste à extraire et à purifier les métaux contenus dans le concentré obtenu. Elle a recours à des opérations qui sont réalisées en combinant un ensemble de techniques où interviennent soit des phases aqueuses (hydrométallurgie), soit l'action des hautes températures (pyrométallurgie).

La lixiviation du sulfure de zinc a été souvent étudier que ce soit la lixiviation par une solution de chlorure ferrique, la lixiviation non oxydante en milieu chlorhydrique ((Mizoguchi et Habashi, 1981; Majima et al., 1981) ou sulfurique (Forward et Veltman, 1959; Parker, 1961; Begar et al., 2015) et l'acide nitrique (Bjorling, 1954).

Creative Commons Attribution-NonCommercial-NoDerivatives 4.0 International License (CC BY-NC-ND)

Les prétraitements des sulfures pour l'hydrométallurgie peuvent être effectuées par différentes méthodes (Havlik et Kammel, 2000 ; Havlik et al, 2001a, b).

PAWLEK et PIETSCH ont étudier la lixiviation de 10 sulfures (CoS, CuS,MoS_2, NiS, SnS, SnS_2,WS_2, et ZnS) à 120°C sous 2.10^5 Pa d'oxygène. Ils ont observé la formation de soufre élémentaire lors du lessivage des sulfures de manganèse et molybdène
Comparé à l'intérêt porté à d'autre sulfures métalliques, le sulfure de zinc fut un peu négligé jusqu'en 1957. Von discher et pawlek ont étudié un concentré de Blend-galène et un autre de zinc-cuivre. Ces concentrés contenaient de fortes proportions de fer et un peu de cuivre, plomb et manganèse. Les essais furent effectués à 160-180°C et sous 6.106 Pa de pression d'oxygène. Le produit de la réaction était du sulfate de zinc.

Forward et weltman ont travaillé sur des concentrés de sulfures zinc –cuivre et zinc-plomb et récupéré 95 à 99 % de zinc, en deux à quatre heures et à 110-115°C, en présence de quantités stœchiométrique d'acide sulfurique (pH 1 à 2) et sous une pression de 1,4 .105 Pa d'oxygène.

Dans le même temps, Pawlek et Pietsch ont étudié la lixiviation de cinq sulfures de zinc différents à forte concentration en fer. Les opérations ont été menées de 115 à 135 °C sous 2.10^5 Pa à 5.10^5 Pa d'azote. Dans chaque cas, il se formait de l'hydrogène sulfuré et du sulfate de zinc.

Dans les résidus solides, le zinc peut se trouver sous plusieurs formes, ZnS (insoluble), (ZnO) (soluble dans H_2SO_4 et insoluble dans l'eau), $ZnSO_4$(soluble dans l'eau), et $ZnO.Fe_2O_3$ (insolubles dans les conditions normales). Ces formes de zinc, principalement la dernière forme, il est souvent difficile d'extraire le zinc en solution par le procédé de double lixiviation. Il sera nécessaire de compléter l'extraction humide par un autre procédé tel que le procédé Jarosite, goethite ou hématite qui consiste à former un complexe de fer facilement filtrable.

La jarosite est une phase minérale, de formule $AFe_3(SO4)_2(OH)_6$ avec (A = K, Na, H_3O, NH_4, 1/2 Pb). Dans de nombreuses usines de production de zinc par voie hydrométallurgique, la jarosite est générée par ajout de sels (tels que Na_2SO_4 ou K_2SO_4 par exemple) afin d'éliminer le fer du filtrat riche en zinc. En plus du fer, la jarosite contient du zinc (4 à 6%) et du plomb (6 à 7%) ainsi que d'autres métaux (à l'état de traces) qui sont co-précipités. Afin de mener à bien ce travail, une démarche expérimentale a été mise en place.

Matériels et méthodes

. Matériaux et analyse

La ZLR utilisée dans cette étude a été obtenue à partir d'une usine hydrométallurgique de zinc à Ghazaouat, en Algérie. Les échantillons ont été séchés avant de broyer et tamiser pour obtenir les fractions requises. La composition des éléments du résidu a été déterminée par absorption volumétrique, atomique et spectrophotométrie. Les différents éléments trouvés sont résumés dans le tableau 1. Les phases cristallines des échantillons de poudre ont été étudiées par diffraction des rayons X. L'examen de la poudre naturelle

Creative Commons Attribution-NonCommercial-NoDerivatives 4.0 International License (CC BY-NC-ND)

montre que Franklinite, Anglesite, gypse et bianchite sont les principales phases minérales cristallines dans le résidu. Dans un deuxième temps nous avons analysé l'échantillon à une température de 500°C c'est à dire le calciné pour confirmer la présence de gypse. La réflexion principale du gypse disparait, une réflexion nouvelle apparait vers 3,504° qui pourrait être attribuée à la forme anhydre du sulfate de Zinc, la zincosité $ZnSO_4$.

La composition des éléments du résidu après le grillage a été déterminée par absorption volumétrique, atomique et spectrophotométrie. Les différents éléments trouvés sont résumés dans le tableau 2.

Éléments	Teneur (Wt. %)	Éléments	Teneur (Wt. %)	Éléments	Teneur (Wt. %)
Zn (Total)	**17.82**	**Cu**	**0.24**	**K**	**0.281**
$Zn(H_2O)$	**4.19**	**Ag**	**408.75**	**As**	**0.051**
$Zn(H_2SO_4)$	**8.33**	**Ni**	**0.014**	**Mg**	**1.02**
Fe	**20.82**	**Co**	**0.0032**	**Al**	**0.505**
Ca	**2.08**	**Mn**	**1.325**	**$Si(SiO_2)$**	**8.153**
Pb	**7.697**	**Tl**	**0.0026**	**S(ZnS)**	**1.15**
Cd	**0.177**	**Na**	**0.032**	**Cl**	**0.0078**

Table 1 Composition chimique des résidus

Éléments	Teneur (Wt.%)	Éléments	Teneur (Wt. %)	Éléments	Teneur (Wt. %)
Zn (Total)	**17.82**	**Cu**	**0.24**	**K**	**0.281**
$Zn(H_2O)$	**4.19**	**Ag**	**408.75**	**As**	**0.051**
$Zn(H_2SO_4)$	**8.33**	**Ni**	**0.014**	**Mg**	**1.02**
Fe	**20.82**	**Co**	**0.0032**	**Al**	**0.505**
Ca	**2.08**	**Mn**	**1.325**	**$Si(SiO_2)$**	**8.153**
Pb	**7.697**	**Tl**	**0.0026**	**S(ZnS)**	**1.15**
Cd	**0.177**	**Na**	**0.032**	**Cl**	**0.0078**

Table 2 Composition chimique des résidus après torréfaction

. Procédure expérimentale

Les résidus de lixiviation neutre sont traités avec de l'H_2SO_4 assez concentré à température élevée (95°C) de sorte que les ferrites de zinc se dissolvent. La concentration de cet acide doit être de 160 à 250 g/l, ce qui nous permet d'utiliser le retour cellule complète avec l'acide sulfurique concentré. A la fin du traitement est appelé lixiviation acide à chaud. Après cette opération on a une séparation solide liquide. Le solide contenant environ 15% de pb passe au stockage, la solution passe à la précipitation de Jarocité, ou le fer est précipité sélectivement sous forme de jarosité, à température élevée par ajout d'ions ammoniums selon l'équation suivante :

$$3Fe_2(SO_4)_3 + 2NH_4OH + 10H_2O \rightarrow (NH_4)_2[Fe_6(OH)_{12}(SO_4)_4] + 5H_2SO_4$$

Creative Commons Attribution-NonCommercial-NoDerivatives 4.0 International License (CC BY-NC-ND)

Pour ne pas contaminer la solution, on n'ajoute pas plus d'ions ammoniums que ce qui nécessaire pour la formation de la Jarosité.

L'acide sulfurique formé lors de la précipitation du fer, de plus l'acide sulfurique contenu dans la solution avant la précipitation rend la précipitation de la Jarosite très difficile, donc on est amené à ramener l'acidité du milieu à un pH de 1,5 à 2 par ajout de l'oxyde de zinc ou plutôt le grillé car le ZnO est trop cher. Le précipité de Jarosite obtenu contenant toutefois d'autres composés de zinc tels que le ZnO mis en excès qui n'à pas réagi au cours de la neutralisation et les ferrites de zinc, ce qui nous donne encore un résidu de zinc.

Durant toutes nos expériences, on a travaillé avec les réactifs suivants :

95% de H_2SO_4 avec une densité de 1,83, concentré de NH_4OH, HCl, NaClO, $CaCl_2$, Grillé, MnO2 et poudre d'aluminium.

L'équipement utilisé est un agitateur magnétique chauffant sur lequel on a reporté un bêcher d'un litre avec à l'intérieur un aimant permettant l'agitation et un thermomètre pour régler la température désirée.

L'échantillon avant d'être mis on solution il est pesé, une fois l'échantillon pesé, il subit une attaque dans un bécher par de l'acide sulfurique. L'agitation de l'échantillon se fait à l'aide d'un aiment et ceci afin de permettre une bonne mise en solution. La température est réglée à l'aide d'un thermomètre.

Le temps d'attaque est d'environ 4 heures. Ensuite la solution passe à la filtration, une fois filtrée la solution est neutralisé à l'aide du grillé avec un ajout d'une petite quantité de MnO_2 ou de $KMnO_4$ afin de permettre une bonne oxydation. Par ajout d'ions ammoniums, sodium ou potassium, le fer est précipité sous forme « jarosité ».

Après la précipitation du fer sous cette forme on le passe à la filtration, le précipité restant sur le filtre est soumis à un lavage à l'acide sulfurique à 40 g/l afin de récupérer le maximum de Zn. La solution obtenue est ensuite analysée pour connaitre la qualité de Zinc mis en solution.

Résultats et discussion

. Influence de la concentration

Dans le conduit de notre travail, nous avons été amené à choisir plusieurs concentrations afin de définir une concentration qui nous permet de récupérer le maximum de Zinc

Les concentrations d'H_2SO_4 étudiées sont 250, 240, 220 et 200g/l.

Dans un premier temps, on a fixé la température avec une agitation moyenne pendant un temps fixe.

Le principe d'attaque consiste à mettre en solution le maximum de Zinc.

Les résultats obtenus sont la moyenne de deux concentrations.

De fait de la forte teneur en fer présenté dans le résidu et qui représente l'effet principal de la perte en Zinc dans les résidus de lixiviation. Le fer est en combinaison avec le Zinc sous forme de ferrite de Zn ($ZnO.Fe_2O_3$).

Creative Commons Attribution-NonCommercial-NoDerivatives 4.0 International License (CC BY-NC-ND)

Algerian Journal of Engineering Architecture and Urbanism Vol. 5 Nr. 3 2021
ISSN: 2588-1760

De fait de tout cela nous avons déterminé aussi la quantité de fer en gramme par litre qui peut passer inévitablement dans la solution finale ou bien causée par une mauvaise précipitation de fer.

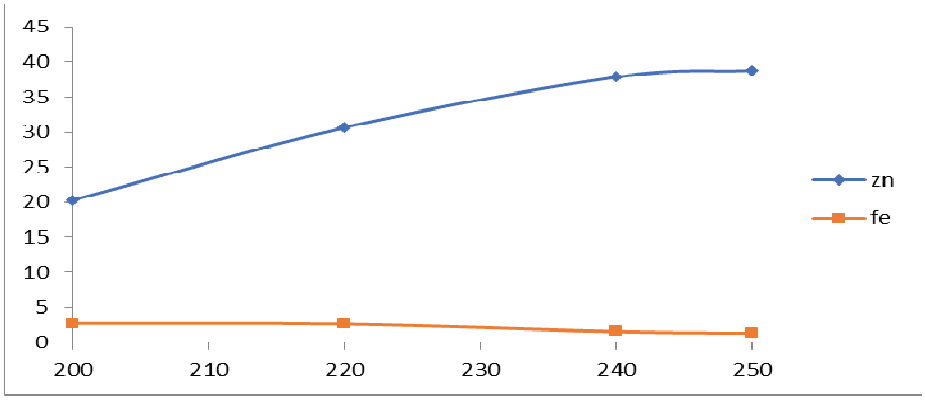

Figure 1 Influence de la concentration

Après les essais faisant varier la concentration de l'acide sulfurique et d'après les résultats obtenus, on a constaté qu'une concentration allant de 240 à 250 g/l permet d'obtenir une bonne dissolution de Zn.

La dissolution de Zn est presque la même pour les deux concentrations et pour des raisons économiques, on est décidé de fixer la concentration à 240g/l pour les essais qui suivent.

. Influence de la température

Après la détermination de la meilleure concentration avec laquelle on peut dissoudre le maximum de Zn, nous avons vairés la température en fixant le temps, la concentration est fixée à 240g/l.

La variation de la température permet de définir la meilleure température avec laquelle on peut obtenir une dissolution maximum de Zinc sans que le matériau utilisé ne soit épuisé.

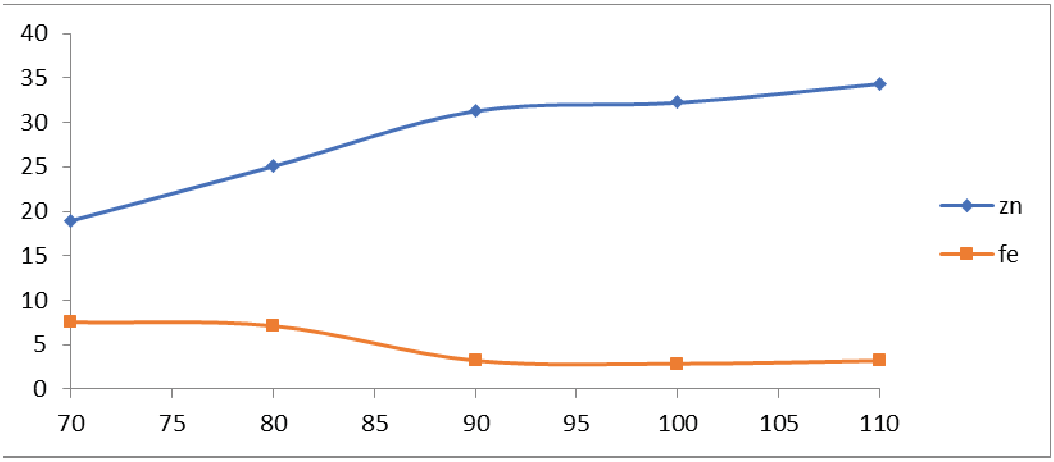

Figure 2 Influence de la température

Creative Commons Attribution-NonCommercial-NoDerivatives 4.0 International License (CC BY-NC-ND)

En faisant varier la température, on Remarque que plus la température est en croissance et plus on a une forte dissolution de Zn.

De fait de la grande énergie qu'il faut fournir pour augmenter la température, il est préférable de prendre une température allant de 90 à 95°C. En effet, prendre une telle température exige l'emploi d'un matériel qui doit résister à ces températures.

La teneur en zinc de la solution à la fin de l'opération est de 34.37g / l.

. Influence du temps par une attaque à chaud

Après avoir déterminé la meilleure concentration et la meilleure température avec lesquels on peut obtenir une bonne dissolution des ferrites de zinc et donc une forte teneur en Zn qui passe en solution, on est amené à étudier un troisième paramètre qui présente lui aussi une grande importance

Le temps est un facteur primordial pour la dissolution des ferrites de zinc. De fait du temps très court qui nous à été donné on a pu travailler qu'avec quatre temps différents.

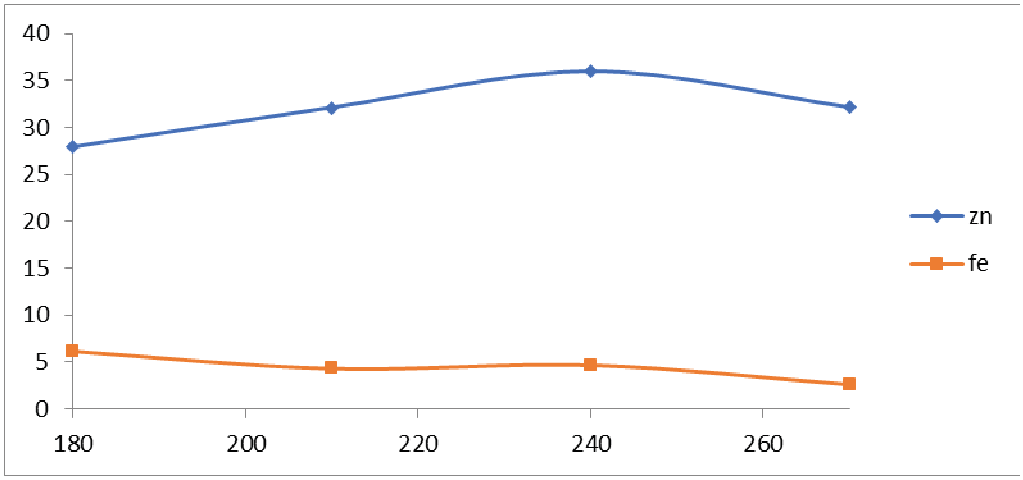

Figure 3 Influence du temps par une attaque à chaud

D'après les résultats obtenus, on constate que le temps nécessaire pour obtenir une dissociation maximum des ferrites de zinc est compris entre 3H30 et 4h. Cela nous permet de choisir un temps minimum avec un dissolution maximale de Zn.

. Influence du temps par une attaque à froid

Comme il à été signalé, le temps est un facteur essential pour le bon déroulement d'une telle expérience. Pour mieux connaitre le rôle du temps seul et à froid pour la récupération du zinc à partir des résidus de lixiviation, on a été intéressé par la variation du temps ou tout simplement l'influence de l'agitation à froid sur la dissociation des ferrites de zinc.

Creative Commons Attribution-NonCommercial-NoDerivatives 4.0 International License (CC BY-NC-ND)

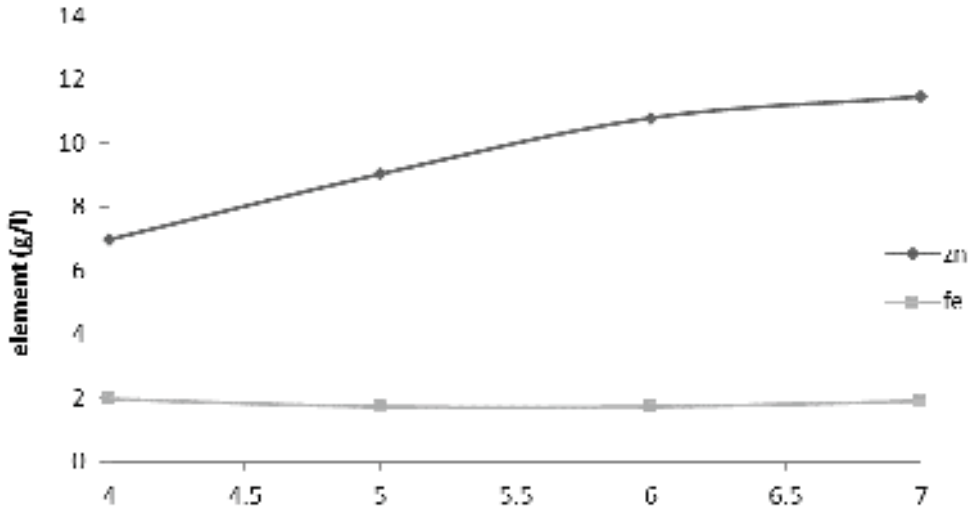

Figure 4 Influence du temps par une attaque à froid

En jouant sur l'agitation à froid on a constaté que même si on laisse l'échantillon plusieurs heures, le taux de dissociation n'est pas très intéressé. En effectuant nos expériences on a remarqué aussi que lorsqu'on ajoute l'ammoniaque pour précipiter le fer, la précipitation de fer ne se fait pas ou quelque fois on observe la précipitation de fer que dans un milieu basique. Cela nous permet de constater que le zinc qui passe en solution n'est que le Zn sous forme d'oxyde (ZnO) ou (ZnSO4), mais le Zn se trouvant sous forme de ferrites ne passe en solution qu'en petite quantité.

. Schéma de la lixiviation proposée

Après l'étude expérimentale qui a donné des résultats encourageants, il est nécessaire d'incorporer le procède dit à la jarosite dans le circuit de lixiviation tout en évitant de grandes modifications.

Pour cela on a proposé le schéma suivant :

Après la première étape dite lixiviation neutre, la solution ou l'overflow passent à la lixiviation acide à chaud, l'inderflow contenant surtout le Pb et Ag passe au stockage.

L'overflow de la lixiviation acide à chaud passe à la précipitation de la jarosite par ajout d'ions ammonium ou sodium. La pulpe formée est retournée à la tête de la lixiviation neutre.

Cependant les solides venant de la précipitation jarosite entrent dans l'étape de la lixiviation acide à chaud avec l'inderflow neutre.

. Avantages d'un tel procédé

La pulpe de la précipitation jarosite contenant le zinc sous forme de ferrites ou d'oxyde mis en excès lors de la neutralisation est recyclé et donc on peut récupérer le zinc lors de la lixiviation acide à chaud.

Il permet aussi d'avenir un seul résidu

Le résidu obtenu peut contenir beaucoup de Pb et d'Ag qui peuvent être récupérer.

Creative Commons Attribution-NonCommercial-NoDerivatives 4.0 International License (CC BY-NC-ND)

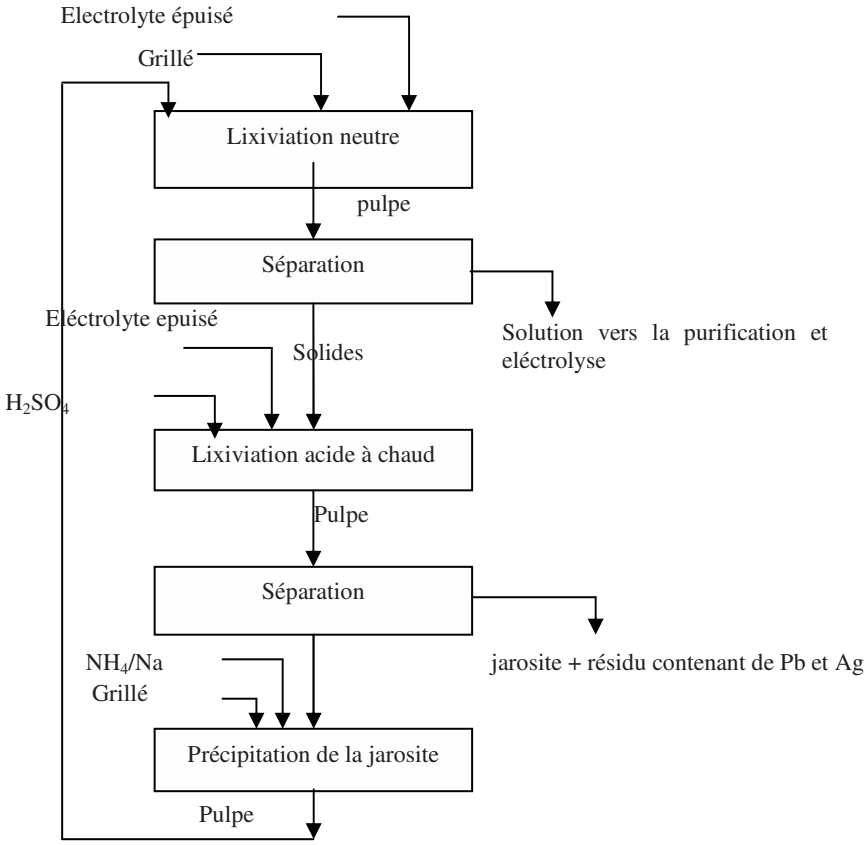

Figure 5 Schéma de la lixiviation proposée

Récupération de l'Ag à partir des résidus

Pour mettre en solution directe l'Ag sans être gêné par les chlorure et sulfures liée à l'Ag, on choisit un milieu de lixiviation chargé en chlorure de calcium acidulé par HCl, Ce milieu permet de dissoudre de nombreux élément dont le Fe, le Zn, le Pb et l'Ag tous ces métaux forment des complexes en milieu chlorure.

Le résidu est attaqué dans un milieu chlorure avec ajout de l'acide chlorhydrique et NaclO. L'attaque se fait à chaud PH=2.

Avant d'ajout la poudre d'Al on ajout e de la poudre de Fe afin de réduire le fer trivalent en fer dévalant pour permettre une bonne décantation du cément d'Ag;

Après des analyses , nous remarquant qu'une quantité d'Ag reste en solution et elle n'est pas cémenté et ceci est l'invitable . Ceci qui nous permet de dire qu'avec la quantité d'Ag se trouvant dans le résidus et qui dépasse rarement les 400g/l que la récupération n'est pas intéressante.

Creative Commons Attribution-NonCommercial-NoDerivatives 4.0 International License (CC BY-NC-ND)

Conclusion

Les résultats de notre étude sur la récupération du zinc à partir des résidus de lixiviation sont encourageants.

Ces résultats ont été obtenus par un procédé dit de la jorasite " lixiviation acide à chaud pendant un temps donné, suivi d'une filtration, le filtrat passe à la précipitation du fer comme Jarosite"

En premier lieu, nous remarquons que plus nous augmentant la concentration de l'acide et plus La dissolution du zinc augmente. Ceci s'explique par le fait que les ferrites de zinc se dissocient à une forte concentration.

En faisant varier la température on remarque que plus on augmente la température, plus la dissolution du zinc augmente.

De ce fait il est nécessaire de travailler à une température convenable.

La variation du temps permet aussi de déterminer le meilleur temps avec lequel on a une grande dissolution du zinc.

Nous sommes persuadés qu'avec un tel procédé et dans les conditions de travail suivantes:

• L'acide concentre 240 g / l.
• La température allant de 90 à 95 ° c.
• Avec un temps compris entre 3h30 et 4h.

On peut obtenir une très bonne dissolution de Zn et donc un bon rendement d'extraction.

L'intégration d'un tel procédé dans le circuit de lixiviation de l'unité d'électrolyse de Ghazaouat est donc possible tout en évitant de grandes modifications.

Concernant la récupération d'Ag, nous faisons remarquer qu'il est pour le moment difficile d'arrivé à des résultats signifiant de ceci du essentielles à la quantité d'Ag continu dans les résidus et qui dépasse rarement les 400g/l .

References:

Abdelhakim Begar , M. Djeghlal , M. Ould Hamou, Study of the reaction of dissolution of Sphalerite in the absence of oxygen. Russian Journal of Non-Ferrous Metals, Sep 2015.

Bjorling, G. Lixiviation of sulphidic minerals under oxygen pressure. Metallurgie 8, 781–784.(1954).

Forward f.a. veltman h. A process for direct leaching Zinc sulfide concentrates with sulfuric acid and oxygen under pressure. Intrn. Sympos. On the Phys,

Forward, F.A., Veltman, H. Direct leaching of zinc sulphide concentrate by Sherrit Gordon. J. Met. 11,836– 840 (1959).

Creative Commons Attribution-NonCommercial-NoDerivatives 4.0 International License (CC BY-NC-ND)

Havlik, T., Kammel, R. Procedure for selective copperrecovery from tetraedrite. Metall 54, 26– 29.(2000).

Havlik, T., Miškufová, A., Tatarka, P. Modern methods of oxidative chalcopyrite leaching. Acta Metall.

Majima, H., Awakaura, Y., Misaki, N. A kinetic study on nonoxidative dissolution of Sphalerite in aqueous hydrochloric acid solution. Metall. Trans. 12B, 645–649.(1981).

Mizoguchi, T., Habashi, F. The aqueous oxidation of complex sulfide concentrates in hydrochloric acid. Int. J. Miner. Process. 8, 177– 193.(1981).

Parker, E.G. Oxidative pressure leaching of zinc concentrate. CIM Bull. 74 (5), 145– 150. (1961).

Pawlek, f. And Pietsch, h. Erzmetall, 10 (1957), 373/83.(pawlek, f. And pietsch, h., z. Für erzbergbau und metalhuttenwesen. 1957 10, 373 anwendung des

Von discher e. Pawlek f. Drucklaugung von sulfidischen Erze. Z. Für Erzbergbau und Metalhuttenwesen 10.373-83(1957)

Creative Commons Attribution-NonCommercial-NoDerivatives 4.0 International License (CC BY-NC-ND)

Algerian Journal of Engineering Architecture and Urbanism Vol. 5 Nr. 3 2021
ISSN: 2588-1760

Machine Learning for Optimization of Flow-Rack AS/RS Performances

Zakarya AMARA
Phd Student, Manufacturing Engineering Laboratory of Tlemcen, Tlemcen University, Algeria, e-mail: zakarya.amara@univ-tlemcen.dz

Latefa GHOMRI
Lecturer, Manufacturing Engineering Laboratory of Tlemcen, Tlemcen University, Algeria, e-mail: latefa.ghomri@univ-tlemcen.dz

Ali RIMOUCHE
Teaching Assistant, Dynamic Systems and Applications Laboratory, Tlemcen University, Algeria, e-mail: ali.rimouche@univ-tlemcen.dz

Abstract:
In this paper we are interested in flow rack automated storage/retrieval systems, which are multi-deep automated storage/retrieval systems. For this type of systems, we have used a machine learning method to store the loads inside the system so that their retrieval time is optimal. In order to be able to predict the total times of retrieval and the best location, three methods were used: The Decision Tree, Multi-variable Linear Regression and Multi-variable Polynomial Regression, which gave us very satisfactory results. This can be used as a comparison basis to later work in this area.

Key words: Flow rack AS/RS, Retrieval time prediction, Supervised machine learning, Regression, classification

Introduction:

Automated storage/retrieval systems (AS/RS) are widely used in manufacturing systems for storing raw materials, tools, work in process, finished products, etc. They mainly combine two parts: automatic operational equipment, used to carry, store and retrieve materials, and a control system whose main characteristics are the high precision and the high speed. AS/RS are actually attracting much attention in modern manufacturing thanks to their numerous advantages, namely low labour cost, low storage cost, best space exploitation and high throughput. In the basic shapes of AS/RS, each cell is used for the storage of only one load. This class, called unit-deep AS/RS, is the most studied in literature.

Industrial engineering has many objectives, one of which is the improvement of the performance of industrial processes: Scheduling tasks, optimizing spaces in warehouses, automating storage and retrieval systems… Many researches have been conducted up to date in order to come up with better results. (Sari, 2003) used modern techniques like computer simulations in order to develop travel-time expressions for flow-rack AS/RS. In another paper, (Bessenouci et al., 2012) decided to use tabu search and simulated annealing, two known Metaheuristics algorithms, in order to minimize retrieval cycle times by controlling the retrieval machine of the AS/RS. In a paper written by (Chen et al., 2016), the objective was to minimize travel time of operations in a flow-rack AS/RS, and in order to achieve that, the two-step heuristic “group-matching” was used. In a comparative study, (Meghelli-Gaouar and

Creative Commons Attribution-NonCommercial-NoDerivatives 4.0 International License (CC BY-NC-ND)

Sari, n.d.) assessed the performance of a heuristic using a simulation between three types of storages (a handpicked storage, a class-based storage and a random storage); and (Cardin et al., 2012) presented the In-Deep Class Storage for Flow-Rack AS/RS and evaluated its performance through a simulation study. Researchers and engineers have been using these methods to get better performances and assessment techniques, and now with the emergence of Machine Learning and its applicability in the different fields, it is an opportunity for the industrial engineering field to develop even better models and techniques to solve many (Kim et al., 2018) of its problems; (Wuest et al., 2014) presented a ML-based approach to monitor quality in a manufacturing system using Cluster Analysis and Supervised Machine Learning. (Park et al., 2015) studied the consumption of energy in a milling machine, and came up with a ML-powered model to predict the effects of machining parameters on energy consumption using Gaussian Process. (Jurkovic et al., 2018) compared multiple ML methods used in high-speed turning processes, like the polynomial regression, SVR (support vector regression) and ANN (artificial neural network); the study showed that the polynomial regression outperformed the other two methods. In this paper, the objective is to minimize the average retrieval time of a multi-deep AS/RS, in this case we consider the flow-rack AS/RS, using methods and algorithms developed through many years of research and breakthroughs in the Machine Learning field.

This paper is organized as follows: In section 2 notions about machine learning are presented. In section 3, we present a description of flow rack AS/RS. The software we have used for experiments (Python Jupyter) is presented in section 4. Method of this study is presented in section 5. The results of this study are summarized in section 6.

Machine learning:

In order to understand what machine learning is as a term used in journals and articles, we need to look at its two parts 'Machine' and 'Learning' individually:

- Defining the learning process may prove to be a very difficult task, just like the definition of intelligence, which is the end-product of learning, is. The simplest definition one can find for learning in its broader meaning would be "*the acquisition of knowledge or skills through study, experience, or being taught*" (*Dictionary of Harvard*, n.d.);
- Whereas a machine could be defined as a mechanical system, apparatus, structure, device. That transforms a power source into an action mechanical or otherwise. Computers are also considered machines alongside sensors… These systems have inputs, outputs and functions that work cohesively in order to produce the desired effect (main function(s)) of the machine.

Machine learning, taken as a whole term, is one of Artificial Intelligence's main subsets and aims to give the ability of learning to computer systems by using predefined data, examples and even experience that helps these systems "predict" and "make decisions". The whole process of "learning" is repetitive, just like for humans and animals; with each new chunk of correct information, the machine becomes better at predicting with better performance; for example, we say that a ML-powered text-recognition software is learning when it becomes better and faster at recognizing texts; The main and innovative difference between ML-powered machines (and software) and the conventional solutions is that the latter use pre-programmed algorithms to perform tasks, whereas the former is self-dependent, much like a human being.

Machine learning is highly used when the problems, or task require an unconventional way of solving them, like recognition, diagnosis, planning, robot control, prediction, etc (Nilsson, 1998).

Creative Commons Attribution-NonCommercial-NoDerivatives 4.0 International License (CC BY-NC-ND)

With more research and groundbreaking solutions relating to this field, Machine Learning has become one of the most powerful tools in the different fields where it can be applied (IT, medicine, business, security and cybersecurity, …); It is noteworthy that the more advances there are in the field of computers (more powerful GPUs, CPUs and APUs coming out every couple of months), the performance of ML algorithms grows exponentially; as a result, newer systems that are reliant on Machine Learning can nowadays perform even better than humans in tasks where they didn't have much use in the past (Royal Society (Great Britain), 2017).
In a very similar way that people learn new things, either formally by going to a specialized institution or by using the different available ways for self-education (online courses and documentations…), machines have the same options depending on the algorithms they use in order to learn; Consequently, Machine learning algorithms can be divided into three major categories, each with its own purpose:

Supervised learning:

In order to understand supervised learning better, the following analogy can be used: in the same way kids are taught in elementary schools especially in their earliest years, where teachers have to be present at every level of the kids' education in order to give them examples, make sure they get the answers right and to validate those answers, the children will then memorize and learn to derive the correct answers on their own; when a machine learning algorithm needs to be supervised and its results validated by humans, then we are talking about "supervised learning"; But what does it mean and how does it work technically?
It is imperative to know what datasets are before diving deeper into the machine learning processes. Simply put, datasets are "collections of data, examples, information..." used to train models, which are usually files containing previous results that are the product of applying a ML algorithm over the training dataset. By using those models, a ML algorithm can have a performance boost, giving much better predictions and making more accurate decisions. In the case of supervised learning, these datasets are associated to "correct" answers and responses, technically representing the "behavior/result" desired by the supervisor;
The supervisors will prepare target answers that can be of any type (qualitative or quantitative; like numbers, weights, colors, labels, classes, ... (Mueller & Massaron, 2016)) and present them as datasets to the system they want to "teach"; the system will then use these labelled examples to learn how the different data points are connected and structured ; at this point, we say that a model has been trained; this model will then be used by the system to predict results of new given inputs (Royal Society (Great Britain), 2017);

Supervised Learning Using Classification:

Just as the name suggests, classification translates to putting sets of information in categories; the categories are usually decided upon attributes that these data points have in common. For example, we have to classify objects according to their color; in this instance, the colors represent the categories and could be white, black, red, blue, etc. The minimum number of classes required is 2 with no maximum bounds (Bishop, 2006).
The type of data in this case is discrete (Royal Society (Great Britain), 2017). This is an important piece of information and needs to be considered before training a model and putting to work in real applications like objects/features recognition, medical applications, face recognition, etc.

Decision Trees for Classification:

A decision tree is a graphical structure that looks like a flowchart and has nodes and branches.

Creative Commons Attribution-NonCommercial-NoDerivatives 4.0 International License (CC BY-NC-ND)

It is used for mapping information and is a very important tool in many fields including business, mathematics, safety operations, AI… The different nodes represent "tests" (for example, we observe whether a coin toss results in heads or tails) and the outcome of the test is represented by the branch (es) that follow(s).

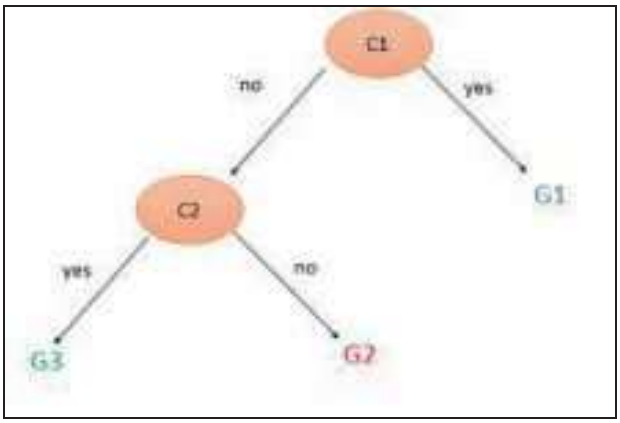

Fig1. Examples of decision trees

Each outcome can also be called a class (aka: leaf node), resulting from a test that precedes it; for example, the node C2 in the following figure (Nilsson, 1998) is a result of C1 (Fig1), and it has two outputs one that represents the class G3 and G2.
If the input patterns are tested for one and only one feature (like color), then they are called univariate tests; whereas more features (weights, shapes, color intensity, etc.) mean that the tests are multivariate. These features can be quantitative or qualitative. Also, depending on the number of outcomes, the complexity of the tree and the algorithms that use it may increase since there could be as little as two outcomes with no upper limit whatsoever In case all the tests have only two outputs, the decision tree is called "a binary tree"(Nilsson, 1998).

Supervised Learning Using Regression:
while classification is used for data that is essentially discrete, input data that can be classified as "continuous" is dealt with by Regression analysis. This kind of analysis is actually used in predicting stocks and market changes, sales and revenue, etc.

Linear Regression:
Out of the three known regression methods, linear regression is considered the least complex, where the variable in question is of a continuous nature (Royal Society (Great Britain), 2017). Here are some key points about this kind of regression: the part "linear" comes from the relationship that the decision variable has with the independent variables ; there is a binding rule that independent variables should not be arbitrary and must be measured flawlessly (no tolerance for error) (Sinha, 2013) ; the residual value (which is the vertical line connection each point to the regression line) should be constant and must not correlate throughout all observations, and these values must identify as a normal distribution.

Depending on the number of the independent variables, we can divide Linear Regression to two major categories, which are:

- **Simple Linear Regression** when one variable that is dependent and another that is independent;

Creative Commons Attribution-NonCommercial-NoDerivatives 4.0 International License (CC BY-NC-ND)

- **Multiple Linear Regression** when one variable that is dependent and there are more than one independent variables;

Non-Linear Regression:

If the equation is not linear, then the classic linear regression method wouldn't help to predict new values and estimates; in this case, the polynomial regression methods and models are used to fit the curves of the nonlinear equation by determining the polynomial functions of the independent variable, one by one (Sinha, 2013).

The equations in this type of regression have independent variables to a power of 2 or more, for instance y = a+b*x^2 is a polynomial equation, and because of that it cannot be represented by a line but rather by a curve (Sinha, 2013).

When fitting a polynomial equation, it is considered a bad practice to go overboard with this method. The objective is to find the best way to explain the phenomenon at hand using statistics while minimizing errors; The higher the degree of the polynomial, the harder it is to find the best curve to fit its equation, so it is best to try and understand the nature of the problem before applying the method arbitrarily.

Unsupervised Learning:

Contrary to the ones that rely on supervised learning, algorithms that are based on unsupervised learning use models trained by datasets with examples that aren't associated with any response; meaning that in this case, systems will have to learn without relying on labels and they will have to determine whether the different pieces of information within a dataset follow specific patterns with no human judgement to rely on (Mueller & Massaron, 2016). An interesting aspect of this kind of algorithms is that more often than not, they find links and relations between the provided datasets that prove to be very useful in training better models for the supervised machine learning algorithms.

Rather than explicitly "learning", systems powered by unsupervised learning algorithms try to "figure out" the patterns as they take in new data from the dataset; In order to make this work, the algorithm tries to find features, characteristics or classes that the data points may have in common (similarities) by assigning them to clusters and groups, rather than analyzing each point individually (Royal Society (Great Britain), 2017)

Reinforcement learning:

This type is very similar to unsupervised learning, where the algorithm is provided with datasets and examples with no labels to determine the right outputs. The difference in reinforcement learning is that feedback can be given every time the algorithm comes with a response. The algorithm learns by trial and error, and works on improving the quality of its answers by aiming for better feedback (Mueller & Massaron, 2016); it's very similar to a human being learning from experience. In this case, the algorithm tries to maximize the objective function and is given a penalty every time it fails to give a good response (through positive/negative feedback); The best analogy maybe a game where the player wins on getting the highest score: in order to get to that goal, the player may choose the trial and error approach to find the best way to beat the game (Royal Society (Great Britain), 2017).

Flow Rack AS/RS:

It is an AS/RS that comes with a gravity conveyor (GC) (Fig2). It has one long and profound rack with numerous bins on its sides. Each bin is equipped with a GC. There are multiple

Creative Commons Attribution-NonCommercial-NoDerivatives 4.0 International License (CC BY-NC-ND)

locations for the bin, and each location is used to store a single product. The system can store products thanks to a machine located on one side of the rack (the front side) as it can retrieve products via a machine installed on the other side of the rack (the rear side). The two sides of the rack are associated by a reestablishing conveyor slanted the other way of the racks. Products are put away by the storage machine and move (slide) along the gravity conveyor until they arrive at the first empty location of the bin (Kouloughli et al., 2017).

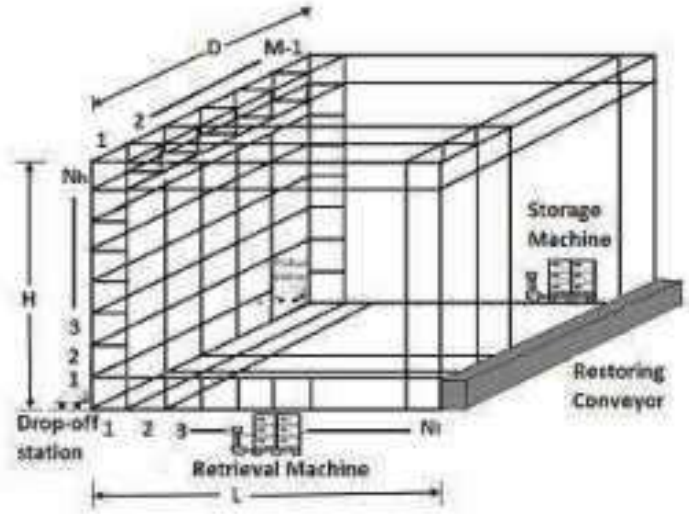

Fig2. Configuration and components of an AS/RS with a gravity conveyor

The method of destocking in AS/RS:

The exiting station is on the left corner and, the restocking conveyor will be on the right corner, the retrieval machine will be in an initial position (center, corner...).

When a part is to be retrieved, the machine will search for the location of the requested part at the end of the range up to the exit point.

But when there are other parts in front of the requested part, the machine will automatically free the space by bringing the other parts at the same time to the restocking conveyor in order to reach the requested part.

$$Etd + Etr = Etotal \quad (1)$$

Etotal: Total retrieval time.
Etd: Direct retrieval time.
Etr: Restocking time.

Python Jupyter:

The open-source application Jupyter Notebook allows the creation and the sharing of code, equations, visualizations and narrative text. This software can be used in: data cleaning and transformation, numerical simulation, statistical modeling, data visualization, machine learning, and much more (Kluyver et al., 2016).

Methodology :

Our goal is to develop a program to predict the empty location that has a minimum total retrieval time, steps to be taken from several stages.

Creative Commons Attribution-NonCommercial-NoDerivatives 4.0 International License (CC BY-NC-ND)

In the first step, we taught the system a model classification using the decision tree, so that we could estimate our data from this classification; in the second step, we also taught the system a method of calculating the direct retrieval time without counting the restocking time, then we predicted the direct retrieval time of the group that has a restocking action (from the total time and the retrieval time, we determine the restocking time); the third model predicts the restocking time.
The system, after the learning process, will be able to show us the empty location, predict the total time of retrieval and will provide us with a better choice of location.
In the following, we will present the piece of code written in Python Jupyter after each step.

Date Collection:

We use the data of an AS / RS with gravity conveyor, containing 2 types of products, number of the layer is 10, number of the bins horizontally is 2, number of the bins vertically is 2 and initial fill rate of the rack is 75%. Our system can learn from the provided data and we will achieve the same result.
This table (Fig3) represents a set of columns used to indicate the role of each column in relation to the data.

1. The first column represents the type of product (piece), where (0) represents an empty location.
2. (x), represents the number of the layer (location) in the AS/RS.
3. (y), shows the number of the bin horizontally.
4. (z), tells us the bin number vertically.
5. (Label), informs us the time of retrieval of a certain piece if there was one.
6. (M), represents the number of different articles in front of the article.
7. (G), represents the group of each location.

Our data was put into a table in Excel, to be imported into our Python Jupyter program, then we made the table description (Fig4).

```
import NumPy as np
import pandas as p
d = p.read_excel("C:/Users/amara/Desktop/asrs3.xlsx")
print(d)
d.describe()
```

Creative Commons Attribution-NonCommercial-NoDerivatives 4.0 International License (CC BY-NC-ND)

	type	x	y	z	label	G
0	1	1	1	1	1.5	2
1	1	2	1	1	1.5	2
2	1	3	1	1	1.5	2
3	2	4	1	1	13.5	3
4	1	5	1	1	5.5	3
5	2	6	1	1	17.5	3
6	2	7	1	1	17.5	3
7	1	8	1	1	13.5	3
8	1	9	1	1	13.5	3
9	0	10	1	1	0.0	1
10	2	1	2	1	2.5	2
11	1	2	2	1	8.5	3
12	2	3	2	1	8.5	3
13	2	4	2	1	8.5	3
14	2	5	2	1	8.5	3

Fig3. The data

	type	x	y	z	label	G
count	40.00000	40.000000	40.00000	40.00000	40.000000	40.000000
mean	1.07500	5.500000	1.50000	1.50000	7.012500	2.250000
std	0.79703	2.908872	0.50637	0.50637	7.653127	0.869718
min	0.00000	1.000000	1.00000	1.00000	0.000000	1.000000
25%	0.00000	3.000000	1.00000	1.00000	0.000000	1.000000
50%	1.00000	5.500000	1.50000	1.50000	5.000000	3.000000
75%	2.00000	8.000000	2.00000	2.00000	11.500000	3.000000
max	2.00000	10.000000	2.00000	2.00000	26.500000	3.000000

Fig4. The description of the data

Before the training phase, we created an M vector which contains the number of pieces to be restocked in each location, then we added it to our data.

Part1:

In this part, the model will learn how to classify our data set into 3 groups:

a. Group 1 (G1): contains the empty slots.
b. Group 2 (G2): contains the parts that will be directly retrieved in order.
c. Group 3 (G3): where a two-step operation takes place, the first one of restocking, the second one of retrieval.

1.The input matrix and the vector (G): we selected the inputs (Fig5) and the vector (G) to have a classification method from our data.

```
xt1 = d.drop(['G'],axis=1)
```

Creative Commons Attribution-NonCommercial-NoDerivatives 4.0 International License (CC BY-NC-ND)

```
yt1= d['G']
```

	type	x	y	z	label	M
0	1	1	1	1	1.5	0
1	1	2	1	1	1.5	0
2	1	3	1	1	1.5	0
3	2	4	1	1	13.5	3
4	1	5	1	1	5.5	1
5	2	6	1	1	17.5	4
6	2	7	1	1	17.5	4
7	1	8	1	1	13.5	3
8	1	9	1	1	13.5	3
9	0	10	1	1	0.0	0
10	2	1	2	1	2.5	0

Fig5. Features

2.To estimate the dataset, we divided our data in two parts in a random way, 80% for the training, and the other 20% for the test.

```
from sklearn.model_selection import train_test_split
x_trains,x_test,y_trains,y_test=train_test_split(xd1,yt1,
test_size = 0.8 )
```

3.Decision tree: this method was applied from the training to arrive at a classification.

```
clf=tree.DecisionTreeClassifier()
clf = clf.fit(x_trains, y_trains)
```

To finalize this part, we must divide our data from the classification into three groups.

Part2:

In this part the model will learn how to calculate the DIRECT retrieval time from group 2 (obtained from Classification results).

1.Group 2 data: in this exercise (Fig6), we will eliminate the column of the group (G).

Creative Commons Attribution-NonCommercial-NoDerivatives 4.0 International License (CC BY-NC-ND)

	type	x	y	z	label	M
0	1	1	1	1	1.5	0
1	1	2	1	1	1.5	0
2	1	3	1	1	1.5	0
10	2	1	2	1	2.5	0
20	2	1	1	2	2.5	0
21	2	2	1	2	2.5	0

Fig6. Data from Group 2

2.The matrix of inputs and the vector (label) of group 2: we selected the inputs (Fig7) and the vector (label) to have a method of calculation from our data.

	type	x	y	z	M
0	1	1	1	1	0
1	1	2	1	1	0
2	1	3	1	1	0
10	2	1	2	1	0
20	2	1	1	2	0
21	2	2	1	2	0

Fig7. Features of group 2

3.To estimate the dataset, we divided our data in two parts in a random way, 80% for the training, and the other 20% for the test.

```
from sklearn.model_selection import train_test_split
x_trains,x_test,y_trains,y_test=train_test_split(xd1,yt1,
test_size = 0.8 )
```

4.Multi-variable linear regression: Since the nature of the resulting values is continuous (Royal Society (Great Britain), 2017), we decided to use Regression to predict retrieval times, and knowing that our model uses more than one variable for prediction (x, y, z, M, type), Multi-variable Regression was the best way for solving the equations (2), and following a step-by-step method to create a better model starting with the simplest form of linear Regression to more complex forms (non-linear), we chose our final model that is based on Multivariable Linear Regression. Given by:

$$\beta_0 + \beta_1 x + \beta_2 y + \beta_3 z + \beta_4 M + \beta_5 type = Label \qquad (2)$$

```
from sklearn import linear_model
from sklearn.metrics import confusion_matrix
regr = linear_model.LinearRegression()
```

Creative Commons Attribution-NonCommercial-NoDerivatives 4.0 International License (CC BY-NC-ND)

```
regr.fit(x_traind,y_traind)
print('Intercept: \n', regr.intercept_)
print('Coefficients:\n',regr.coef_)E1=regr.predict(d.drop(
['label',],axis=1))
```

Part3:

In this part, we will predict from the last model the time of retrieval of group 3 (Fig8) only (without counting the time of restocking).

```
E1 = regr.predict(d.drop(['label',],axis=1))
```

	type	x	y	z	label	E1	M
3	2	4	1	1	13.5	1.5	3
4	1	5	1	1	5.5	1.5	1
5	2	6	1	1	17.5	1.5	4
6	2	7	1	1	17.5	1.5	4
7	1	8	1	1	13.5	1.5	3

Fig8. Time of retrieval of group 3 only

Subtraction: we are going to subtract the retrieval time from the total time to have the restocking time.

```
d4['label'] = (d4['label'] - E3
```

Part4:

In this part, the model will learn how to calculate the restocking time from the group 3 data obtained from the Classification results.

1. Group 3 data (Fig9).

	y	z	label	M
3	1	1	12.0	3
4	1	1	4.0	1
5	1	1	16.0	4
6	1	1	16.0	4
7	1	1	12.0	3
8	1	1	12.0	3
11	2	1	6.0	1
12	2	1	6.0	1

Fig9. Data from group 3

Creative Commons Attribution-NonCommercial-NoDerivatives 4.0 International License (CC BY-NC-ND)

2. The matrix of inputs and the vector (label) of group 3: we selected the inputs (Fig10) and the vector (label) to have the method of calculating restocking time from our data.

	y	z	M
3	1	1	3
4	1	1	1
5	1	1	4
6	1	1	4
7	1	1	3
8	1	1	3
11	2	1	1

Fig10. Features of group 3

3. To estimate the data set we are going to divide our data in two parts in a random way, one for the training 80%, and the other for the test 20%.

```
from sklearn.model_selection import train_test_split
x_trains,x_test,y_trains,y_test=train_test_split(xd1,yt1,test_
size = 0.8 )
```

4.Multi-variable Polynomial Regression: We used the same way as in Part 2 to decide on which algorithm to use for this part. The only difference is that the Linear Regression didn't give us good results, which is why we trained and tested our model using Multivariable Polynomial Regression(3) (2nd degree) and obtained much better results.

$$\beta_0 + \beta_1 x + \beta_2 xy + \beta_0 xz + \beta_0 xM + \beta_0 x\hat{}2 + \beta_0 y + \beta_0 yz + \beta_0 yM + \beta_0 y\hat{}2 + \beta_0 z + \beta_0 xzM + \beta_0 z\hat{}2 + \beta_0 M + \beta_0 M\hat{}2 = Label \quad (3)$$

```
from sklearn.preprocessing import PolynomialFeatures
poly = PolynomialFeatures(2)
xpoly = poly.fit_transform(x_trains)
poly.fit(xpoly,y_trains)
```

Results:

We tested the system with new data from a larger AS/RS, the configuration was always the same, the positioning of the retrieving machine and the restoring conveyor have not been changed.

Decision tree:

After training our model (the decision tree), we performed an evaluation test.

Creative Commons Attribution-NonCommercial-NoDerivatives 4.0 International License (CC BY-NC-ND)

```
from sklearn.metrics import accuracy_score
accuracy_score(y_test,clf.predict(x_test))
```

We got:
Accuracy = 1. (100% correct)

Multi-variable linear regression model:

After training our model (multivariate linear regression), it gave us the following coefficients (Fig11).

```
Intercept:
 [-0.5]
Coefficients:
 [[7.23131496e-16 1.99840144e-15 1.00000000e+00 1.00000000e+00
  0.00000000e+00]]
```

Fig11. The coefficients of the model

This model has been evaluated with:

```
ypred = regr.predict(x_test)
from sklearn.metrics import r2_score
r2_score(y_test, ypred)
```

From the following equation:

$$R^2 = 1 - U/V$$

$$U = ((y\_test - y\_pred) \wedge 2).sum()$$

$$V = ((y\_test - y\_test.mean()) \wedge 2).sum()$$

We got:
R^2 = 1. (100% correct)

Multi-variable linear polynomial model:

After training our model (Multi-variable polynomial regression), it gave us the following coefficients (Fig12).

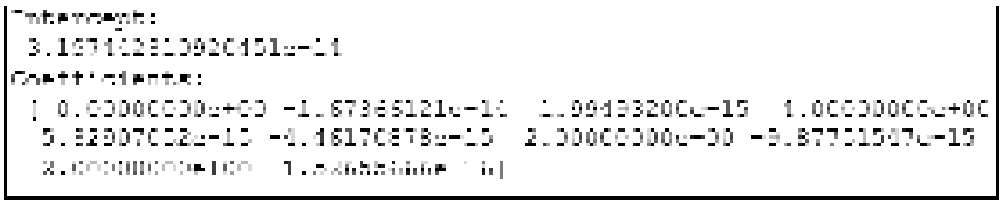

Fig12. The coefficients of our third model

This model has been evaluated with:

```
ypred2 = regr2.predict(poly.fit_transform(x_test))
```

Creative Commons Attribution-NonCommercial-NoDerivatives 4.0 International License (CC BY-NC-ND)

```
r2_score(y_test ,ypred2 )
```

We got:
R^2 = 1. (100% correct)

Conclusion:

In this work, we are interested in the optimization of the retrieval time of a flow rack AS/RS using a method of machine learning. Our approach was to build a database with an AS/RS of a fixed size and filled at multiple load rates. The goal is to teach the machine to choose the best location each time so that the retrieval time is optimal. We used three methods: the Decision Tree, Multi-variable Linear Regression and Multi-variable Polynomial Regression. Some of the data was spent on learning and the rest on testing. The sizes of AS/RS used in the test phase were varied and the result was 100% correct

References:

Bessenouci, H. N., Sari, Z., & Ghomri, L. (2012), *Metaheuristic based control of a flow rack automated storage retrieval system*, Journal of Intelligent Manufacturing, *23*(4), 1157–1166. https://doi.org/10.1007/s10845-010-0432-1

Bishop, C. M. (2006). *Pattern recognition and machine learning*. Springer.

Cardin, O., Castagna, P., Sari, Z., & Meghelli, N. (2012), *Performance evaluation of In-Deep Class Storage for Flow-Rack AS/RS*, International Journal of Production Research, *50*(23), 6775–6791. https://doi.org/10.1080/00207543.2011.624561

Chen, Z., Li, X., & Gupta, J. N. D. (2016), *Sequencing the storages and retrievals for flow-rack automated storage and retrieval systems with duration-of-stay storage policy*, International Journal of Production Research, *54*(4), 984–998. https://doi.org/10.1080/00207543.2015.1035816

Dictionary of harvard. (n.d.).

Jurkovic, Z., Cukor, G., Brezocnik, M., & Brajkovic, T. (2018), *A comparison of machine learning methods for cutting parameters prediction in high speed turning process,* Journal of Intelligent Manufacturing, *29*(8), 1683–1693. https://doi.org/10.1007/s10845-016-1206-1

Kim, D.-H., Kim, T. J. Y., Wang, X., Kim, M., Quan, Y.-J., Oh, J. W., Min, S.-H., Kim, H., Bhandari, B., Yang, I., & Ahn, S.-H. (2018), *Smart Machining Process Using Machine Learning: A Review and Perspective on Machining Industry,* International Journal of Precision Engineering and Manufacturing-Green Technology, *5*(4), 555–568. https://doi.org/10.1007/s40684-018-0057-y

Kluyver, T., Benjamin, R.-K., Fernando, P., Brian, G., Matthias, B., Jonathan, F., Kyle, K., Jessica, H., Jason, G., Sylvain, C., Paul, I., Dami{\'a}n, A., Safia, A., & Carol, W. (2016), *Positioning and Power in Academic Publishing: Players, Agents and Agendas* (F. Loizides and B. Schmidt).

Kouloughli, I., Castagna, P., & Sari, Z. (2017), *Reducing retrieval time in Automated Storage and Retrieval System with gravitational conveyor based on Multi-Agent Systems,* Journal of Applied and Computational Mechanics, Online First. https://doi.org/10.22055/jacm.2017.22183.1131

Meghelli-Gaouar, N., & Sari, Z. (2010), *Assessment of Performance of a Class-Based Storage in a Flow-Rack AS/RS*. 9.

Mueller, J., & Massaron, L. (2016), *Machine learning for dummies*. John Wiley & Sons, Inc.

Nilsson, N. J. (1998). *MLBOOK - INTRODUCTION TO MACHINE LEARNING*. https://www.coursehero.com/file/5996903/MLBOOK/

Park, J., Law, K. H., Bhinge, R., Biswas, N., Srinivasan, A., Dornfeld, D. A., Helu, M., & Rachuri, S. (2015), *A Generalized Data-Driven Energy Prediction Model With Uncertainty for a Milling Machine Tool Using Gaussian Process*, *Volume 2:* Materials; Biomanufacturing; Properties,

Creative Commons Attribution-NonCommercial-NoDerivatives 4.0 International License (CC BY-NC-ND)

Applications and Systems; Sustainable Manufacturing, V002T05A010. https://doi.org/10.1115/MSEC2015-9354

Royal Society (Great Britain). (2017), *Machine learning: The power and promise of computers that learn by example.*

Sari, Z. (2003), *MODELISATION, ANALYSE ET EVALUATION DES PERFORMANCES D'UN AS/RS A CONVOYEUR GRAVITATIONNEL.*

Sinha, P. (2013), *Multivariate Polynomial Regression in Data Mining: Methodology, Problems and Solutions*. *4*(12), 4.

Wuest, T., Irgens, C., & Thoben, K.-D. (2014), *An approach to monitoring quality in manufacturing using supervised machine learning on product state data*, Journal of Intelligent Manufacturing, *25*(5), 1167–1180. https://doi.org/10.1007/s10845-013-0761-y

Creative Commons Attribution-NonCommercial-NoDerivatives 4.0 International License (CC BY-NC-ND)

Algerian Journal of Engineering Architecture and Urbanism Vol. 5 Nr. 3 2021
ISSN: 2588-1760

MODELLING AND OPTIMIZATION OF A STAND-ALONE PV-DIESEL HYBRID SYSTEM WITH HYDROGEN STORAGE: CASE OF ALGERIA.

Adel MOKRANE
Ph.D Student, Laboratoire d'Automatique de Tlemcen, University of Tlemcen (LAT), Algeria, adeljc8@gmail.com

Abdellatif ZERGA
Professor, Pan African University Institute of Water and energy Sciences (PAUWES), University of Tlemcen, Algeria, abdellatif.zerga@gmail.com

Ismael JUMARE
Ph.D, Pan African University Institute of Water and energy Sciences (PAUWES), University of Tlemcen, Algeria, shehius61@yahoo.com

Abstract:
The aim of this study is to find the optimum system configuration of a hybrid power system that can supply electricity to a rural community in south of Algeria. A rural village from the region of Adrar containing 15 households is selected with a daily electricity demand of 145.44 kWh and a day-time peak of 39.80 kW. HOMER Pro. computer modeling software was used to model the power system. The hybrid system configuration has been found to be 21.7kW-PV, three 10kW-diesel genset, 20.0kW-electrolyzer and 380kg-hydrogen tank. The total Net Present Cost NPC of this hybrid power system was found to equal $823.744 and electricity can be supplied at an approximate cost of energy LCOE of 0.60 $/kWh.

Key words: PV, diesel generator, hydrogen, hybrid power system, HOMER Pro,

Introduction:

Algeria is the largest country in Africa, about 80% of its area is a desert or Sahara. Its geographic location has many advantages for massive use of most of renewable energy sources (solar and wind). The crucial economical changes, which have been experienced these last years on both levels national and international, have led Algeria to get on structural amendments that aim to adapt progressively to these changes especially in the energy sector (fossil and renewable energies) (Boudghene, 2007).

Photovoltaic (PV) generators, which convert the solar radiation directly into electricity, have a set of major advantages like being silent, inexhaustible, pollution free and size-independent electric conversion efficiency (Abou El-Maaty, 2005). PV generators are substituting electricity produced by fossil fuels thanks to their harmless environmental effect. However, PV power generation suffers from large variations in its output power due to weather conditions intermittency. Therefore, the nature fluctuation of the solar radiation imposes the use of purely PV power generators for off-grid applications in large scale. Although hydrogen is not a primary energy source like oil and gas, it has the ability to turn into one of the main energy carriers in the near future. In stand-alone hybrid power systems (Geovanni, 2010), PV systems and electrolysers can be combined with hydrogen storage and a diesel generator.

Creative Commons Attribution-NonCommercial-NoDerivatives 4.0 International License (CC BY-NC-ND)

Unlike batteries, which are considered as flexible and fast response back up storage but very costly, the diesel genset can generate electricity for limitless time to support the PV generator. Hence, combining all of the PV generator, the diesel generator and the hydrogen storage will assure a continuous supply of high quality power generation and an effective storage of energy in form of gas. The combination of the listed power sources is referred to as hybrid power system HPS.

The focus of this project is on modeling and designing a PV/diesel hybrid power system associated with hydrogen storage to fulfill the electricity demand of fifteen (15) households in Boukazine, Adrar in affordable, reliable and sustainable way with cost-effective solution.

Problematic:

According to the Renewable Energy and Energy Efficiency Partnership (REEEP), the average annual solar radiation ranges between 2,000 and 3,900 hours and an average solar energy of 6.57 kWh/m2/day. The German Space Center (DLR) assessed the potential power of 169,440 TWh/year and 13.9 TWh/year (Energy & Mines, 2007). Therefore, it is thought that solar has the greatest potential in Algeria. Unfortunately, this potential is not exploited. On the other hand, few solar energy projects were realized in the past few years. One example is the mini grid solar power plant, which has the capacity of 28 kW, was installed on the rooftop of a reaserch division in Wilaya of Adrar (Lydia, 2017).

In order to increase the exploitation of the solar energy potential in Algeria while mitigating the climate changes effect and reducing the toxic pollutants, the installation of hybrid systems represents an excellent option especially in remote areas where the national grid is not available. Coupling a PV generator with a diesel genset is one of the best combinations for night and day electricity generation. In most cases, PV systems electricity generation may lead to an excess. This excess can be stored in different forms using several technological storage systems. Hydrogen gas is one of these forms. Electricity can be converted to hydrogen gas by the use of an electrolyser and stored in hydrogen tank.

Materials and methods:

Currently, there are many state of the art software packages that are used for assisting in the dimensioning, optimization and financial analysis of renewable energy projects. Among these packages, there are HOMER, Hybrid2, RETScreen, PVSyst, INSEL, TRNSYS, Solargis and HYBRID DESIGNER (Costa, 2020). HOMER which stands for Hybrid Optimization of Multiple Energy Resources is a computational model developed by the United States National Renewable Energy Laboratory (NREL). It allows the simultaneous simulation of a higher number of non-renewable and renewable energy sources in the same project. It consists mainly of three steps: simulation, optimization and sensitivity analysis.

Technical modelling of the hybrid PV-diesel-hydrogen system

Creative Commons Attribution-NonCommercial-NoDerivatives 4.0 International License (CC BY-NC-ND)

Modelling of the PV generator

Due to the changing in the meteorological conditions, the output power of a PV module varies for different days in different seasons. In order to have better understanding of the PV system performance, sufficient information on the daily and seasonal pattern must be known before. The model that takes in into account the effect of both solar radiation and temperature is given by the following expression:

$$P_{PV} = Y_{PV} f_{PV} \frac{G_T}{G_{T,STC}} [1 + \alpha_p (T_c - T_{c,STC})] \quad (1)$$

Where, Y_{PV} is the nominal capacity of the photovoltaic module under standard test conditions (kW), f_{PV} is the photovoltaic energy reduction factor (%), G_T is the solar radiation incident on the photovoltaic panel in real conditions (kW/m^2), $G_{T,STC}$ is the incident irradiance under standard test conditions (1 kW/m^2), α_p is the temperature coefficient of power (%/˚C), T_C is the photovoltaic cell temperature in real conditions (˚C), $T_{C,STC}$ is the photovoltaic cell temperature under standard test conditions (25 ˚C).

Modelling of the diesel generator

The diesel generator fuel consumption depends on the generator size and the load at which it operates. The linear equation that gives the fuel consumption CC_{DG} in [units/h] vs. the output power P_{DG} in [kW] is described by the equation below (Weldemariam, 2010). The unit of the fuel consumption can be kg/h, l/h or m^3/h.

$$CC_{DG} = a_0 P_{DG} + b_0 PN_{DG} \quad (2)$$

Where, PN_{DG} the electrical output of the diesel generator (kW), a_0 and b_0 are coefficients of fuel consumption curve in [units/h*kW].

Modelling of the electrolyser

The alkaline electrolyser, which will be used in this work for hydrogen production, is the most widely used technology for water electrolysis. This type of electrolysers is advantageous; it can be made of abundant and inexpensive materials like nickel and iron. The cell voltage can be obtained as the sum of the overvoltages that appear in the cell and the reversible voltage V_{rev}.

$$V_{cell} = V_{rev} + V_{act} + V_{ohm} \quad (3)$$

Where, V_{act} is the activation overvoltage and V_{ohm} is the ohmic loss overvoltage.
Based on the chemical equation of electrolysis, a minimum electric voltage is applied to both electrodes of the electrolyser. This voltage is referred to as the reversible voltage and can be determined using Gibbs equation (Tijani, 2014):

$$\Delta G = zFV_{rev} \quad (4)$$

Creative Commons Attribution-NonCommercial-NoDerivatives 4.0 International License (CC BY-NC-ND)

Where, ΔG is the Gibbs energy, z is the number of electrons and F is the Faraday's Constant. At standard conditions, the Gibbs energy used for splitting water equals to 237.21 kJ.mol^{-1}, the Faraday's constant equals to 96485.37 C.mol^{-1} and z is just 2. Therefore, V_{rev} is found to be 1.229V.

The activation voltage V_{act} is produced due to the electrochemical kinematics of both the anode and the cathode during the simultaneous half-reactions.

$$V_{act} = s \log\left(\frac{t_1 + \frac{t_2}{T} + \frac{t_3}{T^2}}{A} I + 1\right) \quad (5)$$

Where: s, t_1, t_2, t_3 are the coefficient for overvoltage on electrodes, I is the current density, T is the cell temperature and A is the electrode area.
The ohmic loss overvoltage V_{ohm} can be reduced by shortening the distance between the cathode and the anode. It is proportional to the current that flows through the cell and it is given by:

$$V_{ohm} = \frac{r_1 + r_2 T}{A} I \quad (6)$$

Where: $r_1$and r_2 are the overpotential coefficients.

The hydrogen production rate inside the alkaline electrolyser is directly proportional to the electrical current I. It can be determined by the following equation (Ulleberg, 2003):

$$\dot{n}H_2 = \eta_F \frac{n_c I}{2F} \quad (7)$$

Where n_c is the number of cells inside the electrolyser, η_F is the Faraday's efficiency.

Economic modeling using HOMER PRO

Hybrid power system economics has an important role in simulation process in HOMER, in which the system is operated so as the total Net Present Cost NPC is minimized. In addition, the economics of HPS are used in the HOMER's optimization process, in which it looks for the system combination that has the lowest total NPC. The technical modeling of any HPS is insufficient. Economical issues are essential when selecting the final choice of the combination of components during the design (Lambert, 2006).

Modelling of the total Net Present Cost NPC

Total Net Present Cost is defined as the costs' present value minus the revenue' present value during the lifetime of the project. The costs, which are positive values, comprise capital costs, replacement costs, operating and maintenance costs (O&M), fuel costs, emissions penalties, and the cost of purchasing power from the grid. Revenues, which are negative, comprise salvage value and income from selling power to the grid.
The total NPC is the main economic output of HOMER; it is the value by which the system configurations are ranked in the optimization results. It is given by the equation below:

$$C_{NPC} = \frac{C_{ann,tot}}{CRF_{(i,R_{proj})}}$$

Creative Commons Attribution-NonCommercial-NoDerivatives 4.0 International License (CC BY-NC-ND)

(8)

Where, $C_{ann,tot}$ is the total annualized cost, CRF (i, $R_{proj)}$ is the Capital Recovery Factor. It is used to calculate the present value of an annuity (a series of equal annual cash flows) and is given by:

$$CRF(i,N) = \frac{i(1+i)^N}{i(1+i)^N - 1} \quad (9)$$

Where, N is the number of years, *i* is the annual real interest rate which is the discount rate used for converting between one-time costs and annualized costs in [%].

Modelling of the Levelized Cost of Energy LCOE

The Levelized Cost of Energy LCOE is defined by HOMER as the average cost per kWh of useful electrical energy generated by the system. Therefore, LCOE is referred to as the cost of producing energy for a particular system. Its equation is given by (Lambert, 2006):

$$COE = \frac{C_{ann,tot}}{E_{prim} + E_{def} + E_{grid,sales}} \quad (10)$$

Where, E_{prim} is the annual primary that must be met by the system, E_{df} is the annual deferrable load, the load that does not need to be met by the system at specific times throughout one year. This type of load needs a certain amount of power within a specific time period. Loads which are associated with storage are deferrable loads. $E_{grid,sales}$ is the annual electricity which is sold to the grid.

Hybrid system design

In the present work, the selection and sizing of hybrid power system's components has been done using HOMER software. HOMER is hybrid system design software that facilitates design of electric power systems for stand-alone applications. Input information to be provided to HOMER comprises: electrical loads (one year of load data), renewable resources, component technical details and costs, constraints, controls, type of dispatch strategy, etc. HOMER designs an optimal power system to serve the desired loads (Satish, 2014).

Case study

The case study for this thesis is a remote area in Wilaya of Adrar which is the second largest province located in the western south of Algeria. The area of this province covers 427,968 km^2 which represents 18% of the total area of the country. It is divided into 28 communes or districts and each commune contains a certain number of cities and villages called K'sars. Among the K'sars, Boukazine, which is located in Commune of Talmine (north-west of the main Commune Adrar), is selected for this research (29°18' N, 0°8' W). The region of Adrar has a hot desert climate according to Kppen climate classification BWh. Winters are mild with average temperature around 14 °C. Summers are very hot; the temperature can reach its maximum of 51°C. Rainfall is very light and intermittent, and summers are dry (National Oceanic and Atmospheric Administration, 2016). Many sites in Adrar, which are isolated and

Creative Commons Attribution-NonCommercial-NoDerivatives 4.0 International License (CC BY-NC-ND)

the distance between them is far way, are not connected to the grid. Thus, this leads to think of hybrid systems for generating electricity for the people living in this region.

Load profile

In this research, the hybrid power system is for providing electricity for fifteen (15) households. But first, the load profile of a single household should be obtained. A new plan is required in order to get the monthly and annual profile for 15 households. This can be done by multiplying the load profile of single household by 15 households supplied by the system. The monthly energy demand of a single household is shown in the Fig.1.

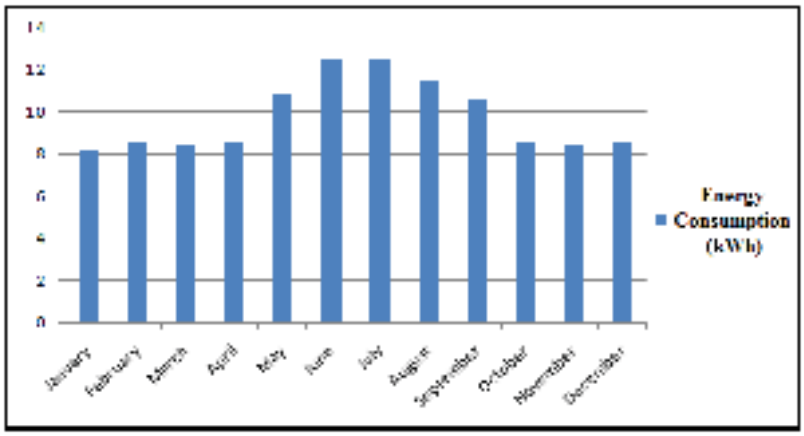

Fig1. Monthly energy consumption variations

Resource input

Before sizing our PV system, we will first analyze the solar resource potential available and the monthly temperatures in Boukazine, Adrar. The climatic data for this study is obtained from Meteonorm 7.2 software. This latter can generates accurate and representative global climatic data for any place on earth.

	Global Horizontal Irradiance GHI [kWh/m^2]	**Average Temperature [°C]**
Jan.	141	12.9
Feb.	146	16.2
Mar.	202	21.4
Apr.	221	25.3
May	241	30.5
Jun.	240	35.2
Jul.	245	38.2
Aug.	225	37.2
Sep.	192	33.1
Oct.	166	27.5
Nov.	139	19
Dec.	127	14.4
Annual	2282	-

Creative Commons Attribution-NonCommercial-NoDerivatives 4.0 International License (CC BY-NC-ND)

Average	190.4	25.9

Table 1. Horizontal radiations and average temperature in Boukezine, Adrar

System description

HOMER is a simplified optimization model, which performs thousands of hourly simulations over and over (to sort the best possible matching between supply and demand) in order to design the optimum system. It uses life cycle cost to rank order these systems. The model has been developed using HOMER, consists of: a PV generator, three (3) diesel gensets, a bi-directional inverter, an electrolyzer and a hydrogen tank as shown in Fig. 2. The goal of the optimization process is to determine the optimal value of each decision variable that interests the modeler. A decision variable is a variable over which the system designer has control and for which HOMER can consider multiple possible values in its optimization process. The objective of the optimization is to minimize the net present cost (NPC) of the system with 2% capacity shortage, 10% reserve as the electrical load and 25% reserve as output solar energy.

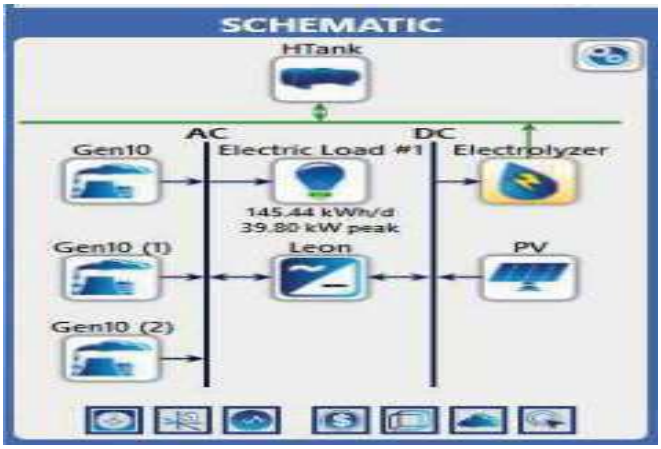

Fig2. HOMER system configuration

Results and discussions:

In our case, lots of simulations have been performed by HOMER Pro. to find out the most optimized and cost effective configuration of the hybrid power system considering all of the system components, their sizes and their costs assumptions. HOMER Pro. displays a list of categorized optimization results which shows the least-cost system of each type. It enables us to compare the system category with other system category alternatives. Fig. 3 gives the categorized optimization results and shows the most cost effective configuration of each system type. As in the overall optimization result, HOMER Pro. considers the system type of three diesel generators as the optimum one.

It can be seen that some system types have only either an electrolyzer or a hydrogen tank. These system are economically feasible but practically not since, in reality, the electrolyzer and the hydrogen tank are needed both at the same type for efficient production and storage of hydrogen. Thirdly, hydrogen can be produced by using the PV generator and either two or three generators. In our case, we are interested in the system type that considers the PV generator, the three generators, the inverter, the electrolyser and the hydrogen tank. Such

Creative Commons Attribution-NonCommercial-NoDerivatives 4.0 International License (CC BY-NC-ND)

Algerian Journal of Engineering Architecture and Urbanism Vol. 5 Nr. 3 2021
ISSN: 2588-1760

system type uses a PV generator output power of 21.7kW, a 16kW MPPT-converter, three 10kW diesel generators, 20kW electrolyzer, hydrogen tank of 380kg and an inverter of 8.00 kW. The Load Following strategy is adopted in this system. The total Net Present cost NPC is found to be $823,744 and a LCOE of $0.602/kW. The ecotechnical analysis results can be accessed by double click on the corresponding system type.

The different outflows and inflows through the entire project lifetime can be displayed in HOMER Pro. either in tabular or graphical form. Fig. 4 below gives the nominal cash flow outputs of the considered system type components. The capital cost for our project is estimated to be $456,283. The share of the hydrogen tank only represents 83% of the total capital cost.

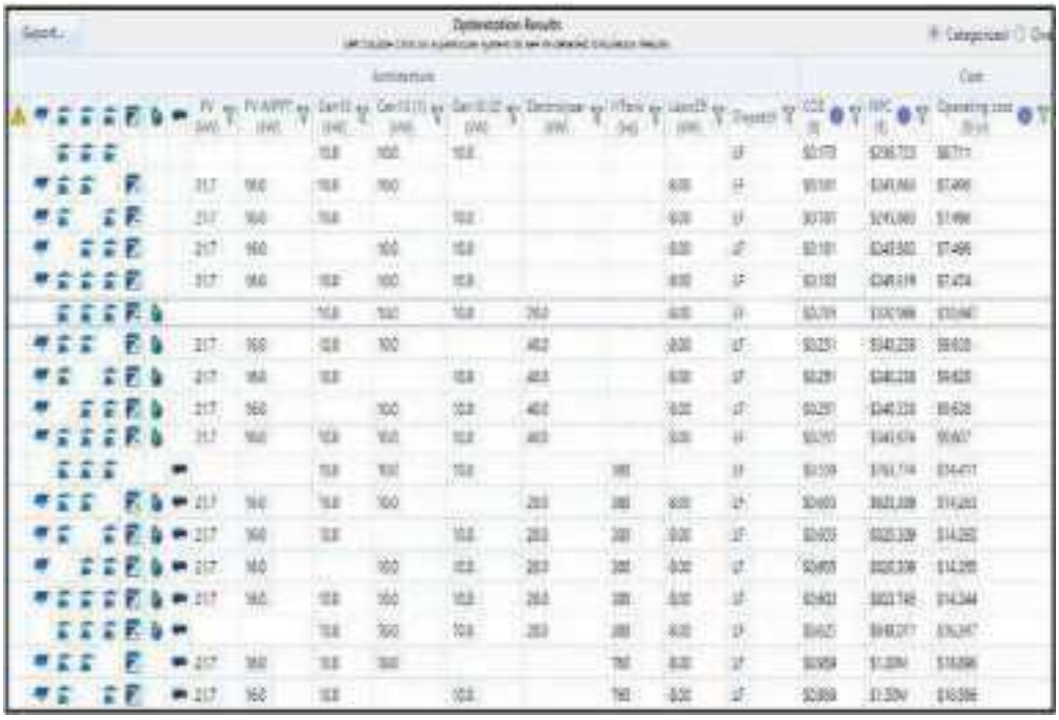

Fig3. HOMER categorized optimization solutions

The PV generator produces the highest percentage of 51.3% of the total annual energy generation. As stated by the Table 2, the capacity shortage of this system is 0.188% which is very small resulting only 10 hours of load shedding during the entire year due to the incapability of generating enough power to satisfy the load. The PV tab shows the operation characteristics of the PV generator. The capacity factor of the PV system is 19.7% which is relatively low. Other characteristics are summarized in Table 3.

Creative Commons Attribution-NonCommercial-NoDerivatives 4.0 International License (CC BY-NC-ND)

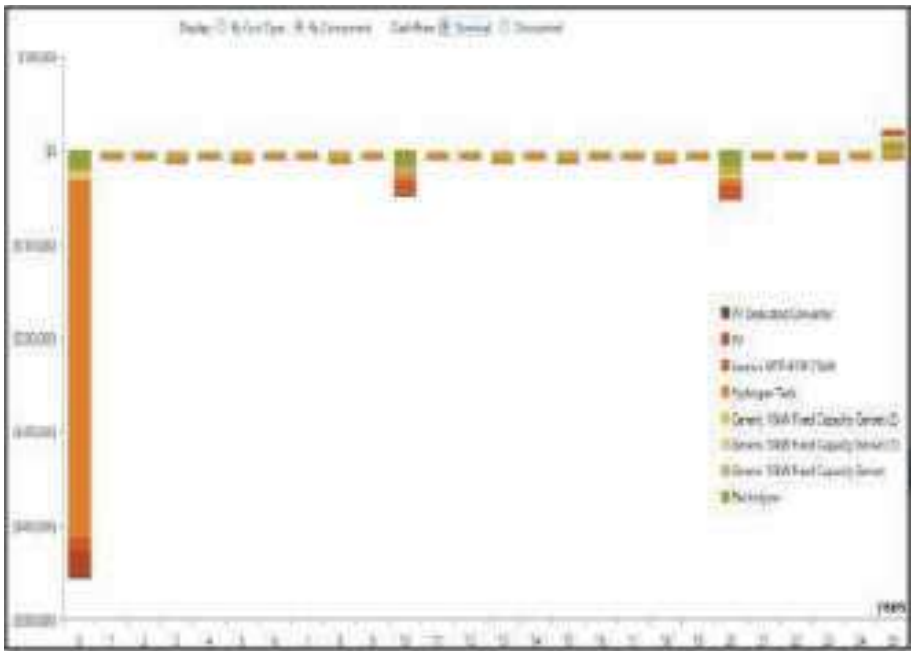

Fig4. Project nominal cash flow by components

Production	kWh/yr	%
PV	37,354	51.24
Genset 1	31,342	43.0
Genset 2	3,437	4.72
Genset 3	759	1.04
Capacity shortage	-	0.188

Table 2. Energy produced by different energy sources and their shares

Quantity	Value	Units
Rated Capacity	21.7	kW
Total Production	37,354	kWh/yr
Hours of Operation	4,383	Hrs/yrs
Levelized Cost	0.0416	$/kWh

Table 3. PV system characteristics

According to the HOMER Pro. simulations above, it has been found that the optimal hybrid configuration, which can supply the load and produce hydrogen at lower cost, contains PV arrays with a size of 21.7kW. The PV arrays generate DC electricity; they are connected to the DC bus bar. They can be divided into two arrays. In our case, we are going to use a converter that has a range of 230-400V and a PV module that has a capacity of 210W and a voltage of 24.6V. Hence, 13 solar modules can be connected in series to adjust the array output voltage. Since an 11kW PV system requires 52 PV modules, they can be arranged into 4 strings each containing 13 series connected PV modules. The total fuel consumed by the three genset can be calculated resulting 13,545 liters of diesel. Hence, the average fuel consumed per day and the average fuel consumed per hour is calculated by HOMER: 37.1L/day and 1.55L/h, respectively.

Creative Commons Attribution-NonCommercial-NoDerivatives 4.0 International License (CC BY-NC-ND)

In the electrolyzer tab, several quantity values are tabulated. Table 4 below shows some of these values.

Quantity	Value	Units
Rated Capacity	20.0	kW
Mean input	2.18	kW
Total input energy	19,099	kWh/yr
Capacity Factor	10.9	%
Hours of operation	3,973	h/yr
Total production	353	Kg/yr

Table 4. Electrolyser system characteristics

Fig. 5 gives the D-map of the input power to the electrolyzer. It can be seen that the maximum input power can attain 12kW and this happens usually during winter. However in summer, the input power of the electrolyzer is low. This is mainly because the hybrid system priority is to satisfy the load. In case of peak load, the electrolyzer input power turns to be zero. The hydrogen quantity produced by the electrolyzer (353 kg) is sent directly to the hydrogen tank that contains initially a quantity of hydrogen of 19.0 kg. The energy storage capacity is found to be 12,667 kWh and the tank autonomy, which the ration of the energy storage capacity and the average electric load (6.06 kW in our case), is calculated to be 2,090 hours

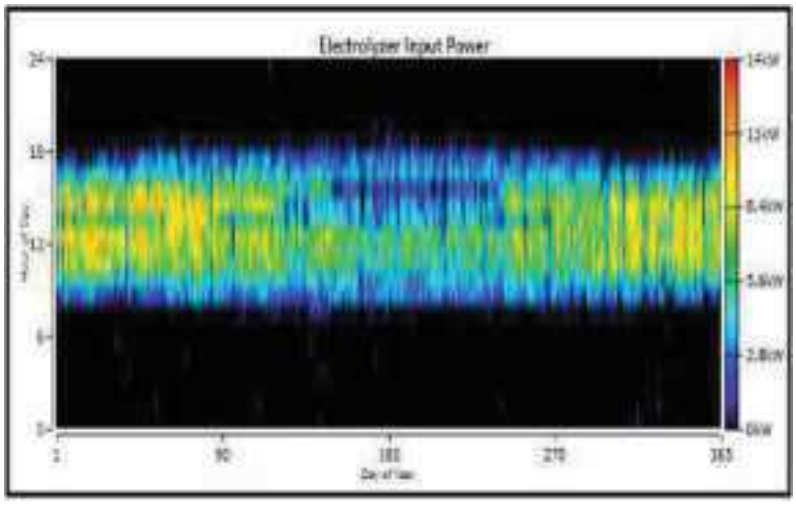

Fig5. The yearly electrolyser input power

According the simulation results, the optimum system configuration for both electricity and hydrogen generation was found to be: PV capacity of 21.7kW, MPPT converter of 16.0kW, 3 Diesel generator of 10kW each, Inverter 8.00kW, Electrolyzer of 20.0kW and Hydrogen tank of 380 kg.

The diesel generators were required to generate a total of 48.76% of the total system energy generation. Since there was no power source other than solar PV, the operations hours of the diesel gensets were find to be considerable. This was mainly in order to compensate the absence of solar energy during night times and solve the issue of peak load especially during summer. On the other hand, the solar PV generator produced 51.24% of the total system

Creative Commons Attribution-NonCommercial-NoDerivatives 4.0 International License (CC BY-NC-ND)

energy generation. Part of this energy was used by the electrolyzer to produce hydrogen where a total production of hydrogen of 353 kg/yr was recorded. A 20.0kW rated capacity electrolyzer could reach a maximum input of power of 13.3kW. HOMER Pro. estimated the capacity shortage to be only 0.188% which implies only 10 hours of power outage during a year. Homer Pro, does not take in consideration all of the region remoteness, the power interruptions due to the harsh environment or the shut downs for maintenance in the calculation of such parameter. Otherwise, the power outage hours would increase significantly.

The HOMER Pro. simulation results revealed that the hybrid power system can supply electricity at a cost of energy of 0.602 $/kWh, which is almost nine (9) times the cost of energy from the national grid (0.07 $/kWh). The lifetime cost analysis of the system has demonstrated that the project requires a capital investment of $456,283, where 83% of this capital cost represents only the capital cost of the hydrogen tank. The replacement and the O&M costs were estimated to be $118,051.55 and $207,695.50, respectively. The lifetime fuel and the salvage costs were found to be $69,888.35 and $28,174.00, respectively. Overall, the project NPC is worth $823,744.56.

The optimized hybrid power system uses three diesel generators than have a total hours operation of 7044 hours/years. The presence of this conventional technology yields a considerable emissions of pollutants mainly CO2. Simulation results have been shown that the three diesel gensets can generate 35,386 kg of CO2. The emission penalty was not taken into consideration in this work. However, further analysis has shown that the implication of such penalties may increase the system NPC and LCOE on one hand.

One of the most important aspects of the considered hybrid power system is the presence of the hydrogen system. This latter can be seen as a renewable energy source and bountiful in supply. Hydrogen is a clean and non-toxic energy; it does not cause any harm to human health. This feature makes it the most preferred fuel compared to other sources of fuels. In addition, hydrogen energy is very efficient and hence an ideal fuel source for energy production than can be used for different applications. At national level, hydrogen technology can offer several benefits like diversifying the national energy mix.

The hybrid system in this project was able to produce a total weight of 353 kg of hydrogen. The Net Calorific Value (or the Low Heat Value LHV) and the Gross Calorific Value (or High Heat Value HHV) of hydrogen at a temperature of 25°C and a pressure of 1 atm are 119.93 MJ/kg and 141.88 MJ/kg, respectively. Thus, the energy that can be release by the total weight produced of hydrogen is 30,342.3 MJ (or 11,760.7 kWh) using the LHV. This huge energy can be used to supply the load of the 15 households considered in this study for at least 80 days without using the other sources of power (neither PV nor diesel generator) during that period.

Conclusion:

The aim of this work was to model a PV-diesel hybrid system with hydrogen storage. From the lifetime cost analysis, the estimated levelized cost of electricity LCOE has been found to be 0.602 $/kWh. At present, hybrid power systems with hydrogen storage are not

Creative Commons Attribution-NonCommercial-NoDerivatives 4.0 International License (CC BY-NC-ND)

cost-competitive against both standalone conventional fueled system and grid utility power source. The hydrogen quantity produced by the hybrid system under this study is considerable. This hydrogen gas would be converted to other forms of energy like electricity if the system was integrated with hydrogen power generation technologies like fuel cells or hydrogen combustion engine.

References:

Abou El-Maaty M., Abd El-Aal (2005), *Modelling and simulation of a photovoltaic fuel cell hybrid system,* Ph.D dissertation at University of Kassel.

Boudghene Stambouli (2007), *An overview of different energy sources in Algeria*, United Nations, Index 382958.

Costa T.S., A Villalva M.G. (2020), *Technical evaluation of a PV-Diesel hybrid system with energy storage: Case study in Tapajos-Arpiuns Extractive Reserve, Amazaon, Brazil*, Energies, 13(11), 2969.

Energy & Mines Book (2007), *www.mem-algeria.org*, (accessed in March 2018).

Geovanni S., Orlando L., Rafael P., Albersto S., Sebastian P. (2010), *Analysis of the current methods used to size a wind/hydrogen/fuel cell integrated system: A new perspective*, International Journal of Energy Research vol(34) , pp.1042-1051.

Lambert T. (2006), *Micropower system modelling with HOMER*, Mistaya Engineering Inc, National Renewable Energy Laboratory**.**

Lydia V.O., Magyari V., Adriaan L. N. (2017), *Facts & figures: Solar energy in Northern Africa 2017*, Solar Plaza.

National Oceanic and Atmospheric Administration (2016), *Adrar climate normals, 1961-1991*, Urbanism Retrieved October 21st, 2016.

Satish K. R., Jagadish K. (2014), *Optimal economical sizing of a PV-wind hybrid energy system using genetic algorithm and teaching learning based optimization*, International Journal of Advanced Research in Electrical, Electronics and Instrumentation Engineering,Vol. 3, Issue 2, pp.7352-67.

Tijani A. S., Yusup N. A. B., Rahim. A. H. A. (2014), *Mathematical modeling and simulation analysis of advanced alkaline electrolyzer system for hydrogen production*, Procedia Technology, vol. 15, pp. 798-806.

Ulleberg O. (2003), *Modeling of Advanced Alkaline Electrolyzers: A System Simulation Approach*, International Journal of Hydrogen Energy; 28:21–33.

Weldemariam (2010), *Genset-solar-wind hybrid power system of off-grid power station for rural applications*, Electrical Power Engineering. PhD thesis, Department of Electrical Power Engineering, Delft University of Technology, Delft, The Netherlands.

.

Creative Commons Attribution-NonCommercial-NoDerivatives 4.0 International License (CC BY-NC-ND)

Algerian Journal of Engineering Architecture and Urbanism Vol. 5 Nr. 3 2021
ISSN: 2588-1760

Set INVERSION FOR THE CALIBRATION OF A 3-AXIS ROBOT

Salima BORSALI
PhD, University of Tlemcen ALGERIA,
Faculty of Technology, Automatic laboratory
Email: borsali.salima@gmail.com

Abstract:
In this study, a set method based on interval arithmetic is proposed for the geometric calibration of a robot with three degrees of freedom. This method, called set inversion, makes it possible to frame each parameter to be estimated within an interval whose width depends on the uncertainty on the collected measurements, on modeling errors and on the pessimism inherent in set methods. The problem of geometric calibration is presented and formalized as a problem of constraint satisfaction. Since the smallest box surrounding all the solutions is not necessarily obtained, an addition of redundant constraints based on the principle of constraint projections is proposed in order to improve the results obtained by the set inversion
Key words: Calibration, robotics, set inversion, interval arithmetic.

Introduction:

En robotique, en vue d'une simulation ou d'une commande, l'identification des paramètres inertiels est indispensable. Lorsque nous effectuons une mesure, elle est toujours entachée d'un bruit qui se surajoute aux erreurs structurelles ou de modélisation, il est donc indispensable de faire appel, pour identifier les paramètres, à des techniques d'estimation dont l'efficacité dépend en partie de la modélisation du problème ainsi que de l'algorithme d'estimation choisi. Pour l'identification des paramètres comme dans plusieurs applications [1] [2] [3] on va utiliser le modèle dynamique ou énergétique qui en robotique est linéaire par rapport aux paramètres minimaux [4].

La technique ensembliste que nous allons appliquer est une approche qui est connue depuis plusieurs années mais ses bases ont été fondées par R. Moore [4] puis Neumaier [5] et Hansen[6]. Dans ce contexte une variable est représentée uniquement par un ensemble $\mathbb{X}$, appelé ensemble de vraisemblance ou domaine, supposé contenir la valeur réelle x. La manipulation des variables aléatoires par les méthodes ensemblistes demande moins de connaissances statistiques que celles exigées habituellement par les méthodes probabilistes.

Les méthodes ensemblistes trouvent actuellement des applications dans plusieurs domaines. On peut citer des applications en électrochimie [7][8] pour l'estimation de paramètres incertains, elles sont aussi utilisées pour l'intégration numérique d'équations différentielles ordinaires en présence d'incertitudes [9], beaucoup plus récemment des approches ensemblistes ont permit l'analyse et une estimation plus robuste de systèmes hybrides non linéaires [10] [11]. Il existe aussi des application dans le domaine de la robotique pour la résolution de problèmes d'étalonnage [12], d'estimation et d'identification[13] [14] [15]ainsi que les planifications de trajectoires et la localisation [16] [17] .

Plus connue par méthode d'estimation à erreurs bornée [18][19], l'approche ensembliste permet de résoudre en automatique des problèmes d'estimation non linéaire dont le traitement par une approche probabiliste reste difficile voir impossible.

Dans notre article nous allons comparer deux techniques d'estimation une méthodes ensemblistes basées sur l'arithmétique par intervalles en particulier l'inversion ensembliste

Creative Commons Attribution-NonCommercial-NoDerivatives 4.0 International License (CC BY-NC-ND)

[21][22] associé à une propagation de contraintes[20] et l'approche probabiliste notamment la méthode des moindres carrés.
Dans la première section nous donnons d'abord quelques définitions concernant l'approche ensembliste et l'arithmétique par intervalle [23][24]. Dans la section suivante nous décrivons le model du robot plan trois axes dont on veut identifier les paramètres dynamiques. Par la suite nous présentons notre méthode d'estimation ensembliste que nous comparons avec la méthode des moindres carrés.
Des résultats de simulation, suivis d'une discussion sont donnés dans la dernière section.

Problématique:

II. Analyse par intervalles.

2-1 Opérations ensemblistes pures.

Soit $\mathbb{A}$ et $\mathbb{B}$ deux sous-ensembles de $\mathbb{R}^n$. Rappelons que $\mathbb{A}$ est inclus dans $\mathbb{B}$ si et seulement si tout élément de $\mathbb{A}$ appartient à $\mathbb{B}$. Il vient de ce fait

$$\mathbb{A} \subset \mathbb{B} \iff (\forall\, x \in \mathbb{A}, x \in \mathbb{B}) \qquad [1]$$

Les opérations suivantes s'appliquent sur des sous-ensembles de $\mathbb{R}^n$ en général. Elles concernent l'union, l'intersection, le produit scalaire et la projection. Étant donnés $\mathbb{X}$ et $\mathbb{Y}$ deux sous-ensembles de $\mathbb{R}^n$ et de $\mathbb{R}^m$; Nous avons :

$$\begin{aligned}
&\mathrm{Proj}_i\ (\mathbb{X}) = \{\ xi \in \mathbb{R} / \exists\ x = (x_1, ..., x_i, ..., x_n)^T \in \mathbb{X}\ \}\\
&\mathbb{X} \cap \mathbb{Y} = \{\ x \in \mathbb{R}^n \mid x \in \mathbb{X} \text{ et } x \in \mathbb{Y}\ \}, \text{ avec } n = m,\\
&\mathbb{X} \cup \mathbb{Y} = \{\ x \in \mathbb{R}^n \mid x \in \mathbb{X} \text{ ou } x \in \mathbb{Y}\ \}, \text{ avec } n = m, \qquad [2]\\
&\mathbb{X} \times \mathbb{Y} = \{\ (x,y)^T \in \mathbb{R}^{n+m} \mid x \in \mathbb{X} \text{ ou } x \in \mathbb{Y}\ \}
\end{aligned}$$

2-2 Arithmétique des intervalles

Un intervalle, noté par $[x]$ est un ensemble connexe et borné de $\mathbb{R}$, il est défini par :

$$[\mathbf{x}] = (\ \underline{\mathbf{x}}, \overline{\mathbf{x}}\ ) = \{x \in \mathbb{R} \mid \underline{\mathbf{x}} \leq x \leq \overline{\mathbf{x}}\ \} \qquad [3]$$

Les nombres réels $\underline{\mathbf{x}}$ et $\overline{\mathbf{x}}$ sont respectivement les bornes inférieure et supérieure de $[x]$.
L'ensemble des intervalles de $\mathbb{R}$ est noté par $\mathbb{IR}$.
Les opérations mathématiques élémentaires sont étendues aux intervalles.
Soit $[x] \in \mathbb{IR}$, on définit alors:

- sa borne inférieure : $\inf([\mathbf{x}]) = \underline{\mathbf{x}}$
- sa borne supérieure : $\sup([\mathbf{x}]) = \overline{\mathbf{x}}$
- sa largeur : $w([\mathbf{x}]) = \overline{\mathbf{x}} - \underline{\mathbf{x}} \geq 0$ [4]
- son milieu : $\mathrm{mid}([\mathbf{x}]) = (\overline{\mathbf{x}} + \underline{\mathbf{x}}\ ) / 2$
- son rayon : $\mathrm{rad}([\mathbf{x}]) = (\ \overline{\mathbf{x}} - \underline{\mathbf{x}}\ ) / 2 \geq 0$

Un pavé (ou vecteur intervalle) [x] est un compact de $\mathbb{R}^n$ défini par le produit cartésien de n intervalles. On a :

$$\begin{aligned}
[\mathbf{x}] &= [\ \underline{\mathbf{x}}_1, \overline{\mathbf{x}}_1\ ] \times [\ \underline{\mathbf{x}}_2, \overline{\mathbf{x}}_2\ ] \times \ldots \times [\ \underline{\mathbf{x}}_n, \overline{\mathbf{x}}_n\ ] \qquad [5]\\
&= [\mathbf{x}_1] \times [\mathbf{x}_2] \times ... \times [\mathbf{x}_n]
\end{aligned}$$

Soient $[x], [y] \in \mathbb{IR}$, et $\circ \in \{+, -, *, /\}$, alors :

$$[x] \circ [y] = \{\ x \circ y \,/\, x \in [x],\ y \in [y]$$

On obtient ainsi les équations suivantes, plus utilisables en pratique que la définition abstraite

$$[\mathbf{x}] + [\mathbf{y}] = [\ \underline{\mathbf{x}} + \underline{\mathbf{y}}\ ,\ \overline{\mathbf{x}} + \overline{\mathbf{y}}\ ]$$

Creative Commons Attribution-NonCommercial-NoDerivatives 4.0 International License (CC BY-NC-ND)

$$[\mathbf{x}] - [\mathbf{y}] = [\ \underline{x} - \overline{y}\ ,\ \overline{x} - \underline{y}\ ]$$

$$[\mathbf{x}] * [\mathbf{y}] = [\min\{\ \underline{x}\,\underline{y}\ ,\underline{x}\,\overline{y}\ ,\overline{x}\,\underline{y},\ \overline{x}\,\overline{y}\ \},\ \max\{\ \underline{x}\,\underline{y}\ ,\underline{x}\,\overline{y}\ ,\overline{x}\,\underline{y}\ ,\ \overline{x}\,\overline{y}\ \}] \qquad [6]$$

$$[\mathbf{x}]^2 = [\min(\underline{x}^2, \overline{x}^2)\ ,\ \max(\underline{x}^2, \overline{x}^2)\ ]\ \text{si}\ 0 \notin [\underline{x}\ ,\ \overline{x}\ ]$$

$$= [0,\ \max(\underline{x}^2, \overline{x}^2)\ ]\ \text{sinon}$$

La division est définie par :

$$1/[y] = \emptyset \quad \text{si } [y] = [0, 0]$$

$$= [\ 1/y,\ 1/y\ ] \quad \text{si } 0 \notin [y] \qquad [7]$$

$$= [\ 1/y,\ \infty[\quad \text{si } y = 0 \text{ et } y > 0$$

$$[x]\ /[y] = [x] * (1/[y]) \quad \text{si } 0 \notin [y]$$

Soit f une fonction de $\mathbb{IR}^n$ dans $\mathbb{IR}^m$. La fonction d'intervalle [**f**] de $\mathbb{IR}^n$ dans $\mathbb{IR}^m$ est dite **fonction d'inclusion** pour f si :

$$\forall\ [x] \in, \mathbb{IR}^n\ \ \mathbf{f}\ (\ [x]\ ) \subseteq\ [\ \mathbf{f}\ ]\ (\ [x]\ )$$

Ou bien : $$[f\ ]\ ([x]) \supset \{f(x) \mid x \in [x]\} \qquad [8]$$

2-3 Inversion ensembliste

Considérons un ensemble $\mathbb{X}$ dans $\mathbb{R}^n$ et une fonction $f : \mathbb{R}^n \longrightarrow \mathbb{R}^m$. Soit Y un sous ensemble de $\mathbb{R}^m$ défini comme suit :

$$\mathbb{Y} = f(\mathbb{X}) \qquad [9]$$

L'inversion d'ensembles permet de caractériser l'ensemble $\mathbb{X}$, comme l'image réciproque par la fonction f, de l'ensemble $\mathbb{Y}$:

$$\mathbb{X} = \{x \in \mathbb{X} \mid f(x) \in \mathbb{Y}\ \ \} = f^{-1}(\mathbb{Y}) \qquad [10]$$

Le problème d'inversion ensembliste peut être résolu par le biais de l'algorithme SIVIA (*Set Inversion Via Interval Analysis*) [26]. SIVIA est un algorithme Récursif permettant d'obtenir, en partant d'un pavé initial assez large, deux sous-ensembles encadrant l'ensemble solution X, tel que L'approximation, ou encadrement, **intérieure** $\underline{\mathbb{X}}$ représente l'ensemble des pavés dont on a pu prouver qu'ils étaient **acceptables**. Les éléments de $\underline{\mathbb{X}}$ sont tous solutions, mais il peut y avoir des solutions admissibles qui ne sont pas contenues dans $\underline{\mathbb{X}}$. Un pavé est acceptable s'il vérifie le relation $[x] \subseteq \mathbb{X}$. A l'opposé si on démontre que $[x] \cap \mathbb{X} = \emptyset$, alors le pavé [x] est **inacceptable** et sera supprimé. Dans le cas ou le pavé est ni acceptable ni inacceptable, on dit que le pavé [x] est **ambigu**. L'algorithme va donc découper le pavé ambigu en deux sous-pavés, et ils seront testés à leur tour pour déterminer s'ils peuvent être gardés ou rejetés. Le processus est réitéré à nouveau jusqu'à obtenir un pavé dont la largeur atteint un certain seuil, $\varepsilon > 0$, fixé par l'utilisateur. Dans tous les autres cas, le pavé sera dit **indéterminé**.

The Algorithm Sivia

SIVIA (Input: [*t*], [**x**], η, Output: $\underline{\mathbb{X}}$, $\overline{\mathbb{X}}$)
1. If [*t*] ([**x**]) = [0], rejected [**x**]
2. If [*t*] ([**x**]) = [1], $\underline{\mathbb{X}} := \underline{\mathbb{X}} \cup [\ \mathbf{x}\ ]$, $\overline{\mathbb{X}} := \overline{\mathbb{X}} \cup [\ \mathbf{x}]$
3. If *w* ([**x**]) ≤η, $\overline{\mathbb{X}} := \overline{\mathbb{X}} \cup [\ \mathbf{x}\ ]$
4. Bisected [**x**] en ($[x_1]$ $[x_2]$)
SIVIA (I:[t] , x_1 ,η; O : $\underline{\mathbb{X}}$, $\overline{\mathbb{X}}$)
SIVIA (I : [t] , x_2 ,η; O : $\underline{\mathbb{X}}$, $\overline{\mathbb{X}}$)

Creative Commons Attribution-NonCommercial-NoDerivatives 4.0 International License (CC BY-NC-ND)

Algerian Journal of Engineering Architecture and Urbanism Vol. 5 Nr. 3 2021
ISSN: 2588-1760

2-4 Propagation de contraintes

La propagation des contraintes sur les intervalles permet, sur un domaine de variables prédéfini, une réduction considérable de la taille d'un pavé [x] sans avoir recours à des bissections. Le contracteur que nous utilisons dans notre étude est basé sur le principe de la projection de contraintes. Soit un ensemble, notons C_s ([x]) le plus petit pavé contenant $\mathbb{S} \cap$ [x] .C_s est appelé opérateur de contraction. Cet operateur est capable de remplacer un pavé [x] par un pavé C_s ([x]) de taille inferieur tout en préservant l'intégralité de l'ensemble solution.
La méthode est basée sur le principe de projection des contraintes.

2-4-1 Problème de satisfaction de contraintes

Un problème de satisfaction de contraintes est caractérisé par un triplet (*X,D, C*). Si n est le nombre de variables et m le nombre de contraintes, alors :

- $X = \{x_1, x_2, ..., x_n\}$ représente l'ensemble des variables,
- $D = \{D_1, D_2, ..., D_n\}$ est l'ensemble de domaines associés à chaque variable [11]
- $C = \{C_1, C_2, ..., C_m\}$ correspond à l'ensemble des contraintes.

Si $x \in \mathbb{X} \subset \mathbb{R}^m$ et, f une fonction définie de $\mathbb{R}^n \longrightarrow \mathbb{R}^m$

Résoudre un problème de satisfaction de contraintes c'est rechercher de l'ensemble des solutions de [12] contenues dans $\mathbb{X}$

$$H : (f(x) = 0 , x \in \mathbb{X}) \quad [12]$$

2-4-2 Projection de contraintes.

Le calcul de C_s ([x]) est communément appelé projection. Un ensemble pour lequel on dispose d'un contracteur optimal est appelé ensemble primitif.
L'exemple suivant illustre cette notion de projection pour un ensemble S primitif.
Exemple :

Soient 3 variables x, y et z telles que : $x \in [1, 5]$, $y \in [2,4]$ et $z \in [6,10]$

La méthode est la suivante:

$z \in [6,10] \cap ([1,5] + [2,4])$
$=[6,10] \cap [3,9] = [6,9]$
$x \in [1,5] \cap ([6,10] - [2,4])$
$= [1,5] \cap [2,8] =[2,5]$
$y \in [2,4] \cap ([6,10] - [1,5])$
$= [2,4] \cap ([1,9]-[1,5]) =[2,4]$

Une propagation de contrainte consiste à projeter les contraintes jusqu'au blocage.
Par l'ajout d'une étape de contraction à l'algorithme Sivia, on obtient l'algorithme SiviaP :

Algorithme SiviaP (entrée : *C*,[p] ,[y], ε ; sorties : $\underline{\mathbb{X}}$, $\overline{\mathbb{X}}$)
1. [x] = *C*([p])
2. Si [p] = ∅ rejeter [p]
3. Si [f] ([p]) ⊆ [y] alors $\underline{\mathbb{X}} := \underline{\mathbb{X}} \cup [x]$, $\overline{\mathbb{X}} := \overline{\mathbb{X}} \cup [x]$
4. si w ([p]) < ε, $\overline{\mathbb{X}} := \overline{\mathbb{X}} \cup [x]$
5. Bissecter [p] en [p_1] et [p_2]
6. **SiviaP** ([p_1]) ; **SiviaP** ([p_2])

Creative Commons Attribution-NonCommercial-NoDerivatives 4.0 International License (CC BY-NC-ND)

Materials and methods:

3-1 Description du robot

Le robot étudié est un robot plan de 3 axes de rotation (Fig:1). Pour définir sa structure on a adopté les conventions de Denavit-Hartenberg modifiées [24], les paramètres articulaires sont regroupés dans le tableau [1].

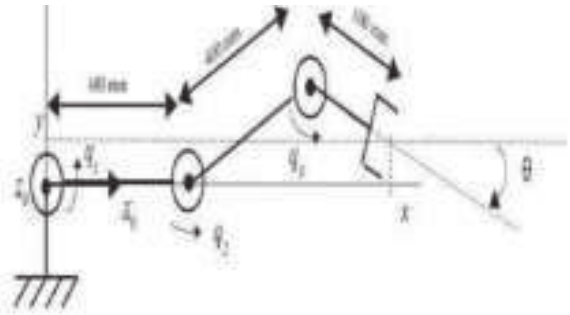

Fig1 :Robot plan 3 axes

Articulation	θ_i	l_i	d_i	α_i
C_1	q_1	0	r1	0
C_2	q_2	0	r2	0
C_3	q_3	0	r3	0

Tableau1 : Paramètres articulaires

La matrice de transformation homogène obtenue à partir du tableau des paramètres articulaires, nous permet de définir les coordonnées du TCP (Tool center point), correspondant au modèle géométrique direct

$$ {}^{0}T_3 = \begin{bmatrix} C(q1+q2+q3) & -S(q1+q2+q3) & r1Cq1 + d2C(q1+q2) + r3C(q1+q2+q3) \\ S(q1+q2+q3) & C(q1+q2+q3) & r1Sq1 + d2S(q1+q2) + r3S(q1+q2+q3) \\ 0 & 1 & 0 \\ 0 & 0 & 1 \end{bmatrix} $$

On en déduit le modèle géométrique direct :

$$x = r1Cq1 + d2C(q1+q2) + r3C(q1+q2+q3)$$

$$y = r1Sq1 + d2S(q1+q2) + r3S(q1+q2+q3)$$

avec : q_i les paramètres articulaires, c=cos, s=sin

Results and discussions:

Le principe de notre application est d'appliquer l'inversion ensembliste sur un robot plan trois axes. Nous choisissons d'étalonner le robot en essayant de déterminer des encadrements pour les longueurs des trois segments. Les valeurs à priori pour ces segments sont :

r1= 450 mm
r2= 250mm

Creative Commons Attribution-NonCommercial-NoDerivatives 4.0 International License (CC BY-NC-ND)

r3=240mm

Nous disposons de mesures expérimentales dans plusieurs cas : un axe mobile et les deux autres immobiles, puis les trois mobiles en même temps. Les simulations ont été exécutées sous Matlab avec la Toolbox Intlab. Dans le but d'augmenter la précisons des intervalles et d'améliorer le temps de simulation qui est une des contraintes quand on utilise les méthodes ensemblistes, on améliore l'algorithme Sivia utilisé en lui associant une étape de contraction qui diminuent le nombre des bissections, cet Algorithme est SiviaP.

Dans le premier cas, nous considérons l'axe 1 mobile et les axes 2 et 3 immobiles. Le pavé de recherche initiale est :

p0 = [0.3, 0.5] × [0.2, 0.4] × [0.2,0.4]

L'erreur additive choisie est e=0.01 et la précision de l'algorithme Sivia et SiviaP est ε = 0.01; r_i représente les longueurs des axes qu'on cherchent à étalonner, on obtient des intervalles pour chaque valeur r_i

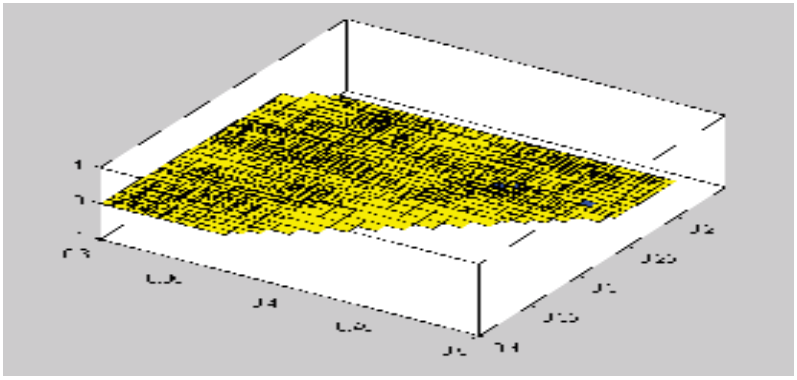

Fig 2 : Pavés solutions relatifs aux paramètres r1, r2 et r3 obtenu par SiviaP

Les pavés solutions sont représentés en bleu, les pavés jaunes sont indéterminés.

On obtient dans ce cas les pavés suivants pour un temps de simulation T= 184.793112 s

r1= [0.4288, 0.4891]
r2= [0.1999, 0.3]
r3= [0.1999, 0.3]

Dans le deuxième cas, on considère l'axe 2 mobile et des deux autres immobiles

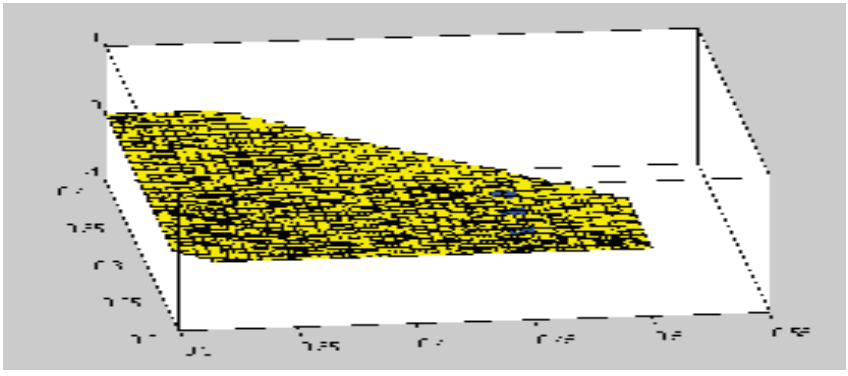

Fig 3 Pavés solutions relatifs aux paramètres r1, r2 et r3 obtenu par SiviaP

r1= [0.4437, 0.4607]
r2= [0.1999, 0.2876]
r3= [0.1999, 0.2876]

Creative Commons Attribution-NonCommercial-NoDerivatives 4.0 International License (CC BY-NC-ND)

Pour un temps T = 231.187013 s.
Pour le troisième cas, c'est l'axe 3 qui est mobile et les deux autres immobiles.

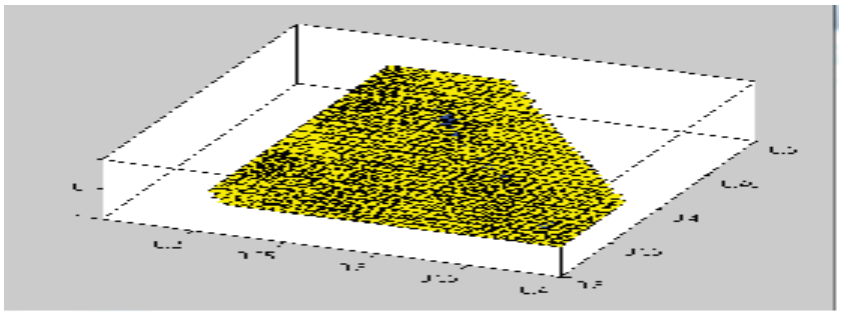

Fig 4: Pavés solutions relatifs aux paramètres r1, r2 et r3 obtenu par SiviaP

Dans ce cas, on obtient, pour un temps T= 243.207279 s, les pavés suivants.
r1 = [0.3050, 0.5000]
r2 = [0.2062, 0.4]
r3 = [0.2292, 0.2472]
Dans le dernier cas, c'est tous les axes qui sont mobiles. Nous testons d'abord l'algorithme Sivia qui nous fourni le résultat suivant :

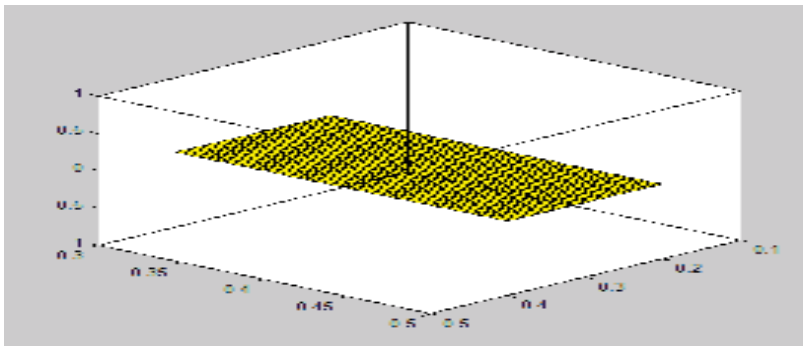

Fig 5 : Pavés solutions relatifs aux paramètres d'intervalle p obtenu par Sivia
Les encadrements relatifs à chaque axe sont les suivants :
r1= [0.3126, 0.5000]
r2 = [0.2062, 0.4000]
r3 = [0.2312, 0.2376]
Obtenus pour un temps de simulation T = 4420.237812 s.
On constate que le temps de simulation est trop grand, afin de l'améliorer et aussi diminuer le nombre de bissections, on a introduit un contracteur basé sur des projections, l'Algorithme SiviaP

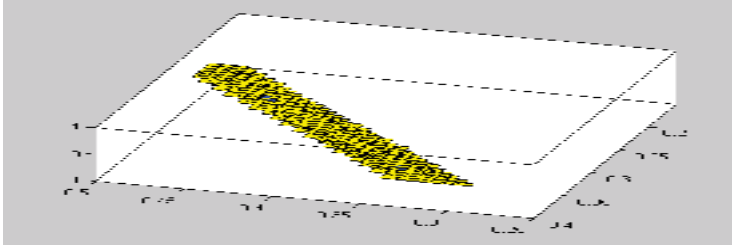

Creative Commons Attribution-NonCommercial-NoDerivatives 4.0 International License (CC BY-NC-ND)

Fig 6 : Pavés solutions relatifs aux paramètres d'intervalle p obtenu par SiviaP

r1= [0.3463, 0.4647]
r2 = [0.2459, 0.3564]
r3 = [0.2276, 0.2468]
Pour T= 74.332108 s
On constate que le temps est nettement amélioré ainsi que la largeur de l'intervalle.
On peut donc augmenter la précision aussi.
Pour une précision, ε = 0.005, on obtient :

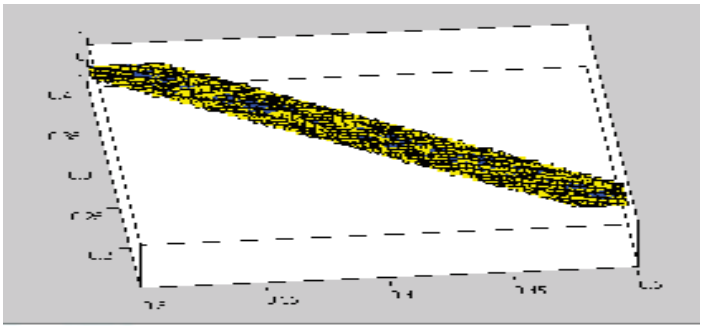

Fig 7 : Pavés solutions relatifs aux paramètres d'intervalle p obtenu par SiviaP

r1= [0.2999, 0.5000]
r2 =[0.1999, 0.4000]
r3 =[0.2410, 0.2500]
Pour un temps T= 399.553832 s
Afin de confirmer nos résultants, nous avons ensuite testé un solveur appelé Proj2D conçu par Masse Dao et Luc Jaulin [30]
Nous avons obtenu les résultats suivants. Les pavés solutions sont en rouge et ceux indéterminé en bleu

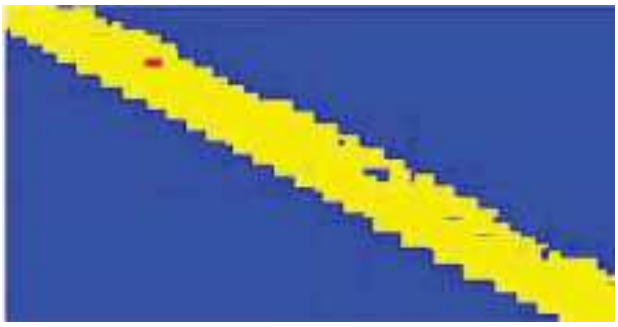

Fig 8 : Pavés solutions relatifs aux paramètres r1, r2, r3 testé par un solveur Proj2D
Les solutions sont représentées par des boites rouges.
Les boites jaunes sont indéterminées
r1=[0.344980866853, 0.350280347979123]
r2= [0.361310466292726, 0.366451909929]
r3= [0.226166498771732, 0.232190388042873]
Temps de calcul T= 3.198s, pour une précision epsilon ε= 0.01
Puis en améliorant la précision ε=0.005, on obtient :

Creative Commons Attribution-NonCommercial-NoDerivatives 4.0 International License (CC BY-NC-ND)

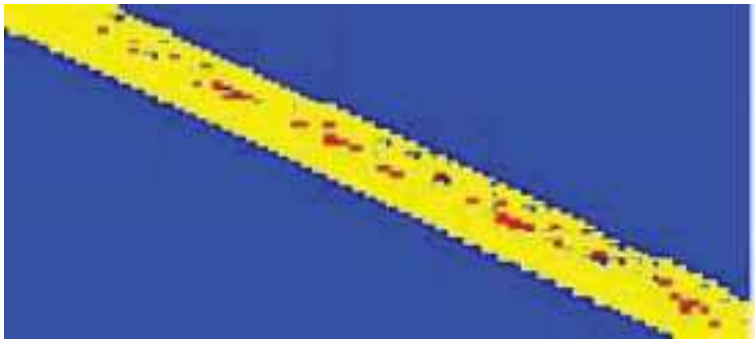

Fig 9 : Pavés solutions relatifs aux paramètres p1, p2, p3 testé par un solveur Proj2D

r1= [0.3, 0.5]
r2=[0.2, 0.4]
r3= [0.223341070194639, 0.250573339261123]
Pour T= 15.772s

A part le temps qui est très court, il existe beaucoup de similitudes avec ceux obtenue par lignes de commandes

Conclusion:

Ce travail nous a permis d'expérimenter la méthode d'identification des paramètres inertiels d'un robot plan 3 axes par les méthodes ensemblistes, plus particulièrement l'inversion ensembliste décrit par l'algorithme SIVIA puis amélioré par l'association de propagations de contraintes par l'algorithme SIVIAP.

Nous avons utilisé deux solveurs afin de projeter nos paramètres sur le plan et vérifier les résultats obtenus par Intlab.

Bien qu'on soit pénalisé en termes de temps quand le nombre de paramètres augmente les méthodes ensemblistes permettent d'obtenir des résultats garantis donc plus fiables.

La propagation de contrainte a permis d'obtenir de bons résultats donc cette technique ouvre une bonne perspective concernant les problèmes d'identification et d'estimation pour les robots possédant beaucoup de paramètres.

Références:

[1] M.Gautier, « *Identification of Robot Dynamics*, »Proc.of IFAC Symposium on theory of Robots, Vienne, Austria :1986, pp. 351-356.

[2] M. Gautier, « *Contribution à la modélisation et à l'identification des robots* », thèse de Doctorat d'état, Université de Nantes, Ecole National Supérieur de mécanique, 1990.

[3] W. Khalil, E. Dombre, « *Modélisation , identification et commande des Robots* », Hermes,Paris ,1999.

[4] R. E. Moore, « *Interval Analysis* », Prentice Hall, Englewood Cliffs, New Jersey, 1966.

[5] A. Neumaier, « *Interval Methods for Systems of Equations* », Encyclopedia of Mathematics and its Applications, Cambridge 1990.

[6] E. R. Hansen, « *Global Optimization Using Interval Analysis* », Marcel Dekker, New York, 1992.

[7] I.Braems, N.Ramdani, A.Boudenne, M.Kieffer, L.Jaulin, L.Ibos, E.Walter « *New Set-Membership Techniques For Parameter Estimation In Presence Of Model*

Creative Commons Attribution-NonCommercial-NoDerivatives 4.0 International License (CC BY-NC-ND)

Uncertainty », Proceedings 5th Int. Conf. Inverse Problems In Engineering: Theory & Practice, July 2005, Cambridge, Leeds University Press, Leeds, ISBN 085316242, Volume I, pp. B09.

[8] I. Braems, F. Berthier, L. Jaulin, M. Kieffer and E. Walter (2001). « *Guaranteed estimation of electrochemical parameters by set inversion using interval analysis* » , Journal of Electroanalytical Chemistry, Volume 495, Issue 1, Pages 1-9

[9] N. Nedialkov, K. Jackson, and G. Corliss, « *Validated solutions of initial value problems for ordinary differential equations*, » Appl. Math. Computat., vol. 105, pp. 21–68, 1999.

[10] N. Meslem & N.Ramdani, « *Interval observer design based on nonlinear hybridization and practical stability analysis*, » International Journal of Adaptive Control and Signal Processing, 25(3): 189–294, 2011.

[11] N.Ramdani & N.S.Nedialkov, « *Computing reachable sets for uncertain nonlinear hybrid systems using interval constraint propagation techniques*, » Nonlinear Analysis: Hybrid Systems, 5(2): 149-162, 2011.

[12] Baguenard, X., Dao, M., Jaulin, L., and Khalil, W. (2003). « *Méthodes ensemblistes pour l'étalonnage géométrique*. » *JESA*, 37(9):1060–1074

[13] Jaulin et al, 1993] L. Jaulin et E. Walter, « *Guaranteed nonlinear parameter estimation from bounded-error data via interval analysis*, » Journal Mathematics and Computers in Simulation, No.35, pp.123-137, 1993.

[14] P.Poignet, N.Ramdani & A.Vivas (2003) « *Robust Estimation Of Parallel Robot Dynamic Parameters With Interval Analysis*, » Proceedings 42th IEEE Conference on Decision and Control, CDC2003, Maui, pp. 6503-6508.

[15] Milanese, M. and Vicino, A. (1991). « Estimation theory for nonlinear models and set membership uncertainty. » *Automatica*, 27(2):403–408.

[16] Kieffer, M. (1999). « *Estimation ensembliste par analyse par intervalles, application à la localisation d'un véhicule*. » PhD dissertation, Université Paris-Sud, Orsay, France.

[17] L. Jaulin (2009), « *A nonlinear set-membership approach for the localization and map building of an underwater robot using interval constraint propagation»,* IEEE Transactions on Robotics, vol. 25, no 1, Feb 2009, 88-98.

[18] L. Jaulin (2001). « *Path planning using intervals and graphs*». Reliable Computing, issue 1, volume 7, 1-15

[19] T.Raïssi, N.Ramdani «Parameter Estimation For Nonlinear Continuous-Time Systems In A Bounded Error Context, » Proceedings 42th IEEE Conference on Decision and Control, CDC2003, Maui, pp.2240-2245. Automation,1986 ,San Francisco,pp.1174-1180

[20] N.Ramdani, T.Raïssi, Y.Candau, L.Ibos (2005) « *Complex Interval Constraint propagation For Non Linear Bounded-Error Parameter Identification*, » Proceedings Of 44th IEEE Conference on Decision and Control and European Control Conference, December 2005, Sevilla, pp.3590-3595.

[21] L. Jaulin, «*Le Calcul Ensembliste par Analyse par Intervalles et ses Applications*, »
Habilitation à Diriger des Recherches (http://www.istia.univangers.), Université d'Angers, Paris, 2000.

[22] L. Jaulin, M. Kieffer, O. Didrit et E. Walter,(2001) « *Applied Interval Analysis, » Springer, 2001*.

Creative Commons Attribution-NonCommercial-NoDerivatives 4.0 International License (CC BY-NC-ND)

[23] L.Jaulin « *Interval constraint propagation with application to bounded-error* estimation. *Automatica*, » 36, 1547-1552, 2000

[24] W.Khalil ,J.F.,Kleinfinger, « *A New Geometric Notation for open and Closed Loop Robots* »,Proceeding of IEEE Internationnal Conference on Robotics and Automation.

[25] R. E. Moore, « *Methods and Applications of Interval Analysis, Studies in Applied Mathematics*, » Philadelphia, Pennsylvania, 1979.

[26] N. Revol and F. Rouillie « *Motivations for an arbitrary precision interval arithmetic and the MPFI library,* » Reliable Computing, vol. 11, no 4, pp 275--290, 2005.

[27] S.M. Rump. INTLAB - « Interval Laboratory, the Matlab toolbox for verified computations, »Version 5.3, 2006 . http://www.ti3.tu-harburg.de/rump/intlab/

[28] http://www.boost.org/

[29] http://www.emn.fr/z-info/ibex/

[30] Massa Dao «*Caractérisation d'ensembles par des méthodes intervalles. Applications en Automatique* » Thèse de Doctorat , 2006
http://www.ensta-bretagne.fr/jaulin/demo.html

[31] Xavier Baguenard « *Propagation de contraintes sur les intervalles, application à l'étalonnage des robots* » Thèse de Doctorat,2005

Creative Commons Attribution-NonCommercial-NoDerivatives 4.0 International License (CC BY-NC-ND)

Algerian Journal of Engineering Architecture and Urbanism Vol. 5 Nr. 3 2021
ISSN: 2588-1760

MODELLING OF POLYMER SOLUTION USED IN MEMBRANE ELABORATION

Fedia BEKIRI
PhD, CRSTRA, Campus of Mohamed Khider University, e-mail: sandi_elamel@yahoo.fr

Hanane RAHALI
Dr, Mohamed Khider University, e-mail: h.rahali@univ-biskra.dz

Abstract:
The flow of fluids in a network of pipes of different sizes, is a major problem and widely studied throughout the engineering industry، particularly in the development of hollow fiber ultrafiltration membranes. Computational fluid dynamics (CFD) is an extremely powerful tool for solving problems associated with flow, mixing, heat, mass transfer and chemical reaction. Recently. To be able to predict the flow behavior of complex fluids and investigate ways of improving their processing, CFD simulation is carried out to track the evolution of velocity within the capillary rheometer at different inlet velocities then see the influence of these velocities on the nature of the regime at the end of capillary die.The results of model concluded that the inlet velocity remains constant in the upper part of the capillary (the tank), but it increase in the lower part of the capillary (capillary die), this is due to the flow conservation law (Bernoulli theorem). On tne other hand, for a minimum inlet velocity the system established at the outlet is laminar for non-ne wtonien fluid which becomes non uniform wher the inlet velocity is increased.

Key words: Fluid, capillary rheometer, CFD, membrane

Introduction:

Membrane filtration has become firmly established as primary technology for ensuring the purity, safety and efficiency of water or effluent treatments. As an example, water desalination is one of the major applications of this technology around the word. An important objective in membrane technology is to control the structure and the performance of the elaborate membranes. The completion of these objective depends on various factors such as : the choice of the dopping component, the elaboration conditions (Temperature (Qin, Wang, & Chung, 2000), shear stress, shear rate, pressure, velocity…), where many experimental studies have been completed to get the knowledge about velocity distribution, pressure drop and turbulent flow behavior (Ahsan, 2015) the choice of the constituents of the spinning solution (polymer , solvent and non solvent (Torrestiana-sanchez, Ortiz-basurto, & Fuente, 1999), (Kajekar et al., 2015) and the spinneret geometry and its dimensions (Mckelvey, Clausi, & William, 1997). For straight annular spinneret, the highest shear stress usually occurs at the wall of the spinneret since the dope solution is normally a non-Newtonian fluid (Yu, Matsuura, Chung, & Fen, 2004), at the output of the spinneret Almin and al have studied the effect of phase separation behavior on morphology and performance of polymer

Creative Commons Attribution-NonCommercial-NoDerivatives 4.0 International License (CC BY-NC-ND)

membrane (Idris, Man, Maulud, & Khan, 2017), (Hee, 2014). Other researchers have found that the increase in shear during the fabrication increase the molecular orientation which can enhance the membrane selectivity (Shilton, 1996), (Suresh, Selvam, & Karunanithi, 2019).
The flow instability inside the annular area of the spinneret lead to fiber breakage during the spinning process and generate non-uniform cross section diameter along the leading length of the fiber (Suffian, M, S, I, & Santha, 2013), (Chaudhuri, 2006), (Suresh et al., 2019).

Computational fluid dynamics (CFD) is an extremely powerful tool for solving problems associated with flow, mixing, heat, mass transfer and chemical reaction. Recently, CFD was a very much research tool and most of the early work was aimed at developing numerical methods, solution algorithms and Reynolds-average turbulence models.

The rheological flow of complex fluid in industrial equipment poses a number of challenges, not least from a modeling point of view. Research is needed to further understand and be able to predict the flow behavior of such materials and investigate ways of improving their processing validated CFD simulation were used to study the effect of rotational and transversal mechanical vibrations on the pipe flow of viscous power law fluids.

Materials and methods:

In the context of this work, it was chosen to use capillary rheometer at imposed pressure. The aim being to be in the experimental conditions close to elaboration conditions of hollow fibers. Fig. 1 presents the diagram of installation.

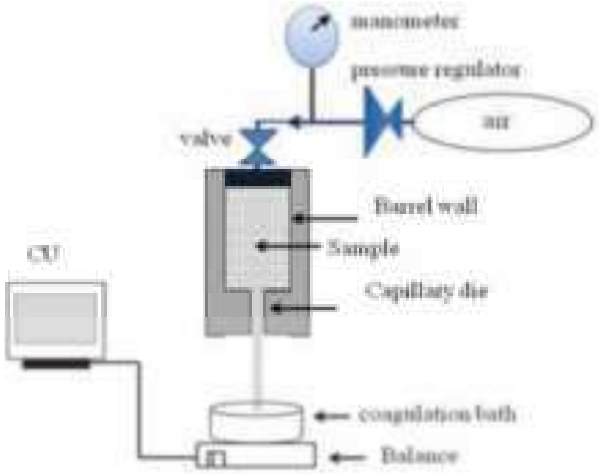

Fig1. Capillary rheometer schematic diagram

Creative Commons Attribution-NonCommercial-NoDerivatives 4.0 International License (CC BY-NC-ND)

The measurements were carried out at ambient temperature 300K, an expansion valve place upstream of the tank containing the suspension, it makes possible to control the total pressure of compressed applied air. The testes are carried out at different pressures ranging from 1 to 6 bar relative; the characteristics are summarizing in table 1:

Tab 1.: Capillary rheometer characteristics.

Capillary lenght	Lc	20 cm
Capillary diameter	Dc	9mm
Capillary die diameter	Dd	1 mm
Capillary die lenght	Ld	20 mm
Pressure	P	1 – 6 bars
Température	T	300K

The velocity U_c in the tank is calculated from the mass flow at the exit of the die by applying the formula below:

$$U_c = \frac{4Q_m}{\rho D_c^2}$$

Where ρ $[Kg/m]^3$ is the density of the fluid. Mass flow is obtained from computer acquisition of mass over time.

After the pressurizing of the polymer by the piston sliding without friction in the cylinder, the die limits the flow of the polymer, if $D_c >> D_d$ (typically : $D_c = 9$ mm et $D_d = 1$ mm.

The flow of the fluid is given by :

$$Q = \frac{U_c \pi D_c^2}{4}$$

In this study pseudo plastic power law model was used to describe the flow properties for spinning suspension containing Polyethersulfone (PES) as polymer, N-Methyl2-Pyrrolidone (NMP) as solvent and Stainless Steel (SS) as doped particles.

Power law model , also known as the Ostwald de Waele relationship, the relationship of shear stress τ and shear rate $\dot{\gamma}$ as :

$$\mu = \frac{\tau}{\dot{\gamma}} = K\dot{\gamma}^{n-1}$$

Where μ $[Pa.s]$ is the apparent visosity of the fluid, K is the consistency index and n $[unitless]$ is the flow behavior index; $n < 1$ for a shear-thinning fluid (pseudo plastic fluid), $n > 1$ for a shear-thickening fluid (dilatants fluid), and $n = 1$ for a Newtonian fluid. The rheological fluid parameters are presented in table 2:

Results and discussions:

Creative Commons Attribution-NonCommercial-NoDerivatives 4.0 International License (CC BY-NC-ND)

The effect of inlet velocity on outlet velocity and pressure drop is studied for spinning solution. The results show that increasing of inlet velocity leads to increase pressure drop and outlet velocity as shown in figure 2 and 3.

For all curves of velocity and pressure in the capillary, we note that the velocity values are almost stable figure 5. On the other hand, there is an increase in the velocity in the die which reaches its maximum value at the exit of the die, on the other hand, it is noted that the values of the pressure in the capillary tank are practically stable for an inlet velocity equal to $1.06e^{-4}$ m / s, and a slight increase when increasing the inlet velocity. On the other hand, there is a sudden decrease in the pressure in the die which reaches the zero value at the exit.

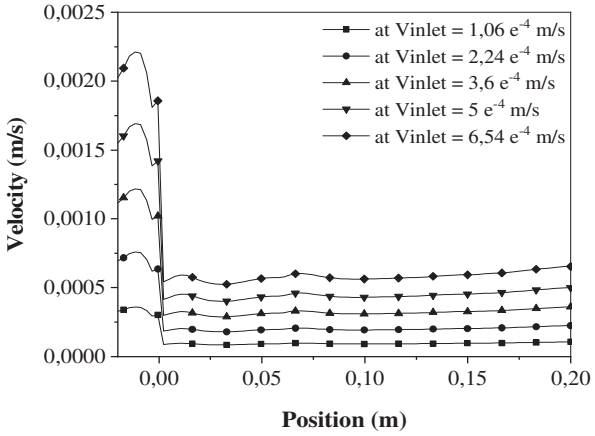

Fig2. Velocity evolution along the length at various inlet velocities

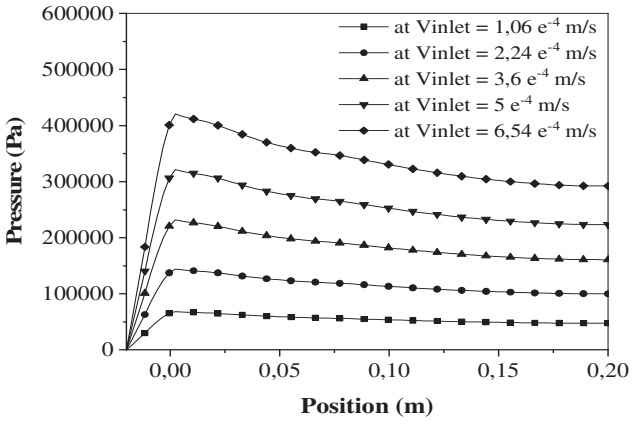

Fig3. Pressure drop evolution along the length at various inlet velocities

The simulation results of the velocity profile at the outlet of the capillary die is shown in figure 4. The velocity profile is parabolic, as commonly experienced in the laminar flow. The velocity profile in the die is flattening around the cross-section area and the velocity gradient near the wall is high compared with the rest point located in the horizontal axis of the exit of the die. it is clear that when increasing the velocity of entry we observe an in homogeneity of the distribution of the velocity at the exit, according to these profiles we can conclude that at a

Creative Commons Attribution-NonCommercial-NoDerivatives 4.0 International License (CC BY-NC-ND)

minimum speed of 1.06 e^{-4} m / s we have an uniform distribution of the velocity which leads to a seine extrusion of the solid fiber membranes

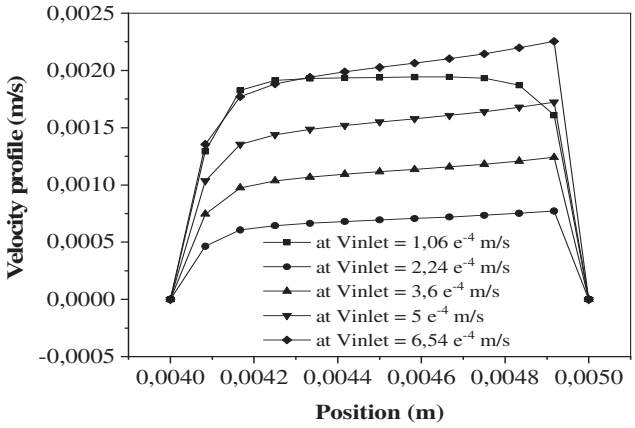

Fig4. Velocity profile at the end of the capillary die

Capillary dimension, D_d: 0.001 m, D_C: 0.009 m, Total length: 0.2 m, Fluid velocity (m/s): 1.06 e^{-4}

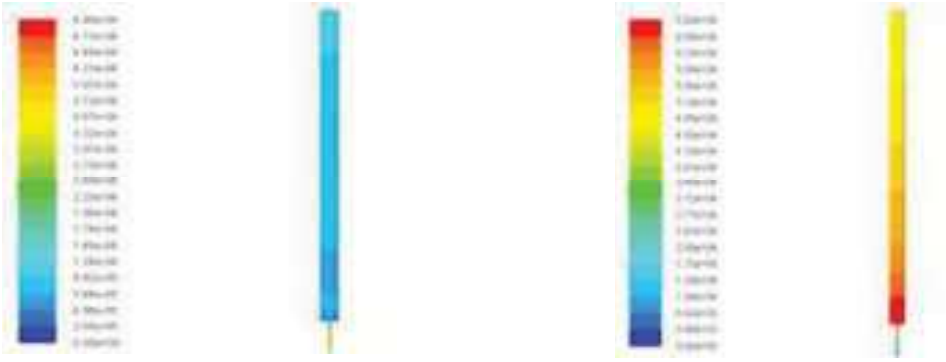

Fig5. Contours plot of Velocity along the length (at the left), Contours plot of static pressure along the length (at the right)

Conclusion:

The CFD simulation study made it possible to understand the flow behavior of a suspension fluid that follows the power law through a capillary rheometer consisting of a cylinder and a die. According to the evolution of the velocity in the two geometries the velocity marks an uniform distribution in the upper part (capillary tank) and an increase in the lower part (capillary die). The preliminary result obtained from this study suggests that 3D simulations are necessary for this type of solution that is sensitive to low flow shear. The methodology can adopt for different geometrical configuration which leads to the understanding of the behavior of the flow inside the die.

Creative Commons Attribution-NonCommercial-NoDerivatives 4.0 International License (CC BY-NC-ND)

References:

Ahsan, M., (2015), *Numerical analysis of friction factor for a fully developed turbulent flow using k –ε turbulence model with enhanced wall treatment ScienceDirect Numerical analysis of friction factor for a fully developed turbulent flow using k e ε turbulence model with*. Journal of Basic and Applied Sciences, N°3, pp.269–277.

Chaudhuri, J. B., (2006), *Effects of Common Sterilization Methods on the Structure and Properties of Poly (D , L Lactic-Co-Glycolic Acid)* Scaffolds. Tissus Engineering, N°12.

Hee, K. O., (2014). *Effect of shear, elongation, and phase separation in hollow fiber membrane spinning*.

Idris, A., Man, Z., Maulud, A. S., & Khan, M. S., (2017), *Effects of Phase Separation Behavior on Morphology and Performance of Polycarbonate Membranes.*

Kajekar, A. and al., (2015), *Preparation and characterization of novel PSf / PVP / PANI-nano fi ber nanocomposite hollow fi ber ultra fi ltration membranes and their possible applications for hazardous dye rejection*. Journal of Desalination, Vol 365, pp.117–125.

Mckelvey, S. A., Clausi, D. T., & William, J., (1997), *A guide to establishing hollow fiber macroscopic properties for membrane applications*. Journal of Membrane Science, Vol 124, pp. 223–232.

Qin, J., Wang, R., & Chung, T., (2000), *Investigation of shear stress effect within a spinneret on flux , separation and thermomechanical properties of hollow fiber ultrafiltration membranes*. Journal of Materials Chemistry A, Vol 175, pp. 197–213.

Shilton, S. J., (1996), *Flow Profile Induced in Spinneret During Hollow Fiber.* Journal of Applied Polymer Science, 1359–1362.

Suffian, M., M, R., S, M. A., I, C. B. L., & Santha, P. H. Y., (2013), *Flow instability of dope solution in hollow fiber spinning*. Borneo Science, pp. 1–13.

Suresh, K., Selvam, K., & Karunanithi, B., (2019), *CFD simulation studies on the flow behavior of power-law fluids used to extrude the polymeric hollow fiber membrane through an angular spinneret*. The 11th National Conference on Mathematical Techniques and Applications, 20160.

Torrestiana-sanchez, B., Ortiz-basurto, R. I., & Fuente, E. B. La., (1999), *Effect of nonsolvents on properties of spinning solutions and polyethersulfone hollow fiber ultrafiltration membranes*. Journal of Membrane Science, Vol 152.

Yu, K., Matsuura, T., Chung, T., & Fen, W., (2004), *The effects of flow angle and shear rate within the spinneret on the separation performance of Polyethersulfone(PES) ultrafiltration hollow fiber membranes*. Journal of Membrane Science, Vol 240, pp. 67–79.

Creative Commons Attribution-NonCommercial-NoDerivatives 4.0 International License (CC BY-NC-ND)

Algerian Journal of Engineering Architecture and Urbanism Vol. 5 Nr. 3 2021
ISSN: 2588-1760

IMPACT OF DFB LASER PARAMETERS ON FTTH-GPON SYSTEM

Attaouia BENTAHAR
Dr, Department of Electronic, LEPO Laboratory, Mascara university , bentaha_1011@yahoo.fr
Malika KANDOUCI
Pr, Department of Electronic, LEPO Laboratory, Sidi Bel Abbes University, maikand04@gmail.com
Samir GHOUALI
Dr, Department of Electronic, STIC laboratory, Mascara university, ghtelec@yahoo.fr
Radia MADJIDI
Department of Electronic, LEPO Laboratory, Mascara university, madjidi_r@yahoo.fr

Abstract:
DFB (Distributed Feed Back) lasers are commonly used in most telecommunication devices for their single-longitudinal mode, narrowband line width and high-power optical signal. DFB laser diode was developed for use in current generation high speed FTTx and 10G PON optical networks in OLT units. With highly optimized performance up to 85°C, this laser exhibits low threshold current and excellent slope efficiency. The purpose of this paper is to demonstrate an implementation of DFB as transmitter can provide an extended reach and a high split-ratio for the cost-effective implementation of GPON technology. Moreover in this paper, was study different characterizations of DFB laser, which depend essentially on the physical parameters, such as confinement factor, quantum of efficiency and the effect of those parameters to optimize the power, quality factor Q and eye diagram. Our analysis shows that the optimum DFB laser (for confinement factor F = 0.2 , Photon lifetime estimation τp = 12 ps and quantum of efficiency η = 0.2) was able to reach transmission distance over 60 Km with best BER value around 10^{-9} , Q factor around 8 and good eye diagram.

Key words: Laser, DFB, FTTH, Eye diagram.

Introduction:

Single wavelength emission allows to favor a single mode of emission, and to avoid multimodal broadcasting; this show cannot be do that with a selective resonator obtained in introducing into the cavity a network selecting only one wavelength. This notion transposed semiconductor lasers gave birth to Bragg grating laser diode. These laser diodes are at the base of two types: DFB (Distributed feedback) and DBR (Distributed Bragg Reflector).
When the network is engraved above or below of the active layer, the laser is called "DFB", which means "distributed feedback". When the network is etched out of the active layer, along the axis of the cavity, the laser is called "DBR" which means "distributed Bragg reflector [1]:

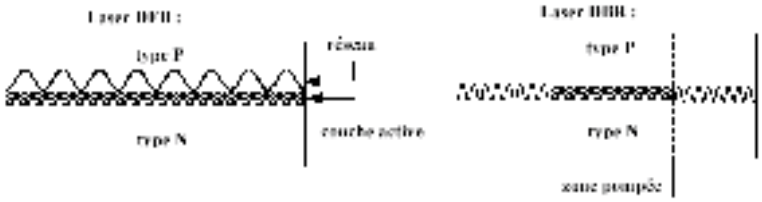

Fig.1: presentation of DFB laser and DBR laser.

Creative Commons Attribution-NonCommercial-NoDerivatives 4.0 International License (CC BY-NC-ND)

Principle of DFB:

DFB laser has better properties spectral; its structure is the same as that of a Fabry-Perot laser only the two mirrors of the cavity are removed and replaced by a reflector distributed Bragg allowing the selection of a wavelength [3, 4]. We obtain this network by doing periodically vary the thickness of a layer of the hetero structure which, in turn, creates a variation periodic refractive index [5, 6]. This periodic variation of the refractive index results in reflecting a specific wavelength, called the Bragg wavelength defined by equation (1)

$$\lambda_B = 2 \cdot n_{eff} \cdot \Lambda \qquad (1)$$

Where:

n_{eff} is the effective index of the fundamental mode and Λ is the period .

Physical characterization of DFB laser:

It is possible to describe a DFB laser either by 'system' quantities or by its physical parameters (differential gain coefficient, gain compression factor, photon lifetime), or by its physical parameters (wavelength, differential gain coefficient, confinement factor, carrier lifetime). The characteristic parameters for the description of the DFB laser, depending on the type of system definition or physical definition, are given in table (1).

System parameters	Physical parameters
Wavelength	Wavelength
Threshold current	Coefficient de gain différentiel (cm^{-3})
Power / current efficiency	Volume of the active layer (cm^2)
Line width	Damping rate
Containment factor	Gain compression factor (cm^3)
-3 dB band	Photon lifetime (s)
Spacing between modes	Spontaneous emission factor
Chirp	Lifespan of carrier (s)
RIN noise	Line broadening factor

Table1. parameters of DFB

These physical parameters are obtained after calculations from system parameters which require knowledge of certain internal physical data specific to the component.

Puissance optique d'émission du Laser :

Solving the following system of evolutionary equations [2] :

$$\begin{cases} \frac{dP}{dt} = 0 \\ \frac{dN}{dt} = 0 \\ \frac{d\Psi}{dt} = 0 \end{cases} \qquad (3)$$

In statics, this resolution makes it possible to determine for each polarization current the pair of variables N and P solution of this system of equations. The number of photons P thus

Creative Commons Attribution-NonCommercial-NoDerivatives 4.0 International License (CC BY-NC-ND)

obtained makes it possible to calculate the instantaneous optical power at the output of the laser diode by the relation:

$$P_{opt} = \frac{P.h.c.\eta}{2.\lambda.\tau_p} \quad (4)$$

P: The number of photons
η: The differential quantum efficiency,
h: Planck constant = 6.62 $.10^{-34}$J.s
C: speed of light in vacuum = 3.10^{8} m / s.

The power emitted as a function of the current:

We can then visualize the curve which makes it possible to know the relationship between the injected current and the emitted power.

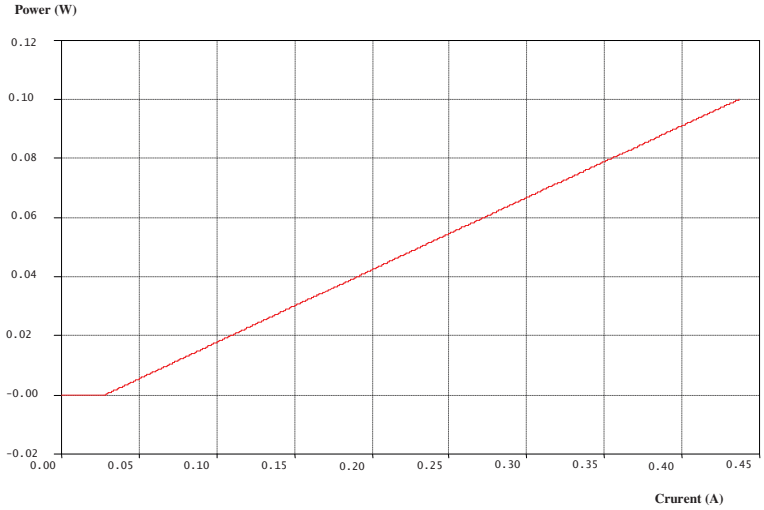

Fig. 2 : optical power as a function of the injected current.

Simulation of GPON:

The block diagram of the basic link that we are going to simulate is represented in the figure above, the generator block and the NRZ encoder generate pseudo-random data at a rate of 2.5Gb/s. The laser is a continuously modulated DFB, emitting at 1550 nm delivering an output power of 10 dBm. Typically a splitter sharing rate of 64 users and a total loss of 30 dB over a 20 km distance of G.652 fiber and with a linear attenuation of 0,2 dB/km. The receiving module includes signal conversion by an APD photodiode with a sensitivity of 0.9 A/W, a filter and performance evaluation modules to determine the eye diagram and the received power. In order to characterize the optical power emitted by the laser, we will first intervene on some physical parameters of the laser such as the confinement factor, the differential efficiency and the duration of photons. The synoptic diagram of the simulated link is represented by figure (3)

Creative Commons Attribution-NonCommercial-NoDerivatives 4.0 International License (CC BY-NC-ND)

Algerian Journal of Engineering Architecture and Urbanism Vol. 5 Nr. 3 2021
ISSN: 2588-1760

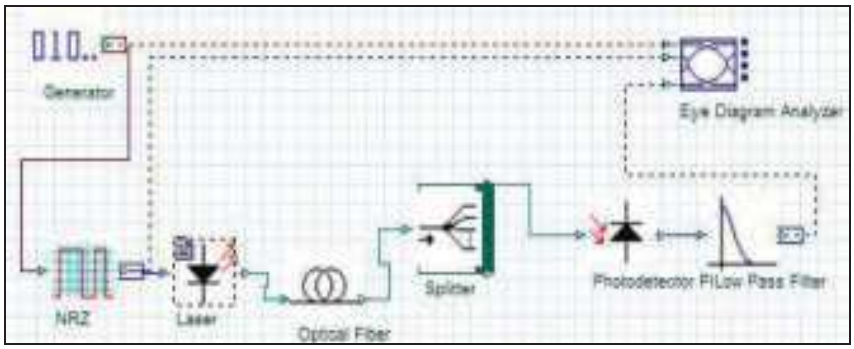

Fig. 3: Block diagram of the link studied.

Results and discussions:

The effect of differential quantum efficiency on optical power

Differential quantum efficiency measures the energy efficiency of converting electrical energy into light energy in a semiconductor laser. To see the effect of the differential efficiency on the optical power at the output of the laser, we will vary η and we visualize the shape of the power at the output of the laser..

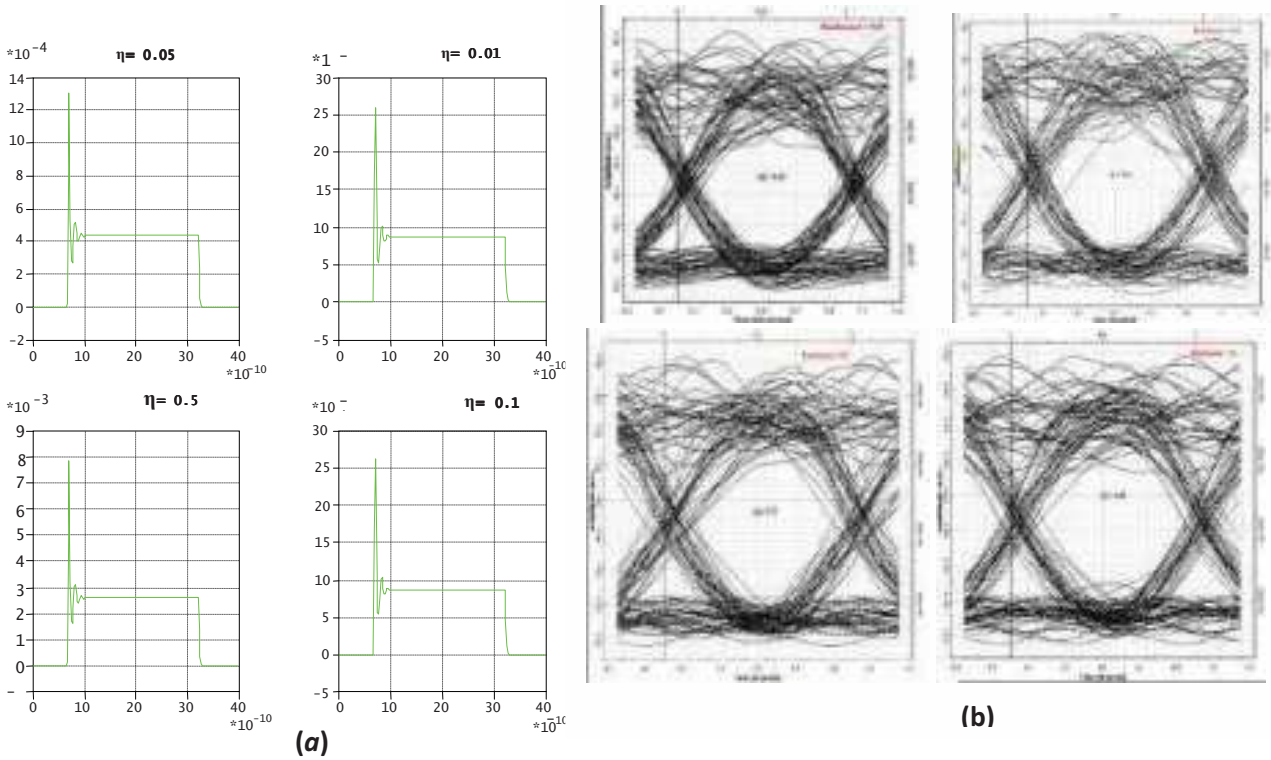

Fig. 4 : a) optical power as a function of the differential quantum efficiency , b) diagrams of the eye for differential quantum efficiency at 20km..

Creative Commons Attribution-NonCommercial-NoDerivatives 4.0 International License (CC BY-NC-ND)

Algerian Journal of Engineering Architecture and Urbanism Vol. 5 Nr. 3 2021
ISSN: 2588-1760

Figure (4) represents the optical power at the output of the laser for different values of the differential quantum efficiency (η = 0.01, η = 0.05, η = 0.10, η = 0.60), we can see that the output power is linearly related to l 'increase in efficiency η as shown by relation (4). It is always in the interest of having the highest possible differential efficiency to achieve a given light power.

The effect of optical confinement factor on optical power:

The optical confinement factor, F is defined as the ratio of the optical power confined in the active layer to the total power. According to the results shown in figure (5), a smaller optical confinement factor is also observed which contributes considerably to a delay time of the output of the pulses. In the case of F = 0.1, the response time of the laser is a little greater compared to the response time for F = 0.9. Thus, by increasing the optical confinement factor in the active layer of the semiconductor, we can significantly reduce the delay time of the laser response.

This delay reflects the fact that the stimulated emission did not take place until the concentration of carriers reached its threshold value. It can be said that a design high performance laser source should maximize optical confinement in the active layer with a reasonable value. We obtain a high quality factor (around 7. 30), and a high received power (30.10^{-4} w) for a confinement factor of 0.2. The eye diagram is wide open with a higher detection threshold in this case.

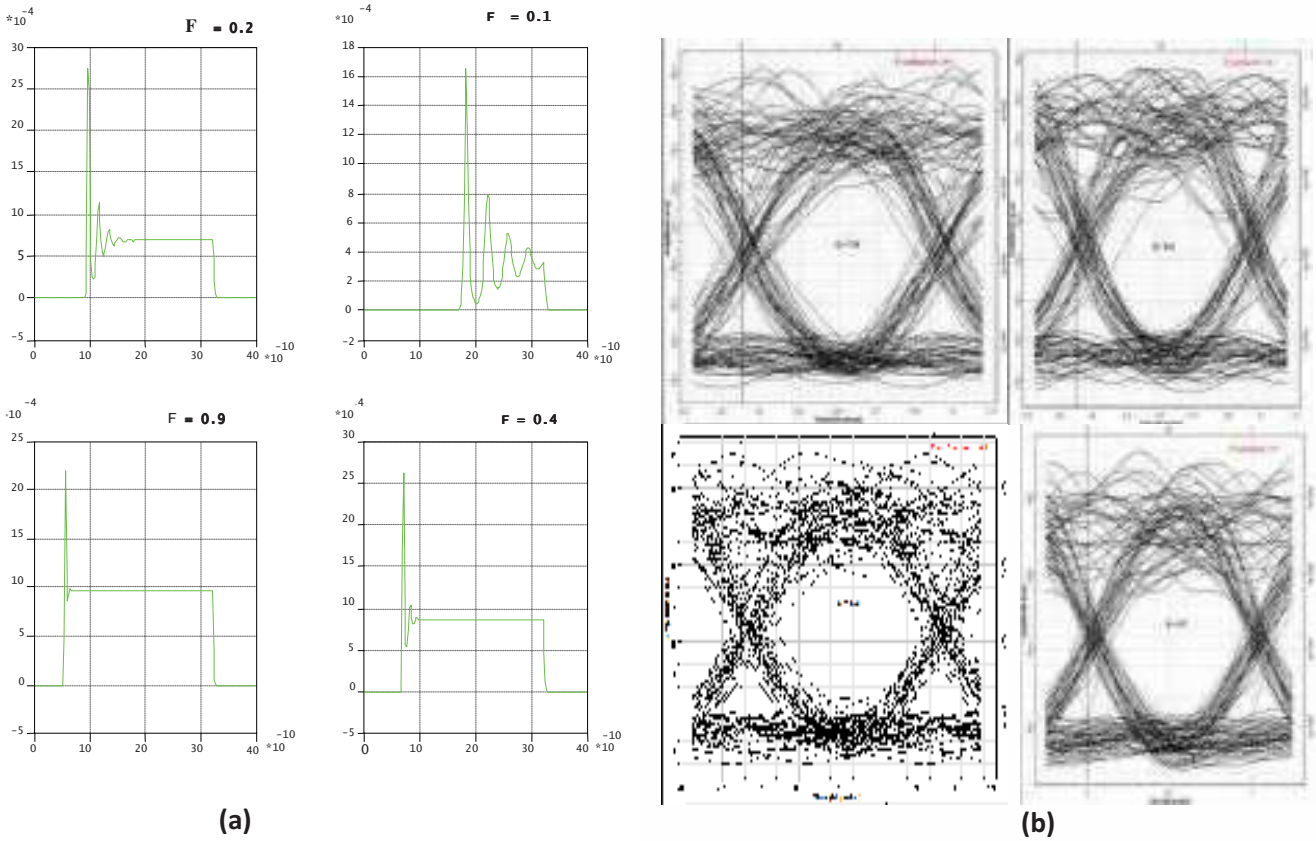

Fig .5: a)optical power as a function of the variation of the confinement factor.b) eye diagrams as a function of the containment factor at 20km.

Creative Commons Attribution-NonCommercial-NoDerivatives 4.0 International License (CC BY-NC-ND)

Algerian Journal of Engineering Architecture and Urbanism Vol. 5 Nr. 3 2021
ISSN: 2588-1760

The effect of photon lifetime on optical power:

The lifespan of photons in a laser cavity reflects the ability of the cavity to trap light. The curves in figure (6) represent the optical power for different lifetimes of the photon, it can be seen that the higher the lifespan of the photon at the input, the more the optical power at the output of the laser decreases (the duration of photon life τp is inversely proportional to the output power) which we always see in relation (4) for optical power.

According to the results obtained, it can be seen that the laser diode has a characteristic response but with an overshoot and a small delay, the response of the laser is therefore not instantaneous. In fact, this delay corresponds to the time necessary for the concentration of carriers to reach its threshold value, this value will be reached all the more rapidly as the flow of injected carriers and the greater the injected current. It has been noticed that the more the lifetime of the photon increases, the more the quality factor increases, The maximum quality factor is obtained for τ_p = 12 ps with a good opening of the eye diagram.

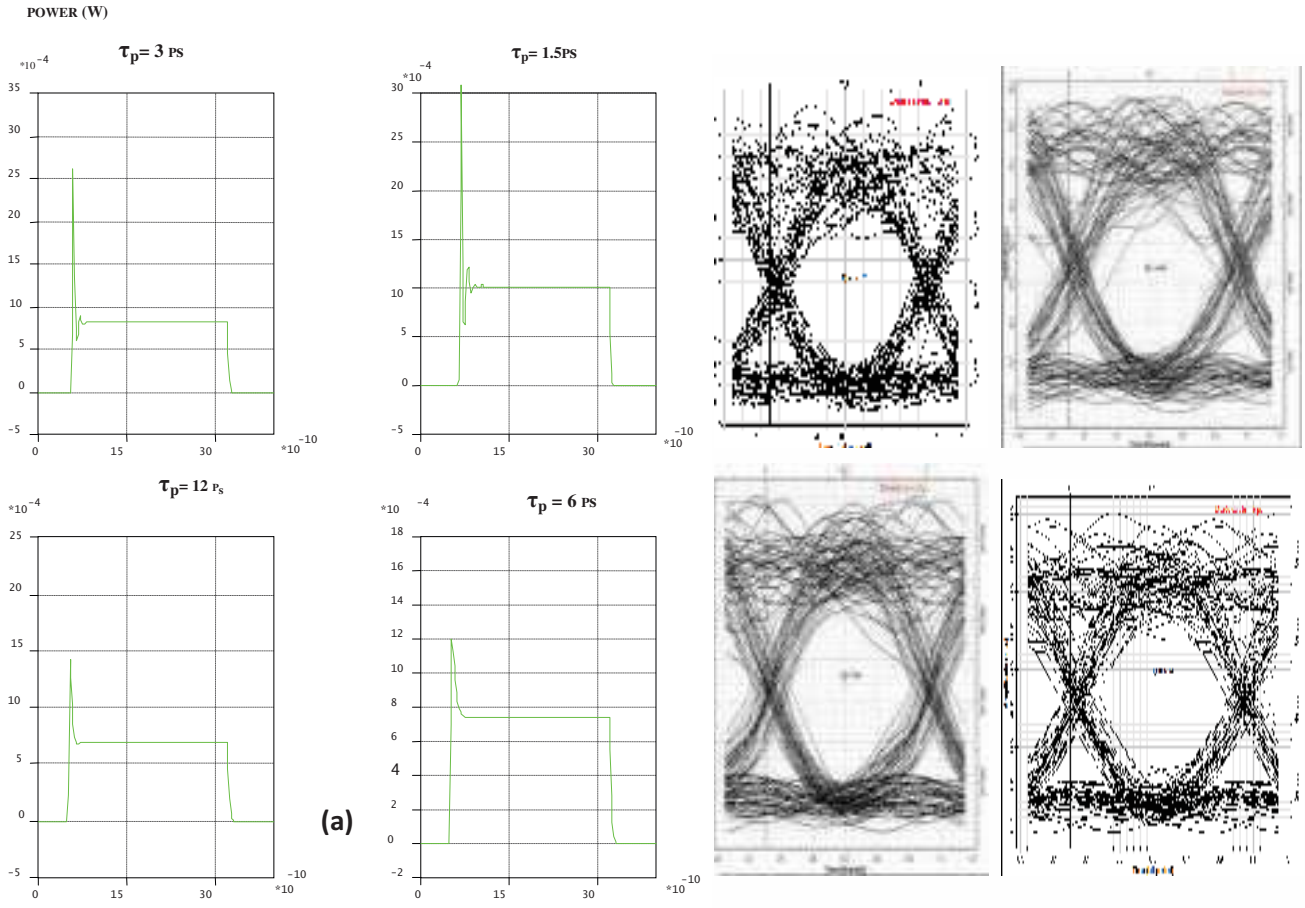

Fig. 6: a) optical power as a function of the variation of photon lifetime.b) eye diagrams as a function of the photon lifetime at 20km.

Creative Commons Attribution-NonCommercial-NoDerivatives 4.0 International License (CC BY-NC-ND)

Conclusion:

This simulation work clearly showed us the different variations of the characteristics of the distributed feedback laser. The simulation results provide information on the choice of physical parameters to be used in optimizing the emitted optical power, which is the main factor in calculating the signal-to-noise ratio of the system. The table summarizes the parameters used in our simulation, and which allow us the post-amplification of a GPON link with a good quality factor around 7.6 up to 60 km for 64 users.

F = 0.2	confinement factor
τ_p= 12 ps	photon lifetime
η= 0.6	Differentialquantum efficiency

References:

[1]. Grégory Mourat "Study of laser diodes for metrological applications of optical feedback". Doctoral thesis from the University of Toulouse, Defended on June 25, 1999.
[2]. Iréne and Michel Joindot "Telecommunications by optical fibers", Dunod, Paris, 1996.
[3]. Laurent Mendizabal "Reliability of 1.55µm DFB laser diodes for telecommunications applications: Statistical approach and component-system interaction". Doctoral thesis from the University of Bordeaux1, defended on March 03, 2006.
[4]. Stéphane. Calvez, "Fiber laser for wavelength multiplexed telecommunications: study of wavelength tunability and the generation of multi-wavelength pulse trains by electro-optics", Thesis of Doctorate from the University of Franche-Comté, 2002.
[5]. Fabien Kéefélian "Correlation of the phase noise of Bragg grating lasers by optical injection. Application to the generation and transport on fiber of radio-frequency signals ". Doctoral thesis from the National School of Telecommunications defended on December 05, 2005
[6]. Carlos Alberto Palavicini Cham "Analysis of photonic components by phase-sensitive low coherence reflectometry". Doctoral thesis from the National School of Telecommunications defended on April 26, 2004.
[7]. David Barat "GaSb-based single-frequency lasers emitting at 2.6 µm for gas analysis". Doctoral thesis from the University of Montpellier II, Defended on November 22, 2007
[8]. System software manual.

Creative Commons Attribution-NonCommercial-NoDerivatives 4.0 International License (CC BY-NC-ND)

Algerian Journal of Engineering Architecture and Urbanism Vol. 5 Nr. 3 2021
ISSN: 2588-1760

DIMENSIONAL ANALYSIS OF A PARABOLIC TROUGH COLLECTOR WITH A SINUSOIDAL ABSORBER TUBE

Lyes BORDJA

Department of mechanics, Faculty of Science and Applied Sciences.University Of Larbi Ben M'hidi, Oum El Bouaghi, Algeria, E-mail : bordjalyes@gmail.com

Yassine DEMAGH

LESEI, Department of mechanics University of Batna 2, Batna, Algeria,

E-mail : yassine.demagh@yahoo.fr

El Wardi BITAM

LESEI, Department of mechanics University of Batna 2, Batna, Algeria,

E-mail : bitam.ew@gmail.com

Redjem HADEF

Department of mechanics, Faculty of Science and Applied Sciences.University Of Larbi Ben M'hidi, Oum El Bouaghi, Algeria, E-mail : rhadef@rocketmail.com

Abstract:

To reduce the investment cost of parabolic trough technology and to improve the thermal performance of solar receivers, a new design is proposed to achieve a high photo-to-thermal conversion level. The proposed solar receiver has a sinusoidal absorber tube, a concept completely different from conventional receivers with their straight absorber shapes. Dimensional analysis with similarity considerations will be discussed to highlight thermal performances of the new tube compared to the former. The construction of the dimensional analysis is based on the quantification of the heat transfer rate between the inner wall and the HTF (heat transfer fluid) and to assume the same operating conditions and the same useful thermal power in order to estimate the aspect ratio of the new absorber tube. The pressure drop will also be estimated for both tubes to establish the relationship between them. The pressure drop penalty and heat transfer improvement of the new tube compared to the conventional straight tube will be evaluated using the performance evaluation criteria.

Key words: Sinusoidal shape absorber, parabolic trough concentrators, dimensional analysis.

Introduction :

Plusieurs travaux de recherche ont été menés pour étudier le transfert de chaleur et l'écoulement de fluide dans les tubes courbés en tant qu'application technique pratique. Les applications potentielles des géométries courbés dans les processus industriels comprennent les bobines hélicoïdales, les tubes courbés, les tubes serpentins, les tubes en spirale et les tubes torsadés (Abou-Arab et al. 1991) et (Yang et al. 2002).

L'énergie du rayonnement solaire est transformée à travers ces tubes en une énergie interne réalisée par le HTF. L'énergie du HTF peut alors être utilisée directement comme eau chaude ou pour d'autres applications. Les capteurs solaires peuvent être classés comme non concentrateurs (stationnaires) ou concentrés (Kalogirou 2004). La principale différence est

Creative Commons Attribution-Non Commercial-No Derivatives 4.0 International License (CC BY-NC-ND)

que les capteurs fixes ont la même surface pour intercepter et pour absorber le rayonnement solaire, tandis que les capteurs concentrateurs ont un rapport de concentration beaucoup plus élevé jusqu'à 1500, qui est essentiellement le rapport de la zone d'interception à la zone de réception.

La structure des collecteurs doit être suffisamment robuste pour supporter des différentes charges, elle doit être plus légère pour l'optimisation des coûts et les défis de fabrication doivent être soigneusement évalués. Un certain nombre de concepts structurels ont été proposés tels que les structures d'ossature en acier avec des tubes de torsion centraux ou doubles fermes en V, (Kalogirou et al. 1994, Adrian et Randy 2009).

Récemment, des études numériques menées par (Demagh et al. 2015), (Bitam et al. 2018), (Demagh et al. 2020) sur une nouvelle configuration avec la forme incurvée en S pour optimiser la température de sortie des fluides caloporteurs et le comportement thermo-hydraulique de ce tube en tant qu'élément collecteur de chaleur.

Notre étude est basée sur une analyse dimensionnelle et des considérations de similitude afin de découvrir les avantages du nouveau tube absorbeur en termes de performances par rapport au tube droit conventionnel. La constitution de l'analyse dimensionnelle quantifiant le taux de transfert de chaleur entre la paroi interne de l'absorbeur et celle transportée par le fluide caloporteur comme chaleur utile, il est possible sous les mêmes conditions de fonctionnement et pour la même puissance thermique utile d'estimer le rapport de la longueur du nouveau Tube. La perte de charge est également estimée pour les deux tubes afin d'établir la relation intermédiaire. La combinaison de la perte de charge et du gain de transfert de chaleur du nouveau tube par rapport au tube conventionnel droit est évaluée à l'aide des critères d'évaluation des performances (PEC).

Configuration Géométrique du nouveau tube absorbeur :

Le tube absorbeur est défini par une section transversale circulaire (plan xy) le long d'une ligne médiane sinusoïdale, représentée sur la figure. 1. Il est entièrement caractérisé par une amplitude 2A et une périodicité λ. Les sections extraites sont perpendiculaires à la direction z. ce dernier est utilisé en acier inoxydable admet une forme selon l'équation (1), et ayant les propriétés suivantes: Conductivité thermique : $k = 54\ w/m^2$, Chaleur spécifique à pression constante : $C_p = 502.48\ KJ/Kg.K$, la masse volumique : $\rho = 8030\ Kg/m^3$ (SYLTHERM 800).

$$y(z) = A\left(\cos(\frac{2\pi}{\lambda}.z\right) - A$$

(1a)

Le rayon de la courbure (R_C) est défini par:

$$R_C = \frac{\left(1+(\frac{2\pi}{\lambda})^2 A^2 \sin(\left(\frac{2\pi}{\lambda}\right) Z)\right)^{3/2}}{((\frac{2\pi}{\lambda})^2 A\ cos(\left(\frac{2\pi}{\lambda}\right) Z)}$$

(1b)

Creative Commons Attribution-Non Commercial-No Derivatives 4.0 International License (CC BY-NC-ND)

R_C : n'est pas constant pour un trajet sinusoïdal, mais varie le long de la direction Z.

Le tube récepteur représente le cas de l'étude expérimentale LS-2, citée dans (Dudley et al 2004). Ces paramètres sont regroupés dans le tableau 1.

L'écoulement de fluide est turbulent et en régime permanent dans les conditions d'essai. Les équations gouvernantes comprennent, l'equation de la continuité, les équations de la quantité de mouvement, l'équation d'énergie et les équations du modèle K-ε réalisable. Afin de réaliser notre étude, on adopte les conditions aux limites comme il est indiqué sur la Figure 2.(Yang et al 1995, Ebadian et al 1996, Chen et al 2009, Jayakumar et al 2010).

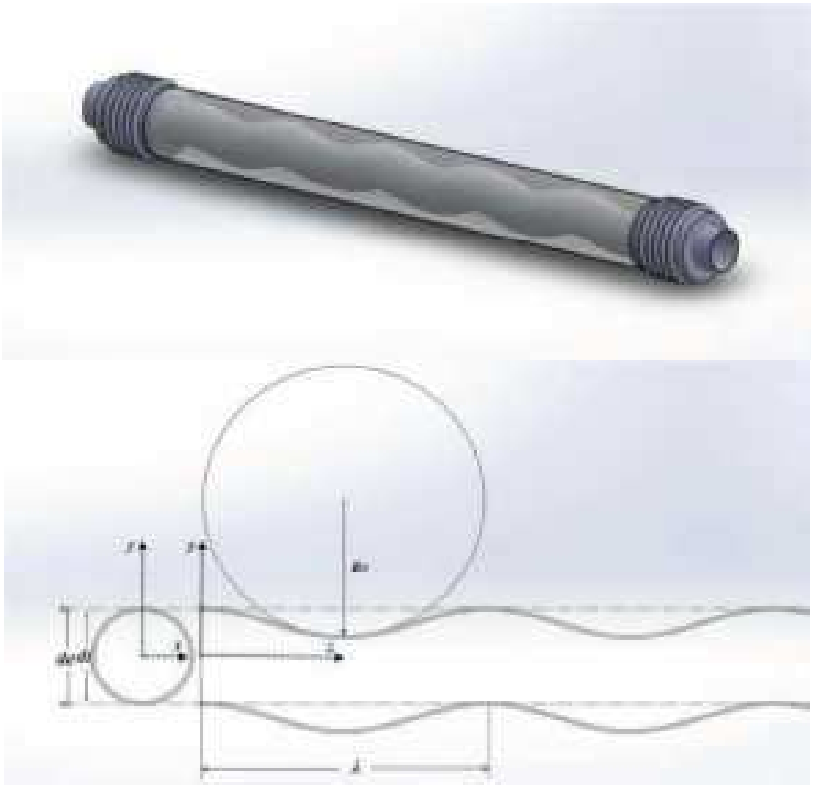

Fig 1. Schéma du nouveau Tube absorbeur.

La condition à la limite imposée à la surface externe est en réalité mixte : un flux entrant dû à la réflexion du rayonnement solaire par le miroir du CCP et un rayonnement de cette même paroi en raison de la température élevée qu'il peut atteindre.

	Paramètres	Cas de validation	Cas Réel
Diamètre extérieur	D_e	0.0227	0.070
Diamètre intérieur	D_i	0.020	0.066
Longueur de période	λ	0.3065	0.195
Amplitude d'onde	A	0.0235	0.01
Longueur de Tube	L	1	0.975
Rayon de courbure	R_c	0.101258936	0.09631845

Creative Commons Attribution-Non Commercial-No Derivatives 4.0 International License (CC BY-NC-ND)

Table 1. Valeurs des paramètres du nouveau tube absorbeur

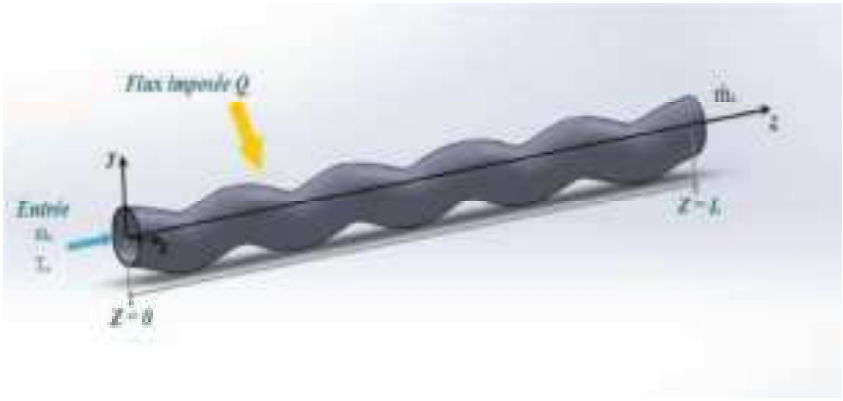

Fig 2. Conditions aux limites sur le tube absorbeur

Le rayonnement entre la face externe de l'absorbeur et la face interne du vitrage est maintien le vide. (Modest et al 2003, Tao et al 2001, Cheng et al 2012).

Résultat et validation:

Les résultats numériques sont comparés avec différents corrélations expérimentales présentés dans la bibliographie. La figure 3 représente le nombre de frottement en fonction de Reynolds.

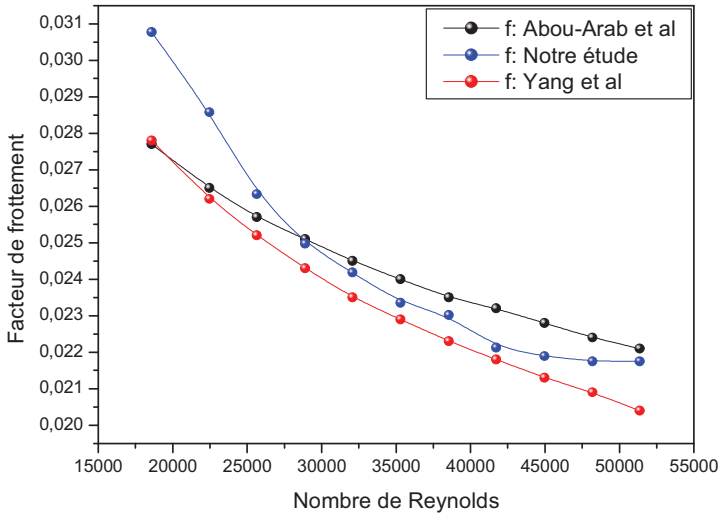

Fig 3. Facteur de frottement en fonction du nombre de Reynolds.

Les résultats numériques obtenus sont en bon accord avec les corrélations expérimentales, avec une erreur relative de 3% pour la corrélation de (Abou-Arab et al. 1991). Alors que celle (Yang et al. 2002) la plus défavorable à Reynolds élevé, avec 20% d'erreur.

Analyse dimensionnelle et considérations de similarité :

Creative Commons Attribution-Non Commercial-No Derivatives 4.0 International License (CC BY-NC-ND)

Il est très intéressant de pouvoir quantifier les avantages et les impacts du nouveau tube absorbeur sur les dimensions du récepteur solaire, le module solaire et le champ solaire ; ceci peut être obtenu par une analyse dimensionnelle (Bitam 2019).

Le taux moyen de transfert de chaleur Q dans tout le tube est défini comme :

$$Q = \dot{m}C_p(Text - Tint)$$
(2)

$\dot{m} = \rho u_{int}$S, le débit massique à travers la section d'entrée, $s = 4\pi/D_{int}$, d'autre part, en supposant des conditions d'un régime permanent, le transfert de chaleur par convection interne est exprimé comme suit :

$$Q = \dot{h}A(Tp - Tm)$$
(3)

$A = \pi D_{in}L$, C'est la zone d'échange interne du tube, avec L est sa longueur équivalente.

Le rapport des équations résultant de l'expression (2) lorsqu'elle est appliquée à la première configuration et à la seconde configuration conduit à :

$$\frac{Q_1}{Q_2} = \frac{(\rho u_{in}c_p)_1}{(\rho u_{in}c_p)_2}\frac{(Text-Tint)_1}{(Text-Tint)_2}\left(\frac{(D_{in})_1}{(D_{in})_2}\right)^2$$
(4)

De même, en utilisant l'équation (3)

$$\frac{Q_1}{Q_2} = \frac{(h)_1}{(h)_2}\frac{(Tp-Tm)_1}{(Tp-Tm)_2}\left(\frac{(D_{in})_1}{(D_{in})_2}\right)\frac{L_1}{L_2}$$
(5)

Les expressions (4) et (5) peuvent être combinées pour supprimer le terme $\frac{Q_1}{Q_2}$, on obtient :

$$\frac{L_2}{L_1} = \frac{(\rho u_{in}c_p/h)_2}{(\rho u_{in}c_p)_1}\left(\frac{(D_{in})_2}{(D_{in})_1}\right)\frac{(Text-Tint)_2}{(Text-Tint)_1}\frac{(Tp-Tm)_1}{(Tp-Tm)_2}$$
(6)

En supposant $\theta = (Text - Tint)$ et $\theta_p = (Tp - Tm)$, il s'ensuit que

$$\frac{L_2}{L_1} = \frac{(St)_1}{(St)_2}\left(\frac{(D_{in})_2}{(D_{in})_1}\right)\frac{(\theta)_2}{(\theta)_1}\frac{(\theta_p)_1}{(\theta_p)_2}$$
(7)

$St = h/\rho u_{in}c_p$, Étant le nombre de Stanton.

Selon la deuxième formule du nombre de Stanton, $St = Nu/Re.Pr$, l'équation (7) devient :

$$\frac{L_2}{L_1} = \frac{(St=Nu/Re.Pr)_1}{(St=Nu/Re.Pr)_2}\left(\frac{(D_{in})_2}{(D_{in})_1}\right)\frac{(\theta)_2}{(\theta)_1}\frac{(\theta_p)_1}{(\theta_p)_2}$$
(8)

Creative Commons Attribution-Non Commercial-No Derivatives 4.0 International License (CC BY-NC-ND)

Ce résultat est très utile ; cela suggère que le taux de transfert de chaleur proportionnel entre deux échangeurs différents peut être converti en égalité en introduisant des groupes sans dimension. Pour de nombreuses applications, il est pratique d'évaluer les propriétés du fluide caloporteur à la température d'entrée.

En introduisant le rapport d'aspect, défini comme L/D, une autre forme utile de l'expression (8) peut être atteinte,

$$\left(\frac{L}{D_{int}}\right)_1 \left(\frac{Nu}{Re.Pr}\right)_1 \left(\frac{\theta_p}{\theta}\right)_1 = \left(\frac{L}{D_{int}}\right)_2 \left(\frac{Nu}{Re.Pr}\right)_2 \left(\frac{\theta_p}{\theta}\right)_2 \quad (9)$$

La réduction possible de la taille de l'absorbeur :

Dans le cadre de la présente étude, les échangeurs seraient l'absorbeur conventionnel à tube droit et le nouveau conçu avec un tube longitudinalement courbé.

La question immédiate est de savoir quelle serait la taille de l'absorbeur courbé pour atteindre la hausse température similaire du fluide caloporteur pour les deux absorbeurs, c'est-à-dire $\frac{\theta_{nouvel\ absorbeur}}{\theta_{\ absorbeur\ standar}} = 1$, en considérant: la température d'entrée du fluide caloporteur similaire, $\frac{Pr_{nouvel\ absorbeur}}{Pr_{\ absorbeur\ standar}} = 1$, et un régime d'écoulement uniforme, $\frac{Re_{nouvel\ absorbeur}}{Re_{\ absorbeur\ standar}} = 1$, l'équation (8) est réduite à,

$$\frac{L_2}{L_1} = \frac{(Nu)_{absorbeur\ standar}}{(Nu)_{nouvel\ absorbeur}} \left(\frac{(D_{in})_{nouvel\ absorbeur}}{(D_{in})_{absorbeur\ standar}}\right) \frac{(\theta_p)_{absorbeur\ standar}}{(\theta_p)_{nouvel\ absorbeur}} \quad (10)$$

comme $Nu = hD_{int}/\lambda$, l'équation (10) devient,

$$\frac{L_2}{L_1} = \frac{(h)_{absorbeur\ standar}}{(h)_{nouvel\ absorbeur}} \frac{(\theta_p)_{absorbeur\ standar}}{(\theta_p)_{nouvel\ absorbeur}} \quad (11)$$

En supposant une paroi similaire avec une différence de température du fluide, $(\theta_p)_{absorbeur\ standar} = (\theta_p)_{nouvel\ absorbeur} = 1$, $(h)_{nouvel\ absorbeur}$, devrait être supérieur à $(h)_{absorbeur\ standar}$ l'équation (11) devient,

$$\frac{L_2}{L_1} = \frac{(h)_{absorbeur\ standar}}{(h)_{nouvel\ absorbeur}} < 1 \quad (12)$$

L'équation (12) peut donner une mesure de la longueur que le nouveau récepteur devrait absorber une quantité d'énergie utile similaire à celle absorbée par le récepteur droit dans les conditions de fonctionnement mentionnées précédemment. En utilisant l'équation (12), le changement potentiel de la longueur du nouvel absorbeur, tout en faisant varier le nombre de Reynolds, à T = 450 K est illustré sur la figure 4. Jusqu'à Re = 71000, la tendance augmente de, $\frac{L_2}{L_1} = 0{,}61$ à $0,71$; à partir de cet endroit, il diminue et devient relativement, environ 0,69.

Creative Commons Attribution-Non Commercial-No Derivatives 4.0 International License (CC BY-NC-ND)

Algerian Journal of Engineering Architecture and Urbanism Vol. 5 Nr. 3 2021
ISSN: 2588-1760

Pour obtenir la même augmentation de température du fluide caloporteur pour l'absorbeur droit classique, la longueur du nouvel absorbeur L_2 sera considérablement réduite, suite à l'amélioration du transfert de chaleur. Avec une longueur moyenne de L_2= 69% L_1, la taille du champ du capteur solaire devrait être réduit d'environ 31%.

Une autre question pourrait découler de l'analyse précédente: quel serait le diamètre du nouvel tube absorbeur en supposant une élévation de température du fluide caloporteur similaire à θ, la même température d'entrée du fluide caloporteur, la même longueur et le même débit massique.

Pour répondre à cette question, il est préférable d'utiliser l'équation (6) au lieu de l'équation (8). Compte tenu des hypothèses précédentes, il devient,

$$\frac{L_2}{L_1} = \frac{(u_{int}/h)_{nouvel\ absorbeur}}{(u_{int}/h)_{absorbeur\ standar}} \left(\frac{(D_{in})_{nouvel\ absorbeur}}{(D_{in})_{absorbeur\ standar}}\right) \frac{(\theta_p)_{absorbeur\ standar}}{(\theta_p)_{nouvel\ absorbeur}} \quad (13)$$

Pour plus de commodité, la différence de température de la paroi est supposée similaire, donc :

$\frac{(\theta_p)_{absorbeur\ standar}}{(\theta_p)_{nouvel\ absorbeur}} = 1$ et la vitesse est remplacée par, $u_{int} = 4\dot{m}/\rho\pi {D_{int}}^2$, Le débit massique étant inchangé, l'équation (13) est simplifiée,

$$\frac{(D_{in})_{nouvel\ absorbeur}}{(D_{in})_{absorbeur\ standar}} = \frac{h_{absorbeur\ standar}}{h_{nouvel\ absorbeur}} \quad (14)$$

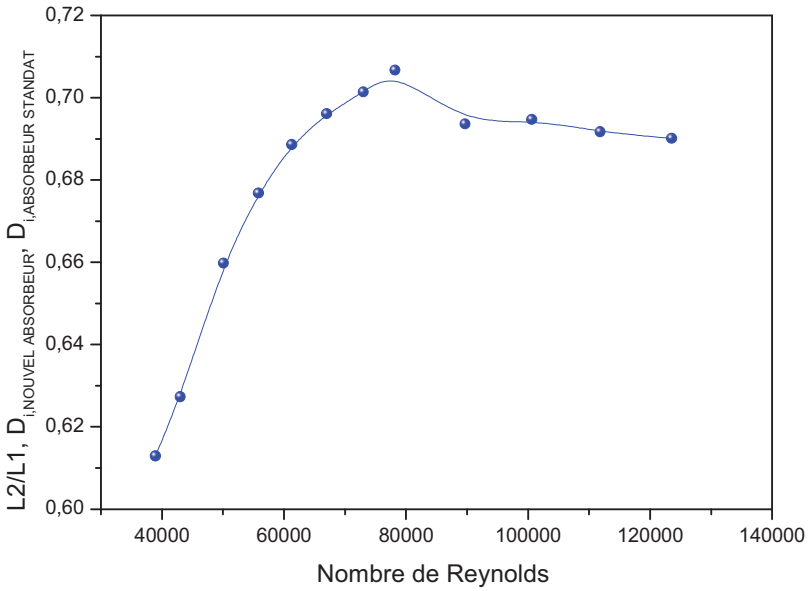

Fig 4. Réduction de la taille de l'absorbeur solaire.

Le résultat est similaire à l'équation (12) et la tendance par rapport au nombre de Reynolds serait similaire, comme le montre la figure 4. Pour obtenir la même augmentation de la

Creative Commons Attribution-Non Commercial-No Derivatives 4.0 International License (CC BY-NC-ND)

température du fluide caloporteur de l'absorbeur droit classique, tout en prenant la même longueur du nouvel absorbeur, son diamètre doit être diminué. Selon les hypothèses citées, la réduction moyenne du diamètre de récepteur devrait être d'environ 31%.

Il est également important de spécifier que la longueur du nouvel absorbeur L_2 est identifiée comme la longueur d'arc du tube sinusoïdal ; ce qui signifie que sa longueur droite équivalente devrait être légèrement inférieure en raison de la courbure.

Le rééquilibrage de la chute de pression :

L'augmentation de la perte de charge du nouveau tube d'absorbeur solaire, devrait être rééquilibrée par la réduction, de sa longueur. Pour renforcer cette affirmation, il vaut mieux utiliser la perte de charge $(-\Delta p)$ plutôt que le facteur de frottement f, la chute de pression à travers le nouveau tube, compte tenu du facteur de frottement f, s'écrit:

$$(-\Delta P)^{L_1}_{nouvel\ absobeur} = f.(\rho u^2_{int}/2)(L_1/(D_{int})_1) \quad (15)$$

Le facteur de frottement étant indépendant de la longueur, multipliant et divisant le côté droit de l'équation (15) par L_2,

$$(-\Delta P)^{L_1}_{nouvel\ absobeur} = f.\left(\frac{\rho u^2_{int}}{2}\right)\left(\frac{L_2}{(D_{int})_1}\right)\left(\frac{L_1}{L_2}\right) = (-\Delta P)^{L_2}_{nouvel\ absobeur}\left(\frac{L_1}{L_2}\right) \quad (16)$$

Donc,

$$(-\Delta P)^{L_1}_{nouvel\ absobeur} = (-\Delta P)^{L_2}_{nouvel\ absobeur}\left(\frac{L_1}{L_2}\right) \quad (17)$$

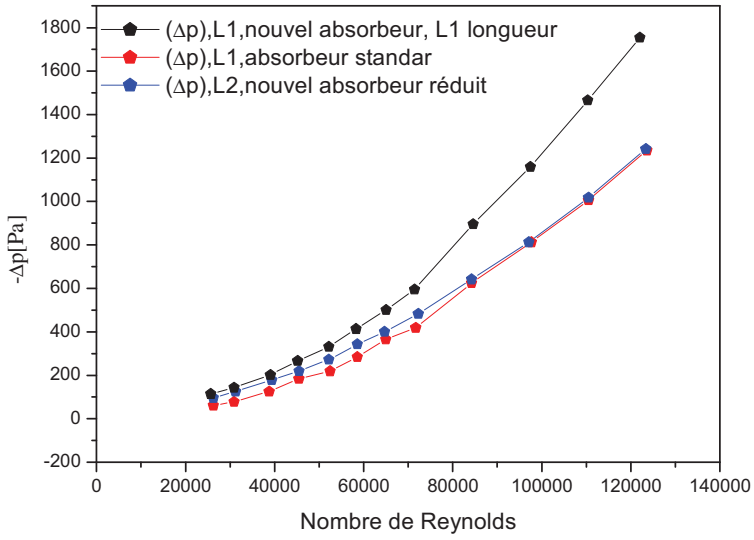

Creative Commons Attribution-Non Commercial-No Derivatives 4.0 International License (CC BY-NC-ND)

Fig 5. Similitude de la chute de pression à travers les absorbeurs et l'effet de la réduction de la taille sur le nouvel absorbeur.

Compte tenu de la réduction de taille du nouvel absorbeur, la perte de charge tout au long du nouveau tube $(-\Delta P)^{L_1}_{nouvel\ absobeur}$, calculé par l'équation (15) le tube doit être reconsidéré en tenant compte de sa longueur réduite. La chute de pression est rééquilibrée par la réduction de la taille et diminue comme le montre la figure 5. Comme supposé précédemment, les pertes de charge du nouveau tube (avec la longueur réduite L_2) et le tube droit (avec la longueur droite L_1) sont similaires.

Analyse de performance :

Pour une meilleure évaluation des nouvelles performances du nouvel absorbeur, il convient d'évaluer les critères d'évaluation des performances (PEC).

L'amélioration du transfert de chaleur est définie comme suit:

$$E_{Nu} = {Nu_{nouvel}}/{Nu_{standart}}$$

(18)

$Nu_{nouvel}\ et\ Nu_{standart}$, étant les nombres moyens de Nusselt pour le nouveau tube et le tube droit, respectivement.

La perte de charge relative encourue pour le nouveau tube, de longueur et de diamètre égaux avec un tube droit, est donnée par :

$$E_f = {f_{nouvel}}/{f_{standart}}$$

(19)

La combinaison de ces deux nombres sans dimensions, conduit aux critères d'évaluation des performances (PEC) à une puissance de pompage donnée.

$$PEC = \frac{{Nu_{nouvel}}/{Nu_{standart}}}{\left({f_{nouvel}}/{f_{standart}}\right)^{1/3}}$$

(20)

Creative Commons Attribution-Non Commercial-No Derivatives 4.0 International License (CC BY-NC-ND)

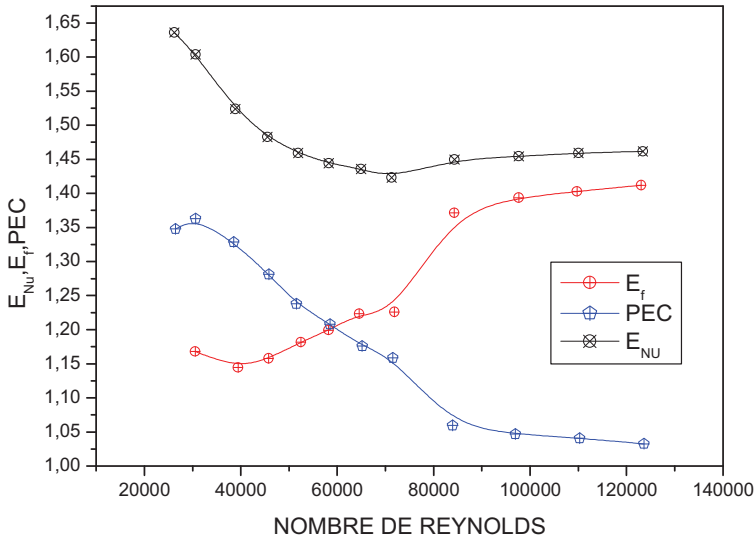

Fig6. L'amélioration moyenne du transfert de chaleur, la perte de charge et le PEC du nouvel absorbeur par rapport au nombre de Reynolds à Tint = 450 K.

L'amélioration moyenne du transfert de chaleur, la perte de charge et le PEC par rapport aux nombres de Reynolds sont illustrés dans la figure 6. Le PEC atteint un maximum de 135%, il diminue tandis que le Re augmente et devient presque uniforme à Re = 84160. Ce résultat est cohérent avec le comportement d'écoulement observé à Re = 84160 où le flux s'établit sans l'apparition de nouveaux tourbillons (Bitam et al. 2018).

Conclusion :

Grâce à une relation de similitude établie entre le nouveau tube absorbeur et le tube conventionnel droit. En termes de taux de transfert de chaleur, il a été constaté, dans les hypothèses et les conditions de fonctionnement considérées, que la nouvelle longueur du nouveau tube pouvait être réduite de 31%. L'amélioration du transfert de chaleur du nouveau tube accompagnée également de l'augmentation de la chute de pression par rapport à l'absorbeur conventionnel à tube droit, mais en général, le PEC a montré une grande amélioration de l'efficacité thermique pour le nouveau tube.

References :

Abou-Arab T.W., Aldoss T.K., Mansour A. (1991), *Pressure drop in alternating curved tubes*, Applied Scientific Research **48:** 1-9.

Yang R., Chiang F.P. (2002), *An experimental heat transfer study for periodically varying-curvature curved-pipe*, Int. J. Heat MassTransfer **45:** 3199–3204.

Adrian F., Randy G. (2009), *The SkyTrough™ Parabolic Trough Solar Collector, proceedings of the ASME 2009,* 3rd International Conference of Energy Sustainability, San Francisco, California, USA.

Kalogirou S.A. (2004), *Solar thermal collectors and applications*, Progress in Energy and Combustion Science **30:** 231–295.

Creative Commons Attribution-Non Commercial-No Derivatives 4.0 International License (CC BY-NC-ND)

Kalogirou S.A., Lloyd S., Ward J., Eleftheriou P. (1994), *Design and Performance Characteristics of a Parabolic-Trough Solar-Collector System*, Applied Energy **47:** 341-354.

Demagh Y., Bordja I., Kabar Y., Benmoussa H. (2015), *A design method of an S-curved parabolic trough collector absorber with a three dimensional heat flux density distribution*,Sol Energy **122:** 873 –884.

Bitam E. W., Demagh Y., Hachicha Ah. A., Benmoussaa H., Kabar Y. (2018), *Numerical investigation of a novel sinusoidal tube receiver for parabolictrough technology*, Applied Energy **218:** 495 –510.

Demagh Y., Bitam E. W., Bordja L. (2020), *Comparative numerical study on pressure drop in helically coiled and longitudinally C-shaped pipes*,SN Applied Sciences **2:**1570.

SYLTHERM 800. (2012), *heat transfer fluid*: product technical data.

Dudley V., Kolb G.,Sloan M., Kearney D. (1994), *SEGS LS2 solar collector-test results*, Tech. Report of Sandia National Laboratories SANDIA **94:**1884.

Yang G., Dong F., Ebadian M.A. (1995), *Laminar forced convection in a helicoidal pipe with finite pitch*, Int. J Heat Mass Transfer **38**: 853–62.

Yang G., Ebadian M.A. (1996), *Turbulent forced convection in a helicoidal pipe with substantial pitch*, Int. J Heat Mass Transfer **39:** 2015–2022.

Wu S.Y., Chen S.J., Li Y.R., Li L .J. (2009), *Numerical investigation of turbulent flow heat transfer and entropy generation in a helical coiled tube with larger curvature ratio*, Heat Mass Transfer **45:** 569–578.

Jayakumar J.S., Mahajani S.M., Mandal J.C., Iyer K.N., Vijayan P.K. (2010), *CFD analysis of single-phase flows inside helically coiled tubes*, Computers and Chemical Engineering **34:** 430–446.

Modest M.F. (2003), *Radiative heat transfer*, 2nd Ed., New York Academic Press.

Tao W.Q. (2001), *Numerical Heat Transfer*, 2nd Ed., Xi'an Jiaotong University Press, Xi'an.

Cheng Z.D., He Y.L., Cui F.Q., Xu R.J., Tao Y.B. (2012), *Numerical simulation of a parabolic trough solar collector with nonuniform solar flux conditions by coupling FVM and MCRT method*, Solar Energy **86:** 1770–1784.

Bitam E. W. (2019), *ConfigurationsStudy of Parabolic Trough CollectorsField for Optimizing Heat Transfer FluidsOutlet Temperature*, Thesis of Sciences, Faculty of Material Science, University Hadj Lakhder-Batna1, Algeria.

Creative Commons Attribution-Non Commercial-No Derivatives 4.0 International License (CC BY-NC-ND)

Algerian Journal of Engineering Architecture and Urbanism Vol. 5 Nr. 3 2021
ISSN: 2588-1760

CHEMICAL RECOVERY OF CADMIUM IONS FROM CHARGED BIOSORBENT

Asma1 BOUDAOUD1
PhD, Laboratory of Process Engineering, Faculty of Technology, Amar Telidji University, P.O. Box 37G, Route de Ghardaïa, 03000, Laghouat, Algeria, e-mail: asmaboudaoud@gmail.com

Mebrouk2 DJEDID2
PhD, Laboratory of Process Engineering, Faculty of Technology, Amar Telidji University, P.O. Box 37G, Route de Ghardaïa, 03000, Laghouat, Algeria, e-mail: m.djedidg@gmail.com

Chifaa3 AD3
PhD, Laboratory of Process Engineering, Faculty of Technology, Amar Telidji University, P.O. Box 37G, Route de Ghardaïa, 03000, Laghouat, Algeria, e-mail: chiffaad@gmail.com

Abstract:
The aim of current study was to recover cadmium (II) ions from palm fibres powder biosorbent. We have tested many desorbing chemical agents for changing the pH of solution to recover cadmium (II) ions such as nitric acid, hydrochloric acid and sulfuric acid under the same operating conditions such as contact times and stirring speeds, etc.., the reusability of the biosorbent was tested by repeating adsorption–desorption study up to five cycles, the results showed that the sulfuric acid solution is the optimal agent for this desorption with optimum pH for maximum desorption was found around 1, and 72 % of cadmium ions was recovered.
Key words: Desorption, Adsorption, Cadmium ions, Regeneration.

Introduction:

The success of wastewater treatment no longer depends solely on the use of the best methods in terms of high efficiency and low cost, but also depends on the use of eco-friendly biomaterials, and the most important not leave the toxic waste after the treatment that caused the spread another danger to the environment.

Many researchers have used an important method to remove toxic residues by recycling the biosorbent used in the adsorption process by desorption (Yu, 2002; Mishra, 2014).

The desorption process is the reverse process of adsorption based primarily on the modification of the experimental conditions of the adsorption process to guide this process in a completely opposite direction include the variation of pH solution (Xie, 2018), temperature (Srivastava, 1990) and solution ionic strength Blume (Srivastava, 2005).

The purpose of this study is to recycle of palm fibers powder charged by cadmium ions using the variation of pH solution after selecting the best chemical agent for the recuperation of cadmium ions.

Creative Commons Attribution-NonCommercial-NoDerivatives 4.0 International License (CC BY-NC-ND)

Materials and methods:

1. Preparation of Biosorbent

Palm fibers (PF) are perennial, a member of the palm family, were obtained from Laghouat region, Algeria. The PF were washed with distilled water three times and boiled for 30 min in order to remove the impurities and dried in the oven at 105°C to constant weight; the PF were crushed before use.

2. Preparation of adsorbate

All the chemicals used were of analytical reagent grade. Stock solution of 1000 ppm of Cd (II) was prepared by dissolving weighed quantity of Cd hydrated salts in distilled water, and then the desired concentrations were provided with diluting the stock solution. (Fig. 1)

3. Adsorption-Desorption experiments

The Adsorption- Desorption experiments were carried out in a batch system, the agents chemical effects were studied with variation of pH. Beakers containing 100 ml of HNO3, HCl and H2SO4 solutions with a concentration of 0.1mol/L are placed and the 1g of palm fibers powder charged by Cd ions was added to the solutions. The mixture was shaken mechanically at 25°C.

After the adsorption and desorption, the samples are filtered to measure the residual concentration of the metal ions using an atomic adsorption spectrophotometer, Elemental analyzes was carried out by atomic absorption (ANALYTIK JENA AG GERMANY AAS NOVAA 350) at the Laboratory of Process Engineering at Amar Telidji University in Laghouat.Subsequent paragraphs, however, are indented (here insert the second paragraph).

Results and discussions:

1. Choice of desorbent

In order to estimate the possibility of adsorbent regeneration and the reversibility of Cd (II), desorption experiments using various desorbing agents were tested at room temperature. For the regeneration of this adsorbent, three desorbing agents were tested in order to choose the best one. Their results are shown in Fig.1.

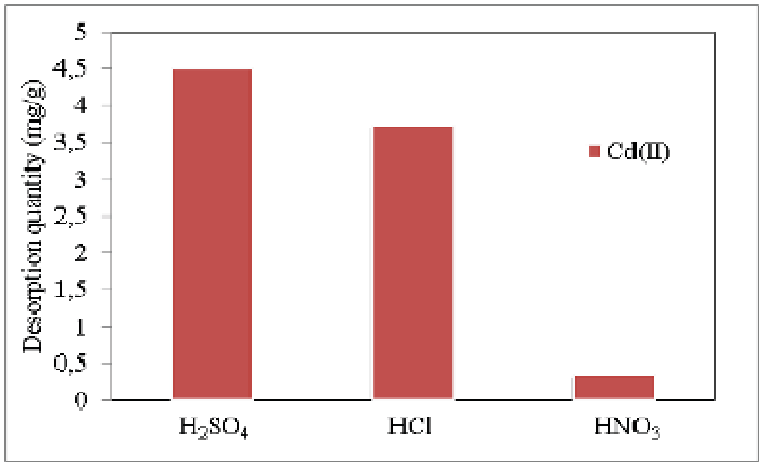

Fig1. Effect of various desorbing agents on desorption of Cd (II) under the operating conditions: t = 4h, m = 1 g, T = 293K and stirring speed = 500 rpm.

Creative Commons Attribution-NonCommercial-NoDerivatives 4.0 International License (CC BY-NC-ND)

Fig. 1 show that for Cd (II), the maximum desorption reaches 4.5 mg /g for one treatment cycle. We can conclude that adsorption is a reversible process and the recovery of Cd (II) from PFP is more efficient with the H_2SO_4 solution. From which it can be deduced that the PFP can be regenerated with sulfuric acid in order to reuse it another time.

2. Effect of pH

The regeneration desorbent found is sulfuric acid, tests of variation pH were carried out to determine its effectiveness. The results are shown in Fig. 2.

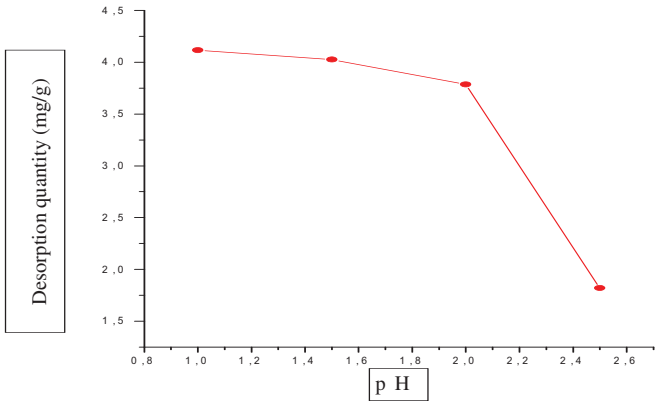

Fig2. Effect of pH on the amount of Cd (II) desorption under the operating conditions: t = 4 h, C0 = 100 mg / l, T = 293 K, stirring speed = 500 rpm.

The results in Fig. 2 indicate that the best desorption of Cd (II) at pH = 1. In addition, the desorption of Cd (II) seems to detach more easily which confirms a better affinity. Although it should be noted that at low pH, some of metals ions can be displaced by H^+ ions.

3. Determining the number of regeneration cycles

After selection of the Cd (II) desorption agent and the optimal pH, five adsorption-desorption cycles were examined (Fig. 3).

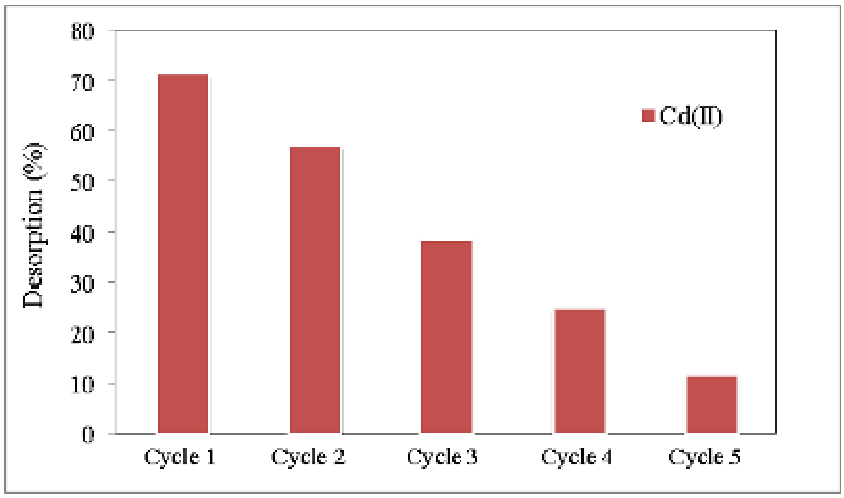

Fig3. Regeneration Cycles on Cd (II) desorption under the operating conditions: t = 4 h, m = 1 g, T = 293K and stirring speed = 500 rpm.

Creative Commons Attribution-NonCommercial-NoDerivatives 4.0 International License (CC BY-NC-ND)

Fig. 3 shows in the first cycle, desorption of Cd (II) was 72%. Then, the adsorbent was used again for the adsorption-desorption process for the other cycles up to the fifth cycle. However, the Cd (II) level was reduced to 10.87 % after five regeneration cycles. The adsorption-desorption process was stopped at the five cycles in order to avoid mass loss of the adsorbent dosage. In addition, the desorption of the metal ions has been slowly reduced from one cycle to the next and it can cause by the efficiency of the presence of functional groups which has resulted in a decrease of the adsorption sites.

Conclusion:

The desorption of cadmium ions by sulfuric acid studied here presented high Cd (II) ions desorption efficiency than the nitric acid and hydrochloric acid. Furthermore, the desorption Cd (II) did not in a wide range of pH, desorption of Cd (II) decreased with an increase in pH. Sequential desorption experiments also revealed that the PFP can be regenerated with sulfuric acid in order to reuse it up to five time.

References:

Yu S., He Z. L., Huang C. Y., Chen G. C., Calvert D. V. (2002), *Adsorption-desorption behavior of copper at contaminated levels in red soils from China*, Journal of Environmental Quality **31:** 1129-1136.

Mishra S. P. (2014), *Adsorption–desorption of heavy metal ions.* Current science **107:** 601-612.

Xie S., Wen Z., Zhan H., and Jin M. (2018*), An Experimental Study on the Adsorption and Desorption of Cu(II) in Silty Clay*, Geofluids **2018(4)**: 1-12.

Srivastava A., Srivastava P. C. (1990), *Adsorption-desorption behaviour of zinc (II) at iron (III) hydroxide-aqueous solution interface as influenced by pH and temperature*, Environmental Pollution **68:** 171-180.

Blume T., Weisbrod N., Selker J. S. (2005), *On the critical salt concentrations for particle detachment in homogeneous sand and heterogeneous Hanford sediments*, Geoderma **124:** 121-132.

Creative Commons Attribution-NonCommercial-NoDerivatives 4.0 International License (CC BY-NC-ND)

Algerian Journal of Engineering Architecture and Urbanism Vol. 5 Nr. 3 2021

ISSN: 2588-1760

THE SCALE AND THE SHAPE EFFECTS USING THE UDEC MODELING OF AN UNDERGROUND MINING PILLAR

Youcef CHEIKHAOUI
PhD student, Department of Mining Engineering, National Higher School of Mining and Metallurgy Amar Laskri-Annaba, Algeria, e-mail: youcef.cheikhaoui@ensmm-annaba.dz

Hamza CHENITI
PhD, Department of Mining Engineering, National Higher School of Mining and Metallurgy Amar Laskri-Annaba, Algeria, e-mail: hamza.cheniti@ensmm-annaba.dz

Salim BENSEHAMDI
Professor, Department of Mining Engineering, National Higher School of Mining and Metallurgy Amar Laskri-Annaba, Algeria, e-mail: salim.bensehamdi@ensmm-annaba.dz

Souhib LORABI
PhD student, Department of psychology, UMMTO, Algeria, e-mail: sohaib.lorabi@gmail.com

Abstract:

This study involved modeling mining pillars with varying shape and size values to determine the strength that develops in an underground rock masses. The modeling was performed using Itasca's UDEC distinct element software, which allows explicit modeling of blocks of rock and how they interact with each other. In this method, a model consists of an assembly of distinct blocks (rigid or deformable) interconnected by discontinuities considered boundary conditions. From constituent models, different properties can be associated with the blocks (mechanical properties) as well as the joints (mechanical and hydraulic properties).
The distinct method is appropriate for known structures with known (discontinuities) plans that can be modeled by joints. The method makes it possible to calculate the large displacements which is an advantage over the finite element method.

The analyses included three different factors such as the size (volume) and the shape (width to high ratio of pillar) and presence of the joint sets in pillars, the results show that the presence of joints can have a pronounced effect on the strength of a pillar.

Two important results were observed: as the width to height ratio of the pillar increases, the strength of pillar increases. The size effect becomes important in presence of discontinuities in which the strength is reduced with increasing size. However, as numerical modeling results confirms of empirical laws used in literature of pillar strength the validation is done.

Key words: Strength, Size effect, Shape effect, Pillars stability

Algerian Journal of Engineering Architecture and Urbanism Vol. 5 Nr. 3 2021

ISSN: 2588-1760

Introduction

The scale effects in rock masses are rather similar to that observed for intact rock, and they are mostly due to the presence of rock joints. Like cracks at a smaller scale, joints are weak elements that reduce the failure strength and the deformation modulus. The usual approaches take into account the scale effects through the use of geomechanical classifications. Over the years, several authors have proposed empirical equations to estimate the scale effects on strength (e.g. Hoek and Brown, 1997) or on the deformation modulus (e.g. Bieniawski 1978, Barton 2002). Hudson et al. (1972) also exarnined the "shape effect" which considers the effects of varying the length to diameter ratio of rock cores with a constant diameter (varying the Iength). They found that varying the length to diameter ratio had a significant effect on the compressive strength of the rock as well as the shape of the stress-strain curve in the post-peak region. Figure 2 presents the results of the tests, the smaller the length to diameter ratio the higher the compressive strength of the sample.

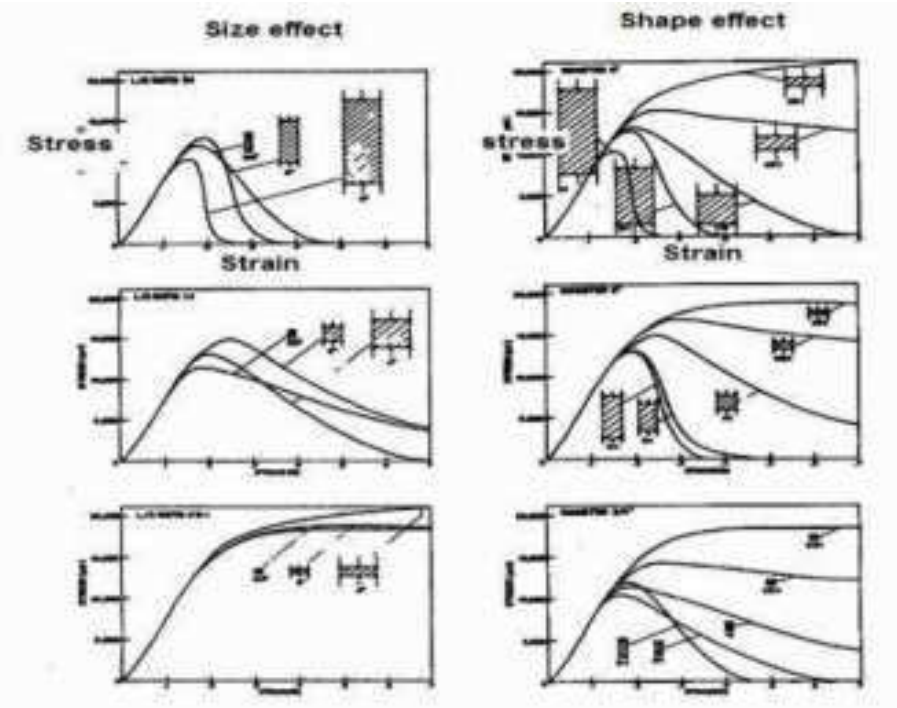

Figure 1: Influence of specimen size and shape on the complete stress-strain curve for marble loaded in uniaxial compression (Hudson et al., 1972)

Discontinuities are observed at all scale in rocks and they greatly affect its properties. For instance, when the density of discontinuities increases, a decrease of the strength is observed. The unconfined compressive strength of rocks is also known to be dependent on the scale at which it is tested. A non-uniform distribution of discontinuities can also induce en important strength

anisotropy within the rock mass. In this study an underground mining pillar in rock was modeled to determine the difference in strength expected when the size and shape of pillars varies.

The development of the discrete element methods of numerical modeling have greatly increased our ability to model the behavior of discontinuous materials like blocky rock. One way to use these tools is to perform parametric studies to facilitate growth of our understanding of the behavior of rock masses. Another use is to provide validation for empirical design guidelines. This study made use of one particular discrete element method, the distinct element method in the form of Itasca's UDEC software, for both of these purposes.

Model Description

Dimensions and Loads

Modeling has been performed using the UDEC software to represent a uni-axial compression test on a pillar to observe the variation of strength, for two cases (rectangular and square) with an increasing in volume (Fig. 2) In the case of absence of discontinuities and presence of one or two joint families (Fig.3). The loading is done by a vertical displacement speed (represents the applied charge), also the gravity load was applied rather. The following tables represent the characteristics of the material and joints used.

The model was specified using a homogenous material with dimensions 4 metres width by 4, 8 m height. All of the boundaries were fixed. In order to minimize computer run time, we applied 6 Mpa to represent the loads of the upper land.

There were three parameters of interest in this investigation: friction angle of joints and material, joint spacing, and joint orientation. The tables 1 and 2 shows parameter values that were varied in the suite of models.

Table 1. Model parameters varied for parametric study.

Friction Angle, Degrees	Orientation, Degrees from Horizontal	Joint Spacing, Meters
25	-30	1
25	-50	1

Table 2: Model parameters of the material and joints.

Algerian Journal of Engineering Architecture and Urbanism Vol. 5 Nr. 3 2021

ISSN: 2588-1760

Material Parameter	value	Joint parameters	Joint fictif	Joint normal
Density (Kg/m^3)	2500	-	-	-
Isostatic modulus of elasticity 'Bulk ' E (Pa)	6.66E9	Normal stiffness jkn (Pa)	1E10	1E9
Shear modulus 'Shear' G (Pa)	7.69E8	Tangential stiffness jks (Pa)	1E9	5E8
Cohesion C (Pa)	2e6	Cohesion C (Pa)	1E5	1E6
Friction Angle ϕ (°)	35	Tensile strength T (Pa)	1E5	1E6
Tensile strength T (Pa)	5e5	Friction Angle ϕ (°)	-	25

Example UDEC File

Table 3 shows the commands used in a typical UDEC analysis file. The first lines define the corner rounding, the model block external dimensions, and the cracks used to create the pillar. The save files are used throughout the code to facilitate rerunning the analyses without having to start over from the beginning, which saves a lot of time in some models. Next are lines that define the rock material and joint properties followed by the fixed boundaries section. Gravity is set to -10 [m/s^2] and a title is added to the computation. After all of the data is input an initialization solve is performed to make sure that all of the blocks are in equilibrium before the main part of the analysis is started. After the initial solve is done the excavation is removed and a second solve is initiated to allow the blocks to move, if necessary, to attempt to reach equilibrium. The final state of the model is then saved.

Table 3. Commands used in a typical UDEC analysis file.

```
round 0.05
block 0,-2 0,7 5,7 5,-2
crack 0,1 5,1
crack 1,1 1,4
crack 0,4 5,4
crack 4,1 4,4
jregion id 1 1,1 1,4 4,4 4,1
jset 50,0 1,0 0,0 1,0 1,1 range jreg 1
jset -30,0 1,0 0,0 1,0 1,1 range jreg 1
generate edge 0.5 range 0.1,5.1 1.1,3.9
generate edge 1
prop mat 1 density 2.5E3 bulk 6.66E9 shear 7.69E8 friction 35 coh 2e6 ten 5e5
Change mat=1 cons=1
prop jmat=1 jkn=1e10 jks=1e9 jcoh=1e5 jten=1e5
Change jmat=1 cons=1
prop jmat=5 jkn=1E9 jks=5E8 jfric=25 jcoh=1E6 jtens=1E6
change jmat=5 range ang 49,51
change jmat=5 range ang -21,-19
;bound stress 0, 0,-3e6 range -0.1,5.1 6.9,7.1
```

Algerian Journal of Engineering Architecture and Urbanism Vol. 5 Nr. 3 2021

ISSN: 2588-1760

```
bound xvel=0.0 range -0.1,0.1 -2.1,7.1
bound xvel=0.0 range 4.9,5.1 -2.1,7.1
bound yvel=0 range -0.1,5.1 -2.1,-1.9
hist syy 1.5,2.5
set gravity 0 -9.81
damp auto
solve
```

Extraction and plastic calculation

```
Reset damp hist disp jdisp rota time
Change mat 1 cons 3
del bl 757
del bl 342
solve
```

Type of load and take results

```
hist syy 1.5,2.5
def iterations
  t = 0.03
  loop nn (1,10)
     new_time = t
      command
       boundary yvel -1e-3 range -0.1,5.1 6.9,7.1
      step time new_time
      boundary yfree range -0.1,5.1 6.9,7.1
      boundary yvel 0 range -0.1,5.1 6.9,7.1
      cycle 1000
         set log res_dep.txt
         set log on
         set pline 0.9 2.5 4.1 2.5 15
         print pline 3 syy
         set log off
     endcommand
  endloop
end
iterations
```

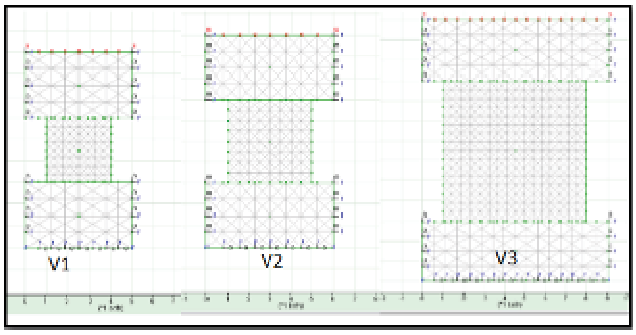

Figure 2: Square pillars modeled in UDEC

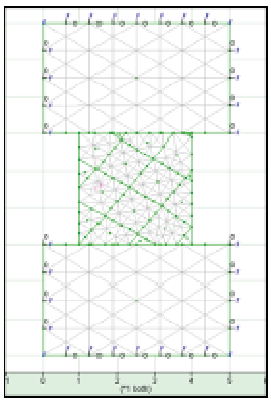

Figure 3: Models of a square pillar with 2 families of cracks (50° and -30° orientation) in the UDEC.

Algerian Journal of Engineering Architecture and Urbanism Vol. 5 Nr. 3 2021

ISSN: 2588-1760

At this point more code was required to observe what actually happened during the analysis. The objective was to determine the configuration of the model after equilibrium is reached, or after a substantial number of time steps have been run.

Plotting the block configuration is done by using the "plot block" command. The "nc" helps the plot function work faster because it doesn't show the rounding of the corners of the blocks in the file (rounded corners take longer to draw on the screen). The "disp red" shows red arrows that display the displacement vectors of blocks indicating the direction and magnitude of movement. Setting the plot to "jpg" creates a jpeg image file. "Set output" allows the user to name the file and, if necessary, specify the file location. "Copy" sends the previous screen plot to the jpeg output file.

Results and Discussion

The results of this modeling (presented in Figures 4, 5, 6 and 7), allowed us to conclude 3 points, such as:

1 Size effect: in presence of joints, an increase in compressive strength is observed with volume, which is coherent to previous literature.

2 Shape effect: the slender rectangular pillar is less resistant than the square pillar (comparison between figures 6 and 7); the numerical model therefore reproduces well a decrease in resistance following the increase in slenderness h/w.

Effect of the existence of cracks: a reduction in compressive strength, if one compares the effect of one family and two families of cracks in the same pillar (Figure 4)

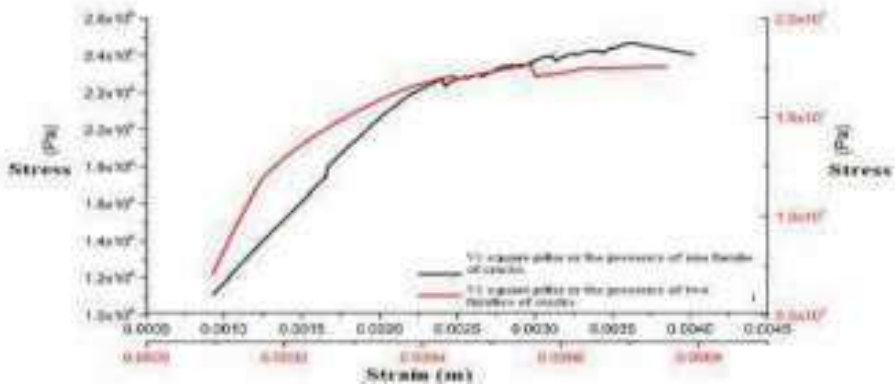

Figure 4: Stress-strain curve of a UDEC calculation for a square pillar in the presence of one and two families of cracks.

Algerian Journal of Engineering Architecture and Urbanism Vol. 5 Nr. 3 2021

ISSN: 2588-1760

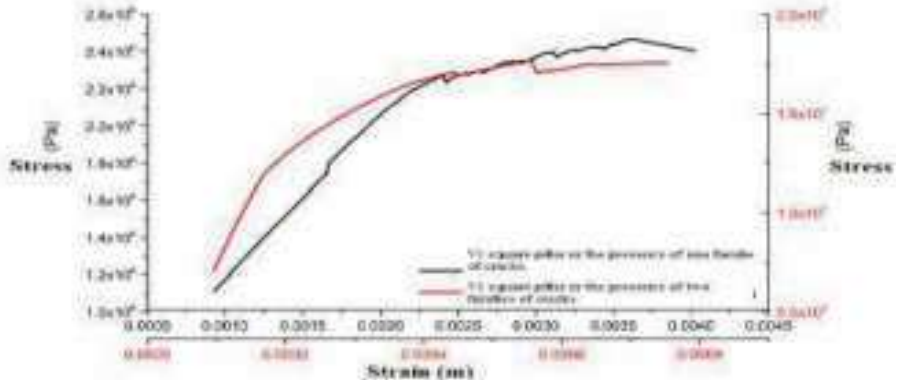

Figure 4: Stress-strain curve of a UDEC calculation for a square pillar in the presence of one and two families of cracks.

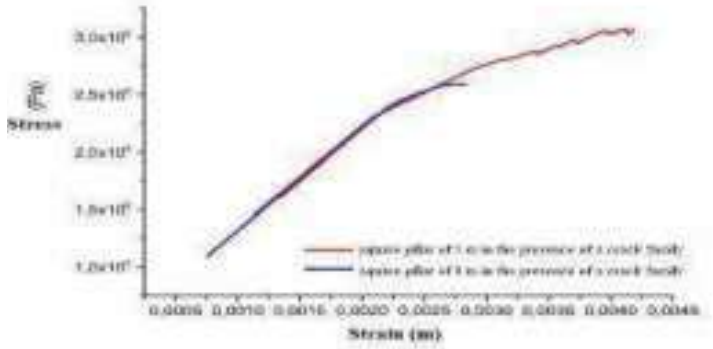

Figure 5: Stress-strain curve of a calculation with UDEC for a square pillar in the presence of a crack family

Algerian Journal of Engineering Architecture and Urbanism Vol. 5 Nr. 3 2021

ISSN: 2588-1760

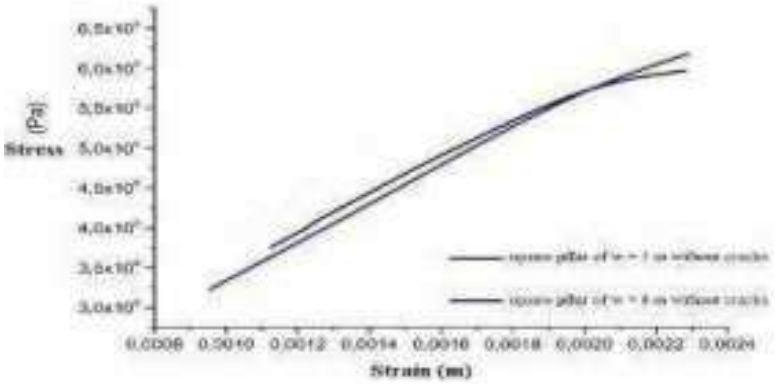

Figure 6: Stress-strain curve of a design with UDEC for a square pillar without cracks.

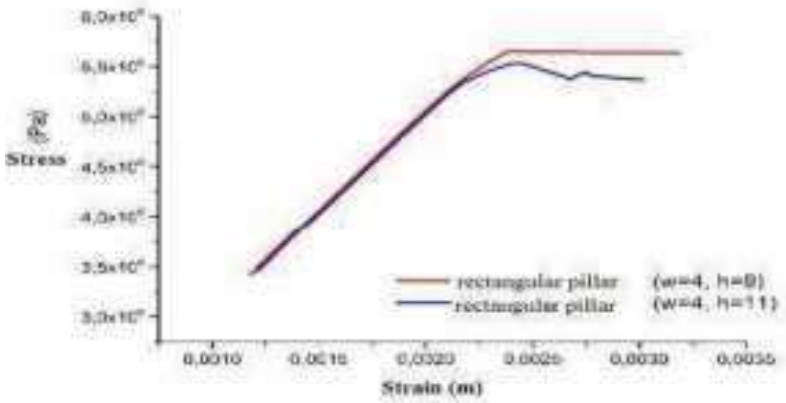

Figure 7: Stress-strain curve of a calculation with UDEC for a rectangular pillar without cracks.

Algerian Journal of Engineering Architecture and Urbanism Vol. 5 Nr. 3 2021

ISSN: 2588-1760

The use of UDEC allows us to represent the effect of discontinuities which is the major influential factor in the scaling effect. This result is explained by the method of calculation of the distinct elements which takes into account the difference between the scales where there is an increase in the presence of heterogeneities with the increase of the volume.

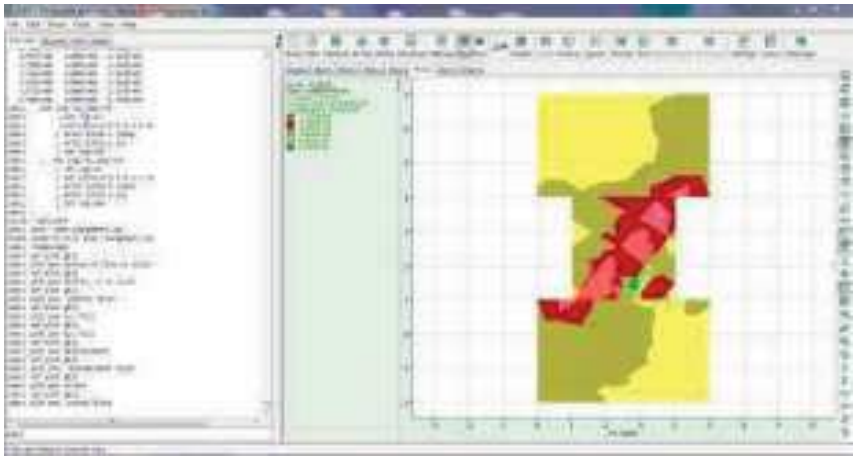

Figure 8: Example of the output showing complete yielding of a pillar with a W=H ratio of 1, shear failure and tensile failure.

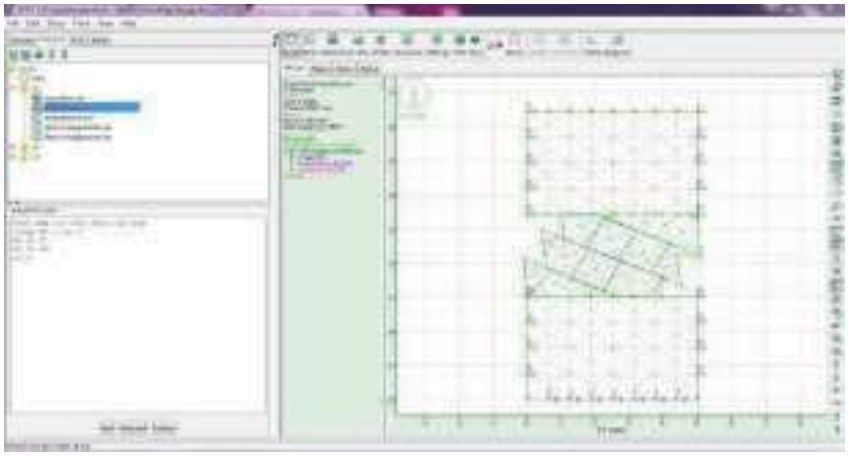

Figure 9: Example of the output showing the type of failure in pillar

During the modeling it was found that the models that collapse completely take much more time to run than the models that only drop the roof and sides of the excavation. The smaller the joint spacing, the longer the models took just because there are more blocks moving so it takes many more calculations to run the model.

Observations of the extent of the failed zone indicate that the joint orientations have a large influence on the results. The failure is done on the freest discontinuity planes in our model case,

the discontinuity family of -50° dip is blocked by the lower block of the model for that the rupture is amplified on the planes of 30°. It should be noted, however, that the models assume that both sets of joints are perfectly persistent, which is not very common in nature.

Conclusion

The effect of discontinuities on strength was numerically investigated using a Discrete Element Method. The model integrates structural effects induced by discontinuities which are known to produce strong behaviour changes in rock-like materials, scale dependency above all.

The study focused on the relationship between the strength and the set of pre-existing discontinuities in a numerical sample. Comparisons with experimental data have shown that the model can reproduce a strength dependency on the density of discontinuities.

When increasing the size of the numerical sample, it has been observed that the strength is decreasing when discontinuities are present. This conclusion is in good agreement with the results recently obtained by (Martin et al. 2000) and (Zhang et al. 2011), where the role of the density of fractures has been explicitly considered in the scale effects on the strength of disordered fractured rock mass.

References

Bieniawski, Z.T. (1974). Geomechanics Classification of Rock Masses and the Application is Tunneling. *Proc. Third Intl. Congress on Rock Mechanics*, ISRM, Denver, Vol 11A, pp. 27-32.

Cheikhaoui Y., Deck O., Omraci K., Cheniti H. (2021).The Scale and Shape Effects on the Characteristic Strength of a Rock Mass: Application to Mining Pillars. In: Abdel Wahab M. (eds) Proceedings of 1st International Conference on Structural Damage Modelling and Assessment. Lecture Notes in Civil Engineering, vol 110. Springer, Singapore. https://doi.org/10.1007/978-981-15-9121-1_23

Cheikhaoui Y. Characteristic strength of mining pillars in the presence of size and shape effects / Y. Cheikhaoui, O. Deck, K. Omraci, H. Cheniti // Український гірничий форум – 2020 : матеріали міжнар. конф., 4-5 листоп. 2020 р. – Дніпро : Журфонд, 2020. – С. 134-139

Hoek, E., P.K. Kaiser, and W.F. Bawden (1987). *Support of Underground Excavations in Hard Rock*, Rotterdam:Balkema, 215 pp.

Hudson JA, Crouch SL, Fairhurst C (1972) Soft, stiff and servo-controlled testing machines: a review with reference to rock failure. Eng Geol 6:155–189. https://doi.org/10.1016/0013-7952(72)90001-4

Itasca (2000). *UDEC User's Guide (Version 3.1).* Minneapolis:Itasca Consulting Group Inc.

Waltham, A.C. (2002). *Foundations of Engineering Geology, 2nd Ed.*, Spon Publishing, 90 pp.

Martin, C. D., & Maybee, W. G. (2000). The strength of hard-rock pillars. International Journal of Rock Mechanics and Mining Sciences, 37(8), 1239–1246. https://doi.org/10.1016/S1365-1609(00)00032-0

Zhang Q, Zhu H, Zhang L, Ding X (2011) Study of scale effect on intact rock strength using particle flow modeling. Int J Rock Mech Min Sci 48:1320–1328. https://doi.org/10.1016/j.ijrmms.2011.09.016

Algerian Journal of Engineering Architecture and Urbanism Vol. 5 Nr. 3 2021
ISSN: 2588-1760

OPTIMISATION OF TRANSPORTATION, PRODUCTION, STORAGE AND DISTRIBUTION IN AGRIFOOD SUPPLY CHAIN: AN ALGERIAN CASE STUDY

Mohamed Amine Cherier
1, PhD student, Manufacturing Engineering Laboratory of Tlemcen, Abou Bekr Belkaid University of Tlemcen, Algeria), e-mail: mohamedamine.cherier@univ-tlemcen.dz

Mohammed Bennekrouf
2, Doctor, Manufacturing Engineering Laboratory of Tlemcen, High School of Applied Science of Tlemcen, Algeria),
e-mail: mbenkrouf@gmail.com

Sidi Mohammed Meliani
3, Professor, Manufacturing Engineering Laboratory of Tlemcen Abou Bekr Belkaid University of Tlemcen, Algeria),
e-mail: smed.meliani@gmail.com

Abstract:
The optimisation of agrifood supply chain is one of the most difficult tasks almost when the handled product is perishable. The flow of the raw material from the farms to table of final client -passing to production, storage and distribution operations- as manufactured products to consumption is complicated cycle must be optimised. In this paper, a mathematical model has been proposed to optimise tomato agrifood supply chain. This study is applied in real case study in Algeria. This paper principally consists to maximise the company profits with: (1) minimise the transportation cost between tomato production zones-plants, plants-warehouses and warehouses-final clients, (2) minimise the storage cost in warehouses, and (3) minimise the cost of production. The results have shown that the proposed model has given a remarkable profit to the company.

Key words: Optimisation; Agrifood; Supply Chain; Tomato

Introduction:

The agrifood supply chain can be presented as a set of agricultures and production activities from the farms to customer table (Aramyan et al., 2006). The perishable agrifood supply chain is more complex comparing with the non-perishable one due to the freshness (fast degradation in effect of temperature and humidity) and high variability of the price. In fact, the optimisation of this kind of agrifood supply chain need more attention about all chain parties in order to keep it more efficient.

The tomato processing industry is one of the most complex agrifood supply chains, where the fruit maturation lasts few days, which make the harvest planning complex. Therefore, the tomatoes skin is very fragile, it can be damaged which the minimum of pression almost in harvesting and transportation phases. Thus, the optimisation of this tomato processing industry is very required.

Creative Commons Attribution-NonCommercial-NoDerivatives 4.0 International License (CC BY-NC-ND)

In literature, several researchers have been contributed in this field. A survey has been presented by Ahumada et al., (2009). The review presented the most recent scientific reputed papers in the field of agrifood supply chain. In addition, their survey has concentrated to the application of operational research approaches in AFSC. One of the most recent survey in AFSC is presented by Soto et al., (2016). The authors have illustrated operational research models applied in perishable AFSC to face to real problems of agrifood industry.
Rocco and Morabito (2016) have proposed a mathematical model for support decision of production and logistic planning in real case study in tomato company in Brazil. Another article of Rocco and Morabito (2016), presented two models (linear programming and robust optimisation) to deal with industrial tactical decision in tomato processing industry in Brazil.
In this contribution, we propose a linear mathematical model applied in tomato processing company to support operational and tactical decision such as transportation of fresh raw material from farms to plants, from plants to warehouses and from warehouses to final clients. It is also noteworthy to mention that this study is applied in real case study in Algeria.

Problem description:

In tomato processing industry, the demands of product based to tomato are throghout all year, but the harvesting of it is seasonable. So, the agricultures want to maximise their productions and the company want to meet all demands in year. For set this conflict, the company product a product with high concentration for dilute it throughout the period off-harvest. For more clarification, in harvest period, the company produce just one product called Triple Concentrate of Tomato (TCT) with 36 of Brix (one degree brix is equivalent to 1 gram of sucrose in 100 grams of solution). This product is considered as a semi-finished product, which will be used to produce other finished tomato-based products using the dilution of TCT.

An Algerian processing tomato company aim to minimise the dispenses inventory costs and the transportation costs between different facilities. The company assure the movement of the raw material (fresh tomatoes) from agricultural production zones to different plants for produce TCT. One the fresh tomatoes arrive to plants, the production line begins to product the semi-finished product. Then, the TCT produced must be sent to warehouses to storage. The company can send the enough quantity from the warehouses to final clients according to the demands of customers. The scheme of our case is shown in the Fig. 1. The objective of the contribution is to minimise the number of trips between facilities and minimise the number products stored in warehouses.

Creative Commons Attribution-NonCommercial-NoDerivatives 4.0 International License (CC BY-NC-ND)

Algerian Journal of Engineering Architecture and Urbanism Vol. 5 Nr. 3 2021
ISSN: 2588-1760

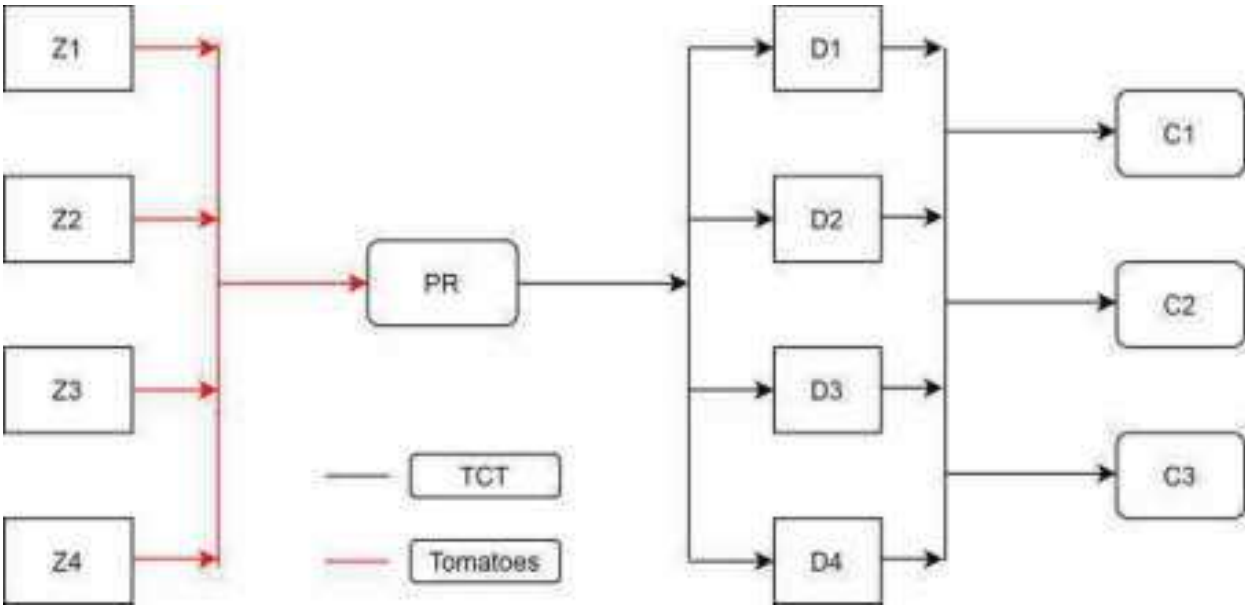

Fig1.: Algerian tomato processing industry scheme (real case study)

Mathematical model:

In this section, the proposed mathematical model presents the real case study. The objective function, constraints are presented below, and the decision variables and all parameters used in this model can be found in Appendix.

Objective function:

The main objective of Z is to maximise the revenue of the tomato company. It is composed with several elements. The first one is the cost of selling the TCT product, the second one is the purchasing cost. The third one represents the number of trips between production zones and plants, the fourth one is the number of trips between plants and warehouses, the fifth component refer to the number of trips between warehouses and final customers. The last element of objective function is the inventory dispense. Briefly speaking, our objective is to minimise the dispenses in order to maximize the profits.

Creative Commons Attribution-NonCommercial-NoDerivatives 4.0 International License (CC BY-NC-ND)

$$
\begin{aligned}
Max\ Z = & \sum_{c}\sum_{t} D_{c,t}^{FP} C^{FP} \\
& - \sum_{z}\sum_{v}\sum_{t} QT_{zvt} C_{zvt}^{p} \\
& - \sum_{z}\sum_{u}\sum_{t} NJ_{zut} C_{zut}^{TRP} \\
& - \sum_{u}\sum_{k}\sum_{t} NJ_{ukt} C_{ukt}^{TRP} \\
& - \sum_{k}\sum_{c}\sum_{t} NJ_{kct} C_{kct}^{TRP} \\
& - \sum_{k}\sum_{t} I_{kt}^{FP} C_{I}^{FP}
\end{aligned} \qquad (1)
$$

Constraints

$$Q_{ut}^{FP} = \sum_{z}\sum_{v} QT_{zvt} \times \frac{Bx_v}{Bx^{FP}} \quad \forall u,t \qquad (2)$$

The quantity manufactured of the FP product is presnted with equation 1.

$$NJ_{zut} = \frac{1}{Cap_{zu}^{tk}} \times \sum_{v} QT_{zvt} \quad \forall z,u,t \qquad (3)$$

The number of trips between tomato farms and the plants is shown by equation 2. It is express by the quantity harvested transported by the trucks, respecting the trucks' capacity.

$$\sum_{k} QMv_{ukt}^{FP} \leq Cap_{Prod}^{FP} \quad \forall u,t \qquad (4)$$

Creative Commons Attribution-NonCommercial-NoDerivatives 4.0 International License (CC BY-NC-ND)

The quantity sent between the plant u to warehouse k must respect the capacity of FP production.

$$\sum_{u} QMv_{ukt}^{FP} \geq d_{kt}^{FP} \quad \forall k,t \tag{5}$$

The quantity sent between the plant u to warehouse k must be superior to warehouse demand.

$$NJ_{uk} = \frac{1}{Cap_{uk}^{tk}} \times \sum_{t} QMv_{ukt}^{FP} \quad \forall u,k \tag{6}$$

The number of trips between the plant u and the warehouses k can be calculated using the equation 6, respecting the truck capacity.

$$\sum_{c} QMv_{kct}^{FP} \leq Cap_{k}^{FP} \quad \forall k,t \tag{7}$$

The quantity sold to final costumers is transported by trucks between the warehouse k and the client c respecting the capacity of warehouse.

$$\sum_{k} QMv_{kct}^{FP} \geq d_{c}^{FP} \quad \forall c,t \tag{8}$$

The quantity sent between the warehouse k and client c must satisfy the customer demand.

$$NJ_{kc} = \frac{1}{Cap_{kc}^{tk}} \times \sum_{t} QMv_{kct}^{FP} \quad \forall k,c \tag{9}$$

The number of trips between two facilities (warehouses and clients) is presented with equation 9.

$$I_{kt}^{FP} = \sum_{u} QMv_{ukt}^{FP} + \sum_{k} I_{t-1}^{k} - \sum_{c} QMv_{kct}^{FP} \quad \forall k,t \tag{10}$$

The inventory in warehouses can be calculated using equation 10. It can be managed with addition of sent quantity of FP from the plant t plus the ancient quantity minus the quantity delivered to final clients.

Creative Commons Attribution-NonCommercial-NoDerivatives 4.0 International License (CC BY-NC-ND)

Results and discussions:

The mathematical model presented in previous section have been explained the all operations of the case study. As mentioned before, the tomatoes harvested must be sent to several plants using trucks of different capacity. The transportation cost between facilities depend essentially to quantity transported and distance travelled.

Actually, the company use the trucks with same capacity (15 Tons) between all facilities (farms, plants and clients). Hence, We propose to increase the capacity of truck for minimise the transportation cost in hand and increase the company in other hand.

The Fig.2 present difference of transportation cost between real case (using 15 Tons of trucks) and the proposed solution (20 Tons). It is remarkable that the proposed solution can give a significant minimisation of cost of transport which influence directly to objective function.

The Fig.3 present the influence of minimisation of the transportation cost by increase the capacity of the tucks used. The company can earn 66 \% (equivalent to the two-thirds) of money -using trucks with capacity of 20 tons comparing with other ones with capacity of 15 tons- due the transportation dispenses. This results can give an major advantage to the company to take the lion share in competitive market by diminution of price of final products.

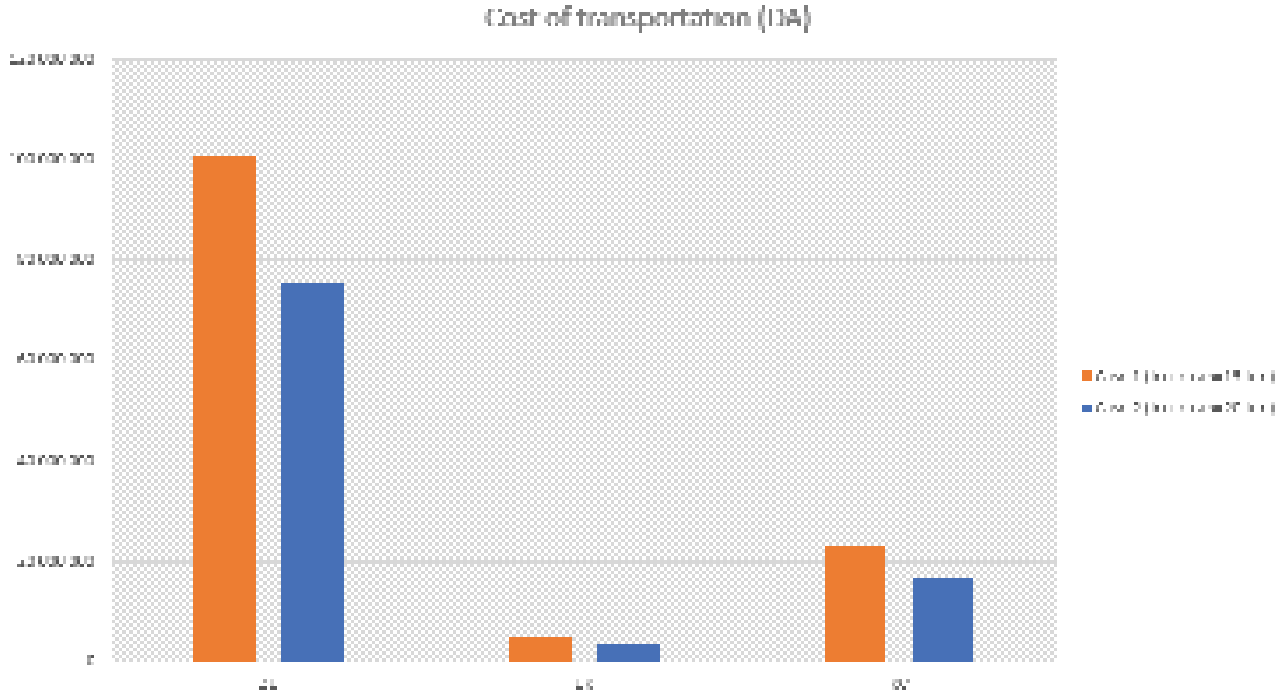

Fig2.: Transportation costs between different facilities with two trucks capacity.

Creative Commons Attribution-NonCommercial-NoDerivatives 4.0 International License (CC BY-NC-ND)

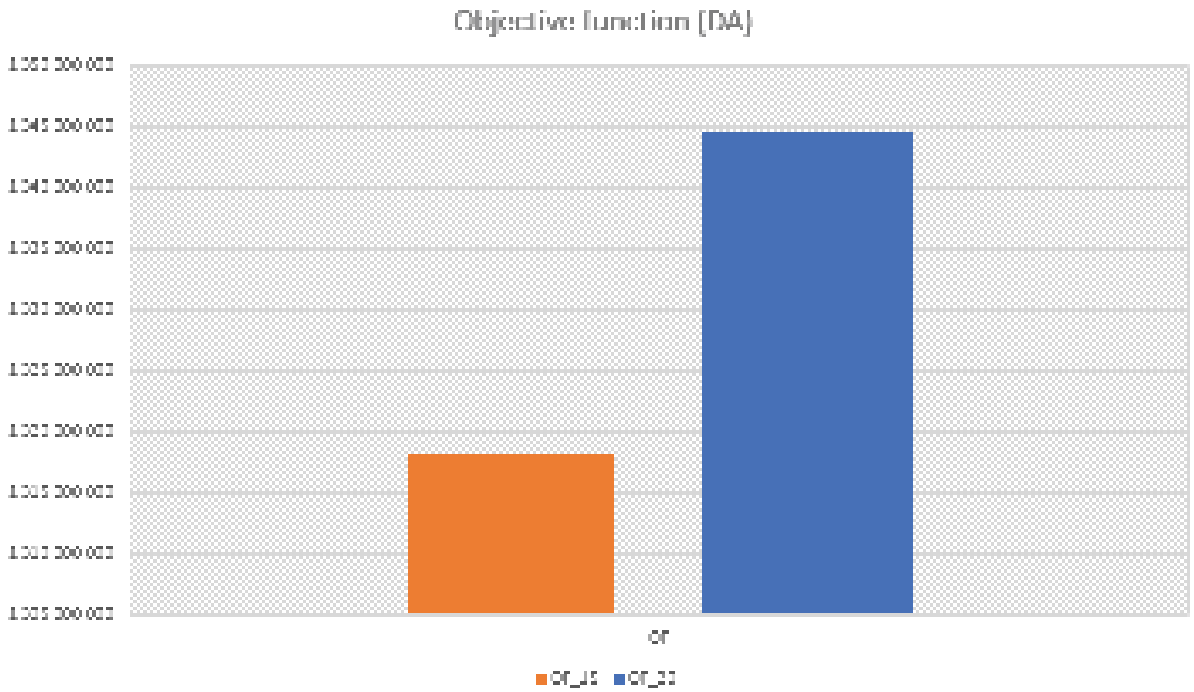

Fig3.: The variation of objective function according two trucks capacity

Conclusion:

In this paper, a mathematical model is presented to deal with the problem of minimisation inventory cost and optimise the transportation between the facilities. The model is applied in a real case study in Algeria. The results prove that the minimisation of number of trips and the number of products stored in warehouses of this supply chain can increase significantly the profit of this company.

This study can be considered as a decision support for tomato processing industry and any other type of agricultural product with same characteristic's tomato. As perspectives, the losses of tomato between the farms and production line is relatively considerable, for this reason, the minimisation of losses is primordial.

Creative Commons Attribution-NonCommercial-NoDerivatives 4.0 International License (CC BY-NC-ND)

Algerian Journal of Engineering Architecture and Urbanism Vol. 5 Nr. 3 2021
ISSN: 2588-1760

Appendix A

Indices and sets

$v \in V$	Tomato varieties
$z \in Z$	Produce zones
$u \in U$	Different plants
$k \in K$	Available warehouses for storage
$c \in C$	Customers
$t \in T$	Planning periods

Data parameters

Cap_k	Storage capacity in the warehouses
C^{FP}	Cost of FP
C^{zvt}_{p}	Cost of purchase
C^{FP}_{fab}	Cost of fabrication of FP
C^{FP}_{I}	Cost of inventory of FP
Bx_v	Brix of variety v
Bx^{FP}	The Brix of the FP product
C^{TRP}_{zu}	The cost of trip between the producing zone z and the plant u
C^{TRP}_{uk}	The cost of trip between plant u and the warehouse k
C^{TRP}_{kc}	The cost of trip between warehouse k and the customer c
I^k_{t-1}	Initial stock in warehouse k
QT_{zvt}	The quantity of tomato harvested in region z for the variety v harvested in period t
Cap^{tk}_{uk}	Capacity of truck for the transportation the FP between plants and warehouses
d^{FP}_{k}	Demand of warehouses of FP
d^{FP}_{c}	Demand of FP of customers c
Cap^{FP}_{Prod}	Capacity of production of FP per day
Cap^{tk}_{zu}	Capacity of truck for the transportation the fresh tomatoes between the
$C^{prchase}_{Tom}$	Purchase's mean cost of Tomatoes

Decision variables

Q^{FP}_{uvt}	The quantity produced of FP with variety v in plant u in period t
QMv^{FP}_{ukt}	The quantity of FP moved from the plant u to the warehouse k in period t
I_{kt}	Inventory on warehouse k in period t
QMv^{FP}_{kct}	Quantity of FP moved from the warehouse k to the customer c in period t
$I^{FP}_{k,t}$	Inventory of the FP in warehouse k in period t
NJ_{zu}	Number of journeys between the producing zone z and plant u
NJ_{uk}	Number of journeys between plant u and warehouse k
NJ_{kc}	Number of journeys between warehouse k and customer c

Creative Commons Attribution-NonCommercial-NoDerivatives 4.0 International License (CC BY-NC-ND)

References:

Aramyan, L., Ondersteijn, C. J., Van Kooten, O., & Lansink, A. O. (2006). *Performance indicators in agri-food production chains*. Frontis, 47-64.

Ahumada, O., & Villalobos, J. R. (2009). *Application of planning models in the agri-food supply chain: A review.* European journal of Operational research, **196(1):** 1-20.

Soto-Silva, W. E., Nadal-Roig, E., González-Araya, M. C., & Pla-Aragones, L. M. (2016). *Operational research models applied to the fresh fruit supply chain.* European Journal of Operational Research, **251(2):** 345-355.

Rocco, C. D., & Morabito, R. (2016). *Production and logistics planning in the tomato processing industry: A conceptual scheme and mathematical model.* Computers and Electronics in Agriculture, **127:** 763-774.

Rocco, C. D., & Morabito, R. (2016). *Robust optimisation approach applied to the analysis of production/logistics and crop planning in the tomato processing industry.* International Journal of Production Research, **54(19):** 5842-5861.

Creative Commons Attribution-NonCommercial-NoDerivatives 4.0 International License (CC BY-NC-ND)

Algerian Journal of Engineering Architecture and Urbanism Vol. 5 Nr. 3 2021
ISSN: 2588-1760

HOW TO DETECT AND TREAT THE BACTERIAL CORROSION RESULTING OF WATER SEPARATED FROM PETROLEUM?

Dekhili Nourelhouda
PhD Mechanical Engineering, e-mail: nourelhouda.dekhili@univ-biskra.dz
Dekhili Mariem
Master Hydraulic and Civil Engineering, Biskra University
mimadekhili16@gmail.com

Abstract:
The problem of bacterial corrosion at distribution and transport pipes frequently is caused by bacterial corrosion of distribution and transport pipes. The bacterial corrosion leads to the formation of deposits on the inner surface of the pipes which causing a risk of clogging. This work studies the effects of bacterial corrosion of distribution and transport pipes. For this aim, we analyses the water separated from petroleum to detect the presence of Sulphate-Reducing Bacteria (SRB). Then, we prepared the appropriate environment for live bacteria for purposes for analysis it. Finally, we measured the pH and we analyzed by SEM/EDX/ machines to detect the presence (SRB).

Key words: Water analysis, Bacterial Corrosion; Sulphate-Reducing Bacteria; Steel N 80.

Introduction:

The oil industry is an important driving force of the Algerian economy. However, this industry is faced with numerous challenges. One of these challenges is bacterial corrosion. Corrosion, in general, can be defined as a phenomenon of materials degradation under the effect of the physical, chemical or electrochemical actions of the surrounding environment. Corrosion is responsible for an annual cost up to 5% of the Gross National Product (GNP) of an industrial country (Marconnet et al 2005; Maluckov et al, 2012).

The process where bacterial metabolic acts help creating favourable conditions for corrosion to occur is called bacterial corrosion (Chantereau et al, 1973; Videla et al, 2005). The main bacterial type associated with this deterioration is the anaerobic Sulfate-Reducing Bacteria (SRB). In low oxygen environments and in the presence of sulfate, SRBs contribute to the mineralization of organic material by the process of sulfate reduction (Videla et al, 2005; Karr et al, 2003; King et al, 1971; Enning et al, 2014). Furthermore, these bacteria are known for their exceptional enzymatic capability that allows them to grow in rather complex conditions and to adhere to various surfaces, including metallic based materials (Santegoeds et al, 1998; Davey et al, 2000; Busscher et al, 2006). This bacterial corrosion is widely observed in petroleum pipelines which might result in pipes clogging and other severe losses in the oil and gas industries (Galvão et al, 2014).

In order to avoid the harmful effects of BSR on metallic materials and installations, a chemical treatment with biocides is applied. The term biocide or bactericide includes all the chemicals which destroy or prevent the development of microorganisms (Hulak, 1999).

Creative Commons Attribution-NonCommercial-NoDerivatives 4.0 International License (CC BY-NC-ND)

Quaternary ammonium compounds (QUATS), formaldehyde, glutaraldehyde, acrolein, amines and diamines in addition to methyl chloromethyl-isothiazolone (MCMI) and 4,5-dichloro-2-n-octyl-4-isothiazolin-3-one (DCOI) are some of the widely used compounds in industrial biocides (Uliasz et al, 2010; Turkiewicz et al, 2013).

The purpose of this work was to study the deposit resulting from bacterial corrosion on the surface of N80 steel samples and determine the elements contributing to the formation of this deposit. Furthermore, this study evaluated the effectiveness of the industrial inhibitor (NORUST 720) and biocide (biocide 2 CHIMEC 7660) in the removal of these deposits.

We organize the rest of paper as follows: Section 2 represents our approach followed, Section 3 explains some obtained results with discussion, and Section 4 concludes the paper.

Problematic:

The main contribution in this paper is the trying to answer the following questions: How to detect and how treat the bacterial corrosion resulting of water separated from petroleum?

Materials and methods

We conducted this study on samples of oil pipe that carry crude oil during the extraction (steel N 80) that having a high resistance to the pressure. In addition, it can be used during drilling of oil wells and can withstand the wall of a well after the completion of the latter, to ensure a normal operation in all the wells. Note that, the surface of the samples is rectifies, degreasers and dried, whose chemical composition (%) represent in the Table1.

Components	Weight (%)
C (Carbon)	0.24
Si (Silicon)	0.22
Mn (Manganese)	1.19
P (Phosphorus)	0.013
S (Sulfur)	0.004
Cr (Chromium)	0.036
Mo (Molybdenum)	0.021
Ni (Nickel)	0.028
Nb (Niobium)	0.006
V (Vanadium)	0.017
Ti (Titanium)	0.011
Cu (Copper)	0.019

TABLE 1. THE CHEMICAL COMPOSITION OF THE BASE METAL (%)

Table 2 represents a description about the situation of each sample of our experimentations. However, Table 3 gives the different amounts of chemical composition of the culture environment of bacteria.

Creative Commons Attribution-NonCommercial-NoDerivatives 4.0 International License (CC BY-NC-ND)

Sample number	Description of situation
Sample 1	N80 steel was placed in SRB contaminated environment for90 days at 37°C.
Sample 2	N80 steel was placed in SRB contaminated environment for60 days at 37°Cthen treated by NORUST 720 and left for another 30 days at 37 °C.
Sample 3	N80 steel was placed in SRB contaminated environment for60 days at 37°Cthen treated by biocide2 CHIMEC 7660 and left for another 30 days at 37 °C.

TABLE 2. DESCRIPTION OF THE SAMPLES

Components	Quantity
Magnesium Sulfate MgSO4, 7H2O	1 g
Ammonium sulphate (NH4)2SO4	1 g
Sodium citrate trisodium Na3C6H5O7, 2H2O	1 g
DI-potassium Hydrogenophosphate K2HPO4	1 g
Ascorbic acid	0.2 g
Yeast extract	0.2 g
Agar	0.1 g
Sodium Lactate	4 ml
Distilled water	1 l

TABLE 3. CHEMICAL COMPOSITION (CULTURE ENVIRONMENT)

We have filled 9 ml of environment prepared in vials penicillin's; to add metal nail defatted by acetone in these vials. We have plugged the vials to using capsules of rubber, capsuling then were blocked by the aluminum. After that, we have purged the vials with nitrogen to create the anaerobic environment and sterilize by autoclaving under wet pressure at 120°C for 50 minutes. Then, using a syringe, we collected 1 ml of water and we eliminated the trapped air bubbles possibly in the syringe. Subsequently, we injected the contents of the latter through the capsule in the rubber stopper of the vial containing 9 ml of culture environment. Finally, we have labeled the vials. They have incubated in the incubator at 37°C for 28 days. We found blackening deposit in the vials with increased pH of environment showing the presence SRB in the analyzed water.

After confirming bacteria in the water, we repeat the same operation of Kit test, but we add our samples instead of nail metal. Also, we collected 1 ml of water contains bacteria. They have incubated in the incubator at 37°C for 60 days. Then, we added the biocide or inhibitor used against the problems caused by the SRB and left it another 30 days in the incubator at 37°C.

Creative Commons Attribution-NonCommercial-NoDerivatives 4.0 International License (CC BY-NC-ND)

Algerian Journal of Engineering Architecture and Urbanism Vol. 5 Nr. 3 2021
ISSN: 2588-1760

Results and discussions:

pH measurement

The pH of the sample environment was measured before and after incubation as following: 7.10 before incubation and 8.54 after incubation. The pH measurement shows that it is increases, and this environment is suitable for the multiplication of bacteria and the formation of a biofilm (biofilms have complex structures consisting of cells and clusters of bacteria, distributed randomly) . This biofilm develops or can develop under extreme conditions which are: temperature (12 ° C to 115 ° C), pH (0 to 13) and hydrostatic pressure.

Analysis surface by scanning electronic microscope

The determination of the morphology of deposit that formed on the surface of the steel N80 has been carried out by scanning electron microscopy (Figure 1). We have achieved for each sample an image with expansions of (500X). It is clear that the images of the surface sample (Figure 2,3 and 4).Show the existence of a stable adherent deposit in the form of colonies.

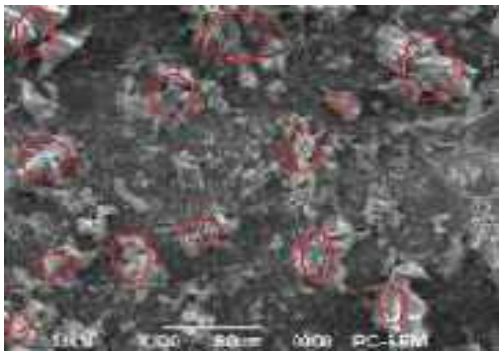

Fig 1. SURFACE OF THE SAMPLE 1 (37 ° C FOR 30 DAYS OF INCUBATION)

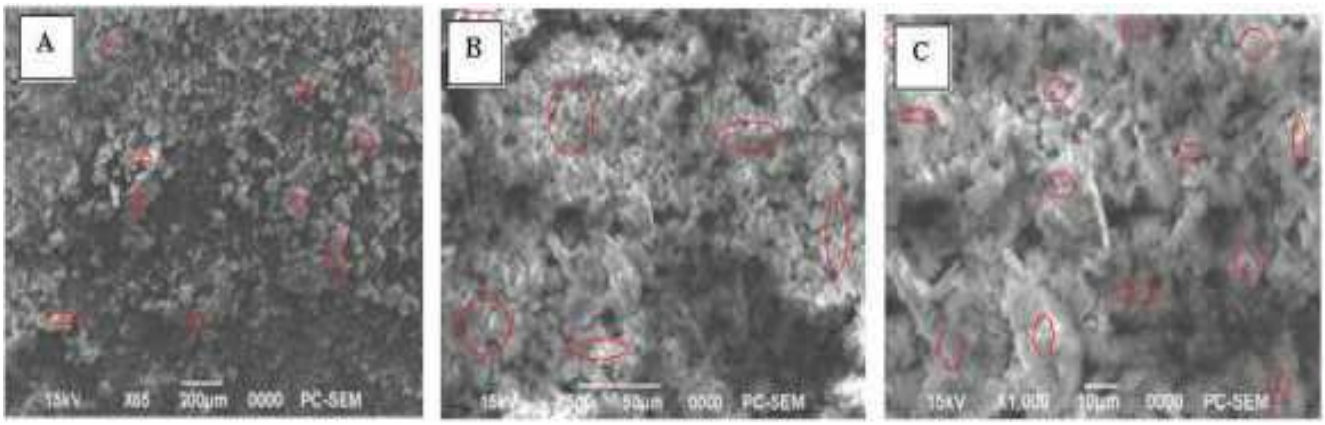

Fig 2. MICROGRAPHS OF N80 STEEL SAMPLES INCUBATED IN SRB CONTAMINATED ANAEROBIC ENVIRONMENT FOR 90 DAYS AT 37 °C, (A) REPRESENT AN X65 MAGNIFICATION WITH A SCALE BAR OF 200 µM, (B) REPRESENT AN X500 MAGNIFICATION WITH A SCALE BAR OF 50 µM, (C) REPRESENT AN X1000 MAGNIFICATION WITH A SCALE BAR OF 10 µM.

Creative Commons Attribution-NonCommercial-NoDerivatives 4.0 International License (CC BY-NC-ND)

Algerian Journal of Engineering Architecture and Urbanism Vol. 5 Nr. 3 2021
ISSN: 2588-1760

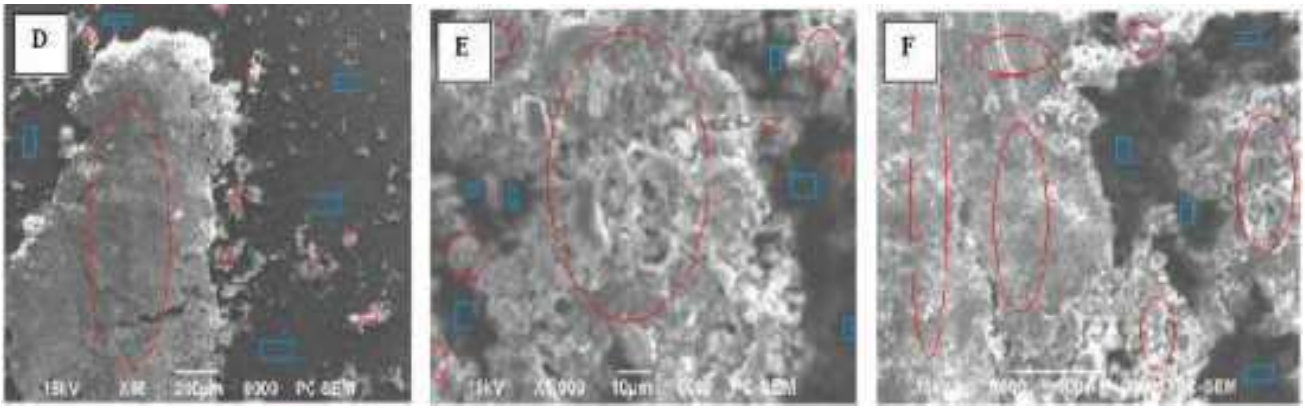

Fig 3. MICROGRAPHS OF N80 STEEL SAMPLES INCUBATED IN SRB CONTAMINATED ANAEROBIC ENVIRONMENT FOR 60 DAYS AT 37 °C THEN TREATED BY NORUST 720 AND LEFT FOR ANOTHER 30 DAYS AT 37 °C. (D) REPRESENT AN X65 MAGNIFICATION WITH A SCALE BAR OF 200 µM, (E) REPRESENT AN X500 MAGNIFICATION WITH A SCALE BAR OF 50 µM, (F) REPRESENT AN X1000 MAGNIFICATION WITH A SCALE BAR OF 10 µM.

Fig 4. MICROGRAPHS OF N80 STEEL SAMPLES INCUBATED IN SRB CONTAMINATED ANAEROBIC ENVIRONMENT FOR 60 DAYS AT 37 °C THEN TREATED BY BIOCIDE2 CHIMEC 7660 AND LEFT FOR ANOTHER 30 DAYS AT 37 °C. (G) REPRESENT AN X65 MAGNIFICATION WITH A SCALE BAR OF 200 µM, (H) REPRESENT AN X500 MAGNIFICATION WITH A SCALE BAR OF 50 µM, (I) REPRESENT AN X1000 MAGNIFICATION WITH A SCALE BAR OF 10 µM.

Analysis surface by Energy Dispersive X-ray

In order to know the chemical compositions of the layer that form on the surface of the samples, we observed the samples by EDX spectrometry (Figure 5).

Creative Commons Attribution-NonCommercial-NoDerivatives 4.0 International License (CC BY-NC-ND)

Algerian Journal of Engineering Architecture and Urbanism Vol. 5 Nr. 3 2021
ISSN: 2588-1760

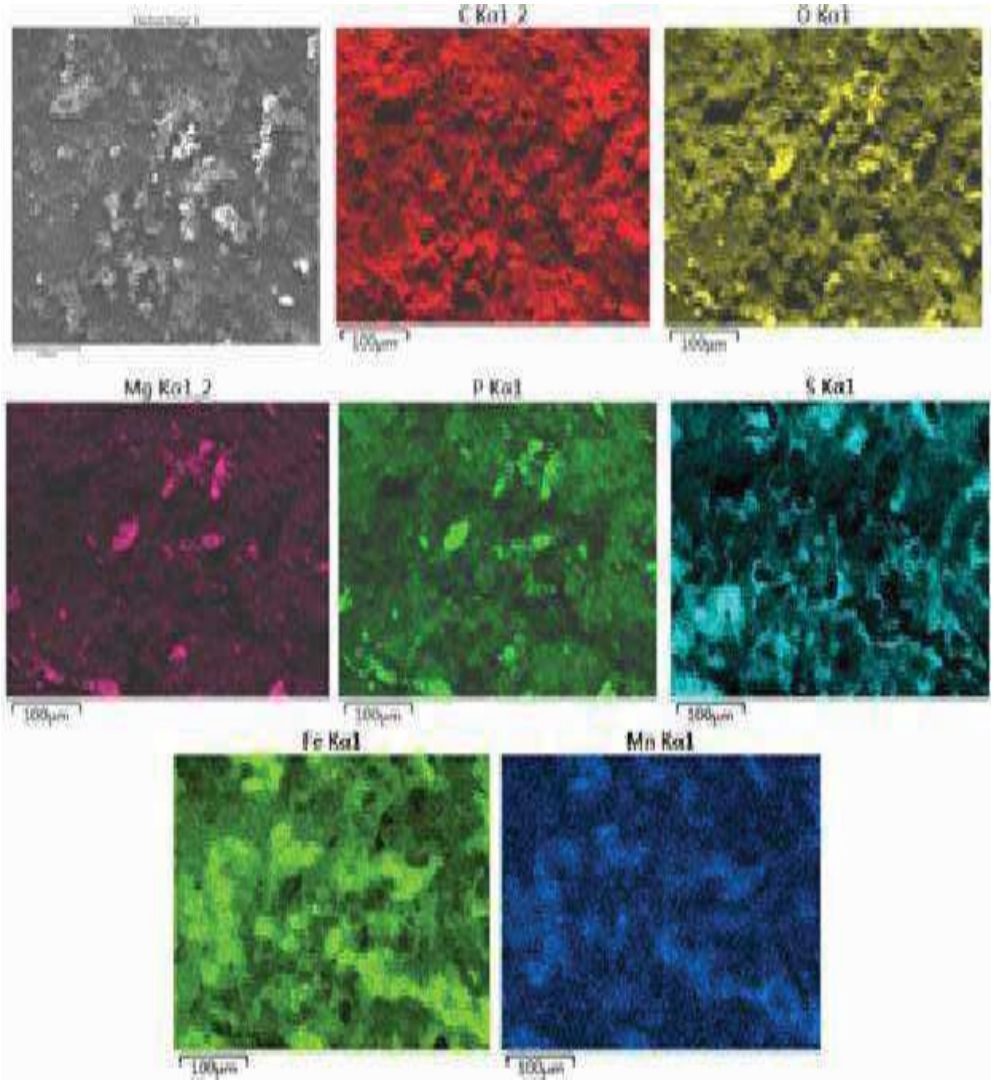

Fig 5. SURFACE OF THE SAMPLE 1 AFTER 30 DAYS OF INCUBATION AT 37

We observe in Figure 5 that the elements present in the deposition layer are: oxygen (O), iron (Fe), Carbon (C), Manganese (Mn), Magnesium (Mg), Phosphorus (P) and Sulfur (S

Conclusion:

This current work focus to detect the presence of bacteria in the water extracted from petroleum, in order to avoid the phenomenon of bacterial corrosion. To confirm the presence of bacteria, we measured the environmental pH and observe deposits on the surface of the sample using SEM and EDX devices. We concluded that: the pH is high, we found that the deposits are largely stable in the form of colonies on the surface and the main chemical components involved in the formation of sediments formed on the surface of the samples are oxygen, sulfur and iron.

Creative Commons Attribution-NonCommercial-NoDerivatives 4.0 International License (CC BY-NC-ND)

References:

Marconnet, C., Dagbert, C., Roy, M., & Féron, D. (2005). *Comportement d'aciers inoxydables en eaux naturelles*. Matériaux & Techniques, 93, s-83.

Maluckov, B. S. (2012). *Corrosion of steels induced by microorganisms*. Metallurgical and Materials Engineering, **18(3),** 223-232.

Chantereau, J., & Bouffard, A. M. (1977). *Corrosion bactérienne-bactéries de la corrosion* (pp. 262-262).

Videla, H. A., & Herrera, L. K. (2005). *Microbiologically influenced corrosion: looking to the future*. International microbiology, **8(3),** 169.

Karr, E. A., Sattley, W. M., Jung, D. O., Madigan, M. T., & Achenbach, L. A. (2003). *Remarkable diversity of phototrophic purple bacteria in a permanently frozen Antarctic lake*. Appl. Environ. Microbiol., **69(8),** 4910-4914.

King, R. A., & Miller, J. D. A. (1971). *Corrosion by the sulphate-reducing bacteria*. Nature, **233(5320),** 491-492.

Enning, D., & Garrelfs, J. (2014). *Corrosion of iron by sulfate-reducing bacteria: new views of an old problem*. Appl. Environ. Microbiol., **80(4),** 1226-1236.

Santegoeds, C. M., Ferdelman, T. G., Muyzer, G., & de Beer, D. (1998). *Structural and functional dynamics of sulfate-reducing populations in bacterial biofilms*. Appl. Environ. Microbiol., **64(10),** 3731-3739.

Davey, M. E., & O'toole, G. A. (2000). *Microbial biofilms: from ecology to molecular genetics. Microbiol.* Mol. Biol. Rev., **64(4),** 847-867.

Busscher, H. J., & van der Mei, H. C. (2006). *Microbial adhesion in flow displacement systems*. Clinical microbiology reviews, **19(1),** 127-141.

Galvão, M., & Lutterbach, M. T. S. (2014). *Application of the qPCR technique for SRB quantification in samples from the oil and gas industries*. Applications of molecular microbiological methods. Skovhus TS, Caffrey SM and Hubert CRJ (eds.), Caister Academic Press, 215, 69-77.

Hulak, I. (1999). *Protection contre la dégradation et la prolifération des microorganismes*. XXIIe Journée Technologique. Les polymères à usage médical.

Uliasz, M. (2010). *Wykorzystanie związków aminowych w technologii płuczek wiertniczych*. Nafta-Gaz, **66(7),** 577-585.

Turkiewicz, A., Brzeszcz, J., & Kapusta, P. (2013). *The application of biocides in the oil and gas industry*. Nafta-Gaz, **69(2),** 103-111.

Creative Commons Attribution-NonCommercial-NoDerivatives 4.0 International License (CC BY-NC-ND)

Algerian Journal of Engineering Architecture and Urbanism Vol. 5 Nr. 3 2021
ISSN: 2588-1760

ELABORATION DE MATERIAUX COMPOSITES BIFONCTIONNELS

Chahrazed DJILANI
Research Professor, Université du 20 Août 1955 Skikda, Faculté de Technologie, e-mail: chahrazed_dj@yahoo.fr

Rachida ZAGHDOUDI
Professor, Université du 20 Août1955 Skikda, Faculté des sciences, e-mail: zeg_rach@yahoo.fr

Fayçal DJAZI
Professor, Laboratoire LRPCSI, Université du 20 Août 1955 Skikda , Faculté de Technologie, e-mail: djazi_faycal@yahoo.fr

Abstract:
Acetic acid is one of the major pollutants in petroleum, fine chemicals, textiles and Pharmaceutical industry. Various methods used to remove acetic acid include adsorption, ion exchange, evaporation, precipitation and membrane techniques. Adsorption by using various adsorbents is also attractive alternative. Use of low cost adsorbents is very important attribute because of which the research in this field has gained an importance. The efficiency of prepared nanocomposites from banana peels/ titanium dioxide (BP/TiO_2) and animal bones/titanium dioxide (AB/TiO_2) for the adsorption of acetic acid from aqueous solution was investigated. The effect of different parameters including initial concentration and contact time on the adsorption capacity were studied. The BP/TiO_2 and AB/TiO_2 were characterized for the following parameters: pH, iodine number and specific surface. The adsorption data for acetic acid fitted Freundlich isotherm. The kinetic data were examined. It was found that pseudo-second-order kinetic model was found to adequately explain the adsorption kinetic of acetic acid from aqueous solution.

Key words: Adsorption, Nanocomposites, TiO_2, Acetic acid.

Introduction:

L'eau est le constituant majeur de notre planète. C'est un élément qui a une très grande importance pour les besoins de l'homme et l'équilibre des écosystèmes aquatiques. Mais, elle est malheureusement très facile à polluée par les activités industrielle, agricoles, ainsi que les déchets urbains comprenant de nombreuses substances toxiques qui provoquent une dégradation de ses propriétés physiques, chimiques ou biologiques. La pollution des eaux issues des rejets est un sérieux problème dans le monde. Cette pollution peut provoquer des effets nocifs sur l'environnement **(Syeda S. A., 2017).** Pour réduire les effets néfastes de ces polluants, plusieurs procédés de traitement des eaux usées, notamment physico-chimiques, sont mis en œuvre. Parmi les procédés de traitement adaptés aux rejets, l'adsorption reste une technique relativement utilisé et facile à mettre en œuvre **(Sunil J. K., 2016).** Les charbons actifs sont connus comme étant les adsorbants les plus largement utilisés en raison de leur importante surface spécifique et de leur volume poreux élevé **(Folahan A. A., 2017).** La présente étude consiste à utiliser des nouveaux matériaux nanocomposites à base des déchets biologiques adsorbants et biodégradables à base de la peau de banane, l'os et l'oxyde de titane

Creative Commons Attribution-NonCommercial-NoDerivatives 4.0 International License (CC BY-NC-ND)

dans un procédé physico-chimique d'adsorption, pour éliminer les acides organiques. Les essais ont été réalisés sur l'acide acétique qui est un polluant organique, ils ont montrés une élimination remarquable. L'influence de différents paramètres expérimentaux ont été étudiés. L'étude des isothermes et les modèles cinétiques d'adsorption ont montrés que l'isotherme d'adsorption de Freundlich et le modèle cinétique de pseudo-premier-ordre décrivent bien le processus de l'adsorption de l'acide acétique sur BP/TiO_2 et OS/TiO_2. .

Problématique:

L'augmentation progressive de la technologie industrielle se traduit par augmentation relative de la pollution de l'environnement et un grand effort a été fait pour minimiser les polluants dangereux et, par conséquent, éviter leurs effets dangereux sur les animaux, les plantes et les humains. La pollution de l'eau représente un grand défi et le charbon actif est un adsorbant couramment utilisé pour éliminer les contaminants dangereux des eaux usées. La presence d'acide acétique dans les effluents industriels pose un sérieux problème environnemental. Les principaux effets néfastes causés par cet acide sont la formation de calculs rénaux, les vomissements et la faiblesse générale du corps. Ainsi, il est impératif qu'ils soient retirés des déchets industriels avant de les rejeter dans le plan d'eau. De nombreuses techniques ont été utilisées dans le passé pour le traitement des eaux usées contenant ce polluant, mais se sont avérées inefficaces. L'adsorption est une technique efficace pour l'élimination des polluants dissous (organiques ou inorganiques) de l'eau. Parmi de nombreux types d'adsorbants, les charbons actifs sont les plus largement utilisés, en raison de leur grande capacité d'adsorption et de leur faible coût.

Matériels et méthodes :

Préparation de la peau de banane

Après la collecte de la peau de banane directement, on a retiré tous les résidus indésirables. Ensuite, on a étend la peau à l'air libre pour quelques heures, le temps qu'elle sèche complètement. La peau de banane séché est broyé à l'aide d'un moulin à café de manière à optimiser la surface de contact des adsorbants ultérieurement produit et un tamisage du broyat jusqu'à obtenir une poudre fine.

Préparation des matériaux nanocomposites (PB/TiO_2)

Une quantité de TiO_2 a été dissous dans 100 ml d'acide acétique (1%), ou il a été converti en cations de titane. A cette solution, une masse de la poudre de la peau de banane a été ajouté. Le mélange a été agité pendant 30 min. Après agitation magnétique, une solution de NaOH 1 M a été ajoutée goutte à goutte jusqu'à ce que la solution atteigne un pH de 10. La solution a été chauffée dans un bain d'eau à 80 °C pendant environ 3 heures. Ensuite, il a été filtré et lavé plusieurs fois avec de l'eau distillée et séché à l'étuve à 50 °C pendant 1 heure.

Préparation de l'os et le nanocomposite (OS/TiO_2)

Les os recueillies ont été nettoyés de la viande avec l'eau de robine, et séché à une température ambiante, puis coupés à des tailles comprise approximativement entre 1-2 cm.

Par la suite, bouillis dans l'eau distillé pendant 2 heures, afin d'éliminer la graisse et la chaire, cette opération répétée plusieurs fois jusqu'à l'obtention d'une eau claire. Après séchage dans

Creative Commons Attribution-NonCommercial-NoDerivatives 4.0 International License (CC BY-NC-ND)

l'étuve, le matériau obtenu est broyé à l'aide d'un moulin à café. On a suivi les mêmes étapes de préparation de nanocomposite (PB/TiO_2) avec l'os.

Activation des matériaux nanocomposites par micro-onde

L'activation par micro-onde est une méthode de chauffage réactionnelle et performante en chimie organique. Elle permet l'atteinte de températures beaucoup plus élevées en très peu de temps ce qui accélère considérablement la cinétique des réactions et, par le fait même, les temps de réaction. Après le séchage des matériaux nanocomposites (PB/TiO_2 et OS/TiO_2) à 50 °C pendant 1 heure, les nanocomposites ont été placés dans une micro-onde. Ces échantillons ont été exposés à une puissance de 650 W pendant 6 minutes.

Les caractéristiques physico-chimiques de PB/TiO_2 et OS/TiO_2

Mesure du pH

La mesure du pH de surface des matériaux avant et après préparation donne une première indication sur la nature acido-basique des espèces présentes.

On place 1 g du matériau (PB/TiO_2 et OS/TiO_2) dans 100 ml d'eau distillé, la solution est agité pendant 1 heure, le mélange est ensuite filtré. Le solide est récupérer et le pH de la solution résiduelle est déterminé à l'aide d'un pH mètre.

Détermination de l'indice d'iode

L'indice d'iode donne des informations sur le degré d'activation du CA et les surfaces d'adsorption disponibles dans les micropores. En règle générale, l'adsorbant avec l'indice d'iode le plus élevé présentera la surface spécifique la plus importante **(Sumrit M., 2015).** La détermination de l'indice d'iode est un test simple et rapide, donnant une indication sur la microporosité des matériaux **(Cleiton A. N., 2011)** et leur capacité d'adsorption. Cet indice se réfère à la quantité en milligrammes d'iode adsorbés par un gramme de matériaux. Pour déterminer l'indice d'iode de chaque nanocomposite (PB/TiO_2 et OS/TiO_2), en utilisant une solution d'iode (I_2) de 0.1 N. 10 ml d'acide chlorhydrique est mis en contact avec 1g de chaque matériau (PB/TiO_2 et OS/TiO_2) dans un bécher de 250 ml. La suspension est agitée jusqu'à ce que le matériau soit mouillé, le bécher est ensuite placé sur une plaque chauffante pour bouillir le mélange qui contient, après 30 secondes d'ébullition puis la refroidissement à la température ambiante, un volume de 100 ml de la solution titrée de l'iode 0.1N a été ajouté dans le bécher fermé. L'ensemble est laissé sous agitation pendant 30 secondes à température ambiante. A la fin de cette durée, la suspension est filtrée. 50 ml d'iode restant dans le filtrat a été titré par 0.1 N de thiosulfate de sodium jusqu'à ce que la solution devienne jaune pâle, on ajoute à la fin de titrage 2 ml d'amidon fraîchement préparé et titré goutte à goutte jusqu'à ce que la solution devienne transparente on lire le volume final de thiosulfate versé. L'indice d'iode est donné par les formules suivantes :

$$R = 0.001 \cdot V'$$

$$D = \left(\frac{0.01}{R}\right)^{0.165}$$

$$X'_{meq} = 100 \cdot N_1 - \frac{110 \cdot N_2 \cdot V}{vt}$$

$$X = 12693 \cdot X'$$

$$ID = \frac{X}{m} \times D$$

Creative Commons Attribution-NonCommercial-NoDerivatives 4.0 International License (CC BY-NC-ND)

Où :
R : La molarité du filtrat
D : Le facteur de correction
V' : Volume final de thiosulfate versé (ml)
N_1 : La normalité d'iode (M)
N_2 : La normalité de la solution de thiosulfate utilisée(M)
X' : La quantité d'iode adsorbée
X : La quantité en mg d'iode adsorbée
ID : l'indice d'iode (mg/g)
m : La masse de matériaux (g).

Résultats et discussions :

Caractérisation des nanocomposites préparés

Les résultats obtenus par le pH pour les deux nanocomposites sont regroupés dans **le Tableau 1.**

Nanocomposites	PB/TiO_2	OS/TiO_2
pH	11.11	7.19

Tableau 1. Les valeurs du pH de PB/TiO_2 et OS/TiO_2.

Les résultats obtenus montrent que Le pH de PB/TiO_2 est basique ceci traduit par la présence des groupements fonctionnels de type basique à la surface de PB/TiO_2, par contre le pH de OS/TiO_2 est neutre.
Les indices d'iode exprimés en (mg/g) de nanocomposites préparés (PB/TiO_2 et OS/TiO_2) obtenus par l'iodométrie sont reportés dans **le Tableau 2.** A partir de ces résultats nous permettent de constater que les valeurs d'I_2 des deux matériaux élaborés sont plus importantes que celle de test à blanc. PB/TiO_2 à un ID plus élevé que le nanocomposite OS/ TiO_2, donc il présente la surface spécifique la plus importante.

Nanocomposite	PB/TiO_2	OS/TiO_2	Test à blanc
Indice d'iode (mg /g)	386.949	306.408	18.558

Tableau 2: Les valeurs de l'indice d'iode de PB/TiO_2, OS/TiO_2 et le test à blanc.

Etude des performances d'adsorption de nanocomposites préparés

Variation du temps d'équilibre

Puisque l'adsorption est un procédé de transfert du polluant de la phase liquide vers la phase solide, le temps entre les deux phases joue le rôle d'un facteur limitant. Le choix d'étudier l'influence du temps de contact pour les différentes concentrations sur l'adsorption de l'acide acétique sur nos adsorbants est de déterminer le temps requis pour l'établissement de l'équilibre ainsi que la concentration optimale en acide et pour déterminer la capacité d'adsorption expérimentale à l'équilibre.
Dans une séries des béchers, on place une masse m = 1g de chaque matériau (PB/TiO_2, OS/TiO_2) à pH de solution et température ambiante, avec 50 ml de solution d'acide acétique

Creative Commons Attribution-NonCommercial-NoDerivatives 4.0 International License (CC BY-NC-ND)

de concentration connue 0,15 mol/L. Les béchers sont mis sous une agitation magnétique égale à 250 tr/min, les échantillons sont prélevés à des intervalles de temps variables de 1 à 30 min. Les mélanges sont enfin filtrés, après un volume de 10 ml de solution est titré par une solution d'hydroxyde de sodium (0.1N) avec 3 goutte de l'indicateur colorée phénolphtaléine pour calculer la capacité d'adsorption à chaque instant (t).

La quantité de l'acide acétique adsorbée par gramme d'adsorbant à l'instant (t) est donnée par la relation suivante :

$$q_e = \frac{C_i - C_e}{m} \times V$$

Où:

q_e : la quantité fixée des adsorbats en mg par gramme d'adsorbant **(mol/g)**

C_i et C_e : sont respectivement les concentrations initiales et instantanées **(mol/L)**

V : le volume de la solution **(L)**

m: la masse de l'adsorbant utilisé **(g)**

Les résultats obtenus pour notre polluant organique étudié, qui est l'acide acétique sont représentés sur la Figure 1, on remarque que l'équilibre est atteint pratiquement au bout de 12 min avec une capacité d'adsorption $q_e = 2.5.10^{-3}$ mol/g pour PB/TiO_2 et 10 min avec une capacité d'adsorption $q_e = 2.9.10^{-3}$ mol/g pour OS/TiO_2. Les résultats obtenus montrent aussi l'existence de deux phases ; la première ou la vitesse d'adsorption est plus rapide pendant 1 minute, puis la deuxième ça décélère de plus en plus jusqu'à atteindre un état d'équilibre ; ceci revient à la disponibilité d'un grand nombre de sites actifs sur la surface de PB/TiO_2 et OS/TiO_2 au début du processus. Celui-ci devient de plus en plus lent jusqu'au temps d'équilibre. Au-delà, on observe un palier qui est dû à la saturation des sites actifs.

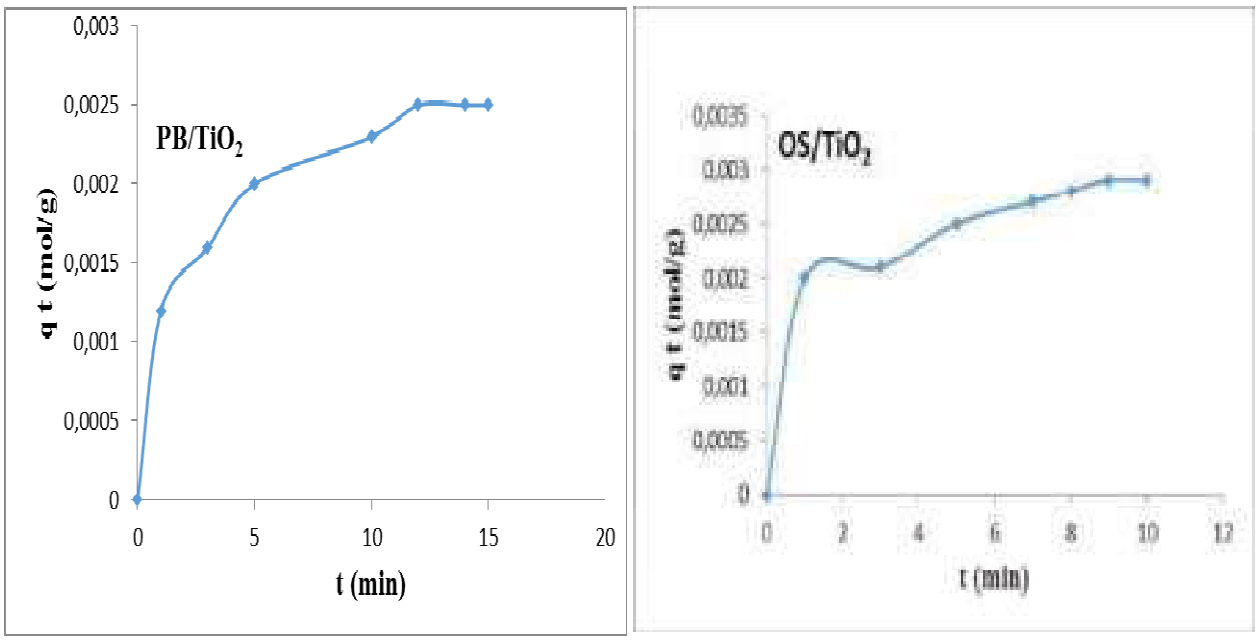

Fig 1. *Variation de la capacité d'adsorption de l'acide acétique sur PB/TiO_2 et OS/TiO_2 en fonction du temps de contact.*

Creative Commons Attribution-NonCommercial-NoDerivatives 4.0 International License (CC BY-NC-ND)

Les modèles cinétiques d'adsorption

Afin d'étudier la cinétique d'adsorption de l'acide acétique sur PB/TiO_2 et OS/TiO_2, et pour mettre en évidence l'influence de certains paramètres susceptibles d'affecter le processus, nous sommes intéressés à l'influence du temps de contact et la concentration initiale.

La compréhension du mécanisme cinétique dans des opérations fondées sur les phénomènes d'adsorption présente un intérêt pratique considérable pour la mise en œuvre optimale d'un adsorbant ainsi que pour connaître les facteurs qu'il faut optimiser pour fabriquer ou améliorer un adsorbant conduisant à la cinétique la plus rapide possible. Le processus d'adsorption se produit aussi selon une succession d'étapes qui déterminent la vitesse globale du processus **(Güler N. 2017).** Nous avons adopté deux modèles de cinétique. Ces modèles sont : modèles de pseudo-premier-ordre et pseudo-deuxième-ordre.

Le modèle du pseudo-premier-ordre

Ce modèle a été proposé par Lagergren en 1898, il est basé sur une relation linéaire entre la quantité de soluté (adsorbat) fixé à la surface du matériau (adsorbant) en fonction du temps**.** De nombreux auteurs ont utilisé ce modèle cinétique de pseudo-premier-ordre pour décrire l'adsorption de solutés organiques et inorganiques sur des surfaces solides hétérogènes. Dans la plupart des études sur les cinétiques d'élimination, ce modèle n'est pas adapté à toute la gamme de temps de contact, mais il est généralement applicable au début de l'adsorption, soit pour les 20 ou 30 premières minutes. Au-delà, les capacités expérimentales ne sont plus correctement extrapolées. Le modèle pseudo-premier-ordre (P1O) est donné par l'expression :

$$\frac{dq_t}{dt} = k_1(q_e - q_t)$$

Où**:**

$\mathbf{k_1}$: Constante de vitesse (min^{-1}).

$\mathbf{q_e}$: Quantité d'adsorbat à l'équilibre (mol/g).

$\mathbf{q_t}$: Quantité d'adsorbat à l'instant t (mol/g).

t: Temps de contact (min).

La linéarisation de l'équation de Lagergren est exprimée par l'équation suivante :

$$ln(q_e - q_t) = lnq_e - k_1 t$$

Les constantes du pseudo-premier-ordre ont été déterminées par extrapolation du tracé de $ln(q_e - q_t)$ en fonction du temps (t) (Figure 2). Pour les deux nanocomposites étudiées, les valeurs des quantités adsorbées q_e, les constantes de pseudo-premier-ordre k_1 et les coefficients de corrélation R^2 sont regroupées dans le **Tableau 3**.

Creative Commons Attribution-NonCommercial-NoDerivatives 4.0 International License (CC BY-NC-ND)

Algerian Journal of Engineering Architecture and Urbanism Vol. 5 Nr. 3 2021
ISSN: 2588-1760

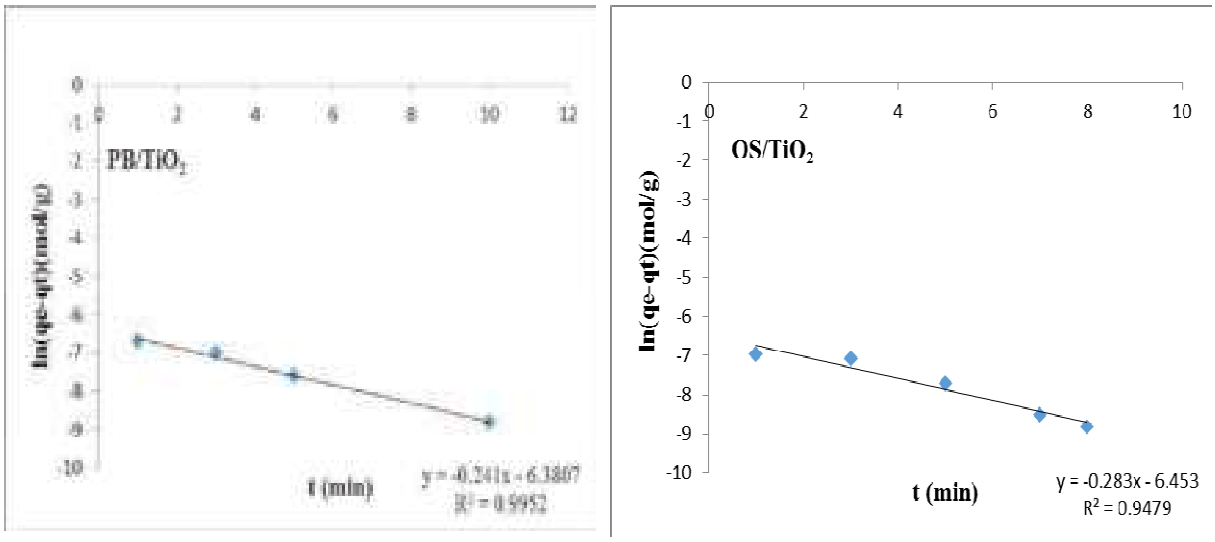

Fig 2. *Modélisation de la cinétique d'adsorption selon le modèle du pseudo-premier-ordre pour PB/TiO_2 et OS/TiO_2.*

Les valeurs de R^2 ont été trouvées entre 0,94 et 0,99. Le calcul de q_e pour les nanocomposites (PB/TiO_2 et OS/TiO_2) montre que les quantités adsorbées de l'acide acétique sont plutôt faibles par rapport aux quantités expérimentales. Ces observations nous amènent à dire que l'adsorption n'adéquat pas pour un processus de diffusion contrôlée.

Le modèle du pseudo deuxième ordre

Le modèle de pseudo-deuxième-ordre permet de décrire correctement la fixation des molécules de soluté sur la surface solide du matériau. L'analyse des données cinétiques relève qu'un modèle irréversible de second ordre fournit des résultats de meilleure qualité que les modèles d'ordre inférieu**.** Cette meilleure description des cinétiques s'explique par l'hétérogénéité réelle des sites de fixation, ces vitesses de transfert se caractérisent globalement par deux phases :

- Une première phase correspondant à la fixation rapide des solutés sur les sites les plus réactifs.
- Une seconde phase plus lente qui implique la fixation sur les sites de faible énergie.

Ce modèle est donné par l'expression suivante :

$$\frac{dq_t}{dt} = k_2(q_e - q_t)^2$$

Où

q_e: Quantité adsorbée à l'équilibre (mol/g).

q_t: Quantité d'adsorbée à l'instant t (mol/g).

t : Temps de contact (min).

k_2 : Constante de vitesse de pseudo-second-ordre (g/mol.min).

La linéarisation de l'équation précédente donne :

$$\frac{t}{q_t} = \frac{1}{k_2 \times q_t^2} + \frac{1}{q_t} t$$

Creative Commons Attribution-NonCommercial-NoDerivatives 4.0 International License (CC BY-NC-ND)

Algerian Journal of Engineering Architecture and Urbanism Vol. 5 Nr. 3 2021
ISSN: 2588-1760

La figure 3 illustre les résultats de l'application du modèle cinétique de pseudo-deuxième-ordre relatifs à l'adsorption de l'acide acétique sur PB/TiO_2 et OS/TiO_2. Les valeurs calculées des quantités adsorbées q_e, les constantes de pseudo-deuxième-ordre k_2 et les coefficients de corrélation R^2 sont regroupées dans le **Tableau 3**.

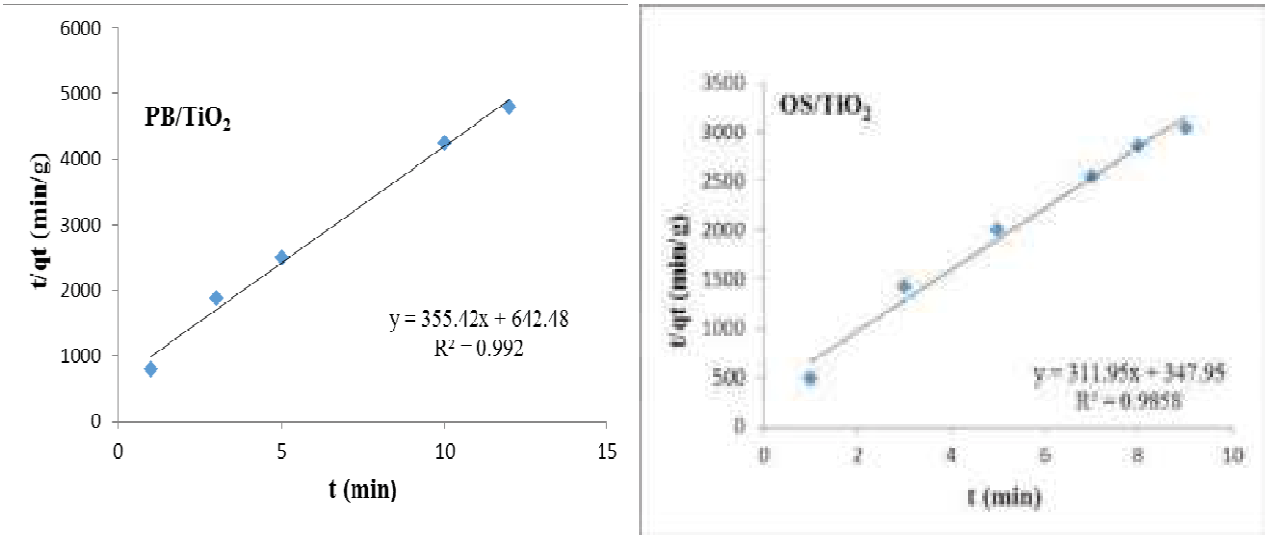

Fig 3. *Modélisation de la cinétique d'adsorption selon le modèle du pseudo-deuxième-ordre pour PB/TiO_2 et OS/TiO_2.*

D'après ces résultats, il apparait que les valeurs de R^2 sont très élevées et sont de l'ordre de 0,98 pour TiO_2 et 0.99 pour TiO_2 et dépassent de celles obtenues avec le modèle du pseudo-premier-ordre. Les quantités fixées à l'équilibre q_e sont très proches des valeurs retrouvées expérimentalement. Ces deux dernières constatations nous amènent à penser que le processus d'adsorption suit bien le modèle de pseudo-deuxième-ordre.

Nanocomposites	Modèle P1O				Modèle P2O			
	$k_1(min^{-1})$	R^2	q_e (mol/g)		$k_2(g.mol^1.min^{-1})$	R^2	q_e (mol/g)	
			q_e(théo)	q_e (exp)			q_e(théo)	q_e(exp)
PB/TiO_2	0.5550	0.9952	0.0016	0.0025	197.21	0.9920	0.0028	0.0025
OS/TiO_2	0.6517	0.9479	0.0015	0.0029	280.27	0.9858	0.0032	0.0029

Tableau 3: Les paramètres cinétiques du modèle de pseudo-premier-ordre et pseudo-deuxième-ordre pour PB/TiO_2 et OS/TiO_2.

La cinétique d'adsorption

Toutes les cinétiques d'adsorption sont réalisées suivant le même protocole expérimental **(Avom J., 2001).** Dans des erlenmeyers, on place une masse m = 0.5g de nanocomposites (PB/TiO_2 et OS/TiO_2), avec 50 ml de solution d'acide acétique de concentration connue variant entre 0.015, 0.025, 0.05, 0.10 et 0.15 mol/L. Ces erlenmeyers sont ensuite fermés, et agités sous une agitation magnétique égale à 250 tr/min à température ambiante pendant 30 minutes. Les mélanges sont enfin filtrés. A l'issue de la filtration, on prélève 10 ml de la

Creative Commons Attribution-NonCommercial-NoDerivatives 4.0 International License (CC BY-NC-ND)

solution. Après, on ajoute trois gouttes de phénolphtaléine et on fait le dosage acido-basique par une solution d'hydroxyde de sodium de concentration 0.1 mol/L. La quantité adsorbée q_e est déterminée par la relation suivante :

$$q_e = \frac{C_i - C_e}{m} \times V$$

Etude des isothermes d'adsorption

Les isothermes d'adsorption jouent un rôle important dans la détermination des capacités maximales d'adsorption et dans la conception de nouveaux adsorbants ; il est donc indispensable dans notre étude de les déterminer pour chacun des nanocomposites utilisés.

Il existe de nombreux modèles théoriques qui ont été développés pour décrire les isothermes d'adsorption. Cependant dans cette partie, nous nous intéresserons au modèle de Langmuir et Freundlich, car ils sont les plus simples et les plus répandus. Ces isothermes d'adsorption peuvent être obtenues par la représentation graphique de $q_e = f(C_e)$.

D'après la classification de Giles et al, les isothermes sont de type C (classe de Langmuir) dans le sous-groupe 3 sans le plateau de saturation. Cette forme d'isotherme indique que l'adsorption de ces composés s'effectue selon un processus de "mouillage" du système microporeux (rayon des pores < 20A°) et de la surface externe.

La figure 4 présente l'isotherme d'adsorption de l'acide acétique sur PB/TiO_2 et OS/TiO_2.

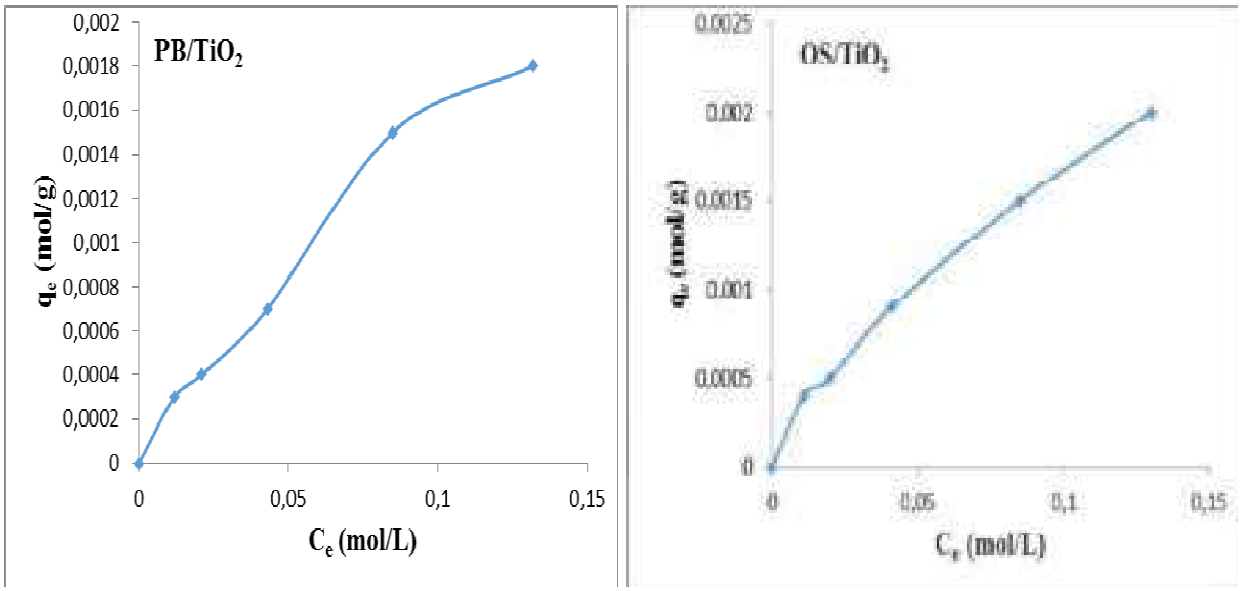

Fig 4. *L'isotherme d'adsorption de l'acide acétique sur PB/TiO_2 et OS/TiO_2.*

Nous observons ainsi une augmentation de l'efficacité lorsque la concentration d'adsorbant introduite augmente. Pour une concentration de 0.13 mol/L de l'adsorbant, la quantité adsorbée atteint $1.8.10^{-3}$ mol/g. Cette amélioration peut être justifiée par l'augmentation des sites d'adsorption avec l'augmentation de la concentration. Nous observons que les isothermes d'adsorption de l'acide acétique sur PB/TiO_2 et OS/TiO_2, ont la même allure : la quantité de l'acide acétique adsorbée augmente plus au moins rapidement pour de faibles concentrations en solution, ce qui traduisant une adsorption en monocouche. Ces résultats

Creative Commons Attribution-NonCommercial-NoDerivatives 4.0 International License (CC BY-NC-ND)

indiquent que l'adsorption de ce composé est de type chimisorption et se réalise avec formation d'une monocouche moléculaire. Il s'agit d'une adsorption localisée sur des sites de même énergie, sans interaction entre les molécules adsorbées. L'adsorption, dans ce cas, semble être favorisée par la présence des groupements carboxyliques des molécules. Ceci peut s'expliquer par le fait que l'adsorption d'acide acétique est gouvernée par les interactions entre le plan basal du matériau et le groupement carboxylique du soluté. Dans ce mécanisme « donneur-accepteur » par interactions entre la surface PB/TiO_2, OS/TiO_2 et le groupement carboxylique de la molécule, le nanocomposite joue le rôle de donneur d'électrons et l'adsorbat le rôle d'accepteur. Dans le cas de l'acide acétique, le groupement carboxylique peut jouer le rôle d'attracteur d'électrons ce qui accentue le caractère « Accepteur d'électrons » de ce dernier et facilite l'adsorption (contrairement au groupement hydroxyle qui augmente la densité électronique de la molécule).

Modélisation des isothermes d'adsorption

La modélisation des équilibres d'adsorption consiste à représenter, par des lois mathématiques, la relation à l'équilibre entre la quantité de polluant en phase liquide C_e et celle adsorbée sur le matériau q_e. Dans cette étude, l'équilibre d'adsorption est analysé par application du modèle de Langmuir et celui de Freundlich qui sont couramment utilisés par les chercheurs pour l'étude des isothermes d'adsorption des systèmes adsorbant/adsorbât.

Isotherme d'adsorption de Langmuir

La théorie de l'isotherme de Langmuir suppose que l'adsorption est monocouche et a lieu aux sites homogènes spécifiques de l'adsorbant. Les résultats des tests d'adsorption d'acide acétique sur PB/TiO_2 et OS/TiO_2 ont été traités par le modèle de Langmuir représenté par l'équation suivante :

$$\frac{C_e}{q_e} = \frac{1}{k \times q_{max}} + \frac{C_e}{q_{max}}$$

Où:

C_e : La concentration d'équilibre en (mol/L),

q_e : La quantité adsorbée à l'équilibre (mol/g),

k : La constante d'équilibre relative au modèle de Langmuir,

q_{max} : La quantité maximale adsorbée (mol/g).

Les valeurs de q_{max} et k sont déterminées à partir de l'intersection avec l'axe des ordonnées et la pente de la droite $\frac{1}{q_e} = f\left(\frac{1}{C_e}\right)$ dans le **Tableau 5**. Les courbes $\frac{1}{q_e} = f\left(\frac{1}{C_e}\right)$ de BP/TiO_2 et OS/TiO_2 sont représentées dans la Figure selon le modèle de Langmuir.

Creative Commons Attribution-NonCommercial-NoDerivatives 4.0 International License (CC BY-NC-ND)

Algerian Journal of Engineering Architecture and Urbanism Vol. 5 Nr. 3 2021
ISSN: 2588-1760

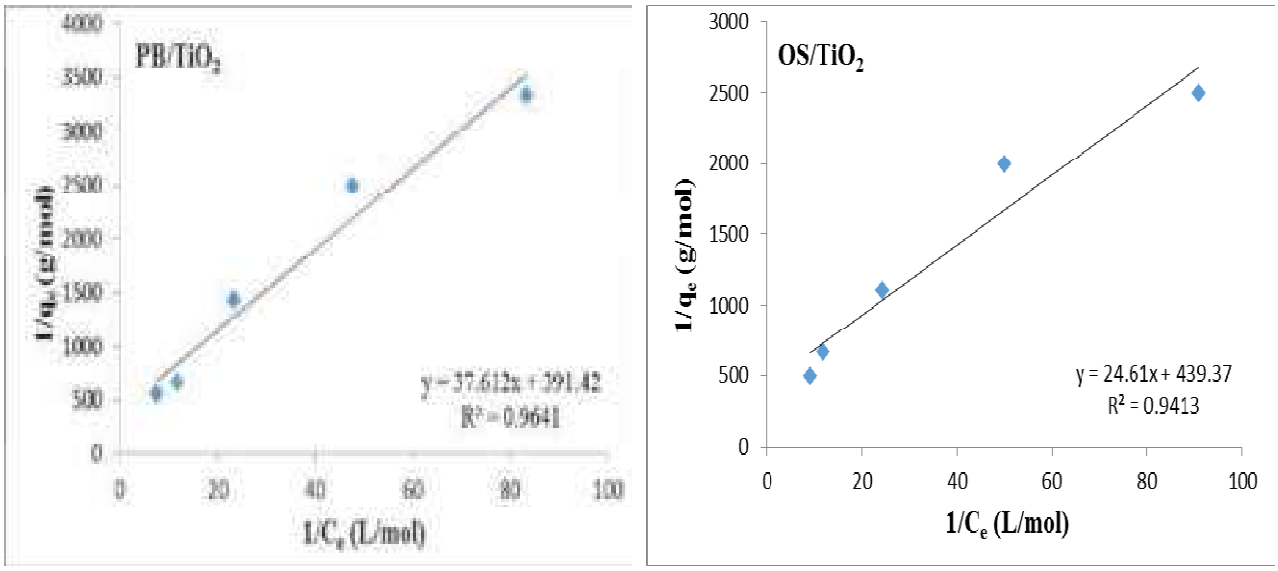

Fig 5. *Linéarisation de l'isotherme d'adsorption de Langmuir de l'acide acétique sur PB/TiO₂ et OS/TiO₂.*

Nanocomposites	Les paramètres de Langmuir		
	q_{max}	k	R^2
PB/TiO₂	0.0025	10.41	0.964
OS/TiO₂	0.0022	17.85	0.941

Tableau 4. Les valeurs de l'isotherme d'adsorption de Langmuir.

A partir des valeurs de coefficients de corrélation de PB/TiO_2 et OS/TiO_2, Nous observons que la linéarisation de l'isotherme d'adsorption de Langmuir de l'acide acétique sur le nanocomposite PB/TiO_2 est décrite de manière satisfaisante que le nanocomposite OS/TiO_2.
L'étude des isothermes d'adsorption a montré que le modèle de Langmuir est adapté pour les isothermes expérimentales, confirmant le phénomène d'adsorption par chimisorption. Nous pouvons dire que le modèle de Langmuir, est adéquat pour une description de cette isotherme d'adsorption sur PB/TiO_2.

Isotherme d'adsorption de Freundlich

L'isotherme de Freundlich suppose que l'adsorption est multicouche et que la surface de l'adsorbant est hétérogène. Elle peut s'exprimer par la relation suivante :

$$lnq_e = lnk_f + \frac{1}{n} lnC_e$$

La représentation graphique de $\ln q_e$ en fonction de $\ln C_e$ pour l'adsorption d'acide acétique sur PB/TiO_2 et OS/TiO_2 est une droite dont la pente est $\frac{1}{n}$ et d'ordonnée à l'origine $\ln k_f$ ***(Figure 6)***. La valeur de $\frac{1}{n}$ donne une indication sur la validité de l'adsorption du système adsorbant-adsorbât, et comprise entre 0 et 1 indique une adsorption favorable.

Creative Commons Attribution-NonCommercial-NoDerivatives 4.0 International License (CC BY-NC-ND)

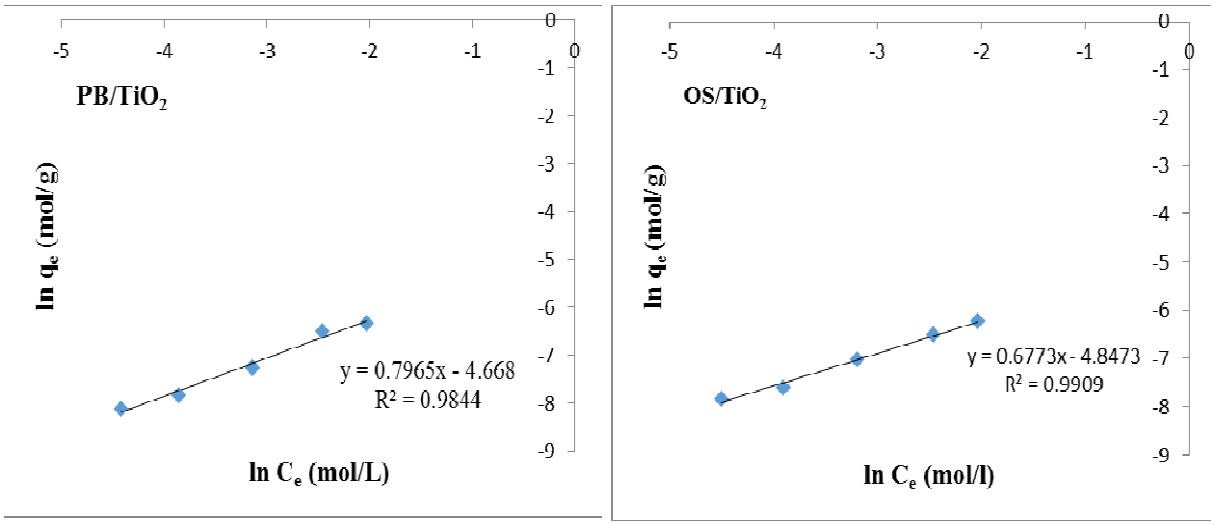

Fig 6. *Linéarisation de l'isothermed'adsorption de Freundlich de l'acide acétique sur PB/TiO₂ et OS/TiO₂.*

Les valeurs numériques de k_f et $\frac{1}{n}$ calculées respectivement, à partir de l'intersection avec l'ordonnée à l'origine et la pente de la droite de l'isotherme sont regroupées dans le **Tableau 5**.

Nanocomposites	Paramètres de Freundlich		
	$\frac{1}{n}$	k_f	R^2
PB/TiO₂	0.79	0.0093	0.980
OS/TiO₂	0.67	0.0078	0.990

Tableau 5. Les valeurs de l'isotherme de Freundlich.

D'après ces résultats on note que les valeurs numériques de $\frac{1}{n}$ de PB/TiO_2 et OS/TiO_2 sont respectivement (0.79 et 0.67) indique que l'adsorption est favorable. Les coefficients de corrélation R^2 sont de (0.98 et 0.99), ils sont supérieurs à celles du modèle de Langmuir. Ceci indique que l'adsorption d'acide acétique sur PB/TiO_2 et OS/TiO_2 suit bien le modèle de Freundlich que celui de Langmuir pour les deux nanocomposites.

La surface spécifique

Le calcul de la surface spécifique se base sur le traitement analytique de l'isotherme d'adsorption déterminé expérimentalement ; il est ainsi possible de définir la quantité de l'acide acétique adsorbé en une monocouche complète, puis de calculer l'aire de cette couche, donc la surface spécifique de la poudre ou du solide.

On peut alors déduire q_{max} à partir de la pente et de l'ordonnée à l'origine des courbes $\frac{1}{q_e} = f\left(\frac{1}{C_e}\right)$. La connaissance de q_{max} conduit à la détermination de la surface spécifique S_n par la relation suivante :

Creative Commons Attribution-NonCommercial-NoDerivatives 4.0 International License (CC BY-NC-ND)

$$S_n = q_{max} \times \omega \times N_a$$

q_{max} : La capacité maximale d'adsorption **(mol/g).**
ω : L'aire de l'acide acétique **(ω = 21 Å^2)**.
N_a : Le nombre d'Avogadro **($6.023.10^{23}$).**

Nanocomposites	PB/TiO_2	OS/TiO_2
q_{max} (mol/g)	0.0025	0.0022
S_n (m^2/g)	316.20	278.26

Tableau 6. Les valeurs de la surface spécifique de PB/TiO_2 et OS/TiO_2.

Les résultats du **Tableau 6** montrent que la surface spécifique de PB/TiO_2 est supérieure à celle de OS/TiO_2. Donc, il se produit un développement plus étendu de la porosité des nanocomposites. Ce constat est confirmé par la valeur élevée de la capacité d'adsorption du nanocomposite PB/TiO_2 préparé à partir de la peau de banane. On constate que la nature de la biomasse joue un rôle important dans le développement de la structure de PB/TiO_2 et OS/TiO_2.

Conclusion :

Cette étude a mis en évidence l'efficacité des nanocomposites PB/TiO_2 et OS/TiO_2 pour éliminer les acides organiques en milieu aqueux. L'influence des paramètres liés aux conditions opératoires tels que le temps de contact et la concentration initiale de l'acide acétique ont été étudiés. L'étude cinétique montre que l'équilibre s'établit au bout de 10 et 12 minutes et que le mécanisme d'adsorption peut être décrit par une cinétique de pseudo-deuxième-ordre. L'application des isothermes d'adsorption montre que le modèle de Freundlich représente parfaitement la cinétique d'adsorption de l'acide acétique sur les deux nanocomposites PB/TiO_2 et OS/TiO_2. Les paramètres obtenus indiquent que l'adsorption de l'acide acétique sur les PB/TiO_2 et OS/TiO_2 est efficace et applicable les déchets biologiques fonctionnalisés par TiO_2 se sont avérées comme un support qui a une affinité d'adsorption généralement importante vis-à-vis l'acide acétique. L'abondance de ces déchets biologiques, peut offrir un matériau adsorbant et alternatif à faible coût qui peut éventuellement contribuer au traitement des eaux usées pour l'élimination des acides organiques.

Références :

Syeda S. A., Sadiya M., Noorunnisa B. (2017)**,** *Adsorption Studies of Acetic Acid Removal from Waste Water Using Seeds of Brassica Nigra,* Journal of Engineering Research and Application **7(8)** : 1-3.

Sunil J. K., Mrunmai J., Nikita M. (2016), *Acetic Acid Adsorption on Rice Husk Adsorbent,* International Journal of Science and Healthcare Research **1(1)** : 18-21.

Folahan A. A., Ismaila A. O. (2017), *Biosorption of formic and acetic acids from aqueous solution using activated carbon from shea butter seed shells***,** Applied Water Science **7** : 2727–2736.

Gao X., Hua X., Gong C., Xue Bao. (2008), *Recovery of acetic acid from wastewater by adsorption and heating regeneration,* Journal of Chemical Engineering of Chinese Universities **22(4)** :580-584.

Creative Commons Attribution-NonCommercial-NoDerivatives 4.0 International License (CC BY-NC-ND)

Sumrit M., Phansiri M., Wanwimon P., Sataporn K. (2015), *Characterization and Properties of Activated Carbon Prepared from Tamarind Seeds by KOH Activation for Fe(III) Adsorption from Aqueous Solution,* ScientificWorld Journal **2015:** 415961.

Cleiton A. N., Mário C. G. (2011), *Estimation of surface area and pore volume of activated carbons by methylene blue and iodine numbers*, International Year of Chemistry **34 (3)** : 472-476.

Güler N. (2017), *Removal of acetic acid from dilute aqueous solutions using zeolite 13X*, Journal of the turkish chemical society section B **1(2):** 159-190.

Avom J., Ketcha Mbadcam J. K., Matip M.R.L., Germain P. (2001), *Adsorption isotherme de l'acide acétique par des charbons d'origine végétale***,** African Journal of Science and Technology **2(2) :** 1-7.

Creative Commons Attribution-NonCommercial-NoDerivatives 4.0 International License (CC BY-NC-ND)

Algerian Journal of Engineering Architecture and Urbanism Vol. 5 Nr. 3 2021
ISSN: 2588-1760

DESIGN OF A NEW DIRECT TORQUE CONTROL USING SLIDING MODE THEORY FOR DOUBLE STAR INDUCTION MOTOR

Farid BELOUAHCHI
PhD student, Materials physics laboratory, radiation and nanostructure, Electromecanical department, university Mohamed El Bachir El Ibrahimi of Bordj Bou Arreridj, Algeria, farid.belouahchi@univ-bba.dz

Elkheir MERABET
Professor, Materials physics laboratory, radiation and nanostructure, Electromecanical department, university Mohamed El Bachir El Ibrahimi of Bordj Bou Arreridj, Algeria, elkheir34@gmail.com

Abstract:
This paper describes a new Direct Torque Control (DTC) scheme to the synthesis of controllers based on the theory of sliding mode control (SMC) for two level inverter fed double star induction motor (DSIM) drive. The controllers' synthesis method is totally analytical, and is based on non-linear models of the DSIM. The proposed sliding mode control scheme requires creation of the space attractors and artificial manifolds that reflect the desirable operating modes of the DSIM. The combination between the DTC and the SMC laws provides asymptotic stability with respect to the required operating regimes, reduces the THD of stator currents, invariance to external disturbances, and robustness to variation of DSIM parameters. The performance of the proposed approach has been tested under different operating conditions. With respect to their dynamic characteristics, sliding mode controllers (SMCs) are superior to the existing types of PI and Fuzzy Logic (FL) controllers.

Key words: (DSIM) double star induction motor, (SMC) sliding mode control, (FLC) fuzzy logic control, Lyapunov's theory, (THD) total harmonic distortion.

Introduction:

In recent years, the double star induction motor has been largely replaced asynchronous machines, it is the dominant technology used today [1, 2], indeed, this priority due to numerous factors such as, great power, power segmentation, minimizing torque ripples, high reliability, ruggedness, low cost and minimal loss...etc. [3, 4].This type of machines is constituted by two windings shifted between them by an angle of 30 degrees. These windings are usually fed by a six-phase inverter supply in variable speed. The main benefits of DSIM are higher torque density, higher efficiency, reduced harmonic content of the DC link voltage [5].

Currently, several moderns control techniques have been proposed to control the double star induction motors such as, direct torque control, feedback control, vector control, adaptive

Creative Commons Attribution-NonCommercial-NoDerivatives 4.0 International License (CC BY-NC-ND)

control …etc. [6]. Among these approaches, the DTC technique has been proposed by Takahashi and Depenbrock in 1985 which considered a solution for the problems of vector control [6]. This technique does not look the voltages to be applied to the machine, but the best switching state of the inverter to satisfy the user's requirements [7]. The method supplies direct control of the stator flux and torque and gives a systematic solution to improve the operating characteristics of the motor and the voltage source inverter. This method is not a complex structure compared to field orientation control (FOC) [8], DTC gives a very fast and accurate torque response, simple to introduce, torque, flux ripples and acoustic noise produce significant stable state [9]. The principal advantage of DTC is not requiring speed or position encoders and uses the measured voltage and current only. Flux, torque, and speed are estimated [10]. Direct torque control allows fast and efficient control of the stator flux and torque by optimal selection of the inverter switch states in each sampling period. The additional inverter is available for multiphase machines, allows greater flexibility in their selection and therefore more narrow adjustment of stator flux and torque. The control is realized by only eight possible inverter states in three phases on the other hand at several of inverter states means that a more elaborate selection criterion is required. For this reason, a small research was presented on a switching-table-based direct torque control of multiphase drives [7]. Due to the parametric sensitivity of PID regulator, minimal research has been done to avoid this inconvenient such as in the papers [11-13], to solve these problems, the use of a non-linear technique is essential, among them the fuzzy logic, which considered one of the most successful artificial intelligence technique for controlling nonlinear systems, sliding mode control (SMC) which ensuring good system and robustness to external disturbance and parametric variations [14-16].

In this paper, a direct torque control (DTC) scheme based on sliding mode approach for the two-level inverter fed double star induction motor (DSIM) drive has been proposed. The purpose of this work is to exploit the benefits of DTC control and to make a combination between DTC control and sliding mode approach to obtain more performances of control applied. The performances of the proposed approach have been tested under different operating conditions. To illustrate the effectiveness and the superiority of the proposed approach, a comparative study has been done with PI and fuzzy logic control (FLC) and by using MatLab/Simulink the simulation results are presented and analyzed.

The structure of present paper is classified as follow: The description and the modeling of the DSIM have been presented in section 2. The control strategy applied to DSIM (DTC) is set in section 3. The design of sliding mode control of DSIM is developed in section 4. Moreover, the simulation results are discussed on Matlab/Simulink for the proposed control scheme in section 5. Finally, a general conclusion summarizes this work.

Modeling of the DSIM

The DSIM dynamic équations in the reference d-q can be writing as follow:

Creative Commons Attribution-NonCommercial-NoDerivatives 4.0 International License (CC BY-NC-ND)

$$
\begin{aligned}
V_{ds1} &= R_{s1} i_{ds1} + \frac{d\phi_{ds1}}{dt} - \omega_s \phi_{qs1} \\
V_{qs1} &= R_{s1} i_{qs1} + \frac{d\phi_{qs1}}{dt} + \omega_s \phi_{ds1} \\
V_{ds2} &= R_{s2} i_{ds2} + \frac{d\phi_{ds2}}{dt} - \omega_s \phi_{qs2} \\
V_{qs2} &= R_{s2} i_{qs2} + \frac{d\phi_{qs2}}{dt} + \omega_s \phi_{ds2} \\
V_{dr} &= 0 = R_r i_{dr} + \frac{d\phi_{dr}}{dt} - (\omega_s - \omega_r)\phi_{qr} \\
V_{qr} &= 0 = R_r i_{qr} + \frac{d\phi_{dr}}{dt} + (\omega_s - \omega_r)\phi_{dr}
\end{aligned}
\tag{1}
$$

The fluxes equations are:

$$
\begin{aligned}
\phi_{ds1} &= L_{s1} i_{ds1} + L_m (i_{ds1} + i_{ds2} + i_{dr}) \\
\phi_{qs1} &= L_{s1} i_{qs1} + L_m (i_{qs1} + i_{qs2} + i_{qr}) \\
\phi_{ds2} &= L_{s2} i_{ds2} + L_m (i_{ds1} + i_{ds2} + i_{dr}) \\
\phi_{qs2} &= L_{s2} i_{qs2} + L_m (i_{qs1} + i_{qs2} + i_{qr}) \\
\phi_{dr} &= L_r i_{dr} + L_m (i_{ds1} + i_{ds2} + i_{dr}) \\
\phi_{qr} &= L_r i_{qr} + L_m (i_{qs1} + i_{qs2} + i_{qr})
\end{aligned}
\tag{2}
$$

For studying the dynamic behavior, the following équation of mouvement was added:

$$
J \frac{d\Omega_r}{dt} = T_{em} - T_L - K_f \Omega_r \tag{3}
$$

The model of the DSIM has been completed by the expression of the electromagnetic torque Tem given below:

$$
T_{em} = P \frac{L_m}{L_m + L_r} (\phi_{dr} (i_{qs1} + i_{qs2}) - \phi_{qr} (i_{ds1} + i_{ds2})) \tag{4}
$$

A schematic representation of the stator and rotor windings axis of double star induction motor in the synchronous reference frame (d, q) has been illustrated in Figure 1.

Direct torque control of DSIM

In its basic principle, the direct torque control is a method based on the switching tables wich its inputs are hysteresis torque and stator flux. Using this method led us to the minimizing of the inverter switching number, torque/stator fluxes decoupling, the inverter controlled without PWM generator, open loop parameters estimation in the referential related only to the stator and control is provided without need a mechanical sensor [17-18].

Creative Commons Attribution-NonCommercial-NoDerivatives 4.0 International License (CC BY-NC-ND)

Algerian Journal of Engineering Architecture and Urbanism Vol. 5 Nr. 3 2021
ISSN: 2588-1760

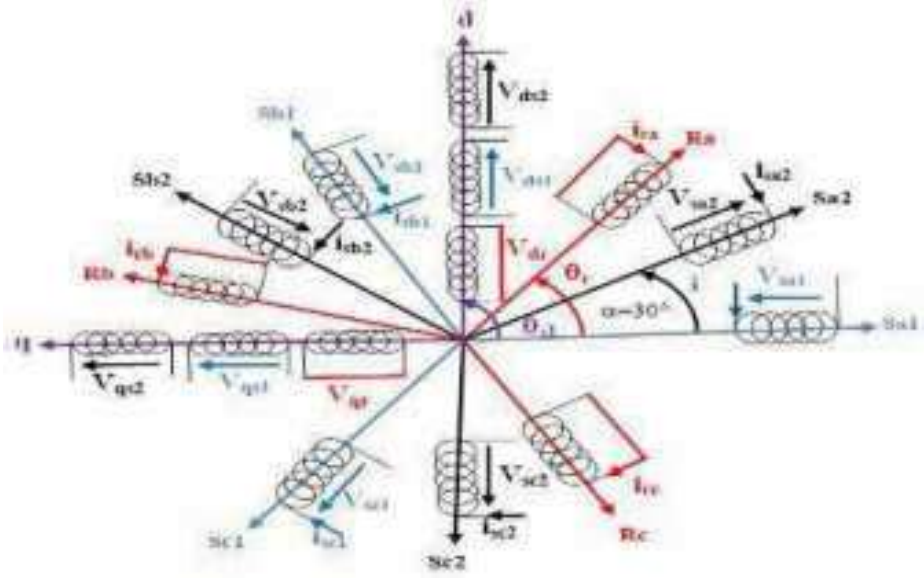

Fig. 1. Schematic representation of DSIM in abc and d-q reference

Figure 2 illustrates the synoptic diagram of the DTC of DSIM. In addition, Table I shows the sequences corresponding to the position of the stator flux vector to the different sectors.

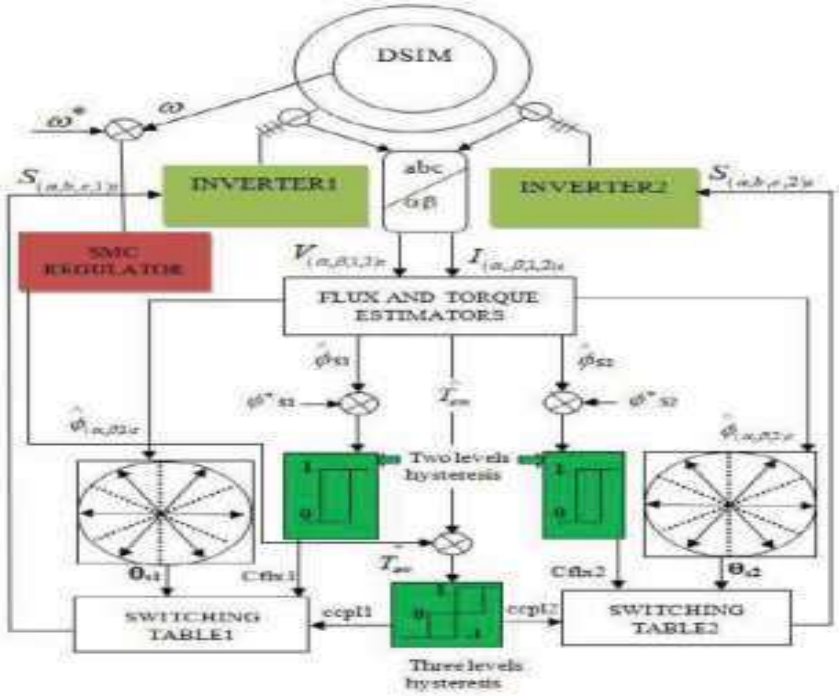

Fig. 2. Block diagram of DSIM speed SMC under DTC

The expression of the stator flux is given by the following équations:

$$\begin{aligned} \phi_{s\alpha 1,2} &= \int_0^t (V_{s\alpha 1,2} - R_s i_{s\alpha 1,2})\, dt \\ \phi_{s\beta 1,2} &= \int_0^t (V_{s\beta 1,2} - R_s i_{s\beta 1,2})\, dt \end{aligned} \tag{5}$$

Creative Commons Attribution-NonCommercial-NoDerivatives 4.0 International License (CC BY-NC-ND)

Where, $V_{s\alpha 1.2}$ and $V_{s\beta 1.2}$ are the estimated components of the stator vector voltage. They are expressed from the model of the inverter.

Corrector	Cflx	Ccpl	1	2	3	4	5	6
2levels	1	1 0 -1	V2	V3	V4	V5	V6	V1
			V7	V0	V7	V0	V7	V0
3levels			V6	V1	V2	V3	V4	V5
2levels	0	1 0 -1	V3	V4	V5	V6	V1	V2
			V7	V0	V7	V0	V7	V0
3levels			V5	V6	V1	V2	V3	V4

Table 1.SWITCH TABLE OF DTC CONTROL

Sliding mode control design:

1. Sliding Mode Control Theory [14]:

The sliding mode control is based on the convergence of system state trajectory to a sliding surface. The state vector is kept around this surface by the switching control effort in order that the trajectory slides to the origin through the sliding surface. The design of SMC can be reach in two successive steps:

First step: definition of sliding surfaces. The following equation is the most used surface S(x) in the literature:

$$s(t) = (\lambda + \frac{d}{dt})^{r-1}(x_{ref} - x) \tag{6}$$

Where x is the state vector, xref is the reference state vector, r is the degree of the sliding mode and λ is the weighting factor.

Second step: Control law design

The sliding mode control has two command components and can be written as follows:

$$s(t) = u_{eq}(t) + u_N(t) \tag{7}$$

The component u_{eq} called the equivalent control (decoupling control) is obtained by putting surface derivate equals zero $s(t)^{\bullet} = 0$, its role is holding the system on the sliding surface which is definite by $s(t) = 0$. The other constituent u_N is the discontinuous control

Creative Commons Attribution-NonCommercial-NoDerivatives 4.0 International License (CC BY-NC-ND)

(switching control) it ensures the convergence of system state trajectory toward sliding surface. The reaching condition is based on Lyapunov theory stability and must verify $s^{\bullet} \cdot s < 0$.

2. Application of SMS on DSIM

The électromagnétique torque can be expressed as:

$$T_{em} = P \frac{L_m}{L_m + L_r} \phi^*_r (i_{qs1} + i_{qs2}) = K i_{qs} \tag{8}$$

Where, k is the torque constant and ϕ^* is the flux référence.

To design a sliding mode speed controller for the double star induction motor FOC drive, consider the mechanical équation:

$$\frac{J}{P} \Omega_r^{g} + \frac{K_f}{P} \Omega_r + T_L = T_e \tag{9}$$

Where Ωr is the rotor speed in electrical rad/s, rearranging to get.

$$\Omega_r^{g} = -\frac{K_f}{J} \Omega_r - \frac{P}{J} T_L + \frac{P}{J} T_e \tag{10}$$

Considering Δa and Δb as bounded uncertainties introduced by system parameters J and Kf, (10) can be rewritten as:

$$\Omega_r^{g} = (a + \Delta a) \Omega_r + (b + \Delta b) T_L + c T_e \tag{11}$$

Where :

$$a = -\frac{K_f}{J}, b = -\frac{P}{J}, c = -\frac{P}{J}$$

Error speed is as follow :

$$e(t) = \Omega_r(t) - \Omega^*_r(t) \tag{12}$$

Combining the sign function with Lyapunov condition Yields :

$$e^{g}(t) = a e(t) + b\left(\overline{T}_e + d(t)\right) \tag{13}$$

Where d(t) is the lumped uncertainty defined as:

$$d(t) = \frac{\Delta a}{b} \Omega_r + \frac{\Delta b}{b} T_e + \frac{c}{b} T_L \tag{14}$$

And:

$$\overline{T_e}(t) = T_e(t) + \frac{a}{b} \Omega_r^* \tag{15}$$

The switching surface s(t) of system parameters a and b [19-21]:

$$S(t) = e(t) + \int_0^t (a + bk) e(\Gamma) d\Gamma \tag{16}$$

Such that the error dynamics at the sliding surface :

$$S(t) = S^{g}(t) = 0 \tag{17}$$

Creative Commons Attribution-NonCommercial-NoDerivatives 4.0 International License (CC BY-NC-ND)

Will be forced to exponentially decay to zero, then the error dynamics can be described by:

$$e^{g}(t) = (a + bk)\, e(t) \tag{18}$$

Where k is a linear negative feedback gain [9]. The variable structure speed controller law can be defined as:

$$\overline{T_e}(t) = ke(t) - \beta\, sign\left(S(t)\right) \tag{19}$$

Where β is known as hitting control gain used to make the sliding mode condition possible and the sign function can be defined as [21]:

$$\text{sign(s)} = \begin{cases} 1 \text{ if } s>0 \\ 0 \text{ if } s=0 \\ -1 \text{ if } s<0 \end{cases} \tag{20}$$

The final électromagnétique torque command T_e^* of the output of the sliding mode speed controller can be obtained directly substituting (18) into (15) [22]. Basically, the control law for T_e^* is divided into two parts: equivalent control U_{eq} which defines the control action when the system is on the sliding mode and switching part U_s which ensures the existence condition of the sliding mode. If the friction k_f is neglected expressions for U_{eq} and U_s can be written as:

$$\begin{cases} U_{eq} = ke(t) \\ U_s = -\beta\, sign\left(s(t)\right) \end{cases} \tag{21}$$

Simulation results and discussions:

The control of the drive system has been tested by simulation under DTC scheme using sliding mode controller; the results are performed in this paper by using MATLAB/SIMULINK. The used double star induction motor has the following parameters, the nominal power Pn is 4.5kw, nominal voltage Vn is 220V, stator resistances Rs1 and Rs2 are 3.72 Ohm, rotor resistance Rr is 2.12 Ohm, mutual inductance Lm is 0.3672H, rotor inductance Lr is 0.006H, moment of inertia J is 0.0662kg.m2, and friction coefficient Kf is 0.001.The simulation results have been obtained for two tests conditions. The performances of the proposed approach have been compared with PI and fuzzy logic control (FLC).

1. Tracking the performance of sliding mode controller:

This test is the no load start then under load with load torque is T_L= 14 N.m and reference speed are w_{ref}=100rd/sec.

Figure 3 presents different réponses of electromagnetic torque, speed, stator flux and stator current for this test.

Figure 3 illustrates the simulation results of the first test, the electromagnetic torque has the same form of the load torque which shows that it compensates the load torque and the friction in the established regime (Figure 3(a)), the speed reaches the reference speed at t=0.3s and follows it perfectly, it also noticed that the speed controller rejects the load disturbance quickly (Figure 3(b)), the stator current has a peak value at the start up of 21A, in the presence of load its peak value is 7A and 1.5A in the absence of theme (no load) (Figure 3(c)), the

Creative Commons Attribution-NonCommercial-NoDerivatives 4.0 International License (CC BY-NC-ND)

stator flux follows its reference perfectly.

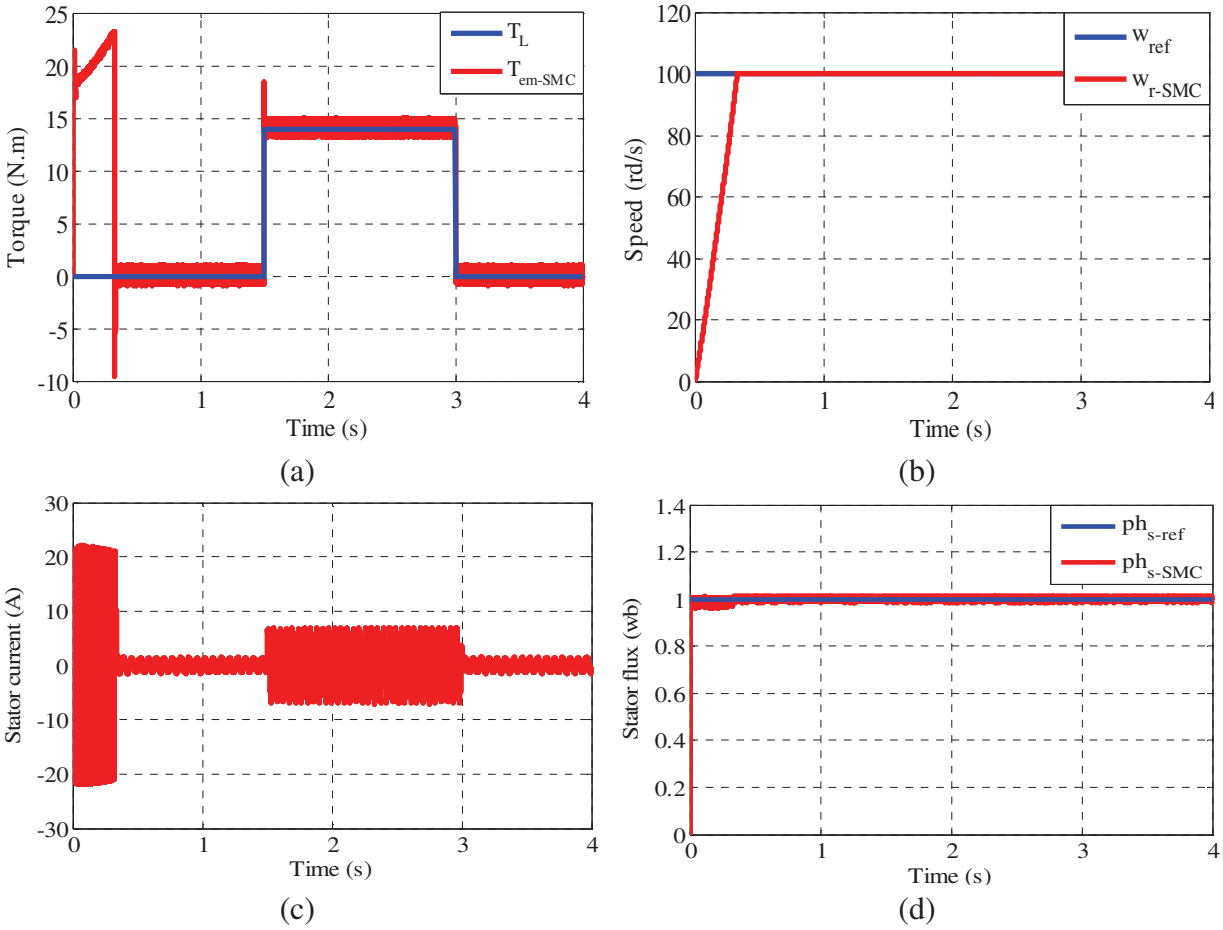

Fig3. Torque, speed, stator flux and current responses for the first test

2. Assessment the performance of sliding mode controller with others techniques:

In this part of simulation, the performances of the used approach (SMC) have been compared with others techniques under the following test:

In this section, the form of reference speed is chosen as a stair curve with amplitude of 100rd/s, -100rd/s, 0rd/s and 50rd/s.

Figure 4 presents different responses of speed, torque, stator current and stator flux for the reference tracking test.

Figure 4 shows the performance of each controller when the chosen form of reference speed is a stair curve. It noticed that the sliding mode controller has the best performances in following of wire speed (Figure 4(a)), the wire speed achieves its reference value quickly which prove the rapid convergence and the shirt time response of the proposed approach, the electromagnetic torque and the stator current track the chosen variation of wire speed (Figures 4(b), 4(c)), despite these changes the stator flux follows its reference value perfectly (Figure 4(d)).

Table II summarizes the main current THD and table III illustrate the amplitude of ripples for each controller.

Creative Commons Attribution-NonCommercial-NoDerivatives 4.0 International License (CC BY-NC-ND)

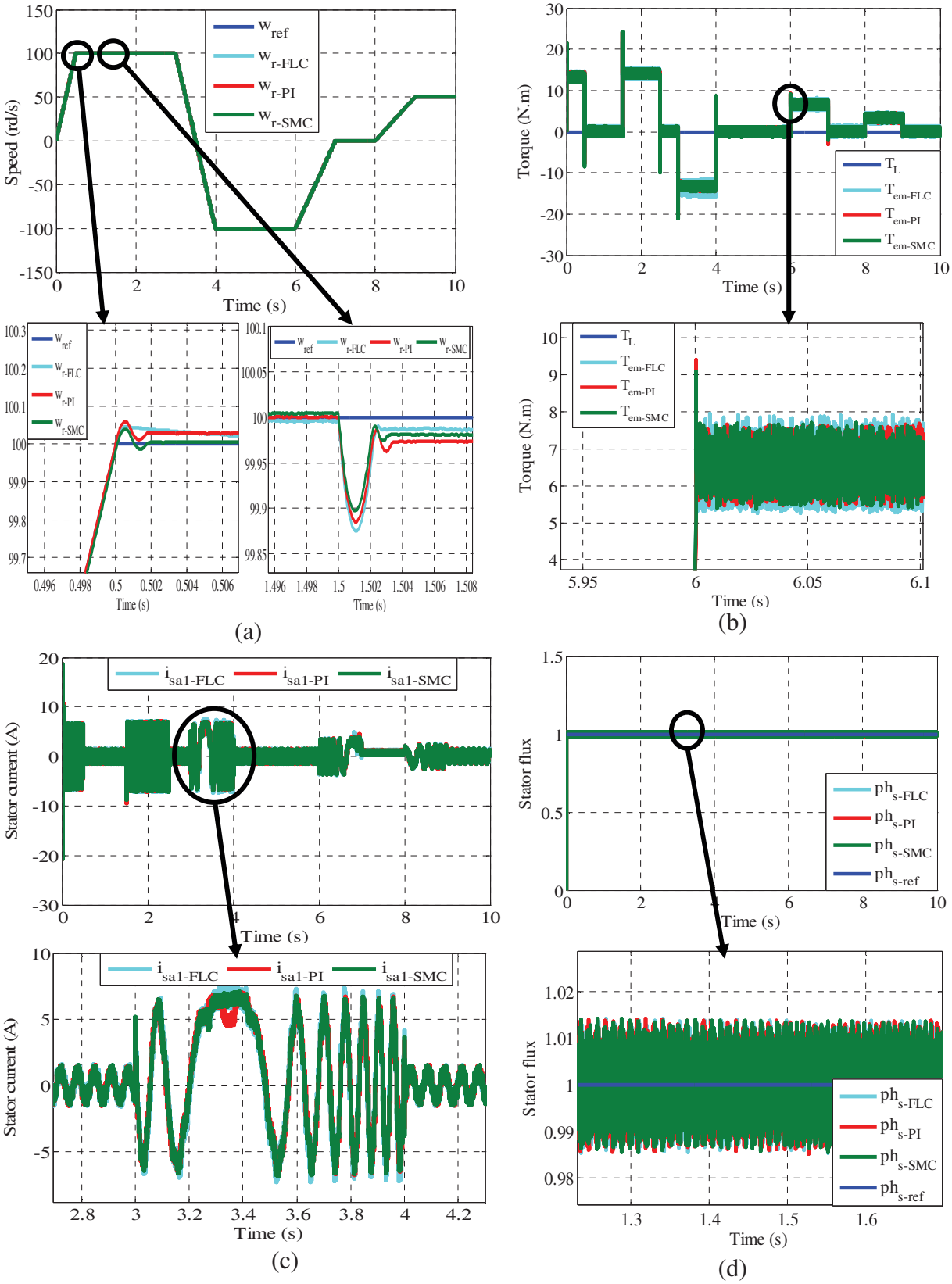

Fig4. Speed, torque, stator current and flux responses for the second test

These results show that the use of sliding mode control has led us to the reduced ripple amplitude and THD current, in addition to an improvement in rise time.

Creative Commons Attribution-NonCommercial-NoDerivatives 4.0 International License (CC BY-NC-ND)

	SMC	PI	FLC
Torque ripples (N.m)	***13.35-14.66***	***13.48-14.86***	***12.96-15.22***
	(1.31)	***(1.38)***	***(2.26)***
Stator Flux ripples (Wb)	***0.9898-1.009***	***0.9861-1.006***	***0.9874-1.011***
	(0.0192)	***(0.0199)***	***(0.0236)***

Table2. AMPLITUDE OF RIPPLES

Techniques	**SMC**	**PI**	**FLC**
Current THD %	***4.71%***	***6.1%***	***6.34%***

Table3. SMC, PI AND FLC CORRESPONDING PHASE CURRENT THD

Conclusion:

A new approach for the DTC scheme of DSIM based on sliding mode control theory (SMC) was investigated in this paper. Application of the SMC allowed us to design analytical control strategy using a nonlinear model of DSIM that regulates the speed and flux continuously. These controllers guarantee asymptotic stability of the closed loop system through Lyapunov's theory. In the first part of simulation, the performances of the used approach have been tracked and evaluated. In the second part of simulation, the controllers were assessed and compared with the classic PI and Fuzzy Logic (FL) controllers considering state and transients behaviors in DSIM. From the simulation results, it was observed that the controllers based on SMC showed better performance in all cases considered compared to the classic PI and FL controllers such as: overload torque, stator current, stator flux and electromagnetic torque ripples.

References:

[1] **Kortas I., Sakly A., Mimouni MF.** (2017), *Optimal vector control to a double-star induction motor. Energy,* Elsevier vol 131, pp.279-288.

[2] **Hammache H., Moussaoui D., Marouani K., Hamdouche T.** (2008), *Magnetic properties in double star induction machine*, 18th International Conference on Electrical Machines IEEE, pp.1-6.

[3] **Azib A., Ziane D., Rekioua T., Tounzi A.** (2016), *Robustness of the direct torque control of double star induction motor in fault condition*, Revue Roumaine des Sciences Techniques, vol 61, pp.147-152.

[4] **Hamidia F., Abbadi A., Boucherit M.S.** (2016), *Direct torque controlled dual star induction Motors (in open and closed loop),* In 4th International Conference on Electrical Engineering (ICEE) IEEE, pp.1-6.

[5] **Youb L., Belkacem S., Naceri F., Cernat M., Pesquer L.G.** (2018), *Design of an adaptive fuzzy control system for dual star induction motor drives,* Advances in Electrical and Computer Engineering, vol 18, pp.37-44.

[6] **Lazreg M.H., Bentaallah A.** (2019), *Sensorless speed control of double star induction machine with five level DTC exploiting neural network and extended Kalman filter*, Iranian Journal of Electrical and Electronic Engineering, vol 15, pp.142-152.

[7] **Zheng L., Fletcher J.E., Williams B.W., He X.** (2010), *A novel direct torque control scheme for a sensorless five-phase induction motor drive,* IEEE Transactions on Industrial Electronics, vol 58, pp.503-

Creative Commons Attribution-NonCommercial-NoDerivatives 4.0 International License (CC BY-NC-ND)

513.

[8] **Vasudevan M., Arumugam R., Paramasivam S.** (2006), *Development of torque and flux ripple minimization algorithm for direct torque control of induction motor drive,* Electrical Engineering, vol 89, pp.41-51.

[9] **Gowri K.S., Reddy T.B., Babu C.S.** (2010), *Direct torque control of induction motor based on advanced discontinuous PWM algorithm for reduced current ripple,* Electrical Engineering, vol 92, pp.245-255.

[10] **Araria R., Berkani A., Negadi K., Marignetti F., Boudiaf M.** (2020), *Performance analysis of DC-DC converter and DTC based fuzzy logic control for power management in electric vehicle application,* Journal Européen des Systèmes Automatisés, vol 53, pp.1-9.

[11] **Boukhalfa G., Belkacem S., Chikhi A., Benaggoune S.** (2018), *Direct torque control of dual star induction motor using a fuzzy-PSO hybrid approach,* Applied Computing and Informatics.

[12] **Yue Y.T., Lin Y.** (2015), *A novel sensorless fuzzy sliding-mode control of induction motor,* International Journal of Control and Automation, vol 8, pp.1-10.

[13] **Hamouda N., Babes B., Hamouda C., Kahla S., Ellinger T., Petzoldt J.** (2019), *Optimal tuning of fractional order proportional-integral-derivative controller for wire feeder system using ant colony optimization optimal tuning of fractional order proportional-integral-derivative controller for wire feeder system using ant colony optimization,* Journal Européen des Systèmes Automatisés, vol 53, pp.157-166.

[14] **Amimeur H., Aouzellag D., Abdessemed R. Ghedamsi K.** (2012), *Sliding mode control of a dual-stator induction generator for wind energy conversion systems,* International Journal of Electrical Power & Energy, vol 42, pp.60-70.

[15] **Cherifi D., Miloud Y.** (2020), *Hybrid control using adaptive fuzzy sliding mode control of doubly fed induction generator for wind energy conversion system,* Periodica Polytechnica Electrical Engineering and Computer Science, vol 64, pp.374-381.

[16] **Rahali H., Zeghlache S., Benyettou L., Benalia L.** (2019), *Backstepping sliding mode controller improved with interval type-2 fuzzy logic applied to the dual star induction motor,* International Journal of Computational Intelligence and Applications, vol 18, pp.1950012.

[17] **Benalia L., Chaghi A., Abdessemed R.** (2013), *A Robust DTC Applied to the Doubly Stator Asynchronous Motor Based on RST Regulator,* Journal of Electrical and Control Engineering, Vol. 3, pp. 25-30.

[18] **Zaimeddine R., Berkouk E.M.** (2007), *A Novel DTC Scheme of Double Star Induction Motors Using Three Level Voltage Source Inverter,* Journal of Engineering and Applied sciences, Vol. 1, pp. 136-142.

[19] **Bojoi R., Lazzari M., Profumo F., Tenconi A.** (2003), *Digital Field-Oriented Control for Dual Three-Phase Induction Motor Drives,* IEEE Trans. On INDUSTRY Appl., Vol. 39, pp. 752-760.

[20] **Singh G. K., Nam K., Lim S. K.** (2005), *A simple indirect fieldoriented control scheme for multiphase induction machine,* IEEE Trans Ind.Electron vol. 52, pp. 1177–1184.

[21] **Hazzab A., Bousserhane I. K., Kamli M.** *Design of a fuzzy sliding mode controller by genetic algorithms for induction machine speed control,* Int. Journal Emerging Elec. Power Syst.

[22] **Massoum A., Meroufel A., Bentaallah A.** (2012), *Sliding Mode Speed Controller for a Vector Controlled Double Star Induction Motor,* Electrical Review PRZEGLĄD ELEKTROTECHNICZNY, ISSN, 0033-2097.

Creative Commons Attribution-NonCommercial-NoDerivatives 4.0 International License (CC BY-NC-ND)

Algerian Journal of Engineering Architecture and Urbanism Vol. 5 Nr. 3 2021
ISSN: 2588-1760

High Speed Transmissions over RoF-OCDMA Networks using ZCZ Spreading Code

GHALIFodil
PhD Student, Telecommunications and Digital Signal Processing Laboratory, Djillali Liabes University, Sidi Bel Abbes, Algeria, e-mail: ghali.abouka2019@gmail.com

DRIZ Samia
Doctor, Telecommunications and Digital Signal Processing Laboratory, Djillali Liabes University, Sidi Bel Abbes, Algeria, e-mail: samia.driz@univ-sba.dz

FASSI Benattou
Doctor, Telecommunications and Digital Signal Processing Laboratory, Djillali Liabes University, Sidi Bel Abbes, Algeria, e-mail: benattou.fassi@univ-sba.dz

Abstract:
This paper presents the performance analysis of Optical Code Division Multiple Access (OCDMA) based on Radio over Fiber (RoF) for GigabitPassive Optical Networks (GPON) application. The implementation of OCDMA into RoF system allows propagation of Radio Frequency (RF)signal through low loss optical fibers to achieve long reach. This coexistence of RF/optics systems promised secure, cost-effective, high-capacity mobile and multimedia wireless services. In the other hand, the integration of OCDMA-RoF technology in PON networks, allows a mix of services, technologies and efficiently supporting multi-rate traffic with different QoS requirements.Furthermore, an innovative codingcalled ZeroCorrelation Zone (ZCZ) codehavebeen proposedfor OCDMA systems. This class of codes ensures goodautocorrelation and cross-correlation properties within the correlation zone.The Bit Error Rate (BER) performance of the RoF ZCZ-OCDMA system was measured through OptiSystem software simulation. The achieved results demonstratethatthe proposed framework can accomplishes successfully transmission with acceptable Bit Error Rate up to 20 km. The proposed scheme provides up to eight simultaneous users with a bit rate of 1.244 Gb/s, achieving a total network capacity of 9.95 Gb/s.
Key words: RoF, OCDMA, ZCZ, PON, GPON, OptiSystem.

Introduction:

During the previous century, coaxial cables and microwave links were very popular. However, with the fast-growing technology in the communication industry and the emergence of new services related to the development of multimedia throughout the world, such as mobile telephony, High Definition (HD) and internet television, has involved incredible accelerating data transmission rates. To meet such demand, the idea of transmitting information through light called Radio over Fiber technology (RoF) have been proposed. This technique integrate the wireless network and the fiber network (low signal loss) for enhancing mobility and data rate (Singh, 2017; Driz, 2019; Paredes-Pàliz, 2020).

RoF technology consists of transporting, over optical fibers, radio frequency (RF) microwave/millimeter waves (3 to 30 GHz or 30 to 70 GHz) of which cellular wireless networks (GSM, UMTS) constitute an important field of application to increase the number of

Creative Commons Attribution-Non Commercial-NoDerivatives 4.0 International License (CC BY-NC-ND)

subscribers, accompanied by a strong demand for broadband services thro2017;ugh these networks (Aragon-Zavala, 2011).

The main advantage of RoF technology lies in its centrally managed architecture, which makes it possible to centralize the RF signal processing function at different Base Stations (BS) and antenna sites in one shared Central Office (CO) (Sharma, 2012; Wake, 2010; Pooja, 2015). Thus, RoF technique can simplify significantly the antenna sites by using remote-antenna-units (RAUs: simple and low-cost) and extend the reach of the transmission by using one low-loss optical fiber (Chow, 2011).

In the other hand, optical CDMA schemes have recently garnered significant interest because of their inherent capability of multiplexing multiple users on the same asynchronous access network, secure network connection, flexibility and multimedia services. Numerous parameters such as the data bit rate, simultaneous number of active users and the type of codes govern transmission performance analysis of the OCDMA systems (Driz, 2019). In consequence, OCDMA technique can be combined with the RoF system to form the OCDMA-RoF system to enhance the security problem of the traditional RoF frameworks (Rashidi, 2017; Ibrahim, 2017).

However, the main cause of degradation of optical CDMA performance is the interferences such as Inter Symbol Interference (ISI) and Multiple Access Interference (MAI), which can be reduced by using a good optical codes family having a large number of users with maximum weight and the good correlation properties (Driz, 2019; Fassi, 2018).

Recently, an interesting code called Zero Correlation Zone (ZCZ) code is proposed. This class of codes is an innovative coding, which ensures ideal autocorrelation and cross-correlation properties within the correlation zone. Various constructions of ZCZ codes such as binary, ternary, polyphase and optical codes have been constructed (Driz, 2019; Maeda, 2010; Matsumoto, 2013; Fassi, 2018; Fassi, 2015; Fassi, 2014). By taking advantage of the ZCZ spreading sequences having less Periodic Auto Correlation Function (PACF) and Periodic Cross Correlation Function (PCCF), implementing ZCZ-OCDMA into RoF framework is seen as a promising technique. This hybrid system allows high spectral efficiency and meanwhile enhance the optical fiber length and data rates (Ibrahim, 2019).

In this paper, the application of OCDMA technique using ZCZ codes in radio fiber network is explored. To achieve that goal, the paper is divided into six sections. The general architecture of RoF technology is presented in Section II followed by Section III that introduces the concept of Zero Correlation Zone sequences. Section IV gives the simulation model of the RoF ZCZ-OCDMA system. Simulation results are reported in section V and finally, the conclusion is presented in Section VI.

RoF Architecture:

Fig 1 depicts the general framework of RoF network. The concept of this technology is based on the modulation of light by a radio signal, which is transmitted between Central Unit (CU) and Remote Unit (RU) through optical fiber (Bonghyuk, 2017).

Creative Commons Attribution-Non Commercial-NoDerivatives 4.0 International License (CC BY-NC-ND)

Algerian Journal of Engineering Architecture and Urbanism Vol. 5 Nr. 3 2021
ISSN: 2588-1760

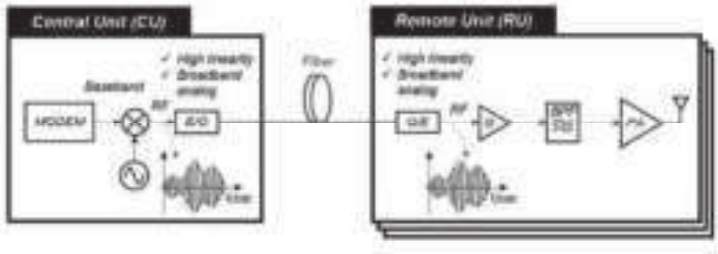

Fig1. Block diagram of a RoF system; PA: Power Amplifier (Bonghyuk, 2017).

At the transmitter side, optical signal is modulated by the RF signal (E/O) using an intensity modulation scheme via direct or external modulation of a laser. Where transmission over the link is at the radio carrier frequency, the choice of the RF frequencies becomes an important parameter because it determines the type of optoelectronic components that can be used (Wake, 2010; Reddy, 2015).

After that, the modulated signal will pass through optical fiber toward the BSs where is detected. The operations of both the electrical to optical (E/O) conversion (uplink) and optical to electrical (O/E) conversion (downlink) take place (Driz, 2019).

ZCZ Spreading sequences:

ZCZ codes differ from traditional spreading codes due to their correlation functions that contain a region called Z_{CZ} where the correlation values are zero (Fig2). In these regions, spreading codes are considered ideal because ISI and MAI interferences are reduced (Fassi, 2013).

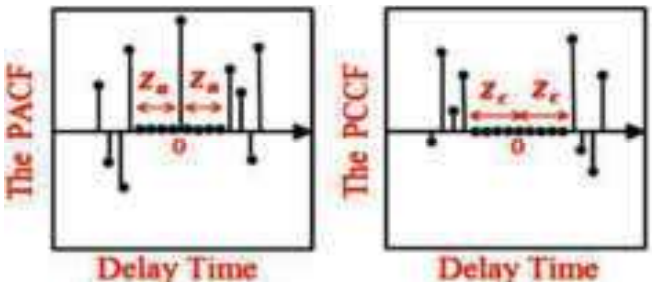

Fig 2. Definition of Zero-Correlation Zone (Fassi, 2013)

The Periodic Correlation Function (PCF) between two sequences b_i and $b_{i\prime}$, of length L, at a lag τ is determined by (Driz, 2019) :

$\forall \tau \geq 0$

$$\begin{cases} \theta(b_i, b_{i'})(\tau) = \sum_{j=0}^{L-1} b_{i,j} b_{i\prime,(j+\tau) mod\ L} \\ \theta(b_i, b_{i'})(-\tau) = \theta(b_{i'}, b_i)(\tau) \end{cases} \quad (1)$$

and $\forall \tau$

$$\theta(b_i, b_{i'})(\tau) = \varphi(b_i, b_{i'})(\tau mod L) + \varphi(b_i, b_{i'})\big((\tau mod L) - L\big) \quad (2)$$

The Aperiodic Correlation Function (ACF) $\varphi(b_i, b_{i'})(\tau)$ is defined as follows (Driz, 2019):

Creative Commons Attribution-Non Commercial-NoDerivatives 4.0 International License (CC BY-NC-ND)

$$\varphi(b_i, b_{i'})(\tau) = \begin{cases} \sum_{j=0}^{L-\tau-1} b_{i,j} b_{i',(j+\tau),} & 0 \le \tau < L \\ \sum_{j=0}^{L+\tau-1} b_{i,(j-\tau)} b_{i',j,} & -L < \tau < 0 \\ 0 & |\tau| \ge L \end{cases} \quad (3)$$

Fig. 3 shows an example of the correlation properties, in terms of PACF and PCCF functions, of $C_4^{3,1}$ code (Feng, 2015). The PACF of Code1 (C1) and PCCF of (C1, C2), (C3, C2) and (C3, C4), confirm that the set of codes is an OZCZ set with $Z = 1$.

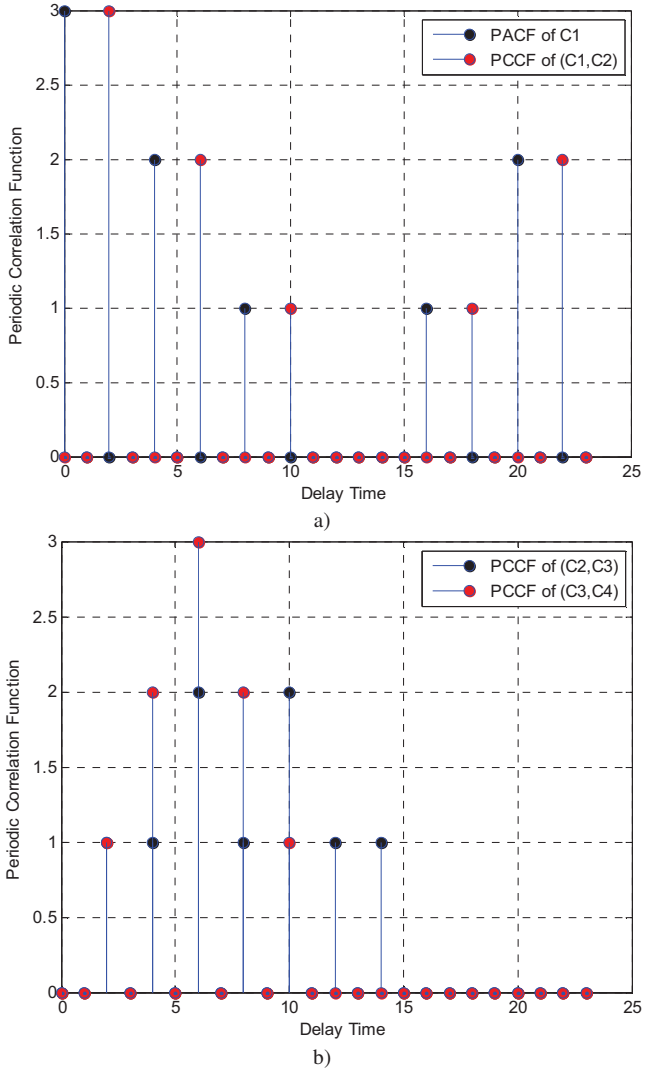

Fig 3. The periodic correlation function : a) PCF of codes C1 and C2 ; b) PCCF of codes C2, C3 and C4.

RoF ZCZ-OCDMA System model:

Fig. 4 shows the overall architecture of the RoF ZCZ-OCDMA topology with direct detection using OptiSystem7.

Creative Commons Attribution-Non Commercial-NoDerivatives 4.0 International License (CC BY-NC-ND)

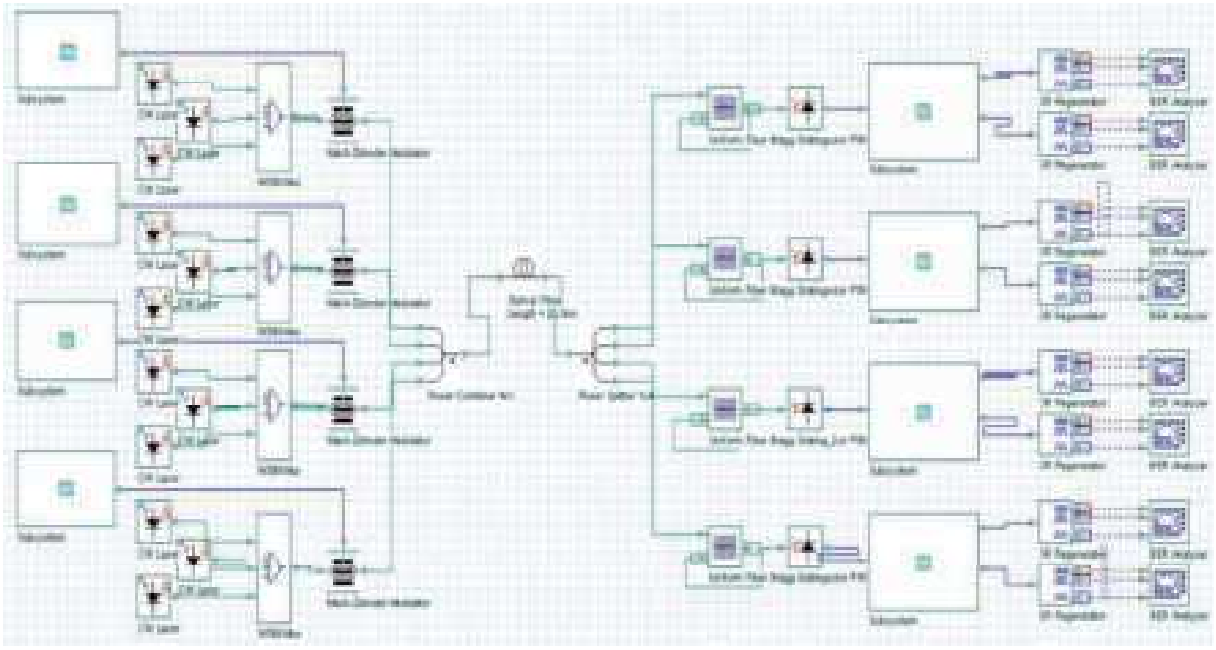

Fig 4. Proposed RoF ZCZ-OCDMA system architecture

In this configuration, four Central Station (CS) will be used (Fig 4). Each CS consists of two Optical Line Terminal (OLT) where the two pseudo-random bit generator (PRBG) are used to modulate two different electrical carriers (subcarrier radio frequency). This electrical carriers are then added together using electrical adder (Fig 5). Two low RF frequencies are selected according to the specifications of the Wireless Local Area Networks (WLAN). Therefore, in order to work in the band ISM 5 GHz for WiFi (IEEE 802.11), the carrier frequencies are taken of 5.18 GHz and 5.2 GHz corresponding to the channels 36 and 40 (each channel has a width of 20 MHz).

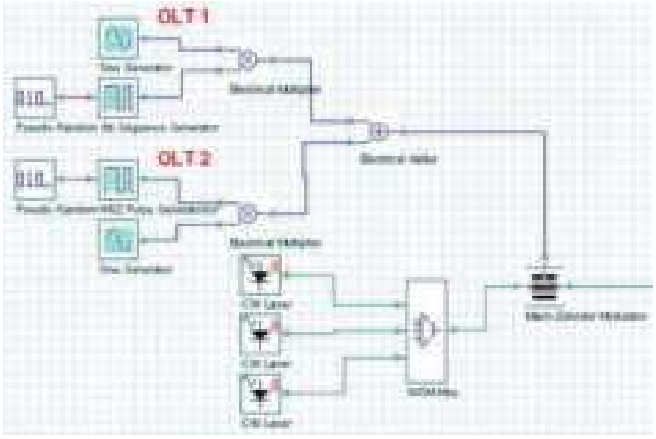

Fig 5. Proposed RoF ZCZ-OCDMA system : first CS

The external Mach-Zehnder Modulator (MZM) is then used to modulate the combined RF signal with a unique optical ZCZ code sequence. The four ZCZ sequences, $C_4^{3,1}$ used in the simulation are as follow (Feng, 2015):

Creative Commons Attribution-Non Commercial-NoDerivatives 4.0 International License (CC BY-NC-ND)

$$C_1 = [1\ 0\ 0\ 0\ 1\ 0\ 0\ 0\ 1\ 0\ 0\ 0\ 0\ 0\ 0\ 0\ 0\ 0\ 0\ 0\ 0\ 0\ 0\ 0]$$
$$C_2 = [0\ 0\ 1\ 0\ 0\ 0\ 1\ 0\ 0\ 0\ 1\ 0\ 0\ 0\ 0\ 0\ 0\ 0\ 0\ 0\ 0\ 0\ 0\ 0]$$
$$C_3 = [0\ 0\ 0\ 0\ 0\ 0\ 0\ 0\ 0\ 0\ 0\ 0\ 1\ 0\ 1\ 0\ 1\ 0\ 0\ 0\ 0\ 0\ 0\ 0]$$
$$C_4 = [0\ 0\ 0\ 0\ 0\ 0\ 0\ 0\ 0\ 0\ 0\ 0\ 0\ 0\ 0\ 0\ 0\ 0\ 1\ 0\ 1\ 0\ 1\ 0]$$

In the proposed system, due to the characteristics of the used ZCZ codes, the encoders are based on continuous wave (CW) laser sources as the optimal choice instead of one white light source (LED). In fact, the ZCZ codes are generated with three different wavelengths provided by three different CW lasers.

On the other side, the received optical signal is uniformly distributed into four optical band signal using power splitter since we have four CS at the transmitter side. Each optical band is then passed decodes using OCDMA decoders consisting of Fiber Bragg Gratings (FBG) because of their low fabrication cost (Fig6). After the photo-detection, one splitter is used to split and distribute the electrical RF signal to two optical Network Units (ONU). Later filtered by Band Pass Filter (BPF), mixed with an electrical local microwave frequency and finally filtered using low pass filter (LPF).

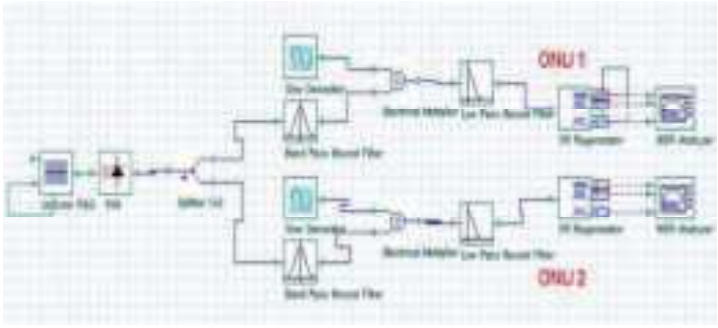

Fig 6. Proposed RoF ZCZ-OCDMA system : first two ONUs

Channel physical parameters such as fiber loss, chromatic dispersion, noise and others simulation parameters are set in (Table 1).

Bit rate	1.244 Gb/s
Number of OLT and ONU	8
Optical channel spacing	0.4 nm
Fiber loss	0.2 dB/km
Fiber dispersion	17 ps/nm/km
Dark courant	5 nA
Thermal noise	18×10^{-23} W/Hz
MZM insertion loss	3 dB
Filters insertion loss	1 dB
MUX/DEMUX insertion loss	2 dB
Splitter insertion loss	$3 \times \log_2$(number of pins) dB

Table 1. Simulation Parameters

Creative Commons Attribution-Non Commercial-NoDerivatives 4.0 International License (CC BY-NC-ND)

Simulation results:

To evaluate the performances of proposed system, Bit Error Rate (BER) transmission measurements are performed. The downlink RoF ZCZ-OCDMA network at bit rate 1.244 Gbps (I.T.U, 2019) has been simulated using OptiSystem7. In the case of the wavelength spacing of 0.4 nm (corresponding to 50 GHz), the spreading ZCZ sequence of the first CS is shown in Fig 7. The optical spectrum of the first CS is shown in Fig 8.

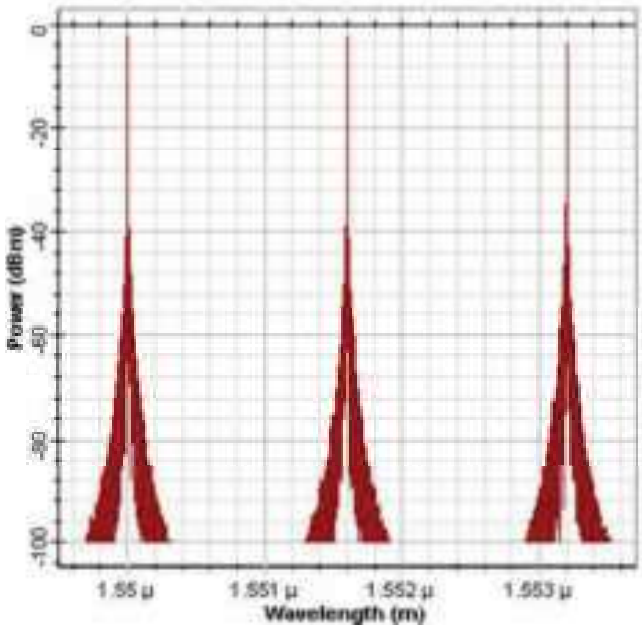

Fig 7. Spreading code of the first ZCZ-OCDMA central station

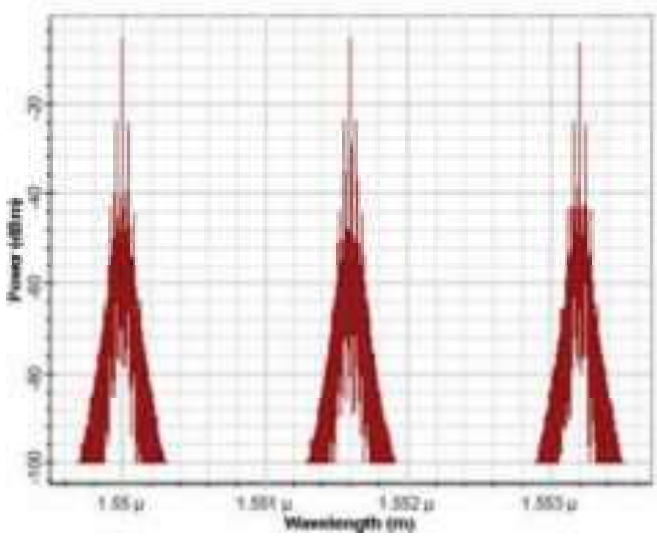

Fig 8. Optical spectrum of the first CS

The performance of the system was evaluated referring to the Q-factor, the BER and the eye pattern diagram. Fig 9 shows the eye diagram of the two first ONUs. It can be seen that, the

Creative Commons Attribution-Non Commercial-NoDerivatives 4.0 International License (CC BY-NC-ND)

proposed system has good performance in term of BER and can perform adequately for 20 km fiber length. The obtained BER of the two first ONUs is about 2.89997e-012 and 3.04336e-012 (BER ≤ e-09) respectively corresponding to a Q-factor of 6.84404 and 6.84263 (Q > 6) respectively.

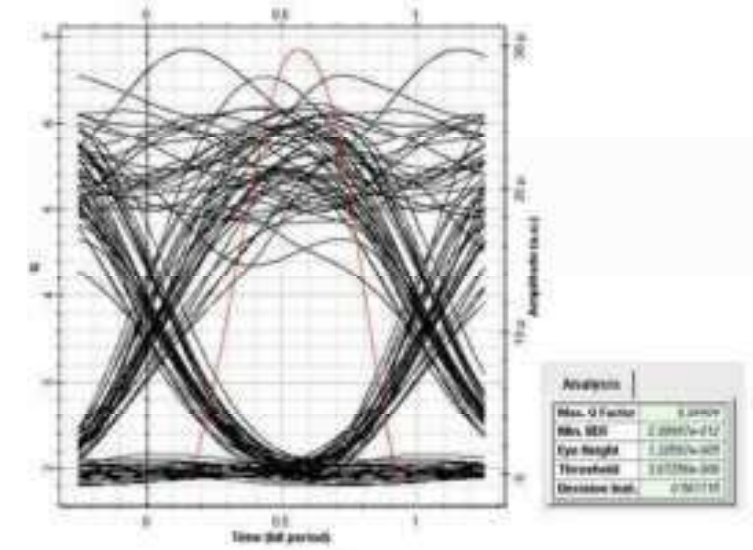

a)

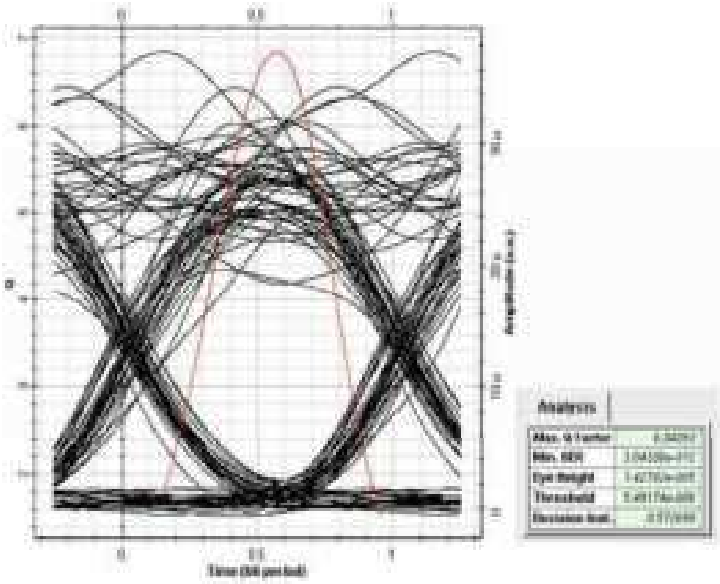

b)

Fig 9. Eye diagram at 20km for : a) the first ONU; b) second ONU

Conclusion:

In this paper, the performances of the ZCZ-OCDMA system using RoF scheme at bit rate 1.244 Gb/s for 8 OLT/ ONU have been presented using OptiSystem software simulation. The outcomes showed that the RoF system based on ZCZ codes can accomplishes successfully transmission up to 20 km (PON network) achieving an acceptable BER threshold.

Creative Commons Attribution-Non Commercial-NoDerivatives 4.0 International License (CC BY-NC-ND)

Acknowledgment

This work was supported by Directorate General for Scientific Research and Technological development (DGRSDT).

References:

Aragon-Zavala A., Castanon G., Beas J. (2011), *Radio-over-Fiber Systems for Wireless Communications*, Recent Patents on Electrical Engineering **4**(5):114 – 124.

Bonghyuk Park S. J. , Hong, S. (2017*), Digital Radio-over-Fiber System with Multipulse Manchester Encoding-Assisted Deltasigma Modulation*, Optics Express **25**(7): 8335-8349.

Chow C. W., Yeh C. H., Stanley M. G. Lo , Li C., Tsang, H. K. (2011), *Long-reach Radio-over-Fiber Signal Distribution using Single-Sideband Signal Generated by a silicon-Modulator*, Optics Express **19**(12): 11312-11317.

Driz S., Djebbari A. (2019), *Performance Evaluation of Sub-carrier Multiplexed SAC-OCDMA System Using Optimal Modulation Index*, J. Opt. Commun. **40**(1): 83–92.

Driz S., Fassi B., Mansour M. A., Taleb-Ahmed A. (2019), *FPGA Implementation of a Novel Construction of Optical Zero-Correlation Zone Codes for OCDMA Systems*, J. Opt. Commun., aop. in press. https://doi.org/10.1515/joc-2019-0048

Fassi B., Taleb-Ahmed A. (2018), *New Design of Optical Zero Correlation Zone Code*, the 2nd International Conference OPAL, USTO, ORAN, Algeria.

Fassi B. , Taleb-Ahmed A. (2018), *A New Construction of Optical Zero Correlation Zone Codes*. J Opt Commun. **39**(3):359–368.

Fassi B., Mimoun H., Messaoudi R., Addad A. (2015), *A New Class of Ternary Zero Correlation Zone Sequence Sets Based on Mutually Orthogonal Complementary Sets*, IOSR J Electron Commun Eng (IOSR-JECE) **10**(3): 08–13.

Fassi B., Djebbari A. , Taleb-Ahmed A. (2014), *Ternary Zero Correlation Zone Sequence Sets for Asynchronous DS-CDMA*, J Commun Netw. **6**(4): 209–217.

Fassi B., Djebbari A., Taleb-Ahmed A. , Dayoub I. (2013), *A New Class of Binary Zero Correlation Zone Sequence Sets*, IOSR Journal of Electronics and Communication Engineering (IOSR-JECE) **5**(3): 15-19.

Feng L., Wang J. , Hu R. Q. , Liu L. (2015), *New design of optical zero correlation zone codes in quasi-synchronous VLC CDMA systems*, EURASIP Journal on Wireless Communications and Networking **120**(2015): 1–7. DOI: https://doi.org/10.1186/s13638-015-0360-z

Ibrahim Z., Rashidi C. B. M., Aljunid S. A., . Rahman A. K, Anuar M. S. (2017), *Performance analysis of optical CDMA based on radio over fiber (RoF) technique*, 3rd International Conference on Electronic Design (ICED), IEEE. DOI: 10.1109/ICED.2016.7804622

Ibrahim Z., Rashidi C.B.M., Aljunaid S.A., Rahman A.K. , Anuar M.S. (2019), *Performance Evaluation of Flexible Cross Correlation (FCC) OCDMA Code Based on Radio over Fiber (RoF) Simulation System*, Indonesian Journal of Electrical Engineering and Computer Science **13**(2): 543-550.

Maeda T., Kanemoto S. , Hayashi T. (2010), *A novel Class of Binary Zero-Correlation Zone Sequence Sets*, Proc. IEEE TENCON: 708–711.

Matsumoto T., Torii H., Matsufuji S. (2013), *Theoretical Analysis of BER Performance of Optical ZCZ-CDMA System*, Int J Comput Commun. **1**:18–25.

Creative Commons Attribution-Non Commercial-NoDerivatives 4.0 International License (CC BY-NC-ND)

Paredes-Páliz D. F., Royo G., Aznar F., Aldea C. , Celma S. (2020), *Radio over fiber: an alternative broadband network technology for IoT*, Electronics **9(11):** 1-8.

Pooja, Saroj and Manisha (2015), *Advantages and Limitation of Radio over Fiber System*, International Journal of Computer Science and Mobile Computing **4**(5):506–511.

Rashidi C. B. M., Aljunid S. A., Rahman A. K, Anuar M.S, Yaakob S. (2017), *Effective Design for Optical CDMA Based on Radio over Fiber (RoF) Technique*, Engineering Technology International Conference, MATEC Web of Conferences **97**: 6. DOI: 10.1051/matecconf/20179701100

Rec I.T.U. (2019). G. 984.2; *Gigabit-capable Passive Optical Networks (GPON): Pysical Media Dependent (PMD) layer specification*, International Telecommunication Union, ITU-T.

Reddy V. , Jolly L. (2015*), Radio over Fiber (RoF) Technology an Integration of Microwave and Optical Network for Wireless Access*, International Conference and Workshop on Emerging Trends in Technology (ICWET): 8–13.

Sharma V., Singh A. , Sharma A. K. (2012), *Challenges to Radio over Fiber (RoF) Technology and its Mitigation Schemes – A review*, Optik **123**: 338– 342.

Singh R., Ahlawat M. , Sharma D. (2017), *A Review on Radio over Fiber communication System*, International Journal of Enhanced Research in Management & Computer Applications **6**(4) : 23–29.

Wake D., Nkansah A., Gomes N. J. (2010), *Radio over Fiber Link Design for Next Generation Wireless Systems*, Journal of Lightwave Technology **28**(16): 2456-2464.

Creative Commons Attribution-Non Commercial-NoDerivatives 4.0 International License (CC BY-NC-ND)

Algerian Journal of Engineering Architecture and Urbanism Vol. 5 Nr. 3 2021
ISSN: 2588-1760

Effeciency of coagulants aid for the removal of a Cationic dye From synthetic solutions

Sarah GOUDJIL[1] (PhD)

Research Laboratory in Subterranean and Surface Hydraulics, University of Biskra, Department of Civil Engineering and Hydraulics, P.B 145 RP, 07000, Biskra - Algeria.

[1]Sarah.goudjil@univ-biskra.dz;

Saadia GUERGAZI[2] (professor) and **Toufik MASSMOUDI[3]** (doctor)

[2,3] Research Laboratory in Subterranean and Surface Hydraulics, University of Biskra, Department of Civil Engineering and Hydraulics, P.B 145 RP, 07000, Biskra - Algeria.

[2]s.guergazi@univ-biskra.dz;[3] toufik.masmoudi@univ-constantine3.dz

Abstract:
The rejection of synthetic dyes has been one of the most important categories of aquatic pollutants in recent years, due to various commercial uses; the impact and toxicity of dyes released into the environment have been studied extensively. Treatment will therefore be essential to eliminate these dyes which are harmful to the environment and humans. In this research paper, the potential of $FeCl_3$ and coagulants aid for efficient removal of Methyl Violet (MV) dye commonly used in the textile industry from aqueous solutions by Coagulation-Flocculation was investigated. The removal of MV was determined by varying several parameters such as coagulant dosage and coagulants aid like powdered activated carbon (PAC) and lime ($Ca(OH)_2$). The experiments demonstrated that 80 mg/l of ferric chloride was found as optimum coagulant dose for the removal of MV with 24.66%. Studies of dye removal efficiency were higher when coagulant and coagulants aid were used together. In this regard, the use of ferric chloride in conjunction with coagulants aid has shown that MV is effectively removed. The results demonstrated that the removal dye increases from 24.66 %to 87.52 % for 0.5g/l of PAC, and the yield exceeds 88 percent for 0,8 g/l of lime.

Key words: Methyl Violet, removal, Coagulation-Flocculation.

Introduction:

Synthetic dyestuffs can exist in the effluents of wastewater from different industries such textiles, paper, leather, plastics, etc. [1]. Which use dyes and pigments are characteristically high in both colour and organic content [2].Today there are more than 10,000 dyes available commercially, and over 7×10^5 tons are produced annually world-wide. It has been estimated that about 10–15% of these dyes are released as effluents during the dyeing processes [3]. Removal of dyes has attracted significant attention in recent years but most of these quantities are difficult to biodegrade due to their complex aromatic molecular structure and synthetic origin [4]. Also some dyes and their metabolites are mutagenic, carcinogenic and potentially dangerous to the health of living creatures [5]. The discharge of wastewaters with a high concentration of dye compounds into the environment is considered as one of the important environmental problems [6]. Textile factories are one of the industries which its wastewater

Creative Commons Attribution-NonCommercial-NoDerivatives 4.0 International License (CC BY-NC-ND)

treatment is a challenging issue, especially in developing countries [7]. Such as the discoloration of this kind of reject is often difficult since conventional treatments do not easily degrade organic dyes [8]. There are several methods for dye removal such as biological treatment [9-11], coagulation/flocculation [9,12], chemical oxidation and photocatalytic processes [13-16], ozone treatment [9,12], membrane processes [9,17-21], electrocoagulation [22, 23] and adsorption [9, 18, ,24-26].

The most of the techniques mentioned above are limited by methods, costs or difficulties during the operation, unlike the coagulation–flocculation process, which is a traditional technique [22]. This process can be used as a pre-treatment, a post-treatment or even a main treatment [27]. Coagulation extracts dissolved and colloidal compounds of wastewater by merely raising the ionic pressure, which overcomes the interparticle repulsive energy barrier and destabilizes colloids by neutralizing the forces that drive them apart. Flocculation is the process of bridging particles together to form larger flocs that can then be sedimented [28]. It is interesting to note that the effectiveness of flocculation coagulation depends on the characteristics of the water to be treated, the dose of coagulant, and the pH [22].

In this research, we'll look at the best conditions for removing a cationic dye called Methyl Violet (MV) from synthetic solutions, as well as the efficiency of ferric chloride and the Coagulation-Flocculation process. In order to increase the removal of the MV dye, this step will be accompanied by a mixture of two coagulants aid, such as PAC and lime.

Materials and methods:

All experiments were performed at Research Laboratory Underground and Surface Hydraulics (LARHYSS) at Biskra University in Algeria

1.1. Solutions and reagents

Stock solutions

Stock solutions were prepared periodically at laboratory.

Methyl violet dye and ferric chloride $FeCl_3$ were purchased with high purity from Merck (Sigma-Aldrich, Germany). Methyl Violet is one of the most important pollutants responsible for destabilizing aquatic ecosystems, and it is poisonous to most of the animals [29]. This dye is widely used in textile industries in Algeria. The main physicochemical properties of this dye are shown in Table 1. Synthetic wastewater was prepared by dissolving 1g of (MV) in 1L of distilled water.

In this research, we chose $FeCl_3$ as a coagulant. Ferric chloride is an orange to brown-black solid. With the formula ($FeCl_3$, $6H_2O$) and a molar mass of 162.2 g/mol. The coagulant solution was prepared by using distilled water. We have prepared in a large volume flask (1 L) a stock solution of coagulant at a concentration of 20 g/L.

Creative Commons Attribution-NonCommercial-NoDerivatives 4.0 International License (CC BY-NC-ND)

Coagulants aid

In order to test the performances of coagulants aid in combination with the coagulant on the elimination of MV. The coagulants aid tested are PAC, a commercial product. It is a mesoporous adsorbent characterized by a particle size of 20 µm and a specific surface of 658 m^2/g and the lime ($Ca(OH)_2$), which is a commercial chemical.

Table 1: Characteristics of MV dye [30]

Name	**Description of characteristics and Chemical structures of MV dye**
Chemical name	Methyl Violet
Appearance	green to dark-green powder
Molecular formula	$C_{24}H_{28}ClN_3$
Molecularweight(g/ mol)	393.96
pKa	9.4
λmax	584 nm
solubility	soluble in : water, ethanol
Utility	Textile
Molecular structure	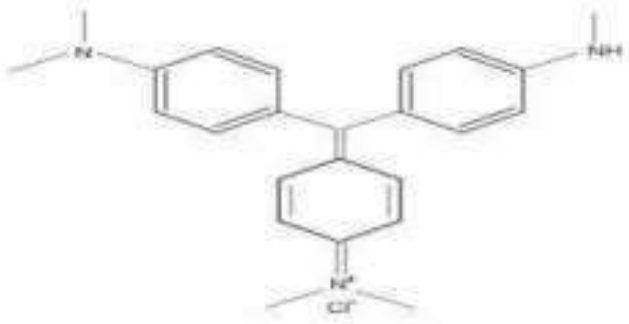

Description of coagulation tests

All coagulation-flocculation tests were executed according to the "Jar-Test" protocol on a flocculator with 6 stirrers (Ficher 1198) under an individual speed rotation varying between 0 and 200 rpm [22]. This apparatus allows the solutions contained in a series of 250 mL beakers to be agitated simultaneously. The solutions enriched in MV and in reagents (coagulant and coagulants aid) are subjected for 3 min to rapid stirring of 150 rpm. The speed has then reduced to 45 rpm for duration of 17 min. In the next step, different concentrations of PAC and lime (0.05-0.1-0.15-0.2-0.25-0.5 g/L), (0.2-0.4-0.6-0.8-1-2 g/L) respectively were added to the samples to enhance the removal of MV dye. For the tests with the coagulant alone, even in combination with the coagulants aid, and after decantation for 30 min, the supernatant is recovered to be filtered under vacuum on an OSMONICS INC membrane with a porosity of

Creative Commons Attribution-NonCommercial-NoDerivatives 4.0 International License (CC BY-NC-ND)

0.45 µm. The filtrate has then been assayed by analysis with a spectrophotometer. The % removal of MV is calculated according to Equation (1) as follows [22]:

$$R(\%) = \left(\frac{(C_0 - C_f)}{C_0}\right) \times 100 \quad (1)$$

Where C_0 and C_f, respectively, represent the initial and final concentrations of MV expressed in mg/L. Different reaction parameters will also be studied, such as:

-Effect of the variation in the dose of the coagulant, we considered a range going from 8 to 130 mg/L of ferric chloride;

-The last trial concerns the hybrid effect of $FeCl_3$ coagulant and two coagulants aid, namely: PAC and lime ($Ca(OH)_2$).

Results and discussions:

1.1. The effect of coagulant dose on the dyes removal efficiency and the final pH of samples studied

Before starting the tests concerning the effect of coagulants aid, the effect of the variation of the optimum coagulant dose on dye removal was studied, like the figure 1 (a) shows that the optimum dose is 80mg/L, where the elimination efficiency exceeds 24%. This value guided us to use coagulants aid to increase the removal efficiency, while pHf was decreased with the increasing of coagulant doses (figure 1 (b))

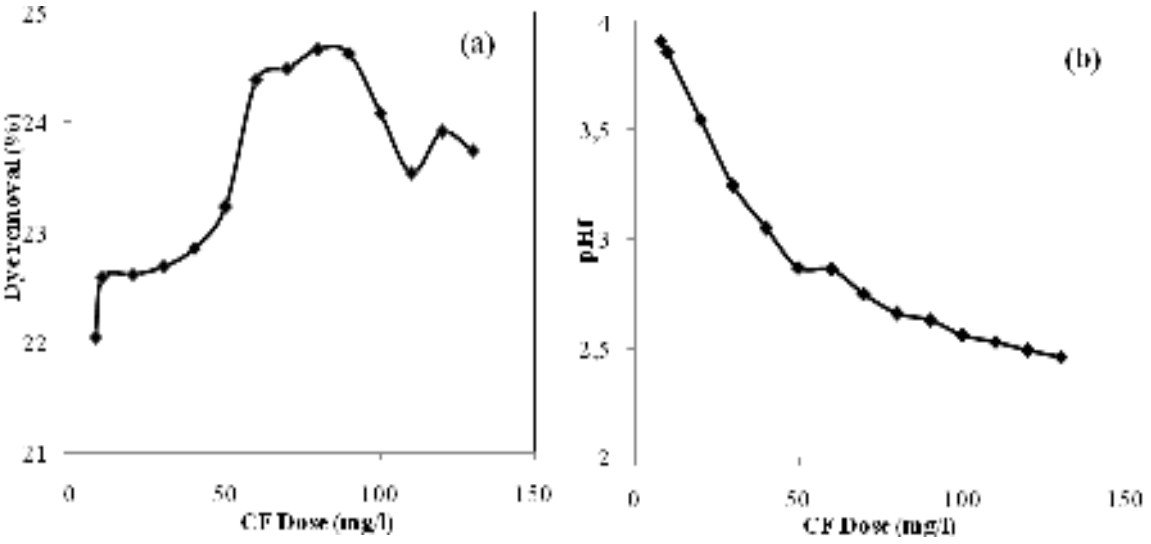

Fig.1. (a) Effect of the variation of coagulant doses, (b) final pH (MV= 30 mg/L, $FeCl_3$= 80 mg/L, pH=5,4)

Creative Commons Attribution-NonCommercial-NoDerivatives 4.0 International License (CC BY-NC-ND)

1.2. Effect of coagulants aid on the dye removal efficiency

1.2.1. *Effect of PAC*

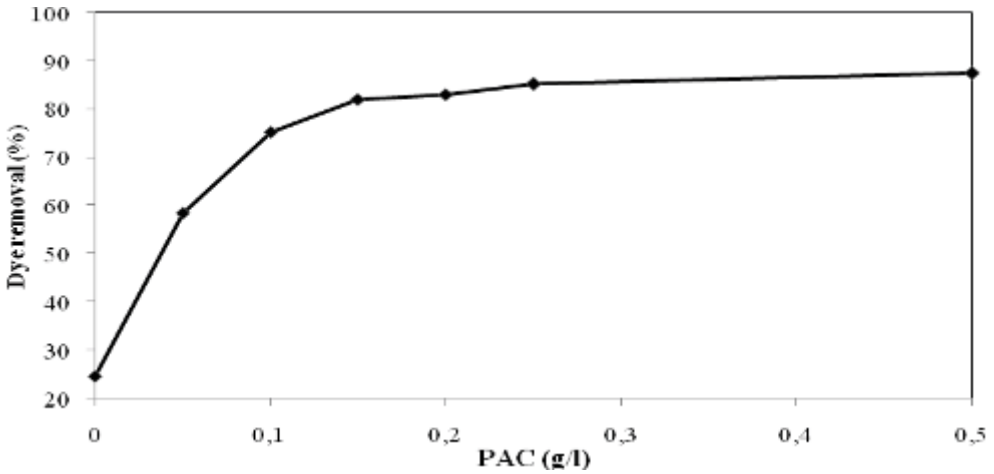

Fig.2. Effect of PAC variation (MV= 30 mg/L, $FeCl_3$= 80 mg/L, pH=5,4)

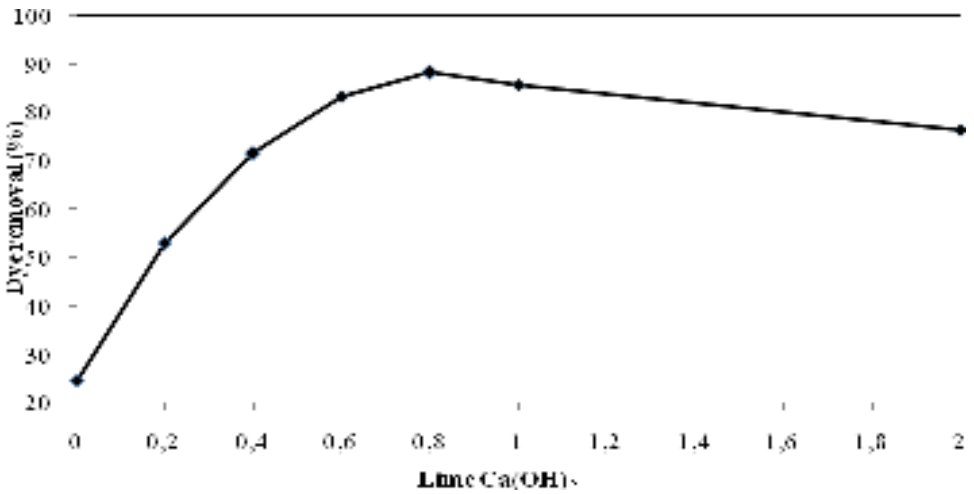

Fig.3. Effect of the variation of lime ($Ca(OH)_2$) MV removal (MV= 30 mg/L, $FeCl_3$= 80 mg/L, pH=5,4)

This step was performed to determine the influence of coagulants aid such as PAC and lime on dye removal efficiency; they are used in coagulation/flocculation process, usually to obtain higher efficiency, to reduce the amount of required coagulant, and to form stronger and more settleable flocs [31].

The results given in figures (2-3) show that the best elimination is quoted in the small amounts of the added heading, as it has been observed the dye removal efficiencies by the low head masses are greater than those obtained when the coagulant is used alone, The results found confirm this, since the removal dye increase from 24,66% to 87,52% for 0.5g/L of PAC and for 0,8 g/L of lime the yield exceed 88%.

Creative Commons Attribution-NonCommercial-NoDerivatives 4.0 International License (CC BY-NC-ND)

Conclusion:

This study was conducted to evaluate the effect of some parameters such as coagulant dose, the effect of initial pH and coagulants aid (PAC) and ($Ca(OH)_2$) on the removal of MV. According to results these conclusions were obtained:

1- 24.66% elimination of the dyes was observed for a dose of 80 mg /L of ferric chloride (optimal dose);

2- The combination of ferric chloride with coagulants aid has shown that there is a very strong elimination of MV by 0,5 g/L of PAC in combination with a coagulant dose at a pH of 5,4. Although the yield that it exceeds 88 percent for 0,8 g/l of lime.

Using of this coagulant aid to remove dyes has the unfavorable effect of elevating the pH above 10. As a result, it has been determined that treating by lime is not commended because it results in large quantities of sludges. As a consequence, improved color removal and less sludge generation are two of the benefits of PAC.

References:

[1] Guiza S., Bagane M. (2012), Sorption Kinetics for Dye Removal from Aqueous Solution Using Natural Clay, Journal of Environment and Earth Science, 2(3): 30-39.

[2] Papic´ S., Koprivanac N., Loncaric´ Bozic´ A., Metes A. (2004), Removal of some reactive dyes from synthetic wastewater by combined Al (III) coagulation/carbon adsorption process, Science direct, Dyes and Pigments 62: 291–298

[**3] Gomez V., Larrechi M.S., Callao M.P.** (2007), Kinetic and adsorption study of acid dye removal using activated carbon, Chemosphere 69: 1151–1158.

[4] Nigam P., Armour G., Banat I.M., Singh D., Marchant R. (2000)**,** Physical removal of textile dyes from effluents and solid-state fermentation of dye-adsorbed agricultural residues, Bioresource Technology 72: 219-226.

[5] Moghaddam S.S., Moghaddam M.A., Arami M. (2011)**,** Response surface optimization of acid red 119 dye from simulated wastewater using Al based waterworks sludge and polyaluminium chloride as coagulant, Journal of Environmental Management 92: 1284-1291.

[6] Dalvand A., Ehrampoush M.H., Ghaneian M.T., Mokhtari M., Ebrahimi A.A., Ahmadi R.M., Mahvi A.H. (2017)**,** Application of chemical coagulation process for direct dye removal from textile wastewater, J Environ Health Sustain Dev, 2(3): 333-339.

[7] **Asadollahfardi G., Zangooei H., Motamedi V., Davoodi M.**(2018), Selection of coagulant using jar test and analytic hierarchy process: A case study of Mazandaran textile wastewater, Advances in Environmental Research, 7 (1): 1-11.

[8] **Guiza S., Bagane M.** (2013), Étude cinétique de l'adsorption du rouge de Congo sur une bentonite, J. Water Sci, 26 : 39–50.

[9] **Allegre C., Moulin P., Maisseu M., Charbit F.** (2006), Treatment and reuse of reactive dyeing effluents, J. Membr. Sci, 269: 15.

Creative Commons Attribution-NonCommercial-NoDerivatives 4.0 International License (CC BY-NC-ND)

[10] **Pala A., Tokat E.** (2002), Color removal from cotton textile industry wastewater in an activated sludge system with various additives, Water Res, 36 : 2920.

[11] **Kapdan I.K., Kargi F.** (2002), Simultaneous biodegradation and adsorption of textile dyestuff in an activated sludge unit, Process Biochem, 37: 973.

[12] Cooper P. (1993), Removing colour from dyehouse waste waters—a critical review of technology available, J. Soc. Dyers Colourists, 109: 97.

[13] Liu H.L., Chiou Y.R. (2006), Optimal decolorization efficiency of reactive red 239 by UV/ZnOphotocatalytic process, J. Chin. Inst. Chem. Eng. 37: 289.

[14]Clark T., Bruce M., Anderson S. (1994), Decolorisation of extraction stage bleach plant effluent by combined hypochlorite oxidation and anaerobic treatment, Water Sci. Technol. 29 (5–6): 421.

[15]Solozhenko E.G., Soboleva N.M. (1995), Goncharuk V.V., Decolourization of azodye solutions by Fenton's oxidation, Water Res, 29: 2206.

[16] Mokif L.A. (2019), Removal methods of synthetic dyes from industrial wastewater: a review, Mesopotamia Environ. J., 5: 23–40.

[17] Buckley C.A. (1992), Membrane technology for the treatment of dyehouse effluents, Water Sci. Technol, 25 (10): 203.

[18] Cooper P. (1993), Removing colour from dyehouse waste waters—a critical review of technology available, J. Soc. Dyers Colourists, 109: 97.

[19] Jiraratananon R., Sungpet A., Luangsowan P. (2000), Performance evaluation of nanofiltration membranes for treatment of effluents containing reactive dye and salt, Desalination, 130: 177.

[20] Koyuncu I. (2002), Reactive dye removal in dye/salt mixtures by nanofiltration membranes containing vinylsulphone dyes: effects of feed concentration and cross flow velocity, Desalination, 143: 243.

[21]Treffry-Goatley K., Buckley C.A., Groves G.R. (1983), Reverse osmosis treatment and reuse of textile dyehouse effluents, Desalination, 47: 313.

[22]Goudjil S., Guergazi S., Masmoudi T., Achour S. (2021), Effect of reactional parameters on the elimination of Congo Red by the combination of coagulation-flocculation with aluminium sulphate, desalination and water treatment, 209: 429-436.

[23] Yuan-Shing P., Ha-Manh B. (2014), Decolorization of Reactive Red 195 solution by electrocoagulation process, J. Viet. Environ., 5: 22–26.

Creative Commons Attribution-NonCommercial-NoDerivatives 4.0 International License (CC BY-NC-ND)

[24]Karcher S., Kornmuller A., Jekel M. (2001), Screening of commercial sorbents for the removal of reactive dyes, Dyes Pigments 51: 111.

[25] Netpradit S., Thiravetyan P., Towprayoon S. (2003), Application of 'waste' metal hydroxide sludge for adsorption of azo reactive dyes, Water Res. 37: 763.

[26] Wu J.S., Liu C.H., Chu K. H., Suen S.Y. (2008), Removal of cationic dye methyl violet 2B from water by cation exchange membranes, Journal of Membrane Science 309: 239–245.

[27]Szygu A., Guibal E., Palacı´n M. A., Ruiz M., Sastre A. M. (2009), Removal of an anionic dye (Acid Blue 92) by coagulation–flocculation using chitosan, Journal of Environmental Management 90: 2979–2986.

[28]Lee K. E., Hanafiah M. M., Halim A. A., Mahmud M. H. (2015), Primary treatment of dye wastewater using aloe vera-aided aluminium and magnesium hybrid coagulants, Procedia Environmental Sciences 30: 56 – 61.

[29]Mehr, H. V., Saffari, J., Mohammadi, S. Z.,Shojaei, S. (2020). The removal of methyl violet 2B dye using palm kernel activated carbon: thermodynamic and kinetics model, *International Journal of Environmental Science and Technology*, *17*(3): 1773-1782.

[30] Doğan, M., Mahir A. (2003), Adsorption kinetics of methyl violet onto perlite, *Chemosphere* 50 (4): 517-528.

[31] Zonoozi M. H., Moghaddam M. R. A., Arami M. (2008), Removal of acid red 398 dye from aqueous solutions by coagulation/flocculation, Environmental Engineering and Management Journal, 7(6): 695-699.

Creative Commons Attribution-NonCommercial-NoDerivatives 4.0 International License (CC BY-NC-ND)

Algerian Journal of Engineering Architecture and Urbanism Vol. 5 Nr. 3 2021
ISSN: 2588-1760

GROUNDWATER QUALITY OF MIH-OUENSA, EL OUED (SOUTHEAST OF ALGERIA)

QUALITÉ DES EAUX SOUTERRAINES DE MIH-OUENSSA, EL OUED (SUD –EST DE L'ALGÉRIE)

Lynda HECINI[1,2]
[1]Centre de recherche scientifique et technique sur les régions arides, CRSTRA, B.P. 1682, R.P. 7000, Biskra, Algérie. e-mail: lindahecini@yahoo.fr;
[2]Laboratoire de recherche en hydraulique souterraine et de surface - LARHYSS Faculté des Sciences et de la Technologie - Université de Biskra - B.P. 145 R.P, 07000, Algérie

Wahida KHERIFI[1]
[1]Centre de recherche scientifique et technique sur les régions arides, CRSTRA, B.P. 1682, R.P. 7000, Biskra, Algérie. e-mail: wahidakherifi@yahoo.fr

Khadidja BOUZID[1]
[1]Centre de recherche scientifique et technique sur les régions arides, CRSTRA, B.P. 1682, R.P. 7000, Biskra, Algérie. e-mail: khadidja_07@yahoo.fr

Abstract:

In the area of Mih Ouensa located southwest of the wilaya of Oued Souf, the groundwater are the main water resource for the supply of drinking water to the population and for the irrigation of agricultural land. This work aims to study the physico-chemical quality of the drilling in this area. To achieve this, water sampling at the level of ten boreholes was carried out in Mih Ouensa during the month of March 2017. Various physicochemical parameters were measured: temperature, pH, electrical conductivity, hardness and ions major (Na^+, K^+, Ca^{2+}, Mg^{2+}, HCO_3^-, NO_3^-, SO_4^{2-}, Cl^-) were analyzed according to the water quality assessment techniques described by Rodier et al (2009). The results showed that the boreholes studied have concentrations higher than the standards recommended by WHO (2006) and the Algerian standard (JORA, 2014). The Mih Ouensa groundwater is classified Sodium Chloride, Sodium Potassium and Sodium Sulphate for all sampled drill holes. From a qualitative point of view these waters appeared to be very mineralized and excessively hard, with high levels of chlorides and sulphates and high salinity exceeding 3g/l.

Key words: Groundwater, physico-chemical quality, Mih Ouensa, Terminal Complex

Creative Commons Attribution-NonCommercial-NoDerivatives 4.0 International License (CC BY-NC-ND)

Introduction:

Les eaux souterraines constituent une provision d'eau potable inestimable pour l'humanité. Dans plusieurs pays, c'est pratiquement la seule source d'approvisionnement. L'exploitation anarchique des ressources en eau et en particulier les ressources en eaux souterraines augmente, principalement en raison de l'augmentation de la demande et de la détérioration de la qualité de l'eau. L'accès général à l'eau potable, l'irrigation, l'étalement urbain et industriel, le développement et le tourisme sont autant de facteurs qui aggravent cette situation (Yasser et al, 2021).

les eaux souterraines sont traditionnellement les ressources en eau privilégiées pour l'eau potable car sont plus à l'abri des polluants que les eaux de surface (Guergazi et al., 2005). Dans les territoires à climat aride du Sud Algérien, en particulier dans la région d'Oued Souf (situé au Sud-Est de l'Algérie), le rôle des eaux souterraines est d'autant plus important qu'elles constituent souvent la seule source d'approvisionnement en eau potable (Bouchemal et al., 2011). La qualité naturelle des eaux souterraines peut être altérée par l'activité humaine ou par les divers éléments dont l'eau se charge au contact des terrains qu'elle rencontre. La détérioration de la qualité de l'eau est appréciée par les mesures des paramètres physico-chimiques. La qualité d'une eau est définie par des paramètres physiques, chimiques et biologiques, mais également par son usage (Beauchamp, 2006). Le présent travail s'intéresse à l'étude de la qualité physico-chimique des eaux de forages de Mih Ouensa située au Sud-Ouest d'El Oued, ainsi qu'à la détermination des principaux faciès chimiques. Il est important de connaître certains paramètres physico-chimiques, qui pourraient être la cause de nombreux problèmes, car la mauvaise qualité de l'eau de boisson est un problème de santé publique. L'étude menée prend en compte les propriétés physico-chimiques de cette zone.

Problematic:

Le territoire Algérien couvre en effet une superficie de 2.380.000 km^2 dont 85% correspondent à la zone désertique. Les disparités régionales en matière de ressources hydriques seraient ainsi particulièrernent liées à une répartition zonale nord/sud de la pluviomiétrie et à l'existence d'une forte évaporation des apports hydrique dans le sud du pays. Par ailleurs, l'acroissenient des besoins en eau (pression démographique, urbanisation accélérée, agriculture en irrigué...) a provoqué d'énormes déficits en eau. Les différents secteurs utilisateurs et consomniateurs peuvent également induire des effets plus ou moins négatifs sur la qualité de ces eaux (rejets urbains et industriels, pratiques agricoles). II importe donc que les eaux naturelles, déjà en quantités réduites, puissent faire l'objet d'analyses systéimatiques et régulières de leur qualité ou de surveillance (le pollution par certains effluents. Nos travaux s'inscrivent donc dans le cadre global de l'appréciation de la qualité phiysico-chimique des eaux naturelles Algériennes. Ils ont surtout pour objectif de mettre en exergue les problèmes de qualité des eaux souterraines spécifiques à la région du Sahara septentrional tel que la zone d'El-Oued.

Creative Commons Attribution-NonCommercial-NoDerivatives 4.0 International License (CC BY-NC-ND)

Materials and methods:

2.1 Géographie de la zone d'étude

La ville de Mih Ouensa est située au Sud-Ouest d'El Oued, à 25 km du chef lieu de la wilaya. Elle est limitée au Nord par la commune d'Ourmès, et la commune d'Oued Alenda à l'Est, et par la wilaya d'Ouargla à l'Ouest, et au Sud par la commune d'Oued Allenda et la wilaya d'Ouargla (Figure 1). Elle occupe une superficie de 1111 Km^2, avec une population de 17045 habitants en 2009 (ONS, 2010) (Fig. 1).

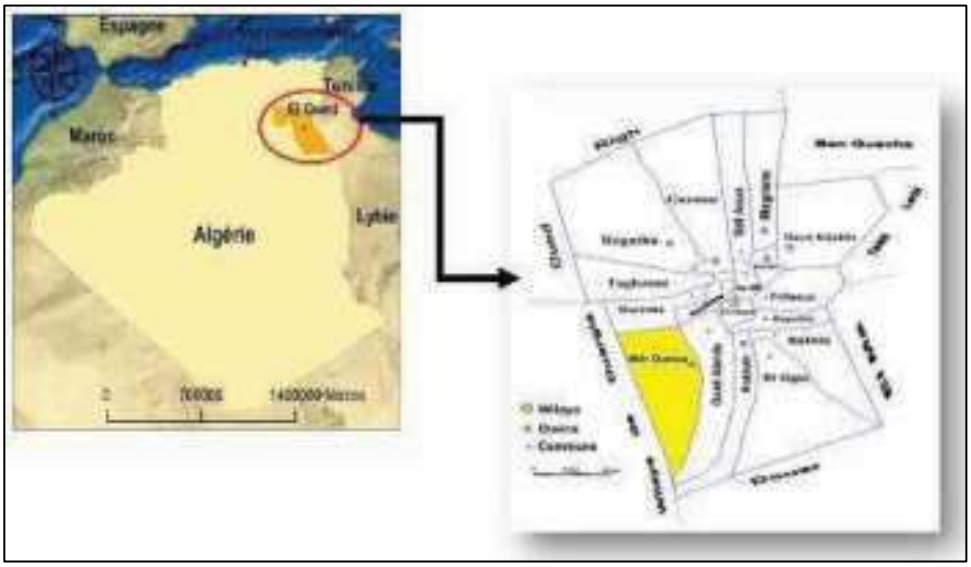

Fig1. Situation géographique d'El-Oued et la position de Mih Ouensa

2.3 Echantillonnage et méthodologie

Dix campagnes d'échantillonnage d'eau ont été effectuées sur des forages couvrant la zone d'étude (figure 2), les coordonnées géographiques (X, Y, Z) de chaque point d'eau illustré dans le tableau 1. Le prélèvement a été effectué manuellement pendant le mois de Mars 2017 dans des bouteilles en plastiques (1litre) identifiées et conservées au froid (2 à 4°C). Les analyses des différentes caractéristiques physico-chimiques de l'eau ont été effectuées au sein du laboratoire central du Centre De Recherche Scientifique Et Technique Sur Les Régions Aride (CRSTRA) de Biskra, selon les méthodes standard d'évaluation de qualité décrites par Rodier et al (2009). La température, le pH, et la conductivité ont été mesurées à l'aide d'un Multiparamètre de type Multi 3430 SET K. Pour les éléments majeurs, les méthodes utilisées sont : la complexométrie pour le TH et le calcium, la volumétrie pour le bicarbonate et les chlorure (méthode de Mohr), la spectrophotométrie DR 5000 (HACH) pour les sulfates et les nitrates et la photométrie à émission de flamme sur appareil (photomètre à flamme JENWAY) pour le sodium et le potassium.

Creative Commons Attribution-NonCommercial-NoDerivatives 4.0 International License (CC BY-NC-ND)

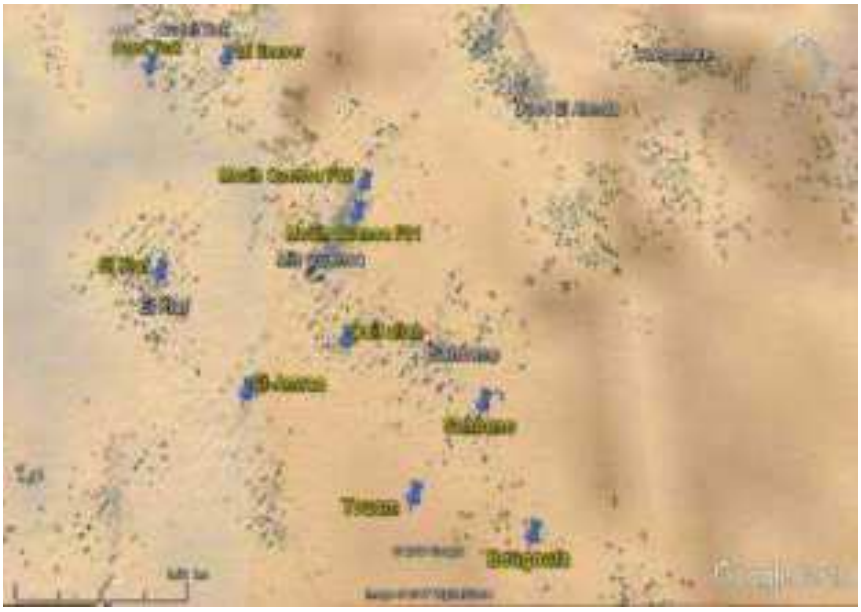

Fig 2. Carte des points de prélèvement (Google Earth)

Results and discussions:

3.1 Etude de la variation des paramètres physiques

***pH et conductivité électrique**

Les valeurs des pH des eaux souterraines de la région de Mih Ouensa sont assez voisins de la neutralité (figure 2), sont comprises entre 6.93 et 7.37 ce qui indique une variabilité faible pour ces eaux. Toutes les eaux de forages se trouvent dans la plage de pH recommandé par l'OMS (6.5-9) et les normes Algériennes (2014).

Les valeurs de conductivité électrique obtenues varient entre de 4760 à 7210 µS/cm, le minimum enregistré au forage (Sahbane) et le maximum enregistré au forage (Oued Turk) (figure 3). Les résultats d'analyses des paramètres physico-chimiques des eaux montrent des valeurs élevées de la conductivité électrique qui dépasse 1000 µs/cm (OMS, 2006) et 2800 µs/cm (JORA, 2014).

Creative Commons Attribution-NonCommercial-NoDerivatives 4.0 International License (CC BY-NC-ND)

Algerian Journal of Engineering Architecture and Urbanism Vol. 5 Nr. 3 2021
ISSN: 2588-1760

Tableau 1 : Cordonnées géographiques des points d'eau
NS : Niveau statique
ND : niveau dinamique

Nom de forages	Coordonnées			Profondeur	Année	Debit	NS	ND	Usage
	X	Y	Z	(m)	de réalisation	(L/S)	(m)	(m)	
Mih Ouensa F1	6°42' 46"	33°12'02"	91	285	1984	/	11	12	AEP
Dif Allah	6°42' 38,54"	33°10'29,44"	/	52	2009	10	10,9	20,22	AEP
Mih Ouensa F2	6° 42' 52"	33°12'26"	80	220	1992	31,0	/	/	AEP
Bougoufa	6°45' 15"	33°8'26"	85	56	2009	9	10,8	26,15	AEP
Touam	6° 41' 53"	33°08' 49"	101	198	2010	52	28,58	38,32	AEP
El Katef	6°39' 46"	33°11'18"	96	225	2011	50	30	61,08	AEP
El Amra	6°41'14,39"	33°9' 55,12"	/	48	2008	8	16,9	21,92	AEP
Oued Turk	06°39'7,16"	33°14' 9,95"	88	254	2013	35	37	43,11	AEP
Cité el Nassar	6°40' 24,73"	33°14' 16,01"	/	64	2010	10	9,8	20,6	AEP
Sahbane	6°44'39"	33°09'46"	95	/	2011	40	41	/	AEP

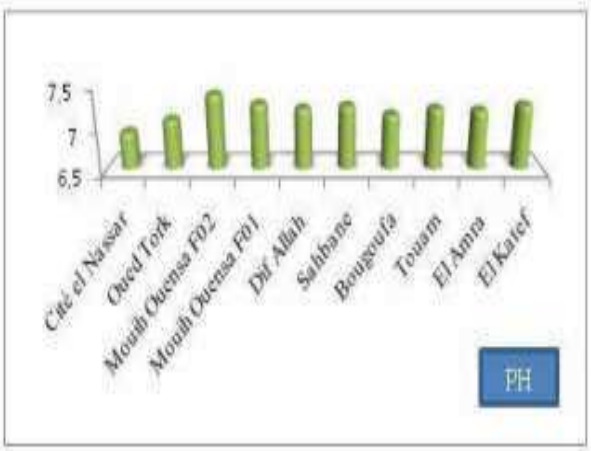

Figure 2 : Variation des valeurs de pH des eaux souterraines du Mih Ouensa

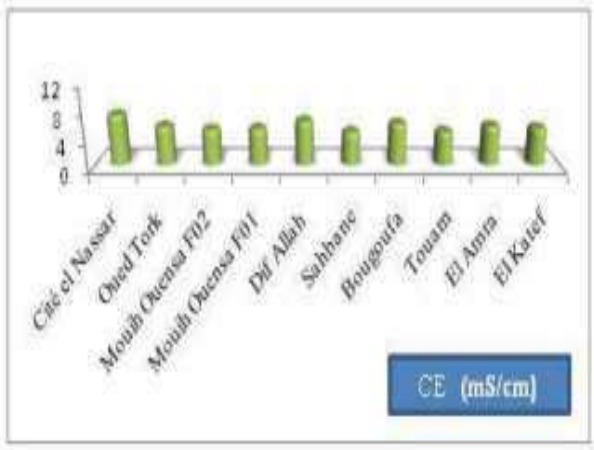

Figure 3 : Variation des valeurs de la conductivité des eaux souterraines du Mih Ouensa.

3.2 Etude de la variation des paramètres chimiques

1. Dureté totale

La dureté totale d'une eau est produite par les sels de calcium et de magnésium qu'elle contient. La dureté de l'eau influe essentiellement sur l'état des canalisations et des appareils de chauffage, et sur le lavage du linge. Les teneurs en dureté varient de 128 à 262 °F (figure 4). Elle est supérieure à la norme 50 °F (OMS, 2006). Tous les échantillons d'eau

Creative Commons Attribution-NonCommercial-NoDerivatives 4.0 International License (CC BY-NC-ND)

présentent des fortes valeurs de dureté et sont des eaux très dures. Des études épidémiologiques relatives à la dureté et aux risques de maladies cardiovasculaires ont trouvé une association protective entre la mortalité due aux maladies cardiovasculaires et l'augmentation de la dureté de l'eau (OMS, 2004).

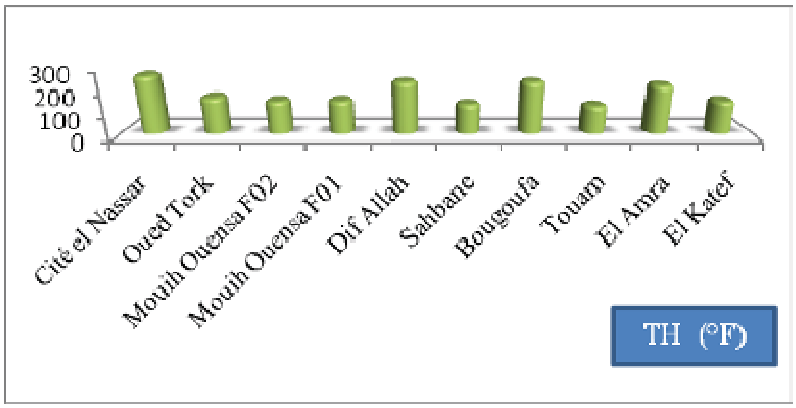

Figure 4 : Variation des valeurs de la dureté totale des eaux souterraines du Mih Ouensa

2. Calcium et Magnésium

Le calcium : est un métal alcalinoterreux extrêmement répandu dans la nature et en particulier dans les roches calcaires sous forme de carbonates (Rodier et al, 2009). C'est le composant majeur de la dureté de l'eau. Dans nos échantillons d'eau, les teneurs en calcium varient de 280 mg/l à 640 mg/l (Figure 5). Ces eaux présentent des concentrations supérieures à la norme OMS (2006) et les normes Algériennes (2014) qui est de 200 mg/l.

Le Magnésium : constitue le deuxième élément significatif de la dureté de l'eau après le calcium. Il est présent dans les eaux de cette région à des teneurs allant de 140,94 à 247,86 mg/l (Figure 6). Ces teneurs sont supérieures la norme admise par l'OMS pour le magnésium, qui est de 150 mg/l.

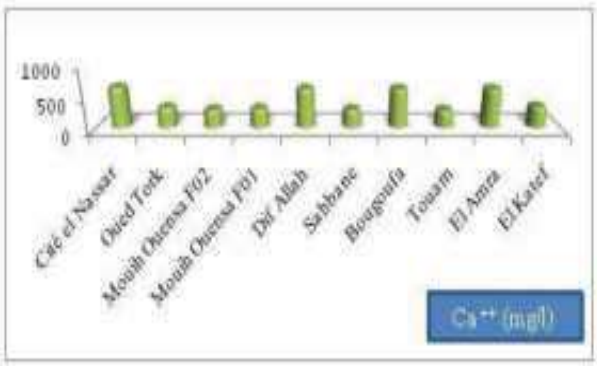

Figure 5 : Variation des teneurs en calcium des eaux souterraines du Mih

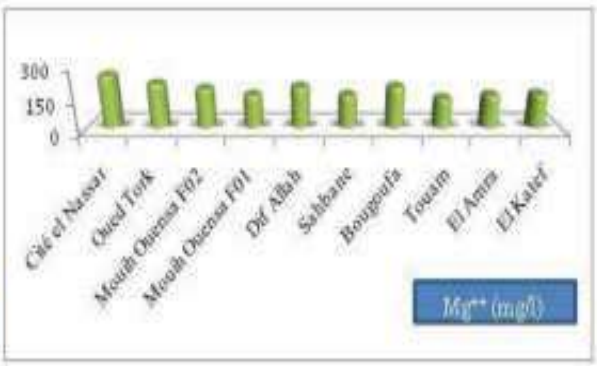

Figure 6 : Variation des teneurs en magnésium des eaux souterraines du Mih

3. Sodium et Potassium

L'analyse des données a montré que les teneurs de sodium dans les eaux étudiés varient de 718,46 mg/l à 1053,17 mg/l (Figure 7). Nous avons remarquée que tous les échantillons dépassaient les normes de potabilités. La présence exagérée de sodium dans les eaux peut

Creative Commons Attribution-NonCommercial-NoDerivatives 4.0 International License (CC BY-NC-ND)

affecter certaines populations (sujets souffrant d'hypertension par exemple), et peut aussi affecter certains sujets normaux (augmentation de la tension sanguine chez les adolescents) (Montiel, 1999).

Pour le potassium : Les valeurs de ce paramètre dans les eaux étudiées sont variables et oscillent entre 38,71 et 56,05 mg/l (Figure 8). Le potassium présente des valeurs élevé et dépasse les normes algériennes (soit 12 mg/l).

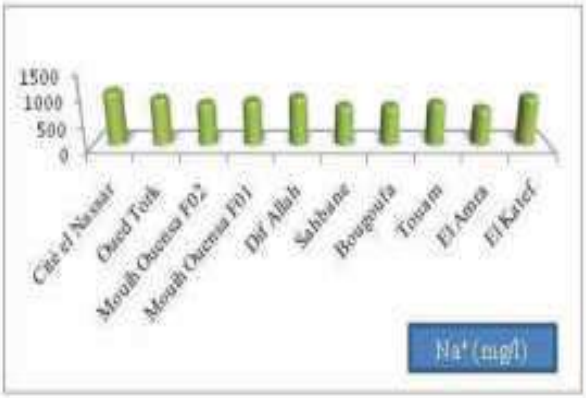

Figure 8 : Variation des teneurs en potassium des eaux souterraines du Mih Ouensa

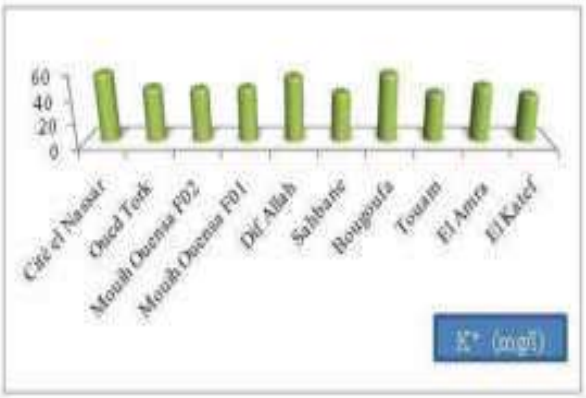

Figure 7 : Variation des teneurs en sodium des eaux souterraines du Mih Ouensa

4. Bicarbonates

La teneur en bicarbonates dans les eaux souterraines dépend surtout de la présence des minéraux carbonatés dans le sol et l'aquifère, ainsi que la teneur en CO_2 de l'air et du sol dans le bassin d'alimentation. La teneur en bicarbonates des eaux souterraines non soumises aux influences anthropiques, varie entre 50 et 400 mg/l. Les valeurs médianes des teneurs en bicarbonates se situent autour de 302 mg/l dans le domaine habituel des eaux souterraines non polluées. Les teneurs en bicarbonates des points étudiés (figure 9) variaient globalement entre un minimum de 146,4 mg/l et un maximum de 317,2 mg/l. Les valeurs élevées sont dues vraisemblablement à la circulation de ces eaux dans le réservoir aquifère de nature calcaro-dolomitique.

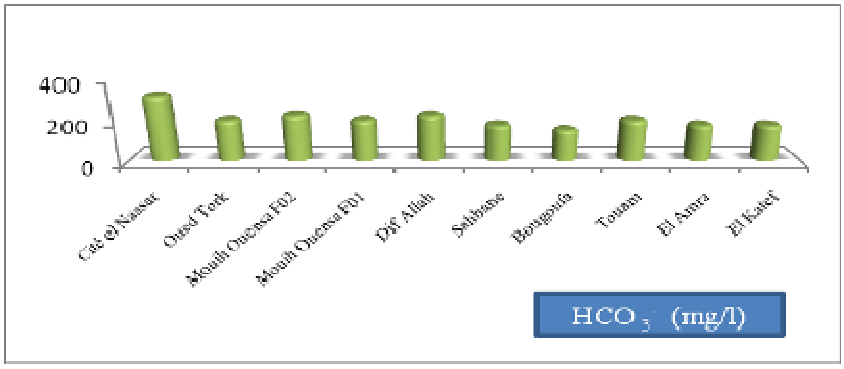

Figure 9 : Variation des teneurs en bicarbonates des eaux souterraines du Mih Ouensa

Creative Commons Attribution-NonCommercial-NoDerivatives 4.0 International License (CC BY-NC-ND)

5. Chlorures

Les eaux trop riches en chlorures sont laxatives et corrosives (Humbert et Pommier, 1988; Tarik, 2005), La concentration des chlorures dans l'eau dépend aussi du terrain traversé. Sur la base des résultats des analyses effectuées pour les échantillons des eaux, les teneurs en chlorures est de l'ordre de 975,15 mg/l (Bougoufa) à 1488,9 mg/l (Cité el Nassar) (Figure 10). Nous avons remarqué toute les valeurs dépassaient les normes de potabilités Algérienne (soit 400 mg/l).

Leurs teneurs dans les eaux naturelles sont susceptibles de subir des variations en zones arides suite au lessivage superficiel en cas de fortes pluies. Elles peuvent avoir aussi comme origine, selon Dib (2009), une contamination par les eaux usées. L'inconvénient majeur des chlorures, est la saveur désagréable, qu'elles communiquent à l'eau à partir de 250 mg/l (OMS, 2006), surtout lorsqu'il s'agit de chlorure de sodium. Pour une quantité équivalente de chlorures, la saveur peut être moins marquée en présence de calcium et de magnésium (Rodier et al., 2009).

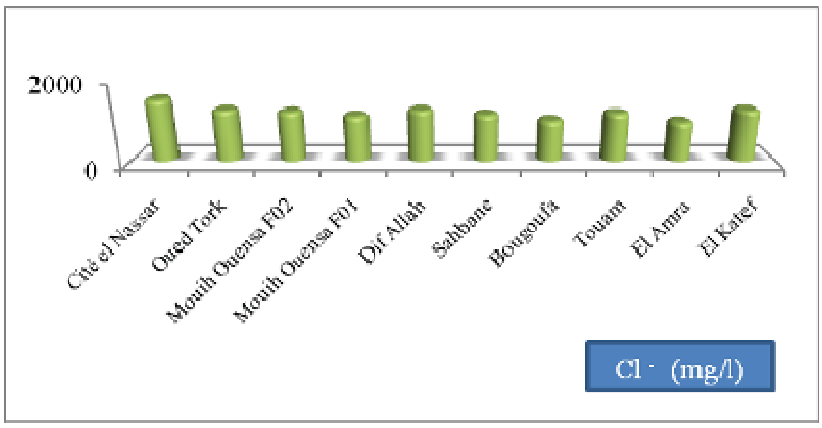

Figure 10 : Variation des teneurs en Chlorures des eaux souterraines du Mih Ouensa

6. Sulfates

La présence du ion SO_4^{2-} dans les eaux souterraines naturelles peut avoir deux origines que sont la dissolution des sulfates et l'oxydation des sulfures. La dissolution des sulfates est caracteristique des aquifères en roches évaporitiques (qui contiennent du gypse, de l'anhydrite et d'aurtes types de sulfates), l'oxydation de sulfures par contre est typique des roches riches en pyrite ou des minéralisations secondaires peuvent se produire dans les diaclases (Rodier et al., 2009; Dib, 2009). Les valeurs de ce paramètre dans les eaux étudiées sont variables entre 836,36 mg/l (Touam) et 2072,73 mg/l (Bougoufa) (Figure 11). Nous avons remarqué toute les valeurs dépassaient les normes de potabilités Algérienne (soit 500 mg/l). La présence de sulfate en quantité supérieure à 300 mg/l peut entrainer dans certaines conditions l'altération des matériaux de construction (corrosion des réservoirs de stockage) et accélérer la corrosion du fer (Rodier et al., 2009).

Creative Commons Attribution-NonCommercial-NoDerivatives 4.0 International License (CC BY-NC-ND)

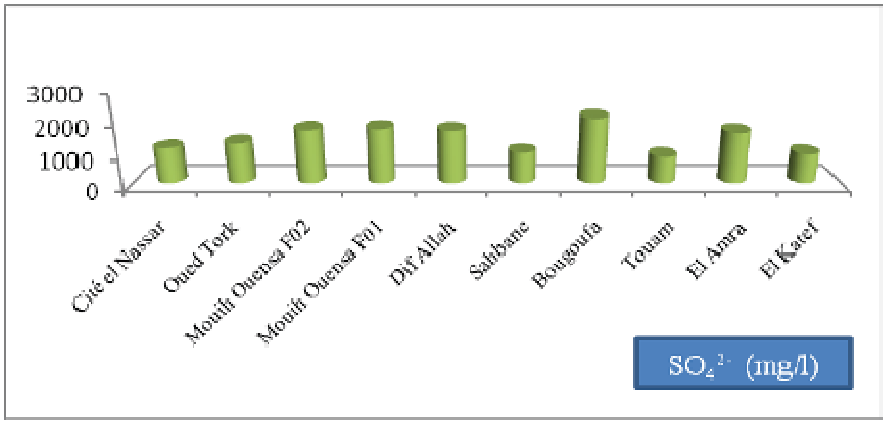

Figure 11 : Variation des teneurs en sulfates des eaux souterraines du Mih Ouensa

7. Nitrates

Les nitrates constituent la forme azotée la plus dominante dans les nappes d'eau souterraine. Ils proviennent généralement de la décomposition de la matière organique par oxydation bactérienne des nitrites et constituent ainsi l'ultime produit de la nitrification. Des valeurs supérieures indiquent des rejets d'eaux usées dans les milieux aquatiques superficielles et souterraines, et surtout une utilisation excessive de fertilisants utilisés en agriculture, (Chapman et al, 1996). Les teneurs en nitrates présentent des concentrations variables entre 7.2 mg/l et 41.37 mg/l, inférieur à la valeur limite dans les normes de (l'OMS, 2006) et les normes algériennes (JORA, 2014) soit 50 mg/l (Figure 12) mais reste des valeurs importante.

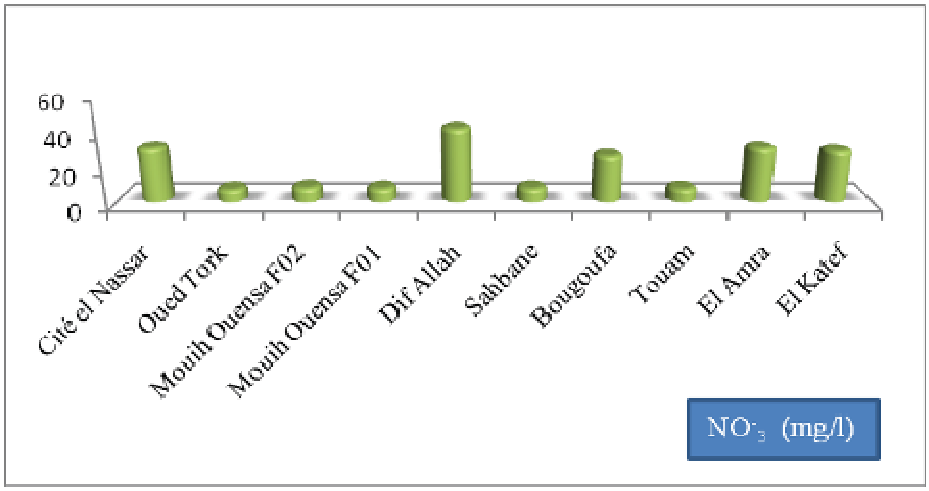

Figure 12: Variation spatiale des teneurs en nitrates des eaux souterraines du Mih Ouensa

Les nitrates peuvent se trouver dans le sol et les eaux soit à la suite d'un apport d'engrais, soit comme la conséquence de processus biochimique naturels qui dépendent étroitement des conditions pédoclimatiques et écologiques régionales. Par ailleurs, Selon, le transfert des nitrates vers les nappes est conditionné par un excès d'eau d'irrigation

Creative Commons Attribution-NonCommercial-NoDerivatives 4.0 International License (CC BY-NC-ND)

ou de pluie (El-Bardai et al, 2004). Dans notre étude cette observation est confirmée par la présence de la forte concentration en nitrates dans la nappe Phréatique par le lessivage des sols cultivée dans les forages suivants (Cité El Nacer, Dif Allah, Bougoufa et El Amra), et dans le forage d'El Katef du Miopliocéne. La forte concentration en élément provient du phénomène d'infiltration des engrais utilisé dans l'agriculture par le lessivage des sols.

3.3 Facies hydrochimiques

Dans le but de bien identifier les faciès hydrochimiques et d'avoir une indication sur l'aspect qualitatif des eaux souterraines, la représentation graphique des résultats d'analyses s'avère un outil inévitable. Pour atteindre cet objectif, on a eu recours au diagramme de Piper. La réalisation de ces diagrammes a été faite en utilisant le logiciel Diagrammes 5.6, conçu par Simler (2007). Le diagramme de Piper permet de représenter le faciès chimique d'un ensemble d'échantillons d'eaux. Il est composé de deux triangles permettant de représenter le faciès cationique et le faciès anionique et d'un losange synthétisant le faciès global. Les nuages de points concentrés dans un pôle représentent pour les différents échantillons la combinaison des éléments cationiques et anioniques. Ce type de diagramme est particulièrement adapté pour étudier l'évolution du faciès des eaux lorsque la minéralisation augmente ou bien pour indiquer les types de cations et anions dominants et pour distinguer des groupes d'échantillons.

Selon le diagramme de Piper (figure 13), La nappe captive des eaux de forages de la zone d'étude présente un faciès chloruré sodique et potassique avec la tendance de 4 forages vers le pôle chloruré et sulfaté calcique et magnésien.

Figure 13: Piper des eaux souterraines de la région de Mih Ouensa

Le report de 10 forages d'eau sur le diagramme de Schoeler (Figure 14) montre que tous les points analysés sont caractérisés par des eaux de type sulfaté sodique. Ce faciès indique une dissolution évaporitique riche en sels et en gypse.

Creative Commons Attribution-NonCommercial-NoDerivatives 4.0 International License (CC BY-NC-ND)

Algerian Journal of Engineering Architecture and Urbanism Vol. 5 Nr. 3 2021
ISSN: 2588-1760

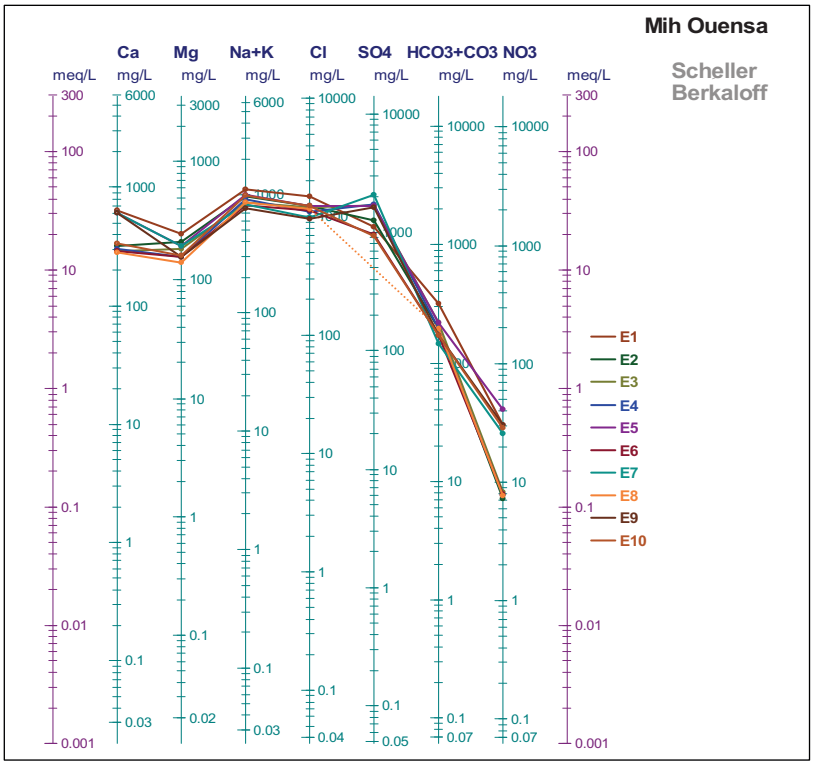

Figure 14 : Schoeller-Berkaloff des eaux souterraines (Mih Ouensa)

Les ions dominants (Tableau 2) sont les chlorures et les sulfates pour les anions et le sodium et potassium pour les cations**.**

Tableau 2: Classification des eaux selon Schoeller-Berkaloff

Forage	Anions	Cations	Faciès Chimique
Cité el Nassar	$Cl^- > SO_4^- > HCO_3^- > NO_3^-$	$Na^+ + K^+ > Ca^+ > Mg^+$	Chloruré sodique
Oued Tork	$SO_4^- > Cl^- > HCO_3^- > NO_3^-$	$Na^+ + K^+ > Ca^+ > Mg^+$	Sulfaté sodique
Mih Ouensa F2	$SO_4^- > Cl^- > HCO_3^- > NO_3^-$	$Na^+ + K^+ > Ca^+ > Mg^+$	Sulfaté sodique
Mih Ouensa F1	$SO_4^- > Cl^- > HCO_3^- > NO_3^-$	$Na^+ + K^+ > Ca^+ > Mg^+$	Sulfaté sodique
Dif Allah	$SO_4^- > Cl^- > HCO_3^- > NO_3^-$	$Na^+ + K^+ > Ca^+ > Mg^+$	Sulfaté sodique
Sahbane	$Cl^- > SO_4^- > HCO_3^- > NO_3^-$	$Na^+ + K^+ > Ca^+ > Mg^+$	Chloruré sodique
Bougoufa	$SO_4^- > Cl^- > HCO_3^- > NO_3^-$	$Na^+ + K^+ > Ca^+ > Mg^+$	Sulfaté sodique
Touam	$Cl^- > SO_4^- > HCO_3^- > NO_3^-$	$Na^+ + K^+ > Ca^+ > Mg^+$	Chloruré sodique
El Amara	$SO_4^- > Cl^- > HCO_3^- > NO_3^-$	$Na^+ + K^+ > Ca^+ > Mg^+$	Sulfaté sodique
El Katef	$Cl^- > SO_4^- > HCO_3^- > NO_3^-$	$Na^+ + K^+ > Ca^+ > Mg^+$	Chloruré sodique

Creative Commons Attribution-NonCommercial-NoDerivatives 4.0 International License (CC BY-NC-ND)

Conclusion:

Dans ce travail, nous avons analysé les paramètres physico-chimiques des eaux souterraines destinées à l'alimentation en eau potable du commun de Mih Ouensa situé au Sud-Ouest de la wilaya d'Oued souf en vue d'évaluer la qualité de ces eaux.

Les ressources de ces eaux souterraines sont représentées par la nappe du Complexe Terminale. Ce dernier représente l'unique ressource en eau potable dans toute la région. La comparaison des résultats des analyses chimiques des eaux souterraines de Mih Ouensa avec les normes recommandé par l'OMS et les normes Algériennes nous a permis d'observé que ces eaux sont très dures (TH>>50°F) avec des pH assez voisins de la neutralité et des conductivités sont globalement élevées, souvent supérieures à 4 mS/cm. Les teneurs en chlorure, en sodium et en sulfates présentent des concentrations élevés dépassent souvent les seuils de potabilité. L'évaluation de ces eaux présente une qualité médiocre, résultant d'une forte salinité dépassant 3 g/l influencée par la lithologie de la nappe et les facteurs anthropiques (exploitation intensive). Les eaux de la nappe du Complexe Terminale de cette région sont caractérisées par la présence de deux faciès: Chloruré sodique et potassique et sulfaté sodique. Les cations majeurs présentent un ordre d'abondance du type : $Ca^{2+} > Mg^{2+} > Na^{+} > K^{+}$. Cette étude a montré que ces eaux souterraines ne sont pas conseillées à la consommation comme eau de boisson, donc on déduit que dans cette région d'étude il n'y a pas un problème de quantité mais plutôt de qualité, pour cela il faut exiger des rigoureux critères pour améliorer la qualité chimique de l'eau et garantir sa potabilité dans les normes avant de la mobiliser aux consommateurs humains, et nécessitant aussi un traitement pour réduire les concentrations excessives de certains éléments minéraux d'origine naturelle.

References:

ANAT (2007), *Plan Directeur d'Aménagement et de l'Urbanisme PDAU du groupement de Tlemcen, Mansouarh, Chetouane*, Direction de l'Urbanisme et de la Construction, Tlemcen.

Baker J. L. (2012), *Climate change, disaster risk, and the urban poor: cities building resilience for a changing world (urban development),* World Bank Publications, Washington, ISBN: 978-0821388457

Boukerche D. (1989), *Evolution de la ville de Tlemcen pendant la période coloniale éléments de croissance et de transformation*, Mémoire de magister, Ecole Polytechniques d'Architecture et d'Urbanisme, Alger.

Gouvernement Algerien (2009), *Décret n° 09-403 du 29 novembre 2009 portant création et délimitation du secteur sauvegardé de la vieille ville de Tlemcen*, Journal Officiel de la République Algérienne Démocratique et Populaire **48(71):** 6–7.:

Hamma W., A Djedid D., Ouissi M. N. (2016), *Intervention on historical city Tlemcen during 1960-2009: Impacts and applicability*, Urbanism Architecture Constructions **7(2):** 109-124.

Amin N.C., Lekadou K.S., Attia A.R., Claon J.S., Agbessi K. et Kouadio K.l. (2008). *Qualité physico-chimique et bactériologique des eaux d'adduction publique de huit communes en Côte d'Ivoire. J.sci.pharm.biol., vol.9, n°1.*

Beauchamp J. (2006). *Qualité et Pollution des Eaux Souterraines. Université de Picardie Jules-Verne.*

Bouchemal F, Bouchahm N, Achour S. (2011). *Qualité des eaux des nappes aquifères de la région de BISKRA. Revue des Sciences Fondamentales et Appliquées, 3(1): 34- 44.*

Chapman d., kimstach v. (1996). *Selection of water quality variables. Water quality assessments : a guide to the use of biota, sediments and water in environment monitoring, Chapman edition, 2nd ed. E & FN Spon, London, pp. 59-126*

Creative Commons Attribution-NonCommercial-NoDerivatives 4.0 International License (CC BY-NC-ND)

DIB I., (2009). *L'impact de l'activité agricole et urbaine sur la qualité des eaux souterraines de la plaine de Gadaine- Ain Yaghout (Est Algérien). Mémoire de magister en hydraulique. Université Hadj Lakhdar Batna, 127 p.*

El-Bardai S, Lyoussi B, Wibo M, Morel N (2004). *Comparative Study of the antihypertensive activity of Marrubium Vulgare and of the dihydropyridine calcium antagonist amlodipine in spontaneously hypertensive rat. Clin. Exp. Hyprtens.26(6): 465-474.*

Guergazi S., Achour S., (2005). *Caractéristiques physico-chimiques des eaux d'alimentation de la ville de Biskra. Pratique de la chloration. Larhyss journal. 4, pp 119-127.*

JORA (2014). *Journal Officiel De La République Algérienne N°18. Décret exécutif n° 11- 125, du 23 mars 2014, relatif à la qualité de l'eau de consommation humaine.*

OMS, (2006). *Directives de qualité pour l'eau de boisson, troisième édition. Recommandations. Organisation mondiale de la Santé, Genève, 78 p.*

O.N. S (2010), *Office nationale de statistique de la Wilaya d' El-Oued.*

Rodier J., Legube B., Merlet N., Brunet R., (2009) ; *L'analyse de l'eau - 9ème édition,- Eaux naturelles, eaux résiduaires, eau de mer: Analyse de l'eau, 9ème édition, Paris, Dunod.*

Yasser M., Nouioua I., Kahoul I (2021); *Assessment of groundwater quality of the karst aquifer of Cherea, Tebessa (northeast of Algeria). Int. J. Hydrology Science and Technology, Vol. 11, No. 3.*

Creative Commons Attribution-NonCommercial-NoDerivatives 4.0 International License (CC BY-NC-ND)

Algerian Journal of Engineering Architecture and Urbanism Vol. 5 Nr. 3 2021
ISSN: 2588-1760

Experimental study on the effect of spraying distance on microstructural and tribological behavior of flame sprayed Ni alloy coatings.

Abdelhek IDIR[1, a *], Francesco DELLORO[2, b], Mohand Amokrane BRADAI[1, c,] Rassim YOUNES[1, d], Abdelhamid SADEDDINE[1, e]

[1] Laboratory of Mechanics, Materials and Energetic, Faculty of Technology, University of Bejaia, 06000 Bejaia, Algeria.
[2] MINES ParisTech, PSL Research University, MAT-Centre des Matériaux CNRS UMR 7633, BP 87, 91003, Evry, France.
[a*] abdelhek.idir@univ-bejaia.dz

Abstract

Thermally sprayed Ni-based coatings have shown their potential for use in wear applications due to their good tribological properties, cost efficiency and positive environmental aspects. In this study, the microstructural details and tribological performances of two flame sprayed Ni-based coatings (Ni-W-Cr-B-Si-Fe-C), obtained by process under reducing stoichiometric conditions and at different spraying distances, were evaluated. Microstructural investigations were conducted by using scanning electron microscopy coupled with energy dispersive X-ray spectroscopy and X-ray diffraction analysis. Microhardness measurements of the coatings were made and their tribological behavior was investigated in dry sliding wear test (ball-on-disc) at room temperature. Results showed that the as-sprayed coatings consisted of lamellar inhomogeneous microstructure, containing pores, unmelted particles and carbides. Main wear mechanisms were inferred by wear track characterization, results shows that the predominating wear mechanism of the coating sprayed at shorter distance was controlled by local delamination and re-growth of a dense, smooth and oxidized tribo-layer. But increasing in spraying distance, the main wear mechanism was massive exfoliation of large coating portions.

Keywords: Ni alloy; Microstructure; coating; Wear performance.

Introduction

Creative Commons Attribution-Non-Commercial-No Derivatives 4.0 International License (CC BY-NC-ND)

Machine parts, such as sealing, impellers, pump bodies, hydraulic pistons, petrochemical valves, coal-fired boilers, heat exchangers, turbines, tools, extruders, components for the food and packaging industry, etc., are often protected against wear and corrosion by thermal spray coatings **[1-7],** providing excellent performances in many severe environments **[4].** In flame spray technique a wide range of materials can be thermal sprayed for a variety of applications. When wear and corrosion resistance are required, Ni based coatings are widely used to provide enhancements in surface properties of materials. In the past decades, extensive attention has been given towards NiCrBSi alloy coatings, due to several advantages in comparison with other alloys. Its composition makes the alloy easy to remelt, specifically due to the content of boron and silicon, which decrease the melting temperature and enhance wettability by combining with oxides **[8, 9].** Moreover, the presence of carbon enables the creation of carbides, increasing hardness and wear resistance **[10].** The presence of chromium is responsible for the corrosion resistance of this material, specifically in alkali environments **[11].** NiCrBSi alloy coatings can be deposited by different technologies, as flame spraying **[8, 12-14],** atmospheric plasma spraying (APS) **[15-16]** and HVOF **[17-18**]. Several extensive studies have already been carried out on tribological behaviour of Ni-based and composite coatings under different conditions, such as dry sliding **[19-20],** slurry erosion **[21],** liquid impingement erosion **[22],** solid-particle erosion **[23]** and others. In this paper, NiWCrBSi coatings, sprayed onto a mild steel substrate using a reducing flame with two different spraying distances, were compared in terms of microstructure and wear resistance. Coating microstructures were characterized using scanning electron microscopy (SEM). Dry sliding ball-on-disk wear tests were performed on a tribometer, to investigate coating wear behavior. Furthermore, worn surfaces were characterized using digital microscope, SEM and by energy dispersive X-ray spectrometry (EDS), to determine the main mechanisms taking place during wear.

Materials and methods

In this study, E355 mild steel cylindrical samples, with 10mm diameter and 20 mm length, were used as substrates. This material presents a tensile strength of 335 MPa and the nominal chemical composition (wt % max) is: C 0.1%, Mo 0.007%, Mn 0.231 %, P 0.050%, N 0.03%, Cu 0.119%, Si 0.044%, V 0.01%, S 0.010% and Fe balance. Feed-stock material for flame spray was commercially available Ni-based super-alloy (Saint-Gobain, France) in rod shape

Creative Commons Attribution-Non-Commercial-No Derivatives 4.0 International License (CC BY-NC-ND)

with 4.75 mm diameter, with a composition of W 9.5%, Cr 14.3%, B 2.8%, Si 3.7%, Fe 3.5%, C 0.6% and Ni balance. Before spraying, samples were degreased with acetone and alcohol and grit blasted with Al_2O_3 particles to obtain a surface with mean roughness of Ra < 2µm. The coatings deposition was performed using oxyacetylene flame spraying technique using a Master Jet 2 (Saint Gobain, France) spray gun. During deposition, the operating pressure of the gases was kept constant to 4 bar for oxygen and 1.4 bar for acetylene. The gas flow was set measuring ball heights for, respectively, acetylene (99 mm) and oxygen (55 mm). With these settings, a reducing flame was obtained. Two spraying distances were tested (70 and 300 mm) and corresponding samples will be referenced in the following as, respectively, P03 and P05. Coating thickness was set to 10 mm for both spraying conditions.

Prior to metallographic observations, sample surfaces were polished on SiC abrasive papers from P400 down to P2000 and then finished with a 1 µm diamond paste. Microstructure observations were performed by SEM equipped with an EDAX detector for EDS analysis. Vickers micro-hardness was measured on coating top surfaces by using a (B 3212001 type Zwick machine), with a load of 3N during 15 s. For each sample the micro-hardness value was the average of 3 measurements. A CSM instrument tribometer was used to measure coating friction coefficients. Tests were performed using a 6 mm diameter WC steel ball with a hardness of 63 HRC, under dry friction conditions. The sliding distance was 50 m with a displacement rate of 25m/min and a load of 10 N. Coating roughness before the wear test, the wear track depth and width were investigated using a 3D profilometer.

Results and discussion

As-sprayed coatings morphologies and XRD Analysis

Flame sprayed coatings are obtained by sequential stacking of molten or semi-molten particles. For this reason, their microstructure consists of lamellar structure type **[13].** Figure. 1 illustrates the typical microstructure observed for coatings of the present study. It is predominantly heterogeneous, with the presence of pores, carbide particles, cracks and splats boundaries. Porosity can be due to the high cooling rate or to gas trapping during solidification. Spherical particles could be observed only in the coating P 05 (Figure. 1), corresponding to unmelted particles. This can be explained by the shorter spraying distance of

Creative Commons Attribution-Non-Commercial-No Derivatives 4.0 International License (CC BY-NC-ND)

P 05 conditions as compared to P 03 (170 mm versus 300 mm), resulting in shorter dwell time of particles in the flame. XRD spectra, that are not shown in this work, revealed for both coatings the presence of three different phases, labeled (Ni, Cr, Fe), WC and $Ni_{31}Si_{12}$. It can, thus, be claimed that the spraying distance did not significantly affect the formation of coating phases. Nevertheless, a certain difference was observed in the relative repartition of these phases.

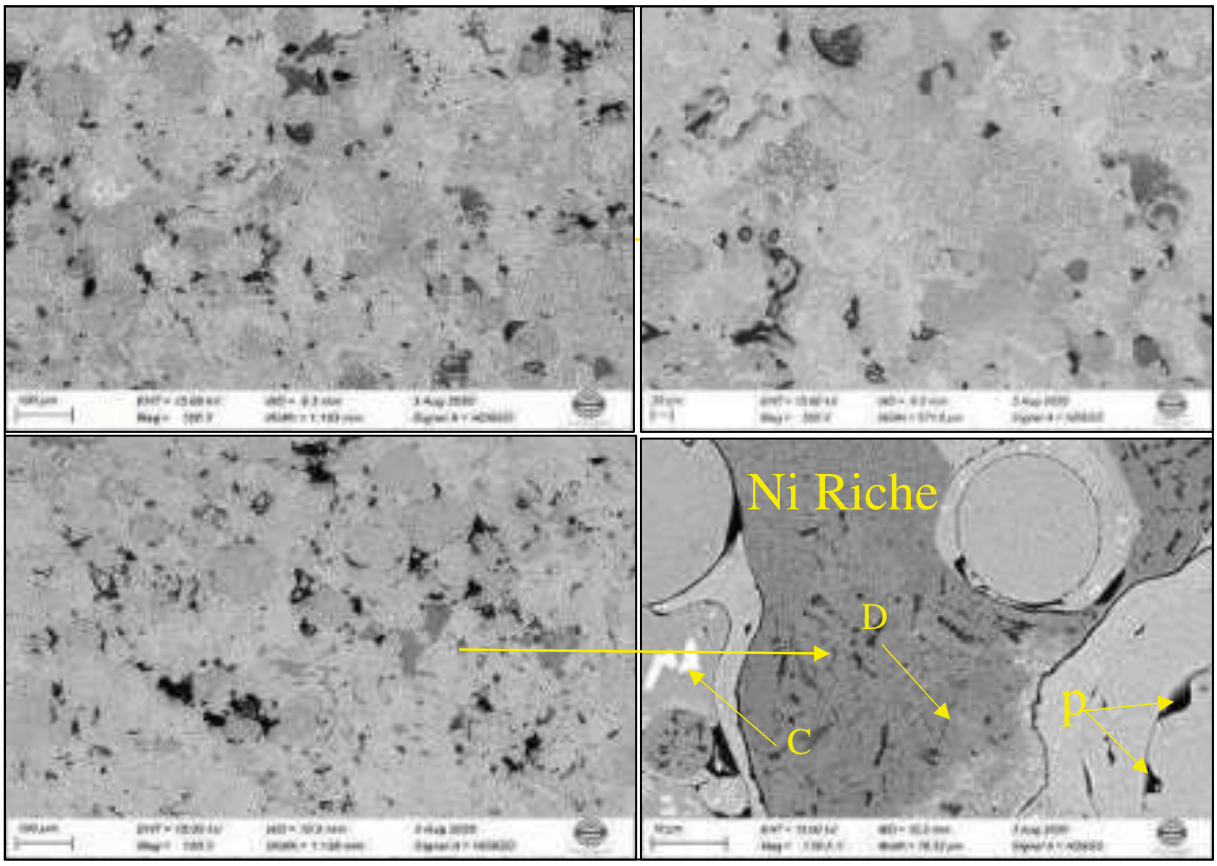

Fig. 1. SEM (backscattered electron) micrograph of as-sprayed NiWCrBSi coatings with different spraying distances (300 mm for P03, 170 mm for P 05).

SEM observations in chemical contrast of all deposits, combined with analyses (EDS) shows areas with different levels of grayscale. They have been listed in Figure.3-10 as follows: light gray area, granular area, bright particles and black area. Chemical phase identification was performed by EDS (Energy Dispersive Spectrometer). The quantitative elemental composition of each phases is listed showed in Figure. 2 and Figure.3 respectively. These light grey contrasts have been identified to be Ni-rich, and they are mainly formed by Ni (61.7

Creative Commons Attribution-Non-Commercial-No Derivatives 4.0 International License (CC BY-NC-ND)

wt-% for coating P 03) and Ni (65.8% for the coating P 05) corresponding to the Ni matrix, with small quantities of Fe, Cr and Si. Some particles still retain their angular morphology and have incorporated randomly into coatings matrix. The semi-quantitative (EDS) analysis of the brightest particles which had angular morphologies was corresponded to carbides and could be MxCy type phases. The black area was identified as the coating porosity. In overall, we can conclude that no significant influence of spraying distance in terms of phases formation, but theses coating shows slight difference in the distribution of chemical elements constituting each phase.

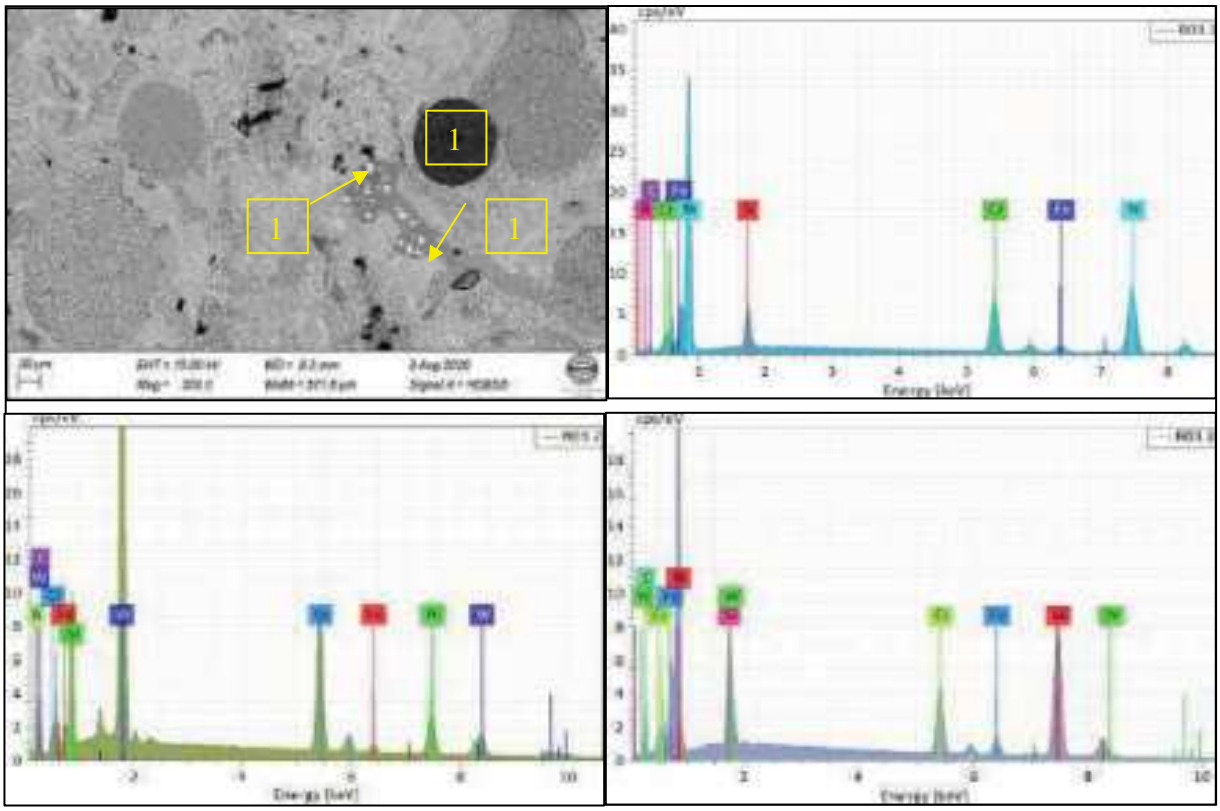

Fig.2. EDS analysis of coating P 03

Creative Commons Attribution-Non-Commercial-No Derivatives 4.0 International License (CC BY-NC-ND)

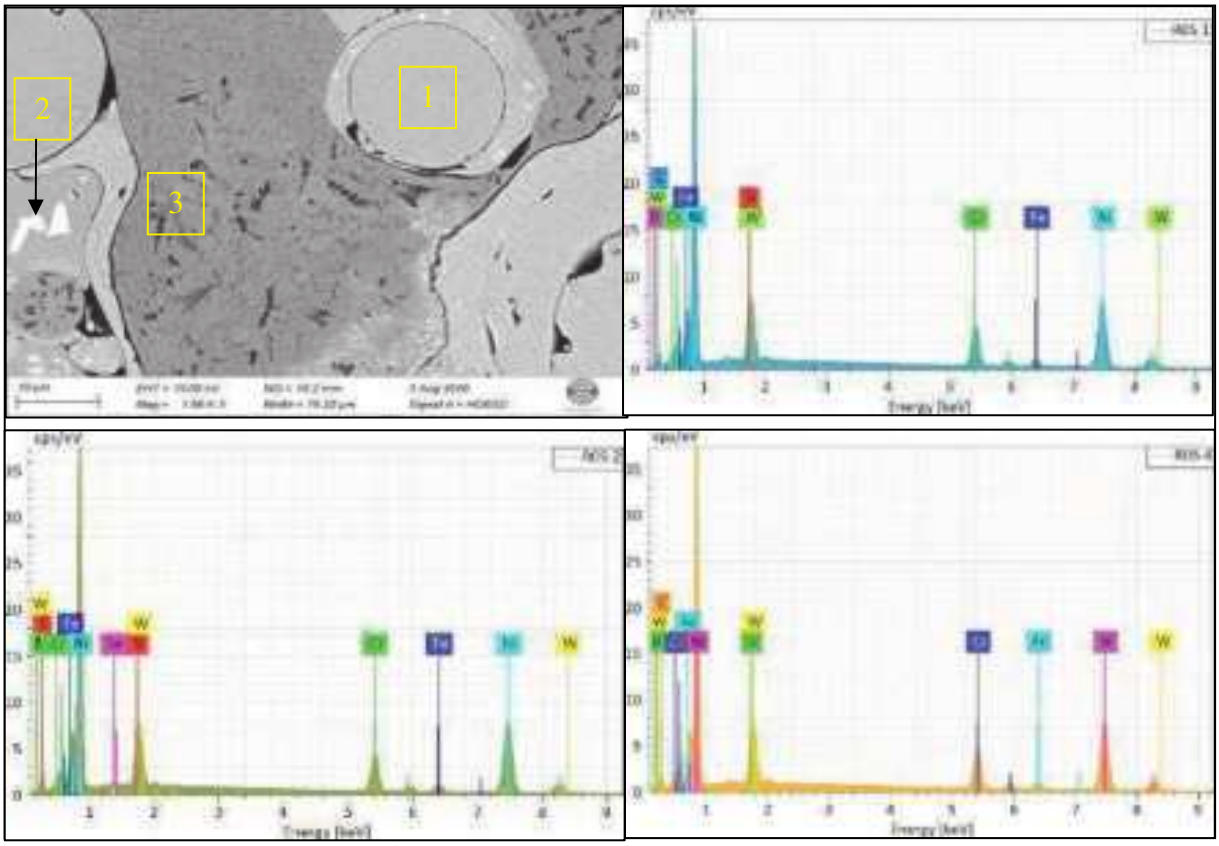

Fig.3. EDS analysis of coating P 05

Mechanical characterization

Microhardness measurements are carried out on polished surfaces of coatings (Vickers scale) using a Vickers B 3212001 type Zwick hardness tester with a 3N load. The loading and unloading speed were 0.5 mm/min and the waiting time was 15 sec. Figure.4 shows the microhardness measurements of the two coatings. Each value is a mean of five measurements. Values fluctuated from one point to another, which might be justified by the carbides phases randomly distributed through the coating microstructure. The two coatings showed a much higher hardness than the substrate. It is also to note that the coating (P03) showed the highest hardness than coating (P05) this difference might be justified by the coating cohesion. In fact, through the coatings microstructure as clearly obvious in Figure.1 a and b, the coating (P03) shows relatively uniform microstructure, when the major of spalts were melted flattened to form coating. However, the coating (P05) has a higher rate of unmelted particles than the coating (P03), which mainly explains the poor cohesion of the coating lamella and may also affect the coating hardness.

Creative Commons Attribution-Non-Commercial-No Derivatives 4.0 International License (CC BY-NC-ND)

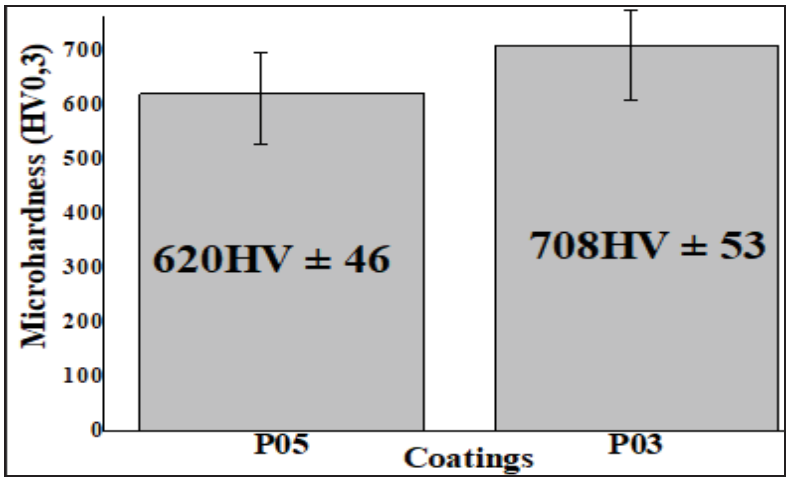

Fig. 4. Microhardness measurement of the two coatings.

Figure. 5 shows the evolution with time of the coefficient of friction for the two coatings, under a loading of 10 N, for a total sliding time of 33 minutes. Two main periods can be identified from these curves, namely (1) the early period and (2) the steady state period. During the first period, corresponding to a time of approximately 471 s for the coating P 03 and 582 s for P 05, friction coefficient rose up rapidly to the maximum values of 1.2 and 1.25, respectively, for coating P03 and P05. were caused by an interface which might also involve oxides. After reaching its maximum value, friction coefficient began to decrease slightly. Here, the contact area became smooth due to the shearing of asperities and the elimination of oxides. Tribolayer oxidation, which contributes in decreasing friction coefficient. When friction coefficient stabilizes, wear entered in the steady state regime. During this stage, the average friction coefficient was 0.94 ± 0.12 for P 05 and 1.01 ± 0.08 for P 03. Wear parameters and 3D profile of wear scars are illustrated in Table 3. and Fig. 7 respectively.

Type de revêtement	P 03	P 05
Coefficient de frottement	0.97 ± 0.092	0.910 ± 0.157
Taux d'usure (mm^3 /Nm)	9.804×10^{-5}	7.790×10^{-5}
Profondeur du sillon (µm)	30	20
Largeur du sillon (µm)	400	200

Table.1 Wear parameters

Creative Commons Attribution-Non-Commercial-No Derivatives 4.0 International License (CC BY-NC-ND)

Algerian Journal of Engineering Architecture and Urbanism Vol. 5 Nr. 3 2021
ISSN: 2588-1760

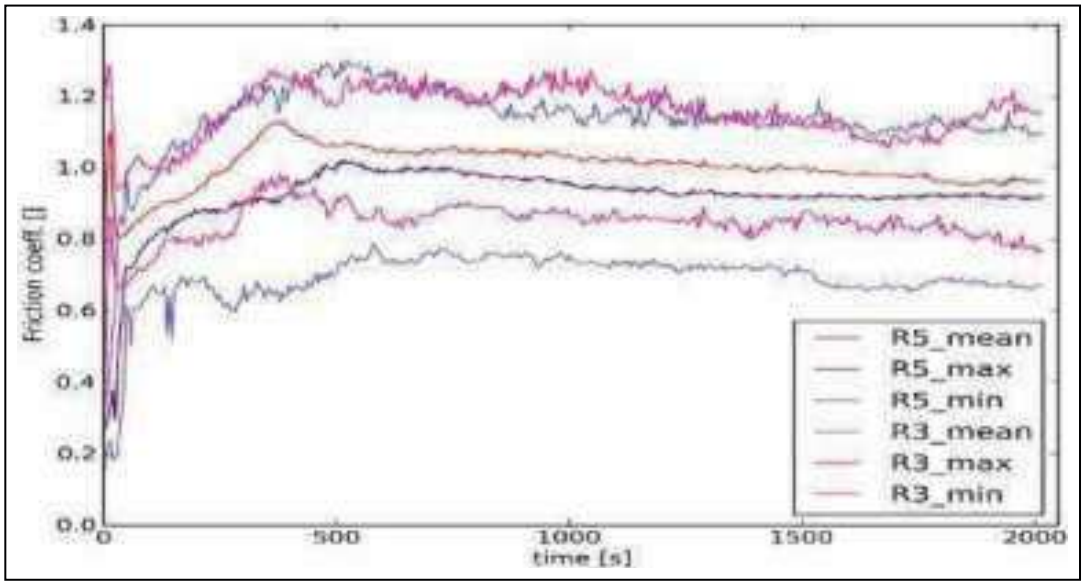

Fig.5. Evolution of friction coefficient as function of sliding time

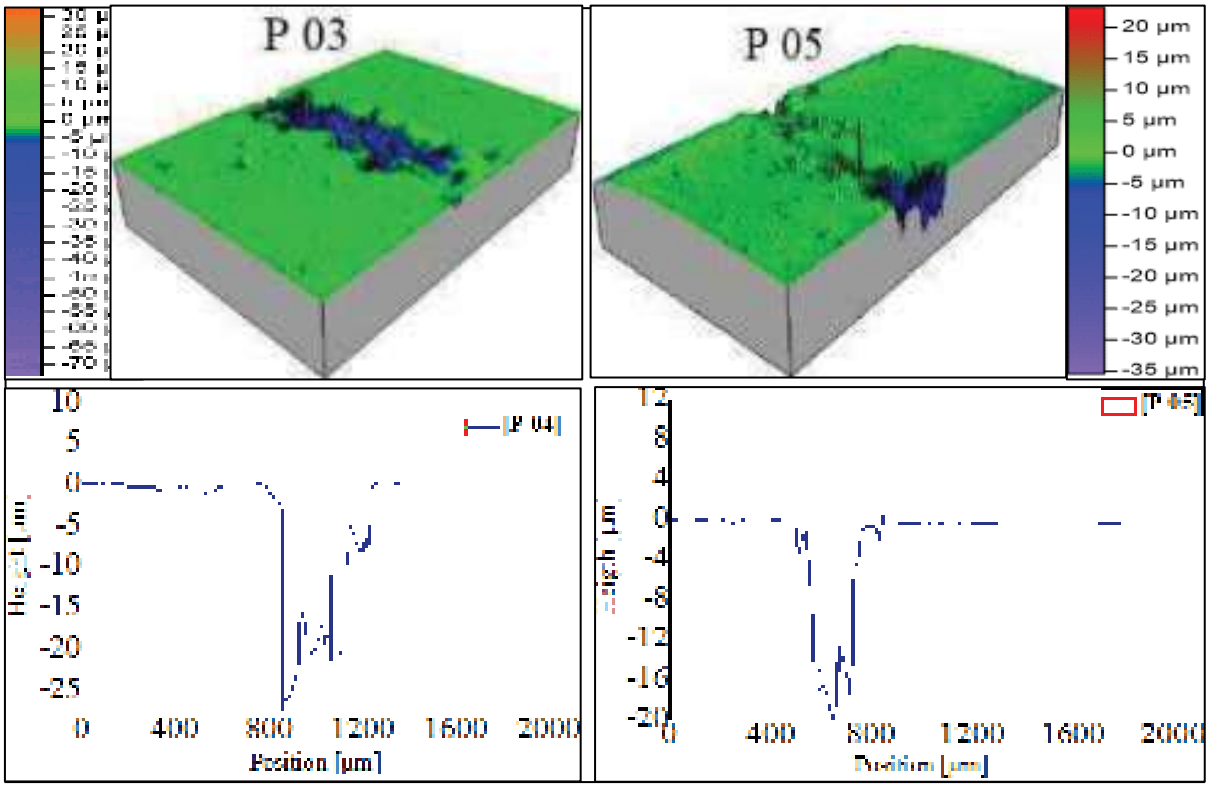

Fig.6. 3D Profile of the worn scar

To better understand wear performance and the mechanisms governing coating wear behavior, worn scars obtained after the wear test were examined by SEM and EDS, as shown

Creative Commons Attribution-Non-Commercial-No Derivatives 4.0 International License (CC BY-NC-ND)

in (Figure 6 and 7). Figure 6 shows a SEM top view micrograph of P 03 coating, in secondary electron image mode (a) and in backscattered electron image mode (BSE) (b), at higher magnification. The wear track appeared relatively rough and contained small smooth cavities. Cracks were observed on the whole coating surface. Some lamellae could also be observed and might be due to brittle fracture of large parts of coating layers. Worn surfaces also presented interlamellar interfaces and relatively smooth patches. These micrometer-sized defects in the coatings, such as pores, interlamellar interfaces and cracks, might have acted as cracking starting points during the sliding test. This can be connected to higher friction forces registered before the steady state, caused by severe damage and brittle fracturing of coating layers. Debris and very fine fragments could also be observed, caused by shear stresses acting on coating layers. These could lead to abrasive wear, as suggested by the presence of some shallow grooves (Figure 6b). In contrast, during the steady state period, friction coefficient showed a slight reduction, probably as a consequence of a transition from brittle fracture to soft abrasive wear mechanism. Detailed study of the wear scar (Figure 6b) suggested the formation of compacted layers of oxide particles on the sliding surfaces. EDS analysis of the worn scar in the zone indicated by 1 (Figure 6b) revealed the presence of Ni, Cr, Si, Fe and O. The presence of oxygen is probably due to the silicon and chromium, easily forming oxides especially in a metal-to-metal contact [15]. Tribo-layer characteristics depend on the temperature at the coating/ball interface and on the friction force. After the shearing of the surface asperities, the contact process seems to take place between the coating layers and ball counter-body, after having been a contact between the surface asperities and the ball, so that the Ni matrix suffers heavy wear as the sliding distance increases. In this case, pits could be observed on the worn scar, as shown in (Figure 6b), corresponding to the pullout of WC particles. Thus, the predominating wear behaviour of P 03 coating was controlled by the local delamination and oxide tribo-layer. However, abrasive wear mechanism might also have played an important role. Anyway, its effect was masked by delamination, due to high rate of brittle fracture and tribo-oxide renewal.

Creative Commons Attribution-Non-Commercial-No Derivatives 4.0 International License (CC BY-NC-ND)

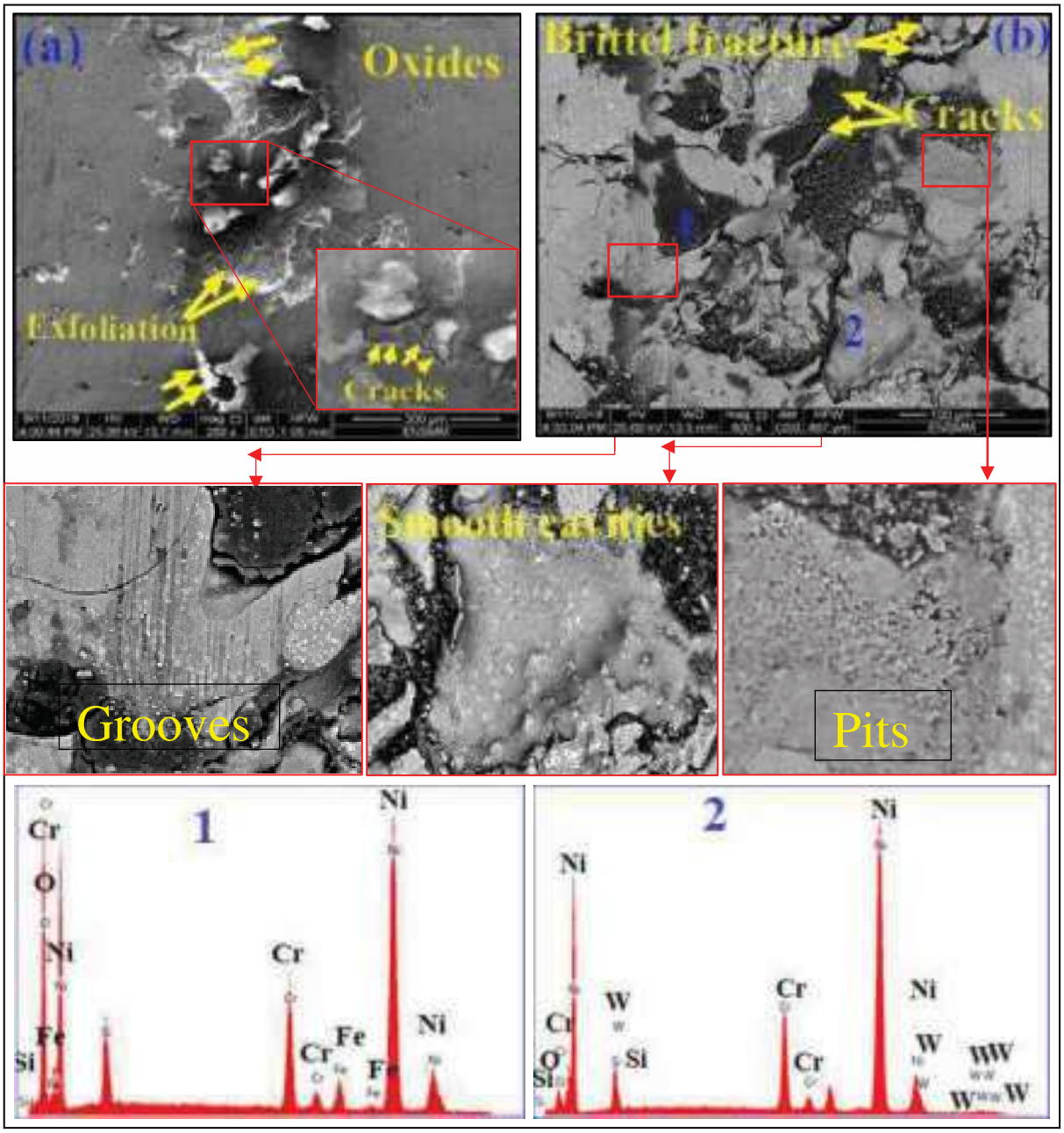

Fig. 6. SEM top view micrograph of the wear track of the as-sprayed **(P03)** coating produced after ball-on-disk testing at room temperature against WC steel balls. **(a)** Secondary electron image mode (SE). **(b)** Backscattered electron image mode (BSE).

The same analysis was also performed on P 05 coating, in an attempt to identify the wear mechanisms taking place during dry sliding wear test (Figure. 7a and b). Some differences in wear scar morphology related to microstructural aspects could be observed, as well as a higher friction coefficient, influenced by lower inter-splat cohesion. EDS analysis results of the worn track (zone pointed by 1 in Figure. 7a) revealed the presence of Fe, Si and O; in the

Creative Commons Attribution-Non-Commercial-No Derivatives 4.0 International License (CC BY-NC-ND)

zone pointed by 2 revealed the presence of Fe, O and W. The relatively high quantity of oxygen (44.11 %) indicated that important tribo-oxydation have been taking place. At the same time, under the repeated action of shearing forces due to friction, coating layers were also suffering from an exfoliation of large parts and splats. This can be related to coating microstructure and, in particular, to the presence of more numerous unmelted particles, micro-cracks and pores when compared to P 03 coating. Thus, results in (Figure. 7) clearly show that the predominating wear mechanism was the massive exfoliation of large parts of the coating (single or multiple splats).

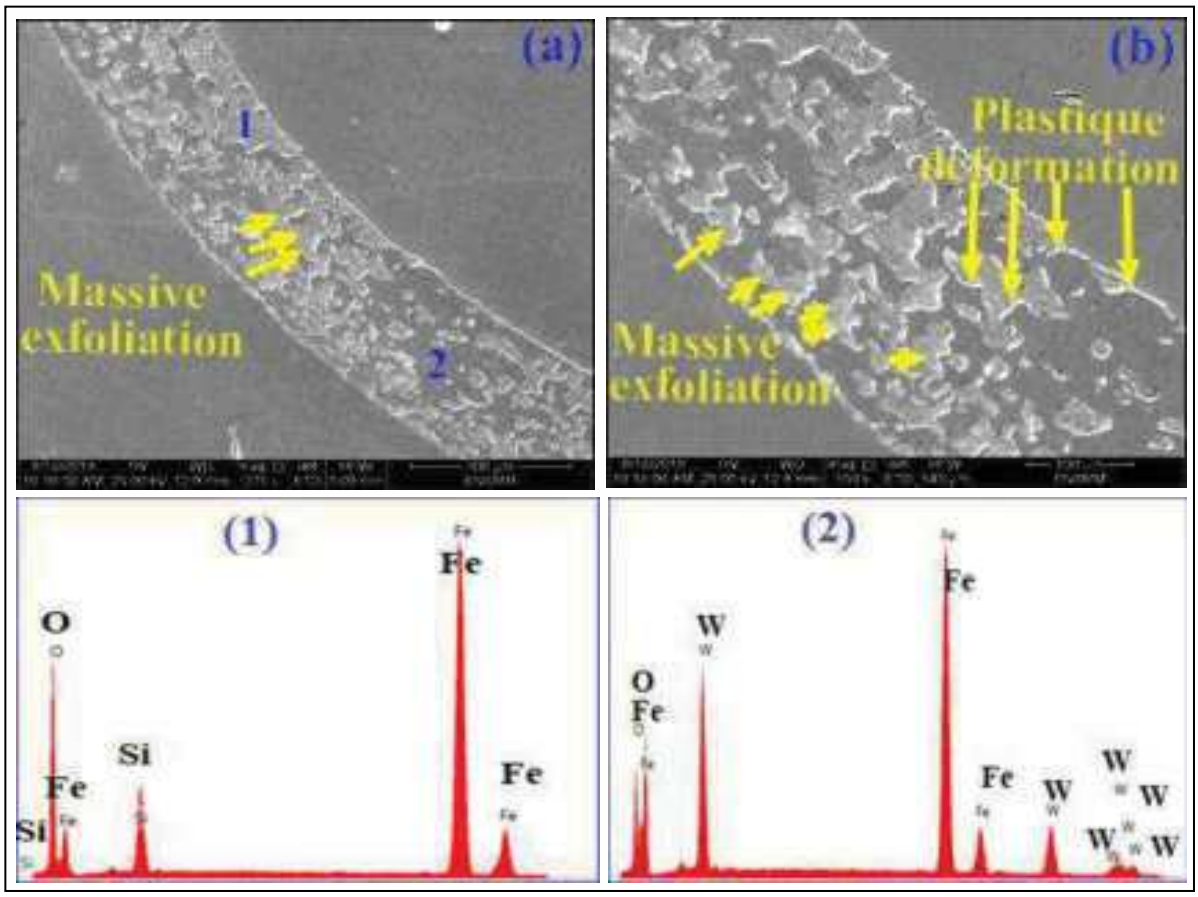

Fig. 7. Backscattered electron image mode (BSE) SEM micrograph of the wear track of the as-sprayed **(P05)** coating produced after ball-on-disk testing at room temperature against WC steel balls.

Creative Commons Attribution-Non-Commercial-No Derivatives 4.0 International License (CC BY-NC-ND)

Conclusions

Two NiWCrBSi coatings were successfully sprayed onto a mild steel substrate, using oxyacetylene flame spray process with a reducing flame stoichiometry and two different spraying distances. Coatings underwent dry sliding ball-on-disk wear test. Microstructures and wear scars were investigated by SEM, EDS. The following conclusions can be drawn:

- A typical lamellar microstructure was found for both coatings. The P 05 coating was characterized by a higher level of unfused particles.
- A better friction coefficient is obtained by the P05 coating
- The predominant wear mechanism for the P 05 coating was controlled by local delamination and the growth of a dense, smooth, oxidized tribolayer. For the P 03 coating, the predominant wear mechanism was massive exfoliation of large portions of the coating.
- A high spray distance was not beneficial to the wear performance of the coating.
- A high spraying distance was not beneficial to the coating wear performance.

References:

[1] Davis, J. R. ***(Ed.).*** *(2004). Handbook of thermal spray technology. ASM international.*

[2] Scrivani, A., Ianelli, S., Rossi, A., Groppetti, R., Casadei, F., & Rizzi, G. *(2001). A contribution to the surface analysis and characterisation of HVOF coatings for petrochemical application. Wear,* ***250(1-12),*** *107-113.*

[3] Mann, B. S., Arya, V., Maiti, A. K., Rao, M. U. B., & Joshi, P. *(2006). Corrosion and erosion performance of HVOF/TiAlN PVD coatings and candidate materials for high pressure gate valve application. Wear,* ***260(1-2),*** *75-82*.

[4] Mann, B. S., Arya, V., & Joshi, P. *(2005). Advanced high-velocity oxygen-fuel coating and candidate materials for protecting LP steam turbine blades against droplet erosion. Journal of materials engineering and performance,* ***14(4),*** *487-494.*

[5] Rastegar, F., & Richardson, D. E. *(1997). Alternative to chrome: HVOF cermet coatings for high horse power diesel engines. Surface and Coatings Technology,* ***90(1-2),*** *156-163.*

[6] Bolelli, G., Bonferroni, B., Laurila, J., Lusvarghi, L., Milanti, A., Niemi, K., & Vuoristo, P. *(2012). Micromechanical properties and sliding wear behaviour of HVOF-sprayed Fe-based alloy coatings. Wear,* ***276,*** *29-47.*

[7] Kim, H. J., Hwang, S. Y., Lee, C. H., & Juvanon, P. *(2003). Assessment of wear performance of flame sprayed and fused Ni-based coatings. Surface and Coatings Technology,* ***172(2-3),*** *262-269.*

[8] Houdková, Š., Smazalová, E., Vostřák, M., & Schubert, J. *(2014). Properties of NiCrBSi coating, as sprayed and remelted by different technologies. Surface and Coatings Technology,* ***253,*** *14-26.*

[9] Otsubo, F., Era, H., & Kishitake, K. *(2000). Structure and phases in nickel-base self-fluxing alloy coating containing high chromium and boron. Journal of Thermal Spray Technology,* ***9(1),*** *107-113.*

Creative Commons Attribution-Non-Commercial-No Derivatives 4.0 International License (CC BY-NC-ND)

[10] Serres, N., Hlawka, F., Costil, S., Langlade, C., & Machi, F. *(2011). An investigation of the mechanical properties and wear resistance of NiCrBSi coatings carried out by in situ laser remelting. Wear,* ***270(9-10),*** *640-649.*

[11] Zhao, W. M., Wang, Y., Han, T., Wu, K. Y., & Xue, J. *(2004). Electrochemical evaluation of corrosion resistance of NiCrBSi coatings deposited by HVOF. Surface and Coatings Technology,* ***183(1),*** *118-125.*

[12] Bergant, Z., & Grum, J. *(2009). Quality improvement of flame sprayed, heat treated, and remelted NiCrBSi coatings. Journal of thermal spray technology,* ***18(3),*** *380-391.*

[13] Habib, K. A., Cano, D. L., Heredia, J. A., & Mira, J. S. *(2019). Effect of post-coating technique on microstructure, microhardness and the mixed lubrication regime parameters of thermally-sprayed NiCrBSi coatings. Surface and Coatings Technology,* ***358,*** *824-832.*

[14] Rachidi, R., El Kihel, B., & Delaunois, F. *(2019). Microstructure and mechanical characterization of NiCrBSi alloy and NiCrBSi-WC composite coatings produced by flame spraying. Materials Science and Engineering: B,* ***241,*** *13-21.*

[15] Serres, N., Hlawka, F., Costil, S., Langlade, C., Machi, F., & Cornet, A. *(2009). Dry coatings and ecodesign: Part. 2—Tribological performances. Surface and Coatings Technology,* ***204(1-2),*** *197-204.*

[16] García, A., Cadenas, M., Fernandez, M. R., & Noriega, A. *(2013). Tribological effects of the geometrical properties of plasma spray coatings partially melted by laser. Wear,* ***305(1-2),*** *1-7.*

[17] Zhao, W. M., Wang, Y., Dong, L. X., Wu, K. Y., & Xue, J. *(2005). Corrosion mechanism of NiCrBSi coatings deposited by HVOF. Surface and Coatings Technology,* ***190(2-3),*** *293-298.*

[18] Miguel, J. M., Guilemany, J. M., & Vizcaino, S. *(2003). Tribological study of NiCrBSi coating obtained by different processes. Tribology international,* ***36(3),*** *181-187.*

[19] Houdková, Š., Zahálka, F., Kašparová, M., & Berger, L. M. *(2011). Comparative study of thermally sprayed coatings under different types of wear conditions for hard chromium replacement. Tribology Letters,* **43(2),** *139-154.*

[20] Huang, S. W., Samandi, M., & Brandt, M. *(2004). Abrasive wear performance and microstructure of laser clad WC/Ni layers. Wear,* ***256(11-12),*** *1095-1105.*

[21] Lu, S. P., Kwon, O. Y., & Guo, Y. *(2003). Wear behavior of brazed WC/NiCrBSi (Co) composite coatings. Wear,* ***254(5-6),*** *421-428.*

[22] Grewal, H. S., Singh, H., & Agrawal, A. (*2013). Understanding Liquid Impingement erosion behaviour of nickel–alumina based thermal spray coatings. Wear,* ***301(1-2),*** *424-433.*

[23] Paul, C. P., Mishra, S. K., Tiwari, P., & Kukreja, L. M. *(2013). Solid-particle erosion behaviour of WC/Ni composite clad layers with different contents of WC particles. Optics & Laser Technology,* ***50,*** *155-162.*

Creative Commons Attribution-Non-Commercial-No Derivatives 4.0 International License (CC BY-NC-ND)

Algerian Journal of Engineering Architecture and Urbanism Vol. 5 Nr. 3 2021
ISSN: 2588-1760

IMPACT OF DRILLING ON A CARBON-ORTHOCRYL COMPOSITE MATERIAL FOR THE PRODUCTION OF AN ORTHOPAEDIC PROSTHESIS

Younès MENAIL
Enseignant-chercheur, (Dr), *University Badji Mokhtar, Sidi Ammar, BP 12, 23000 - Annaba, Algerie.*
menailyounes43@gmail.com

Abstract:
The production of a carbon-orthocryl orthopaedic prosthesis requires two holes of different diameters. The large diameter is used to fix the leg shaft and the small diameter is used to fix a valve.
In order to study the impact of the large bore, which carries the full weight of the disabled person, on the small bore, we made a series of carbon-orthocryl test pieces. We then carried out cross-sections, frontal and longitudinal sections on the different specimens in order to detect the various degradations within the material.
The microscopic study on SEM allowed us to detect interlaminar laminations at the beginning and at the end of the drilling in mode I. Matrix and fibre breaks were also detected.
The propagation of delamination from the large bore to the small bore is very difficult to quantify and requires an appropriate investigation methodology. Our objective is to find the best way to monitor and quantify this propagation. The work we are doing is not yet complete and is part of a research project that is still ongoing.

Key words: Carbone, époxy, orthopédie, traction, MEB

Introduction:

Composite materials have established themselves as materials of the 21st century. Due to their performance and consumption, they have far surpassed conventional materials such as wood, metals, alloys, etc. These materials are so efficient that they are used in various fields. Aviation alone uses more than half the weight of its machines in composite materials. The assembly of a commercial aircraft requires a large number of holes to be drilled. A large number of studies have investigated the drilling of composite materials and have revealed that the initial defects and damage potentially generated by drilling penalise the strength of the machined composite material. This is because the drilling process generates defects at the entrance, on the wall and at the exit of the hole in the composite laminate.
Carbon fibre composite material is very efficient, light, strong, does not corrode and is easy to mould. These are all requirements for this material to be used in orthopaedic prostheses. The only drawback is the price. But the price-quality ratio makes this composite an irreplaceable element.
The ONAAPH Company, which makes these prostheses, has opted for carbon fibers, after having used wood, metal and glass fibers. This choice responds to a physical and psychological need for the motor handicapped. It is the only material that ensures comfort and autonomy, two criteria that change a man's life.

Translated with www.DeepL.com/Translator (free version)

Problematic:

Creative Commons Attribution-NonCommercial-NoDerivatives 4.0 International License (CC BY-NC-ND)

The prosthesis is made by infusion moulding of the carbon fibres with an orthocryl resin, which gives good results. The socket, which receives the thigh of the disabled person, has to be drilled twice with different diameters. It is known from the literature and research results that the drilling causes double lamination and other damage. In order to contribute to the increase of the life span of these prostheses and to the safety of the users, we opted for a practical study based on the identification of the various degradations. For this purpose, we proceeded to the census of the degradations caused by the drillings and the propagation of these degradations in the material.

The use of the SEM allows us to detect and follow the different degradations with precision.

Materials and methods:

The carbon plates were made in-house by the technicians who make the orthopaedic prostheses. They used the same percentage of fibre and carbon to maintain the same characteristics.

Moulding

We made laminated composite plates with three plies of twisted carbon fibers by infusion moulding, with a vacuum of 0.8 bar for six hours. These plates were cured in an oven at 80°C for 8 hours in an autoclave.

Plates

After polymerization, these plates were cut into test tubes of 220x30x2mm3. Then they were drilled with two holes Ø 8 and Ø 12, with the following characteristics, table 1

Fiber	weaving	surface density [g/m^2]	mass fraction [%]	Resin	supplier	Dimensions [mm^3]	Layer	weight [g]
Carbon	taffeta	300	35	Epoxy c-orthocryl	Otto bock Germany	220x30x2	3	12

Table 1. Characteristics of the plates

Protocol

The protocol to be followed consists of cutting the specimens in five planes, Figure 1.

Plane 1, longitudinal section along the length.

This section gives us an idea of the interior of the material away from the drilling area. It can be used as a comparison with the machined area.

Plan 2, front cut according to thickness.

The frontal cut touches a larger surface of the material. It gives us an idea of the quality of the moulding and the existing defects.

Plan 3, cross section according to the width, passing through the axis of the small hole.

Creative Commons Attribution-NonCommercial-NoDerivatives 4.0 International License (CC BY-NC-ND)

This section allows us to see the impact of the drilling on the material. The shots are taken at the bottom of the hole, to see in detail the different degradations.

Plan 4, cross-section along the width, passing through the axis of the large hole.

This section, like the one for the small hole, allows us to see the different degradations caused during drilling.

Plan 5, cross-section along the width, passing between the two holes.

This section allows us to follow the progression of delamination between the holes. Several cuts are normally necessary with a precise pitch to really confirm this progression.

All sections will be examined under the SEM electron microscope to detect the various defects existing after moulding and to detect the defects generated within the material by the drilling.

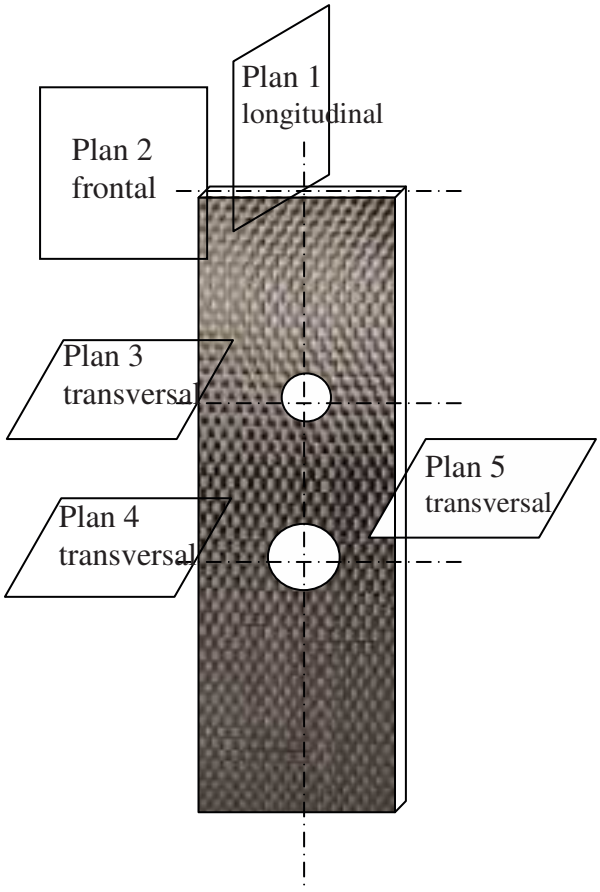

Fig1. Sectional drawings

Results and discussions:

The results obtained from the interpretation of the SEM photographs allow different degradations to be distinguished. Interpretations will be made according to the cross-sectional drawings, figures 2-6.

Section according to plan 1:

Creative Commons Attribution-NonCommercial-NoDerivatives 4.0 International License (CC BY-NC-ND)

Algerian Journal of Engineering Architecture and Urbanism Vol. 5 Nr. 3 2021
ISSN: 2588-1760

This sectional plane allows us to see a certain homogeneity of the surfaces. This implies that the material is well moulded and that it does not present any apparent defects. Figure 2a shows the different facies of the three plies that form the composite. It is a twill and is balanced. Figure 2b shows a higher magnification, and the carbon fibre pieces are due to the cutting of the specimen.

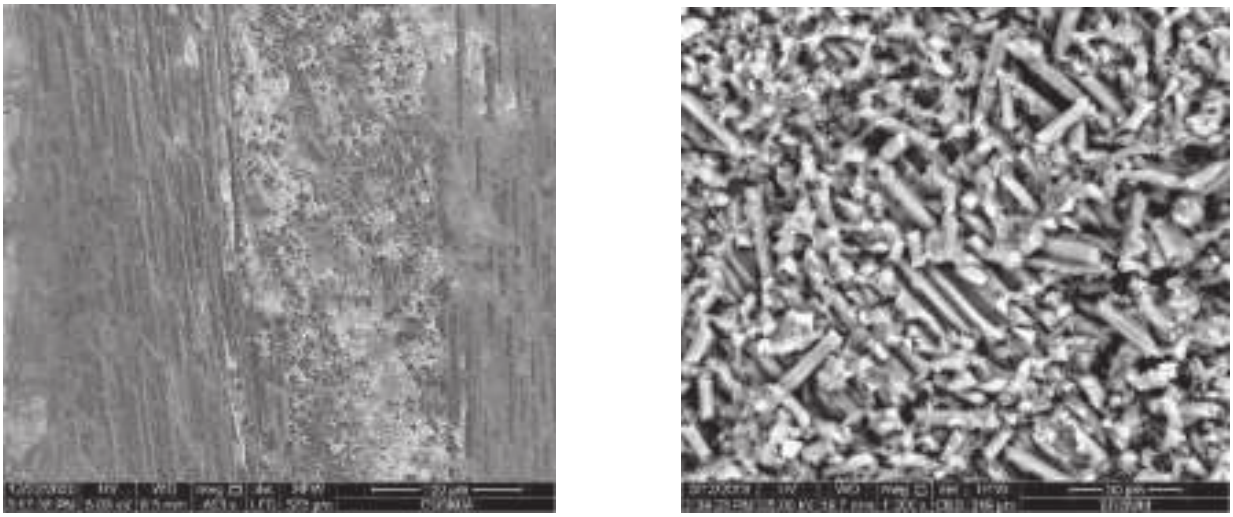

(a) (b)

Fig 2: Different facies along sectional plane 1 (longitudinal)
(a) Different fiber orientations of the carbon twill
(b) Fiber cross-section in the plane orthogonal to the figure

Section according to plane 2:

This section gives us an idea of the cohesion of the material and the distribution of the resin within the fibres. Figure 3a shows a relatively uniform surface with a good distribution of resin. Figure 3b (at high magnification x1200) shows the boundary between two bundles of carbon fibres which are welded together and show no defects such as matrix breakage or delamination. This demonstrates good moulding, cohesion and wetting.

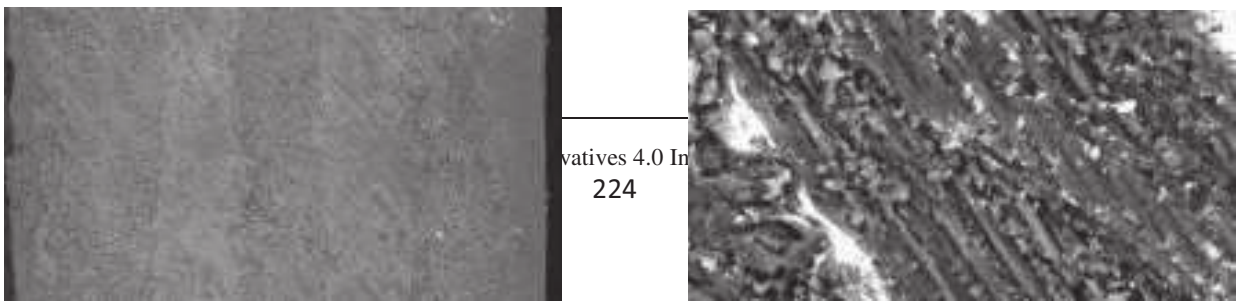

vatives 4.0 In

Algerian Journal of Engineering Architecture and Urbanism Vol. 5 Nr. 3 2021
ISSN: 2588-1760

Fig 3. Different facies according to section plane 2 (frontal)
(a) Section along the large surface
(b) Detail of section (a)

Section according to plan 3:

This cross-section at the bottom of the 8 mm diameter hole shows significant delamination caused by the drill bit during drilling. Figure 4a shows two interlaminar delaminations in mode 1, at the entrance and exit of the hole. Between the two we see another delamination between the fibre strands. Figure 4b shows delamination in Mode 2, where the fibres are oriented in the direction of rotation of the drill. There is some resistance from the fibres which elongate before yielding to the cutting force which increases as the drill penetrates the composite.

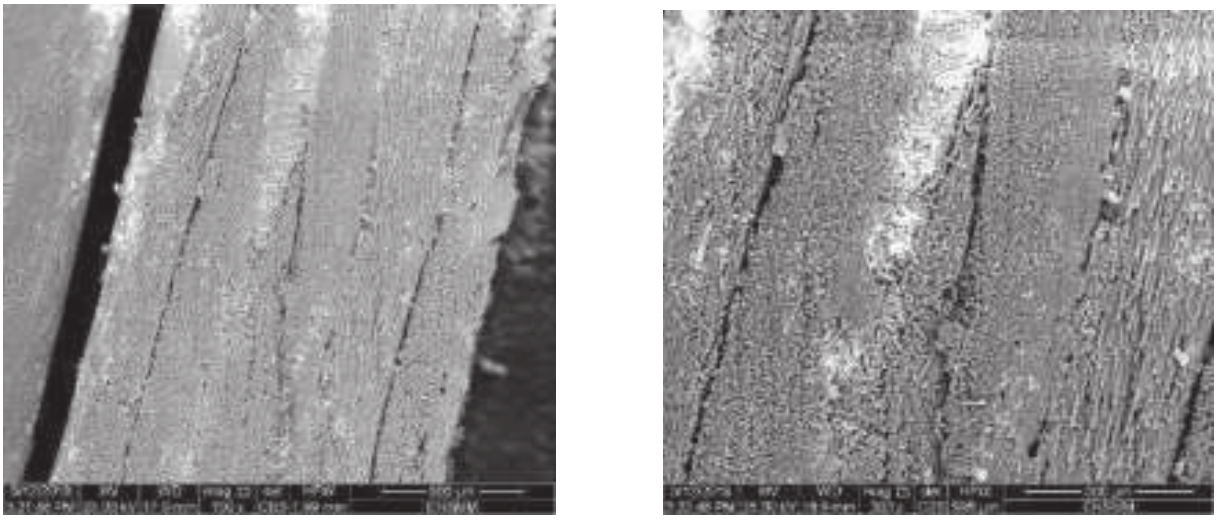

Fig 4. Different facies according to cutting plane 3 (transverse)
(a) Section according to the hollow transverse plane of the Ø 8 hole
(b) Detail of cutting plane 3a

Section according to drawing 4:
The section according to plane 4 at the bottom of the 12 mm diameter hole shows delamination all along the section. Figure 5a shows a double delamination caused by the drill bit during drilling. The first delamination occurs during drill penetration and the second

Creative Commons Attribution-NonCommercial-NoDerivatives 4.0 International License (CC BY-NC-ND)

Algerian Journal of Engineering Architecture and Urbanism Vol. 5 Nr. 3 2021
ISSN: 2588-1760

delamination occurs during drill exit. Figure 5b also shows a double delamination. We also show a matrix break parallel to the delamination.

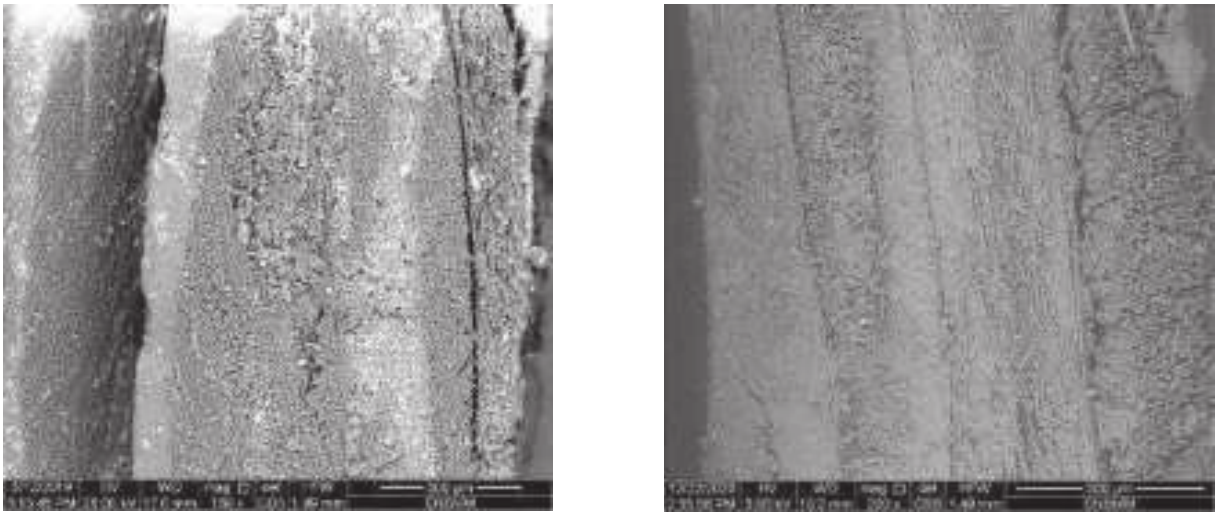

Fig 5. Different facies according to cutting plane 4 (transverse)
(a) Section according to the hollow transverse plane of the Ø 12 hole
(b) Detail of cutting plane 4a

Section according to plane 5:
The section according to plane 5, the plane between the two holes, shows interlaminar delamination. It turns out that a single cutting plane between the two holes is not sufficient to follow the delamination progression between the two holes.

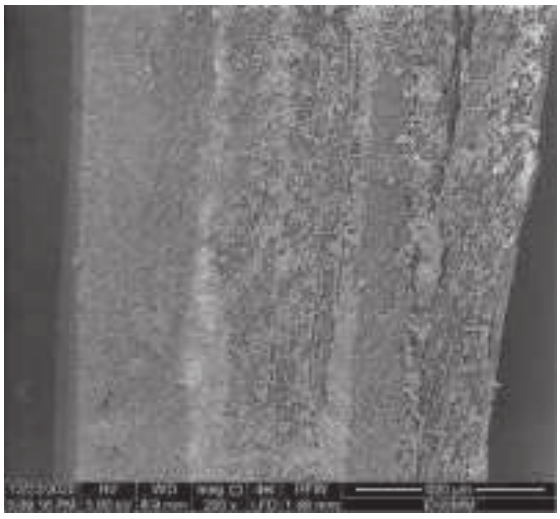

Fig 6. Facies along section 5 (transverse)

Conclusion:
This work allowed us to highlight the various degradations suffered by the carbon fibre and C-Orthocryl resin material. The material itself before drilling shows good cohesion and good wetting of the fibres. It does not have any defects that affect its integrity.

Creative Commons Attribution-NonCommercial-NoDerivatives 4.0 International License (CC BY-NC-ND)

After drilling, the material shows various degradations induced by this machining. The different sections in the different planes, longitudinal, frontal and transverse, show delaminations, matrix and fibre breaks. These different degradations, by creating cracks in mode 1 and 2 will weaken the material. These induced defects require solutions adapted according to the machining parameters (cutting speed, feed rate, etc.), according to the drilling techniques (pre-hole, different diameters, ...), according to the machining fixtures (drill bush, clamping, ...). These adapted and combined solutions make it possible to reduce the effects of drilling.

We can conclude that the C-Orthocryl carbon composite material withstands the effects of drilling well, despite the various degradations, and that it can play its role as an orthopaedic prosthesis well. It should be noted that its various degradations will be inhibited by mechanical parts during the assembly of the prostheses.

References:

Berthelot J.-M. (2005), Matériaux composites: comportement mécanique et analyse des structures. Paris; Londres: Editions Tec & Doc.

Persson E., Eriksson I., and Zackrisson L. (1997), Effects of hole machining defects on strength and fatigue life of composite laminates," Compos. Part Appl. Sci. Manuf., vol. 28, no. 2, pp. 141–151,.

Gohorianu G. (2008), Interaction entre les défauts d'usinage et la tenue en matage d'assemblages boulonnés en carbone/époxy," Université Toulouse III.

Piquet R., Ferret B., Lachaud F. and Swider P. 2000, Experimental analysis of drilling damage in thin carbon/epoxy plate using special drills, Composites: Part A, 31, 1107-1115.

Landon Y. and Chérif M. 2013, Characterization of the surface quality of holes drilles in CFRP laminates, Adv. Mater. Res., vol. 698, pp. 107–116.

Benezech L., Landon Y., Rubio W. (2012) Study of manufacturing defects and tool geometry optimisation for multi-material stack drilling, International Journal Advanced Materials Research, 423, 1-11

Han, S. H., Oh H. J. and Kim S. S. (2014), Evaluation of the impregnation characteristics of carbon fiber-reinforced composites using dissolved polypropylene, Compos. Sci. Technol., vol. 91, pp. 55–62.

Baudrye, P. (2004), Etude du résidu carboné et de la liaison fibre/matrice lors de la pyrolyse de composites carbone/phénolique. Thèse de doctorat de l'Ecole doctorale de sciences chimiques de l'université Bordeaux 1.

Poyyathappan, K., Bhaskar, G.B., Pazhanivel1 K., Rajesh S. and Sagadevan, S. (2018), Mechanical and Microstructural Characteristics of the Glass – Carbon Fiberous Composite Materials. Taga journal vol. 14 pp 2684-2696.

Ihiawakrim, D. (2019), Etude par les techniques avancées de microscopie électronique en transmission de matériaux fragiles. Matière Condensée [cond-mat]. Université de Strasbourg France.

Turla, P. Sampath Kumar S., Harshitha Reddy P., Chandra Shekar K.. (2014), Processing and Flexural Strength of Carbon Fiber and Glass Fiber Reinforced Epoxy-Matrix Hybrid Composite, International Journal of Engineering Research & Technology (IJERT) Vol. 3 Issue 4.

Creative Commons Attribution-NonCommercial-NoDerivatives 4.0 International License (CC BY-NC-ND)

Algerian Journal of Engineering Architecture and Urbanism Vol. 5 Nr. 3 2021
ISSN: 2588-1760

CHOICE BETWEEN TWO GLASS-EPOXY COMPOSITES WITH SERGE AND UD TEXTURE FOR THE REALISATION OF A BOAT HULL

Younès MENAIL
Enseignant-chercheur, (Dr), *University Badji Mokhtar, Sidi Ammar, BP 12, 23000 - Annaba, Algerie.* *menailyounes43@gmail.com*

Abderahim EL MAHI
Enseignant-chercheur, (Pr), *University of Maine, av. O. Messiaen, 72085 Le Mans, France.* *menailyounes43@gmail.com*

Bachir REDJEL
Enseignant-chercheur, (Pr), *University Badji Mokhtar, Sidi Ammar, BP 12, 23000 - Annaba, Algerie.* *menailyounes43@gmail.com*

Abstract:
In order to make a boat hull, we opted for a glass epoxy composite material. In order to make a better choice, we had to choose between two different textures, 2-2 twill texture and UD unidirectional.
For this purpose we made two series of specimens of the same nature and dimensions, with two different textures. We subjected them to the same number of tensile fatigue cycles and to the same ageing times in salt water. The study of the impact of tensile fatigue and salt water ageing of the two materials is based on the results of the stress-strain relationship within the materials. The evolution of the Young's modulus and the stress gives us an idea of the strength of these materials. In order to refine the results of this study, we used the acoustic tool to get a precise idea of the effect of salt water after fatigue on the structure of both materials.

Key words: Epoxy glass, fatigue, ageing, salt water, acoustic

Introduction:

Composite materials are used in a wide range of fields: aerospace, aeronautics, car manufacturing, transport, shipbuilding, etc.
The choice of the material and its components according to its use, its life span, its cost and its method of production has led researchers to optimise its performance as much as possible, through simulations and practical research in situ. This was done in order to compare the two materials in the study, UD glass and twill glass, to determine which is more resistant.
The influence of moisture on the change in the behaviour of the composite has been studied by several researchers, Bunsell, among others, has dealt with this phenomenon well. The various studies have shown that while the intake of water generally increases the mass of the specimen, in other cases, the opposite effect is manifested by a decrease in weight due to the destruction of the resin following leaching. This degradation occurs through plasticisation or physical ageing, followed by hydrolysis or chemical ageing resulting in damage by osmotic cracking.
In order to fully understand how the different damages manifest themselves, a quantitative approach to the acoustic emission technique has been developed by some authors.

Creative Commons Attribution-NonCommercial-NoDerivatives 4.0 International License (CC BY-NC-ND)

The work of Åberg and Gudmundson De Groot et al, Che et al, Kim and Lee, Karger-Kocsis et al, Kotsikos et al and Benzeggagh et al. classified the amplitudes into three or four groups, from the lowest to the highest.

The purpose of this paper is to determine the effect of salt water on two Ud-glass laminates and glass twilled with an epoxy amine resin, aged for 5 to 7 months at pressure and ambient temperatures (15 to 25°C). Tensile fatigue to failure highlights the effect of ageing.

Problematic:

The experimental study is conducted by a destructive method in quasi-static tension and tensile fatigue before natural ageing in synthetic seawater at 37‰, in order to determine the evolution of the mechanical characteristics in the longitudinal direction of the reinforcement of the studied laminates (modulus of elasticity and rupture). This study is carried out with the aim of comparing two materials and making a choice based on the criteria of resistance to salt water and its hazards and the stresses to which its materials will be subjected at sea.

Materials and methods:

Materials

The materials used are epoxy glass laminates, with two different laminations, UD and twill, made of 4 plies with a mass per unit area of 300g/m^2. The mixture developed for the production of our specimens is based on SR 1500 epoxy resin combined with SD 2505 amine hardener. It was processed by contact moulding under vacuum, at a pressure of 0.3 bar for 6 hours. Polymerization took place in an oven at 80°C for 8 hours. The specimens were then cut to the dimensions 200x20x1 mm^3.

Fatigue

Tensile fatigue was carried out under loading at a constant speed of 1mm/min, under controlled displacement up to 50% of the static displacement at failure. Then we imposed fatigue amplitude of 10% of the displacement at failure. For this article, we opted for 10,000 cycles out of the ten actually performed.

Natural ageing

The specimens are separated into two batches to be immersed in synthetic seawater at 37‰. Each batch is immersed for 1000h. Damage by osmotic cracking linked to a very important water uptake was identified beyond 120h of ageing. These results therefore confirm the state of damage of the material. At 20°C, the specimens quickly reached equilibrium (35 days), at 0.35% absorption, and a Frick model was used to correctly describe the absorption kinetics.

Static testing

The stress-strain curves for Ud 300 and twill 300 are shown in Figure 1, table 1. It is manifested by a quasi-linear variation of the stress as a function of the strain. This behaviour is the result of the progressive rupture of the matrix, the most brittle element of the composite, followed by decohesions and possible delaminations. Once embrittled, the material fails under the effect of the stress, characterised by a sudden drop, which implies a rupture of the fibres and the end of the specimen's life.

Creative Commons Attribution-NonCommercial-NoDerivatives 4.0 International License (CC BY-NC-ND)

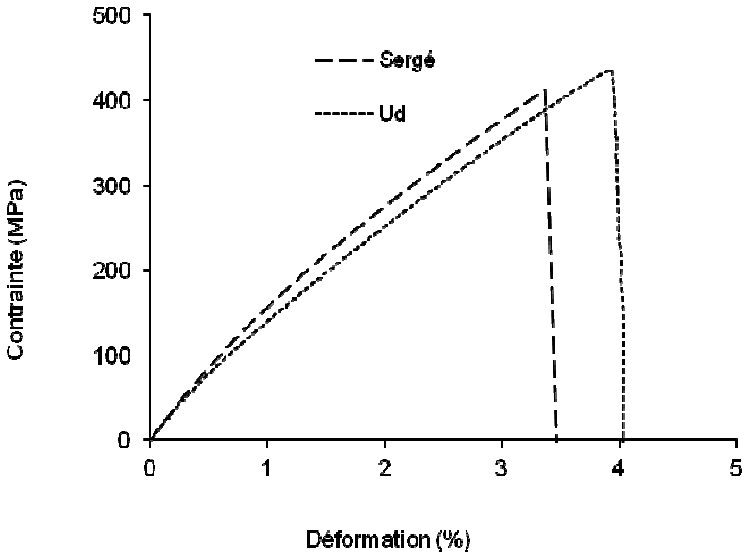

Fig 1: Stress-strain curve

Fiber	Nature	density[g/m^2]	Mass Fraction [%]	Resin	Supplier	Dimensions [mm]	Ply	weight [g]
Glass E	Twill	300	65	Epoxy SR 1500 Hardener SD 2505	Sicomin France	200x20x1	4	7.2
Glass E	Ud	300	67				4	7,2

Table 1 Specimen characteristics

Fatigue tests

Tensile fatigue was carried out under loading at a constant speed of 1mm/min, under controlled displacement up to 50% of the static failure displacement. Then we imposed fatigue amplitude of 10% of the displacement at failure.

Creative Commons Attribution-NonCommercial-NoDerivatives 4.0 International License (CC BY-NC-ND)

Fig. 2 Fatigue machine and acoustic acquisition system

The control and data acquisition are done by computer to record the evolution of the stress as a function of the deformation. The tests are performed at room temperature (15 to 25°C).

The curves of the fatigue test results are shown in Table 1. The results obtained show that the loss of stiffness, measured by the Fmax/F0max ratio until the specimen breaks, takes place in three phases. Initially, it is manifested by a sudden decrease in the Fmax/F0max ratio from the first cycles, figure 2. The decrease then becomes very slow in the second phase, which corresponds to the stable propagation of the latter, as well as the initiation of delamination, corresponding to almost the entire life of the specimen.

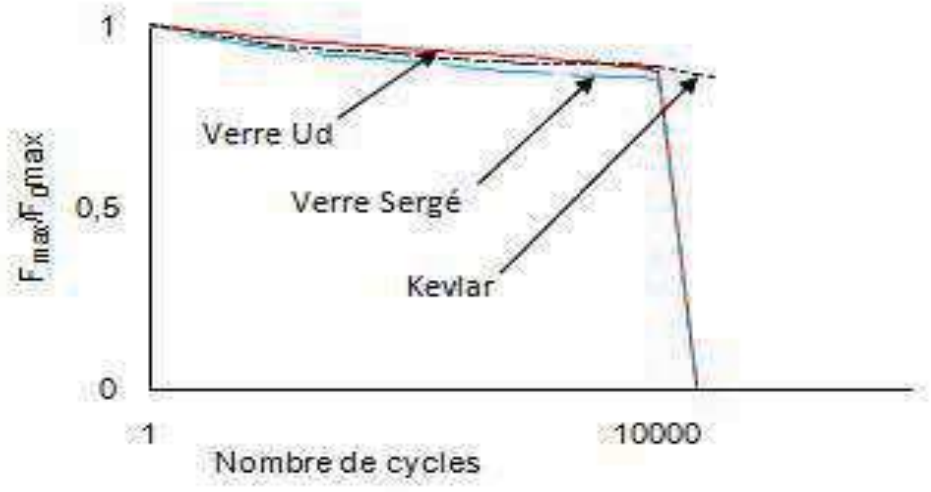

Fig. 2 Fatigue of the three materials

Monitoring by acoustic emission

Creative Commons Attribution-NonCommercial-NoDerivatives 4.0 International License (CC BY-NC-ND)

Acoustic monitoring is very valuable, as it allows us to visualise the different damages suffered by the different materials. Three piezoelectric sensors are placed along the specimen and connected to amplifiers. The monitoring and acquisition of the acoustic data is done in parallel with the mechanical tests, using another software and another computer. The acquisition system must be calibrated before use, using a lead breaker, to determine the safety threshold, to avoid spurious noise.

It is very easy to distinguish the effects of the two operations of loading and fatigue. The first operation manifests itself from the outset by a matrix break followed by delamination and then fibre breakage, over a very short time corresponding to the sudden loading of the specimen. Then fatigue begins, which manifests itself in matrix failure throughout the operation. Delamination is very low and fibre breakage is very rare. Based on these results, we can say that the material is not very resistant to sudden stresses and is better adapted to long and constant fatigue.

- Using the acoustic tool, Figure 3 allows us to visualise the different types of degradation of the two materials and to understand the different stages each material has to go through before failure.
- The Ud-glass specimen, is the specimen that exhibits all types of stresses from the beginning to the end. This is due to the nature and texture of the material.

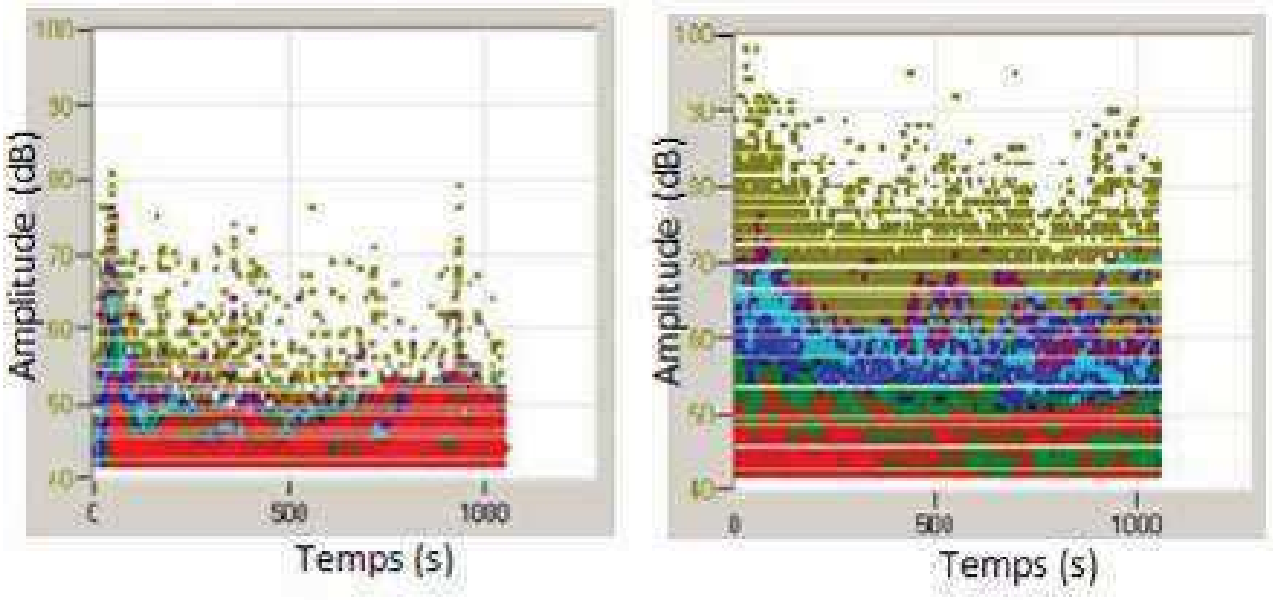

Fig. 3 Fracture after 10,000 fatigue cycles
(a) Twill glass (b) Ud glass

Conclusion:

Creative Commons Attribution-NonCommercial-NoDerivatives 4.0 International License (CC BY-NC-ND)

The strength of the material depends on its nature and texture. The Ud-glass specimen and the twill glass specimen with identical nature, equal dimensions and different texture do not show the same fatigue profile. This allows us to say that the evolution of the degradation of a material (matrix rupture, delamination, decohesion and fibre rupture) as a function of fatigue is indicative of the behaviour of the material and its characteristics. This degradation depends on its nature and texture. Hence the interest of the choice of material for the realization of the parts according to their use. The acoustic tool has enabled us to highlight the resistance of Ud glass compared to twill glass.

The various studies to which we referred showed that the osmotic origin of the degradation process of composite materials was confirmed by preliminary tests in sea water and distilled water. The progressive fall in mechanical characteristics is attributed to the plasticization of the structural resin by water when the material is saturated. The progressive decline in mechanical properties is attributed to the plasticisation of the structural resin by the water when the material is saturated, followed by the attack of the resin in the laminate between two plies, leading to a decline in the mechanical properties.

In conclusion, we can say that, based on the static tests, fatigue tests and acoustic results, the UD-textured glass-epoxy composite material is stronger than the twill-textured material. And that this material is safer for boat building.

References:

Bunsell A. R. *(1989), L'absorption d'eau par les matériaux composites à matrice organique- CODEMAC, 2ème Ecole d'automne, GUETARY.*

Perreux D., Suri C., Varchon D. et Oytana C., *"Endommagement mécanique de matériaux composites. Role sur les propriétés hygrothermiques" La construction navale en composites. Paris, 7-9 décembre 1992, IFREMER, Actes de colloques n°15, communication n°36.*

Vigier G. and Tatibouet J., *"Physical ageing of amorphous and semicrystalline poly(ethylene terephtalate) ". Polymer, vol. 34, n° 20, 1993, pp. 4257-4266.*

Gautier L., Mortaigne B., Bellenger V. and Verdu J., *(2000), Osmotic cracking nucleation in hydrothermal-aged polyester matrix. Polymer, vol. 41, pp. 2481-2490.*

Odru P., Dewimille B., Grosjean F. et Huvey M*. (1996) Canalisation composites pour applications pétrolières marines : les problèmes de durabilité. Journées Scientifiques et Techniques AMAC. Moret sur Loing 30-31 mai 1996. France.*

Talreja R., *(1981).Fatigue of composite materials: damage mechanisms and fatigue-life Diagrams". Proceedings of Royal Society London, A378, pp 461-475.*

Gaumet S., Siampiringue N. and Lemaire J., *(1996)"Durabilité des matériaux composites. Comment réaliser un photovieillissement accéléré fiable. Un exemple précis : la résine époxy (DGEBA)"Annale des composites, AMAC, France, , pp. 85-90.*

Benzeggagh M.-L., Barre S., Echalier B. et Jacquemet R (*1992****).*** *Etude de l'endommagement de matériaux composites à fibres courtes et à matrice thermoplastique. In: AMAC Journées Nationales Composites, Paris , vol. 8, pp.703-714*

Kline R. A., Green R. E. et Palmer, C. H. (*1981****)*** *Acoustic emission waveforms from cracking steel: experiment and theory. Journal of Applied Physics Volume 52,p. 141–146.*

Wadley H. N. G., Scruby C.B. et Shrimpton, G. *(1981) Quantitative acoustic emission source characterisation during low temperature cleavage and intergranular fracture., Acta Meterialia, Volume 29, p. 399–414.*

Ceausescu-Ersen *(2004) E.A. Application de la technique d'émission acoustique à la caractérisation de matériaux céramiques évolutifs thèse de l'Université de Limoges,.*

Åberg M. et Gudmundson P.(*2000) Micromechanical modeling of transient waves from matrix cracking and fiber fracture in laminated beams. International Journal of Solids and Structures, , Volume 37, Issue 30, pp 4083-4102.*

Creative Commons Attribution-NonCommercial-NoDerivatives 4.0 International License (CC BY-NC-ND)

Algerian Journal of Engineering Architecture and Urbanism Vol. 5 Nr. 3 2021
ISSN: 2588-1760

NUMERICAL STUDY INVESTIGATING THE PERFORMANCE OF HVIGBT-NPT UNDER FUNCTIONAL AND THERMAL STRESS

Lynda BENBAHOUCHE 1
Chef Equipe Laboratory Intelligent Systems LSI, Dr Enseignant at Faculty of technology, U.F.A.S University, Setif1, 19000, Algeria
e-mail: lybenbah@yahoo.fr

Billal BISBIS 2
Master Diploma at Electronics Department U.F.A.S University, Setif1, 19000, Algeria,
e-mail: bisibis03@gmail.com

Abstract:

In recent decades, the reliability of electrical systems has been the focus of many research projects. Indeed, the importance of the reliability of electrical systems is nowadays unequivocal, since a degradation of these systems is likely to cause enormous technological, financial and human damage.

The main goals of this paper are to study, to optimize the design of the news generations available HVIGBT NPT from IXYS according to a criterion of reliability associated with a functional and thermal stress coupling. The interest of this study is to provide a rigorous framework for analyzing the performance of the HVIGBTs in question by comparing the different static and dynamic parameters before, after stress and under the coupling effect of the two stresses.

Discussions and results presented in this paper show that the stress coupling (functional and thermal stress) could therefore reduce the value gap of some parameters caused by thermal stress. We attribute this behavior to an implemented compensation mechanism. Thus the choice of stress conditions can induce an optimization of the performances of HVIGBTs.

Key words: HVIGBT- NPT, avalanche capability, thermal stress, functional stress, breakdown

Introduction:

The arrival on the market of large-gap components makes it possible to consider the manufacture of power electronics modules with high compactness or high power density. In addition, the level of maturity of components such as IGBTs has increased significantly, making it possible to produce in industrial applications as well as integration into optimized functions. Thus, new technological solutions, chosen to allow operation under a constrained environment, become the critical factors of such assemblies and aim to identify the modes of failure[. IGBT transistors are the most frequently used power switches in different types of industrial applications : transport systems, from rail to aeronautics. In all these applications, the reliability of these components is still a critical point.

Problematic:

In this context, the aim of this paper is to highlight the most popular stresses: functional stress and thermal stress in HVIGBT-NPT and their effects on the chip and on its immediate neighborhood to evaluate the effects of damage and identify the failure modes. Subsequently, we focused on the functional stress and thermal stress where we showed in a detailed manner the different effects induced on several varieties of HVIGBT (low, medium, and high frequency) and very high IGBT belonging to the IXYS firm.

Creative Commons Attribution-NonCommercial-NoDerivatives 4.0 International License (CC BY-NC-ND)

Algerian Journal of Engineering Architecture and Urbanism Vol. 5 Nr. 3 2021
ISSN: 2588-1760

Results and discussions:

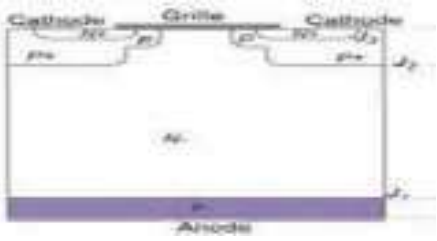

Fig1. Cross section of NPT IGBT device

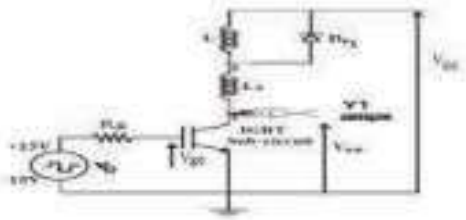

Fig2. Chopper Mounting for HVIGBT-NPT device.

Constructor	IXYS NPT	HVNPT-IGBT
Reference	IXGT32N170A	IXLF19N250A
Technology : Epitaxy Parts	A1: NPT	A2: NPT
Type & caliber	1700V/32A	2500V/ 32A
Series	1600V-1700V	2500V-4000V

Table 1. NPT-IGBTS Devices chosen in this study

The functional stress is based on an integrated chopper function based on an IGBT (Fig.2).

To further conduct our study, we will present as an illustration the static characteristic for a gate voltage V_g = 15V at 27 ° C and at 200°C for NPT and HVNPT IGBT.

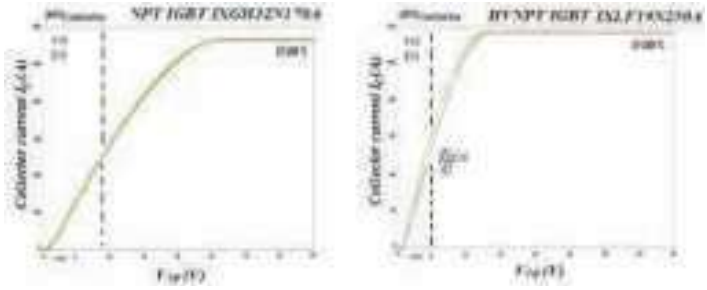

Fig. 3. Collector current versus collector– emitter voltage

As shown in Fig.3, the output characteristics of NPT-IGBT do not present an intersection point occurs between the characteristics at 27 ° C and that at 200 ° C. On the other hand, for the HVNPT-IGBT an intersection point occurs which corresponds to zero temperature coefficients dV_{ce}/dT. This is verified by the equation below:

$$\frac{dV_{CE}}{dT} = 0 \quad \Leftrightarrow \quad I_C = \frac{-\alpha}{\beta} \tag{1}$$

$$\frac{dV_{CE}}{dT} = \alpha + \beta * I_C \tag{2}$$

In addition, it is worthily important to note that the low temperature coefficient of the static voltage drop at the high current level is favorable to ensure the homogeneous distribution of the current in the chips and to achieve a good current sharing for the component in parallel mounting.

Static parameters:

This section aimed at in the coupling of the two stresses studied above. This operating mode is therefore extremely restrictive because of the very high energy level that the component must then dissipate.

Creative Commons Attribution-NonCommercial-NoDerivatives 4.0 International License (CC BY-NC-ND)

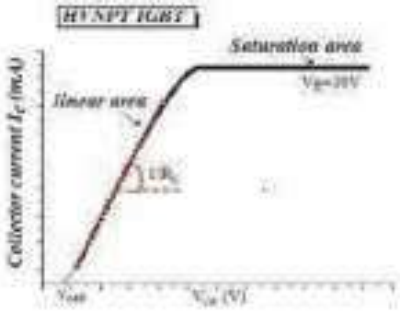

Fig.4. I-V Characteristics for HVIGBT-NPT device.

As can be seen in Fig.4, that the voltage drop V_{ce} across the IGBT can be model in the linear area by a straight line with slope 1/ R_0 and abscissa at the origin V_{ce0}. The voltage drop V_{ce} is then expressed by the following equation:

$$V_{ce} = V_{ce0} + R_0 I_C \quad (3)$$

Thus, we will represent the variations of the static parameters V_{ce0} and R_0 as a function of the temperature from 27 ° C to 200 °C for HVNPT IGBTs implanted and studied in this paper. From the simulation results, the variation laws V_{ce0} and R_0 can be approximated by the following relation:

$$\begin{aligned} V_{ce} &= V_{ce00} + \alpha\theta_j \\ R_0 &= R_{00} + \beta\theta_j \end{aligned} \quad (4)$$

Where

V_{ce00} : threshold voltage at 0 ° C,
R_{00} : resistance at 0°C,
α, β : Sensitivity coefficient at temperature T,
θ_j : Junction temperature ° C.

$$\frac{dV_{ce}}{dT} = \frac{dV_{ce0}}{dT} + \frac{dR_0}{dT} * I_C = \alpha + \beta * I_C \quad (5)$$

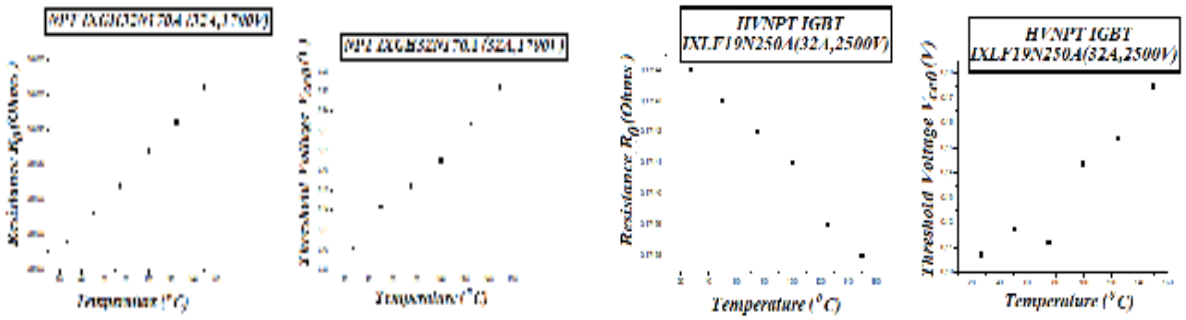

Fig.5. Variation of V_{ce0} and R_0 as a function of temperature for NPT and HVNPT-IGBT.

The set of results presented provides objective resources for calculations by extracting important parameters which characterize the operation of an HVNPT IGBT such as: threshold voltage V_{th}, the transconductance coefficient Kp, aiming at optimizing its performance and to an understanding of the evolution of these parameters on the degradation mechanism.

Creative Commons Attribution-NonCommercial-NoDerivatives 4.0 International License (CC BY-NC-ND)

Algerian Journal of Engineering Architecture and Urbanism Vol. 5 Nr. 3 2021
ISSN: 2588-1760

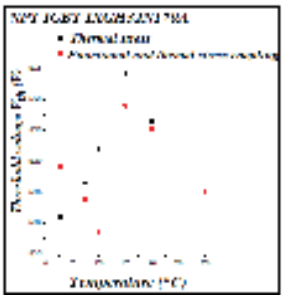
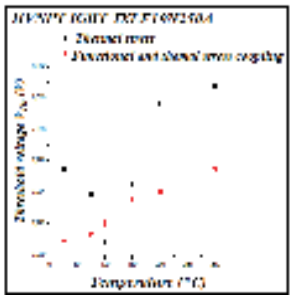

Fig.6. Extraction of threshold voltage V_{th}

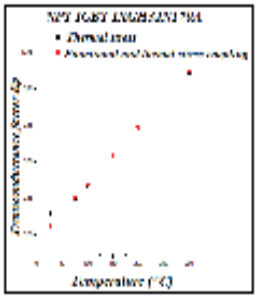
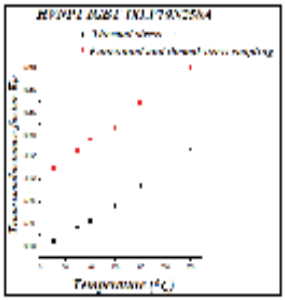

Fig.7. Transconductance factor K_p extraction

of an NPT and HVNPT-IGBT after coopling stress

From the comparison results obtained, we observe a significant shift in the threshold voltage V_{th} of NPT-IGBT under thermal stress than compared to the coupling of the two stresses, this decrease of V_{th} in particular under the coupling of stress. The explanation for this decrease lies in the location of a significant amount of the trapped negative charges.

From the characteristic ($\sqrt{I_c} = f(V_{ge})$), the slope in the linear region is proportional to the product ($K_p(\beta+1)$). Note that this slope decreases with increasing temperature. The decrease in K_p is therefore due to the decrease in the mobility of carriers in the canal. Further, we observe that the K_P transconductance factor of HVNPT-IGBT increased more under stress coupling than under thermal stress.

Dynamics parameters:

The main goal of this section is to evaluate the overall performance of each device in Table.1, for technologies NPT IGBT, which will be investigated by considering the trade off among the following dynamics parameters. I_C-V_{ce} waveforms are translated PC running MATLAB (fitting parameters for each curve), for example the power dissipation of each device is calculated from the product of collector emitter voltage and collector current.

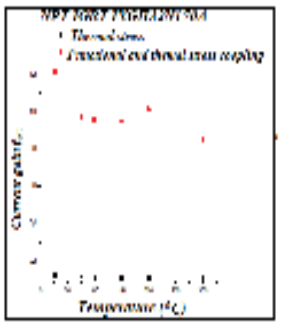
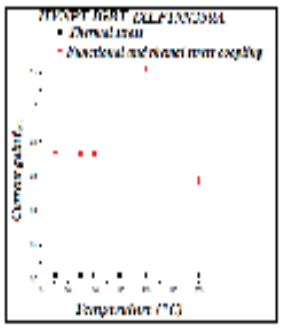

Fig.8. Extraction of β_{PNP} gain currant

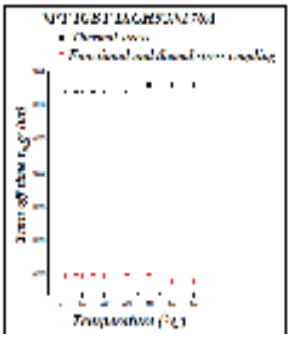
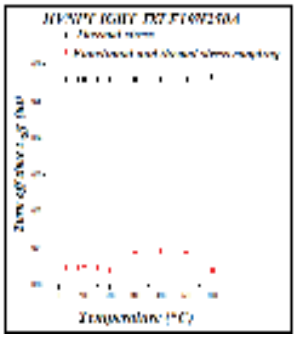

Fig.9. Turn off time t_{off} extraction

of an NPT and HVNPT-IGBT after coopling stress

From the simulation results presented in Fig.8. we note that β_{PNP} decreases with temperature, particularly at temperatures above 200 ° C. These results show us that thermal stress alone could therefore reduce β_{PNP} significantly compared to stress coupling. For this purpose, the optimization of IGBT performance under functional stress is done by the choice of conditions that allows the best compromise between the closing time and the current density I_c. This compromise is expected, a factor in the intended application.

Creative Commons Attribution-NonCommercial-NoDerivatives 4.0 International License (CC BY-NC-ND)

Further, in Fig.9, we notice that t_{off} decreases with temperature for both devices but the decrease is relative. The closing time is improved under the effect of stress coupling only under the effect of thermal stress alone. Also, we note that the both IGBT structures, the dV_{ce}/dt decreases with increasing temperature T ° as the stored charge increases.

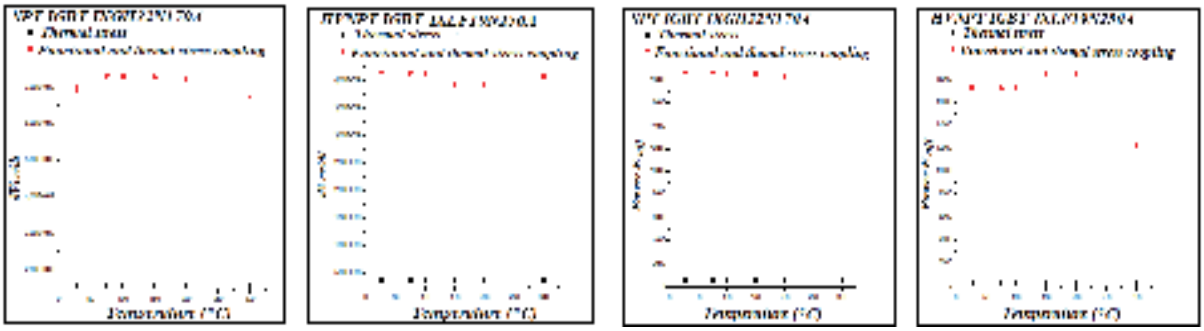

Fig.10. dV_{ce} /dt parameter extraction of an NPT and HVNPT-IGBT after coupling stress

Fig.11. E_{off} extraction

Conclusion:

Emphasis has been placed in this paper on the importance of HVIGBTs reliability in various industrial applications where their characteristics are suitable for a wide range of power levels. For this purpose, the results obtained in this study provide a confirmation of the origin of defects and lead to provide monitoring of operation of an electronic system in an industrial environment. These results show the need for a hardening of the components exposed to the natural environment to long-term operations.

Finally, the study presented in this document also brought some surprises. It is important to note that through the deduced results, we also found that, stress coupling (functional and thermal stress) could therefore reduce the value gap some parameters caused by themal stress. We attribute this behavior to an implemented compensation mechanism. Thus the choice of stress conditions can induce an optimization of the performances of IGBTs.

References:

T. Funaki, J-C. Balda, J. Junghans, A-S. Kashyap, H-A. Mantooth, F. Barlow, T. Kimoto, T. Hikihara, (2007), *Power Conversion With SiC Devices at Extremely High Ambient Temperatures*, IEEE Transactions on Power Electronics,vol. 22, n^0 4, 1321-1329,

Ly.Benbahouche (2011), ‘‘*Contribution à l`étude du comportement électrothermique et analyse du mécanisme de vieillissement dans les transistors de puissance IGBTs,* Thèse de doctorat, Université UFAS Setif1, Algérie,

Deboy G, Marz M, Stengel JP, Strack H, Tihanyi J, Weber H, (1998). *A new generation of high voltage MOSFETs breaks the limit line of silicon*. In: Proc. IEDM, 683–5.

Marina Antoniou, Florin Udrea, (2006), *Simulated Superior Performance of Superjunction Bipolar Transistors*. International Semiconductor Conference, 2006, 27-29 Sept, 293 - 296.

A,Maouad, A.Hoffmann, A.Khoury, J.P.Charles, (2000), *Characterization of high density current stressed IGBT and simulation with an adapted SPICE sub-circuit,* Microelctro Reliability,Vol.40, 973-979, Pergamon.

F. Blaabjerg and M. Pecht, (2015), “*Special Issue on Robust Design and Reliability of Power Electronics, IEEE Trans. on Power Electronics*, May 2015”, IEEE Trans. on Power Electronics, Vol. 30, No. 5, 2373-2374.

H. Akagi,(2001) “*Large Static Converters for Industry and Utility Applications*”, *Proc. IEEE, Vol. 89,* 976–983,

Vijay Bolloju, Ritu Sodhi, Chiu Ng, Jie Zhang, (2006), *Trench IGBTs Improve Appliance Motor Drives*, Power Device Department, International Rectifier, El S | Aug 01.

J. Thébaud, E. Woirgard, C. Zardini, S.Azzopardi, O. Briat, and J. Vinassa,(2003), *“Strategy for Designing Accelerated Aging Tests to Evaluate IGBT Power Modules Lifetime in Real Operation Mode”,* IEEE Transactions on Components and Packaging Technologies, Vol. 26, No. 2, 429-438.

S. Lefebvre, F. Miserey, (2004), “*Composants à semi-conducteur pour l’électronique de puissance*”. Tec & Doc Lavoisier.

Creative Commons Attribution-NonCommercial-NoDerivatives 4.0 International License (CC BY-NC-ND)

Algerian Journal of Engineering Architecture and Urbanism Vol. 5 Nr. 3 2021
ISSN: 2588-1760

COMPUTER SIMULATIONS OF BLOOD FLOW IN HUMAN ARTERIAL BIFURCATION

Khellaf BELKHIRI
Associate Professor, Dr, Mechanical Engineering Department, University of M'Sila, Laboratory of Materials and Mechanics of Structures, University of M'Sila, Algeria, e-mail: khellaf.belkhiri@univ-msila.dz

Abstract:
Hemodynamic factors play a role in atherogenesis and the localization of atherosclerotic plaques. The human aorta and coronary arteries are susceptible to arterial disease, and there have been many studies of flows in models of these vessels. Atherosclerosis is a systemic disease occurring in specific sections of the cardiovascular tree such as the carotid and the coronary arteries.
This paper aims to simulate the human arterial bifurcation and investigates some hemodynamic parameters as blood propagates from the aortic artery toward the carotid artery. We analyze the velocity, static pressure, shear stress. The simulation results showed disturbed flow (such as flow separation, stagnation) as well as abnormal hemodynamic parameters (HPs) distributions (including the low and high wall shear stress (WSS) and oscillation of wall shear stress.
Based on our simulating characteristic results, the CFD tools can not only monitor the hemodynamic parameters obviously, but also help to analyze the diagnostic for the treatment of vascular diseases. CFD can be an effective technology for the examination and treatment of patients with failure of blood supply of the head and brain.

Key words: Arterial Bifurcation, Atherosclerosis, Blood Flow, Numerical Investigation, Wall Shear Stress

Introduction:

Hemodynamic factors play a role in atherogenesis and the localization of atherosclerotic plaques. The human aorta and coronary arteries are susceptible to arterial disease, and there have been many studies of flows in models of these vessels. Atherosclerosis is a systemic disease occurring in specific sections of the cardiovascular tree such as the carotid and the coronary arteries (Jaffrin et al., 1995). The thromboembolic complications have been linked to abnormal fluid dynamic stresses in the flow chamber.
Computational fluid dynamics provides an alternative technique in which more detailed analysis of fluid dynamic effects of flow within an arterial bifurcation can be evaluated.
As an initial attempt to analyze the effect of the blood flow past an arterial bifurcation, the present study was restricted to steady flow in a simplified three-dimensional model of the bifurcation considering the flow to be laminar (Hyun et al., 2000).

Theory:

In this initial attempt to describe the laminar blood flow within an arterial bifurcation, a 3-D simplified geometry was employed as shown in Fig.1.

Creative Commons Attribution-NonCommercial-NoDerivatives 4.0 International License (CC BY-NC-ND)

Numerical simulation was performed by a Finite Volume solver, CFD-Ansys Fluent by solving the transport equations - the Navier-Stokes equations. The wall is considered rigid, the blood flow was treated as an incompressible and Newtonian with a density of 1056 kg/m3 and a dynamic viscosity of 0.0034 Pa·s (Perktold et al., 1990).

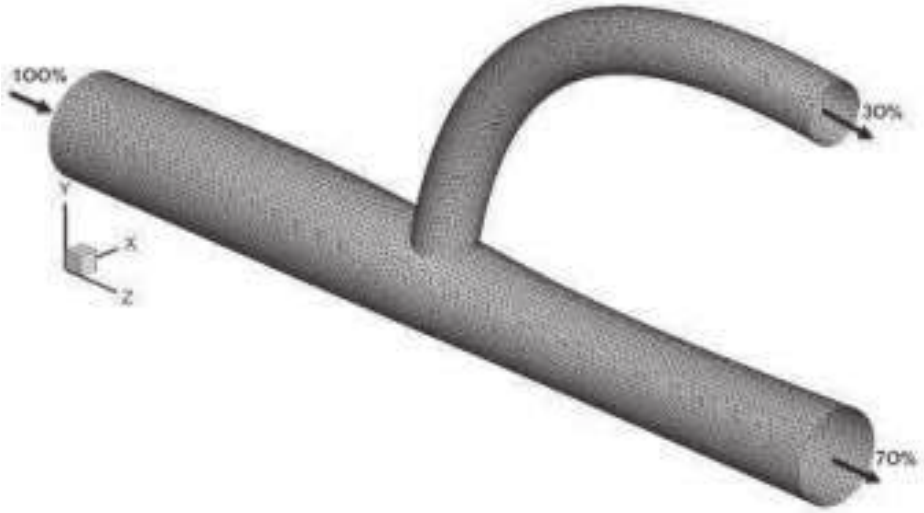

Fig.1. Geometry of the arterial bifurcation

The Navier-Stokes equations (Kleinstreuer, 1997) read:

$$\nabla . \boldsymbol{V} = 0 \quad (1)$$

$$\rho(\boldsymbol{V}.\nabla \boldsymbol{V}) = -\nabla p + \nabla . \boldsymbol{\tau} \quad (2)$$

where $\boldsymbol{V}$ is the velocity vector, $\boldsymbol{p}$ is the pressure and $\boldsymbol{\tau}$ is the shear stress tensor.

For three-dimensional flows, equations (1) and (2) comprise four equations for four flow variables, that is, three velocity components and pressure. Together with appropriate boundary conditions these equations are numerically solvable.
The choice of appropriate boundary conditions is important in obtaining the flow field of interest. For the flow problem treated here the boundary conditions include:

- The inlet boundary condition is a specified velocity, where the velocity profile being a fully developed laminar profile.
- At the outflow boundaries, the mass flow boundary conditions were specified where the flow rate ratio between the two branches was known.
- The arterial wall is considered rigid with a no-slip boundary condition.

The computational domain is subdivided into multiple control volumes or finite volumes. Proper mesh generation is one of the most challenging tasks in computational fluid dynamics analyses. In this study, an unstructured mesh, which consists of arbitrarily shaped eight-node elements, has been used. All flow equations were spatially discretized to be second-order accurate using a higher-order upwind scheme. The upwind scheme used has been derived by integrating the fluxes over a control volume (Patankar, 1980). The procedure for solving the

Creative Commons Attribution-NonCommercial-NoDerivatives 4.0 International License (CC BY-NC-ND)

discrete equations is iterative and based on the SIMPLE method. A preconditioned conjugate gradient algorithm is adopted to calculate the pressure corrections.

Results and discussions:

Streamlines which exemplify the basic blood flow features in the arterial bifurcations can give insight into the flow pattern. Fig. 2 illustrates these trajectories colored by the amplitude of the axial velocity.

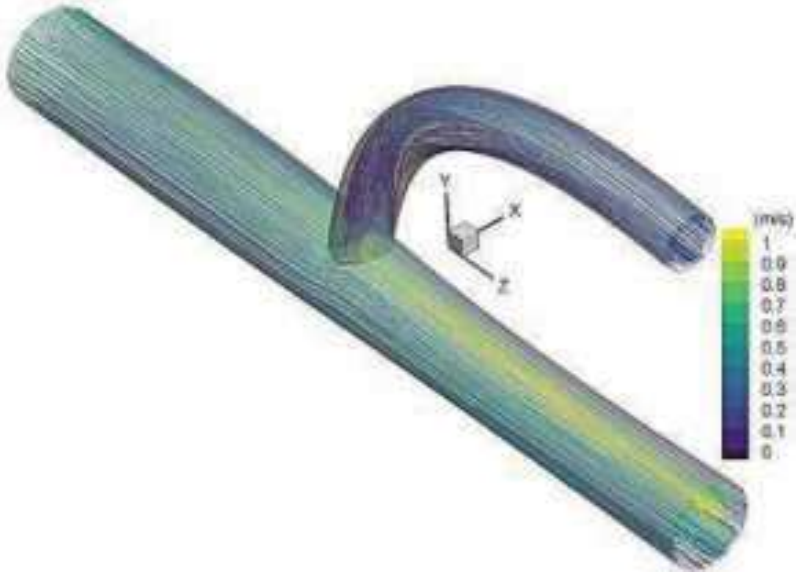

Fig.2. Computed streamlines contours

Fig. 3 shows the velocity vectors and contours at the longitudinal section of the bifurcation (plane of symmetry). The flow, which is directed to the lower part of the common artery, generates vortices in the branching region of the bifurcation and a large separated region along the upper wall of the branch vessel. Since separated and low-flow regions have potential for thrombus formation, clotting may occur on the upper region of the bifurcation and the lower wall of the branch vessel.

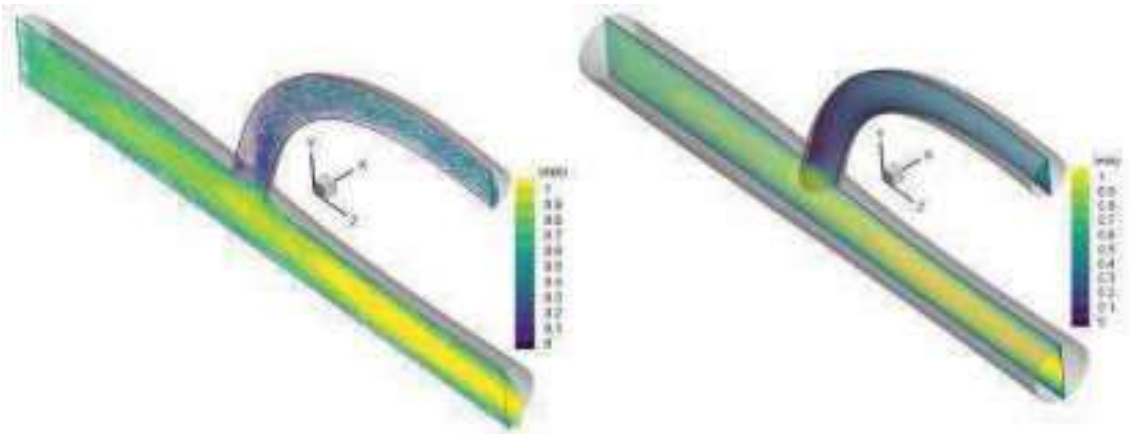

Fig.3. Axial velocity vectors and contours

Creative Commons Attribution-NonCommercial-NoDerivatives 4.0 International License (CC BY-NC-ND)

There is a clear identification of stagnation flow zone in the carotid sinus, in these sites are the most possible growing of the atherosclerosis if patient has already beginning stadium of this disease (Filipovic et al., 2004).
Regarding the WSS distribution shown in Fig. 4, the maximum WSS can be found at the branch vessel entrance region near the flow divider and at the upstream side of the branching in the main vessel.

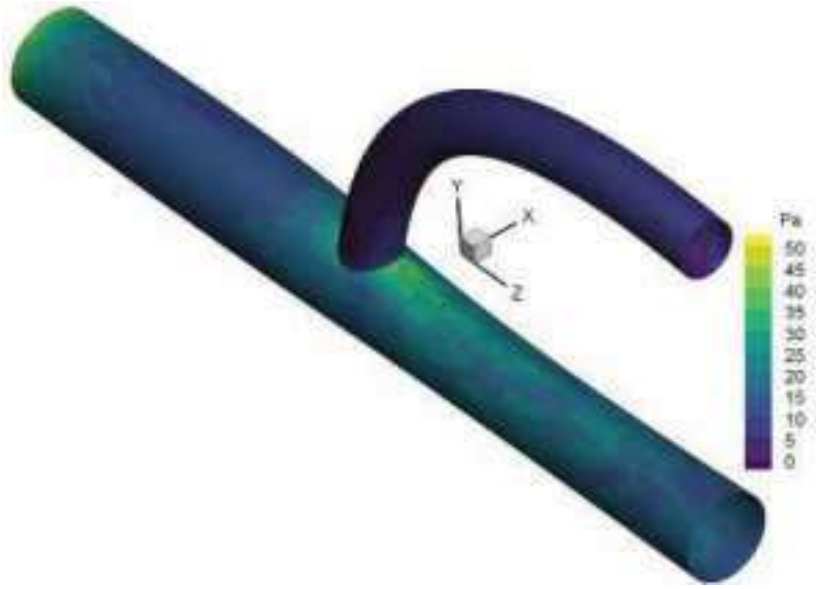

Fig.4. Wall shear stress (WSS) contours

Computational analyses show that atherosclerotic plaques, and other heterogeneities, lead to increased local stress in the artery wall. This is clinically significant, because the so-called stress concentration within the plaque region increases the probability of plaque rupture, which can lead to sudden thrombotic occlusion or distal embolization.

Conclusion:

Based on our simulating characteristic results, the CFD tools can not only monitor the hemodynamic parameters obviously, but also help to analyze the diagnostic for the treatment of vascular diseases. Computational stress modeling has helped in our understanding of atherogenesis and its sequelae. CFD can be an effective technology for the examination and treatment of patients with failure of blood supply of the head and brain.

References:

Filipović Nenad D., Kojić M. (2004), *Computer Simulations of Blood Flow with Mass Transport Through the Carotid Artery Bifurcation*, Theoretical and Applied Mechanics **31(1):**1-33.

Hyun S., Kleinstreuer C., Archie Jr J. P. (2000), *Hemodynamics Analyses of Arterial Expansions with Implications to Thrombosis and Restenosis*, Medical Engineering & Physics **22(1):**13-27.

Jaffrin Michel Y., Colin G. Caro (1995), *Biological Flows,* Springer, New York, US.

Kleinstreuer C. (1997), *Engineering Fluid Dynamics: An Interdisciplinary Systems Approach*, New York: Cambridge University Press.

Patankar S.V. (1980), *Numerical Heat Transfer and Fluid Flow*, Hemisphere Publishing Corporation. New York.

Perktold K., Peter R. (1990), *Numerical 3D-Simulation of Pulsatile Wall Shear Stress in an Arterial T-Bifurcation Model*, Journal of Biomedical Engineering **12(1):** 2-12.

Creative Commons Attribution-NonCommercial-NoDerivatives 4.0 International License (CC BY-NC-ND)

Algerian Journal of Engineering Architecture and Urbanism Vol. 5 Nr. 3 2021
ISSN: 2588-1760

EXPERIMENTAL AND THEORETICAL CONTRIBUTION OF FRICTION WELDING

Abdelhak Roubi[1],
Phd student, Department of Mechanical Engineering, University Saad Dahlab Blida 1, Blida, Algeria, e-mail: roubi_abdelhak@yahoo.com
Abderrazak Allali[2],
Professor, Department of Mechanical Engineering, University Saad Dahlab Blida 1, Blida, Algeria, e-mail: yasminallali2011@yahoo.fr

Abstract:
In this paper, we study the mechanical and metallurgical characteristics of Rotary Friction Welding (RFW) welded joints for homogeneity and heterogeneous joints. We have studied the A60 steels and the aluminum alloys of the 2017A series. The welds obtained are similar in appearance in that they have several distinct microstructural areas. Thus, the results show that by increasing the rotational speed employing 1000 and 1600 rpm, the mechanical properties during the RFW process are slightly improved, favored by the increased heat flow. In the same sample, the micro hardness distribution is usually slightly changed between the projection weld of the centerline of the welded tube and near their borderline. This is due to the non-uniformity of the temperature distribution in the cross section. Thus, the plastic deformation of the heated part of the metal plays an important role in the process of friction welding and their quality. Microstructural analysis reveals grain growth in the WCZ joint and in the heat affected HAZ zone due to the non-uniform distribution of heat flow in both directions (transverse and longitudinal of the tube). Finally, by using RFW, manufacturers make it possible to produce and maintain mechanical components at low cost and retain their welding quality compared to conventional fusion welding. A medialization with ABAQUS, then an experimental modal analysis is established. The obtained results will be compared to two cases: absence and presence of the weld and conclusions will be drawn regarding changes in dynamic properties under the influence of RFW welding.

Key words: Dynamic, Rotary Friction Welding (Rfw), Plasticized Material, Heat Flux, Characterization

Introduction:

Friction welding makes it possible to carry out butt joints of two parts, at least one of which is rotationally symmetrical. It implements the thermal effect generated in their joint plane by the rapid rotation under pressure of the parts on each other or by friction welding. The heating power results from the resistive torque and the speed of rotation, which is kept constant in principle. It is a comprehensive joining process which is classified as one of the forging processes. Due to the creep of the material during friction and forging, the melting temperature is never reached. The principle is as follows: One of the two parts to be joined is rotated. The two parts are brought into contact by a defined axial force. By friction the parts heat up on both sides of the parting line (V = 100 m/min). Friction speed: Physically, for a given material and pressure, the torque passes through a maximum depending on the speed. These conditions are to be determined in a pre-test carried out on a tubular assembly of a given diameter. Thus, for steels in general, we obtain a speed of 2 m/s for a force of 5 daN/mm2. To apply these values to a full section of diameter D for which the friction speeds will vary from zero at the center to a maximum at the periphery, a so-called friction diameter of 2 D/3 is chosen. In practice, for a solid steel section, the transverse thermal diffusion

Creative Commons Attribution-NonCommercial-NoDerivatives 4.0 International License (CC BY-NC-ND)

intervenes favorably in the total friction time. The above value is not critical and this makes it possible to have standard machines whose speed of rotation is fixed by construction or adjustable in steps to be globally related to the section to be welded and the capacity of the machine. In the case of tubular workpieces, the speed must be determined more precisely in relation to the average diameter. Friction duration: This is determined experimentally and shown. Too short a time results in an uneven heat-affected zone; too long a time results in excessive metal consumption. A bead begins to form. After a sudden stop of the rotating part, the axial force is increased. This is the forging phase of the weld, which results in the formation of a very characteristic bead. This bead is then removed by machining. This process is applied for mechanisms requiring high resistance. Examples are: Drive shafts; Gears; Studs on hubs; Piston rods etc. Or the simulation of the friction welding process. According to its general definition. Welding is defined as an operation consisting in bringing together two or more constituent parts of an assembly in such a way as to ensure continuity between the parts to be assembled, either by heating, pressure or both, with or without the use of a filler material.

This study contributes to the numerical modeling of friction welding for the identification of welding parameters. The modeling is based on the calculation of the amount of heat generated by friction and on the special heat distribution taking into account the variations in the thermal properties of the material. Study of the optimal welding parameters, including the goal of having welds with a mini-mum of defects detected by non-destructive testing methods and their characterization namely: Friction speed; Duration of friction; Friction effort; Forging effort and duration; Presentation of specimens; Dimensions, Materials, Machining of specimens; Testing of specimens; Ultrasonic testing; Tensile test.

A study of the dynamic behavior of the two bars (welded and non-welded) with two methods is also conducted: Numerical simulation using ABAQUS software and experimental modal analysis under a Spectral Dynamics platform. Friction welding makes it possible to carry out butt joints of two parts, at least one of which is rotationally symmetrical. It implements the thermal effect generated in their joint plane by the rapid rotation under pressure of the parts on each other or by friction. The heating power results from the resistive torque and the rotation speed maintained at a constant principle. It is a global assembly process that ranks among the forging processes. Due to the creep of the material during friction and forging, the melting temperature is never reached. The principle of this study is as follows: One of the two parts to be joined is rotated. The two parts are brought into contact by a certain axial force. By friction the parts heat up on both sides of the parting line (V = 100 m/min).

Friction speed: Physically, for a given material and pressure, the torque passes through a maximum depending on the speed. These conditions are to be determined in a preliminary test carried out on a tubular assembly of a given diameter. Thus, for steels in general, a speed of 2 m/s is obtained for a force of 5 daN/mm2. To apply these values to a full section of diameter D for which the friction speeds will vary from zero in the center to maxi-mum at the periphery, a so-called friction diameter of 2 D/3 is chosen. In practice, for a solid steel section, the transverse thermal diffusion favorably intervenes in the total friction time. The above value is not critical and this makes it possible to have standard machines whose speed

Creative Commons Attribution-NonCommercial-NoDerivatives 4.0 International License (CC BY-NC-ND)

is fixed by construction or adjustable in steps in order to be globally related to the section to be welded and the capacity of the machine. In the case of tubular workpieces, the speed must be determined more precisely according to the average diameter. Friction duration: This is determined experimentally and shown. Too short a time results in an uneven heat-affected zone; too long a time results in an overabundant metal consumption. A bead begins to form. After a sudden stop of the rotating part, the axial force is increased. This is the forging phase of the weld, which results in the formation of a very characteristic bead. This bead is then removed by machining. This process is applied for mechanisms requiring high resistance. Examples are: Drive shafts; Gears; Studs on hubs; Piston rods etc. Or the simulation of the friction welding process. According to its general definition. Welding is defined as an operation consisting in bringing together two or more parts of an assembly, in such a way as to ensure continuity between the parts to be assembled, either by heating, pressure or both, with or without the use of a filler material. This study contributes to the numerical modeling of friction welding for the identification of welding parameters. The modeling is based on the calculation of the amount of heat generated by friction and on the special heat distribution taking into account the variations in the thermal properties of the material.

Problematic:

Aim of the study First of all, it is a question of studying the vibratory behaviour by determining the dynamic parameters of an Aluminum bar (2017A) and a steel bar (A60) to redo the test once the bar has been cut and welded by the RFW technique. We can summarize the objectives of this experimental modal analysis of aluminum and steel bar in the following points:

- Determination of the natural frequencies and damping of an aluminum bar and steel bar.
- Visualization of the modal deformations corresponding to the Eigen frequencies.

Materials and methods:

1. **Aluminum (2017A):**

- **Length:** 300 mm before installation And 280 mm after installation.
- **Thickness:** 10 mm
- μ = 7.8e-009kg mm-3
- M = 0.195 kg
- E = 210000 Mpa

2. **Acier (A60):**

- **Length:** 300 mm before installation And 280 mm after installation
- **Thickness:** 10 mm
- μ = 7.8e-009 kg mm-3
- M = 0.195 kg
- E = 210000 Mpa

Creative Commons Attribution-NonCommercial-NoDerivatives 4.0 International License (CC BY-NC-ND)

Sensitivity (mV/N)	1.16	**Resonance frequency (Hz)**	75
The range of use (N)	4450	**Max output impedance (Ω)**	100
The maximum force (N)	9900	**Power source (V)**	+18 à 30
Humidity (%)	36	**Intensity (mA)**	2 à 20
Temperature (°C)	22	**Material (Head, wrist)**	Acier inoxydable, Fibre de verre
Connector(Coaxial)	BNC	**Head weight (g)**	100

Table 1. Impact Hammer Specification

Sensitivity (mV/g)	102
Relative cross-sectional sensitivity (%)	4
Resonance frequency (kHz)	42.9
Measuring range (Hz)	2 à 27400
Frequency range (Hz)	5 à 20000
Maximum Amplitude (g peak)	50

Table 2. Technical data, accelerometer (Wilcoxon 736T). Doc CRD/MA].

Results and discussions:

The shock is applied to the structure with a hammer. The kinetic energy of the hammer gives rise at the moment of impact to a force whose intensity is measured by a cell that delivers an electrical signal that constitutes the input of the system. The response of the system is measured by an accelerometer attached to the structure. The analyzer then calculates the transfer function and modal deformations.

The Measuring Technique, by user fixes the sensor at one point and excites the structure at various locations, it can determine the transfer functions and deformations.

In our study, we chose the impact hammer as a means of excitation of the bar to be studied and an acceleration sensor (accelerometer) for the measurement of its vibratory response. [CRD-MA]. In order to acquire and analyze the signals delivered by the two sensors; force sensor and acceleration sensor, we used a vibration analysis platform "SPECTRAL DYNAMICS". The main objective of the use of the acquisition card is the transfer of the signals from the sensors to the PC to analyze them.

The experimental modal analysis system of SPECTRAL DYNAMICS Company is equipped with two software packages; PUMA & CATSMODAL

Mode of fixation & Discretization of the bar: realized the embedded-free fixation mode of the bar with the help of a fixation support. We discretized the bar in eleven (11) points at equidistant distances. The bar has the following geometrical and mass characteristics the two signals (force & acceleration) are acquired as follows and analyzed by the PUMA software in order to calculate the frequency response functions (FRFs)

Determination of modes Case of the un-welded bar: After treatment of the FRF curves (curve-fitting), using the polynomial technique for the determination of Eigen frequencies. The results obtained are presented in the Figure1:

Creative Commons Attribution-NonCommercial-NoDerivatives 4.0 International License (CC BY-NC-ND)

Algerian Journal of Engineering Architecture and Urbanism Vol. 5 Nr. 3 2021
ISSN: 2588-1760

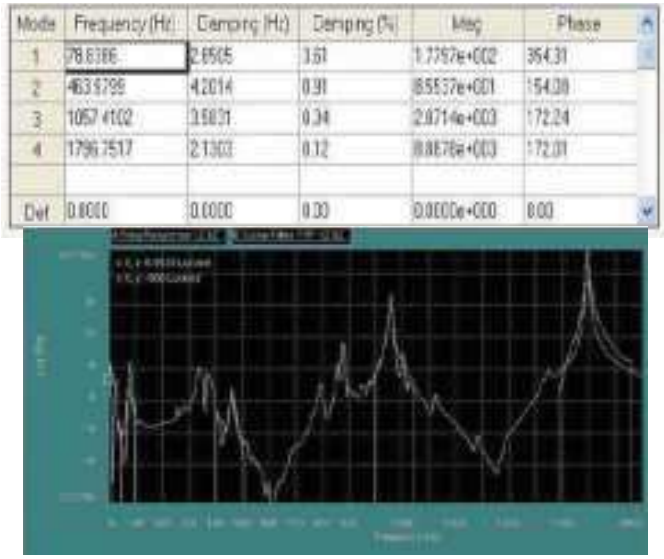

Figure 1: Modal parameters

Table 3 shows a comparison between the modal deformations obtained previously and the theoretical deformations:

Mode	frequency propre	Experimental deformations	Theoretical deformations
1	78.84 Hz		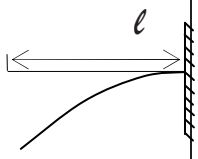
2	463.98 Hz		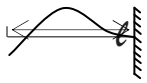
3	1057.41 Hz		

Table 3. Three appropriate deformations for the different mode of unwelded bar

Case of Bar welded by Rotary Friction Welding (RFW): The smoothing of the curves makes it possible to redesign them in order to facilitate the extraction of the modes (the peaks).

Determination modes: After processing the curves of the frequency response functions FRFs (curve-fitting), using the polynomial technique for the determination of frequencies. The results obtained are presented in the Figure 2:

Creative Commons Attribution-NonCommercial-NoDerivatives 4.0 International License (CC BY-NC-ND)

Algerian Journal of Engineering Architecture and Urbanism Vol. 5 Nr. 3 2021
ISSN: 2588-1760

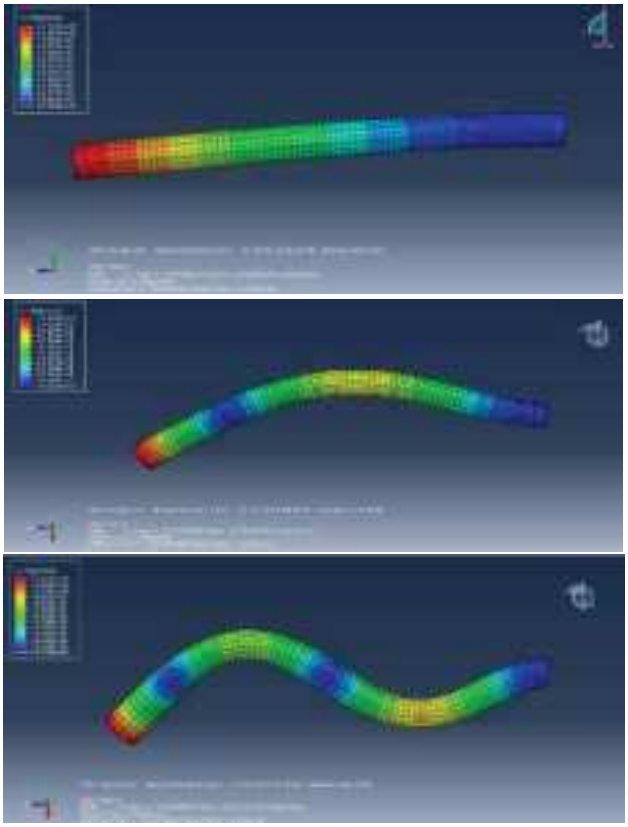

Figure 2: (a) the first modes (unwelded bar), (b) the second modes (unwelded bar) and (c) the third modes (unwelded bar).

Determination modes: After processing the curves of the frequency response functions FRFs (curve-fitting), using the polynomial technique for the determination of frequencies. The results obtained are presented in the Figure 3:

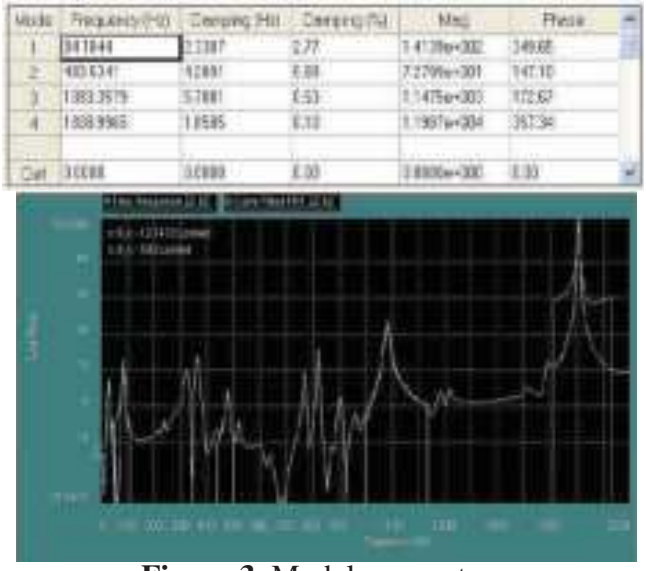

Figure 3. Modal parameters

Modal distortions: Table 4 shows a comparison between the modal deformations obtained ex-periodically and the theoretical deformations

Creative Commons Attribution-NonCommercial-NoDerivatives 4.0 International License (CC BY-NC-ND)

Algerian Journal of Engineering Architecture and Urbanism Vol. 5 Nr. 3 2021
ISSN: 2588-1760

Mode	Fréquence propre	Experimental deformations	Theoretical deformations
1	84.10 Hz		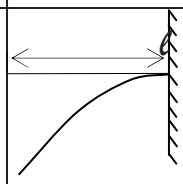
2	480.53 Hz	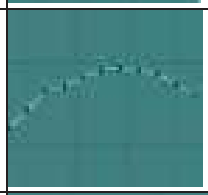	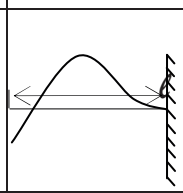
3	1083.36 Hz	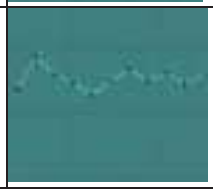	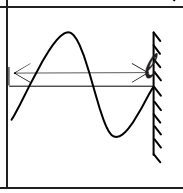

Table 4. Appropriate deformations for the different modes of welded bar.

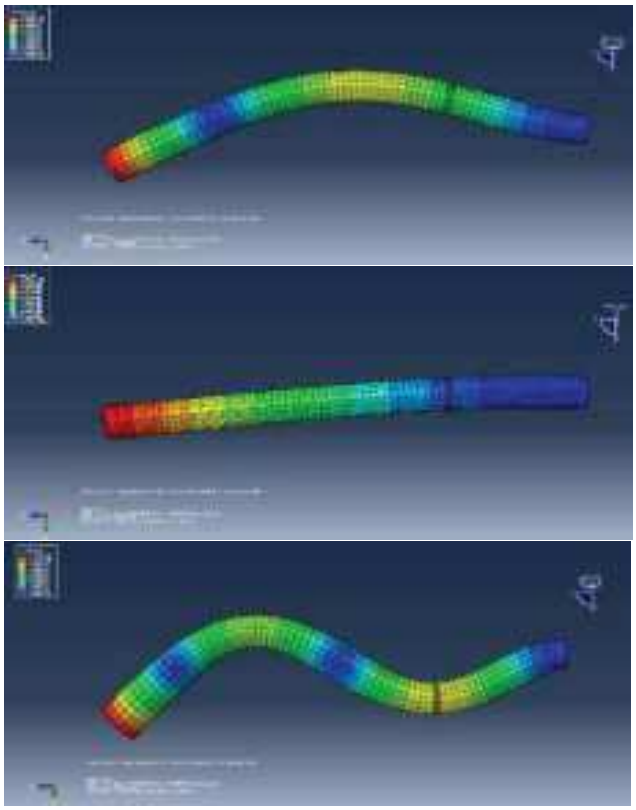

Figure 4. the first modes (unwelded bar), (b) the second modes (unwelded bar) and (c) the third modes (unwelded bar).

Interpretation this table represents the different frequency values found during simulation.

Creative Commons Attribution-NonCommercial-NoDerivatives 4.0 International License (CC BY-NC-ND)

	Method of resolution	Modes		
		1	2	3
Frequency (Hz)	Reference bar	77.99	483.85	1004.30
	Welded bar	78.074	484.30	1007.40
Taux d'erreur (%) $\left\|\frac{f1-f2}{100}\right\|$		0.00084	0.0045	0.031

Table 5. Comparison between frequency values

The table below shows the dynamic parameters of the two bars (unwelded and welded).

	Reference bar			Welded bar		
Mode	**Frequency propre (Hz)**	**Amortization (Hz)**	**Amortization %**	**Frequency propre (Hz)**	**Amortization (Hz)**	**Amortization %**
1	78.84	2.8505	3.61	84.10	2.3307	2.77
2	463.98	4.2014	0.91	480.53	4.289	0.89
3	1057.41	3.5831	0.34	1083.36	5.7081	0.53

Table 6. Experimental Results

According to the results obtained, the dynamic parameters of the two bars (unwelded and welded) are almost identical, in terms of frequency and damping ; By observing the modal deformations of the two bars we notice a similarity between the different modes for those of the experimental study as well as those of the theory on all modes. This confirms the veracity of the results of the experimental modal analysis. Convergence of the results between the two unwelded and welded bars (negligible error rate) implies that the RFW welding process does not affect the dynamic parameters as well as the vibration behavior.

Conclusion:

The results of the parametric study, although they allowed us to identify the influence of some operating parameters such as the increase of the welding speed within a defined weldability range, also show the difficulty to identify the impact of each parameter on the mechanical characteristics of the beads. This difficulty is explained by the coupling of the physical phenomena resulting from these operating parameters. Microscopic observations of the bead have identified the different zones of the friction weld seam. They led to the identification of the boundaries between these different spaces by the change of microstructure and orientation of the grains. At the end of the uniaxial tensile tests, the friction welded joints showed acceptable mechanical properties of our welds.

Experimental modal analysis is used to validate numerical simulation models, in order to make the necessary adjustments to create reliable models. However, this validation technique requires a good mastery of the signal processing on the one hand, and a judicious choice of

Creative Commons Attribution-NonCommercial-NoDerivatives 4.0 International License (CC BY-NC-ND)

the measurement and excitation points, representative of the whole structure on the other hand.

- Convergence of the results between the two unwelded and welded bars (ne-slippable error rate) implies that the RFW welding process does not affect the dyna-mic parameters as well as the vibration behavior.

The results obtained were satisfactory and in line with the literature. Further studies are still possible, it would be interesting to carry out additional fatigue tests in order to be able to predict the influence of RFW welding on the dynamic behaviour of structures over time.

References:

Luc. Fairon, *Introduction au soudage* – Techni futur ASBL.

Helal, Y., thèse « *L'effet de soudage par friction malaxage sur la microstructure et les propriétés mécaniques d'un joint soudé composé d'un alliage d'aluminium industriel et un acier* ». Université MOHAMMED KHAIDER Biskra (2017).

Camille Routhier & Gilles Desjardins. WEMAN, *Soudage et assemblage-soudage – Guide d'auto-apprentissage. Comité sectoriel de la main-d'oeuvre dans la fabrication métallique industrielle (CSMOFMI),* Bibliothèque et Archives nationales du Québec, 2010

Merry, G., *Soudage et soudabilité métallurgique des métaux*. Technique de l'ingénieur, 10 janvier 1994 (M715).

Obtention des pièces mécano soudés (Soudage autogène). (12 avril 2018).

Creative Commons Attribution-NonCommercial-NoDerivatives 4.0 International License (CC BY-NC-ND)

Algerian Journal of Engineering Architecture and Urbanism Vol. 5 Nr. 3 2021
ISSN: 2588-1760

INDIRECT VECTOR CONTROL OF A DFIG BASED IN AWIND ENERGY CONVERSION SYSTEM

Sakina AOUN
PhD student, LABGET laboratory, Department of Electrical Engineering, University of Tebessa, Algeria, e-mail: sakina.aoun@univ-tebessa.dz

Aziz BOUKADOUM
PhD,LABGET laboratory, Department of Electrical Engineering, University of Tebessa, Algeria, e-mail: azizboukadoum@yahoo.fr

Laatra YOUSFI
PhD, LABGET laboratory, Department of Electrical Engineering, University of Tebessa, Algeria, e-mail: yousfi_laatra@yahoo.fr

Abstract:
This paper presents the study of a doubly fed induction generator control (DFIG) which may be integrated in wind system. The main objective of AC machines vector control is to give the possibility of controlling these machines to achieve dynamic performance as good as that of DC machines, the application of this command consists in performing a decoupling between the rotor flux and the electromagnetic torque. In our study, indirect vector control of doubly fed induction generator (DFIG) in a wind energy system is simulated in closed loop using conventional PI controllers of active, reactive power and rotor currents components.
The simulation results show the effectiveness of the proposed DFIG control method.

Key words: Doubly fed induction machine, Indirect vector control, PI controller, Simulation, Performances.

Introduction:

Following the strong industrialization, electric energy will always reside an energy that humanity cannot do without it. Fossil fuels have long been used in the production of electrical energy; these fossil fuels are causing harmful damage to the environment [1]. To meet the high demand of energy and at the same time keep the environment safe, the majority of countries has opted for the use of renewable energies. These energies are inexhaustible, clean and do not create greenhouse gases unlike fossil fuels [2][3].

Among the renewable energies, wind energy is experiencing a significant growth and is considered as a mature and economical technology [4]. However, the problem is that this resource is characterized by variable wind speed [5]. For this reason, we have opted for the generator doubly fed induction, as well as other advantages such as; reducing the sizing of the converters, and improving the quality of the energy produced. On the other hand, the control of this machine remains the most important and complex phase [6][7].

Creative Commons Attribution-NonCommercial-NoDerivatives 4.0 International License (CC BY-NC-ND)

In that, way we will start our study by modeling the wind turbine. Then, the modeling of the DFIG, and the power control, which is done by the vector control. Finally, the results of the simulations will be presented in the Matlab / Simulink environment in order to infer the control efficiency on the system.

System modelling:

The proposed wind energy conversion chain consists mainly of a wind turbine, a doubly fed induction generator and a PWM controlled converter.

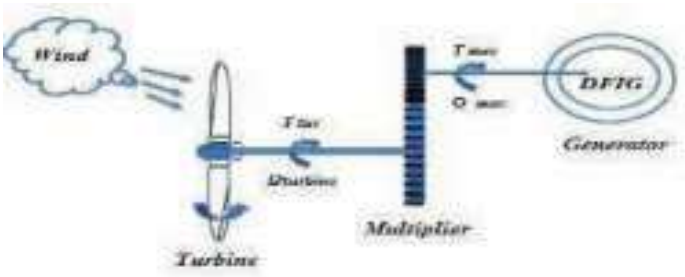

Fig1. Structure of wind power conversion system.

Turbine modelling :

The wind turbine allows the transformation of kinetic energy into mechanical energy and then into electrical energy through a generator. Wind power depends on the surface to be swept (S), wind speed (v) and air density (ρ). Based on the fluid mechanics equations we have the following equation [8][9]:

- The aerodynamic power P_{tur} captured by the wind turbine is given by [10]:

$$P_{tur} = \frac{1}{2} C_p(\lambda,\beta).\rho.S.v^3 \quad (1)$$

Where:

ρ is the air density (1.22 kg/m^3) ; S is wind turbine blades swept area in the wind (m^2) ; R is the turbine radius (m) ; v is wind speed(m/s) ; β blade pitch angle (°) and λ is the tip-speed ratio defined by:

$$\lambda = \frac{\Omega_{tur}.R}{v} \quad (2)$$

C_p is the power coefficient of wind is treated in bibliographies for a wind of 1.5MW by:

$$C_p(\lambda,\beta) = 0.5\left[\left(\frac{116}{\lambda_i} - 0.4\beta - 5\right)e^{\frac{-21}{\lambda_i}} + 0.0068\lambda\right] \quad (3)$$

With:

$$\frac{1}{\lambda_i} = \frac{1}{\lambda+0.08\beta} - \frac{0.035}{\beta^3+1} \quad (4)$$

Expression of the aerodynamic torque is given by [10]:

$$T_{tur} = \frac{P_{tur}}{\Omega_{tur}} = \frac{\pi}{2\lambda}\rho.R^3.C_p(\lambda,\beta) \quad (5)$$

The multiplier is the connection between the turbine and the generator modeled by [17]:

$$T_{mec} = \frac{T_{tur}}{G} \quad (6)$$

$$\Omega_{mec} = G.\Omega_{tur} \quad (7)$$

Creative Commons Attribution-NonCommercial-NoDerivatives 4.0 International License (CC BY-NC-ND)

Where: T_{mec} is mechanical torque,Ω_{tur}, Ω_{mec} are the turbine and generator speed, and G is the multiplier ratio.

The equation of system dynamics can be written as [10]:

$$J\frac{d\Omega_{mec}}{dt} + f.\Omega_{mec} = T_{mec} - T_{em} \quad (8)$$

Where: f is the viscous friction coefficient, T_{em} is the electromagnetic torque of the generator.

Modelling of doubly fed induction generator:

The stator of the machine is directly connected to the power grid, but the rotor is connected through the power electronics. The mathematical model of DFIG in the park referential (d-q) is given by the following equations [11][12][13][14]:

The electrical equations of the stator and rotor voltages of the DFIG are written:

$$\begin{cases} V_{sd} = R_s.I_{sd} + \frac{d}{dt}\Phi_{sd} - w_s.\Phi_{sq} \\ V_{sq} = R_s.I_{sq} + \frac{d}{dt}\Phi_{sq} - w_s.\Phi_{sd} \\ V_{rd} = R_r.I_{rd} + \frac{d}{dt}\Phi_{rd} - w_r.\Phi_{rq} \\ V_{rq} = R_r.I_{rq} + \frac{d}{dt}\Phi_{rq} + w_r.\Phi_{rd} \end{cases} \quad (9)$$

The stator and rotor flux are expressed by:

$$\begin{cases} \Phi_{sd} = L_s.I_{sd} + M.I_{rd} \\ \Phi_{sq} = L_s.I_{sq} + M.I_{rq} \\ \Phi_{rd} = L_r.I_{rd} + M.I_{sd} \\ \Phi_{rq} = L_r.I_{rq} + M.I_{sq} \end{cases} \quad (10)$$

Where: $R_s, R_r, L_s$and $L_r$are respectively the resistance and inductance of the stator and the rotor; M is the mutual inductance, $I_{sd}, I_{sq}, I_{rd}, I_{rq}$represent the d and q components of the stator and rotor currents; w_s is the stator angular frequency ($w_r = w_s - p\Omega_{mec}$) w_r is rotor angular frequency. and p number of pole pairs.

Equation (11) represents the expression of electromagnetic torque:

$$T_{em} = p\frac{M}{L_s}(\Phi_{sd}I_{rd} - \Phi_{sq}I_{rd}) \quad (11)$$

The active and reactive powers in the stator and rotor of the DFIG are given respectively:

$$\begin{cases} P_s = (V_{sd}.I_{sd} + V_{sq}.I_{sq}) \\ Q_s = (V_{sq}.I_{sd} + V_{sq}.I_{sq}) \\ P_r = (V_{rd}.I_{rd} + V_{rq}.I_{rq}) \\ Q_s = (V_{rq}.I_{rd} - V_{rd}.I_{rd}) \end{cases} \quad (12)$$

Creative Commons Attribution-NonCommercial-NoDerivatives 4.0 International License (CC BY-NC-ND)

Algerian Journal of Engineering Architecture and Urbanism Vol. 5 Nr. 3 2021
ISSN: 2588-1760

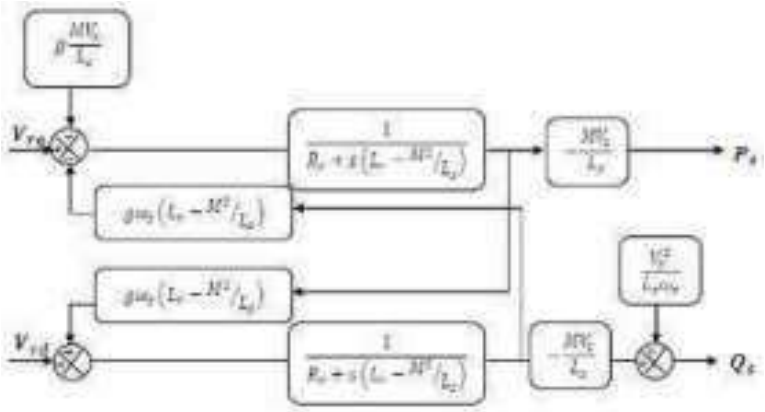

Fig2. Block diagram of the DFIG.

Field oriented control :

Vector control is one of the most widely used techniques for controlling electrical machines. It is based on the fact that the machine is similar to a DC machine with separate excitation; this latter ensures a natural decoupling between currents and flux [15][16].

According to the equation (11), we see clearly the strong coupling between the fluxes and the currents rotoric and statoric which generates a difficulty in the control of the DFigure The principle of vector control is to orient the flux of the machine in one of the two axes d or q. In our case and in order to simplify the control of stator power (active or reactive), we use an orientation on the d axis [2][13].

However:

$$\Phi_{sq} = 0 \text{ and } \Phi_{sd} = \Phi_s \tag{13}$$

The expressions of the electromagnetic torque becomes:

$$T_{em} = -\frac{3}{2} p . \frac{M}{L_s} . \Phi_{sd} . I_{rq} \tag{14}$$

The expressions of the stator voltages becomes:

$$\begin{cases} V_{sd} = R_s . I_{sd} + \frac{d}{dt} \Phi_{sd} \\ V_{sq} = R_s . I_{sq} + w_s . \Phi_{sd} \end{cases} \tag{15}$$

For medium and high power machines, stator resistances are neglected [9], therefore the stator voltage equations become:

$$\begin{cases} V_{sd} = \frac{d}{dt} \Phi_{sd} \\ V_{sq} = w_s . \Phi_{sd} \end{cases} \tag{16}$$

In steady state, it is assumed that the flow is constant, thus:

$$\begin{cases} V_{sd} = 0 \\ V_{sq} = w_s . \Phi_{sd} = V_s \end{cases} \tag{17}$$

$$\Phi_{sd} = \Phi_s = L_s . I_{sd} + M . I_{rd}$$
$$\Phi_{sq} = 0 = L_s . I_{sq} + M . I_{rq} \tag{18}$$

From the (18), we deduce the equations linking between stator and rotor currents:

Creative Commons Attribution-NonCommercial-NoDerivatives 4.0 International License (CC BY-NC-ND)

$$\begin{cases} I_{sd} = \frac{\Phi_s}{L_s} - \frac{M}{L_s}.I_{rd} \\ I_{sq} = -\frac{M}{L_s}.I_{rq} \end{cases} \quad (19)$$

The relations of the powers become:

$$\begin{cases} P_s = V_{sq}.I_{sq} \\ Q_s = V_{sq}.I_{sd} \end{cases} \quad (20)$$

To express the power relations as a function of the rotor currents, we replace in the previous equation the currents by the (19):

$$\begin{cases} P_s = -V_s.\frac{M}{L_s}I_{rq} \\ Q_s = \frac{V_s}{L_s}\Phi_s - V_s.\frac{M}{L_s}.I_{rq} = \frac{V_s^2}{L_s.w_s} - V_s.\frac{M}{L_s}.I_{rq} \end{cases} \quad (21)$$

By replacing flux and stator currents in the (10) by the expression (19) we obtain:

$$\begin{cases} \Phi_{rd} = (L_r - \frac{M^2}{L_s}).I_{rd} + M\frac{V_s}{L_s.w_s} \\ \Phi_{rq} = (L_r - \frac{M^2}{L_s})I_{rq} \end{cases} \quad (22)$$

In order to control the generator, these expressions are established showing the relationship between the currents and the rotor voltages that will be applied to it.

$$\begin{cases} V_{rd} = R_r.I_{rd} + L_r\sigma\frac{dI_{rd}}{dt} - gw_sL_r\sigma I_{rq} \\ V_{rq} = R_r.I_{rq} + L_r\sigma\frac{dI_{rq}}{dt} - gw_sL_r\sigma I_{rd} + g.\frac{V_sM}{L_s} \end{cases} \quad (23)$$

Where: $\sigma = (1 - \frac{M^2}{L_sL_r})$ is the dispersion coefficient.

It exists two methods of Field Orientation Control [17].

- **Direct field orientation control (DFOC)**

This method consists on regulating the active and reactive stator powers of DFIG independently, by using a PI controller on each axis, while neglecting the coupling terms between the two axes. This method is called direct because the PI controller act directly on the voltages [16][17].

- **Indirect field orientation control(IFOC)**

Unlike direct control and in order to regulate the powers as well as the currents rotor. This method takes into consideration the coupling terms and puts two PI controllers on each axis [2].The figure bellow shows the model of indirect field orientation control which we chose in our study.

Creative Commons Attribution-NonCommercial-NoDerivatives 4.0 International License (CC BY-NC-ND)

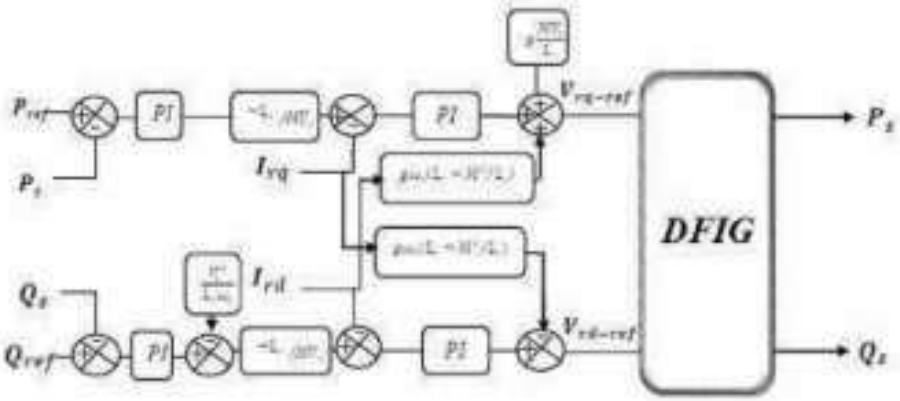

Fig.3.Block diagram of the closed loop indirect control.

Controllers synthesis:

PI regulators used for the adjustment of active and reactive power and I_{rd} I_{rq} currents. Offers several advantages in particular speed and simplicity to implement, as well as it offers acceptable performance for the regulation of the system considered [18].The regulators of each axis have the role of canceling the difference between the reference active and reactive powers and the measured active and reactive power.

The PI regulator equation is:

$$R(s) = K_p + \frac{K_i}{s} \quad (24)$$

Where:

- K_p: is the proportional gain controller.
- K_i: is the integral controller gain.

The corrected closed loop system is shown in Fig4.

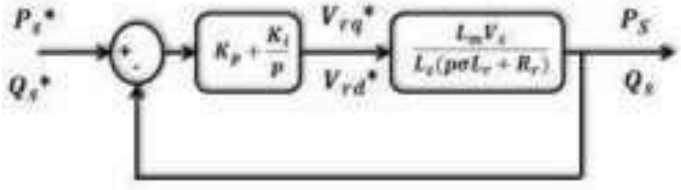

Fig4. Structure of PI controller.

Results of the simulation

The proposed IFOC scheme is implemented with Matlab/Simulink in order to evaluate its performances.DFIG used for the simulations has the following parameters:

Parameter name and symbol	Numerical value
Nominal power P_n	1.5 MW
Rated current I_n	1900 A
Nominal stator voltage V_s	398/690V
Nominal stator frequency	50 Hz
Nominal rotor voltage V_r	225/389 V
Stator resistance R_s	0.012 Ω

Creative Commons Attribution-NonCommercial-NoDerivatives 4.0 International License (CC BY-NC-ND)

Rotor resistance R_r	0.021Ω
Stator inductance L_s	0.0137 H
Rotor inductance L_r	0.0136 H
Mutual inductance L_m	0.0135 H
DFIM viscous friction coefficient	0.0024 N.m/s
Number of P pole pairs	2

Table 1.DFIG parameters.

The generator is driven at a fixed speed equal to 1455 rpm with an application of a reference active power P = −500000W at time t = 0s and t = 5s then P =1000000W between t= 3s and t = 5s and a zero reactive power.

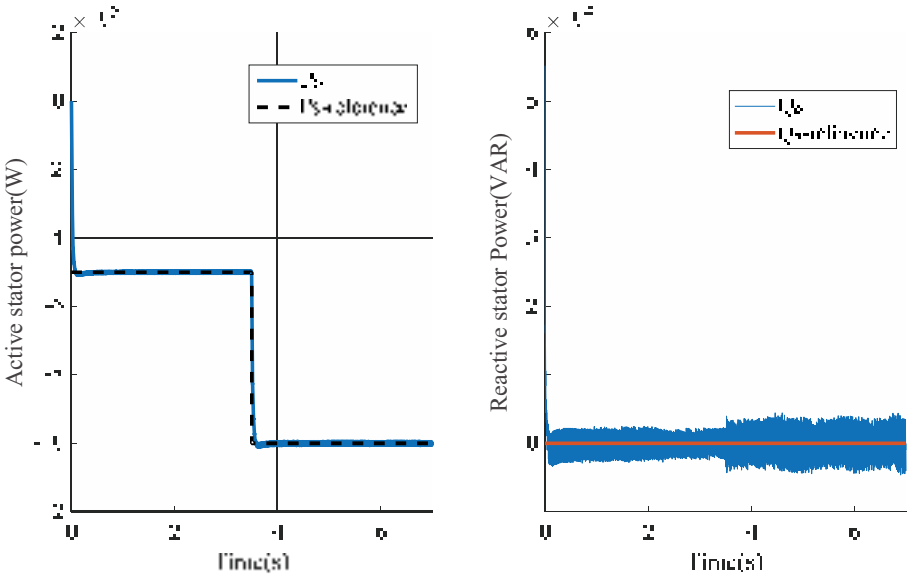

Fig5. Comparison between Active and reactive stator power and their references.

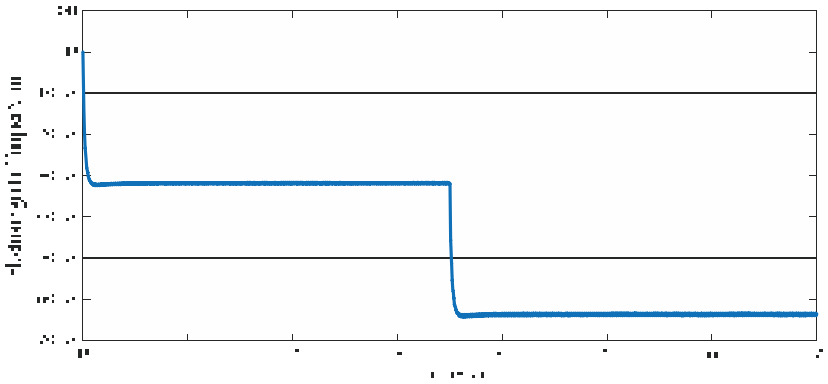

Fig6. Electromagnetic Torque.

Creative Commons Attribution-NonCommercial-NoDerivatives 4.0 International License (CC BY-NC-ND)

Algerian Journal of Engineering Architecture and Urbanism Vol. 5 Nr. 3 2021
ISSN: 2588-1760

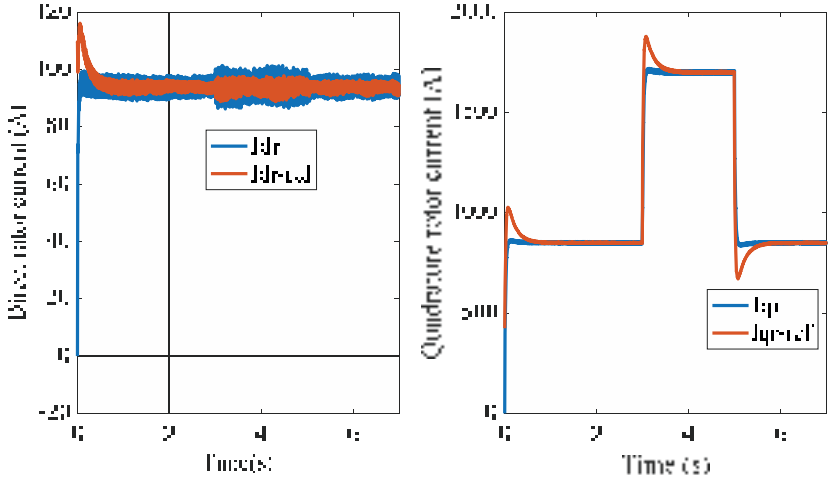

Fig7. The components of rotor current.

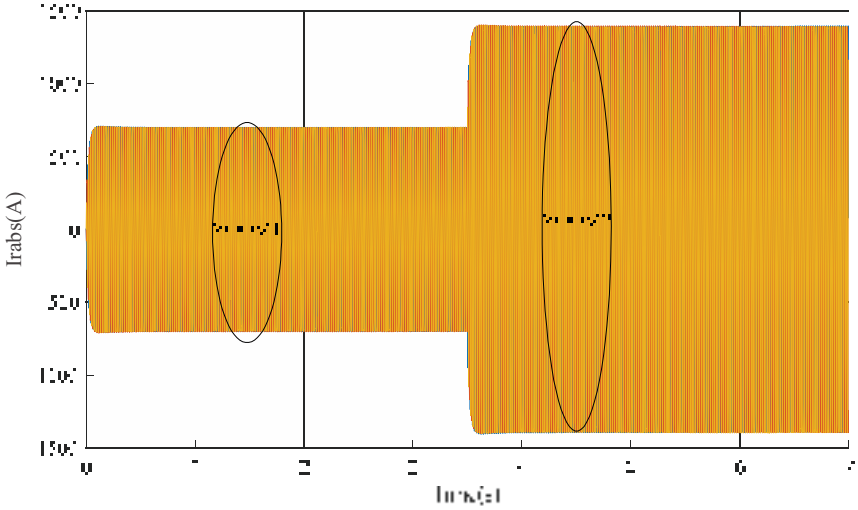

Fig8. Phase rotor currents.

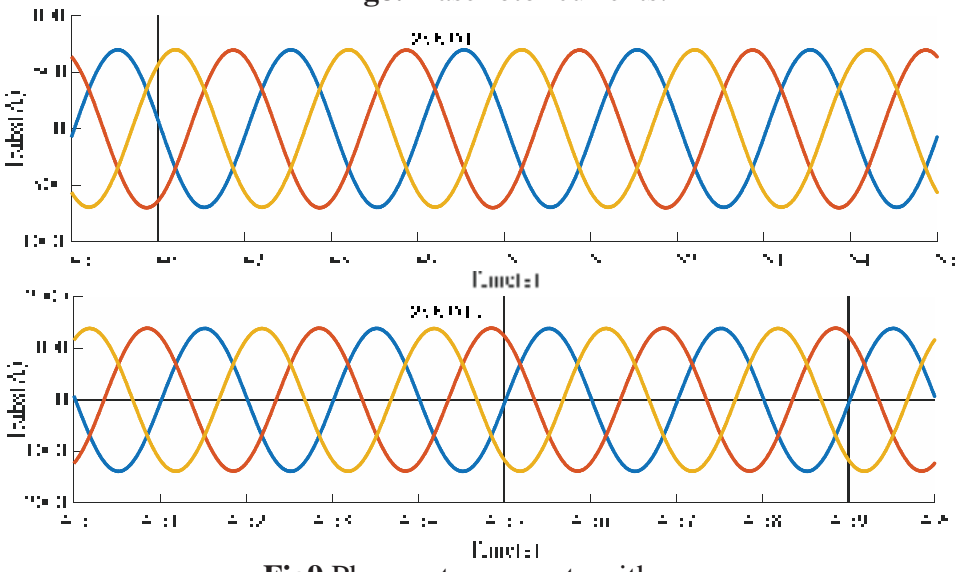

Fig9. Phase rotor currents with zoom.

Creative Commons Attribution-NonCommercial-NoDerivatives 4.0 International License (CC BY-NC-ND)

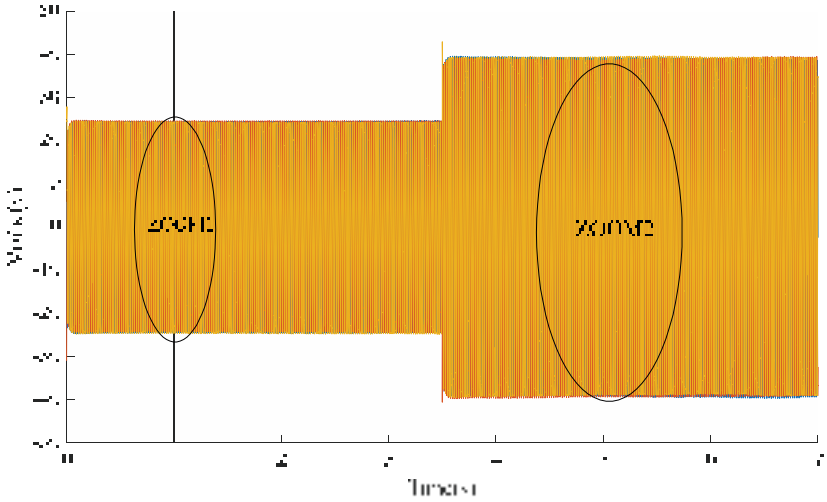

Fig10. Phase rotor voltages.

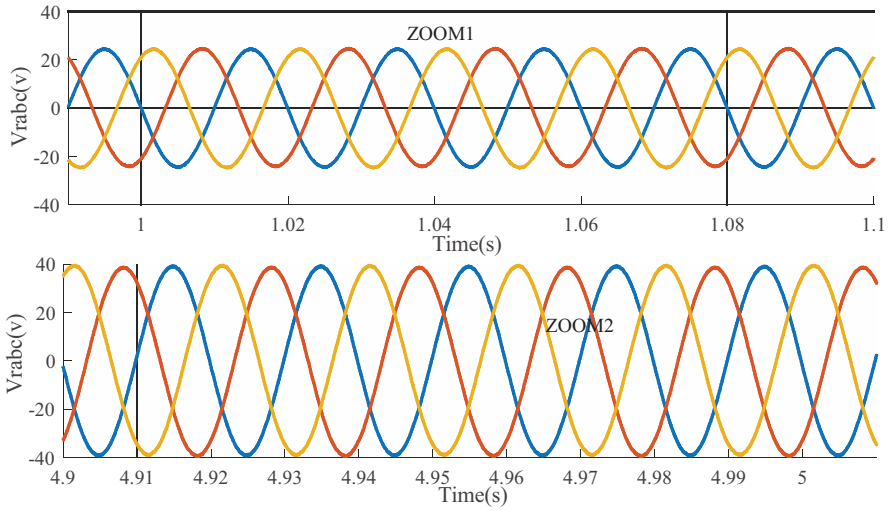

Fig11. Phase rotor voltages with zoom.

The figures above show the variations of the various quantities when the vector control makes it possible to decouple the expressions of the active and reactive power of the generator. Fig.6 shows that the active and reactive powers issued by the DFIG follow the corresponding references. This is due to the control quadrature and forward components of the DFIG current.

Conclusion:

In this paper, we developed the DFIG model and its indirect vector control. The simulation results showed very encouraging performance and conform to those found in the literature. We note that the indirect control using PI controller presents a good decoupling in the adjustment of the active and reactive powers at the stator level and a good tracking at their imposed reference values.

Creative Commons Attribution-NonCommercial-NoDerivatives 4.0 International License (CC BY-NC-ND)

References:

[1]:*T. Ackermann and Soder, L." An Overview of Wind Energy-Status 2002", Renewable and Sustainable Energy Reviews, 6(1-2), 67-127 (2002).*

[2]:*S.Mensou, A.Essadki, T.Nasser, B.B.Idrissi,"An Efficient Nonlinear Backstepping Controller Approch of a wind Power Generation System based on a DFIG", International Journal of Renewable Energy Research, Vol.7, No 4, pp.1520-1528, December 2017.*

[3]:*H.Alami, E.Ziani, B.Bossoufi,"Speed control of the doubly fed induction generator applied to a wind system" Journal of Theoretical and Applied Information Technology, pp426-433, Vol.83 No.3, January 2016.*

[4]:*A. Boualouch, A. Essadki, T. Nasser, A. Boukhriss, A. Frigui, "Power Control of DFIG in WECS Using Backstipping and Sliding Mode Controller", International Journal of Electrical Computer Energetic Electronic and Communication Engineering, vol. 9, pp. 612-618, 2015.*

[5]:*B.Bossoufi, S.Ionita, H.Alami Arroussi, M.El Ghamrasni, Y.Ihedrane "Managing voltage drops a variable speed wind turbine connected to the grid", IJAAC International Journal of Automation and Control ,Vol.11, No. 1, January 2017.*

[6]:*B.Bossoufi, M.Karim, A.Lagrioui, M.Taoussi, A.Derouich"Observer Backstepping control of DFIG Generators for Wind Turbines Variable-Speed: FPGA-Based Implementation", Renewable Energy Journal (ELSIVER), pp 903-917, Vol. 81, September 2015.*

[7]:*M. El Azzaoui, H. Mahmoudi, K. Boudaraia, "Backstepping Control of wind and photovoltaic hybrid Renewable Energy System".International Journal of Power Electronics and Drive Systems, Vol.7, pp 677-686, September 2016.*

[8]:*B.Bossoufi, M.Karim, A.Lagrioui, M.Taoussi, M.L.El Hafyani "Backstepping control of DFIG Generators for Wide-Range Variable-Speed Wind Turbines " IJAAC International Journal of Automation and Control, pp 122-140, Vol.8 No.2, July 2014.*

[9]:*S. Mensou, A. Essadki, I. Minka, T. Nasser and B. B. Idrissi,"Backstepping Controller for a Variable Wind Speed Energy Conversion System Based on a DFIG," IEEE International Renewable and Sustainable Energy Conference (IRSEC), pp. 1-6, December 2017.*

[10]:*S. AIMANI," Modelling of different wind turbine technologies integrated in a medium voltage network ", Doctoral thesis, University of Science and Technology of Lille. 06/12/2004.*

[11]:*B.Bossoufi, M.Karim, A.Lagrioui, M.Taoussi "FPGA-Based Implementation nonlinear Backstepping control of a PMSM Drive" IJPEDS International Journal of Power Electronics and Drive System, pp 12-23 Vol.4 No.1, March 2014.*

[12]:*G. Poddar and V. T. Ranganathan, "Sensorless Double-Inverter-Fed Wound-Rotor Induction-Machine Drive," IEEE Trans. Ind. Electron., Vol. 53, No.1, pp. 86–95, February 2006.*

[13]:*N. El Ouanjli, A. Derouich, A. El Ghzizal, A. Chebabhi, M. Taoussi, "A comparative study between FOC and DTC controls of the Doubly Fed Induction Motor (DFIM) ", IEEE International Conference on Electrical and Information Technologies, Rabat- Morocco 2017.*

[14]:*N. El Ouanjli, M. Taoussi, A. Derouich, A. Chebabhi, A. El Ghzizal, B. Boussoufi "High Performance Direct Torque Control of Doubly Fed Induction Motor using Fuzzy Logic", Gazi university journal of science 31(2),2018.*

[15]:*M. Taoussi, M. Karim, D. Hammoumi, C. Elbakkali, B. Bossoufi, N. El Ouanjli,"Comparative study between Backstepping adaptive and Field-oriented control of the DFIG applied to wind turbines", 3rd IEEE International Conference on Advanced Technologies for Signal and Image Processing , May 2017.*

[16]:*M. Nadour, A. Essadki, T. Nasser. "Comparative Analysis between PI & Backstepping Control Strategies of DFIG Driven by Wind Turbine", International Journal of Renewable Energy Research Vol. 7, No 3, pp.1307-1.*

[17]:*Y. Ihedrane, C. El Bekkali , B. Bossoufi, "Power Control of DFIGGenerators for Wind Turbines Variable Speed", International Journal of Power Electronics and Drive Systems, Vol. 8, pp. 444-453. March 2017.*

Creative Commons Attribution-NonCommercial-NoDerivatives 4.0 International License (CC BY-NC-ND)

Algerian Journal of Engineering Architecture and Urbanism Vol. 5 Nr. 3 2021
ISSN: 2588-1760

OPTIMIZATION OF WIRELESS SENSOR NETWORK COVERAGE BASED ON A NEW OPTIMAL SENSOR PLACEMENT STRATEGY

Asma MESMOUDI
Dr, HASSIBA BEN BOUALI University of Chlef, Faculty of technology, Department of electronic, a.mesmoudi@univ-chlef.dz

Samira MESMOUDI
Dr, AMAR TALIDJI University of Laghouat, Faculty of technology, Department of electronic, s.masmoudi@lagh-univ.dz

Chaima MADAOUI
Student, HASSIBA BEN BOUALI University of Chlef, Faculty of technology, Department of electronic, chaimamada9@gmail.com

Abstract:
Wireless sensor networks (WSNs) have recently gained a lot of attention by scientific community due to their very wide spectrum of applications. In such networks, the deployment of sensors nodes is a crucial phase that can affects significantly the coverage quality of network monitoring area. Recently, many works focused specifically on the optimization of Network Coverage while maximizing the lifetime of the Wireless Sensor Network. In this context, we propose a new placement strategy of sensors based on geometric methods. Hence, our approach aims to optimize two essential criteria, namely the number of nodes deployed and the redundant monitoring areas. Our proposal outperforms exiting approaches. Indeed, the simulation results confirmed that our approach guaranty a higher coverage ratio of the monitored area with a lower number of nodes deployed.

Key words: Wireless Sensor Networks; network lifetime; coverage; placement strategy.

Introduction:

A Wireless Sensor Network (WSN) is a wireless network consisting of a large number of small sensors with low-power transceivers. They are expected to be an effective tool to cooperatively monitor physical or environmental conditions (Xu G., Shen W., Wang X. ,2014) WSNs are rapidly emerging technologies with potentials for many different distributed applications, such as detection of chemical or biological agents, fire detection, or tracking of enemy vehicles, which renders them a hot research topic over the past few years (Labraoui N., Gueroui M., Aliouat M., Petit J, 2011). Every application in WSN requires a particular placement strategy for sensor nodes to ensure an optimum performance system.

The issue of placement of sensor nodes in a network is a strategy that is used to define the topology of the network. Therefore, the coverage of the monitored region, and network connectivity, and power consumption are also directly affected by the network topology.

Creative Commons Attribution-NonCommercial-NoDerivatives 4.0 International License (CC BY-NC-ND)

Recently, Many related works are primarily aimed at ensuring full or acceptable coverage and optimal network connectivity. For instance, there are several solutions based on geometric methods to deal with the node placement problem; They are based on geometric concepts and calculations (Khoufi I., Minet P., Laouiti A., Mahfoudh S, 2017). Among these methods, we find the placement of (NGOM D., Lorenz P., Gueye B, 2015), a new deterministic node placement model that not only reduces the number of sensors needed to completely cover a given surveillance area but also maintains optimal network connectivity. However, this algorithm suffers from two major problems. The first problem concerns the high percentage of the Redundant Coverage Area. The second is that the network production cost is high.

To address the above problems, we propose in this paper, a novel network placement method based on geometric concepts. Our proposed approach minimizes both the number of required sensors and the Redundant Coverage Area to ensure: the entire coverage of the monitored region and optimal network connectivity.
Our technique achieves a higher percentage of the area covered under lower sensor node density, compared to the proposed approach in (NGOM D., Lorenz P., Gueye B, 2015).

The remainder of this paper is organized as follows: section 2, discusses the related work. A detailed description of the model placement proposed in (NGOM D., Lorenz P., Gueye B, 2015) is presented in section 3. Section 4 presents our approach. The simulation results are reported in section 5. Finally, section 6 concludes the paper.

Related Works:

Several works are proposed in the literature to Improve Lifetime in Wireless Sensor networks based on Geometric Placement of Sensors with Coverage and Connectivity Constraints.

Authors in (Akewar M. C., Thkur N. V, 2012) have presented a detailed study on different strategies for deploying sensor nodes in WSN. These strategies based on algorithmic geometry computation methods provide a good reference and overview of the coverage and connectivity issues in WSN. However, they did not integrate the problems of coverage redundancies.

Authors in (Khasteh S. H., Shouraki S. B., Hajiabdorahim N., Dadashnialehi E, 2012) have focused on the node placement strategies to ensure good coverage and connectivity properties. The authors proposed a new approach integrated with the coverage problems. This approach is based on a deterministic deployment of the sensor nodes, indeed the assumed convex area of interest allowed to determine the relation that binds the complete coverage of the area of interest. This relation, which links the communication radius of each sensor Rc and its detection radius Rs, is a sufficient condition for the coverage to be complete.

Creative Commons Attribution-NonCommercial-NoDerivatives 4.0 International License (CC BY-NC-ND)

Authors in (Wang X., Xing G., Zhang Y., Lu C., Pless R., Gill C, 2003), showed that the 1-coverage of a convex region is sufficient to guarantee the 1-connectivity of the network if and only if, the communication radius Rc of each sensor is at least twice its detection radius Rs, thus, $Rc \geq 2Rs$.

Authors in (NGOM D., Lorenz P., Gueye B, 2015) presented a method for deterministic placement of nodes in the area of interest, This method is based on a partition of the area of interest into grids of the same size, and each sensor is placed according to its coordinates (x, y) in the center of some well-chosen grids. It allowed to reduce the number of sensors needed to cover a given monitoring area, moreover, it ensured optimal connectivity of the wireless sensor network.

To demonstrate the effectiveness of our Geometric Placement, the proposed placement cited in (NGOM D., Lorenz P., Gueye B, 2015) is selected and compared to ours. In the next section, a brief description of the proposed strategy of placement in (NGOM D., Lorenz P., Gueye B, 2015) is given.

Sensors placement model based on grids:

In (NGOM D., Lorenz P., Gueye B, 2015), the authors have proposed a new method for the optimal placement of sensor nodes. In this geometric placement method, the monitoring area is partitioned into grids with equal dimensions. The sensor nodes are placed according to their coordinates in the center of some well-chosen grids such that the entire monitoring area remains fully covered and the graph formed by the set of sensor nodes is k-connected ($k \leq 4$) (Fig. 1).

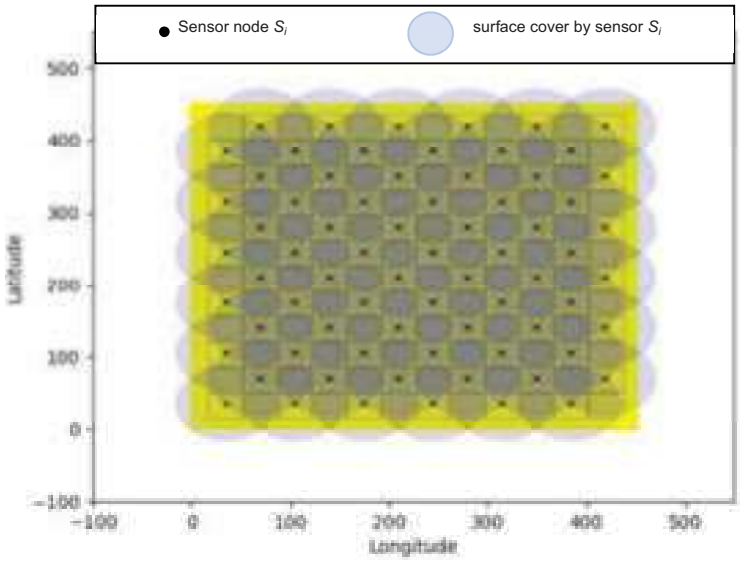

Fig1. The geometric placement model of the nodes.

Creative Commons Attribution-NonCommercial-NoDerivatives 4.0 International License (CC BY-NC-ND)

Algerian Journal of Engineering Architecture and Urbanism Vol. 5 Nr. 3 2021
ISSN: 2588-1760

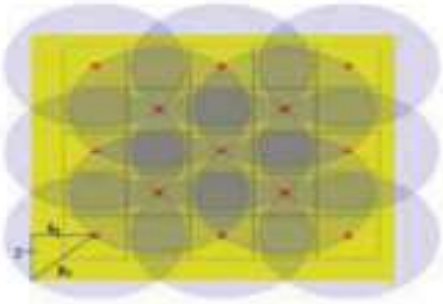

Fig2. Illustration of the N_1 sensor coordinate.

.

To calculate the coordinates (x,y) of the first sensor N_1 in the monitoring area, the Pythagorean theorem applies to the isosceles rectangle triangle with equal side measures (x=y), and Rs the measure of the hypotenuse (Fig. 2). Therefore, the coordinates (x,y), corresponding to the following equation :

$$x = y = \frac{\sqrt{2}}{2} R_s \qquad (1)$$

the distance between the two neighboring sensors N_i and N_j located on the same row or column is given by the following equation:

$$d(N_i, N_j) = \sqrt{2}\, R_s \qquad (2)$$

According to the model of (NGOM D., Lorenz P., Gueye B, 2015), the placement of the sensors is brought to intersecting circles. The intersection of these circles caused regions of redundant coverage (Fig. 3).

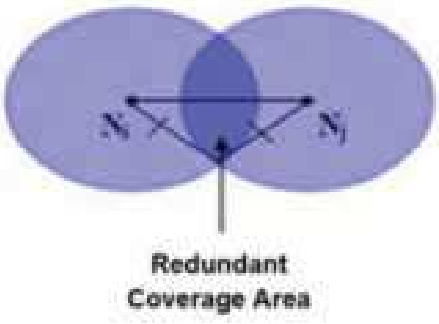

Fig3. Example illustrates the area covered by two neighboring sensors according to the proposed model cited in (NGOM D., Lorenz P., Gueye B, 2015)

We show that according to our placement method an area may be covered by many sensor nodes at the same time; this is due to overlapping coverage areas of neighbor sensor nodes. To optimize the energy consumption in the network, we propose a new placement model while maintaining the full coverage of the monitored region and optimal network connectivity to ensure robustness in the communication.

Creative Commons Attribution-NonCommercial-NoDerivatives 4.0 International License (CC BY-NC-ND)

Algerian Journal of Engineering Architecture and Urbanism Vol. 5 Nr. 3 2021
ISSN: 2588-1760

Our proposed sensors placement model:

In our deployment model. Previous knowledge of the monitoring area is required, the deployment of the nodes is deterministic (uniform). We assume an area of interest of surface L×L. This is partitioned into 1m×1m grids and each sensor is placed in the center of each grid. Where each sensor is characterized by its coordinates (x, y) and two different radius, one to ensure the communication noted Rc, and the other to ensure the coverage noted Rs, we assume that Rc=2Rs. Fig. 4 represents the placement used in our solution.

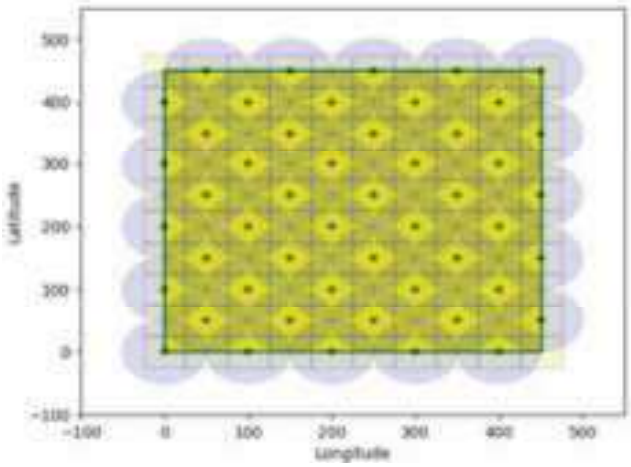

Fig4. Our improved geometric sensor placement model

According to the placement that is illustrated in the previous figure, it has been noted that to cover the point having the coordinates (0,0) it has been taken into consideration that the distance between two neighboring sensors N_i and N_j located on the same line and same column, is the double of the detection radius Rs.as mentioned in the following equation

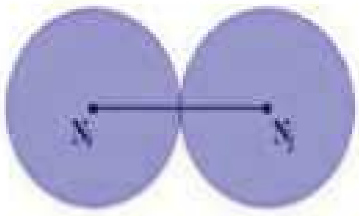

Fig5. Example illustrates the area covered by two neighboring sensors according to our placement model

In our solution, more precisely in the placement of the sensors located in the same row and the same column, we have based on the following equations:

$$x_{i+1} = x_i + 2R_S \qquad (3)$$

Creative Commons Attribution-NonCommercial-NoDerivatives 4.0 International License (CC BY-NC-ND)

$$y_{j+1} = y_j + 2R_S \qquad (4)$$

i: Line index
j:column index ;
x_i ,y_j : sensor coordinates.

The coordinates (x, y) of the sensors located in the same column and different adjacent rows or the same row and different adjacent columns, are given by the following equations:

$$x_{i+1} = x_i + R_S \qquad (5)$$

$$y_{j+1} = y_j + R_S \qquad (6)$$

With the mentioned strategy of node placement, some uncovered surfaces are detected (Fig. 6). To solve this problem, we have placed other nodes at the borders of the network area (Fig.4).

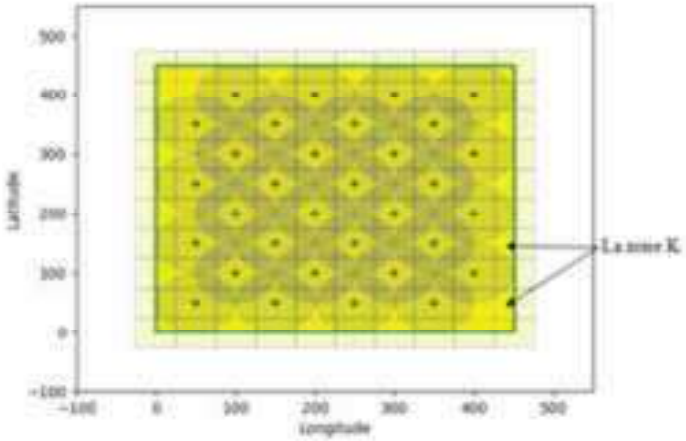

Fig6. An example illustrates the problem of uncovered areas.

Simulation Results

In the simulation environment, which is developed in Python 2.7,ó nodes are uniformly deployed, within an area of size Z. Two node densities are considered by changing Z, high density (250m × 250m) and low density (450m × 450m). The transmission range of a sensor is 100 m. In all of our graphs, each plotted point represents the average value of 30 trials. The performance of our approach is evaluated in terms of the following metrics:Area covered.
Area covered in %: is the most important metric to evaluate the performance of proposals that solve the coverage problem in wireless sensor networks. It is defined as the average percentage of the area of interest covered (Elhabyan R., Shi W., St-Hilaire M, 2019).

The first placement represents the solution proposed by (NGOM D., Lorenz P., Gueye B, 2015) and the second placement represents our improvement of the latter. The main metric

Creative Commons Attribution-NonCommercial-NoDerivatives 4.0 International License (CC BY-NC-ND)

evaluated in our simulations is the rate of the covered area. And to evaluate the performance, we had to vary the number of nodes. The high density corresponds to the surface network of (250m x 250m) and the low density corresponds to the surface network (450m x 450m).

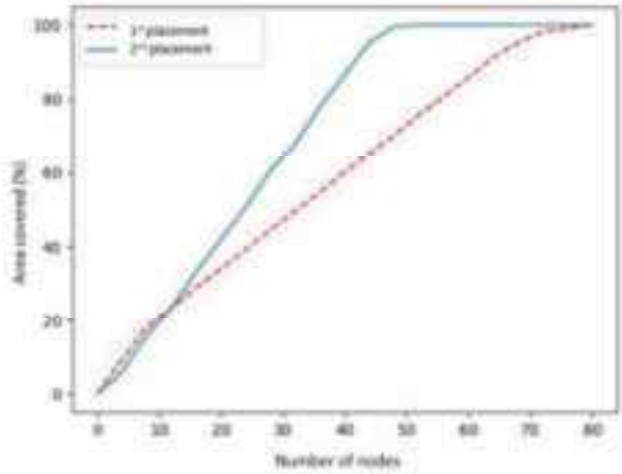

Fig7. Evolution of the rate of the covered surface according to the number of nodes in a surface network (450m x 450m)

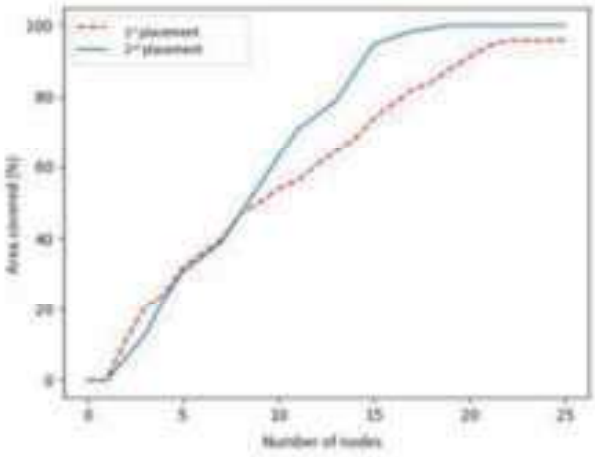

Fig8. Evolution of the rate of the covered surface according to the number of nodes in a surface network (250m x 250m)

Fig. 7 and Fige. 8 show the area coverage rate as a function of the number of nodes in two areas (450m x 450m) and area (250m x 250m) networks, respectively. By analyzing these figures, we could notice that the rate of the area covered increases with the number of nodes deployed. This is because nodes increase their chances of having areas to cover.
Fig. 7 and Fig. 8 show the good results of our placement method. This is because sensors placed at the border of the area to be monitored can plug coverage holes.

Conclusion:

In this paper, we have presented an improved version of a placement model proposed by (NGOM D., Lorenz P., Gueye B, 2015). It is based on the same grid placement process. On the other hand, the optimization provided by our approach concerns the reduction of the

Creative Commons Attribution-NonCommercial-NoDerivatives 4.0 International License (CC BY-NC-ND)

redundancy in the covered area, the increase of the covered area rate, minimization of the number of deployed sensors. This optimization strategy is adaptive for a low density of nodes in the network. The simulation results showed a significant gain in the covered area rate. We can conclude that our placement leads to very good coverage performance and outperforms the approach (NGOM D., Lorenz P., Gueye B, 2015).

References:

Xu G., Shen W., Wang X. (2014), *Applications of wireless sensornetworks in marine environment monitoring: a survey*,Sensors **14(9) :**16932–16954.

Labraoui N., Gueroui M., Aliouat M., Petit J. (2011), *RAHIM: Robust Adaptive Approach Based on Hierarchical Monitoring Providing Trust Aggregation for Wireless Sensor Networks*, J. UCS **17(11) :** 1550-1571.

Khoufi I., Minet P., Laouiti A., Mahfoudh S. (2017), *Survey of deployment algorithms in wireless sensor networks: Coverage and connectivity issues and challenges*, Int. J. Auton. Adapt. Commun. Syst. **10(4)** :341–390.

NGOM D., Lorenz P., Gueye B. (2015)**,** *A Distributed Scheduling Algorithm to Improve Lifetime in Wireless Sensor Network based on Geometric Placement of Sensors with Coverage and Connectivity Constraints*, Ninth International Conference on Sensor Technologies and Applications, SENSORCOMM‟15, Venice, Italy, ISBN: 978-1-61208-425-1.

Akewar M. C., Thkur N. V. (2012), *Study of Wireless Sensor Network Deployments,* International Journal of Computer and Communication **2(4)** : 533-541.

Khasteh S. H., Shouraki S. B., Hajiabdorahim N., Dadashnialehi E. (2012), *A new approach for integrated coverage and connectivity in wireless sensor networks,* in Journal Computer Communications **36(1):**113-120.

Wang X., Xing G., Zhang Y., Lu C., Pless R., Gill C., (2003), *Integrated Coverage and Connectivity Configuration in Wireless Sensor Networks* , SenSys'03,Los Angeles, California, USA,

Elhabyan R., Shi W., St-Hilaire M. (2019), *Coverage protocols for wireless sensor networks: Review and future directions*. J. Commun. Netw. **21(1) :** 45–60.

Creative Commons Attribution-NonCommercial-NoDerivatives 4.0 International License (CC BY-NC-ND)

Algerian Journal of Engineering Architecture and Urbanism Vol. 5 Nr. 3 2021
ISSN: 2588-1760

THE PERFORMANCE OF THE DESALINATION PLANT CHATT EL-HILLAL-BENI-SAF
LA PERFORMANCE DE LA STATION DE DESSALEMENT CHATT EL-HILLAL-BÉNI-SAF

ZIREG Hanane (masterante)
Institut de Maintenance et de Sécurité Industrielle / Université Oran 2 - Mohamed Ben Ahmed
zireghanane@gmail.com

MANSOUR Mohamed (masterant)
Institut de Maintenance et de Sécurité Industrielle / Université Oran 2 - Mohamed Ben Ahmed
midohido23@gmail.com

HEBBAR Chafika (Professeur)
Laboratoire d'Ingénierie en Sécurité Industrielle et Développement Durable/Institut de Maintenance et de Sécurité Industrielle / Université Oran 2 - Mohamed Ben Ahmed
hebbar.chafika@univ-oran2.dz

Résumé:
Le dessalement de l'eau de mer en Algérie revêt un caractère stratégique et remplacera la ressource naturelle dans la majorité des villes du nord algérien et surtout l'ouest. Quel que soit le procédé utilisé (membranaire ou de distillation), toutes les stations de dessalement produisent des quantités considérables de saumure.
Ce travail a pour objectif le renforcement des ressources hydriques, l'étude de la performance de la station de dessalement « Chatt El-Hillal » par le suivi de l'évolution de la qualité physico-chimique de son eau brute et de l'eau obtenue par osmose inverse sans oublier l'amélioration de la qualité des eaux distribuées pour Oran et Ain-Temouchent. Cette station constitue l'un des grands projets réalisés par le gouvernement algérien en matière d'approvisionnement en eau potable, avec une capacité de 200 000 m^3/ jour.
A la lumière des résultats obtenus, les eaux issues de dessalement de l'eau de mer présentent une qualité physico-chimique adéquate comparée aux normes nationales. En revanche, les analyses chimiques révèlent des teneurs relativement élevées en brome, chlorures et en certains ions (calcium, magnésium, sodium et phosphore).

Mots clefs : Eau de mer, saumure, dessalement, paramètres physicochimiques, Station Béni-Saf « Chatt El-Hillal ».

Abstract :
The desalination of seawater in Algeria is strategic and will replace the natural resource in the majority of cities in northern Algeria and especially in the west. Whatever process is used (membrane or distillation), all desalination plants produce considerable quantities of brine.

Creative Commons Attribution-NonCommercial-NoDerivatives 4.0 International License (CC BY-NC-ND)

This work aims to strengthen water resources, study the performance of the "Chatt El-Hillal" desalination plant by monitoring the evolution of the physicochemical quality of its raw water and water. Obtained by reverse osmosis without forgetting the improvement of the quality of the water distributed for Oran and Ain-Temouchent. This station is one of the major drinking water supply projects carried out by the Algerian government, with a capacity of 200,000 m3 / day.
In the light of the results obtained, the water resulting from seawater desalination has an adequate physicochemical quality compared to national standards. On the other hand, chemical analyzes reveal relatively high contents of bromine, chlorides and certain ions (calcium, magnesium, sodium and phosphorus).

Keywords: Seawater, brine, desalination, physicochemical parameters, Béni-Saf "Chatt El-Hillal" station.

Introduction :

L'eau vitale, base du développement socioéconomique durable, recouvre environ 75% de la surface de la terre, dont 94% d'eau salée provient des océans et 6% d'eau douce. Les besoins en eau douce dans le monde comme en Algérie augmentent parallèlement avec l'augmentation de l'agriculture, de l'industrialisation et de la croissance de population humaine (**Boyé**, **2008**). Selon l'inventaire mondial de l'Association Internationale de Dessalement (IDA), il existe plus de 15 000 unités de dessalement dans le monde produisant environ 56 millions de m^3/j, dans 120 pays réparties comme suit : 60,6% de l'eau de mer employée dans ces usines, 22,8% est de l'eau saumâtre et 16,6% d'eaux superficielles et résiduelles (**Morsli**, **2013**). L'Algérie sera à l'abri grâce aux méga-stations dont la plus grande station de dessalement de la Mactâa d'une capacité de production de 500 000 m^3/j permettant la couverture à long terme des besoins de cinq millions de personnes en eau potable, et plus de 30 stations d'une capacité allant de 25000 à 500 000 m^3/j, et produire plus de 2,5 millions de m^3/j à travers ce vaste programme (**Bessenasse et Belkacem Filali, 2014**).

L'eau de mer est la matière première d'une usine de dessalement qui constitue le pilier de la stratégie d'approvisionnement d'eau en Algérie en général, et dans l'ouest algérien en cas particulier et garantit la fourniture de l'eau dans les zones à déficit hydrique avec un coût minimal (**Frenkel**, **2011**). Les constituants présents dans les eaux résiduaires rejetées par les usines de dessalement dépendent de la qualité de l'eau d'alimentation, de la qualité de l'eau douce produite et du procédé de dessalement adopté ; Ils comprennent l'effluent de saumure concentrée, des désinfectants et des agents antisalissures, des eaux chaudes et des effluents aqueux (distillats et condensats d'éjecteurs) (**Dawoud** et **Al Mulla**, **2012**). L'eau dessalée peut être destinée vers de nombreux usages comme : la consommation humaine, l'industrie, l'irrigation, la production de l'eau embouteillée, la production de l'eau distillée (**Metaiche**, **2006**). Le dessalement de l'eau de mer en Algérie, a permis notamment l'augmentation de la ressource en eau douce disponible, de fournir une solution en cas de sécheresse et de faire face aux situations de stress hydrique ou pénuries et de crises.

Ce travail a pour objectif l'étude de la performance de la station de dessalement « Chatt El-Hillal » par le suivi de l'évolution de la qualité physico-chimique de son eau brute

Creative Commons Attribution-NonCommercial-NoDerivatives 4.0 International License (CC BY-NC-ND)

et de l'eau obtenue par osmose inverse, le renforcement des ressources hydriques sans oublier l'amélioration de la qualité des eaux potables distribuées pour les deux villes Oran et Ain-Temouchent. Cette station constitue l'un des grands projets réalisés par le gouvernement algérien en matière d'approvisionnement en eau potable, avec une capacité de 200 000 m^3/ jour.

Problématique :

Plus d'un milliard de personnes dans le monde n'ont pas accès à des ressources d'eau douce ; la raison pour laquelle il faut donc leur assurer un minimum de 5l/j/hab (**Kara Omar** et **Khaldi**, **2017 ; OMS, 2011**). C'est dans cette thématique que les stations de dessalement des eaux s'inscrivent puisqu'elles permettent de produire de l'eau potable à partir de l'eau de mer (**Rerolle**, **2010**) ou d'eau saumâtre grâce à des procédés membranaires par osmose inverse et de distillation et assurent un approvisionnement correct en eau. Le dessalement, procédé moins énergivore, est en pleine expansion avec une progression d'environ 7% par an (**Mandri**, **2011**). L'Algérie, région aride et semi-aride, est soumise à des conditions physiques et hydroclimatiques défavorables, appuyées par des périodes de sécheresse chronique ; elle enregistrera un déficit en eau d'un milliard de m^3 d'ici l'an 2025 (**Remini, 2010**) ; elle complète alors son stress hydrique par l'obtention de l'eau douce à travers l'implantation des stations de dessalement de l'eau de mer (devenu une nécessité vitale) sur tout son littoral de façade maritime de 1622km.

Matériel et méthodes :

Zone d'étude :

La construction de la station de dessalement d'eau de mer de Béni Saf (SDEM) entre dans le programme de réalisation des quatorze stations lancées par le gouvernement algérien. La SDEM est réalisée par la société de projet Beni Saf Water Company Spa «BWC» qui est constituée à partir du consortium Algéro-Espagnol en l'occurrence GEIDA COBRA (espagnole) avec 51% des actions et de l'AEC (Algérienne) avec 49 % des actions. Par ailleurs, l'exploitation de l'usine durant 25 ans est confiée à l'entreprise espagnole UTE desaladora Beni saf operation y mantemeniento. L'usine est implantée dans la commune de Sidi-Adda (W. Ain Temouchent) d'une superficie de 51 118 m^2, mise en service totale le 04 avril 2010, de capacité de production annuelle : 200 000 m^3/jour (à faible coût pour subvenir aux besoins des populations de la région d'Ain-Temouchent et d'Oran) et d'une consommation électrique : 4,15 KW/m^3 (fig.1). La construction de l'usine a été effectuée conformément à la législation concernant l'hygiène et la sécurité ; il n'existe pas de rejets atmosphériques engendrés par l'usine. Elle est soumise à une autorisation ministérielle selon le décret exécutif 07-144 du mois de mai 2007. Le climat de la zone côtière se caractérise par une saison relativement pluvieuse s'étalant du mois d'octobre à avril, la saison sèche s'étale sur une période de 5 mois (mai-juin, juillet-août-septembre). La température moyenne annuelle est de 300mm avec 49mm au mois de janvier et 1mm au mois le plus sec juillet. L'humidité est assez importante au cours de l'année : elle varie entre 72 et 76% avec une moyenne de 73,4%.

Creative Commons Attribution-NonCommercial-NoDerivatives 4.0 International License (CC BY-NC-ND)

Algerian Journal of Engineering Architecture and Urbanism Vol. 5 Nr. 3 2021
ISSN: 2588-1760

Creative Commons Attribution-NonCommercial-NoDerivatives 4.0 International License (CC BY-NC-ND)

Sous l'action d'un gradient de concentration, le transfert de l'eau, à travers une paroi semi-perméable, se fait naturellement de la solution la moins concentrée vers la plus concentrée. Ce gradient de concentration correspond à la pression osmotique.

L'osmose inverse est l'application sur le liquide concentré d'une pression supérieure à la pression osmotique ; Cette fois-ci un flux d'eau douce dessalée passe dans l'autre sens. L'osmose inverse reste en compétition avec les procédés thermiques (multi flash ou multi effet). Le choix entre ces deux technologies dépend essentiellement des coûts énergétiques (électricité et vapeur), de la qualité de l'eau brute à traiter ou de l'eau dessalée à obtenir (**Jamaly** et ***al.***, **2014**).

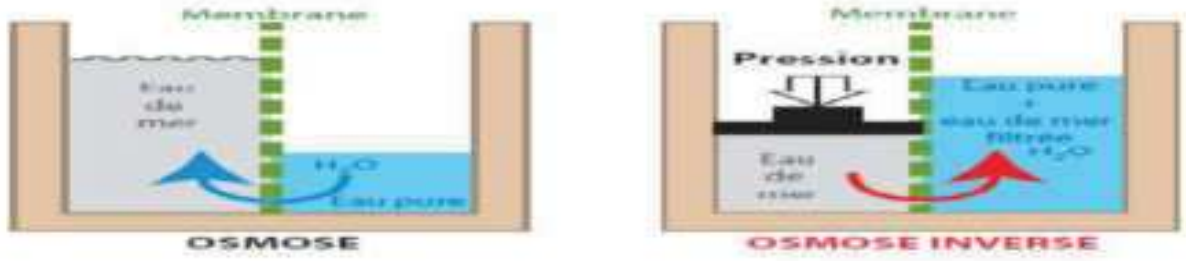

Fig.3. Principe de l'osmose et de l'osmose inverse (Bushnak, 2012).

Echantillonnage

L'objectif de l'échantillonnage à des fins d'analyse est l'obtention des renseignements sur un milieu donné à l'aide d'échantillons représentatifs. Les échantillons d'eau de mer ont été prélevés à l'entrée et à la sortie de la station durant 3 mois (mars, avril, mai) de l'année 2017. A l'entrée de la station : c'est l'eau d'alimentation avant dessalement (l'eau de mer brute). A la sortie de la station en trois points de la station : c'est l'eau produite après dessalement (l'eau dessalée) et l'eau des rejets (la saumure). Trois points (P1, P2, P3) prédéfinis de la zone d'étude pour étudier la performance de la station et l'impact des rejets des eaux saumures depuis la côte jusqu'au large de la mer.

-P1 : point à une distance de 3m environ du trait de côte ;
-P2 : point à une distance de 20m de la côte (milieu marin) ;
-P3 : point à une distance de 50m de la côte (milieu marin).

Les méthodes d'analyse des paramètres physicochimiques sont réalisées selon l'objectif recherché. La température, le pH, la conductivité et la salinité sont mesurés in situ. Les échantillons d'eau sont analysés au laboratoire pour évaluer les teneurs moyennes en magnésium (Mg^{++}), phosphates, bicarbonates ($CaCO_3$), chlorures, sulfates (SO_4^-) et autres.

Resultats et discussion :

En décembre 2009, le taux de production d'eau potable par la station de dessalement « Chatt El-Hillal » était de 5,9%, 10,06% en janvier 2010 puis il y a eu un arrêt total en février 2010. Ceci est dû au fonctionnement partiel de la station avec seulement 10 modules. A partir de l'année 2011, la station a connu une progression marquée dans sa production. Les causes des différentes pannes de la station sont dues aux cassures survenues sur les conduites et aux

Creative Commons Attribution-NonCommercial-NoDerivatives 4.0 International License (CC BY-NC-ND)

pannes des automates, aux coupures d'électricité par Sonelgaz, à un manque de produits chimiques (acide sulfurique) (**Morsli, 2013**).

Après le processus de dessalement, l'eau est séparée en deux compartiments : permeat (fraction de l'eau qui a été dessalée) et le concentrât (de concentration élevée et est rejetée à la mer) qui contient une concentration élevée en sels car il contient les quantités de sels enregistrées dans l'eau d'alimentation d'entrée avant dessalement accompagnées de produits chimiques utilisés dans le pré et le post-traitement de l'eau produite. Pour la plupart des prélèvements, les paramètres physicochimiques des eaux varient sensiblement d'un point et d'un mois à l'autre.

Analyse physicochimique de l'eau de mer brute

Les résultats des variations mensuelles des paramètres physico-chimiques de l'eau brute prélevée au niveau de la station sont présentés dans la figure 4.

Le pH est un paramètre très important donnant une idée sur l'équilibre de l'eau et sur la qualité de l'eau produite ; c'est un facteur d'investigation de l'acidité ou de l'alcalinité d'une eau. Les valeurs moyennes du pH et de la température correspondant à 8.25 et 22.3°C ; elles restent inférieures aux normes algériennes (JORADP, 2014); ceci ne présente aucun danger pour le traitement biologique de l'environnement marin.

La valeur moyenne enregistrée de MES est de 0,87mg/l ; elle est très négligeable à la norme qui est de 35mg/l ; ceci indique une faible charge en matières minérales et organiques des effluents liquides de la station.

Les faibles concentrations enregistrées de la DBO5 et de la DCO respectives à 28.33mg/l et 74.33 restent inférieures aux normes algériennes (35 et 120 mg/l ; ceci indique une faible charge en matières minérales et organiques des effluents liquides de la station et aussi une faible charge en matières organiques biodégradables.

La concentration moyenne enregistrée des hydrocarbures totaux est de 1mg/l ; elle reste toujours inférieure à la norme.

Nos résultats obtenus s'approchent de ceux obtenus dans les deux stations : El Hamma et zeralda de l'an 2009 (**Bessenasse et Belkacem Filali, 2014**). En revanche, les travaux de **Mehtougui** et ***al.*** (**2018**) enregistrent des valeurs élevées de conductivité, salinité, calcium, magnésium et des chlorures. A cela s'ajoutent les concentrations élevées de bicarbonates dans les rejets, dues à l'utilisation de différents traitements chimiques, ainsi que l'augmentation du NaCl de 10500 mg/l à 12500 mg/l et du TDS entre 13625 mg/l et 13600 mg/l.

Creative Commons Attribution-NonCommercial-NoDerivatives 4.0 International License (CC BY-NC-ND)

Pour l'heure actuelle, nous pouvons dire que les concentrations semblent être inférieures aux normes algériennes mais seront-elles les mêmes après une longue durée ? Ça reste à vérifier par d'autres analyses sur autres périodes.

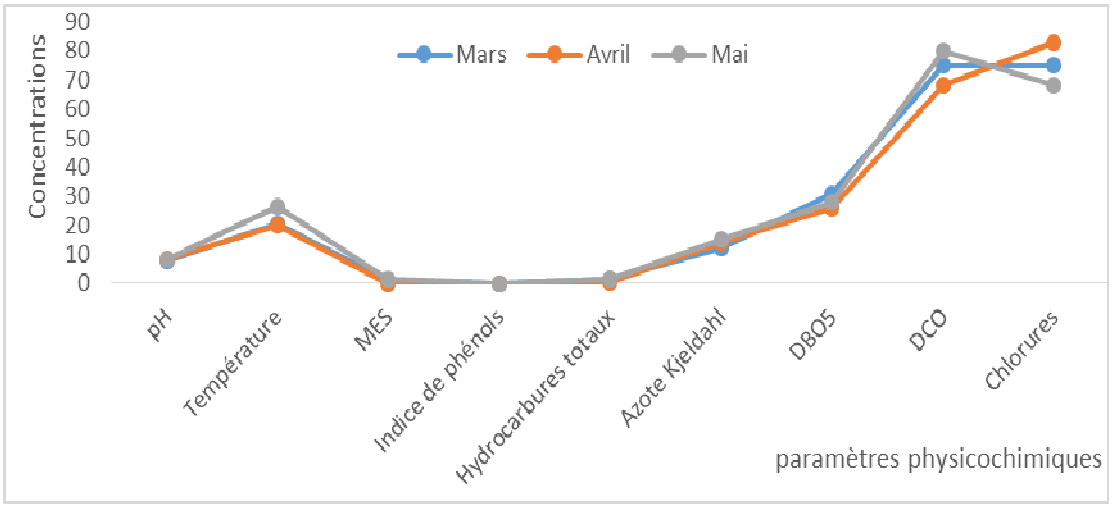

Fig.4. Analyse physicochimique de l'eau de mer brute.

Analyse physicochimique de l'Eau Saumure (ES)

Parmi les impacts négatifs d'une station de dessalement, nous citons surtout le rejet direct de la saumure dans la mer, sans dilution et sans aucun traitement.

Les résultats des variations mensuelles des paramètres physico-chimiques de l'eau brute prélevée au niveau de la station sont présentés dans la figure 5. La température de l'eau saumure est de 20°C, elle reste inférieure à la norme algérienne.

La salinité de l'eau saumure varie de 33 à 37 mg/l ; elle est proche de la salinité de l'eau de mer. La salinité de la saumure dépend du procédé de dessalement utilisé. Dans le cas des usines à osmose inverse, la salinité de la saumure dépend de la capacité de conversion de l'usine et elle est de 1,2 à 3 fois supérieure à la salinité de l'eau d'alimentation.

On note des concentrations élevées moyennes en sodium variant de 250 à 406 mg/l et en chlorures (16856mg/l). Le sodium est l'élément le plus dominant dans les cations et il existe dans la totalité des eaux car la solubilité de ses sels est très élevée. Selon **Kara Omar** et **Khaldi** (**2017**), il a été constaté que les rejets de la station d'El-Mactâa provoquent une augmentation de la concentration en sels de 5 à 10 mg/l autour de la zone de rejet.

Les teneurs initiales mesurées du calcium pour l'eau brute pour les trois de prélèvements varient entre 177 et 183 mg/l. Ces résultats montrent que les trois analyses restent faibles et présentent des concentrations en calcium conformes à la norme algérienne.

Creative Commons Attribution-NonCommercial-NoDerivatives 4.0 International License (CC BY-NC-ND)

Les eaux saumures prélevées sont très sulfatées avec des teneurs en sulfates variant entre 285 et 584mg/l. On note que le procédé d'osmose inverse n'est pas très efficace pour l'élimination des sulfates pour cette pèriode d'échantillonnage.

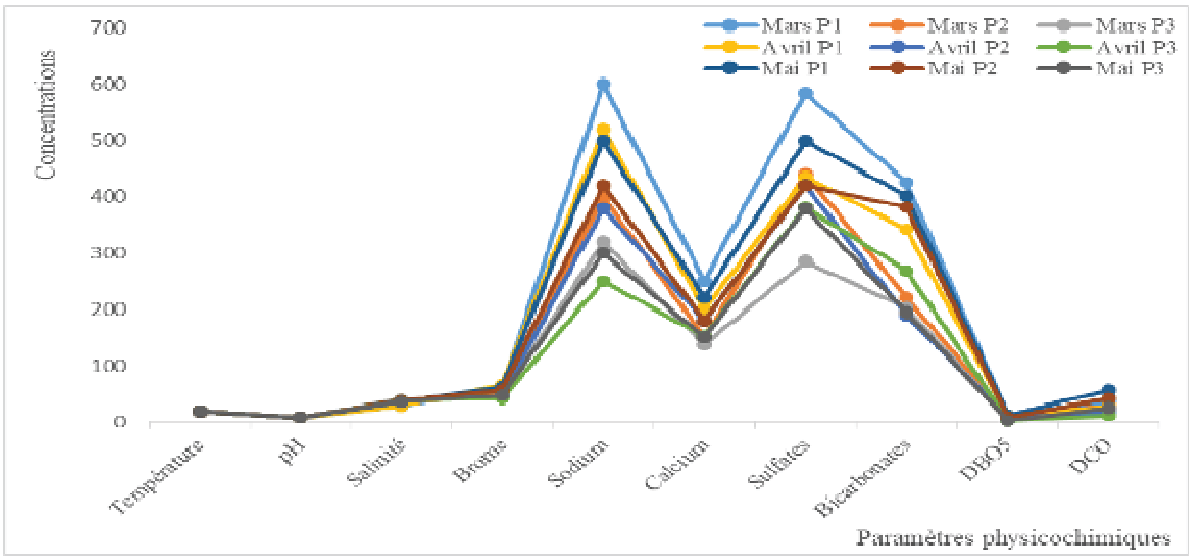

Fig.5. Analyse physicochimique de l'eau saumure.

Conclusion :

Le dessalement d'eau de mer fait partie des solutions envisagées pour limiter la surexploitation des nappes et constituer une source supplémentaire d'eau de bonne qualité ; c'est donc un des enjeux majeurs pour le développement économique et social de notre pays. Certes qu'il apporte une solution rapide et idéale à la pénurie d'eau douce, mais apporte aussi avec lui beaucoup d'inconvénients tels que : un besoin énergétique important, un problème de dégradation du paysage, du bruit, des émissions de gaz (CO, NO), une forte utilisation de produits chimiques (dérivés chlores surtout) et présence de métaux traces (cuivre) dans les rejets sans oublier l'absence de législation nationale spécifique au rejet de saumure. La saumure entraînera une détérioration supplémentaire de la qualité de l'eau de mer, ce qui affectera directement ou indirectement les activités opérationnelles des usines de dessalement.

Nous en concluons que l'eau saumure si elle est rejetée directement dans la nature, elle peut causer des effets indésirables sur la faune, la flore et le sol du milieu récepteur. Pour cela, certaines recommandations sont utiles, tels que :

-Le choix d'un procédé de dessalement en considérant une station de neutralisation de la saumure avant son rejet à la mer pour préserver les ressources écologiques marines en particulier et diminuer les impacts environnementaux en général.

-Prendre des précautions pour ne pas altérer la vie végétale et animale de l'écosystème local.

-Dilution de la saumure avec les rejets de la STEP de la zone d'étude.

-Amélioration des stations de dessalement par un gain d'énergie en utilisant l'énergie solaire.

-Suggestion du rejet de l'eau saumure, une fois l'eau de mer est turbide.

Creative Commons Attribution-NonCommercial-NoDerivatives 4.0 International License (CC BY-NC-ND)

Références:

Bessenasse M., Belkacem Filali M, (2014), *Impact du dessalement sur l'environnement en Algérie*. Revue Agrobiologia 2014 ; N°6, 75-81.

Boyé H, (2008), *Eau, énergie, dessalement et changement climatique en méditerranée.* Plan bleu, France.

Bushnak A, (2012), *Évaluation des meilleures technologies disponibles pour le dessalement en zones rurales/ locales.* Rapport final, Gestion Intégrée Durable de l'Eau – Mécanisme de Soutien (SWIM - SM).

Dawoud M.A., Al Mulla M, (2012), *Environmental Impacts of Seawater Desalination: Arabian Gulf Case Study,* International Journal of Environment and Sustainability | Vol. 1, No. 3, pp. 22□37.

Frenkel V, (2011), *Seawater Desalination: Trends and Technologies, Desalination. Trends and Technologies,* M. Schorr (Ed.), ISBN : 978-953-307-311-8, 2011.

Jamaly S., Darwish N.N., Ahmed I., Hassan S.W, (2014), A short review on reverse osmosis pretreatment technologies, Desalination.vol. 354 1 December 2014, Pages 30–38.

Kara Omar A., Khaldi A, (2017), *Dessalement de l'eau de mer et impacts environnementaux : cas de la station d'El-Mactaâ.* J. Wat. Env. Sci. Vol. 1, (Numéro spécial ICWR 2) (2017), 249-253.

Mandri Y, (2011), *Etude paramétrique du procédé de dessalement de l'eau de mer par congélation sur paroi froide*, Thèse de doctorat. Université Claude Bernard Lyon.

Maurel A, (2006) - *Dessalement de l'eau de mer et des eaux saumâtres*. 2ème édition, Paris, Ed. Tec & Doc-Lavoisier. 286p.

Mehtougui M.S., Kerfouf A., Mehtougui F., Ardjoum S., Benyahia M, (2013), *Impacts du Dessalement D'eau de mer sur les Écosystèmes Littoraux: Cas de Deux Unités de L'ouest Algérien (Bousfer et Bouzedjar).* European Journal of Scientific Research , ISSN: 1450-216X, Volume 96, No 2, 245-249.

Mehtougui M.S., Kerfouf A., Ardjoum S., Mehtougui F, (2018), *Assessment of the Quality of Water Discharges from a Desalination Plant: Case of Honaine Station (Western Algeria).* International Journal of Sciences: Basic and Applied Research (IJSBAR) ISSN 2307-4531.

Metaiche M, (2006), *Optimisation des systèmes de dessalement par osmose inverse : conception, paramètres de fonctionnement et simulation numérique*. Thèse de doctorat. Ecole Nationale Polytechnique d'Alger. 139p.

Morsli M.S, (2013), *Impact des arrêts techniques de l'usine de dessalement de l'eau de mer sur l'entreprise et l'Environnement.* Mémoire de Magister. Université d'Oran. 203p.

OMS (2011), *Guidelines for drinking-water quality.* Fourth edition. ISBN 978 924 1548151.

Remini B, (2010), *La problématique de l'eau en Algérie du nord*, Larhyss Journal, ISSN 1112-3680, n° 08, Juin 2010, pp. 27-46.

Rerolle A, (2010), *Quelle gestion de l'eau pour les pays du Sud ? Notes* à l'attention du groupe de pilotage de campus plein sud. 78 P.

Creative Commons Attribution-NonCommercial-NoDerivatives 4.0 International License (CC BY-NC-ND)

Algerian Journal of Engineering Architecture and Urbanism Vol. 5 Nr. 3 2021
ISSN: 2588-1760

DISTRIBUTION OF THE MAGNETIC FIELDS INTENSITY AROUND OVERHEAD POWER TRANSMISSION LINES

Salah-Eddine HOUICHER
PhD, University Ammar Telidji, LACoSERE Laboratory, Department of Electrical Engineering, Laghouat, Algeria, e-mail:houichersalah@gmail.com

Rabah Djekidel
Professor, University Ammar Telidji, LACoSERE Laboratory,Department of Electrical Engineering, Laghouat, Algeria, e-mail: r.djekidel@lagh-univ.dz

Abstract:
In this paper, we examine and calculate the lateral profile of magnetic field distribution produced around overhead transmission lines horizontal configuration in single circuit recently will be analytically computed. The approximate computations will be done using the image method and applying Ampere's law considering quasi-static fields and an infinite line sources parallel to a perfectly conducting flat ground plane. The computation domain considered is the 2D free space in the lateral directions perpendicular to the line conductors at 1 and 4m above ground level, and study the factors affecting the magnetic induction. The resulted field values considering different loads current are much less than the general public exposure level limit (B=100μT) recommended by the ICNIRP.

Key words: overhead transmission line; high voltage; magnetic field; exposure limit; simulation.

Introduction:

High voltage overhead transmission lines travel long distances and generally cross regions that are very different in terms of their relief (topography of the land, altitude, etc.), their climate (temperature, pressure, wind, etc.), their environment (industrial zones, coastal regions, etc.). Therefore, electrical power transmission equipment is exposed to various forms and degrees of stress. the development and enormous advancement of power plants are requires the construction of various new energy transmission networks and power production sources, therefore this results the continuous and increasing consumption of different types of energy. The augmentation demand for electric power has resulted in the increase of operating voltage for transmission lines (HV and VHV). These overhead transmission lines create electric and magnetic fields, and therefore raised serious questions regarding the potential health and environmental possible effects associated with the resulting higher levels of field strength around these lines. The influences of electric and magnetic fields produced by overhead power lines (HV and VHV) on human health and the environment are well known and analyzed in several research works and numerous experimental locations. High overhead electric power lines covers and extends nearly to the whole places where industry developing and people live. The usually maximum high voltage used for overhead power transmission lines is the 400-KV 50Hz system with single and double circuits with triple bundled conductors. The electromagnetic fields generated around high-voltage transmission lines in general have received many investigations focused their intensities and their influence to

Creative Commons Attribution-NonCommercial-NoDerivatives 4.0 International License (CC BY-NC-ND)

human beings. In some situations, especially where people live just under or near by these lines, the introspection of the effects of fields produced by these lines becomes a serious problem. Neither the government nor any other nongovernmental local organization has set any exposure level limits to electromagnetic fields. The government has agreed only the corridor width (Right Of Way, ROW) that extends 30 meters from both sides of the center-line of a high voltage transmission lines. The international standards are established for general public exposure limits as set by the ICNIRP, are 5kV/m for the electric field and 100μT for the magnetic field. On the other hand for professional exposure limits are 10kV/m for the electric field and 200μT for the magnetic field. In a recent study, the electric field intensity around the same 400kV power transmission line system was computed analytically using the static laws of electromagnetic. In this present work, the static technique will also be used to analytique compute the magnetic flux density, B, in 2D profile using Ampere's law (Biot-Savart). To simplify the integration of field components around the exciting lines, the -component of the magnetic field intensity will be decomposed into two x- and y- components in a Cartesian coordinates system assuming electric power transmission is along z-direction. The human population augmentation in the world has caused an increase and successful demand for the introspection of electrical energy, which requires the high quantities and various resources production of energy, therefore the implementation of power transmission networks. Become an essential aspect of their daily operations lives, our technological and economic development. The quasi-static analysis of low frequency electromagnetic fields invites that the electric and magnetic field components behave independently, and are realized in separately way. The electric field strength generated by three-phase overhead transmission lines (HV and VHV) depends mainly on the operating voltage level carried by the conductors, while the magnetic field intensity has a great dependence on the electric current magnitude flowing in the conductors. The alternating current electric and magnetic fields engendered by these HV overhead power lines induce currents in human bodies. Through two capacitive and inductive couplings, with very high induced current levels, undesirable effects may present damage and constitute a menace to the human body in the long term. The accurate evaluation of electric and magnetic fields produced by high voltage overhead transmission lines is very important in many research regions, necessary in different applications in the design, maintenance and electrical and electronic equipments. There are various experimental and simulation projects studies on operation of electromagnetic characteristics of the high voltage overhead power lines. The majority of works is based on the assessment and comparison of the product field under the high voltage transmission lines with the guidelines and international standards, there are some research studies have also been conducted on decreasing the fields electric power lines by the technical solutions. Our main of this article is to calculate and examine the lateral profile of magnetic fields distribution created around and in the vicinity of high voltage overhead transmission line at 1m above the ground, in order study the numerous factors affecting the magnetic induction values under electric power lines. We present the numerique simulation based in the GARSON method, are obtained by MATLAB software which makes it possible to better analyze and represent the transverse profile of the magnetic flux density distribution underneath electric power transmission lines.

Creative Commons Attribution-NonCommercial-NoDerivatives 4.0 International License (CC BY-NC-ND)

Problematic:

Plot the lateral profile of magnetic field distribution under three-phase overhead transmission lines single circuit horizontal configuration at height 1m above the ground level, and study the factors affecting the magnetic induction at any point in space surface or ground.

Materials and methods:

The quasi-statique regime analyze of low frequency electromagnetic fields propose that the electric and magnetic field components behave independently, and are realized separately, the magnetic field of overhead transmission line has a great dependence on the courant passage which circulates in the line conductors. Magnetic field intensity is evaluated using image method and the superposition theorem. The magnetic field value above the ground is equal to source magnetic field plus its complex image. A simple application of the Ampere's law calculates the value of magnetic field intensity around a single phase conductor, and then we apply the superposition theorem of three partial fields for get the total magnetic field.

For calculate the magnetic field in the vicinity of high voltage transmission lines, we consider a long overhead power line with loading current and the conductors are cylindrical, the radius of phase conductors is weak compared to its length and height above the ground level . The magnetic field expression is given by the following equation describes below:

$$H = \frac{I}{2.\pi.r} \tag{1}$$

As shown in figure1 the current intensity (I) in the point (x_i, y_i), created at observation point p(x_j, y_j) of space a magnetic field, the magnetic induction is defined by the following relation formula show in this equation:

$$B = \mu_0.H = \frac{\mu_0.I}{2.\pi.r} \tag{2}$$

Where:

μ_0: is the magnetic permeability of vacuum (N/A2).

We can use the conductors image theory for plot the lateral profile distribution of magnetic induction in the vicinity of high voltage overhead transmission line at 1m above the ground, is based in currents return on ground, in taking into account the depth of penetration. The rotating magnetic field of the line generates induces return currents in the ground, at the same time generate a magnetic field that is composed to that produced by the line. The precise calculation of magnetic field intensity requires the use of Garson method, which is based on the notion of return currents through earth. We consider a fictitious plane of currents return, parallel to the ground plane and placed at penetration depth in the complex distance D_{erc} (see Fig.1), The image conductors are placed at a skin depth given by D_{erc}+ y_i below the ground level, as expressed in equation (4), is depends on resistivity of sol ρ and the frequency f. its relation is defined in this following formula describes below:

$$D_{erc} = 658.87\sqrt{\frac{\rho_s}{f}} \tag{3}$$

Where; ρs: the resistivity of earth expressed as Ω.m; *f*: electric frequency of source line (Hz).

Creative Commons Attribution-NonCommercial-NoDerivatives 4.0 International License (CC BY-NC-ND)

Algerian Journal of Engineering Architecture and Urbanism Vol. 5 Nr. 3 2021
ISSN: 2588-1760

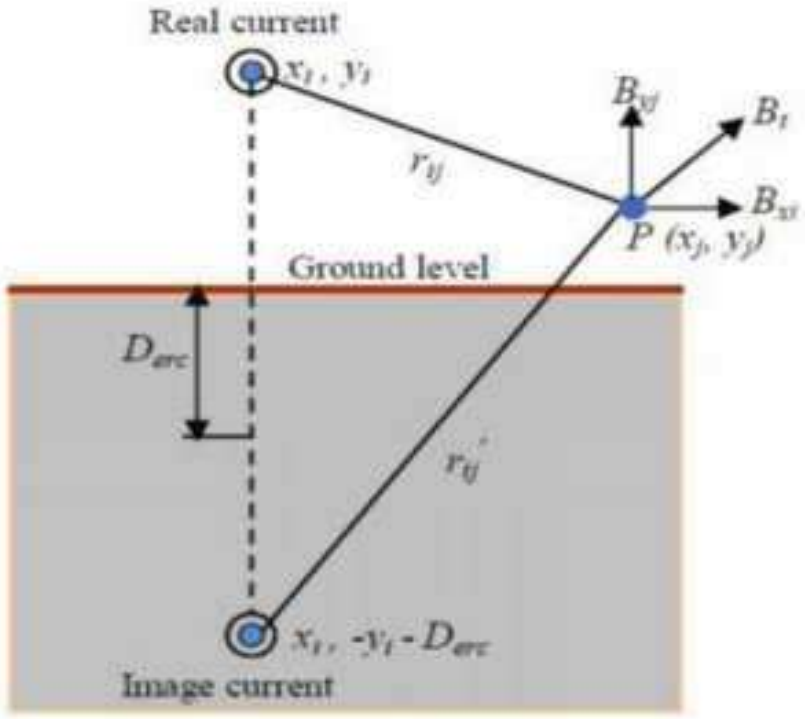

Fig1. Magnetic intensity engender by the current circulate in the reel conductor and its image.

In the numerique simulation, are obtained for a balanced system in which the currents in phase conductors are symmetric and in direct succession at a phase angle φ of 120^0 to one another. For the power line situation, symmetrical load current of 1000A and electric resistivity of sol 100Ω.m and the frequency 50Hz are used for the numerical computation. The circuit line is assumed to carry the same amount of current magnitude, and earth wires effects on the circuit are neglected. The effect of transmission line current unbalance is not considered, because it is usually low. The lateral profile distribution of magnetic field intensity depends on the phases arrangement. Underneath power lines the same phases arrangement produces the highest magnetic field; the magnetic flux density can be reduced either underneath or far from the lines by changing the phase arrangement.

The horizontal and vertical components of the magnetic field are calculated by using the following equations describe below:

$$B_{xj} = -\frac{\mu_0}{2.\pi} \cdot \sum_{j=1}^{3.n.m} I_n \left[\frac{y_i - y_j}{r_{ij}^{\,2}} - \frac{y_i + y_j + D_{erc}}{r'^{\,2}_{ij}} \right]$$

$$B_{yj} = \frac{\mu_0}{2.\pi} \cdot \sum_{j=1}^{3.n.m} I_n \left[\frac{x_i - x_j}{r_{ij}^{\,2}} - \frac{x_i - x_j}{r'^{\,2}_{ij}} \right] \qquad (4)$$

Where, (x_i, y_i) and (x_j, y_j) are the coordinates of the observation point above the ground and the location of simulation line current carry conductors, respectively; r_{ij} is the distance between each conductor and observation point above ground; r'_{ij} is the distance between each image conductor and observation point.

Creative Commons Attribution-NonCommercial-NoDerivatives 4.0 International License (CC BY-NC-ND)

Algerian Journal of Engineering Architecture and Urbanism Vol. 5 Nr. 3 2021
ISSN: 2588-1760

The resultant magnetic field is the summe of the horizontal and vertical components in each phase conductors is calculated by using this expression defined as following:

$$B_t = \sqrt{B_{xj}^{\ 2} + B_{yj}^{\ 2}} \tag{5}$$

Results and discussions:

In this work study we consider a three-phase high voltage overhead transmission line in single circuit horizontal configuration, the phase conductors are arranged on the same horizontal plane, that is to say the same height above the ground. This type it is usually used for electric power transmission lines. We have three phases(R,S,T) contains a horizontal bundle of two subconductors in each phase are separated by 0.4m between them, the radius of conductor is 1.34cm. According to the coordinates system presented in Fig.2, the phase conductors are horizontally positioned at distance -10m, 0m, +10m, and at vertically separation distance 26m. the radius of guard cable is 0.7cm positioned horizontally at -8m and +8m, at height 36m above the ground, the span length of single circuit power line is of 300m.The schema geometry of high voltage overhead power line used in this study, with the arrangement and geometric coordinates are shown in Fig.2. Its parameters are used in table.1.

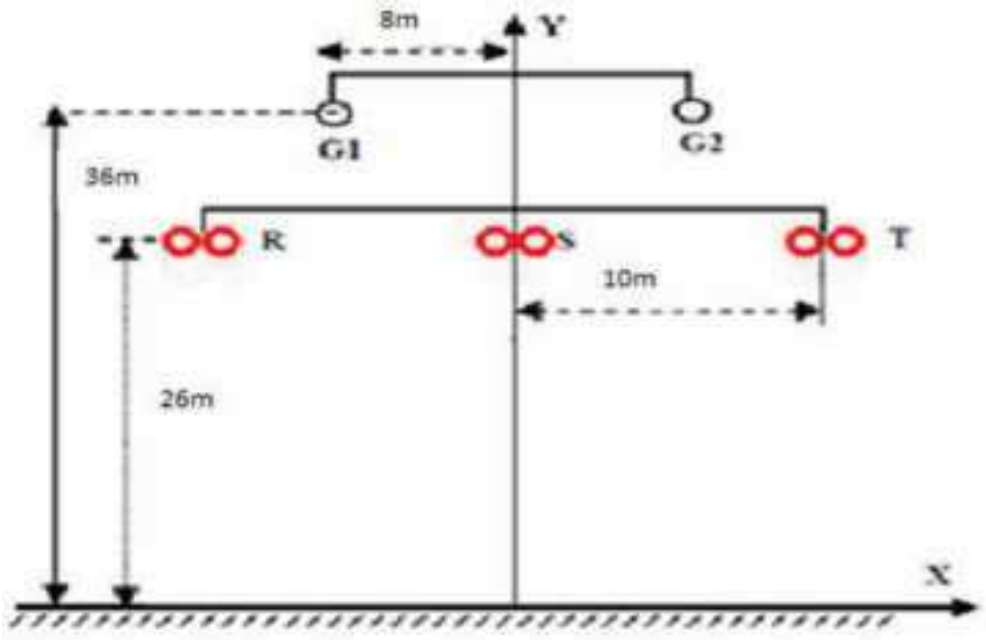

Fig2. Single circuit three-phase high voltage overhead transmission line horizontal arrangement.

Parameter	Value (m)
Height of conductors	26
Distance between phase conductors	10
Spacing between subconductors	0.4
Height of guard cable	36
Distance between guard cable	8

Table 1. Parameters used for overhead power single circuit line

Creative Commons Attribution-NonCommercial-NoDerivatives 4.0 International License (CC BY-NC-ND)

For the simulation computation of magnetic field we found the following results are illustrates the lateral profile distribution of magnetic flux density underneath three- phase high voltage overhead transmission lines in single circuit horizontal configuration of phase arrangement. Fig 3 illustrates the lateral profiles distribution of the horizontal, vertical and total components (Bx, By, Bt) of the magnetic field intensity at height 1m above the ground level in the vicinity of three-phase high voltage overhead power line, as a function of the lateral distance of circuit line, accordining the nemurique simulation, it is very clear the magnetic field strenght increases in symmetrically and continuous manner in the two sides positive and negative of the high voltage overhead transmission line single circuit line for the significative decreases of the lateral distance of the line. On observe in this curve for the total component Bt of the magnetic induction undrer overhead power line, we show very clear the maximum total value directly under middle phase conductor is about 4.64µT register at the center distance(x=0m), accounting for only 4.64% of the exposure limit established by ICNIRP for the general public 100µT, then reduces rapidly in symmetrically and continous way when one moves away from the conductors, to reach at distance 75m far from the center distance a very low value about 0.56µT approximetly recorder ten times lower than the maximum value found under the line. For the horizontal component Bx of the magnetic induction in the x-axis of single circuit horizontal arrangement of phase conductors, the maximum value of lateral profile of magnetic field intensity distribution Bmax = 3.23µT is registered at a distance located between the lateral and central conductor x=17m near under the side phase conductor accounting for only 3.22% of the exposure limit established by ICNIRP for the general public 100µT , then it slowly reduces until register minimum value Bmin = 1.10µT in the point of symmetry (center distance x=0m) accounting for only 1.10% of the exposure limit established by ICNIRP for the general public 100µT is less intense under the middle phase conductor from where it increase slowly again in symmetric manner in the two sides positive and negative of the high voltage overhead transmission line, until to register the peak intensity value of the magnetic induction Bmax=3.22µT near under the side phase conductor at the lateral distance x= 17m, then decrease rapidly with significative increase of the lateral distance of high voltage tranmsmission line, when one moves away from the conductors, to reach at a lateral distance of 75 meters far from the circuit line a very low value is about 0.35µT almost negligible approximetly accounting ten times lower than the maximum value that found under the line. For the vertical component By of the magnetic induction in the y-axis of of single circuit horizontal arrangement of phase conductors, the values of magnetic field intensity increase in symmetrically manner in two sides positive and negative of the circuit line, then decreases rapidly with increase of the lateral distance, on observe the maximum value of the magnetic induction Bmax=4.74µT is registered in the center point (x=0m) under the middle phase conductors, accounting for only 4.74% of the exposure limit established by ICNIRP for the general public 100µT, takes the values max than that recorder at the level in the horizontal component (x-axis), then it is strongly attenuated to reach a low value 0.26µT at a lateral distance of 28m, elsewhere which the magnetic induction increases slightly again, after begins to decrease as a the distance increases, if when one moves away from the conductors, to reach at a distance of 75meters far from the conductors a value is about 0.45µT almost negligible.

Creative Commons Attribution-NonCommercial-NoDerivatives 4.0 International License (CC BY-NC-ND)

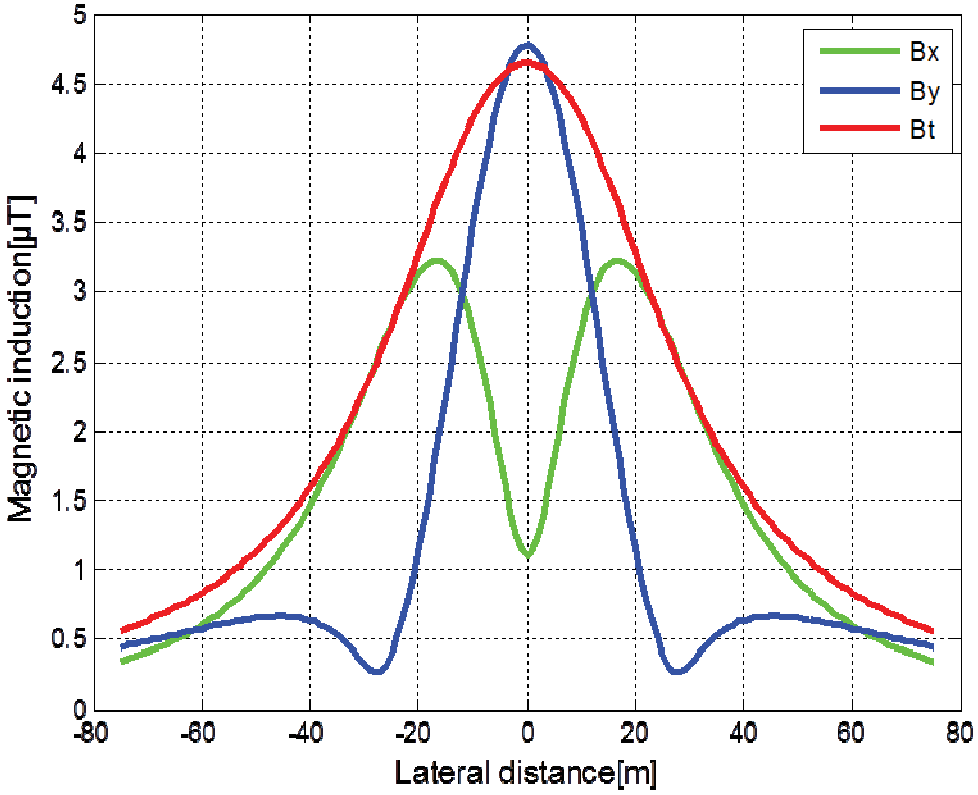

Fig3. Lateral profile of the magnetic induction distribution under overhead transmission lines.

The magnetic flux density generated around the 50Hz, 400kV single- circuit power transmission line described above is analyzed and computed in the aforementioned way. The computations where done for 1.0 and 4.0m above ground .The computer program results are shown in Figs (4,5,6,7) for the single circuit. The field quantities were assumed quasi-static fields and computed on this basis at discrete time instances corresponds to a maximum value along a full time period. The magnetic flux density was designed twice for different minimum possible clearances of the line conductors H=20, 22, 24, 26, and 28 meters for currents magnitude 215A and 1000A. For the single circuit line configuration system, the results for line currents of 215A shows a maximum magnetic flux density values within the transmission corridor of 1.538µT and 1.95µT at 1 and 4m above ground respectively. The maximum values at 1000A line currents are 7.152µT and 9.068µT at 1 and 4m above ground respectively. Outside the transmission corridor (at the ROW edges) for line currents of 215A shows a maximum magnetic flux density values of 0.6138µT and 0.6812µT at 1 and 4m above ground respectively. Which are about 99.38% and 99.31%, respectively, below the general public exposure level limit, 100µT, set by the ICNIRP. the maximum values is 2.726µT and 3.104µT at 1 and 4m above the ground respectively for line currents of 1000A which are about 97.27% and 96.89%, respectively, below the general public exposure level limit, 100µT, set by the ICNIRP. Within the transmission corridor, and for line currents of 1000A, the maximum magnetic flux density, B, is 92.15% and 89.29%, respectively, less than the ICNIRP exposure level limit 100µT established by the general public exposition for the 1 and

Creative Commons Attribution-NonCommercial-NoDerivatives 4.0 International License (CC BY-NC-ND)

4m heights above ground level respectively. For line currents of 215A, these percentages go even higher those in case of 1000A line currents flowing throught the phase conductors.

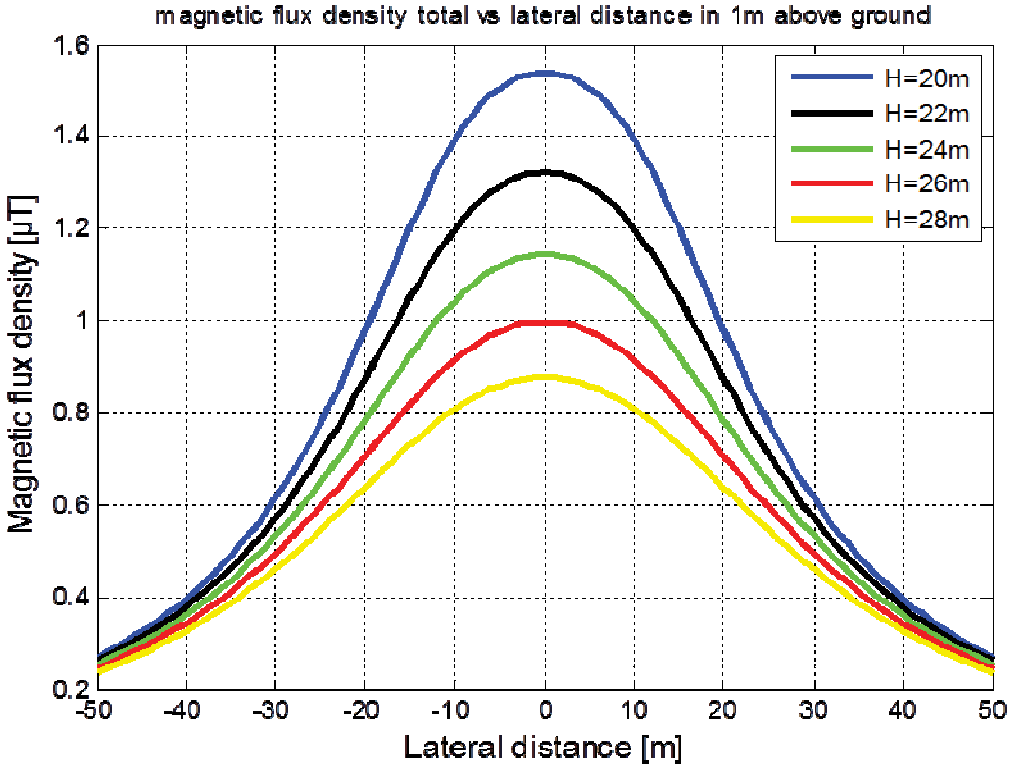

Fig4. Magnetic Field around single circuit 400kV Transmission Lines, 1m above ground, Io=215A.

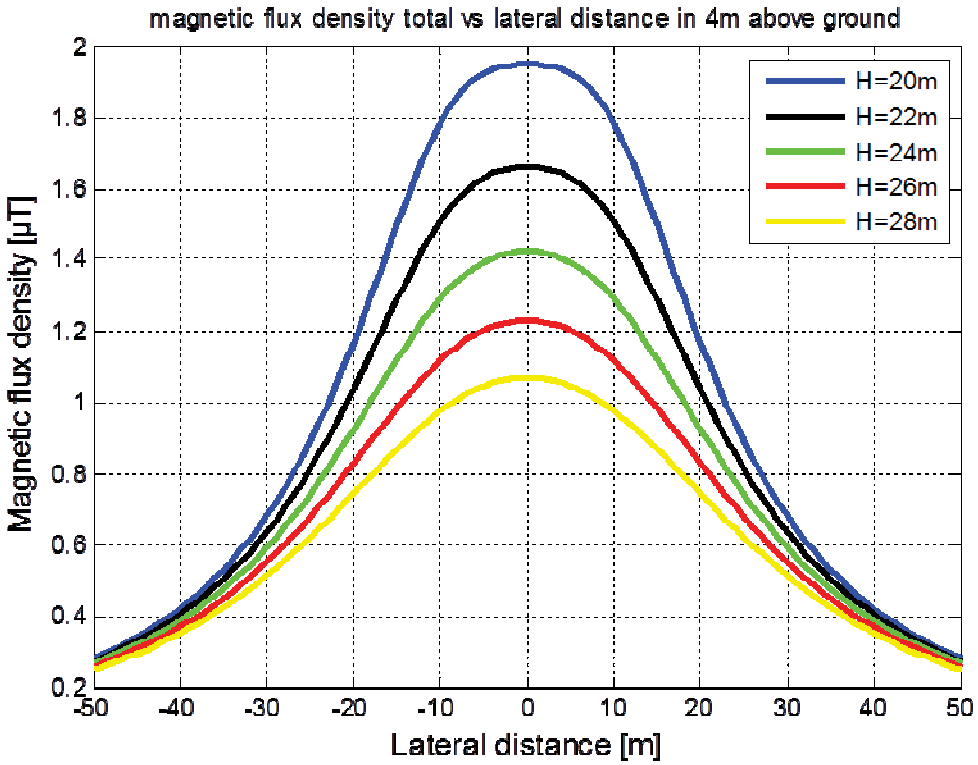

Fig5. Magnetic Field around single circuit 400kV Transmission Lines, 4m above ground, Io=215A.

Creative Commons Attribution-NonCommercial-NoDerivatives 4.0 International License (CC BY-NC-ND)

Algerian Journal of Engineering Architecture and Urbanism Vol. 5 Nr. 3 2021
ISSN: 2588-1760

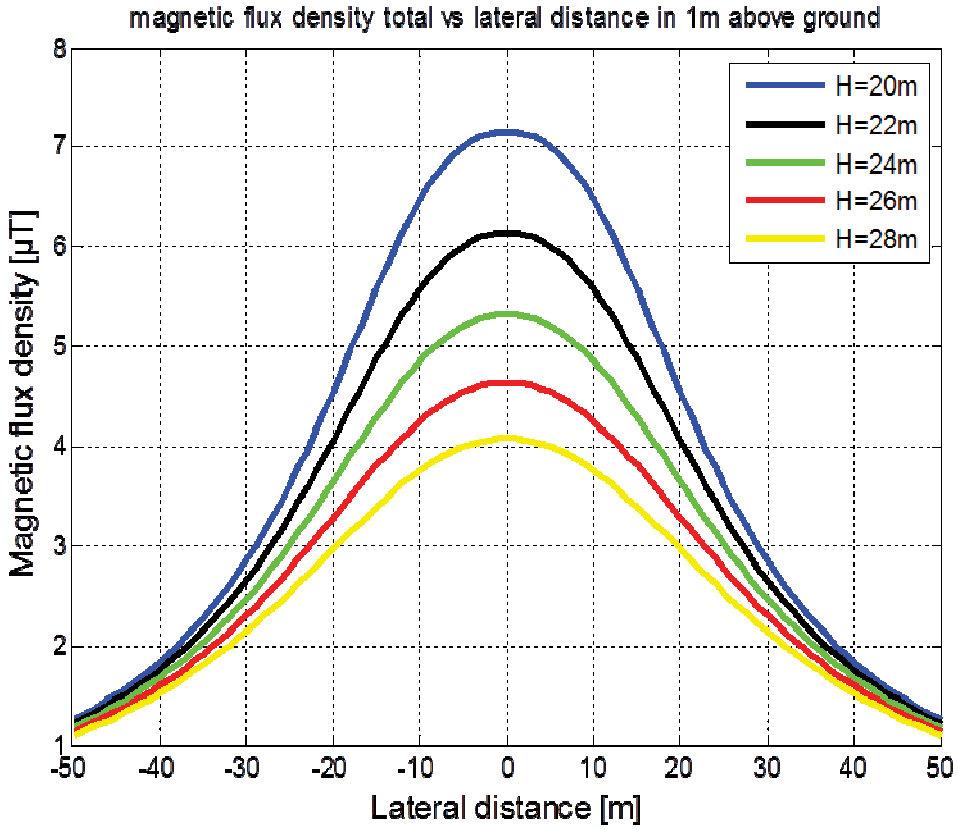

Fig6. Magnetic Field around single circuit 400kV Transmission Lines, 1m above ground, Io=1000A.

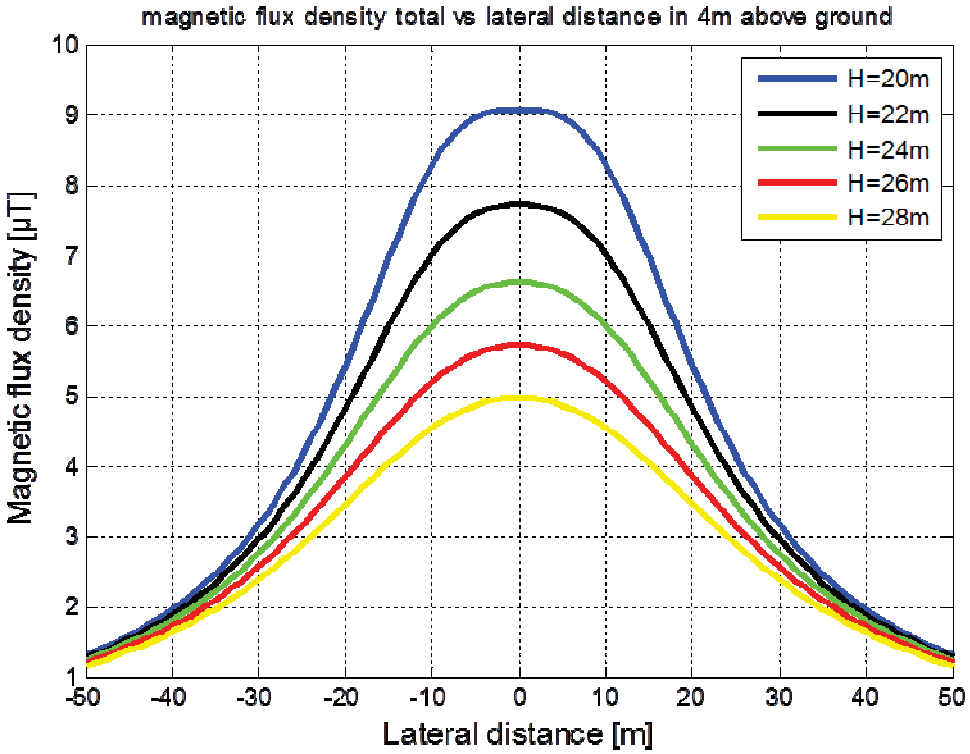

Fig7. Magnetic Field around single circuit 400kV Transmission Lines, 4m above ground, Io=1000A.

Creative Commons Attribution-NonCommercial-NoDerivatives 4.0 International License (CC BY-NC-ND)

In this figures below show the factors effects on the magnetic field intensity at any point on the ground surface or the space around and in the vicinity of the high voltage overhead transmission lines, it mainly depends on the geometry of the power line, the height of conductors, their size and spacing between phase conductors, together with the location of the observation point where the field is to be calculated. the loading currents also impact the magnitude of the components by increase or reduce the field strength under transmission line. Fig8 plots the lateral profile of magnetic induction distribution at 1m height above the ground as a function of different loading currents of phase conductors 500, 1000, 1500, and 2000A. The maximum magnetic flux density values corresponding to these current amplitude values are 2.32, 4.64, 6.96 and 9.28μT respectively. It is clear that as this graph curve symmetric in the two sides positive and negative of single circuit power line, it observe the currents increase, the magnetic field intensity increases until to reach the maximum values for all this four values of electric current flowing the conductors in the center distance under the middle phase conductors, then decreases rapidly with significative increase of the lateral distance, to reach the minimum values when one moves away from the conductors, a very far for the center lateral distance of circuit line. On note the maximum magnetic flux density at 400kV applied voltage of the power line is found to be about 9.28μT corresponding to maximum current of conductors I=2000A, On the other hand, the minimum magnetic flux density is found to be about 2.32μT corresponding to minimum current of conductors I=500A flowing the power line in all the corridor right of way of the high voltage three-phase overhead transmission line. it see a significant linear relationship between the magnetic induction and current magnitude circulate in the line, more the current is higher, the magnetic field intensity is intense, it is proportional to the electric current intensities that pass them in all types circuit lines configurations of electric power transmission line and arrangement of phase conductors.

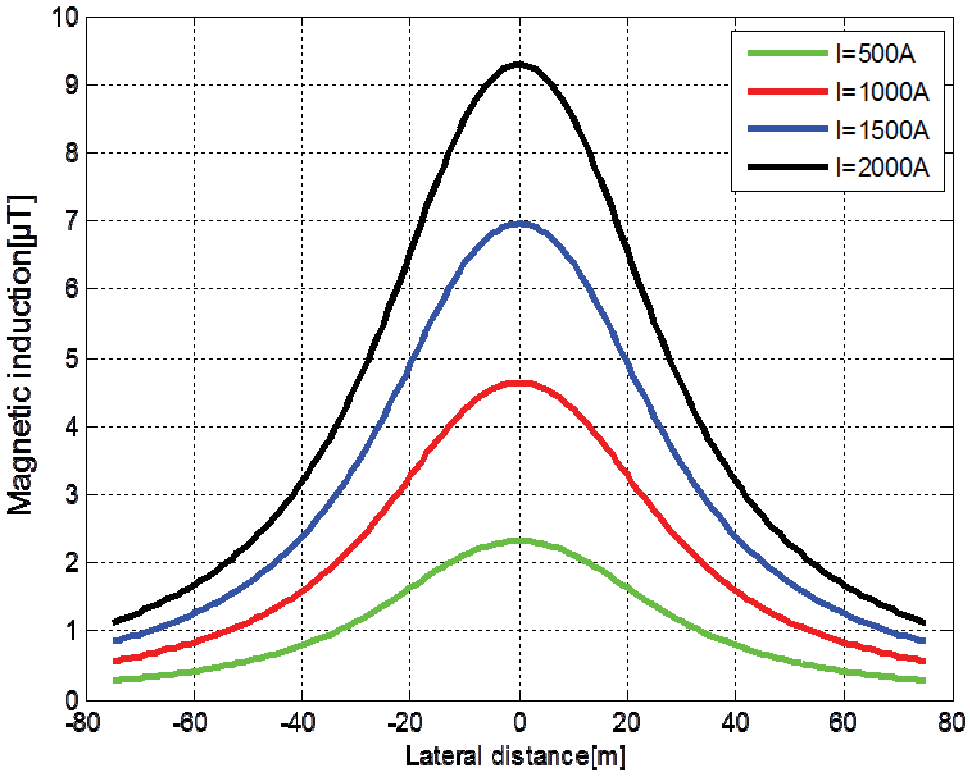

Fig8. Lateral profile of magnetic induction as a function of current flowing the conductors.

Creative Commons Attribution-NonCommercial-NoDerivatives 4.0 International License (CC BY-NC-ND)

In Fig9 shows the lateral profile of magnetic induction distribution at 1m height above the ground level as a function of different heights of phase conductors 20, 22, 24, 26 and 28m. The maximum magnetic flux density values corresponding to these conductors' heights are 7.15, 6.14, 5.32, 4.64 and 4.07µT respectively. It is clear that as the heights of conductors increase, the maximum magnetic field intensity decreases in symmetrically and continuous manner with a significative increase in lateral distance of the single circuit line, to reach the maximum values in the center distance under the middle phase conductors, then decrease rapidly to reach the minimum values when one moves away from the conductors, a very far for the center lateral distance of circuit line in all this conductors heights. it see an opposite relationship between the magnetic induction and the height of conductors for all circuit lines configurations and phase conductors arrangement. accordinate to this curve, on observe the maximum magnetic flux density at 400kV applied voltage of the power line is found to be about 7.15µT corresponding to minimum height of conductors H=20m, On the other hand, the minimum magnetic flux density is found to be about 4.07µT corresponding to maximum height of conductors H=28m in all the corridor right of way of the high voltage three-phase overhead transmission line. Increasing the line height is the most effective parameter in line design, which reduces the maximum field strength in ground. the changement of conductors height have great impact in the field intensity variation by increase or minimize the field stress under electric power transmission lines, therefore optimize or modify the line geometry.

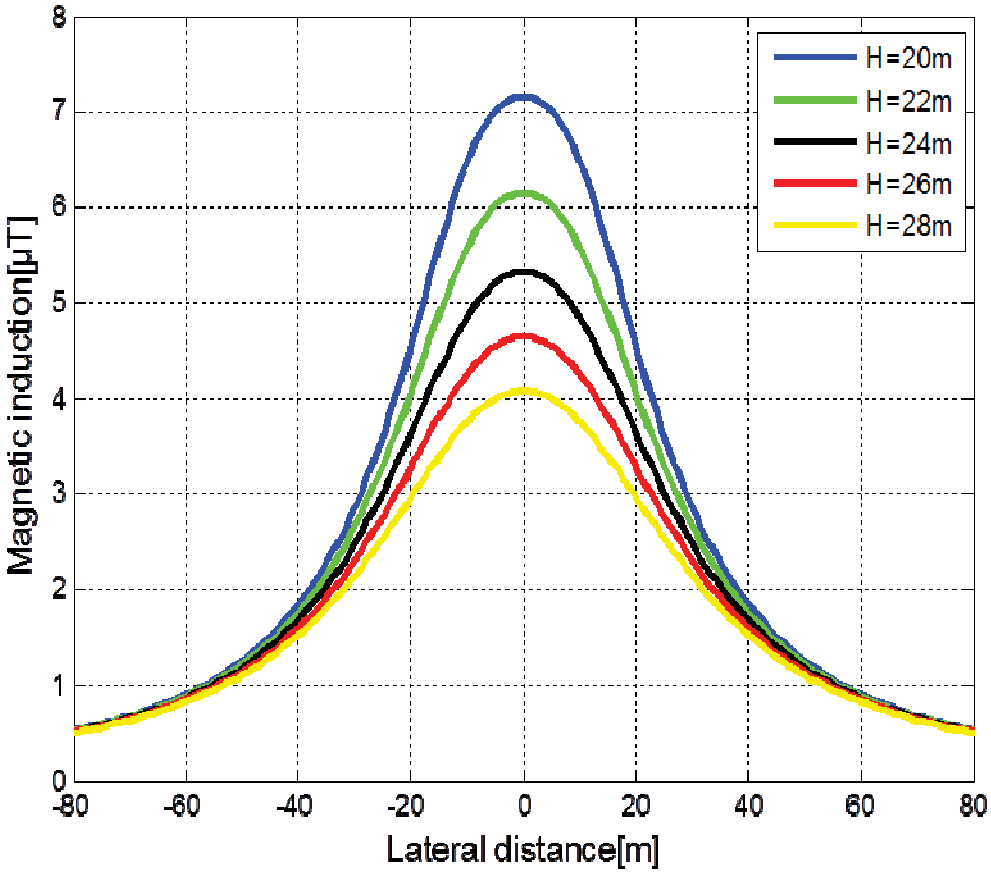

Fig9. Lateral profile of magnetic induction as a function for various heights of phase conductors.

Creative Commons Attribution-NonCommercial-NoDerivatives 4.0 International License (CC BY-NC-ND)

Fig.10 shows the lateral profile of magnetic induction as a function of different separation distances between phase conductors 6, 8, 10 and 12m. The maximum magnetic flux density values corresponding to these separation distances of phase conductors are 3.10, 3.94, 4.64 and 5.18µT respectively. It is clear that as the phase spacing between conductors increases, the maximum magnetic field intensity increases in symmetrically and continuous manner in the two sides positive and negative of single circuit power line, to reach the maximum values in the center distance under the middle phase conductors for all this four values of separation distances between phase conductors, then decreases rapidly for increase the lateral distance of the circuit line to register the minimum values when one moves away from the conductors, a very far for the center distance of power line. in this curve on observe that as the maximum magnetic flux density at 400kV applied voltage of the overhead power line is found to be about 5.18µT corresponding to maximum separation distance between the phase conductors D=12m. On the other hand, the minimum magnetic flux density is found to be about 3.10µT corresponding to minimum separation distance between the phase conductors D=6m. This is a significative linearity relationship between them in the corridor right of way of power transmission line, for all the types of circuit lines configurations and phase conductors arrangement. Changement of the separation distances between phase conductors have a great impact in the line design for increases or reduces the field strength, elsewhere optimization the field intensity under high voltage overhead transmission lines in each phases arrangement.

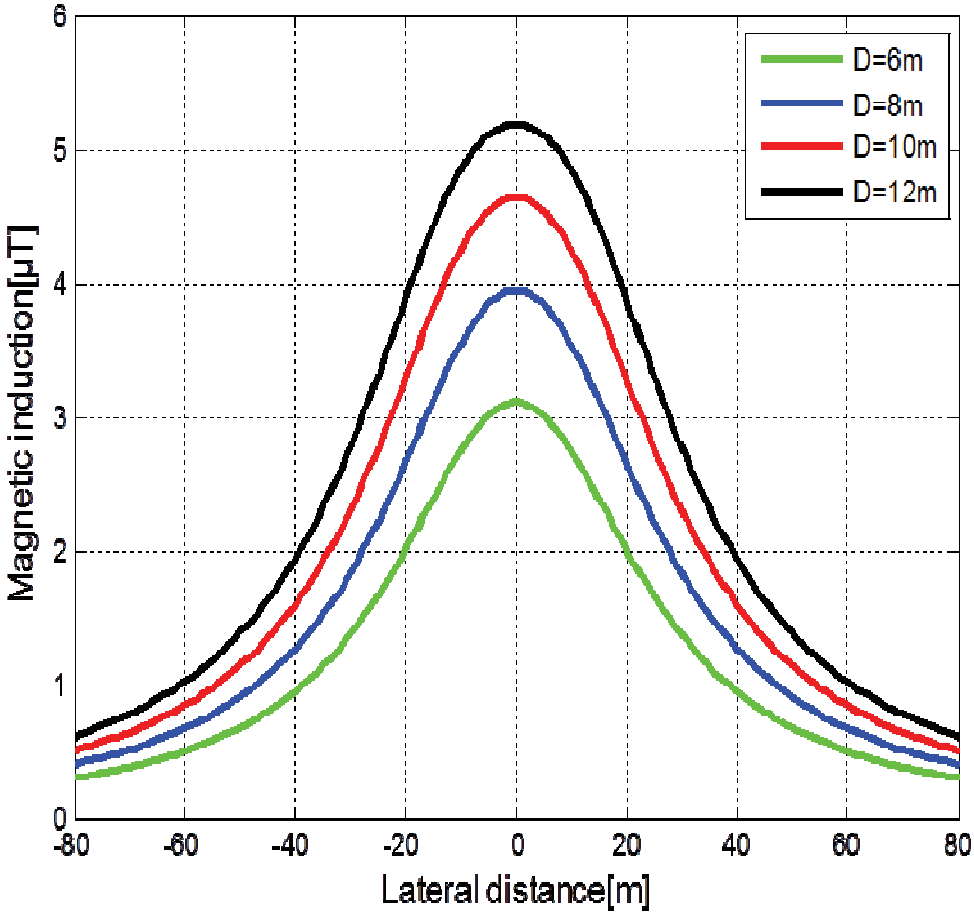

Fig10. Lateral profile of magnetic induction as a function of phase spacing between conductors.

Creative Commons Attribution-NonCommercial-NoDerivatives 4.0 International License (CC BY-NC-ND)

Fig.11 shows the lateral profile of magnetic induction as a function of different observation point heights of phase conductors above the ground 0, 1, 1.5, 1.8 and 2m. The maximum magnetic flux density values corresponding to these heights of observation point (calculation point of the magnetic field intensity) are 4.34, 4.64, 4.8, 4.89 and 4.96µT respectively. According to the curve it is very clear that as the observed point heights above the earth increase, the maximum magnetic field intensity increases, in symmetrically and continuous manner in the two sides positive and negative of the power line, to reach the max values for all this observation point heights in the center distance, then decreases rapidly with a significative increase in the lateral distance of single circuit power line, to register the lower values when one moves away from the conductors, a very far for the center lateral distance, this is linearity relationship between them. On observe the maximum magnetic flux density at 400kV applied voltage of the power line is found to be about 4.96µT corresponding to maximum observed point height above the ground z=2m. On the other hand, the minimum magnetic flux density is found to be about 4.34µT corresponding to minimum observed point height above the ground z=0m. Note accordinate to the simulation results obtained that the magnetic induction values under and in the vicinity of the high-voltage three-phase overhead transmission line, depending on the distance to several levels starting with the beginning level 0m at the ground level, therefore on show a two-dimensional plot of the lateral profile magnetic field intensity distribution for the five following levels as a function of the lateral distance of transmission line in all types of configurations and phase conductors arrangement.

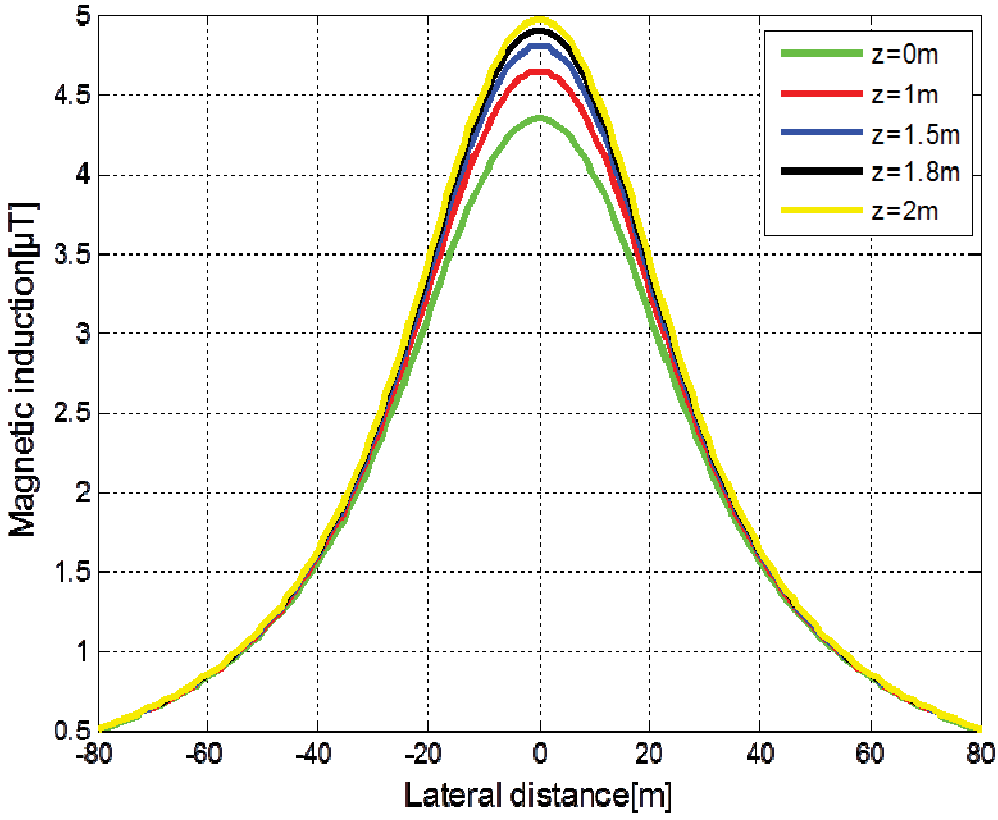

Fig11. Lateral profile of magnetic induction as a function of observation point heights above earth.

Creative Commons Attribution-NonCommercial-NoDerivatives 4.0 International License (CC BY-NC-ND)

Fig.12 illustrates the lateral profile of magnetic induction distribution in four different phase configurations of high voltage overhead transmission line: horizontal, vertical, triangular, and inverted triangular circuit line at 1m from the ground level. On observe in this curve the magnetic field intensity increases in symmetrically and continuous way in the two sides positive and negative of the line, to reach the maximum values in the center lateral distance under the middle phase conductors for all this phases arrangement of the circuit line, then decreases rapidly for significative increase of the lateral distance, to register the lower values when one moves away from the conductors, a very far for the center distance of circuit line. By comparing the simulation results obtained, it can be show that the magnetic induction values are higher for the horizontal configuration in all points of the corridor right of way transmission line, and the magnetic induction values for the inverted triangular configuration are lower in comparison with the magnetic induction values registered in the other configurations (vertical, triangular), this is the last recorder the values 2.93µT for vertical configuration, and 1.94µT for triangular configuration, respectively. Accordinate the grave below it is very clear that the horizontal phase arrangement causes the high values of the magnetic flux density with a maximum value of 4.64µT. On the other hand, the inverted triangular phase arrangement causes the low values of the magnetic flux density with a maximum value of 1.70µT in the center lateral distance of single circuit line in all points of right of way power transmission line, this is for the same loading current amplitude of 1000A. This deviation is due to difference in the height of phase conductors above the ground in each configuration. The geometry in inverted triangular line should be the best solution in the modification case of the basic geometry for obtained the reduced values under the power line.

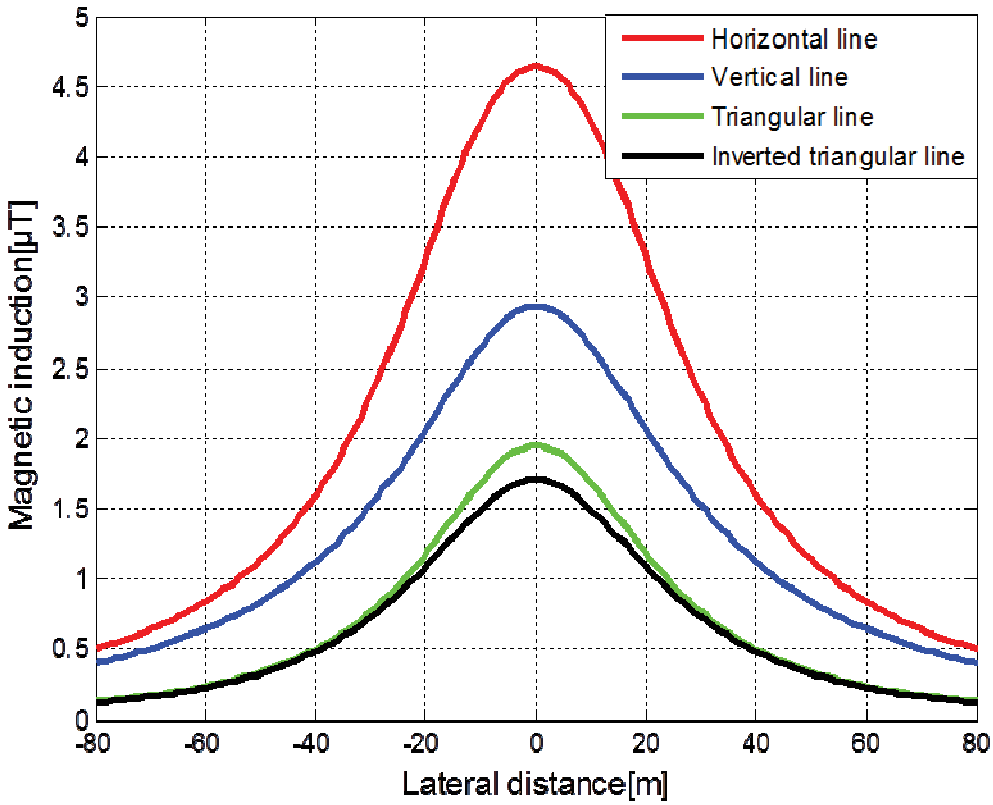

Fig12. Lateral profile of magnetic induction calculated in 1m from the ground level for different configurations of overhead transmission lines

Creative Commons Attribution-NonCommercial-NoDerivatives 4.0 International License (CC BY-NC-ND)

Conclusion:

In this article we plot the lateral profile of magnetic field distribution under the high voltage overhead transmission lines at 1m above the ground.accordinate the simulation results obtained it is very clear the magnetic induction values are maximum in the center distance under the middle phase conductors, then decrease rapidly in symmetrically and continuous manner with a significative increase of the lateral distance, to reach the minimum values when one moves away from the conductors, a very far for the lateral distance, in order study the several factors affecting the magnetic induction under and in the vicinity of the high voltage overhead transmission line, such as the loading current, the height of conductors, the phase spacing between conductors, observation point height above the ground, and the arrangement of phase conductors, on observe the horizontal configuration produce the maximum values of magnetic induction, on the other hand the inverted configuration produce the minimum values of magnetic induction. According the simulation results the horizontal configuration creates the high magnetic induction values due to all conductors being near to the ground level, on other hand the inverted triangular configuration produces the lowest magnetic field values. Generally, the low frequency magnetic fields underneath 400kV overhead power lines with loading phase current of 1000A is below and does not exceed the proposed value 20µT,which is five times lower of the exposure limit established by ICNIRP for the general public 100µT.

References:

Tourab W., Babouri A. (2016), *Measurement and modeling of personal exposure to the electric and magnetic fields in the vicinity of high voltage power lines*, Safety and Health at Work **7(2):** 102-110.

Grellier J., Ravazzani P., Cardis E. (2014), *Potential health impacts of residential exposures to extremely low frequency magnetic fields in Europe,* Environment International ,science direct, vol.62,55-63.

Huang J., Tang T., Hu G and al. (2013), *Association between exposure to electromagnetic fields from high voltage transmission line and neurobehavioral function in children*, PLoS One Journal.

Al-Bassam E., Elumalai A., Khan A and al. (2016), *Assessment of electromagnetic field levels from surrounding high-tension overhead power lines for proposed land use,* Environmental Monitoring and Assessment, Springer **188(5):** 188–316.

Rifai A.B., Hakami M.A. (2014), *Health Hazards of Electromagnetic Radiation*, Journal of Biosciences and Medicines, Scientific Research **2(8):** 1-12.

CIGRE. (1980), *Electric and magnetic fields produced by transmission systems*, Description of phenomena, Practical Guide for calculation, WG 36-01, Paris.

ICNIRP. (2010), *International Commission on Non-Ionizing Radiation Protection, Guidelines for limiting exposure to time-varying electric and magnetic fields (1Hz to 100 kHz)*, Health Physics **99(6):** 818-836.

Abdel-Salam E., Abdallah H., El-Mohandes M.Th and al. (1999), *Calculation of magnetic fields from electric power transmission lines*, Electric Power Systems Research **49(2):** 99–105.

Yao D., Li B., Deng J and al. (2008), *Power Frequency Magnetic Field of Heavy Current Transmit Electricity Lines Based on Simulation Current Method*, Automation Congress IEEE, 1–4. Print ISSN: 2154-4824.

Radwan R., Abdel-Salam., Mahdy M and al. (2011), *Laboratory Validation of Calculation of Magnetic Field Mitigation Underneath Transmission Lines Using Passive and Active Shield Wires*, Innovative Systems Design and Engineering **2(4):** 218–232.:

Amiri R., Hadi H., Marich M. (2006), *The influence of sag in the electric field calculation around high voltage overhead transmission lines*, Annual Report Conference on Electrical Insulation and Dielectric Phenomena.

Riba-Ruiz J.R., Espinosa A.G. (2009), *Magnetic field generated by sagging conductors of overhead power lines*, Wiley Periodicals, Inc. Computer Applications in Engineering Education. **19(4):** 787–794.:

Creative Commons Attribution-NonCommercial-NoDerivatives 4.0 International License (CC BY-NC-ND)

Algerian Journal of Engineering Architecture and Urbanism Vol. 5 Nr. 3 2021
ISSN: 2588-1760

COMPARATIVE STUDY BETWEEN TWO HYPERELASTIC MODELS OF AN ELASTOMERIC SPECIMEN)

Sara BOUDJIT
PhD student, Laboratory of Mechanics, Materials and Energetic (L2ME).Faculty Technology, University of Bejaia, 06000 Bejaia, Algeria, Departement of mechanical engineering,
e-mail: boudjitsara7@gmail.com

Rassim YOUNES
Lecturer, Laboratory of Mechanics, Materials and Energetic (L2ME).Faculty Technology, University of Bejaia, 06000 Bejaia, Algeria, Departement of mechanical engineering,
e-mail: rassimyounes@yahoo.fr

Issam BOUKLOUCHE
PhD student, Laboratory of Mechanics, Materials and Energetic (L2ME).Faculty Technology, University of Bejaia, 06000 Bejaia, Algeria, Departement of mechanical engineering,
e-mail: issamboukelouche2018@gmail.com

Mohand Amokrane BRADAI
Professor, Laboratory of Mechanics, Materials and Energetic (L2ME).Faculty Technology, University of Bejaia, 06000 Bejaia, Algeria, Departement of mechanical engineering,
e-mail: mokbrad@yahoo.fr

Abstract:
Due to the great richness of their behavior, the use of elastomeric material as hyperelastic is more and more widespread in many industrial fields, in particular in the leisure industry to the aerospace passing by the automobile and aeronautics. Most rubbers are considered to be incompressible, that is to say they deform at constant volume. There is a number of strain energy density expressions reported in the literature for rubbers. An efficient hyperélastic material model is one which can lead to good agreement with experimental results for any stress state, with the same set of material parameters.

The objective of this work is to carry out a comparative study between two hyperelastic models proposed in the literature (Mooney Rivlin and Arruda-Boyce) to reproduce the mechanical behavior of hyperelastic polymer (latex) using the finite element method (FEM). To do this, we have carried out a comparative study of the results calculated analytically with the results obtained numerically thanks to the mechanical tests of traction and compression uni-axial. The results obtained were carried out on a cylindrical specimen 10mm in diameter and 70mm in length by varying the varying displacements in order to record the stress distribution. However for reasons of simplicity, we have chosen to use the equivalent stress of Von Mises to model the mechanical behavior of materials in order to approach the numerical model to the analytical results. The Mooney Rivlin and Arruda-Boyce analytical models reproduce satisfactorily the numerical results of traction and compression in the whole range of

Creative Commons Attribution-NonCommercial-NoDerivatives 4.0 International License (CC BY-NC-ND)

elongations, the numerical results for both models are in goog agreement with the theory. Recall that the parameters of the models were taken from the Marckmann publication.

Key words: elastomer, hyperelastic, FEM.

Introduction

Elastomers are called rubbers in the common language are widely used in industrial applications, especially in automotive and aerospace. Their properties are used for various applications such as sealing, damping, insulation,etc(CHEVALIER, M. 2003)**.** thse applications take advantage of the particular mechanical brhavior of these materials, characterized mainly by the ability to withstand very large reversible deformation(servel hundred percent)(Verron, E. 2003)**.** Thus the prediction of the mechanical behavior of elastomers in finite element calculation software requires the use of highly nonlinear behavior models, this non-linearity is the result of both the large deformation that induce strong changes in geometry and the relationship between these deformations and stresses (Raoult, I. (2005)**.** For the characterisation of the statistical or quasi-statique behavior of these materials, we use models or laws of hyperelastic behavior widespread in the literature. Some of them were based on experimental observations and mathematical properties of isotropy and incompressibility, others were derived from microstructural considerations and reflect the essentially entropic origin of rubber elasticity **(** Gacem, H. (2007).

The objective of this work is to perform a comparative study between two hyperelastic models proposed in the literature (Mooney Rivlin and Arruda-Boyce) to reproduce the mechanical behavior of hyperelastic polymer (latex) using the finite element method. To do this we have made a comparative study of the results calculated analytically to the results obtained numerically through mechanical tests of traction and compression uni-axial; knowing that the parameters of the models were taken from the publication of Markmann (Marckmann, G et al., 2006). The analytical models Mooney Rivlin and Arruda-Boyce reproduce satisfactorily the numerical results of traction and compression in the whole range of elongations, the numerical results for both models are in good agreement with the theorie.

In the next section, we present some notions on hyperelasticity behavior laws. Then the numerical simulation in traction and compression uni-axial, we present the geometry and the mesh used in this study as well as the analytical method, the results obtained are discussed followed by a conclusion.

Creative Commons Attribution-NonCommercial-NoDerivatives 4.0 International License (CC BY-NC-ND)

Materials and methods:

Material used:

The material used for this study is the latex of the volumic mass ρ=940 kg/m^3 , it is mainly composed of 30 to 40% of polymer and 2 to 3% of protein.

Presentation of the hyperelastic models used in the study:

We can separate the hyperelastic models that are expressed in terms of invariants and chose that are expressed in terms of principal elongations:

W = (I_1, I_2, I_3) or W = (λ_1, λ_2, $\lambda 3$), Where I_1, I_2, I_3 are the invariants of the Cauchy Green tensor, and λ_i (i =1, 3) are the principal elongations.

In all our study we have assumed that the medium is incompressible, which implies that I_3 = 1. The law of behavior for an incompressible medium is expressed by:

$$\boldsymbol{\sigma} = 2\mathbf{B}\frac{\partial w}{\partial \mathbf{B}} - p\mathbf{I} \qquad (1)$$

The hyperelastic potential of each model is given by the following relations:

- **Mooney Rivlin model** (Marckmann, G. 2004)**:**

$$W = C_1(I_1 - 3) = \frac{\mu}{2}(I_1 - 3) \qquad (2)$$

- **Arruda-Boyce model :**(BOUZIDI, S)

$$W = \mu_0 N_B \left(\lambda_r \beta + \ln\left(\frac{\beta}{\sinh\beta}\right)\right) - C_g^* \qquad (3)$$

Analytical calculation:

In the case of uni-axial loading along the x direction, the gradient tensor of the deformation is:

$$F = \begin{bmatrix} \lambda & 0 & 0 \\ 0 & \lambda^{-1/2} & 0 \\ 0 & 0 & \lambda^{-1/2} \end{bmatrix}$$

The right Cauchy Green tensor is defined by:

$$\mathbf{B} = \mathbf{F}\mathbf{F}^T = \begin{bmatrix} \lambda^2 & 0 & 0 \\ 0 & \lambda^{-1} & 0 \\ 0 & 0 & \lambda^{-1} \end{bmatrix}$$

The boundary conditions of the uni-axial tensil test (uni-axial compression) are:

$$\sigma_1 = \sigma \,, \quad \sigma_2 = \sigma_3 = 0$$

The stress-strain relationship of each model is determined from relationship (1) where the hydrostatic pressure is eliminated from the boundary conditions:

Creative Commons Attribution-NonCommercial-NoDerivatives 4.0 International License (CC BY-NC-ND)

- **Mooney Rivlin model:**

$$\sigma = 2\left(C_1 + \frac{C_2}{\lambda}\right)\left(\lambda^2 - \lambda^{-1}\right) \quad (4)$$

The parameters of the model are C_1 and C_2

For the material used, according to the Marckmann publication we have: $C_1 = 0.162MPa$ and $C_2 = 0.0059MPa$

- **Arruda-Boyce model:**

Using the padé approximation:

$$\beta = L^{-1}(\lambda_r) = \frac{\lambda_r(3 - \lambda_r{}^2)}{1 - \lambda_r{}^2}$$

We find that: $\sigma = \frac{\mu_0}{3}\left(\frac{3-\lambda_r{}^2}{1-\lambda_r{}^2}\right)\left(\lambda^2 - \lambda^{-1}\right)$ (5)

Where $\lambda_r = \frac{\lambda_{chaine}}{\lambda_l} = \sqrt{\frac{I_1}{3N_s}}\lambda_r = \sqrt{\frac{\lambda^2 + 2\lambda^{-1}}{3N_s}}$

With:

λ_r: Relative dillatation of a chain ,

λ_l: Limit elongation of the network $\lambda_l = \sqrt{N_s}$.

μ_0 and N_s are the parameters that define this model.

According to the Marckmann publication we have: $\mu_0 = 0.28$ et $N_s = 25.4$

Von Mises equivalent stress:

It is very interesting to compare the stresses obtained on structure either numerically or theoretically to the characteristics of the material that constitutes it. For this purpose the moste used criterion. In the case of uni-axial tension (uni-axial compression), the equivalent Von Mises stress is equal to the tension stress (compression).

$\sigma^{vm} = \sqrt{\frac{3}{2}\boldsymbol{\sigma}^D : \boldsymbol{\sigma}^D} = \sigma$ (III.13)

Where $\boldsymbol{\sigma}^D = \boldsymbol{\sigma} - \left(\frac{1}{3}\text{Trace}\,(\boldsymbol{\sigma})\right)\boldsymbol{I}$: is the deviator of the tensor $\boldsymbol{\sigma}$.

Numerical simulation of uni-axial traction (uni-axial compression):

Presentation of the geometry;

We consider a cylindrical specimen of 10mm diameter and 70mm length (Fig1)

Creative Commons Attribution-NonCommercial-NoDerivatives 4.0 International License (CC BY-NC-ND)

Algerian Journal of Engineering Architecture and Urbanism Vol. 5 Nr. 3 2021
ISSN: 2588-1760

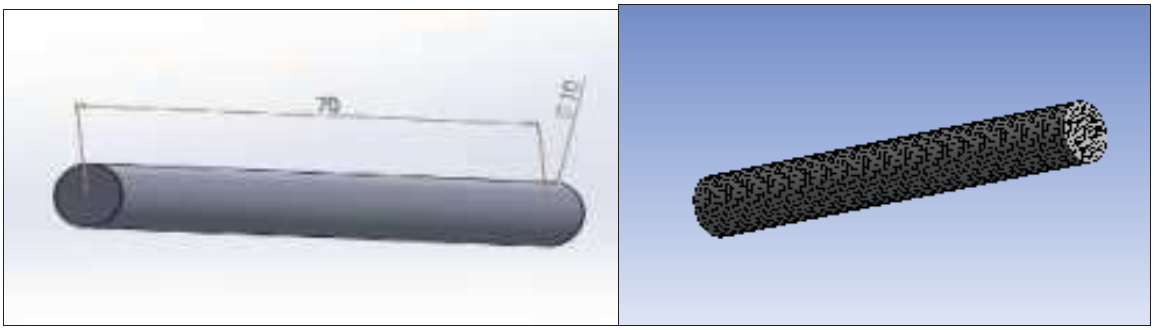

Fig1.3D mesh model

After entering the parameters into the finite element software, we generated an adaptive, quadratic mesh

Nodes	38059
Elements	8540

Results and discussions:

Result of the numerical simulation of the uni-axial traction:

We present here the results of the numerical simulation. Note that the medium is assumed to be quasi-incompressible with a fish coeffecient very close to 0.5

So $\nu = 0.4995$ which gives $D = 0.0015MPa^{-1}$

With : $D = \frac{2}{k_0} = \frac{6(1-2\nu)}{E}$ (E ≈ 1.2 MPa)

Mooney Rivlin model:

Figure (3) shows the distribution of numerical constraints (Von Mises) for the different elongations

Creative Commons Attribution-NonCommercial-NoDerivatives 4.0 International License (CC BY-NC-ND)

Algerian Journal of Engineering Architecture and Urbanism Vol. 5 Nr. 3 2021
ISSN: 2588-1760

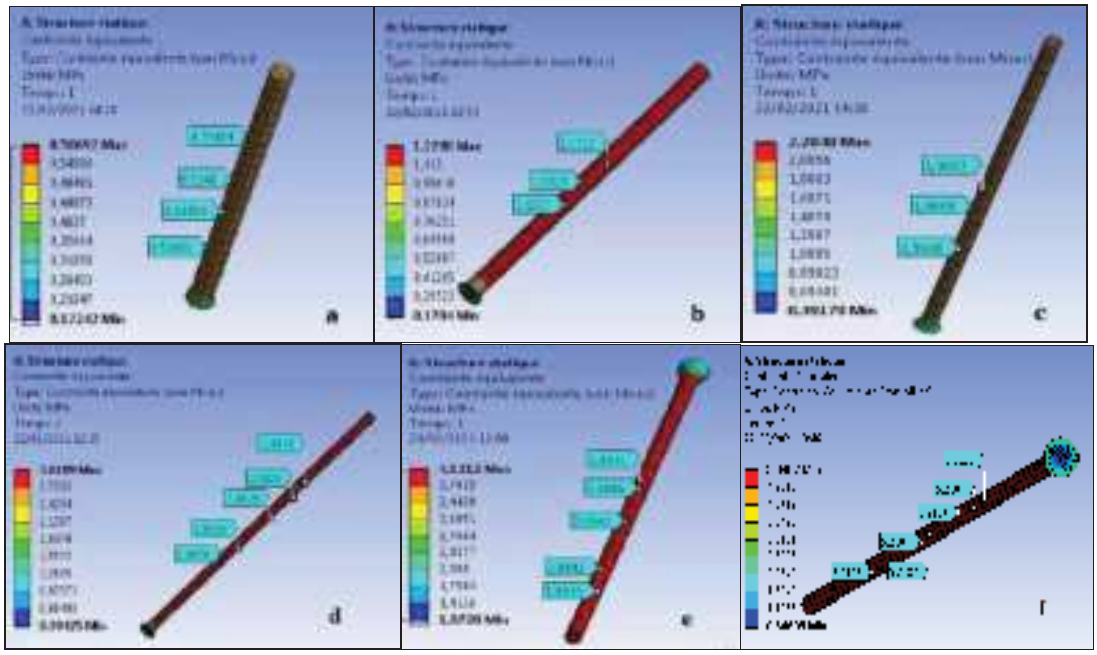

Fig2. Distribution of numerical constraint (VM) for the different elongation **a)** λ=1.5 **b)** λ =2 **c)** λ=2.5 **d)** λ=3 **e)** λ=3.5 **f)** λ=4

Figure (3) shows the evolution of the different stresses calculated (analytically and numerically) as a function of elongations.

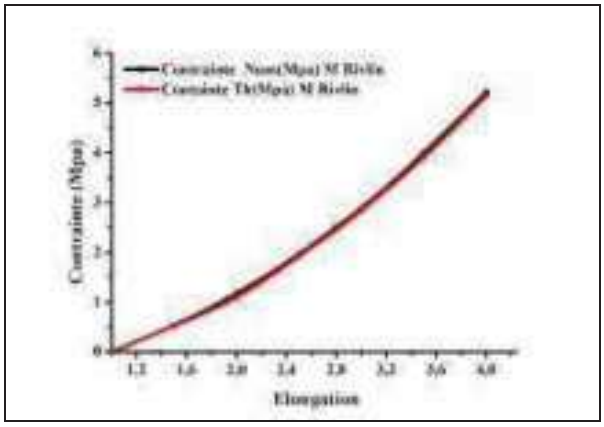

Fig3. Evolution of equivalent stresses(Von-Mises) as a function of elongations

The results obtained analytically are compared with the numerical results in the case of uni axial traction.It can be seen the numerical model reproduces the theorical results in a very satisfactory way for all values of elongations.

It should be noted that the numerical simulations were carried out with the same parameters of the theoretical model.

Arruda-Boyce model (8 chains) :

Creative Commons Attribution-NonCommercial-NoDerivatives 4.0 International License (CC BY-NC-ND)

Algerian Journal of Engineering Architecture and Urbanism Vol. 5 Nr. 3 2021
ISSN: 2588-1760

Figure (3) shows the distribution of numerical constraints (Von Mises) for the different elongations

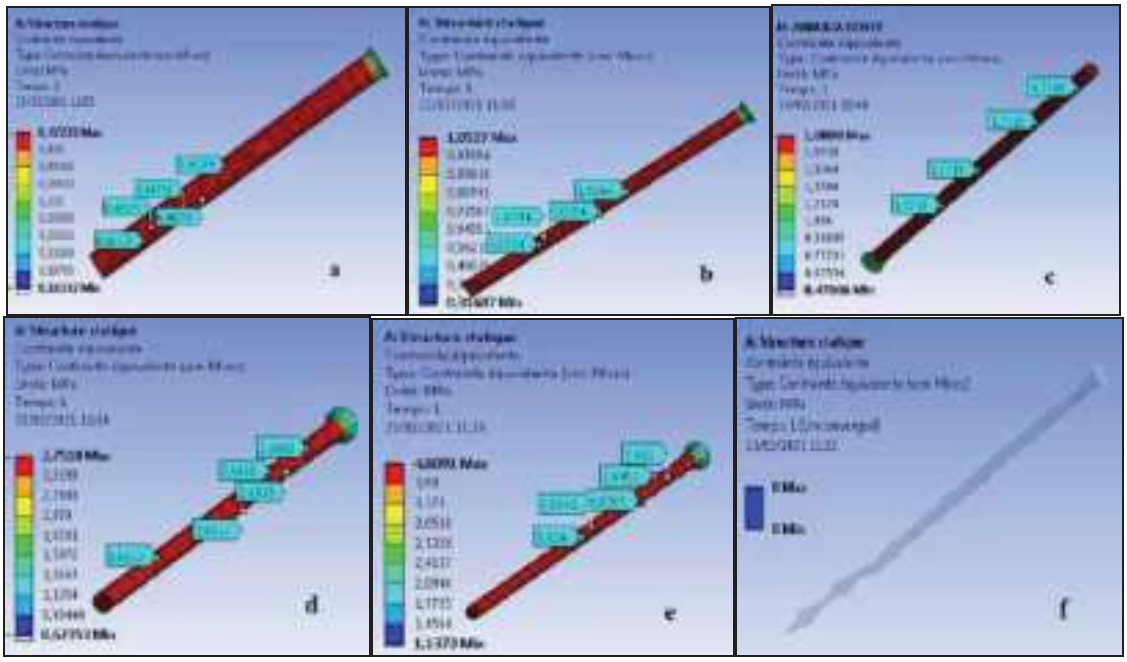

Fig4. Distribution of numerical constraint (VM) for the different elongation **a)** λ=1.5 **b)** λ =2 **c)** λ=2.5 **d)** λ=3 **e)** λ=3.5 **f)** λ=4

Figure (5) shows the evolution of the different stresses calculated (analytically and numerically) as a function of elongations.

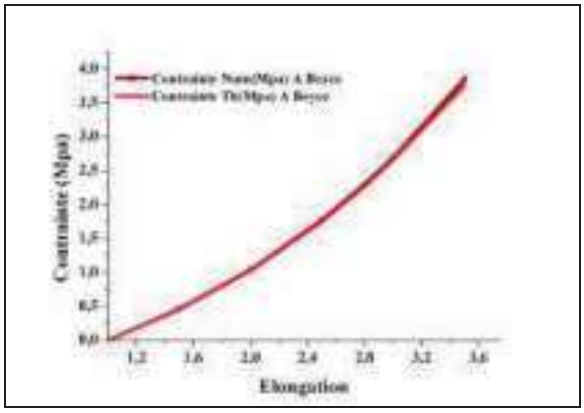

Fig5. Evolution of equivalent stresses(Von-Mises) as a function of elongations.

From figure (5) we can see that the analytical results are compared with the numerical results in the case on uni-axial traction.

It can be seen that the Arruda-Boyce analytical model reproduce the nulerical results of uni-axial traction test in a very sastisfoctory way in the whole range of elongation.

Creative Commons Attribution-NonCommercial-NoDerivatives 4.0 International License (CC BY-NC-ND)

Figure (6) shows the evolution on the different stresses calculated analytically an numerically for the two models as a function of elongation.

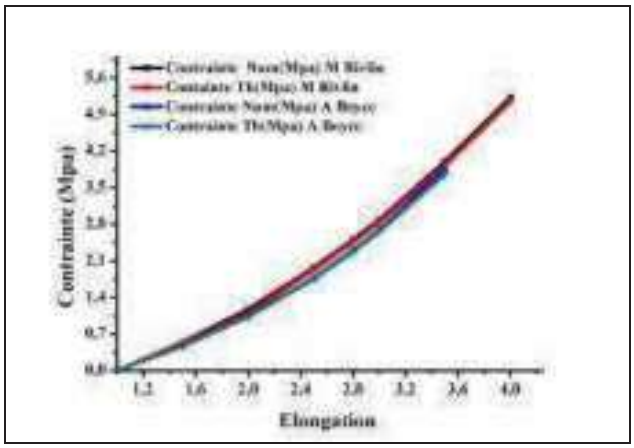

Fig6. Comparison of numerical and theorical curves in the uni-axial traction case for the two models.

The cuves presented in figure (6) show the evolution of the theorical and numerical stresses as a function of elongation for the two models Arruda-Boyce and Mooney Rivlin.

From the figure it can be seen that the analytical results are compared with the numerical rsults in the case of uni-axial traction for both models up to an elongation λ=3.8. beyond this value the simulation does not give any results for the Arruda-Boyce model (deterioration of the part (Fig 4-f)). This deformation is explained the validity range of the plane stress calculations, in the case the finite element calculation does not give results. The diameter of the specimen must be small compared to its length.

Result of the numerical simulation of the uni-axial traction:

Mooney Rivlin model:

Figure (7) shows the distribution of numerical constraints (Von Mises) for the different elongations under uni-axialncompressive loading.

Creative Commons Attribution-NonCommercial-NoDerivatives 4.0 International License (CC BY-NC-ND)

Algerian Journal of Engineering Architecture and Urbanism Vol. 5 Nr. 3 2021
ISSN: 2588-1760

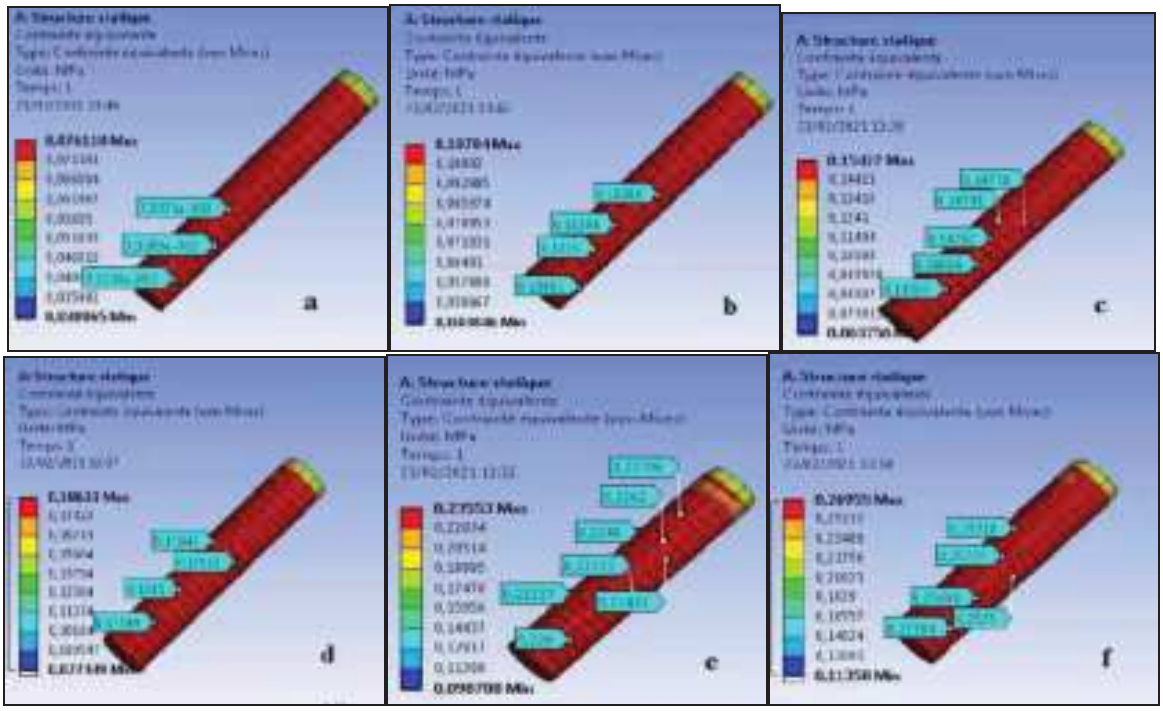

Fig7. Distribution of numerical constraint (VM) for the different elongation **a)** λ=0.92 ; **b)** λ =0.9 ; **c)** λ=0.85 ; **d)** λ=0.82 ; **e)** λ=0.78 ; **f)** λ=0.75

Figure (8) shows the evolution of the theorical and numerical stresses as a function of the elongation

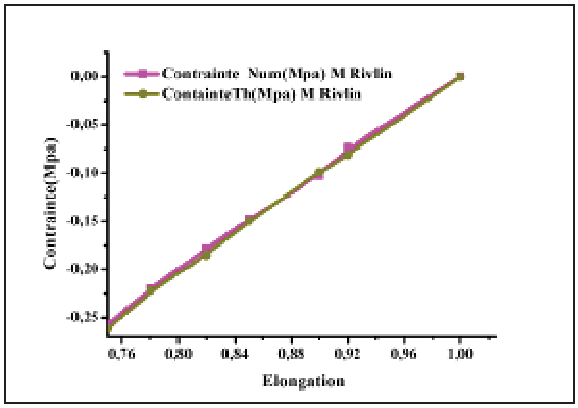

Fig8. Evolution of equivalent stresses(Von-Mises) as a function of elongations.

In the case of a uni-axial compression test , the numerical results obtained are compared with the theorecal results.

It is found that the numerical model reproduces the theoretical results for the Mooney Rivlin model in a very satisfactory way for all the values of elongation.

Creative Commons Attribution-NonCommercial-NoDerivatives 4.0 International License (CC BY-NC-ND)

Arruda-Boyce model (8 chains) :

Figure (9) shows the distribution of numerical constraints (Von Mises) for the different elongations under uni-axialncompressive loading.

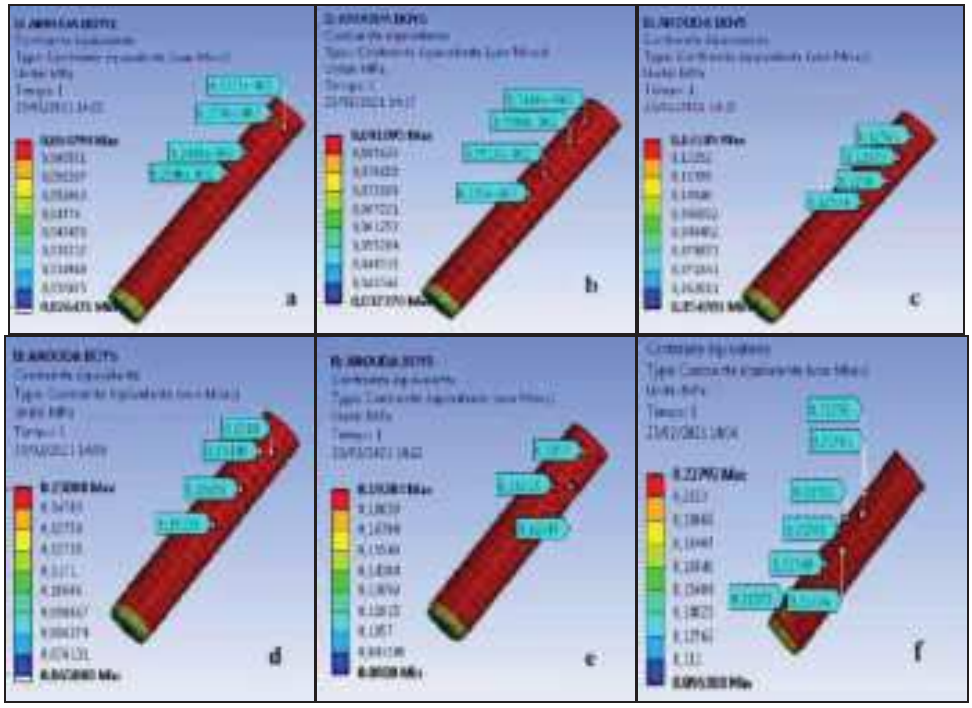

Fig9. Distribution of numerical constraint (VM) for the different elongation **a)** λ=0.92 ; **b)** λ =0.9 ; **c)** λ=0.85 ; **d)** λ=0.82 ; **e)** λ=0.78 ; **f)** λ=0.75

Figure (10) shows the evolution of the theorical and numerical stresses as a function of the elongation.

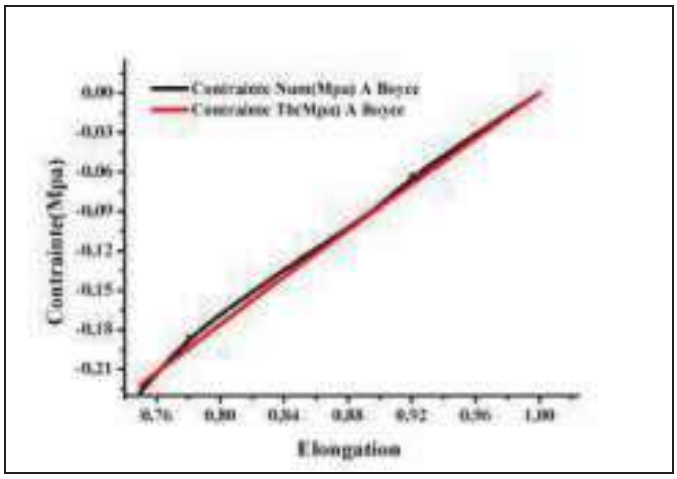

Fig10. Evolution of equivalent stresses(Von-Mises) as a function of elongations.

Creative Commons Attribution-NonCommercial-NoDerivatives 4.0 International License (CC BY-NC-ND)

The numerical results obtained are compared with the analytical results in the case of a uni-axial compression test for the Arruda-Boyce model.

The curves obtained by the numerical simulation are merged with the analytical curve for all values of elongations.

Figure (11) shows the evolution of the different stresses calculated analytically and numerically for the two models as a function of elongation.

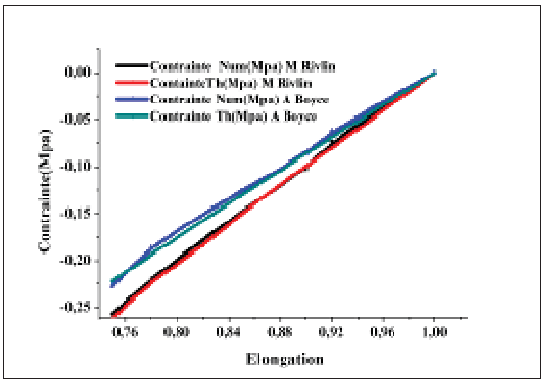

Fig 11. Comparison of numerical and theorical curves in the uni-axial compression case for the two models.

From the figure a slight difference between the stress values for the two models is observed up to an elongation of λ=0.96, beyond this value the results are in goog agreement.

It can be seen that the numerical results obtained are almost in agreement with the analytical results in the case of uni-axial compression test.

Conclusion:

This work is devoted to the comparative study between two hyperelastic models (Mooney Rivlin and Arruda-Boyce). To carry out this study, a cylindrical specimen made of elastomer (latex) was chosen for different deformation modes (uni-axial traction and compression).

We found that the results of the numerical simulation are in good agreement with the theoretical results for both models. The distribution of the stress and strain fields is homogeneous along the entire length of the specimen.

Creative Commons Attribution-NonCommercial-NoDerivatives 4.0 International License (CC BY-NC-ND)

We have shown that for very large displacements, the diameter of the specimen must be small compared to its length in order to avoid the deterioration of the simulation part.

It is also important to note that a behavior law capable of simulating the mechanical respons with a minimum of parameters is the main objective of modeling.

References:

CHEVALIER, M. (2003). Modélisation et identification du comportement non linéaire des cales en caoutchouc (Doctoral dissertation, École Centrale de Lyon).

Verron, E. (2003). Modélisation du comportement des structures et des matériaux élastomères (Doctoral dissertation, Université de Nantes).

Raoult, I. (2005). Structures élastomères sous chargement cyclique: comportement, fatigue, durée de vie (Doctoral dissertation, Ecole Polytechnique X).

Marckmann, G. (2004). Contribution à l'étude des élastomères et des membranes soufflées (Doctoral dissertation, Ecole Centrale de Nantes (ECN); Université de Nantes)

Gacem, H. (2007). Comportement visco-hyperélastique des élastomères : viscoélasticité non linéaire, application aux multicouches (Doctoral dissertation, Paris 6).

Masson, I. (2008). Contribution à la modélisation mécanique du comportement dynamique, hyperélastique et anisotrope de la paroi artérielle (Doctoral dissertation, Paris

BOUZIDI, S. Modelisation micro mécanique du comportement hyper elastique des élastomères composites (Doctoral dissertation, Université de Béjaia-Abderrahmane Mira).

Marckmann, G., **&Verron, E**. (2006). Comparison of hyperelastic models for rubber-like materials. Rubber chemistry and technology, 79(5), 835-858.

Creative Commons Attribution-NonCommercial-NoDerivatives 4.0 International License (CC BY-NC-ND)

Algerian Journal of Engineering Architecture and Urbanism Vol. 5 Nr. 3 2021
ISSN: 2588-1760

Numerical study of the use of composite piston and estimation of the lifetime.

Tablit bassima
dept génie mécanique ,laboratoire mécanique des solides et systèmes (lmss).
Algeria,email tablitbassima@gmail.com

chellil ahmed
dept génie mécanique,Laboratoire dynamique des moteurs vibroacoustiques LMDV algeria
email cchellil@yahoo.fr

lecheb samir
dept génie mécanique,Laboratoire dynamique des moteurs vibroacoustiques LMDV algeria
email samir_lecheb@yahoo.fr

Brihmat chahira
dept génie mécanique,laboratoire mécanique des solides et systèmes (lmss). Algeria
email c.brihmat@univ-boumerdes.dz

Abstract:
The paper presents the results of inverstigations concerning the possibilities of application of composite materials in construction and industry engines, a piston is an integral part of an engine which reciprocates at very high speed thus producing combusion resulting in movement of the vehicle,the main in this study the first we give in statically part the distribution of stress, displacement field and strain of composite piston made in (carbon/carbon) also in dynamical part the first ten modes shapes,secondly in this work the goal is to estimate the lifetime of composite piston based on the fatigue analysis to do this aims to discover the theory of fatigue with different analysis methods and we determined the life time based on finite element methode on software abaqus and analytical approches (S-N) (E-N) when provide the composite material are best material in damage

Key words: composite piston ,lifetime,fatigue,frequencies.

Introduction:

A composite material is made by combining two or more materials often ones that have very different properties.the two materials work together to give the composite unique properties.however,within the composite you can easily tell the different materials apart as they do not dissolve or blend into each other.[1]

I.1.Characteristics of composite materials

- High specific strenght and modulus,as well as high fatigue strength and fatigue damage tolerance.
- Anisotropic
- Designable or tailorable materials for both microstructure and properties.

Creative Commons Attribution-NonCommercial-NoDerivatives 4.0 International License (CC BY-NC-ND)

- Production of both material and structure or component in a single operation manufacturing flexible ,net –shape,complex geometry
- Corrosion resistance and durable.
- Other unique functional properties damping, low CTE(coefficient of the thermal expansion).[2][3]

II.Carbon-carbon pistons

II.1Piston concept

A new piston concept has been developed that overcomes a number of the shortcomings of aluminium pistons.the new piston concept is made of carbon-carbon refractory composite material [4-9] the carbon-carbon piston was developed as a replacement for an aluminum piston used in a two stroke cycle engine .the engine was used to power a us army remotely piloted vehicle.the aluminum piston and its carbon piston a cooperative effort.called the advanced carbon-carbon piston program,was started in 1986 inolving nasa langley research center and the us the first objective was to develop and test an all carbon piston engine.the second objective was to transfer the carbo-carbon technology to engines used in light aircraft,automobiles and other types of transportvehicles

II.1Piston crown damage

- Anisotropic
- Designable or tailorable materials for both microstructure and properties.
- Production of both material and structure or component in a single operation manufacturing flexible ,net –shape,complex geometry
- Corrosion resistance and durable.
- Other unique functional properties damping, low CTE(coefficient of the thermal expansion)

Fig 1.damage piston.

- Overheating due to combustion defaults
- Bent/blocked oil injection jet
- Installation of incorrect pistons
- Malfunctions in the cooling system
- Clearance restriction in the upper sliding surface area

II.2Fatigue estimation methods

General on fatigue and estimation of lifetime

Fatigue or fatigue damage is the modification of mechanical properties of materials resulting from the repeated application of stress cycles, these applications which may lead to the breakage of parts made of these materials. Two fields of study can then be distinguished, the

Creative Commons Attribution-NonCommercial-NoDerivatives 4.0 International License (CC BY-NC-ND)

first field is that so-called “oligocyclic” fatigue which corresponds to the greatest forces, at the elastic limit of the material and where the breakage occurs around 104 -105 cycles. Second domain, that of "polycyclic" fatigue We distinguish there two subdomains, that of limited endurance is fatigue with large numbers of cycles that is referred to. The break then occurs between 105 - 107 cycles and endurance unlimited is that of fatigue with very large numbers of cycles where the rupture do not intervene before 108 cycles. When the limited endurance is treated, We consider that the initiation of a crack in the structure determines its lifetime since statistically, the appearance of a crack generally represents more than 90% the life of a structure. [10] Stress

The constraint is then characterized by

* Alternating stress: σa
* Average stress: σm
* Stress ratio: R = σmin/ **σmax**

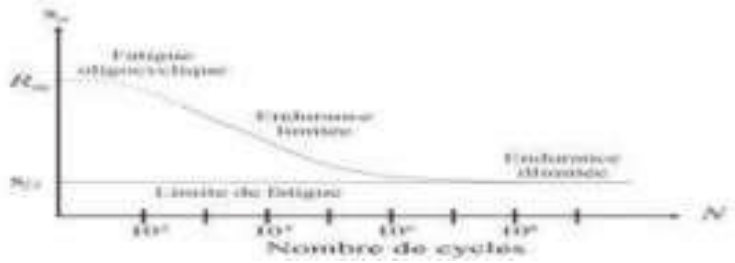

Fig2.Fatigue study areas.

The most representative way to report the endurance of a material is to plot the Wöhler curve or S-N curve. Indeed, to characterize fatigue parameters of a material, the simplest test is to submit "smooth or notched" specimens of this material with stress cycles periodicals, of maximum amplitude and constant frequency and to be reported on a curve, the number of cycles at the end of which the rupture occurs according to the magnitude of the applied force. Various analytical expressions have been proposed to represent the curves de Wöhler in the areas of limited and unlimited endurance. The most commonly used analytical representation was proposed by Basquin in 1910 [11] by the following relation:

ln Sa = a – b ln Nr a > 0, b > 0 (1)

GOODMAN model or Goodman line, It is the most appropriate model to model the effects of the mean compressive stress: Sa / Se+ Sm / Rm = 1 or Sm <Rm. GERBER model or Gerber parabola, C 'is the most appropriate model to model the effects of stress

moy: Sa /Se + (Sm /Rm) 2 = 1 ou Sm < Rm (2)

III. Numerical parts

The piston is designed in solidworks as it the platform for designing parts and many component accurately with the required dimensions the software give the idea of a part manifactured in reality as it serves like a prototype.

Creative Commons Attribution-NonCommercial-NoDerivatives 4.0 International License (CC BY-NC-ND)

Geometry of piston

Fig3. geometry piston.

Fig3. geometry model of piston.

III.1Load and BC

Loads consist of any of the forces, moments, concentrated or distributed tractions, fluxes, or more generally, influences, including predefined fields imposed upon a structure or body that cause deformation, displacement, or change the state of the structure from the unloaded state. For the first force we applied P= 0.05 (MPa), pressure

Fig 4. Load and boundary conditions.

III.2Results:

III.2.1.Statical part:Von Mises : $S_{max= 1.832e+01}$

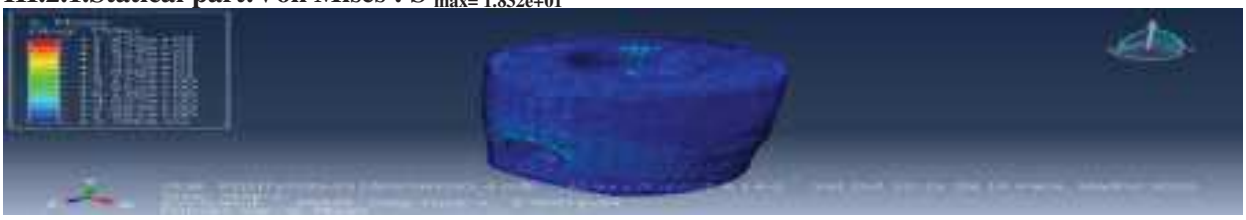

Fig 5. Von Misses stress.

Displacement:U=2.633 e -2 .

Fig 6. Displacement.

Deformation: $E_{max=}$ 4.233E+02.

Creative Commons Attribution-NonCommercial-NoDerivatives 4.0 International License (CC BY-NC-ND)

Fig7. Max strain.

III.2.2Dynamical part ¸Mode of deformation :

Mode1 :Umax=1.092e+00,Freq=617.15 hz

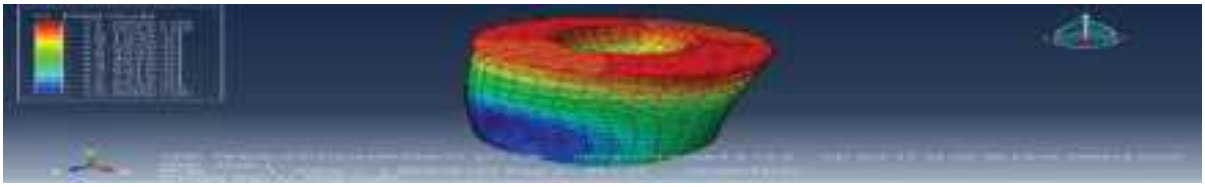

Fig8 first mode shape.

Mode 2 :Umax=1.032e+00,Freq=910.71 hz.

Fig.9 : second mode shape .

Mode 3 Umax=1.285e+00 ;Freq=1499.8 hz

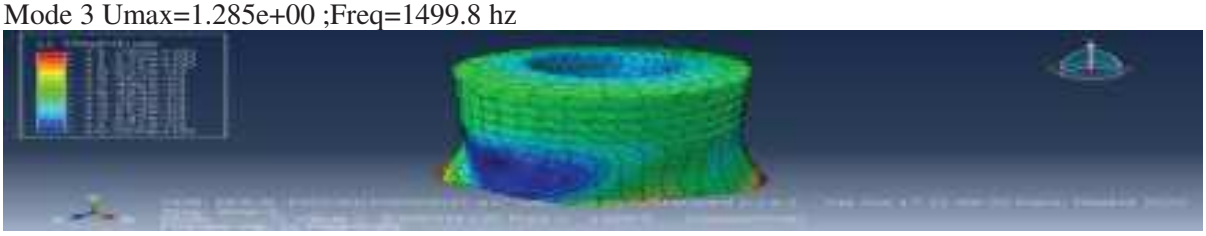

Fig.10 : Third mode shape.

Mode 4 Umax=1.210e+00,Freq=1589.4 hz

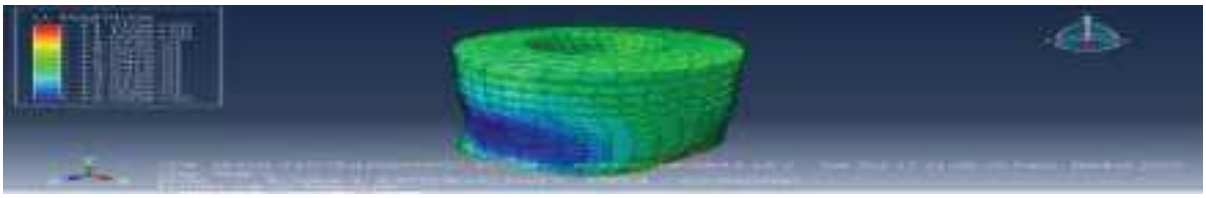

Fig.11 :Forth mode shape .

Mode 5 Umax=1.347e+00,Freq=1727.7 hz.

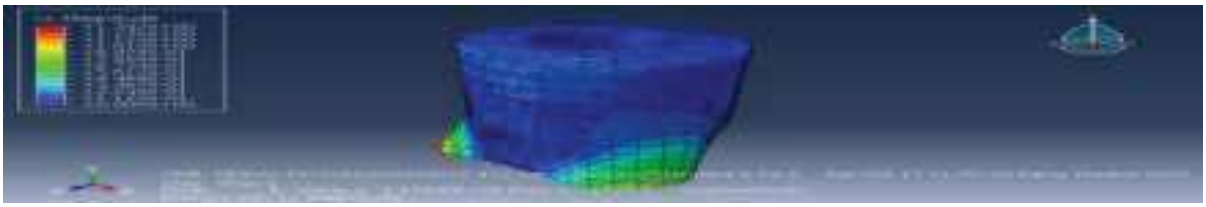

Creative Commons Attribution-NonCommercial-NoDerivatives 4.0 International License (CC BY-NC-ND)

Fig.12 : Five mode shape .

Mode 6 Umax=1.338e+00,Freq=1847.3 hz.

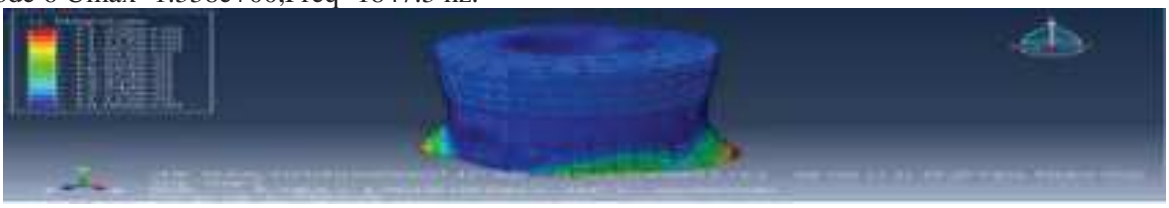

Fig.13: Sixe mode shape .

Mode 7Umax=1.074e+00,HZ=2109.9 hz.

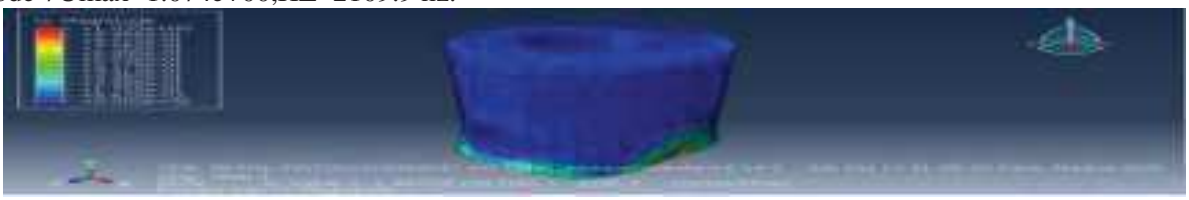

Fig.14: Seven mode shape.

Mode 8 Umax=1.035e+00,Freq=2246.9 Hz.

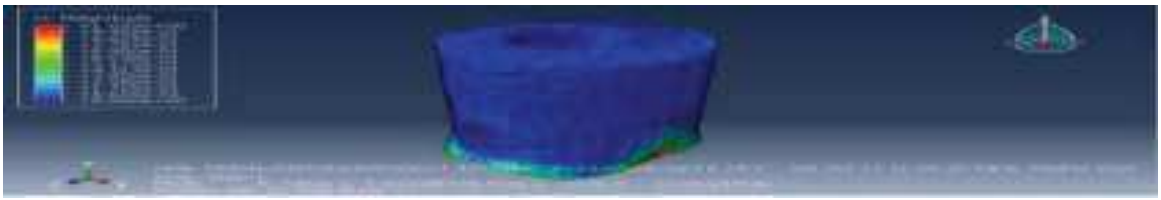

Fig.15 : eight mode shape.

Mode 9 Umax=1.079e+00.Freq=2393.6hz

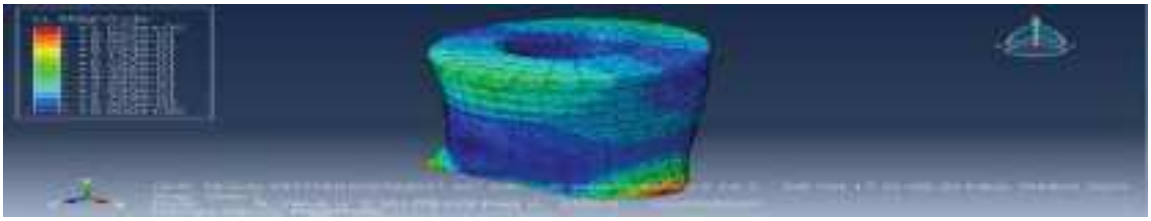

Fig.16 nine mode shape.

Mode 10 Umax=1.01e+10 Freq=2464.3 Hz.

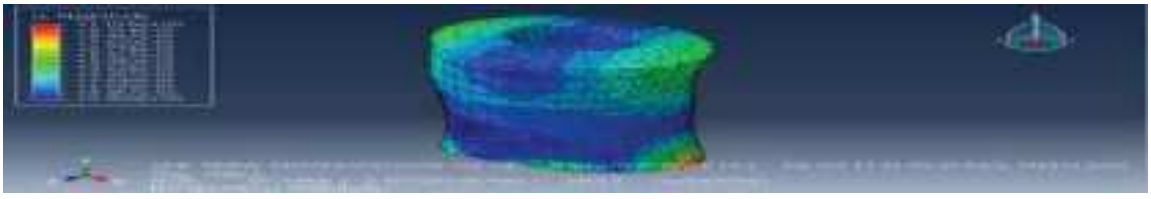

Fig.15 ten mode shape.

Graph of frequency as function of modes

Creative Commons Attribution-NonCommercial-NoDerivatives 4.0 International License (CC BY-NC-ND)

Algerian Journal of Engineering Architecture and Urbanism Vol. 5 Nr. 3 2021
ISSN: 2588-1760

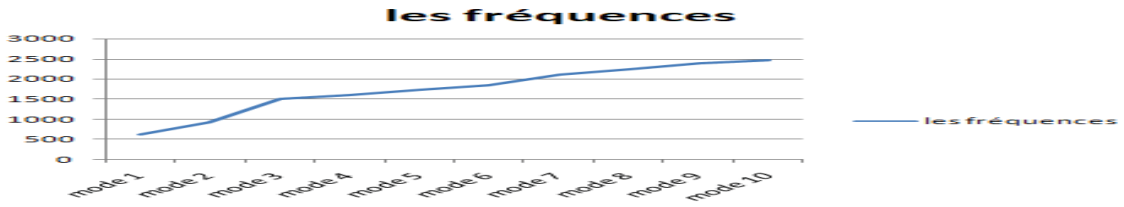

Fig.16 graphe Frequency vs modes.

results given by software deduce that the maximum stresses , and also the behavior during deformation of the composite piston ,and deduce the maximum displacement or deformation will be request inflection, and we deduce that the frequencies increase proportionally with each mode

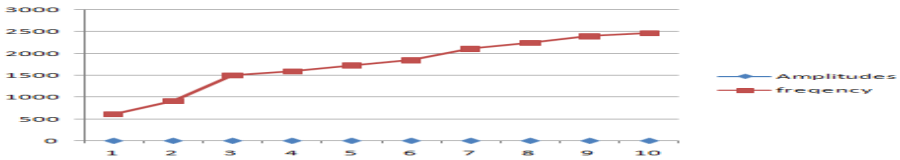

II. the goal of this work is to estimate the servise life of composite piston.

Determination of the service life of stiffeners by S-N and E-N analysis methods

By the S-N method To determine the shelf life, we took the following steps: • Determine the characteristic equation connecting S and Nf:

$$S_{NF} = \sigma'_f (2N_f)^b$$

Fatigue resistance coefficient which depends on the material. b is determined by the relation of BASQUIN:

Knowing that the duration of each cycle is 75s.

ln **Sa** = **a** + **b** ln **Nr.** **(4)**

FOR n=1, **Sa** = = **a** + **bln(1)** = **a**
N = **Nc** = **2.105**

$$b = \frac{-a + \ln \Delta\sigma_e}{\ln N_c} = \frac{\ln \Delta\sigma_e - \ln \sigma'_f}{\ln N_c}$$

b=-0.2

Determination of the endurance constraint SNf and estimation of Nf we have recourse to use the Goodman equation to take into account the effect of the average stress given by the following relation:

$$\frac{S_a}{S_{Nf}} + \frac{S_m}{R_m} = 1 \quad \text{et} \quad S_m < R_m \qquad (5)$$

Creative Commons Attribution-NonCommercial-NoDerivatives 4.0 International License (CC BY-NC-ND)

$$S_a = \frac{\sigma_{max} - \sigma_{min}}{2} \qquad S_m = \frac{\sigma_{max} + \sigma_{min}}{2}$$

$$S_{Nf} = \frac{S_a}{1 - \frac{S_m}{R_m}} \Longrightarrow$$

Nf=50000000 cycles.

Knowing that the duration of each cycle is 75s, we deduced the duration of life in days:

50000000*75/3600*24=1041 days.

That is, after 1041 days, there will be a total break.

TABLE .1 Results of estimation the lifetime..

equations	**Results**		
	$\varepsilon_a \sigma_{max} = \frac{\sigma_f^2}{E}(2N_f)^{2b} + \varepsilon_f'(2N_f)^{}$		
results	NF=456050 cycles 228 days there will be crack initiation	0.28	-0.17

The work of this study is to determine the behavior of Composite materials use in piston (carbon) have attractive aspects like the relatively high compressive strength, good adaptability in fabricating thick composite shells, low weight, low density and corrosion resistance.and finally we will carry out a fatigue analysis of the piston in the place most damaged, the aim is to determine their fatigue life, by based on simulation calculation results and we provied the lifetime is more resistant among other damaged materials.

.References

[1] Boulic,A ;Quantitative Morphology of impact damage to composite aircraft structure, unpublished report, polytech orlèans, France ,2007.
[2] Nikhil VN ayak,UG student,Mechanical B.V. bhvonaraddi college of engineering& technology.
[3] Composite material in aerospace construction,mechanical technology.
[4] Tayor,allanH,Fabrication and performance of advanced carbon-carbon piston structure Fiber-tex 1988,john D buckley ed,Nasa CP-3038,1989,pp,375-395.
[5] Tayor,Allan H :carbon-carbon pistons for internal combustion engines nasa tech briefs vol ,9,no,4 winter 1985,pp,156-157.
[6] Savage ,Gray,carbon-carbon composites first chapman and hall,inc,1993.
[7] Taylor,AllanH: light piston.us patent1.686,809, august 87.
[8] Tayor,allan H. Composite piston.us patent4,736,676 april88.
[9]Taylor,allanH lightweiht piston architecture. U.s1990.
[10] Frederik Rusek. Advances in Fatigue and Fracture Mechanics. PhD thesis, Aalto University ,Espoo, Finland, 2014.
[11] Robert Basan Tea Marohnic et Marina Franulovi. Evaluation of Methods for Estimation of Cyclic Stress-Strain Parameters from Monotonic Properties of Steels. PhD thesis, Faculty of Engineering, University of Rijeka, Vukovarska 58, HR-51000 Rijeka, Croatia, January 2017.

Creative Commons Attribution-NonCommercial-NoDerivatives 4.0 International License (CC BY-NC-ND)

Algerian Journal of Engineering Architecture and Urbanism Vol. 5 Nr. 3 2021
ISSN: 2588-1760

STUDY OF A NON-PREMIXED METHANE/AIR PILOT FLAME

Bendadi Mohammed El Khalil
Auteur, PhD mechanical engineering, department of mechanical engineering, university of MASCARA, e-mail: mohammed.bendadi@univ-mascara.dz

Merouane Habib
Co-auteur, doctor mechanical engineering, department of mechanical engineering, university of MASCARA, e-mail: mer_habib@yahoo.fr

Abstract:

Principle use of the pilot flame is to control combustion in systems having continuous ignition and maintain main flame by providing heat or chemical species and prevention from cold air. This paper study the numerical simulation of non-premixed methane/air piloted flame comparatively with piloted methane/air flame of Sandia National Laboratories. Two-dimensional (2D) simulation used to study the diffusion of piloted flame and measure temperature, pressure, velocity and mass fraction CH4, O2, CO2 and NO including axial and radial profiles. The results describe the propagation of methane/air combustion in the burner and stoichiometric flame length using axial and radial profiles x/D, the factors influence on the flame: the flux of initial jet, the stoichiometric mixture fraction methane/air and diameter of initial jet, that result the reducing of soot in the reaction zone.

Key words: pilot flame, diffusion, combustion, flame length

Introduction:

Piloted flame is used in several technological fields, including continuous combustion engines, as this flame facilitates its work by ensuring a prepared interaction zone, such as providing the necessary heat and energy transfer and avoiding the cold air that negatively affects the main flame and there is another goal to use piloted flame where it reduces the proportion emissions NO and soot. This work studied piloted flame at a mixture of methane and air by using the Sandia National Laboratory model**[2],** which indicates the necessary length of stoichiometric flame includes simultaneous point measurements of T, N2 , O2 , CH4 , CO2 , H2O, and H2 by Rayleigh/Raman scattering and of OH, NO, and CO by laser-induced fluorescence **[1,2]**. Two-component LDV data where measured during the past year at TU Darmstadt. The burner and a set of calibrated flow controllers were loaned from Sandia in order to insure equivalence of flow conditions **[2].**

Creative Commons Attribution-NonCommercial-NoDerivatives 4.0 International License (CC BY-NC-ND)

Materials and methods:

Experimental part

Flame D is one in a series piloted jet flames operated using the Sydney University piloted burner geometry **[1,2].** This burner has a nozzle diameter of D_i=7.2 mm and a premixed pilot that extends to a diameter of 18.2 mm. The main jet composition is 25% CH4 and 75% air, selected to reduce the level of fluorescence interference from soot precursors.
The complete series of six flames spans jet Reynolds numbers from 1,100 (laminar) to 44,800 (turbulent with significant localized extinction). Flame D has a jet Reynolds number of 22,400 and has only a small probability of localized extinction. **[1]**

Numerical setup

Turbulence Model: Viscous standard k-Ɛ Eddy-Dissipation.
Coupling Model: Solved via a CFD code, 2D space planar finite volume code, coupled method, fluent15.0 solver.
Solution Domain: Steady(2D) space planar; grid: 30000 quadrilateral cells, 600 wall faces, 600 symmetry faces, 50-pressure outlet 30651 nodes, L_x=600mm, L_y=25mm.
Location of Start of Computation: Computation starts at x = 0:0 mm.
Length of Calculation: Procedure takes about 10000 iterations for time 1h: 14mn:37s.
Machine used and Approx. CPU Time: about 240h on MEDION ERAZER DESKTOP-CRMPM3V.

Main jet inner diameter	Pilot annulus inner diameter	wall thickness	Pilot annulus outer diameter	Burner outer wall diameter	wall thickness
D_i[mm]	D_{pi}[mm]	E_p[mm]	D_{po}[mm]	D_b[mm]	E_b[mm]
7.2	7.7	0.25	18.2	18.9	0.35

TABLE1.BURNER GEOMETRY **[2]**

Flow velocity	Temperature	Pressure	Main jet composition	Main jet speed	Temperature	Pressure	Kinematic viscosity
U_f[m/s]	T_f[k]	P_f[pa]	V[m^3]	U_j[m/s]	T_j[k]	P_f[pa]	ν[m^2/s]
0.9	291	10e+5	25% CH4, 75% dry air	49.6	294	10^5	1.58e-5

TABLE2.FLOW CONDITIONS **[2]**

Creative Commons Attribution-NonCommercial-NoDerivatives 4.0 International License (CC BY-NC-ND)

Algerian Journal of Engineering Architecture and Urbanism Vol. 5 Nr. 3 2021
ISSN: 2588-1760

Results and discussions:

The propagation of the temperature and pressure in the burner:

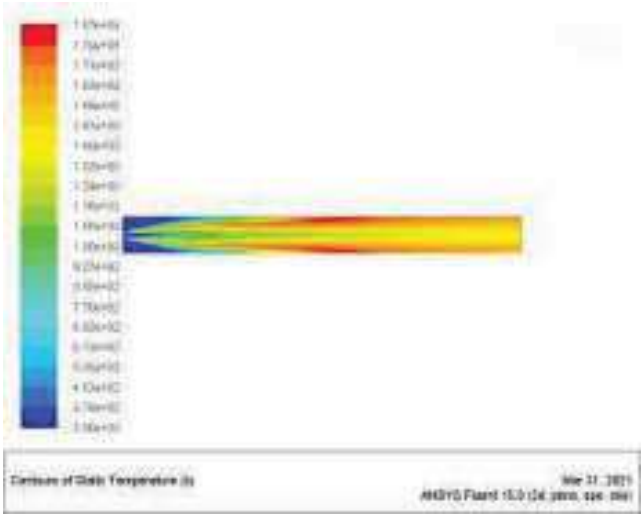

FIGURE 1: CONTOURS OF STATIC TEMPERATURE

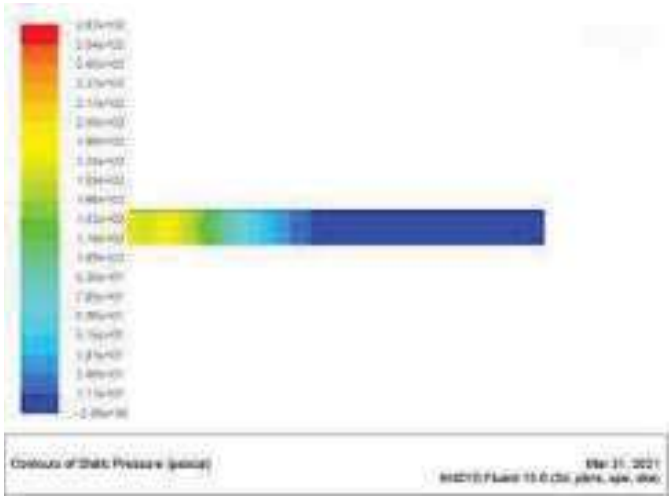

FIGURE2: CONTOURS OF STATIC PRESSURE

In a diffusion flame, the reactants are initially separated, and reaction occurs only at the interface between the fuel and oxidizer, where mixing and reaction both take place**. [3]**
Factors Affecting Flame Length For vertical flames created by a fuel jet issuing into a quiescent environment, four primary factors determine flame length:

- Relative importance of initial jet momentum flux and buoyant forces acting on the flame
- Stoichiometry
- Ratio of nozzle fluid to ambient gas density
- Initial jet diameter**. [3]**

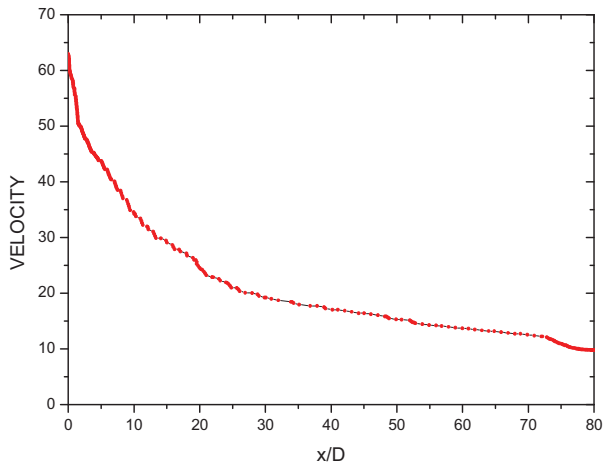

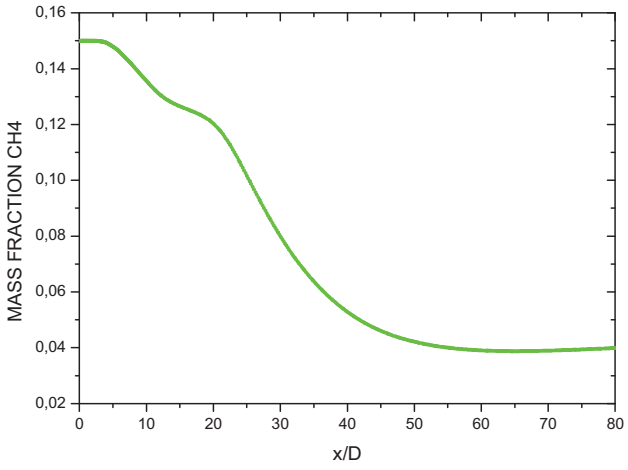

Creative Commons Attribution-NonCommercial-NoDerivatives 4.0 International License (CC BY-NC-ND)

Algerian Journal of Engineering Architecture and Urbanism Vol. 5 Nr. 3 2021
ISSN: 2588-1760

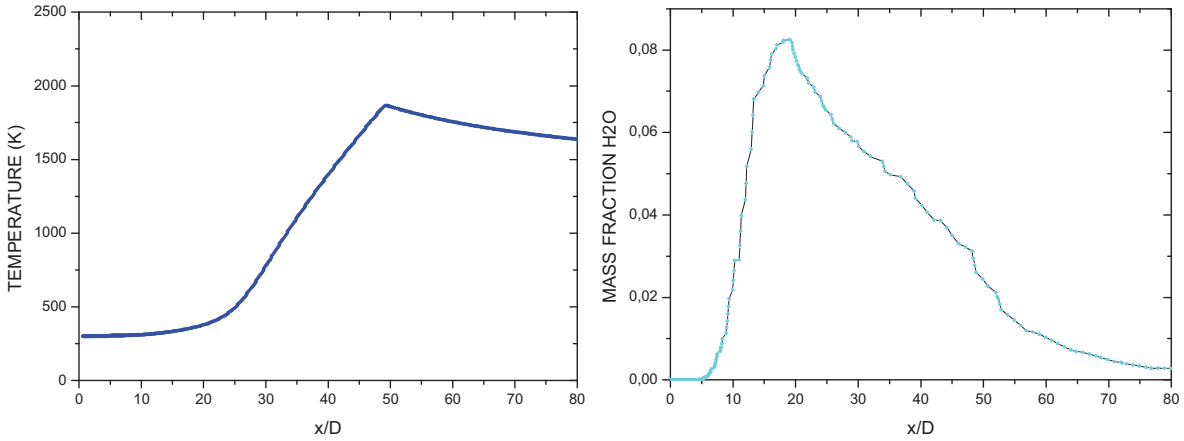

FIGURE 3: AXIAL PROFILES OF U, F, and T

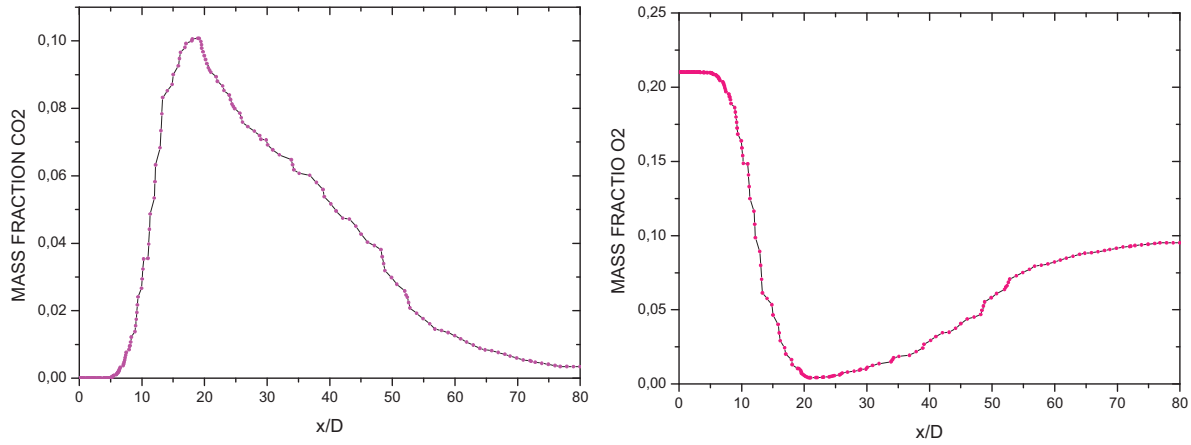

FIGURE 4: AXIAL PROFILES OF SPECIES MASS FRACTION

Figure 3and 4 show the fluctuation of velocity, temperature, and species mass fraction by the axial profiles x/D. The graphical curves represents the changes and distribution of the temperature, velocity and species mass fraction of water ,carbon, methane ,and oxygen according to the axial values We note that the highest degree for pilot flame combustion was 1800 K, while the flow velocity gradually decreases during combustion, and the formation of chemical parts begins.

Creative Commons Attribution-NonCommercial-NoDerivatives 4.0 International License (CC BY-NC-ND)

Algerian Journal of Engineering Architecture and Urbanism Vol. 5 Nr. 3 2021
ISSN: 2588-1760

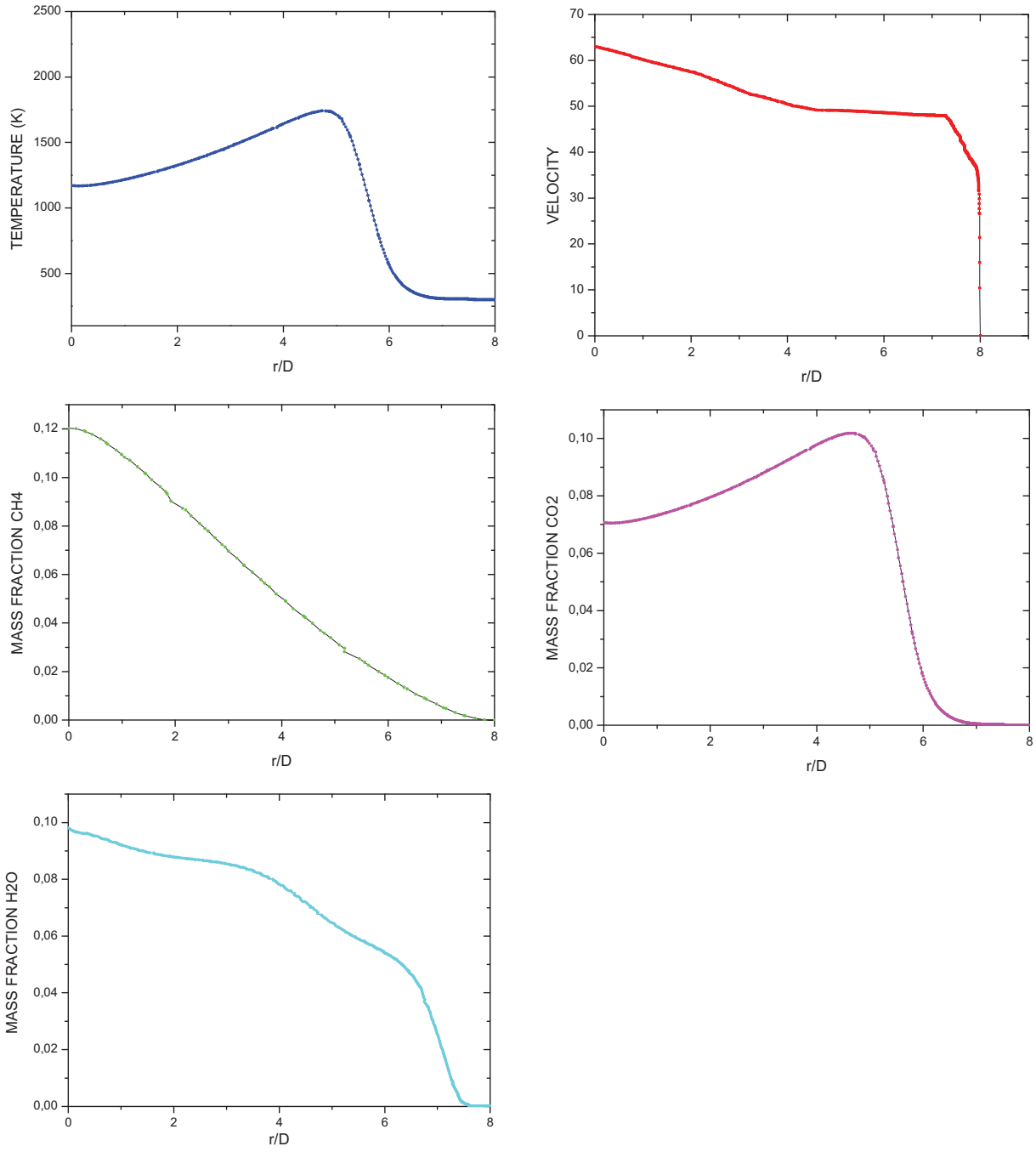

FIGURE 5: RADIAL PROFILES OF TEMPERATURE, VELOCITY, AND SPECIES MASS FRACTION x/D=45

Creative Commons Attribution-NonCommercial-NoDerivatives 4.0 International License (CC BY-NC-ND)

Algerian Journal of Engineering Architecture and Urbanism Vol. 5 Nr. 3 2021
ISSN: 2588-1760

The stoichiometric quantity of oxidizer is just that amount needed to completely burn a quantity of fuel. If more than a stoichiometric quantity of oxidizer is supplied, the mixture is said to be fuel lean, or just lean**;** while supplying less than the stoichiometric oxidizer results in a fuel-rich, or richmixture. The stoichiometric oxidizer– (or air–) fuel ratio (mass) is determined by writing simple atom balances, assuming that the fuel reacts to form an ideal set of products. For a hydrocarbon fuel given by C*x* Hy, the stoichiometric relation can be expressed as:

$$C_xH_y + a\,(O_2 + 3.76\,N_2) \rightarrow xCO_2 + (y/2)\,H2O + 3.76aN_2 \quad (1)$$

Where:

$$a = x + y/4. \quad (2)$$

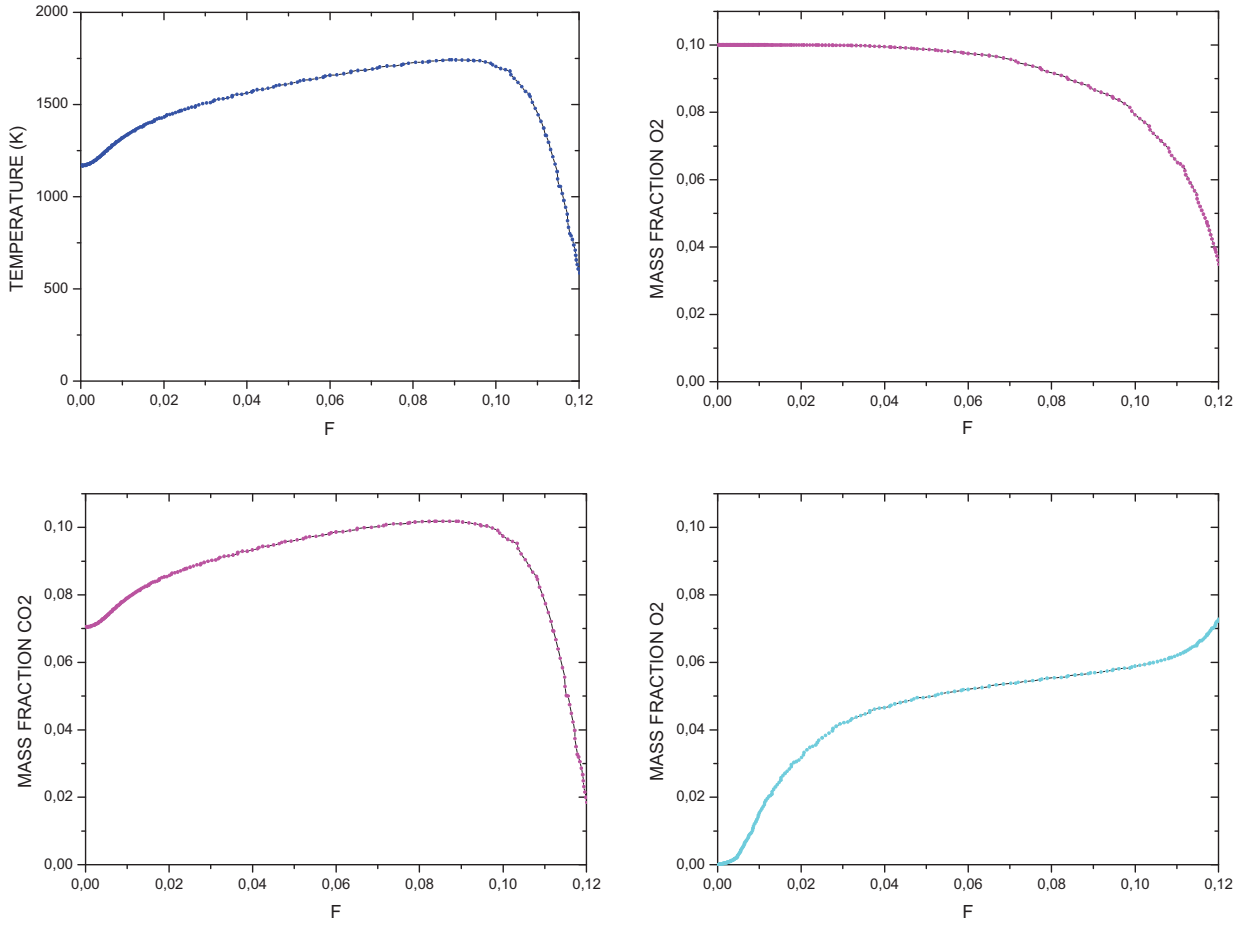

FIGURE 6: CONDITIONAL MEANS AT x/D=45

Creative Commons Attribution-NonCommercial-NoDerivatives 4.0 International License (CC BY-NC-ND)

The total flame heat transfer calculated by fluent version 15 and resulted:

Total mass flow rate: 1.99 e-7 [kg/s]

Total heat transfer rate: 8.95 [W]

Heat of reaction source: 455 [kW]

Total sensible heat transfer rate: 22.37 [W]

CONCLUSION

The effect of pilot flame is to control combustion in systems having continuous ignition and maintain main flame by providing heat or chemical species and prevention from cold air. The equivalence ratio is commonly used to indicate quantitatively whether a fuel–oxidizer mixture is rich, lean, or stoichiometric. Methane is unique tetrahedral molecular structure with large C–H bond energies; it exhibits some unique combustion characteristics. It has a high ignition temperature, low flame speed, and low reactivity in photochemical smog chemistry compared to other hydrocarbons.

Numerical simulation of methane/air piloted flame including the axial profile and radial profiles at x/d=1, x/d=2, x/d=15, and x/d=45 discerned the stoichiometric flame length ~47D.

REFERENCES

[1] Barlow, R. S. and Frank, J. H., “Effects of Turbulence on Species Mass Fractions in Methane/Air Jet Flames,” Twenty-Seventh Symposium (International) on Combustion, the Combustion Institute, Paper 4A10 (1998).

[2] www.ca.sandia.gov/tdf/Workshop.html

[3]Turns, Stephen R, An introduction to combustion: concepts and applications / Stephen R. Turns.—third Ed.

Creative Commons Attribution-NonCommercial-NoDerivatives 4.0 International License (CC BY-NC-ND)

Algerian Journal of Engineering Architecture and Urbanism Vol. 5 Nr. 3 2021
ISSN: 2588-1760

Etudes structurales et optiques de nanoparticules $Zn_{1-x}Fe_xO$ préparées par la méthode Sol-Gel: Applications à la photodégradation du colorant Rhodamine B (RhB) sur la lumière solaire

Soufiane BOUDJEMAA
Enseignant chercheur, Docteur en science (MCA), Département des Sciences de la Matière, Faculté des Sciences et de la Technologie, Université Mohamed El-Bachir El-Ibrahimi de B.B.A, Algérie,
e-mail: bsouf77@yahoo.fr

Hamoudi MEKHALFI
Enseignant chercheur, Docteur en science (MCB), Département des Sciences de la Matière Faculté des Sciences et de la Technologie, Université Mohamed El-Bachir El-Ibrahimi de B.B.A, Algérie,
e-mail: hammek7@yahoo.fr

Ammar BENAMRANI
Enseignant chercheur, Docteur en science (MCB), Département des Sciences de la Matière Faculté des Sciences et de la Technologie, Université Mohamed El-Bachir El-Ibrahimi de B.B.A, Algérie,
e-mail: quantum.ammar@gmail.com

Abstract:
Fe doped ZnO with different percentages of Fe content (Zn1-xFexO) thin films have been fabricated on ultrasonically cleaned quartz substrates by the sol-gel technique. The as-formed Zn1-xFexO nanopowder was characterized by Powder X-ray diffraction (PXRD), Scanning electron microscopy (SEM), Fourier transform infrared spectroscopy (FTIR), Raman, and UV- VIS. The as-formed nanopowder was used as photocatalyst for the degradation of the dye Rhodamine B (RhB), under solar irradiation, in an aqueous suspension at room temperature. The different characterization methods (DRX, FTIR, Raman) confirmed the formation of the ZnO compound of hexagonal structure (würtzite type).The visible light activity of Zn1-xFexO (1, 3, 5, 7) was identified through studies of Rhodamine B (RhB) degradation under visible light photocatalysis, which highlight that $Zn_{0.97}Fe_{0.O3}O$ shows the best activity.

Key Words: Photo-catalysis, Pollutants, $Zn_{1-x}Fe_xO$, Rhodamine B, Under Solar Irradiation, Environment

1. Introduction

De nos jours, la pollution est devenue un des problèmes environnementaux les plus graves. Grâce à leur structure, les photocatalyseurs à base de semi-conducteurs tels que le dioxyde de titane (TiO_2) et l'oxyde de zinc (ZnO) ont été utilisés pour plusieurs procédés environnementaux comme l'élimination de contaminants organiques de l'eau et la destruction de microorganismes (Fusjishima, A- Liao, S. C). Le ZnO nanostructuré est un semi-conducteur à large bande interdite et à gap direct. Il est devenu un matériau prometteur en photocatalyse

Creative Commons Attribution-NonCommercial-NoDerivatives 4.0 International License (CC BY-NC-ND)

en raison de son efficacité catalytique élevée, de son faible coût et de son inertie chimique et biologique.

Dans ce travail, nous avons employé une approche chimique simple fondée sur un processus sol-gel en utilisant l'acétate de zinc et de nitrate de fer pour préparer des nanopoudres de ZnO. Ces nanopoudres de ZnO obtenues ont été caractérisées par DRX, FTIR, Raman et par photoluminescence. L'activité photocatalytique de ces nanopoudres de ZnO a été étudiée en utilisant la Rhodamine B comme modèle de polluant, sous irradiation solaire. Les nanopoudres de ZnO dopées 3% Fe ont montré une bonne activité photocatalytique.

2. Problematic

L'oxyde de Zinc (ZnO) est un matériau semi-conducteur à bande interdite large et direct, il est actuellement l'un des matériaux les plus étudiés grâce à son vaste potentiel d'applications. Ces propriétés optiques sont de loin celles qui ont lui confèrent le plus d'importance. Le ZnO est un matériau dont l'utilisation s'est accrue dans plusieurs domaines d'applications tels que les dispositifs optoélectroniques, acousto-optiques, piézoélectriques et comme détecteur de gaz ainsi que catalyseur photochimique.

Toutes ces propriétés sont directement liées à la structure, la morphologie, la taille et les défauts dans les cristallites de ZnO lesquels dépendent largement de la méthode de préparation. Le ZnO peut être obtenu par des méthodes physiques et chimiques sous forme massive, couche mince et poudre …

Dans ce travail, nous avons opté pour la méthode sol-gel, vue sa simplicité et son faible coût, pour l'élaboration caractérisations structurales et optiques des nanoparticules (NPs) de ZnO dopés au fer et des couches minces de $Zn_{1-x}Fe_xO$. Comme application, le $Zn_{1-x}Fe_xO$ est utilisé pour tester la photodégradation de la Rhodamine B sous irradiation solaire. Le mécanisme de photodégradation sera discuté.

3. Matériels et méthodes

3. 1. Produits

Acétate de zinc dihydraté [Zn $(CH_3COO)_2 2H_2O$] (Sigma-Aldrich, 98%), Méthanol(Alfa Aesar, 99%)[CH_3OH], Aacide citrique (Sigma-Aldrich, 97%) [$C_6H_8O_7$], Nitrate ferrique [$Fe(NO_3)_3$]

3. 2. Elaboration des poudres du ZnO pur

Les poudres de ZnO ont été obtenues en utilisant le procédé sol-gel. Le sol a été préparé en utilisant de l'acétate de zinc dihydraté [Zn $(CH_3COO)_2 2H_2O$] comme produit source, le méthanol comme solvant, et l'acide citrique ($C_6H_8O_7$) en tant que stabilisant. La solution de précurseur a été mélangée à fond avec un agitateur magnétique à 80°C jusqu'à la formation d'un sol.

Le sol a été préchauffé dans une étuve à 80°C pendant 12 h pour évaporer le solvant et enlever les résidus organiques. Un produit solide de couleur blanche se forme au fond du bécher. Le matériau solide (ZnO) est broyé à l'aide d'un mortier jusqu'à l'obtention d'une poudre(ZnO).

Les poudres obtenues à partir du sol séché ont ensuite subi un recuit à 500° C pendant 2 heures à l'air ambiant.

Creative Commons Attribution-NonCommercial-NoDerivatives 4.0 International License (CC BY-NC-ND)

3. 3. Elaboration de ZnO dopé Fe

Pour préparer des poudres de ZnO dopées Fe nous avons utilisé le même processus que précédemment (c.à.d. celui de ZnO pur) tout en dopant avec différentes concentration de nitrate de fer.

La solution de précurseur a été mélangée avec un agitateur magnétique à 80 °C jusqu'à la formation d'un sol.

Le sol a été préchauffé dans un four à 80 ° C pendant 7 jours afin d'évaporer le solvant et éliminer les résidus organiques. Un produit solide de couleur variante du blanc à l'orangé foncé « caramélisé » en fonction de la teneur en fer se forme.

Enfin, une série des poudres de Zn1-xFexO (x = 0, 1%, 3%, 5%, 7%) sont obtenues après un recuit à 500 ° C pendant 2 heures à l'air ambiant.

4. Caractérisation de ZnO et ZnO DOPE Fe

4. 1. Spectroscopie FTIR

Les échantillons sont préparés sous forme de pastilles fines en mélangeant 96 % (massique) de KBr avec 4 % de l'échantillon à analyser, préalablement broyé et séché pendant au moins vingt-quatre heures à 100 °C. Ces pastilles ont été obtenues par pression à 10 torr/cm^2 pendant deux minutes.

Les spectres IRTF ont été réalisés à l'aide d'un spectrophotomètre IRTF-8300 à transformée de Fourier SHIMADZU, dans un domaine de nombre d'onde allant de 400 à 4000 cm^{-1}.

4. 2. Diffraction des rayons X (DRX)

Nous avons utilisé pour toutes les caractérisations par DRX un diffractomètre de type Philips PW-1710, alimenté par un courant de 40 kV sous une intensité de 40 mA. Travaillant avec la raie monochromatique Kα du cuivre à une longueur d'onde de λ = 1,54Å. Les paramètres choisis sont une faible vitesse de rotation avec un pas de 0,05°. Le domaine observé de l'angle 2 Thêta est compris entre 2 et 30°.

4. 3. Microscopie à balayage électronique (MEB)

Les images MEB ont été obtenues en utilisant un Zeiss ULTRA 55 équipé d'un émetteur à émission de champ thermique et de haute efficacité.

4. 5. Suivi la diminition de la concentration de rhodamine B

Nous avons suivi la diminution de l'intensité du pic d'absorption la Rhodamine B à λ_{max}= 554 nm en fonction du temps d'exposition solaire. Les mesures de l'absorbance de la RhB ont été effectuées chaque 20 minute. Ce qui permet d'étudier la cinétique de dégradation photocatalytique de RhB sous irradiation solaire en utilisant la spectrophotométrie UV-vis.

Les spectres d'absorption optique qui interviennent à notre travail sont réalisés à l'aide d'un spectrophotomètre UV-Visible de type UV-1800 dont la gamme spectrale s'étale sur un domaine allant de 190-1100 nm.

Creative Commons Attribution-NonCommercial-NoDerivatives 4.0 International License (CC BY-NC-ND)

Algerian Journal of Engineering Architecture and Urbanism Vol. 5 Nr. 3 2021
ISSN: 2588-1760

5. Résultats et discussion

5. 1. Caractérisation de ZnO et Zn1-xFexO

5. 1. 1. Diffraction des rayons X (DRX)

La figure.1 montre un diffractogramme DRX du ZnO non dopé. Ce diffractogramme montre qu'on a bien un composé cristallisé, correspondant au système hexagonal, de structure würtzite. L'indexation de ces pics de diffraction donne les plans cristallographiques suivants (100), (002), (101), (102), (110) et (103) de la structure hexagonale de ZnO.

La figure.2 montre que l'addition du fer ne conduit pas à la formation d'une nouvelle structure cristalline avec des nouvelles orientations de (figure.1). Il n'y a pas des pics correspondant à Fe comme α-Fe, α-Fe_2O_3, γ-Fe_2O_3 ou Fe_3O_4. Ceci indique que soit tous les ions Fe^{3+} ont été incorporées dans le réseau du cristal d'accueil (Mishra, A.K) soit que la quantité du dopant ajouté est trop faible pour être détecté par DRX (Ni, M-Linsebigler, A. L). L'intensité des pics de diffraction de ZnO a diminué et leur largeur à mi-hauteur (FWHM) a augmenté avec l'augmentation de la quantité de dopage Fe surtout pour les dopages supérieurs à 3%, ce qui révèle que le dopage Fe contribue à la dégradation de la qualité cristalline du ZnO. Cet effet peut être expliqué par l'introduction d'un trouble au réseau et par la déformation induite par des atomes interstitiels de Fe ou la substitution des atomes Fe aux atomes de Zn (Zeng, H).

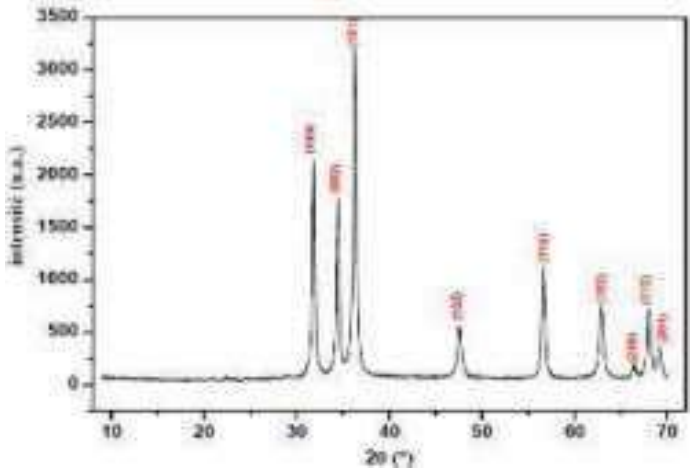

Fig1. Diagramme DRX des nanoparticules de ZnO non dopé.

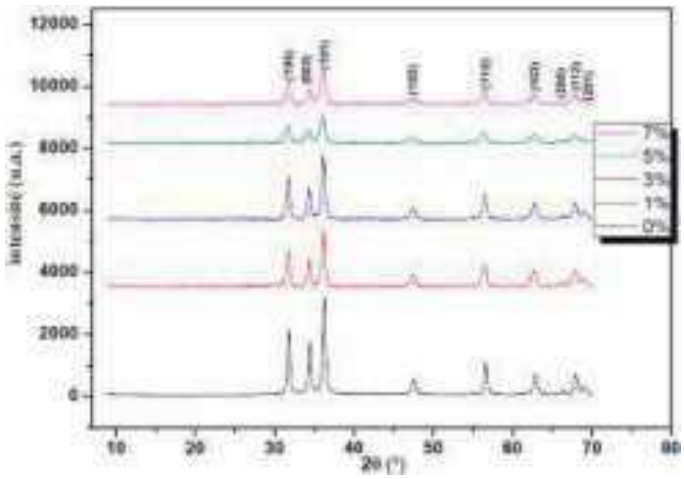

Creative Commons Attribution-NonCommercial-NoDerivatives 4.0 International License (CC BY-NC-ND)

Fig2. Diagramme DRX des nanoparticules Zn1-xFexO.

5. 1. 2. Etude par MEB

La morphologie des nanoparticules Zn1-xFexO a été étudiée par MEB (figure.3). L'image MEB de la poudre $Zn_{0,97}Fe_{0,03}O$ montre une agglomération des particules sous forme de nanotubes avec différentes tailles.

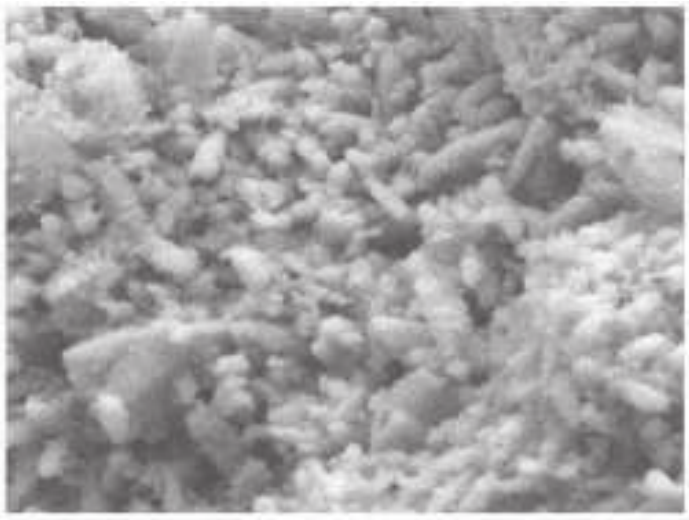

Fig3. Image MEB de $Zn_{0,97}Fe_{0,03}O$.

5. 1. 3. Etude par spectroscopie infrarouge (FTIR)

Comme c'est indiqué dans la figure.4, le pic large à 3443 cm^{-1} est attribuée à l'absorption du groupement hydroxyle (-OH) (Zeng, H). L'activité photocatalytique de tout photocatalyseur est étroitement liée à la quantité du groupe -OH parce que les groupes -OH peuvent fournir un trou photogénéré et le transfert à un radical réactif ·OH. La vibration à 2356 cm^{-1} résulte de l'interaction entre le dioxyde de carbone atmosphérique et l'eau (Liu, H). La bande localisée à 502 cm^{-1} peut être attribuée à la vibration Zn-O. A partir de ces spectres d'absorption on remarque l'effet du dopage sur l'intensité de la bande de vibration Zn-O. En effet, cette bande est très intense dans le cas de ZnO dopé Fe^{3+} (3%).

La largeur à mi-hauteur de la bande de vibration Zn-O (figure.5) a été influencée par l'addition des ions Fe^{3+}. En effet, une diminution de la largeur à mi-hauteur est remarquable suite au dopage 3%. Ce qui indique que le dopage 3% est spécifique pour le ZnO et donne des résultats remarquables par comparaison avec les autres pourcentages de dopage.

Creative Commons Attribution-NonCommercial-NoDerivatives 4.0 International License (CC BY-NC-ND)

Algerian Journal of Engineering Architecture and Urbanism Vol. 5 Nr. 3 2021
ISSN: 2588-1760

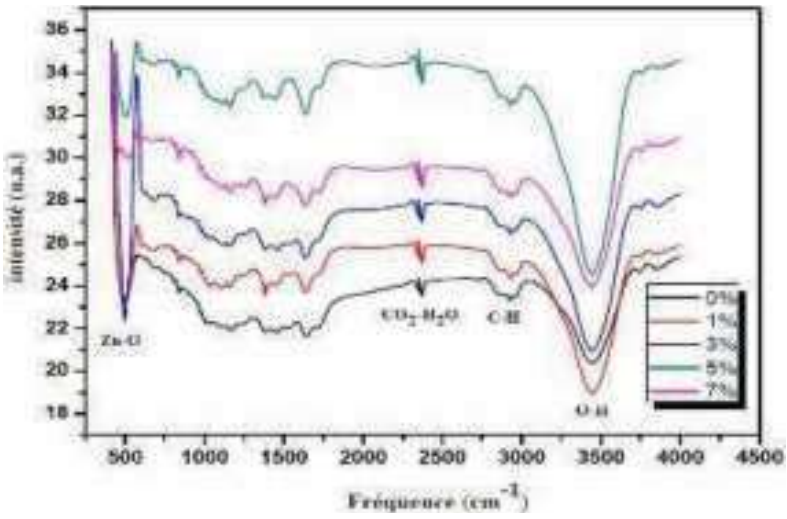

Fig4. Spectre FTIR des nanopaticules $Zn_{1-x}Fe_xO$.

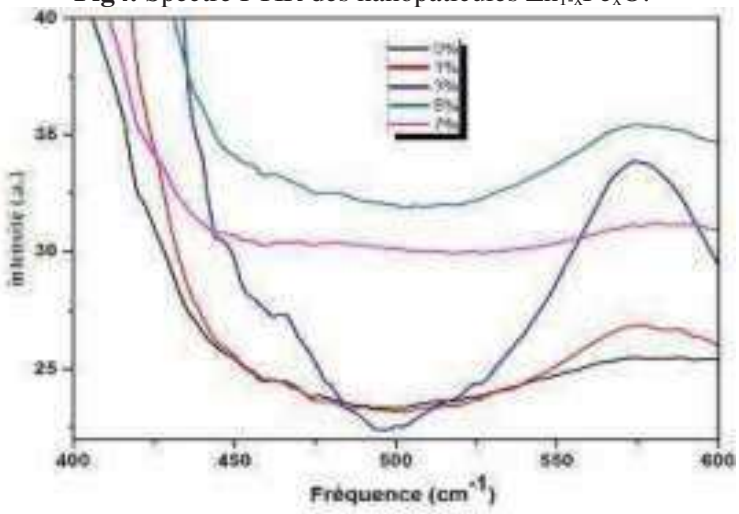

Fig5. Zoom de la gamme 400-600 cm-1 du spectre FTIR des nanoparticules $Zn_{1-x}Fe_xO$.

5. 2. Cinétique de la dégradation photocatalytique

Le modèle de Langmuir-Hinshelwood est le plus souvent appliqué à la photocatalyse hétérogène et peut être expliqué sur la base de la production d'électrons et de trous par photo-excitation de la surface du catalyseur pour former des radicaux réactifs. La constante d'adsorption et la concentration du polluant entrent en jeu (Haddou, M- Rauf, M.A). Dans ce modèle, le recouvrement de la surface θ et la concentration initiale C_0 du polluant sont reliés à sa constante d'adsorption selon l'équation suivante :

$$\theta = \frac{KC_0}{(1+K.C_0)} \qquad (1)$$

Dans le cas du modèle de Langmuir-Hinshelwood, l'étape limitante est la réaction de dégradation du polluant sur le site actif situé à la surface du photocatalyseur. La vitesse de cette réaction est donc donnée par l'équation suivante:

Creative Commons Attribution-NonCommercial-NoDerivatives 4.0 International License (CC BY-NC-ND)

$$\Gamma = \frac{dC}{dt} = k\theta = \frac{k(KC_0)}{(1+K.C_0)} \qquad (2)$$

Où, k représente la constante de vitesse de la réaction sur le site actif.
Dans le cas des solutions concentrées en polluant ($C_0 > 5.10^{-3}$ mol. L^{-1}), le terme $K.C_0$ est très grand devant 1, la réaction est d'ordre pseudo-zéro.

Dans le cas des solutions diluées en polluant ($C_0 < 10^{-3}$ mol. L^{-1}), le terme $K.C_0$ est négligeable devant 1. Par conséquent, la réaction est du pseudo-premier ordre.

Cette équation peut alors être simplifiée et transformée pour avoir une équation d'ordre apparent 1 :

$$C = C_0.e^{-k_{app}t} \qquad (3)$$

$$\frac{C_0}{C} = k.K.t = k_{app}.t \qquad (4)$$

La variation de $\ln\left(\frac{C_0}{C}\right)$ en fonction du temps est une droite. La pente de cette régression linéaire donne la constante de vitesse de premier ordre kapp.

Généralement, une cinétique du premier ordre est appropriée pour une gamme de concentrations qui peut aller jusqu'à quelques ppm et plusieurs études ont confirmé qu'on pouvait utiliser ce modèle cinétique (Haddou, M- Rauf, M. A - Konstantinou, I. K).

5. 3. Etude des propriétés photocatalytiques des nanoparticules de ZnO

La performance des nanoparticules de ZnO non dopées et dopées au fer pour la photodégradation de la Rhodamine B, un polluant typique dans l'industrie textile, sous irradiation solaire a été étudiée.

Les solutions obtenues ont été préparées en dissolvant une masse des nanopoudres de ZnO non dopées et dopées au fer (concentration du catalyseur est de 0,25 g/L) dans une solution de Rhodamine B de concentration $C_{RhB} = 5.10^{-6}$ mol.L^{-1}.

Nous avons suivi la diminution de l'intensité du pic d'absorption de la Rhodamine B à λ_{max} = 554 nm en fonction du temps d'exposition solaire. Les mesures de l'absorbance de la RhB ont été effectuées chaque 20 minute. Ce qui permet d'étudier la cinétique de dégradation photocatalytique de RhB sous irradiation solaire en utilisant la spectrophotométrie UV-vis.

5. 3. 1. Efficacité photocatalytique

La dégradation de la solution aqueuse de RhB a été évaluée en suivant la diminution de la bande d'absorption à 554 nm caractéristique de la RhB en fonction du temps d'irradiation.

Les spectres d'absorption du RhB avec et sans exposition au rayonnement solaire sont représentés dans la figure.6 (a). Aucun changement significatif n'a été remarqué dans le spectre enregistré après 2h d'irradiation, ce qui indique que la solution de RhB pur ne peut pas être facilement dégradée par la lumière solaire. Les spectres d'absorption de la solution de RhB en présence de ZnO pur et de $Zn_{0.97}Fe_{0.03}O$ sous différentes durées d'irradiation de la

Creative Commons Attribution-NonCommercial-NoDerivatives 4.0 International License (CC BY-NC-ND)

Algerian Journal of Engineering Architecture and Urbanism Vol. 5 Nr. 3 2021
ISSN: 2588-1760

lumière solaire sont présentées dans les figures.6 (b) et (c), respectivement. Ces résultats montrent clairement que la dégradation de la solution de RhB a été induite par l'addition du photocatalyseur $Zn_{1-x}Fe_xO$. En outre, les figures.6 (b) et (c) montrent une diminution de la bande d'absorption à 554 nm accompagné d'un déplacement hypsochrome progressive. Le décalage vers le bleu de la bande d'absorption sous irradiation est attribué à une déséthylation progressive de RhB. En effet, les groupes éthyle de RhB sont déséthylé un par un (les pics correspondant sont : N, N, N'- triethyle RhB à 539 nm, N, N'- diethyle RhB à 522 nm et N-éthyle RhB à 510 nm). La molécule entièrement déséthylé affiche une bande d'absorption caractéristique à 498 nm (Barras, A).

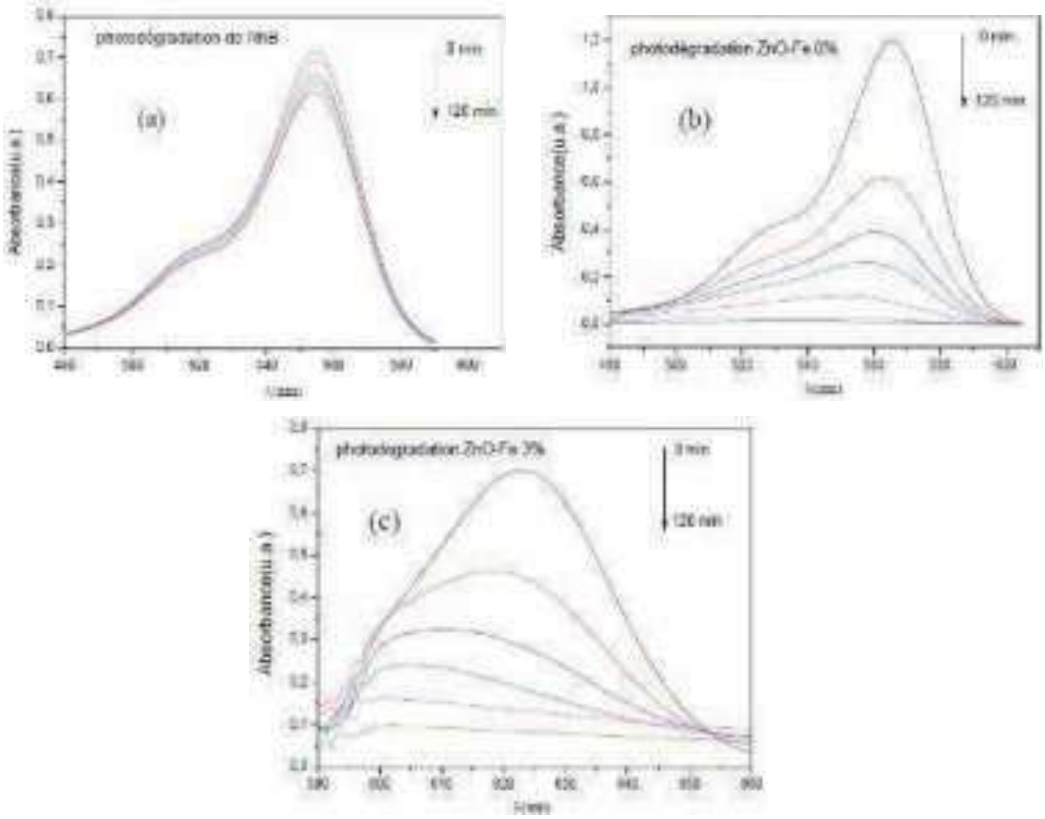

Fig6. Evolution de l'intensité d'absorption du RhB en solution : (a) en absence de catalyseur (b) en présence de ZnO non dopé (c) en présence de ZnO dopé 3% Fe.

La figure.7 affiche l'évolution temporelle de la dégradation photocatalytique de la RhB à différentes concentrations de $Zn_{1-x}Fe_xO$. On remarque que l'activité photocatalytique ne change pas de façon monotone avec l'augmentation de la concentration de Fe, et 3% est la concentration de dopage optimum. La bande d'absorption du RhB diminue rapidement et disparaît après 40 min. Ainsi, les nanoparticules de $Zn_{0,97}Fe_{0,03}O$ présente la plus grande efficacité de la dégradation photocatalytique.

Creative Commons Attribution-NonCommercial-NoDerivatives 4.0 International License (CC BY-NC-ND)

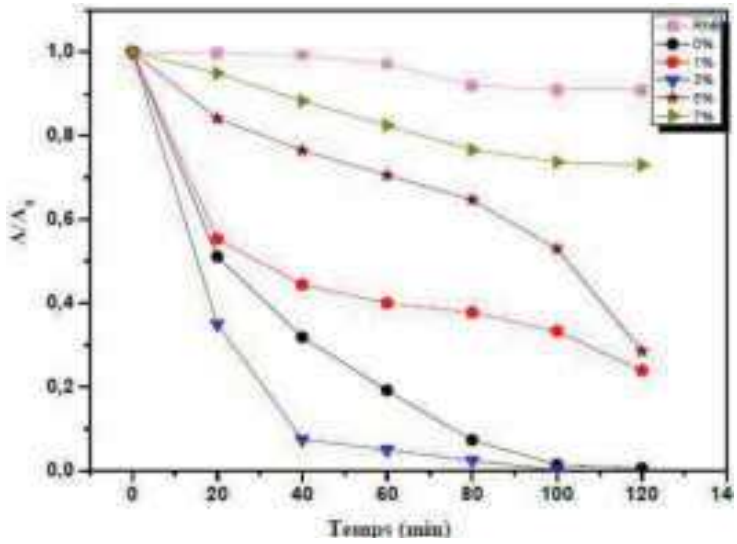

Fig7. Dégradation photocatalytique d'une solution de Rhodamine B en absence et en présence de Zn1- xFexO

Lorsque les résultats de cette réaction de dégradation de la RhB en fonction du temps d'exposition solaire sont représentés sous forme de logarithme, ln (A_0/A), en fonction du temps (A_0/A étant le rapport entre la concentration initiale et la concentration lors de la réaction), des courbes linéaires sont obtenues (figure .8). Ceci indique que la réaction de décomposition suit une cinétique de premier ordre.

La figure.8 montre l'augmentation de Ln (A_0/A) en fonction du temps, ce qui nous permet de calculer les coefficients de vitesse afin de comparer les performances du matériau élaboré. Notamment, il y a une amélioration de la vitesse d'oxydation photocatalytique de la Rhodamine B surtout en présence du ZnO dopé 3%, ce qui prouve bien l'influence du dopage et son importance dans la photodégradation du polluant.

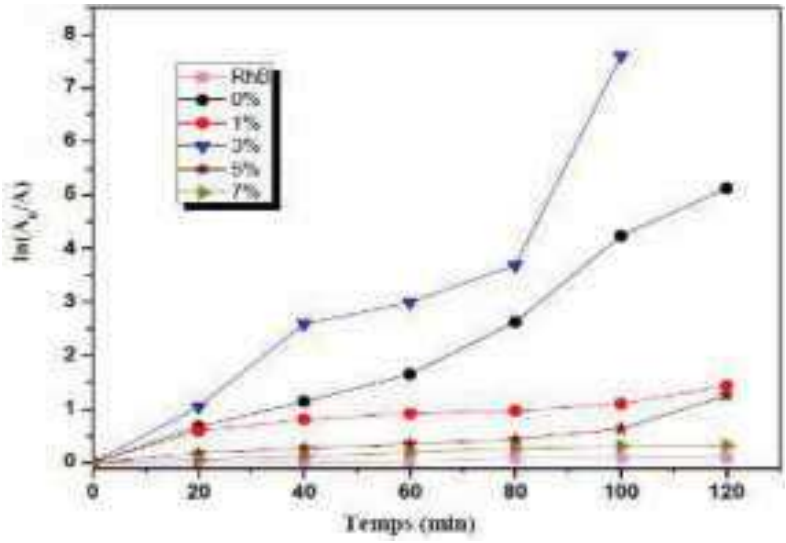

Fig8. Variation de Ln (A_0/A) en fonction du temps d'irradiation solaire de la solution de Rhodamine B en absence et en présence de $Zn_{1-x}Fe_xO$

Creative Commons Attribution-NonCommercial-NoDerivatives 4.0 International License (CC BY-NC-ND)

En effet, Q. Xiao et al. ont synthétisé du ZnO dopé Fe par un procédé de précipitation à pH = 7, et ils ont évalué l'activité photocatalytique en mesurant les taux de dégradation de KEX (xanthate d'éthyle de potassium) sous irradiation de la lumière visible. Ils ont constaté que le dopage Fe peut améliorer l'activité photocatalytique et les valeurs de coefficient de vitesse de premier ordre sont les suivantes: 4 > 5 > 2> 3 > 1 % en mole, ce qui indique que les nanopoudres $Zn_{0,96}Fe_{0,04}O$ présentent la plus haute efficacité photocatalytique (Xiao, Q).

Système photocatalytique	Constante de vitesse (10^{-3} min^{-1})
RhB sans catalyseur	1,23
RhB en présence du ZnO non dopé	33
RhB en présence du ZnO-Fe 1%	6,21
RhB en présence du ZnO-Fe 3%	44,13
RhB en présence du ZnO- Fe 5%	5
RhB en présence du ZnO-Fe 7%	3,08

Table 1. Constantes de vitesse pour les Systèmes photocatalytiques $Zn_{1-x}Fe_xO$

5. 3. 2. Effet de l'irradiation visible > 420nm

La figure.9 montre la dégradation photocatalytique d'une solution de Rhodamine B en absence et en présence du photocatalyseur en fonction du temps d'irradiation sous lumière visible avec puissance de la lampe 0,5W/cm^2.

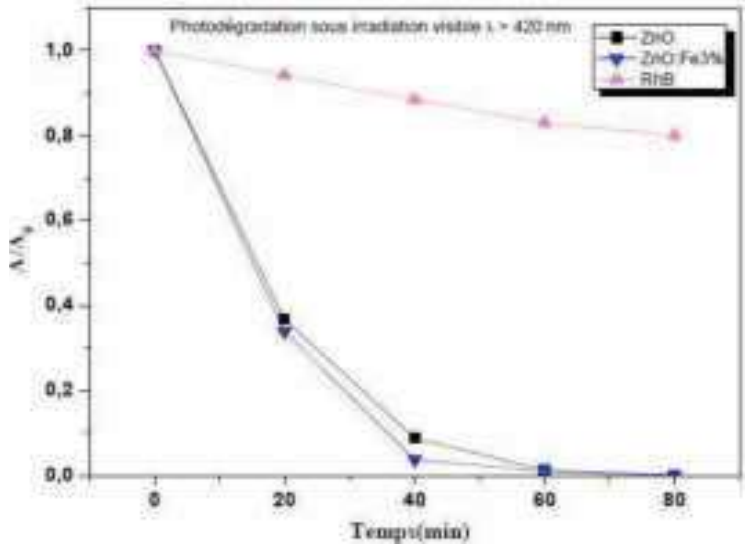

Fig9. Dégradation photocatalytique d'une solution de Rhodamine B en absence et en présence de Zn1- xFexO(x=0 et 3%) sous lumière visible avec puissance de la lampe 0,5W/cm^2.

En absence du photocatalyseur, l'irradiation directe de la solution de RhB dans le domaine du visible induit une diminution d'environ 20% de son intensité au bout de 80 min. En présence de ZnO non dopé, la photodégradation est accélérée, et elle est plus rapide par rapport à l'irradiation solaire. Le dopage au fer de ZnO n'a pas d'influence significative sur la vitesse de photodégradation de la RhB sous irradiation visible.

Creative Commons Attribution-NonCommercial-NoDerivatives 4.0 International License (CC BY-NC-ND)

5. 3. 3. Effet de la concentration du catalyseur

L'effet de la concentration en catalyseur sur la dégradation photocatalytique de RhB est étudié en faisant varier la quantité des nanopoudres de $Zn_{0,97}Fe_{0,03}O$.

La figure.10 montre le profil de dégradation de RhB avec une concentration initiale de 5.10^{-6} M sous différentes concentrations de catalyseur (de 0,125 à 0,375 g L^{-1}).

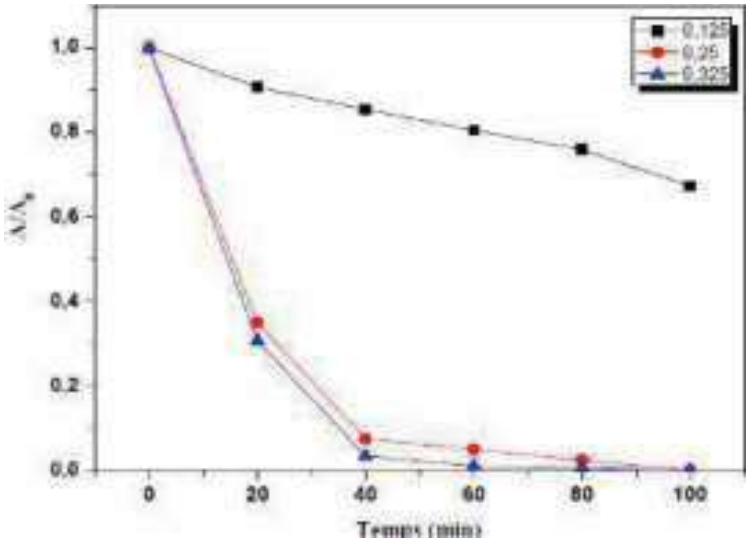

Fig10. Dégradation photocatalytique d'une solution de Rhodamine B sous différentes concentrations de catalyseur

5. 4. Mécanisme de la photodégradation en présence de ZnO : Fe

L'efficacité photocatalytique dépend de deux processus: l'un est la concurrence entre la recombinaison et la capture des électrons et des trous photogénérés, l'autre est la compétition entre la recombinaison des électrons et des trous capturées et le transfert de charge en surface. Le temps de recombinaison des porteurs photogénérés et l'augmentation de leur taux de transfert sont à la fois favorable à l'amélioration de l'efficacité photocatalytique.

Le temps de séparation des recombinaisons électrons-trou peut être augmenté par divers défauts intrinsèque ou extrinsèque. Les défauts intrinsèques comprennent les lacunes d'oxygène dans les nanostructures (oxydes réductibles), et les défauts extrinsèques sont les dopants du nanomatériau avec des impuretés appropriées. Il a été remarqué que le ZnO pur est un exemple semi-conducteurs de type n qui est toujours associé à des défauts intrinsèques comme grandes quantités de lacunes d'oxygène. La perte de l'oxygène dans la matrice de ZnO à haute température de recuit peut produire d'additionnelles lacunes d'oxygène. Dans le cas de ZnO dopé Fe, les ions Fe pénètrent dans le réseau cristallin de ZnO et conduisent à la formation des lacunes de Zn (VZn) et plus des lacunes d'oxygène (VO). Par conséquent, les défauts sur la surface de catalyseurs sont également responsables des paires électron-trou photogénéré sous irradiation. Le retard de la recombinaison électron-trou va augmenter l'efficacité photocatalytique de ZnO et, par conséquent, accélère la formation des radicaux hydroxyles qui permettra d'améliorer le taux de dégradation de RhB. En effet, les radicaux hydroxyles sont connus puissant agents oxydant et peuvent réagir avec des molécules de colorant pour provoquer leur complète dégradation (Kim, J- Tatsuma, T).

Creative Commons Attribution-NonCommercial-NoDerivatives 4.0 International License (CC BY-NC-ND)

D'après la figure.7, on a pu constater que l'activité photocatalytique dépend de la quantité de Fe introduite. Lorsque le dopage Fe était de 3% dans le ZnO, l'activité photocatalytique a augmenté en comparaison avec le ZnO non dopé. Des augmentations supplémentaires de la concentration en dopant conduisent à une diminution progressive de l'activité photocatalytique. Ce résultat a été attribué au fait qu'une petite concentration d'ions Fe peut fonctionner comme un piège d'électron et de trou photogénéré, ce qui inhibe la recombinaison électron-trou (Mehedi, H), comme décrit par les équations ci-dessous:

$$ZnO + h \rightarrow e^- + h^+ \quad (5)$$

$$Fe^{3+} + e^- \rightarrow Fe^{2+} \text{ (piège à électrons)} \quad (6)$$

$$Fe^{2+} + O_2 \rightarrow Fe^{3+} + O_2^{\cdot-} \text{ (libération d'un électron)} \quad (7)$$

$$Fe^{3+} + hvb^+ \rightarrow Fe^{4+} \text{ (piège de trou)} \quad (8)$$

$$Fe^{4+} + OH^- \rightarrow Fe^{3+} + OH^{\cdot} \text{ (libération d'un trou)} \quad (9)$$

$$RhB + OH^{\cdot} \rightarrow \text{RhB intermédiaire} \rightarrow CO_2 + H_2O \quad (10)$$

6. Conclusion

Les nanoparticules de $Zn_{1-x}Fe_xO$ ont été préparées en utilisant le procédé sol-gel. Les effets du dopage Fe sur les propriétés structurales et optiques ont été étudiés. Les différentes méthodes de caractérisation structurales (DRX, FTIR, Raman) ont confirmé la formation du composé ZnO de structure hexagonale (type würtzite). Pour les nanoparticules de ZnO dopées par du Fer, la formation et la cristallisation est ralentie par la présence du dopage et ce phénomène a été observé par M. Mehedi Hassan et al. (Mehedi, H. M). Les propriétés optiques ont été étudiées par des mesures de réflectance. Les mesures de l'énergie d'Urbach indiquent que la densité d'impuretés ionisées augmente avec le dopage. Enfin, nous avons étudié l'activité photocatalytique de Zn1-xFexO pour la dégradation de la Rhodamine B, sous irradiation solaire. On constate que $Zn_{0.97}Fe_{0.03}O$ possède la meilleure activité photocatalytique.

Références

Fusjishima A., **Honda K**. (1972), Nature **37** : 238.

Liao S. C., Lin H. F., Hung S. W., Hu C. T., J. (2006), Vac. Sci. Technol. B **24**: 1322.

Mishra A.K., Das D. (2010), Mater. Sci. Eng. B **171**: 5–10.

Ni M., Leung M. K. H., Leung D. Y. C., Sumathy K. A. (2007), Renewable Sust. Energy. Rev. **11**: 40.

Linsebigler A. L., Lu G., Yates J. T. (1995), Chem. Rev., **95:** 735.

Zeng H., Cai W., Liu P., Xu X., Zhou H., Klingshirn C., Kalt H. (2008), ACS Nano **2** : 166.

Liu H., Yang J., Zhang Y., Yang L., Wei1 M., Ding X. (2009), J. Phys.: Condens. Matter., **21**: 145803– 145807.

Haddou M. (2010) thèse de Doctorat d'état, Université de Toulouse.

Rauf M. A., **Ashraf S. S.** (2009), Chem. Eng. J. **10**: 151.

Konstantinou I. K., Albanis T. A. (2004), Appl. Catal. B: environmental, **49:** 1.

Barras A., Cordier S., Boukherroub R. (2012), Appl. Catat. B: Environ. **1**: 123-124.

Xiao Q., Yao C. (2011), Materials Chemistry and Physics **130:** 5–9.

Creative Commons Attribution-NonCommercial-NoDerivatives 4.0 International License (CC BY-NC-ND)

Kim J., Lee C.W., Choi W. (2010), Environmental Science and Technology **44**: 6849.

Tatsuma T., Tachibana S., Miwa T., Tryk D.A., Fujishima A. (1999), The Journal of Physical Chemistry. B **103:** 8033.

Mehedi H. M., Khan W., Azam A., Naqvi A. H. (2014), Journal of Luminescence **145**: 160–166.

Creative Commons Attribution-NonCommercial-NoDerivatives 4.0 International License (CC BY-NC-ND)

Algerian Journal of Engineering Architecture and Urbanism Vol. 5 Nr. 3 2021
ISSN: 2588-1760

UNSUPERVISED SEGMENTATION OF IMAGES BY MARKOV SEGMENTATION INTO REGIONS

Dr. Lalaoui Lahouaoui
Dept electronics, Laboratory LGE department electronics University of M'sila 28000 City Ichbilia M'sila, Algeria,
e-mail: lahouaoui.lalaoui@univ-msila.dz

djaalab abdelhak
Dept electronics, Laboratory LGE department electronics University of M'sila 28000 City Ichbilia M'sila, Algeria,
e-mail: abdelhak.djaalab@univ-msila.dz

Dib Fouad
Dept electronics, Laboratory LGE department electronics University of M'sila 28000 City Ichbilia M'sila, Algeria,
e-mail: fouad.dib@univ-msila.dz

Abstract:
Image segmentation is a preliminary and fundamental step in computer aided magnetic resonance imaging (MRI) images analysis. Markov random field model (MRF) has attracted great attention in the field of image segmentation. Such super pixel-based or region-based MRF models have their own advantages and disadvantages. In order to complement advantages of each other, a unified Markov random field (UMRF) model proposed in this paper. However, the performance of most current image segmentation methods easily depreciated by noise in MRI images. In this paper, we proposed the hidden Markov random field (HMRF) model based on KMeans and Expectation-Maximization (EM) algorithm for image segmentation. We implement a MATLAB toolbox named HMRF-EM-image for 2D image segmentation using the HMRF-EM framework2. This toolbox also implements edge-prior preserving image segmentation, and can be easily reconfigured for other problems, such as 3D image segmentation. We have applied this algorithm segmented different type of image, to evaluate the method a validation of the results provided, demonstrating the strength of the algorithm for image with noise.

Key words: segmentation, level set and watershed, evaluate.

I. Introduction:

In recent years, methods of acquiring medical images have developed rapidly, including methods such as x-ray computed tomography (CT), magnetic resonance imaging (MRI), ultra-sound (US), positron emission tomography (PET) and single photon emission tomography. With the production of more and more images medical, automatic image processing and analysis techniques have become essential [Jiang, 2021]. The field of probability it possible to introduce a segmentation class where the characteristics of regions can be modeled, the random fields of Markov (MRF: Markov Random Field), ([Dubes and Jain, 1990] [Gao J.et al, 2002]), using conditional random fields (CRF: Conditional Random Field) ([Zhang L. et al, 2010][Lee S.H., et al, 2010] or with Gaussian mixture models (GMM: Gaussian Mixture Models) ([Carson C. et al, 2002] [Khan J.F. et al, 2009]).

Creative Commons Attribution-NonCommercial-NoDerivatives 4.0 International License (CC BY-NC-ND)

Although optical image processing technology has been widely used in robotics, most of these methods cannot be used to process medical images. Mage segmentation is a process of partitioning an image into several segments with the aim of simplifying the representation of the image or extracting meaningful objects. Image segmentation is one of the most important tasks of computer vision and it has many applications in many other fields, including pattern recognition, remote sensing, medical diagnostics, computer vision, remote sensing and medical imaging (Gribben, Miller, 2009) etc…, has proposed a fuzzy treatment of masked image segmentation based on an MRF model. Image segmentation is a process of partitioning an image into several segments with the aim of simplifying the representation of the image or extracting meaningful objects (Zhang and Brady, 2001).

Thus, the novelty of this work is threefold, namely, we propose (i) an interface level estimation and prediction approach using MRF, (ii) using an approach simultaneously estimating the parameters of the GMM using using the EM Algorithm to account for MRF spatial constraints, and (iii) validation of the proposed approaches on medical and synthetic images. Markov Random Field Theory (MRF) has been widely used in image segmentation and analysis [Ahmadvand and Daliri, 2015]. The Markov Random Field Model (MRF) is a probabilistic graphical model, which provides a statistical means of model spatial contextual constraints as prior information. For pixel based MRF model, spatial context, but it is time consuming and cannot describe long distance interactions between pixels, i.e. macro texture model. On the contrary, the region-based MRF can capture the macro texture pattern using the region-based information, but it suffers from the irregular spatial context. Image segmentation is a process of partitioning an image into several segments with the aim of simplifying the representation of the image or extracting meaningful objects. We use the expectation maximization (ME) algorithm for parameter estimation, a well-practiced approach to compute model parameters within a maximum likelihood estimation framework (Demrsrsa et al., 1977). MRFs have proven to be a suitable method for solving computer vision tasks such as image segmentation. [Sridhar, B., Reddy, 2013] Showed that with certain user-defined starting values, objects can segmented using strict constraints and histograms for the object and the background. In [16], Gaussian mixture models (GMM), one for the background and one for the foreground; replaced the user seed histograms and a border matting algorithm has been developed to fix the transparency on the edges of segmented objects.

The region-level MRF model has proposed in [Ocegueda, and Fang, 2013]. [Wang C, Ni J, Zhang, 2018] Proposed an approach for fusion of multispectral and panchromatic images exploiting local spatial information using the FCM clustering algorithm based on the MRF. However, their notion of label uncertainty cannot generalized to generic MRF models. In the context of image segmentation, a general notion of uncertainty can be considered as the variance or inequality (Yousif, and Ban, 2014) in the label assignments resulting from the distribution posterior of the label image. In [. Xia and Sun, 2006] they applied FCM with MRF for the detection of change in synthetic aperture radar (SAR) images. They classified the modified and unchanged regions using FCM with a defined random Markov field energy function. An improved method for color texture image based segmentation on FCM aggregation and for medical image segmentation, we propose an MRI segmentation method combining EM and Markov random field. It is different from [Siyal, 2005], which modified the fuzzy clustering membership of each pixel by the MRF energy function; we keep the standard form of FCM and integrate it into the MAP-MRF framework as a component of extraction and analysis of gray level information in our algorithm.

Major disadvantage of the Markov field model is that approximation algorithms they induce are iterative and very computationally intensive.

Creative Commons Attribution-NonCommercial-NoDerivatives 4.0 International License (CC BY-NC-ND)

In order to reduce the amount of computation and to obtain non-iterative computational algorithms, we can use the hidden Markov chains. The remainder of this article structured as follows: A brief review of the MRF model discussed in section two. The new regional feature of the UMRF model presented in section three. Details of the UMRF model given in section four. The algorithm described in section five. The experiments presented in section six and the conclusion given in section seven.

Problematic:

Problematic, MRF model and image segmentation

Let S denote a set of sites. $Y = \{ys| s \in S\}$ is the observed image defined on S. $X = \{Xs| s \in S\}$ is the label random field defined on S. Each random variable Xs in X represents the class of site s and takes value from the set $\Lambda = \{1, 2, , n\}$, where n is the number of classes. Let $x = \{xs| s \in S\}$ denote a realization of X. In the MRF model, the image segmentation is converted into the estimation of a best realization $\hat{x}$ given the observed image Y, i.e. $\hat{x} = \arg\max xP(x | Y)$.

According to the Bayesian rule, the posterior probability

$P(X | Y)$ is equal to $(P(Y | X) P(X))/ P(Y)$. Since the probability P(Y)is a constant, the estimation of the best realization $\hat{x}$ can be obtained by maximizing $P(Y | X)P(X)$, which needs to determine the forms of P(X)and $P(Y | X)$. First, the joint probability P(X) is used to model the label random field X. Since X is assumed to possess the Markov property in the MRF model, P(X) is of Gibbs distribution according to the theorem of Hammersley –Clifford [21]. That is

$P(X = x) = (1/ Z) \exp (- U(x))$, where $Z = \sum xU(x)$ is the normalisation factor and $U(x) = \sum s \in SU(xs,$ xNs) is the energy function. Here $U(xs, xNs) = \sum t \in Ns V (xs, xt)$, where Ns is set of sites neigh bouring site s and each V (xs, xt) is the potential function between site s and site t, $t \in Ns$. The multilevel logistic (MLL) model [21] is usually employed to define the potential function V (xs, xt), which is

$V (xs, xt) = \beta$ if $xs \neq xt - \beta$ if $xs \neq xt$, (1)

Where $\beta > 0$ is the potential parameter and $t \in Ns$. Based on the MLL model, P(X) would have a large value if the local neighbor labels were same, otherwise small. This characteristic encourages the adjacent pixels to be classified into the same label, which would make the MRF model resist noise and reduce the impact of intraclass variations. Second, the likelihood function $P(Y | X = x)$ is a conditional probability function. It is used to measure the probability that how the observed image Y match a given realization X = x. The sites of the likelihood function are assumed to be independent when the label field is given. That is

$P(Y | X = x) = \prod s \in S P (y_s| x) = \prod s \in S P (ys| xs)$.

For the pixel-based MRF model, each site $s = (i, j) \in S$ in the above equation denotes a pixel, and its feature ys is the vector that consists of spectral values of each band at site s, i.e. ys= (ys1, ys2, …, ysD). Here, ysi denotes the value of spectral band i, and D is the number of spectral bands for the observed image. The Gaussian distribution is usually employed to model P(ys| xs)in the above equation, i.e.

$P(ys| xs) = (2\pi) - D/2\Gamma - 1/2\exp - 12(ys - \mu)T\Gamma - 1(ys - \mu)$,where $\mu = E(Xs)$, and Γis the covariance matrix of Xs. At the pixel-based MRF model, the site set $S = \{s | , 1 \leq i \leq M, 1 \leq j \leq N\}$ is an $M \times N$ discrete rectangular lattice. Due to the regular spatial context, one can conveniently define the neighborhood system $N = \{Ns| s \in S\}$ as the four- or the eight-neighborhood system. However, the pixel-based neighborhood relationship is limited to describe the macro texture pattern of an image. To model complex and macro texture patterns, the multi-resolution MRF (MRMRF) model is introduced into the MRF model [19, 21, 24, 37]. The MRMRF model improves the MRF model by considering the image information at different resolutions. Although the MRMRF model can describe interactions in a lager neighborhood compared with the MRF model, it is still pixel-based method. This would lead to some misclassifications and limit the segmentation accuracy. The region-based MRF models proposed to improve the MRF model by using over-segmented regions as the basic site unit. They are defined on the site set $R = \{r\}$ of regions, where each r is an over-segmented region and $\bigcup r \in R r = Y$, $r \cap t = \emptyset (\forall r \neq t,$ and $r, t \in R)$. It could make the region-based MRF model to describe more macro spatial interactions. However, the region-based MRF model also suffers disadvantages. First, the initially over segmented regions may be imprecise. As mentioned in [35], the approaches used for initially segmentation, such as watershed, have some imprecise segments that would lead

Creative Commons Attribution-NonCommercial-NoDerivatives 4.0 International License (CC BY-NC-ND)

to the unfavourable result. Second, the spatial context relationships between regions are irregular. It will be difficult to define the neigh bourhood system for these regions.

3. THE PROPOSED FRAMEWORK

parameter set, k indicates the Gaussian component in the mixture model, K is the total number of Gaussian distributions constituting the mixture model, and w*k* is the weight of each Gaussian distribution, which satisfies - K k=1wk= 1. Each Gaussian component has the standard normal distribution form as:

Pk(ds| θk)=1σk√2πe−(ds−μk) 22σ2 k (4)

Consequently, the observation parameter set θd includes the distribution parameter rθk, which consists of the mean μk and the variance σk, and the weight for each distribution wk. Let S denote a set of sites. Y ={ys|s∈S} is the observed image defined on S. X ={Xs|s∈S} is the label random field defined on S. Each random variable Xs in X represents the class of site s and takes value from the set Λ={1,2,…,n}, where n is the number of classes. Let x={xs|s∈S} denote a realization of X. In the MRF model, the image segmentation is converted into the estimation of a best realisation x ^ given the observed image Y, i.e. x ^ =arg maxx P(x|Y). According to the Bayesian rule, the posterior probability P(X|Y) is equal to (P(Y|X)P(X))/P(Y) . Since the probability P(Y) is a constant, the estimation of the best realisation x ^ can be obtained by maximising P(Y|X)P(X), which needs to determine the forms of P(X) and P(Y|X). First, the joint probability P(X) is used to model the label random field X. Since X is assumed to possess the Markov property in the MRF model, P(X) is of Gibbs distribution according to the theorem of Hammersley–Clifford [21]. That is

P(X = x)=(1/Z)exp(−U(x)), where Z = ∑xU(x) is the normalisation factor and U(x)= ∑s∈SU(xs,xNs) is the energy function. Here U(xs,xNs)= ∑t∈NsV(xs,xt), where Ns is set of sites neighbouring site s and each V(xs,xt) is the potential function between site s and site t, t ∈ Ns. The multilevel logistic (MLL) model [21] is usually employed to define the potential function V(xs,xt), which is

V(xs,xt)= β if xs ≠ xt −β if xs ≠ xt, (1)

where β >0 is the potential parameter and t ∈ Ns. Based on the MLL model, P(X) would have a large value if the local neighbour labels are same, otherwise small. This characteristic encourages the adjacent pixels to classified into the same label, which would make the MRF model resist noise and reduce the impact of intraclass variations. Second, the likelihood function P(Y|X = x) is a conditional probability function. It is used to measure the probability that how the observed image Y match a given realization X = x. The sites of the likelihood function assumed independent when the label field is given. That is P(Y|X = x)= ∏ s∈S P(ys|x)= ∏ s∈S P(ys|xs). For the pixel-based MRF model, each site s=(i, j)∈S in the above equation denotes a pixel, and its feature ys is the vector that consists of spectral values of each band at site s, i.e. ys =(ys 1,ys 2,…,ysD). Here, ys i denotes the value of spectral band i, and D is the number of spectral bands for the observed image. The Gaussian distribution is usually employed to model P(ys|xs) in the above equation, i.e. P(ys|xs)=(2π)−D/2Γ−1/2exp −1 2(ys−μ)TΓ−1(ys−μ) , where μ= E(Xs), and Γ is the covariance matrix of Xs. At the pixel-based MRF model, the site set S={s|,1≤i≤ M,1≤ j ≤ N} is an M×N discrete rectangular lattice. Due to the regular spatial context, one can conveniently define the neighbourhood system N ={Ns|s∈S} as the four- or the eight-neighborhood system. However, the pixel-based neighborhood relationship is limited to describe the macro texture pattern of an image. To model complex and macro texture patterns, the multi-resolution MRF (MRMRF) model is introduced into the MRF model [19, 21, 24, 37]. The MRMRF model improves the MRF model by considering the image information at different resolutions. Although the MRMRF model can describe interactions in a lager neighborhood compared with the MRF model, it is still a pixel-based method. This would lead to some misclassifications and limit the segmentation accuracy. The region-based MRF models are proposed to improve the MRF model by using over-segmented regions as the basic site unit. They are defined on

Creative Commons Attribution-NonCommercial-NoDerivatives 4.0 International License (CC BY-NC-ND)

the site set R={r} of regions, where each r is an over-segmented region and ⋃r∈Rr =Y, r∩t =∅(∀r ≠t, and r,t ∈ R). It could make the region-based MRF model to describe more macro spatial interactions. However, the region-based MRF model also suffers disadvantages. First, the initially over segmented regions may be imprecise. As mentioned in [35], the approaches used for initially segmentation, such as watershed, have some imprecise segments that would lead to the unfavourable result. Second, the spatial context relationships between regions are irregular. It will be difficult to define the neighborhood system for these regions. (3.14)

2.2. The MAP-MRF framework

Markov random field theory provides a convenient and consistent way of modelling context-dependent entities such as image pixels and correlated features [26]. Geman advocates the maximum a posteriori Markov random field (MAP-MRF) framework for statistical image analysis problems [27]. For segmentation, it can be considered to be a labeling problem and the segmented result can be retrieved by seeking the maximum a posteriori estimation of the labeling problem.

Let the rectangular lattice for a 2D image of size MN be defined as follows: S¼fðm;nÞj1mM;1nNg (5) For a lattice S, the set of neighbors of element i is defined as the set of sites within a radius of ▪ ▪ rp from i Ni ¼fpixeli0 2Sj½distðpixeli0;pixeliÞ2 r;i0 6¼ig (6) Clique c in S defined as a subset of sites in S. Single-site clique c ¼f ig, pair-site clique c¼f i;i0g, triple-site clique c ¼f i;i0;i00g,(i;i0;i00 2S and neighbor each other), and so on. The collections of all single-site cliques, pair-site cliques, and triple-site cliques can be denoted as C1; C2 and C3. The collection of all cliques C ¼C1 [C3 [C3: In MAP-MRF framework, the MRI segmentation can be converted to a labeling problem which gives different labels to pixels e.g. WM, GM, CSF etc. The joint probability of each pixel's label in the MR image is modeled by the MRF, denoted by PðfÞ¼Pðf1;:::;fMNÞ (7) where, N and M are the height and the width of the MR image in pixels. S¼fðm;nÞj1mM; 1nNg;fi2S 2f 1;:::;LKg, where i is a pixel in S, and LK;k 21;:::;K, corresponding to labels of the different tissues in the brain. According to markovianity, for each i 2S, PðfijfS figÞ equals to Pðfij fNiÞ, where Ni denotes the neighborhood system of i. By the Hammersley-Clifford theorem, PðfjdÞ¼ 1 Ze 1 TUðfjdÞ (8) where, d ¼d1;:::;dMN is the observation, Z and T are constants. The energy function UðfjdÞ¼X c2C VcðfjdÞ¼X i2S X c2C Vcðfijdi0Þ;i0 2c (9) is the sum of clique potentials VcðfjdÞ over all possible cliques in C. Then, the solution of the original segmentation or labelling problem can be denoted as : f ¼argmax f PðfÞ¼argmin f UðfÞ (10) The computation would take a long time if calculated over all cliques. In practice, execution of the computation over single site cliques and pair site cliques is widely adopted. In other words, the second order neighborhood system is adopted, where the label of i is only decided by the elements in Ni ¼ fi0 2Sj½distðpixeli0; pixel iÞ2 2; I0 6¼ig and i itself. In this situation, the model also called an auto model.

3.2 MAP-MRF Framework

The Bayesian framework helps to obtain statistical inferences, synthesizing the maximum a posteriori (MAP) solution, and incorporating the prior information Greig et al. (1989). The objective of the MAP solution is to maximize the posterior probability, which can be represented as: arg max f ∈F P(f | d) (5) According to the Bayes rule, the posterior probability is P(f | d) ∝ P(d | f)P(f) (6) As a result, the MAP estimation problem becomes: argmax f∈F{P(d | f)P(f)} (7) By applying Hammersly-Cli▪ ord theorem, the posterior probability can be expressed as: P(f | d) ∝ e−U(d|f)e−U(f) (8) Consequently, the posterior probability can be written as: P(f | d) ∝

Creative Commons Attribution-NonCommercial-NoDerivatives 4.0 International License (CC BY-NC-ND)

e−U(f|d) (9) where U(f | d)=U(d | f)+U(f) (10) is defined as the posterior energy and U(d | f) is called the likelihood energy. Therefore, maximizing the posterior probability P(f | d) is equivalent to minimizing the posterior energy function U(f | d), which is given by: argmin f U(f | d)

3.1 Gaussian Mixture Model

Pixel values of an image for segmentation purpose usually have significant di□erences among distinct regions; therefore, the mixture of Gaussian distribution becomes a reasonable choice for modeling the observed image. As a result, the observation model can be formulated in the following form (Bishop, 2006):

P(ds | θd)= K - k=1

wkPk(ds | θk) (3) where ds represents an observed pixel, θd is the observation parameter set, k indicates the Gaussian component in the mixture model, K is the total number of Gaussian distributions constituting the mixture model, and wk is the weight of each Gaussian distribution, which satisfies K k=1 wk = 1. Each Gaussian component has the standard normal distribution form as: Pk(ds | θk)= 1 σk√2πe−(ds−μk)2 2σ2 k (4) Consequently, the observation parameter set θd includes the distribution parameter θk, which consists of the mean μk and the variance σk, and the weight for each distribution wk.

Results and discussion

In this work, we presented the segmentation of images by Markov fields based on the KMeans and EM algorithms and the results obtained. We used the Matlab tool to present the segmentation methods by region that we have proposed. The objective of this introduction to image processing in Matlab to present the notion of image and to perform simple image analysis operations. Image processing is a research topic located between computer science and signal processing. To make an objective comparison of the different methods proposed, we propose to opt as evaluation criteria: mean squared error (MSE), signal to noise ratio (PSNR Peak Signal to Noise Ratio), normalized cross-correlation (NCC), structural content (SC) and normalized absolute error (NAE). We present in tables the values of the validation criteria for all the proposed methods. This will be followed by an interpretation of the results, in order to be able to make a comparison between the segmentation methods used. First, we define the evaluation criteria that we mentioned above.

IV.3 Quality measurement:

The objective of this part is to study and define evaluation criteria to quantify the quality of image segmentation results. There is a multitude of segmentation methods whose effectiveness remains difficult to assess. It seems important to be able to measure the quality of the images. However, there is no ideal solution, especially when there is no reference image for this difficult problem. In this part, we will define some basic metrics. [10]

IV.4 Objective evaluation:

Objective quality measurement (as opposed to subjective assessment of quality by human observers) seeks to determine the quality of images algorithmically. The goal objective assessment quality research is to design algorithms whose quality prediction is consistent with the subjective assessment of human observers. The methods of assessing image quality can be classified into three broad categories:

Creative Commons Attribution-NonCommercial-NoDerivatives 4.0 International License (CC BY-NC-ND)

IV.4 . 1 Methods with full reference,

In which the algorithm has access to a perfect version of the image with which it can compare degraded aversion. The perfect version usually comes from a high quality acquisition device; afterwards it degraded by compression and transmission errors.

IV.4 .2 Methods without reference,

In which the algorithm has access to distorted signal and must estimate the quality of the signal without knowledge of the perfect version.

Since non-reference methods do not require any reference information, they can used in any application where quality measurement is required.

IV.4 .3 Methods with reduced reference,

In which partial information about the perfect version is available.
A channel side exists through which some information about the reference can made available to the quality assessment algorithm.
Reduced reference algorithms use this partial reference information to judge the quality of the distorted signal.
The most widely used quantitative measures are: the mean squared error (MSE), the peak signal to noise ratio (PSNR), the signal to noise ratio (Signal to Noise Ratio: SNR) etc. [50]

IV.5 Methods with reduced reference,

Image quality measurement plays an important role in the development of image processing algorithms and in evaluating the performance of the processed image. Image quality is defined as a characteristic of an image that measures the degradation of the processed image by comparing it to an ideal image. Humans are generally the observers and users of the majority of imaging systems, therefore subjective assessment of image quality considered the reliable method. Temporal applications, the use of the subjective method is limited due to its complexity and difficulty of implementation. Therefore, objective methods have used more widely for the assessment of image quality in recent years. In this work, we consider several measures of image quality and analyze their statistical behavior for eight targeted measures of the SFF method. [48]

IV.5.1 Erreur quadratique moyenne (MSE)

The degraded image Î is always compared to the original I to determine its likeness ratio, this criterion is the most used.

It based on the mean square error (MSE) measurement calculated between the original and gradient pixels:

$$M = \frac{1}{M * N} \sum_{m=1}^{M} \sum_{n=1}^{N} \left(I(m,n) - \hat{I}(m,n) \right)^2$$

Creative Commons Attribution-NonCommercial-NoDerivatives 4.0 International License (CC BY-NC-ND)

Where (M × N) the size of image, et I p et Î p are respectively the amplitudes of the pixels on the original and degraded images.

It is likely that the eye takes much more account of errors at large amplitudes, which favors quadratic measurement.

[50]

IV.5.2 The peak signal to noise ratio **(PSNR)**

The PSNR operator measures the relationship between information and noise in an image, calculated from an initial image img_I, which includes the image and noise, and from an image img_O, which is the segmented version of the initial image img_I.
The images img_I and img_O must have the same dimension and the same type.

The PSNR is to quantify the performance of the algorithms by measuring the quality of reinsertion of the segmented image compared to the original image.

PSNR defined by:

$$PNSR = 10log_{10}\frac{d^2}{EQM} \qquad (\mathbf{IV.2})$$

- d is the dynamics of an image.
In the standard case of an image where the components of a pixel are encoded on 8 bits, d = 255.
- EQM is the mean squared error and defined for two images I image and O image of size M × N.
Maximizing the PSNR amounts to minimizing the squared error.
Typical PSNR values for good quality images vary between 30 and 40 dB. [49]

IV.5.3 Structural content:

This quality metric expressed as follows:

$$SC = \frac{\sum_{i=1}^{m}\sum_{j=1}^{n}(A_{ij})^2}{\sum_{i=1}^{m}\sum_{j=1}^{n}(B_{ij})^2} \qquad (\mathbf{IV.3})$$

A higher value of SC (Structural Content) shows that the image is of poor quality.

IV.5.4 Normalized Cross Correlation:

The NCC (Normalized Cross Correlation) measurement shows the comparison of the processed image and the reference image.
NCC expressed as follows: [48]

$$NCC = \sum_{i=1}^{m}\sum_{j=1}^{n}\frac{(A_{ij} \times B_{ij})}{A^2{}_{ij}} \qquad (\mathbf{IV.4})$$

IV.5.5 Maximum difference:

Creative Commons Attribution-NonCommercial-NoDerivatives 4.0 International License (CC BY-NC-ND)

MD (Maximum Difference) provides the maximum error signal (i.e. difference between the image references). MD defined as follows:

$$MD = Max\left(\left|A_{ij} - B_{ij}\right|\right) \qquad \textbf{(IV.5)}$$

$$i = 1,2 \ldots\ldots m \ , \ j = 1,2 \ldots\ldots n$$

The higher the value of the maximum difference, the higher the quality of the image.

IV.5.6 Normalized absolute error

This quality measure can expressed as follows:

$$NAE = \frac{\sum_{i=1}^{m}\sum_{j=1}^{n}\left(\left|A_{ij} - B_{ij}\right|\right)}{\sum_{i=1}^{m}\sum_{j=1}^{n}A_{ij}} \qquad \textbf{(IV.6)}$$

A higher NAE value shows that the image is of poor quality.

IV.6.1 synthetic image Segmentation

In this part, we started to apply the two segmentation methods on the synthetic images and after that; we evaluated these methods by evaluation criteria that we saw previously.
From the values in the table (Table IV.1) (PSNR = 21.5514) and (SC = 170.5034) in can see that the quality of the segmented image is poor by the ICM method based on the EM algorithm versus ICM. An infinite PSNR value corresponds to an undegraded image. In addition, this value decreases according to the degradation of the PSNR therefore links with MSE the maximum energy of the image. Regardless of the value of MSE, the value of PNSR is large.

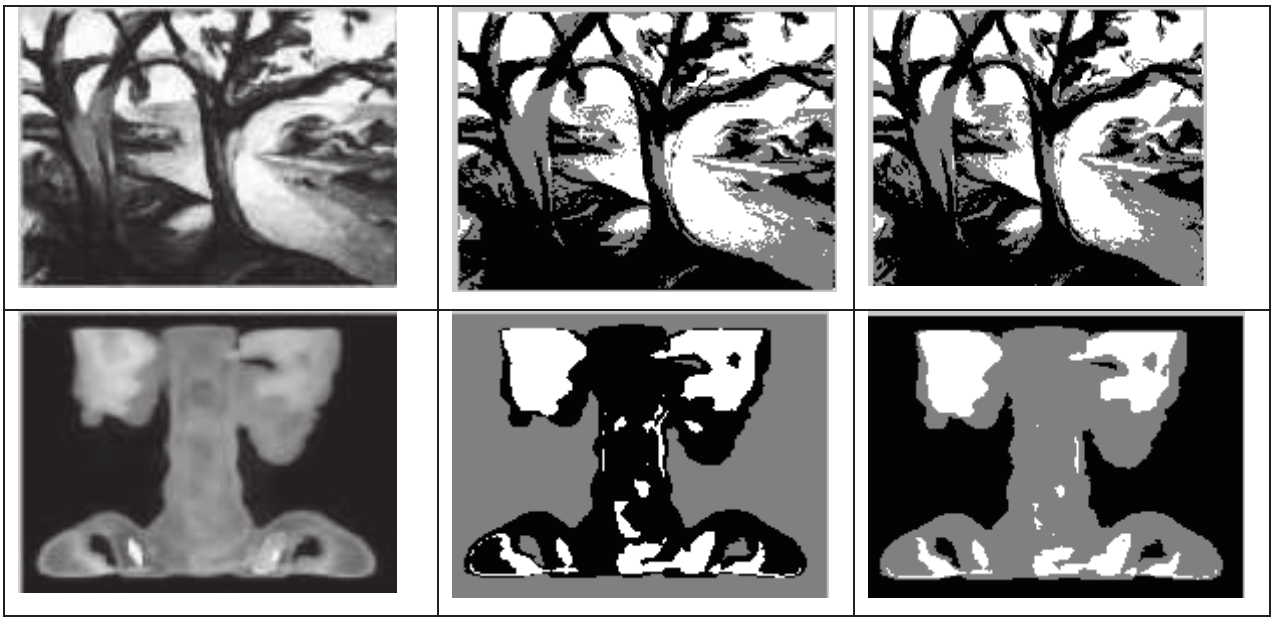

Creative Commons Attribution-NonCommercial-NoDerivatives 4.0 International License (CC BY-NC-ND)

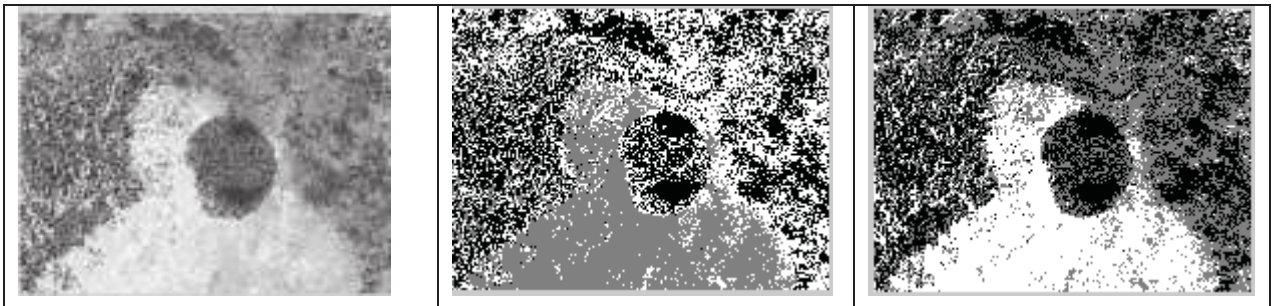

a) Image original	b) MRF based K-Means	c) MRF based EM

Figure IV.1 a) Image original, b) Segmentation par MRF basée K-Means, c) Segmentation par MRF basée EM based on the KMeans algorithm for synthetic images.

Critères\ Algorithmes	MSE	PSNR	NCC	SC	NAE
KMeans	2.4853e+004	4.1770	0.0132	5.6493e+003	0.9866
EM	2.5019e+004	4.1482	0.0099	5.3427e+003	0.9862
KMeans	454.9593	21.5511	0.0695	170.5034	0.9468
EM	454.9253	21.5514	0.0696	169.8783	0.9466

Tableau IV.1 the Values of the evaluation criteria for image segmentation**.**

IV.7 Real image Segmentation

IV.7.1 Image Segmentation

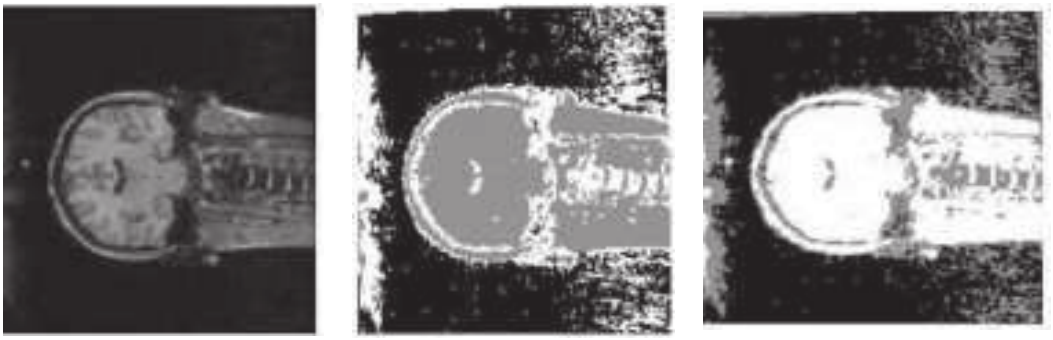

a) Image originale **b) MRF basée KMeans** **c) MRF basée EM**

Figure IV.2 a) Image original, b) Segmentation parMRF base KMeans, c) MRF base EM

Creative Commons Attribution-NonCommercial-NoDerivatives 4.0 International License (CC BY-NC-ND)

In this part we started to apply the two segmentation methods on real images and synthetic images and then we evaluated these methods by evaluation criteria that we have seen previously the results obtained in the table which shows that the

ICM algorithm based on EM method is better compared to ICM based method for KMeans the actual images.

	K-Means	EM
MSE	2.9142e+003	2.8690e+003
PSNR	13.4856	13.5535
NCC	0.0247	0.0321
SC	809.7124	753.9953
MD	253	252
NAE	0.9558	0.9532

Tableau IV.2 the Values of criteria for image segmentation

In order to benefit from the advantages of the two methods presented in the previous paper, we decided to use them to segment the images, and we made a table for each result, this table presents the values of some evaluation criteria on the segmentation results the two optimal values (taking into account the direction of variation of the criteria).

We can observe in figure (IV.2) the interest of the segmentation by the method of KMeans it allows to keep precise borders.

The outline image as it appears is a typical image for this kind of segmentation with similar EMs. The values of KMeans are large relative to the value of EM.

So the quality is good and the best EM algorithm.

IV.7.2 image Segmentation

a) Image original

b) MRF based with K-Means

c) MRF based with EM

Creative Commons Attribution-NonCommercial-NoDerivatives 4.0 International License (CC BY-NC-ND)

Figure IV.3 a) Image original, Segmentation par b) MRF base K-Means, c) MRF base EM

The results obtained presented in the previous figures where we have presented the segmentation evaluation criteria in the following table: It concluded that the ICM algorithm based on the EM method better compared to ICM based on the method for KMean image real.

Critères	K-means.	EM
MSE	4.8045e+003	4.7178e+003
PSNR	11.3143	11.3934
NCC	0.0112	0.0196
SC	683.0782	1.8686e+003
MD	254	252
NAE	0.9492	0.9678

Tableau IV.3 the Values of criteria for image segmentation

The values of the criteria give the information that the EM algorithm is better than the KMeans algorithm.

IV.8 Conclusion

The work is applied on synthetic and real images, after we carried out a comparative study between the method MRF based on KMeans and MRF based on EM to evaluate these results we used the following criteria: MSE, PNSR, NCC, SC, MD and NAE and two algorithms: KMeanS and EM. The results obtained show that the MRF method sometimes gives bad results (under-segmentation, over-segmentation). The cooperation of these two approaches, which are by nature dual, improves the segmentation result.

In this thesis, we presented different segmentation approaches by region-contour cooperation. Whether sequential or mutual, cooperative segmentation integrates the two types of information (regions and contours) in order to allow better consideration of the characteristics of the objects in the image. The homogeneous zones, as well as the transitions between them, are respected simultaneously. In comparison with segmentation by regions or by contours, the result of cooperative segmentation is more faithful to the reality of the image.

Conclusion and discusion

In this, work we have presented the results of the region segmentation algorithm based on Markov fields, the work applied on synthetic and real images, after we have carried out a comparative study between the MRF method based on KMeans and any image analysis process. It consists of preparing the image in order to make it more usable by an automatic process such as interpretation. There are two main purely local approaches. The contour approach consists in locating the borders of the regions; it based on the notion of dissimilarity. Among these strengths: its simplicity and speed but it sometimes gives open contours. The region approach consists in bringing together the related pixels in a homogeneous region; it

Creative Commons Attribution-NonCommercial-NoDerivatives 4.0 International License (CC BY-NC-ND)

based on the notion of similarity. It is quick and simple, but using only local information MRF based on EM to evaluate these results we used the following criteria: MSE, PNSR, NCC, SC, MD and NAE and two algorithms: KMeans and EM. This work describes the unsupervised classification of images in the framework of hidden Markov models and estimation.

Hidden Markov fields frequently used to impose spatial regularity constraints in parameter estimation and classification steps. This approach produces excellent results in many cases, but our experiences indicate that the estimation of the regularity parameter is a delicate problem. Another disadvantage is the considerable calculation time. The methods based on hidden Markov chains, applied to the Hilbert-Peano traversal of the image, constitute an interesting alternative. The estimation of the regularity parameters, which represent the elements of a transition matrix, seems to be much more robust. Region boundaries are often slightly irregular with this approach, but excellent structures generally better preserved than in the case of hidden Markov fields. In addition to the robust estimation of the regularity parameters, the computational speed is the main advantage of the hidden Markov chain approach. In our experiments, this was about 25 times faster than the program based on hidden Markov fields. Several facts emerge from this experimental study. First, the value of considering spatial information for the classification of the pixels of an image appears clearly in the various examples treated. As expected, the choice of a Gaussian mixture model leads to acceptable segmentations and we observe a clear improvement in the homogeneity of the segmentation with a spatial model. This result is satisfactory because it confirms, in the case of the field, and shows, in the case of strings, that the approximations of a hidden Markov model used preserve Markovian information. In this work, we presented the results of the region segmentation algorithm based on Markov fields. The results obtained show that the MRF method based on EM is better than that based on KMeans.

Reference

Jiang Z, Xie M and Sainju A (2021) Geographical Hidden Markov Tree, IEEE Transactions on Knowledge and Data Engineering, 33:2, (506-520), Online publication date: 1-Feb-2021.

Dubes,R. Jain,A. Nadabar, S. and Chen, C. 1990), MRF model-based algorithms for image segmentation, Pattern Recognition. Proceedings., 10th International Conference on, IEEE, pp. 808–814.

Gribben, H., and Miller,(2009), Map-MRF segmentation of lung tumours in pet/ct images, Biomedical Imaging: From Nano to Macro. ISBI'09. IEEE International Symposium on, IEEE, pp. 290–293.

Ahmadvand, A. ***and*** **Daliri**, **M.R.** (2015) Improving the runtime of MRF based method for MRI brain segmentation, Appl Math Comput 256, 808–818.

Yousefi, S., Azmi, R., ***and*** **Zahedi, M.** (2012), Brain tissue segmentation in MR images based on a hybrid of MRF and social algorithms, *Med Image Anal* **16**, 840–848.

Ryali, S., Chen, T., Supekar, K., and Menon, V. (2013), "A parcellation scheme based on von Mises-Fisher distributions and Markov random fields for segmenting brain regions using resting-state fMRI", Neuroimage, 65 (2), pp. 83-96.

Creative Commons Attribution-NonCommercial-NoDerivatives 4.0 International License (CC BY-NC-ND)

Ashraf, A. B., Gavenonis, S. C., Daye, D., Mies, C., Rosen, M. A., and Kontos, D. (2013), "A multichannel markov random field framework for tumor segmentation with an application to classification of gene expression-based breast cancer recurrence risk", Medical Imaging, IEEE Transactions on, 32 (4), pp.637-648.

Sridhar, B., Reddy, V.S., and Prasad, A. M. (2013), "Automated Medical image segmentation for detection of abnormal masses using Watershed transform and Markov random fields", International Journal on Signal and Image Processing, 4 (3), pp. 56.

Simmons, J., Przybyla, C., Bricker, S., Kim, D. W. (2014), and Comer, M., "Physics of MRF regularization forsegmentation of materials microstructure images". Image Processing (ICIP), IEEE International Conference on, Paris, France: IEEE, pp. 4882- 4886.

Yousif, O., and Ban, Y. (2014), "Improving SAR-Based Urban Change Detection by Combining MAP-MRF Classifier and Nonlocal Means Similarity Weights", IEEE Journal of Selected Topics in Applied Earth Observations and Remote Sensing, 7 (10), pp.4288-4300.

Siyal, M.Y. and Yu, L.; (2005), An intelligent modified fuzzy c-means based algorithm for bias estimation and segmentation of brain MRI, Pattern Recogn Lett 26, 2052–2062

Ocegueda, O., Fang, T., Shah, S. K., and Kakadiaris, I. A. (2013), "3D face discriminant analysis using Gauss-Markov posterior marginals", Pattern Analysis and Machine Intelligence, IEEE Transactions on, 35 (3), pp.728-739.

Wang C, Ni J, Zhang, .X and Huang, .Q (2018), Efficient Compression of Encrypted Binary Images Using the Markov Random Field, IEEE Transactions on Information Forensics and Security, 13:5, (1271-1285), Online publication date: 1-May-2018.

Xia, G.-S., C. He, and Sun, H. (2006), An unsupervised segmentation method using Markov random field on region adjacency graph for sar images, Radar, 2006. CIE'06. International Conference on, IEEE, , pp. 1–4.

Creative Commons Attribution-NonCommercial-NoDerivatives 4.0 International License (CC BY-NC-ND)

Algerian Journal of Engineering Architecture and Urbanism Vol. 5 Nr. 3 2021
ISSN: 2588-1760

Co-Evolution Binary Particle Swarm for RFM Optimization of Satellite Images Ortho-rectification

Oussama Mezouar
PHD Student, Communication Networks, Architectures and Multimedia Laboratory,
University of Djillali Liabes, Sidi Bel Abbes, Algeria,
e-mail: ousama31@gmail.com

Fatiha MESKINE
MCA, Communication Networks, Architectures and Multimedia Laboratory,
University of Djillali Liabes, Sidi Bel Abbes, Algeria,
e-mail: me_fatiha2010@hotmail.fr

I. Boukerch
MRB, Spatial Technical Center, Arzew, Oran, Algeria
e-mail: issam.boukerch@yahoo.fr

Abstract:
The Rational function models (RFMs) are one of the most efficient methods used for ortho-rectification of very high-resolution satellite imagery, unlike the rigorous models the RFM don't require any information or parameters about the physical sensors, however, RFM requires a lot of accurate well-distributed ground control points (GCPs) which is a time-consuming and costly operation, there is also the issue of the over-parameterization errors because so many coefficients are used. In addition, RFM coefficients or also known as rational polynomial coefficients (RPCs) have no physical significance which makes it difficult to find their best combination. Recently, a variety of meta-heuristic algorithms have been proposed to overcome these problems and find the optimum combination of RPCs as particle swarm optimization and genetic algorithm. In this paper, we propose a new co-evolution binary particle swarm optimization with a multiple inertia weight strategy to determine the best rational polynomial coefficients for RFMs, increase the convergence speed and avoid the local optimum phenomenon. The results showed that the proposed method gives a higher accuracy which is appropriate for photogrammetric and remote sensing applications.

Key words: satellite images, ortho-rectification, rational function model, binary particle swarm optimization, multiple inertia weight.

I. Introduction

In recent years, a significant number of high-resolution satellite images (HRSI) have become available, therefore they are used in several applications fields both scientifically and commercially (Belfiore & Parente, 2016). Among this field, the geographic information system (GIS) where the HRSI constitutes one of the most popular sources because it contains various information (Jayaseeli & Malathi, 2020). On the other hand, the raw images often involve major geometrical distortions. This distortion depends on the device (airplane or satellite), type of sensor, and the overall field of view so the raw images can't be used directly for map products in GIS (Thierry, 2010).

Creative Commons Attribution-NonCommercial-NoDerivatives 4.0 International License (CC BY-NC-ND)

In order to georeference the images and correct the geometric deformations introduced during acquisition, careful orientation and ortho-rectification are necessary (Belfiore & Parente, 2016). These errors and geometric deformations can be corrected generally with two types of models named rigorous and empirical models (Tao & Hu, 2001). The rigorous models also called physical models are based on a traditional photogrammetric approach, in which collinearity equations relate the image coordinates and ground coordinates, and the parameters used have physical significance. Furthermore, They will need anxillary data from the satellite platform such as ephemeris, altitude, and other parameters that aren't always given by the vendors which making their implementation costly, time-consuming, and error-prone (Thierry, 2010). All of these disadvantages support the use of empirical models.

The rational function model (RFM) is the most commonly used empirical model to replace rigorous models since, unlike rigorous models, the RFM does not involve any physical knowledge about the sensor or the satellite. Instead, the RFM needs a large number of accurate and well-distributed ground control points (GCPs), which is a time-consuming and expensive process. There's also the problem of over-parameterizing errors, which arises from the RFM structure's use of too many coefficients known as rational polynomial coefficients (RPCs). Moreover, these RPCs have no physical significance which makes it difficult to find their best combination (Yavari et al., 2012). Recently, a variety of meta-heuristic methods based on particle swarm optimization (PSO) have been proposed as (Gholinejad et al., 2019; Yavari et al., 2013) to surmount the issue and find the optimum RPCs.

In this paper, we trying to tackle the limitations of PSO in RFM optimization by proposing a novel co-evolutionary binary particle swarm optimization algorithm with a multiple inertia weight strategy to improve the convergence speed and avoid the risk of stuck in the local minima, while also preserving the diversity of the population. The remaining of the paper is organized as follows: an overview of the RFM and a brief description of the binary PSO for RFM optimization is presented in section II, the proposed method of RFM optimization is depicted in section III, therefore the implementation and different simulation results are provided in section IV. Finally, we give our conclusion in section V.

Problematic:

The rational function model (RFM) has a lot of unnecessary parameters namely rational polynomial coefficients (RPCs), hence these RPCs have no physical meaning which creates the presence of the over parameterization phenomena and makes it difficult to determine the best rational polynomial coefficients(RPCs) for the RFM. Therefore, it is necessary to increase the number of ground control points (GCPs) to calculate the RPCs. As result, it appears that certain RPCs must be removed to improving the RFM structure. In this paper, a co-evolution particle swarm is proposed based on the multiple inertia weight strategy in order to find and select the optimum RPCs for RFMs within a predefined number of GCPs.

II. The RFM theoretical model

Creative Commons Attribution-NonCommercial-NoDerivatives 4.0 International License (CC BY-NC-ND)

Rational function model (RFM) is composed of two mathematical equations which define the spatial relationship between ground space and image space and vice versa using a ratio polynomial (C. Tao & Hu, 2001) as follows :

$$r = \frac{P_1(X,Y,Z)}{P_2(X,Y,Z)}$$
$$c = \frac{P_3(X,Y,Z)}{P_4(X,Y,Z)} \quad (1)$$

Where r and c are the row and column index of pixels in the image respectively, X Y and Z are reference point coordinates in ground space, and the polynomial P_i (i=1,2,3,4) defined as

$$P_1 = a_0 + a_1X + a_2Y + a_3Z + a_4XY + a_5XZ + a_6YZ + a_7X^2 + a_8Y^2 + a_9Z^2 + a_{10}XYZ + a_{11}X^3 + a_{12}XY^2 + a_{13}XZ^2 + a_{14}X^2Y + a_{15}X^3 + a_{16}YZ^2 + a_{17}X^2Z + a_{18}Y^2Z + a_{19}Z^3 \quad (2)$$

$$P_2 = b_0 + b_1X + b_2Y + b_3Z + b_4XY + b_5XZ + b_6YZ + b_7X^2 + b_8Y^2 + b_9Z^2 + b_{10}XYZ + b_{11}X^3 + b_{12}XY^2 + b_{13}XZ^2 + b_{14}X^2Y + b_{15}X^3 + b_{16}YZ^2 + b_{17}X^2Z + b_{18}Y^2Z + b_{19}Z^3 \quad (3)$$

$$P_3 = c_0 + c_1X + c_2Y + c_3Z + c_4XY + c_5XZ + c_6YZ + c_7X^2 + c_8Y^2 + c_9Z^2 + c_{10}XYZ + c_{11}X^3 + c_{12}XY^2 + c_{13}XZ^2 + c_{14}X^2Y + c_{15}X^3 + c_{16}YZ^2 + c_{17}X^2Z + c_{18}Y^2Z + c_{19}Z^3 \quad (4)$$

$$P_4 = d_0 + d_1X + d_2Y + d_3Z + d_4XY + d_5XZ + d_6YZ + d_7X^2 + d_8Y^2 + d_9Z^2 + d_{10}XYZ + d_{11}X^3 + d_{12}XY^2 + d_{13}XZ^2 + d_{14}X^2Y + d_{15}X^3 + d_{16}YZ^2 + d_{17}X^2Z + d_{18}Y^2Z + d_{19}Z^3 \quad (5)$$

The a_i b_i c_i d_i Are the polynomial coefficients named rational function coefficients (RFCs) where b_0 =1 and d_1=1, unknown RPCs can be solved with the linearized RFM form (Long et al., 2015; Tengfei et al., 2014) as in the following :

Firstly, Equation (1) is rewritten as follows :

$$r = \frac{(1\ Z\ Y\ X \dots Y^3\ Z^3).(a_0\ a_1 \dots a_{19})^T}{(1\ Z\ Y\ X \dots Y^3\ Z^3).(1\ b_1 \dots b_{19})^T}$$
$$c = \frac{(1\ Z\ Y\ X \dots Y^3\ Z^3).(c_0\ c_1 \dots c_{19})^T}{(1\ Z\ Y\ X \dots Y^3\ Z^3).(1\ d_1 \dots d_{19})^T} \quad (6)$$

Next, we can reformulate the Equation (6) into linearized RFM form to get the error equations (7) and (8):

$$v_r = \left[\frac{1}{B}\frac{Z}{B}\frac{Y}{B}\frac{X}{B} \dots \frac{Y^3}{B}\frac{X^3}{B} - \frac{rZ}{B} - \frac{rY}{B} \dots - \frac{rY^3}{B} - \frac{rX^3}{B}\right].J - \frac{r}{B} \quad (7)$$

$$v_c = \left[\frac{1}{D}\frac{Z}{D}\frac{Y}{D}\frac{X}{D} \dots \frac{Y^3}{D}\frac{X^3}{D} - \frac{cZ}{D} - \frac{cY}{D} \dots - \frac{cY^3}{D} - \frac{cX^3}{D}\right].K - \frac{c}{D} \quad (8)$$

Where :

$B=(1\ Z\ Y\ X \dots Y^3\ X^3).(1\ b_1 \dots b_{19})^T$

Creative Commons Attribution-NonCommercial-NoDerivatives 4.0 International License (CC BY-NC-ND)

$J= (a_0\ a_1\ \dots\ a_{19}\ b_1\ b_2\ \dots\ b_{19})^T$

$D=(1\ Z\ Y\ X\ \dots\ Y^3\ X^3).(1\ d_1\ \dots\ d_{19})^T$

$K= (c_0\ c_1\ \dots\ c_{19}\ d_1\ d_2\ \dots\ d_{19})^T$

Equation (7) can be represented in the matrix form by using n GCPs as follows:

$$\begin{bmatrix} v_{r1} \\ v_{r2} \\ \vdots \\ v_{rn} \end{bmatrix} = \begin{bmatrix} \frac{1}{B_1} & 0 & \cdots & 0 \\ 0 & \frac{1}{B_2} & 0 & \vdots \\ \vdots & 0 & \ddots & 0 \\ 0 & \cdots & 0 & \frac{1}{Bn} \end{bmatrix} \cdot \begin{bmatrix} 1 & Z_1 & \cdots & X_1^3 & -r_1 Z_1 & \cdots & -r_1 X_1^3 \\ 1 & Z_2 & \cdots & X_2^3 & -r_1 Z_2 & \cdots & -r_2 X_2^3 \\ \vdots & \vdots & \ddots & \vdots & \vdots & \ddots & \vdots \\ 1 & Z_n & \cdots & X_n^3 & -r_n Z_n & \cdots & -r_n X_n^3 \end{bmatrix} J - \begin{bmatrix} \frac{1}{B_1} & 0 & \cdots & 0 \\ 0 & \frac{1}{B_2} & 0 & \vdots \\ \vdots & 0 & \ddots & 0 \\ 0 & \cdots & 0 & \frac{1}{Bn} \end{bmatrix} \cdot \begin{bmatrix} r_1 \\ r_2 \\ \vdots \\ r_n \end{bmatrix} \tag{9a}$$

$$V_r = W_r\, MJ - W_r\, R = 0 \tag{9b}$$

where W_r considered as the weight matrix.

Equation (9b) could then be written in the following form :

$$M^T W_r^2 MJ - M^T W_r^2 R = 0 \tag{10}$$

If we take W_r as the unit matrix, we can solve Equation (10) in this case by using direct least square (LS) then the direct solution of RFCs is as follows :

$$J = (M^T M)^{-1} M^T R \tag{11}$$

Therefore, the complete system is set up into the following form:

$$\begin{bmatrix} V_r \\ \cdots \\ V_c \end{bmatrix} = \begin{bmatrix} W_r & \vdots & O \\ \cdots & + & \cdots \\ O & \vdots & W_c \end{bmatrix} \cdot \begin{bmatrix} M & \vdots & O \\ \cdots & + & \cdots \\ O & \vdots & N \end{bmatrix} \cdot \begin{bmatrix} J \\ \cdots \\ K \end{bmatrix} - \begin{bmatrix} W_r & \vdots & O \\ \cdots & + & \cdots \\ O & \vdots & W_c \end{bmatrix} \cdot \begin{bmatrix} R \\ \cdots \\ C \end{bmatrix} \tag{12}$$

Where : $V = WTI - WG$

The normal equation becomes:

$$T^T W^2 TI - T^T W^2 G = 0 \tag{13}$$

The above equation can then be solved using a standard least-squares method :

$$I = (T^T T)^{-1} T^T G \tag{14}$$

III. The proposed technique for RFM optimization

Particle swarm optimization (PSO) is one of the most common meta-heuristic optimization algorithms inspired by social intelligence and cooperative behavior displayed by various

Creative Commons Attribution-NonCommercial-NoDerivatives 4.0 International License (CC BY-NC-ND)

species to fill their needs in the search space The first version of the particle swarm algorithm developed by James Kennedy and Russell Eberhart in 1995 (Kennedy & Eberhart, 1995). For RFM optimization the binary version of PSO (BPSO) is used, in which a population (swarm) is initialized randomly with values of {0,1}, this means that each particle in the population is a string of ones and zeros, with a "one" indicating the presence of the corresponding RPC coefficient in RFM and a "zero" indicating the absence of the corresponding RPC coefficient in RFM.

Each particle in BPSO is characterized by two fundamental parameters, namely the velocity and position (location), where the velocity of particle *i* is bounded between a minimum and maximum velocity [v_{min}, v_{max}], and is determined at the iteration (*t*) by using the following equation:

$$v_{ij}(t+1) = w(t)v_{ij}(t) + c_1 r_1 \left(P_{ij}(t) - x_{ij}(t)\right) + c_2 r_2 \left(Pg(t) - x_{ij}(t)\right) \quad (15)$$

Where:

***w*(t) :** is the inertia weight that changes over time

c1 , ***c2:*** are the acceleration factors.

i : is the index of a particle in the population.

j : is the index of bits in each particle.

***t* :** is the number of iterations.

r1 , ***r2*** : are two uniform random values in the range [0,1];

$\boldsymbol{P_g}$: denotes the best particle of the swarm

P : the best previous position of the i^{th} particle

x : is the present position (solution) of particle *i.*

Inertia weight is one of the important parameters of PSO algorithm, which is useful for balancing the algorithm. A nonlinear inertia weight (w) is used to adjust the effect of the current velocities in the computation of the new velocity values (Yavari et al., 2012). There is no universal inertia weight technique that can provide optimum efficiency for all engineering problems currently available (Too et al., 2019).

In this paper, we propose a new co-evolution Binary Particle Swarm Optimization with Multiple Inertia Weight for RFM optimization (CPSO-RFO). To solve the over-parameter in RFM and select the optimum RPC for RFM, a multiple inertia weight strategy was introduced, this is advantageous in terms of increasing diversity and avoiding the local optimum. Three inertia weight schemes were used in this study, and they are as follows:

$$w1 = 0.7 \quad (19)$$

$$w2 = 0.5 + \frac{\text{rand()}}{2} \quad (20)$$

$$w3 = w_{min} + (w_{max} - w_{min}).\frac{t_{max} - t}{t} \quad (21)$$

Creative Commons Attribution-NonCommercial-NoDerivatives 4.0 International License (CC BY-NC-ND)

Where : w_{max} and w_{min} are two constant experimental parameters, and t_{max} is the maximum number of iterations. In each iteration, we used a random selection technique to choose an inertia weight scheme (w) for each particle. The random selection strategy can be expressed mathematically as follows:

$$w = \begin{cases} w1, \text{if randi}([1,3],1) = 1 \\ w2, \text{if randi}([1,3],1) = 2 \\ w3, \text{if randi}([1,3],1) = 3 \end{cases} \quad (22)$$

RFM optimization aims to reduce the number of terms (RPCs) while maintaining adequate accuracy, the normalizing function should be designed more likely to omit terms rather than keep them. Indeed, the tangent hyperbolic function (***tanh***) is used as the normalizing function in our CPSO-RFO algorithm since it produces good results as shown in (Yavari et al., 2013) and the bits updating is done with it. Until a termination condition is met, the algorithm is updated repeatedly.

The position of each particle is updated as follow:

$$x_{ij}(t+1) = \begin{cases} 1, & \text{if } r_{ij} < \emptyset(v_{ij}) \\ 0, & \text{otherwise} \end{cases} \quad (23)$$

$$\emptyset(v_{ij}) = \begin{cases} \tanh(v_{ij}), & \text{if } v_{ij} > 0 \\ 0, & \text{otherwise} \end{cases} \quad (24)$$

We can summarize the steps of the proposed algorithm as follow:

1. The velocity of each particle is set to zero in the first step, and an initial population of N particles is randomly initialized (1 or 0).
2. Evaluate the fitness value of each particle.
3. Pbest and Gbest are set, Gbest is the overall best particle from all particles in population and Pbest is the best previous position of the i^{th} particle.
4. Apply the inertia weight scheme (*w*) depicted by Equation (22) and calculated using equations (19)-(21) to update the velocity in equation (15).
5. The fitness of each particle is then assessed in the next step. The Pbest and Gbest have also been updated again.
6. The algorithm is repeated until it reaches the maximum number of iterations which is the end criteria in this study.

IV. Experimental results & discussion

In this paper, we used an image over Winterthur city (Switzerland) consisting of 20 control points (CPs) acquired by the Algerian satellite ALSAT2. The distribution and the location of the CPs into the image are shown in fig.1. To assess the efficiency of the proposed algorithm, we work with the RFM version which has 78 parameters because it is used mostly in remote sensing; hence each particle is represented by a string of 78 binary values. The Root Mean

Creative Commons Attribution-NonCommercial-NoDerivatives 4.0 International License (CC BY-NC-ND)

Square Error (RMSE) is used as a cost function to evaluate the fitness of each particle given by this equation:

$$RMSE = \sqrt{\frac{\sum_{i=1}^{N}(x_i - \hat{x}_i)^2 + (y_i - \hat{y}_i)^2}{N}} \quad (25)$$

Where: N is the total number, x_i, y_i the estimated coordinate(x, y), $\hat{x}_i, \hat{y}_i$ denote the actual coordinate (x, y).

The set of CPs are divided into three groups:

1. Ground CPs (GCPs) are used in conjunction with Least Square method to calculate RFM coefficients.
2. The fitness value for each particle is calculated using Dependent Checkpoints (DCPs), and the cost function is defined as the RMSE of DCPs.
3. Independent Checkpoints (ICPs) are used to test the method's accuracy.

We chose some well-distributed GCPs and ICPs to test the proposed algorithm BPSO-RFO, so different combinations of GCP/ICP were chosen, 20% of the GCPs were chosen at random as DCPs to determine the particle's cost function. The quality of the results is determined by the RMSE measured over ICPs which determines the accuracy of the obtained results.

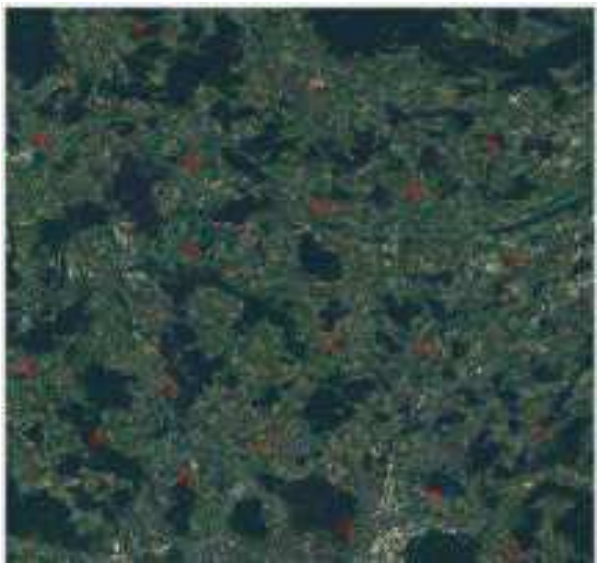

Fig.1. CPs location in Winterthur image.

The table below lists the parameters of the proposed algorithm.

Population size		30
v	v_{max}	+3
	v_{min}	-3
t_{max}		200
C1		1.5
C2		1.5

Creative Commons Attribution-NonCommercial-NoDerivatives 4.0 International License (CC BY-NC-ND)

Table1. Parameters of the proposed algorithm

To evaluate the performance of our algorithm, a comparison was conducted with conventional PSO in terms of accuracy and convergence speed. The tests were carried out using MATLAB software on a personal computer with an Intel Core i3 processor 2.40GHz and 8GB of RAM.

❖ ***The accuracy analysis***

As each execution of the meta-heuristic algorithms yielded a different result, the algorithm was executed 10 times, the best one with the lowest cost function was selected as the best and mentioned in table 2.

GCP/ICP	RMSE over ICPs		RMSE over GCPs		Number of RPC in P1, P2, P3, P4		Performance time (s)	
	CPSO-RFO	The conventional PSO	CPSO-RFO	The conventional PSO	CPSO-RFO	The conventional PSO	CPSO-RFO	The conventional PSO
15/5	0.9015	**0.8365**	**0.1594**	0.3305	9,3,7,2	8,4,8,5	**42.155202**	45.582184
12/8	**1.0120**	3.5756	**0.1736**	0.6151	5,3,6, 2	9, 5,10,3	**32.607638**	44.673478
10/10	**1.1717**	20.0519	**0.2398**	8.2241	5,3,5,2	9,3,11,3	**27.058844**	43.738477
8/12	**1.7355**	849.1055	**0.0463**	73.6354	3,2,4,3	11,11,8,13	**23.372941**	36.554056

Table2. The results obtained over Winterthur image.

As shown in table above, the value of RMSE demonstrates the high accuracy of the proposed method, CPSO-RFO can optimize the RFM to obtain subpixel accuracy when a few numbers of GCPs are used (15 GCPs), and 1.73 pixel in the worst case with just 8 GCPs. unlike the conventional PSO when the number of GCPs is less than 12 GCP the accuracy value degraded to 800 pixel with 8 GCPs this due to the stuck in local minima, according to the 8^{th} and 9^{th} column of Table 2. The CPSO-RFO algorithm achieve the good accuracy by using less total coefficients than conventional PSO in most cases, this is an important argument since, as compared to conventional PSO results, CPSO-RFO results have more degrees of freedom and are therefore more accurate. This is due to the multiple inertia weights used in CPSO-RFO which help them to minimize the number of RPC in the minimum with acceptable accuracy.

❖ **Convergence speed analysis**

The best run among the ten runs is chosen for convergence speed analysis in this section, fig.2 shows the convergence curve of the literature methods using a different combination of GCPs (15,12,10,8). The conventional PSO, as shown in fig.2(b), has a slower convergence than the CPSO-RFO (fig.2a), which is much faster with less than 20 iterations in all cases and confirm the performance time mentionned in (Table 2). Our algorithm performs well not only in terms of accuracy but also in terms of convergence speed.

Creative Commons Attribution-NonCommercial-NoDerivatives 4.0 International License (CC BY-NC-ND)

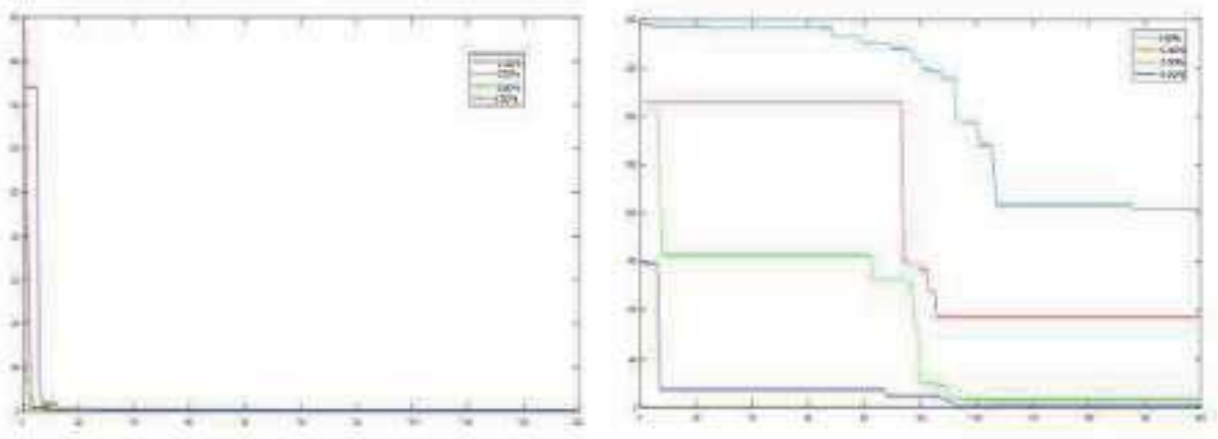

(a) (b)

Fig.2. The convergence curve: (a) CPSO-RFO method and (b) the conventional PSO

V. Conclusion

In this paper, we have presented a new co-evolution binary particle swarm optimization (CPSO-RFO) with a multiple inertia weight strategy to increase the accuracy of ortho-rectification by presenting the optimum RFM coefficients. Our tests showed that the CPSO-RFO was better than conventional PSO in terms of accuracy and convergence speed. Our algorithm shows significant performances due to the multiple inertia weight that does not just improve the accuracy but also the convergence speed.

The main advantage of CPSO-RFO is to provide satisfactory results with a limited number of GCPs (less than ten GCP) with a speed convergence (less than 20 iterations) which makes the proposed algorithm more suitable for photogrammetric and remote sensing applications.

References:

Belfiore O. R. and Parente C. (2016), *Comparison of Different Algorithms to Orthorectify WorldView-2 Satellite Imagery*. Algorithms, ***9*(4)**, 67. DOI: 10.3390/a9040067

Gholinejad S., Naeini A. A., and Amiri-Simkooei A. (2019), *Robust Particle Swarm Optimization of RFMs for High-Resolution Satellite Images Based on K-Fold Cross-Validation,* IEEE Journal of Selected Topics in Applied Earth Observations and Remote Sensing, ***12*(8)**, 2594–2599.

Jayaseeli J. D. D. and Malathi D. (2020), *An Efficient Automated Road Region Extraction from High Resolution Satellite Images using Improved Cuckoo Search with Multi-Level Thresholding Schema*. Procedia Computer Science, ***167***, 1161–1170.

Kennedy J. and Eberhart R. (1995), *Particle swarm optimization,* Proceedings of ICNN'95-International Conference on Neural Networks, 27 Nov.-1 Dec 1995, Perth, WA, Australia, 1942‑1948.

Long T., Jiao W., and He G. (2015), *RPC Estimation via l_1-Norm-Regularized Least Squares (L1LS),* IEEE Transactions on Geoscience and Remote Sensing, **53(8)**, 4554–4567.

Creative Commons Attribution-NonCommercial-NoDerivatives 4.0 International License (CC BY-NC-ND)

Moghaddam S. H. A., Mokhtarzade M., and Moghaddam S. A. A. (2018), *Optimization of RFM's Structure Based on PSO Algorithm and Figure Condition Analysis,* IEEE Geoscience and Remote Sensing Letters, **15(8)**, 1179–1183.

Tao C. and Hu Y. (2001), *A Comprehensive Study of the Rational Function Model for Photogrammetric Processing,* Photogrammetric Engineering and Remote Sensing, **67**, *1347-1357.*

Tao C. V. and Hu Y. (2001), *Use of the Rational Function Model for Image Rectification,* Canadian Journal of Remote Sensing, **27(6)**, 593–602.

Tengfei L., Weili J., Guojin H. (2014), *Nested Regression Based Optimal Selection (NRBOS) of Rational Polynomial Coefficients,* Photogrammetric Engineering and Remote Sensing. **80(3)**, 261-269.

Too J., Abdullah A. R., and Mohd Saad N. (2019), *A New Co-Evolution Binary Particle Swarm Optimization with Multiple Inertia Weight Strategy for Feature Selection, Informatics*, ***6*(2)**, 21.

Toutin T. (2010), *Review article: Geometric processing of remote sensing images: Models, algorithms and methods,* International Journal of Remote Sensing, **25(10)**, 1893-1924.

Yavari S., Zoej M. J. V., Mohammadzadeh A., and Mokhtarzade M. (2013), *Particle Swarm Optimization of RFM for Georeferencing of Satellite Images,* IEEE Geoscience and Remote Sensing Letters, ***10*(1)**, 135–139.

Yavari S., Zoej, M. J. V., Mokhtarzade M., and Mohammadzadeh A. (2012), *Comparison of Particle Swarm Optimization and Genetic Algorithm in Rational Function Model Optimization*, ISPRS - International Archives of the Photogrammetry, Remote Sensing and Spatial Information Sciences, **39B1**, 281–284.

Creative Commons Attribution-NonCommercial-NoDerivatives 4.0 International License (CC BY-NC-ND)

Algerian Journal of Engineering Architecture and Urbanism Vol. 5 Nr. 3 2021
ISSN: 2588-1760

STUDY AND CONTROL OF AERODYNAMIC FLOW IN AUTOMOTIVE VEHICLES

Brahim ROSTANE

Dr, laboratoire MECACOMP, Département de Génie Mécanique, Faculté de Technologie, Université de Tlemcen, Algerie. e-mail: *r_brahim75@yahoo.fr*

Abdelkrim BENMANSOUR

Dr,*département de physique, Faculté des sciences, Université de Tlemcen , 13000 Tlemcen, Algerie.* e-mail:*abdelkrim.benmansour@gmail.com*

Said ABBOUDI

Pr, laboratoire Interdisciplinaire Carnot de Bourgogne-UTBM, CNRS et Université de Bourgogne Franche Comté (UBFC), Dijon, France e-mail: *said.abboudi@utbm.fr*

Rima LAZZOUNI

Département de Génie Mécanique, Faculté de Technologie, Université de Tlemcen, Algerie.

Asma BOUZZIZA

Département de Génie Mécanique, Faculté de Technologie, Université de Tlemcen, Algerie.

Abstract:
This paper concerns the study of the flow around a simplified model of a cars . Numerical developments have enabled the identification of the topology of the flow and associated pressure coefficient.
The present work is based on a numerical analysis with FLUENT software. The turbulence model SST-kw is used for solving the Navier-Stokes equations averaged in order passive control by the spoiler and the angle of inclination of the rear window.
The Annalyse the results obtained it was concluded that the drag reduction (or increase the pressure coefficient) for the rear window is due to spoiler since it delayed the release, but its influence is not significant to improve the flow around the car knowing that the our study cars is already optimized because it is a sports cars.

Key words: *controle of the flow, drag, pressure coefficient, FLUENT, SST-Kω, passive controle*

Introduction:

The first phenomenological identifications and classifications associated with aerodynamic flows around motor vehicles appear shortly after the first oil crisis of 1973. At this time, the world became aware of the scarcity of petroleum products and the automobile industry rapidly sought to reduce the levels of petroleum products. Consumption exceeding 10 liters over 100 kilometers traveled for mid-range vehicles.

In this context and from 1976, industrial and research wind tunnels were made available to automobile manufacturers who then used them to try to reduce the aerodynamic drag of vehicles.

Improving the understanding of the physical phenomena required to work on simplified geometries capable of reproducing the complexity of flows and detachments encountered in automotive aerodynamics. It thus appears particularly important to better understand the unsteady physical mechanisms at the origin of detachments, the mechanisms linked to the vortex wake dynamics and to the interactions between the vortex structures.

Creative Commons Attribution-NonCommercial-NoDerivatives 4.0 International License (CC BY-NC-ND)

Reductions are obtained from a spoiler, flexible blade or deflector before being able to integrate the form recommendations resulting from the first feedback into the Design. this work is based on a digital study of flow control
on the rear of a generic basic motor vehicle model.
Passive control is the method used for the analyzer of the influence of rear window tilt angle and spoiler influence on flow topology and drag forces.

II. Geometry, boundary conditions and Numerical approaches:

For our study, we were inspired by a sports vehicle and we designed a simplified 2D model, the obstacle is placed in a rectangular digital vein (Fig.1) of length l = 2.7m and height h = 0.8m.

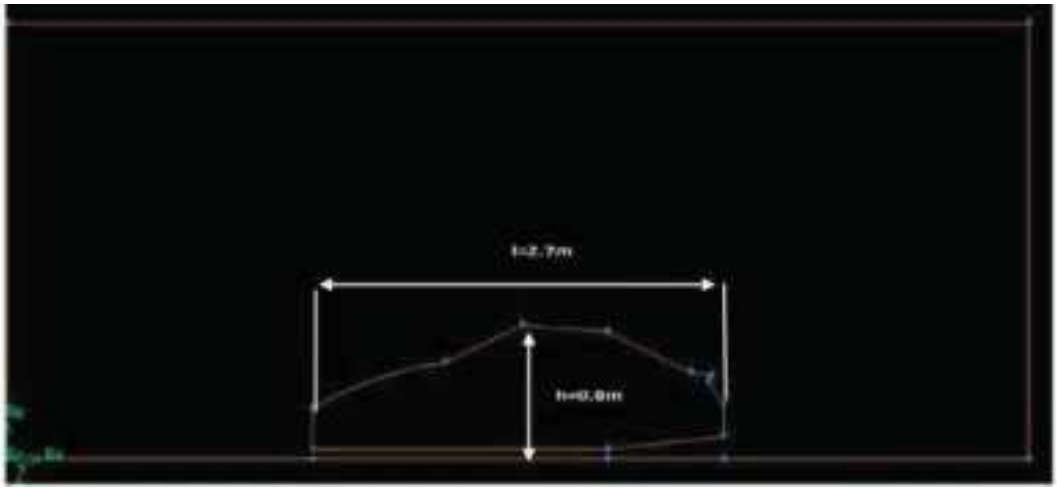

Fig1. DIMENSION OF THE CONSIDERED VEHICLE

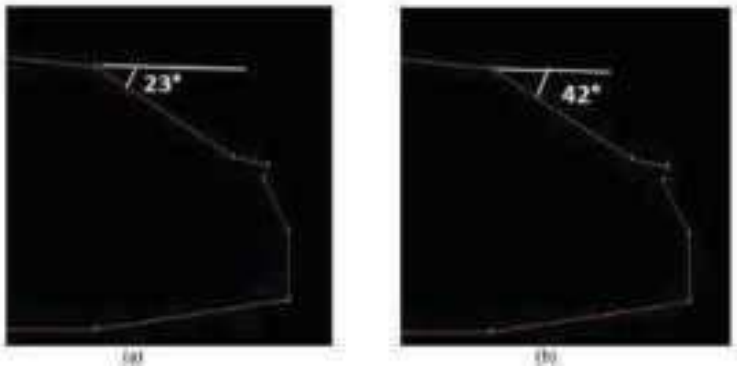

Fig2. DIFFERENT ANGLES OF THE REAR WINDOW: (a) α = 23 ° ,(b) α = 42 °

Creative Commons Attribution-NonCommercial-NoDerivatives 4.0 International License (CC BY-NC-ND)

Algerian Journal of Engineering Architecture and Urbanism Vol. 5 Nr. 3 2021
ISSN: 2588-1760

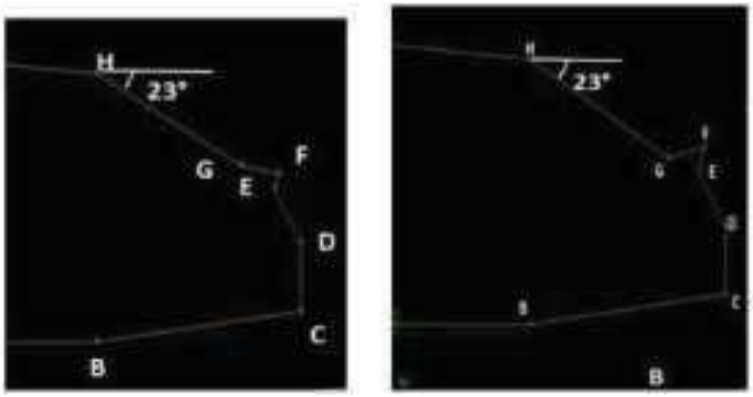

Fig3.SPOILER.

It was first varies the angle of the rear window (Fig.2).
We took our 1st geometry considered with α = 23 ° then we added a spoiler to the trunk, so our point (f) was raised by 3cm (Fig.3).

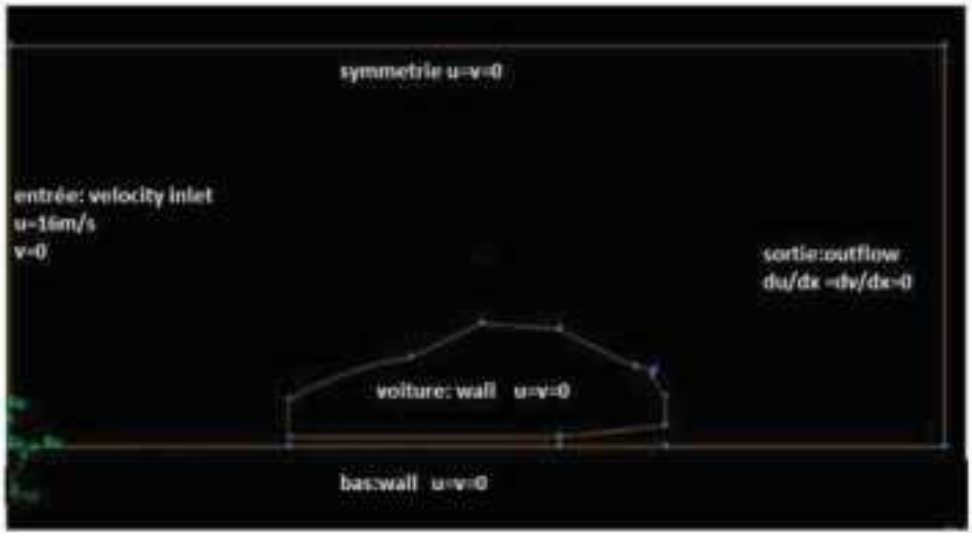

Fig4. BOUNDARY CONDITIONS

As shown in fig.4 the boundary conditions taken are:
The Input: velocity-inlet with a speed of 16m / s
The output: outflow
The top of the domain: symmetry
The bottom of the domain: wall
The car: wall.
The simulation study was carried out in unsteady mode with a time step Δt = 0.004s and a number of steps N = 200 steps.
The equations used in this study are Unsteady Reynolds Averaged Navier Stokes Equations (URANS) et and the turbulence model used is the The Shear Stress Transport Turbulence Model (Kω- SST).
the Urans equations were solved using the FLUENT code employing the finite volume method with a refined quadratic mesh near the solid walls

Creative Commons Attribution-NonCommercial-NoDerivatives 4.0 International License (CC BY-NC-ND)

The discretization scheme, the pressure interpolation method and the pressure-speed coupling method are summarized in table 1.

The discretization scheme	Seconde order upwind
The pressure interpolation	SIMPLE
The pressure-velocity coupling	SIMPLE

Table 1. CHOICE OF GRID CONFIGURATION AND RESOLUTION

Results and discussions:

1. Comparisons of streamlines

Fig. 5, 6 and 7 show the streamlines around the vehicle for the different configurations (α = 23 °, α = 42 ° and spoiler).

The second figure (Fig.5) shows us the detachment at the rear of the car with the appearance of three vortex zones A, B and C.

The second figure (Fig.6) shows us an amplification of the separation which is characterized by the appearance of three vortex structures at the rear of the car, one near the rear window (A1) and the other near the base (B1) and the last one

located a little further (C1) with a significant scope. Here we notice that the detachment zone is larger compared to the 1st case (Fig.5).

The third figure (Fig. 7) also shows the detachment at the rear of the car with the appearance of three vortex zones A2, B2 and C2.

Creative Commons Attribution-NonCommercial-NoDerivatives 4.0 International License (CC BY-NC-ND)

Algerian Journal of Engineering Architecture and Urbanism Vol. 5 Nr. 3 2021
ISSN: 2588-1760

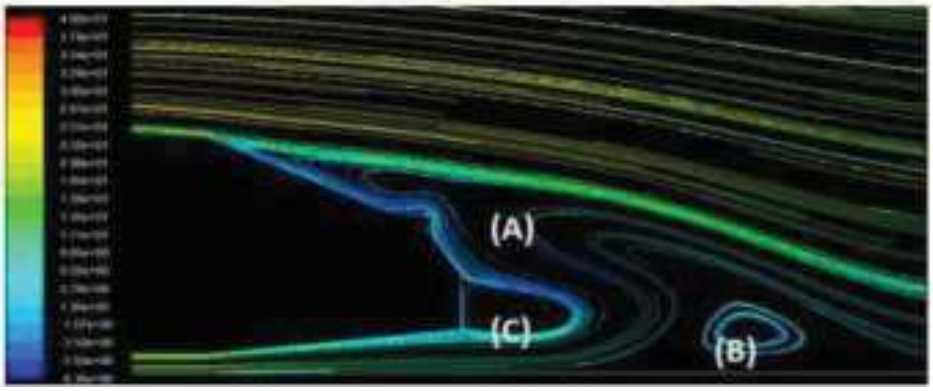

Fig5. STREAMLINES $\alpha = 23$ °

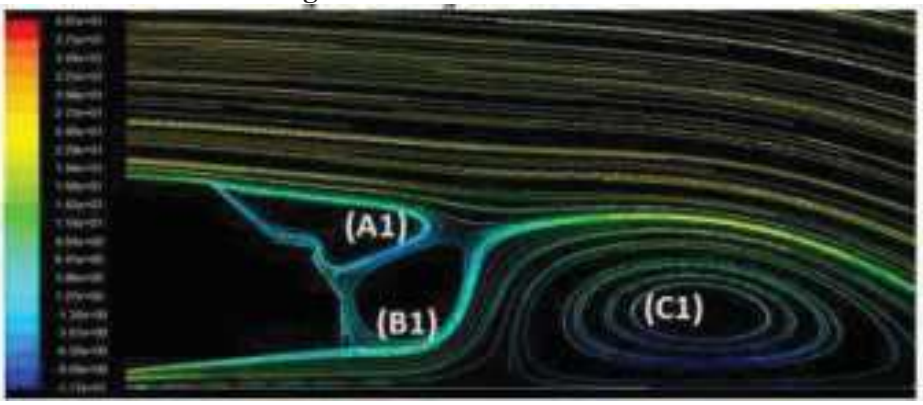

Fig6. STREAMLINES $\alpha = 42°$

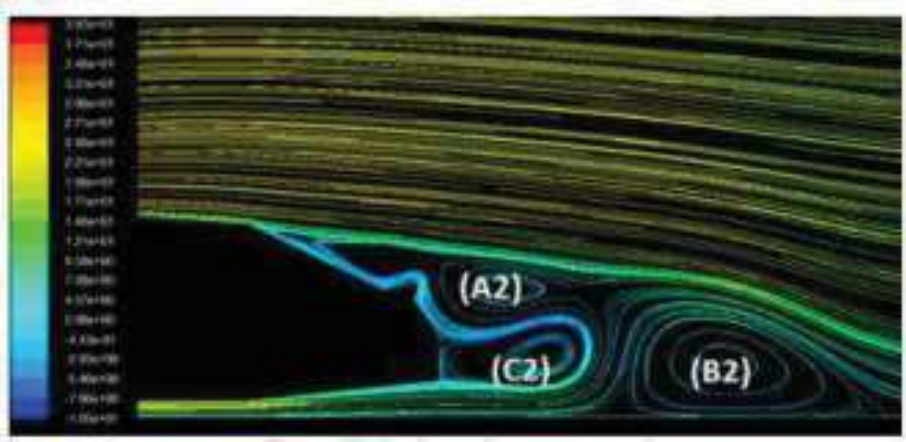

Fig7. STREAMLINES WITH SPOILER.

2 pressure coefficient (Cp)

The evolution of the static pressure generated at the surface of the geometry is due to the volume energy loss observed in the wake, this evolution is given in the form of the coefficient of static pressure Cp (Fig. 8 and fig.9).
The distribution of the coefficient cp on the rear window and the base are shown as a function of the dimensionless height (y / h).

Creative Commons Attribution-NonCommercial-NoDerivatives 4.0 International License (CC BY-NC-ND)

Algerian Journal of Engineering Architecture and Urbanism Vol. 5 Nr. 3 2021
ISSN: 2588-1760

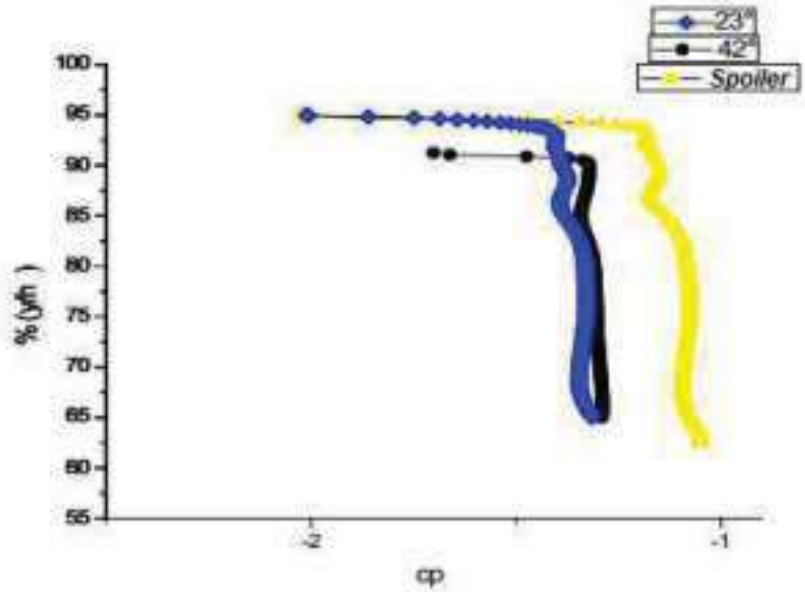

Fig 8. PRESSURE COEFFICIENT DISTRIBUTION ON THE REAR WINDOW FOR THE THREE CONFIGURATIONS.

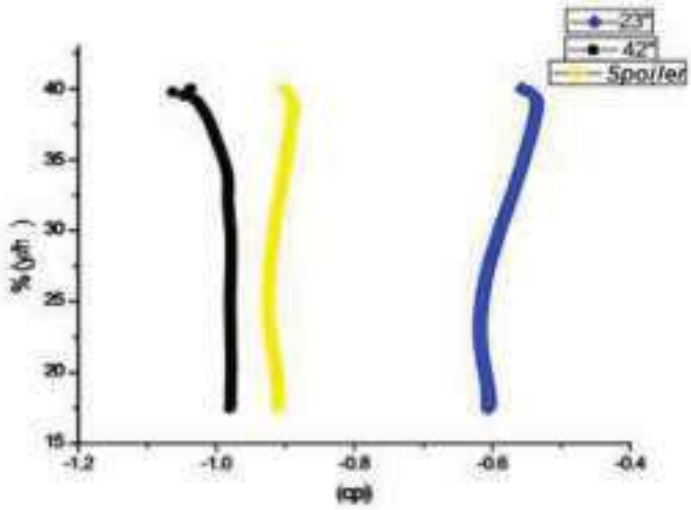

Fig 9. PRESSURE COEFFICIENT DISTRIBUTION ON THE BASE FOR THE THREE CONFIGURATIONS

Fig. 8 shows the distribution of cp along the rear window for the three configurations it varies between -2.2 and -1.3 for the 23 ° configuration and from -2.2 and -1.1 for the spoiler and from -1.8 and -1.3 for the configuration 42 °. This shows that the pressure coefficient is lower at the start of the rear window and this is due to the start of the separation of the flow. According to the figure of Cp for spoiler is more important than the other 23 ° and 42 ° configurations because the separation of the flow on the rear window is slightly delayed compared to the other two configurations.

Creative Commons Attribution-NonCommercial-NoDerivatives 4.0 International License (CC BY-NC-ND)

For the distribution at the base (Fig. 9), the values vary between -1.1 and -0.9 for 42 ° and -1 and -0.9 for the spoiler and between -0.7 and -0.5 for 23 °, so the pressure coefficient is greater for the case 23 ° and this is due to the presence of cavitation (low velocity implies high pressure).

Conclusion:

The aerodynamic study of a vehicle makes it possible to reduce its resistance to forward movement at speeds: the better its penetration into the air; the less the engine is required to maintain its speed and therefore, the less it consumes.

2D numerical exploration is done using the Fluent computer code. The digital model chosen is the RANS model using the SST-kw turbulence model.

For the rear window, we obtained an optimum pressure coefficient for the spoiler configuration, a cp = -1.1 therefore an increase of 16% of Cp which means that our drag has been reduced.

For the base we found that our geometry considered at the beginning is the best configuration with a Cp = -0.5.

it deduced the drag coefficient from the result of the pressure coefficient since our fluent gives an average drag coefficient of the car and since our study is only on the wake and the drag coefficient depends on Cp. If the pressure increases at wake this will create the 1st thrust for the car and therefore a reduction in drag force.

References:

Spohn A. , Gilliéron P. (2002), *Flow Separations Generated by a Simplified Geometry of an Automotive Vehicle,* Congress IUTAM Symposium on Unsteady Separated Flows, April 8-12, ,Toulouse, France.

Howard G.(1986) , *Aérodynamique automobile3 : Théorie et pratique* .(Aerodynamics, from theories to formula ones) – Paris : Editions E.P.A..

Faure T. (2008), *Dynamique des fluides appliquée : Applications à l'aérodynamique,* Édition DUNOD .

Eulali Y. (2014), *étude aérodynamique et contrôle de la trainée sur un corps d'Ahmed, culot droit*. Thèse de l'Université de Bordeaux.

Leclerc C., Levallois E. & Kourta A.(2006), Drag *reduction by synthetic jet : a 2D Numerical Study Around a Simplified Car*, AIAA 2006-3337.

Creative Commons Attribution-NonCommercial-NoDerivatives 4.0 International License (CC BY-NC-ND)

Algerian Journal of Engineering Architecture and Urbanism Vol. 5 Nr. 3 2021
ISSN: 2588-1760

IDENTIFICATION OF THE PARAMETERS OF THE DYNAMIC BEHAVIOR LAW OF AN AL6061-T6 ALUMINUM USING THE TAYLOR IMPACT TEST

Leila KERDJA
PhD student, Institute of Optics and Precision Mechanics, Laboratory of Applied Precision Mechanics 'LMPA' University Ferhat Abbas UFAS1, e-mail: kerdjaleila1@gmail.com

Yazid FIZI
Doctor of Engineering, Institute of Optics and Precision Mechanics, Laboratory of Applied Precision Mechanics 'LMPA' University Ferhat Abbas UFAS1, e-mail: fizi_yazid19@yahoo.fr

BOUALEM KESKES
Professor, Institute of Optics and Precision Mechanics, Laboratory of Applied Precision Mechanics 'LMPA' University Ferhat Abbas UFAS1,
e-mail : b_keskes@yahoo.fr

Abstract:
The objective of this work is to optimize by inverse analysis the mechanical behavior of an Al6061-T6 Aluminum under dynamic loads. The methodology proposed to identify the behavior law is based on the combination of experimental tests, finite element and optimization. In a first step, numerical results of Taylor impact tests performed according to the classical analysis have been presented. In a second step, numerical simulations of the impact tests coupled with a finite element calculation and an optimization algorithm to identify the different parameters of the Johnson-Cook behavior law were performed. Concerning the projectile profiles, the numerical results using the optimal parameters of the mechanical behavior present a good consistency with the experimental results presented in the literature.

Key words: Taylor test, inverse analysis, finite elements, Johnson-Cook model

Introduction:

The characterization of the behavior of materials under dynamic loads is one of the current concerns, which are the subject of much advanced work, in the context of the development of numerical and experimental tools. For the explicit numerical simulation of a high strain rate event requires the use of a constitutive material model and its associated material parameters, including the models: Johnson-Cook model [1], the modified Johnson-Cook model [2], and the Cowper-Symonds model [3]. These models predict the deformation and damage process of components and structures at strain rates applied during an event. Engineers and scientists working on these types of simulations must overcome the difficult task of extracting material parameters from a constitutive model, based on experimental techniques. Thus, the challenge is to choose an appropriate combination of an experimental technique and an optimization procedure to determine the most suitable set of material parameters that describes their mechanical behavior. Sasso et al [4] determined the material parameters of the Johnson-Cook and Zerilli Armstrong constitutive model for steel from experimental Split Hopkinson pressure tests. They used a finite element model of the test and an optimization module to fit the material constants. Milani et al [5] presented a multi-objective identification strategy to estimate the parameters of the Johnson-Cook constitutive

Creative Commons Attribution-NonCommercial-NoDerivatives 4.0 International License (CC BY-NC-ND)

model. They used data from Split Hopkinson pressure bar tests with varying temperatures and strain rates as a characterization strategy. Shrot et al [6] presented an inverse identification method of Johnson Cook parameter based on the Levenberg- Marquardt algorithm. They created a finite element model for high-speed machining using a particular set of Johnson-Cook parameters to describe the material behavior. The goal of this method is to re-identify the original set of Johnson-Cook parameters by examining chip morphology and cutting force. The Taylor test is still often used to study the mechanical behavior of materials under high strain rate loading conditions. Recently, the final deformed geometry of an impact specimen from this test has been used with numerical simulations and inverse analyses to determine the constitutive parameters of the materials [7,8]. Similarly, Hernandez et al [9] combined a genetic algorithm optimization method with a numerical model to determine Cowper-Symonds material model parameters from the deformed shape of the specimens. Acosta et al [10] validated the constitutive parameters of AISI 1010 steel materials found by inverse analysis from Taylor tests. They compared the Vickers hardness profile along the axis of a deformed specimen and the numerically calculated hardness from a Taylor impact finite element model, which uses the constitutive parameters found by inverse analysis. Piao et al [11] proposed a new method to obtain reliable hardening behavior at ultra-high strain rates through an inverse optimization process by comparing the results of numerical simulation including the thermal softening effect at different strain rates with the experimental results of sequentially deformed shapes of a projectile during the Taylor impact test. Nistor et al [12] proposed a procedure for identifying the parameters of the Johnson-Cook behavior law for 42CrMo4 steel and 2017-T3 aluminum. This work then led to further developments in the work conducted by Lu Ming [13]. Taylor impact tests were used to conduct high strain rate compression experiments, and the difference between the numerically deformed shape and the experimentally deformed shape was minimized by a combined Monte-Carlo and Levenberg-Marquardt algorithm.

Problematic:

Nowadays, the modeling of mechanical behavior is becoming more and more important in the process of product design and in the definition of safety criteria for structures. A major problem in the process lies, on the one hand, in the choice of the behavior law and, on the other hand, in the identification of the parameters of this law.

The main objective of this study is to determine the parameters of the Johnson-Cook model for Aluminum Al6061-T6 from the deformed shape of a projectile during the Taylor impact test. The optimization procedure used in this work is described in Fig1.

Creative Commons Attribution-NonCommercial-NoDerivatives 4.0 International License (CC BY-NC-ND)

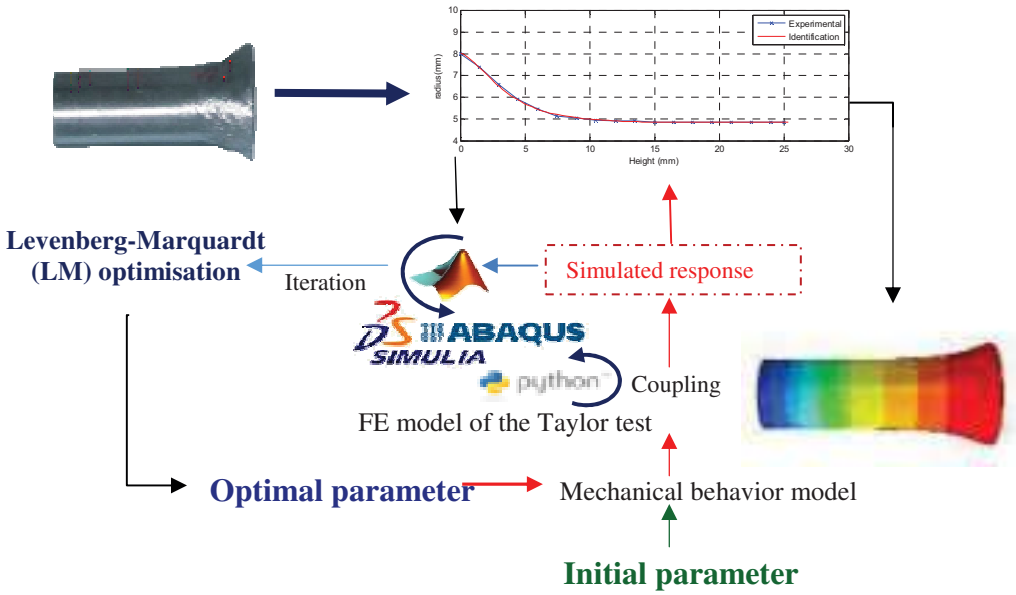

Fig1. The optimization procedure used to determine the material's mechanical properties from the Taylor test

Materials and methods:

1.Taylor impact test:

The Taylor test [14 ,15] was developed as an experimental method for measuring the dynamic yield strength of metallic materials at high strain rates, reaching strain rates in the range of $10^4 S^{-1}$ to $10^6 S^{-1}$The test consists of impacting a straight circular cylinder, at a known velocity, against a rigid barrier. The experimental work used in this paper was presented in detail by Konokman et al [16] the projectiles are made of 6061-T6 aluminum and have a nominal length of 30 mm and a nominal diameter of 9.7mm. A compressed gas gun was used to accelerate the projectiles in an impact chamber at velocities up to 300 m/s. Fig7 shows the experimental results for different impact velocities.

2.Finite element model:

A 3D numerical model of the Taylor impact test was implemented in the ABAQUS code using an explicit solution strategy, based on the experimental test. A cylindrical rod, measuring 30 × 4.85 mm, impacts a rigid wall at an initial velocity of v =250 m/sec applied to the nodes of the specimen. The rod is meshed with C3D8R elements and the wall is modeled as a rigid surface and the contact frictionless. The material model used to represent the mechanical behavior of the Taylor sample was the Johnson-Cook model.

Creative Commons Attribution-NonCommercial-NoDerivatives 4.0 International License (CC BY-NC-ND)

Algerian Journal of Engineering Architecture and Urbanism Vol. 5 Nr. 3 2021
ISSN: 2588-1760

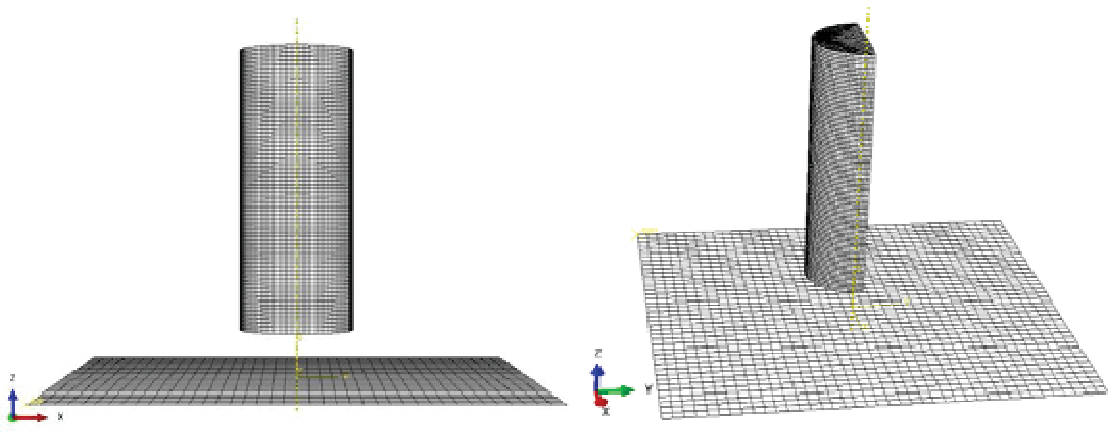

Fig2. Finite element model of the Taylor impact test

The model that is chosen for the study (Eq.1) is in the form:

$$\sigma = \left[A+B\left(\varepsilon^{pl}\right)^{n}\right]\left[1+C\ln\left(\frac{\dot{\varepsilon}^{pl}}{\dot{\varepsilon}_0}\right)\right]\left[1-\left(\frac{T-T_0}{T_f-T_0}\right)^{m}\right] \quad \text{Eq.1}$$

Where ε^{pl} is the plastic deformation, $\dot{\varepsilon}^{pl}$ is the strain rate, $\dot{\varepsilon}_0$ is the reference strain rate, A, B, n, C, m are the constants dependent on materials, T is the temperature of the material, T_0 is the ambient temperature et T_f is the melting point of the material.

In addition, extremely high plastic stresses develop at the crushed end of the rod, resulting in severe local mesh distortion. Adaptive mesh is used to reduce the element distortion and to obtain an accurate and economical solution to the problem.

Density ρ (kg. m^{-3})	2700
Elastic modulus E (GPa)	70
Poisson's ration ν	0.3
Specific heat C_v (J/kg K)	896
Yield strength A (MPa)	300
Hardening coe□cient B (MPa)	290
Strain-hardening exponent n	0.3
Strain rate C	0.02
Softening exponent m	1
Melting temperature T_f (K)	925.4
Reference temperature T_0 (K)	294.2
Reference strain rate (s^{-1})	1.0

Table 1. Material properties of the metal used in this simulation.

3. An optimization procedure for determining material properties:

Creative Commons Attribution-NonCommercial-NoDerivatives 4.0 International License (CC BY-NC-ND)

In this study, we used a nonlinear optimization technique using MATLAB®, which provides an excellent interface to finite element codes such as ABAQUS®. Analysis based on the Levenberg-Marquardt (LM) inverse method [17] is used to estimate the material properties. The use of this method in this work is illustrated by the flowchart shown in Fig1. From the modeling of the Taylor test in finite elements, the software allows to write the function (difference between the predictions of the model and the test results) to be minimized.

In this work, the objective is the identification of the parameters of the Johnson-Cook model. For this model, four parameters have to be determined; the material yield strength A, the strain hardening modulus B, the strain rate sensitivity parameter C and the strain hardening coefficient n. For simplicity, the value of the parameter m concerning the influence of temperature, has not been taken into account for the identification. The initial values of A, B, C and n were chosen arbitrarily. The optimization algorithm is used to determine the mechanical properties, using an iterative procedure to produce the best fit between the experimental Taylor impact data and the optimized Taylor impact data produced by the finite element analysis. The method consists of minimizing the mean square error on the Taylor test profile using an optimization method. The "Lsqnonlin" function of MATLAB® [18] was used for this study. This function allows to find the coefficients U that minimize the squared error J(U) between the experimental and calculated values. U is the vector of parameters of the behavioral laws. This problem can be formulated as follows:

$$J(U) = \frac{1}{2}\sum_{i=1}^{N}[P_i^{EF}(U) - P_i^{EXP}]^2$$

Where, P_i^{EF} and P_i^{EXP} represent the simulated and experimental Taylor test profile respectively, n is the number of experimental points and U is a vector that contains the unknown parameters, $U^T = [A, B, C, n]$. The material parameters that lead to the best agreement can be considered as the mechanical behavior law of the material.

Results and discussions:

1.Taylor impact procedure:

The Taylor impact can be decomposed into several steps (Fig3). The deformation process during specimen / target contact induces an increase in stress, the stress exerted first leads to elastic deformation of the specimen. Once the yield strength is reached, the material will deform plastically.

Creative Commons Attribution-NonCommercial-NoDerivatives 4.0 International License (CC BY-NC-ND)

Algerian Journal of Engineering Architecture and Urbanism Vol. 5 Nr. 3 2021
ISSN: 2588-1760

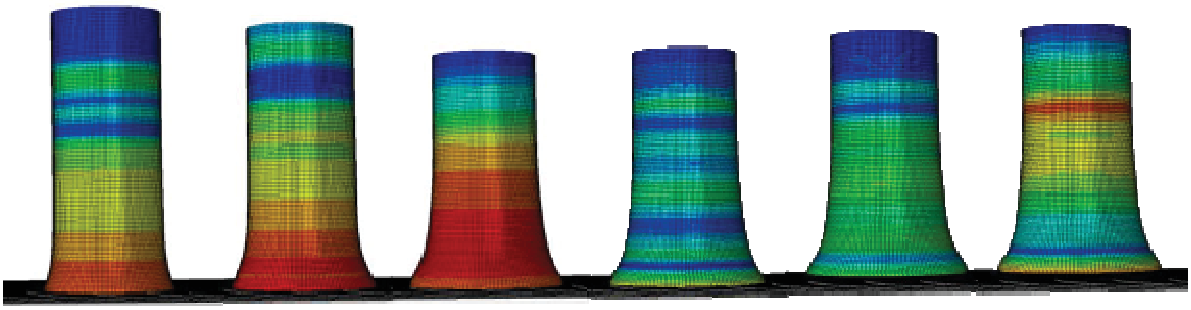

Fig3. Morphological evolution during the impact of an Al6061 -T6 projectile at *250 m.s*$^{-1}$.

From the instant t = 51µs, the deformation indicates that the specimen has rebounded.A follow-up of the evolution of the kinetic energy of the specimen during the impact, makes it possible to identify this instant t where the minimum of the energy is reached (Fig4.).

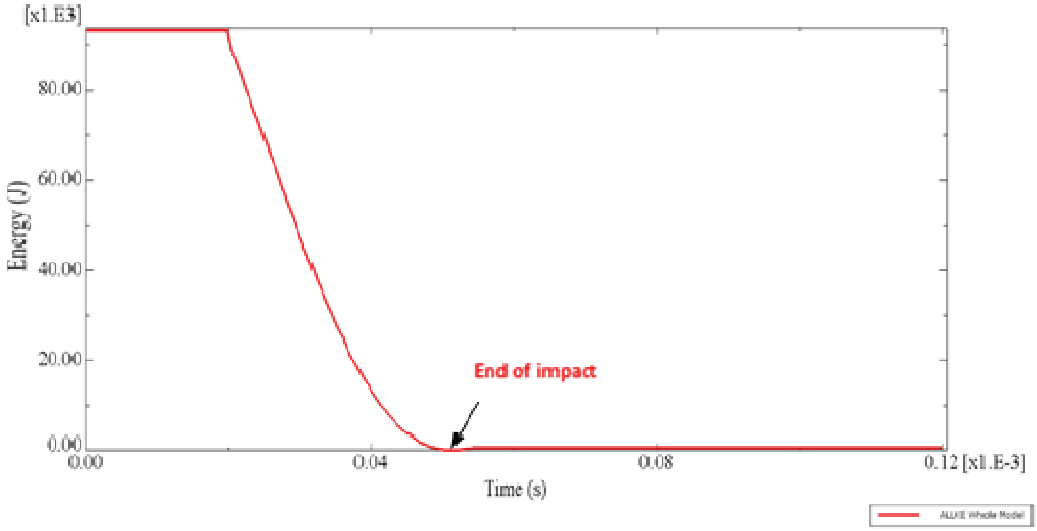

Fig4. Evolution of the kinetic energy during the impact of an Al60611 -T6 projectile at 250 m.s^{-1}.

The simulation shows that the impact induces a zone of high deformation on the impact surface (Fig5.a). This zone corresponds to the one undergoing the maximum stress (Von-Mises). The finite element calculation determines the length L_f and the diameter D_f after the impact. We notice that, at the end of the impact, the ratio of L_0/L_f and D_0/D_f are 1.148 and 0.776, respectively. Figure (5.b) shows the deformation of a projectile after the Taylor impact for a speed of 250m/s.

Creative Commons Attribution-NonCommercial-NoDerivatives 4.0 International License (CC BY-NC-ND)

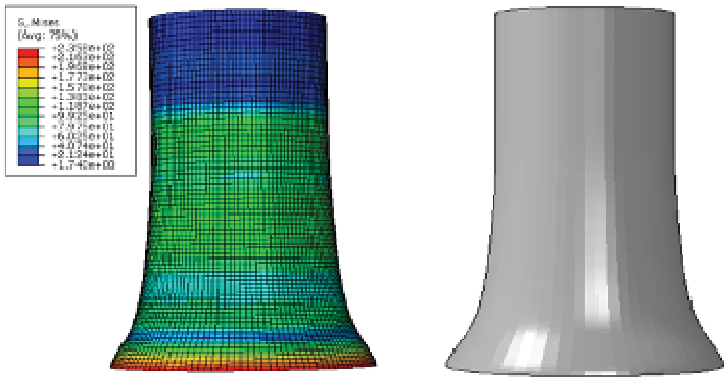

Fig5. Numerical results: a) Von-mises stress contours, b) projectile deformation

1.1 Effect of impact velocity:

Changing the velocity of the projectiles results in a change in its kinetic energy. A different equivalent stress is observed for different impact velocities used (Fig6.). The higher the impact velocity, the higher the specimen deformation. During impact, a tangential stress deforms the specimen laterally. A strong specimen stress is then present resulting in a strong deformation. We find that with the change in impact velocity from 250 to 288 m/s, the equivalent stress increases from 235.8 to 405.1 MPa.

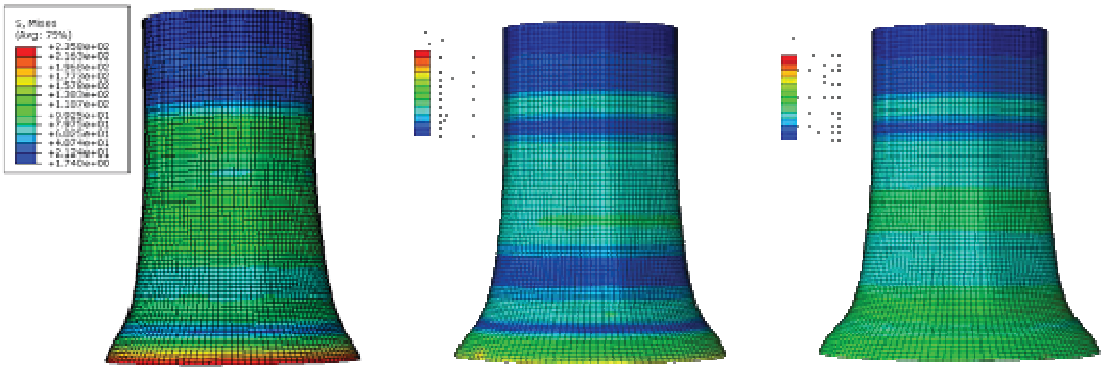

Fig6. Numerical results in Von-mises stresses (MPa) for different impact velocities

1.2 Validation of the numerical model:

The validation of the numerical model is based on the experimental work presented by Konokman et al [16]. Fig7 shows the comparison of the projectile morphology after impact between the experimental and numerical results for different impact velocities. The experimental and numerical values of L0/Lf ratio show that the maximum deviations are 4.25 %, 3.86 % and 1.48 % for an impact velocity of 250, 275 and 288, respectively.

Creative Commons Attribution-NonCommercial-NoDerivatives 4.0 International License (CC BY-NC-ND)

Algerian Journal of Engineering Architecture and Urbanism Vol. 5 Nr. 3 2021
ISSN: 2588-1760

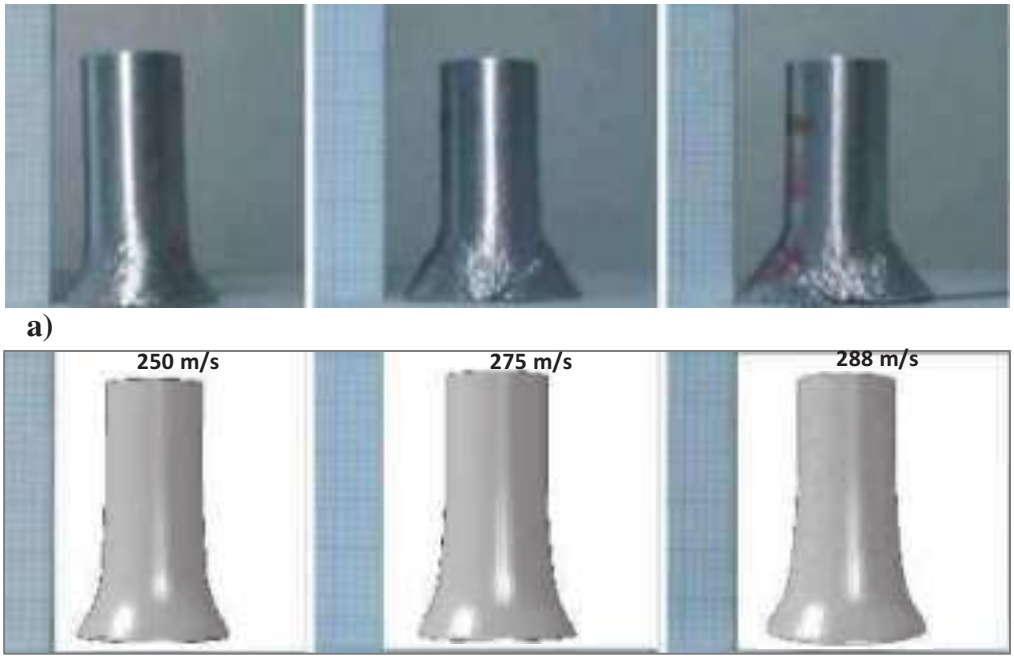

Fig7. Comparison of projectile deformation for different impact speeds: a) experimental result [16], b) numerical result.

For the experimental results, shear cracks were observed with the initial velocities of 275 and 288 m/s, on the other hand the deformation was carried out without rupture during the course of calculation. This can be explained by the absence of the damage criterion during the simulation.

2. Results of identification procedures:

In order to minimize the deviation between numerical and experimental results, we used the optimization technique proposed in section 1. The optimization of the desired parameters is obtained after 19 iterations. Fig8.b shows the numerical response of the profile evolution of the Taylor test for different iterations.

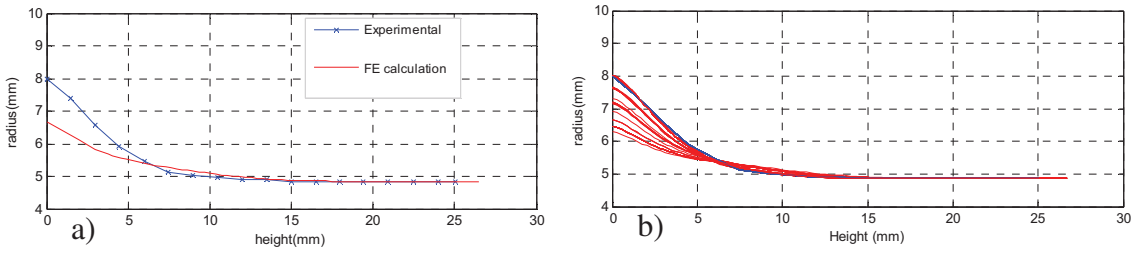

Fig8. Comparison between experimental and simulation data: a) initial profile b) profiles for different numbers of iterations

Creative Commons Attribution-NonCommercial-NoDerivatives 4.0 International License (CC BY-NC-ND)

Fig9 shows the experimental profile and the simulated profile after the identification of the parameters of the law of behavior. A good consistency between the experimental profile and the corresponding predicted profile is observed. The results of the identification procedures are presented in Table 2.

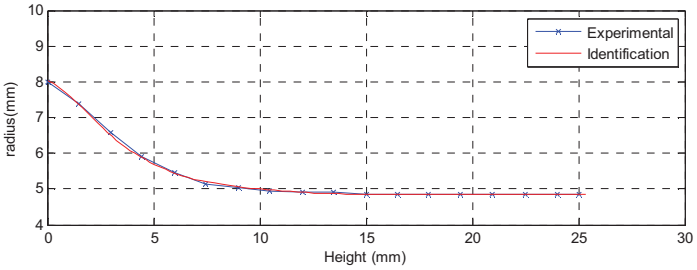

Fig9. Comparison between experimental [16] and simulation data for the projectile profile

Fig10. Comparison of impact morphology between the experimental observation [16] and the numerical result

	A (MPa)	B (MPa)	n	C	Gap(Difference)
Initial values	300	290	0.3	0.02	$2.68.10^{-3}$
Valeur optimales	289.4	203.12	0.305	0.019	

Table 2. Results of identification procedures.

From the numerically identified parameters of the behavior law, the variations of stresses and strains can be determined by FE simulation. Fig11 and Fig12 show the contour of the equivalent strain and stress with the use of the parameters of the optimal behavior law.

Fig11. Contour of the equivalent plastic

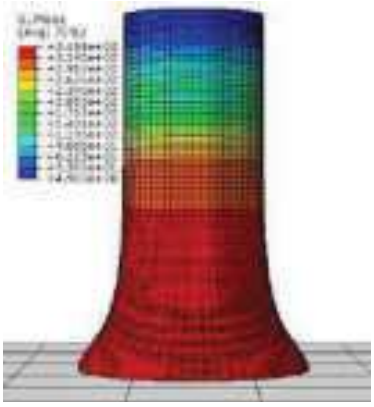

Fig12. Contour of the equivalent Von-mises stress

Conclusion :

Creative Commons Attribution-NonCommercial-NoDerivatives 4.0 International License (CC BY-NC-ND)

To characterize the behavior of metallic materials under dynamic loads, a parametric identification procedure consisted of numerical and experimental tools was developed. une application sur l'aluminium Al6061-T6 à a été présentée dans ce document en déterminant les paramètres de la loi de visco-plasticité de Johnson-Cook à partir de la forme déformée d'un projectile pendant l'essai de choc de Taylor. The results obtained during the identification show the effectiveness of this identification procedure.

References:

[1] **Johnson GR., WH Cook.** (1983), A constitutive model and data for metals subjected to large strains, high strain rates and high temperatures. In: Proceedings of the 7th International Symposium on Ballistics. The Netherland: The Hague;.p. 541–7.

[2] **Kang W., Cho S., Huh H., Chung DT. (**1999), Modified Johnson–Cook model for vehicle body crashworthiness simulation. Int J Veh Des: 4(4):424–35.

[3] **Cowper G., Symonds P.** (1957), Strain hardening and strain-rate effects in the impact loading of cantilever beams, Tech. Rep., Brown University Divisionof Applied Mathematics.

[4] **Sasso M., Newaz G., Amodio D.** (2008), Material characterization at high strain rate by Hopkinson bar tests and finite element optimization, Mater. Sci. Eng.: A 487 (1–2) 289–300.

[5] **Milani A., Dabboussi W., Nemes J., Abeyaratne R.** (2009), An improved multi-objective identification of Johnson–Cook material parameters, Int. J. Impact Eng.36 (2) 294–302.

[6] **Shrot A., Bäker M.** (2012), Determination of Johnson–Cook parameters from machining simulations, Computational Materials Science 52 298–304.

[7] **Grazka M., Janiszewski J.** (2012), Identification of Johnson-cook equation constants usingfi-nite element method, Eng. Trans. 60 (3) 215–223.

[8] **Šlais M., Dohnal I., Forejt M.** (2012), Determination of Johnson-cook equation parameters, Acta Metall. Slovaca 18 (2–3) 125–132.

[9] **Hernandez C., Maranon A., Ashcroft I., Casas-Rodriguez J.** (2013), A computational determi-nation of the cowper–symonds parameters from a single Taylor test, Appl. Math. Model. 37 (7) 4698–4708.

[10] **Acosta C., Hernandez C., Maranon A., Casas-Rodriguez J.** (2016), Validation of material constitutive parameters for the AISI 1010 steel from Taylor impact tests, Materials and Design 110 324–331.

[11] **Piao M., Huh H., Lee I., Ahn K., Kim H., Park L.** (2016), Characterization offlowstress at ultra-high strain rates by proper extrapolation with Taylor impact tests, Int. J. Impact Eng.V91 142–157.

[12] **Nistor I., Pantalé O., Caperaa S., Sattouf C.** (2003), Identification of a dynamic viscoplastic flow law using a combined levenberg-marquardt and monte-carlo algorithm. In VII International Conference on Computational Plasticity, COMPLAS.

[13] **Ming L.** (2018), A numerical platform for the identification of dynamic non-linear constitutive laws using multiple impact tests: application to metal forming and machining. Thèse Université de Toulouse.

[14] **Taylor G.** (1948), The use of flat-ended projectiles for determining dynamic yield stress. I. Theoretical considerations. Proc. R. Soc. London Ser. A 194, 289–299.

[15] **Carrington W., Gayler M**. (1948), The use of flat-ended projectiles for determining dynamic yield stress. III. Changes in microstructure caused by deformation under impact at high-striking velocities. Proc. R. Soc. London, Ser. A 194, 323–331.

[16] **Emrah Konokman H., Murat Çoruh M. Altan K.** (2011), Computational and experimental study of high-speed impact of metallic Taylor cylinders, Acta Mech (220), 61–85.

[17] **Marquardt D.** (1963), An Algorithm for least squaresestimation of nonlinear parameters, J. Soc. Ind. Appl. Math., 11, pp. 431-441.

[18] **Matlab** (2008) Optimisation Toolbox TM4 Users (T.M.Inc.).

Creative Commons Attribution-NonCommercial-NoDerivatives 4.0 International License (CC BY-NC-ND)

Algerian Journal of Engineering Architecture and Urbanism Vol. 5 Nr. 3 2021
ISSN: 2588-1760

DIGITAL IMPLEMENTATION OF MULTICELL SERIAL CONVERTER

Ismail BOUYAKOUB
Dr. Electrical Engineering Department, Hassiba Benbouali University, Chlef, Algeria
Laboratoire Génie Electrique et Energies Renouvelables (LGEER)
ism.bouyakoub@gmail.com

Rachid TALEB
Prof. Electrical Engineering Department, Hassiba Benbouali University, Chlef, Algeria
Laboratoire Génie Electrique et Energies Renouvelables (LGEER)
rac.taleb@gmail.com

Maamar SOUAIHIA
Dr. Electrical Engineering Department, Hassiba Benbouali University, Chlef, Algeria
Laboratoire Génie Electrique et Energies Renouvelables (LGEER)
m.souaihia@univ-chlef.dz

Izzeddine CHERCHAR
Mr. Electrical Engineering Department, Hassiba Benbouali University, Chlef, Algeria
Laboratoire Génie Electrique et Energies Renouvelables (LGEER)

Wissam NABED
Ms. Electrical Engineering Department, Hassiba Benbouali University, Chlef, Algeria
Laboratoire Génie Electrique et Energies Renouvelables (LGEER)

Abstract:
This article deals with multicellular converters. This new structure of energy conversion is now present in different fields of applications. Therefore, due to these important characteristics, it was able to compete with other multi-level structures and allowed to consider a much wider field of applications and can be adapted to all conversion configurations.

Our goal is to make a three-cell inverter. After the general presentation of multi-level converters and their different topologies, the article is divided into two parts. The first part proposes on the control and the structure of the floating capacitors followed by the simulation of the multicellular inverter. In the second part, a test bench of this inverter is carried out, the stages of realization are detailed. Finally, a general conclusion summarizing the validation of the results obtained in the two parts is presented.

Key words: Multicellular converter, PWM control, Dspace DS1104, THD.

Introduction:

Depuis de nombreuses années dans le domaine de l'électronique de puissance, nous assistons à une augmentation sans cesse des puissances commutées par les convertisseurs statiques afin de répondre aux exigences industrielles.

Ces convertisseurs de puissance sont utilisés comme des interfaces entre la source et la charge. Ils permettent d'adapter la puissance nécessaire à celle consommée. A partir d'une source d'énergie brute, ils doivent alimenter les différents circuits en énergie avec un flux

Creative Commons Attribution-NonCommercial-NoDerivatives 4.0 International License (CC BY-NC-ND)

maîtrisé et adapté aux conditions de fonctionnement. Un intérêt remarquable a été donc donné à l'amélioration des convertisseurs de puissance. En effet, la dernière décennie a été marquée par des avancées technologiques sans précédents dans le domaine de l'électronique de puissance : apparition de nouveaux interrupteurs capables de commuter rapidement et supportant une grande tension et un grand courant, apparition de nouvelles structures de conversion (structures multiniveaux), (Vizzaccaro, Armando, Pellegrino, & Savio, 2018) et développement de nouvelles stratégies de commande.

Une nouvelle topologie de convertisseurs apparue au début des années 90, les convertisseurs multicellulaires série. Cette structure est basée sur la mise en série de cellules de commutation entre lesquelles une source de tension flottante est insérée. La structure multicellulaire série a permis d'envisager un champ d'application beaucoup plus vaste, et peut être adaptée à toutes les configurations de conversions.

En effet, en entrelaçant des signaux de commande, les tensions aux bornes des condensateurs flottantes s'équilibrent, c'est le phénomène d'équilibrage nature. Il a pour effet la réduction des contraintes en tension sur chaque interrupteur, et d'augmenter le nombre de niveaux en sortie de bras, cette structure permet aussi d'améliorer les formes d'ondes en sortie et notamment le contenu harmonique en utilisant un déphasage adéquat des ordres de commande (Yodwong, Guilbert, Kaewmanee, & Phattanasak, 2019).

Cette régulation est assurée par une commande convenable. Il existe une commande en boucle ouverte très simple permettant d'assurer la stabilité de ce convertisseur. Elle est connue sous le nom de commande MLI (Modulation de Largeur d'Impulsions). Cette commande permet l'équilibrage naturel des tensions aux bornes des condensateurs.

L'objectif de ce travail est de simuler un onduleur à 3 cellules commandé par la commande MLI et réaliser une maquette de celui-ci avec la carte Dspace DS1104

Problématique :

1- Le modèle instantané de l'onduleur

Le modèle exact ou instantané prend en compte les commutations des interrupteurs et les grandeurs instantanées des variables d'état du convertisseur. Il permet de représenter l'état de chacune des cellules de commutation du convertisseur à l'échelle de la période de découpage et les phénomènes harmoniques liés à la commutation des interrupteurs (Abraham & Jose, 2018).

Ce modèle est utilisé pour valider en simulation des lois de commande mises en œuvre à partir du modèle moyen. La figure ci-dessous présente un convertisseur multicellulaire série fonctionnant en onduleur associé à une charge R-L. L'onduleur est dit à point milieu de la source de tension. Ce convertisseur représente une association de p cellules de commutation.

Creative Commons Attribution-NonCommercial-NoDerivatives 4.0 International License (CC BY-NC-ND)

Algerian Journal of Engineering Architecture and Urbanism Vol. 5 Nr. 3 2021
ISSN: 2588-1760

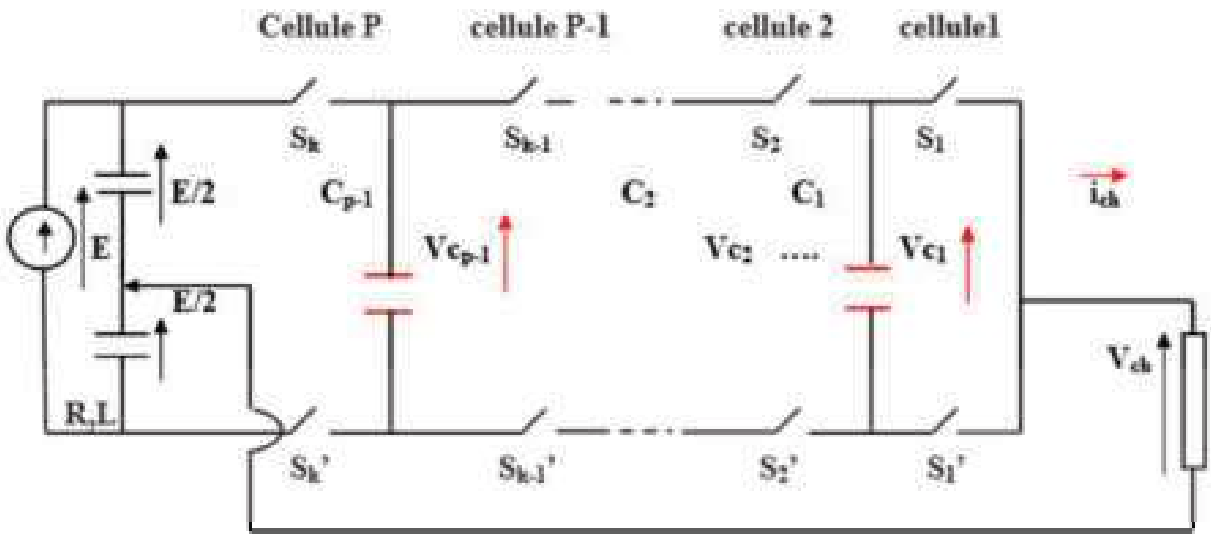

Fig1. Onduleur à p cellules associé à une charge R-L.

Le modèle instantané représentant un bras multicellulaire série à p cellules fonctionnant en onduleur associée à une charge R-L.

L'évolution de la tension aux bornes du condensateur C_k est liée à l'évolution du courant i_{Ck}, ce dernier étant fonction des deux cellules adjacentes et du courant i_{ch}, le courant de charge d'un condensateur C_k est fonction des signaux de commande u_{k+1}et u_k :

$$\boldsymbol{i_{ck} = (u_{k+1} - u_k) * i_{ch}} \quad (1)$$

La tension aux bornes du condensateur C_k est liée au courant i_{Ck} par :

$$\boldsymbol{i_{Ck} = C_k \frac{dv_{Ck}}{dt}}$$

Donc, il vient :

$$\boldsymbol{\frac{dv_{Ck}}{dt} = \frac{(uk+1 - uk) * i_{ch}}{C_k}} \quad (2)$$

Cette équation est généralisée aux (p-1) condensateurs flottants.

D'après la loi des mailles, la tension de sortie Vch est la somme des tensions aux bornes des interrupteur Sk' diminuée de E/2. Ces tensions sont définies par :

$$V_{Sk}' = (v_{Ck} - v_{C(k-1)}) * u_k \quad (3)$$

D'où la tension aux bornes de la charge V_{ch} :

$$V_{ch} = \sum_{k=1}^{p} VSk' - E/2 = \sum_{k=1}^{p} (v_{Ck} - v_{C(k-1)}) * u_k - E/2 \quad (4)$$

Creative Commons Attribution-NonCommercial-NoDerivatives 4.0 International License (CC BY-NC-ND)

Avec $v_{C0}= 0$ et $v_{Cp}= E$.

$$V_{ch} = (u_1- u_2)*v_{C1} + (u_2- u_3)*v_{C2} +\ldots+ (u_{p-1}- u_p)*v_{Cp-1} + u_p*E - E/2 \quad (5)$$

Dans le cas d'une charge R-L, l'évolution du courant dans la charge est donnée par :

$$\frac{di_{ch}}{dt} = \frac{V_{ch}}{L} - \frac{R}{L} i_{ch} \quad (6)$$

$$\begin{cases} \frac{dv_{c1}}{dt} = \frac{1}{C_1} * (u2 - u1) * ich \\ \frac{dv_{c2}}{dt} = \frac{1}{C_2} * (u3 - u2) * ich \\ \vdots \\ \frac{dv_{cp-1}}{dt} = \frac{1}{C_{p-1}} * (up - up-1) * ich \\ \frac{dich}{dt} = \frac{1}{L} * (u1 - u2) * VC1 + \frac{1}{L} * (u2 - u3) * VC2 + \cdots + \frac{1}{L} * (up - 1 - up) * \\ VCp - 1 + \frac{u_p}{L} * E - \frac{1}{L} * \frac{E}{2} - \frac{R}{L} * ich \end{cases} \quad (7)$$

Matériels et méthodes :

1-La stratégie de la commande de l'onduleur multicellulaire :

Dans cette partie, nous élaborons une stratégie de commande de convertisseur multicellulaire a trois cellules qui permettent de générer une source de tension la plus sinusoïdale possible et qui est Commande MLI.

1-1 Commande des interrupteurs par modulation largeur d'impulsion

La commande par MLI consiste à découper la tension de sortie générée par le convertisseur en une série de motifs élémentaires de période très faible, et de rapport cyclique variable dans le temps. L'évolution temporelle du rapport cyclique de chaque interrupteur est alors déterminée par un signal modulant que l'on choisit en général sinusoïdal.

Les ordres de commande de chaque cellule sont générés par l'intersection entre une porteuse triangulaire et le signal modulant. Selon la stratégie adoptée, ce dernier peut être échantillonné en synchronisme avec la porteuse triangulaire, ou comparé directement à celle-ci. Chaque interrupteur commute à une fréquence imposée par celle de la porteuse (notée$f_{déc}$) (Jday, Vidal, Haggège, & Rotella, 2019; Rouabah, Rahmani, Toubakh, & Duviella, 2019).

La commande MLI utilise P porteuses triangulaires pour commander les P cellules de commutation d'un onduleur multicellulaire série. De plus, ces porteuses sont toutes régulièrement déphasées entre elles de 2π/P.

La porteuse no 2 est en retard de 2π/P par rapport à la porteuse no 1. La porteuse no 3 est en retard de (3-1).2π /P par rapport à la porteuse no 1, … jusqu'à la porteuse P qui aura un déphasage de (P-1).2π/P par rapport à la porteuse no 1. Ce déphasage régulier des porteuses les unes par rapport aux autres est utile pour deux raisons :

Creative Commons Attribution-NonCommercial-NoDerivatives 4.0 International License (CC BY-NC-ND)

- D'une part, il permet à la tension multi niveaux de sortie d'atteindre ses niveaux intermédiaires.
- D'autre part, le déphasage régulier permet aussi de multiplier la fréquence apparente de découpage de la tension de sortie

Les équations permettant de générer les signaux triangulaires notés Tri évoluant sur l'intervalle [-1,1] sont (Yodwong et al., 2019):

$$T_{r1} = \frac{2}{л} \arcsin(\cos(2л. f_{déc}.t)). \quad (8)$$

$$T_{r2} = \frac{2}{л} \arcsin(\cos(2л. f_{déc}.t - \frac{2л}{p})). \quad (9)$$

$$T_{rp} = \frac{2}{л} \arcsin(\cos(2л. f_{déc}.t - (p-1)\frac{2л}{p})). \quad (10)$$

1-2 Implémentation de la commande MLI par DSPACE 1104 sure l'onduleur multicellulaire

Le banc d'essai de notre expérience est constitué d'un DSPACE1104 relie à un ordinateur pour commande celle-ci et une alimentation four fourni la tension d'entrée et un oscilloscope pour capturer les signaux de la tension de sortie et un banc de condensateurs nécessaire pour la réalisation de ce convertisseur de 3 niveaux ou bien cellules.

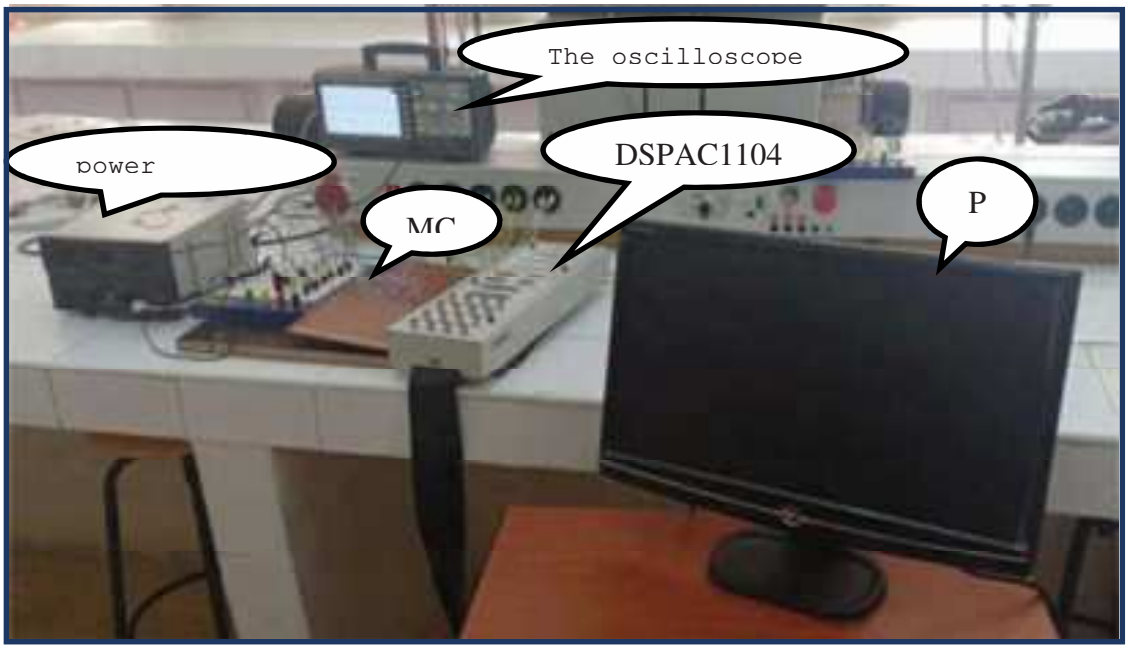

Fig2. Simulation and implémentation

Creative Commons Attribution-NonCommercial-NoDerivatives 4.0 International License (CC BY-NC-ND)

Algerian Journal of Engineering Architecture and Urbanism Vol. 5 Nr. 3 2021
ISSN: 2588-1760

Résultat de simulations :

- Pour *f*=25Hz

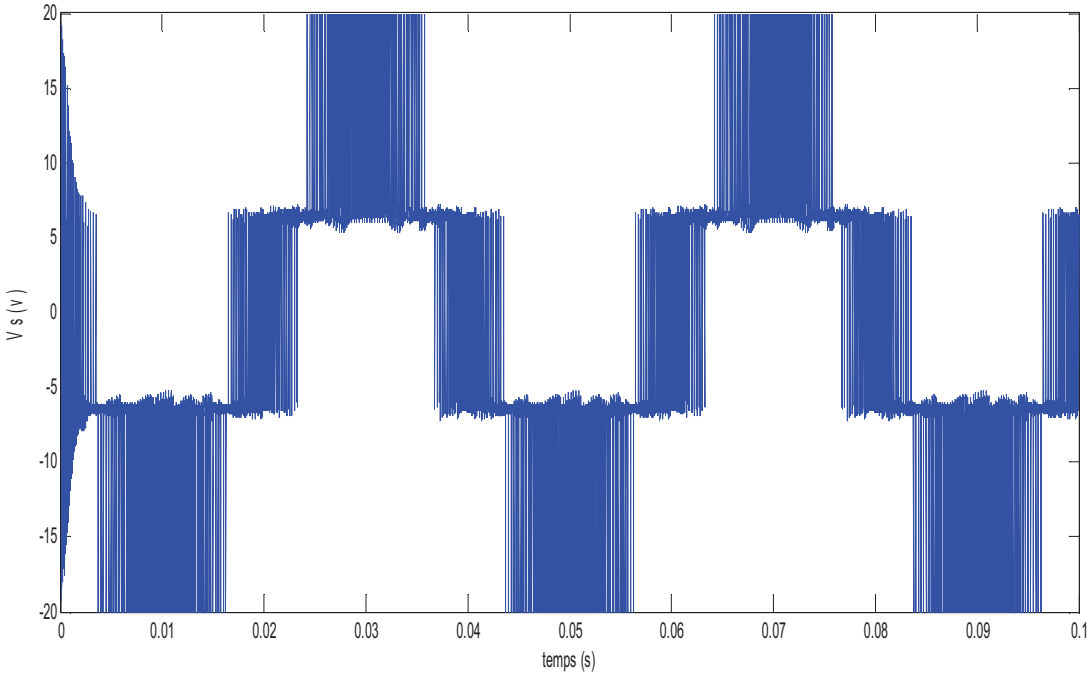

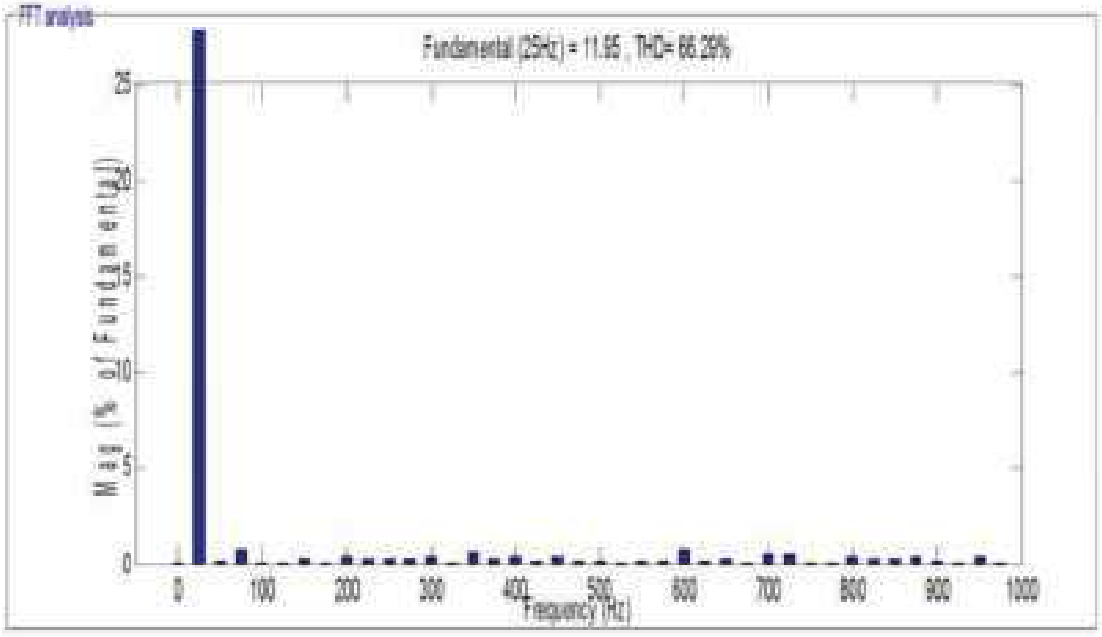

Fig3. Les harmoniques de tension de l'onduleur ont 3 cellules pour f=25 Hz

Creative Commons Attribution-NonCommercial-NoDerivatives 4.0 International License (CC BY-NC-ND)

Algerian Journal of Engineering Architecture and Urbanism Vol. 5 Nr. 3 2021
ISSN: 2588-1760

Schéma bloc de la simulation implémentée par DSPACE 1104

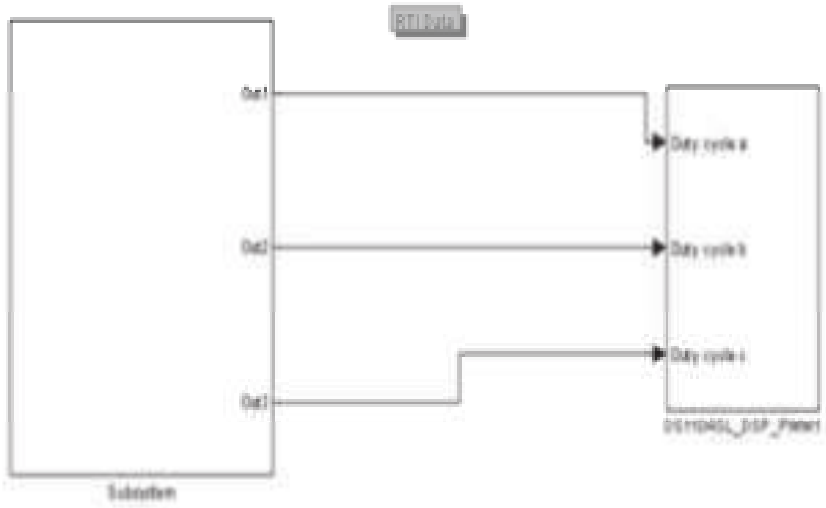

Fig4. Schéma bloc de la simulation implémentée par DSPACE 1104

Résultats expérimentaux des tensions de sortie

Nous présentons les tests expérimentaux que nous avons effectués au cours de la réalisation, et à l'aide d'un oscilloscope numérique on a pu récupérer les signaux de tension de la charge ainsi que les allures des tenions flottantes.

- Pour *f*=25Hz

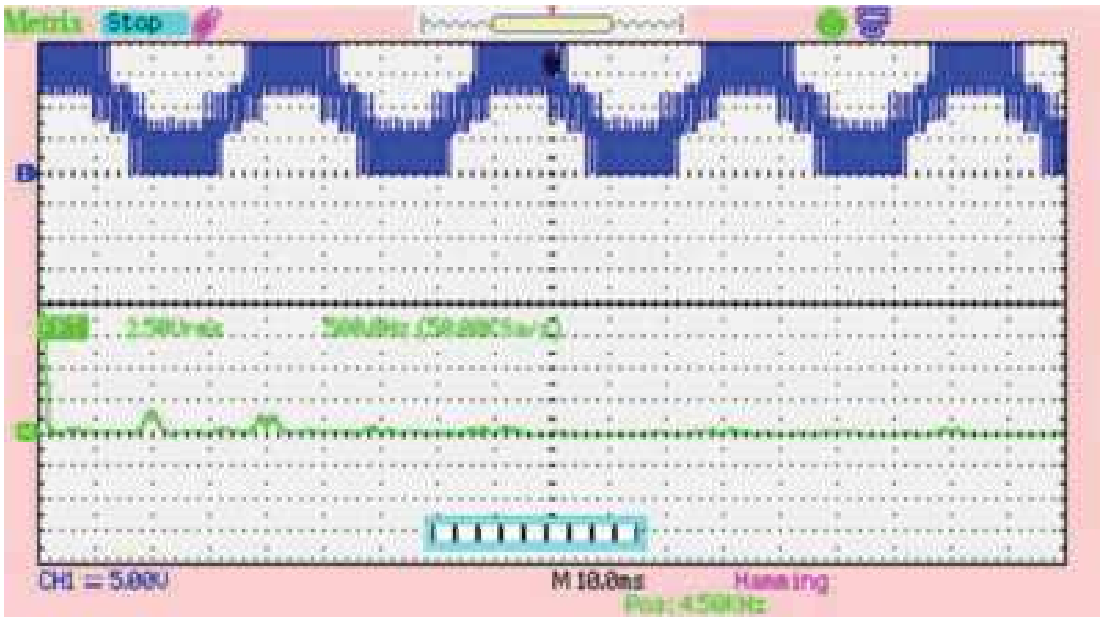

Fig5. Tension de sortie pour *f*=25 Hz

Creative Commons Attribution-NonCommercial-NoDerivatives 4.0 International License (CC BY-NC-ND)

Les caractéristiques du cet onduleur est les suivantes :

- La tension d'alimentation E=20V
- Une charge résistive R=1KΩ
- C1=C2=47 µF

Les figures (Fig. 7) et (Fig. 8) et (Fig. 9) représente les allures de tensions de sortie de l'onduleur multicellulaire, et on voit bien que les forme de ces derniers sont multi niveaux dans les fréquences 25 Hz, 50 Hz, 100 Hz.

La figure (Fig. 9) représente les allures des deux tensions flottantes, et on voit bien que la somme des tensions aux bornes des condensateurs égale à la tension de la source VC1+VC2≈E

Conclusion :

Dans cette partie nous avons présenté les différents organes qui constituent notre banc d'essai réalisé. Nous avons essayé d'expliquer au mieux les étapes suivis pour la réalisation de l'onduleur multicellulaire commandé par DSPACE 1104.

D'après les résultats obtenus pratiquement on peut dire que les modèles réalisés ont été validés, noté qu'on a utilisé des valeurs réduites afin d'éviter le risque sur les appareils utilisés. Grace à cette réalisation, nous avons amélioré et renforcé nos connaissances théoriques.

References:

Abraham C. (2018), *Design, modeling and analysis of multiple input buck boost switched capacitor based converter*, Thesis of doctorat,cochin university, India.

Jday M., Vidal P.-E., Haggège J. (2019), *Observability and sliding mode observer design for multi-cell series converter,* 6th international conference on control, decision and information technologies (CoDIT).

Rouabah B., Rahmani L., Toubakh H., Duviella E. (2019), *Adaptive and Exact Linearization Control of Multicellular Power Converter Based on Shunt Active Power Filter*. Journal of Control, Automation and Electrical Systems **30(6):** 1019-1029.

Vizzaccaro E., Armando E. G., Pellegrino G., Savio, P. (2018), *Remotized Control of Power Electronic Devices Exploiting a Plastic Optical Fiber Photonic Bus*. Thesis of doctorat, Politecnico di Torino, Italy.

Yodwong B., Guilbert D., Kaewmanee W., Phattanasak, M. (2019), *Energy efficiency based control strategy of a three-level interleaved DC-DC buck converter supplying a proton exchange membrane electrolyzer,* Electronics **8(9):** 933.

Creative Commons Attribution-NonCommercial-NoDerivatives 4.0 International License (CC BY-NC-ND)

Algerian Journal of Engineering Architecture and Urbanism Vol. 5 Nr. 3 2021
ISSN: 2588-1760

APPLICATION OF THE HETEROGENEOUS PHOTOCATALYSIS TO THE DEGRADATION OF DYE (Purple Ethyl) IN AQUEOUS MEDIUM

Soumia Fassi, Ibtissem Bousnoubra and K.Djebbar
Laboratory science and technology environment. Department of Chemistry. Faculty of Sciences. University of Brother's Mentouri- Constantine. Algeria.

Abstract:
In recent years, research in the field of photocatalysis has grown considerably. Today, it is considered as a future technology, resulting in research and applications, especially, in the environment. It has the great advantage over other technics in use, to achieve total mineralization of the pollutants, while respecting the integrity of the environment. In this work we focused on the effectiveness of TiO_2 to eliminate a cationic dye: the Purple Ethyle (PE) in aqueous medium. The results obtained showed that adsorption of PE (10 ppm) on TiO_2 (1g/l) in absence of UV radiation, is low (19%). These results are important because they allow to situate the system PE/TiO_2/UV in its proper contribution in this process at 365 nm compared to direct UV photolysis (365 nm), where discoloration of PE (10ppm) was significantly faster in the presence of TiO_2/UV and for the same experimental conditions. The study of factors such as the initial concentration of the pollutant, the catalyst and the addition of H_2O_2, have showed a positive impact on process of photocatalytic discoloration of PE. However, the influence of other parameters such as: organic salts, as chlorides and alcohol have been also studied.
Keywords: Purple Ethyle, UV radiation, photocatalysis, Environment.

Introduction:

L'utilisation massive des colorants synthétique dans le secteur industriel, particulièrement celui du textile, a engendré une pollution de l'environnement aqueux par le rejet de ses effluents dans les rivières. De ce fait, ils peuvent conduire par voie de conséquence à une destruction importante de la faune et de la flore [Sauer.T ,Galindo,C].Cependant ces substances toxique ont pu être réduite à des doses non dangereuses voire éliminées grâce d'une part, à une législation rigoureuse et d'autre part, aux traitements chimiques mis en oeuvre antérieurement : les échanges ioniques [Dusart.O , Perineau.F] les procédés de floculation/coagulation [Linsheng.Z], les procédés d'adsorption sur différents supports [Mc kay.G , Specchiar,V, Sethuraman.V.V, McKay.G] les procédés biologiques [Paprowicz.J, Porter.J.J, Ogawa.T] et plus récemment la dégradation par les radiation UV et par les procédés d'oxydation avancées [Milano.J.C, Al-Quaradawi.S, .Daneshvar.N, Gomes.C].L'efficacité de ces derniers systèmes résident essentiellement en la production in situ des radicaux hydroxyles, qui sont considérés comme espèces très réactives vis-à-vis de plusieurs composés organiques [Buxton.G.U].Le traitement par photocatalyse est une alternative prometteuse pour l'élimination de ces composés organiques solubles. Dans ce travail nous avons examiné les cinétiques de la photodégradation de l'Etyhle Violet en présence de TiO_2 (1g/l) irradié dans le domaine des longueurs d'onde (λ ›300 nm). L'étude des facteurs tels que la concentration initiale du polluant et du catalyseur ainsi que l'ajout de H_2O_2, a indiqué que ces derniers ont influé positivement sur le processus photocatalytique de décoloration de l'EV. Cependant, l'influence d'autres paramètres comme les sels inorganiques tels que les chlorures et l'alcool ont été étudié.

Creative Commons Attribution-NonCommercial-NoDerivatives 4.0 International License (CC BY-NC-ND)

Algerian Journal of Engineering Architecture and Urbanism Vol. 5 Nr. 3 2021
ISSN: 2588-1760

Materiéles et methodes:

Les solutions mères en EV de concentration de 100 ppm, ont été préparées par dissolution respective de leur sel dans l'eau bidistillé à l'obscurité et sous agitation magnétique pour faciliter la dissolution. L'Isopropanol (99%) fourni par prolabo et le chlorure de sodium (99,5%) fourni par Labosi.

Le systéme d'irradiation est une enceinte réfléchissante cylindrique munie de trois lampes à vapeurs de mercure haute pression 125 W. La surface de la suspension est à 10 cm approximativement des lampes. L'émission est filtrée par un globe noir se situant principalement à 365 nm. Le réacteur est en pyrex, équipé d'une jaquette permetant la circulation d'eau afin de maintenir la température 20± 2 °C. Le mélange réactionnel contient 100 ml de EV (10ppm) et 0,1 g de TiO_2 agité à l'obscurité pendant 30 minutes avant illumination afin atteindre l'équilibre d'adsorption. Les particules de TiO_2 sont éliminées par filtration à travers des filtres Millipore 0,45 µm.

L'evolution spectrale et les mesures de la D.O des solutions du colorants, à différents temps de réaction ont été suivies par spectromètre UV de type " Helios α- Unicam spectronic".

Resultats et discussion:

1.Optimisation de la masse de TiO_2

L'efficacité de la photocatalyse hétérogène dépend directement de la quantité du catalyseur en suspension, d'où l'utilité d'optimiser la concentration en catalyseur

À différentes concentrations en TiO_2 allant de 0,5 jusqu 'à 2 g. L^{-1}, nous avons irradié la solution de colorant à 365 nm et les résultats expérimentaux sont représentés dans la **Figure (1)**.

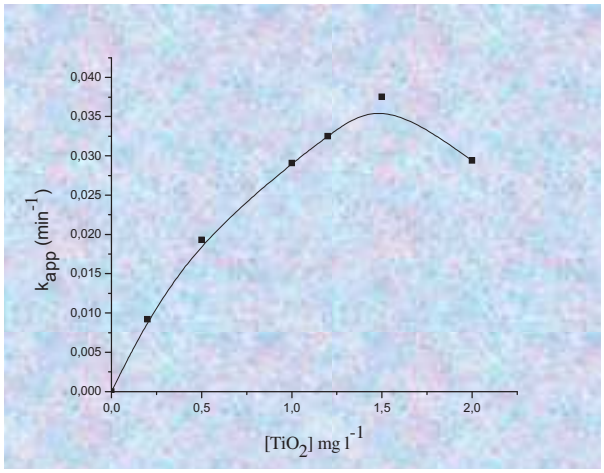

Figure 1 : Influence de la masse du catalyseur sur le processus de décoloration en présence de TiO_2/ UV (λ= 365nm)

Les résultats illustrés dans cette figure, montrent que :

- le taux de dégradation de l'EV est proportionnelle à la concentration de TiO_2 où ce comportement est une conséquence d'une augmentation de la surface de particules à illuminer, produisant ainsi une plus grande quantité de paires "électron-trou" et donc une plus grande quantité de $^{\bullet}OH$.

Creative Commons Attribution-NonCommercial-NoDerivatives 4.0 International License (CC BY-NC-ND)

- le taux de d'élimination augmente en fonction de la concentration en catalyseur TiO_2 jusqu'à un optimum de 1 g L^{-1}. Au delà de cet optimum, on remarque que les taux commencent à diminuer. En effet, à des concentrations élevées en TiO_2, l'agrégation des particules TiO_2 réduit la surface de contact entre la solution et le catalyseur conduisant ainsi à une réduction du nombre de sites actifs à la surface.

2- Influence de la concentration initiale de l'EV

L'influence de la concentration initiale De l'Ethyle violet a été étudiée à température ambiante et pour une concentration fixe en TiO_2 (1g/l). La cinétique de la décoloration rapportée dans la figure (2), démontre que la disparition de l'EV est plus rapide pour les concentrations faibles. Ceci peut s'expliquer par la plus grande disponibilité des espèces réactives photogénérées comme : $^{\bullet}OH$, h^+, $O_2^{\bullet -}$. De plus à forte concentration, la diminution de taux de dégradation peut être attribuée à la diminution des sites actifs due à la compétition entre les photoproduits, souvent plus facilement à dégrader et le substrat restant.

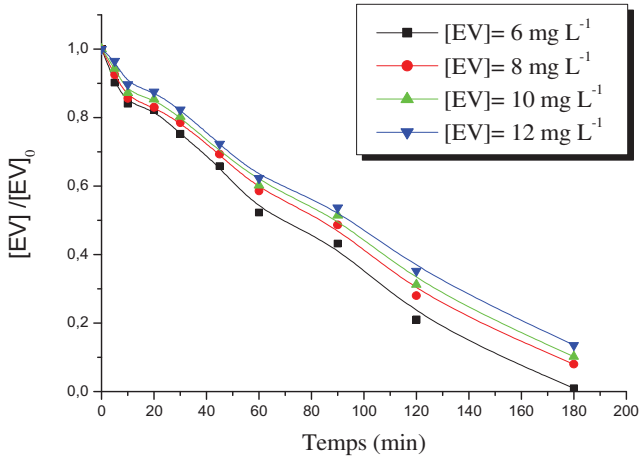

Figure 2 : Influence de la concentration initiale de l'EV sur le processus de décoloration ($[TiO_2]_O$= 1g/l)

3- Influence de l'ajout du peroxyde d'hydrogène

La dégradation photocatalytique de l'EV à été étudiée à différentes concentrations en peroxyde d'hydrogèn (de 5 10^{-1} jusqu'a 10^{-3}M). Les résultats représentés dans la figure (3), ont prouvé que le pourcentage de processus de décoloration du substrat, augmente avec l'élévation de la concentration de H_2O_2. Cette accélération, pourrait être liée à l'inhibition de la recombinaison de électron-trou et également par la production de plus de radicaux $OH^{\bullet}$ dans le milieu .

$$TiO_2 + h\nu \rightarrow TiO_2 + e^- + h^+ \quad (1)$$

$$H_2O_2 + e^- \rightarrow HO^{\bullet} + OH^- \quad (2)$$

Creative Commons Attribution-NonCommercial-NoDerivatives 4.0 International License (CC BY-NC-ND)

Algerian Journal of Engineering Architecture and Urbanism Vol. 5 Nr. 3 2021
ISSN: 2588-1760

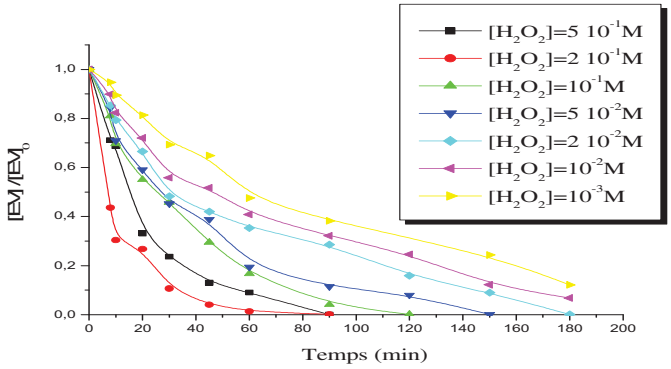

Figure 3: Effet de la concentration de H_2O_2 sur le procédé de décoloration de l'EV en présence de TiO_2(1g/l)

Pour une grande concentration en peroxyde d'hydrogène (5 10^{-1} M), plusieurs auteurs [Lee.S.O, Lunar.L, Hislop .K. A] ont observé l'inhibition des cinétiques de la photodégradation. Ceci est attribué à la consommation des radicaux $HO^{\bullet}$ et la formation des radicaux $HO_2^{\bullet}$, beaucoup moins réactif que l'oxygène moléculaire selon les réactions suivantes :

$$H_2O_2 + HO^{\bullet} \rightarrow HO_2^{\bullet} + H_2O \quad (3)$$

$$HO_2^{\bullet} + HO^{\bullet} \rightarrow H_2O + O_2 \quad (4)$$

En conclusion, on peut affirmer que le système $TiO_2/H_2O_2/UV$ est plus efficace que le système TiO_2/UV seul, cependant, dans le cas des doses optimales de H_2O_2. Cette conclusion est conforme à celle obtenue par plusieurs auteurs travaillants sur différentes substances organiques.

4-Influence des alcools

Les résultats représentés dans la figure (4), ont montré l'effet de ralentissement pour une faible concentration de Isopropanol (5% v/v). On peut donc conclure, que le processus de dégradation par décoloration photocatalytique pourrait se produire selon deux voies : une première, majoritaire, due aux radicaux $OH^{\bullet}$ et une seconde, minoritaire due aux trous positifs (h^+) formés par l'irradiation de la surface de photocatalyseur.

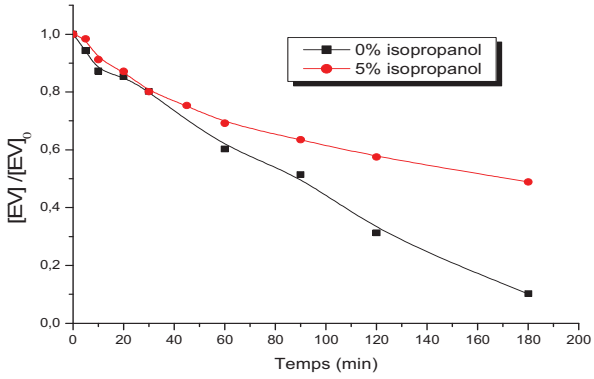

Figure 4: Inhibition de l'action des radicaux hydroxyles par l'isopropanol dans le système TiO_2/UV : [EV] = 10 ppm, λ_{irr} = 365 nm.

Creative Commons Attribution-NonCommercial-NoDerivatives 4.0 International License (CC BY-NC-ND)

5 -Influence des sels

Dans le but de mieux comprendre l'impact des sels sur le processus de rétention de l'éthyle violet sur l'adsorbant, des expériences ont été effectuées, en mélangeant le colorant à des sels cations monovalents (NaCl). Outre cela, il convient de mentionner, que des études thermiques doivent être menées sur ces mélanges. Cela consiste, à suivre en fonction du temps et en absence de support, leur évolution, afin de pouvoir déceler d'éventuelles interactions.

Des expériences préliminaires ont été conduites sur des mélanges constitués par des sels de cations monovalents (NaCl) avec une concentration de (10^{-1} M) et de l'éthyle violet (10ppm) pour un temps de réaction de 120 minutes et en l'absence de support. D'après les résultats obtenus, nous avons constaté aucune variation significative de la densité optique (figures 5) on peut conclure l'absence d'interaction susceptible de mener à des modifications de structure de notre colorant.

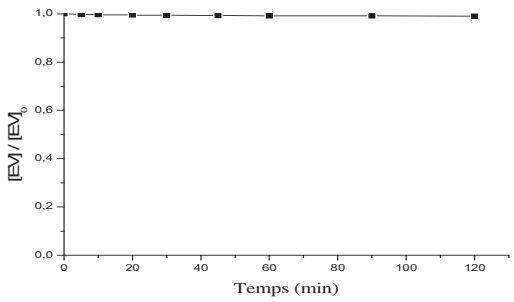

Figure 5 : Evolution thermique du mélange : Nacl (10^{-3}M) + EV (10ppm) en fonction du temps.

La photocatalyse de l'EV en lumière artificielle, n'a pas donné les résultats escomptés. Pour cela, nous avons associé le rayonnement UV (365 nm) et un sel monovalent à 10^{-3} M.Les résultats obtenu ont montré que l'influence est pratiquement insignifiante tant sur la vitesse que sur la décoloration de L'EV (Figure 6).Ce qui montre l'absence de compétitivité entre le substrat et les sels pour l'occupation des sites de support.

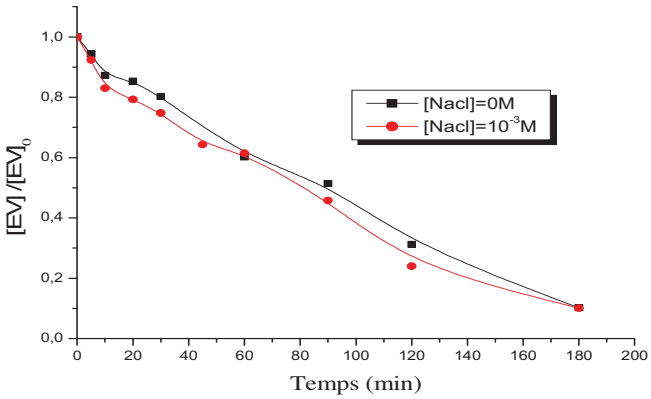

Figure 6 : Cinétique de décoloration de l'EV (10 ppm) par le procédé TiO_2/UV. Effet de l'ajout des sels..

Creative Commons Attribution-NonCommercial-NoDerivatives 4.0 International License (CC BY-NC-ND)

Conclusion

La dégradation des polluants organiques par photocatalyse hétérogène permet, d'une façon générale, d'effectuer la destruction totale de la pollution organique en composés minéraux (eau, gaz carbonique et ions minéraux). Cette étude nous a permis de mettre en évidence l'influence de la structure chimique des colorants organiques sur l'efficacité de leur dégradation photocatalytique en présence du photocatalyseur TiO_2 PC 500.Les essais menés sur ces deux substrats, ont démontré que ce procédé était plus efficace pour ce processus. Ainsi l'ensemble de ces résultats montre que :

- La disparition de l'EV est plus rapide pour les concentrations faibles en colorant.
- La concentration optimale en TiO_2 PC 500 pour notre réacteur est de 1g. L^{-1}.
- l'addition de H_2O_2dans la solution améliore les performances de dépollution de la technique de photocatalyse. L'excès de H_2O_2 crée un effet d'autoinhibition qui annule l'effet accélérateur
- l'inhibition significative de la réaction photocatalytique par l'addition du Isopropanol confirme que la voie majoritaire de la dégradation des colorants est due aux radicaux $^{\bullet}OH$ formés par l'irradiation de la surface du photocatalyseur.
- l'influence de l'ajout de NaCl est pratiquement insignifiante tant sur la vitesse que sur la décoloration de L'EV.

Référence:

Al-Quaradawi.S and Salman.R.S. (2002), *J photochem . photobiol. A Chemistry:* **148,161-168**
Buxton.G.U , Greenstock.C.L , Helman.W.P and Ross.A.B.(1983), *J .Phys. Chem*. **17(2) , 513-886.**
Daneshvar.N, Salari.D and Khataee.A.R.(2003) , *J photochem. Photobiol. A: Chemistry ;* **157,111-116.**
Dusart.O and serpaud.B.(1991), *J la tribune de l'eau*. **44 , 15-22**
Galindo.C , Jasques.P and Kalt.A.(2002)*, J Chemosph* **45,997**
Gomes Da Silva .C and Luis Faria.J.(2003), *J photochem. Photobiol. A: Chemistry*, **157 , 133-143.**
Lee.S.O, Tran.T, Jung.B.H, Kim.S.J, et Kim.M.J.(2007) « Dissolution of iron oxide using oxalic acid » *Hydrometallurgy* **87, 91- 99.**
Hislop .K. A and Bolton. J.R. (1999) « The Photochemical Generation of Hydroxyl Radicals in the UV-vis/Ferrioxalate/H_2O_2 System », *Environ. Sci. Technol*, **33,3119-3126.**
Linsheng.Z and Dobias.B.(1992), *J Water Treatment*. **7 ,221- 232.**
Lunar.L, Sicilia.D, Rubio.S, Pérez-Bendito.D and Nickel.S.(2000) « Degradation of photographic developers by Fenton's reagent: condition optimization and kinetics for metol oxidation », *Water Res,* **34 ,1791-1802.**
Mc kay.G and al Duri.B.A.A.(1988). *J Colourage*. **35, 24- 28.**
McKay .G, Otterburn.M.C.(1985), *J Water, Air and Soil Pollution.* **24, 307-322.**
Milano.J.C, Loste-Berdot.P and Vernet.L.(1994), *J Environ. Techn.* **16,329-341.**
Ogawa.J.C, Yatom.C, Idaka.E and Kamiya.H.(1986), *J S.D.C.* **102, 12-14.**
Paprowicz.J and Slodezyk.S .(1988), *J Env. Tech .Let*. **9 ,271- 280.**
Perineau.F,Moliner.J and Gazet.A.(1983), *J Wat. Res*., **17(5),559-567.**
Porter. J.J and Snider.E.H.(1976),J W.P.C.F. **5 ,926-935.**
T.Sauer.T , Gesconato.G, Neto.H,jose.J , Moreira.M.(2002) *J photochem. Photobiol A: Chemistry*, **149,147-154**
Sethuraman.V.V and B. C.Raymahashay.(1975), *J Env. Sci.Tech*. **9 (1975) 1139-1140.**
Specchiar.V, Ruggeri.B.and Gianetto. (1988), *J Chem. Eng. Comm*. **68,99-117.**

Creative Commons Attribution-NonCommercial-NoDerivatives 4.0 International License (CC BY-NC-ND)

Algerian Journal of Engineering Architecture and Urbanism Vol. 5 Nr. 3 2021
ISSN: 2588-1760

OPTIMISATION PAR LE PLAN DE BOX-BENKHEN DE L'ÉLECTROCOAGULATION DES POLLUANTS DES EAUX USÉES DE LA VILLE DE GUELMA

Ilhem DJAGHOUT
PhD
Laboratoire d'Analyses Industrielles et Génie des Matériaux, Université 8 Mai 1945 Guelma,
Département de Génie des Procédés, Université Mohamed Chérif Messaadia, Souk Ahras,
i.djaghout@univ-soukahras.dz

Rabah KSOURI
Laboratoire de chimie appliquée, Département de Génie des Procédés, Université 8 Mai 1945 Guelma,
ksourira@hotmail.com

Abstract :
L'objectif de ce travail est le traitement par électrocoagulation des polluants des eaux usées de la ville de Guelma. L'influence des paramètres opératoires à savoir ; la densité de courant, le temps d'électrolyse, la concentration de l'électrolyte support et la surface de l'électrode sur le processus d'électrocoagulation ont été étudiés par la méthodologie de la surface de réponse. Un plan expérimental appelé Box-Benkhen est utilisé pour modéliser le rendement d'abattement. La signification du modèle et des coefficients de régression a été testé par l'analyse ANOVA. Les résultats prédits par les modèles se sont révélés en bon accord avec ceux obtenus expérimentalement (R^2 = 96,7 %), Nous avons également trouvé que la contribution de la densité de courant est la prédominante, elle est de 60,03 %. Les résultats d'optimisation des paramètres d'électrolyse du processus d'électrocoagulation ont révélé des valeurs de facteurs correspondants à un rendement d'abattement maximal avec des valeurs de désirabilité qui sont proche de l'unité.

Key words : Eaux usées ; Electrocoagulation ; Plan d'expérience ; Rendement d'abattement.

Introduction :

Les eaux usées sont des milieux extrêmement complexes, altérées par les activités anthropiques à la suite d'un usage domestique, industriel ou agricole. [1]. Les eaux polluées devraient être dirigées vers des stations d'épuration dont le rôle est de concentrer la pollution sous la forme d'un petit volume de résidu, sous forme des boues, et de rejeter une eau épurée répondant à des normes bien précises, et cela grâce à des procédés physico-chimiques ou biologiques. Parmi les différentes solutions envisageables, l'électrocoagulation permettent de répondre à de nombreuses situations [2-4]. Le procédé d'électrocoagulation crée, au sein de l'eau que l'on souhaite épurer, des flocs d'hydroxydes métalliques par électrodissolution d'anodes solubles. À des valeurs de pH proches de la neutralité ou légèrement acide, l'aluminium et le fer dissous sous forme cationique, réagissent avec l'eau pour former des complexes de type $Al_2(OH)^{5+}$, $Al_2(OH)_2^{4+}$, ou des hydroxydes peu solubles $Al(OH)_3$, $Fe(OH)_2$ ou $Fe(OH)_3$. Ce sont ces dernières formes qui jouent le rôle de coagulant, des agrégats de particules sont alors formés et peuvent décanter pour laisser place à une eau claire et épurée [5]. L'objectif de ce travail est la modélisation par le plan d'expérience de Box-Benkhen du processus d'électrocoagulation, les modèles de prédiction obtenus permettent d'évaluer l'effet des facteurs d'électrolyses sur le rendement d'abattement, ils permettent également d'optimiser le processus en question.

Creative Commons Attribution-NonCommercial-NoDerivatives 4.0 International License (CC BY-NC-ND)

Algerian Journal of Engineering Architecture and Urbanism Vol. 5 Nr. 3 2021
ISSN: 2588-1760

Résultats et discussions :

Modélisation du procédé d'électrocoagulation

Les variables les plus signifiants qui peuvent agir sur le procédé d'électrocoagulation sont : la densité de courant (I), le temps d'électrolyse (t), la concentration de l'électrolyte (C) et la surface immergée de l'électrode (S). Dans ce travail, nous combinons tous les facteurs dans une matrice d'expérience dont chaque facteur prend trois niveaux, un niveau bas, un niveau moyen et un niveau haut, symbolisé par (-1), (0) et (+1) respectivement (Tableau 1).

Tableau 1 : Facteurs et niveaux de plan Box-Benkhen

Facteurs	Niveaux		
	-1	0	+1
Densité de courant (I)	10	20	30
Temps (t)	10	20	30
Concentration (C)	0,01	0,015	0,02
Surface (S)	400	600	800

La variation du rendement d'abattement en fonction des facteurs étudiés a été modélisée par une régression quadratique avec interaction, l'équation de régression obtenue est la suivante :

$$Rd = 75{,}158 + 9{,}348\,I + 1{,}582\,t + 2{,}081C + 3{,}505 + 0{,}282\,I * t - 1{,}865\,I * C - 0{,}042\,I * S - 0{,}352\,t * C - 3{,}317\,t * S + 3{,}637\,C * S + 2{,}527\,I^2 + 0{,}781\,t^2 + 0{,}822\,C^2 + 1{,}701\,S^2$$

Le coefficient de détermination (R^2) est 96,7 % ceci indique que seulement 3,3 % de la variabilité totale n'est pas expliqué par le modèles de prédiction, la figure 1 montre la comparaison entre les valeurs mésurés et prédite du rendement d'abattement. Il ressort que les valeurs expérimentales et les valeurs estimées sont proches. Donc la régression quadratique avec interaction est adéquate et peuvent être utilisé pour la prédiction dans cette étude.

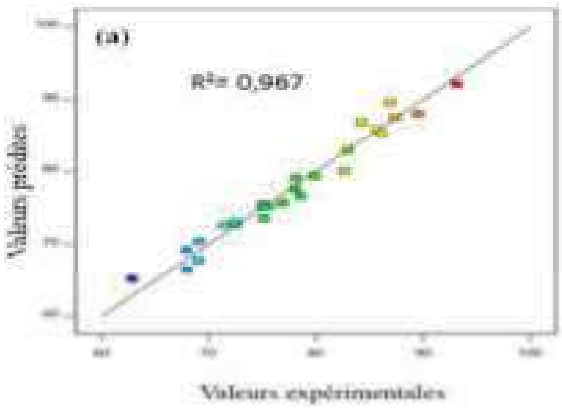

Fig1. RENDEMENT PREDIT EN FONCTION DU RENDEMENT REEL

Analyse de la variance (ANOVA) du rendement d'abattement

L'analyse de variance du procédé d'électrocoagulation a été faite dans le but d'analyser l'effet de la densité de courant, le temps d'électrolyse, la concentration de l' électrolyte support

Creative Commons Attribution-NonCommercial-NoDerivatives 4.0 International License (CC BY-NC-ND)

et la surface de l'electrode sur la fonction réponse, Le tableau 2 montre les résultats de la variance, cette analyse a été faite pour un niveau de signification de 5%, c'est-à-dire un niveau de confiance de 95% [6], Dans ce tableau, les degrés de liberté (ddl), la somme des carrés des écarts (SCE), la somme des carrés moyenne (SCM), Fisher (F-value), la probabilité (P), et le pourcentage de contribution de chaque facteur et interaction sont présentés, Donc le modèle est extrêmement signifiant. Par ailleurs l'analyse ANOVA, montre aussi que tous les facteurs étudiés affectent le rendement d'abattement, concernant les interactions, deux interactions sont signifiantes, qui sont (S×C et S×I).

Tableau 2 : Analyse des variances ANOVA pour le rendement d'abattement.

Source	SCE	DL	SCM	F value	Prob	Cont %	Remarque
Modèle	1441,62	14	102,97	29,27	< 0,0001		Signifiant
I	1048,7	1	1048,7	298,11	< 0,0001	60,03	Signifiant
T	30,050	1	30,050	8,540	0,0111	10,96	Signifiant
C	52,000	1	52,000	14,78	0,0018	08,70	Signifiant
S	147,49	1	147,49	41,93	< 0,0001	11,14	Signifiant
I×t	0,319	1	0,319	0,090	0,7677	0,216	non signifiant
I×C	13,910	1	13,910	3,950	0,0666	0,212	non signifiant
I×S	44,020	1	44,020	21,48	0,0033	3,576	signifiant
t×C	0,497	1	0,497	0,141	0,7126	0,579	non signifiant
t×S	0,007	1	0,007	0,001	0,9645	0,779	non signifiant
C×S	52,930	1	52,930	15,04	0,0017	1,059	signifiant
I^2	41,430	1	41,430	11,78	0,0040	01,019	signifiant
t^2	3,960	1	3,960	1,120	0,3069	0,058	non signifiant
C^2	4,390	1	4,390	1,250	0,2830	0,109	non signifiant
S^2	18,77	1	18,77	5,340	0,0367	0,428	signifiant
Résiduel	49,250	14	3,520			0,105	
total						100	

Effet principaux des facteurs

L'effet d'un facteur est statistiquement significatif si P < 0,05 [7]. La figure 2 montre les effets principaux des facteurs étudiés sur le rendement d'abattement. On peut voir d'après les figures que tous les facteurs ont un effet positif sur le rendement d'abattement et cela avec un degré plus au moins élevé. Egalement il apparait clair que la densité de courant affecte considérablement la réponse étudiée, sa contribution 60,03 % tandis que les trois autres facteurs ont un pourcentage de contribution qui ne dépasse pas 11 %. Concernant les interactions on remarque que la surface d'électrode immergée entre dans les deux interactions signifiantes avec un pourcentage de contribution relativement faible qui ne dépasse pas 5 %.

Creative Commons Attribution-NonCommercial-NoDerivatives 4.0 International License (CC BY-NC-ND)

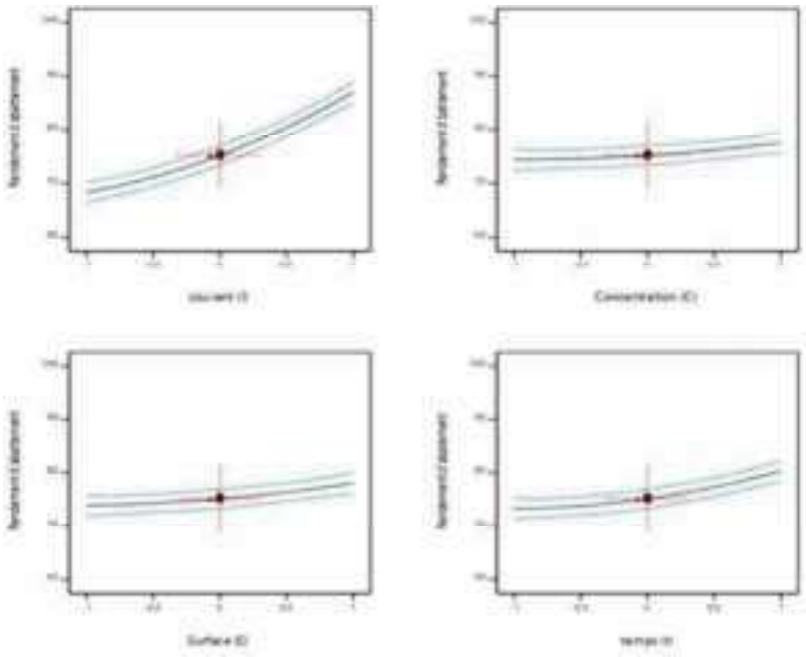

Fig2. EFFETS PRINCIPAUX DES FACTEURS SUR LE RENDEMENT D'ABATTEMENT.

Surfaces de réponse

Les surfaces de réponse sont établies afin d'étudier les effets d'interactions des facteurs sur la fonction réponse [8]. Celle-ci est représentée comme fonction de deux facteurs, en tenant les deux autres facteurs dans le niveau intermédiaire. La figure 3(a) illustre la surface de réponse du rendement d'abattement. A des faibles valeurs de la concentration, l'augmentation de la surface de l'électrode immergée conduit à une légère augmentation du rendement, tandis que pour des valeurs élevées de la concentration, la croissance de la surface conduit à une augmentation signifiante du rendement. Donc la meilleure surface de réponse est obtenue par la combinaison de la valeur la plus élevé de la concentration avec la surface la plus élevé. La figure 3(b), à des valeurs faibles de la surface de l'électrode, l'augmentation du courant d'électrolyse conduit à une légère augmentation de la réponse, mais à des valeurs élevées de la concentration de la surface, l'augmentation du courant d'électrolyse conduit à une augmentation significative du rendement d'abattement. Donc le meilleur rendement est obtenu par la combinaison de la surface de l'électrode la plus élevé avec le courant d'électrolyse le plus élevé.

Creative Commons Attribution-NonCommercial-NoDerivatives 4.0 International License (CC BY-NC-ND)

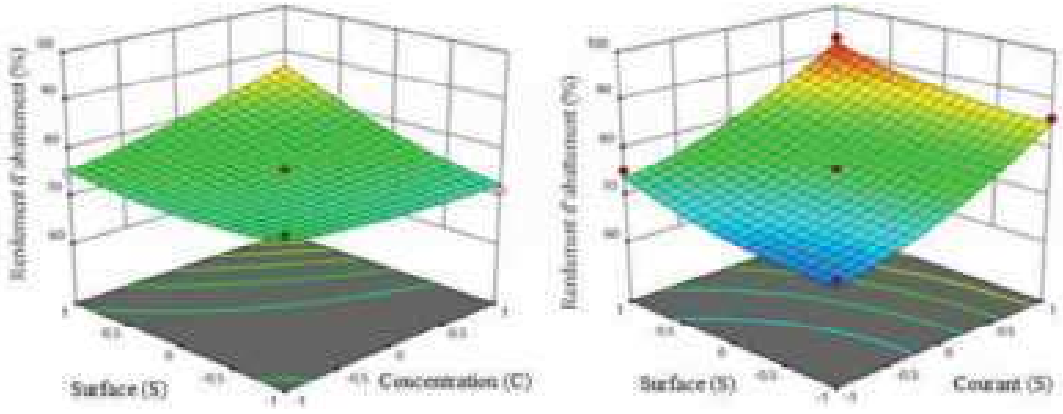

Fig3. Surface de réponse des interactions signifiante

Optimisation des paramètres d'électrolyse

L'optimisation des paramètres d'électrolyse dans le processus d'électrocoagulation est effectuée par la fonction désirabilité qui donne des multi-réponses pour optimiser différentes combinaisons de paramètres du procédé. Les gammes des facteurs sont résumées dans le tableau 3 tandis que les résultats de l'optimisation en valeurs codées sont présentés dans le tableau 4 et la représentation graphique est dans la figure 4.

Condition	Objectif (i)	Objectif (ii)	Niveau bas	Niveau haut
Densité de courant (I)	Minimiser	La gamme	10	30
Temps d'électrolyse (t)	Minimiser	La gamme	10	30
Concentration de l'électrolyte (C)	Minimiser	La gamme	0,01	0,02
Surface de l'électrode (S)	Minimiser	La gamme	400	800
Rendement d'abattement	Maximiser		62,87	93,13

Tableau 4: L'optimisation des paramètres.

Densité de courant	Temps d'électrolyse	Concentration de l'électrolyse support	Surface de l'électrode	Rendement d'abattement
0,792	-0,999	-0,999	-0,999	81,5427 %
-0,999	-0,999	-0,997	-0,999	
0,937	0,986	0,616	0,999	93,166 %
-0,983	-0,529	-0,976	-0,015	

Creative Commons Attribution-NonCommercial-NoDerivatives 4.0 International License (CC BY-NC-ND)

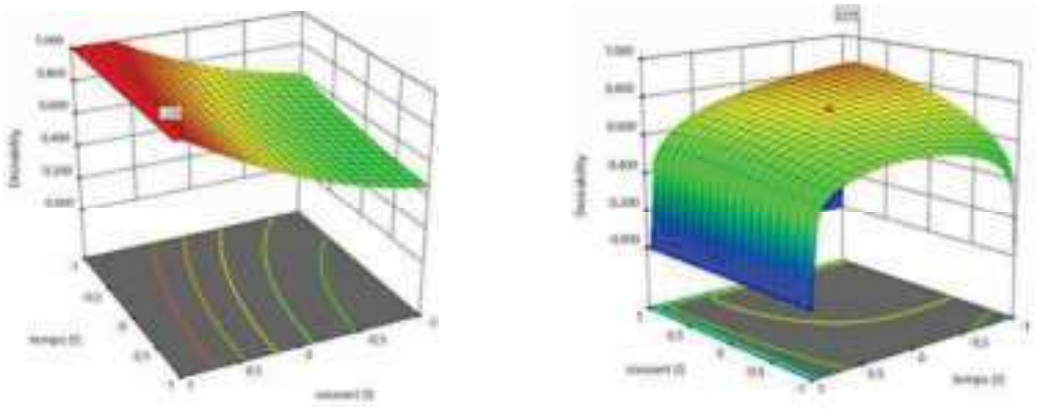

Fig4. OPTIMISATION DU RENDEMENT D'ABATTEMENT

Conclusion :

L'influence des paramètres d'électrolyse à savoir ; la densité de courant, le temps d'électrolyse, la concentration de l'électrolyte support et la surface de l'électrode sur le processus d'électrocoagulation a été étudiés. La fonction réponse choisie étant le rendement d'abattement. Le plan d'expérience utilisé est le plan Box-Benkhen de surface de réponse avec un nombre de 29 essais, ceci permet de modéliser et d'optimiser la fonction réponse. Le modèle de régression quadratique avec interaction ont fourni d'excellentes relations entre les facteurs étudiés et les deux fonctions réponse. Basant sur l'outil d'analyse ANOVA, le modèle de prédictions est signifiant. L'analyse effectuée montre aussi que tous les facteurs étudiés sont signifiants, mais le pourcentage de contribution varie d'un facteur à un autre, la contribution de la densité de courant est la prédominante, leur pourcentage de contribution est 60,03 %. Les quatre facteurs étudiés ont un effet positif sur le rendement d'abattement, tandis que la variation des facteurs du niveau bas vers le niveau haut entraine une augmentation du rendement d'abattement. L'optimisation des paramètresd'électrolyse dans ce processus d'électrocoagulation est effectuée par la fonction désirabilité qui donne des multi-réponses pour optimiser différentes combinaisons de paramètres du procédé. Nous sommes intéressés à deux approches d'optimisation que nous avons nommée : optimisation économique et optimisation qualité. Les résultats d'optimisation ont donné les valeurs des facteurs correspond à un rendement d'abattement maximal pour ces deux approche d'optimisation avec des valeurs de désirabilité qui sont proche de l'unité. Donc ces derniers indiquent à nouveau la concordance entre les résultats expérimentaux et les modèles de prédictions.

Références :

Salghi R. (2001), Différentes filières de traitement des eaux, ed univ iz rabat,
Meneses E.S.(2005), Arguelho M.L.P.M., Alves J.P.H., Talanta 67: 682-685.
Bouaouine O., Khalil F., Chtioui H., Zaitan H. (2015), Larhyss Journal 23:53-67.

Creative Commons Attribution-NonCommercial-NoDerivatives 4.0 International License (CC BY-NC-ND)

Alinsafi A., Khemis M., Pons M.N., Leclerc J.P., Yaacoubi A., Benhammou A., Nejmeddine A. (2005), Chemical Engineering and Processing 44: 461-470.

Debillemont P. (1996), Récents Progrès en Génie des Procédés 10 : 129-136.

Brereton R. (2003), Chemometrics: data analysis for the laboratory and chemical plant, john wiley and sons limited, England,.

maria P. S., gutta S., gutt G., cretescu I., cojocaru C. (2011), chemical engineering research and design 89 136–147.

Djaghout I., Affoune A.M., Chelaghmia M.L., Bendjaballah M. (2015), Portugaliae Electrochimica Acta 33:209-222.

Creative Commons Attribution-NonCommercial-NoDerivatives 4.0 International License (CC BY-NC-ND)

Algerian Journal of Engineering Architecture and Urbanism Vol. 5 Nr. 3 2021
ISSN: 2588-1760

NUMERICAL STUDY OF THE CAVITANT FLOW IN THE VENTURI TUBE

Brahim ROSTANE

Dr, laboratoire MECACOMP, Département de Génie Mécanique, Faculté de Technologie, Université de Tlemcen, Algerie. e-mail: *r_brahim75@yahoo.fr*

Khaled ALIANE

Pr, laboratoire MECACOMP, Département de Génie Mécanique, Faculté de Technologie, Université de Tlemcen, Algerie. e-mail: *kh_aliane@yahoo.fr*

Said ABBOUDI

Pr, laboratoire Interdisciplinaire Carnot de Bourgogne-UTBM, CNRS et Université de Bourgogne Franche Comté (UBFC), Dijon, France e-mail: *said.abboudi@utbm.fr*

Abdelhakim TAZOUTA

Département de Génie Mécanique, Faculté de Technologie, Université de Tlemcen, Algerie.

Abdelhakim BOUGHRARA

Département de Génie Mécanique, Faculté de Technologie, Université de Tlemcen, Algerie.

Abstract

Cavitating venturis are simple apparatus that can be used for controlling the mass flow of fluids. The aim of this work is to carry out a numerical simulation of the two-phase flow in a cavitating venturi. This study was performed with the ANSYS-Fluent code that solves the equations of Navier stocks. The effects of turbulence were taken into account by using the turbulence model k-ω- (SST) with Schnerr and Sauer as a cavitation model. A good agreement was found after the confrontation between the numerical results and experimental measurements of the literature. The results show that the pressures at the outlet of the venturi have a direct influence on the cavitation zone.

Key words: Cavitating venturi, Cavitating, ANSYS Fluent, mass flow, pressure

Introduction

Cavitation phenomena occur during the flow of liquids in machines and hydraulic systems. They are usually caused by a drop in pressure accompanied by a local phase change, and, in most cases, by noise and erosion of metal walls. This phenomenon has been the subject of a large number of analytical and numerical studies, including those relating to the dynamics of the bubble (Rayleigh, 2009)

Local over speeds imposed by geometry, by shear, acceleration or vibration phenomena can cause local pressure drops in the fluid. When at certain points in the flow the pressure is lower than the vapor pressure of the fluid, partial vaporization occurs and vapor structures are formed. The structures thus formed are carried away by the flow and when they reach a zone of higher pressure they condense and implode violently. Cavitation leads to significant losses in plant performance, problems with unstable machine operation and erosion of the

Creative Commons Attribution-NonCommercial-NoDerivatives 4.0 International License (CC BY-NC-ND)

component walls. It is thus a source of fundamental technical problems in the field of hydraulic turbomachines and shipbuilding. Given the complexity of the physical phenomena involved in cavitation, and despite excellent studies conducted on the subject, the basic physical mechanisms of cavitation are not yet fully understood.

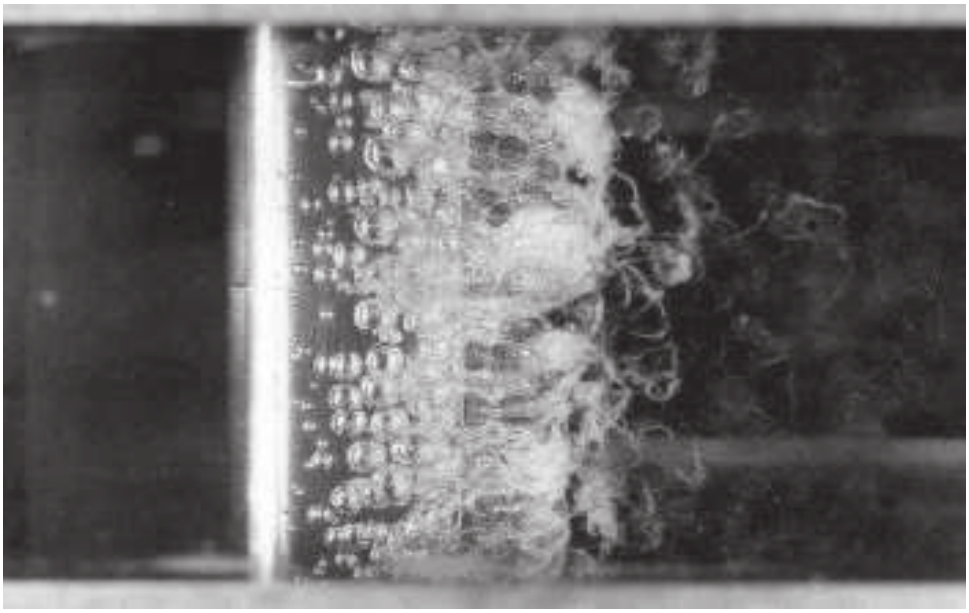

Fig1. EXAMPLE OF CAVITATION ON A PROFILE (BRENNEN, 1995),

The introduction of a dimensionless formulation allowed (Chahine, 1983) to express the influence of various parameters on the behavior of the bubble through the expression of three dimensionless numbers: the Reynolds number, the Weber number and the number cavitation. The Reynolds number has been taken in a more complete form, allowing the influence of most of the parameters that make up the equation of motion of a bubble in an incompressible fluid to be analyzed. Studied cavitating flow with nucleation of bubbles through a converging-diverging nozzle.

The Venturi generally corresponds to the measurement of flow rates in single-phase flow. Its study in the case of a flow with bubbles makes it possible to visualize the effect of the convergent and divergent angles (through the dimensionless radius β of the Venturi) on the parameters of the mixture.

A review of previous studies in this area shows that the study of venturis has aroused great interest. However, less attention has been given to small venturis. Therefore, the main goal of this work is to study the flow in a small cavitating venturi with a view to determining its performance. The study makes it possible to verify the capacities of the cavitating venturis in the flow control under different pressures upstream and downstream. In addition, the application range of small cavitating venturis is also studied.

The venturi is made up of three distinct parts: a divergent, a part of constant section representing the neck and a divergent. Fig.1 schematically represents the configuration of the venturi showing its main dimensions.

The neck has a diameter of 1 mm and a length of 1 mm. The angle of the convergent is fixed at 15 ° while that of the divergent is equal to 7 °. The diameter of the inlet and outlet sections

Creative Commons Attribution-NonCommercial-NoDerivatives 4.0 International License (CC BY-NC-ND)

is equal to 4 mm as shown in Figure III.1 This configuration has been the subject of experimental and numerical studies published by(Ashrafizadeh and Ghassemi , 2015)

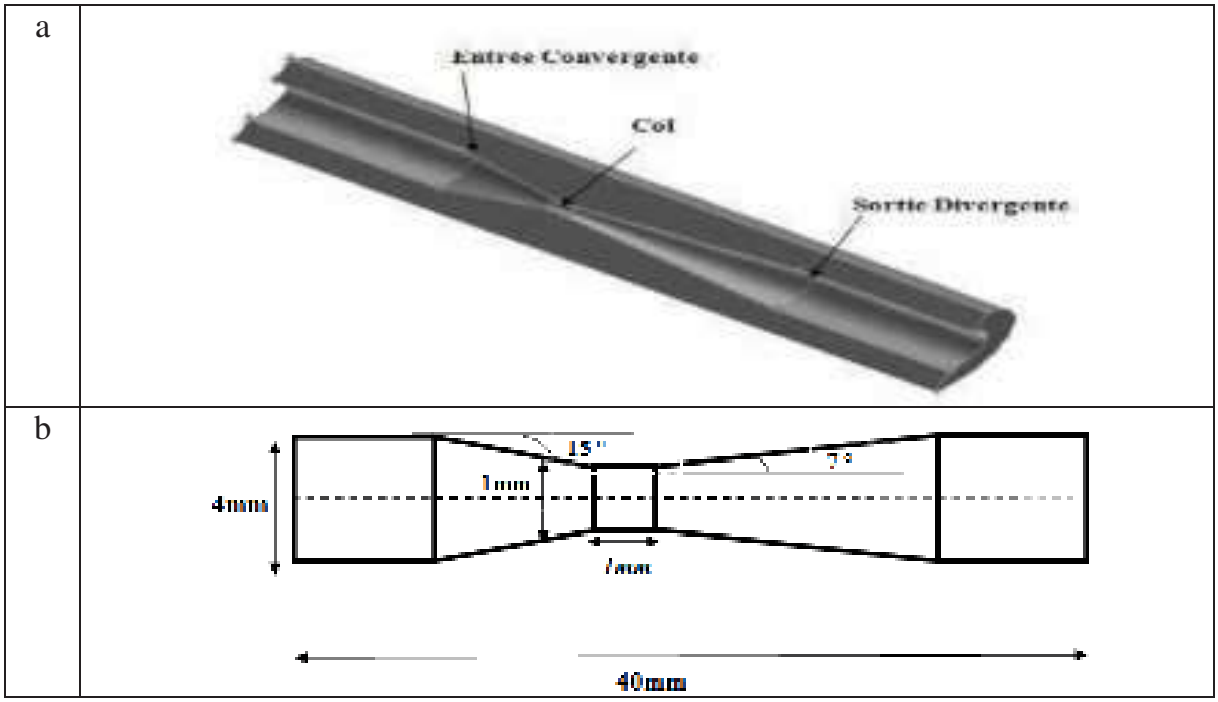

Fig2. DESCRIPTION OF THE VENTURI STUDIED: a. OVERVIEW ; b. DIMENSIONS

The governing equations

The equations governing the flow of fluid in the venturi include the equations of continuity and motion. Since the flow through the cavitating venturi is two-phase, the multiphase mixing approach is used in order to simulate the two-phase flow in the venturi. It should be noted that the primary phase is liquid water and the secondary phase is water vapor.

1. Continuity equation

The continuity equation for the mixture is given by:

$$\frac{\partial}{\partial t}(\rho_m)+\nabla\cdot(\rho_m\cdot\vec{v}_m)=0 \quad (1)$$

$\vec{v}_m$ the velocity of the mixture expressed by**:**

$$\vec{v}_k=\frac{\sum_{k=1}^{n}\alpha_k\rho_k\vec{v}_k}{\rho_m} \quad (2)$$

And ρ_m is the density of the mixture which is expressed by:

$$\rho_m=\sum_{k=1}^{n}\alpha_k\rho_k \quad (3)$$

Creative Commons Attribution-NonCommercial-NoDerivatives 4.0 International License (CC BY-NC-ND)

Where n is the number of phases and α_k is the volume fraction of phase k.

2. Equation of motion

The equation of motion of the mixture can be obtained by summing the individual equations of motion of all phases. It takes the following form:

$$\frac{\partial}{\partial t}\left(\rho_m \vec{v}_m\right) + \nabla \times \left(\rho_m \vec{v}_m \vec{v}_m\right) = -\nabla p + \nabla \times \left[\left(\mu_m + \mu_t\right)\left(\nabla \vec{v}_m + \nabla \vec{v}_m^T\right)\right] \quad (4)$$

Where μ_m is the viscosity of the mixture:

$$\mu_m = \sum_{k=1}^{n} \alpha_k \mu_k \quad (5)$$

The RANS equations were solved using the FLUENT code employing the finite volume method with a refined quadratic mesh near the solid walls

The discretization scheme, the pressure interpolation method and the pressure-speed coupling method are summarized in table 1.

The discretization scheme	Seconde order upwind
The pressure interpolation	SIMPLE
The pressure-velocity coupling	SIMPLE

Table 1. CHOICE OF GRID CONFIGURATION AND RESOLUTION

Results

The comparison that we made between the characteristic curve of the cavitating venturi obtained by the numerical model with that obtained experimentally by (Ashrafizadeh and Ghassemi, 2015) for the purpose of validating our results. In Fig. 3 this comparison is shown between the characteristic curve of the studied cavitating venturi obtained numerically with that resulting from the measurements of the cited reference. At first glance, the digital model allows us to faithfully represent the shape of the characteristic curve of a cavitating venturi. The mass flow ratio has remained almost constant with increasing pressure ratio to a critical value, from which the mass flow ratio drops rapidly. However, he found that the digital model overestimates the mass flow ratio especially in the region of the cavitating fluid where the maximum error is 8.77%. It does not exceed 4.30% in the region of all liquid flow. The two approaches give very close critical pressures (Pr, crit = 0.71). They correspond to an outlet pressure of 14 bars and an inlet pressure of 20 bars.

Creative Commons Attribution-NonCommercial-NoDerivatives 4.0 International License (CC BY-NC-ND)

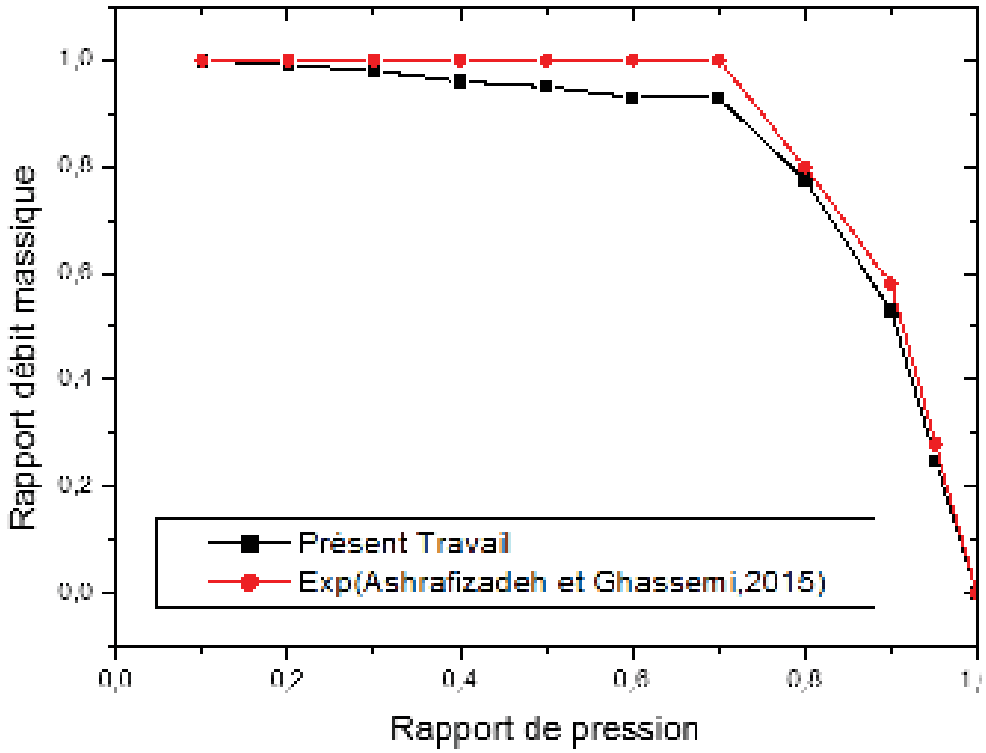

Fig3. COMPARISON OF THE NUMERICAL AND EXPERIMENTAL CHARACTERISTIC CURVES OF THE STUDIED VENTURI

Fig. 7 show the influence of the outlet pressure on the appearance and development of the cavitation zone, for an inlet pressure of 20 bar and an outlet pressure of 14 bar. We notice that towards the exit of the convergent one has a decrease in pressures until they reach their low values at the level of the neck. In this part the pressure of the fluid reaches the saturation pressure of water at 27 ° C, that is to say 3.54 kPa. This causes the water to evaporate. The evaporation phase occurs at the neck and towards the entrance of the divergent.
by changing the outlet pressure by 1, 5, , 14 and 20 (Fig4, Fig5, Fig6, Fig7), it noticed that the decrease in the outlet pressure causes a larger cavitation zone which can reach the outlet of the venturi.

Creative Commons Attribution-NonCommercial-NoDerivatives 4.0 International License (CC BY-NC-ND)

Algerian Journal of Engineering Architecture and Urbanism Vol. 5 Nr. 3 2021
ISSN: 2588-1760

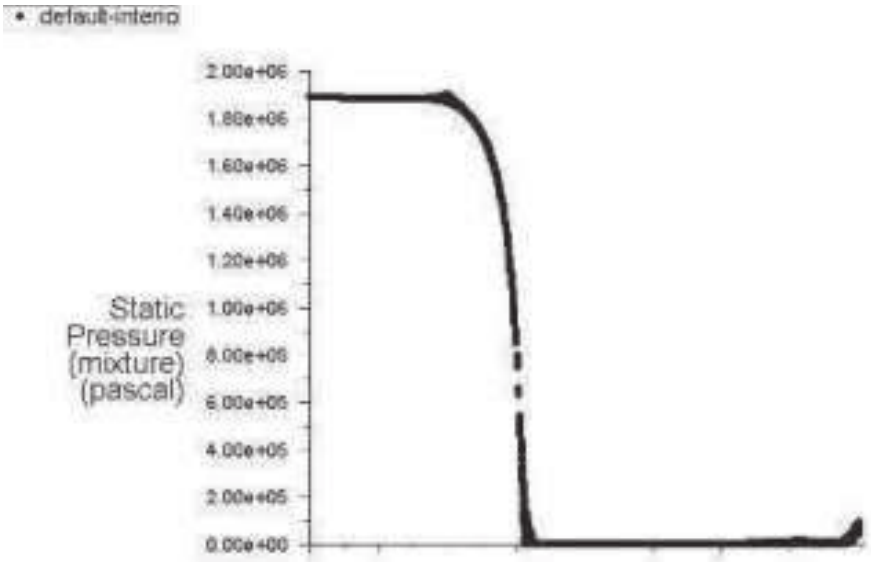

Fig4 . PRESSURE VARIATION FOR AN INLET PRESSURE OF 20 BAR AND AN OUTLET PRESSURE OF 1 BAR IN THE VENTURI TUBE

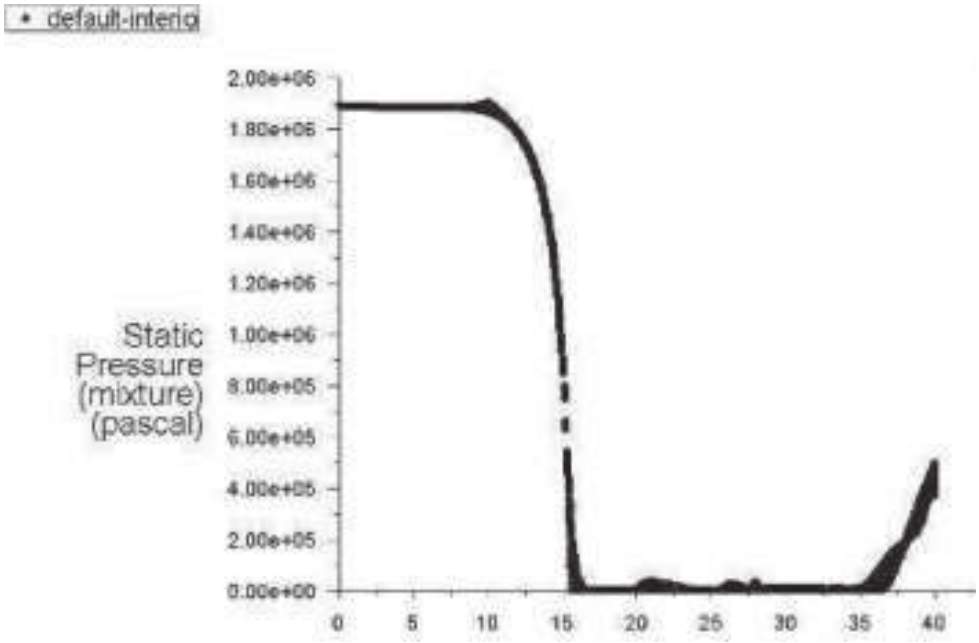

Fig5 . PRESSURE VARIATION FOR AN INLET PRESSURE OF 20 BAR AND AN OUTLET PRESSURE OF 5 BAR IN THE VENTURI TUBE

Creative Commons Attribution-NonCommercial-NoDerivatives 4.0 International License (CC BY-NC-ND)

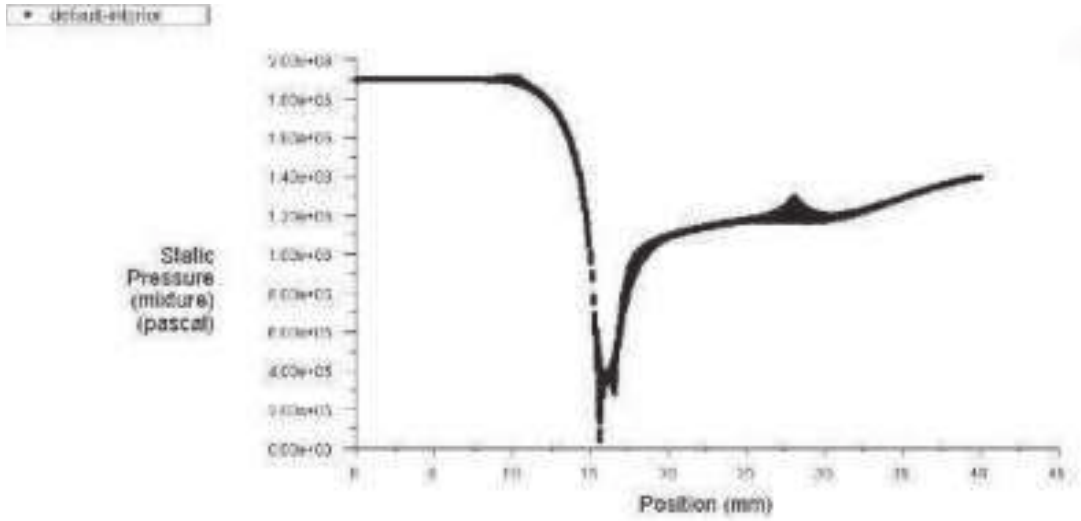

Fig6 . PRESSURE VARIATION FOR AN INLET PRESSURE OF 20 BAR AND AN OUTLET PRESSURE OF 14 BAR IN THE VENTURI TUBE.

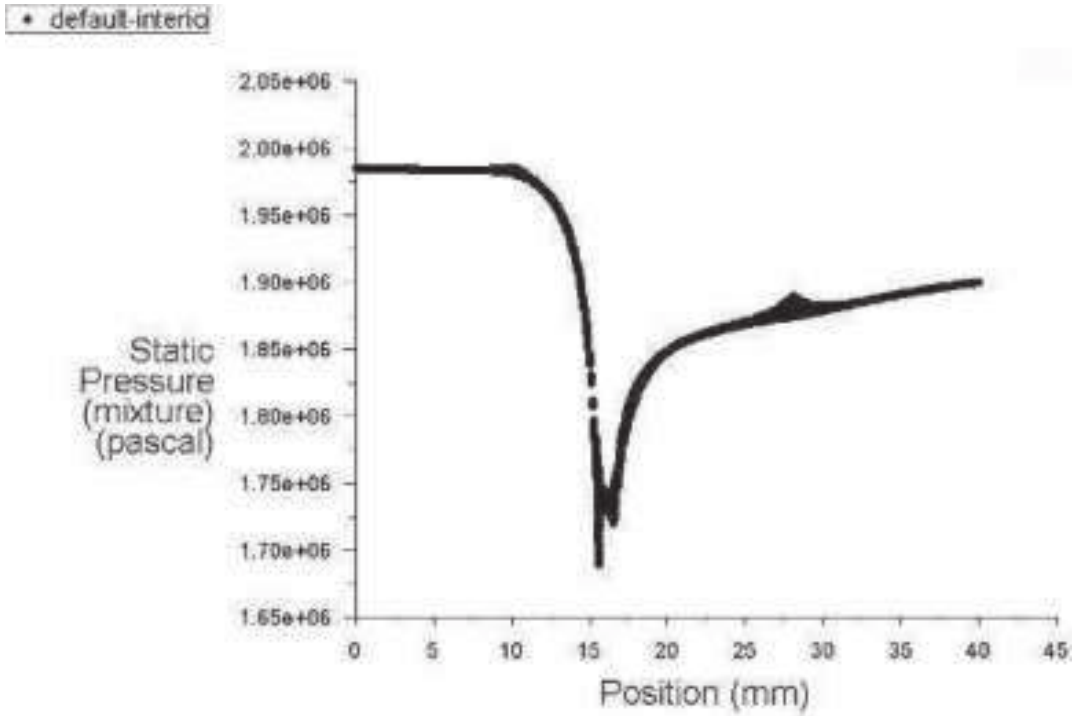

Fig7 . PRESSURE VARIATION FOR AN INLET PRESSURE OF 20 BAR AND AN OUTLET PRESSURE OF 20 BAR IN THE VENTURI TUBE.

Fig.8 shows the evolution of the void fraction as a function of the outlet pressure for an inlet pressure set at 20 bars and outlet pressures of 1, 5, 10, 15 and 20 bars, such as pressure static, For low outlet pressures we notice that the cavitation zone is wider. As for example, the case where the outlet pressure is equal to 1 bar, the vacuum fractions spread out and take maximum values almost throughout the area of the divergent (downstream of the throat up to the outlet of the venturi). Each time we increase the outlet pressure, we notice that the cavitation region is limited to a region of the divergent very close to the neck.

Creative Commons Attribution-NonCommercial-NoDerivatives 4.0 International License (CC BY-NC-ND)

Algerian Journal of Engineering Architecture and Urbanism Vol. 5 Nr. 3 2021
ISSN: 2588-1760

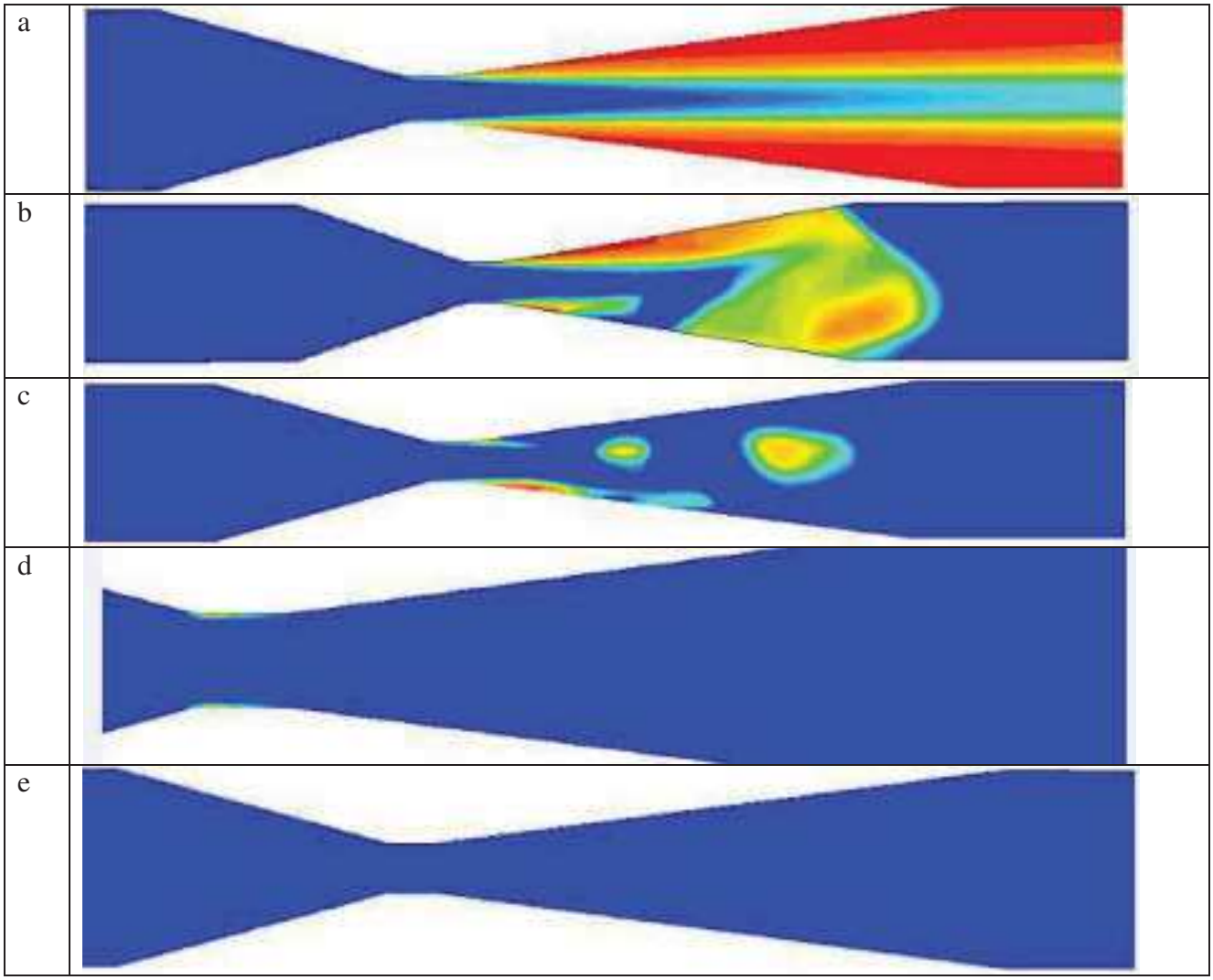

Fig8. INFLUENCE OF THE OUTLET PRESSURE ON THE CONTOURS OF THE VACUUM FRACTION IN THE VENTURI:
a. $p(out) = 1$; b. $p(out) = 5$; c. $p(out) = 10$; d. $p(out) = 15$; e. $p(out) = 20$

Conclusion

A wide variety of flow metering means exists, among these means there is the cavitating venturi. This diversity of use of several or different types of flowmeters is the result of certain criteria such as: the nature of the fluids transported, the type of flow rates measured, the measurement accuracy as well as the installation and service conditions.

To fully understand any phenomenon, it is essential to perform numerical simulations. So the same is the case for the small size cavitatnt venturi, we performed a digital simulation on this device to get an idea of the reliability of the latter in controlling the mass flow with the change in downstream pressure.

Creative Commons Attribution-NonCommercial-NoDerivatives 4.0 International License (CC BY-NC-ND)

Based on experimental results of a cavitating venturi from the literature, a numerical simulation of the flow in a cavitating venturi was undertaken. The numerical results were successfully compared with experimental measurements from the literature.

Analysis of the results in terms of static pressure and the vacuum fraction obtained by the simulation allowed us to clearly see the cavitation zone in the cavitating venturi. It has been shown that the downstream pressures have a direct influence on the cavitation zone. For low downstream pressures the cavitation zone is wider, while it tends to disappear for high pressures. Basically, it has been shown that numerical simulation can be a very interesting tool for the design and study of cavitating venturis, in general, and those of small sizes in particular.

References:

Rayleigh L, O.M. , F.R.S. (2009), *The pressure developed in a liquid during the collapse of a spherical cavity,* the London, Edinburgh, and Dublin Philosophical Magazine and Journal of Science ,Series 6,Volume 34, 1917 - Issue 200, Pages 94-98 .

Brennen C. E. (1995), *Cavitation and Bubble Dynamics*. Oxford University Press, NewYork, .

Chahine, G.L. (1983), *Cloud cavitation : theory*. 14th Simp. On Naval Hydrodynamics.

Ashrafizadeh S.M.,. Ghassemi H. (2015), *Experimental and numerical investigation on he performance of small-sized cavitating venturis,* Flow Measurement and Instrumentation, vol. 42, pp. 6–15.

Da Silva EG. (2011), *Numerical Study of Unsteady Turbulent Cavitating Flow, European Journal of Mechanics - B/Fluids*, Elsevier, 2011, 30, pp.26-40.

Goncalves E , P. RF (2010). *Numerical study of cavitating flows with thermodynamic effect*. Comput. Fluids, 39:99-113.

Creative Commons Attribution-NonCommercial-NoDerivatives 4.0 International License (CC BY-NC-ND)

Algerian Journal of Engineering Architecture and Urbanism Vol. 5 Nr. 3 2021
ISSN: 2588-1760

CARBONATE-HOSTED PB-ZN-FE (CU, F, BA) DEPOSITS OF THE NORTHERN EAST ALGERIA: METALLOGENY, STRUCTURAL AND GRAVIMETRIC /AEROMAGNETIC LINEAMENTS CONTROLS

Saadia YSBAA[1], Omar HADDOUCHE[2], Abdelhak BOUTALEB[2], Madjid CHEMAM[3]

[1] Laboratory of Mineral Resources and Energy, University M'hamed Bougara of Boumerdes, Algeria , e-mail: s.ysbaa@univ-boumerdes.dz

[2]Metallogeny and Magmatism Laboratory, University of Sciences and Technology Houari Boumediene (USTHB), Algiers, Algeria

[3]Abitibi Géophysique inc, Abitibi, Canada

Abstract:
The northern east of Algeria constitutes the most important metallogenical zone for Pb-Zn-Fe (Cu, F, Ba). Mineralization is mainly in vein fillings in fractures and in epigenetic lenticular or stratabound ores that can be classified as Mississippi Valley Type "MVT" deposits. The orebodies are preferentially associated with small surface NE-SW/NW-SE and E-W-trending faults, mainly located in the margins of the subsiding basins/synclines, at the apex or along the anticline structures. The relationship between deep lineaments, surface faults and associated mineral deposits has been investigated in these regions, through the analysis of regional gravimetric/aeromagnetic surveys, metallogenic and geological data. Mineral deposits occurred along the margin of geological structures (e.g., subsiding basins) deduced from the gravimetric data. In Hodna/Setifian and Belezma Mounts, mineralization is generally lie along or near NW-SE oriented regional-scale deep lineaments. In the neighbouring regions (e.g., Batna/Aures, Tebessa Mounts and diapiric zone), mineral deposits are located along or near (or at intersections of) NE-SW/NW-SE deep lineaments. The deeper lineaments that are plausible structural controls on the mineralization in these regions play probably an important role in providing pathways for focusing mineralised fluids into the upper crust to depositional sites along surface smaller faults. It is suggested that mineral deposits appear to be regionally controlled by these structural limits, which reflect trending major deformation corridors, and can indicate a potential target in mining exploration.

Key words: Geology, metallogenical, geophysical data, ore-deposit, tectonic, exploration.

Introduction:

Many small polymetallic ore deposits of Pb-Zn-Fe- (Cu, F, Ba) have been discovered in the northern east of Algeria. The mineral deposits were mined since eighteen century for mainly Fe and Pb, Zn. These deposits are closely associated with the Jurassic and Cretaceous carbonate rocks, related to hydrothermal processes. Mineral deposits show a spatial relationship with the major faults that would have controlled the circulation of the hydrothermal fluids responsible for the emplacement of mineralization (Bouzenoune, 1993; Boutaleb, 2001; Haddouche, 2010; Haddouche et al., 2016; Sami, 2011).

This spatial relation with major faults has been successfully used as a guide in exploration for decades (e.g., National Office of Geologic and Mining Research of Algeria, ORGM). In this study we have used geological, metallogenical and geophysical data (gravimetric and aeromagnetic data) to identify structural/lineaments control on mineralization. Currently, in many other parts, several authors used similar approach in the study of ore genesis, metallogenical regularity and mineral resource prediction (e.g., Blakely and Jachens, 1991; Lü et al., 2012; Shah et al., 2013, Wang et al., 2011, Cheng, 2012; Gunn et Dentith, 1997; Chernicoff et al., 2002; Bierlein et al., 2006; Austin and Blenkinsop, 2009; Joly et al., 2012; Chen et al., 2015). For example, Austin and Blenkinsop (2009) used correlation analysis between mineralization and structures to recognize structural controls on mineralization, in the eastern Mount Isa Inlier (Australia). These studies may be combined with other

Creative Commons Attribution-NonCommercial-NoDerivatives 4.0 International License (CC BY-NC-ND)

techniques. Thus, Crafford and Grauch (2002) used geological, geophysical and isotopic data to suggest a fundamental link between the locations of world-class Carlin gold deposits and concealed deep crustal fault zones in north central Nevada (USA). Vos et al. (2004) employed combination of structural–tectonic, geophysical and geochronological data in northeastern Queensland (Australia) to establishing linkages between orogenic gold deposits and concealed crustal breaks. The aeromagnetic data used were made by the American firm Aero Service Limited (1971-1974) whose measurement step is 150 feet, or about 46 m. The gravimetric maps have been reinterpreted, based on the gravimetric data made by Zerdazi (1990). The Bouguer data are regional, with an overall accuracy of -113.10 to 3.55 mgal, interpolated at the nodes of a regular grid of 500X500 m.

This paper reviews the geologic setting, metallogenical characteristics of these areas and the importance of major geophysical lineaments (by processed gravimetric/aeromagnetic data) and aimed at distinguishing the spatial relationship between mineral deposits, fault systems and structural/lineaments that control mineralization. A GIS of ArcView was applied for visualization of the spatial distribution of the mineral deposits and to aid interpretation. The spatial distribution of mineralization was analyzed by a plot on which each data point (e.g., mineral deposits) is marked relative to every other data (geologic, tectonic, gravimetric and aeromagnetic maps). These techniques have been successfully used by several authors and might be used as an exploration guide for this type of mineralization.

Geological and tectonic setting

The study area is mainly composed of Mesozoic sedimentary rocks, with locally dispersed intrusions of Triassic rocks (Fig.1).

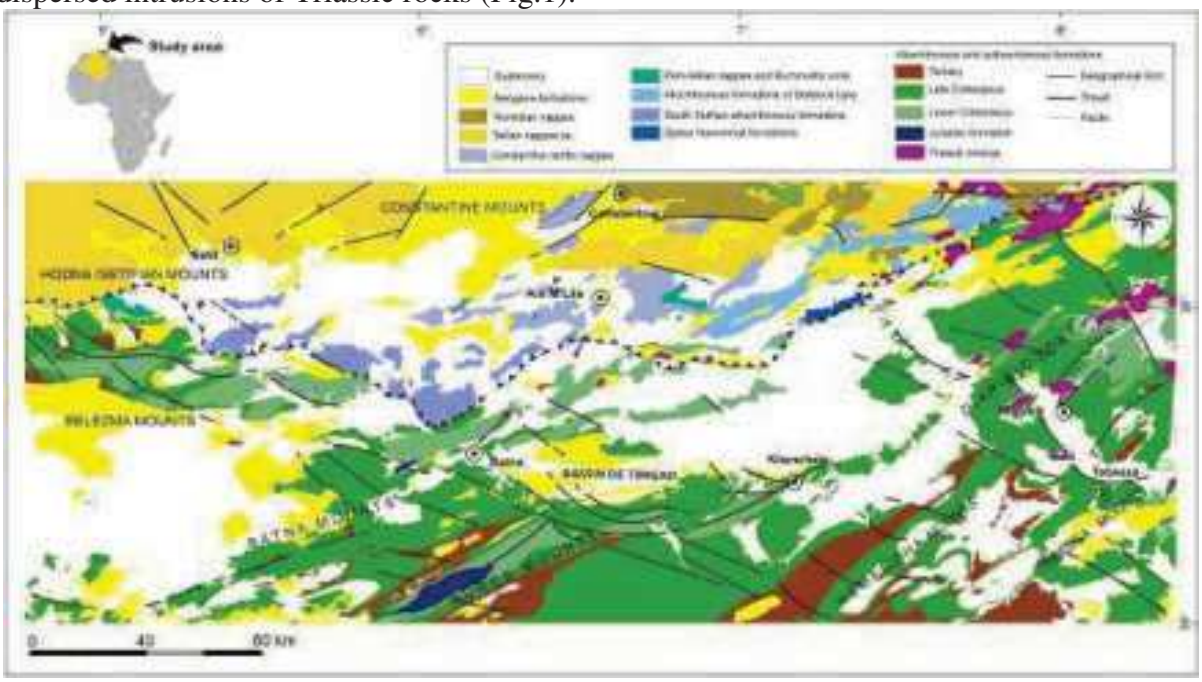

Fig.1 Simplified geological map of Northern East Algeria. Modified from Vila (1980) and Haddouche and al., (2014).

The structural evolution of this part of North Eastern of Algeria, results from the superposition of several polyphase tectonic events. The first phase (Neo-Cimmerian phase)

Creative Commons Attribution-NonCommercial-NoDerivatives 4.0 International License (CC BY-NC-ND)

known in northeastern Algeria discovered at the Jurassic-Cretaceous limit and marked by discordances. This is followed by the Austrian phase, occurred in the Middle Albian, responsible for the structuring of NNW-SSE folds. On the other hand, the Lower Cretaceous period was mainly marked by the development of extensional structures with tilted blocks and grabens (Herkat, 1999). Sharp variations in thickness and facies towards the north-east indicate that basin subsidence was driven by regional tectonic movements along NE-SW, ENE-WSW and E-W- trending normal faults that placed sub basin (Herkat, 1999). The overall evolution during Cretaceous is also maintained by halokinesis of Triassic salt creating subsident rim-synclines, where organic-rich facies prevail. The post Lutetian-ante Miocene phase (Laffite, 1939; Guiraud, 1990; Vila, 1980; Marmi and Guiraud, 2006) represents the most important episode in the north-eastern Algeria, preceded by an extensional regime responsible of the large sedimentary basin subsidence and ascension of Triassic rocks. In these regions, predominantly NE-SW (N50 to N60°) folded structures were formed (Fig.2), related to a late Eocene compressive event. The Belezma anticline was starting to form at the base of Late-Eocene and thrusts developed during Miocene (intra-Tortonian, Guiraud et al., 2005).

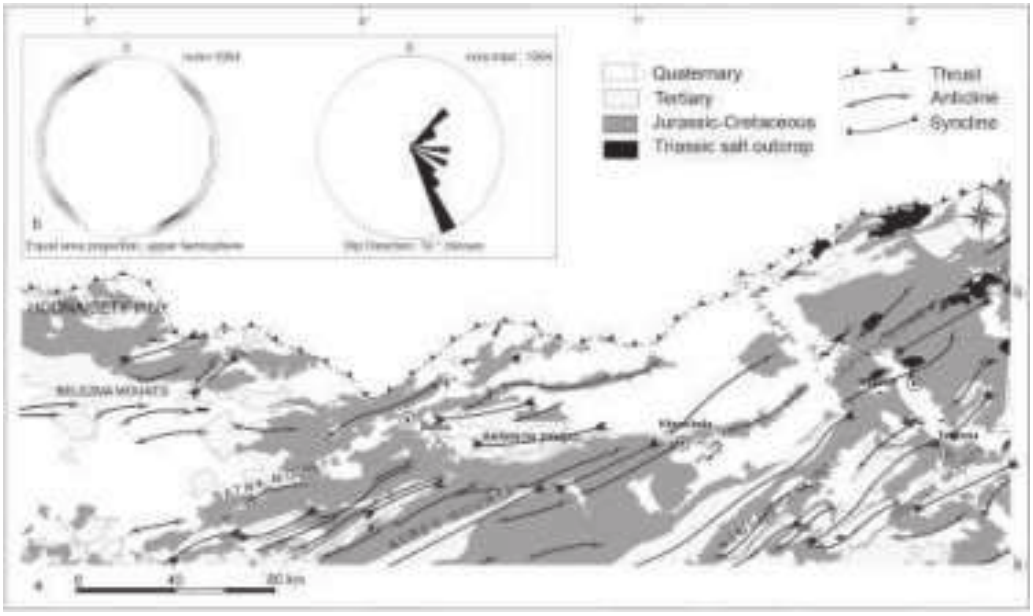

Fig.2 (a) Regional geological sketch map of north eastern Algeria, showing the locations of regional-scale folds, and the extent of Jurassic-Cretaceous and Tertiary rocks (b) Average rose diagrams showing orientations of 1064 faults in the study area

In the eastern Saharan Atlas (e.g., Aures, Batna, Nemenchas and Tebessa Mounts), the compressive phase is responsible for the structuring of NE-SW folds. It is followed in the north of Algeria and in the Constantine Mounts (Coiffait, 1992; Aris et al., 1997) by a large compressive tectonic phase during the Miocene, which continues until the Quaternary in Southern Saharan Atlas (Adoum, 1995).

This with large extension is responsible for structuring EW to WNW-ESE folds, clearly visible on the southern edge of the Aures-Nemencha and the Timgad basin. Recent work by Aris et al., 1997, revealed a regional extension phase (N140° -150° E) during the Miocene and late

Creative Commons Attribution-NonCommercial-NoDerivatives 4.0 International License (CC BY-NC-ND)

Pliocene-Quaternary, followed by a compressive phase (N130° -150° E) during the quaternary and the present.

The diapiric structures are numerous and can locally influence the sedimentary and structural evolution of the sedimentary cover. In the Khenchela region, diapiric movements allow the development of santonian reefs (Camoin et al, 1990; Guiraud, 1990). In the "diapiric zone", these phenomena are important, affecting Upper Cretaceous and Tertiary formations (Perthuisot, 1978-1992; Perthuisot and Rouvier, 1988; Thibieroz and Madre, 1976; Bouzenoune, 1993; Rouvier et al., 1985, Sami, 2011).

Faults that affect these regions are numerous (Fig.2a). There is a wider of orientations for NW-SE, NE-SW, E-W and rarely ENE-WSW/NS trending faults (Aissaoui, 1984; Kazi-Tani, 1986; Addoum 1995; Vila, 1980; Boutaleb, 2001; Haddouche, 2010; Sami, 2011). The NW-SE-trending faults are mainly composed by normal or strike-slip faults, intersecting locally NE-SW-trending faults.

Metallogenical aspect

Many small Pb-Zn-Fe (Cu, F, Ba) ore-deposits and showings are located in Setifian/Hodna, Batna/Aures, Tebessa, Belezma Mounts and diapiric zone (Fig.3a), majority hosted in Jurassic and lower Cretaceous (Hauterivian, Barremian, and Albo-Aptian) carbonate rocks. Mineralization occurs in veins (veinlets) fillings in fractures and in lenticular or stratabound ores, related to epigenetic hydrothermal system. Most of the orebodies (veins, lenticular and stratabounds ores) are developed mainly along the NW- SE/NE-SW and E-W-directions (Fig.3b).

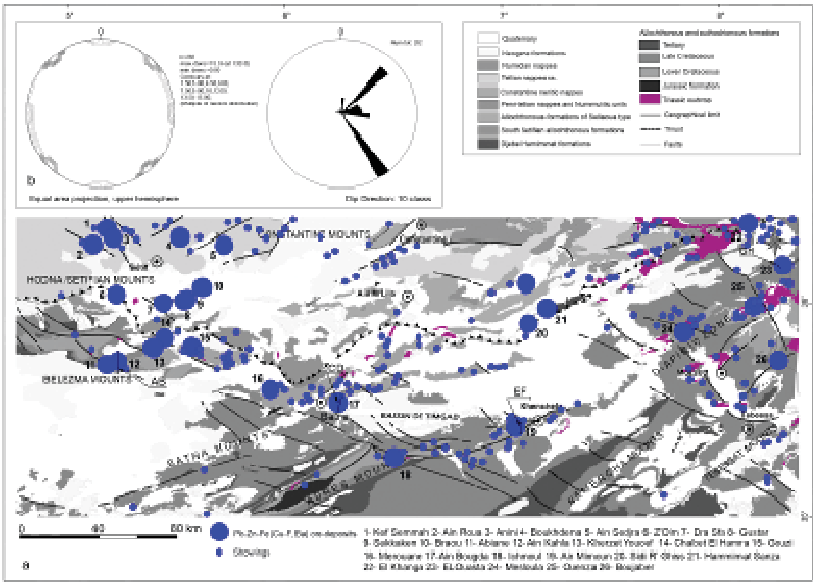

Fig.3 Simplified geological map of North Eastern Algeria, mainly showing: (a) the spatial distributions of major Pb-Zn-Fe (Cu, F, Ba) mineral deposits (b) Average rose diagrams showing orientations of major Pb-Zn-Fe (Cu, F, Ba) orebodies in north eastern Algeria.

The orebodies are dominated by banded ores (Fig.4a, b, c, d) breccias or hydraulic breccias ore (Fig.4e, f, g) and disseminated ore (Fig.4h, i), but fracture-filling (Fig.4j), veinlets (Fig.4k), massive and collomorphic textures (Fig4l) are also common in most orebodies (Boutaleb, 2001; Haddouche, 2010; Sami, 2011).

Creative Commons Attribution-NonCommercial-NoDerivatives 4.0 International License (CC BY-NC-ND)

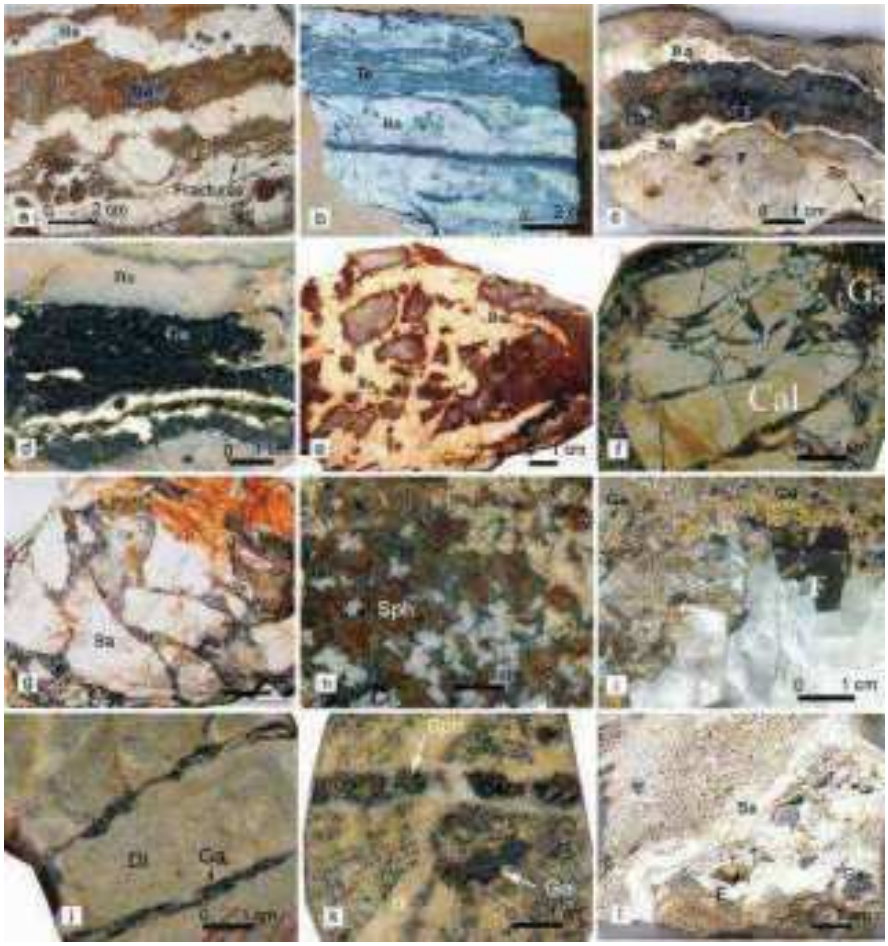

Fig.4 Major textures of ores from some ore-deposits. (a) Banded ore from Ichmoul ore-deposit [Galena (Ga)+Barite (Ba)] affected by later deformation. (b) Banded ore from Ain Mimoun ore-deposit [Barite+ tetrahedrite (Te)]. (c) Banded ore from M'Khiriga ore-deposit [Barite+ Galena+fluorite (F)]. (d) Banded ore from Ain Kahla ore-deposit [Barite+ Galena]. (e) Breccia ore from Hamimat ore-deposit (Morsott-diapiric zone) at contact Triassic rocks/Aptian [Barite]. (f) Hydraulic breccia ore from Boutaleb (Setifian) ore-deposit [Galena+ calcite (cal)]. (g) Breccia ore from Ichmoul ore-deposit [Barite+ calcite]. (h) Disseminated ore from Gustar ore-deposit [Sphalerite (Sph)] (i) Disseminated ore from Ouenza ore-deposit (diapiric zone) [Galena+ fluorite]. (j) Fracture filling ore from Boukhdema ore-deposit [Galena+ Dolomite (Dl)]. (k) veinlet ore from Boukhdema ore-deposit [Sphalerite] cutting veinlet dolomite [Dolomite]. (l) Collomorphic ore from M'khiriga ore-deposit [Galena+barite+ fluorite].

In Setifian area, the best-known ore-deposits are those of Boukhdéma, Ain Roua, Ain Sedjra, Kef Semmah, and Anini. Boukdéma is the most important and economical ore-deposit, characterized by a mineral association with sphalerite, galena and pyrite, as a "stratabound" (Boutaleb, 2001). There is also a Cu-As-Sb-Ba mineralization related to fissure fillings and veinlets.

In Hodna region, economic carbonate-hosted Zn-Pb deposits occur at several stratigraphic horizons in carbonate rocks (dolomitic) of Jurassic, lower Cretaceous and Miocene age. As for all mineral deposits of Setifian, mineralization of Hodna is located at limited subsiding basins (Boutaleb, 2001). The lower Cretaceous (Hauterivian and Barremian) horizons contain

Creative Commons Attribution-NonCommercial-NoDerivatives 4.0 International License (CC BY-NC-ND)

the economically most important base metal ore-deposits. Mineral deposits are mainly as stratabound orebodies, and in vein type filling (Boutaleb et al., 1999). The most important ore-deposits are those of Ain Kahla, Kherzet Youcef, Chabet El Hamra, Abiane, Z'Dim, Braou, Dra Sfa, and Sekkaken. Mineralization is mainly composed by galena and sphalerite, associated locally with pyrite, smithsonite, cerusite, and hydrozincite.

The Ain Kahla mineralization consists of ore bodies that are embedded in the Upper Liassicand in the Dogger dolomites. The most significant base metal concentration is emplaced within regional unconformities (Fig.5), such that of the infra-Toarcian (Boutaleb et al., 2006).

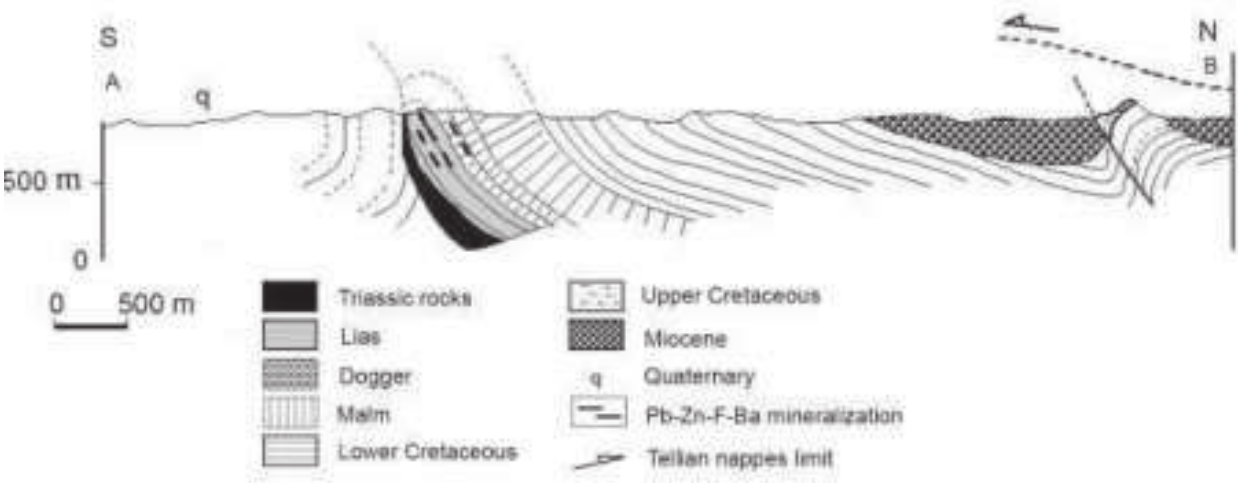

Fig.5 Geological cross-section in the Ain Kahla Pb-Zn-F-Ba ore-deposit (Boutaleb et al., 2006).

In the Belezma Mounts, there are several Pb-Zn mineral deposits. Merouana is hosted in dolomitic rocks of Upper-Aptian, related to fracture fillings with various directions (Glaçon, 1967; Boutaleb, 2001). Mineralization is reflected principally by sphalerite, pyrite and galena associated with white dolomite. During 1992 to 1998, ORGM (National Office of Geologic and Mining Research) exploration work has been concentrated in the Batna Mounts, based mainly on geophysical analysis and drilling work. As a result of this work, a new Pb-Zn ore-deposit (Ain Bougda) was discovered, hosted in limestone dolomitized of Aptian. Ore-bodies are mainly lenticular "stratabound" (Fig.6), located in the margin of the subsiding basin. Mineralization consists essentially of marcasite, pyrite, melnicovite, sphalerite, and galena, related to open spaces filling and breccia cement.

Creative Commons Attribution-NonCommercial-NoDerivatives 4.0 International License (CC BY-NC-ND)

Algerian Journal of Engineering Architecture and Urbanism Vol. 5 Nr. 3 2021
ISSN: 2588-1760

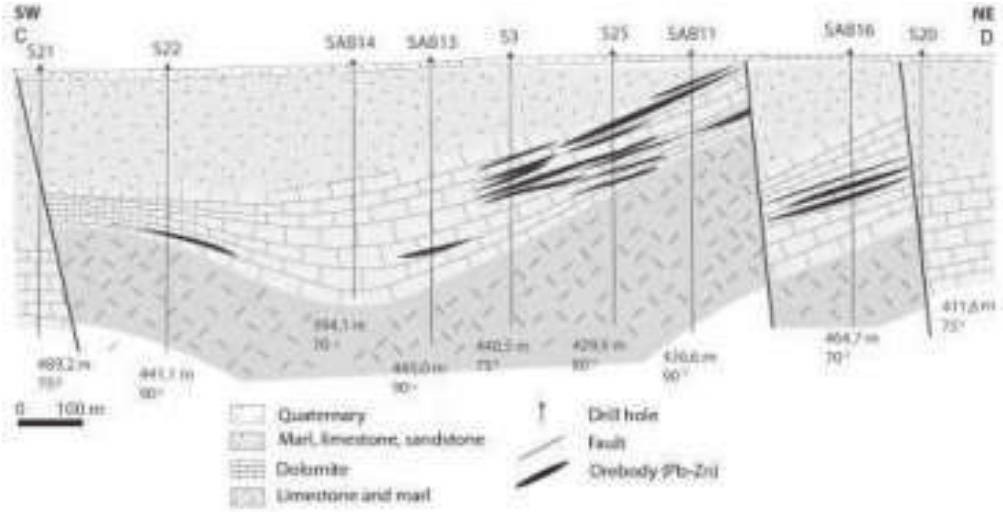

Fig.6 Geological cross-section in the Ain Bougda Pb-Zn ore-deposit.

In the Aures Mounts, there are several deposits of Ba-Pb-Zn (Hg) hosted in carbonate formations of Cretaceous and Miocene. There are two principal deposits (1) Ichmoul ore-deposit essentially composed by barite and galena, in form of lenticular piles of direction E-W. These minerals are associated with disseminated red sphalerite in black shales rich in organic matter (Haddouche, 2010). (2) Aïn Mimoun ore-deposit is related to NW flank of Khenchela anticline (Djebel Aidel) or provided on the edges of syncline structure (Fig.7). Mineralisation is located in veins along normal fractures (NE-SW, NW-SE and E-W), characterized by barite, galena and gray copper. It's hosted in calcareous-dolomitic and sandstone of Albo-Aptian age.

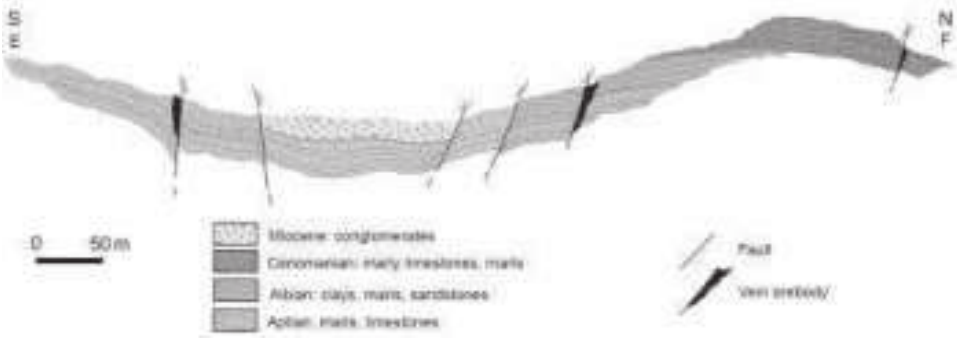

Fig.7 Geological cross-section in the Ain Mimoun Pb-Zn ore-deposit (Haddouche, 2010)

In the diapiric zone, there are many lead, zinc and iron (siderite) ore-deposits, mostly controlled by diapiric structures according to NE-SW axis. Major ore-deposits are those of El Ouenza, Boukhadra, El Ouasta, Mesloula, M'khiriga, M'Zeita and Boudjaber. All these ore-deposits are hosted in carbonate of Aptian-Albian, related to fracture fillings or veins. Recent studies of mineralization related to Tunisian and north-east of Algeria diapirism (Perthuisot and Rouvier, 1988; Hatira, 1988; Shepard et al., 1996; Haddouche et al., 2003) show analogies with mineralization related to the "Cap rocks" of the "Gulf Coast" salt-dome, variant of Mississippi Valley type deposits "MVT" (Kyle and Price, 1986; Posey et al., 1994;

Creative Commons Attribution-NonCommercial-NoDerivatives 4.0 International License (CC BY-NC-ND)

Kyle and Saunders, 1996). Concentrations type "Cap rock", related to cortical salt dome is characterized by impregnation of Pb-Zn, Fe (Ba-Sr) mineralization, near the diapirs-sedimentary cover interface (e.g., Djebel Ressas, El Ouasta and Hameimat) (Fig.8). These types of concentrations whose bodies included in "Cap rock" formation or near the sedimentary cover are the subject of particular attention, due to their importance in the oil fields and mineral exploration.

Fig.8 Geological cross-section in the Ouasta (diapiric zone) Pb-Zn-Fe (Ba, Sr) ore-deposit

Mineralization with no visible connection with diapiric systems are also numerous in the Northern East of Algeria. This is especially NW-SE and NE-SW orebodies of Es Souabah and Hdjar Merakeb (Sami, 2004). At Ouenza, polymetallic mineralization (veins) is always related to N50 and N140 fractures affecting the Aptian limestones (Bouzenoune 1993; Sami, 2011). They show a simple paragenesis with galena, pyrite, chalcopyrite, sphalerite, tetrahedrite, barite and fluorite. Mineralization is also represented by dissolution filling for fluorite, quartz and barite and by dissemination for galena and tetrahedrite. The polymetallic mineralization intersects the iron mineralization and would be of Miocene age (Sami, 2011).

Geophysical data analysis

Gravimetric and aeromagnetic data of the study area were used to remap the main geological units, infer the subsurface geology and to interpret the structural patterns which serve as potential mineralization zones in these regions. The Bouguer data are regional, with an overall accuracy of -113.10 to 3.55 mgal, interpolated at the nodes of a regular grid of 500X500 m. The high values of the Bouguer anomaly (-30 mgal) were located in the regions of Ouenza-Boukhadra. As for the low values (-90 mgal), they were located in the South-West of the studied region. The Gravimetric data analysis shows the presence of a large sedimentary cover. In the central part, linear structures (anticlines NE-SW) give values oscillating between -40 and -55 mgal. Linear gravity troughs directed to the NW-SE give values between -60 and -75 mgal.

The modeling software "Geosoft" was used to reverse the residual anomaly. The basement model of the study area was divided into small rectangular cells of dimensions 1000 X 1000 X 500 m (X, Y and Z). Figure 9 shows the projection of the surface density contrast distribution obtained by 3D inversion.

Creative Commons Attribution-NonCommercial-NoDerivatives 4.0 International License (CC BY-NC-ND)

Algerian Journal of Engineering Architecture and Urbanism Vol. 5 Nr. 3 2021
ISSN: 2588-1760

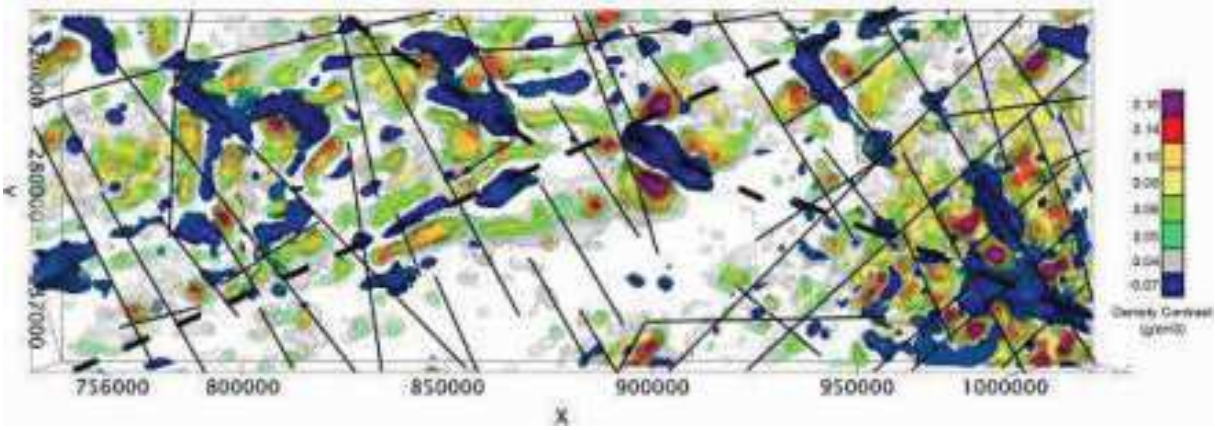

Fig.9 3D inversion contrast map interpretation of Setifian/Hodna, Batna/Aures, Tebessa, Belezma Mounts and diapiric zone

The interpretation of density contrast map obtained by 3D inversion, show numerous lineaments, mainly N135° to N170° and N40° to N60°. These lineaments have average lengths varying between 12 km and 120 km.

The blue anomalies of a more or less structure reflect probably the diapiric structures, or subsidence/tectonic troughs. The other density contrasts reflect linear geological structures (mainly anticlines N50°).

A large portion of the study area was covered by adjacent magnetic surveys carried out by the American firm Aero Service Limited (1971-1974). Raw aeromagnetic data were digitally-processed by "Geosoft" software. Visual inspection of the magnetic lineament map (Fig.14, 15) indicates similar linear trends (NE-SW and NW-SE-trending lineaments). Locally, the NE-SW-trending lineaments are intersected by NW-SE lineaments.

Spatial analysis and discussion

In this study, geological, metallogenical and geophysical analysis were employed to study the spatial pattern of known Pb-Zn (Cu, F, Ba) mineral deposits of the Setifian/Hodna and neighbouring regions (e.g., Batna/Aures, Tebessa, Belezma Mounts and diapiric zone).

The orebodies are located along small normal NE-SW/NW-SE and E-W faults cutting the lower Cretaceous carbonate rocks (Fig.10a, b, c, d). The correlation between Pb-Zn (Cu, F, Ba) mineralization density and the surface faults system show two main trends mineral occurrences (Fig.11a, b): (1) NW-SE trending at Hodna/Setifian and Belezma Mounts (2) NE-SW/NW-SE trending at Batna/Aures, Tebessa Mounts and diapiric zone.

Creative Commons Attribution-NonCommercial-NoDerivatives 4.0 International License (CC BY-NC-ND)

Algerian Journal of Engineering Architecture and Urbanism Vol. 5 Nr. 3 2021
ISSN: 2588-1760

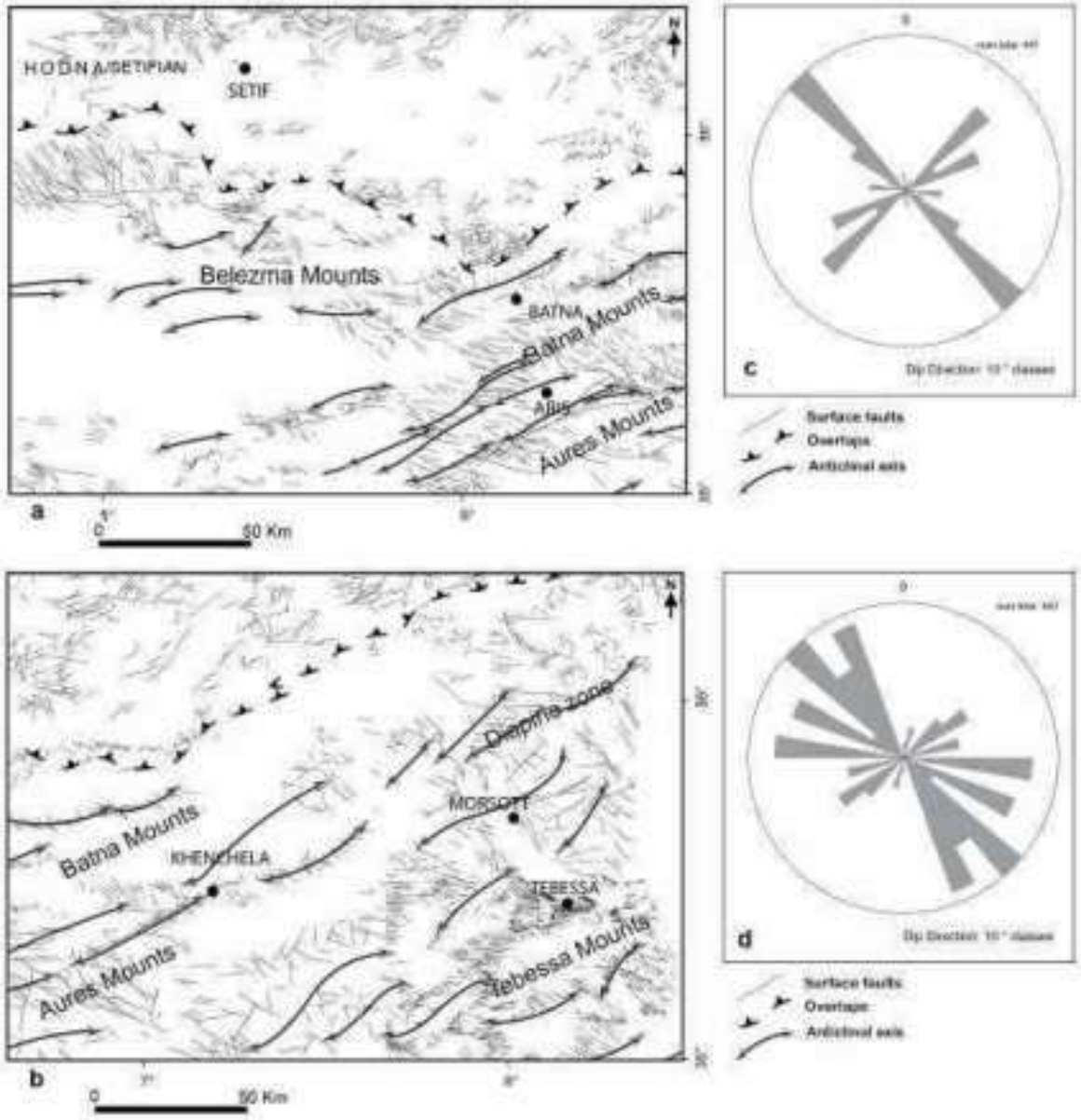

Fig.10 Tectonic maps (surface faults/fractures) of the Setifian, Hodna and neighbouring regions (a) Setifian/Hodna, Belezma and west of Batna/Aures Mounts (b) Batna, Aures, Tebessa Mounts and diapiric zone (c, d) Average rose diagrams showing orientations of surface faults cutting Jurassic-Cretaceous and Tertiary rocks

Creative Commons Attribution-NonCommercial-NoDerivatives 4.0 International License (CC BY-NC-ND)

Algerian Journal of Engineering Architecture and Urbanism Vol. 5 Nr. 3 2021
ISSN: 2588-1760

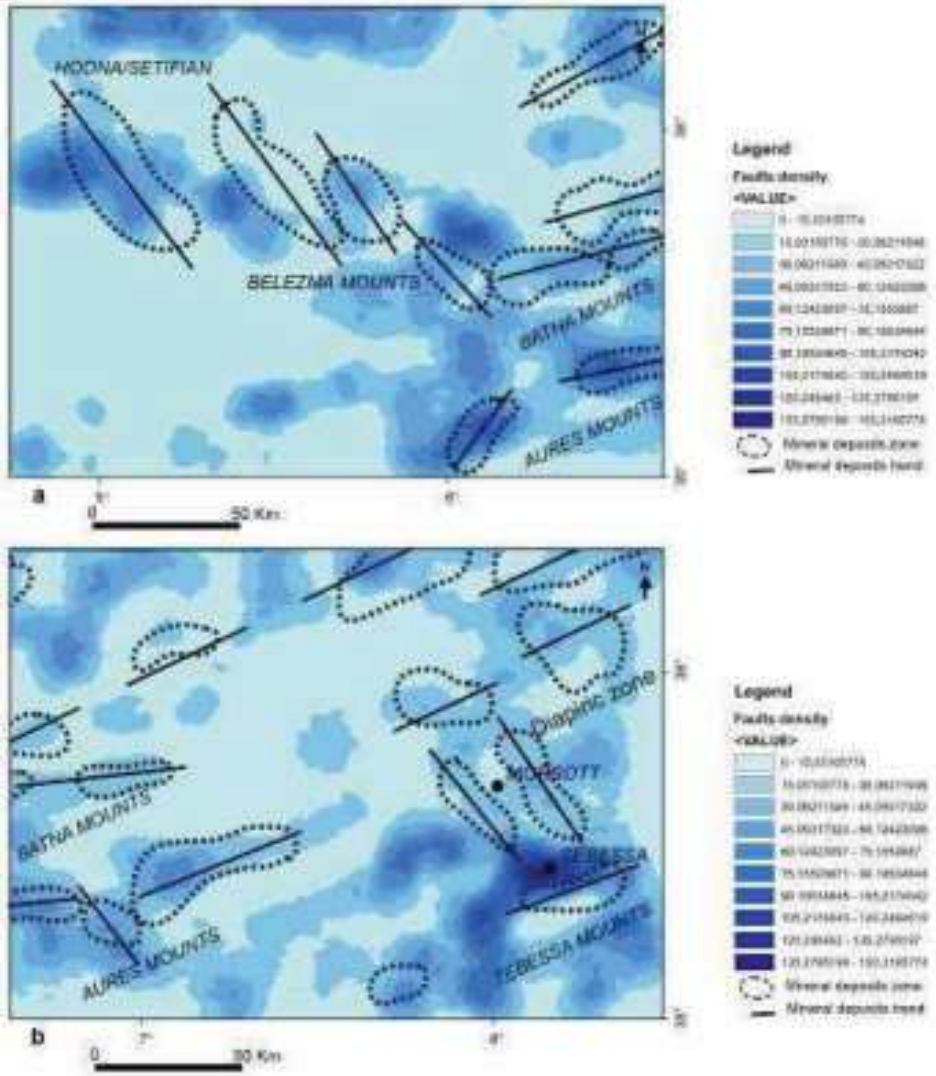

Fig.11 Correlation between Pb-Zn-Fe (Cu,F,Ba) mineralization density and surface faults trending (a) Setifian/Hodna, Belezma and west of Batna/Aures Mounts (b) Batna, Aures, Tebessa Mounts and diapiric zone

The regional-scale gravimetric lineaments show consistent spatial association with mineralization. In the Setifian/Hodna and Belezma Mounts, a large part of the mineral deposits occurs near or along deep NW-SE-trending lineaments and at margin basin, as shown by the gravimetric maps (Fig.12a, b).

In the Southern central (Batna Mounts) and in the East (Diapiric zone and Tebessa mounts) a number of mineral deposits occur near or at the intersection of NW-SE/NE-SW trending lineaments, at margin of subsiding basins/synclines and on the apex or along the anticline structures (Fig.13a, b). Other aspect of relevance to distribution of the mineralization, mineral deposits was deposited near or along NW-SE tectonic troughs (e.g., Morsott trough) (Fig.11b).

Creative Commons Attribution-NonCommercial-NoDerivatives 4.0 International License (CC BY-NC-ND)

Algerian Journal of Engineering Architecture and Urbanism Vol. 5 Nr. 3 2021
ISSN: 2588-1760

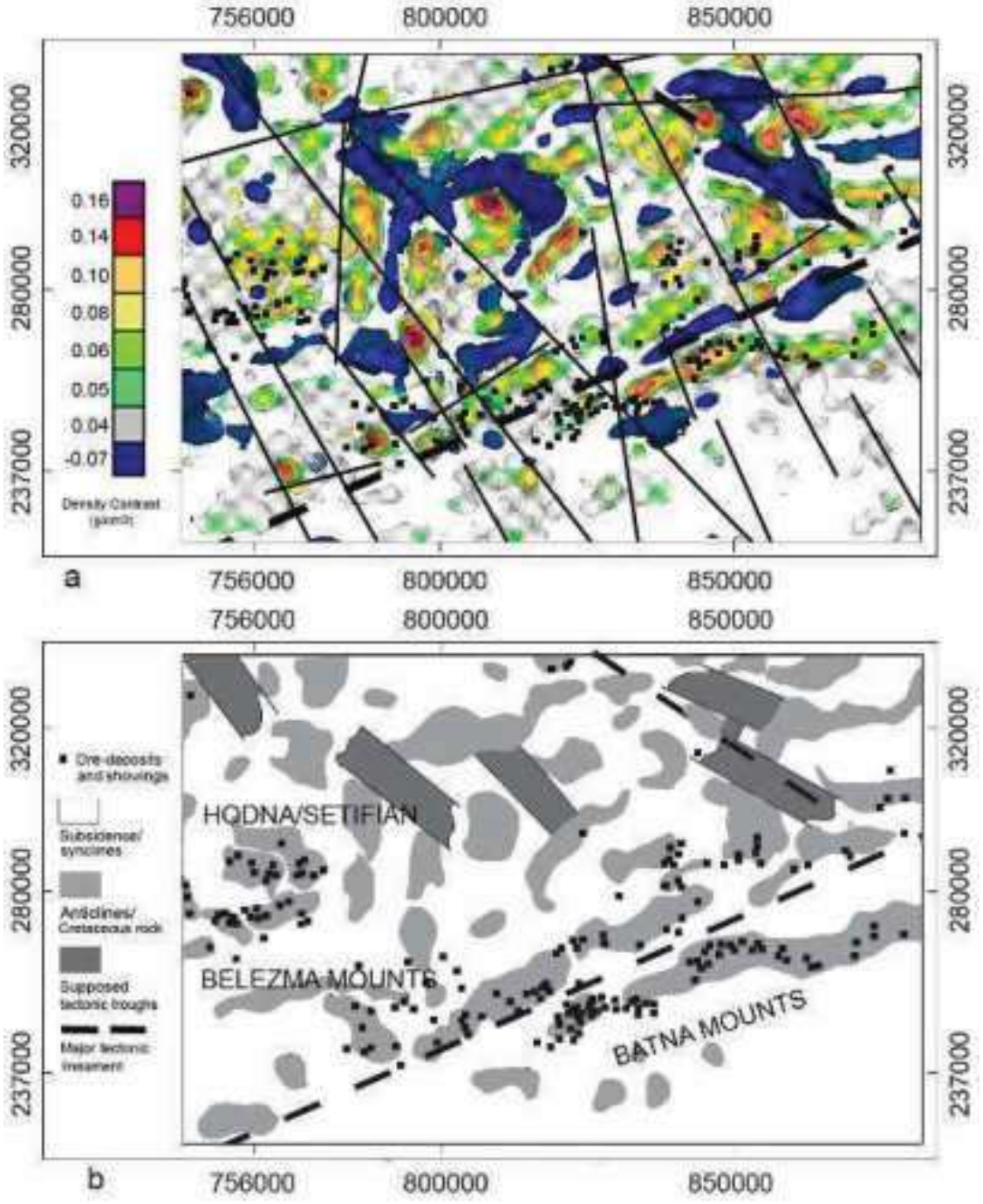

Fig.12 3D inversion contrast map interpretation of Setifian/Hodna, Belezma and west of Batna Mounts, showing the spatial relationship between Pb-Zn-Fe (Cu, F, Ba) mineral deposits and geophysical deep lineaments/structures (a, b). Small black dots indicate the locations of Pb-Zn-Fe (Cu,F, Ba) mineral deposits

Creative Commons Attribution-NonCommercial-NoDerivatives 4.0 International License (CC BY-NC-ND)

Algerian Journal of Engineering Architecture and Urbanism Vol. 5 Nr. 3 2021
ISSN: 2588-1760

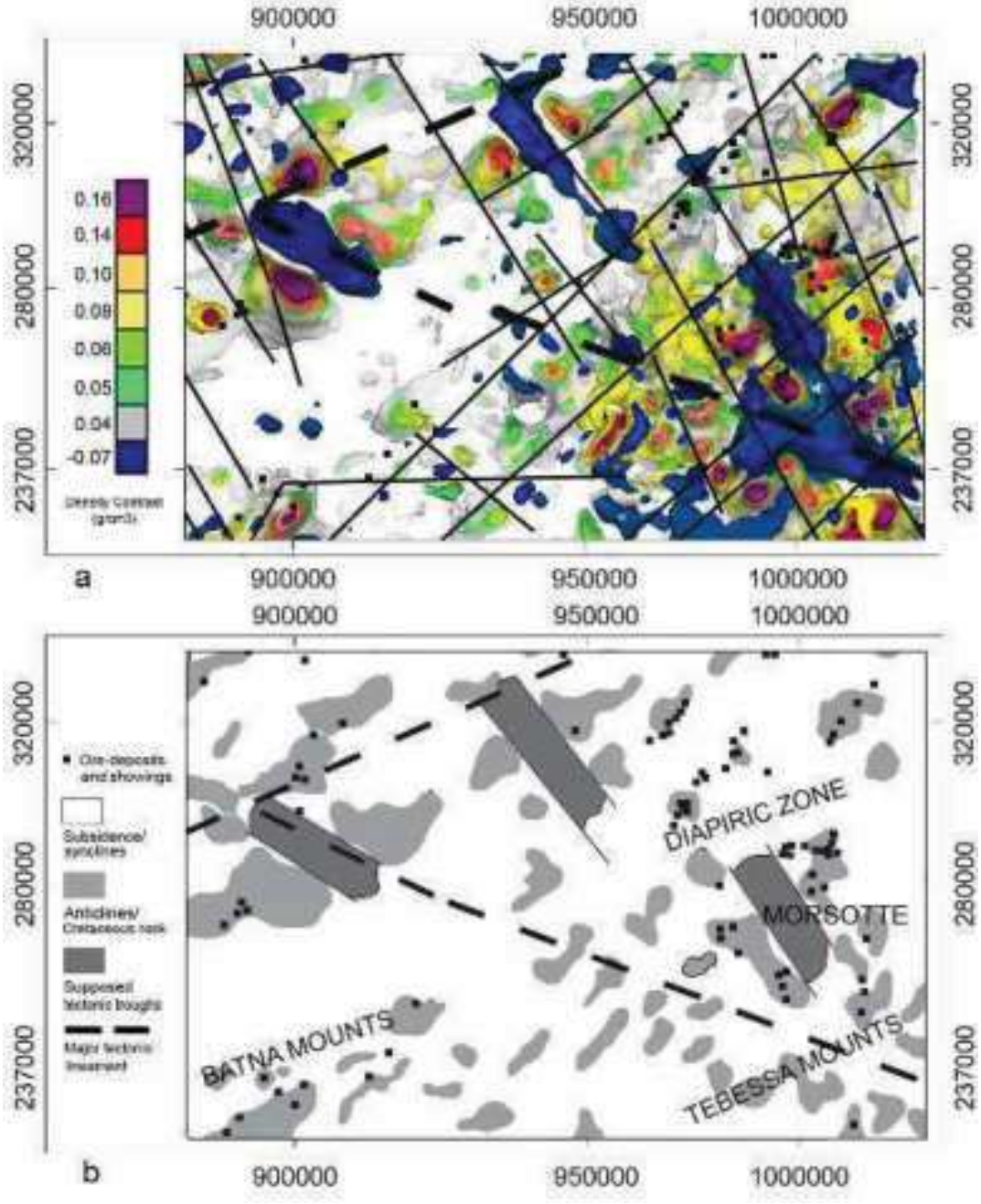

Fig.13 3D inversion contrast map interpretation of Batna, Aures, Tebessa Mounts and diapiric zone, showing the spatial relationship between Pb-Zn-Fe (Cu, F, Ba) mineral deposits and geophysical deep lineaments/structures (a, b). Small black dots indicate the locations of Pb-Zn-Fe (Cu,F, Ba) mineral deposits

This interpretation is supported by the spatial coincidence of some of the regional-scale of the first vertical derivative of the magnetic field (Fig.14a, b). Analysis of this aeromagnetic map helped to delineate deep lineaments and shows essentially NE-SW and NW-SE-trending lineaments which play a pivotal role in the localization of mineralization in the studied area. Mineral deposits are mainly located along or near these deep faults.

Creative Commons Attribution-NonCommercial-NoDerivatives 4.0 International License (CC BY-NC-ND)

Algerian Journal of Engineering Architecture and Urbanism Vol. 5 Nr. 3 2021
ISSN: 2588-1760

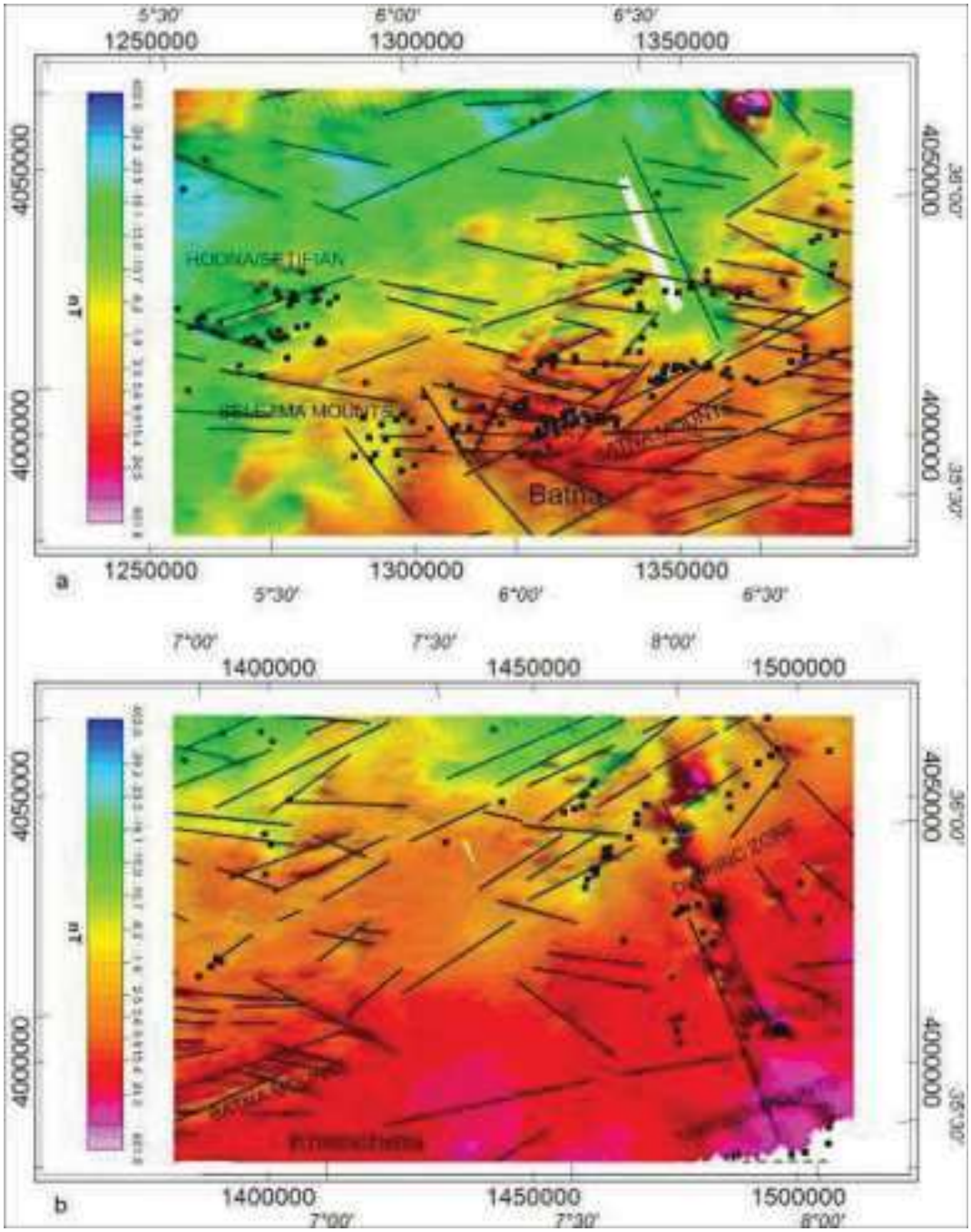

Fig.14 Interpretation of the first vertical derivative of the magnetic field in the North Eastern of Algeria. Small black dots indicate the locations of Pb-Zn-Fe (Cu,F, Ba) mineral deposits (a) Hodna/Setifian, Belezma and Batna Mounts (b) Batna, Tebessa Mounts and diapiric zone

Correlation between mineral deposits and lineaments deduced from aeromagnetic map (Aero Service Limited, 1971-1974, to a scale of 1.500.000) show a broadly similar pattern (Fig.15). In Hodna/Setifian and Belezma Mounts, mineralization is located along or near NE-SW-trending deep faults.

Creative Commons Attribution-NonCommercial-NoDerivatives 4.0 International License (CC BY-NC-ND)

Algerian Journal of Engineering Architecture and Urbanism Vol. 5 Nr. 3 2021
ISSN: 2588-1760

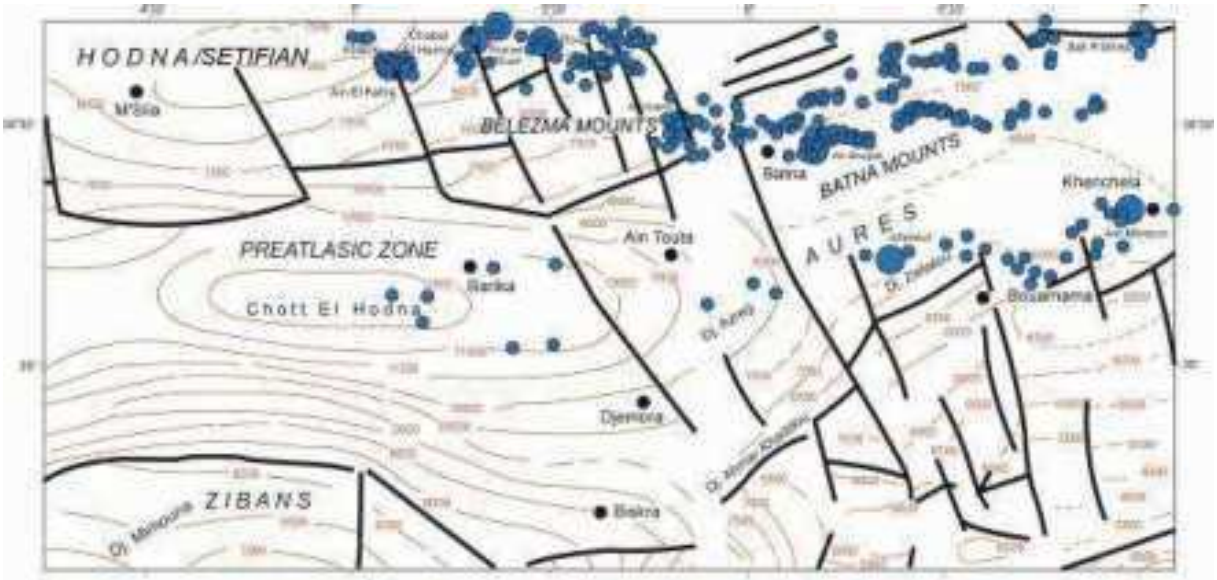

Fig.15 Correlation between mineral deposits and lineaments deduced from aeromagnetic map (Aero Service Limited, 1971-1974, to a scale of 1.500.000). Small blue dots indicate the locations of major Pb-Zn (Cu, Ba) mineral deposits

In the framework of the structural evolution outlined above, the NE-SW regional scale-gravimetric and magnetic lineaments can be interpreted as major faults (block-tilted system) that have controlled the evolution of the sedimentary basins of this region Herkat (1999). In addition, these faults may be favoured ascension of Triassic rocks from the bottom (Bouzenoune, 1993; Vila, 1980) in North Eastern part of Algeria.

NE-SW and NW-SE-trending lineaments systems have probably played a major role in the localization of mineral deposits in this area. Mineral deposits are usually either inside anticline hinge zones (example, Ichmoul and Ain Mimoum ore deposits) or on the flanks of anticline structures (example, Ain Bougda ore-deposit), related to carbonate formations of lower Cretaceous.

In the diapiric zone, the mineralized deposits are generally on the edges of the Triassic bodies, and sometimes related to NE-SW/NE-SW and E-W-trending faults (Mesloula, Es Souabaa and Hameimat ore-deposits).

These results suggest that Pb-Zn-Fe (Cu, F, Ba) are preferentially associated with smaller faults that are within close proximity of major deep lineaments. However, probably these deposits are regionally controlled by the major lineaments but locally by the combination of small faults under the influence of long deep faults. Major deep lineaments provide probably metal transport or create open spaces for fluid flow, and these fluids solution migrate or diffuse away from large deep faults to depositional sites along smaller faults. In the Setifian/Hodna and Belezma Mounts, the spatial distribution of the mineralization is along NW-SE axes, probably controlled by lineaments of the same direction at limited small subsiding-basins. In Batna/Aures Mounts and diapiric zone, mineral deposits appear to be regionally controlled by (or at intersections of) NE-SW and NW-SE-trending lineaments at limited margin of sedimentary subsiding-basins.

Conclusion

Creative Commons Attribution-NonCommercial-NoDerivatives 4.0 International License (CC BY-NC-ND)

The demonstrated association between significant signatures derived from the geological, metallogenical and geophysical (gravimetric and aeromagnetic) data analysis exhibit significant spatial correlations with the locations of Pb-Zn-Fe (Cu, F, Ba) mineral deposits and confirms the spatial link between these deposits, surface faults and major deep lineaments. Orebodies are preferentially located in the margins of the subsiding basins, at the apex or along the anticline structures, mainly associated with surface NE-SW/NW-SE and E-W-trending faults system. We suggest (i) in Setifian/Hodna and Belezma Mounts; mineralization occurs near or along NW-SE deep lineaments and mineral deposits appear to be regionally controlled by structural trends (subparallel NW-SE-trending). (ii) in the Batna/Aures, Tebessa Mounts and diapiric zone, mineral deposits are located within close proximity at (or at intersections of) major NE-SW/NW-SE deep lineaments.

These deeper lineaments play probably an important role in providing pathways for focusing mineralised fluids into the upper crust to depositional sites along surface smaller faults. Thus, the axial trends (NE-SW/NW-SE) reflect probably deformation corridors that have controlled the emplacement of mineralized deposits in these areas. These results may help to predict the potential mineralization targets by integrating other geo-information such as geochemical data in future mineral exploration.

References:

Abed, A.M. Saffarini, G.A., Sadaqah R.M., (2013). *Spatial distribution of uranium and vanadium in the upper phosphorite member in Eshidiyya basin, southern Jordan.* Arab J. doi.org/10.1007/s12517-013-0837-1.

Addoum, B. (1995). *L'Atlas saharien Sud-oriental : Cinématique des plis chevauchements et reconstitution du bassin du Sud-Est constantinois (Confins algéro-tunisiens). Thèse. Doct ès Sc.* Univ. Paris XI, Centre d'Orsay, *200 p.*

Afzal, P., Fadakar Alghalandis, Y., Khakzad, A., Moarefvand, P., Rashidnejad Omran, N.(2011). *Delineation of mineralization zones in porphyry Cu deposits by fractal concentration–volume modeling*. J Geochem Explor 108:220.

Aissaoui, D. (1984). *Les structures liées à l'accident sud-atlasique entre Biskra et le Djebel Manndra, Algérie. Evolution géométrique et cinématique. Thèse de 3 ème cycle*, Univ. Louis Pasteur, Strasbourg.

Aoudjehane, M.(1991). *Distribution des gîtes à Pb-Zn et fer sidéritique dans le NE algérien. In: Source, Transport and disposition of metals. Page l & J. Leroy (eds)*, Belkema, Rotterdam, pp.419-422.

Aris, Y., Coiffait, P.E., Guiraud, M.(1998). *Characterisation of Mesozoic-Cenozoic deformations and palaeostress fields in the Central Constantinois, northeast Algeria*. Tectonophysics 290, 59-85

Austin, J.R., Blenkinsop, T.G.(2009). *Local to regional scale structural controls on mineralisation and the importance of a major lineament in the eastern Mount Isa Inlier, Australia: Review and analysis with autocorrelation and weights of evidence*. Ore Geology Reviews 35, 298–316

Bierlein, F.P., Murphy, F.C., Weinberg, R.F., Lees, T.(2006). *Distribution of orogenic gold deposits in relation to fault zones and gravity gradients: targeting tools applied to the Eastern Goldfields, Yilgarn Craton, Western Australia.* Miner Deposita, Volume 41, Issue 2, pp.107-126

Boutaleb, A., Aïssa, D.E., Touahri, B.(1999). *Les gîtes plombo-zincifères du Hodna : Minéralisations comparables au type « Vallée du Mississippi »*. Bull. Serv., Géol., Algérie. Vol. 10, n°1, pp55 – 71, 6 fig., 2 tab.

Boutaleb, A.(2001). *Les minéralisations Pb-Zn du domaine Sétifien-Hodna : Gîtologie, pétrographie des dolomies, microthermométrie et implications métallogénique. Thèse. Doct. D'Etat*, USTHB (FSTGAT), Alger. Algérie.

Creative Commons Attribution-NonCommercial-NoDerivatives 4.0 International License (CC BY-NC-ND)

Boutaleb, A., Afalfiz, A., Aïssa, D.E., Kolli, O., Marignac, C.H., Touahri, B. (2000). *Métallogénie et évolution géodynamique de la chaîne tellienne en Algérie*. Bull. Serv., Géol., Algérie. Vol. 11, n°1, pp. 3 – 27, 7 fig., 2 pl.

Boutaleb, A., Aissa, D.E., Marignac, C. (2006). Caractérisation microthermométrique des minéralisations à Pb-Zn (f et ba) de Aïn kahla (Hodna) - NE Algerien. Bull. Serv., Géol., Algérie. Vol. 17, n° 2, pp. 1 - 15, 10 fig., 3 tabl.

Bouzenoune, A.(1993). *Minéralisations péridiapiriques de l'Aptien calcaire: les carbonates de fer du gisement hématitique de l'Ouenza (Algérie orientale).* Thèse Doct. Univ. Paris VI, France.

Camoin, G., Bouju, J.P., Maurin, A.F., Perthuisot, V., Rouchy, J.M.(1990). Relation récifs-diapirs : l'exemple du Sénonien de Khenchela (Algérie centre-orientale). Bull. Soc. Géol. France (8), VI, n°5, pp. 831-841.

Chen, G., Cheng, Q., Zuo, R., Liu, T., Xi, Y. (2015). *Identifying gravity anomalies caused by granitic intrusions in Nanling mineral district, China: a multifractal perspective. Geophys. Prospect*. 63, 256–270.

Cheng, Q. (2012). *Singularity theory and methods for mapping geochemical anomalies caused by buried sources and for predicting undiscovered mineral deposits in covered areas*. J. Geochem. Explor. 122, 55–70.

Chernicoff, J.C., Richards, J.P., Zappettini, E.O. (2002). *Crustal lineament control on magmatism and mineralization innorthwestern Argentina: geological, geophysical, and remotesensing evidence*. Ore Geology Reviews 21. 127 – 155.

Crafford, A.E.J., Grauch, V.J.S.(2002). *Geologic and geophysical evidence for the influence of deep crustal structures on Paleozoic tectonics and the alignment of world-class gold deposits, northcentral Nevada, USA*. Ore Geol Rev 21:157–184.

Glaçon, J.(1967). Recherches sur la géologie et les gîtes métallifères du Tell Sétifien (Algérie). Bull. Serv., Géol., Algérie, Nlle. série, n°32, 2 tomes.

Guiraud, R. (1990). *L'évolution post-triasique de l'avant-pays de la chaîne alpine, d'après l'étude du bassin du Hodna et des régions voisines : Thèse Doct. Sci. Univ. Nice, 259 p. Mém. n°3*, Publ. ONIG, Alger.

Guiraud, R., Bosworth, B., Thierry, J., Delplanque, A. (2005). *Phanerozoic geological evolution of Northern and Central Africa*: an overview. J. Afr. Earth Sc. 43, 83-143.

Gunn, P., Dentith, M. (1997). *Magnetic responses associated with mineral deposits*. AGSO J. Aust. Geol. Geophys. 17, 145–158.

Haddouche, O.(2010). *Les minéralisations à Ba, Pb-Zn, Cu, Hg liées au segment NE du Djebel Azreg-Djebel Khenchela (NE de l'Algérie) : géologie, gitologie et apport de l'étude des inclusions fluides. Thèse*. Doct. FSTGAT (USTHB), 175p.

Haddouche, O., Boutaleb, A., Benhamoud, I. (2014). *Contexte structural des minéralisations liées à la bordure nord des Monts des Aures (NE de l'Algérie) et des régions voisines : Exemple des gisements à Ba-Pb (Zn-Cu) d'Ichmoul et d'Ain Mimoun*. Bull. Serv., Géol., Algérie, Vol. 25, n°1, pp3 - 19, 10.

Haddouche, O., Boutaleb, A., Chamam, M., Ysbaa, S., Hammouche, H., Boubaya, D. (2016). *Pb-Zn (Ba) deposits of the oriental Saharan Atlas (north-east of Algeria): distribution, control and implications for mining exploration*. Arab J. doi.org/10.1007/s12517-016-2406-x.

Hatira, N., (1988). *Les concentrations de Zn, Pb, Sr (Ba) dans le cortex de Diapirs de Trias salifère : exemple du diapir de Sakiet-Coucha (Tunisie septentrionale), comparaison avec d'autres massifs et avec les cap rocks de la Golf Coast (USA)*. Thèse Univ. P. & M. Curie, Paris, 288 p.

Herkat, M., (1999). *La sédimentologie du haut niveau marin du Crétacé supérieur de l'Atlas saharien oriental et de l'Aurès : Stratigraphie séquentielle, analyse quantitative des biocénoses, évolution paléogéographique et contexte géodynamique*. Thèse. Doct., FSTGAT (USTHB), Alger. Algérie.

Holden, E., Wong, J.C., Kovesi, P., Wedge, D., Dentith, M., Bagas, L. (2011). *Identifying structural complexity in aeromagnetic data: An image analysis approach to greenfields gold exploration*. J.Oregeorev. 46, 47–59. doi:10.1016.

Jachens, R.C. (1991). *Regional study of mineral resources in Nevada: insights from three-dimensional analysis of gravity and magnetic anomalies*. Geol. Soc. Am. Bull. 103, 795–803.

Creative Commons Attribution-NonCommercial-NoDerivatives 4.0 International License (CC BY-NC-ND)

Joly, A., Porwal, A., McCuaig, T.C. (2012). *Exploration targeting for orogenic gold deposits in the Granites–Tanami Orogen: mineral system analysis, targeting model and prospectivity analysis*. Ore Geol. Rev. 48, 349–383.

Kazi-Tani, N. (1986). *Evolution géodynamique de la bordure nord-africaine : le domaine intraplaque nord-algérien. Approche mégaséquentielle.* Thèse Doct.ès Sciences, Univ. Pau et des pays de l'Adour, 2 tomes.

Kyle, J.R., Price, P.E. (1986). *Metallic sulfide mineralization in sald-dome cap-roks, Gulf Coast. USA*. Trans. Inst. Min. Metall., Sect. B, N°95, pp. B6-B16

Creative Commons Attribution-NonCommercial-NoDerivatives 4.0 International License (CC BY-NC-ND)

Algerian Journal of Engineering Architecture and Urbanism Vol. 5 Nr. 3 2021
ISSN: 2588-1760

Comparative study of the physicochemical and organoleptic characteristics of two similar creams

Imene HARRATE
PhD student, Department of Process Engineering, Faculty of Technology,
Food Technology Laboratory, University of Bejaia, 06000, Algeria
E-mail: harrateimene@gmail.com

Sofiane FATMI
Lecturer A, Department of Process Engineering, Faculty of Technology, Pharmaceutical Technology Laboratory, University of Bejaia, 06000, Algeria
E-mail: fatmi.sofiane@gmail.com

Nacera CHIBANI
Lecturer B, Department of Process Engineering, Faculty of Technology, Technological Laboratory for Advanced Polymer Materials, University of Bejaia, 06000, Algeria
E-mail: chibaninacera83@gmail.com

Abstract:
The development of the field of reconstituted dairy creams has given rise to similar creams, products identical to dairy creams in which the milk fat is replaced by vegetable fat. The present work, carried out in the laboratory, consists first of all of preparing a cream similar to those marketed and then a comparative study between the latter two is carried out. It consists of an evaluation of the physicochemical parameters (pH, total dry extract, density, fat content, viscosity and diameter of the droplets) as well as the organoleptic parameters (odor, color, flavor and appearance).
The study carried out showed that the cream prepared in the laboratory had better physicochemical and organoleptic parameters than that marketed on the market, in other words, the cream prepared is more stable than the model marketed.
The difference between the parameters of the two creams studied is probably due to: raw materials used, the manufacturing process (time and speed of agitation) or storage conditions.
The phase shift noticed on the marketed cream is due to the coalescence or the ripening of Ostwald.

Key words: Similar creams, culinary preparation, UHT vegetable cream, emulsion, stability.

Creative Commons Attribution-NonCommercial-NoDerivatives 4.0 International License (CC BY-NC-ND)

Introduction:

Milk is a highly nutritious foodstuff which occupies a preponderant place in the human diet, due to its balanced composition of basic nutrients (carbohydrates, proteins and lipids) and its richness in certain vitamins and minerals, in particular calcium. [1].

Nevertheless, milk is easily perishable and constitutes an environment conducive to microbial proliferation, which is why it is transformed into various products by various processes in order to preserve it and extend its shelf life for several days, several weeks or even several. Months [2].

Among the dairy derivatives, is cream. In family agricultural productions of cream, raw milk is left to stand for several hours; the fat, which is lighter, rises over time and concentrates on the surface: this is "creaming"; this phenomenon is natural. In industrial cream processing, the process is accelerated by centrifugation of the milk before it is “homogenized”. [3]

The consumption of dairy creams has seen a considerable increase in recent years, hence the creation of reconstituted dairy creams.

The development of the field of reconstituted dairy creams gave birth to similar creams, products identical to dairy creams in which the milk fat is replaced by vegetable fat.

These creams are sold under different names on the packaging depending on the total fat content and the processing it has undergone. It sometimes contains thickeners and emulsifiers to compensate for the lack of fat and stabilizers. It should be noted that the storage time of the latter varies from a few weeks to a few months.[2]

Our work aims to manufacture a cream in the laboratory and compare the physicochemical, organoleptic and microbiological parameters of the model marketed and the one prepared.

Problematic:

The majority of creams marketed are unstable, they have phase separation problems (oily phase and aqueous phase) due to the physical mechanisms of rupture which are:

• **Creaming**: it is the separation by gravity of fatty particles and aqueous particles, in other words it is the spontaneous rise of the fat to the surface of the cream at rest. [4]

• **Sedimentation**: (settling) is also one of the separation processes. These are all the phenomena that lead to the formation and deposition of raw materials used under the action of gravity. [4]

• **Flocculation**: this is the reversible association of droplets with one another due to the elimination of the surface charges of the droplets (from a certain size, the flocs cause creaming). This phenomenon is reversible because the forces which govern it are weak. [4]

• **coaless**: this is the mechanism by which two or more fatty globules merge after breaking their interfacial film to form a larger globule.

Unlike flocculation, coalescence is an irreversible phenomenon. This is the main mechanism by which a dispersion of fat evolves to its thermodynamically most stable state because it causes a decrease in the contact area between the aqueous and lipid phases. Coalescence accelerates the creaming of fatty globules by increasing their size. It can possibly lead to phase separation. [4]

• **Ostwald ripening**: it occurs during the aging of creams. The Laplace pressure difference which exists between droplets of different diameters will cause the molecules constituting the smaller droplet to migrate to the larger droplet, through the continuous phase. This phenomenon causes an increase in the average size of the dispersed phase droplets, and a tightening of the particle size distribution of the cream. [4]

- The problems encountered prompted me to try to produce a cream with better stability over time.

Creative Commons Attribution-NonCommercial-NoDerivatives 4.0 International License (CC BY-NC-ND)

Materials and methods:

The purpose of quality control of food products is to ensure that the products meet both professional standards on the one hand and legislation on the other. It can also be used to compare the products obtained with those of the competition. Finally, certain chemical determinations make it possible to see whether the products meet the rules set by export or by the specifications of certain administrations.

The cream prepared in the laboratory is a reconstituted cream, it is obtained by mixing different raw materials such as:

• **Process water**: The water was sampled at the water station, the analysis of the raw and treated water was carried out three times during the internship period. Flambé the sampling tap, let it run, and take aseptic sample in a sterile bottle at the rate of 250 ml. [4]

• **Milk powder**: the milk powder used is that of 0% and 26% fat.

Physicochemical analyzes are carried out on the ready-to-use bags.

The sample is initially taken at the bacteriological laboratory, the bag is opened next to the bunsen burner with sterile scissors and a sterile ladle is plunged into the bottom of the bag to take a sample which will be used for all the analyzes. [4]

• **Vegetable fat**: The physicochemical analysis of the peroxide value is carried out on the barrel ready for use. [4]

• **Starch**: Sampling and analysis are done in the same way as the milk powder explained above.

Product marketed and product produced:

A sample of cream marketed in Algeria "X" was chosen and studied from a physicochemical point of view. Thus, we performed the following analyzes on the two products: pH, density, EST, fat content, viscosity, droplet size (stability).

Table 1: The results of the physicochemical parameters of the cream prepared and marketed

Crèmes / Paramètres	Marketed cream (X)	Prepared cream
pH		
Dry total extract (g/l)		
Fat (%)		
Density		
Viscosity (cP)		
Droplet size (µm)		

Creative Commons Attribution-NonCommercial-NoDerivatives 4.0 International License (CC BY-NC-ND)

- **Physical and chemical analyzes**

- **The water**

The water temperature should be 25 °C for physical and chemical analyzes.

PH measurement

After calibrating the pH meter with two buffer solutions (pH4 and pH7); Put the water to be analyzed in a beaker; then we immerse the pH probe and the temperature probe in the water. If the water temperature is below 25 ° C, the cup is placed in hot water, and if it is above 25 ° C, in this case, it is placed in ice water, so to adjust the temperature. [5]

Determination of conductivity

The water to be analyzed is poured into the beaker; then the conductivity meter probe is immersed. The conductivity is expressed in micro siemens per centimeter (µS / cm). [5]

Determination of total hardness (hydrotimetric titer)

Using a 50ml volumetric flask, measure 50ml of the water to be analyzed and pour it into an Erlenmeyer flask. We add 2 ml of the ammoniacal buffer solution at pH 10 and a pinch of the colored indicator NET (Eriochrome T black), then titration with the solution of Ethylene Diamine Tetra-acetic acid (EDTA) (0.02 N)) until a color change appears, from purple to persistent solid blue. [5]
The result is expressed in French degrees ° F:

$$TH = V \times 2$$

V: EDTA titration volume used to obtain the turn (directly read the burette drop).

Chlorides

The test is carried out according to the Mohr method: 50ml of water to be analyzed is placed in an Erlenmeyer flask and 2 to 3 drops of phenolphthalein are added. A first titration is carried out with 1 ml of K2CrO4 (0.014N potassium chromatin), then a second titration with AgNo3 (silver nitrate). [5]
The result is given by the expression:

$$Chlorides = V1 \times 10$$

V1: fall of the burette

Alkalimetric title (TA)

2 to 3 drops of phenolphthalein are added to 10 ml of water to be analyzed in an Erlenmeyer flask. If the water does not color, then the TA = 0, and if a pink color appears, we proceed to titration with 0.02N H2SO4 sulfuric acid. [5]
The result, expressed in French degrees ° F, is given by the expression:

$$TA = V2 \times 10$$

V2: burette fall.

Creative Commons Attribution-NonCommercial-NoDerivatives 4.0 International License (CC BY-NC-ND)

Complete Alkalimetric Title (TAC)
2-3 drops of methyl orange are added to the previously processed sample. If the water turns orange, so the TAC = 0F °, on the other hand, if it turns yellow, it is titrated with sulfuric acid H2SO4 (0.02N) until it has an orange-red color. [5]
The result, expressed in French degrees ° F, is given by the following expression:

$$\mathbf{TAC = V3 \times 10}$$

V3: burette fall.

- **Milk powder**

The test solution is prepared at a rate of 10%. In fact, a test portion of 25g of milk powder is placed in a 500 ml beaker and then added with reconstitution water until a volume of 250 ml is obtained.

Humidity level
Weigh 5g of milk powder using a dish, and distribute it over the latter. Using the desiccator, the moisture content of the powder is determined. The result is shown as a percentage on the device screen. [5]

PH measurement
The same procedure is followed for measuring the pH of water, except that in this test reconstituted milk is used instead of water, and the temperature should be 20 ° C. [5]

Titratable acidity
10 ml of reconstituted milk are transferred to a beaker and the temperature is checked, which must be at 20 ° C, then 3 to 4 drops of phenolphthalein are added before inserting the electrode of the pH meter, and finally the titration is titrated. solution with soda (N = 1.009). The titration must be stopped as soon as the pH reaches 8.3. The acidity of milk is expressed in Dornic degree (D °). [5]
The result is given by the following expression

$$\mathbf{Acidity = V4 \times 10 \times Correction\ factor}$$

V4: fall of the burette

Determination of composition
The reconstituted milk is placed in a beaker, the probe of the milkoscan apparatus is introduced into the sample. The result is displayed on the microcomputer one minute after saving the sample data.

Rate of MG "Gerber method"
In a powder butyrometer, we put 10ml of 91% sulfuric acid, then pour 10ml of distilled water, and using a funnel, we add 2.5g of milk powder. Add 1 ml of iso-amyl alcohol, then homogenize manually, so that the mixture is finally centrifuged for 5 minutes. The result is read directly on the butyrometer, and this test is performed for each bag of powder. [5]

Stability test

"Ramsdell" test
In a series of 7 tubes, 10 ml of the reconstituted milk are introduced, then 1.3 is added; 1.4; 1.5; 1.6; 1.8; 2.0; 2.3 ml of mono potassium phosphate (0.02N KH2PO4) in the 6 tubes; the seventh will serve as a witness. These solutions are allowed to heat in a water bath at a temperature of 100 ° C. for 5 minutes. After removing them from the water bath, we put them in cold water. If no clotting is noticed, the milk is stable. [5]

Creative Commons Attribution-NonCommercial-NoDerivatives 4.0 International License (CC BY-NC-ND)

Oil bath test

At 140 ° C. 20ml of the reconstituted milk are distributed in 5 tubes (4ml in each), closed and placed in an oil bath. Shake the tubes, watching for the appearance of clotting in each; and from 5 minutes of heating, one begins to withdraw the tubes one by one, at different times, up to a time of 30min, to determine the time necessary for coagulation if it takes place. [5]

- **Vegetable fat**

The rancidity of fat is an oxidation of fatty acids to butyric acid and peroxide radicals. It is all the faster when the fat is exposed to the oxygen in the air, to light, and to heat. The analysis of the peroxide number is essential in order to characterize the quality of the fat. [5]

Determination of the peroxide number (PI)

Weigh 3g of MGV and add 10ml of chloroform, 15ml of pure acetic acid and 1ml of KI (potassium iodide) solution, shake for one minute protect from light for 5min. Add 75ml of distilled water and a few drops of starch starch and titrate with 0.01N sodium thiosulfate (Na2S2O3) solution until the color disappears. [5]

The peroxide number (PI) is expressed in milliequivalent of active oxygen per kilogram and is calculated using the following equation:

$$\mathbf{IP\ (meq\ /\ kg) = (V1 - V0) * NThio\ /\ me * 100}$$

V1: volume of the sodium thiosulphate standard solution used for the determination, in milliliters.
V0: volume of the standard sodium thiosulphate solution used for the blank test, in milliliters.
me: sample mass.

- **Starch**

Physico-chemical analyzes are applied to the starch to control the quality of the latter.
These parameters are: pH and humidity, they are measured in the same way as milk powder (explained previously).

- **Prepared cream**

Preparation of tests

1. Materials

- pH meter
- Desiccator
- Centrifuge
- Viscometer
- Laser particle size analyzer

2. Method

- Fill the tank with hot water at a temperature of 45 ° C.
- Incorporate the bags of stabilizer, the bags of powdered milk, the KIT of additives.
- Via a stainless steel rod, introduce the MGV barrels.
- The mixture is sent to a plate heat exchanger where the cold water enters against the current or the temperature is lowered from 32 to 35 ° C.
- The preparation is then sent to another tank passing through a filter to prevent the passage of impurities for heat treatment as well as homogenization and finally conditioning.

Creative Commons Attribution-NonCommercial-NoDerivatives 4.0 International License (CC BY-NC-ND)

Our sample was subjected to several physico-chemical analyzes by which the compliance of the prepared cream with the standards is determined and verified.

- The pH
- The total dry extract
- The fat content
- Density
- Viscosity
- The diameter of the droplets

a. pH

¬ Principle

The freshness of the cream is determined by measuring the pH, the latter is therefore as a result, using an electrode of a pH meter, a chemical reaction brings into play the H + ions released from the solution which are wants to measure his pH.

¬ Method of analysis

- The pH meter is calibrated with two solutions, one at pH 7 and the other at pH 4.
- The electrode is rinsed with distilled water.
- A quantity of the culinary preparation to be analyzed, the temperature of which is 20 ° C, is introduced into a beaker.

- The pH value is displayed on the pH meter. [5]

b. Total Dry Extract (TDE)

¬ Principle

The EST consists in determining the percentage of moisture or solid which is calculated by the difference between the final dry weight and the initial weight using an infrared desiccator, which consists in drying the sample by the emission of radiation to control the weight content using an integrated scale.

¬ Method of analysis

- Using a desiccator, the cup is weighed and then the value of its mass is tared.
- 11g of sterile and dry sand are weighed in the cup to facilitate drying and the standard raccoon yarn is introduced then the displayed value is tared again.
- Using a syringe, add 3g of the culinary preparation, mix and then distribute over the entire surface of the dish using the standard raccoon.
- The dryer is started automatically after closing the cover. [5]

¬ Expression of results

- After a few minutes, the desiccator displays a stable value for the percentage of TDE.

The TDE content expressed in g / l is determined by the following formula:

$$\textbf{TED (g/l) = x.10.d}$$

d: the density of the food preparation.
x: percentage of TED displayed on the desiccator.

Creative Commons Attribution-NonCommercial-NoDerivatives 4.0 International License (CC BY-NC-ND)

c. Fat content

¬ Principle

The principle is based on the dissolution of proteins by the addition of sulfuric acid and the separation of the fat by centrifugation in a butyrometer. Separation is aided by the addition of a small amount of iso-amyl alcohol. The fat collects in a clear, transparent layer.

¬ Method of analysis

- 10ml of 91% sulfuric acid is introduced into a butyrometer using a pipette.
- Add 5g of culinary preparation by flowing through the walls.
- Add 1 ml of iso-amyl alcohol using a pipette.
- Introduce 7ml of distilled water using a pipette.
- The wall of the butyrometer is cleaned before replacing the rubber dust plug.
- Homogenize by stirring and shaking the butyrometer with successive turns.
- Centrifuged for 6 min 30 sec.
- After centrifugation, the fat content is read. [5]

d. Density measurement

¬ Principle

It consists in estimating the ratio between the mass of a quantity of the culinary preparation and the volume occupied by the same mass compared to the density of the water using a lactodensimeter at a temperature of 20 ° C.

¬ Method of analysis

- The flask used is called a pycnometer. It consists of a small balloon onto which is fitted a hollow ground-glass stopper surmounted by a capillary tube.
- When the cap is adjusted on the vial, the excess liquid escapes from the upper end of the tube and since this tube is very thin, the volume of liquid is determined with great precision.
- We start by weighing the empty pycnometer, once it is filled with the sample, replace the cap and let out the excess.
- We weigh the full pycnometer. [5]

The measure of a density is based on the following equation:

Density = (mass of filled pycnometer - mass of empty pycnometer) / volume of pycnometer

e. Viscosity measurement

¬ Principle

The viscometer works by rotating a cylinder or disc (rod) which is immersed in the solution to be analyzed and measures the resistance of this substance at a selected speed.

The resulting resistance is the measure of the viscosity flow, depending on the speed and characteristics of the rod; the device calculates the result and the direct reading of the viscosity is reflected in cP or mPa.s . [5]

¬ Analysis mode

Configure the screen with the touch pen
Choose the speed in 60 RPM
Choose a temperature of 20 °C
Start the test by clicking on EXECUTE
Wait for the end of the test, then validate your measurement.

Creative Commons Attribution-NonCommercial-NoDerivatives 4.0 International License (CC BY-NC-ND)

f. Droplet size

¬ Principle

Laser granulometry is a technique based on the diffraction of light.

Laser diffraction measures particle size distributions by measuring the angular variation in the intensity of scattered light when a laser beam passes through a sample of dispersed particles. Large particles scatter light at small angles to the laser beam and small particles scatter light at higher angles.

The data relating to the intensity diffused as a function of the angle are analyzed to calculate the size of the particles which created the diffraction image and this thanks to Mie's theory. The particle size represents the diameter of the equivalent sphere having the same volume as the particle. [5]

¬ Analysis mode

- Switch on the laser granulometer and the computer.
- Fill the can with distilled water.
- Rinse then fill it.
- Using a micro pipette, we introduce drops of our sample into the device.
- After a few seconds, the diameter of the droplets is displayed in a table on the screen of the computer to which the device is connected.

- **Microbiological analyzes**

The objective of microbiological control is to guarantee a certain hygienic safety for the consumer, and to ensure good preservation of the products.

Aerobic germs at 30 ° C are the only germs sought after in UHT culinary cream.

¬ The search for total flora

The samples to be studied are incubated at 35 ° C for 4 days, on the fifth day the analysis begins.

The upper surface of the bricks to be analyzed is disinfected with alcohol, then the Petri dishes are inoculated with 1 ml of UHT food preparation taken from each brick. The PCA agar is poured and the dishes are incubated at 30 ° C. for 72 hours. [6]

- **Organoleptic analyzes**

This analysis is extremely important in the making of a food preparation, because it allows the arrangement of many aspects.

¬ Settings

In our work, we have studied the following characteristics:

Appearance: First an essential inspection at a glance to detect an anomaly on the sample if it exists then it is necessary to distinguish if the product is consistent or liquid by the simple method of flow of the product and also to determine if the refining was done well so no particles should be found.

Odor: The odor of the product is detected by the odor receptors in the nose whether it is pleasant or unpleasant.

Flavor: It is detected after tasting the product by the taste buds in the mouth, the flavors that can be detected are sweet, salty, sour, bitter and spicy. [6]

Creative Commons Attribution-NonCommercial-NoDerivatives 4.0 International License (CC BY-NC-ND)

Results and discussions:

- **Physicochemical analyzes of raw materials**

a) Process water

The results of the process water analysis are summarized in Table 2.

Table 2. The results of the physicochemical analyzes of the water

Parameters	Samples	Standards	Reference
pH	7.43	**6.5 to 8.5**	**J.O.R.A n°75, 2009**
TA (°F)	0	**< 0.1**	
TAC (°F)	7.8	**12 to 25**	
TH (°F)	11.6	**10 to 15**	
Conductivity (ms/cm)	0.369	**0.03 to 8.0**	
Chlorides (mg/l)	21.3	**< 50**	
Taste and odour	Normaux	**Normaux**	
color	Normal	**Normal**	

The results obtained for all water parameters comply with company standards. Indeed, the pH of the sample is 7.43. The upper standard is 8.5. The same observation concerns the values of TH which is 11.6 (values less than 15 ° F). The water must be of an acceptable level of hardness. In fact, the injection of very hard water does not allow good dissolution of the milk powder. The temperature of the water is also a factor influencing the wettability and dispersion of milk powder.

Due to the deterioration of the proteins, the dispersion of the powder in water is preferably done at a temperature between 40 °C and 50 °C.

The downside of chlorides is the unpleasant flavor they impart to water. They can cause corrosion in the pipes. The regulations recommend a [Cl-] content of the process water not exceeding 50mg / l.

The organoleptic analyzes revealed the absence of unpleasant taste and odor, which confirms that the water is of good organoleptic quality.

Creative Commons Attribution-NonCommercial-NoDerivatives 4.0 International License (CC BY-NC-ND)

b) Milk powder

The results obtained are summarized in Table 3 below

Table 3. The results of the physicochemical analyzes of the milk powder

Parameters	sample (1) 0% MG	standards		sample (2) 26% MG	standards	References
pH	6.69	**6 to 6.9**		6.77	**6 to 6.9**	**J.O.R.A n°69, 1993**
Acidity °D	13.58	**< 15°D**		8.55	**< 15°D**	
Humidity %	4.72	**Max 5%**		2.84	**Max 5%**	
MG (g/l)	0	**< 1.25%**		27	**≥ 26%**	
Ramsdell	1.4	**≥ 1.3**		1.4	**≥1.3**	
Oil bath	18	**≥ 6 min**		25	**≥ 12 min**	
Taste and odour	Frac milk	**Frac milk**		Frac milk	**Frac milk**	
Color	Blanche	**Blanche**		Jaunâtre	**Jaunâtre**	
Aspect	Normal	**Normal**		Normal	**Normal**	

The results presented in the preceding table comply with the standards set by J.O.R.A n ° 69, 1993.

The pH values tell us about the freshness of the milk, especially its stability, because the pH influences the solubility of proteins. In addition, the titratable acidity values of the milk powders are within the standards; it is a natural acidity of normal milk.

The humidity of the milk powders meets the set standard (H (%) ≤ 5%), which gives them protection against any deterioration likely to make them unfit for consumption. In order to avoid the increase in humidity, the powder is packaged in airtight, closed packaging of sufficient strength.

The difference in color between the two powders is explained by the fat content which gives a yellowish color for the 26% powder and a white color for the 0% powder.

The results of the stability tests (Ramsdell, oil bath) tell us that the milk is suitable for undergoing treatment at a high temperature of 140 ° C for a period of time without coagulation.

Therefore, the 0% and 26% milk powders used by the Candia unit are of good physicochemical quality.

The organoleptic analyzes revealed the absence of unpleasant taste and odor, which confirms that the milk powder is of good organoleptic quality.

Creative Commons Attribution-NonCommercial-NoDerivatives 4.0 International License (CC BY-NC-ND)

c) Vegetable fat

The results of the vegetable fat analysis are summarized in Table 4

Table 4. The results of the physicochemical analyzes of the MGV

Parameters	Results	standards	Reference
Peroxide index (meqg/kg)	0	**5**	**Internal standards**
Taste	Normal	**Caracteristic**	
Odour	Normal	**Caracteristic**	
Color	yellow	**Typical**	
Aspect	Normal	**Typical**	

The peroxide index is used to characterize vegetable fat, it is concerned with the number of oxygen active in the organic chains of a fatty substance. This active oxygen can be in the form of an epoxide or in the form of a hydro-peroxide. The higher the index, the more the fat is oxidized.
The results obtained imply that the fat is not oxidized.
The organoleptic analyzes revealed the absence of unpleasant taste and odor, which confirms that the vegetable fat is of good organoleptic quality.

d) Starch

The results of the starch analysis are summarized in Table 5

Table 5. The results of the physicochemical analyzes of starch

Paramètres	Résultats	Norme	Référence
Humidity (%)	11.24	**Max 14**	**pharmacopée Eu.**
pH (20°C)	5.47	**4.5 to 7**	
Aspect	White powder	**Pouder**	
Odour	without	**whithout**	
Color	white	**white**	

The pH value complies with the standard set by the pharmacopoeia.
The humidity of the starch meets the standard set by the pharmacopoeia, (H (%) ≤ 14%), which gives it protection against any deterioration likely to make it unfit for consumption. In order to avoid the increase in humidity, the starch is packaged in airtight, closed packages of sufficient strength.
The organoleptic analyzes revealed the absence of unpleasant taste and odor, which confirms that the starch is of good organoleptic quality.

Creative Commons Attribution-NonCommercial-NoDerivatives 4.0 International License (CC BY-NC-ND)

- **Physicochemical analyzes**

The results of the physicochemical analyzes carried out on the two creams marketed and prepared are summarized in Table 6

Table 6. The results of the physicochemical analyzes of the two creams marketed and prepared

Crèmes / Paramètres	Crème commercialisée (X)	Crème préparée
pH	5.14	6.74
Total dry extract (g/l)	230.27	248.07
Fat (%)	12	18
Density	1.024	1.008
Viscosity (cP)	431.54	590
Droplet size (µm)	19.8	4.65

- From the results obtained, we notice that the pH of the cream sold is low compared to that of the prepared cream.
- The prepared cream is richer in TSE than that marketed, this is due to the constituents it contains.
- The fat content for the prepared cream is higher than that of the marketed cream, this implies that that marketed is light.
- The viscosity as well as the stability (size of the droplets) of the prepared cream are more important than those of the marketed cream, this is probably due to the speed and time of stirring, to the types as well as to the quantities of thickeners and stabilizers used.
- In terms of density, the values of the two products are almost identical.
- The phase separation observed on the marketed cream is due to coal gasoline or Ostwald ripening.

Creative Commons Attribution-NonCommercial-NoDerivatives 4.0 International License (CC BY-NC-ND)

- **Microbiological analyzes**

Table 7: The results of microbiological analysis of the two creams

Germs wanted	Results	standard
Total flora (prepared cream)	Absence	< 100
Total flora (marketed cream)	Absence	< 100

The results of the bacteriological analyzes carried out on the two creams are presented in Table 7, show an absence of the total flora, which confirms their sterility. The regulations specify that the total germ load in 0.1 ml of UHT cream analogues must not exceed 100 germs. These results are explained by the destruction of almost all of the microorganisms present in the UHT culinary preparation, which demonstrates the effectiveness of the heat treatment applied.

- **Analyses organoleptiques**

Tableau 8 : Les résultats d'analyses organoleptiques du produit fini

Produit	Paramètres	Résultats	
Marketed cream	**color**	white	
	Odour	Normal	
	flavor	Slightly acid	
	Aspect	24h	Normal
		48h	Normal
		7 jours	Normal
		30 jours	phase separation
		45 jours	phase separation
Prepared cream	**Color**	white	
	Odour	Normal	
	flavor	Normal	
	Aspect	24h	Normal
		48h	Normal
		7 jours	Normal
		30 jours	Normal
		45 jours	Normal

Creative Commons Attribution-NonCommercial-NoDerivatives 4.0 International License (CC BY-NC-ND)

From the results obtained, it can be seen that the parameters: color, odor and flavor are almost identical for the two creams for the two creams and are stable and no change is observed during the analysis period.
From the thirtieth day, a phase separation is observed on the marketed cream, unlike the prepared cream which was always stable.

Conclusion:

- The raw materials used for the manufacture of the prepared cream
conformed to internal standards and to the Algerian official journal.
- The physicochemical parameters: pH, EST, density and MG vary little between the two creams, unlike the stability (size of the droplets) on which we notice a difference of a factor of almost 4
- The absence of total flora during the microbiological analysis of the marketed cream indicates that the phase separation is not due to bacterial contamination.
- The phase shift noted on the marketed cream, indicating a loss of structural stability, is due to one or both of the physical phenomena of rupture which are: coalescence and ripening of Ostwald.
- The structural stability of the prepared cream is probably due to:

- The good quality of the raw materials used;
- The time and speed of stirring used during the preparation of the cream allowed good homogenization between the different constituents;
- Respect of the stirring temperature during manufacture as well as that of storage once the finished product;
- The quality and quantity of emulsifiers and preservatives used.

References:

[1] Alais, C et Linden,G. (1997). Abrégé de biochimie alimentaire, 4é éditionmasson. Paris.1

[2] CAULLET, L. DOS SANTOS.A, KNIPPER.G, RUSALEN.M, SEIGNEUR.M, (2018). Les émulsions alimentaires et cosmétiques. Projet professionnel. Université de lorraine, France.

[3] C.E.L.P.C 2000. [CENTRE D'ENSEIGNEMENT LAITIER PAR CORRESPONDANCE]. Produit de consommation. Ecole Nationale d'Industrie Laitière et des Industries Agro-Alimentaires.

[4] Delacharlerie S, de Biourge S, Chèné C, Sindic M et Deroanne C. (2009). HACCP organoleptique: Guide pratique. Edition : Presses Agronomiques de Gembloux, 172p.

[5] Doumeix, O. (2011), les émulsions, opérations unitaires en génie biologique, CRDP, biologie technique, France.

[6] Hassainya J, Padilla M et Tozanli S. (2007). Lait et produits laitiers en Méditerranée: des filières en pleine restructuration. Editions : KARTHALA. 385 p.

Creative Commons Attribution-NonCommercial-NoDerivatives 4.0 International License (CC BY-NC-ND)

Algerian Journal of Engineering Architecture and Urbanism Vol. 5 Nr. 3 2021
ISSN: 2588-1760

ÉVALUATION EXPERIMENTALE DES PERFORMANCES D'UN MOTEUR DIESEL ALIMENTE EN ETHANOL/DIESEL ET METHANOL/DIESEL

M'hamed BERIACHE
Associate Professor PhD., Laboratory of Rheology and Mechanics, Department of Mechanical Engineering, Faculty of Technology, University Hassiba Benbouali of Chlef, m.beriache@univ-chlef.dz

Moustefa HADJ HENNI
Master Student, Laboratory of Rheology and Mechanics, Department of Mechanical Engineering, Faculty of Technology, University Hassiba Benbouali of Chlef, mostafa022017@gmail.com

Leila MOKHTAR SAIDIA
PhD Student, Laboratory of Rheology and Mechanics, Department of Mechanical Engineering, Faculty of Technology, University Hassiba Benbouali of Chlef, lmokhtarsaidia@gmail.com

Abstract:
Nowadays, decreasing sources of petroleum fuel has led to innovation of other resources. Alternative fuel can be produced from biomass such as alcohol. In this work, an experimental study on the feasibility and the effects of using Diesel-ethanol and Diesel-methanol blends as alternative fuel for Diesel engine was carried out. Pure Diesel, Diesel-ethanol, D95E5, D90E10 and D85E15 as well as Diesel-methanol, D95M5, D90M10 and D85M15 on Farymann four stroke monocylinder Diesel engine performances was completed. The engine is tested at full load with engine speed ranged from 700 to 3000 tr/min. The effects of ethanol and methanol fraction on diesel engine power, torque, brake specific fuel consumption (BSFC), brake thermal efficiency and exhaust temperature were experimentally investigated. The results showed that mixing ethanol and methanol at different fractions with Diesel fuel have a significant effect on the engine performance, as well as the nature of alcohol, which constitutes a combustion catalyst. Fuel mixtures, D85E15 and D85M15 have the highest improvement rates compared to pure Diesel and other examined fuel mixtures. It has been shown, that, the lowest BSFC than that of pure Diesel, which is an advantage for our proposed fuels, is recorded with D95E5 and D95M5 blends. The different mixtures provide higher exhaust gas and outlet temperature of the coolant proportional to the mixing ratio, which explains why the addition of biofuel improves the calorific value of the fuel. The combustion of the different mixtures increases the outlet temperature of the coolant in proportion to the mixing rates.

Key words: Diesel engine; engine performance; Ethanol-Diesel blend, Methanol-Diesel blend.

Introduction:

L'augmentation de la consommation des carburant et les taux instables de leurs prix ont des impacts directs sur les consommateurs et leur fait subir divers problèmes, ce qui a déclenché une grande attraction vers les bio-carburants alternatives et à faible coût. La consommation excessive de combustibles fossiles a conduit à une réduction des ressources de carbone souterraines. La recherche de carburants alternatifs, qui promettent une corrélation harmonieuse avec le développement durable, la conservation de l'énergie, l'efficacité et la préservation de l'environnement, est devenue très prononcée de nos jours. Les carburants

Creative Commons Attribution-Non Commercial-No Derivatives 4.0 International License (CC BY-NC-ND)

d'origine biologique peuvent apporter une solution réalisable à cette problématique. De plus, les automobiles à essence et au diesel sont les principales sources d'émissions de gaz à effet de serre. En outre, l'utilisation intensive de pétrole brut a également augmenté la pollution de l'air par les émissions d'échappement (Harrod et al., 2005). Ces émissions d'échappement des véhicules ont des effets dangereux sur la santé humaine (Wargo et al., 2006 ; Seagrave et al., 2006; Gauderman et al., 2007; Khieralla, 2005). Les recherches scientifiques de ces dernières années ont exploré plusieurs ressources énergétiques alternatives, qui ont le potentiel de palier aux besoins d'énergie toujours croissants des consommateurs d'aujourd'hui (Farkade and Pathre, 2012; Nik Rosli et al. 2015 ; Yusaf et al., 2013(8) ; Zaharin et al., 2017). De ce fait, plusieurs recherches font la promotion de l'utilisation du méthanol et l'éthanol comme carburants alternatifs pour les moteurs à combustion interne en raison de leur richesse en oxygène à produire de l'énergie avec moins d'émissions. L'utilisation d'alcools comme additifs aux carburants conventionnels de moteurs thermique améliore l'efficacité thermique et réduit les émissions de CO et de HC (Masum et al., 2013). L'éthanol et le méthanol contiennent une teneur élevée en oxygène par rapport au Diesel pure ; ainsi, ils améliorent le processus de combustion dans le cylindre (Yoon et al., 2009 ; Ashraful et al., 2014). D'après ce qui précède, on voit qu'il existe un besoin et une motivation pour explorer le potentiel de l'utilisation des mélanges Diesel-éthanol et Diesel-méthanol dans les moteurs à allumage par compression (CI). Le présent travail vise à étudier par expérimentation le potentiel d'améliorer les performances du moteur Diesel fonctionnant avec ce type de carburants mélanges à base d'alcool. Les performances d'un moteur CI à différents taux de mélange d'éthanol et de méthanol avec du Diesel pure ont été étudiés sur un moteur Diesel à quatre temps monocylindrique.

Propriétés des biocarburants et préparation des mélanges

Plusieurs additifs de carburant oxygénés qui ont été utilisés étaient le méthanol, l'éthanol, l'alcool butylique tertiaire et l'éther méthylique tertiaire butylique (Gong et al., 2014 ; Iliev, 2015). Selon Simeon Iliev (2015), l'utilisation des carburants de remplacement contenant de l'oxygène (oxygénés) est très importante en tant que carburant additif car elle peut augmenter les performances et l'efficacité du moteur. Dasilva et al. (2005), ont déduit que l'éthanol et le méthanol avaient un indice d'octane plus élevé que le Diesel ainsi que l'essence. Ce qui permet aux mélanges de carburants éthanol-Diesel et méthanol-Diesel d'avoir des taux de compression beaucoup plus élevés et augmente le rendement thermique (Thangavelu et al., 2016).

Les carburants mélanges ont été obtenus en mélangeant l'éthanol ensuite le méthanol avec le carburant Diesel Algérie, qui a été obtenu à partir d'une station d'essence locale à Chlef. L'éthanol et le méthanol ont été obtenus du laboratoire du génie des procédés de l'université de Chlef. Les mélanges ont été réalisés dans les rapports E5D95, E10D90, E15D85, et M5D95, M10D90, M15D85 sur une base volumétrique. Par exemple, un mélange E10D90 contient 10% d'éthanol et 90% de carburant Diesel. Les mélanges ont été réalisés simplement en versant les deux carburants dans un récipient aux proportions correctes et en les mélangeant jusqu'à ce que le mélange soit homogène.

Creative Commons Attribution-Non Commercial-No Derivatives 4.0 International License (CC BY-NC-ND)

Le tableau 1 ci-dessous décrit les propriétés du carburant de l'éthanol et du méthanol par rapport au Diesel pure (Yusaf et al., 2013).

Tableau 1. Propriétés comparées des carburants

Properties	**Diesel**	**Ethanol**	**Méthanol**
Formule moléculaire	C_{14}-C_{30}	C_2H_5OH	CH_3OH
Poids moléculaire	-	46	32
Taux d'Oxygène (%)	-	34.7	49.9
Masse volumique (kg/m^3)	845	785	792
Indice de cétane	>50	108	111
Rapport Stœchiométrique air/carburant	14.96	9.0	6.47
Température d'auto-inflammation (°C)	220	425	465
Pouvoir calorifique inférieur (MJ/kg)	43.45	27.00	20.10

Les spécifications du moteur utilisé

Cette étude est réalisée pour tester les performances d'un moteur Diesel à quatre temps monocylindre refroidi par air à injection directe de type Farymann P604. Le tableau 2 présente les spécifications du moteur utilisé. Le moteur est branché à un dynamomètre hydraulique via une liaison et le dynamomètre délaisse la charge sur le moteur pour mesurer la puissance de freinage (Fig.1). L'étude expérimentale est accomplie en utilisant les différents mélanges de carburants préparés, pour des régimes moteur allant de 700 tr/min à 3000 tr/min sous charge moteur constante.

Tableau 2. Spécifications du moteur d'essai

Designation	***Characteristics***
Engine type	*P604*
Fuel	*Diesel*
No. of cylinders	*1*
Bore (mm)	*95*
Stroke (mm)	*100*
Cylinder capacity (cm^3)	*708*
Rated speed, rpm (max)	*3000*
Volumetric ratio	*21±1.5 to 1*
Compression pressure (bars)	*25 to 30*
Engine oil consumption	*1.0 g/kWh*

Dans la présente étude, différents pourcentages de mélanges Diesel-éthanol et Diesel-méthanol de (0%, 5% 10% et 15%) ont été testés pour étudier les effets de mélanges d'alcools sur les performances de moteur Diesel (puissance de freinage, BSFC et BTE) et ce sans la moindre modification sur le moteur originel.

Les objectifs principaux étaient de répondre au problème de l'épuisement des carburants fossiles et de réduire par conséquence leurs effets nuisibles en plus l'idée d'utiliser les biocarburants (éthanol et méthanol) comme carburant alternatif moins nocifs pour

Creative Commons Attribution-Non Commercial-No Derivatives 4.0 International License (CC BY-NC-ND)

l'environnement. A l'issue de cette recherche, les résultats obtenus ont été comparés avec ceux de la littérature.

Materials et méthodes:

Le moteur a été mis en marche pendant environ 10 minutes comme période de chauffe pour que la stabilité de fonctionnement du moteur soit atteinte. L'essai de mélange de carburant a commencé ensuite avec des mélanges éthanol-Diesel, suivis par des mélanges méthanol-Diesel. Le Diesel pure est utilisée après chaque utilisation de mélange de carburant et ce pour nettoyer les traces des mélanges de carburant dans les conduits de carburant. Le moteur a été testé environ 15 min pour chaque essai de mélange avec le régime du moteur dans la plage de 700 à 3000 tr/min à plein régime.

La figure 1 montre la configuration du banc d'essai expérimental. Le moteur est couplé à un dynamomètre à courants de Foucault (modèle Froude Hoffman AG150) d'une puissance maximale de 150 kW pour mesurer le couple et la puissance du moteur. Une burette graduée et chronomètre sont utilisés pour mesurer le débit du carburant consommé. Les températures des fluides (gaz d'échappement, liquide de refroidissement, eau glycolée) sont mesurées par des thermocouples, le liquide de refroidissement est mesuré par deux thermomètres gradués à base de mercure, le premier mesure la température d'eau à l'entré et le second mesure la température d'eau la sortie. Le débit d'air à l'admission est mesuré par un débitmètre basé sur la méthode de la boite à air. La température des gaz d'échappement est mesurée par un thermomètre de type Testo 925.

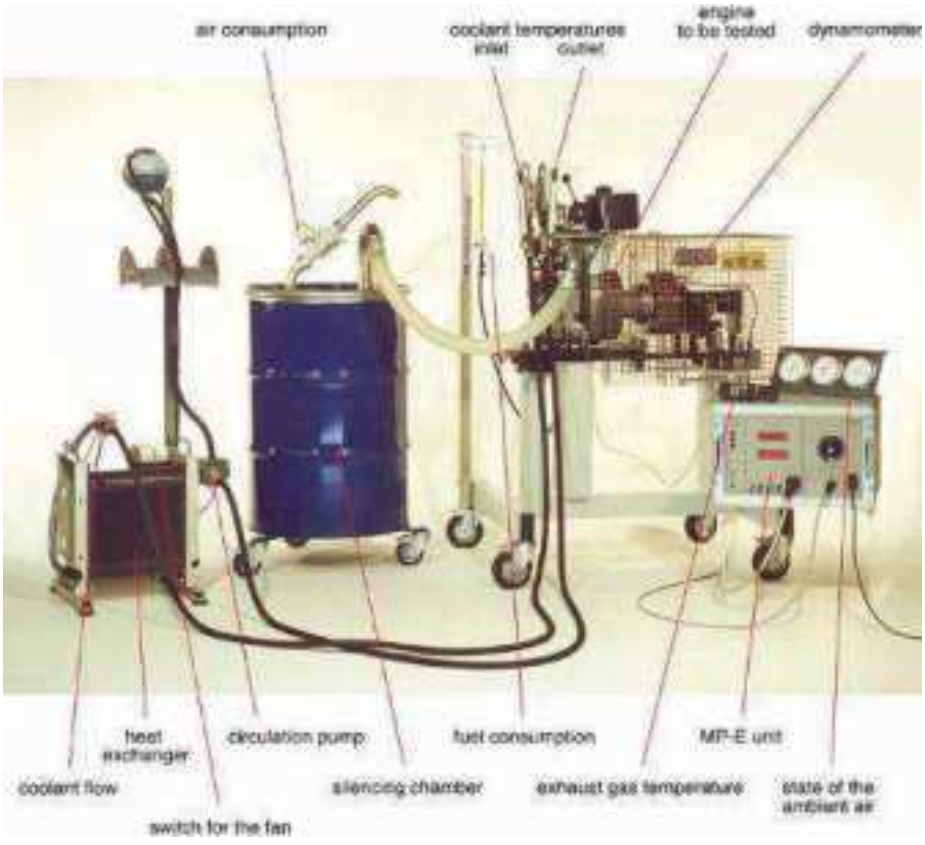

Fig. 1. Banc d'essai experimental

Creative Commons Attribution-Non Commercial-No Derivatives 4.0 International License (CC BY-NC-ND)

Calcul des performances :

La puissance de freinage est utilisée pour indiquer la puissance réellement délivrée par le moteur. La puissance de freinage est définie comme suit (Ganesan, 2004) :

$$P = \frac{2\pi NT}{60000}\ [kW]$$

Avec, N : vitesse du moteur (tr/mn)
T : couple moteur (N.m)

Le BSFC est la caractéristique de consommation de carburant d'un moteur. Elle est exprimée en consommation de carburant en kilogrammes de carburant par kilowattheure (Atmanli et al., 2015).

$$BCFC = \frac{\dot{m}}{B_p}\ \left[\frac{g}{kW.h}\right]$$

Avec, $\dot{m}$: **Débit massique du carburant** $\left(\frac{g}{h}\right)$
B_p : Puissance de freinage du moteur (kW)

Le BTE est le rapport entre la puissance de freinage et l'énergie du carburant d'entrée en unités appropriées (Zaharin et al., 2017).

$$BET = \frac{B_p}{CV.360}\ [\%]$$

Avec, B_p : Puissance de freinage du moteur (kW)
CV : Pouvoir calorifique du carburant $\left[\frac{kJ}{kg}\right]$.

Résultats et discussions :

Cette section englobe les résultats de l'expérience menée sur le moteur Diesel Farymann P604. Le comportement des carburants mélanges ; Diesel, Diesel-Ethanol, D95E5, D90E10 et D85E15 ainsi que Diesel-Méthanol, D95M5, D90M10 et D85M15 est montré dans leurs graphiques relatifs avec discussion. Les résultats illustrent le couple moteur, le couple de freinage, la puissance utile, la consommation spécifique de carburant, l'efficacité thermique de freinage, la consommation d'énergie propre au freinage, la température du liquide de refroidissement moteur et la température des gaz d'échappement et finalement le rendement du moteur.

En vertu des résultats expérimentaux présentés dans les Figs. 2 et 3, pour les mélanges carburants Diesel-éthanol comparé au Diesel pure, le couple moteur est plus élevé que celui dans le cas du Diesel pure, ce couple croit avec l'accroissement du régime moteur ainsi avec le taux du mélange Diesel-éthanol.

Creative Commons Attribution-Non Commercial-No Derivatives 4.0 International License (CC BY-NC-ND)

Algerian Journal of Engineering Architecture and Urbanism Vol. 5 Nr. 3 2021
ISSN: 2588-1760

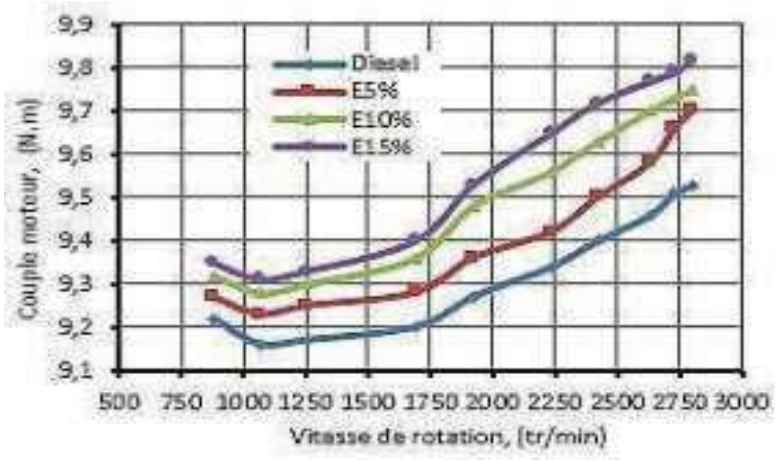

Fig. 2. Couple moteur en fonction du régime moteur pour différents mélanges Diesel-éthanol

Pour le couple de freinage présenté sur la Fig. 3, l'amélioration est moins importante mais la tendance est maintenue.

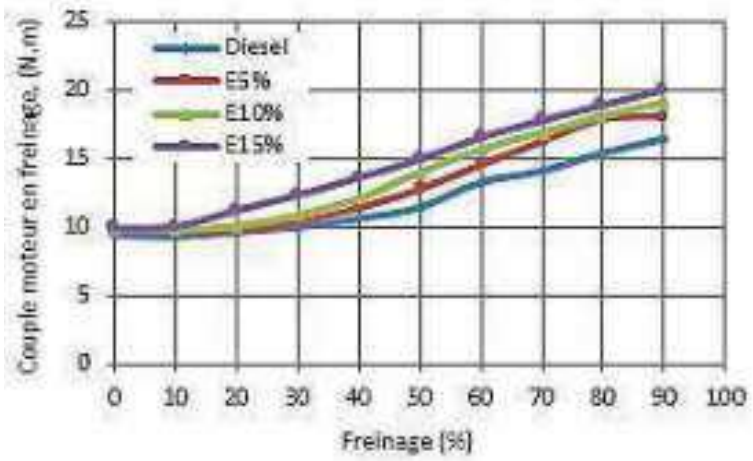

Fig. 3. Couple de freinage pour différents mélanges Diesel-Ethanol

D'après la figure 4, les mélanges d'éthanol améliorent considérablement la puissance du moteur, à savoir, la puissance est une performance clé pour tout moteur. De plus, cette amélioration suit l'accroissement du taux de mélange. Ceci explique la puissance élevée du mélange D85E15 par rapport aux autres mélanges à faible teneur en éthanol.

Creative Commons Attribution-Non Commercial-No Derivatives 4.0 International License (CC BY-NC-ND)

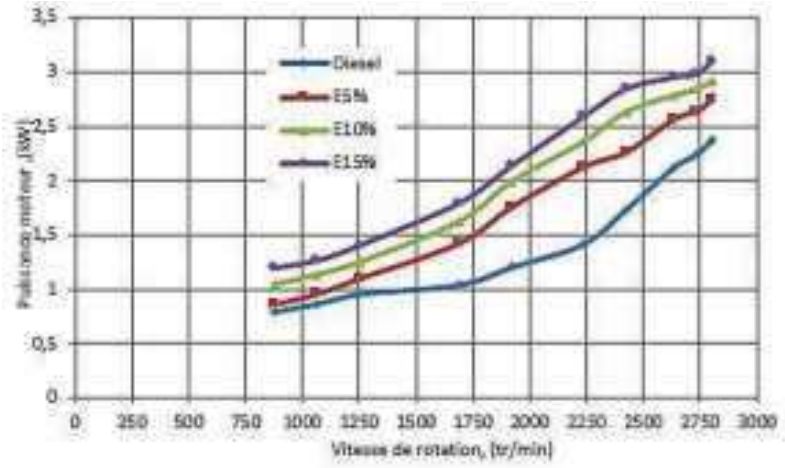

Fig. 4. Puissance en fonction du régime moteur pour différents mélanges Diesel-Ethanol

Selon les résultats de la figure 5, la consommation spécifique des mélanges de carburant de freinage est beaucoup plus élevée que celle du Diesel pure, ce qui est un inconvénient pour les carburants proposés et cela peut être dû au moteur conçu à l'origine pour fonctionner avec le Diesel pure et la nature de l'éthanol qui est un catalyseur de combustion. En revanche, l'éthanol améliore le reste des performances du moteur, chose qui est très appréciable. Le BSFC le plus bas est enregistré avec le mélange D95E5. Selon la littérature, cet inconvénient peut être surmonté en ajoutant certains additifs.

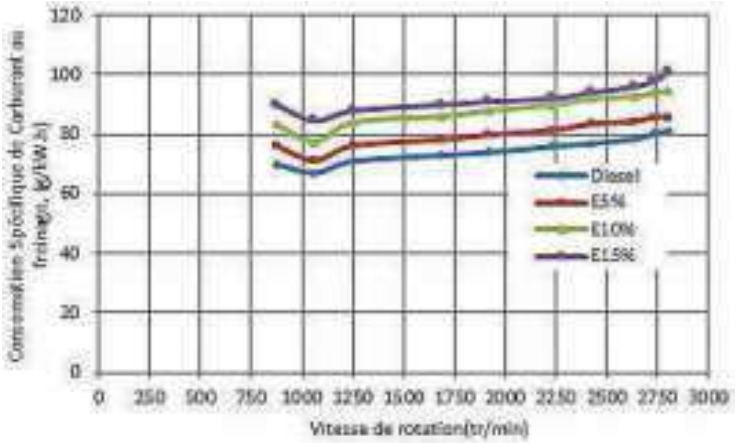

Fig. 5. CSCF en fonction du régime moteur pour différents mélanges Diesel-Ethanol

D'après les résultats de la figure 6, l'augmentation de la température des gaz d'échappement est d'autant plus importante et proportionnelle à l'augmentation de la teneur en éthanol du mélange. La température des gaz d'échappement la plus élevée correspond au mélange D85E15.

Creative Commons Attribution-Non Commercial-No Derivatives 4.0 International License (CC BY-NC-ND)

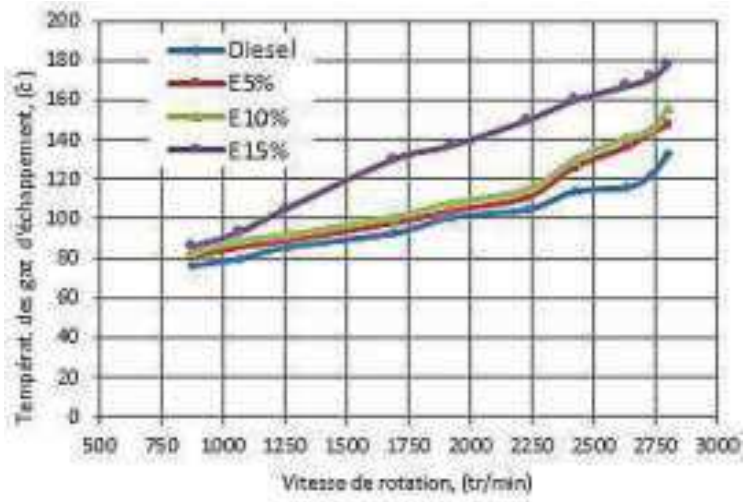

Fig. 6. Température des gaz d'échappement pour différents mélanges Diesel-Ethanol

D'après les résultats présentés sur la figure 7, il est clair que l'utilisation d'éthanol dans ce test a conduit à une meilleure efficacité thermique de freinage par rapport aux autres mélanges carburants. Cela est dû à la combustion complète résultant de l'utilisation d'éthanol dans le mélange carburant. Il est constaté que l'accroissement du taux d'éthanol dans le moteur Diesel est moins bénéfique à des vitesses élevées autour de 3000 tr/min, comme le montre la figure 7, l'ajout de plus de 10% d'éthanol n'améliore pas davantage l'efficacité thermique de freinage contrairement au Diesel pure.

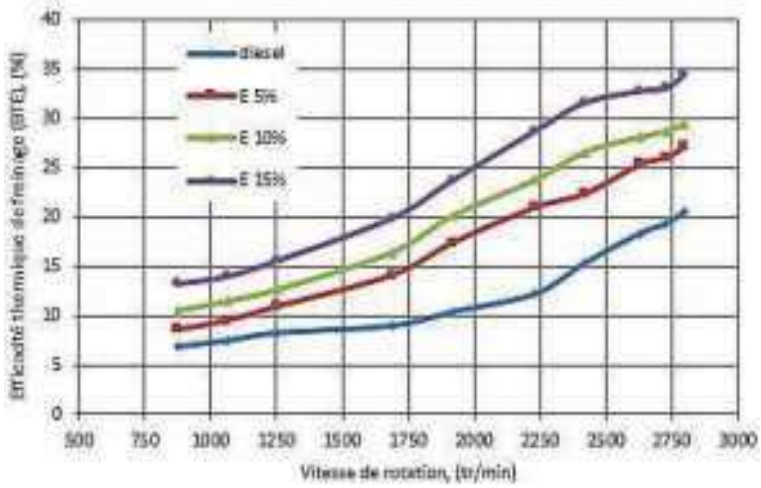

Fig. 7. Efficacité thermique de freinage pour différents mélanges Diesel-Ethanol

D'après les résultats présentés dans la figure 8, l'utilisation d'éthanol dans ces tests a conduit à un meilleur rendement par rapport à celui du Diesel pure avec environ 20% pour le mélange D85E15. La figure 8 montre bien l'augmentation proportionnelle entre l'efficacité du moteur et le régime du moteur ainsi que le rendement avec le taux de mélange en éthanol. Il est observé que pour les vitesses de fonctionnement au-delà de 2400 tr/mn, le rendement est retardé et ce en rapport avec le taux du mélange.

Creative Commons Attribution-Non Commercial-No Derivatives 4.0 International License (CC BY-NC-ND)

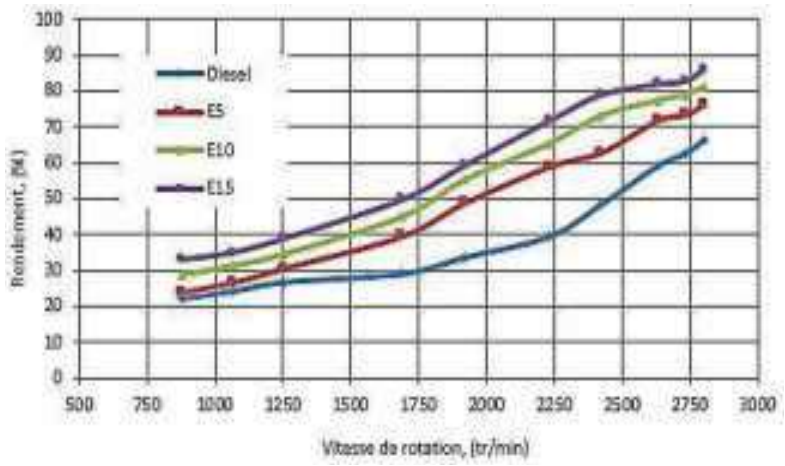

Fig. 8. Rendement du moteur en fonction des différents mélanges Diesel-Ethanol

L'évolution du couple moteur par rapport au régime moteur à différents rapports de mélange Diesel-méthanol est représenté sur La figure 9. Il est bien enregistré que, le couple de démarrage est élevé à bas régime, ce est due à la grande résistance au démarrage, mais une fois elle est surmontée, le couple diminue ensuite il augmente avec l'augmentation du régime moteur. Les résultats expérimentaux obtenus montrent que le taux du mélange en méthanol améliore davantage le couple moteur.

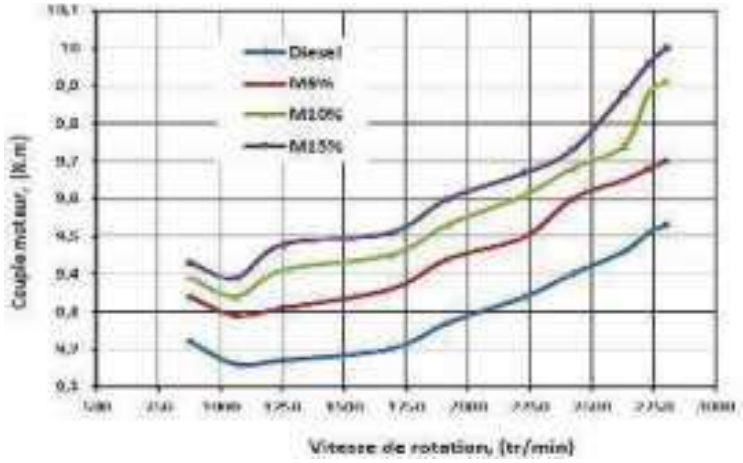

Fig. 9. Le couple en fonction du régime moteur pour différents mélanges Diesel-Méthanol

Cependant, les tendances des résultats sont les même. Pour le Diesel pure, la courbe est assez constante avec un écart entre les valeurs maximale et minimale. Pendant ce temps, le mélange du Diesel-méthanol montre une augmentation du couple à des vitesses plus élevées. Cependant, à tous les régimes moteur, les carburants mélanges Diesel-méthanol dans tous les rapports présentent un couple plus élevé que celui du carburant Diesel pure ceci dit que le recours au méthanol présente un potentiel améliorant les performances du moteur Diesel.

Creative Commons Attribution-Non Commercial-No Derivatives 4.0 International License (CC BY-NC-ND)

Algerian Journal of Engineering Architecture and Urbanism Vol. 5 Nr. 3 2021
ISSN: 2588-1760

Pour le couple de freinage présenté sur la Fig. 10, l'amélioration est moins importante mais la tendance est maintenue.

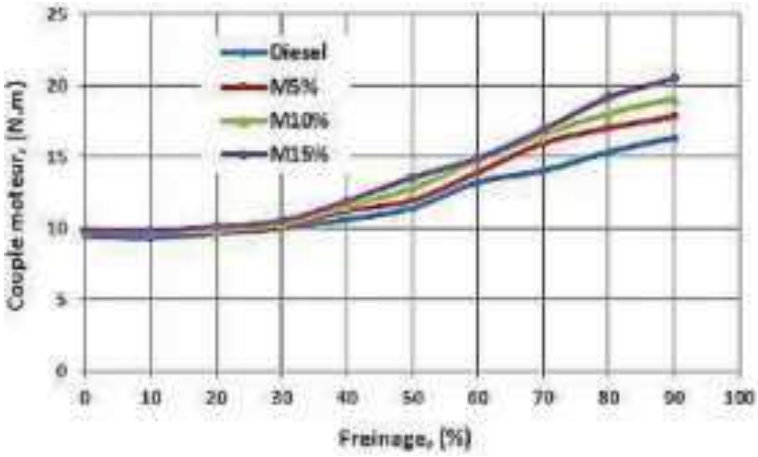

Fig. 10. Comparaison du couple moteur de freinage pour différents mélanges Diesel-Méthanol

La puissance d'entrée du moteur peut être estimée par la quantité de carburant injectée dans celui-ci. Théoriquement, il est déterminé sur la base du débit et du pouvoir calorifique inférieur des carburants mélanges ou pures. Le pouvoir calorifique inférieur du méthanol est environ la moitié de celui du Diesel, avec des valeurs de 23,8 MJ / kg et 44,5 MJ / kg respectivement pour le méthanol et le Diesel. Il est bien connu que la puissance du moteur est fortement contrôlée par l'efficacité de la combustion. Les résultats expérimentaux obtenus, la figure 11 montre l'effet des divers mélanges de carburants sur la puissance du moteur. En général, on peut voir que la puissance de sortie issue des carburants mélanges donne une puissance plus élevée que le Diesel pure. L'amélioration de la puissance de sortie issue des mélanges est nettement supérieure que celle du Diesel pure.

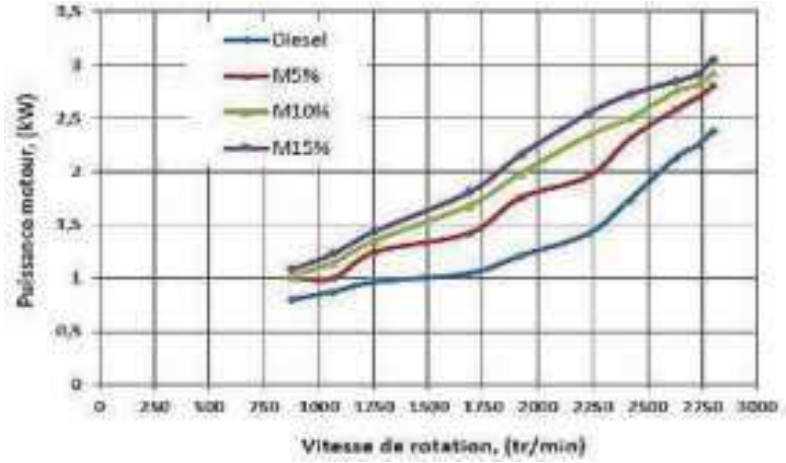

Fig. 11. La puissance du moteur en fonction du régime moteur pour différents mélanges carburants Diesel-Méthanol

Creative Commons Attribution-Non Commercial-No Derivatives 4.0 International License (CC BY-NC-ND)

La consommation de carburant spécifique au freinage (BSFC), qui est définie comme le débit de carburant par heure (kg/h) divisé par la puissance de freinage du moteur (kW), est une mesure de l'efficacité du moteur. Le BSFC en fonction du régime moteur est présenté à la figure 12, qui représente le BSFC aux conditions de fonctionnement maximales. Une différence significative entre les carburants mélanges et le carburant Diesel pure peut être observée sur la figure 12.

De plus, la consommation spécifique de carburant Diesel pure est la plus faible par rapport aux autres mélanges Diesel-méthanol, ces résultats collent bien avec ceux obtenus par Sayin et al. (2010). Cela est dû à la différence des pouvoirs calorifiques inférieures des différents types de carburants comparés.

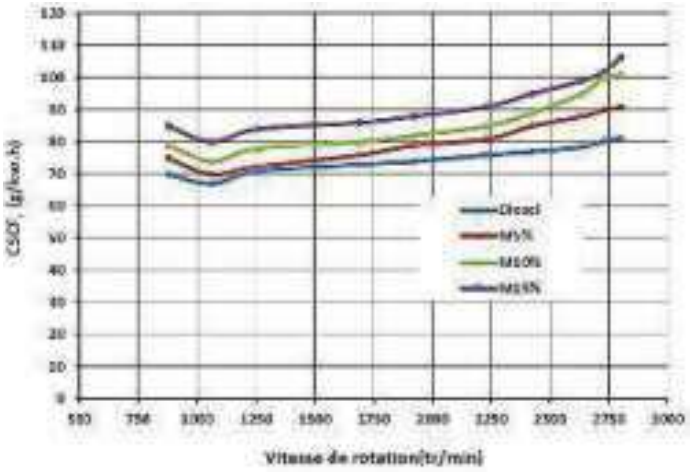

Fig. 12. La CSCF en fonction de la vitesse du moteur pour différents mélanges carburants Diesel-Méthanol

Il est à signaler que les consommations spécifiques relatives au mélanges diesel-méthanol certes sont peux supérieures que celle du Diesel pure mais délivrent des puissances plus importantes que celle issue du Diesel pure voir Fig. 11. Afin d'obtenir la même puissance d'entrée, la quantité de carburant mélange doit être diminuée.

La figure 13 montre l'évolution de la température des gaz d'échappement par rapport au régime du moteur à pleine charge. À toutes les plages de régime du moteur, le meilleur rapport de mélange qui produit la température d'échappement la plus basse est 10% de méthanol et 90% de Diesel. Plus la quantité de méthanol injecté dans la chambre de combustion est importante, plus il y aura d'oxygène disponible, ce qui conduira à une combustion complète.

Creative Commons Attribution-Non Commercial-No Derivatives 4.0 International License (CC BY-NC-ND)

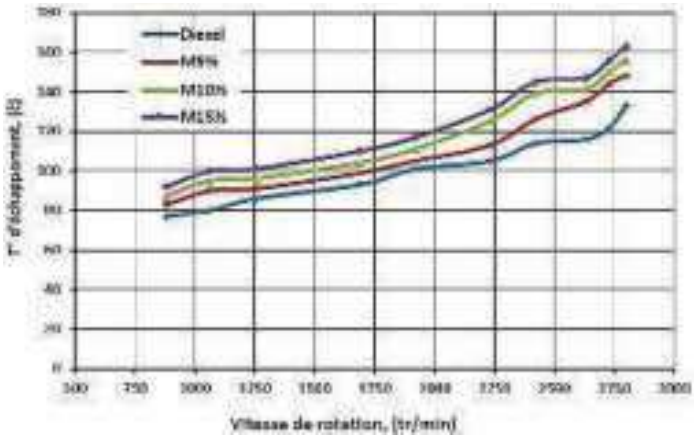

Fig. 13. Température des gaz d'échappement pour différents mélanges Diesel-méthanol

L'efficacité thermique du freinage est le rapport en pourcentage de la puissance de sortie du freinage et de la puissance d'entrée. D'après les résultats présentés sur la figure 14, il est clair que l'utilisation de méthanol dans ce test a conduit à une meilleure efficacité thermique de freinage en comparaison avec le Diesel pure. Cela est dû à la combustion complète lorsque le méthanol est utilisé.

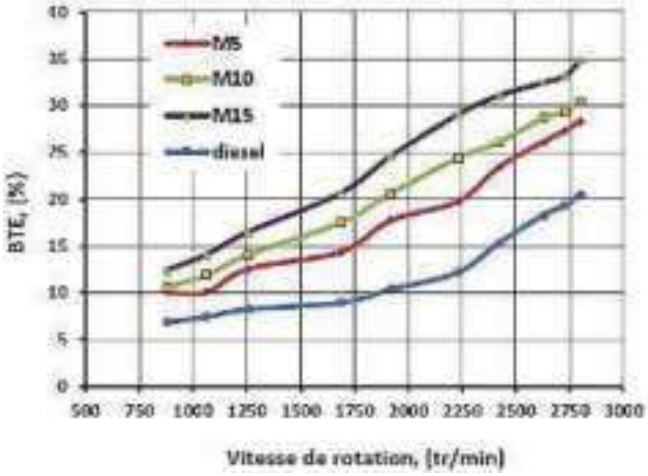

Fig. 14. Evolution de l'efficacité thermique de freinage pour différents mélanges Diesel-Méthanol

D'après les résultats présentés dans la figure 15, l'utilisation du méthanol dans la présente étude a conduit à un meilleur rendement par rapport à celui du Diesel pure avec une amélioration avoisinant les 20% pour le mélange D85M15 comparé au Diesel pure. Les résultats obtenus montrent que le rendement est proportionnel au taux du mélange en éthanol ainsi qu'au régime moteur.

Creative Commons Attribution-Non Commercial-No Derivatives 4.0 International License (CC BY-NC-ND)

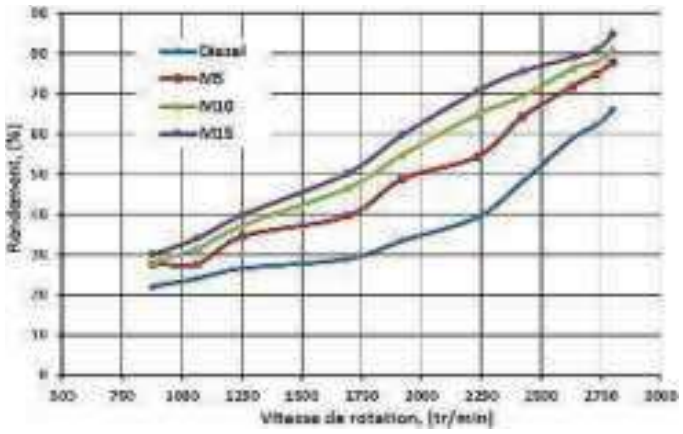

Fig. 15. Le rendement du moteur en fonction des différents mélanges Diesel-Méthanol

Conclusion :

Cette étude s'inscrit dans l'objectif de recherche visant à évaluer l'impact de carburant de nouvelle génération sur les performances des moteurs Diesel. Parmi les carburants envisagés, les mélanges Diesel-Ethanol et Diesel-Méthanol semblent avoir un potentiel important. En effet, ce sont des carburants alternatifs ayant des propriétés physico-chimiques relativement proches de celles d'un gazole traditionnel. De plus, leur haute teneur en oxygène permet une l'amélioration du processus de combustion ainsi la réduction drastique des émissions de particules à l'échappement. L'objectif principal de ce travail était donc de comprendre le comportement des mélanges carburants sur les performances du moteur Diesel. Cette approche est jugée meilleure car elle n'affecte pas le coût du moteur par une éventuelle modification et permettra aux moteurs existants de rester en utilisation.

Les conclusions suivantes peuvent être tirées sur les performances du moteur Farymann Diesel monocylindre de type P604 sans aucune modification du moteur à différents régimes. Les conclusions se présentent comme suit :

- Le couple moteur, la puissance de freinage et le rendement du moteur issus de la combustion des mélanges carburants Diesel-Ethanol, et des mélanges carburants Diesel-Méthanol sont plus élevés que ceux issues du carburant Diesel pure.
- Les mélanges carburants, D85E15 et D85M15 présentent les taux d'amélioration les plus élevés en comparaison au Diesel pure ainsi qu'aux autres mélanges carburants examiné sur notre moteur.
- La consommation de carburant spécifique de freinage pour les carburants mélanges est nettement supérieure à celle issue du Diesel pure ce qui constitue un désavantage pour notre carburants proposés, ceci est peut être due au moteur conçu initialement à fonctionner avec le Diesel pure ainsi qu'à la nature de l'éthanol qui constitue un catalyseur de combustion. En revanche, l'éthanol améliore le reste des performances du moteur. La CSCF la plus faible est enregistrée avec les mélanges D95E5 et D95M5.

Creative Commons Attribution-Non Commercial-No Derivatives 4.0 International License (CC BY-NC-ND)

- Les différents mélanges fournissent des températures de gaz d'échappement plus élevées et proportionnelles aux taux du mélange dans le Diesel. Ceci explique que l'ajout de biocarburant améliore le pouvoir calorifique du carburant, ce qui très recherché.
- La combustion des différents mélanges augmentent la température de sortie du liquide de refroidissement de manière proportionnelle aux taux du mélange. Ceci s'explique par le pouvoir calorifique élevé de mélanges par rapport à celui du Diesel pure.

References :

Ashraful A. M., Masjuki H. H., Kalam M. A., Fattah I. M. R., Imtenan S., Shahir S. A., (2014). *Production and comparison of fuel properties, engine performance and emission characteristics of biodiesel from various non-edible vegetable oils: A review*, Energy Conversion and Management, **80**, pp. 202-228.

Atmanli A., İleri E., and Yüksel B., (2015). *Effects of higher ratios of n-butanol addition to diesel-vegetable oil blends on performance and exhaust emissions of a diesel engine*, Journal of the Energy Institute, **88**, pp. 209-220.

Dasilva R., Cataluna R., Menezes E., Samios D., and Piatnicki C., (2005). *Effect of additives on the antiknock properties and Reid vapor pressure of gasoline*, Fuel, **84**, pp. 951-959.

Farkade H. S., Pathre A. P., (2012). *Experimental investigation of methanol, ethanol and butanol blends with gasoline on SI engine*. International Journal of Emerging Technology and Advanced Engineering. **2**(4).

Ganesan V., (2012). *Internal Combustion Engine*, 4th edition: Tata McGraw-Hill Education Private Limited.

Gauderman W. J., Vora H., McConnell R., Berhane K., Gilliland F., Thomas D., (2007). *Effect of exposure to traffic on lung development from 10 to 18 years of age: a cohort study*, The Lancet, **369**, pp. 571-577.

Gong J., Zhang Y., Tang C., and Huang Z., (2014). *Emission characteristics of iso-propanol/gasoline blends in a spark-ignition engine combined with exhaust gas re-circulation*, Thermal Science, **18**, pp. 269-277.

Harrod K. S., Jaramillo R. J., Berger J. A., Gigliotti A. P., Seilkop S. K., and Reed M. D., (2005). *Inhaled diesel engine emissions reduce bacterial clearance and exacerbate lung disease to Pseudomonas aeruginosa infection in vivo*. Toxicological Sciences, **83**, pp. 155-165.

Iliev S., (2015). *A Comparison of Ethanol and Methanol Blending with Gasoline Using a 1-D Engine Model*, Procedia Engineering, **100**, pp. 1013-1022.

Khieralla A., (2005). *Investigation of Ethanol/Gasoline Blends as Alternative Fuel for Spark Ignition Engine*, International Journal of Environment and Pollution, **23**, pp. 336-344.

Masum B. M., Masjuki H. H., Kalam M. A., Rizwanul Fattah I. M., Palash S. M., and Abedin M. J., (2013). *Effect of ethanol–gasoline blend on NOx emission in SI engine*, Renewable and Sustainable Energy Reviews, **24**, pp. 209-222.

Nik Rosli Abdullah, Zaharin M.S.M., Mamat A.M.I., Nawi M.R.M., Hazim Sharudin, (2015). *Effects of ethanol blends on gasoline engine performance and exhaust emissions*, Jurnal Teknologi, **76**(11), pp. 107-112.

Seagrave J., McDonald J. D., Bedrick E., Edgerton E. S., Gigliotti A. P., Jansen J. J., (2006). *Lung toxicity of ambient particulate matter from southeastern US sites with different contributing sources: relationships between composition and effects*, Environmental Health Perspectives, pp. 1387-1393.

Sayin C., Ozsezen A. N., Canakci M., (2010), *The influence of operating parameters on the performance and emissions of a DI diesel engine using methanol-blended-diesel fuel,* Fuel, **89**(7), 1407-1414. https://doi.org/10.1016/j.fuel.2009.10.035

Thangavelu S. K., Ahmed A. S., Ani F. N., (2016). *Review on bioethanol as alternative fuel for spark ignition engines*, Renewable and Sustainable Energy Reviews, **56**, pp. 820-835.

Yoon S. H., Ha S. Y., Roh H. G., and Lee C. S., (2009). *Effect of bioethanol as an alternative fuel on the emissions reduction characteristics and combustion stability in a spark ignition engine*, Proceedings of the Institution of Mechanical Engineers, Part D: Journal of Automobile Engineering, **223**, pp. 941-951.

Creative Commons Attribution-Non Commercial-No Derivatives 4.0 International License (CC BY-NC-ND)

Yusaf T., Hamawand I., Baker P. and Najafi G., (2013). *The effect of Methanol-Diesel blended ratio on CI engine performance*. International Journal of Automotive and Mechanical Engineering (IJAME), **8**, pp. 1385-1395.

Wargo J., Wargo L., and Alderman N., (2006). *The Harmful Effects of Vehicle Exhaust, A Case for Policy Change*, Environment and Human Health, Inc., USA.

Zaharin M. S. M., Abdullah N. R., Imran Dahalan M., Sharudin Hazim, Asiah A.R., Beriache M., (2017). Experimental Study on the Effects of Methanol and Ethanol on Gasoline Engine Performance and Exhaust Emissions. Journal of Mechanical Engineering, **SI 2** (2), 27-44.

Creative Commons Attribution-Non Commercial-No Derivatives 4.0 International License (CC BY-NC-ND)

Algerian Journal of Engineering Architecture and Urbanism Vol. 5 Nr. 3 2021
ISSN: 2588-1760

DIAGNOSIS OF MECHANICAL FAULTS IN ROTATING MACHINES BASED ON VIBRATION MONITORING IN AN INDUSTRIAL ENVIRONMENT

Mohamed Khemissi BABOURI
Lecturer, Dr, Department of Mechanical Engineering and Productics, FGM& GP, University of Sciences and Technology Houari Boumediene, PO Box 32, El-Alia, 16111 Bab-Ezzouar, Algiers, Algeria, e-mail: babouri_bmk@yahoo.fr

Nouredine OUELAA
Professor and Director LMS, Pr, Mechanics and Structures Laboratory (LMS), May 8th 1945 University, PO Box 401, 24000 Guelma, Algeria, e-mail: n_ouelaa@yahoo.fr

Abderrazek DJEBALA
Professor, Pr, Mechanics and Structures Laboratory (LMS), May 8th 1945 University, PO Box 401, 24000 Guelma, Algeria, e-mail: djebala_abderrazek@yahoo.fr

Abstract:
The implementation of conditional and preventive maintenance of rotating machines based on rigorous vibration monitoring seems an appropriate solution for the early detection of these faults, something which is unfortunately not always obvious. In this study, we propose an advanced and recent method of processing non-stationary and non-linear signals in an industrial environment, based on cyclostationary analysis. The main objective of this work is to meet the request of an industrial group FERTIAL where the vibration analysis was used to analyze the signals measured on the journal bearings of the turbine GMX1164.1 of a turboalternator GZ1164. The problem encountered in this work is due to the decrease in the production of the electric load from 6 MVA to 5 MVA leads to a very strong increase in the level of vibration on all the frequency bands of the bearings of the turbine and of the machine. To remedy this problem, a vibration analysis was used to analyze the signals measured on this turboalternator which operates in real conditions. The results obtained proved the power of the proposed method to highlight the precise nature of the mechanical defect studied and its severity in an industrial environment.

Key words: Spectral analysis, Mechanical defects, Journal bearings, Diagnostic, Cyclostationarity

Introduction

The proper functioning of industrial machines depends on the reliability and safety of their mechanical components, therefore monitoring and controlling them is a crucial and essential step. In this context, the monitoring and diagnosis of rotating machines in operation are of vital importance to ensure continuous production and increase the lifespan of these machines. To do this, it is necessary to ensure a good diagnosis and rely on reliable techniques for detecting defects in mechanical components, which requires the development of measurement, acquisition, analysis and decision support. Many classic tools for processing vibratory signals used in fault diagnosis of rotating machines (Cousinard *et al.,* 2004; Djebala *et al.,* 2015; Boulenger and Pachaud, 1998). On the other hand, denoising methods dedicated to vibratory analysis find the wavelet multiresolution analysis (Babouri *et al.,* 2016; Babouri *et al.,* 2017). Most of these methods have been developed for rotating machines working in a

Creative Commons Attribution-NonCommercial-NoDerivatives 4.0 International License (CC BY-NC-ND)

stationary regime (Khemili and Chouchane, 2005; Babouri *et al.,* 2020; Djebala *et al.,* 2015). Nowadays, several methods have been developed, especially in the case of a variable regime (Wu *et al.,* 2016; Bouhalais *et al.*, 2018; Babouri *et al.*, 2021). In the literature, several works have been carried out through the vibration signals recorded on rotating machines, which contain the necessary information relating to the state of the components of mechanical systems; in general the problem consists in isolating the information relating to each component. In this context, the measured signals have a very complex structure, and are made up of different mechanical components producing cyclic signals according to one or more cycles and on the other hand, random signals, due to parasitic phenomena generated during the operation of these mechanical systems. Overall, these vibratory signals are not stationary. Indeed, the selection of different signal processing methods depends on the two phenomena. Therefore, cyclostationarity offers a framework, particularly suited to the analysis of numerous vibratory signals, filling the limitations of several methods, which have generally been developed to detect specific defects (Antoni *et al.*, 2004; Babouri *et al.*, 2019). This is the context of our work, which focuses on the experimental monitoring of defects in the journal bearings of a turbo-generator GZ1164 in an industrial environment.

Theoretical foundations of Cyclostationarity

The cyclostationarity is an approach based on the distribution intensity modulation (MID) function allowing the identification of the modulations present in a signal s(t). The absolute value of the MID on a two-frequency plane (f, α) is represented as a function of the modulation frequency of order (α) is located with respect to the carrier frequency (f) of the filtered sideband (Tarek *et al.*, 2020).

The spectral correlation density can be defined as follows:

$$SC_x^{\alpha}(f) = \lim_{\Delta f \to 0} \lim_{\Delta t \to \infty} \frac{1}{\Delta t} \int_{-\Delta t/2}^{\Delta t/2} \Delta f \; S_{\frac{1}{\Delta f}}\left(t; f + \frac{\alpha}{2}\right) S^{*}_{\frac{1}{\Delta f}}\left(t; f - \frac{\alpha}{2}\right) dt \qquad (1)$$

Alternatively to the equation (1) the expression of the spectral correlation density can be defined by (Babouri *et al.*, 2019):

$$SC_s^{\alpha}(t,f) = \lim_{\Delta f \to 0} \lim_{T \to \infty} \frac{1}{T\Delta f} \int_T s_{\Delta f}\left(t; f + \frac{\alpha}{2}\right) s^{*}_{\Delta f}\left(t; f - \frac{\alpha}{2}\right) e^{-2j\pi\alpha t} dt \qquad (2)$$

The spectral coherence distribution intensity modulation function (SC_s^{α}) is obtained by:

$$MID_{\Delta f}(f;\alpha) = SC_s^{\alpha}\left(f + \frac{\alpha}{2}\right) SC_s^{\alpha}\left(f - \frac{\alpha}{2}\right), \qquad (3)$$

The integration of distributed MID represents the spectral correlation density, expressed by different sources, is called (IMID). This integration will be selected over the entire carrier frequency band from f_1 to f_2 and which can be defined by:

$$IMID_{f_1}^{f_2}(\alpha;\Delta f) = \int_{f_1}^{f_2} MID_{\Delta f}(f;\alpha) df \qquad (4)$$

Creative Commons Attribution-NonCommercial-NoDerivatives 4.0 International License (CC BY-NC-ND)

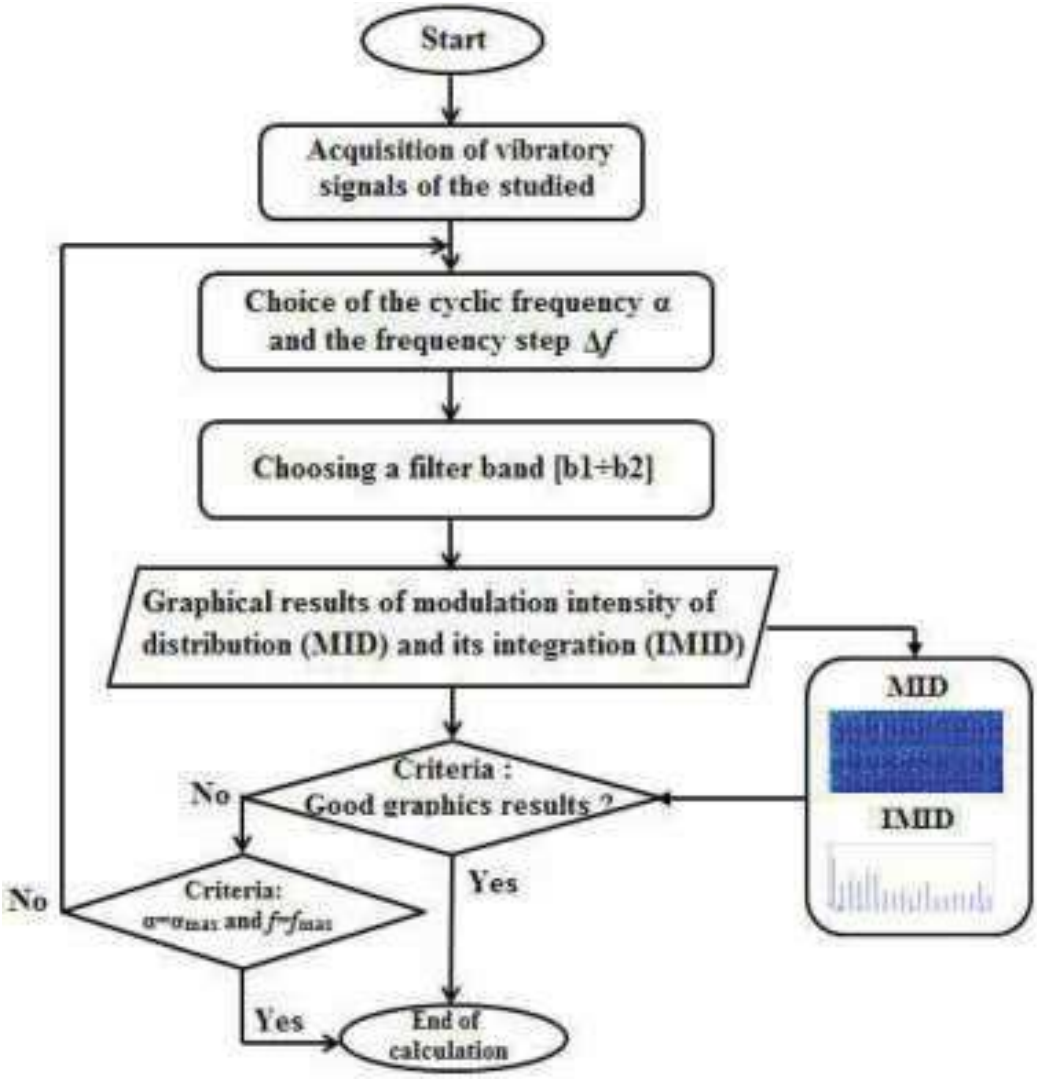

Fig. 1. Flowchart proposed to calculate the two MID indicators and its IMID integration

Figure 1 shows the algorithm of the proposed method for calculating the MID and the integration correspondent (IMID). The ability of these two parameters in the detection of cyclic components will be presented in the following section for the diagnosis of the journal bearings an turboalternator GZ1164 .

Materials and experimental procedures

To validate the proposed method in an industrial environment, an experimental application of the cyclostationarity analysis was carried out on real signals measured under non-stationary conditions on the journal bearings of a turbo-alternator GZ1164. The turboalternator is an essential machine in the production process of fertilizers and complex food fertilizers in Algeria. The main function of the turboalternator is to introduce superheated steam at high pressure through the turbine which turns a generator producing electricity of 5.5 KV. The installation comprises a steam turbine, a speed reducer and an

Creative Commons Attribution-NonCommercial-NoDerivatives 4.0 International License (CC BY-NC-ND)

alternator (Fig. 2). Table 1 gathers the technical characteristics of the steam turbine and of the speed reducer.

Fig. 2. Monoaxial and triaxial accelerometer (A), turboalternator (B), Pulse analyzer type 3160-A-042 (C).

Steam turbine	
Series	GMX1164.1
Number of wheels	16
Number of blades	40 to 112
Speed maxi	9000 tr/min
Blade length	32 mm and 70 mm
Rotation frequency	Fr= 9000/60 = 150 Hz
Number of wheel : 1 th wheel	Fault frequency (F_{bp}) = 6000 Hz
Number of wheel : 5 th wheel	Fault frequency (F_{bp}) = 9600 Hz
Number of wheel : 16 th wheel	Fault frequency (F_{bp}) = 16800 Hz Hz
passage frequency of the number of blades fixed by set (F_{Pbs})	F_{Pbs} =1200 Hz

Table 1. Technical characteristics of steam turbine

The vibration measurements were collected on the journal bearings of the turboalternator (Fig. 2 (B)). Two accelerometers were used; an industrial accelerometer type 4511-001, and another triaxial type 4524B-001 (Fig. 2 (A)). For the collection and processing of measurements, the Bruel & Kjaer PULSE 16.1 analyzer was used (Fig. 2 (C)).

Results and discussions

The main objective of this work is to monitor the specific faults of various mechanical components of the turbo-generator GZ1164. Indeed, we have proposed the vibratory analysis as an in-depth analysis of our study. There are different vibratory analysis methods and tools for detecting and diagnosing the appearance of defects, they are used in our study.

Temporal and frequency analysis

Fig. 3 represents a signal from the journal bearing of the turbine of our machine (Fig. 3a) measured in the rotation frequency of 150 Hz in the frequency band 25600 Hz, and their

Creative Commons Attribution-NonCommercial-NoDerivatives 4.0 International License (CC BY-NC-ND)

spectrum (FIG. 3b). Found frequencies to vary between 467.2 Hz and 3327 Hz, it represents the resonant frequency bands of the turbine and the entire system. On the other hand, we notice that the corresponding spectrum gives no information on the operating state of the turbine. Random noise and other machine components pollute the signal and make detection difficult if not impossible.

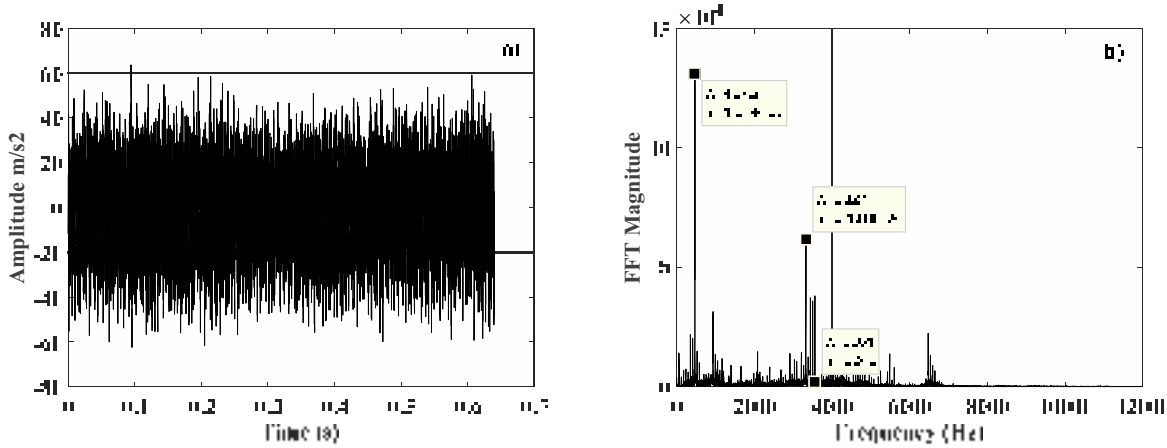

Fig. 3. Signal measured (a), its FFT spectrum (b)

Identifying defects by spectral analysis is difficult. This technique, although it is still used in particular in the context of vibration monitoring, is limited because certain fault frequencies are very close to the frequencies of other components and are generally immersed in each other. In order to make a correct diagnosis, it is useful to push the investigations towards more appropriate techniques such as time-frequency analysis; in particular wavelet multiresolution analysis (WMRA) to filter the measured signal from random noise and others machine components.

Wavelet multiresolution analysis

Wavelet multi-resolution wavelet analysis (WMRA) is like putting the signal under a microscope, cascade filtering allows you to view each part of the signal with a resolution adapted to its scale. The approach used by WMRA is to look for impacts and signs of deterioration of our journal bearing, among several other signal components as well as noise. The goal is to detect these impacts by choosing the detail or the approximation resulting from the wavelet decomposition of the signal and then to perform an envelope spectrum to allow frequency visualization.

Figure 4 shows the scalar indicators before and after the application of WMRA. It appears that the pulse factor is more significant than that of the original turbine bearing signal. For this purpose, the optimal vector of the wavelet multi-resolution decomposition in our case is the reconstructed signal which extracts from the detail D1, the one which allows the detection of the defect in the journal bearings of the turbine with the best possible resolution. One notices an increase of the scalar indicators used according to the reconstructed signal of the detail

Creative Commons Attribution-NonCommercial-NoDerivatives 4.0 International License (CC BY-NC-ND)

(D1). In this case the scalar indicators increase considerably, the impulse factor (IF) remains very sensitive goes from 4.0070 to 6.0311, the kurtosis (K) goes from 2.6190 to 3.7501 and the crest factor (Fc) being more sensitive, increases in rather large proportions, from 3.2713 to 4.6384 compared to Kurtosis.

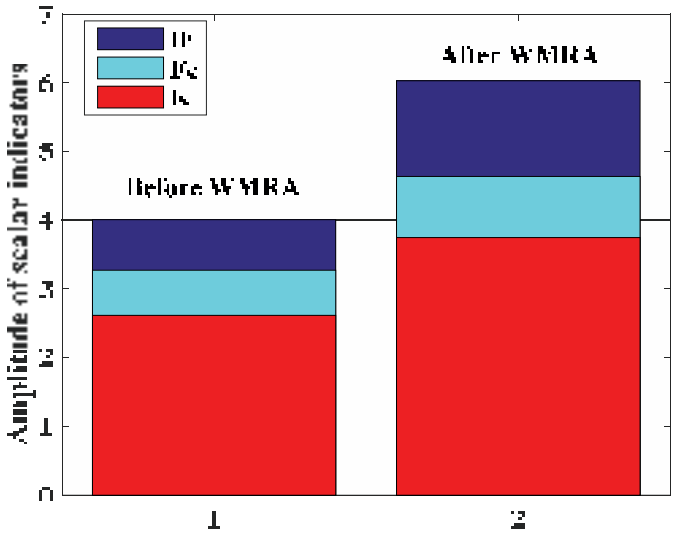

Fig. 4. Scalar indicators before and after WMRA

Fig. 5 (a) represents the optimal reconstructed signal (D1) of the signal measured at the level of the journal bearing the turbine, Fig. 5 (b) and Fig. 5 (c) represents, the envelope of the reconstructed signal and its envelope spectrum of wavelet coefficients which was calculated from the Hilbert transform. The envelope spectrum did not reveal information about the health of the mechanical parts of the turbine.

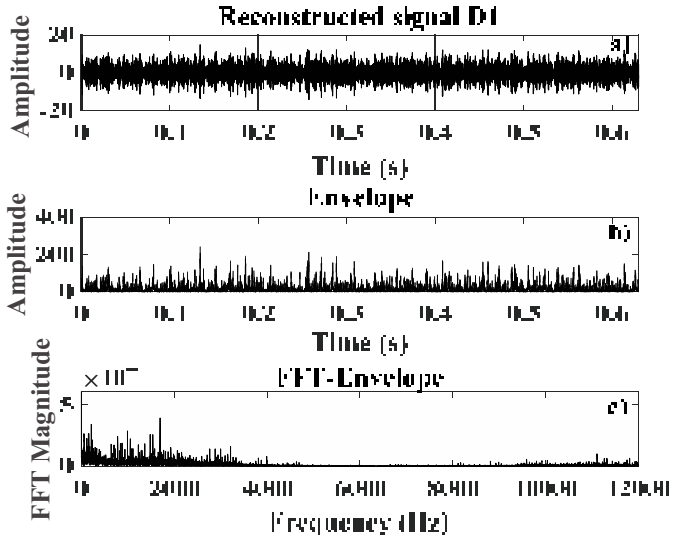

Fig. 5. Signal reconstructed detail D1 (a), Envelope of the wavelet coefficients of the reconstructed signal D1 (b), and FFT envelope of the reconstructed signal D1 (c).

Creative Commons Attribution-NonCommercial-NoDerivatives 4.0 International License (CC BY-NC-ND)

Algerian Journal of Engineering Architecture and Urbanism Vol. 5 Nr. 3 2021
ISSN: 2588-1760

Zooming in the envelope spectrum of the reconstructed signal detail D1 in the frequency band [1000 - 1400 Hz], figure 6 (a), we see the existence of a fault on the blades of the turbine, which is confirmed by l 'appearance of a peak corresponding almost to the passage frequency of the number of blades fixed by set, equal to 1225 Hz. On the zoom (Fig. 6 (b)) of the envelope spectrum in the frequency band [8000 - 11000 Hz], a peak appears equal to 9591 Hz corresponding to the blades passage frequency (Fbp) of the 5th wheel (see Table 1).

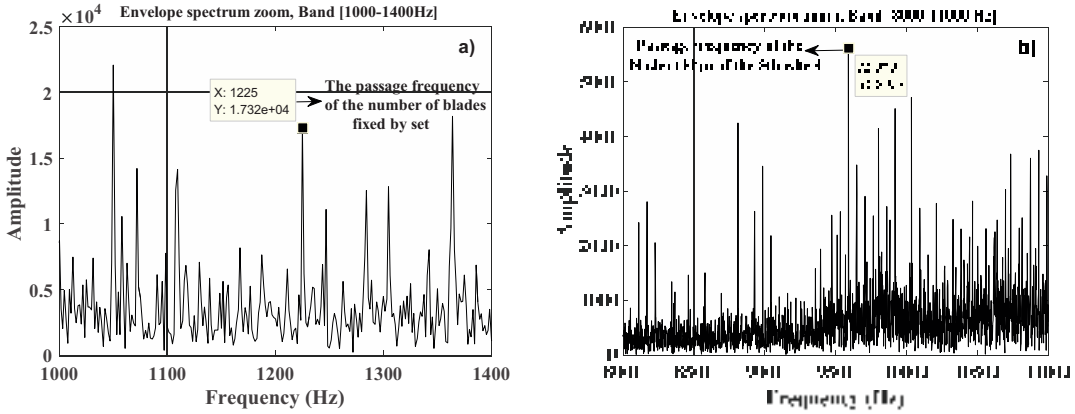

Fig. 6. Zoom on the envelope spectrum in the band [1000 - 1400 Hz] (a), and on the band [8000 - 11000 Hz] (b)

The envelope spectrum did not reveal information regarding the health of journal bearings the turbine. Therefore, a more advanced method has been proposed in signal processing, which also allows the improvement of the monitoring of the journal bearings of the turbine; it is the method of cyclostationary analysis.

Application of cyclostationary analysis

As mentioned earlier, cyclostationarity is a method based primarily on two indicators or distribution intensity modulation function (MID) and its integration (IMID), allowing the detection and identification of modulations present in a signal. The technique (MID) was originally designed for fault diagnosis of gears, rolling bearings and journal bearings. Spectral correlation density focuses on detecting the amplitude modulations of symmetrically spaced sidebands in spectrums. It makes it possible to present the values of the modulation indicator on a frequency plane of the signal as a function of the carrier frequency (*f*) and the modulation frequency of order (α).

Figures 7 (a) and 7 (b) show the distribution intensity modulation (MID) and its integration (IMID) of the measured signal. We can clearly see the appearance of a fundamental cyclic frequency at 149 Hz and several of its harmonics. This component is very close to the frequency of rotation of the turbine (Fr = 150 Hz). This diagnosis was not found by spectral analysis. In this context, we see from Figure 7 (b), frequency components due to the speed of rotation, several of its sub harmonic (0.25 Fr, 0.5 Fr, 0.75 Fr) and their harmonics (2 Fr, 3 Fr), are also visible.

Creative Commons Attribution-NonCommercial-NoDerivatives 4.0 International License (CC BY-NC-ND)

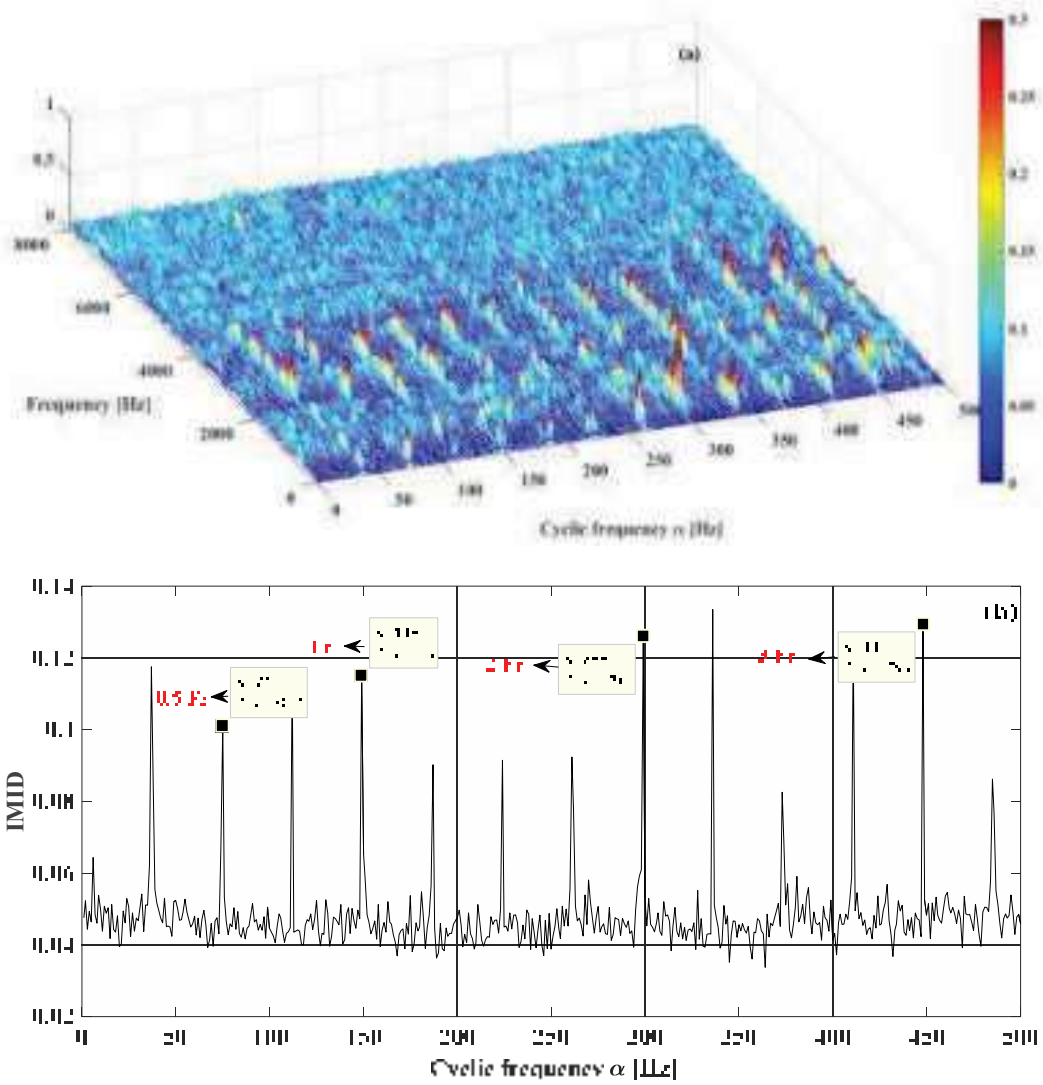

Fig. 7. Distribution intensity modulation MID (a) and its integration IMID (b) of the measured signal (Fig. 3 (a)).

On the other hand, there was a difference in vibration level over the entire frequency band, which can be explained by the presence of two defects, one at low frequency and probably said in the presence of friction in the journal bearing of the turbine and the presence of an oil swirl fault in this bearing and a high-frequency fault closely linked to the blades passages frequency and these harmonics.

Conclusion

The detection of rotating machine faults remains a topical area of research aimed primarily at the development of reliable and practical methods. Several parts of machines produce shocks when they are partially or totally damaged. In this spirit, the objective of this study is the implementation of a conditional and experimental maintenance of the mechanical faults on the journal bearings of the GMX1164.1 turbine of a turboalternator, based on a rigorous vibration monitoring seems a solution suitable for the early detection of these

Creative Commons Attribution-NonCommercial-NoDerivatives 4.0 International License (CC BY-NC-ND)

defects, something which is unfortunately not always obvious. In this context, we also exposed the different techniques for detecting journal bearing defects used in vibration monitoring, namely, the application of signal processing tools used in monitoring rotating machines: the scalar indicators and analysis spectral. On the other hand, we were interested in looking at an advanced method such as wavelet multi-resolution analysis (WMRA) and to have the possibility of applying the cyclostationary analysis of the signals measured in an industrial environment. From the application of these methods, we can draw the following conclusions:

- The temporal analysis of scalar indicators like crest factor (Fc), kurtosis (K) and a proposed new indicator called impulse factor (IF). It is noted that these indicators only guarantee a detection of the first level of alarm, they cannot detect the origin of the failure. On the other hand, the identification of mechanical defects by spectral analysis is difficult. Only observed resonance frequencies of the turbine and the whole system, they vary between 467.2 Hz and 3327 Hz.

- The random noise and other turbine components pollute the signal and make detection difficult if not impossible. Wavelet multiresolution analysis (WMRA) is offered as a solution to this problem. The results of the comparison of the values of the scalar indicators before and after the use of the WMRA, indicated a significant increase in the reconstructed signal of the detail D1. However, the envelope spectrum represents some fault frequencies that are very close to the frequencies of other components and are generally immersed in each other.

- The zoom of the envelope spectrum of the reconstructed signal of detail D1 in the frequency band [1000 - 1400 Hz] and [8000 - 11000 Hz], allows us to have, the existence of a defect on the blades of the turbine, which confirmed by the appearance of a peak corresponding almost to the passage frequency of the number of blades fixed by set, equal to 1225 Hz and on the other hand, a peak is equal to 9591 Hz corresponding to the blades passage frequency of the 5th wheel.

- Finally, we have oriented our diagnosis of the faults in the plain bearings of a GMX1164.1 turbine of a turboalternator towards the application of a recent method called cyclostationarity, this method given very interesting results compared to the previous methods, it makes it possible to highlight the presence of friction and an oil swirl due in the journal bearing faults of the steam turbine, the frequency components due to the speed of rotation (Fr = 150 Hz), several of its sub-harmonics (0, 25 Fr, 0.5 Fr, 0.75 Fr) and their harmonics (2 Fr, 3 Fr), are also visible. This phenomenon can be explained by the presence of two faults, one at low frequency and probably due to the presence of friction and oil swirl in the journal bearings and the other at high frequency closely linked to the frequencies of blade passages and these harmonics.

Creative Commons Attribution-NonCommercial-NoDerivatives 4.0 International License (CC BY-NC-ND)

References:

Antoni J., Bonnardot F., Raad A., El Badaoui M. (2004), *Cyclostationary modelling of rotating machine vibration signals*. Mechanical systems and signal processing **18(6):**1285-1314.

Babouri M. K., Ouelaa N., Djebala A. (2016), *Experimental study of tool life transition and wear monitoring in turning operation using a hybrid method based on wavelet multi-resolution analysis and empirical mode decomposition.* The International Journal of Advanced Manufacturing Technology **82(9-12):**2017-2028.

Babouri M. K., Ouelaa N., Djamaa M. C., Djebala A., Hamzaoui N. (2017), *Prediction of tool wear in the turning process using the spectral center of gravity*. Journal of Failure Analysis and Prevention **17(5):**905-913.

Babouri M. K., Djebala A., Ouelaa N., Oudjani B., Younes R. (2020), *Rolling bearing faults severity classification using a combined approach based on multi-scales principal component analysis and fuzzy technique.* The International Journal of Advanced Manufacturing Technology **107(9):**4301-4316

Babouri M. K., Ouelaa N., Djebala A., Djamaa M. C., Boucherit S. (2017), *Prediction of cutting tool's optimal lifespan based on the scalar indicators and the wavelet multi-resolution analysis*. In Applied Mechanics, Behavior of Materials, and Engineering Systems. Springer, Cham, pp. 299-310.

Babouri M. K., Ouelaa N., Kebabsa T. (2021), *Diagnosis of mechanical defects using a hybrid method based on complete ensemble empirical mode decomposition with adaptive noise (CEEMDAN) and optimized wavelet multi-resolution analysis (OWMRA): experimental study*, The International Journal of Advanced Manufacturing Technology **112:**2657–2681.

Babouri M. K., Ouelaa N., Kebabsa T., Djebala A. (2019), *Application of the cyclostationarity analysis in the detection of mechanical defects: comparative study*, The International Journal of Advanced Manufacturing Technology **103(5):**1681-1699.

Bouhalais M. L., Djebala A., Ouelaa N., Babouri M. K. (2018), *CEEMDAN and OWMRA as a hybrid method for rolling bearing fault diagnosis under variable speed*, The International Journal of Advanced Manufacturing Technology **94:**2475–2489.

Boulenger A., Pachaud C. (1998), *Vibratory diagnosis in maintenance préventive*. Dunod, Paris, ISBN: 2100041053

Cousinard O., Rousseau P., Bolaers F., Marconnet P. (2004), *Paramétrage, utilisation et apport de l'analyse cepstrale en maintenance prévisionnelle*. Mécanique & industries **5(4):**393–406

Djebala A., Ouelaa N., Babouri M. K. (2015), *Optimization of a Maintenance Policy in Industrial Field: Case Study*, In Design and Modeling of Mechanical Systems-II. Springer, Cham, pp. 169-178.

Djebala A., Babouri M. K., Ouelaa N. (2015), *Rolling bearing fault detection using a hybrid method based on empirical mode decomposition and optimized wavelet multi-resolution analysis,* The International Journal of Advanced Manufacturing Technology **79:** 2093–2105

Khemili I., Chouchane M. (2005), *Detection of rolling element bearing defects by adaptive filtering*. European Journal of Mechanics-A/Solids **24:**293–303.

Wu T.Y., Lai C.H., Liu D.C. (2016), *Defect diagnostics of roller bearing using instantaneous frequency normalization under fluctuant rotating speed*, Journal of Mechanical Science and Technology **30:**1037-1048.

Tarek K., Abderrazek D., Khemissi B. M., Cherif D. M., Lilia C., Nouredine O. (2020), *Comparative study between cyclostationary analysis, EMD, and CEEMDAN for the vibratory diagnosis of rotating machines in industrial environment.* The International Journal of Advanced Manufacturing Technology **109(9):**2747-2775.

Creative Commons Attribution-NonCommercial-NoDerivatives 4.0 International License (CC BY-NC-ND)

Algerian Journal of Engineering Architecture and Urbanism Vol. 5 Nr. 3 2021
ISSN: 2588-1760

ASYMMETRICAL AND SYMMETRICAL COPLANAR ISOLATOR BASED ON FERRITE FILMS

Toufik BOUDIAR
Lecturer, Dr, Innovative Technologies Laboratory, ENST, Algiers, Algeria,
toufik.boudiar@enst.dz

Eric VERNEY
Lecturer, Dr, Hubert Curien Laboratory, Jean Monnet University, St-Etienne, France

Abstract:
In this letter, two types of CPW isolator are presented and compared. First, an integrated coplanar isolator using YIG thin films is realized. The component's transmission parameters are measured and compared to the simulation results. The influence of the magnetic film's thickness and the polarizing field on the device performances are evaluated. In the second design where metamaterials are used with a coplanar structure, we measured that the nonreciprocal effect reached higher values for different resonance frequencies than for the first design and that the insertion losses also decreased. Also, the isolation can reach 44.2 dB at 29.2 GHz and 15.8 dB at 16.6 GHz with insertion losses of 2.6 dB and 3.8 dB, respectively.

Key words: Microwave device, nonreciprocal effect, coplanar isolator, metamaterial

Introduction:

For several years, the tremendous growth in electronic telecommunication has generated a lot of interest in developing miniaturized ferrite devices. Isolators (Kirouane, 2012; Courtois, 1975), circulators (Yamamoto, 2004; Wang, 2011), and phase shifters (Yang, 2013) are some non-reciprocal devices that are most commonly used in the telecommunication industries. Among ferrite materials, yttrium iron garnet (YIG) presents some interests in microwave applications (Adam, 2002).

Currently, the integration of non-reciprocal microwave components and the increasing frequency are two important issues of future communication systems. Several configurations of planar isolators are mentioned in the literature, such as slotline (Courtois, 1975), stripline and microstrip (Hines, 1971). In the particular case of coplanar waveguide (CPW) structures the advantages are: simplicity of design, low-cost manufacturing, possibility of integration of discrete elements, compatibility with microwave integrated circuits technology, etc.

Isolator is one of the important ferrite devices whose operation is based on the non-reciprocal effect (NRE). A rf isolator can be considered as a diode for rf energy, allowing signal to go through in one direction only. The problem that power reflecting back to generators may lead to nonlinear effects such as the instability and frequency shifting (Bayard, 2005). To avoid this, an isolator between the generator and the load could be applied in order to attenuate only

Creative Commons Attribution-NonCommercial-NoDerivatives 4.0 International License (CC BY-NC-ND)

the reflected wave and hence protect the generator (Semiconductors, 1998). Other classical applications are to reduce interaction between the transmitter and the antenna or between stages of amplification.

In 1969, Wen proposed a coplanar waveguide with ferrite material (Wen, 1969). A transverse dc magnetic field applied parallel to the surface is required to provide appropriate bias conditions. Under those conditions, the isolation performance is about 37 dB with low insertion losses (< 2 dB). The main obstacle to the use of this structure is the magnetic material which is in the form of rods, located in the slots between the conductors at the air-dielectric interface. An alternative to this problem is to use the magnetic materials in the form of magnetic layers. In addition, CPW technology is widely used in microwave integrated circuits (MIC) and in monolithic microwave integrated circuits (MMIC) (Simons, 2001; Chang, 2005).

For the realization of a coplanar isolator, different studies use 1000 µm-thick YIG substrate at X or Ku band (Kirouane, 2012; Subbiah, 2003; Djekounyoum, 2020). However, the rise in frequency and the increase in the number of communication standards require the design of multiband component. For this purpose, a multiband coplanar isolator with metamaterials such as high impedance wire (HIW) (Safwat, 2007; Safwat, 2010) is also proposed. This structure exploits the non-reciprocal properties of magnetic ferrites as well as those of metamaterials.

In this work, a comparison between coplanar isolator and asymmetric CPW isolator using metamaterials is presented. Firstly, the experimental results of a nonreciprocal CPW using YIG thin film are discussed and compared to the simulation results. Then, the influence of YIG film thickness on the properties of the structure is shown. Finally, an asymmetric design of coplanar isolator is proposed.

Symmetrical coplanar isolator structure:

The operation of microwave isolators is based on ferromagnetic resonance properties of ferrite materials. The behavior of these materials in RF devices is widely understood using the Polder permeability tensor to describe the interaction of the ferrite material with RF excitation fields (Soohoo, 1960; Tsandoulas, 1972). The nonreciprocal behavior of the device is obtained by subjecting a ferrite to a proper magnetic bias field.

The coplanar isolator structure (Fig. 1) consists of a 12.3 µm-thin magnetic film (YIG) deposited on alumina substrate. To obtain a magnetic material, post deposition heat-treatment was carried out at 740°C during 2 h in air at a rate of about 480°C/h. Then, the patterning of the coplanar metallic lines is achieved using a standard lift-off technique. The alumina substrate is 635 µm thick (h_s). The slots (w) and the central strip width (s) are set to 300 µm. The thickness of the gold signal line and the ground planes is around 600 nm. The length and the width of the device are 23 mm and 10 mm, respectively. The isolator characterization is

Creative Commons Attribution-NonCommercial-NoDerivatives 4.0 International License (CC BY-NC-ND)

performed by a 65 GHz vector network analyzer (A37397 Anritsu) and a probing system. For the simulation, the software Ansoft-HFSS was used.

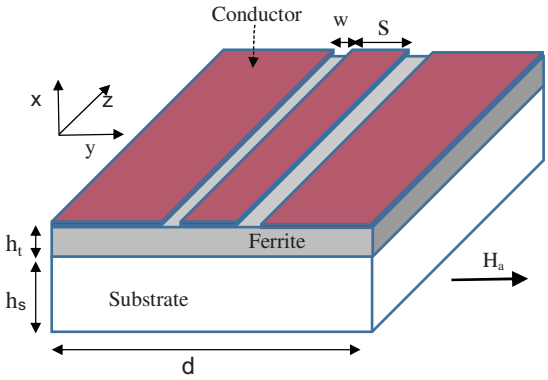

Fig. 1. Coplanar isolator.

Experimental results

Figure 2 shows the transmission coefficients S_{12} (isolation) and S_{21} (insertion loss) of the CPW isolator for different transverse magnetic fields. The gyromagnetic resonance phenomenon is observed when an external field is applied. At 9 GHz, due to the gyroresonance of YIG, the discrepancy between the transmission parameters S_{21} and S_{12} reached a maximum for dc field of 220 kA/m. The non-reciprocal effect measured is about 2 dB for higher magnetic field with an isolation of 8.5 dB. According to figure 3, the non-reciprocal effect increases linearly with the applied magnetic field.

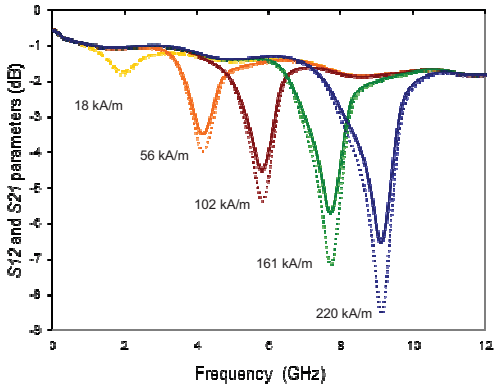

Fig. 2. Experimental measurements of the coplanar isolator transmission coefficients S12 (dashed line) and S21 (solid line) for different applied fields.

Besides, magnetic bias field plays a key role in the design of an isolator. The resonance frequency of the component can be controlled by various magnetic bias fields. Indeed, for a ferrite sample the gyromagnetic resonance frequency is given by the Kittel's equation (Lax,

Creative Commons Attribution-NonCommercial-NoDerivatives 4.0 International License (CC BY-NC-ND)

1962). Since the demagnetization factors could be ignored when the device is transversely biased, so, according this equation, the resonance frequency (f_r) could be written as

$$f_r = \mu_0 \gamma / 2\pi \left[(H_a + (N_x - N_z) M_s)(H_a + (N_y - N_z) M_s) \right]^{1/2}$$

Where H_a is the applied bias field, M_s is the saturation magnetization and γ is the gyromagnetic ratio (28 GHz/T). For a thin film $N_x = N_z = 0$ and $N_y = 1$.

The calculated resonance frequencies are then compared with the measured ones. As shown in figure 4, the two results are in agreement.

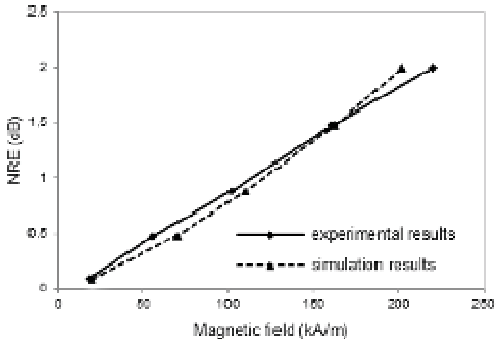

Fig. 3. Nonreciprocal effects obtained in simulation (dashed line) and measurements (solid line) versus internal field and external field respectively.

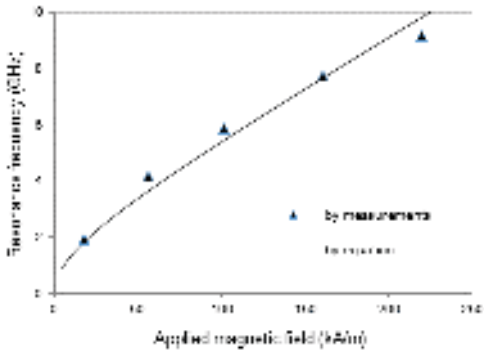

Fig. 4. Resonance frequencies versus applied field.

Numerical results

In the present section, computational results will be given and compared with the experimental results. To estimate the nonreciprocal characteristics of the coplanar isolator, the full wave analysis is carried out with the use of finite element method. The commercial software Ansoft-HFSS is utilized in the simulation. The parameters used in the calculation are as follows: saturation magnetization M_s = 169 mT, dielectric loss tangent tangδ = 2.10^{-4}, and relative permittivity of ferrite ε_r = 15.

Creative Commons Attribution-NonCommercial-NoDerivatives 4.0 International License (CC BY-NC-ND)

For simulations, HFSS uses the internal static magnetic field (H_i) instead of the external applied field (H_a) and it assumed here to be uniformly applied to the YIG thin film. The magnetic field was applied transversal to the coplanar isolator structure.

In figure 5, the comparison of simulated and measured scattering parameters is shown for the applied internal magnetic field of 202.5 kA/m, for which the external magnetic field is 220 kA/m for measurements. It is noted a good agreement between measurements and simulations of S_{12} and S_{21} parameters, except that the simulated bandwidth is lower than the measured one, and a difference in amplitude is also observed. This is probably due to the non-uniform external field applied to the YIG thin film. Besides, the internal magnetic field is relatively different to the external applied field. The variation of NRE against the internal bias field is plotted in Fig. 3. It is estimated from the results that the nonreciprocal effect increases linearly with the internal field. It is also noted that the experimental results match simulation results well.

The variations of the insertion losses and the nonreciprocal effect according to the thickness of ferrite are shown in Fig. 6. In both cases, these parameters increase with the YIG thickness. However, they tend to saturate from around 200 µm thick. This result does not satisfy the requirements of our component.

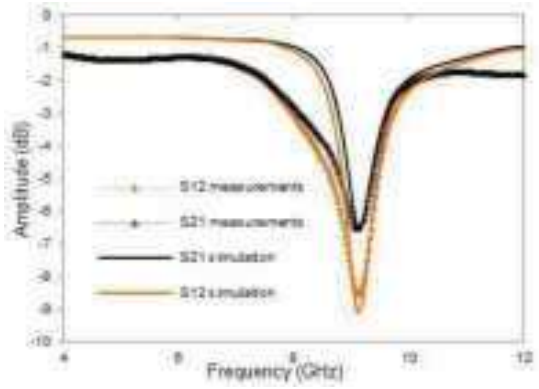

Fig. 5. Transmission parameters obtained in simulation and measurements.

Creative Commons Attribution-NonCommercial-NoDerivatives 4.0 International License (CC BY-NC-ND)

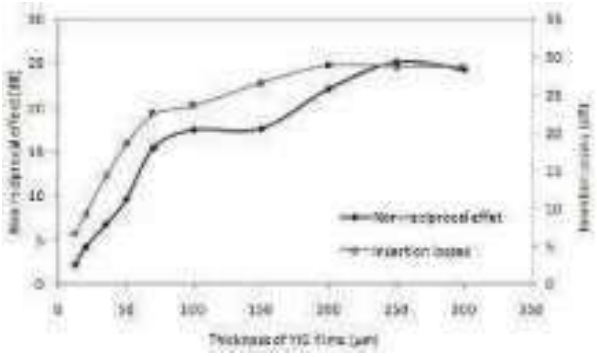

Fig. 6. The NRE and the insertion losses as function of the YIG film thickness at 9 GHz.

Asymmetrical coplanar isolator:

In the previous structure, the NRE was based on the gyromagnetic resonance, and even if a high isolation seemed to have been reached, insertion loss was still too high. In this section, a multiband coplanar isolator is presented, it exploits the nonreciprocal properties of the magnetic material combined with those of metamaterials.

The structure under consideration is shown in figure 7. One of the ground planes is cut via periodic slots, forming a serrated geometry with multiple fingers. The slot grating period is 396 µm and the slots width is 50 µm. The width of the central strip and its length are set to 300 µm and 2.3 cm respectively. The two ground planes are 4.55 mm wide. This metallic electromagnetic structure is known as high-impedance wire. The coplanar isolator was simulated by HFSS, using 300 µm-thick YIG film layer deposited on alumina substrate.

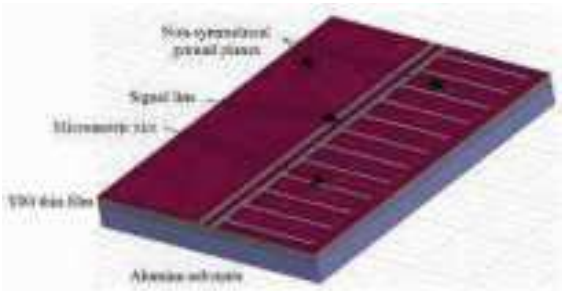

Fig. 7. Non-symmetrical coplanar isolator.

Origin of the phenomenon

For the original coplanar line, the current would flow mainly on the edge along z axis direction, and magnetic field distribution would be dominated by H_x and H_y components (figure 8.a). Whereas for the non-symmetrical structure, the current flowing has been forced

Creative Commons Attribution-NonCommercial-NoDerivatives 4.0 International License (CC BY-NC-ND)

along the new edges created by the presence of slots, which generated rotating magnetic field with H_x and H_z components. When the DC magnetic bias field is applied along y-axis, the left-hand (LHCP) or right-hand (RHCP) circular polarization direction of the magnetic field is depended on the in-plane dc magnetic bias (figure 8). The propagation constant in the stubs takes two different values, depending on the direction of propagation, leading to a nonreciprocal behavior of the structure.

According to the transmission line model of high impedance wire presented by E. Safwat et al (Safwat, 2007), several resonance peaks will occur in the frequency band:

$$f_r \approx (2m+1)\frac{c}{4d_t\sqrt{\mu_{eff}\varepsilon_{eff}}}$$

where m = 0, 1, 2, 3…, c is the velocity of light, d_t is the length of slot, μ_{eff} and ε_{eff} are the effective permeability and permittivity on the slotline stubs, respectively.

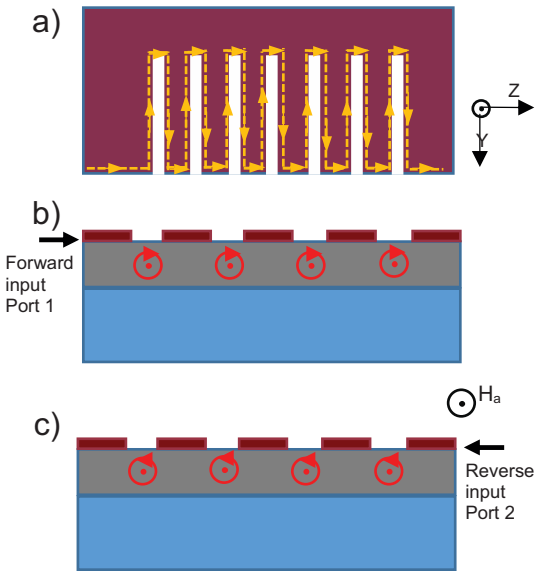

Figure 8. Configuration of microwave magnetic field: a) the dashed line indicates the current flowing on the ground plane, b) LHCP for forward transmission, c) RHCP for reverse transmission.

Simulation results

According to figure 9, the difference between the insertion loss (S_{21}) and the isolation (S_{12}) is observed for different resonance frequencies. The NRE can reach 41.6 dB at 29.2 GHz and 12 dB at 16.6 GHz for an internal magnetic field of 140 kA/m, with insertion losses of 2.6 dB and 3.8 dB respectively. It is also noted that cut-off frequencies appear in the forward and

Creative Commons Attribution-NonCommercial-NoDerivatives 4.0 International License (CC BY-NC-ND)

backward propagation. Indeed, in expression (2) the effective permeability of the polarized ferrite depends on the direction of propagation.

In the forward direction, the cut-off frequencies obtained are: 16.6 GHz and 29.2 GHz respectively, corresponding to the second and third resonant frequencies according to equation 2. The same observation is obtained in the backward propagation at the following frequencies: 30.6 GHz and 18 GHz. Furthermore, the first resonance peak should have appeared at the frequency of 5.53 GHz for the forward propagation and 6 GHz for the reverse direction. This is probably due to the gyromagnetic resonance phenomenon which is observed at 6.6 GHz.

In the operating-frequency ranges of the component, both the forward and backward return losses of S_{11} and S_{22} shown in Fig. 10 are greater than 10 dB, which indicated that the missing energy was dissipated in the YIG film or radiated instead of reflecting back to port 1 and port 2.

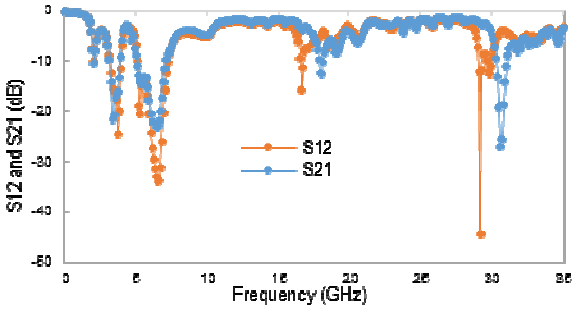

Fig. 9. Transmission coefficients on asymmetrical coplanar isolator.

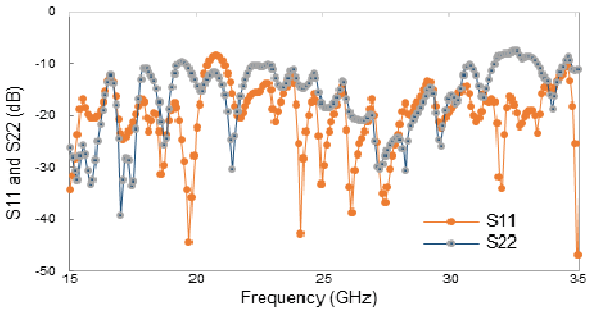

Figure 10. Reflection coefficients on asymmetrical coplanar isolator.

Creative Commons Attribution-NonCommercial-NoDerivatives 4.0 International License (CC BY-NC-ND)

Conclusion:

Two different coplanar isolators are introduced in this letter. First, a symmetrical coplanar isolator based on the gyromagnetic resonance was simulated and realized with YIG thin film. The measured scattering parameters were compared to the simulation results. It was found that the results obtained experimentally are in agreement with those of the simulation. Then, a multiband coplanar isolator was proposed. The simulation results of this structure are as follows: the NRE can reach 41.6 dB at 29.2 GHz and 12 dB at 16.6 GHz with insertion losses of 2.6 dB and 3.8 dB, respectively. Those results pave the way for the realization of multiband microwave isolators using ferromagnetic films.

References:

Kirouane S., Vincent D., Vernet E., Zahwe O., Payet-Gervy B., Chaabi A. (2012), *Design of a new coplanar isolator made from YIG film operating in the X-frequency band*. Eur. Phys. J. Appl. Phys **57**:1-4.

Courtois L., DeVecchis M. (1975), *A new class of nonreciprocal components using slot line*. IEEE Trans. **Microwave** Theory Tech **23**:511-516.

Yamamoto S., Shitamitsu K., Kurisu H., Matsuura M., Oshiro K., Mikami H., Fujii S. (2004), *Proposed new circulator with coplanar waveguie structure*. Trans. Magn. Soc. Japan **4**:56-59.

Wang J., Yang A., Chen Y., Chen Z., Geiler A., Gillette S.M., Harris V.G., Vittoria C. (2011), *Self biased Y-junction circulator at Ku band*. IEEE Microwave Wireless Comp. Lett **21**:292-294.

Yang X., Wu J., Gao Y., Nan T., Zhou Z., Beguhn S., Liu M., Sun N.X. (2013), *Compact and low loss phase shifter with low bias field using partially matgnized ferrite*. IEEE Trans. Magn **49**:3882-3885.

Adam J.D., Davis L.E., Dionne G.F., Schloemann E.F., Stitzer S.N. (2002), *Ferrite devices and materials*. IEEE Trans. Microw. Theory Tech **50**:721-737.

Courtois L., Vecchis M.D. (1975), *A new class of nonreciprocal components using slot line*. IEEE Trans. Microw. Theory Tech **23**:511-516.

Hines M.E. (1971), *Reciprocal and nonreciprocal modes of propagation in ferrite stripline and microstrip devices*. IEEE Trans. Microw. Theory Tech **19**:442-451.

Bayard B., Sauviac B., Vincent D. (2005), *Encyclopedia of rf and microwave engineering*. John Wiley Sons, Inc **6**.

Semiconductors P. (1998), *Circulators and isolators, unique passive devices*. Philips Semiconductors.

Wen C.P. (1969), *Coplanar waveguide: A surface strip transmission line suitable for nonreciprocal gyromagnetic device application*. IEEE Trans. Microw. Theory Tech **17**:1087-1090.

Simons R.N. (2001), *Coplanar waveguide circuits, components, and systems*. John Wiley Sons, New York, NY.

Chang K. (2005), *Encyclopedia of rf and microwave engineering*. John Wiley Sons, Hoboken, NJ.

Subbiah S., Alphones A. (2003), *Tunable isolator using a coupled microstrip line with an obliquely magnetized YIG substrate*. IEE Proc.-Microw. Antennas Propag **150**:219-222.

Djekounyom E., Verney E., Vincent D. (2020), *Coplanar high impedance wire on ferrite substrate: Application to isolators*. IEEE Trans. Magn **56**:1-5.

Safwat A.M., Tretyakov S.A., Raisanen A.V. (2007), *High-impedance wire*. IEEE Antennas Wirel. Propag. Lett **6**:631-634.

Safwat A.M. (2010), *High impedance wire composite right/left-handed transmission lines*. Microw. Opt. Technol. Lett **52**:1390-1393.

Soohoo R.F. (1960), *Theory and application of ferrites*. New Jersey, Prentice-Hall.

Tsandoulas G.N., Willwerth F.G., Ince W.J. (1972), *LSE/sub20/-Mode characteristics in phase-shifter parametrization*. IEEE Trans. Microw. Theory Tech **20**:253-258.

Lax B., Button K.J. (1962), *Microwave ferrites and ferrimagnetics*. McGraw-Hill, New York.

Creative Commons Attribution-NonCommercial-NoDerivatives 4.0 International License (CC BY-NC-ND)

Algerian Journal of Engineering Architecture and Urbanism Vol. 5 Nr. 3 2021
ISSN: 2588-1760

BLIND CLASSIFICATION OF DIGITAL MODULATION FOR D-STBC COOPERATIVE RELAYING NETWORKS

Hakima MOULAY
PhD student, TTNS Laboratory, University of Djillalil Liabes, Sidi Bel Abbes, Algeria, e-mail: hakima8_moulay@hotmail.com

Ahmed Bouzidi DJEBBAR
Professor, TTNS Laboratory, University of Djillalil Liabes, Sidi Bel Abbes, Algeria, e-mail: ahbou_djebbar@yahoo.fr

Brahim DEHRI
PhD in Telecommunications systems, University of Djillalil Liabes, Sidi Bel Abbes, Algeria, e-mail: brahim.dehri@gmail.com

Abstract:
This paper addresses the problem of blind Modulation Classification (MC) approach using single and ensemble-learning algorithms for Distributed Space-Time Block Coding (D-STBC) based Cooperative Relaying Network (CRN). CRN is created by using three nodes namely source, relay and destination. D-STBC matrix is obtained at destination node by concatenation of rows of the STBC matrix used respectively at source and relay nodes. In this paper, the modulation recognition method use High Order Statistics (HOS) to select the features, followed by pattern recognition methods such as Random Forest Classifier (RFC), Adaptive Boosting (AdaBoost) and Decision Trees (DT), to identify modulation type and order. Simulation results compare the performance before and after modulation recognition process. Indeed, the performance of D-STBC-CRN is investigated in terms of Bit Error Rate (BER) before modulation recognition and in terms of Probability of Correct Identification (PCI) after modulation recognition. These results show the effectiveness of our proposed method,

Key words: Modulation Classification (MC), Distributed Space-Time Block Coding (D-STBC), Cooperative Relaying Network (CRN), Random Forest Classifier (RFC), Adaptive Boosting (AdaBoost), Decision Trees (DT).

I. Introduction:
The promise of high spectral efficiency and capability of providing great capacity improvements in a wireless fading environment, as reported by [1], has led to widespread interest in multi-input multi-output (MIMO) communications [2]. However, the practical implementation of a MIMO scheme may be constrained by either the user's equipment size or the hardware complexity. To avoid such constraints, cooperative relaying network (CRN), has been introduced to reach MIMO capability in single-input single-output (SISO) communication [3], by sharing the antennas of multiple distributed transmitters or receivers to create virtual antenna arrays, provides the profits of the diversity gains and relay transmission without employing extra antennas [4].

There are two cooperation protocols that the relay node (R) can pursue, either amplify and forward (AF) or decode and forward (DF) [5]. The relays using amplify and forward (AF) protocol amplify the received signal and retransmit it to the destination node [5], [6]. Decode and forward (DF) schemes refer to cases where the relay explicitly decodes the massages transmitted by the source (S) and forwards the decoded version to destination (D), the decoding process makes the DF systems complex over AF systems [7], [3].

Creative Commons Attribution-NonCommercial-NoDerivatives 4.0 International License (CC BY-NC-ND)

The majority of the AF systems use D-STBC to achieve cooperative diversity because they maintain a reasonable complexity in one hand and they incurs rate loss in another hand [6]-[8].

Thereafter many research attentions have been focalized on D-STBC-CRN systems, where it has been demonstrated in [9] that cooperation using (D-STBC) represents an effective way to introduce spatial diversity in various wireless scenarios where it experiences fast channel variations and frequency selective channels. From this perspective, three fundamental techniques for D-STBC architecture have been count on : the first one request relaying on supplemental number of temporal channels to structure the D-STBC block [10], while the second technique depends on involving multiple antennas in the relay unit [11], whereas the last one entail the participation, of two or more relays [12].

However, seeking a higher number of relays, and/or of antennas at the relays level, might induce many problems because of the demand in terms of nodes, and the limitation on power and high order of complexity. Considering the previous cited research, authors in [13] have proposed a new D-STBC scheme to overcome energy and nodes problems, source and relay nodes are assumed supporting single antenna for each while the receiver (destination node) can support multiple antennas to guarantee a reliable detection.

Furthermore, perfect Channel State Information (CSI) is unavailable at S-R-D nodes in most practical cases. An imperfect CSI may occur because of errors introduced by channel estimation. Moreover, identification of communication parameters constitutes an intermediate step between modulation recognition and signal demodulation [14].

A basic assignment for an intelligent receiver is to identify the modulation in order to perform correctly the decoding of the received signal. Modulation classification (MC) was first encouraged by its applications in military domain, because of electronic struggles, surveillance and threat analysis that requires the recognition of signal modulations. After that, the interest in the civil domain continues to grow due to research developments in Cognitive Radio (CR) [15].

Two major categories of algorithms deals with MC problem namely Maximum-Likelihood (ML) and Feature-Based (FB) algorithms [16]-[17]. The FB methods are not optimal comparing to ML methods, but the lower computational complexity justifies their massive use in MC [15].

Choosing the appropriate features is critical in MC, thus several types of features extraction have been used in MC, e.g. wavelet transforms [18]-[19], Higher Order Moments (HOMs), Higher Order Cumulants (HOCs) and cyclostationarity [20].

Similarly, finding the suitable classification model is crucial. A good classifier can improve the overall recognition results, while a poor one will pull down the classification performance, particularly at low Signal to Noise Ratios (SNRs). Thus, to improve the performance of classifier we resort to the ensemble algorithm instead of single classifier [21]. These algorithms, such as bagging and boosting, have been revealed more significant advantages than single classifiers [22].

The aim of this paper is to evaluate the performance of two types of learning algorithms namely: single and ensemble learning. The ensemble-learning algorithm in turn is presented by two types of algorithms, bagging presented by Random Forest Classifier (RFC), and boosting presented by Adaptive Boosting (Adaboost), while the single learning is presented by Decision Trees (DT). The ensemble algorithms can improve the recognition results by combining a series of base learners (classifiers). Here, both ensemble-learning methods are based on Decision Tree for the comparison of performances.

The data set at the receiver is generated by adopting the D-STBC-CRN based AF protocol with single antenna at source and relay, and multiple antennas at destination node.

The reminder of this paper is organized as follow, in section 2, we introduce the system model, then we present in section 3 modulation classification method.

After that, we display and discuss the performance of the system, and we discuss the obtained

numerical results in section 4. Finally, we conclude in section 5.

Notations: the upper (lower) bold letters indicates matrix (column vector). $E(.)$,$(.)^{-1}$,$(.)^{T}$, $(.)^{*}$ and $(.)^{\mathcal{H}}$ denote expectation, inverse, transpose, conjugate and hermitian operations, respectively. $\mathbf{I}_U$ is an $(U \times U)$ identity matrix, and $\mathcal{CN}(0, \sigma^2)$ denotes zero mean white complex Gaussian (ZMWCG) with variance σ^2.

II. System model:

In this section, we present the mathematical model describing D-STBC cooperative relaying network (D-STBC-CRN) system. The CRN consists of source ($\mathcal{S}$), relay ($\mathcal{R}$) and destination ($\mathcal{D}$) nodes as shown in Fig.1. We suppose that both source and relay are equipped with single antenna, while $\mathcal{D}$ uses N_r antennas [13].

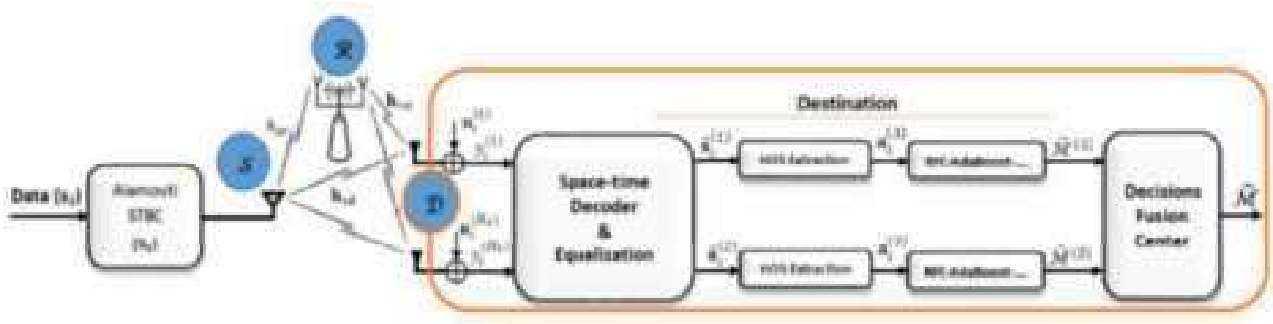

Fig1. D-STBC-CRN system model.

The source signal is transmitted in two time slots through two links, direct link from $\mathcal{S}$ to $\mathcal{D}$ and indirect link from $\mathcal{S}$ to $\mathcal{D}$ with the support of $\mathcal{R}$. For all links, we consider a flat quasi-static Rayleigh channel over a block of two symbol intervals, and a randomly varying channel for every block [9].

We consider the transmission of vectors of N_s data symbols, $\mathbf{s}_i = \left[s_{iN_s}, s_{iN_s+1}, \dots, s_{iN_s+N_s-1}\right]^T$ randomly and independently drawn from the pool of constellations $\Theta = \{\text{BPSK}, \text{8PSK}, \text{8PAM}, \text{16QAM}\}$.

The inputs data are mapped in space and in time by STBC encoder, $\mathcal{C}(\mathbf{s}_i)$, to obtain the $(N_t \times U)$ matrix $\mathbf{C}_{STBC} = \mathcal{C}(\mathbf{s}_i)$ defined by

$$\mathbf{C}_{STBC} = \left\{c_{iU+u}^{(n_t)}\right\}_{u\in\{0,\dots,U-1\}}^{n_t\in\{1,\dots,N_t\}} = \begin{bmatrix} c_{iU}^{(1)} & c_{iU+1}^{(1)} & \dots & c_{iU+U-1}^{(1)} \\ \vdots & \vdots & \dots & \vdots \\ c_{iU}^{(N_t)} & c_{iU+1}^{(N_t)} & \dots & c_{iU+U-1}^{(N_t)} \end{bmatrix} \quad (1)$$

where N_t and U are the number of transmitted antennas and the number of time slots used in $\mathcal{C}(\mathbf{s}_i)$ respectively.

For the number of inputs data symbols $N_s = 2$, $U = 2$ and $N_t = 2$, we obtain Alamouti based STBC encoder ($\mathbf{C}_{Al}$)

$$\mathbf{C}_{Al} = \begin{bmatrix} c_{2i}^{(1)} & c_{2i+1}^{(1)} \\ c_{2i}^{(2)} & c_{2i+1}^{(2)} \end{bmatrix} = \begin{bmatrix} s_{2i} & -s_{2i+1}^{*} \\ s_{2i+1} & s_{2i}^{*} \end{bmatrix} \quad (2)$$

Where the first row of matrix $\boldsymbol{C}_{Al}$ in (2), $\boldsymbol{c}_{2i}^{(1)} = [s_{2i}, \quad -s_{2i+1}^{*}]$, corresponds to the samples of the D-STBC signal transmitted from the $\mathcal{S}$ to $\mathcal{D}$ and to $\mathcal{R}$ during the first time interval, while the second row of $\boldsymbol{C}_{Al}$, $\boldsymbol{c}_{2i}^{(2)} = [s_{2i+1}, \quad s_{2i}^{*}]$, represents the vector generated artificially at $\mathcal{R}$ after applying proper

processing to the vector $\boldsymbol{c}_{2i}^{(1)}$. Indeed, we apply conjugation to s_{2i}, sign reversion and conjugation to $-s_{2i+1}^{*}$, followed by permutation between the positions of the resulting symbols to obtain the vector $\boldsymbol{c}_{2i}^{(2)}$. This vector will be amplified and forwarded (AF) from $\mathcal{R}$ during the second time interval to $\mathcal{D}$. The vectors $(\boldsymbol{c}_{2i}^{(1)}, \boldsymbol{c}_{2i}^{(2)})$ are concatenated at $\mathcal{D}$ in a manner to form the STBC matrix in (2).

A. D-STBC construction

During the first transmission step, the source broadcasts the first row vector $\mathbf{c}_{2i}^{(1)}$ with transmitted power P_s to destination and relay nodes. The received signal by the n_r-th antenna of the destination node, through direct link from $\mathcal{S}$, is given by

$$\mathbf{y}_{sd,i}^{(n_r)} = \left[y_{sd,2i}^{(n_r)}, y_{sd,2i+1}^{(n_r)}\right] \tag{3}$$

where

$$y_{sd,2i+u}^{(n_r)} = \sqrt{P_s}\, h_{sd,i}^{(n_r)} c_{2i+u}^{(1)} + \eta_{sd,2i+u}^{(n_r)} \tag{4}$$

with $u = 0, 1$, and $n_r = 1, \ldots, N_r$. For all links, we assume that the channel remains constant for a block of two symbols intervals and it is randomly varying from block to another [13]. With vector notation of (3), we obtain

$$\mathbf{y}_{sd,i}^{(n_r)} = \sqrt{P_s}\, h_{sd,i}^{(n_r)} \mathbf{c}_{2i}^{(1)} + \boldsymbol{\eta}_{sd,i}^{(n_r)} \tag{5}$$

The received signal at $\mathcal{R}$, through $\mathcal{S}$-$\mathcal{R}$ link, is given by:

$$\mathbf{y}_{sr,i} = \sqrt{P_s}\, h_{sr,i} \mathbf{c}_{2i}^{(1)} + \boldsymbol{\eta}_{sr,i} \tag{6}$$

Mentioning that channels $h_{sd,i}^{(n_r)}$ and $h_{sr,i}$ between $\mathcal{S}$ and $\mathcal{D}$, and between $\mathcal{S}$ and $\mathcal{R}$ respectively are $\mathcal{CN}(0,1)$. $\boldsymbol{\eta}_{sd,i}^{(n_r)} = \left[n_{sd,2i}^{(n_r)}, n_{sd,2i+1}^{(n_r)}\right]$ and $\boldsymbol{\eta}_{sr,i} = \left[\eta_{sr,2i}, \eta_{sr,2i+1}\right]$ are additive ZMWCG noises with $\mathcal{CN}(0, N_0)$ at $\mathcal{R}$ and $\mathcal{D}$ respectively.

During the second transmission step, the signal received by $\mathcal{R}$ is manipulated as previously explained, which leads to the received vector at $\mathcal{D}$ given by

$$\mathcal{A}_{f,i}\sqrt{P_r}\left[-\left(y_{sr,2i+1}\right)^{*}, \left(y_{sr,2i}\right)^{*}\right] \tag{7}$$

where P_r and $\mathcal{A}_{f,i} = \sqrt{P_s\left(P_s\left|h_{sr,i}\right|^2 + N_0\right)^{-1}}$ are a power and the amplification factors at $\mathcal{R}$ respectively. The received signal provided from $\mathcal{R}$ to $\mathcal{D}$, via the indirect link in vector form, is

$$\mathbf{y}_{srd,i}^{(n_r)} = h_{srd,i}^{(n_r)} \mathbf{c}_{2i}^{(2)} + \boldsymbol{\eta}_{srd,i}^{(n_r)} \tag{8}$$

Where the equivalent channel $h_{srd,i}^{(n_r)}$ is defined by

$$h_{srd,i}^{(n_r)} = \mathcal{A}_{f,i}\sqrt{P_s P_r}\, h_{sr,i}^{*}\, h_{rd,i}^{(n_r)} \tag{9}$$

and

$$\boldsymbol{\eta}_{srd,i}^{(n_r)} = h_{rd,i}^{(n_r)} \boldsymbol{\eta}_{sr,i}^{*} + \boldsymbol{\eta}_{rd,i}^{(n_r)} \tag{10}$$

The received signal by N_r antennas of the destination node $\mathcal{D}$ results from the superposition of signals sent through direct and indirect links as follow

$$\mathbf{y}_i = \mathbf{H}_i \mathbf{s}_i + \boldsymbol{\eta}_i \tag{11}$$

where the equivalent channel matrix $\mathbf{H}_i$ is defined by

$$\mathbf{H}_i = \begin{bmatrix} \sqrt{P_s} h_{sd,i}^{(1)} & \mathcal{A}_{f,i} \sqrt{P_s P_r} h_{sr,i}^{*} h_{rd,i}^{(1)} \\ \mathcal{A}_{f,i} \sqrt{P_s P_r} h_{sr,i} \left(h_{rd,i}^{(1)}\right)^{*} & -\sqrt{P_s} \left(h_{sd,i}^{(1)}\right)^{*} \\ \vdots & \vdots \\ \sqrt{P_s} h_{sd,i}^{(N_r)} & \mathcal{A}_{f,i} \sqrt{P_s P_r} h_{sr,i}^{*} h_{rd,i}^{(N_r)} \\ \mathcal{A}_{f,i} \sqrt{P_s P_r} h_{sr,i} \left(h_{rd,i}^{(N_r)}\right)^{*} & -\sqrt{P_s} \left(h_{sd,i}^{(N_r)}\right)^{*} \end{bmatrix} \tag{12}$$

Since $\mathbf{H}_i$ is complex and orthogonal we have

$$\mathbf{H}_i^{\mathcal{H}} \mathbf{H}_i = \left(\sum_{n_r=1}^{N_r} P_s \left| h_{sd,i}^{(n_r)} \right|^2 + \mathcal{A}_{f,i}^2 P_s P_r \left| h_{sr,i} \right|^2 \left| h_{rd,i}^{(n_r)} \right|^2 \right) \mathbf{I}_{N_s} \tag{13}$$

For signal recovery, Zero-Forcing (ZF) equalization matrix $\mathbf{G}_i$ is applied to the received signal as follow

$$\hat{\mathbf{s}}_i = \mathbf{G}_i \mathbf{y}_i \tag{14}$$

where $\mathbf{G}_i$ is defined by $\mathbf{G}_i = \left(\mathbf{H}_i^{\mathcal{H}} \mathbf{H}_i\right)^{-1} \mathbf{H}_i^{\mathcal{H}}$.

III. Modulation classification process:

A. Feature extraction

In order to identify the modulation type and order, modulation recognition process is divided in two steps, namely the feature extraction and the pattern recognition. Previous works [15], [24], have shown that higher order cumulants (HOC) and higher order moments (HOM) of the received signal are one of the best candidates for signal identification, since they present the most appropriate tradeoff between computational simplicity and achieved performance.

In this work, the features employed consists of a combination of HOM up to eight order and HOC up to fourth order which is quite enough for modulation classification. For each block, the p-th order HOM, of the recovered signal is calculated using

$$\mu_{pq}(\hat{s}) = E[\hat{s}^{p-q} (\hat{s}^{*})^{q}] \tag{15}$$

While the p-th order HOC of the zero-mean signal $\hat{s}$ is defined by

$$\kappa_{pq}(\hat{s}) = Cum[\underbrace{\hat{s}, \dots, \hat{s}}_{p-q\ times}, \underbrace{\hat{s}^{*}, \dots, \hat{s}^{*}}_{q times}] \tag{16}$$

On the other hand, to reduce the receiver power's impact and the scale issue the normalized version is adopted:

$$\tilde{\kappa}_{pq}(\hat{s}) = {\kappa_{pq}(\hat{s})}\Big/{\kappa_{21}(\hat{s})^{p/2}} \tag{17}$$

Then, we use the normalized-cumulants-based vector

$$\tilde{\boldsymbol{\kappa}} = [|\tilde{\kappa}_{40}|, |\tilde{\kappa}_{41}|, |\tilde{\kappa}_{42}|, |\tilde{\kappa}_{60}|, |\tilde{\kappa}_{61}|, |\tilde{\kappa}_{62}|] \tag{18}$$

After that, we use the Principal Component Analysis (PCA). This allow us to select the optimal subset of high order statistics (HOS) to improve the identification process [15].

B. Classification tools

MC can be regarded as an important branch of pattern recognition, a lot of results have been reported in a range of opened literature to recognize the modulation type of transmitted signal. In our work a study is done to compare between single and ensemble learning algorithms. With single learning algorithm the classifier is composed of one individual algorithm, while ensemble learning algorithm is a form of hybrid learning method for which we combine multiple weak classifiers intelligently to build a strong one.

The definition of strong and weak learning depends on the probability of false identification, if it is slightly less than 0.5, which means that the accuracy rate is just only better than random guessing, the algorithm can be considered as a weak learner [21].

Recently, the application of boosting and bagging algorithms where both are categorised under the ensemble learning, has become popular among various classifiers owing to their superiority in avoiding overfitting and high probability of classification in high-dimensional space [22].

Next we define the frame work of each algorithm used in our study, thus training data set $\mathfrak{D}_s = \{(\mathbf{a}_1, N_1), (\mathbf{a}_2, N_2), \ldots, (\mathbf{a}_{n_{tot}}, N_{n_{tot}})\}$, with n_{tot} instances, is the total number of realisations for the candidate pool Θ, and $\mathbf{a_i} = [\mu_{p_1q_1}, \kappa_{p_1q_1}, \ldots, \mu_{p_\mathcal{T}q_\mathcal{T}}, \kappa_{p_\mathcal{T}q_\mathcal{T}}]$is an $\mathcal{T}$ -dimensional input feature vector, and $N_i \in \{1, \ldots, \mathrm{card}(\Theta)\}$ is the class identity label associated with $\mathbf{a_i}$ with $\mathrm{card}(\Theta)$ is the cardinal of Θ.

B.1. Decision tree

It's a form of single learning algorithm, DT creates a model based on a tree structure [24]. In the tree, nodes and branches belongs to features and possible values connecting features, respectively. Each leaf is assigned to one class representing the most appropriate target value. A leaf terminates a set of nodes and branches. Thus, tracing the path of nodes and branches to the terminating leaf leads to determine the class of an instance.

Input:	$\mathfrak{D}_s$: set of classified instances.
	Repeat
	maxGain ← 0
	$E(\mathfrak{D}_s)$ ← Entropy (Attributes)
	for all Attributes a_i in $\mathfrak{D}_s$ do
	gain ← InformationGain ($\mathfrak{D}_s$, $E(\mathfrak{D}_s)$)
	if gain >maxGain **then**
	maxGain ← gain
	end if

end for **Update** $\mathfrak{D}_s$ **until** All partitions processed
Table 1. Decision trees algorithm.

B.2. Random forest classifier

In Random Forest Classifier (RFC), each member of the ensemble is constructed from a different training dataset, and the predictions are combined by voting over the class labels [22], [25].

Each dataset d_t is generated by sampling from the n_{tot} data $\mathfrak{D}_s$, choosing n_{tot} items uniformly at random with replacement. Each sample is known as a bootstrap.

For each features vector $\mathbf{a}_i$, the structure of classification based on the random forest is established by the following fundamental steps:

Input: $\mathfrak{D}_s$: set of classified instances.

- A base learning algorithm: WeakLearn;
- Integer T specifying ensemble size after Bootstrap.
For $t = 1,\ldots,T$ **do**
- Obtain Bootstrap sample d_t by randomly drawing n_{tot} instances, with replacement, from the original training set $\mathfrak{D}_s$.
- Call WeakLearn based on d_t to develop hypothesis H_t.
end for

Testing stage: Use the majority voting method to combine the output of T hypotheses $\{H_1,\ldots,H_T\}$ to predict the final class label for each testing instance.
Table 2. RFC algorithm (Bagging).

B.3. Adaboost classifier

Adaboost is designed to boost weak learners, in our case DT, into a strong one to reach the highest degree of accuracy that can be achieved [14].

A certain members of learner are trained sequentially, with a new learner at each round. At the end of each round, misclassified examples are identified and emphasised in a new training set, which is then fed back into the start of the next round, and a new learner (DT) is trained. Training DTs sequentially should be able to compensate for errors made by former learner [22].

Input:	- $\mathfrak{D}_s$: set of classified instances where $N_i \epsilon \{-1,+1\}$. - Required ensemble size T.
	- Define a uniform distribution $d_1(i)$ over elements of $\mathfrak{D}_s$. **For** $t = 1,\ldots,T$ **do** 1) Train a model H_t using distribution d_t; 2) Calculate $\epsilon_t = P_{d_t}(H_t(\mathrm{a}_i) = N_i)$ If $\epsilon_t \geq 0.5$ break

3) Set $\alpha_t = \frac{1}{2}\ln\left(\frac{1-\epsilon_t}{\epsilon_t}\right)$

4) Update

$d_{t+1}(i) = \frac{d_t(i)\exp(-\alpha_t N_i H_t(\mathrm{a}_i))}{Z_t}$

where Z_t is a normalization factor so that d_{t+1} is a valid distribution.

end for

5) For a new testing point $(\mathrm{a}'_i; N'_i)$,

$$H(\mathrm{a}'_i) = \mathrm{sign}\left(\sum_{t=1}^{T} \alpha_t H_t(\mathrm{a}'_i)\right)$$

Table 3. Adaboost Algorithm (Boosting).

IV. Numerical results and discussions:

To assess the performance of D-STBC-CRN, Monte-Carlo simulations in term of bit error rate (BER) and probability of correct identification (PCI) are conducted.

Aiming to discuss the impact of number of antennas N_r at $\mathcal{D}$-node and channel estimation errors on the accuracy of classifiers many scenarios are considered.

A flat quasi-static Rayleigh channel is considered. We assume that the channel remains constant for a block of two symbols intervals and it is randomly varying for every block [13].

In Fig.2, 1000 Monte Carlo trials (MCT) are used to calculate BER. Also 1000 are applied for each modulation scheme, i.e. 4000 iterations in total for Θ in Fig.3 and Fig.4.

The SNR at the $\mathcal{D}$-node antennas is defined by: $\mathrm{SNR_{dB}} = 10\log_{10}\left(\frac{\sigma_s^2}{\sigma_\eta^2}\|\mathbf{H}_i\|_F^2\right)$ [6], where σ_s^2 is the average power of the samples of the transmitted signal on each antenna, σ_η^2 is the noise power, and $\|\mathbf{H}_i\|_F^2$ is the Frobenius norm of the channel matrix [6].

All results are based on transmission of $N = 512$ D-STBC symbols. Target modulation pool is $\Theta = \{\mathrm{BPSK}, \mathrm{8PSK}, \mathrm{8PAM}, \mathrm{16QAM}\}$.

Fig.2 show simulation results acquired by 1×2 antennas configuration for different modulation types and order, one can see that the constellation size M affects the system's performance. It is clear that transition from a high value of M to a low value of M leads to performance improvement. High value of M increases spectrum efficiency, but easily affected by the noise.

Fig.3 shows the effect of the number of received antennas N_r on classification process. It is obvious that all classifiers showed stable results. We can observe that $\mathrm{P_{ci}}$ improves as the SNR values increase and as the number of received antennas N_r increases. RFC presents the best performance regardless of the evaluation measures. For all classifiers, low accuracies of $\mathrm{P_{ci}}$ are observed for 1×1 configuration, while we remark an enhancement in $\mathrm{P_{ci}}$ accuracies for 1×2 and 1×3 antenna configurations. For $N_r = 1$ and $\mathrm{SNR} < 15\mathrm{dB}$, RFC presents the best performance followed by AdaBoost and then DT till they reach 100% $\mathrm{P_{ci}}$ at $\mathrm{SNR} \geq 15\mathrm{dB}$. For $N_r = 2$ and $\mathrm{SNR} < 5\mathrm{dB}$ the classification accuracies of RFC and AdaBoost displayed rather similar performances, where DT presents lower performance then the rest, and all of them reach 100% $\mathrm{P_{ci}}$ at $\mathrm{SNR} \geq 5\mathrm{dB}$. Where for 1×3 antenna configuration at $\mathrm{SNR} \leq 5\mathrm{dB}$ both AdaBoost and DT are headed by RFC, while AdaBoost starts better then DT and they coincide as the SNR increases till all three of them reach 100% $\mathrm{P_{ci}}$ at $\mathrm{SNR} \geq 5\mathrm{dB}$.

Furthermore, one can see from Fig.4 that as the channel estimation error increases the $\mathrm{P_{ci}}$ of all classifiers decreases. Adaboost presents the highest robustness against the channel estimation errors, maintaining it's superiority among them, where DT is the most sensitive to channel estimation errors.

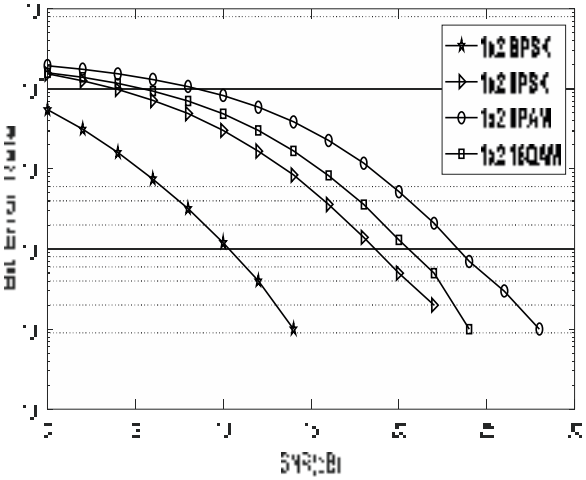

Fig2. BER versus SNR for D-STBC-CRN for 2-PSK, 8-PSK, 8-PAM and 16-QAM, for $N_r = 2$.

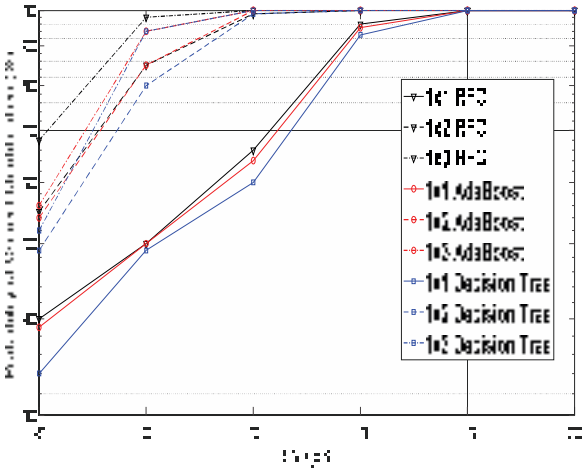

Fig3. P_{ci} versus SNR for RFC, AdaBoost and DT classifiers using D-STBC-CRN for $N_r = 1, 2$, and 3.

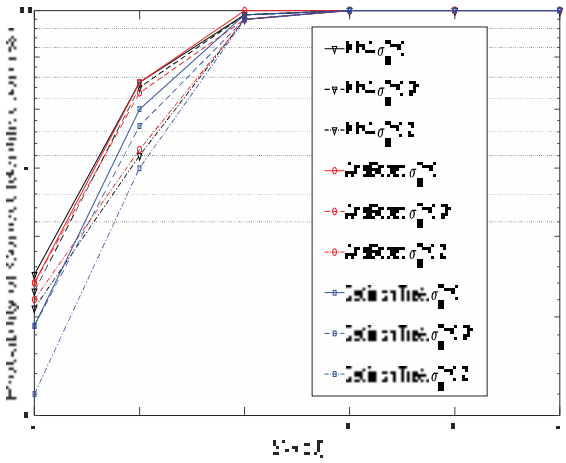

Fig4. P_{ci} versus SNR for RFC, AdaBoost and DT classifiers using D-STBC-CRN for $\sigma_e^2 = 0$, 0.01, and 0.2 for $N_r = 2$.

Conclusion:

In this paper, we have considered the problem of modulation classification for D-STBC-CRN system. Modulation classification is carried out by comparison between three classifiers, DT which is a single learning classifier and two ensemble learning classifiers, namely RFC that joins the Bagging algorithms, and AdaBoost that is associated with the Boosting Algorithms.

In this context, we introduced the comparison while changing in the number of antennas at destination node to guarantee the reliability in our study and maintain the consistency of classifiers. The simulation results showed the superiority of RFC classifier to discriminate among different modulation type and order in perfect CSI where the Adaboost presents the highest robustness to channel estimation errors, which prove that ensemble learning presents higher performance comparing to single learning.

References:

[1] **B. K. Chalise and L. Vandendorpe** (2008), "Outage probability analysis of a MIMO relay channel with orthogonal space-time block codes," IEEE Communications Letters, **12(4)**: 280–282.

[2] **D. Heedong, L . Namyoon and L .Angel** (June 2020), "Capacity of Line-of-Sight MIMO Channels," 2020 IEEE International Symposium on Information Theory (ISIT), USA.

[3] **C. Karunya,T. Aloob *et al***. (Oct. 2017), "A New Amplify and Forward Relay Based OFDMCooperative Communication System," Twenty-third National Conference on Communications (NCC), India.

[4] **T. Lin, , F. Hwang** (Nov. 2018), "Analysis and design of joint CFO/channel estimate techniques for a cooperative STBC-OFDM system," International Journal of Communication System.

[5] **C. Hucher, G. Rekaya, and J.-C. Belfiore** (), "AF and DF protocols based on Alamouti ST Code," IEEE International Symposium Information Theory, pp. 1526–1530, 2007.

[6] **Erik G. Larsson, Petre Stoica** (2003), "Space-Time Block Coding for Wireless Communications," Cambridge University Press.

[7] **G.Ryu, D.Jang, U.Jeong and K.Ko** (2018), "BER Performance Analysis of Orthogonal Space-Time Block Codes in Cooperative MIMO DF Relaying Networks," IEEE International Conference on Communications.

[8] **A. Abdaoui, S. S.Ikki, M. H. Ahmed** (2010), "Performance Analysis of MIMO Cooperative Relaying System Based on Alamouti STBC and Amplify-and-Forward Schemes," IEEE International Conference on Communications.

[9] **A. H. M. Almawgani, M. Alsamawi, W. H. Al-Arashi** (2017), "An Outage Probability in Cooperative MIMO under (Alamouti, Orthogonal and Quasi Orthogonal STBC) Slow Fading Channel," Wireless Pers Commun, **97**: 5277–5287.

[10] **L. Krikidis, H. A. Suraweera** (2013), "Full-Duplex Cooperative Diversity with Alamouti Space-Time Code," IEEE Wireless Communications Letters, **2**: 519 – 522.

[11] **Yunida, Nasaruddin, R.Muharar, Y.Away** (2018), "Implementation of the Alamouti STBC for Multi-Pair Two-Way Wireless Networks with Amplify-and-Forward MIMO Relaying," IEEE International Conference on Information Technology Systems and Innovation.

[12] **M. A. I. Astal, and A. Abu-Hudrouss** (2011), "SIC detector for 4 relay distributed space-time block coding under quasi-synchronization," IEEE Communication Letter, **15(10)**: 1056–1058.

[13] **H. Tayakout, I. Dayoub, K. Ghanem, H. Bousbia-Salah** (2018), "Automatic Modulation Classification for D-STBC Cooperative Relaying Networks," IEEE Communications Letter, **7**: 780-783.

[14] **T. Liu, Y. Guan, Y. Lin** (Nov. 2017), "Research on modulation recognition with ensemble learning," EURASIP Journal on Wireless Communication and Networking, **179**.

[15] **S. Kharbech, I. Dayoub; M. Z. Colin and E. P. Simon** (2016), "On classifiers for blind feature-based automatic modulation classification over multiple-input–multiple-output channels," IET Commun, **10(7)**.

[16] **D. Zhu, V. J. Mathews, D. H. Detienne** (2018), "A Likelihood-Based Algorithm for Blind Identification of QAM and PSK Signals," IEEE Transactions on Wireless Communications, **17**: 3417-3430.

[17] **A. Swami, B. Sadler** (2000), "Hierarchical digital modulation classification using cumulants," IEEE Trans. Commun, **48**: 416-429.

[18] **P. Cheol-Sun, C. Jun-Ho, N. Sun-Phil, *et al.*** (), "Automatic modulation recognition of digital signals using wavelet features and SVM," Proc. 10th ICACT, Phoenix Park, Korea, February 2008, vol. 1, pp. 387–390.

[19] **D. Boutte, B. Santhanam** (2009), "A hybrid ICA-SVM approach to continuous phase modulation recognition," IEEE Signal Process. Lett, **16(5)**: 402–405.

[20] **G. Mingjun, L.Yongzhao, O.A.Dobre, *et al.*** (2018), "Blind identification of SFBC-OFDM signals using subspace decompositions and random matrix theory," IEEE Trans. Veh. Technol., **67(10)**: 9619 - 9630.

[21] **L. Tong, G. Yanan and L. Yun** (2017), "Research on modulation recognition with ensemble learning," EURASIP Journal on Wireless Communications and Networking.

[22] **C. Sammut and G. I. Webb** (2010), "Encyclopedia of Machine Learning," Eds., Springer Press, 393-401.

[23] **L. B. Marinho, N. M. M. Nascimento, J. W. M. Souza, *et al.*** (2019), "A novel electrocardiogram feature extraction approach for cardiac arrhythmia classification," Future Gener. Comput. Syst, **97**: 564-577.

[24] **W. Ben Chikha, I. Dayoub, *et al.*** (Feb. 2014), "Modulation Recognition for MIMO Relaying Broadcast Channels with Direct Link," IEEE Wireless Communications Letters, **3**: 50-53, ,

[25] **K. Triantafyllakis, M. Surligas, G. Vardakis** (March 2017), "Phasma: An automatic modulation classification system based on Random Forest," IEEE International Symposium on Dynamic Spectrum Access Networks (DySPAN), Piscataway, NJ, USA.

Algerian Journal of Engineering Architecture and Urbanism Vol. 5 Nr. 3 2021
ISSN: 2588-1760

CONTROL OF ASYMMETRICAL MULTILEVEL INVERTER BY PWM WITH SELECTIVE HARMONIC ELIMINATION FOR PV APPLICATIONS

Rachid TALEB
Prof. Electrical Engineering Department, Hassiba Benbouali University, Chlef, Algeria
Laboratoire Génie Electrique et Energies Renouvelables (LGEER)
rac.taleb@gmail.com

Taieb BESSAAD
Dr. Electrical Engineering Department, Hassiba Benbouali University, Chlef, Algeria
Laboratoire Génie Electrique et Energies Renouvelables (LGEER)
t.bessaad@univ-chlef.dz

Mohamed MOSTEFAOUI
Dr. Electrical Engineering Department, Hassiba Benbouali University, Chlef, Algeria
Laboratoire Génie Electrique et Energies Renouvelables (LGEER)
m.mostefaoui@univ-chlef.dz

Maamar SOUAIHIA
Dr. Electrical Engineering Department, Hassiba Benbouali University, Chlef, Algeria
Laboratoire Génie Electrique et Energies Renouvelables (LGEER)
m.souaihia@univ-chlef.dz

Abstract :
In order to improve the efficiency of the photovoltaic (PV) system, in other words, to maximize the power delivered to the load connected to the terminals of the photovoltaic generator, several optimization means have been applied, and techniques followed to obtain a good adaptation and a high efficiency. Among these means, improving the quality of the output voltage of the inverter through the use of multilevel inverters. The structures based on multilevel inverters have brought an undeniable advantage to AC-DC conversion, especially in high power applications. This paper presents the control of an eleven-level asymmetrical inverter with uniform step by the harmonic elimination strategy, dedicated to photovoltaic (PV) applications. This inverter is associated with a three-phase induction machine. The performance of the harmonic elimination strategy is analyzed on the basis of a comparison with the triangular-sinusoidal strategy.

Keywords: Photovoltaic system, asymmetrical multilevel inverter, selective harmonic elimination, PWM, Three-phase induction machine.

Introduction :

Depuis plus de dix ans, le marché mondial des systèmes photovoltaïques connaît un taux de croissance très élevé, de l'ordre de 30% à 40% par an, dû en particulier aux installations raccordées au réseau électrique de distribution (Prajapat, Katariya, Kumar, & Shukla, 2011). Cette croissance exceptionnelle passe nécessairement par des innovations

Creative Commons Attribution-NonCommercial-NoDerivatives 4.0 International License (CC BY-NC-ND)

technologiques et une baisse des coûts des modules photovoltaïques, mais également par des efforts significatifs de recherche et de développement, notamment dans le domaine de l'électronique de puissance.

Les performances techniques et la robustesse des onduleurs utilisés pour le raccordement des modules photovoltaïques au réseau de distribution d'électricité sont des éléments-clés qui peuvent fortement impacter la production d'énergie électrique et par conséquent, la rentabilité financière d'un système (Prajapat et al., 2011).

Les interrupteurs de puissance des onduleurs peuvent être soumis à de fortes contraintes en tension. Ces composants doivent en particulier être en mesure de bloquer la pleine tension imposée par le bus continu de la chaîne photovoltaïque. La répétition de ces contraintes peut conduire à la limitation de l'endurance du convertisseur.

Cet article porte sur l'étude des convertisseurs multiniveaux triphasés dont la topologie est basée sur la mise en série de plusieurs onduleurs monophasés (cellules partielles) sur la même phase. La Fig. 1 montre un convertisseur avec k onduleurs partiels en série. Chaque cellule partielle de rang *j*, (*j = 1…k*) est alimentée par une tension continue u_{dj}. Elle montre qu'en alimentant les cellules partielles par des tensions continues de valeurs différentes (alimentation asymétrique), il est possible d'augmenter le nombre de niveaux à la sortie du convertisseur, sans complexité supplémentaire de sa structure (Rodriguez et al., 2009; Rodriguez, Lai, & Peng, 2002). Ces onduleurs sont connus sous le nom d'onduleurs multiniveaux asymétriques.

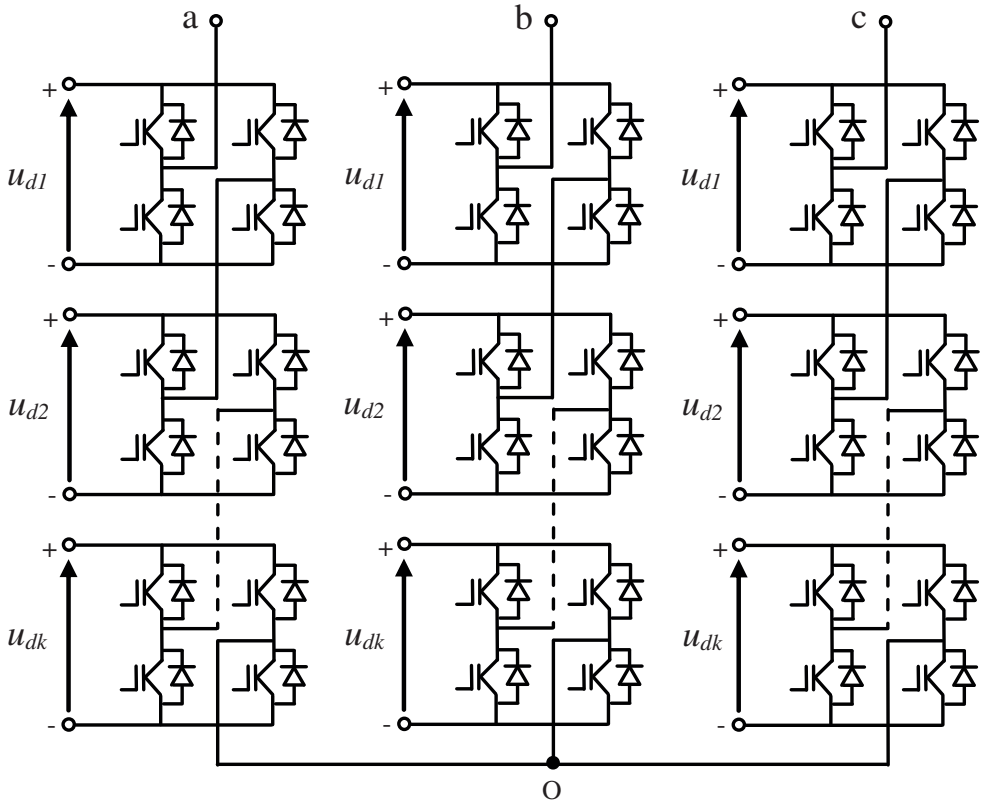

Fig. 1. Mise en série de k onduleurs partiels monophasés par phase

Creative Commons Attribution-NonCommercial-NoDerivatives 4.0 International License (CC BY-NC-ND)

Algerian Journal of Engineering Architecture and Urbanism Vol. 5 Nr. 3 2021
ISSN: 2588-1760

Certaines applications nécessitent des performances de hauts niveaux mais la présence des harmoniques d'ordre peu élevé dans le signal de tension peut dégrader ces performances. Afin d'améliorer la qualité du signal de sortie de l'onduleur multiniveau asymétrique, différentes stratégies de modulation de largeurs d'impulsions ont été proposées par différents auteurs (Mariéthoz, 2005; Song Manguelle, 2004). La plus connue est la stratégie triangulo-sinusoïdale (Mariéthoz, 2005; Song Manguelle, 2004). Elle pousse les harmoniques vers les fréquences élevées, en ayant recours à des porteuses de hautes fréquences.

Cependant, pour les applications de puissance électrique élevée, les composants électroniques sont limités en fréquence de commutation ce qui limite à son tour la fréquence de la porteuse. On peut remédier à ce problème en appliquant la méthode d'élimination d'harmoniques adaptées au cas des onduleurs multiniveaux asymétriques. Cette technique permet d'annuler les harmoniques les plus gênantes et de réguler la composante fondamentale du signal avec l'avantage majeur d'une faible fréquence de commutation des composants électroniques.

Dans cette étude nous allons comparer la stratégie triangulo-sinusoïdale et la stratégie d'élimination d'harmoniques appliquées à la commande d'un onduleur asymétrique à onze niveaux à pas uniforme. De même, sont comparées les performances relatives à l'associative onduleur-MAS pour ces deux stratégies de commandes en MLI. Les résultats obtenus sont très promoteurs dans le domaine de forte puissance et/ou haute tension en particulier pour la traction électrique.

Onduleur multiniveau asymétrique à pas uniforme

La Fig. 2, montre la forme de la tension généralement obtenue à la sortie d'un convertisseur multiniveau. Les valeurs u_{S1}, u_{S2}, …u_{SN} correspondent aux niveaux N possibles de u_S. Le convertisseur est dit à pas uniforme ou régulier si la différence entre deux niveaux consécutifs est constante (relation 1) (Mariéthoz, 2005; Song Manguelle, 2004). Dans le cas contraire, le convertisseur est dit à pas non uniforme ou irrégulier

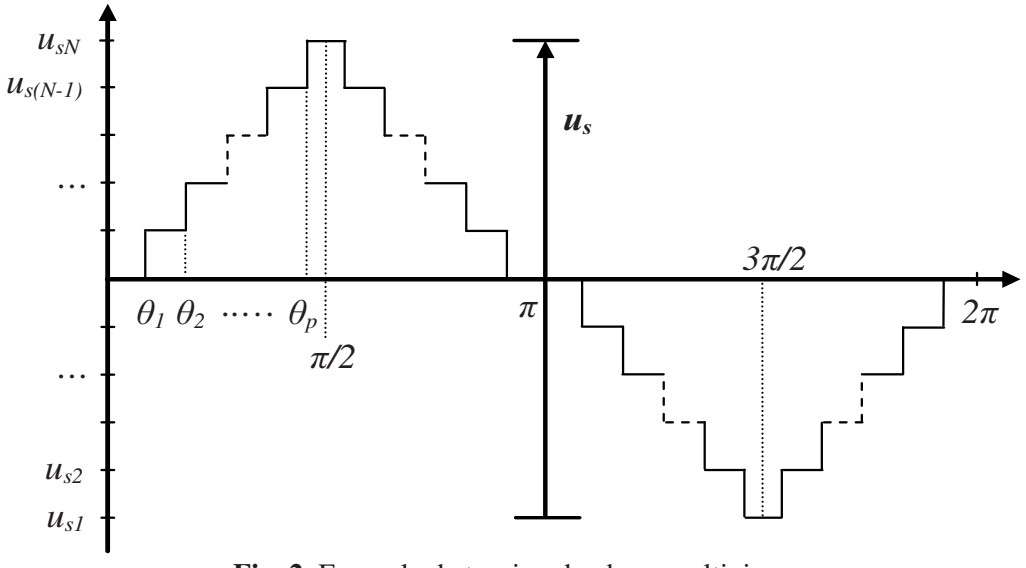

Fig. 2. Exemple de tension de phase multiniveau

Creative Commons Attribution-NonCommercial-NoDerivatives 4.0 International License (CC BY-NC-ND)

Algerian Journal of Engineering Architecture and Urbanism Vol. 5 Nr. 3 2021
ISSN: 2588-1760

$$u_{d1} = \Delta u = u_{s2} - u_{s1} = u_{s3} - u_{s2} = \ldots = u_{sN} - u_{s(N-1)} \quad (1)$$

Pour obtenir un onduleur multiniveaux asymétrique à pas uniforme ou régulier (Uniform Step Asymmetrical Multilevel Inverter : USAMI), les tensions continues d'alimentation des cellules partielles udj ($j = 1...k$) doivent respecter les deux conditions suivantes (Mariéthoz, 2005; Song Manguelle, 2004) :

$$\begin{cases} u_{d1} \le u_{d2} \le \ldots \le u_{dk} \\ u_{dj} \le 1 + 2\sum_{l=1}^{j-1} u_{dl} \end{cases} \quad (2)$$

Le nombre de niveaux pour un groupe de tensions donné, s'obtient à partir de la relation suivante (Mariéthoz, 2005; Song Manguelle, 2004) :

$$N = 1 + 2\sum_{j=1}^{k} u_{dj} \quad (3)$$

La relation donnée par (3) accepte des solutions différentes. Avec $k = 3$, il existe 2 possibilités d'alimentation des onduleurs partiels pour obtenir une tension de 11 niveaux à la sortie du convertisseur, c'est à dire $(u_{d1}, u_{d2}, u_{d3}) \in \{(1, 1, 3), (1, 2, 2)\}$, et 3 possibilités pour obtenir 15 niveaux, c'est à dire $(u_{d1}, u_{d2}, u_{d3}) \in \{(1, 1, 5), (1, 2, 4), (1, 3, 3)\}$. La Fig. 3, représente les différentes possibilités de commutation de trois cellules partielles mises en série sur une phase d'un onduleur asymétrique à 11 niveaux.

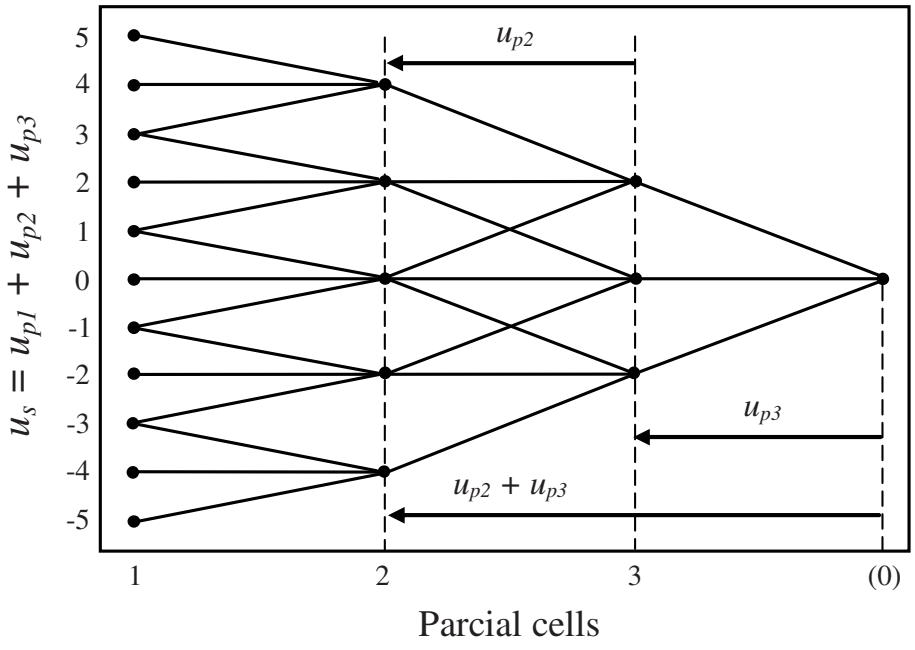

Fig. 3. Possibilités de commutations des 3 cellules partielles d'un USAMI-11 niveaux (k = 3, $u_{d1} = 1$, $u_{d2} = 2$, $u_{d3} = 2$)

Creative Commons Attribution-NonCommercial-NoDerivatives 4.0 International License (CC BY-NC-ND)

La première cellule est alimentée par la tension u_{d1} = 1, la deuxième cellule par u_{d2} = 2 et la troisième par u_{d3} = 2. Chaque cellule ne peut générer qu'au plus trois valeurs : $u_{p1} \in \{-1, 0, 1\}$, $u_{p2} \in \{-2, 0, 2\}$ et $u_{p3} \in \{-2, 0, 2\}$. Il en résulte une tension de phase ayant onze valeurs différentes, $u_s \in \{-5, -4, -3, -2, -1, 0, 1, 2, 3, 4, 5\}$. La génération de certains niveaux de tension peut se faire avec plus d'une séquence de commutation sur les différentes cellules partielles. Par exemple, on voit qu'il est possible de générer la tension us = 3 avec les trois combinaisons suivantes : $(u_{p1}, u_{p2}, u_{p3}) \in \{(-1, 2, 2), (1, 0, 2), (1, 2, 0)\}$. Ces états redondants peuvent être exploités pour l'optimisation des commutations sur le convertisseur.

La possibilité de choisir des tensions intermédiaires différentes les unes des autres, et la possibilité de redondance dans ces choix, sont autant de degrés de liberté qu'offrent les convertisseurs multiniveaux asymétriques à l'utilisateur.

Stratégies de commande

Afin de générer une source de tension la plus sinusoïdale possible, différentes stratégies de commande ont été publiées pour les convertisseurs multiniveaux symétriques. On y retrouve principalement la modulation par gradins (Song Manguelle, 2004), et la modulation par largeur d'impulsions (MLI) (Mariéthoz, 2005; Song Manguelle, 2004).

Dans le cas des convertisseurs multiniveaux asymétriques, les différentes stratégies de modulations existantes peuvent également être utilisées. Dans cette section, nous présentons la stratégie triangulo-sinusoïdale (Sinusoidal Pulse Width Modulation : SPWM) ainsi que la stratégie d'élimination d'harmoniques (Selective Harmonic Elimination Pulse Width Modulation : SHEPWM).

Pour comparer les deux stratégies de commande, nous avons procédé à une étude qualitative par simulation à l'aide du logiciel MATLAB. Il s'agit de générer les signaux de commande des interrupteurs constituant le convertisseur (onduleur asymétrique à onze niveaux à pas uniforme) alimentant la machine asynchrone à entraîner.

A- Stratégie triangulo-sinusoïdale

Pour commander un convertisseur à N niveaux de tension, N-1 porteuses triangulaires unipolaires sont générées. Les signaux triangulaires ont la même fréquence f_p et la même amplitude $A_p = 2/(N-1)$. En plus, ils sont en phase et occupent une bande continue, avec un décalage vertical $\Delta_p = 2/(N-1)$. Celles-ci sont ensuite comparées à un système triphasé de référence d'amplitude Ar et de fréquence f_r. Chaque comparaison donne 1 si une porteuse est supérieure ou égale à une référence, et 0 dans le cas contraire. A la sortie du modulateur la somme des résultats issus des comparaisons donne la valeur de la tension de phase correspondant à chaque niveau. Deux paramètres caractérisent cette stratégie, indice de modulation m et taux de modulation *r* (Lund, 2005) :

$$m = \frac{f_c}{f_r} \tag{4}$$

Creative Commons Attribution-NonCommercial-NoDerivatives 4.0 International License (CC BY-NC-ND)

$$r = \frac{2}{N-1}\frac{A_r}{A_c} \tag{5}$$

Les tensions individuelles à la sortie de chaque onduleur monophasé (u_{p1}, u_{p2} *et* u_{p3}) et la tension simple de la phase a, ainsi que la tension composée et leur spectre sont donnés par les Figs. 4 et 5.

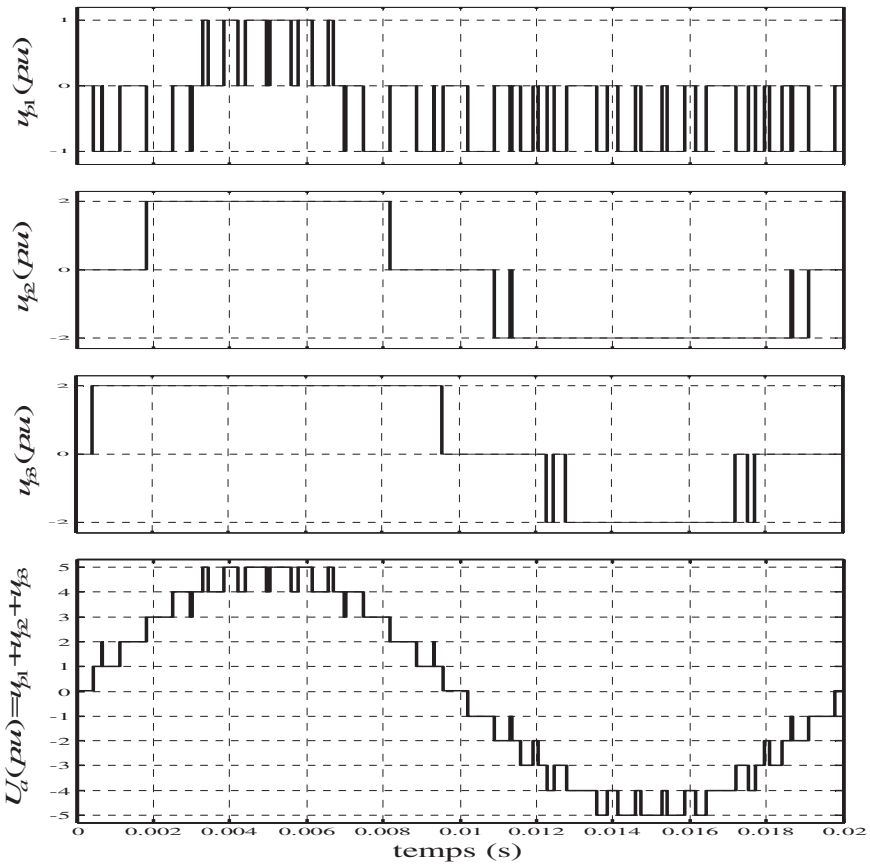

Fig. 4. Tensions partielles et tension de phase d'un USAMI-11 niveaux commandé par SPWM (r = 0.965, m = 30)

Les performances de la MAS alimentée par l'onduleur asymétrique à onze niveaux à pas uniforme commandé par la stratégie triangulo-sinusoïdale sont présentés par la Fig. 6. Les paramètres de la machine sont donnés en annexe.

Creative Commons Attribution-NonCommercial-NoDerivatives 4.0 International License (CC BY-NC-ND)

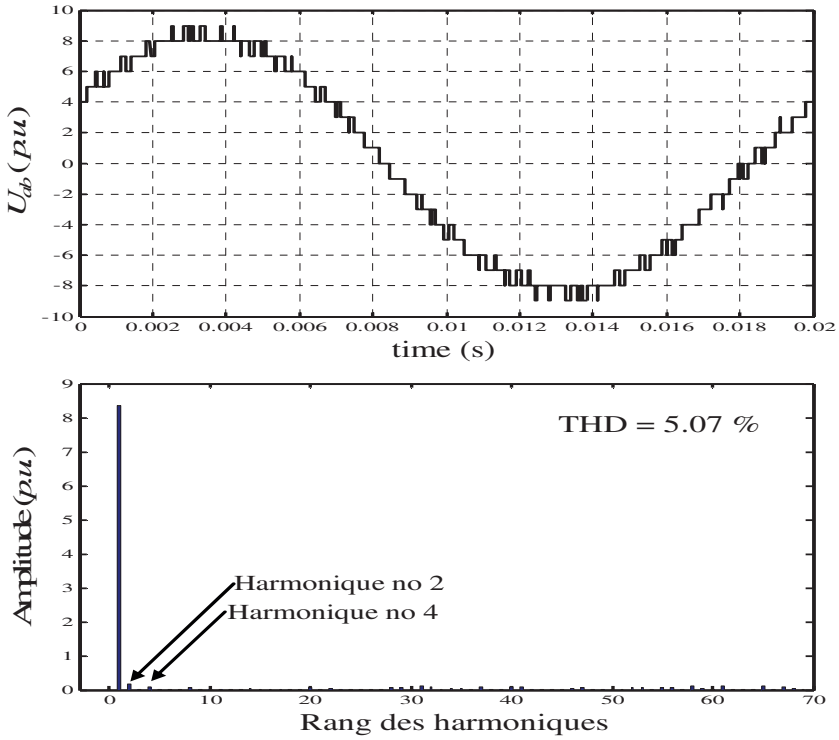

Fig. 5. Tension composée U_{ab} et son spectre d'harmoniques d'un USAMI-11 niveaux commandé par SPWM (r = 0.965, m = 30)

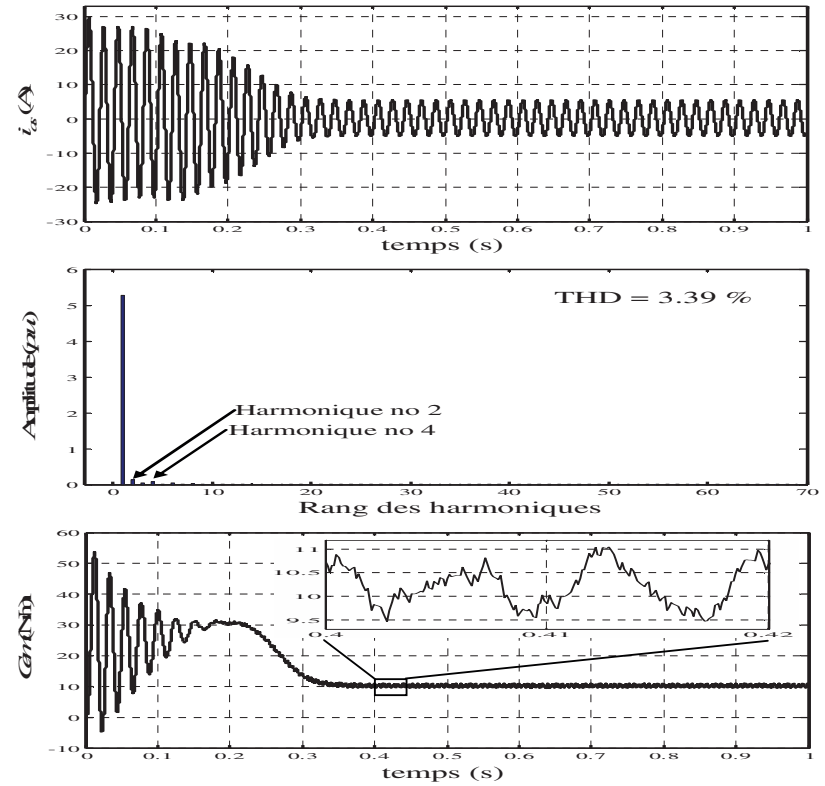

Fig. 6. Performances de la MAS alimentée par USAMI-11 niveaux commandé par SPWM (r = 0.965, m = 30)

Creative Commons Attribution-NonCommercial-NoDerivatives 4.0 International License (CC BY-NC-ND)

B- Stratégie d'élimination d'harmoniques

Le principe de cette stratégie est basé sur le développement en série de Fourier de la tension us à la sortie du convertisseur à pas uniforme ($\Delta_u = u_{d1}$) (Fig. 2) (Chiasson, Tolbert, McKenzie, & Du, 2004; Kato, 1999; Sirisukprasert, Lai, & Liu, 2002). Cette tension admet une symétrie par rapport au demi et au quart de la période. De ce fait, les composantes harmoniques paires en cosinus et en sinus sont nulles. La décomposition en série de Fourier de cette tension est donnée par la relation suivante :

$$\begin{cases} u_s = \sum_{n=1}^{\infty} u_n \sin(n\omega t) \\ u_n = \dfrac{4u_{d1}}{n\pi} \sum_{i=1}^{p} \cos(n\theta_i) \end{cases} \tag{6}$$

avec u_n amplitude de l'harmonique de rang n (n impaire), $p = (N-1)/2$ nombre total de commutations sur un quart de période et θ_i angles de commutation ($i = 1, 2, \ldots, p$).

Les p angles de commutation de la relation (6) sont déterminés en imposant l'amplitude de la composante fondamentale et en annulant les ($p-1$) harmoniques. Par exemple, si l'on veut faire varier la valeur des tensions de sortie d'un onduleur asymétrique triphasé à 11 niveaux constitué de $k = 3$ onduleurs partiels alimentés respectivement par le groupe de tension $u_{d1} = 1$, $u_{d2} = 2$ et $u_{d3} = 2$, alors il faut déterminer les cinq angles de commutation ($\theta_1, \theta_2, \ldots, \theta_5$) de façon à annuler les quatre premières composantes harmoniques impaires autres que celles de rang 3 ou multiples de 3 (5, 7, 11 et 13) de la tension composée. Dans ce cas, cela revient à résoudre le système non linéaire suivant :

$$\begin{cases} \sum_{i=1}^{5} \cos(\theta_i) = \dfrac{5\pi}{4} r \\ \sum_{i=1}^{5} \cos(n\theta_i) = 0 \ \text{ pour } \ n \in \{5, 7, 11, 13\} \end{cases} \tag{7}$$

Où $r = u_1/5u_{d1}$ taux de modulation. La solution recherchée doit satisfaire la condition suivante :

$$\theta_1 < \theta_2 < \theta_3 < \theta_4 < \theta_5 < \frac{\pi}{2} \tag{8}$$

La résolution du système (7) par la méthode de Newton-Raphson donne toutes les solutions possibles pour différentes valeurs de r (Fig. 7). De cette figure, on remarque qu'il existe une double solution pour ($0.65 \leq r \leq 0.74$) et ($0.77 \leq r \leq 0.89$). Pour les valeurs de r inférieures à 0.48 et r compris entre 0.92 et 0.951, aucune solution n'est possible. Ce système accepte une seule solution pour les autres valeurs de r.

Creative Commons Attribution-NonCommercial-NoDerivatives 4.0 International License (CC BY-NC-ND)

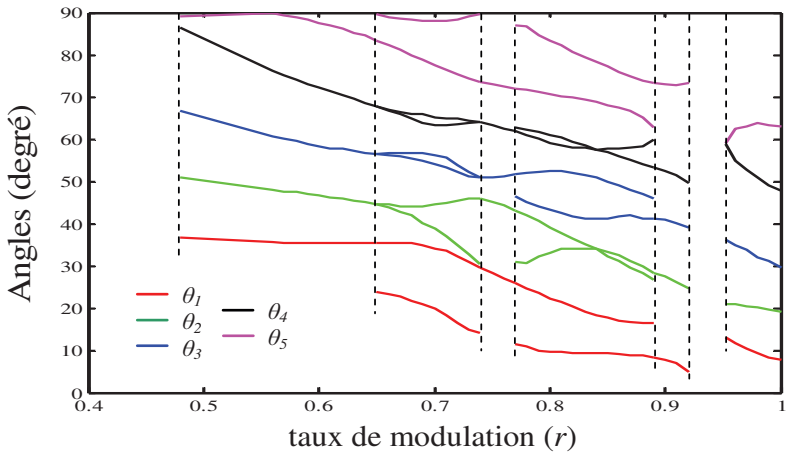

Fig. 7. Angles de commutation en fonction de r

On note que pour $(0.65 \leq r \leq 0.74)$ et $(0.77 \leq r \leq 0.89)$ un critère de choix d'angles adéquats est proposé. Ce critère est basé sur la comparaison des THD (taux d'harmoniques) offerts par les différents angles de ces intervalles. Les angles qui donnent le meilleur THD sont sélectionnés. Pour cela, nous avons calculé les THD (relation 9) données par les solutions déterminées (Fig. 8). La Fig. 9, montre les angles choisis accompagnés de leurs THD (Fig. 10).

$$THD = \frac{\sqrt{\sum_{n=2}^{\infty}\left(\frac{1}{n}\sum_{i=1}^{p=5}\cos(n\theta_i)\right)^2}}{\sum_{i=1}^{p=5}\cos(\theta_i)} \tag{9}$$

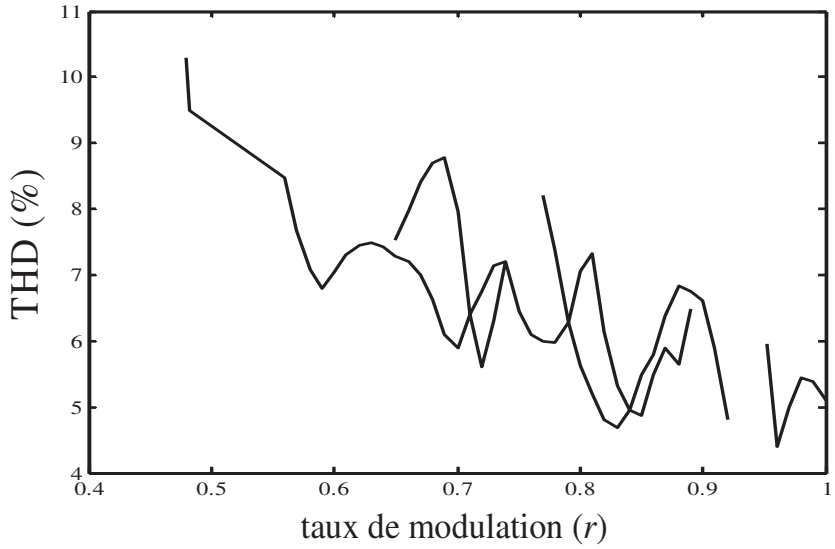

Fig. 8. Variation des THD en fonction de r

Creative Commons Attribution-NonCommercial-NoDerivatives 4.0 International License (CC BY-NC-ND)

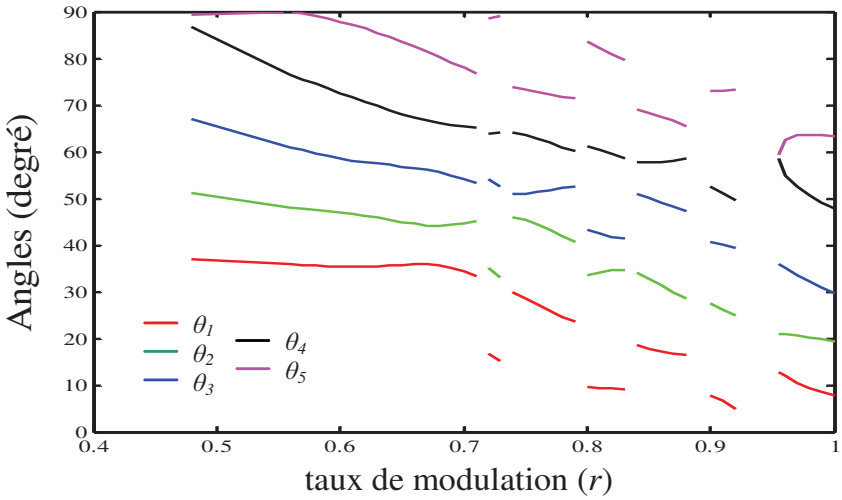

Fig. 9. Angles de commutation sélectionnés en fonction de *r*

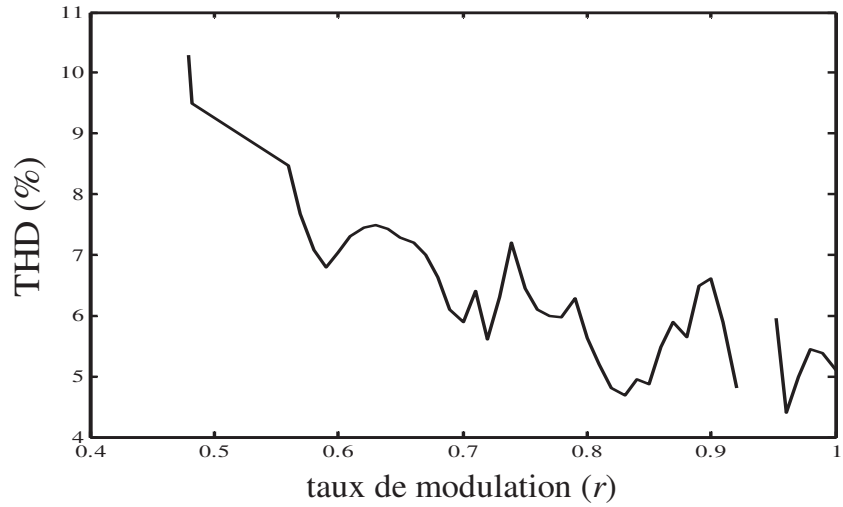

Fig. 10. Variation du plus faible THD en fonction de *r*

Les Figs. 11 et 12 présentent les résultats de simulation de l'onduleur pour une valeur fixe de *r* (*r* = 0.965), c'est à dire pour : θ_1 = 11.1136°, θ_2 = 20.8263°, θ_3 = 34.3041°, θ_4 = 53.4818° et θ_5 = 63.0958°.

Creative Commons Attribution-NonCommercial-NoDerivatives 4.0 International License (CC BY-NC-ND)

Algerian Journal of Engineering Architecture and Urbanism Vol. 5 Nr. 3 2021
ISSN: 2588-1760

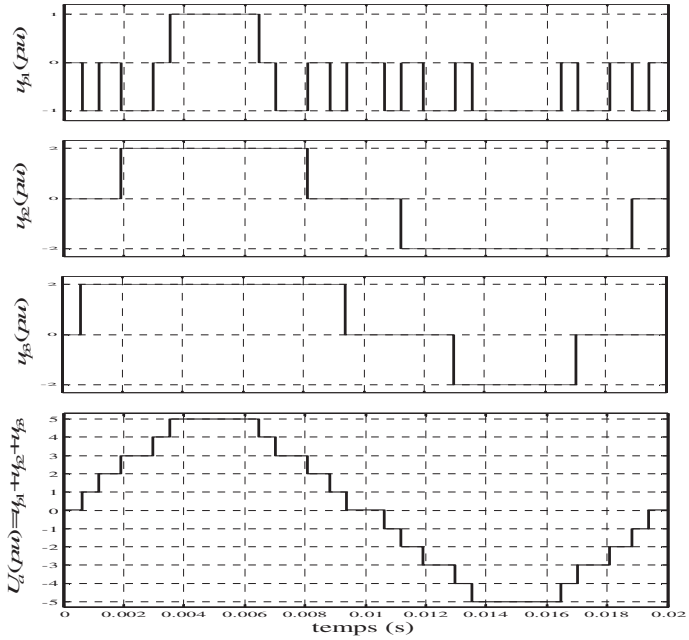

Fig. 11. Tensions partielles et tension de phase d'un USAMI-11 niveaux commandé par SHEPWM (r = 0.965)

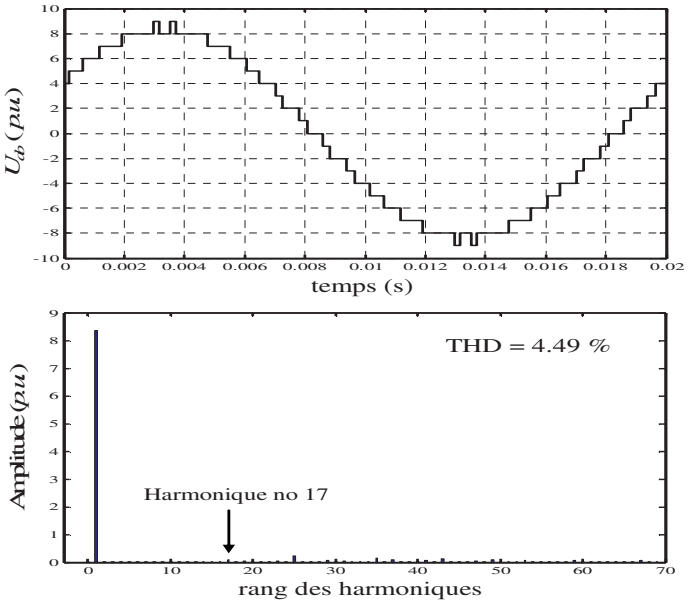

Fig. 12. Tension composée u_{ab} et son spectre d'harmoniques d'un USAMI-11 niveaux commandé par SHEPWM (r = 0.965)

Les performances de la MAS alimentée par l'onduleur asymétrique à onze niveaux à pas uniforme commandé par la stratégie d'élimination d'harmoniques sont présentés par la Fig. 13.

Creative Commons Attribution-NonCommercial-NoDerivatives 4.0 International License (CC BY-NC-ND)

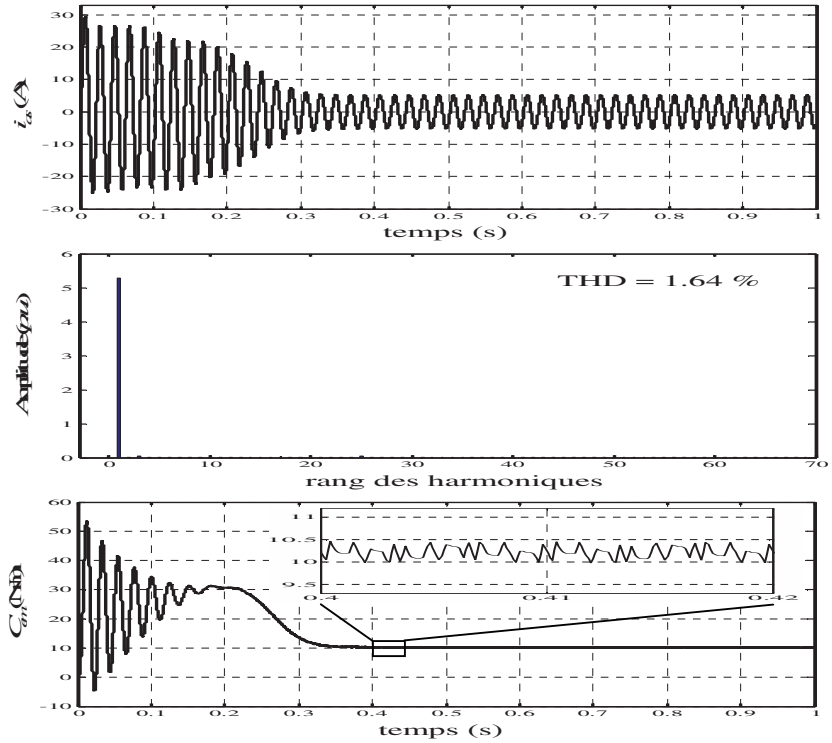

Fig. 13. Performances de la MAS alimentée par USAMI-11 niveaux commandé par SHEPWM (r = 0.965)

Interprétation des résultats:

Dans le tableau 1, nous résumons les résultats de simulation obtenus par les deux stratégies. De l'analyse des figures ainsi que du tableau 1, il ressort que pour la stratégie SHEPWM : 1) l'élimination des harmoniques indésirables (5, 7, 11 et 13) de la tension U_{ab} est assurée, 2) la composante fondamentale suit bien la valeur imposée 8.357 *p.u.* et la première harmonique restante est celle de rang 17, 3) elle présente un taux d'harmoniques est inférieur à celui obtenu par la stratégie triangulo-sinusoïdale, 4) le courant statorique est plus proche de la sinusoïde, 5) elle réduit le nombre d'angles de commutation par période trois fois moins que celle de la SPWM.

Stratégies	U_{ab} THD (%)	i_{as} THD (%)	f_{Cem} (Hz)	Δ_{Cem} (Nm)	Nb θ_i
SPWM	5.07	3.39	f	1.60	60
SHEPWM	4.49	1.64	$2f$	0.45	20

Table 1. COMPARAISON DES RESULTATS OBTENUS

Pour la stratégie SPWM, le couple électromagnétique de la machine oscille autour de sa valeur moyenne à la fréquence f de la tension de sortie de l'onduleur avec une large bande d'oscillation et non $2f$ comme SHEPWM. Cela est dû à la présence des harmoniques 2 et 4 dans la tension de sortie.

Creative Commons Attribution-NonCommercial-NoDerivatives 4.0 International License (CC BY-NC-ND)

Conclusion :

L'amélioration des performances d'un système d'entraînement d'une machine asynchrone passe par le choix d'une bonne stratégie de commande de l'onduleur d'alimentation. Dans ce travail, nous avons montré, par simulation, que la stratégie d'élimination d'harmoniques présente des performances meilleures par rapport à celles de la stratégie triangulo-sinusoïdale. En effet, elle permet de garantir une meilleure qualité du couple, de minimiser les harmoniques de courant et de réduire les pertes de commutation aux bornes des interrupteurs. Ceci a l'avantage d'augmenter leur durée de vie. D'où le choix de cette stratégie dans la commande d'un onduleur multiniveau asymétrique à pas uniforme alimentant une machine asynchrone.

Annexes :

1) Tensions d'alimentations des onduleurs partiels : Tension de base u_{d1} = 70V, $u_{d2} = u_{d3} = 2u_{d1}$ = 140V.

2) Paramètres de la MAS : résistance statorique R_s = 4.850Ω, résistance rotorique R_r = 3.805Ω, inductance statorique L_s = 0.274H, inductance rotorique L_r = 0.274H, inductance mutuelle L_m = 0.258H, nombre de pair de pole $P = 2$, moment d'inertie J = 0,031kg.m², couple de charge C_{ch} = 10Nm, coefficient de frottement K_f = 0,00136 Nm.s.rad^{-1}.

References :

Chiasson J. N., Tolbert L. M., McKenzie K. J., & Du Z. (2004), A unified approach to solving the harmonic elimination equations in multilevel converters, IEEE Transactions on power electronics **19(2):** 478-490.

Kato T. (1999), Sequential homotopy-based computation of multiple solutions for selected harmonic elimination in PWM inverters, IEEE Transactions on Circuits and Systems I: Fundamental Theory and Applications **46(5):** 586-593.

Lund R. (2005), Multilevel power electronic converters for electrical motor drives, Phd thesis, Norwegian University of Science and Technology, Norway.

Mariéthoz J.-S. (2005), Etude formelle pour la synthèse de convertisseurs multiniveaux asymétriques : EPFL, Thèse de Doctorat, EPF-Lausanne, Suisse.

Prajapat K., Katariya A., Kumar A., & Shukla S. (2011), Simulation and testing of photovoltaic with grid connected system. Paper presented at the 2011 International Conference on Computational Intelligence and Communication Networks.

Rodriguez J., Franquelo L. G., Kouro S., Leon J. I., Portillo R. C., Prats M. A. M., & Perez M. A. (2009), Multilevel converters: An enabling technology for high-power applications. Proceedings of the IEEE **97(11):** 1786-1817.

Rodriguez J., Lai J.-S., & Peng F. Z. (2002), Multilevel inverters: a survey of topologies, controls, and applications. IEEE Transactions on industrial electronics **49(4):** 724-738.

Sirisukprasert S., Lai J.-S., & Liu T.-H. (2002), Optimum harmonic reduction with a wide range of modulation indexes for multilevel converters. IEEE Transactions on industrial electronics **49(4):** 875-881.

Song Manguelle J. (2004), Convertisseurs multiniveaux asymétriques alimentés par transformateurs multi-secondaires basse-fréquence : EPFL, Thèse de Doctorat, EPF-Lausanne, Suisse.

Creative Commons Attribution-NonCommercial-NoDerivatives 4.0 International License (CC BY-NC-ND)

Algerian Journal of Engineering Architecture and Urbanism Vol. 5 Nr. 3 2021
ISSN: 2588-1760

ETUDE DE L'IMPACT DU RACCORDEMENT D'UNE PRODUCTION DECENTRALISEE DANS UN RESEAU DE DISTRIBUTION

Mekki Mounira,
(MCB), Université Larbi Ben M'hidi. Oum el bouaghi,
e-mail: mouniramekki9@gmail.com

Résumé:
L'intégration des unités de production distribuée (GED) fournit des avantages potentiels aux réseaux de distribution conventionnels. L'emplacement des unités de la GED devrait être soigneusement déterminé en tenant compte des différentes incitations à la planification.
Ce travail présente une étude et simulation de l'impact de l'intégration de la GED dans un réseau de distribution, et son influence sur le plan de tension et les flux de puissance. Par la suite on a proposé une solution du contrôle de la tension par l'injection ou absorption de la puissance réactive à l'aide des compensateurs de FACTS ; à savoir : le SVC. Les simulations sont effectués sur un réseau de distribution tests IEEE (9 jeux de barre).

Mots clés: Réseau de distribution, générateur d'énergie distribuée (GED), indice de sensibilité de tension , VSI ,SVC

Introduction:

L'électricité est aujourd'hui la forme d'énergie la plus aisée à exploiter. Mais avant de la consommer il aura fallu la produire, en général dans des unités de production de grande puissance, la transporter, puis la distribuer à chaque consommateur. [1]
La nécessité de réduire les émissions de dioxyde de carbone (CO_2) est aujourd'hui devenue une évidence. Cela fait de nombreuses années que le corps scientifique l'annonce, toujours avec plus de force : le réchauffement climatique, dû à ce qu'on appelle communément « l'effet de serre », est étroitement lié à ces émissions. Le CO_2 serait en effet responsable pour 85 % du renforcement de ce phénomène. [2]
Aujourd'hui les pouvoirs publics ne peuvent plus définir une politique énergétique sans considérer cette problématique. Un certain nombre d'accords, pris au niveau international et par lesquels les états signataires s'engagent à limiter leurs émissions de dioxyde de carbone, se traduisent à différents niveaux par une politique volontariste d'utilisation rationnelle de l'énergie. [2]
L'énergie de fission nucléaire, qui ne rejette directement pas de gaz carbonique, souffre généralement d'une mauvaise image médiatique. Certes les risques d'accident lié à leur exploitation sont très minimes mais les conséquences d'un accident, même très peu probable, seraient désastreuses. [1]
C'est dans ce cadre que prennent place à la production décentralisée, les énergies renouvelables offrent la possibilité de produire de l'électricité proprement et surtout dans une moindre dépendance des ressources, à condition d'accepter leurs fluctuations naturelles et parfois aléatoires.

Problématique:

Afin d'évaluer l'impact des productions décentralisées et les changements qu'elles apportent au réseau électrique, une étude de la variation de tension pour le raccordement d'une production éolienne a été faite dans un réseau de distribution. La modélisation mathématique des systèmes non linéaires à résoudre pour l'étude de la répartition de charges,

Creative Commons Attribution-NonCommercial-NoDerivatives 4.0 International License (CC BY-NC-ND)

consiste à faire appel aux outils mathématiques et techniques numériques de calcul de l'écoulement de puissance à savoir la méthode itérative de Newton-Raphson qui sera implantée dans l'environnement MATLAB.

En premier lieu, une étude d'un réseau IEEE à 9 nœuds sera faite pour évaluer l'état du réseau, c'est-à-dire, les tensions aux nœuds et les puissances transitées à travers les lignes électriques ainsi que les pertes de puissance dans les lignes par un calcul d'écoulement de puissance. Par la suite, nous allons intégrer un générateur éolien dans le réseau. Notre but est de faire une analyse paramétrique afin d'étudier l'évolution de ce réseau lorsqu'on lui intègrera une éolienne. Celle-ci sera modélisée par une injection de puissance de forme fluctuante. Un nouveau calcul d'écoulement de puissance sera effectué afin d'évaluer l'impact causé par cette intégration sur la stabilité de la tension aux jeux de barres du réseau et les puissances transitées dans les lignes, ainsi que les pertes de puissance.

Enfin, la solution proposée est d'insérer un dispositif Facts de régulation de tension qui est le SVC [3] [4] pour le réseau test (9 nœuds IEE) dans un emplacement optimal pour obtenir une meilleure stabilité de la tension.

Modèle de simulation:

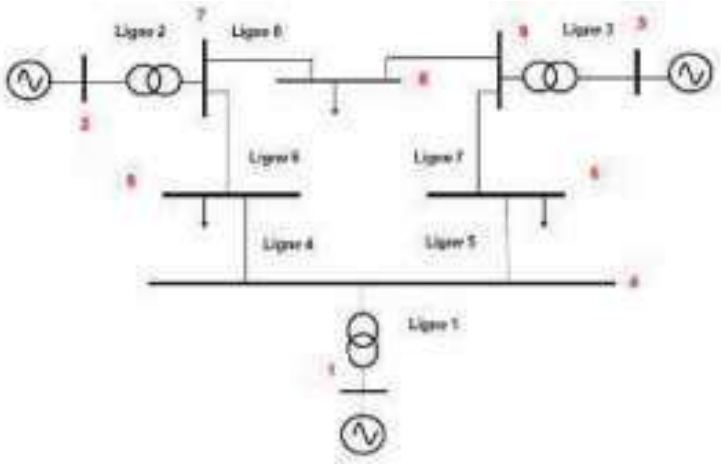

Fig1. STRUCTURE DU RESEAU SIMULE

Résultats et discussions:

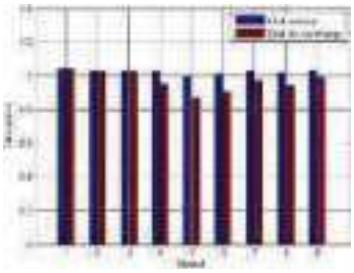

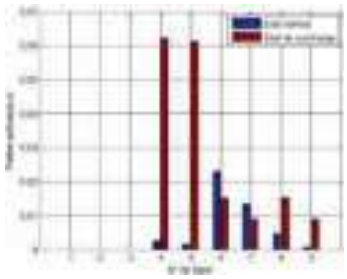

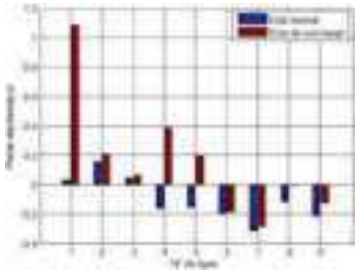

Fig2.TENSIONS DANS LES NŒUDS **Fig3.**PERTES ACTIVES DANS LES LIGNES **Fig4.**PERTES REACTIVES DANS LES LIGNES

Résultats de l'écoulement de puissance et discussions

1. *Etat du réseau sans insertion du générateur éolien*

• Le réseau à l'état normal par la méthode itérative de Newton Raphson.

Creative Commons Attribution-NonCommercial-NoDerivatives 4.0 International License (CC BY-NC-ND)

Algerian Journal of Engineering Architecture and Urbanism Vol. 5 Nr. 3 2021
ISSN: 2588-1760

D'après les résultats obtenus et plus particulièrement les plans de tensions, on remarque clairement que la chute de tension est plus importante pour les nœuds de charge 5.

•Les pertes de puissances actives maximales sont évaluées à 0.0623(p.u) et 0.0613(p.u) , respectivement 6230KW dans la ligne 4 et 6130 KW dans la ligne 5.

•Les pertes de puissances réactives maximales sont évaluées à 1.0799 (p.u) et 0.3832 (p.u) , respectivement 107 ,99KVAR dans la ligne 1 et 383.2KVAR dans la ligne 4.

2. *Etat du réseau avec insertion d'un générateur éolien*

•La puissance injectée par le générateur éolien est prise de forme fluctuante pour représenter l'image réelle de la nature fluctuante du vent.

•D'après certains retours d'expériences, et ce qui est mentionné dans la littérature le taux de pénétration de la production éolienne doit être limité (entre 20 et 30 % de la puissance consommée) afin de pouvoir garantir la stabilité du réseau dans des conditions acceptables.

•Dans le but de voir le comportement du réseau de distribution vis-à-vis d'une intégration éolien.

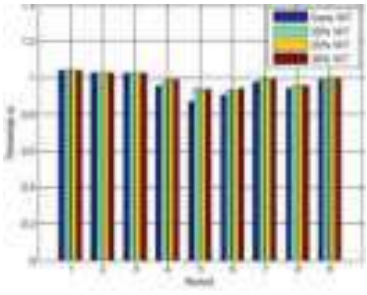

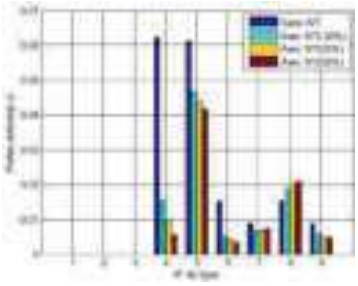

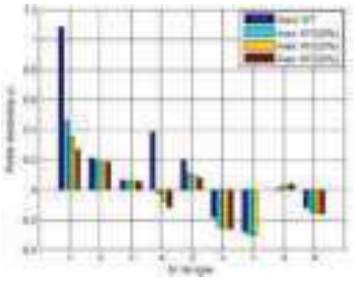

Fig5.TENSIONS DANS LES NŒUDS **Fig6.**PERTES ACTIVES DANS LES LIGNES **Fig7.**PERTES REACTIVES DANS LES LIGNES

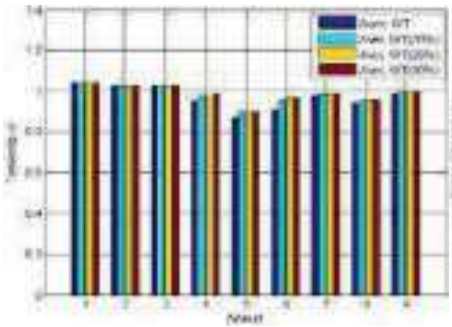

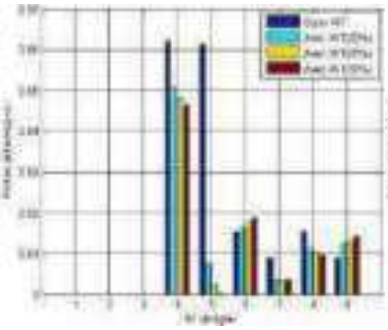

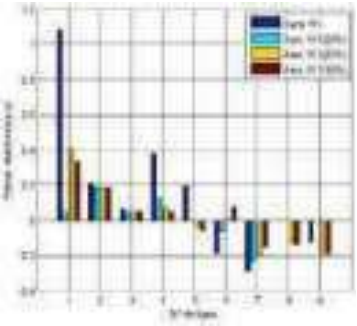

Fig8.TENSIONS DANS LES NŒUDS **Fig9.**PERTES ACTIVES DANS LES LIGNES **Fig10.**PERTES REACTIVES DANS LES LIGNES

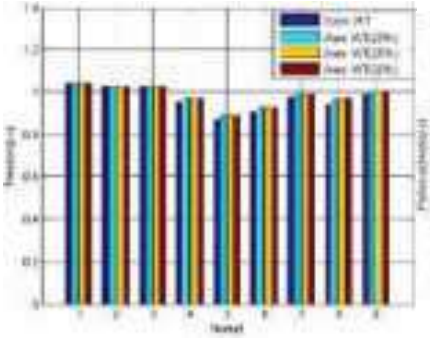

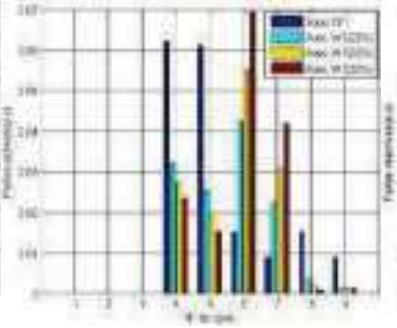

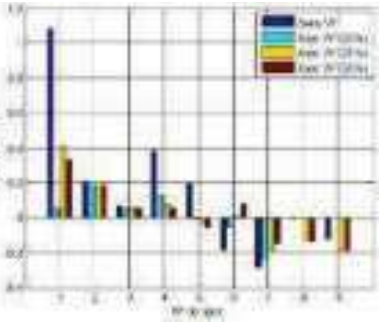

Creative Commons Attribution-NonCommercial-NoDerivatives 4.0 International License (CC BY-NC-ND)

Fig11.TENSIONS DANS LES NŒUDS **Fig12.**PERTES ACTIVES DANS LES LIGNES **Fig13.**PERTES REACTIVES DANS LES LIGNES

3. Interprétation des résultats

La première chose à remarquer dans les résultats d'écoulement de puissance est l'amélioration de l'amplitude des tensions, spécialement le nœud où le générateur éolien a été installé.
Nœud 5 : (de 0.8711 à 0.9245 à 0.9325 à 0.9390). (Fig 5) *Nœud 6 :* (de 0.9059 à 0.9558 à 0.9694). (Fig 8)
Nœud 8 : (de 0.9425 à 0.9669 à 0.9695 à 0.9709). (Fig 11)
Nous observons aussi la diminution remarquable des pertes de puissances actives et réactives dans les branches. Avant et après l'intégration de l'éolienne, la somme des pertes actives et réactives sont évaluées pour le cas de 20% PT à :
Nœud 5 : ΣP_L ont diminué de 0,172 à 0,0988(p.u). (Fig 6) *Nœud 6 :* ΣP_L ont diminué de 0,172 à 0,1016(p.u). (Fig 9) *Nœud 8 :* ΣP_L ont diminué de 0,172 à 0,1282(p.u). (Fig 12)
la somme des pertes réactives sont évaluées à :
Nœud 5 : ΣQ_L ont diminué de 1,3342 à 0,0852(p.u). (Fig 7) *Nœud 6 :* ΣQ_L ont diminué de 1,3342 à 0,5301(p.u). (Fig 10) *Nœud 8 :* ΣQ_L ont diminué de 1,3342 à 1,001(p.u). (Fig 13).

4. Localisation optimale basée sur l'indice de sensibilité de la tension VSI

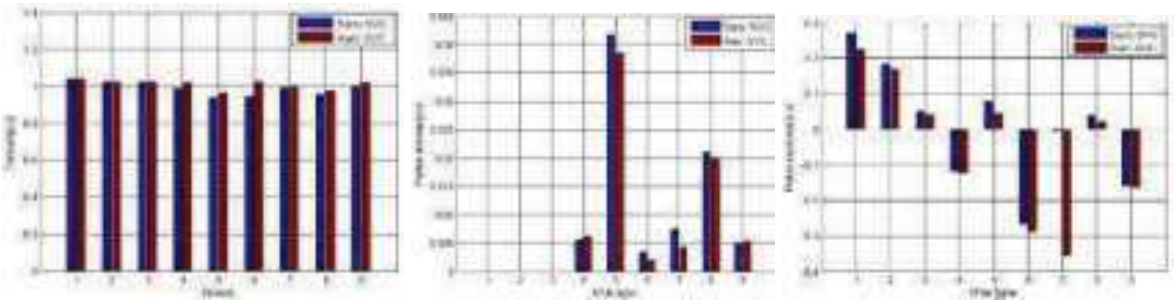

Fig14.TENSIONS DANS LES NŒUDS **Fig15.**PERTES ACTIVES DANS LES LIGNES **Fig16.**PERTES REACTIVES DANS LES LIGNES

Après insertion du dispositif FACTS représenté par le SVC , qui a été inséré dans le nœud 6 ayant pour but l'amélioration du profil de tensions dans les nœuds, on a remarqué que :
➢ Toutes les tensions sont dans les limites admissibles, le nœud 5 passe d'une tension de 0.93 à 0.96 , et le nœud 6 passe d'une tension de 0.94 à 1.02, les autres tensions sont toutes dans las limites admissibles, sachant que la plage de variation est de ±5%.(Voir figure 14.).
➢ On constate qu'il une minimisation des pertes actives au niveau des nœuds 5,6,7 et 8, par exemple pour le nœud 5 les pertes passent de 0.04 à 0.03 , ainsi pour le nœud 6 , les PL passent 0.0033 à 0.0019.(Voir figure 15).
Après calcul, on a pu déterminé que le lieu optimal pour implanter l'éolienne est le nœud 5 parce que la valeur du VSI [5] est minimale pour 30%.

Creative Commons Attribution-NonCommercial-NoDerivatives 4.0 International License (CC BY-NC-ND)

➢ L'implantation du dispositif SVC, au nœud 6 a apporté plusieurs avantages, l'amélioration des tensions qui sont toutes dans les limites admissibles, tels que les nœuds 5 6 et 8, dont les tensions obtenues après compensation sont :

V5=0.96 , V6=1.02 , V8 =0.97 ainsi qu'une minimisation des pertes actives , c'est-à-dire que les pertes totales dans le réseau sont évaluées à : 0.0759(p.u) après insertion du dispositif de compensation le SVC, alors qu'elles étaient de 0.0838.

➢ On a vu que les dispositifs SVC permettent d'améliorer l'exploitation du réseau électrique, d'augmenter la capacité de transport tout en maintenant les tensions des nœuds du réseau d'énergie électrique dans les limites admissibles, et minimiser les pertes actives dans le réseau électrique.

Conclusion:

L'intégration des unités de production distribuée (GED) fournit des avantages potentiels aux réseaux de distribution conventionnels. L'emplacement des unités de la GED devrait être soigneusement déterminé en tenant compte des différentes incitations à la planification.

On a fait un ensemble de programmation numérique (sous Matlab), d'un réseau test (IEEE 9 nœuds) sans éolienne, et avec éolienne puis un réglage par l'un des moyens de FACTS qui est le SVC.

Les résultats d'écoulement de puissance ont été améliorés.

Réferences:

[1] Georges Gerges*, ali el-ali*, nazih moubayed*, rachid outbib. (2007), *L'Energie éolienne au Liban : Bilan annuel, rendement et rentabilité ,* 6th International Conference on Electromechanical and power systems, chi_in_u, rep.moldova.

[2] lsmaèl Daoud, Nicolas Pierreux,(2001), *Analyse des systèmes de micro-cogénération*, Ingénieur Civil Electromécanicien 2000-2001.

[3] Rabah Benabid, (2007), *Optimisation Multiobjectif de la Synthèse des FACTS par les Particules en Essaim pour le Contrôle de la Stabilité de Tension des Réseaux Electriques*, mémoire de magister, option : Analyse, Conduite et Commande des réseaux électriques, université Amar Telidji, Laghouat.

[4] L.Baghli,(2005), *Modélisation et commande de la machine asynchrone* ", notes de cours, université Henri Poincaré Nancy-1..

[5] www.elsevier.com/locate/ijepes, (2008), *Prescriptions technique de conception et de fonctionnement pour le raccordement au réseau de transport d'électricité d'une installation de production d'énergie électrique.*

Creative Commons Attribution-NonCommercial-NoDerivatives 4.0 International License (CC BY-NC-ND)

Algerian Journal of Engineering Architecture and Urbanism Vol. 5 Nr. 3 2021
ISSN: 2588-1760

PRESENTATION OF A THREE-DIMENSIONAL METROLOGY SOFTWARE - APPLICATION TO FLATNESS

Djezouli MOULAI-KHATIR[1,2]
PhD, [1]Abou Bekr Belkaid University, Department of Electrical and Electronics, Faculty of Technology, B.P. 230 Tlemcen, 13000, Algeria
[2]LaRTFM Laboratory, ENP Maurice Audin, B.P. 1523 El M'naouer, Oran,
djezouli.moulai-khatir@univ-tlemcen.dz, moulai_khatir@yahoo.fr

Abstract:
This article presents a three-dimensional metrology software, named « GFDSoft » Geometrical Form Defect Software, developed by MOULAI-KHATIR. GFDSoft implements the least squares adjustment criterion (which is the most commonly used criterion on Coordinate Measuring Machine "CMM" software) and the minimum zone (Chebyshev) criterion. We will present in this work, the mathematical modeling by the criterion of least squares adjustment for the case of the flatness. We will also present applications to measure the flatness defect on industrial parts. Then we will validate our software, comparing our results to results of works of the scientific literature, as well as by performing a comparison of our software with others three-dimensional metrology software's.

Key words: CMM ; form defect ; fitting criterion ; flatness.

Introduction:

Les défauts de forme impactent dans bien des cas la fonctionnalité des assemblages ou des mécanismes, c'est la raison pour laquelle leur détermination connait actuellement une très grande importance dans le domaine industriel. Le contrôle classique (au marbre) des défauts de forme est entaché d'erreurs. Lors de la mesure de la planéité, le métrologue définit la surface géométrique idéale. Ensuite, il palpe des points au niveau de cette surface à contrôler par le palpeur du comparateur en faisant glisser le socle de ce dernier, sur le marbre tout en relevant les écarts de mesure (Moulai-Khatir, 2017). La détermination d'un défaut de forme de manière objective par les méthodes de mesure directes n'est pas possible, ce qui ouvre la porte à toute espèce de contestation entre fournisseur et acheteur (Debongnie, 1998). Le défaut de forme est définit comme étant la distance maximale entre la surface réelle et une surface théorique en contact avec elle du côté extérieur de la matière. La norme exige de choisir cette surface théorique de manière à minimiser cette distance. La détermination de cette surface théorique n'est pas facile en métrologie tridimensionnelle. Les critères imposés par les normes sont nombreux et les cas à traiter sont très diversifiés (Radouani, 2003).

Dans ce contexte, cet article présente un logiciel de métrologie tridimensionnelle, nommé « GFDSoft » Geometrical Form Defect Software (logiciel de détermination des défauts de forme des pièces mécaniques), développé par MOULAI-KHATIR. Il implémente les critères d'ajustement des moindres carrés et de Tchebychev (minimax). Le critère des moindres carrés est le plus pratiqué (et souvent le seul disponible sur les machines à mesurer tridimensionnelles). La surface des moindres carrés passe entre les points palpés. Le plan des

Creative Commons Attribution-NonCommercial-NoDerivatives 4.0 International License (CC BY-NC-ND)

moindres carrés passe par le centre de gravité des points (Anselmetti, 2011). Pour le critère de Tchebychev, la norme ISO 5459-2011 définit le plan tangent à la surface réelle, pour associer une référence à un plan, du côté libre de la matière tel que la distance maximale des points de la surface réelle à ce plan soit minimale. Cette distance maximale est l'écart de planéité (Shunmugam, 2001). Dans cet article nous présentons des applications pour le calcul de la planéité par le critère des moindres carrés, sur des pièces industrielles.

Modélisation mathématique de la planéité:

Mise en situation du problème

La planéité est définie dans la norme ISO 1101 comme étant l'écart minimal entre deux plans parallèles P1 et P2 contenant tous les points prélevés sur une machine MMT (Jalid, 2015), comme le montre la Fig. 1.

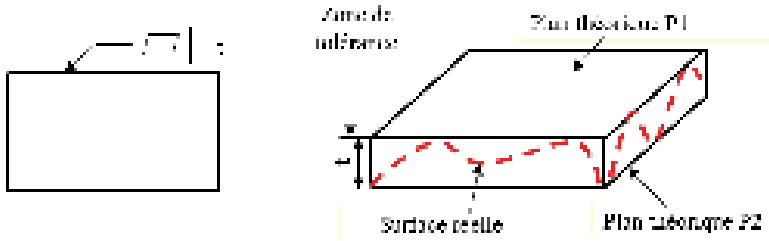

Fig1. Défaut de planéité d'une surface (Jalid, 2015)

Modélisation par les moindres carrés

Nous rappelons que l'équation d'un plan est donnée par l'équation 1 suivante :

$$z = Ax + By + C \tag{1}$$

Le calcul du défaut de planéité par la méthode des moindres carrés consiste à déterminer la distance entre 2 plans parallèles et passants par les deux points extrêmes (intérieur et extérieur matière) à partir d'un nuage de points prélevé sur une MMT.

On se donne a priori « un plan non vertical » $z = f(x, y) = Ax + By + C$ et on pose :

$$S = \sum e_i^2 = \sum (Z - AX - BY - C)^2 \tag{2}$$

La somme S dépend du plan $f(x, y) = Ax + By + C$, donné, i.e. qui dépend de A, B et C. Et le meilleur plan sera donné par un triplet (A, B, C) tel que $S(A, B, C) = \min S(A', B', C')$, i.e. la somme qui minimise le carré des erreurs. Donc, si (A, B, C) existe, on a :

$$\frac{\partial S}{\partial A}(A, B, C) = 0, \qquad \frac{\partial S}{\partial B}(A, B, C) = 0, \qquad \frac{\partial S}{\partial C}(A, B, C) = 0. \tag{3}$$

On obtient alors un système de 3 équations à 3 inconnues :

$$\sum XZ = A\sum X^2 + B\sum XY + C\sum X \tag{4}$$

$$\sum YZ = A\sum XY + B\sum Y^2 + C\sum Y \tag{5}$$

$$\sum Z = A\sum X + B\sum Y + nC \tag{6}$$

Creative Commons Attribution-NonCommercial-NoDerivatives 4.0 International License (CC BY-NC-ND)

Algerian Journal of Engineering Architecture and Urbanism Vol. 5 Nr. 3 2021
ISSN: 2588-1760

La forme matricielle est la suivante :

$$\begin{pmatrix} \sum X^2 & \sum YX & \sum X \\ \sum YX & \sum Y^2 & \sum Y \\ \sum X & \sum Y & n \end{pmatrix} \begin{pmatrix} A \\ B \\ C \end{pmatrix} = \begin{pmatrix} \sum XZ \\ \sum YZ \\ \sum Z \end{pmatrix}$$

Pour résoudre ce système nous utilisons la méthode de Cramer, après calcul on trouve les coefficients A, B et C :

$$A = \frac{\sum XZ(n\sum Y^2-(\sum Y)^2)-\sum YX(n\sum YZ-\sum Z\sum Y)+\sum X(\sum YZ\sum Y-\sum Z\sum Y^2)}{\sum X^2(n\sum Y^2-(\sum Y)^2)-\sum YX(n\sum YX-\sum X\sum Y)+\sum X(\sum YX\sum Y-\sum X\sum Y^2)} \quad (7)$$

$$B = \frac{\sum X^2\,(n\sum YZ-\sum Y\sum Z)-\sum XZ\,(n\sum YX-\sum X\sum Y)+\sum X\,(\sum YX\sum Z-\sum X\sum YZ)}{\sum X^2\,(n\sum Y^2-(\sum Y)^2)-\sum YX\,(n\sum YX-\sum X\sum Y)+\sum X\,(\sum YX\sum Y-\sum X\sum Y^2)} \quad (8)$$

$$C = \frac{1}{n}(\sum Z - A\sum X - B\sum Y) \quad (9)$$

Programmation:

Nous avons réalisé un programme informatique, que nous avons appelé GFDSoft, pour le calcul des défauts de forme des pièces mécaniques. Ce logiciel a été développé sous le langage de programmation Python 3.5 et pour son interface graphique nous avons utilisé la bibliothèque Qt.

Algorithme de calcul du défaut de planéité

La Fig. 2 représente l'algorithme de calcul du défaut de planéité.

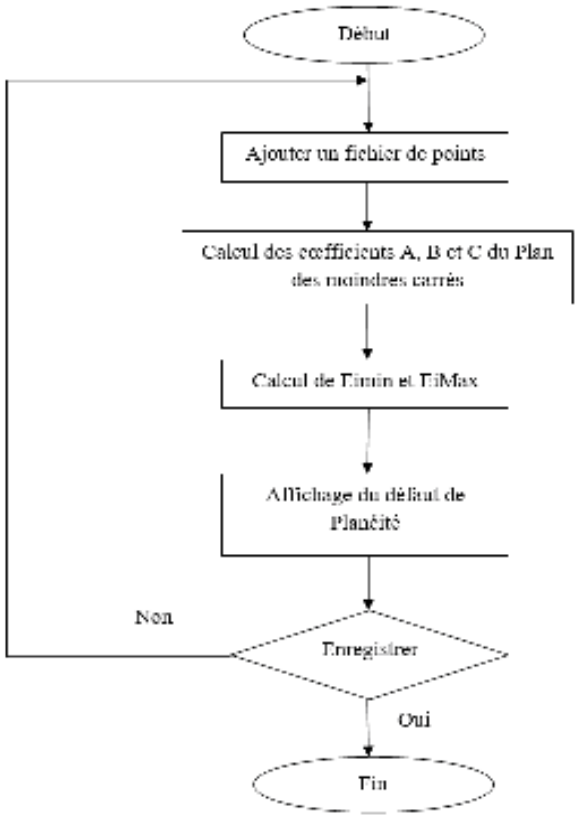

Fig2. Algorithme de calcul du défaut de planéité

Creative Commons Attribution-NonCommercial-NoDerivatives 4.0 International License (CC BY-NC-ND)

Algerian Journal of Engineering Architecture and Urbanism Vol. 5 Nr. 3 2021
ISSN: 2588-1760

Interface du programme

Sur la base de la modélisation mathématique et de l'algorithme cités précédemment, nous avons réalisé notre programme GFDSoft, qui permet de calculer et d'afficher les défauts de forme, selon les deux critères (Moindres carrés et Tchebychev). L'interface du programme est donnée par la Fig. 3.

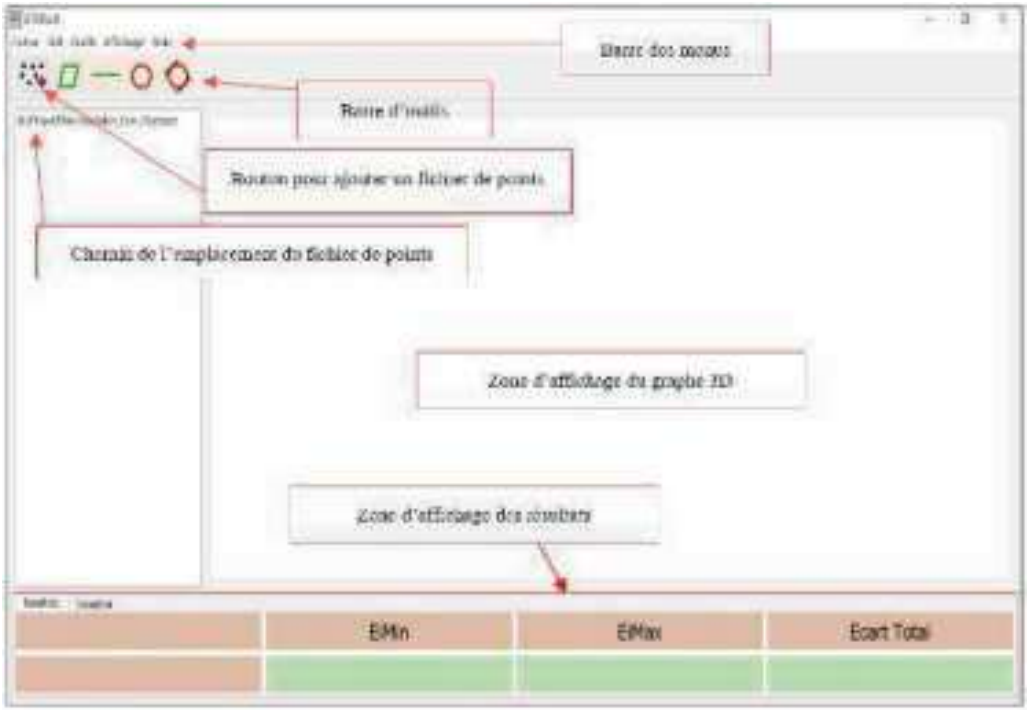

Fig3. Interface du programme

Lors de la conception de l'interface de notre logiciel, nous nous sommes inspirés de l'interface du logiciel expérimental Geoverif (version de prêt), développé par Pairel (Pairel, 1995, 1997, 2005, 2007, 2009), (Moulai-Khatir, 2018), au laboratoire SYMME, de l'université de Savoie (France). L'interface graphique de notre logiciel est très simple. Elle est constituée de boutons permettant l'accès direct aux différents défauts de formes qu'on veut mesurer. Elle réalise l'interactivité avec l'utilisateur, en affichant en 3D la forme du nuage de points ainsi que les différents plans en couleurs différentes (plan des moindres carrés en rouge, plan passant par le point extrême du côté libre matière en bleu et plan passant par le point extrême intérieur matière en vert). Les résultats sont donnés directement sur la zone d'affichage en bas de l'écran.

Résultats & Discussions:

Première application

Nous utiliserons pour première application les résultats de Jalid (Jalid, 2015). Il a pris une pièce industrielle mesurée en 24 points. Le Tableau 1 donne les coordonnées de ces points.

No.	X	Y	Z	No.	X	Y	Z
1	24.921	-29.972	-0.002	13	25.006	-10.003	-0.008
2	-20.204	-30.002	-0.004	14	-24.764	0.008	-0.006

Creative Commons Attribution-NonCommercial-NoDerivatives 4.0 International License (CC BY-NC-ND)

3	-15.013	-30.011	-0.004	15	-20.111	0.002	-0.005
4	-9.999	-30.018	-0.004	16	20.000	-0.004	-0.009
5	-4,962	-30.027	-0.006	17	-9.985	30.001	-0.006
6	-0.025	-30.034	-0.005	18	-4.984	30.000	-0.007
7	4,992	-30.005	-0.006	19	-0.034	30.003	-0.007
8	10.041	-30.000	-0.005	20	5.017	29.997	-0.006
9	-20.218	-9.995	-0.008	21	9.978	30.001	-0.005
10	-15.006	-10.002	-0.007	22	14.996	30.000	-0.007
11	15.015	-9.998	-0.009	23	19.972	30.002	-0.004
12	19.978	-10.002	-0.009	24	25.031	29.999	-0.003

Tableau 1. Coordonnées des points palpés de la pièce de Jalid (Jalid, 2015)

Nous exporterons ce fichier de points dans notre logiciel GFDSoft. A partir du nuage de points prélevé, nous allons mesurer le défaut de planéité de la pièce industrielle suivant le critère des moindres carrés (Sei2), pour 24 points de mesure (palpage).

La Fig. 4, montre le résultat de l'application de GFDSoft au nuage de points de la pièce de Jalid.

Fig4. Résultat du traitement du nuage de points de la pièce de Jalid

Le défaut de planéité trouvé par le critère d'ajustement des moindres carrés, en utilisant le logiciel GFDSoft est le même que celui trouvé par Jalid (Jalid, 2015), à savoir « 0,0068 mm ».

Deuxième application

Nous prendrons pour deuxième application, les résultats de Mangouchi (Mangouchi, 2005). Il a pris pour pièce d'essai, un palier moteur. Il a utilisé la machine à mesurer tridimensionnelle (MMT), du Laboratoire de Métrologie, de l'Ecole Nationale Polytechnique d'Oran, pour avoir le fichier des points palpés. Nous exploiterons ce fichier de points, que

Creative Commons Attribution-NonCommercial-NoDerivatives 4.0 International License (CC BY-NC-ND)

nous exporterons dans notre logiciel GFDSoft. A partir des nuages de points prélevés, nous allons mesurer le défaut de planéité du palier moteur suivant le critère des moindres carrés.
Le tableau 2 montre les résultats du contrôle de la planéité du palier moteur, pour les trois balancements (mesurages), en utilisant le critère des moindres carrés, par les trois logiciels : Metrosoft (Mangouchi, 2005), Geoverif (Pairel, 2005) et GFDSoft.

Balancements	Logiciels		
	Metrosoft	Geoverif	GFDSoft
1er	0.0126	0,012601	0,012601
2ème	0.0131	0,013091	0,013091
3ème	0.0122	0,012136	0,012136

Tableau 2. Résultats du contrôle de la planéité du palier moteur par les logiciels Metrosoft, Geoverif et GFDSoft

La Fig. 5, illustre le graphe de la comparaison des résultats du contrôle de la planéité du palier moteur, pour les trois balancements, en utilisant les trois logiciels Metrosoft, Geoverif et GFDSoft (critère des moindres carrés).

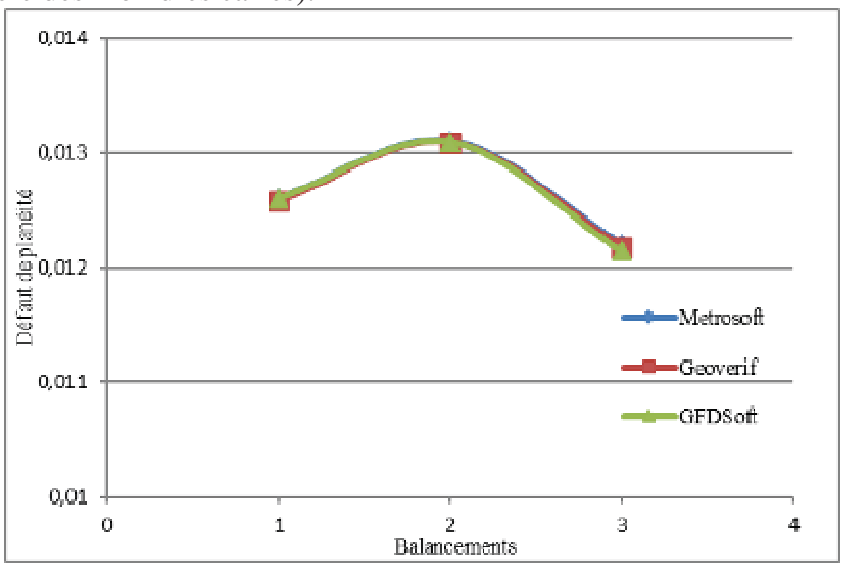

Fig5. Graphe de la comparaison des résultats du contrôle de la planéité par Metrosoft, Geoverif et GFDSoft

Le défaut de planéité trouvé par le critère d'ajustement des moindres carrés, en utilisant le logiciel GFDSoft est le même que celui trouvé en utilisant le logiciel Geoverif, ainsi que par Mangouchi en utilisant le logiciel Metrosoft (Mangouchi, 2005), à savoir « 0,013 mm».

Les résultats trouvés nous permettent de conclure, que les performances de notre logiciel sont prouvées et de confirmer sa validation.

Conclusion:

Cet article présente un logiciel de métrologie tridimensionnelle, nommé « GFDSoft », destiné à la mesure des défauts de forme des pièces mécaniques. Il a été développé sous le langage de programmation Python 3.5 et pour son interface graphique nous avons utilisé la bibliothèque Qt. Il implémente les deux critères d'ajustements, des moindres carrés (Sei^2) et celui de Tchebychev (Minimax). Dans ce travail, nous avons présenté des applications à la mesure du défaut de planéité sur des pièces industrielles. Nous avons pris comme première application une pièce industrielle de la littérature scientifique. Nos résultats sont les mêmes,

Creative Commons Attribution-NonCommercial-NoDerivatives 4.0 International License (CC BY-NC-ND)

donc les performances de GFDSoft sont prouvées. Puis comme deuxième application, nous avons pris un palier moteur. A partir des résultats trouvés, nous avons réalisé une étude comparative entre notre logiciel et deux autres logiciels. Nous avons utilisé le logiciel industriel Metrosoft de la machine « Métromec » et le logiciel expérimental Geoverif. Les résultats de la mesure du défaut de planéité trouvés, en utilisant le critère d'ajustement des moindres carrés, sont identiques entre les trois logiciels, ce qui nous permet la validation de notre logiciel.

Actuellement notre logiciel permet la mesure de : la planéité et la rectitude, en perspectives nous prévoyons d'étendre notre travail aux autres défauts de forme (notamment la cylindricité), ainsi qu'aux autres défauts géométriques (positions et orientations).

Références:

Moulai-Khatir D. (2017), *Etude comparative entre deux logiciels de métrologie tridimensionnelle,* Recueil de mécanique, Centre Universitaire de Tissemsilt, Vol.2-N°002, pp 215–222.

Debongnie J. F., Masset L. (1998), *Sur l'évaluation des défauts de forme à partir de mesures tridimensionnelles*, Eur Jour Mec and Envir Eng, V43-1, pp. 13-21.

Radouani M., Anselmetti B. (2003), *Identification of real surfaces and inspection of the ISO specifications using a solver*, Mechanic&Industry, V4, pp. 249–258.

Anselmetti B. (2011), *Manuel de tolérancement : Métrologie avec les normes ISO*, Volume 5, Edition Lavoisier.

Shunmugam M.S. (2001), *Important aspects of form measurement and assessment of engineering surfaces*, J. Institution of Engineers, India, Part Mc, Mechanical Engineering Division.

Jalid A., Hariri S., Senelaer J.P., El Gharad A. (2015), *Comparaison entre la méthode GUM et Monte Carlo pour l'estimation de l'incertitude en mesure 3D : application à l'étude d'une planéité*, 22ème Congrès Français de Mécanique.

Pairel E. (1995), *Métrologie fonctionnelle par calibre virtuel sur machine à mesurer tridimensionnelle*, Thèse de doctorat en Génie mécanique de l'Université de Savoie, France.

Pairel E. (1997), *The Gauge model: A New Approach for Coordinate Measurement*, XIV IMEKO World Congress, Tampere, Finland, 1-6 June, pp278-283.

Pairel E. (2005), *Présentation d'un logiciel de métrologie tridimensionnelle par calibre virtuel*, 12° congrès international de métrologie, 20-23 Juin, Lyon, France.

Pairel E., Hernandez P., Giordano M. (2007), *Virtual Gauge Representation for Geometric Tolerances in CAD-CAM Systems, in "Models for Computer Aided Tolerancing in Design and Manufacturing* (Selected papers from 9th CIRP seminar on CAT)", Springer, J.K. Davidson (Ed.) , pp. 3-12.

Pairel E. (2009), *Three-dimensional metrology with the virtual fitting gauges*, 11th CIRP International Conference on Computer Aided Tolerancing, March, 26-27, Annecy, France.

Moulai-khatir D., Pairel E., Favreliere H. (2018), *Influence of the probing definition on the flatness measurement*, International Journal of Metrology and Quality Engineering, Volume 9, 15.

Mangouchi A. (2005), *Exploration des moyens d'association de surfaces aux points palpés sur machine à mesurer tridimensionnelle*, Mémoire de magister, université de Tlemcen, Algérie.

Creative Commons Attribution-NonCommercial-NoDerivatives 4.0 International License (CC BY-NC-ND)

Algerian Journal of Engineering Architecture and Urbanism Vol. 5 Nr. 3 2021
ISSN: 2588-1760

FLUIDE ROTATIF SOUMIS A LA MHD AVEC EFFET HALL AUTOUR UNE PLAQUE VERTICALE EN MOUVEMENT

Zohra BENHARKAT
Docteur, Faculté de Technologie Université de Médéa Algérie,
benharkat2011@yahoo.fr

Résumé:
Cet article présente l'étude de la convection stable avec transfert de chaleur et de masse d'un courant de gaz ionisé en rotation autour une plaque semi-infinie se déplaçant avec une vitesse constante en présence d'un fort champ magnétique où l'effet de Hall est présent. Les équations de similarité sont résolues numériquement, en utilisant la méthode des différences finies, afin de prédire les effets de la vitesse de paroi λ et de la force de Coriolis ξ sur les profils de vitesse, de température et de concentration. Les résultats obtenus montrent que toutes les vitesses diminuent avec l'augmentation de ces paramétres, mais les profils de température et de concentration augmentent. Un comportement opposé se produit sur les nombres de Nusselt Nu_x et de Sherwood Sh_x.

Mots Clés: Magnétohydrodynamique, Effet Hall, Vitesse de paroi, Force de Coriolis, fluide tournant en mouvement.

Introduction:

L'étude d'écoulements industrielles magnétohydrodynamiques, où des phénomènes combinés de transfert thermique et de masse ont lieu comme conséquence des diffusions thermique et d'espèces chimiques, ont des applications importantes dans beaucoup de problèmes de l'ingénierie tel que la conversion d'énergie fossile en énergie électrique, la fusion thermonucléaire de la propulsion, les processus de séchage, le contrôle de la couche limite dans l'aéronautique et l'aérodynamique ou encore les techniques industrielles de la métallurgie. Le plus souvent dans ces écoulements, un courant est induit dans une direction normale aux champs électrique et magnétique. Ce phénomène, bien connu dans la littérature, est appelé l'effet Hall où il devient un phénomène prépondérant dans un gaz ionisé avec une densité faible et/ou un fort champ magnétique. Beaucoup d'investigations sur la convection magnétohydrodynamique thermique et massique ont été publiés où les courants de Hall ne sont pas considérés.

La littérature montre qu'il n'existe que très peu d'études faites sur l'effet d'un champ magnétique sur le transfert de chaleur et de masse de la convection ainsi que celle induite par effet Hall autour une plaque fixe, en mouvement ou en rotation. Les seuls travaux disponibles sont ceux d'Aboeldahab et Elbarbary et Megahed et al. sur la convection doublement diffusive autour une plaque fixe. Les travaux de Kinyanjui et al., Kwanza et al. et Sreedevi et al. sur la convection autour une plaque se déplaçant avec une vitesse constante ou variable. Les travaux de Satya Narayana et al. et G.S. Seth et al. sur la convection dans un système en rotation. Pourtant, les domaines d'applications de ce phénomène sont nombreux où les

Creative Commons Attribution-NonCommercial-NoDerivatives 4.0 International License (CC BY-NC-ND)

phénomènes combinés de transfert thermique et de masse sont associés à des courants très importants de Hall et des effets de rotation où la force de Coriolis a une influence significative sur la dynamique de fluide. Cela concerne aussi bien la géophysique, la géothermique, l'océanographie, l'aéronautique que la métallurgie.

Problématique:

L'étude de l'effet magnétique sur la convection thermique et massique induite par effet Hall d'un courant de fluide en rotation produisant des forces de Coriolis autour un solide en mouvement reste très peu documenté malgré l'intérêt pratique de ce phénomène en ingénierie. La littérature présente quelques travaux liés à cette problématique dans une situation où le solide est une plaque verticale semi-infinie. Le mouvement est ascendant et on se propose d'étudier les effets thermiques et de masse sur le comportement global de ce solide qui se déplace avec une vitesse constante.

Dans ce travail, on se propose de connaître les effets de la vitesse de paroi et de la force Coriolis dans une configuration de convection stable pour une plaque verticale semi-infinie se déplaçant avec une vitesse constante dans un courant de gaz ionisé en rotation lors de transfert thermique et de masse combinés. L'ensemble d'équations aux dérivées partielles non linéaires de probléme avec les conditions aux limites sont transformées, en utilisant la méthode de similarité, à un système d'équations différentielles ordinaires non linéaires avec les conditions aux limites appropriées. En outre, les équations de similarité sont résolues numériquement en utilisant la méthode des différences finies. Les profils de température, de concentration et de vitesse seront établis suivant la dépendance du paramètre caractérisant la vitesse de paroi et du paramètre de force de Coriolis.

Modèle mathématique:

Nous considérons le transfert de chaleur et de masse de la convection stable autour une plaque verticale semi infinie. Nous utilisons les coordonnées cartésiennes rectangulaires (x, y, z), les axes de coordonnées x et y sont respectivement orientés suivant les directions parallèle et normal à la plaque (Fig. 1). La pointe de la plaque doit, par conséquent, être pris comme coïncident avec l'axe z, c'est-à dire avec le plan y=0. Les directions des composantes de vitesse (u, v, w) sont orientés respectivement suivant les axes (x, y, z). Cette plaque se déplace avec une vitesse constante U_1 dans la direction de z dans un fluide visqueux, incompressible et électriquement conducteur qui tourne avec une vitesse angulaire constante Ω autour l'axe-y. Ainsi, une vitesse de courant libre uniforme U_2 est parallèle à l'axe-z.

Un fort champ magnétique externe et uniforme avec une densité constante B_0 est appliqué perpendiculairement à la plaque. Donc, l'écoulement est caractérisé par un très petit nombre de Reynolds magnétique de sorte que le champ magnétique induit est négligeable devant celui qui est imposé.

Afin de simplifier la formulation du modèle mathématique, nous allons considérer la température et la concentration d'espèces à la paroi de la plaque sont T_w ($\neq T_\infty$) et C_w ($\neq C_\infty$), où T_∞ et C_∞ sont la température et la concentration d'espèces du courant libre.

Creative Commons Attribution-NonCommercial-NoDerivatives 4.0 International License (CC BY-NC-ND)

Algerian Journal of Engineering Architecture and Urbanism Vol. 5 Nr. 3 2021
ISSN: 2588-1760

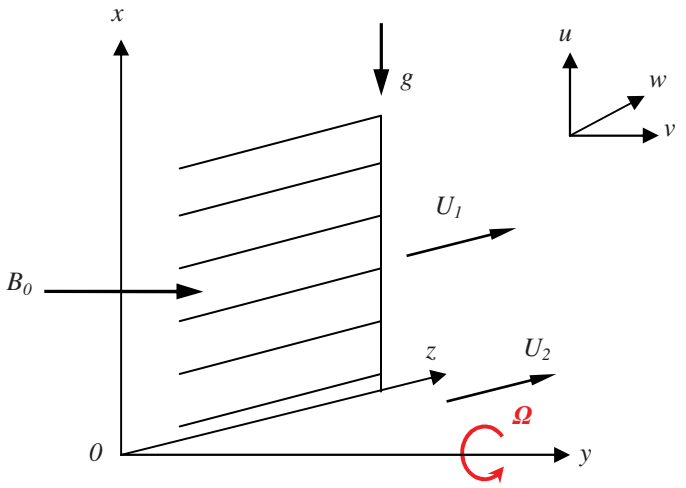

Fig1. Modèle physique et système d'axes

La pression thermoélectrique et le glissement d'ions sont considérés négligeables pour un gaz faiblement ionisé comme notre fluide. Il n'y a aucun champ électrique appliqué, E=0. Les dissipations visqueuse et électrique sont supposées négligeables. La fréquence de collision électron-atome est assumée pour être relativement grand, afin que l'effet de Hall ne puisse pas être négligé. Les effets de courant de Hall donnent l'élévation de force dans la direction z, qui induit un écoulement opposé dans cette direction et d'où, l'écoulement devient à trois dimensions. Pour simplifier le problème, nous supposons qu'il n'y a pas de variation de quantités d'écoulement et du transfert de chaleur dans la direction z.

Ainsi, nous considérons que la plaque est électriquement non-conductrice et par conséquent la densité de courant électrique suivant l'axe y égale à zéro à la plaque, j_y=0. En utilisant les hypothèses simplificatrices précédentes, on obtient le système d'équations qui définie notre problème suivant notre système d'axes:

$$\frac{\partial u}{\partial x}+\frac{\partial v}{\partial y}=0 \tag{1}$$

$$u\frac{\partial u}{\partial x}+v\frac{\partial u}{\partial y}+2\Omega w=-\frac{1}{\rho}\frac{\partial p}{\partial x}+\nu\frac{\partial^2 u}{\partial y^2}+g\beta(T-T_\infty)+g\beta^*(C-C_\infty)-\left(\frac{\sigma B_0^2}{\rho(1+m^2)}\right)(u+mw) \tag{2}$$

$$u\frac{\partial w}{\partial x}+v\frac{\partial w}{\partial y}-2\Omega u=-\frac{1}{\rho}\frac{\partial p}{\partial z}+\nu\frac{\partial^2 w}{\partial y^2}-\left(\frac{\sigma B_0^2}{\rho(1+m^2)}\right)(w-mu) \tag{3}$$

$$u\frac{\partial T}{\partial x}+v\frac{\partial T}{\partial y}=\frac{k}{\rho c_p}\frac{\partial^2 T}{\partial y^2} \tag{4}$$

$$u\frac{\partial C}{\partial x}+v\frac{\partial C}{\partial y}=D\frac{\partial^2 C}{\partial y^2} \tag{5}$$

où ρ est la densité de fluide, ν est la viscosité cinématique de fluide, β et β^* sont respectivement les coefficients d'expansion thermique et de concentration, c_p est la chaleur spécifique à pression constante, D est le coefficient de diffusion d'espèces, k est la conductivité thermique, m est le paramètre de Hall, p est la pression.

Creative Commons Attribution-NonCommercial-NoDerivatives 4.0 International License (CC BY-NC-ND)

Loin de la plaque, un équilibre se produit entre les gradients de pression suivant les directions *x* et *z*, *-∂p/∂x* et *-∂p/∂z*, et les forces de Lorentz et de Coriolis. Cet équilibre est décrit par les équations:

$$-\frac{1}{\rho}\frac{\partial p}{\partial x} = 2\Omega U_2 + \left(\frac{\sigma B_0^2}{\rho(1+m^2)}\right) m U_2 \tag{6a}$$

$$-\frac{1}{\rho}\frac{\partial p}{\partial z} = \left(\frac{\sigma B_0^2}{\rho(1+m^2)}\right) U_2 \tag{6b}$$

Pour les équations (1-5) avec (6a-6b), les conditions aux limites appropriées sont exprimées par

$$\begin{aligned} &u = 0, \quad v = 0, \quad w = U_1, \quad T = T_w, \quad C = C_w \qquad \text{à} \qquad y = 0 \\ &u = 0, \quad w = U_2, \quad T = T_\infty, \quad C = C_\infty \qquad \text{quand} \quad y \to \infty \end{aligned} \tag{7}$$

Pour simplifier la formulation de ce problème on introduit les quantités de similarité utilisées à partir lesquels la variable de similarité η, les vitesses, la température et la concentration prennent la forme

$$\begin{aligned} &\eta = \sqrt{\frac{\Omega}{\nu}}\, y, \quad \psi = \sqrt{\Omega \nu}\, x f(\eta), \quad w = \Omega x h(\eta), \quad \theta(\eta) = (T - T_\infty)/(T_w - T_\infty), \\ &\phi(\eta) = (C - C_\infty)/(C_w - C_\infty), \quad \xi = \Omega x / U, \quad U = U_1 + U_2, \quad \lambda = U_1 / U \end{aligned} \tag{8}$$

où $f(\eta)$, $h(\eta)$, $\theta(\eta)$ et $\phi(\eta)$ sont les fonctions de similarité qui représentent respectivement les composantes de vitesse, λ est la vitesse de paroi, ξ est la force de Coriolis et $\psi(x, y)$ est la fonction du courant relative aux composantes de vitesse exprimée comme suit

$$u = \frac{\partial \psi}{\partial y}, \qquad v = -\frac{\partial \psi}{\partial x} \tag{9}$$

En utilisant les équations (9) et (8), on obtient :

$$u = \Omega x f'(\eta), \qquad v = -\sqrt{\Omega \nu} f(\eta). \tag{10}$$

Les résultats obtenus en termes d'équations de similarité locales sont:

$$f''' - f'^2 + f f'' - 2h + Gr\ \theta + Gc\ \phi - \frac{M}{(1+m^2)}\left[f' + m\left(h + \frac{(\lambda-1)}{\xi}\right)\right] + \frac{2(1-\lambda)}{\xi} = 0 \tag{11}$$

$$h'' + f h' - f' h + 2f' - \frac{M}{(1+m^2)}\left[h - m f' + \frac{(\lambda-1)}{\xi}\right] = 0 \tag{12}$$

$$\theta'' + Pr\, f \theta' = 0 \tag{13}$$

Creative Commons Attribution-NonCommercial-NoDerivatives 4.0 International License (CC BY-NC-ND)

$$\phi'' + Scf\phi' = 0 \tag{14}$$

Les perfections indiquent la différenciation par rapport η, $M=\sigma B_0^2/\rho\Omega$ est le paramètre magnétique, $Gr=g\beta(T_w-T_\infty)/\Omega^2 x$ est le nombre de Grashof dû aux différences de la température, $Gc=g\beta^*(C_w-C_\infty)/\Omega^2 x$ est le nombre de Grashof massique, $Pr=\rho v c_p/k$ est le nombre de Prandtl et $Sc=v/D$ est le nombre de Schmidt.

Les conditions aux limites transformées sont

$$f'(0)=0, \quad f(0)=0, \quad h(0)=\frac{\lambda}{\xi}, \quad \theta(0)=1, \quad \phi(0)=1,$$
$$f'(\infty)=0, \quad h(\infty)=\frac{1-\lambda}{\xi}, \quad \theta(\infty)=0, \quad \phi(\infty)=0. \tag{15}$$

Une attention particulière aux nombre locaux de Nusselt et de Sherwood qui sont exprimés respectivement par

$$Nu_x=\frac{xh_w}{k}=-Re_x^{1/2}\theta'(0), \quad \text{ou} \quad Nu_x Re_x^{-1/2}=-\theta'(0) \tag{16}$$

$$Sh_x=\frac{xh_m}{k}=-Re_x^{1/2}\phi'(0), \quad \text{ou} \quad Sh_x Re_x^{-1/2}=-\phi'(0) \tag{17}$$

où h_w est le coefficient de transfert thermique, h_m est le coefficient de transfert de masse et $Re_x=x^2\Omega/v$ est le nombre de Reynolds local.

Résultats et discussions:

Le système d'équations de similarité (11-14) avec les conditions aux limites (15) sont résolus numériquement en employant l'algorithme de Runge-Kutta d'ordre 4 programmé sous logiciel MATLAB 6.5. Les résultats numériques sont présentés graphiquement. Les figures (Fig. 2)-(Fig. 5) présentent l'effet de paramètre de la vitesse de paroi λ sur le comportement des profils de vitesse f' et h, de température θ et de concentration ϕ de fluide pour $M=m=\xi=1$. La figure (Fig. 2) montre que la vitesse transversale f' diminue progressivement avec l'augmentation de paramètre λ. Nous remarquons clairement sur ces courbes que l'effet de l'augmentation de paramètre λ était d'inverser la vitesse f' qui s'explique par le fait concurrentiel entre les vitesses de plaque et de fluide. Sur la figure (Fig. 3), nous remarquons que lorsque le paramètre λ augmente, la vitesse axiale h augmente pour environ $0\leq\eta\leq0.5$ alors que cette dernière diminue quand $\eta>0.5$.

De plus, sur les figures (Fig. 4) et (Fig. 5), nous observons que les températures et les concentrations sont intensifiées avec l'augmentation de λ et par conséquent les transferts convectifs de chaleur et de l'espèce sont réduits. Ceci est présenté dans le tableau (Table1).

Creative Commons Attribution-NonCommercial-NoDerivatives 4.0 International License (CC BY-NC-ND)

Algerian Journal of Engineering Architecture and Urbanism Vol. 5 Nr. 3 2021
ISSN: 2588-1760

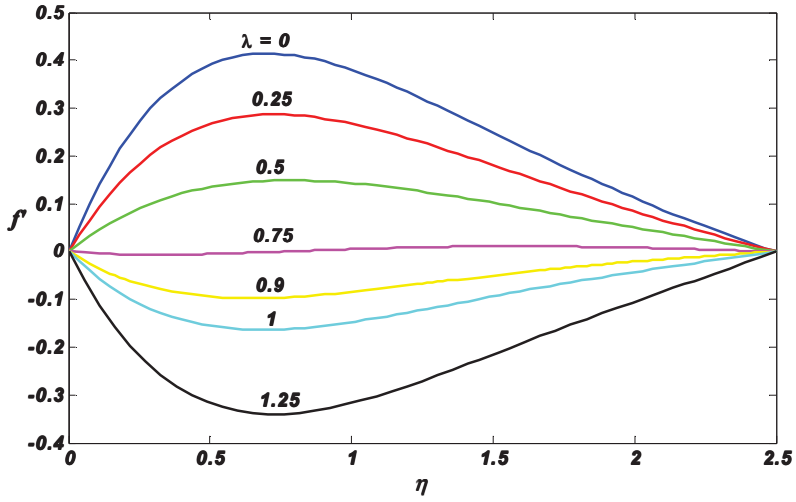

Fig2. Effet de λ sur le profil de x-vitesse pour Pr=0.71, Sc=0.22, M=1, m=1, ξ=1

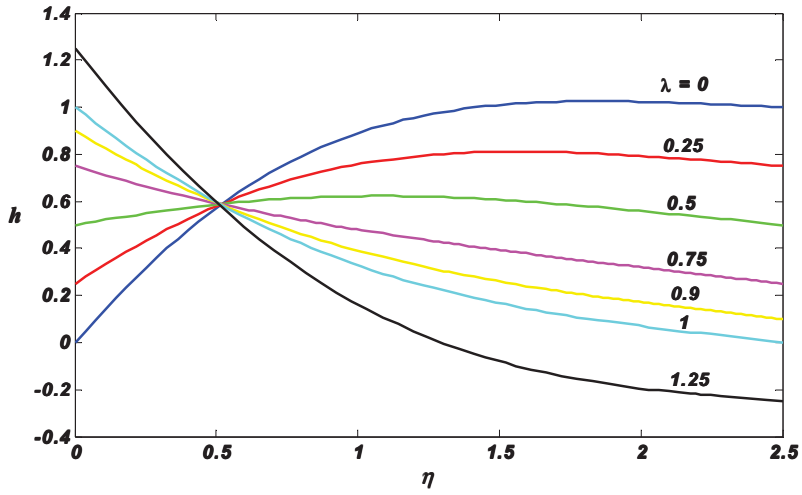

Fig3. Effet de λ sur le profil de w-vitesse pour Pr=0.71, Sc=0.22, M=1, m=1, ξ=1

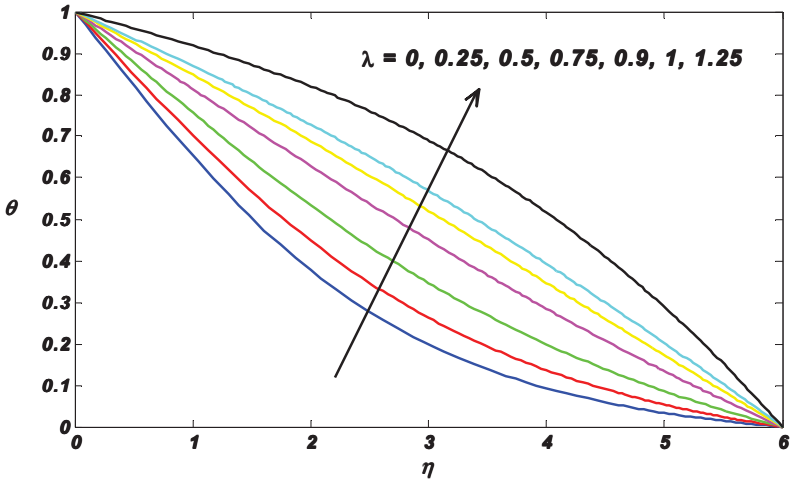

Fig4. Effet de λ sur le profil de température pour Pr=0.71, Sc=0.22, M=1, m=1, ξ=1

Creative Commons Attribution-NonCommercial-NoDerivatives 4.0 International License (CC BY-NC-ND)

Les figures (Fig. 6)-(Fig. 9) présentent l'effet de paramètre de la force de Coriolis ξ sur le comportement des profils de vitesse, de température et de concentration de fluide pour $M=m=\xi=1$ et $\lambda=0.25$. Les figures (Fig. 6) et (Fig. 7) montrent que la vitesse est notablement affectée par la force de Coriolis. Nous constatons clairement sur ces courbes que les profils de vitesse f' et h diminuent avec l'accroissement du ξ. Ceci est montré physiquement, c.-à-d., l'augmentation de la force de Coriolis tend à ralentir les vitesses. D'un autre côté, pour une valeur donnée de ξ, la vitesse h varie fortement près de la plaque. Les figures (Fig. 8) et (Fig. 9) montrent que, à mesure que le paramètre ξ augmente, les profils de température et de concentration augmentent aussi. Donc, les transferts de chaleur et de masse sont réduits aussi, tel que indiqué par le tableau (Table1).

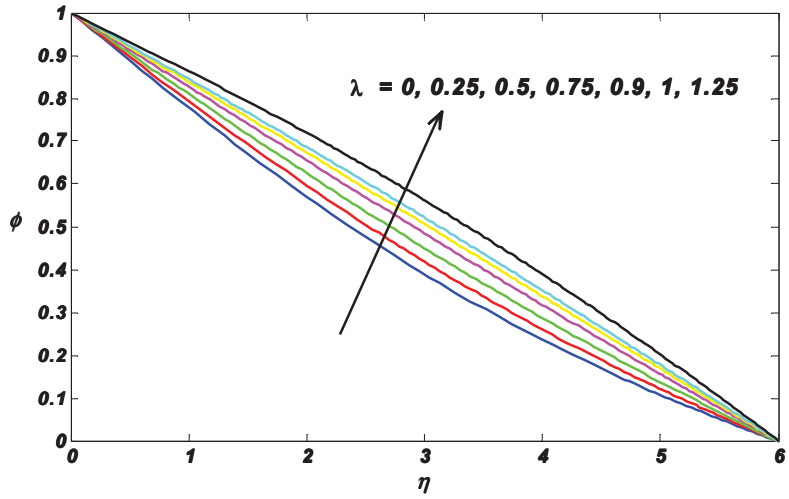

Fig5. Effet de λ sur le profil de concentration pour Pr=0.71, Sc=0.22, M=1, m=1, ξ=1

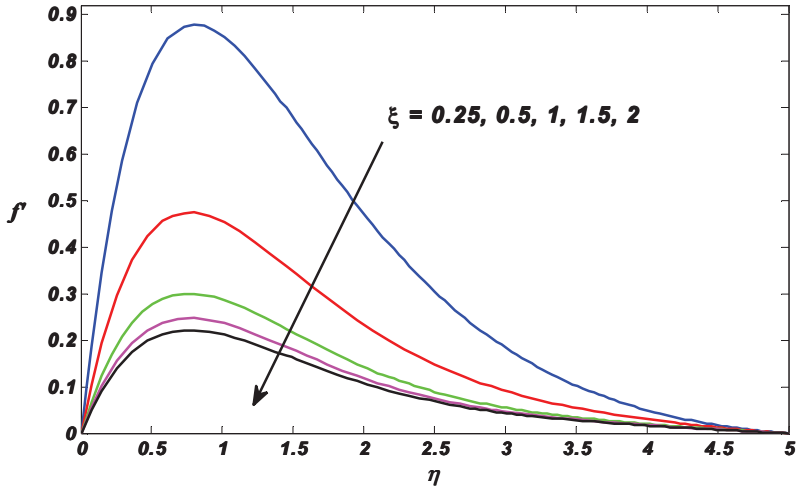

Fig6. Effet de ξ sur le profil de x-vitesse pour Pr=0.71, Sc=0.22, M=1, m=1, λ=0.25

Creative Commons Attribution-NonCommercial-NoDerivatives 4.0 International License (CC BY-NC-ND)

Algerian Journal of Engineering Architecture and Urbanism Vol. 5 Nr. 3 2021
ISSN: 2588-1760

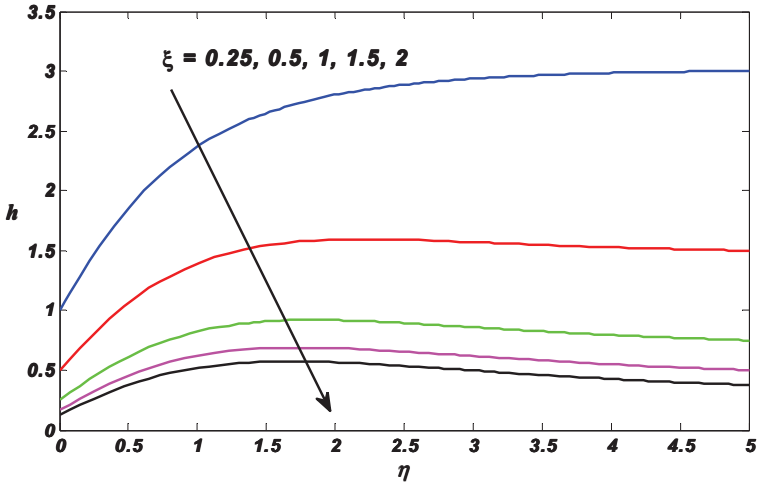

Fig7. Effet de ξ sur le profil de w-vitesse pour Pr=0.71, Sc=0.22, M=1, m=1, λ=0.25

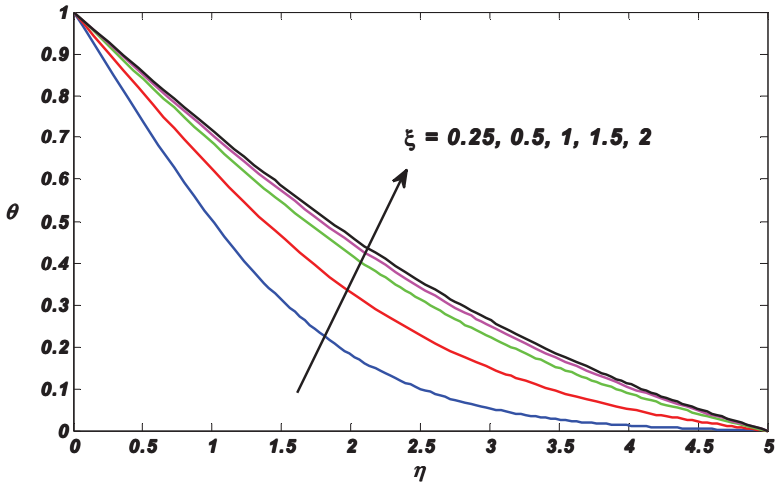

Fig8. Effet de ξ sur le profil de température pour Pr=0.71, Sc=0.22, M=1, m=1, λ=0.25

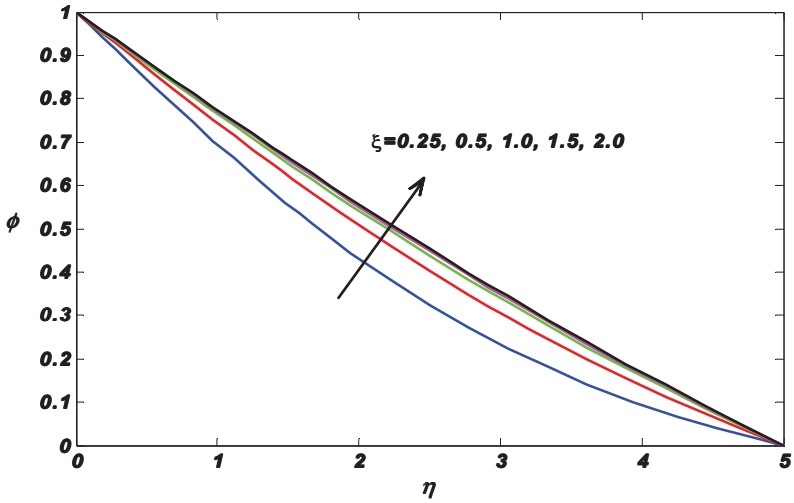

Fig9. Effet de ξ sur le profil de concentration pour Pr=0.71, Sc=0.22, M=1, m=1, λ=0.25

Creative Commons Attribution-NonCommercial-NoDerivatives 4.0 International License (CC BY-NC-ND)

Dans le tableau (Table1), on reporte les valeurs des nombres *Nu* et *Sh* pour des différentes valeurs de λ et ξ. Ces résultats montrent que si on augmente la force de Coriolis ξ, les nombres *Nu* et *Sh*, c'est-à-dire les taux de transferts de chaleur et de l'espèce, augmentent aussi. Un comportement opposé se produit si on augmente la vitesse à la paroi λ. Il est intéressant de noter qu'un excellent taux d'échange de chaleur et de masse peut être obtenu par une grande vitesse de rotation du fluide avec une faible vitesse de la plaque.

λ	ξ	Nu	Sh
0.25	1	0.3485	0.2801
0.5	1	0.3040	0.2666
0.75	1	0.2573	0.2523
0.25	0.5	0.3090	0.2678
0.25	1	0.3485	0.2801
0.25	1.5	0.3622	0.2845

Table 1. Valeurs numériques de *Nu* et *Sh* pour différentes valeurs de λ et ξ avec M=1, m=1, Gr=0.5, Gc=0.5, Pr=0.71 et Sc=0.22.

Conclusion:

Les équations qui régissent la convection stable avec transfert de chaleur et de masse d'un courant de gaz ionisé en rotation autour une plaque semi-infinie se déplaçant avec une vitesse constante en présence d'un fort champ magnétique ont été formulées sans négliger l'effet Hall. Une transformation de similarité a été utilisée pour obtenir un système d'équations différentielles ordinaires ceux qui sont résolu numériquement. Les résultats numériques obtenus indiquent que:

L'augmentation de la vitesse de paroi cause la réduction des vitesses et l'augmentation de la température et de la concentration.

L'augmentation de la force de Coriolis tend à ralentir les vitesses transversale et axiale et à augmenter la température et la concentration.

On observe des effets intéressants en couplant les paramètres spécifiques étudiés sur les coefficients de transfert de chaleur et de masse qui sont accentués ici.

Références:

Aboeldahab E.M., Elbarbary E.M.E. (2001), *Hall current effect on magnetohydrodynamic free-convection flow past a semi-infinite vertical plate with mass transfer*, International Journal of Engineering Science **39(14):** 1641-1652.

Chamkha A. J. (2004), *Unsteady MHD convective heat and mass transfer past a semi-infinite vertical permeable moving plate with heat absorption*, International Journal of Engineering Science **42(2):** 217-230.

Kinyanjui M., Kwanza J. K., Uppal S. M. (2001), *Magnetohydrodynamic free convection heat and mass transfer of a heat generating fluid past an impulsively started infinite vertical porous plate with Hall current and radiation absorption*, Energy Conversion and Management **42(5-6):** 917-931.

Kwanza J. K., Marigi E. M., Kinyanjui M. (2010), *Hydromagnetic free convection currents effects on boundary layer thickness*, Energy Conversion and Management **51(6):** 1326-1332.

Creative Commons Attribution-NonCommercial-NoDerivatives 4.0 International License (CC BY-NC-ND)

Megahed A.A., Komy S.R., Afify A.A. (2003), *Similarity analysis in magnetohydrodynamics: Hall effects on free convection flow and mass transfer past a semi-infinite vertical flat plate*, International Journal of Non-Linear Mechanics **38:** 513-520.

Mohamed R.A., Abo-Dahab S.M. (2009), *Influence of chemical reaction and thermal radiation on the heat and mass transfer in MHD micropolar flow over a vertical moving porous plate in a porous medium with heat generation*, International Journal of Thermal Sciences **48(9):** 1800-1813.

Satya Narayana P. V., Venkateswarlu B., Venkataramana S. (2013), *Effects of Hall current and radiation absorption on MHD micropolar fluid in a rotating system*, Ain Shams Engineering Journal **4(4):** 843-854.

Seth G.S., Sarkar S., Hussain S.M. (2014), *Effects of Hall current, radiation and rotation on natural convection heat and mass transfer flow past a moving vertical plate*, Ain Shams Engineering Journal **5(2):** 489-503.

Sharma R., Bhargava R., Bhargava P. (2010), *Numerical solution of unsteady MHD convection heat and mass transfer past a semi-infinite vertical porous moving plate using element free Galerkin method*, Computational Materials Science **48(3):** 537-543.

Sreedevi G., Raghavendra Rao R., Prasada Rao D.R.V., Chamkha A.J. (2016), *Combined influence of radiation absorption and Hall current effects on MHD double-diffusive free convective flow past a stretching sheet*, Ain Shams Engineering Journal **7(1):** 383-397.

Creative Commons Attribution-NonCommercial-NoDerivatives 4.0 International License (CC BY-NC-ND)

Algerian Journal of Engineering Architecture and Urbanism Vol. 5 Nr. 3 2021
ISSN: 2588-1760

4,4''-bis(pyrrylideneimino)-3,3''-dimethylbiphnyle: Synthesis and application in organic photovoltaic cell

PhD student. Younes BENNACER

Laboratoire de Chimie des Matériaux Constantine (LCMC), Route de Aïn El Bey, Constantine. Algérie.

younes.bennacer43200@gmail.com

Dr. Mounia GUERGOURI

Université des Frères Mentouri de Constantine, Département de Chimie, Laboratoire de Chimie des Matériaux Constantine (LCMC), Route de Aïn El Bey,25000, Constantine. Algérie.

m.guergouri@hotmail.fr

Abstract:
The aim of this study is the synthesis of 4,4"-bis(pyrrylideneimino)-3,3"-dimethylbiphenyle, a new o-tolidine-based fluorescent compound, and its use in Organic Photovoltaic cell (OPV) as acceptor material. The structure identification of the compound has been done by IR and NMR spectroscopies, while the optical properties have been revealed by UV-visible and fluorescence spectroscopies. The compound is a fluorophore that show two absorption peaks, the first in the ultraviolet at and the second in the near ultraviolet. The optical gap was estimated from the absorption thresholds. The electrochemical study was carried out by cyclic voltammetry on a platinum electrode in tetrabutylammonium hexafluorophosphate (0.1M)/ DMSO. The voltammograms obtained allowed us to calculate the energy values of HOMO and LUMO as well as the electrochemical gap. Based on the values of the energy gap estimated by both of optical and electrochemical studies, and based on the values of HOMO and LUMO, this work has led to a conclusion that this compound is a good candidate to be used as an acceptor material in bilayer photovoltaic cells with poly(3-hexylthiophene) as donor material.
Key words: Organic photovoltaic cell, Cyclic voltammetry, Fluorescence.

Introduction:

The use of conjugated organic compounds in photovoltaic cells represents a promising alternative to conventional inorganic components essentially because of their environmental compatibility and low cost [1,2].

In this work, we synthesized a new fluorescent compound, 4,4"-bis(pyrrylideneimino)-3,3"-dimethylbiphenyle (PTO), by the means of a simple method with a good yield. Furthermore, we characterized its photophysical and electrochemical properties to determinate their possible use as acceptor material in a bilayer organic photovoltaic cells, where poly(3-hexylthiophene) is set as donor material.

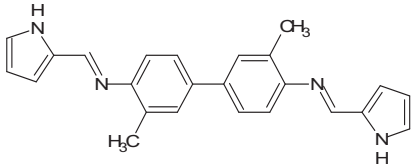

4,4"-bis(furylideneimino)-3,3"-diméthylbiphenyle (PTO)

Creative Commons Attribution-NonCommercial-NoDerivatives 4.0 International License (CC BY-NC-ND)

Algerian Journal of Engineering Architecture and Urbanism Vol. 5 Nr. 3 2021
ISSN: 2588-1760

Materials and methods:

3,3'-dimethyl-1,1'-biphenyl-4,4'-diamine (O-tolidine), Pyrrole-2-carboxaldehyde, Tetrabutyl-ammonium hexafluorophosphate ($TBAPF_6$) (≥ 99.0% for electrochemical analysis), Ethanol and DMSO (Dimethyl Sulfoxide) were obtained from Sigma-Aldrich. All products were used without further purification. UV-visible spectrum was recorded with JASCO V-660 spectrophotometer. Fluorescence spectrum was obtained on a Perkin Elmer LS 50 luminescence spectrometer. Electrochemical experiments were performed using a glassy carbon disk (GCE) as working electrode and Ag/AgCl as reference. A three-electrode cell was used with electrodes connected to a Voltalab Potentiostat, which was interfaced to a computer. All solutions were deaerated by bubbling with argon gas for 10 minutes prior to electrochemical measurements.

Results and discussions:

Synthesis of molecule

PTO was prepared by condensation between o-tolidine and Pyrrole-2-carboxaldehyde in ethanolic medium (Scheme1).

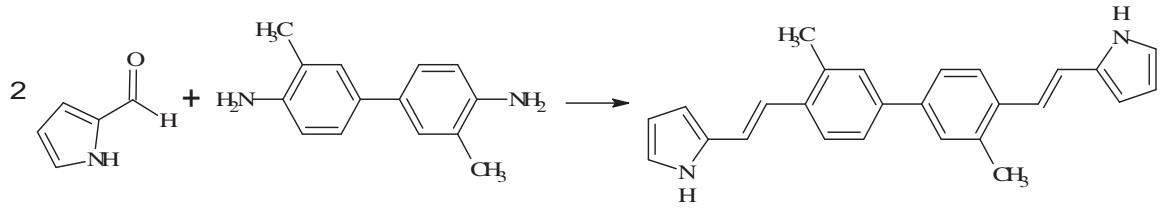

***Scheme 1**: Reaction scheme of the PTO synthesis*

Photophysical properties of PTO

The electrical properties of compounds depend on their structures and on the delocalization of π electrons. The band gap, which is an important factor in determining these properties, can be calculated from cyclic voltammetry or from UV-visible spectroscopy.

The UV-visible measurements were carried out at room temperature with a concentration of 5.10^{-5} M of PTO (Figure 1). The values obtained are listed in Table 1.

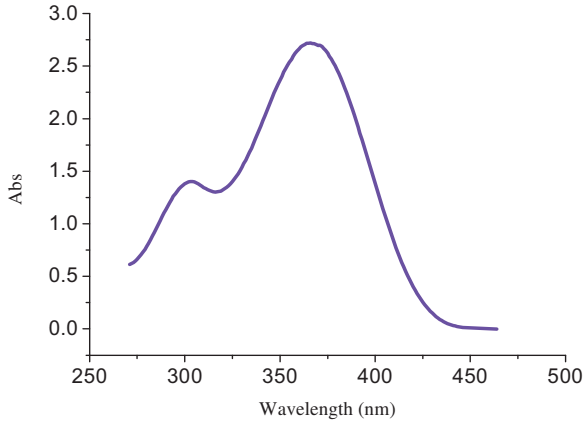

***Figure 1 :** UV-visible spectrum of PTO,*

Creative Commons Attribution-NonCommercial-NoDerivatives 4.0 International License (CC BY-NC-ND)

Table 1. Optical properties of PTO

Compound	λ_{max}	λ_{seuil}	$E_{g\text{-}opt}$
PTO	368	433	2,86

The electronic absorption of PTO exhibit two absorption bands at 304 and 366 nm. The first band was due to a $\pi \rightarrow \pi^*$ transition, while the second was certainely due to $n \rightarrow \pi^*$ transition. The optical bandgap is calculated according to $E_{g\text{-}opt} = 1240/\lambda_{onset}$, where λ_{onset} is obtained from the intersection between the baseline and the tangent of the second band-end.

The fluorescence of the PTO is carried out with a concentration of 5×10^{-6} M. The emission spectrum obtained (Figure 2) shows that the PTO is fluorescent and emits within the visible limit.

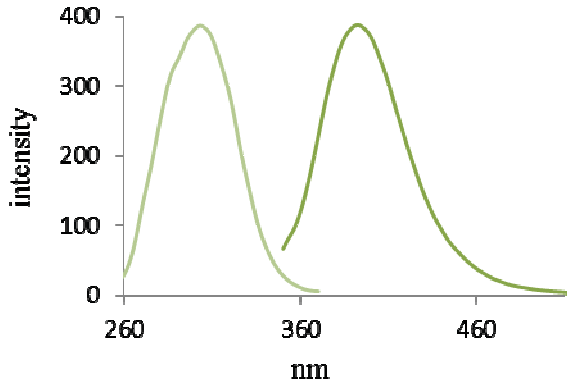

Figure 2 : *Emission spectrum of PTO,*

Electrochemical properties of PTO

The electrochemical behaviour of PTO was investigated on a GCE electrode by cyclic voltammetry (CV).

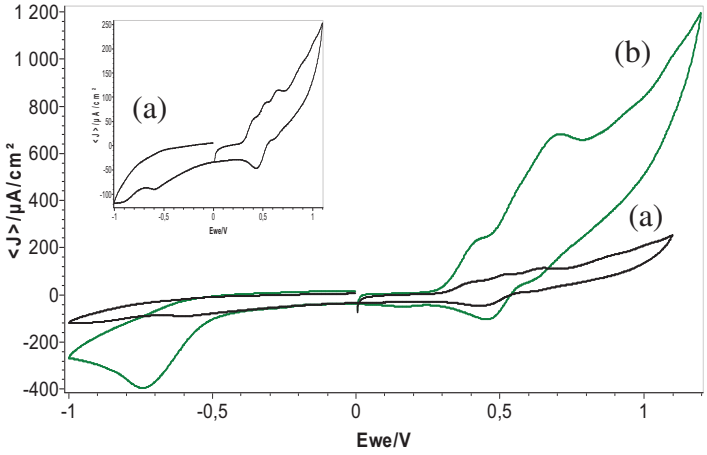

Figure 3: *Voltammograms of PTO recorded in $TBAPF_6$ (0.1M)/ DMSO with v = 50 mV/s. (a) 10^{-3}M, (b)10^{-2} M.*

Creative Commons Attribution-NonCommercial-NoDerivatives 4.0 International License (CC BY-NC-ND)

The voltammogram obtained during electrooxidation of 10^{-3} M of PTO in Bu_4NPF_6 (0.1M)/DMSO, showed two oxidation peaks at 0.44 and 0.712 V and two reduction peaks at 0.455 and -0.74 V, respectively.

HOMO and LUMO energy levels could be estimated from the onsets of oxidation and reduction potentials, respectively [3]. The difference between HOMO and LUMO energies, give the electrochemical gap value (E_{gap}^{el}). The obtained results were summarized in Table 2.

Table 2. Electrochemical properties of PTO

Compound	E_{Onset}^{OX} (eV)	E_{onset}^{Red} (eV)	HOMO (eV)	LUMO (eV)	E_{gap}^{el}
PTO	0,87	-0,2	-5,27	-4,2	1,07

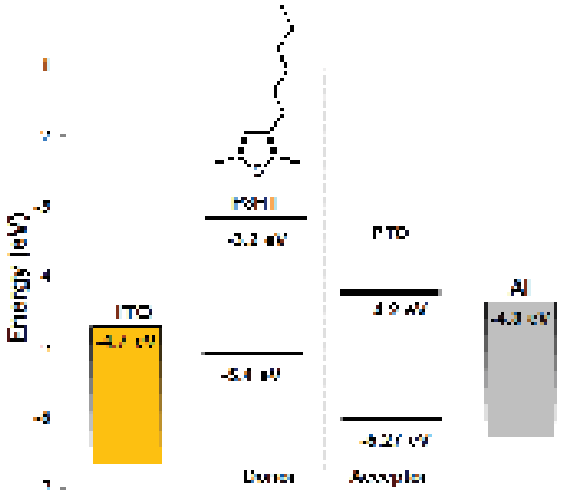

Figure 4: *HOMO and LUMO energy levels calculated for PTO and compared to different components in bilayer organic photovoltaic cell of which P3HT is the donnor material.*

The most critical requirements for this organic compound in order to be used as acceptor material in bilayer photovoltaic cells are a low band gap and harmony between their HOMO/LUMO levels and those of the other cell components [4]. The Fermi level of the electrons in ITO (with a work function of 4.7 eV [5]) was slightly higher than the HOMO energy of P3HT with a difference which allows to an electron to move from the ITO to the HOMO of P3HT. The LUMO level of P3HT is higher than the LUMO level of PTO. The energy offset between these two levels ensures an efficient excitation dissociation and an electron transfer. Indeed, to achieve higher power conversion efficiency, the compound must offer a high open circuit voltage (V_{OC}), which represents the maximum voltage a solar cell can provide to an external circuit [6], and which is proportional to the difference between its LUMO and the donnor's HOMO [7]. The Voc value calculated using a theoretical empirical equation [8] is 0.8V, which is a promising value.

These results satisfy the criteria cited above and place PTO among serious acceptor material candidates for bilayer organic photovoltaic cell with P3HT as donnor, ITO as positive electrode and aluminum as negative electrode [9].

Creative Commons Attribution-NonCommercial-NoDerivatives 4.0 International License (CC BY-NC-ND)

Conclusion:

We have synthesized a new fluorescent compound. Based on the values of the energy gap estimated by both of optical and electrochemical studies, and based on the values of HOMO and LUMO, this work has led to a conclusion that the synthesized compound can be used in bilayer photovoltaic cells as an acceptor material with P3HT as donor material. Indeed, the results show a low band gap of PTO, and harmony between its HOMO/LUMO levels and those of P3HT, as well as between them and the other cell components. Indeed, the energy between the LUMO of PTO and the LUMO of P3HT ensures the excitation dissociation and the electron transfer. In addition, the LUMO of PTO is higher than Fermi level of Al, used as cathode, which ensure the electron transfer from the acceptor to the cathode.

References:

[1] Forrest S. R. (2004), *The path to ubiquitous and low-cost organic electronic appliances on plastic,* Nature. **428:** 911-918.
[2] Shinar R., Shinar, J. (2009), *Organic Electronics in Sensors and Biotechnology,* New York: McGraw-Hill.
[3] Bredas J. L., Silbey R., Boudreux D. S., Chance, R. R. (1983), *Chain-length dependence of electronic and electrochemical properties of conjugated systems: polyacetylene, polyphenylene, polythiophene, and polypyrrole*, J. Am. Chem. Soc. **105:** 6555-6559.
[4] Tang C. W., (1986), *Two-layer organic photovoltaic cell*, Appl. Phys. Lett. **48**: 183-185.
[5] Chirvase D., Chiguvare Z., Knipper M., Parisi J., Dyakonov V., Hummelen J. C.(2003), *Temperature dependent characteristics of poly(3 hexylthiophene)-fullerene based heterojunction organic solar cells*, J. Appl.Phys. **93(6):** 3376-3383.
[6] Bundgaard E., Krebs F. C.(2007), *Low band gap polymers for organic photovoltaics,* Solar Energy Materials and Solar Cells. **91:** 954-985.
[7] Dennler G., Scharbe, M. C., BrabecC. J. (2009) , *Polymer-Fullerene Bulk-Heterojunction Solar Cells,* Adv. Mater. **21:** 1323-1338 (2009).
[8] Scharber M. C., Mühlbacher D., Koppe M., Denk P., Waldauf C., Heege, A. J., Brabec C. J. (2006), *Design Rules for Donors in Bulk-Heterojunction Solar Cells—Towards 10% Energy-Conversion Efficiency,* Adv. Mater. **18:** 789-794 (2006).
[9] Thompson B. C., J. Fréchet M. J. (2008), *Polymer-fullerene composite solar cell,.* Angew. Chem. Int. Ed. **47:** 58-77 (2008).

Creative Commons Attribution-NonCommercial-NoDerivatives 4.0 International License (CC BY-NC-ND)

Algerian Journal of Engineering Architecture and Urbanism Vol. 5 Nr. 3 2021
ISSN: 2588-1760

IMPROVEMENT OF THE MANUFACTURING PROCESS.

Ph.D .Boualamallah Djamal,
Laboratory of materials and reactive system(LMSR), University Djillali liabès of sidi bel abbes (Algeria)-Faculty of sciences of the engineer, Department of Technology BP.89 Cité Larbi Ben Mhidi, 22000 Sidi Bel Abbes, Algeria .
Djamal.Boualamallah@yahoo.com
DR.Ghazi Abdelkader
Department of Mechanical Engineering, University of Mascara.29000.
Laboratory of materials and reactive system(LMSR), University Djillali liabès of sidi bel abbes (Algeria).
ghaziaek@yahoo.fr
DR.Miloudi Abdelkader
Laboratory of materials and reactive system(LMSR), University Djillali liabès of sidi bel abbes (Algeria)-Faculty of sciences of the engineer, Department of Technology BP.89 Cité Larbi Ben Mhidi, 22000 Sidi Bel Abbes, Algeria .
miloudidz@yahoo.fr

Abstract:
The improvement of the manufacturing process is a very delicate operation. It is an operation which must be carried out with much tact especially for a company in full mutation of the unit production (prototyping) to the mass production of complex parts. The improvement of a manufacturing process must meet the needs of the company. In order to propose a commendable improvement to a company, several actions must be taken, the first of which is the analysis of the company's industrial practices at a given time. The analysis of the current industrial practices of the company made it possible to present a reflection of the state of the art. This analysis resulted in the creation of a database that summarizes the way parts are programmed. The analysis of the industrial practices is only an introduction to the development of an optimized manufacturing process. The improvement of the whole manufacturing process starts with the reception of the customer's specifications and ends with the shipment of the finished and good parts to the customer.
The analysis of all the manufacturing steps of the company was carried out. The result of this improvement allowed to improve the steps of the manufacturing process by adding the necessary actions and participants.

Key words: Improvement, manufacturing process, production gesture.

Introduction:

Research on the improvement of machining processes goes back to Taylor, who wanted to minimize production time (Debongnie, 1993). The improvement of a manufacturing process is the search to make it better. A manufacturing process includes all the steps necessary to manufacture a part. The steps necessary to manufacture a part are all the actions from the reception of the customer's specifications to the shipment of the good parts to the customer. The improvement of a manufacturing process allows the elimination of all dead times in the

Creative Commons Attribution-NonCommercial-NoDerivatives 4.0 International License (CC BY-NC-ND)

production chain. Many studies have been done regarding the reduction of machining downtime (Debongnie, 1993). One study shows that machining idle time has been significantly reduced and that machining time itself is now a significant part of the cost (Merchant, 1993).

To begin an improvement process, one must have a goal to achieve. Companies must have a focus on improving the cost and quality of their products. The overriding need is to optimize processes in order to survive in the tough competition of the high precision machining market. The company must implement a policy of continuous improvement of the manufacturing processes it uses. Nash, Poling and Ward, (2006) emphasize that **"good enough today is never good enough for tomorrow".**

Problematic:

The identification of the object to be improved is an important step in the optimization process. It is therefore necessary to clearly identify the object to be improved. The identification of the object to be improved is based on the observation of what is important for the success or even the survival of the company. In the case of APN Inc. the main priority is the production of high quality parts at the lowest possible manufacturing cost in order to obtain the greatest possible profit. The identification of the first priority of the company directs this study towards the improvement of the whole manufacturing process because, a good manufacturing process leads to a stable production in lean, consequently generates good parts and at lower manufacturing cost. One method of improving processes by eliminating losses is the use of Lean.

Lean helps identify and eliminate waste through continuous improvement. The important thing in Lean is not to look at what needs to be added to improve the process, but what is taken away (Nash, Poling and Ward, 2006). Identifying losses is an exercise to be done when using Lean to optimize a process, because there is often a tendency to think that eliminating observed losses will solve the problem (Nash, Poling and Ward, 2006). This is why, in order to identify the causes of losses, we must try to trace the main and not the supposed causes. Some causes are like an iceberg and others like a magic candle. The iceberg causes are those that hide the main reasons for wasted time and the magic candle causes are those that come back even when they are eliminated. There are many steps that are sources of wasted time, but they can only be detected with good management and organization methods of the manufacturing process (Pierrette, 1968). The actions to be taken for the identification and elimination of idle time are the following:

- identify losses and actions that have no value added
- Classify each loss;
- explore the root causes of losses and explore probable and potential solutions;
- streamline and simplify the work;
- eliminate as many unnecessary actions as possible.

The identification of the losses also implies a good knowledge maintained up to date, of the workstations, of their place and importance in the process of manufacture, of the real capacities of the park of the machine tools and of the machinability of the materials used. It was demonstrated by the Germans that the most considerable gains in productivity that could

Creative Commons Attribution-NonCommercial-NoDerivatives 4.0 International License (CC BY-NC-ND)

be expected were not obtained in the long term, thanks to too high standards of output, but essentially by an improvement of the methods, by the reduction of waste and by the training of the personnel as well as that of the senior executives as that of the workers (Pierrette, 1968). Figure 1 shows a breakdown of the total duration of a production or operation (Pierrette, 1968). Figure 2 shows the unproductive time attributable to management or workers .

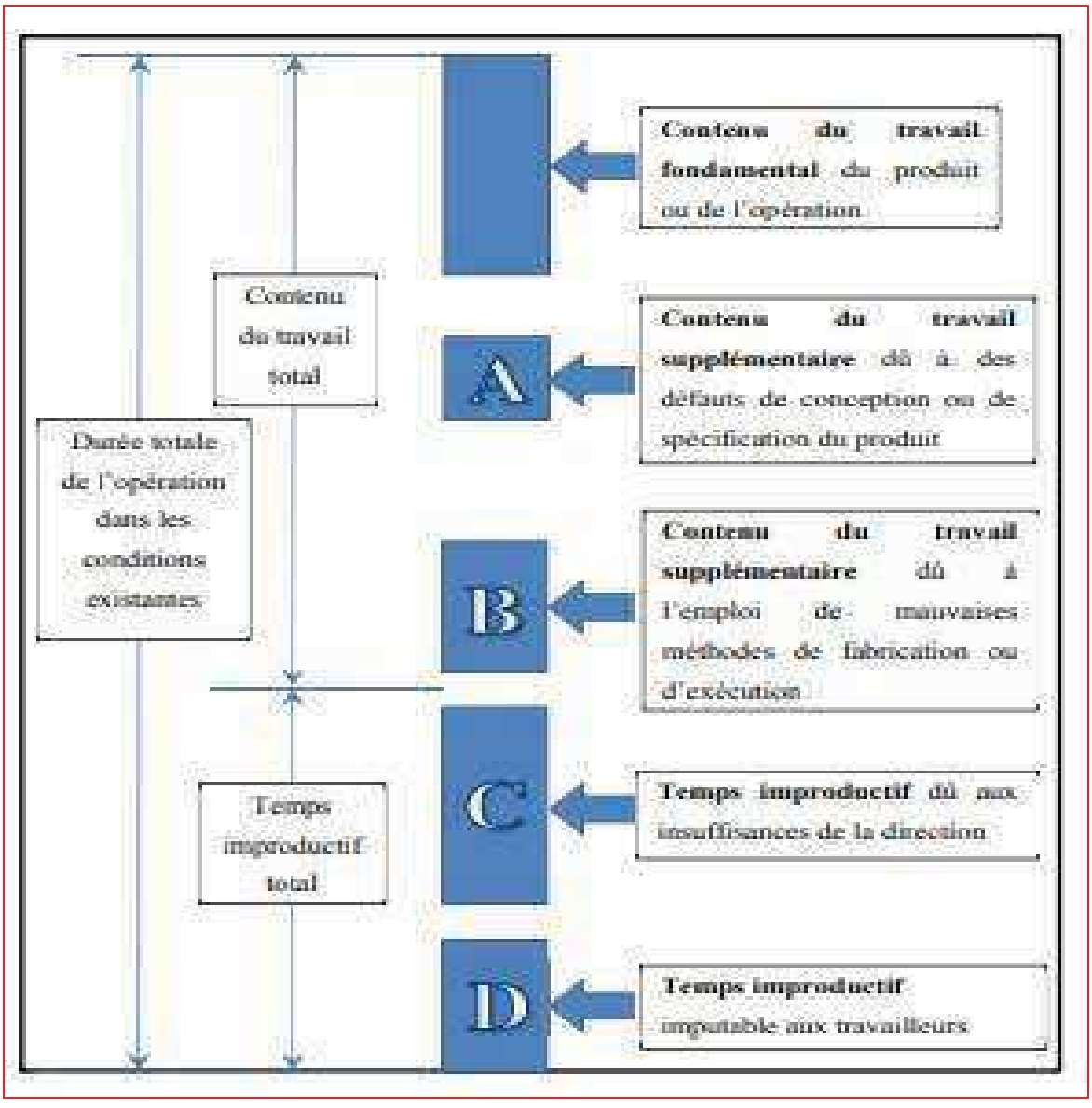

Figure 1: Breakdown of total manufacturing or operation time (Pierrette, 1968) .

Creative Commons Attribution-NonCommercial-NoDerivatives 4.0 International License (CC BY-NC-ND)

Algerian Journal of Engineering Architecture and Urbanism Vol. 5 Nr. 3 2021
ISSN: 2588-1760

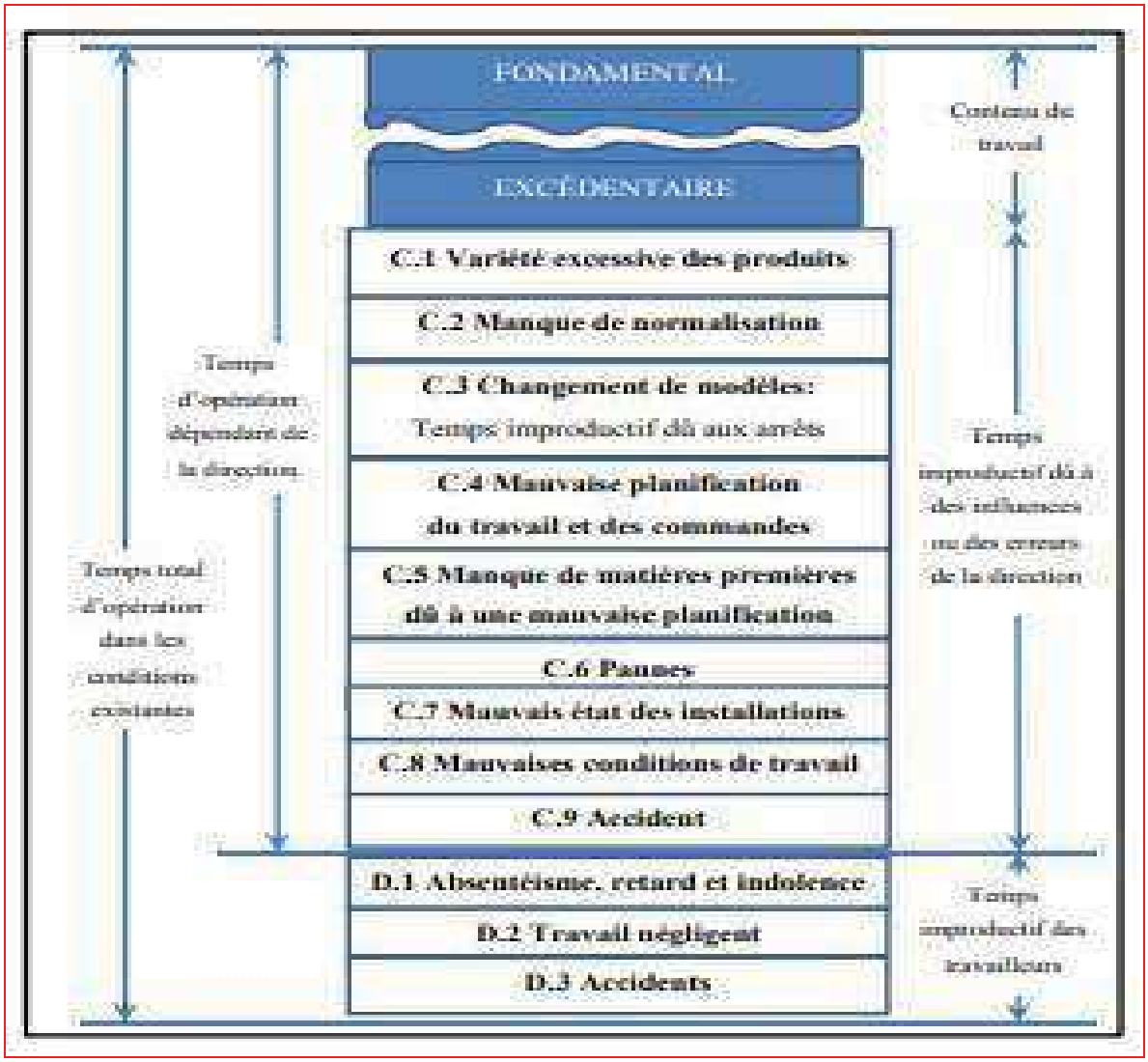

Figure 2: Unproductive time attributable to management or workers (Pierrette, 1968) .

Figures 1 and 2 are very supportive and companies can adapt these figures to their reality to help identify the different idle times observed in the manufacturing process. After the identification of the idle times, figures 1 and 2 help to locate the sources of the time losses. The identification and localization of the time losses and their sources guide the choice of targets for future optimization and significant time savings. The time savings achieved by optimizing the machining processes are quickly reduced or dissolved by a poorly organized production process. This can be seen from the large amount of non-productive time caused by the influence of the management, which is nothing more than the organization of the production process. This organization largely influences the production time. The time of a production is the addition of the basic time and the surplus time. The basic time is also called the real working time. It is the one used if an optimal organization of the production was used. The excess time is still called overtime due to a bad planning of the production. To obtain the time of a production, it is necessary to identify, quantify and measure the work of each step of the manufacturing process. This leads to thinking about optimizing the process by answering the questions of whether the quantity and quality of the tasks at a given level and the time

Creative Commons Attribution-NonCommercial-NoDerivatives 4.0 International License (CC BY-NC-ND)

allocated are optimal. It has been found that, on an eight-hour workday, 62 to 73% of the time is actually used for production in organized firms and 32 to 42% in those that are less well organized (Pierrette, 1968). The reduction or even elimination of wasted time requires a study of it. A good analysis of wasted time requires a good enumeration of its sources.

Enumeration of sources of wasted time

Very often, time losses represent almost one third of the time actually spent to manufacture the product or to carry out the operation. All these time losses lengthen and slow down the production time without any profit. They increase the manufacturing costs and decrease the general productivity of the company. The sources of wasted time are: additional work or rework;

- Poor product design;
- Poor design of operations;
- Too much diversity of models;
- lack of product standardization;
- lack of or non-compliance with work methods
- Incorrect quality standards;
- Poor procurement policy;
- poor execution method;
- poor study of methods;
- downtime;
- poor working conditions;
- poor sales policy;
- voluntary stoppages;
- overproduction;
- over quality;
- lack of tools;
- break;
- lateness and absences;
- indolence at work;
- lack of consideration of the worker's psychology.

Before starting to manufacture a product, it is necessary to make sure that the work has been well prepared, i.e. that the machines have been properly set up, that the tools chosen are adequate and that the manufacturing process is the right one. The reduction of wasted time should not be taken to extremes. Finding solutions to a problem is not always an easy task. Among the methods that exist, the Theory of Inventive Problem Solving (TRIZ) .

TRIZ method

TRIZ is a Russian acronym for "Theory of Inventive Problem Solving". It was invented in the Soviet Union in the 1960s by Genrikh Saulovich Altshuller. The author defines his invention as an alternative to the numerous and less effective methods of searching for variants that simplify the solution of invention problems. It can also be defined as a methodology dedicated

Creative Commons Attribution-NonCommercial-NoDerivatives 4.0 International License (CC BY-NC-ND)

to the analysis and solution of technical problems requiring innovative solutions, as well as a theory of technological evolution of products (Altshuller ,1997). TRIZ is a complex solution research, which consists in gathering different solutions likely to answer the imposed conditions, to concretize them, to simulate their behavior, to finally choose the best one. From this point of view, this method allowed to gather all the data of the company to better understand its needs by detecting its weak links. A limit arises with the quantity and quality of the proposed solutions and the knowledge acquired in the specific field of research, we speak then of psychological inertia. A solution to this limit lies in an essential principle of TRIZ which proposes to use or be inspired by solutions used in other fields to solve similar problems. Thus, in the optimization of the manufacturing process, the study did not only persist in taking only the data and assumptions of optimization of the manufacturing processes of high precision aeronautical parts, but in various areas that require a good organization of production. It is necessary to mention some examples of the bases of TRIZ.

TRIZ is based on:

o the similarity of the principles of the majority of the inventions;

o the resolution of inventive problems is often the result of contradictions between certain requirements;

o the law of evolution of technologies;

o the principle of solving contradictions without the use of compromise.

o TRIZ does not generate new ideas. It suggests ideas resulting from an analysis and a modeling of the existing, ideas that the designers would not necessarily have thought of. It proposes to generalize the observation that when one encounters a technical problem that can be reduced to action that has a harmful side effect, a possible solution path is to perform the action quickly (Altshuller, 1997).

In the search for solutions, TRIZ's originality lies in its refusal to compromise. To avoid compromise, it acts on the root causes of the problem. Advantages of TRIZ:

the ability to identify the nature of the problems

- the ability to orientate the search for solutions without forgetting those that are hardly thought of;
- the knowledge of how to synthesize the search for the necessary information according to the specific problems and the search for adequate solutions
- the ability to find solutions other than the ones most often used;
- the ability to think logically, analogically and systematically
- the effective increase of the ability to think;
- the reduction of the time to solve;
- looking at problems in a different way;
- increasing the perspective of solutions.

The difficulties of using TRIZ:

- the difficulty of identifying precisely where to limit the analysis;
- the absence of clear mechanisms for moving from the formulation of contradictions to their practical resolution;

Creative Commons Attribution-NonCommercial-NoDerivatives 4.0 International License (CC BY-NC-ND)

- the obviousness of choosing the model best suited to the problem at hand.

The TRIZ approach can be summarized in the following three steps:

- Modeling the problem;
- Searching for similar solutions in the catalogs;
- The concretization of the best solution.

Figure 3 summarizes this approach (TRIZ: a methodology to assist invention). For the resolution of technical problems, TRIZ uses the following tools
the technical contradiction resolution table;
the norms for solving problems;
the index of physical effects;
methods for developing creative imagination;
identification and classification of possible options for connections between components of technical systems.

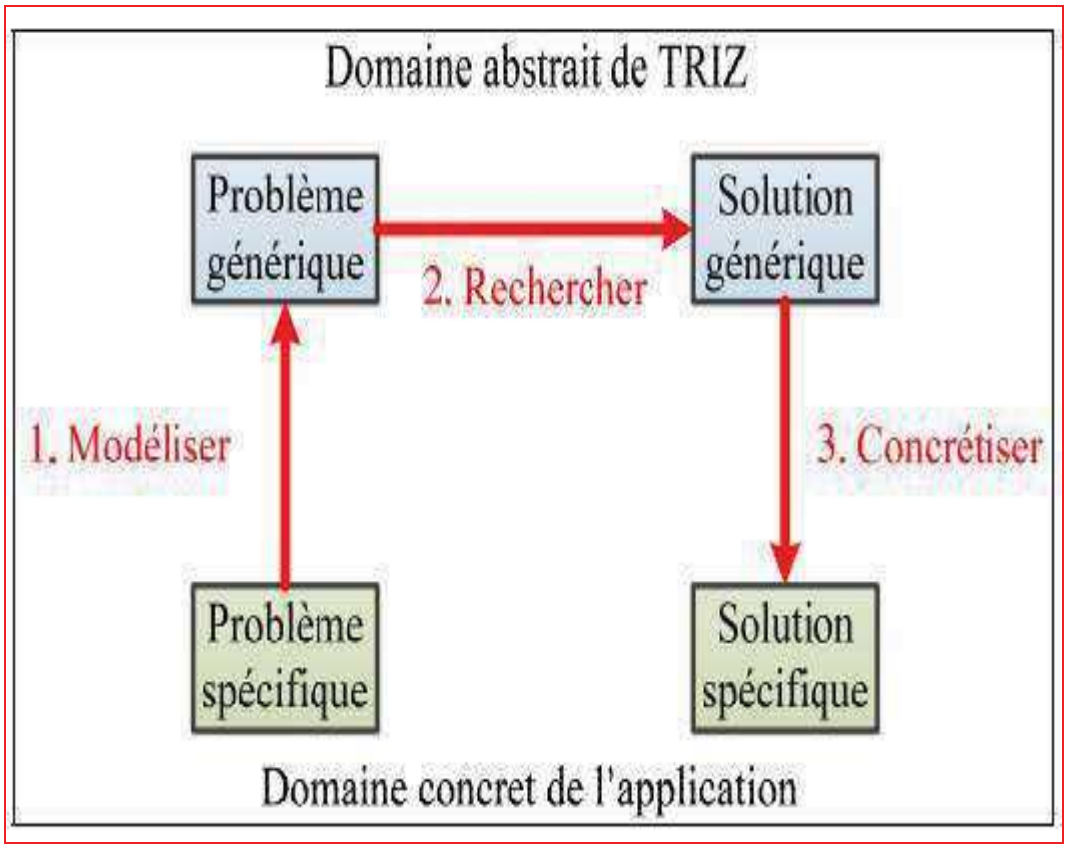

Figure 3 The core of the TRIZ approach: model the problem, seek a solution path, and make it real (TRIZ, n.d.).

TRIZ distinguishes between two types of contradictions: technical and physical. Technical contradictions occur when it is not possible to improve one of the product's performances without unacceptably degrading another. Physical contradictions occur when one part of the product must have two incompatible properties, i.e. when the same physical product is subject to two conflicting requirements.

Creative Commons Attribution-NonCommercial-NoDerivatives 4.0 International License (CC BY-NC-ND)

In order to overcome these difficulties, Alsthuller developed the Inventive Problem Solving Algorithm (ARIZ), which is the main instrument of TRIZ.

Presentation of ARIZ

ARIZ is a detailed industrial methodology based on TRIZ tools, aimed at identifying the problem, analyzing it in different ways, and ensuring the viability of the solutions obtained. ARIZ can also be defined as a logical and consecutive sequence of steps, aimed at detecting and resolving contradictions that exist in technical systems and that hinder their improvement.

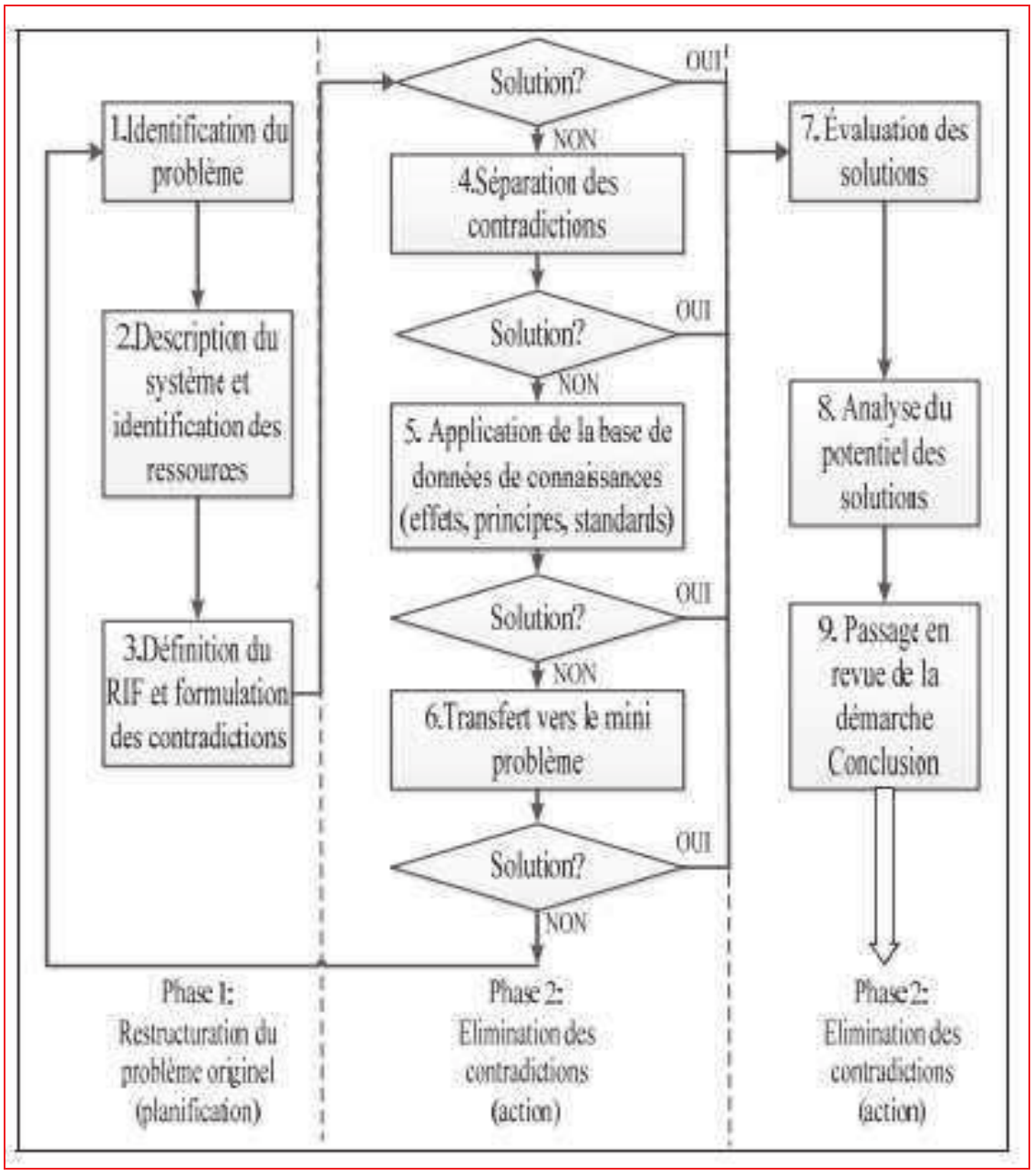

Figure 4: Overview of the ARIZ algorithm (TRIZ, n.d.).

Creative Commons Attribution-NonCommercial-NoDerivatives 4.0 International License (CC BY-NC-ND)

The technical applications of ARIZ have been modified with ARIZ-77 and ARIZ-85B.

Structuring of ARIZ-85B.

ARIZ-85B is divided into nine steps which are presented as follows (Altshuller, 1997):

Step 1. Analysis of the problem

The main objective of the first step of ARIZ is to move from an unclear innovative situation to a well-defined and relatively simple problem model.

Step 2. Analysis of the problem model

The second step of ARIZ is to analyze all the resources that can be used to solve the problem.

Step 3. Determination of the ideal end result and physical contradictions

The application of the third part of ARIZ should lead to a general vision of the ideal final result (RFI). It also allows to highlight the physical contradictions (CP), preventing the achievement of the RFI. It indicates the path towards the ideal solution.

Step 4. The mobilization and use of the SFR (Substance-Fields Rescues)

The fourth step of ARIZ consists in applying a series of operations to increase the number of resources.

Step 5. Use of the database

The fifth step of ARIZ is to use the databases. It allows to obtain a solution directly.

Step 6. Changing or replacing the problem

The sixth step is based on the fact that difficult problems are often solved by changing the meaning of the problem. It is therefore necessary to remove the psychological inertia in order to open up to other sources of ideas.

Step 7. Analysis of the mode of suppression of the CP

The seventh step of ARIZ is aimed at checking the quality of the obtained answers. The physical contradiction should be deleted in an almost ideal way. It is better to spend 2 or 3 more hours to find a better answer than to struggle with the introduction of a weak solution.

Step 8. Developing the maximum use of the resulting solution

The eighth step of ARIZ is to maximize the use of the resulting solution.

Step 9. Analysis of the path taken to produce the solution

The ninth step of ARIZ aims at increasing the inventive potential of the researcher. For this purpose, the analysis of the paths used to record a final solution is necessary.

Conclusion:

It has been pointed out above that even when successful optimization of the machining processes is achieved, other sources of enormous time losses remain and can only be detected, eliminated or reduced by good management and production organization methods. In view of all the theories stated, it is necessary to make a combined study between a good organization of the production and improved machining processes to obtain a significant gain. An improvement of the production organization and of the machining processes gives rise to an improvement of the manufacturing process. In order to reach the desired goal, the TRIZ method allows to group together the possible solutions and to make an optimal choice without compromise to obtain the best expected result.

References:

Debongnie, J.F. (1993). *Optimisation des opérations de tournage: La méthode de la puissance*

Creative Commons Attribution-NonCommercial-NoDerivatives 4.0 International License (CC BY-NC-ND)

disponible. Rapport LMF/D31. Université de liège, 42 p.

Merchant, M Eugene. (1993). *« Some observations on the past and present of research on machining and grinding ».* Applied Mechanics Reviews, vol. 46, no 3, p. 72-73.

Nash, Mark A., Sheila R. Poling et Sophronia Ward.(2006). *Using lean for fast six sigma results : a synchronized approach (2006). Coll. « Using lean for faster six sigma results: a synchronized approach ».* New York: Productivity Press, xiv, 161 p.

Pierrette, Sartin.(1968). *« Les cadres et les directions devant les temps improductifs ».Relations industrielles*, vol. 23, p. 201-220.

Altshuller, Genrich. (1997). T*he innovation algorithm: TRIZ, systematic innovation andtechnical creativity*. Worcester, M.A.: Technical Innovation Center, Inc., 311 p.

Creative Commons Attribution-NonCommercial-NoDerivatives 4.0 International License (CC BY-NC-ND)

Algerian Journal of Engineering Architecture and Urbanism Vol. 5 Nr. 3 2021
ISSN: 2588-1760

SIMULATION NUMERIQUE DES INSTABILITES AEROELASTIQUES DES PLAQUES MINCES SOUS L'EFFET D'UN ECOULEMENT SUPERSONIQUE

Saber ZIARI
Univ. Ouargla, Fac. des Sciences Appliquées, Lab. Dynamique, Interaction et Réactivité des Systèmes, Ouargla 30000, Algeria

Rassim BELAKROUM
Univ. Ouargla, Fac. des Sciences Appliquées, Lab. Dynamique, Interaction et Réactivité des Systèmes, Ouargla 30000, Algeria

Résumé:
On s'intéresse dans ce travail à l'analyse du phénomène de flottement aéroélastique des plaques minces couplées à un écoulement d'air supersonique. Le flottement est un phénomène dit auto-excité qui se manifeste par des vibrations de grandes amplitudes pouvant induire la ruine du système. En raison de la variation de la vitesse d'écoulement, les modes vibratoires se confondent à une vitesse d'écoulement critique et par conséquent un flottement couplé se produit.
Pour la modélisation du sous-domaine solide, on a utilisé une combinaison de la théorie des coques de Sander et de la théorie des éléments finis classiques. Cette méthode hybride consiste à approcher le champ de déplacement membranaire par des polynômes bilinéaires cependant les déplacements transversaux sont interpolés par une fonction exponentielle. Le chargement aérodynamique induit par l'écoulement d'air est prédit grâce à la théorie de piston linéarisée du premier ordre. Les matrices de masse, de rigidité et d'amortissement ont été déterminées par intégration analytique exacte. Le système d'équations aéroélastique résultant est résolu numériquement. Les résultats obtenus grâce à un code développé en FORTRAN sont en bon accord avec d'autres résultats existants en littérature scientifique.

Mots clés : Interaction fluide-structure ; écoulement supersonique ; théorie de piston ; flottement aéroélastique ; théorie de Sander.

Introduction:

Les premiers problèmes de flottement des plaques - étant une oscillation auto-excitée des structures avioniques lorsqu'elles sont exposées à un flux d'air le long de leur surfaces externes- ont été rencontré avec les lancements de missiles allemands V-2 au milieu des années 1940, date à partir de laquelle ont vu éclore les premières investigations autour de ce sujet (Bisplinghoff et al., 2013; Dowell et al., 1989). Les dernières décennies ont vu la mise en œuvre de certaines approches basées sur la formulation par éléments finis pour mieux évaluer les limites du flottement de la plaque sous un flux d'air supersonique.

Creative Commons Attribution-NonCommercial-NoDerivatives 4.0 International License (CC BY-NC-ND)

Olson (M & OLSON, 1967) , a étendu l'approximation éléments finis pour une poutre afin d'évaluer précisément le flottement de la plaque avec seulement quelques éléments. Kariappa et Somashekar (Kariappa & B.R, 1969) ont appliqué une approche éléments finis basée sur la dérivation des matrices de coefficients d'influence aérodynamique pour une plaque simplement appuyée avec différents rapports latéraux en les comparant avec des méthodes conventionnelles. Sander et al. (Sander et al., 1973) ont utilisé l'approche EF pour évaluer les forces aérodynamiques en utilisant la théorie du piston linéarisée, la précision de la méthode est approuvée pour différentes conditions au limite. Cheng (Guangfeng, 2002) a étudié la stabilité du flottement supersonique d'une plaque en utilisant la formulation FE, ils ont conclu que l'influence de l'orientation de l'écoulement est plus grande pour une plaque carrée que pour une plaque rectangulaire. D'autres approches combinées à la formulation EF pourraient être mentionnées, nous citons notamment les travaux de Srinivasan et Babu (Srinivasan & Babu, 1987) avec la technique de l'équation intégrale utilisée pour résoudre l'équation différentielle du mouvement. Abbas et al. (Abbas et al., 2012) avec l'emploi de la formulation basée sur les coordonnées nodales absolues. Pour détecter le flottement Wang et al. (Wang et al., 2011) ont utilisé et validé l'approche d'orientation des vecteurs propres pour une plaque composite simplement appuyée sous un écoulement supersonique. Faroughi et al. (Faroughi et al., 2013) ont amélioré l'évaluation du flottement supersonique d'une aile avec raidisseurs à faible rapport hauteur / largeur avec un élément poutre. Song et al. (Song & Li, 2014) ont comparé la méthode du mode assumée et MEF avec des résultats moins précis pour la première. Notre présente étude vise à utiliser l'élément de plaque développé par Kerboua et al. (Kerboua et al., 2007) pour prédire le comportement aérodynamique d'une plaque carrée soumise à un flux d'air supersonique.

Modélisation aéroélastique:

Modéle structurel

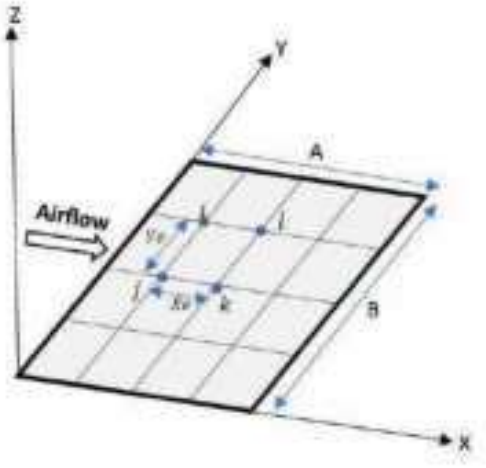

Fig. 1. Elément plaque

L'élément plaque utilisé dans cette étude Fig. 1 est dérivé de la théorie de Sander pour les coques minces qui est basée sur la première approximation de Love (Sanders, 1960). La

Creative Commons Attribution-NonCommercial-NoDerivatives 4.0 International License (CC BY-NC-ND)

Algerian Journal of Engineering Architecture and Urbanism Vol. 5 Nr. 3 2021
ISSN: 2588-1760

forme contractée des équations de Sander pour les coques cylindriques s'écrit: (Sabri & Lakis, 2010)

$$L_j(U,V,W,P_{ij}) = 0 \quad (1)$$

L_j (j=1,2,3), équations aux dérivées partielles linéaires

P_{ij} Sont les éléments de la matrice d'élasticité pour une coque isotrope :

$$[p] = \begin{bmatrix} D & \nu D & 0 & 0 & 0 & 0 \\ \nu D & D & 0 & 0 & 0 & 0 \\ 0 & 0 & \frac{D(1-\nu)}{2} & 0 & 0 & 0 \\ 0 & 0 & 0 & K & \nu K & 0 \\ 0 & 0 & 0 & \nu K & K & 0 \\ 0 & 0 & 0 & 0 & 0 & \frac{K(1-\nu)}{2} \end{bmatrix} \quad (2)$$

Avec

$$K = \frac{E h^3}{12(1-\nu^2)} \qquad D = \frac{Eh}{1-\nu^2} \quad (3)$$

E le module d'élasticité, ν le coefficient de Poisson, et h l'épaisseur de la plaque.

Les composantes du déplacement membranaire sont présentées par les polynômes bilinéaires tandis que celles du déplacement flexionnel sont présentées par une fonction exponentielle. Le champ des déplacements s'écrit alors :

$$U(x,y,t) = C_1 + C_2\frac{x}{A} + C_3\frac{y}{B} + C_4\frac{xy}{AB} \quad (4)$$

$$V(x,y,t) = C_5 + C_6\frac{x}{A} + C_7\frac{y}{B} + C_8\frac{xy}{AB} \quad (5)$$

$$W(x,y,t) = \sum_{i=9}^{24} C_j e^{i\pi\left(\frac{x}{A}+\frac{y}{B}\right)} e^{i\omega t} \quad (6)$$

La solution exacte de l'équation (6) peut-être présentée par :

$$W(x,y,t) = \sum_{q=0}^{3} \frac{A_q}{q!}\left(\frac{x}{A}\right)^q \sum_{p=0}^{3} \frac{B_p}{p!}\left(\frac{y}{B}\right)^p \quad (7)$$

Le développement en série de Taylor de l'équation 7 donne : (Charbonneau et al., 2001a)

$$W(x,y,t) = C_9 + C_{10}\frac{x}{A} + C_{11}\frac{y}{B} + C_{12}\frac{x^2}{2A^2} + C_{13}\frac{xy}{AB} + C_{14}\frac{y^2}{2B^2} + C_{15}\frac{x^3}{6A^3} + C_{16}\frac{x^2y}{2A^2B} + C_{17}\frac{xy^2}{2AB^2} C_{18}\frac{y^3}{6B^3} + C_{19}\frac{x^3y}{6A^3B} + C_{20}\frac{x^2y^2}{4A^2B^2} + C_{21}\frac{xy^3}{6AB^3} + C_{22}\frac{x^3y^2}{12A^3B^2} + C_{23}\frac{x^2y^3}{12A^2B^3} + C_{24}\frac{x^3y^3}{36A^3B^3} \quad (8)$$

Avec U et V représentent les composantes du déplacement membranaire de la surface médiane suivant les directions X et Y, respectivement, et W est le déplacement transversal. A et B sont les dimensions de la plaque suivant les directions X et Y, respectivement. "ω" est la fréquence naturelle de la plaque (rad/s) et "i" est le nombre complexe (i^2=-1), et C_j sont des constantes inconnues.

Creative Commons Attribution-NonCommercial-NoDerivatives 4.0 International License (CC BY-NC-ND)

On peut écrire les équations 4,5 et 8 comme suit :

$$\begin{Bmatrix} U \\ V \\ W \end{Bmatrix} = [R]\{C\} \tag{9}$$

Avec

$$\{C\} = \{C_1, C_2, \dots, C_{24}\}^T \tag{10}$$

Et

$[R]$ est une matrice d'ordre (3×6). Le vecteur des déplacement nodaux est donné par :

$$\{\delta\} = \left\{\{\delta_i\}^T, \{\delta_j\}^T, \{\delta_k\}^T, \{\delta_l\}^T\right\}^T \tag{11}$$

Avec

$$\{\delta_i\} = \{U_i, V_i, W_i, \partial W_i/\partial x, \partial W_i/\partial y, \partial^2 W_i/(\partial x \partial y)\}^T \tag{12}$$

En remplaçant les éqs (4,5 et 8) dans l'éq (9), le vecteur des déplacements nodaux s'écrit:

$$\{\delta\} = [A]\{C\} \tag{13}$$

Les constantes inconnues sont remplacées par le vecteur du déplacement généralisé de l'élément fini quadrilatéral :

$$\{C\} = [A]^{-1}\{\delta\} \tag{14}$$

En remplaçant l'éq (14) dans l'éq (9), l'expression du champ de déplacement devient :

$$\begin{Bmatrix} U \\ V \\ W \end{Bmatrix} = [R][A]^{-1}\{\delta\} = [N]\{\delta\} \tag{15}$$

$[N]$ est une matrice d'ordre (3×24) représente la fonction de forme de forme du déplacement de l'élément fini.

Les relations déformation-déplacement sont données :

$$\begin{Bmatrix} \varepsilon_x \\ \varepsilon_y \\ 2\varepsilon_{xy} \\ \kappa_x \\ \kappa_x \\ \kappa_{xy} \end{Bmatrix} = \begin{Bmatrix} \partial U/\partial x \\ \partial V/\partial y \\ \partial V/\partial x + \partial U/\partial y \\ -\partial^2 W/\partial x^2 \\ -\partial^2 W/\partial y^2 \\ -2\,\partial^2 W/\partial x\,\partial y \end{Bmatrix} \tag{16}$$

De la même manière on peut écrire le champ des déformations :

$$\{\varepsilon\} = [Q][A]^{-1}\{\delta\} = [B]\{\delta\} \tag{17}$$

$[Q]$ est une matrice d'ordre (6×24).

Pour une plaque isotrpe, l'éxpression contrainte-déformation s'écrit :

$$\{\sigma\} = [P]\ \{\varepsilon\} \tag{18}$$

Creative Commons Attribution-NonCommercial-NoDerivatives 4.0 International License (CC BY-NC-ND)

En substituent l'éq (17) dans l'éq(18), on peut exprimer le vecteur de contrainte en fonction des déplacements nodaux :

$$\{\sigma\} = [P][B]\{\delta\} \tag{19}$$

Les matrices de masse et de rigidité sont écrites (Charbonneau et al., 2001b) pour chaque élément comme suit:

$$[m]^e = \rho_m h \int_A [N]^T [N] dA \tag{20}$$
$$[k]^e = \int_A [B]^T [P][B] dA \tag{21}$$

ρ_m est la densité du matériau et dA l'élément de surface. En utilisant les éqs (15 et 17) et les éqs (20 et 21), on obtient :

$$[k]^e = [[A]^{-1}]^T \left(\int_0^{y_e} \int_0^{x_e} [Q]^T [P][Q] dx dy\right)[A]^{-1} \tag{22}$$
$$[m]^e = \rho_m h [[A]^{-1}]^T \left(\int_0^{y_e} \int_0^{x_e} [R]^T [R] dx dy\right)[A]^{-1} \tag{23}$$

Avec x_e and y_e sont dimensions élémentaires suivant les directions X et Y, respectivement.

Modéle aérodynamique

La pression aérodynamique de l'air appliquée sur la surface externe de la plaque est modélisée par la théorie de piston proposée par Ashley and Zartarian (Ashley, 1956). Pour l'analyse du flottement linéaire à de grandes nombres de Mach, cette pression a l'expression suivante :

$$\Delta P = \rho_\infty U_\infty^2 \left\{\frac{1}{\sqrt{M^2-1}}\left[\frac{\partial w}{\partial x} + \frac{(M^2-2)}{(M^2-1)U_\infty}\frac{\partial w}{\partial t}\right]\right\} \tag{24}$$

Avec ρ_∞, U_∞ et M sont la densité du l'air, la vitesse libre du flux d'air et le nombre de Mach, respectivement.
Avec
$M = \frac{U_\infty}{a_\infty}$
a_∞ La Vitesse libre du son.
La forme discrétisée de l'équation du mouvement s'exprime :

$$[m^e]\{\ddot{q}^e\} + g[c_a^e]\{\dot{q}^e\} + [k^e]\{q^e\} + \lambda[k_a^e]\{q^e\} = \{0\} \tag{25}$$

Avec

$$[c_a^e] = h \int_A [N]^T [N] dA \tag{26}$$
$$[k_a^e] = \int_A [N]^T [N, x] dA \tag{27}$$

En remplaçant l'équation (15) dans les équations (26 et 27), on peut écrire :

Creative Commons Attribution-NonCommercial-NoDerivatives 4.0 International License (CC BY-NC-ND)

$$[c_a^e]=h[[A]^{-1}]^T\left(\int_0^{y_e}\int_0^{x_e}[R]^T[R]\,dx\,dy\right)[A]^{-1} \quad (28)$$

$$[k_a^e]=[[A]^{-1}]^T\left(\int_0^{y_e}\int_0^{x_e}[R]^T[R,x]\,dx\,dy\right)[A]^{-1} \quad (29)$$

Avec $\{q^e\}$, $[c_a^e],[k_a^e],g$ et λ sont le vecteur des déplacements nodaux, la matrice d'amortissement aérodynamique élémentaire, la matrice de rigidité aérodynamique élémentaire, le paramètre d'amortissement aérodynamique et le paramètre de pression aérodynamique, respectivement.

$$g = 2Q(M^2-2)/U_\infty(M^2-1)^{3/2} \quad (30)$$

Et $\lambda = 2Q/(M^2-1)^{1/2}$ (31)

Avec Q est la pression aérodynamique libre, est donnée par : $Q = (\rho_\infty U_\infty^2)/2$ (32)

Analyze du flottement

De l'équation 25 et en utilisant la technique d'assemblage avec l'application des conditions aux limites nécessaires, nous obtenons intuitivement la formulation de l'équation qui régit le mouvement dans le système global :

$$[m]\{\ddot{q}\} + g[c_a]\{\dot{q}\} + [k]\{q\} + \lambda[k_a]\{q\} = \{0\} \quad (33)$$

Avec $\{q\},[m],\ [k],[c_a]\ and\ [k_a]$ sont le vecteur de déplacement, la matrice de rigidité, la matrice de masse, la matrice d'amortissement aérodynamique et la matrice de rigidité aérodynamique, respectivement, exprimés dans le système global.
Pour résoudre l'éq (33), on utilise la méthode de réduction, on aura donc :

$$\begin{bmatrix}[0] & [m]\\ [m] & g[c_a]\end{bmatrix}\begin{Bmatrix}\ddot{q}\\ \dot{q}\end{Bmatrix} + \begin{bmatrix}-[m] & [0]\\ [0] & [k]+\lambda[k_a]\end{bmatrix}\begin{Bmatrix}\dot{q}\\ q\end{Bmatrix} = \{0\} \quad (34)$$

On suppose la solution de l'équation 34 de la forme :

$$\{q\} = \{q_0\}e^{\Omega t} \quad (35)$$

La substitution de l'éq (35) dans l'éq (34) nous mène a un problème à valeurs propres avec comme solution:

$$\Omega = \Omega_r + i\Omega_i \quad (36)$$

Avec Ω, Ω_r et Ω_i sont les valeurs propres, les parties réelles et imaginaires des valeurs propres, respectivement. Pour raison de commodité, on représente le paramètre de la pression aérodynamique et la fréquence par la forme adimensionnelle :

$$\lambda^* = \frac{2Qa^3}{K\sqrt{M^2-1}} \quad (37)$$

$$\Omega_i{}^* = \Omega_i a^2\sqrt{\rho_m h/K} \quad (38)$$

Creative Commons Attribution-NonCommercial-NoDerivatives 4.0 International License (CC BY-NC-ND)

Les valeurs propres ainsi obtenues sont des nombres complexes avec la partie imaginaire qui se réfère aux fréquences propres du système couplé et la partie réelle se réfère à son amortissement. Avec l'augmentation de la pression dynamique, une valeur critique est atteinte lorsque la partie réelle de la solution devient positive, ce qui augmente de façon exponentielle l'amplitude du mouvement de la plaque indiquant que le début du flottement.

Résultats et discussions

Les résultats des calculs numériques d'une plaque isotrope carrée en alliage d'aluminium soumis à un flux d'air dans la direction x sont obtenus en utilisant un code de calcul basé sur la méthode des éléments fi,nid. Tout d'abord, une plaque simplement appuyée sur les quatre cotés est considérée. Les propriétés géométriques et physiques du matériau de la plaque sont : A = B = 1 m, h = 0,01 m; E = 70 GPa, ν = 0,3 et ρ_m = 2700 kg / m3.
La variation de la fréquence adimensionnelle par rapport au paramètre de la pression aérodynamique adimensionnel est mise en valeur Fig.2. On peut remarquer que le flottement supersonique se produit lorsque deux modes d'oscillation de la plaque fusionnent à la limite de la valeur du paramètre de la pression aérodynamique adimensionnel, λ = 513.2 qui est une valeur précise par rapport à la solution exacte.

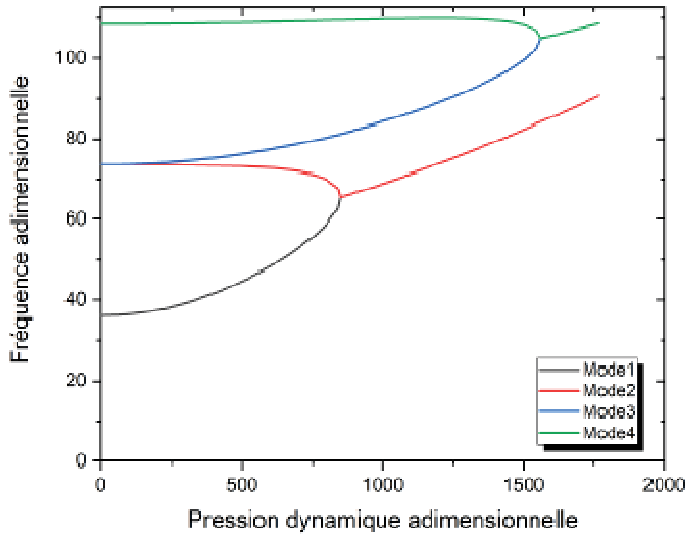

Fig. 2 . La variation de Ω_i^* Vs λ^* pour une plaque SS^*SS.

Pour vérifier la convergence de la méthode pour des plaques carrées simplement appuyées sur les quatre côtés, **Fig.3**, les limites de flottement ont été calculées et analysées par rapport au nombre d'éléments. On constate que le maillage de l'ordre 6 × 6 est acceptable, donc, nos calculs ci-dessous seront effectués avec ce niveau de raffinement.

Creative Commons Attribution-NonCommercial-NoDerivatives 4.0 International License (CC BY-NC-ND)

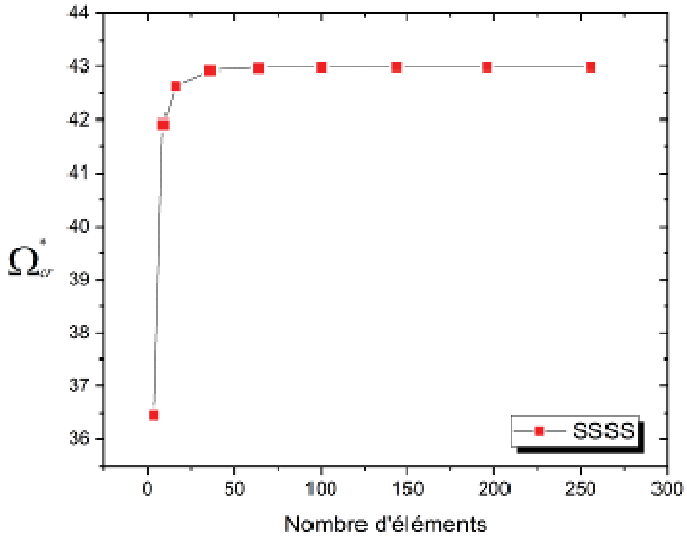

Fig. 3 (Ω_i^*) Vs nombre d'éléments pour une plaque S$\mathcal{S}^*$SS .

Pour explorer les performances de la méthode développée, une campagne de calculs pour différentes configurations de la plaque liées aux conditions aux limites imposées (SSSS, CCCC), **tableau 1**. Les résultats ainsi obtenus, comparés aux différents résultats numériques et analytiques existants dans la littérature, montre une grande précision.

Conditions aux limites	References	Sous-vide		Coalescence	
		Ω1	Ω2	λ^*cr	Ω^*cr
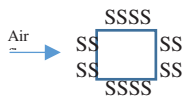	Present element	19.736	49.334	513.231	42.976
	Sander et al (Exact)(Sander et al., 1973)	19.61	49.35	512.6	42.99
	Sander et al (FEM)(Sander et al., 1973)	19.74	49.38	511.8	42.93
	Srinivasan and Babu (Srinivasan & Babu, 1985)	19.31	48.44	521.3	42.86
	Laith K. Abbas et al(Abbas et al., 2012) Kailash Dhital et al.(Dhital et al., 2016)	21.89 –	54.96 –	536.9 512.5	43.96 42.97
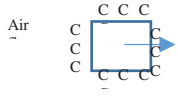	Present element	36.002	73.531	851.926	65.47
	Sander et al(Exact)(Sander et al., 1973)	35.99	73.89	877.0	63.85
	Sander et al (FEM1)(Sander et al.,	37.24	76.50	1058.0	70.49

Creative Commons Attribution-NonCommercial-NoDerivatives 4.0 International License (CC BY-NC-ND)

	1973)				
	Sander et al (FEM2)(Sander et al., 1973)	36.00	73.53	850.0	65.44
	Srinivasan and Babu (Srinivasan & Babu, 1985)	35.99	73.80	877.00	65.44
	Laith K. Abbas et al(Abbas et al., 2012)	40.35	83.04	913.17	68.45
	Durvasula (DURVASULA, 1967)	35.99	73.42	837.73	–

Tableau 1. Résultats numériques pour différentes conditions aux limites

Conclusion

Une méthode hybride combinant une analyse par éléments finis et la théorie des coques de Sander a été mise en œuvre pour la modélisation structurale d'une plaque isotrope carrée élastique soumise à un flux d'air supersonique induisant un chargement aérodynamique modélisé par la théorie des pistons linéarisés du premier ordre. Les résultats des calculs effectués pour différentes conditions aux limites par rapport à ceux de la littérature, montrent une grande efficacité en termes de temps de calcul gagné par la taille de maillage ainsi qu'une grande précision.

References:

Abbas, L.K., Rui, X., Marzocca, P. (2012). *Panel flutter analysis of plate element based on the absolute nodal coordinate formulation.* Multibody System Dynamics, **27**(2), 135-152.

Ashley, H., Zartarian, G. (1956). Piston theory-a new aerodynamic tool for the aeroelastician. *Journal of the Aeronautical Sciences*, **23**(12), 1109-1118.

Bisplinghoff, R.L., Ashley, H., Halfman, R.L. (2013). *Aeroelasticity.* Courier Corporation.

Charbonneau, E., Lakis, A.A.J.J.o.s. (2001). *Semi-analytical shape functions in the finite element analysis of rectangular plates*. **242**(3), 427-443.

Dhital, K., Han, J.-H., Lee, Y.-K. (2016). *Approximation of Distributed Aerodynamic Force to a Few Concentrated Forces for Studying Supersonic Panel Flutter.* Transactions of the Korean Society for Noise Vibration Engineering, **26**(5), 518-527.

Dowell, E.H., Curtiss, H.C., Scanlan, R.H., Sisto, F. (1989). A modern course in aeroelasticity. *Springer*.

Durvasula. S. (1967). Flutter of simply supported, parallelogrammic, flat panels in supersonic flow. *AIAA Journal*, **5**(9), 1668-1673.

Faroughi, S., Malekzadeh, K., Mirzaee, I. (2013). *Finite element supersonic flutter analysis of low aspect ratio stiffened wing.* Journal of Vibration and Control, **19**(14), 2187-2198.

Guangfeng, C. (2002). *Finite element modal formulation for panel flutter at hypersonic speeds and elevated temperatures.* Old Dominion University.

Kariappa, B.R, S. (1969). *Application of matrix displacement methods in the study of panel flutter. AIAA Journal*, **7**(1), 50-53.

Kerboua, Y., Lakis, A.A., Thomas, M., Marcouiller, L.J.N.e. (2007). *Hybrid method for vibration analysis of rectangular plates.* Nuclear Engineering and Design, **237**(8), 791-801.

Creative Commons Attribution-NonCommercial-NoDerivatives 4.0 International License (CC BY-NC-ND)

Olson, M. D. (1967). Finite elements applied to panel flutter. *AIAA Journal*, **5**(12), 2267-2270.

Sabri, F., Lakis, A.A. (2010). *Finite Element Method Applied to Supersonic Flutter of Circular Cylindrical Shells.* AIAA Journal, **48**(1), 73-81.

Sander, G., Bon, C., Geradin, M. (1973). *Finite element analysis of Supersonic panel flutter.* International Journal for Numerical Methods in Engineering, **vol. 7**(3), 379-394.

Sanders, J.L. (1960). An Improved First-Approximation Theory for Thin Shells U.S. Government Printing Office.

Song, Z.-G., Li, F.-M. (2014). *Investigations on the flutter properties of supersonic panels with different boundary conditions*. International Journal of Dynamics and Control, **2**(3), 346-353.

Srinivasan, R., Babu. (1985). *Flutter analysis of cantilevered quadrilateral plates.* Journal of Sound and Vibration, **98**(1), 45-53.

Srinivasan, R., Babu, B. (1987). *Free vibration and flutter of laminated quadrilateral plates.* Computers & Structures, **27**(2), 297-304.

Wang, Z., X. Qin, J.L., Zhang, X. (2011). *Flutter detection of composite plate using finite element and eigenvector orientation method.* International Conference on Mechatronics and Automation. IEEE. pp. 1428-1432.

Creative Commons Attribution-NonCommercial-NoDerivatives 4.0 International License (CC BY-NC-ND)

Algerian Journal of Engineering Architecture and Urbanism Vol. 5 Nr. 3 2021
ISSN: 2588-1760

MODÉLISATION THÉORIQUE DE LA PRODUCTION D'ÉNERGIE PAR CYCLONE SOLAIRE : CAS D'ÉTUDE L'ALGÉRIE

Fatma REZGANE
Ecole nationale polytechnique de Constantine, Département de Génie Mécanique, Constantine 25000, Algeria, e-mail: Rezgane.fatma@gmail.com

Rassim BELAKROUM
Univ. Ouargla, Fac. des Sciences Appliquées, Lab. Dynamique, Interaction et Réactivité des Systèmes, Ouargla 30000, Algeria,
e-mail: Rassim.belakroum@gmail.com

Youcef MOUADJI
Ecole nationale polytechnique de Constantine, Département de Génie Mécanique, Constantine 25000, Algeria, e-mail: ymouadji@yahoo.fr

Résumé
Le présent travail analyse la production d'énergie par cyclone atmosphérique dans certaines régions de l'Algérie. L'étude se base sur une modélisation théorique du principe de conversion d'énergie par vortex atmosphérique solaire. Les investigations concernent quatre différentes villes de l'Algérie situées dans des régions différentes qui sont: Alger, Constantine, Ouargla et Bechar. La centrale solaire étudiée présente un diamètre du collecteur de 122m avec une estimation de la hauteur du cyclone de 1000m. Sous les conditions météorologiques des quatre regions considérées dans cette étude, il a été trouvé que la puissance électrique moyenne produite varie entre 350 et 450kW et que la production annuelle d'énergie électrique se situerait entre 1,3 et 1,4 GWh /an.

Mots Clés : Energie solaire ; Vortex atmosphérique ; Centrale solaire ; Tourbillon ; Cheminée solaire.

Introduction:

Le rôle de la transition énergétique est plus que clair aujourd'hui, il y a une nécessité pour des nouvelles solutions énergétiques, pour pouvoir assurer une gestion intelligente des ressources, et pour prévenir des problèmes climatiques imprévisibles.

Afin d'assurer un développement durable et de diversifier ses ressources énergétiques, le monde s'est engagé dans un important programme de développement des énergies renouvelables. Il est important de noter que les technologies d'énergie renouvelable actuellement disponibles sur le marché sont encore modestes en ce qui concerne l'efficacité globale, et elles sont généralement liées à un investissement global relativement élevé, ce qui entraîne finalement une pénétration plus lente sur le marché (Penga, 2019). En ayant à l'esprit l'amélioration et la mise à niveau des technologies d'énergie renouvelable disponibles sur le marché (en termes d'efficacité et de réduction des coûts), un aspect qui est également important est d'assurer le développement continu de concepts d'énergie renouvelable et alternatifs. Les nouveaux concepts énergétiques alternatifs et renouvelables sont importants

Creative Commons Attribution-NonCommercial-NoDerivatives 4.0 International License (CC BY-NC-ND)

pour un avenir durable et pour réduire la consommation de ressources limitées d'origine fossile.

Le monde vise à augmenter significativement la contribution des énergies renouvelables. L'une des options qui contriburont à répondre à ces demandes sont les systèmes de production d'énergie dite cheminée solaire. Ces méthodes de production d'énergie ont été classées et identifiées en deux types: des systèmes à cheminée et des systèmes de génération de vortex artificiel à court diffuseur (Al-Kayiem, 2018). La naissance du deuxième type est due principalement aux problèmes techniques lié à construction de la cheminée et aussi au cout élevé. Ce dispositif de centrale électrique solaire à cyclone atmosphérique (CSC) transforme l'énergie solaire en électricité. Dans une centrale à vortex on distingue phase conversions d'énergie. Le rayonnement solaire est converti en énergie thermique dans le milieu absorbant, l'énergie thermique est convertie en énergie cinétique dans le passage du collecteur, l'énergie cinétique est convertie en énergie mécanique rotative dans la turbine, et enfin, l'énergie mécanique est convertie en énergie électrique grace à un générateur. D'aprés (Al-Kayiem, 2016) Cette série de conversions a entraîné une efficacité du système aussi faible que 0,1%. De nombreux travaux de recherche ont été rapportés pour tenter d'améliorer les performances du système grâce à des améliorations de tous les processus de conversion à partir du mécanisme d'absorption solaire jusqu'à la production d'énergie électrique.

Moralisation des performances de centrale à cyclone atmosphérique:

Le cyclone solaire atmosphérique est basé sur les mêmes principes que la cheminée solaire. Tous deux sont basés sur la génération d'un courant d'air ascendant naturel, l'étude effectue par (Al-Kayiem, 2018) a démontré que le tourbillon solaire artificiel peut remplacer avec succès la grande tour solaire requise dans la cheminée solaire, et il permet d'obtenir des rendements beaucoup plus élevés à des coûts nettement inférieurs en éliminant la nécessité d'une cheminée physique coûteuse (Michaud, 2013) et (Al-Kayiem, 2018). Le principe de fonctionnement de ces centrales est gérée par le cycle idéale de baryton comme illustre la figure 1.

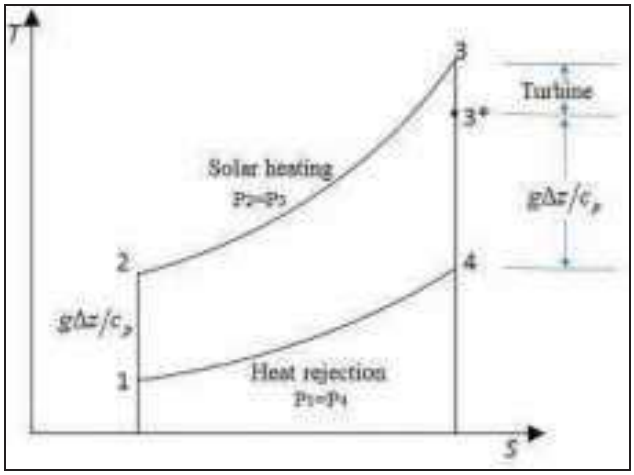

Fig1. Diagramme température –entropie du cycle idéal de Brayton (Guo, 2019).

Le processus isobarique 2-3, représente le gain de chaleur de l'air au niveau de collecteur. La puissance d'expansion 3-4, peut être divisée en deux parties, une patrie de potentiel fait tourner la turbine et un autre exite la turbine en formant un vortex.

Creative Commons Attribution-NonCommercial-NoDerivatives 4.0 International License (CC BY-NC-ND)

d'aprés les résultat des études (Michaud, 2013) et (Al-Kayiem, 2018) on peut considérer que le rendement du cyclone égal au rendement de la cheminée, et s'écrire comme suit :

$$\eta_c = {g\,\Delta z}\Big/{c_p T_2} \quad (1)$$

L'analyse présentée dans ce travail se base sur les hypothèses simplificatrices suivantes :

1. Chauffage uniforme de la surface du collecteur solaire.
2. Aucun gradient de température de l'air à l'intérieur du collecteur.
3. Aucune perte de chaleur le long de l'altitude de cyclone ainsi que un facteur de dissipation de cyclone négligeable.

Le rendement total de la centrale solaire à cyclone atmosphérique (CSC) est défini comme un produit des rendements de ses composants (collecteur, cyclone et turbine) :

$$\eta_{csc} = \eta_{coll}\eta_c\eta_t \quad (2)$$

La puissance totale produite par CSC est calculée à partir de produit de l'énergie solaire totale collectée par le collecteur Q_S et le rendement de la centrale solaire à cyclone atmosphérique :

$$P_{csc} = Q_S\eta_{csc} = Q_S\eta_{coll}\eta_c\eta_t \quad (3)$$

L'énergie solaire totale collectée par le collecteur dépend de la radiation solaire mesurer $G\ (W/m^2)$ et la surface du collecteur $A_{coll}(m^2)$.

$$Q_S = G\,A_{coll} \quad (4)$$

D'après (Azizia, 2019) L'efficacité du collecteur est calculée en divisant la quantité de chaleur transmise à l'air par le collecteur (Q_u) par la quantité de rayonnement solaire introduite par la surface du collecteur (Q_S).

$$\eta_{coll} = {Q_u}\Big/{Q_S} = \alpha - {\beta\,\Delta T_0}\Big/{G} \quad (5)$$

Avec $Q_u = \dot{m}\,C_p\Delta T = \alpha A_{coll}G - \beta\,\Delta T_0 A_{coll}$ (6)

ΔT: La déférence de température entre la température moyen de l'air chaud à l'intérieur de collecteur la température ambiant de l'air.

ΔT_0: La différence de température entre la surface de collecteur et la température ambiante de l'air.

α: Le coefficient d'absorption effectif du collecteur.

β: est un coefficient de transfert de chaleur ajusté qui permet de calculer les pertes par rayonnement et par convection.

Selon (Nizetic, 2008), l'efficacité du capteur pour un toit de collecteur en verre simple peut être exprimée en fonction de deux paramètres, ΔT et G:

$$\eta_{coll} = \eta_{coll}(G, \Delta T) = -13{,}116\left(\frac{\Delta T}{2G}\right)^2 - 6{,}3364\left(\frac{\Delta T}{2G}\right) + 0{,}72 \quad (7)$$

La puissance électrique produite par une centrale à cyclone atmosphérique:

D'une manière générale, la puissance électrique produite par CSC peut être calculée comme l'énergie solaire totale Q_S d'entrée multipliée par les rendements respectifs de collecteur, de cyclone, turbine, et turbogénérateur. Selon (Azizia, 2019) la turbine placée à la sortie de collecteur ou la force d'aire convertit au maximum 2/3 de débit de l'aire en puissance mécanique. Dans la présente étude on considère que le turbogénérateur a un facteur de rendement idéal, la puissance électrique maximale de sortie P_{el-max} peut être calculée comme suit:

Creative Commons Attribution-NonCommercial-NoDerivatives 4.0 International License (CC BY-NC-ND)

$$P_{el-max} = \frac{2}{3}\eta_{coll}\frac{g}{C_p T_0}H_c A_{coll} G \quad (8)$$

Selon (Nizetic, 2008) la quantité moyenne annuelle de puissance obtenue par la centrale P_{av-an} (ou puissance nominale) pour un $\Delta T = 20\,K$ est calculée à partir du P_j mensuel selon l'expression suivante:

$$P_{av-an} = \frac{\Sigma_j P_j t_j}{\Sigma_t t_t} \quad (9)$$

Où $P_j\,(kW)$ est la production électrique mensuelle moyenne; $t_j\,(h/mois)$ heures de travail mensuelles de une CSC et $t_t\,(h/année)$ heures de travail totales (annuelles) de la centrale.

Caractéristiques des zones géographiques considérées:

L'Algérie est l'un des pays de la méditerranée qui dispose d'un énorme gisement solaire. Suite à une évaluation par satellites, l'Agence Spatiale Allemande (ASA) a conclu, que l'Algérie représente le potentiel solaire le plus important de tout le bassin méditerranéen, La durée d'insolation sur la quasi-totalité du territoire Algérien dépasse les 2000 heures annuellement et peut atteindre les 3900 heures sur les Hauts Plateaux et au Sahara (Tableau 1). L'énergie reçue quotidiennement sur une surface horizontale de (1 m^2) est de l'ordre de (5 kWh) sur la majeure partie du territoire Algérien, soit près de (1700kWh/m^2/an) au Nord et(2263 kWh/m^2.an) au Sud du Algérien (Benatiallah, 2019) et (MERAD, 2013).
Quatre zones géographiques caractéristiques sur le territoire Algérien ont été choisis aux fins de cette analyse; qui sont: Alger, Constantine, Ouregla et Béchar. Ces villes ont été choisis car elles sont des échantillons représentatifs de trois régions climatiquement différente. Les données météorologiques sont obtenues grace au logiciel METEONORM 7, avec des données de période (1991-2010) pour les rayonnements solaires et (2000-2009) pour les températures.

Régions	Régions côtières	Hauts-Plateaux	Sahara
Superficie (%)	4	10	86
Durée moyenne d'ensoleillement (h/an)	2650	3000	3500
Energie moyenne reçue (kWh/m^2 /an)	1700	1900	2650

Tableau 1. Potentiel solaire en Algérie (Benatiallah, 2019).

Modèle d'application:

Pour le calcul de la quantité annuelle d'énergie électrique produite par une centrale à cyclone atmosphérique dans les zones géographiques citées, les caractéristiques techniques suivantes ont été adoptées :

- Diamètre du toit du collecteur : 122 m.
- Hauteur de collecteur solaire : 1,85 m.
- L'altitude estimée de cyclone : 1000 m
- La surface totale couverte par le toit collecteur à verre simple : 46000 m^2
- La différence de température choisie est 20 K.

On a adopté les mêmes dimensions géométrique de la structur de collecture de la centrale de manzanares,et on éstime que l'altitudes de cyclone géneréé peut attendre 1000 m.

Creative Commons Attribution-NonCommercial-NoDerivatives 4.0 International License (CC BY-NC-ND)

Algerian Journal of Engineering Architecture and Urbanism Vol. 5 Nr. 3 2021
ISSN: 2588-1760

Selon les paramètres d'entrée adoptés, et avec l'équation 8, les puissances électriques sont calculées mensuellement en fonction des heurs de fonctionnement de la centrale. Les puissance électrique calculées sont représentées graphiquement à la figure 2 sous la forme de colonnes pour les quatre emplacement choisis.

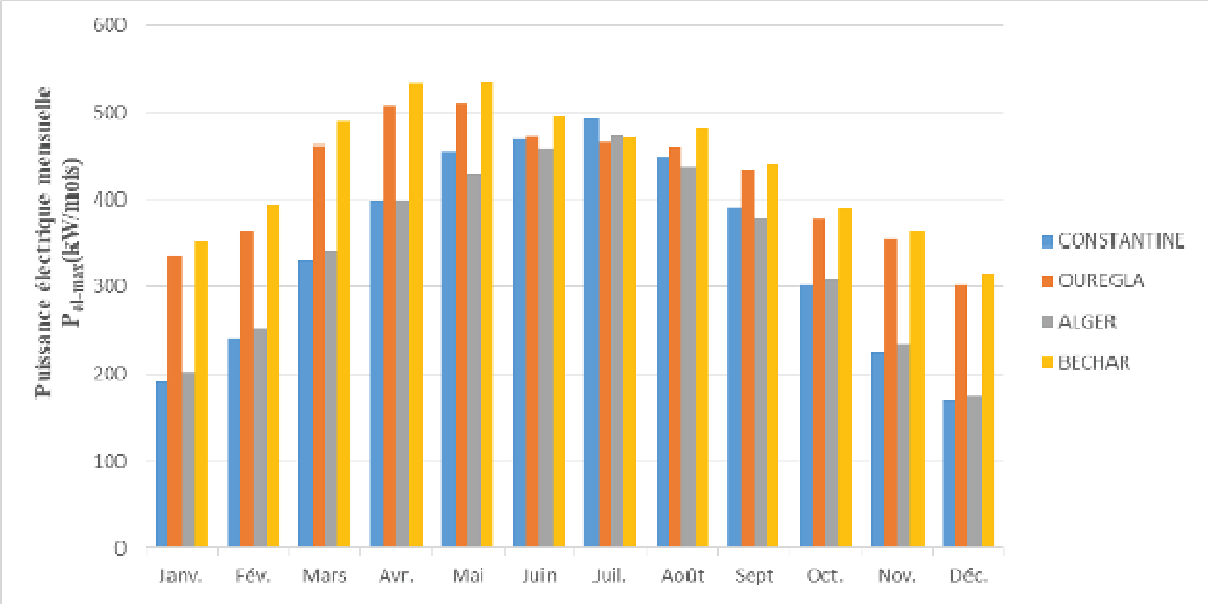

Fig2. Puissance électrique produite mensuellement par CSC

La puissance moyenne annuelle est calculé à partir des puissances mensuelles obtenue, conformément à l'Equation 9. La puissance électrique moyenne annuelle la plus élevée (P_{av-n}= 446,71 kW) est obtenue pour la région de Béchar. Les résultats sont présentés sur la Figure 3.

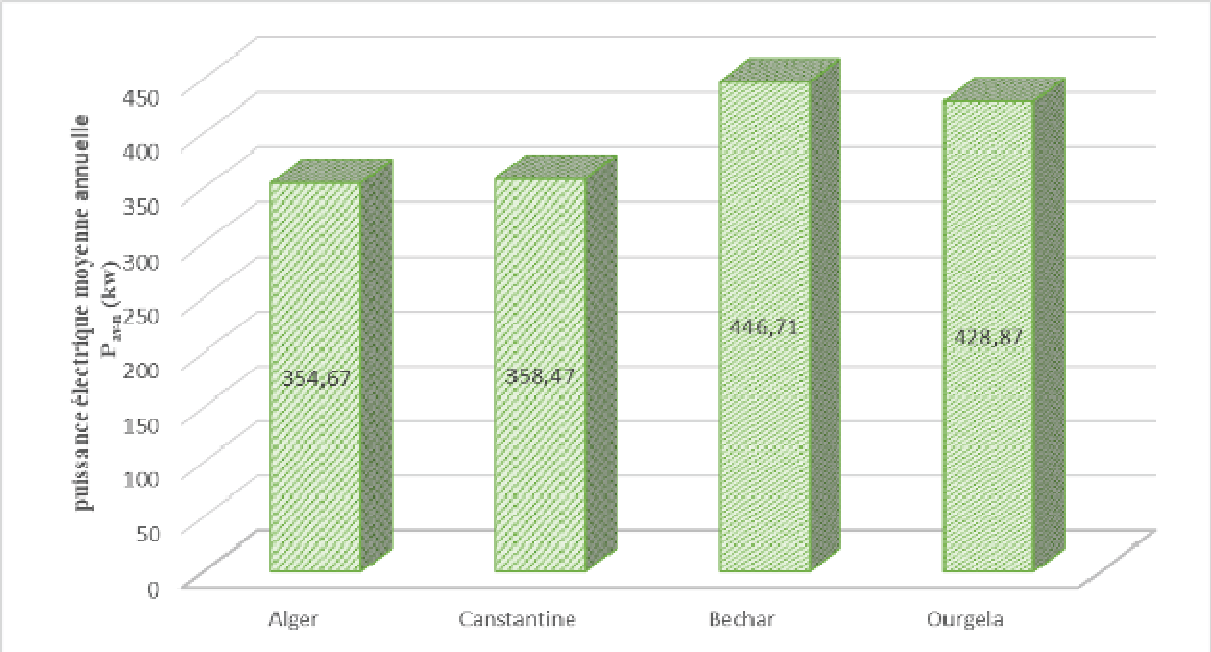

Fig3. La puissance électrique moyenne annuelle produit par CSC

Creative Commons Attribution-NonCommercial-NoDerivatives 4.0 International License (CC BY-NC-ND)

La production annuelle d'électricité cumulée sur une échelle mensuelle pour les différentes régions indiquées, est illustrée à la figure 4.

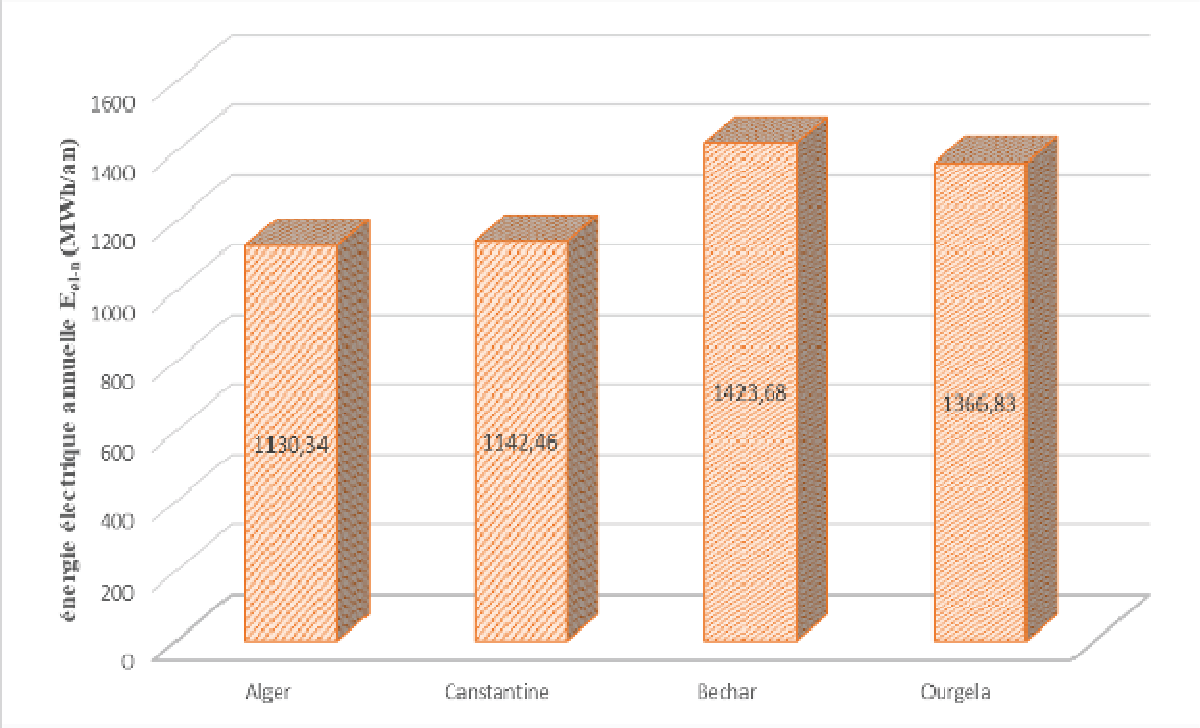

Fig1. La production annuelle d'énergie électrique par CSC

Conclusion:

La centrale électrique à cyclone atmosphériques présentant les caractéristiques techniques considéré dans ce travail produirait une énergie variant de 1,1 à 1,4 GWh/an en Algérie. L'analyse effectuée sur la CSC a montré qu'avec la même surface du collecteur la CSC pourrait produire jusqu'à 30 fois l'énergie produite par le prototype de la cheminée solaire de Manzanares. Sur la base de cette analyse, nous concluons que les centrales électriques solaire à cyclone atmosphérique sont bien adapté aux conditions surtout météorologique de l'Algérie et pourraient présenter une solution plus performante que les cheminées solaires classiques en termes de quantité d'énergie produite.

References:

Penga Z., Nizetic S., Arıcı M. (2019), *Solar plant with short diffuser concept: Further improvement of numerical model by included influence of guide vane topology on shape and stability of gravitational vortex*, Journal of Cleaner Production **212:** 353-361.

Al-Kayiem H.H., Mustafa A.T., Gilani S.I.U. (2018), *Solar vortex engine: experimental modelling and evaluation*, Renew. Energy Architecture **121:** 389-399.

Al-Kayiem H.H., Aja O.C. (2016), *Historic and recent progress in solar chimney power plant enhancing technologies*, Renewable and Sustainable Energy Reviews **58:** 1269-1292.

Michaud L., Monrad B. (2013), Energy from *Convective Vortices*, Applied Mechanics and Materials **283:** 73-86.

Azizia A., Tahrib T., Sellami M.H., Segni L., Belakroum R., Loudiyie K (2019), *Experimental and CFD investigation of small-scale solar chimney for power generation. Case study: southeast of Algeria*, Desalination and Water Treatment **160:** 1-8.

Nizetic S., Ninic N., Klarin B. (2008), *Analysis and feasibility of implementing solar chimney power plants in the Mediterranean region*, Energy **33:** 1680-1690.

Creative Commons Attribution-NonCommercial-NoDerivatives 4.0 International License (CC BY-NC-ND)

Guo P., Li T., Xu B., Xu X., Li J. (2019), *Questions and current understanding about solar chimney power plant: A review*, Energy Conversion and Management **182:** 21-33.

MERAD F. (2013), *Conception d'un programme de calcul du rayonnement solaire, cas particulier de la région de Mostaganem.*, Mémoire de magister, Université Abdel Hamid Ibn Badis, Mostaganem.

Benatiallah D. (2019), *Détermination du gisement solaire par imagerie satellitaire avec intégration dans un système d'information géographique pour le sud d'Algérie*, Thèse de doctorat, Université Africane Ahmed Draia, Adrar.

Creative Commons Attribution-NonCommercial-NoDerivatives 4.0 International License (CC BY-NC-ND)

Algerian Journal of Engineering Architecture and Urbanism Vol. 5 Nr. 3 2021
ISSN: 2588-1760

Study and performance analysis of a hybrid FSO/FO system with spatial diversity under different weather conditions

Amina DJIR
PhD student, Telecommunications and Digital Signal Processing Laboratory,
University of Djillali Liabes, Sidi Bel Abbes, Algeria,
e-mail: djir_amina@yahoo.com

Fatiha MESKINE
MCA, Communication Networks, Architectures and Multimedia Laboratory,
University of Djillali Liabes, Sidi Bel Abbes, Algeria,
e-mail: me_fatiha2010@hotmail.fr

Mohammed Larbi TAYEBI
MCB, Telecommunications and Digital Signal Processing Laboratory,
University of Djillali Liabes, Sidi Bel Abbes, Algeria,
e-mail: tayebi_med@hotmail.com

Abstract:
Free Space Optics (FSO) is a wireless optical communication technology based on the transmission of data in free space. It is based primarily on direct visibility (LOS) between the transmitter and receiver. However, the FSO is sensitive to different weather phenomena, namely fog, snow and rain. Variation of the transmission channel leads to a significant degradation of the performance of the FSO-based system and therefore leads to an increase in the Binary Error Rate (BER) and a deterioration of the quality factor Q. To overcome this handicap, we have adopted hybrid FSO/Fiber Optical architecture with the aim of improving the performance of the system.
Furthermore and in order to achieve as reliable a transmission as possible and thus reduce the effect of these natural phenomena on the quality of the signal, the concept of spatial diversity was used by sending several copies of the signal through different transmission channels. The signal from the FSO is directly connected to erbium-doped fiber optic amplifiers (EDFA). This system was simulated with the simulation software Optisystem v9. 0 and the performance analysis was carried out in terms of the Q factor and the eye diagram.

Key words: FSO, Fiber Optics FO, EDFA, Q Factor, BER.

I. Introduction

In the last few decades, optical wireless communication has become a very popular field with the increasing demand for high-speed technologies (Yu et al., 2015). For this reason, many researchers have shown great interest in this field. Among these technologies, FSO communications which constitute a serious and promising alternative and complement to radio frequency communications due to its advantages. Indeed, FSO has a very high bandwidth, a fast and simplified installation, a low cost and robustness against electromagnetic interferences (Kaushal and Zaddoum, 2017). This is the reason why it can be effectively used in several areas (Malik and Singh, 2015). It should be noted that FSO systems

Creative Commons Attribution-NonCommercial-NoDerivatives 4.0 International License (CC BY-NC-ND)

are designed to make connections between two fixed points (Singh, 2017) in line-of-sight (LOS) in which a laser source is used to transmit light through the atmospheric path and received by a photodiode.

Like all technologies, FSO systems have their own limitations. Weather conditions are one of the most critical factors that negatively impact performance and consequently lead to an increase in the bit error rate (BER) and a deterioration of the Q-factor. Due to these various negative factors, the reliability of FSO systems must be improved. (Khalighi et al., 2014) Studies have shown that optical attenuation can reach 340dB/km in fog with a visibility of 50 m (Kim et al., 2001). The solution proposed in (Tayebi et al., 2020) shows that the link range between the transmitter and receiver is doubled under the same atmospheric conditions.

Furthermore, several research studies have focused on hybrid approaches in order to improve the efficiency of FSO systems, such as RF/FSO (Liang et al., 2019) (Jiang et al., 2019), FSO/FO (Alnajjar et al., 2019) and FSO/VLC (Pesek et al., 2018). The work of (Alnajjar et al., 2020) has presented a hybrid FSO/Fiber Optical link that has been tested under various weather conditions. The combination of these different technologies may be better than one or the other because of the various positive factors that hybrid communication systems offer using the complementary advantages of different communication technologies. Moreover, the results presented in (Grover et al., 2017) showed that the link performance is improved under different weather conditions by using the multi-beam FSO-WDM system. (Kumar and Khandelwal, 2019) (Chatti et al., 2019) have proposed a MIMO-FSO system that has proven its performance compared to the conventional SISO-FSO.

In this paper, we have proposed a hybrid FSO/Fiber optic link. The proposed solution has been developed to improve the performance of the system under different weather conditions. Then, in order to obtain a transmission as reliable as possible and thus reduce the effect of these natural phenomena on the signal quality, the concept of spatial diversity was used by sending several copies of the signal through different transmission channels. This work was designed using the OPTISYSTEM v9.0 simulation software. The paper is organized as follows: the second section presents the theoretical FSO model, the third section is devoted to the description of the proposed model, in fourth section we studies and discusses the different simulation results performed under different weather conditions in order to analyze the performance of the system; and finally we concludes our research work.

Problematic:

Thanks to technological advances, the hybrid communication system has attracted great interest in recent years because of its advantages. The ubiquitous coverage of RF systems, the very low attenuation achieved by fiber optics, the high speed achieved by VLC technology and the low cost provided by FSO systems make these technologies complementary to each other. These mixed systems have recently received considerable attention.

The question that arises in this work is: How to improve the performance of an FSO link? And what hybrid system is used to ensure reliable long-distance transmission?

Creative Commons Attribution-NonCommercial-NoDerivatives 4.0 International License (CC BY-NC-ND)

It should be noted FSO shares the same characteristics as wireless optics such as high data rate, flexible access, high security and robustness against electromagnetic interference. To achieve acceptable Q-factor and BER performance for an FSO link, some major challenges must be overcome. Atmospheric attenuation is one of the challenges of the FSO channel that can lead to the loss of power of the transmitted information signal.

II. FSO theoretical model

Various weather conditions are responsible for disturbing the transmitted information signal. The attenuation phenomenon is the main problem affecting the performance of optical wireless communications. (Alnajjar et al., 2019)

According to Beer Lambert's law, the attenuation experienced by light as it propagates through the atmosphere is defined by the ratio of the received power to the transmitted power.

$$A_{ATM} = \frac{P_R}{P_T} = e^{-\alpha L} \tag{1}$$

Where α is the attenuation coefficient and L is the link distance (in km). Determination of the atmospheric attenuation coefficient values α is possible using an estimate of the visibility range of the link and the wavelength λ. It is given by the following relationship: (Kim et al., 2001)

$$\alpha = \frac{3.912}{V}\left(\frac{\lambda}{550(nm)}\right)^{-q} \tag{2}$$

Where α denotes the attenuation coefficient and V, λ, and q represent the visibility vector in km, wavelength in nm, and the scattering particle size distribution coefficient, respectively. The values of the q coefficient can be calculated using several models. The values of q can be obtained from the KRUSE model (Kruse et al., 1962).

$$q = \begin{cases} 1.6 \ \ for \ V > 50 \\ 1.3 \ \ for \ 6 < V < 50 \\ 0.585.V^{\frac{1}{3}} \ \ for \ V < 6 \end{cases} \tag{3}$$

The parameter q takes the following values, according to the KIM model

$$q = \begin{cases} 1.6 \ \ for \ \ V > 50 \\ 1.3 \ \ for \ \ 6 < V < 50 \\ 0.16V + 0.34 \ \ for \ 1 < V < 6 \\ V - 0.5 \ \ for \ \ 0.5 < V < 1 \\ 0 \ for \ V < 0.5 \end{cases} \tag{4}$$

III. Simulation design model

Creative Commons Attribution-NonCommercial-NoDerivatives 4.0 International License (CC BY-NC-ND)

In this paper, the influence of different weather conditions on the link performance is analyzed through a proposed hybrid system. The designed hybrid multiple Tx/Rx FSO/FO system is shown in Fig.1. The proposed system consists of three parts, the transmitter, the propagation channel and the receiver. The transmission part includes a pseudo-random bit generator that generates the information signal, a non-return-to-zero (NRZ) pulse generator that converts the binary signals into electrical signals. The Mach- zehnder modulator (MZM) receives these electrical signals and modulates them with the optical carrier signal generated by the continuous wave (CW) laser diode with a wavelength of 1550nm. An avalanche photodiode (APD) and a low-pass Bessel shaping filter are used in the receiving system. Finally a BER analyzer to analyze the different parameters of our system such as the BER bit error rate, the Q factor and the eye diagram.

In order to improve the performance of the FSO link, several beams are sent through different paths. Here four FSO channels (4Tx/4Rx) are considered. A Fork is used to duplicate the input beam and at the receiving end, a power combiner is used to combine the optical signals from these different channels. In this research, an optical fiber is used and a 3 km dispersion compensation fiber (DCF) is used to overcome the dispersion problem. In addition, the attenuation in the fiber is compensated by adopting an erbium-doped fiber amplifier (EDFA). The different parameters used in this simulation are listed in table 1:

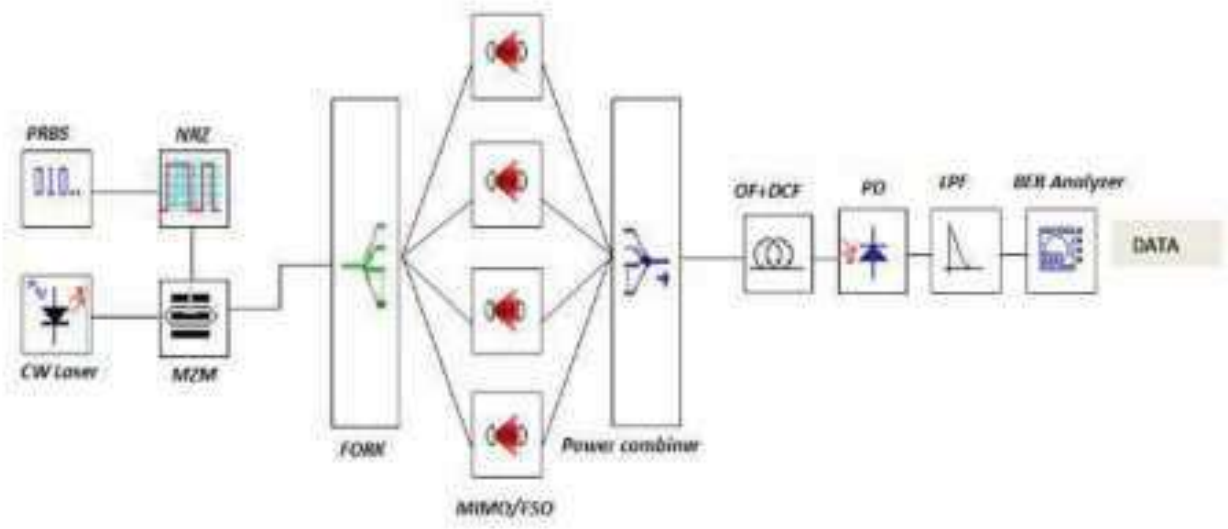

Fig1. Block diagram of a hybrid multiple Tx/Rx FSO / FO system.

Parameters	***Value***
Range (FSO)	***1km à 9km***
Transmitted power	***10 dBm***
Wavelength of laser source	***1550 nm***
Transmission rate	***10 Gbps***
Fiber length	***OF (50km) et DCF (3km)***
Clear Attenuation	***0.24dB/km***

Creative Commons Attribution-NonCommercial-NoDerivatives 4.0 International License (CC BY-NC-ND)

hazy Attenuation	***2.67dB/km***

Table1. Simulation parameters.

IV Results and discussions:

In this paper, the influence of different weather conditions on the performance of a hybrid multiple Tx/Rx FSO/FO link is studied and simulated. The proposed system is designed to operate at the wavelength of 1550 nm. The performance of the system has been analyzed and compared on the basis of Q-factor and BER. A comparison was conducted with the conventional multiple Tx/Rx FSO link. It should be noted that the acceptable bit error rate and Q-factor for telecommunication applications are 10^{-9} and 6 respectively. Initially, the distance of FSO link is set to 15 km. Fig.2 shows the eye diagrams and Q factors of the hybrid and conventional system in a clear environment.

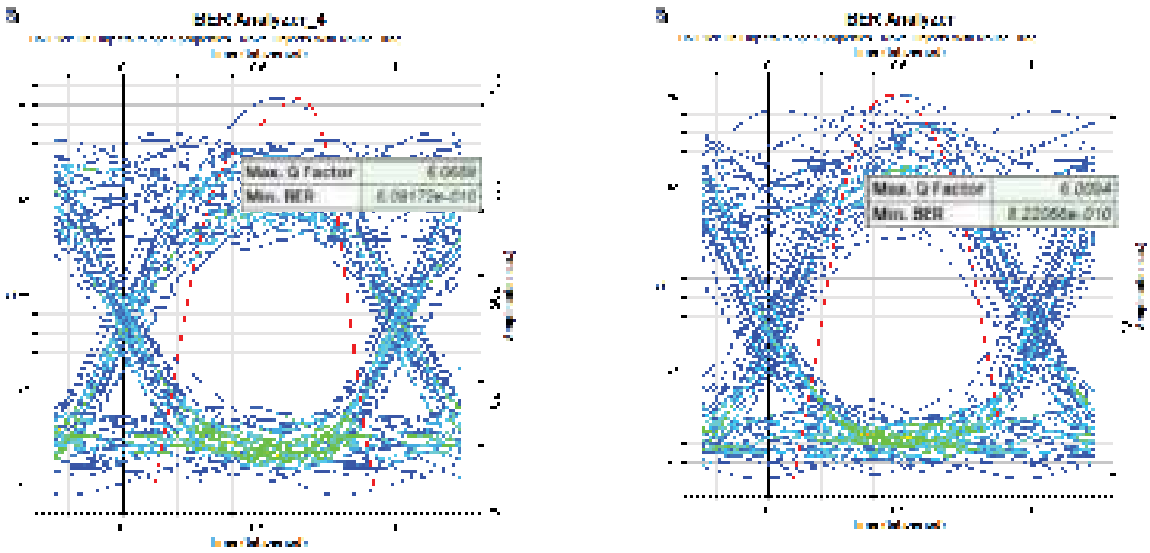

(a) (b)

Fig2. Eye diagram: (a) conventional system after 15km (b) hybrid system after 50 km at 0.24dB/km.

The results obtained using BER analyzers clearly show that distance (range) has a significant impact on system performance, with the Q-factor of the conventional and hybrid FSO systems being approximately 6. After a range of 50 kilometers, the proposed system outperforms the traditional FSO system.

Fig.3 shows the variation of the Q-factor with distance, comparing the multiple Tx/Rx FSO system and the hybrid multiple Tx/Rx FSO / FO system after 50 km at 0.24 dB /km. The numerical results of the different simulations are presented below.

Creative Commons Attribution-NonCommercial-NoDerivatives 4.0 International License (CC BY-NC-ND)

Algerian Journal of Engineering Architecture and Urbanism Vol. 5 Nr. 3 2021
ISSN: 2588-1760

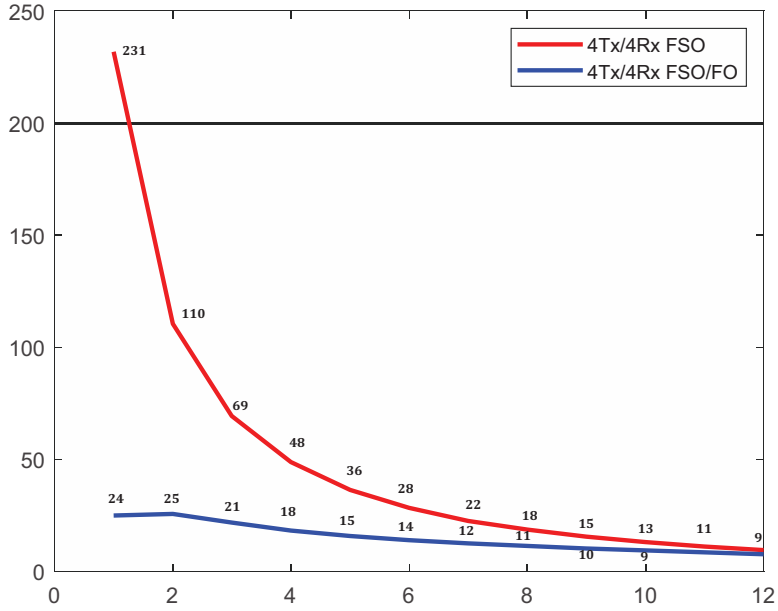

Fig3. Q-factor versus range for a 4TX/4Rx FSO system and a hybrid 4Tx/4Rx FSO /FO system after 50km at 0.24 dB /km.

The proposed link shows a remarkable difference in performance compared to the conventional multiple Tx/Rx FSO link. The communication distance with the hybrid link is increased by 50 km compared to the multiple Tx/Rx FSO communications which does not exceed 13 km. The difference in performance evaluation in the multiple Tx/Rx FSO system is relatively due to the degradation of the information signal in its propagation through the air due to weather changes (according to the Beer-Lambert law), On the other hand, the optical fiber is characterized by a very low attenuation, about 0.2 dB / km. The variation of the attenuation in the fiber is a linear relationship, ie it depends only on the distance.

The haze attenuation is 2.76dB/km and the distance is set to 1 km. The eye diagrams of the two FSO systems under hazy environmental conditions are shown in Fig.4.

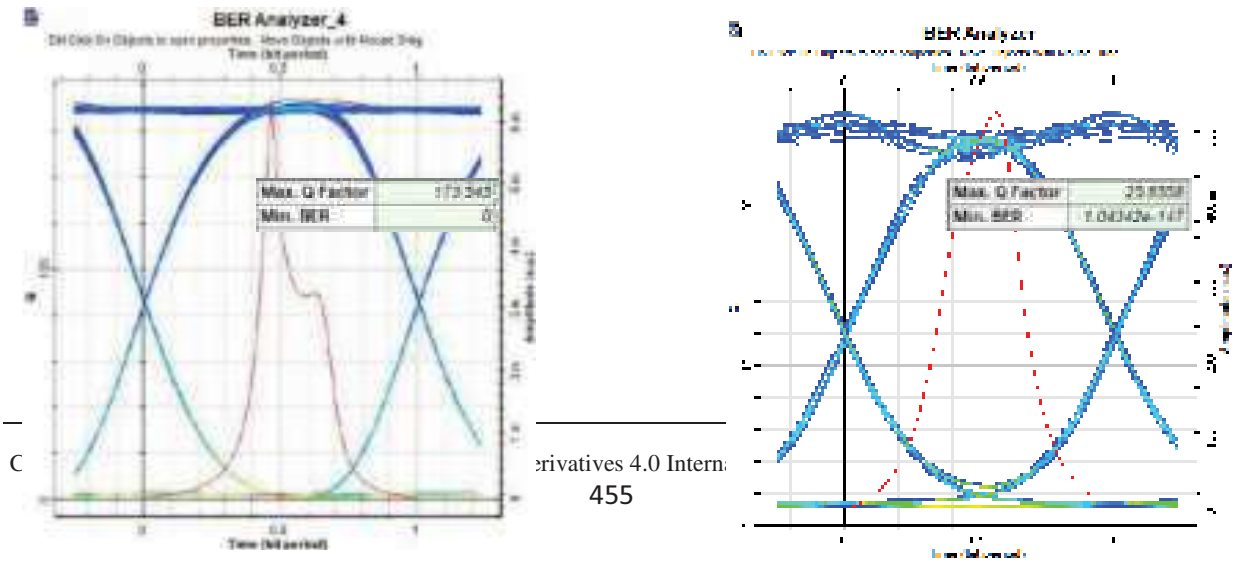

C erivatives 4.0 Interna

(a) (b)

Fig4. Eye diagram (a) multiple Tx/Rx FSO system (b) hybrid multiple Tx/Rx FSO/FO system after 50 km at 2.67dB/km.

From the results obtained using the BER analyzer, Figure 4 clearly shows that the Q-factor of the multiple Tx/Rx FSO system and the hybrid multiple Tx/Rx FSO system are 173.54 and 25.85 respectively. It can be seen that also in this case, the proposed hybrid system is more efficient after 50km. Figure 5 shows the variation of Q-factor with link range for both communication systems under hazy conditions.

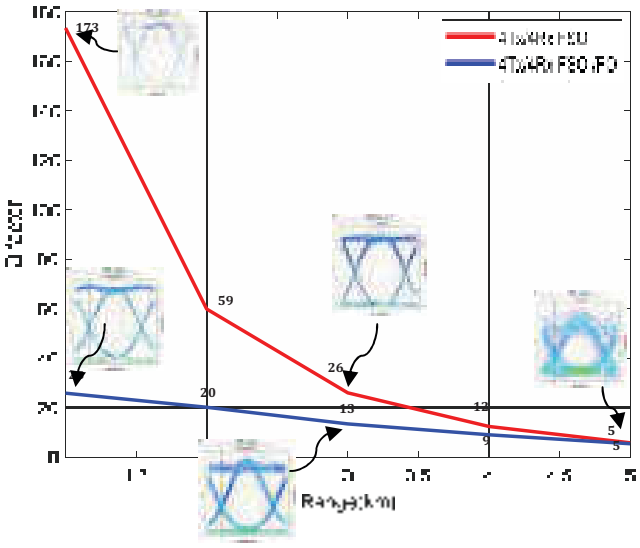

Fig5. Q factor versus range for a 4Tx/Rx FSO system and a hybrid 4Tx/Rx FSO /FO system after 50km at 2.67dB /km.

Based on the curves and eye diagrams presented in the figure above, we conclude that under hazy conditions, the multiple Tx/Rx FSO/FO system gives a better solution after a distance of 50km compared to the conventional system. The obtained Q-factor becomes approximately equal to 6 at the distance of 5km for the multiple Tx/Rx FSO link. On the other hand, an improvement is clearly demonstrated by using the new hybrid design after 50km. It can be seen that this degradation is the result of the increase in attenuation as a function of link distance.

V. Conclusion:

The rapid development of information technology has led to an enormous demand for high-capacity communication systems. FSO has emerged as an attractive alternative to radio frequency (RF) communication. However, like any technology, FSO is very sensitive to

Creative Commons Attribution-NonCommercial-NoDerivatives 4.0 International License (CC BY-NC-ND)

weather conditions which consequently lead to a deterioration of the overall system performance.

In this paper, a new system design has been studied and simulated. The proposed system is designed to transmit the signal to a distance of 50 km under different conditions. Based on the simulation results, the effectiveness against weather change has been approved with the hybrid multiple Tx/Rx FSO/FO system.

References:

Alnajjar S H., Ali M H., Al-obaidi A., and Alsaedi M A. (2020), *Hybrid of Multiple (TX /RX) FSO / Fiber Optic Communication System under Environmental Disturbances*, Journal of Multidisciplinary Approaches in Science, **2(1)**: 7–16.

Alnajjar S H., Ali M H., and Abass A. (2019), *Enhancing Performance of Hybrid FSO/Fiber Optic Communication Link Utilizing Multi-Channel Configuration*, https://doi.org/10.1515/joc-2018-0193.

Chatti I., Baklouti F., Chekir F., Attia R. (2019), *Comparative analysis of MIMO□based FSO and MIMO□based MGDM communications*, Optical Review, **26**: 631–643.

Grover M., Singh P., and Kaur P. (2017), *Performance Analysis of Multibeam WDM-FSO System in Clear and Hazy Weather Conditions*, In Proceeding of international conference on intelligent communication, control and devices, **479**: 189-195.

Jiang T., Zhao L., Liu H., Deng D., Luo A., Wei Z., and Yang X. (2019). *Performance Improvement for Mixed RF–FSO Communication System by Adopting Hybrid Subcarrier Intensity Modulation*, Applied Sciences, **9(18)**: 3724.

Kaushal H and Kaddoum G. (2017), *Optical Communication in Space: Challenges and Mitigation Techniques*, In *IEEE Communications Surveys & Tutorials,* **19(1):** 57–96.

Khalighi M A., Uysal M., Marseille C., and Engineering E. (2014), *Survey on Free Space Optical Communication : A Communication Theory Perspective*, In *IEEE Communications Surveys & Tutorials,* **16(4)**: 2231–2258.

Kim I I., McArthur B., Korevaar. (2001), *Comparison of laser beam propagation at 785 nm and 1550 nm in fog and haze for optical wireless communications*, In Optical Wireless Communications III, **4214**: 26-37.

Kruse P.W. and al. (1962), *Elements of infrared technology: Generation, transmission and detection*, J Wiley and sons, New York.

Kumar N and Khandelwal V. (2019), *Simulation of MIMO-FSO System with Gamma-Gamma Fading under Different Atmospheric Turbulence Conditions*, International Conference on Signal Processing and Communication**, 1(2)**: 117–124.

Liang H., Gao C., Li. Y, Miao M., and Li X. (2019), *Analysis of selection combining scheme for hybrid FSO/RF transmission considering misalignment*, *Optics Communications,* 435: 399-404.

Mahajan S., Parkash D., and Singh H.. *(2020), Design and Investigation of Multiple TX/RX FSO Systems Under Different Weather Conditions,* In proceedings of ICRIC, **397**: 377-388.

Malik A and Singh P. (2015), *Free space optics: current applications and future challenges*, International Journal of Optics, **2015(6):** 1–7.

Pesek P., Zvánovec S., Chvojka P., Ghassemlooy Z. and Haigh P A. (2018), *Demonstration of a Hybrid FSO/VLC Link for the Last Mile and Last Meter Networks*, in IEEE Photonics Journal, **11(1):** 1-7.

Singh M.. (2017), *Mitigating the Effects of Fog Attenuation in FSO Communication Link Using Multiple Transceivers and EDFA*, Journal of Optical Communications, **38(2)**: 169–174.

Tayebi M L., Djir A., and Meskine F.. (2020), *Performance evaluation of a multiple optical link FSO–FSO*, Journal of optical communications, https://doi.org/10.1515/joc-2020-0058.

Creative Commons Attribution-NonCommercial-NoDerivatives 4.0 International License (CC BY-NC-ND)

Yu Y L., Liaw S K., Chou H H., Le-Minh H., and Ghassemlooy Z. (2015), A *Hybrid Optical Fiber and FSO System for Bidirectional Communications Used in Bridges*, IEEE Photonics Journal, **7(6):** 1–9.

Creative Commons Attribution-NonCommercial-NoDerivatives 4.0 International License (CC BY-NC-ND)

Algerian Journal of Engineering Architecture and Urbanism Vol. 5 Nr. 3 2021
ISSN: 2588-1760

EFFECT MPPT CONTROL ON WIND ENERGY CONVENTION SYSTEM BASED IN DFIG CONTROLLED BY VECTOR CONTROL (IFOC)

Moufida SAADI
Laboratoire de Génie Électrique (LABGET), Larbi Tebessi University of Tébessa, e-mail: saadimoufida8@gmail.com
Djalel DIB
Laboratoire de Génie Électrique (LABGET), Larbi Tebessi University of Tébessa, e-mail: dibdjalel@gmail.com
Billel MEGHNI
Department of electrical Engineering. Badji Mokhtar University of Annaba, e-mail: maghni_1990@yahoo.fr

Abstract:
Present in this paper we present effect MPPT control on Wind Energy Convention System based in DFIG controlled by vector control. For wind energy conversion system the control strategy consists of a simple vector control with impressed rotor currents. This strategy allows generating constant frequency and voltage with variable mechanical speed and will make it possible to act on the rotor signals in order to control the exchange of active and reactive power between the stator of the machine and the network. The behaviour of the voltage and frequency, under variable speed are shown. The results confirm the feasibility and effectiveness of the proposed control strategy is validated by the simulation model including a 1.5 MW-DFIG driven by a wind turbine, a PWM back-to-back inverter and the proposed control strategy are developed and implemented using MATLAB/Simulink/SimPowerSystems environment.
Key words: DFIG, MPPT, Wind turbine, IFOC, PWM, SimPowerSystems, Simulink

Introduction:

Wind energy is that the most promising renewable supply of electric power generation for the long run. Several countries promote alternative energy technology through varied national programs and market incentives. Wind energy technology has evolved chop-chop over the past 3 decades with increasing rotor diameters and advanced power physics to permit operation at the variable speed [1]

Wind power generation is subject to fluctuations thanks to the intermittent nature of wind energy and wind speed variations. this is often additional evident once multiple generators are connected to a weak grid [2].

Since twenties years, the thought of the variable speed turbine (VSWT) equipped with a doubly fed induction generator (DFIG) has received increasing attention thanks to its noticeable blessings over different wind turbine ideas.

Fixed-speed induction generators square measure forced to control close to the synchronous speed, as a result of the frequency is obligatory by the network; the rotor speed is sort of constant. Variable-speed turbine systems, on the opposite hand, square measure able to operate over a good vary of wind speeds. What is more, victimisation associate degree acceptable most point chase (MPPT) strategy, variable-speed wind turbines will manufacture most power at varied wind speed conditions. For variable-speed turbine systems with

Creative Commons Attribution-NonCommercial-NoDerivatives 4.0 International License (CC BY-NC-ND)

restricted speed vary, e.g. ± half-hour of synchronous speed, the DFIG may be the answer of selection [3].

Unlike typical wind turbine-driven synchronous generators, the output characteristic of the variable-speed wind energy conversion systems (WECS) depends not solely on the dynamics of the generator however additionally on the convertor management strategy utilized. Management methods of DFIG are extensively mentioned by many authors [4, 5]. In [6], varied management mechanisms for the DFIG are according victimization stator coil flux orientation within the coordinate system α-β.

In [7] and [8], the stator coil flux familiarised management of the generator DFIG has been studied however with none management of the grid facet and DC link voltages. In [9], the authors studied the result of active and reactive powers variations by a decoupling management technique for the active and reactive powers.. This paper presents a comprehensive simulation study of the variations of reactive power on the grid underneath completely different types vector control and analyses the influence of those control on the DFIG power issue that reflects the standard of the facility generated.

In recent years, many robust control techniques have been proposed in the literature to improve the operation performances of the DFIG.[10]

When grid faults appear like unbalanced voltages [11,12] and voltage dips [13]. It has also been shown in [14,15] that glimmer problems could be resolved with suitable control strategies. Many of these works prove that stator reactive power control can be an adapted solution to these diverse problems.

In this paper presents the overall simulation model structure including mathematical models of the wind turbine. The proposed MPPT method used in the model is also presented and modeling DFIG controlled by two control, rotor control (converter), and stator control (vector control) scheme using Park transformation, Finally, simulation results show effect MPPT control on performance DFIG for optimization The quality of the electrical energy produced.

SYSTEM MODELING

The proposed circuit is shown in Figure1. It consists of a three-blade wind turbine connected to a variable-speed DFIG. The stator circuit of the DFIG is directly connected to the grid, whereas the rotor winding is connected to the grid via two PWM-controlled IGBT-converters. The two converters are coupled through a DC link capacitor.

The rotor-side converter controls simultaneously the active and reactive powers by adjusting the amplitude, frequency and phase of the rotor voltages. The aim of the grid-side converter is to regulate the DC link voltage. The inputs to the control system are the voltages and currents on the source side and the voltage on the DC side. These quantities are transformed into their d and q components. A phase-locked loop circuit is used to synchronize the frequency of the system with the network frequency. [16] the vector control is strategy has been widely used for robust control of nonlinear systems.

Creative Commons Attribution-NonCommercial-NoDerivatives 4.0 International License (CC BY-NC-ND)

Algerian Journal of Engineering Architecture and Urbanism Vol. 5 Nr. 3 2021
ISSN: 2588-1760

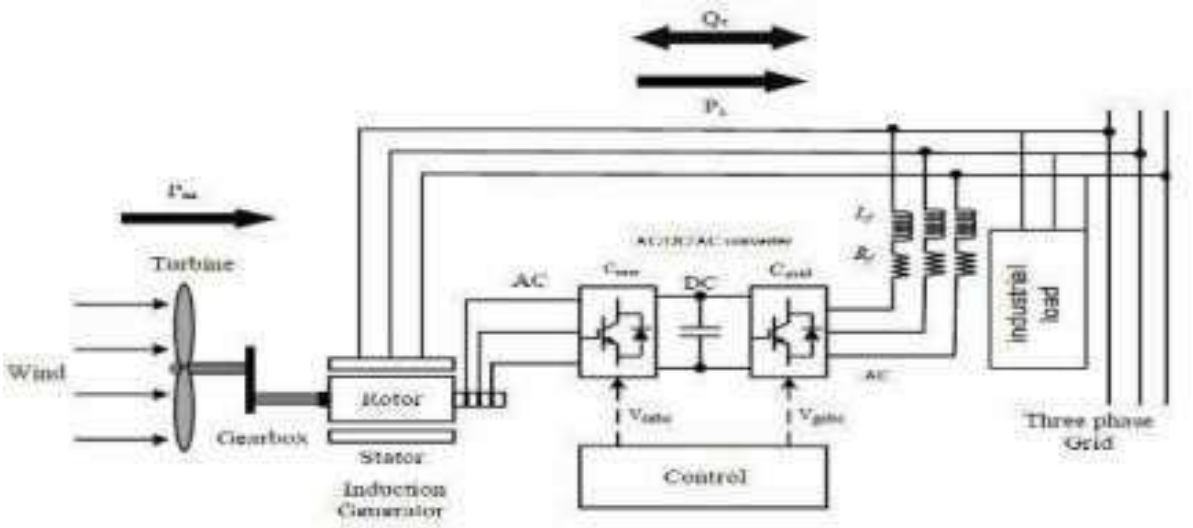

Fig.1. Schematic diagram of wind turbine based on DFIG [16]

1. Wind turbine model with MPPT strategy

The relationship between the wind speed and the aerodynamic mechanical power extracted from the wind can be described as follows [17, 18]:

$$P_m = \frac{1}{2}\rho\pi R^2 . C_p(\lambda, \beta) . v^3 \quad (1)$$

The power coefficient Cp defines the aerodynamic efficiency of the wind turbine. It depends on the characteristic of the turbine and is a function of the speed ratio λ and the orientation angle β of the blade:

$$C_p(\lambda,\beta) = C_1\left(\frac{C_2}{\lambda_i} - (C_3)\beta - C_4\right)e^{-\frac{C_5}{\lambda_{ii}}} + C_6\lambda \quad (2)$$

The values used for the coefficients C1 - C6 are given in Table 1 [19]:

The tip speed ratio is defined by the following relation:

$$\lambda = \frac{\Omega_{turbine} R}{V} \quad (3)$$

It can be observed from Figure 2 that the power coefficient reaches a maximum for a pitch angle of 0° and a particular value λoptimal = 8.1 of the velocity ratio. The power coefficient value corresponding to λoptimal is Cpmax = 0.48.

Creative Commons Attribution-NonCommercial-NoDerivatives 4.0 International License (CC BY-NC-ND)

Algerian Journal of Engineering Architecture and Urbanism Vol. 5 Nr. 3 2021
ISSN: 2588-1760

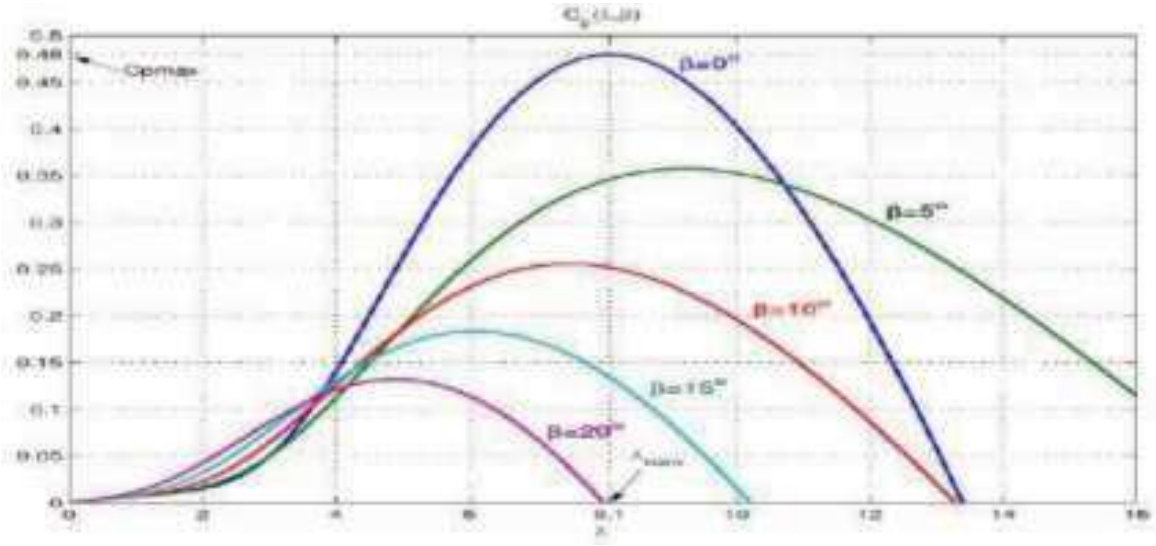

Fig.2. Characteristic of the power coefficient as a function of λ[16]

2. Maximum Power Point Tracking (MPPT)

The principle of this technique is to rotate the turbine over a certain wind speed range in order to maintain the TSR at its optimal value opt which make the turbine operating at CP=Cpmax. Considering equation 1, the captured power from the wind is expressed as a function of the rotational speed [9]:

$$P_t = \frac{1}{2}\rho\,\pi\,R^5\,\frac{C_p(\lambda,\beta)}{\lambda^3}\,\Omega_m^3 \tag{4}$$

Replacing by opt and replacing CP (, β)=Cpmax, the maximum power to be captured is expressed as:

$$P_t^{max} = K_{opt}\,\Omega_m^3 \tag{5}$$

Where $K_{optimal}$ is coefficient

$$K_{opt} = \frac{1}{2}\rho\,\pi\,R^5\,\frac{C_{Pmax}(\lambda_{opt},\beta)}{\lambda_{opt}^3} \tag{6}$$

As a result, the reference electromagnetic turquois given by:

$$T_{em}^{ref} = K_{opt}\,\Omega_m^2 \tag{7}$$

Creative Commons Attribution-NonCommercial-NoDerivatives 4.0 International License (CC BY-NC-ND)

Algerian Journal of Engineering Architecture and Urbanism Vol. 5 Nr. 3 2021
ISSN: 2588-1760

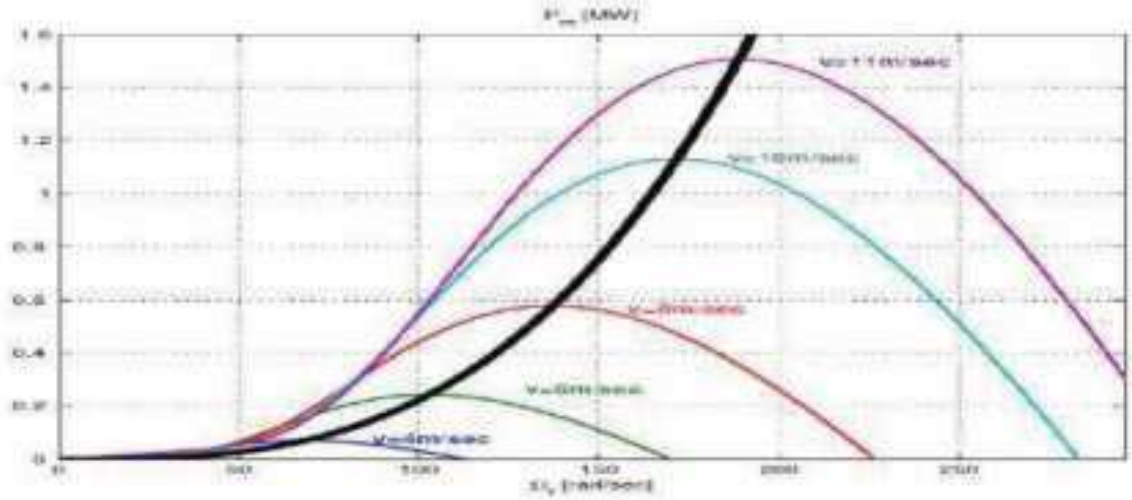

Fig. 3. The characteristics of system optimum turbine[16]

3. Modeling of the DFIG

The equivalent circuit of the DFIG in the synchronous reference frame rotating at the angular synchronous speed ωs is depicted in Fig.1. [10]

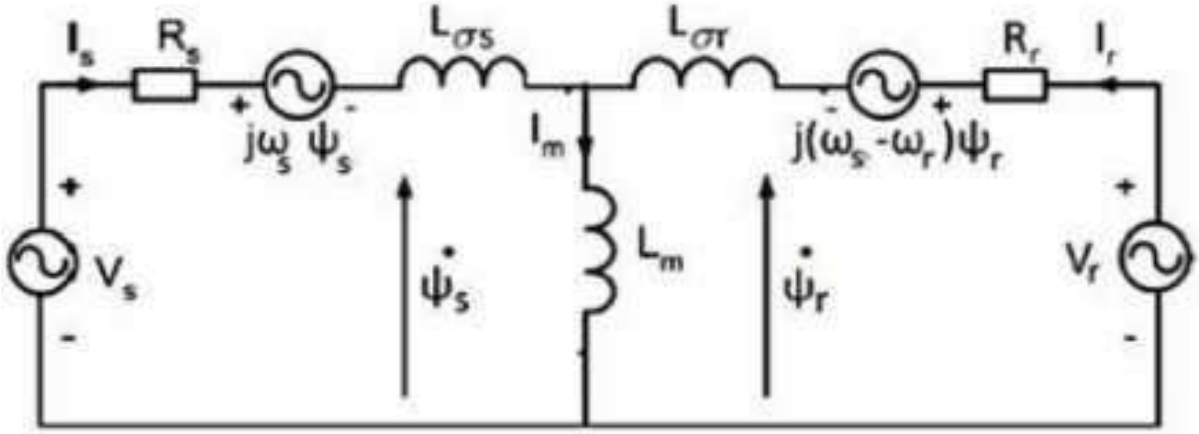

Fig.4. DFIG equivalent circuit in the synchronous reference frame

The model of the DFIG in the synchronous *d-q* reference frame is given by the following equations:

Stator voltage components:

$$\begin{cases} V_{ds} = R_s I_{ds} + \dfrac{d}{dt}\Psi_{ds} - \omega_s \Psi_{qs} \\ V_{qs} = R_s I_{qs} + \dfrac{d}{dt}\Psi_{qs} + \omega_s \Psi_{ds} \end{cases} \quad (8)$$

Creative Commons Attribution-NonCommercial-NoDerivatives 4.0 International License (CC BY-NC-ND)

Rotor voltage components:

$$\begin{cases} V_{dr} = R_r I_{dr} + \dfrac{d}{dt}\Psi_{dr} - (\omega_s - \omega_r)\Psi_{qr} \\ V_{qr} = R_r I_{qr} + \dfrac{d}{dt}\Psi_{qr} + (\omega_s - \omega_r)\Psi_{dr} \end{cases} \quad (9)$$

DFIG electromagnetic torque:

$$T_{em} = \frac{3}{2} P \frac{L_m}{L_s}\left(\Psi_{qs} I_{dr} - \Psi_{ds} I_{qr}\right) \quad (10)$$

Mechanical equation:

$$T_t = T_{em} + J\frac{d\Omega_r}{dt} + f_r \Omega_r \quad (11)$$

The expressions of the generator's active and reactive power on the stator side are:

$$\begin{cases} P_s = \dfrac{3}{2}\left(V_{ds} I_{ds} + V_{qs} I_{qs}\right) \\ Q_s = \dfrac{3}{2}\left(V_{qs} I_{ds} - V_{ds} I_{qs}\right) \end{cases} \quad (12)$$

The rotor-side converter is controlled in a synchronously rotating *d-q* axis frame, with the *d*-axis oriented along the stator flux vector position. The effect of the stator resistance can be neglected and the stator flux can be held constant as the stator is connected to the grid. Consequently (13)

$$\Psi_{ds} = \Psi_s \text{ And } \Psi_{qs} = 0 \quad (13)$$

Since the stator is directly connected to the grid and the stator flux can be considered constant, and if the voltage dropped in the stator resistance has been neglected [20], the voltage equations, flux equations, currents equations and stator active and reactive powers equations can be simplified in study state as:

$$\begin{cases} V_{ds} = 0 \\ V_{qs} = V_s = \omega_s . \Psi_s \end{cases} \quad (14)$$

$$\begin{cases} \Psi_s = L_s I_{ds} + L_m I_{dr} \\ 0 = L_s I_{qs} + L_m I_{qr} \end{cases} \quad (15)$$

Creative Commons Attribution-NonCommercial-NoDerivatives 4.0 International License (CC BY-NC-ND)

$$\begin{cases} I_{ds} = \dfrac{\Psi_s}{L_s} - \dfrac{L_m}{L_s} I_{dr} \\ I_{qs} = -\dfrac{L_m}{L_s} I_{qr} \end{cases} \quad (16)$$

$$\begin{cases} P_s = \dfrac{3}{2} V_s I_{qs} \\ Q_s = \dfrac{3}{2} V_s I_{ds} \end{cases} \quad (17)$$

Replacing the stator currents by their expressions given in (11), the equations below are expressed by:

$$\begin{cases} P_s = -\dfrac{3}{2}\dfrac{L_m}{L_s} V_s I_{qr} \\ Q_s = \dfrac{3}{2} V_s \left(\dfrac{V_s}{L_s . \omega_s} - \dfrac{L_m}{L_s} I_{dr} \right) \end{cases} \quad (18)$$

The electromagnetic torque is as follows:

$$T_{em} = -\frac{3}{2} P \frac{L_m}{L_S} \Psi_s I_{qr} \quad (19)$$

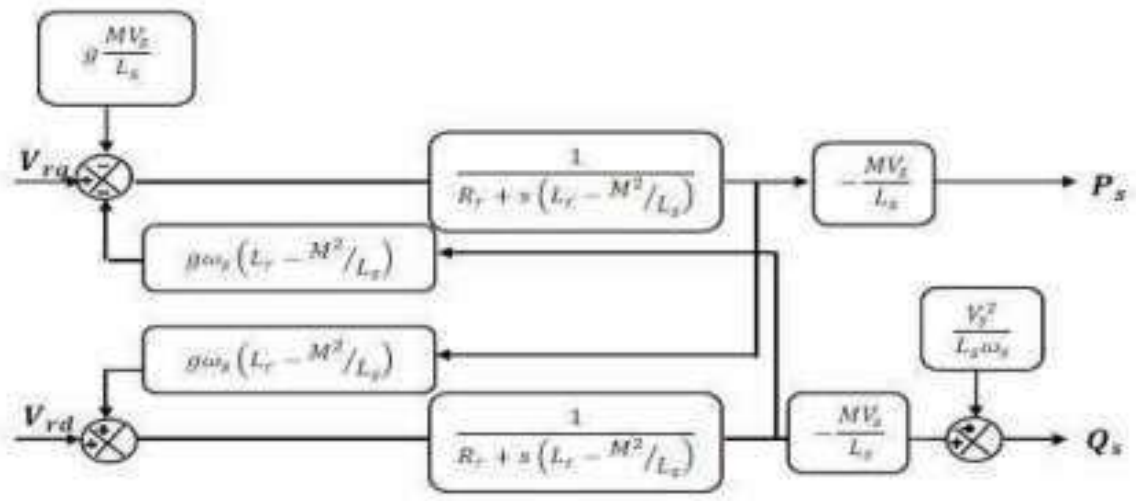

Fig.5. Block diagram of the DFIG.

Creative Commons Attribution-NonCommercial-NoDerivatives 4.0 International License (CC BY-NC-ND)

4. Proposed control strategy

Shows a block diagram of a Doubly-Fed Induction Generator fig1, which consists on a current controlled PWM inverter feeding the rotor windings and the proposed controller. The proposed control strategy is implemented using two independent control loops, one to control stator voltage frequency (frequency control loop) and the other one to control stator voltage magnitude (voltage control loop). Rotor current d and q components, idr and iqr, are used as the independent control variables.

5. The model of the converter with standard IGBTs is defined as

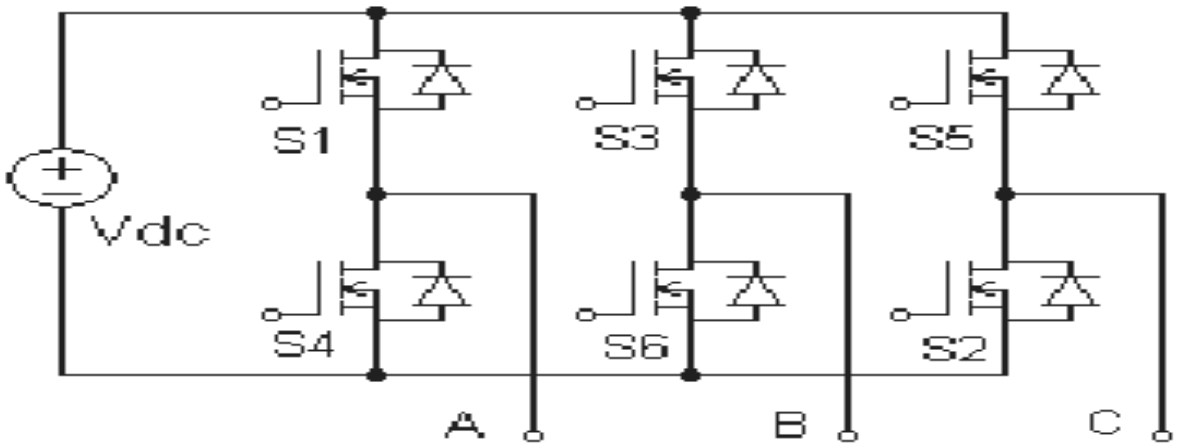

Fig.6. Structure of the two level converters with standard IGBTs

$$\begin{bmatrix} V_{an} \\ V_{bn} \\ V_{cn} \end{bmatrix} = \frac{V_{dc}}{3} \begin{bmatrix} 2 & -1 & -1 \\ -1 & 2 & -1 \\ -1 & -1 & 2 \end{bmatrix} \begin{bmatrix} S_a \\ S_b \\ S_c \end{bmatrix} \tag{20}$$

Where S_a, S_b, and S_c are the command signals, V_{an}, V_{bn}, and V_{cn} are the output voltages and V_{dc} is DC bus voltage.

6. Indirect field-oriented control (IFOC)

$$\begin{cases} I_{qr-r} = -\dfrac{L_s}{M V_s} P_{s\_ref} \\ I_{dr-r} = -\dfrac{L_s}{M V_s} Q_{s\_ref} + \dfrac{V_s}{\omega_s M} \end{cases} \tag{21}$$

Creative Commons Attribution-NonCommercial-NoDerivatives 4.0 International License (CC BY-NC-ND)

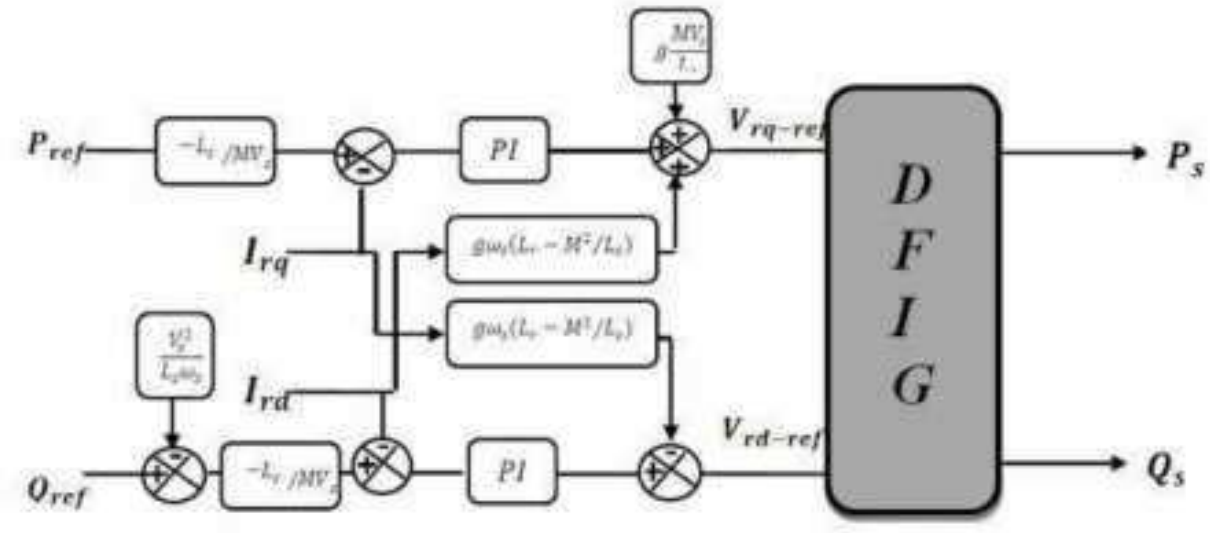

Fig.7. Block diagram of the indirect open loop control.

7. Simulation results and discussion

In this section, the control strategies of 1.5MW DFIG (see Table 1 in appendix) are tested by simulation under MATLAB/SIMULINK software. Both techniques are compared according to three criteria:

1- References tracking test at variable wind speed.

2- Robustness test against the deferent type of vector control the DFIG at variable wind speed.

3- Power quality analysis (chattering effect).

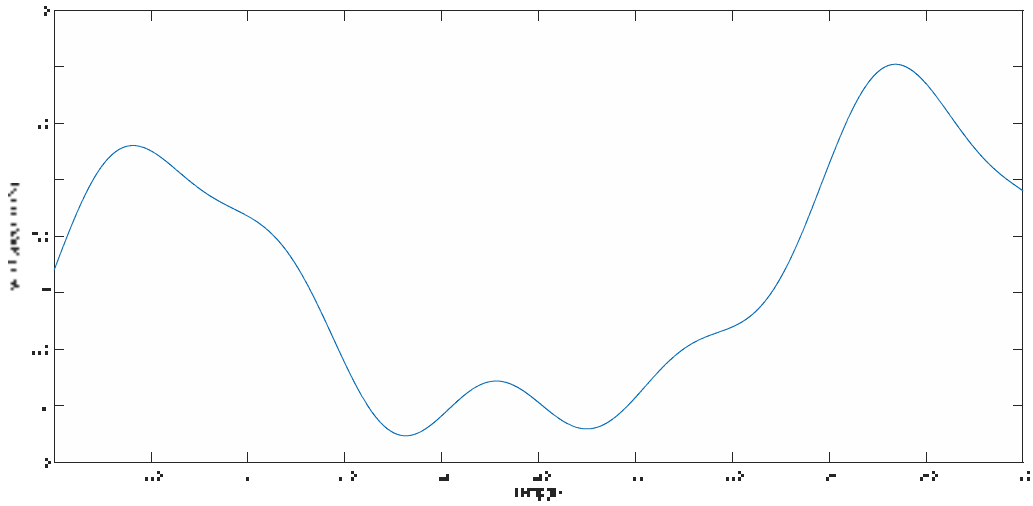

Fig. 8. Simulation results wind speed

Creative Commons Attribution-NonCommercial-NoDerivatives 4.0 International License (CC BY-NC-ND)

Algerian Journal of Engineering Architecture and Urbanism Vol. 5 Nr. 3 2021
ISSN: 2588-1760

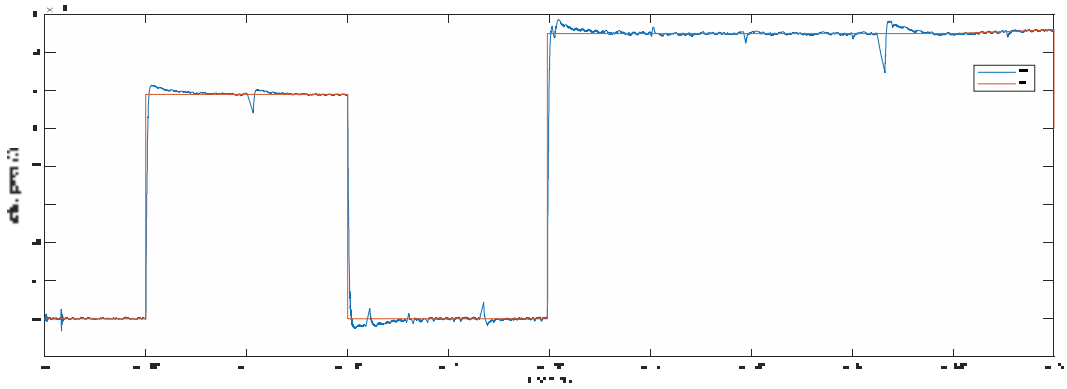

(a) : active power response

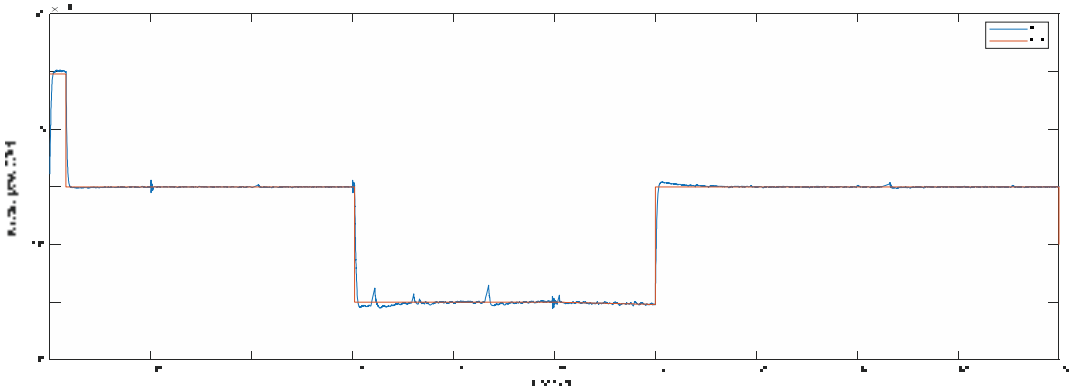

(b) : reactive power response

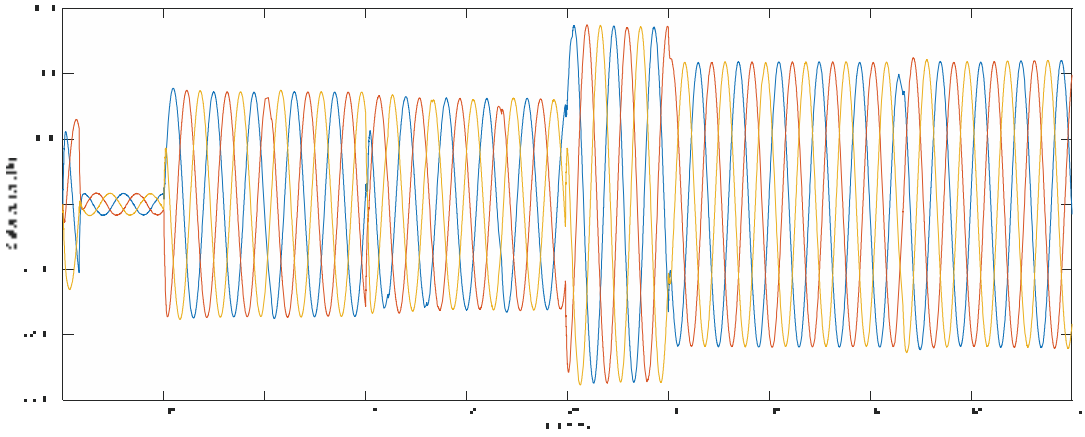

(c) : stator current response

Fig. 9.Simulation results of the robustness test of DFIG for IFOC with MPPT

Creative Commons Attribution-NonCommercial-NoDerivatives 4.0 International License (CC BY-NC-ND)

Algerian Journal of Engineering Architecture and Urbanism Vol. 5 Nr. 3 2021
ISSN: 2588-1760

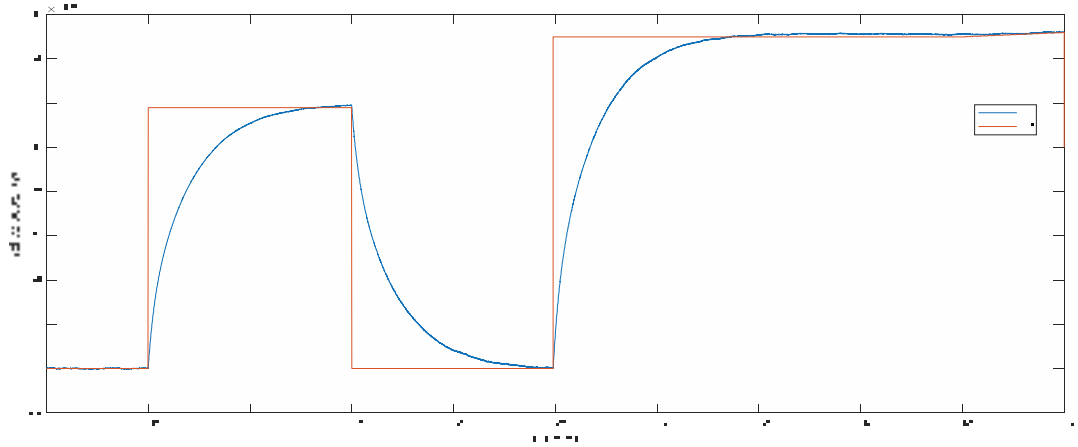

(a) : active power response

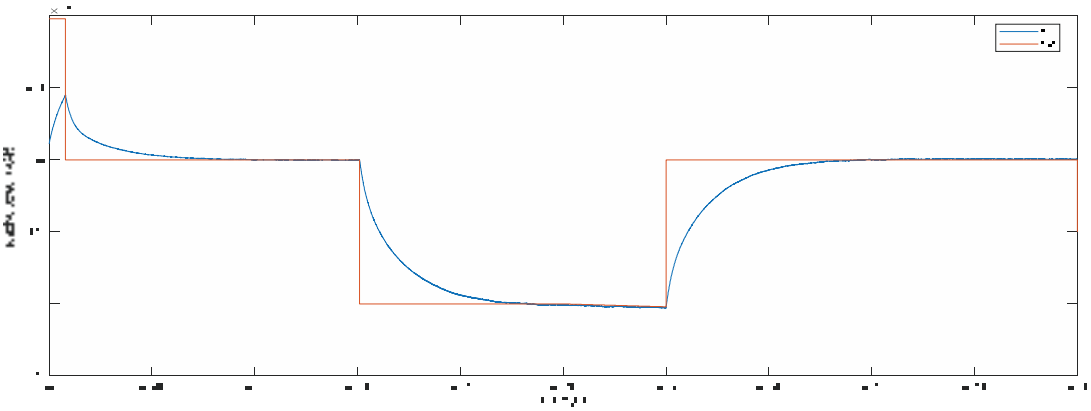

(b) : reactive power response

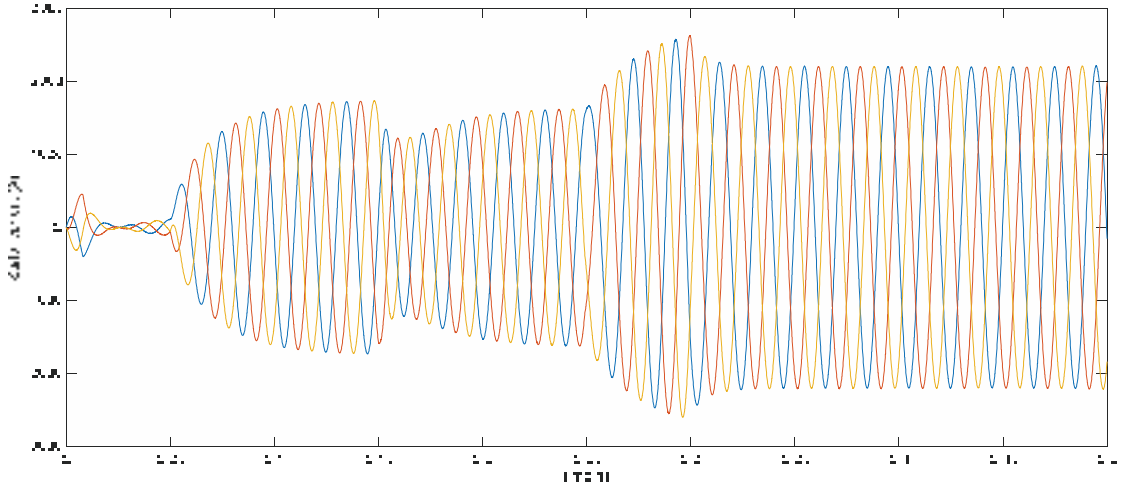

(c) : stator current response

Fig.10. Simulation results of the robustness test of DFIG for IFOC without MPPT

Creative Commons Attribution-NonCommercial-NoDerivatives 4.0 International License (CC BY-NC-ND)

In order to test the robustness of the vector control strategies of the DFIG, we also studied the influence of MPPT controller of the generator on the performances of these last control strategies.

Fig. 9 and 10 show the active power, the reactive power, the stator current and the rotor current responses of DFIG for the vector control strategy where the wind turbine is driven at variable wind speed (m/s). The Fig. 9.a shows a very fast response of the active power, where it follows perfectly its reference generated by the MPPT strategy with a negligible error in sub and super synchronous mode operations of DFIG. The reactive power is maintained at its reference equal to zero (Fig. 9.c), in order to power coefficient (Cpmax=0.48) on the wind turbine These simulation results show the high performances of vector control and the robustness of this strategy of DFIG Compared with the results obtained from the generator without control MPPT look fig.10(a,b).

8. Conclusion

This paper presented the modelling, simulation and control of a DFIG based wind conversion system , the indirect vector control (IFOC) method is used to control the stator flux of the DFIG allowing independent control and hence the active and reactive stator powers of the DFIG, driven by a variable speed wind turbine. The reference of the active power generated by the DFIG is set according to the wind speed using a maximum power point tracking (MPPT) strategy The simulation results show the effectiveness of the decoupling controller and MPPT strategy and can be used to investigate other more robust control strategies to further improve the performance of the system in response to power disturbances , it can be said that the proposed vector control strategy of DFIG is a very simple robust control algorithm which has the advantage of being easily for a real time implementation.

Creative Commons Attribution-NonCommercial-NoDerivatives 4.0 International License (CC BY-NC-ND)

9. APPENDIX

TABLE I
Wind energy conversion system parameters

Parameters	Value	IS-Unit
Rated power, *Pn*	1.5	MW
Blade radius, *R*	35 .25	m
Number of blades	3	-
Gearbox ratio, G	90	-
Total moment of inertia, *J*	1000	$Kg.m^2$
Viscous friction coefficient, *fr*	0.0024	$N.m.s^{-1}$
Stator rated voltage, *Vs*	398/690	V
Rotor rated voltage, *Vr*	225/389	V
Rated current, *In*	1900	A
Stator rated frequency, *f*	50	Hz
Stator inductance, *Ls*	0.0137	H
Rotor inductance, *Lr*	0.0136	H
Mutual inductance, Lm	0.0135	H
Stator resistance, *Rs*	0.012	Ω
Rotor resistance, Rr	0.021	Ω
Number of pair of poles, *p*	2	-

Table 2 Coefficients of the turbine

C_1	C_2	C_3	C_4	C_5	C_6
0.5176	**116**	**0.4**	**5**	**21**	**0.0068**

REFERENCES

[1] BOUDJEMA, Z. – MEROUFEL, A. – DJERIRI, Y. – BOUNADJA, E.: Fuzzy sliding mode control of a doubly fed induction generator for wind energy conversion, Carpathian Journal of Electronic and Computer Engineering, Vol. 6, No. 2, pp.7-14, 2013.

[2] A. Petersson, T. Thiringer, L. Harnefors, T. Petru, "Modeling and Experimental Verification of Grid Interaction of a DFIG Wind Turbine," IEEE Trans. on Energy Conversion, vol. 20, No.4, pp. 878 886, 2005.

[3] G. Yuan, C. Jianyun, Y. Li, "Vector Control and Synchronization of Doubly Fed Induction Wind Generator System," 2004 IPEMC Proceedings, pp. 886-890, 2004.

[4] A. Dendouga, R. Abdessemed, M. L. Bendaas and A. Chaiba, "Decoupled Active and Reactive Power Control of a Doubly-Fed Induction Generator (DFIG)," Mediterranean Conference on Control and Automation, Athens-Greese IEEE, 2007.

Creative Commons Attribution-NonCommercial-NoDerivatives 4.0 International License (CC BY-NC-ND)

[5] A. Abedi, M. Pishvaei, A. Madadi, H. M. Kelk, "Analyzing Vector Control of a Grid-Connected DFIG under Simultaneous Changes of Two Inputs of Control System," European Journal of Scientific Research, vol.45, no. 2, pp.221-231, 2010.

[6] J.P. Barton, D.G., "Infield, Energy storage and its use with intermittent renewable energy," IEEE Transactions on Energy Conversion, vol. 19, no. 2, pp. 441-448, 2004.

[7] C. Abbey, G. Joos, "Supercapacitor energy storage for wind energy applications", IEEE Transactions on Industry Applications, vol. 43, no. 3, 2007.

[8] W. Li, G. Joos, "A power electronic interface for a battery supercapacitor hybrid Energy Storage System for windapplications," in: 39th IEEE PESC, vol. 176, pp. 1762-1768, 2008.

[9] W. Leonhard, "Control of Electrical Drives," 2nd ed. Berlin, Germany: Springer-Verlag, 1996.

[10] Y, DJERIRI "Robust second order sliding mode control of doubly-fed induction generator for wind energy conversion system", Acta Electrotechnica et Informatica, Vol. 20, No. 3, 2020, 30–38, DOI: 10.15546/aeei-2020-0017

[11] M. A. Poller, "Doubly-fed induction machine models for stability assessment of wind farms," In: Power Tech Conference Proceedings, 2003, IEEE, Bologna, vol. 3, 23–26, June 2003.

[12] T. Brekken, N. Mohan, "A novel doubly-fed induction wind generator control scheme for reactive power control and torque pulsation compensation under unbalanced grid voltage conditions," In: IEEE 34th Annual Power Electronics Specialist Conference, 2003, PESC'03, 15-19 June 2003, vol. 2, pp. 760-764.

[13]T. K. A. Brekken, N. Mohan, "Control of a doubly fed induction wind generator under unbalanced grid voltage conditions," In: IEEE Transaction on Energy Conversion, 22 March, 2007 129– 135.

[14] J. Lopez, P. Sanchis, X. Roboam, L. Marroyo, "Dynamic behavior of the doubly fed induction generator during three-phase voltage dips," In: IEEE Transaction on Energy Conversion, 22 September, 2007, 709 717.

[15] T. Sun, Z. Chen, F. Blaabjerg, "Flicker study on variable speed wind turbines with doubly fed induction generators," IEEE Transactions on Energy Conversion, 20 December, 2005, 896–905.

[16] B.Boumerid, A .Allali, M. Boulouiha, D.Mouloud « Modeling, simulation and control of a doubly-fed induction generator for wind energy conversion systems",International Journal of Power Electronics and Drive System (IJPEDS) Vol. 11, No. 3, September 2020, pp. 1197~1210.

[17] C.K. Rai, "Non-Conventional Energy Sources of Energy", Khanna Publishers, 1996.

[18] L. Yazhou, M. Alan, L. Gordon and Y. Robert "Modeling of the Wind Turbine with a Doubly Fed Induction Generator for Grid Integration Studies", IEEE Transactions on Energy Conversion, vol. 21, no. 1, pp. 257-264, 2006.

[19] A. Kuperman, R. Rabinovici and G.Weiss, "A shunt connected inverter based variable speed wind turbine generation," Int. Jour. of electromotion, vol. 13, no. 1, pp. 67-72, 2006.

[20] Laghridat, H., Essadki, A., & Nasser, T. (2019). Comparative Analysis between PI and Linear-ADRC Control of a Grid Connected Variable Speed Wind Energy Conversion System Based on a Squirrel Cage Induction Generator. Mathematical Problems in Engineering, 2019.

Creative Commons Attribution-NonCommercial-NoDerivatives 4.0 International License (CC BY-NC-ND)

Algerian Journal of Engineering Architecture and Urbanism Vol. 5 Nr. 3 2021
ISSN: 2588-1760

VEHICLE EMBEDDED BY A FUEL CELL SYSTEM: A REVIEW

Bilal SOLTANI
PhD Student, Mechanical Engineering, Laboratory of Management, Maintenance and Rehabilitation of Facilities and Urban Infrastructure, Mohamed Chérif Messaadia University, Souk Ahras Mailbox 1553,Souk-Ahras, 41000, Algeria,
b.soltani@univ-soukahras.dz

Nedjem-Eddine BENCHOUIA
Dr, PhD, HDR, Mechanical Engineering, Department of Electrical Engineering, Mohamed Chérif Messaadia University, Souk Ahras Mailbox 1553, Souk-Ahras, 41000, Algeria,
n.benchouia@univ-soukahras.dz

Abstract:
Among the various existing fuel cell, proton exchange membrane (PEM) fuel cells now seem to be the best suited to serve as a basis for the motorization of electric vehicles. This is explained in particular by their low operating temperature (about 70 ° C) and the solid nature of the electrolyte involved. In an emerging context of electromechanical system aspect involving the modeling and simulation of a set of components, the present work consists in developing a model of the system for modeling and optimization of an on-board vehicle by fuel cell system. . In this model, we will model the different parts of the system; PEMFC fuel cell, super-capacitor, converters and a permanent magnet synchronous motor. Validation by simulation is essential for its good analysis and comparison with experimental measurements. Finally, this work focuses on solving the problems of optimization to adapt it to the fuel cell system.

Key words: Fuel cell, Batteries, Super-capacitors, Vehicle, Dimension, Control strategy.

1. Introduction:

During the next decades, hydrogen could be brought to take a bigger place in the field of energy. The reasons for this are multiple. For one, the global demand for energy continues to grow and fossil fuel reserves are finite. It is therefore necessary to optimize their use by increasing the overall efficiency of secondary energy production chains such as electricity.
On the other hand, the areas producing and consuming primary energy have significantly different locations. Countries like France want to enjoy a maximum energy independence rate, for financial and political reasons, linked to the risks that sometimes exist in times of international tension.

Energy consumers are also increasingly aware of the impact of energy production on the environment. This awareness has implications for the government's definition of energy policies. The fight against pollution and the resulting climate change has thus become a priority in the environment, energy and state research policies, even though there are debates on the measures to be taken in order to achieve the desired objectives. The use of fossil fuels, coal in particular, causes significant damage to human health and has an impact on global

Creative Commons Attribution-NonCommercial-NoDerivatives 4.0 International License (CC BY-NC-ND)

warming. New, cleaner and more efficient energy technologies, in particular to reduce greenhouse gas emissions, are to be promoted [see Annex to the Introduction]. Actions are being taken in this direction. They concern fuel cells, bioelectricity (biomass and waste for electricity and heat generation), and the integration of renewable energy sources and decentralized generation, cleaner fuels for transport, storage of electricity and energy, photovoltaic and wind energy. Minimizing costs and the ability of these new concepts to penetrate the market are carefully considered.

Problematic:

- ✓ Energy criteria and sizing: An important part of hydrogen saving is obtained by kinetic energy recovery. The sizing of the secondary source must therefore make it possible to recover as much as possible the braking energy. However, the kinetic energy recoverable and the power demand of the motorization depend on the envisaged use of the vehicle (urban, periurban or highway, mixed...).As a result, the sizing of the power source is specific to a particular application.
- ✓ Vehicle mass problem: Hydrogen consumption is influenced by the mass of the vehicle. The mass of the power source (fuel cell system + secondary energy source) is therefore an important factor in the design process. At the limit, the overweight introduced can go as far as canceling the benefits obtained thanks to the secondary source. Due to the additional weight introduced by the secondary source of energy as well as the increase in the complexity of the powertrain, can be considered the use of a single fuel cell which naturally has a high efficiency over a wide range of use.
- ✓ Energy and Power: It is difficult to advocate the use of battery or super-capacitor, the two technologies having very different characteristics. Some authors favor the use of super-capacitors because of their energy efficiency and specific power, but their low capacity can be a handicap. Conversely, batteries are able to store a large amount of energy but are penalized by their specific power. One solution is to couple batteries and super-capacitors to combine their advantages (power and energy), but this inevitably increases the complexity and cost of the secondary energy source.

2. The field of transport

Oil covers 95% of the needs in this sector, energy consumption related to transport in France represents a quarter of total consumption and this share is one that increases faster. Automakers are making thermal vehicles cleaner by adding new, cleaner engines, catalytic converters and particulate filters. The introduction of these new technologies has led to a significant decrease in emissions of pollutants such as SO2, CO, total hydrocarbons (HC), NOx, particulates and has made it possible to comply with Euro1, Euro2 and Euro3 standards issued by the European Union [1].This despite the simultaneous increase in mass and power of vehicles, despite the generalization of comfort elements such as air conditioning. Upcoming technological innovations, such as the electrical control of valves on engines, and the appearance of hybrid vehicles [2] [3] should further reduce consumption. All-electric vehicles are also available for sale, but the limited performance of their batteries confines them to niche markets.

Creative Commons Attribution-NonCommercial-NoDerivatives 4.0 International License (CC BY-NC-ND)

The evolution of air quality, in terms of pollutant concentration, shows that CO2 emissions are now the main transport challenge in the face of air pollution [4].Transport is the sector that generates the greatest increase in CO2 emissions: a car with a combustion engine releases about one tone of CO2 every 5000 km into the atmosphere. A break in technology seems inevitable.

3. The fuel cell vehicle:

Fueled directly with hydrogen, it generates no local air pollution and is very noisy. It turns out to be a prime candidate in the context.

Fuel cells are still sources of high current and low voltage. Their rational use in vehicle power trains often involves raising the voltage level by means of suitable static converters. In order to optimize these chains globally, it is also necessary to ask the question of the hybridization of the battery by a buffer device allowing intermediate storage of the power. Indeed, the on-board power source must both provide sufficient energy to ensure the autonomy of the vehicle and deliver significant power during transient phases, corresponding to acceleration or a slope crossing. The source must therefore meet these two different needs, while respecting acceptable mass and volume criteria. One solution is to decoupling energy source / power source. Components with appropriate characteristics are then associated with these two sources: fuel cell generator (GE to PAC) and buffers such as super-capacitors. The fuel cell used in transport is most often of the PEM (proton exchange membrane) type; it has the advantage of operating at low temperature and having a solid electrolyte.

The use of super-capacitors is particularly interesting because they are components that have an important ability to accept or restore high energy in very short periods.

PAC GEs can be used in vehicles in different ways. Either they are placed in association with a battery with very limited capacity, comparable to that of the thermal vehicles, and only intended to ensure the startup of the auxiliaries of the group, either they are associated with other elements of energy storage (a stack of more or less large batteries for example) and the two components of the hybrid source together deliver energy to the power train. The architecture chosen and the degree of hybridization largely determine the mode of operation of the EG to PAC. It may be necessary to provide a significant power dynamic or, conversely, to operate as a range extender: it then recharges the batteries by delivering a relatively low power and more or less constant. Hybridization of GE to PAC may also allow for a smaller and therefore less expensive GE. Given the still high price to date of a pile stack, hybridization could allow the launch of the first vehicles to CAP.

- **Hydrogen, an energy vector :**

Certainly, the hydrogen atom is the most abundant element in the universe [5]; it is found in water (lakes, rivers, oceans ...) and in fossil fuels, but hydrogen gas (or Di-hydrogen), in its molecular form, is virtually non-existent in nature. Like electricity, hydrogen must be produced from different sources of primary energy, fossil and non-fossil. The major disadvantage of electricity lies in the difficulty of storing it in large quantities. Assuring an energy storage function, hydrogen could become a second energy vector, complementary to electricity, leading to high yields by limiting the secondary reactions to its transformation into water (oxidation or combustion) and therefore pollutant emissions [6].Fuel cells would convert the chemical energy of hydrogen into electrical energy. Hydrogen production and storage, for example, would allow decoupling over time between consumption and electricity

Creative Commons Attribution-NonCommercial-NoDerivatives 4.0 International License (CC BY-NC-ND)

generation from renewable energies, such as wind energy. The choice of production, storage and distribution methods will determine the development of the hydrogen sector.

After a brief history, the main fields of application of the fuel cell (PAC) will be presented. Vehicle-related usage limits favor the use of a particular technology. Its operating principle and its constraints of use are described. Some of these constraints can be removed by the addition of a secondary energy source (ex: super-capacitors).

- **The early adopters of fuel cell vehicles:**

Several car manufacturers promote FCVs to consumers. Vehicles are often compared to battery electric vehicles (BEVs). Both types of vehicles emit no exhaust, can be powered by renewable energies and are powered by electric motors. The main difference between these vehicles is their range and style of refueling. FCVs have a range of over 300 miles and can be refueled in less than 10 minutes at a hydrogen refueling station [7].

Three FCVs are currently available to consumers. These include the Hyundai Tucson / ix35 FCEV, the Toyota Mirai FCEV and the Honda Clarity FCEV. These vehicles are currently on sale in North America, Europe and Asia. In 2014 sales of these vehicles began. The Toyota Mirai was sold in record numbers with 5233 units delivered to consumers from 2013 to 2017, including 2944 in North America. By the end of 2017, 637 Honda Clarity FCEVs had been delivered to consumers, including 440 in North America.

Finally, 727 Hyundai Tuscon / ix35 FCEVs were delivered, the most important market for these vehicles being Europe with 373 units delivered. Figure 1 provides an overview of the annual sales of these vehicles and the total sales of the three vehicle models.

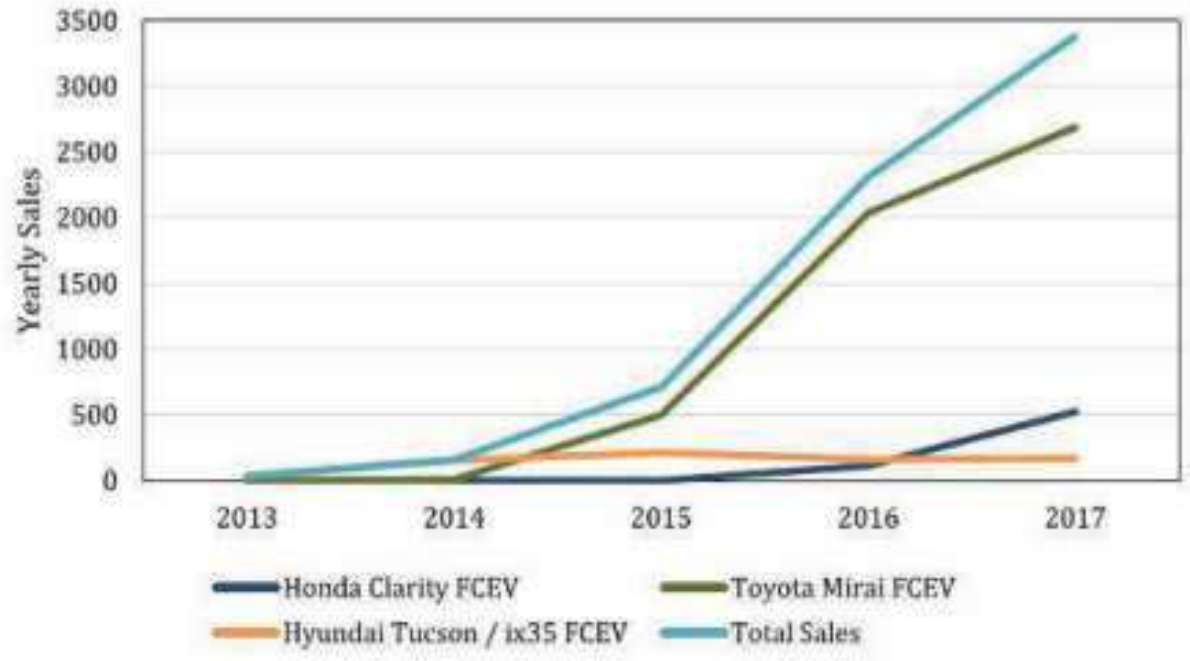

Fig1. Global annual sales of fuel cell vehicles between 2013 and 2017 by vehicle model [8]

Creative Commons Attribution-NonCommercial-NoDerivatives 4.0 International License (CC BY-NC-ND)

The main producers of FCVs are the United States and Japan. In 2017, 2298 vehicles were sold in the United States and 849 in Japan. South Korea is the third largest market with 61 vehicles sold in 2017.Annual sales of these vehicles by country of sale are shown in Figure 2.

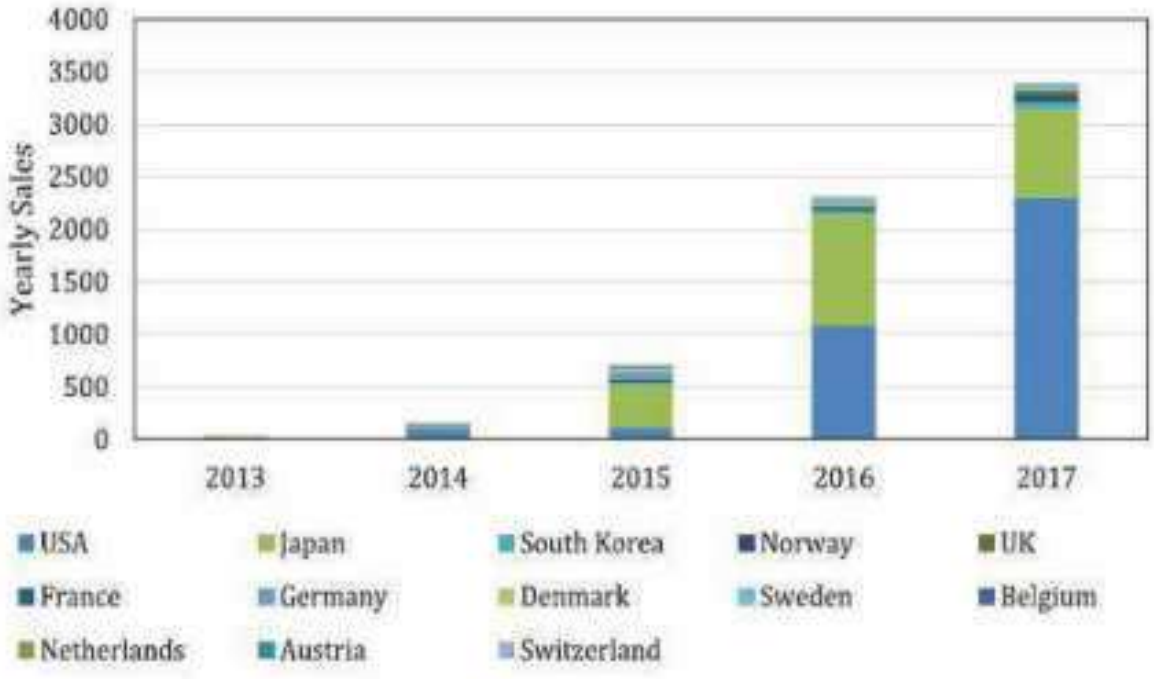

Fig2. Worldwide annual sales of fuel cell vehicles between 2013 and 2017 by country [8]

3.1. The fuel cell, a power full energy converter:

If the hypothesis of the choice of hydrogen as a new energy vector is retained, the fuel cell will become the most efficient converter of hydrogen into usable energy (electricity and heat).

3.1.1. History:

The fuel cell (PAC) converts chemical energy into electrical energy. Its technology has become more and more familiar in recent decades, but has been discovered more than 150 years ago. In 1839, Sir William Grove, an English jurist and amateur chemistry researcher, describes an experiment where water and electricity are produced from oxygen and hydrogen. Grove's experience gives birth to the gas battery (Figure 3), later renamed fuel cell [9] [10].

Creative Commons Attribution-NonCommercial-NoDerivatives 4.0 International License (CC BY-NC-ND)

Algerian Journal of Engineering Architecture and Urbanism Vol. 5 Nr. 3 2021
ISSN: 2588-1760

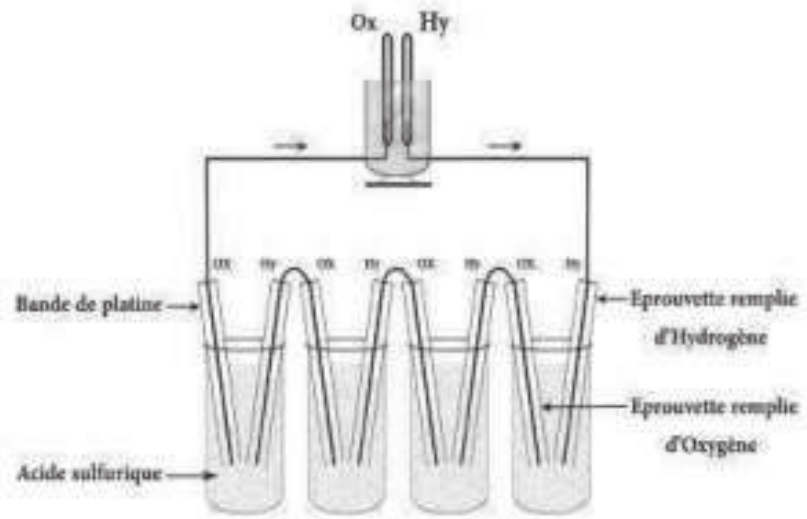

Fig3. The Sir William Grove experience

The discovery of W. Grove, however, was not exploited and was relegated to the rank of scientific curiosity, while the extraction of fossil fuels and the development of the engine were in full swing. In 1932, Dr. Francis Bacon took over the research initiated by W. Grove and managed to build a 5kW fuel cell in 1959.

The fuel cell has emerged with NASA (National Aeronautics and Space Administration, USA) looking for a way to generate electricity on board its spacecraft. The fuel cell appeared as an ideal system because of the presence of oxygen and hydrogen available in the propulsion systems. Fuel cells were successfully used by the Gemini capsule in 1964[11], and the water produced by the reaction between hydrogen and oxygen was consumed by astronauts. This is one of the first concrete uses of fuel cells.

The interest of the use of the fuel cell in the field of transport dates back to 1973.The first oil crisis has led governments, industries and laboratories to seek an alternative to fossil fuels to try to ensure energy independence. Many efforts and means have been provided to reduce the manufacturing costs of fuel cell systems, to increase their reliability and to improve their compactness. In 1993, a fuel cell bus was built by the Ballard company (today one of the world leaders in the field of fuel cells) in partnership with the car manufacturer Daimler-Benz [12]. The fuel cell was of PEM type ("Proton Exchange Membrane").The hydrogen needed to feed the cell was produced by embedded reforming of methanol (Figure 4).

Creative Commons Attribution-NonCommercial-NoDerivatives 4.0 International License (CC BY-NC-ND)

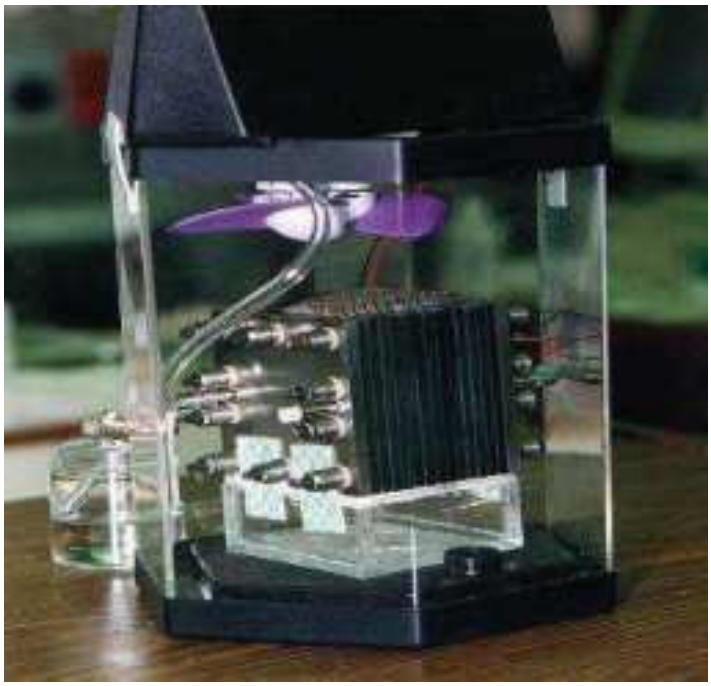

Fig4. Fuel Cell, from NASA to Methanol [13].

Since the 1990s, fuel cells and hydrogen have been considered as possible candidates for the production of sustainable and clean energy, whether for mobile or stationary applications.

Fuel cells are listed based on their operating temperatures, electrolytes, and power ranges. The main fuel cell technologies and their characteristics are given in Table 1 [14] [15]:

	Name	Electrolyte	Power range	Operating temperature	Fields of application
	DMFC(« Direct methanol fuel cell »)	Polymer membrane	1mW to 100 kW	60-90 ° C	Portable
	PEMFC(« Proton exchange Membrane fuel cell »)	Polymer membrane	100W to 500kW	60-90 ° C	Transport Portable Stationary

Creative Commons Attribution-NonCommercial-NoDerivatives 4.0 International License (CC BY-NC-ND)

PAC at low temperatures	AFC («Alkaline fuel cell »)	Aqueous alkaline solution	10kW to 100kW	50-250 ° C	Transport Spatial
	PAFC (« Phosphoric acid fuel cell »)	Phosphoric acid	Up to 10 MW	160-220 ° C	Stationary
High temperature PAC	MCFC (« Molten carbonate fuel cell »)	Molten carbonate	Up to 100 MW	650 ° C	Stationary
	SOFC (« Solid oxide fuel cell »)	Solid Oxide	Up to 100 MW	750-1050 ° C	Stationary

Tab1. The main types of fuel cells

Each type of fuel cell has a preferred field of application (Table 1).fuel cell called low temperatures are more for mobile applications, while so-called high temperature batteries are generally intended for stationary applications.

The main mobile applications concern portable electronic devices (computer, cell phone ...) and the transport sector (car, bus ...); stationary applications concern the decentralized production of electrical energy (collective or individual housing, etc.).In the latter, the heat produced by the high temperature cells can be recovered by cogeneration a process which increases the overall efficiency of the PAC system [14].

In Figure 5, the different types of fuel cells and the power ranges are linked by their possible fields of application.

Creative Commons Attribution-NonCommercial-NoDerivatives 4.0 International License (CC BY-NC-ND)

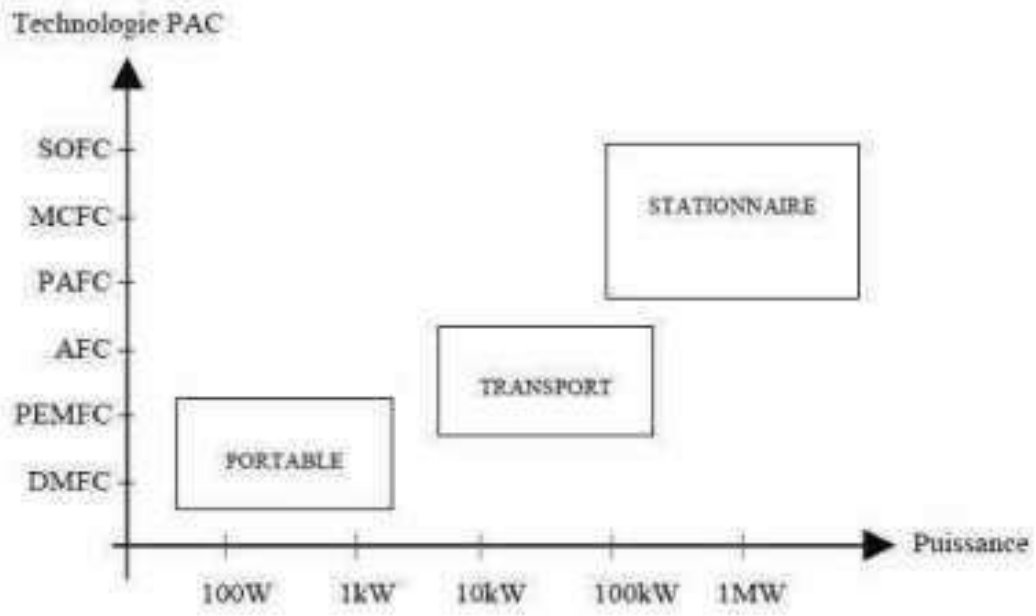

Fig5. Fuel cell technologies and fields of application

Among the different types of fuel cells, the PEM ("Proton Exchange Membrane") type cell, also called PEFC ("Polymer Electrolyte Fuel Cell"), is the technology generally used for automobile use. Several reasons explain this choice [16][17][18]:

- Density of power:

The propulsion of a vehicle requires a power of a few kilowatts to a hundred kilowatts. In addition, the power train must have an acceptable mass and size.

The PEM type is best meets these constraints with a power density of between 1 kg / kW and 3 kg / kW.

- Operating temperature:

The PEM fuel cell has an operating temperature of between 50 ° C and 80 ° C, which is suitable for automotive use.

- Solid structure:

The PEM fuel cell is composed of solid elements (especially the polymer membrane). This solid structure guarantees a certain mechanical resistance with respect to the constraints related to the automotive environment.

3.1.2. The polymer membrane fuel cell (PEM type):

- **Operating principle:**

The fuel cell allows the direct conversion into electrical energy of the free energy of a chemical oxidation-reduction reaction. Like a battery or accumulator, a fuel cell has two electrodes. The negative electrode is the seat of the oxidation drafting of the fuel, usually hydrogen. On the side of the positive electrode is the reduction reaction of the oxidant, usually the oxygen of the air. The two electrodes are separated by an electrolyte. In the case of a PEM cell, a solid membrane performs the function of electrolyte; the faces of the electrodes are covered by a catalyst, platinum. The negative electrode - electrolyte - positive electrode

Creative Commons Attribution-NonCommercial-NoDerivatives 4.0 International License (CC BY-NC-ND)

assembly constitutes the heart of the cell. The supply of the latter in reagents is via distributing plates. The fuel and oxidant are provided to the cell in conditions of pressure, temperature, humidity and purity defined continuously to ensure the production of the current.

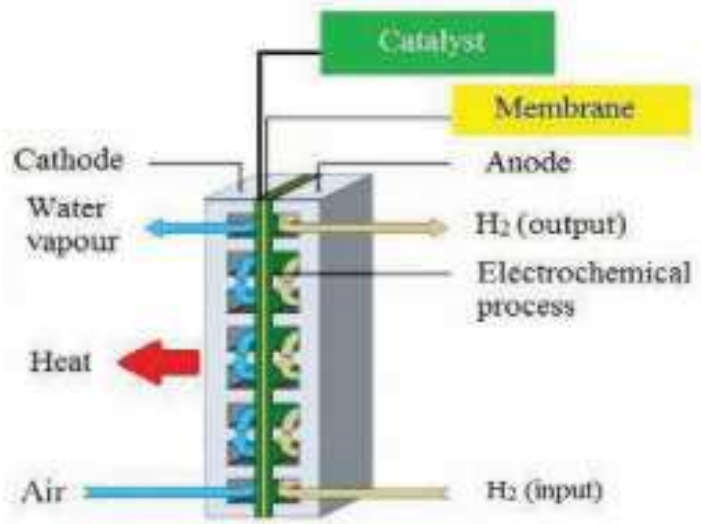

Fig6. Principle of operation of a PEM fuel cell

Depending on the type of cell, the intermediate chemical reactions involved vary but the general principle remains unchanged. The overall reaction of a PEM type fuel cell can be written as follows:

- **Reaction to the anode**

$$H_2 \rightarrow 2H^+ + 2e- \qquad (1)$$

- **Reaction to the cathode:**

$$½\ O_2 + 2H^+ + 2e^- \rightarrow H_2O \qquad (2)$$

- **By combining (1) and (2) the overall reaction is:**

$$H_2 + ½\ O_2 \rightarrow H_2O + heat \qquad (3)$$

Electricity is produced by the 2 electrons released by the hydrogen molecule (1). The H+ hydrogen protons pass through the membrane separating the anode from the cathode and recombine at the cathode with the electrons and the oxygen atoms. Ideally, the only side products

The reaction is water and heat. Figure 6 summarizes the principle of the PEM fuel cell.

Creative Commons Attribution-NonCommercial-NoDerivatives 4.0 International License (CC BY-NC-ND)

The potential difference across each cell is small; in operation, it is less than volt. For most applications, it is therefore necessary to build a stack of cells, commonly called stack, to have a sufficient level of voltage.

a. Elementary cell and assembly of the fuel cell:

The electrochemical reaction takes place within an elementary cell. An elementary cell consists of an Electrode-Membrane-Electrode (EME) assembly pressed between 2 bipolar plates (Figure 7).

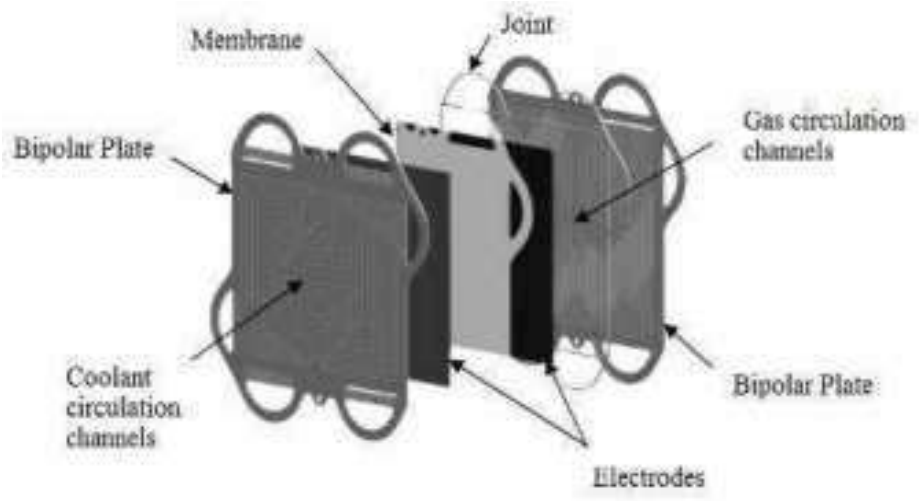

Fig7. Example of assembly of an elementary cell [19]

The membrane is the heart of the elementary cell. The membrane is a polymer electrolyte that is permeable to hydrogen protons H+ and impervious to gases. To guarantee H + proton permeability, the membrane must be permanently moistened. The Nafion® [20] membrane is the most common in PEM fuel cells.

An EME assembly has two electrodes: the anode and the cathode. An electrode is made of two layers of porous material. The Gas Diffusion Layer (GDL) transports and distributes hydrogen and oxygen uniformly over the membrane while discharging the produced water. The catalyst layer (platinum) makes it possible to activate and accelerate the oxidation-reduction reaction.

Bipolar plates fulfill two roles. On the one hand they distribute the gases evenly to the EME assembly through thin channels (Figure 7).On the other hand; they allow the circulation of a cooling fluid to cool the elementary cell.

Bipolar plates must be conductive and withstand a corrosive environment (for example, graphite or stainless steel is used).

The voltage obtained with an elementary cell is less than 1 volt, which is insufficient for most applications. To provide a sufficiently high voltage source, several cells are connected in series to form the fuel cell (Figure 8). To ensure tightness, the cells are pressed against each other by two end plates and tie rods.

Creative Commons Attribution-NonCommercial-NoDerivatives 4.0 International License (CC BY-NC-ND)

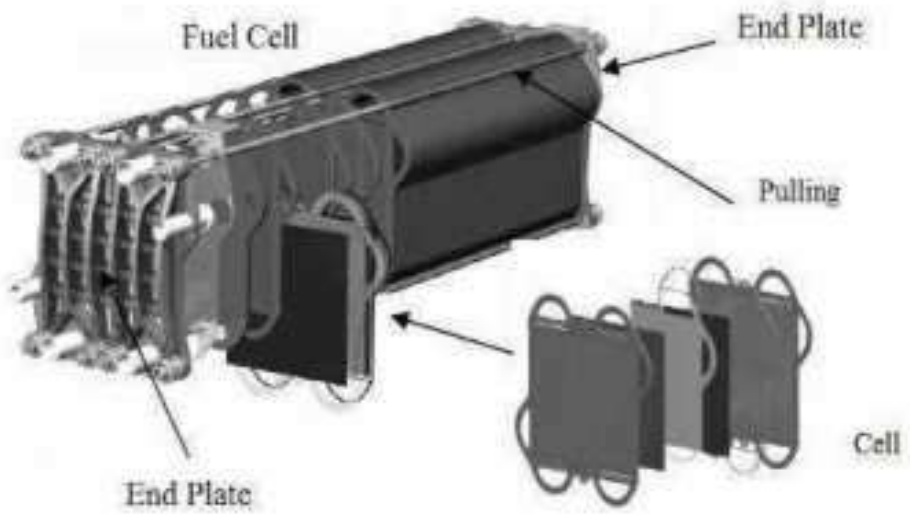

Fig8. Example d'un assemblage de pile à combustible [19]

b. Electrical characteristic of the fuel cell:

The empty voltage of the cell (**Figure 9**) is a function of the electrochemical potential of the oxidation-reduction reaction. Ideally, this electrochemical potential is 1.23 V (standard potential) for standard conditions of temperature and pressure (1 atm, 25 ° C). In practice, the no-load voltage is slightly below **1V** [21].

The polarization curve is the electrical characteristic of a fuel cell. It represents the voltage of the cell as a function of the current density (**Figure 9**) and depends on the operating temperature, the pressure of the reagents and the moisture content of the membrane.

The current density i_{FC} (A / cm²) is defined by:

$$i_{FC} = \frac{I_{FC}}{A_{cell}} \qquad (4)$$

With I_{FC} The fuel cell current and A_{cell} The active surface of a membrane.

Creative Commons Attribution-NonCommercial-NoDerivatives 4.0 International License (CC BY-NC-ND)

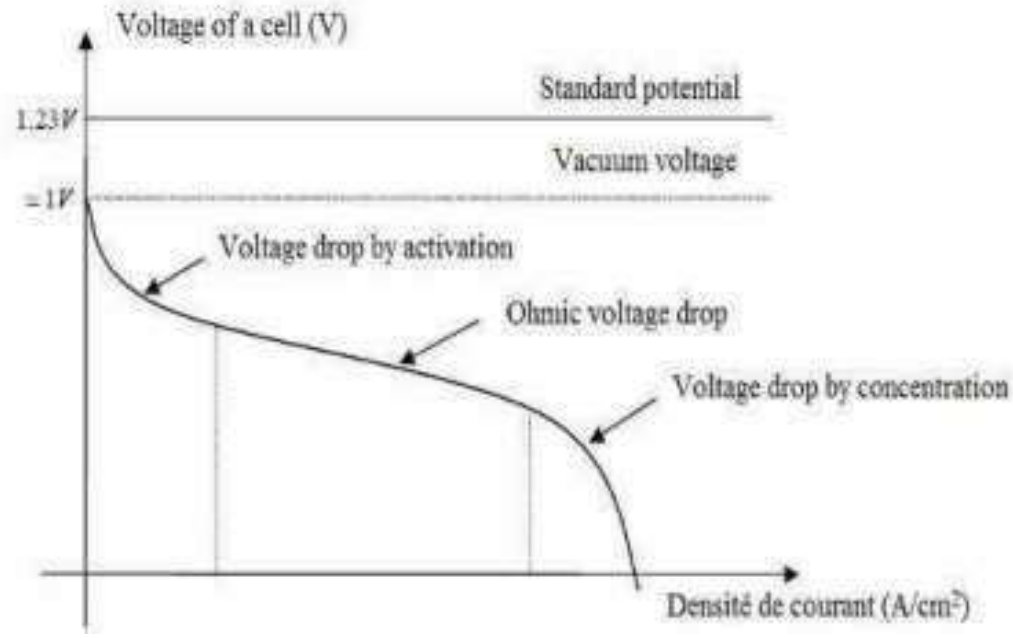

Fig9. Conventional polarization curve of a PEM fuel cell.

The polarization curve (**Figure 9**) can be broken down into three distinct zones, each characterized by preponderant voltage drops **[21]**:

- **Voltage drop by activation:**

The right electrochemical reaction cross a threshold of activation to initiate. This threshold is due to the slowness of the electrochemical reaction at the surface of the electrodes. The catalyst layer present in the electrodes helps to accelerate the reaction.

- **Ohmic voltage drop:**

Ohmic voltage drops are caused by the electrical resistance of the diaphragm and the electrical resistance of the bipolar electrode / plate assembly.

- **Voltage drop by concentration:**

Voltage drops due to concentration result from a lack of reagents. When the current density becomes high the diffusion of the gases in the electrodes is not fast enough to maintain the reaction.

The polarization curve in **Figure 9** is given for an elementary cell. Conventionally, assuming that all cells have the same electrical behavior, the total voltage of the fuel cell V_{FC} is given by:

$$V_{FC}\,(I_{FC}) = N_{Cell} \cdot V_{cell}\,(I_{FC}) \qquad (5)$$

Creative Commons Attribution-NonCommercial-NoDerivatives 4.0 International License (CC BY-NC-ND)

With V_{cell} the elementary voltage of a cell and N_{Cell} the number of cells.

The raw power P_{FC} supplied by the fuel cell is:

$$P_{FC}(I_{FC}) = V_{FC}(I_{FC}).\ I_{FC} \qquad (6)$$

A fuel cell is capable of supplying electrical power as long as it is fed with reagents (oxygen and hydrogen).This implies that a fuel cell cannot operate alone and needs a set of peripheral components to function.

c. Fuel cell system:

The fuel cell needs a set of conditions to produce electrical energy **[18]**: it must be supplied with hydrogen and air, the membrane must be permanently humidified, and the heat produced must be evacuated. The auxiliary components have the role of ensuring the proper functioning of the fuel cell. The fuel cell and auxiliary components assembly is called a fuel cell system.

Fuel cell ***systems*** are typically designed specifically for a particular application. There is therefore much possible architecture. A classical architecture is given in **Figure 10**.

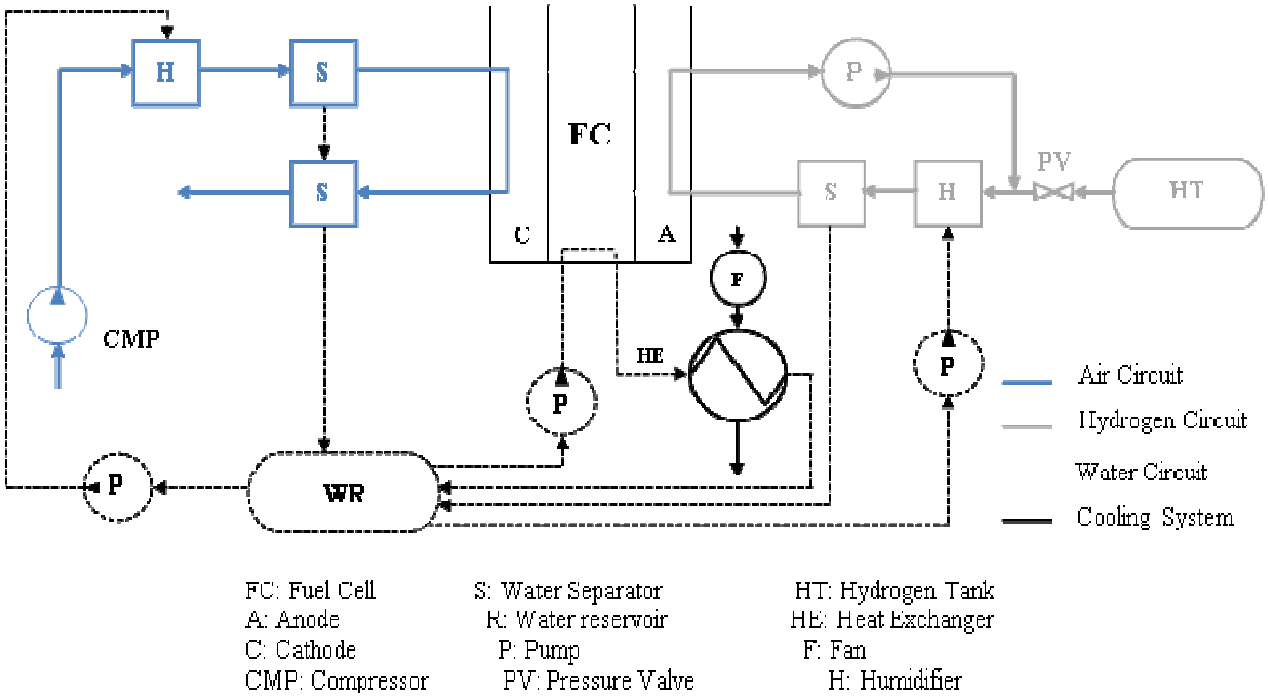

Fig10. Architecture of a fuel cell system [18].

Four main circuits making up a Fuel Cell system **(Figure 10)**:

Creative Commons Attribution-NonCommercial-NoDerivatives 4.0 International License (CC BY-NC-ND)

- **The hydrogen circuit (closed circuit):**

It supplies the anode with gaseous hydrogen. The hydrogen that is not consumed at the outlet of the heat pump can be re-injected at the inlet thereof via a recirculation pump.

- **The air circuit (open circuit):**

Generally, to supply the fuel cell with oxygen, a compressor injects air to the cathode.

- **The cooling circuit:**

The cooling system is an essential part of the fuel cell system **(Figure 10)**.The heat produced by the fuel cell can represent more than **50%** of power losses for high currents. In addition, the limited temperature difference between the fuel cell (about **80 ° C**) and the ambient air does not promote heat exchange and requires the use of large heat exchangers. This represents an important technical constraint in automotive applications.

- **The water circuit:**

Humidification of the membranes is done by the incoming gases (air and hydrogen) via the water circuit **(figure 10)**.The water also contributes to the cooling of the fuel cell as it passes through the heat exchanger.

Auxiliary components are therefore essential for the proper functioning of the fuel cell. They consume some of the energy produced by the fuel cell. The air compressor (Figure 10) is the auxiliary that absorbs the most power **[22]**, and it significantly affects the overall efficiency of the fuel cell system.

The net power available at the output of the fuel cell system (P_{sysFC}) is a function of the gross power (P_{FC}) and the power consumed by the auxiliary components (P_{aux}):

$$P_{sysFC}(I_{FC}) = P_{FC}(I_{FC}) - P_{aux}(I_{FC}) \qquad (7)$$

Paces characteristic of the powers are given in **Figure 11**.

Creative Commons Attribution-NonCommercial-NoDerivatives 4.0 International License (CC BY-NC-ND)

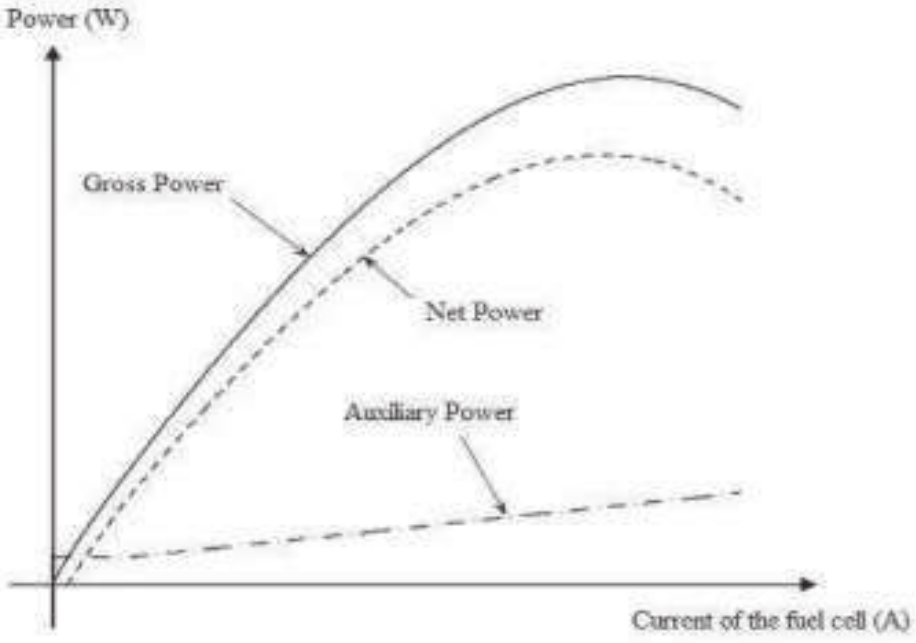

Fig11. Characteristic powers of a fuel cell system
(Gross, net and auxiliary power).

The power losses induced by the power consumption of the auxiliary components affect the overall efficiency of the system **(Figure 12)**.While the fuel cell converts chemical energy into electrical energy with a maximum efficiency of about **70%** for low loads, the fuel cell system achieves a maximum efficiency of about **50%** at around **25%** of the net available power.

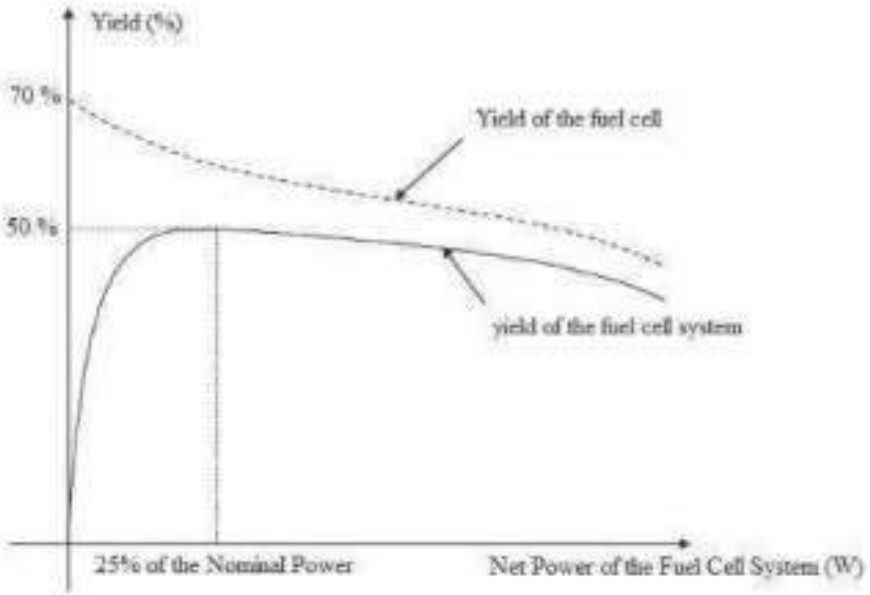

Fig12. Characteristics yield of the fuel cell and fuel cell system.

Creative Commons Attribution-NonCommercial-NoDerivatives 4.0 International License (CC BY-NC-ND)

3.1.3. Fuel Cell Power train:

a. Constraints in automotive applications:

A fuel cell vehicle is primarily an electric vehicle. The motorization is provided by one or more electrical machines and the power is supplied by the fuel cell system. Since the production of electrical energy is done without greenhouse gas emissions, a fuel cell vehicle is considered non-polluting (***locally***).The fuel cell system has a high efficiency (up to **50%**), so its use in a power train appears as an interesting solution for sustainable mobility.

A classic power-train architecture using a fuel cell is given in **Figure 13**.

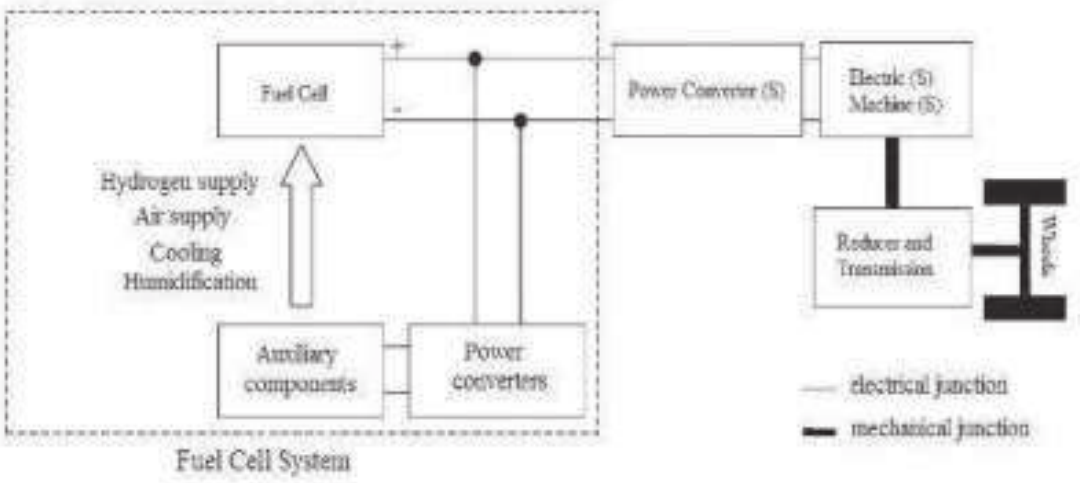

Fig13. Example of Fuel Cell Power train Architecture.

However, certain constraints related to the use of hydrogen and the fuel cell in an automotive environment must be considered:

- **Hydrogen storage:**

Several hydrogen storage technologies have been considered for the automobile **[23] [24] [25]** but do not yet allow storing enough hydrogen to ensure autonomy similar to that of a vehicle conventional:

- ✓ Storage in gaseous form: Hydrogen is stored in metal tanks or composite materials, pressurized between 300 bars and 700 bars. It is the simplest and least expensive solution to store hydrogen.
- ✓ Storage in liquid form: Hydrogen is stored in liquid form at very low temperatures (-253 ° C) in cryogenic tanks.
- ✓ Reforming: Hydrogen is produced in the vehicle by a reformer. A reformer is a "mini-refinery" that extracts hydrogen from hydrogenated liquid fuels (eg methanol).

Creative Commons Attribution-NonCommercial-NoDerivatives 4.0 International License (CC BY-NC-ND)

- ✓ "Solid" storage: Hydrogen can be stored in metal hydride tanks. A metal hydride captures the hydrogen molecules when it is under pressure and releases them when its temperature is increased. The main disadvantage of this solution is the large mass of the tank. The storage of hydrogen in nanostructures and nanotubes is also reported in the literature, but the actual hydrogen absorption capacity is a controversial subject and seems remote from the needs of the automobile **[26]**.

- **Dynamics of the fuel cell system:**

A fuel cell system cannot instantly deliver maximum power. Its dynamics is mainly limited by that of the air compressor **[22]**.Generally the response time of the fuel cell system is of the order of a few seconds and can affect the dynamic performance of the vehicle during strong acceleration.

- **Dimensioning of the fuel cell system and cooling circuit:**

In the case of a fuel cell vehicle without other secondary sources of electrical energy, the fuel cell system is sized to meet the power peaks of the electric motor (during high accelerations).For satisfactory dynamic performance of the vehicle, the rated power of the fuel cell system must be high. Cooling of the fuel cell can therefore become tricky **[27]**.

- **Cold start of the fuel cell system:**

During cold starts, the maximum power of the fuel cell system is limited. The fuel cell needs a few minutes to reach its operating temperature **[28]**. Considers that only 50% of the nominal power is available during the first **2** minutes. The power limitation during a cold start is also described by **[18]**.

Fuel cell vehicles without other secondary sources of electrical energy such as General Motors' Hydrogen3 prototype vehicle, **Table 2**, are therefore uncommon because the constraints related to the automotive environment require specific technological developments. In the context of automobile use, the fuel cell is therefore generally assisted by a secondary source of electrical energy. This type of vehicle is then called "***hybrid fuel cell vehicle***".

Creative Commons Attribution-NonCommercial-NoDerivatives 4.0 International License (CC BY-NC-ND)

Builder	Vehicle	Fuel Cell	Secondary source of energy	Hydrogen storage	Auton-omy	Engines
Honda **[29]**	FCX 	86 kW (Honda)	Super-capacitors	High pressure tank (156.6 l, 350 bar)	430 km	80 kW
Toyota **[30]**	Highlander FCHV* 	90 kW (Toyota)	Batteries Ni-MH	Version 3: Metal hydride Version 4: High tank Pressure Version 5: reformer	300 km 250 km	80 kW
Nissan **[31]**	X-Trail FCHV* 	90 kW (Nissan)	Battery Li-ion	High tank Pressure (700 bar)	500 km	90 kW
General Motors **[32]**	Zafira Hydrogen3 	94 kW	sans	Liquid version: Liquidhydrogentank (68 l) Gas version: High pressure tank (77.4 l, 700 bar)	400 km 270 km	60 kW
Daimler-Chrysler **[5]**	Class A F-Cell 	85 kW (Ballard)	Batteries Ni-MH	High pressure tank (350 bar)	150 km	65 kW
PSA **[33]**	Partner Taxi-PAC 	5,5 kW	Batteries Ni-MH	High pressure tank (300 bar)	250 km	22 kW
Michelin-PSI **[34]** **[35]**	Hy-Light 	30 kW (PSI)	Super-capacitors	High pressure hydrogen tank (200 bar) + High pressure oxygen tank (350 bar)	500 km	2 engines 30 kW wheels at the front.

*: Fuel Cell Hybrid Vehicle

Tab2. Examples of fuel cell vehicles

Creative Commons Attribution-NonCommercial-NoDerivatives 4.0 International License (CC BY-NC-ND)

b. Hybrid fuel cell vehicle:

In a hybrid fuel cell vehicle, it is the power source that is hybrid, the engine remaining fully electric. A hybrid fuel cell vehicle therefore uses a secondary source of electrical power reversible power (charging and discharging).The roles of the secondary source of energy are **[28][36]**:

- **Assist the fuel cell:**

The secondary source provides the additional power when the battery reaches its maximum power (for example during acceleration of the vehicle).

- **Recover kinetic energy during braking:**

The recovery of kinetic energy during braking phases saves hydrogen and increases the range of the vehicle.

- **Introduce a degree of freedom in the distribution of powers:**

Hybridization distributes the power demand between the fuel cell system and the secondary energy source. The operating points of the fuel cell system can thus be shifted to higher yield areas by using appropriate control strategies, thereby reducing hydrogen consumption.

Within the power train of a hybrid fuel cell vehicle (**Figure 14**), several modes of operation can be identified. These modes of operation (traction, braking and stopping) induce different energy flows (**Table 3**).

Mode	Power	Diagram of energy flows	Description
Traction	$P_{EM} > 0$ $P_{sysFC} > 0$ $P_{SSE} = 0$	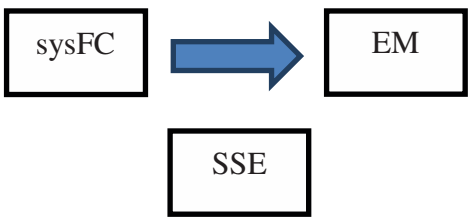	The fuel cell system supplies only the electric machine.
	$P_{EM} > 0$ $P_{sysFC} > 0$ $P_{SSE} > 0$	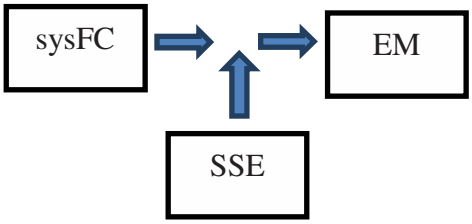	The fuel cell system and the secondary source together power the electric machine.
	$P_{EM} > 0$ $P_{sysFC} = 0$ $P_{SSE} > 0$		The secondary source supplies only the electric machine.

Creative Commons Attribution-NonCommercial-NoDerivatives 4.0 International License (CC BY-NC-ND)

	$P_{EM} > 0$ $P_{sysFC} > 0$ $P_{SSE} < 0$	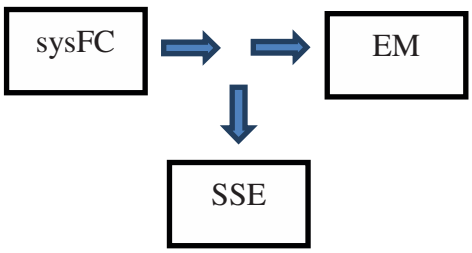	The fuel cell system powers the electric machine and recharges the secondary source.
Braking	$P_{EM} < 0$ $P_{sysFC} = 0$ $P_{SSE} < 0$	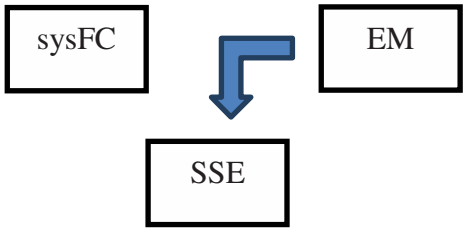	The secondary source recovers the kinetic energy of braking.
	$P_{EM} < 0$ $P_{sysFC} > 0$ $P_{SSE} < 0$	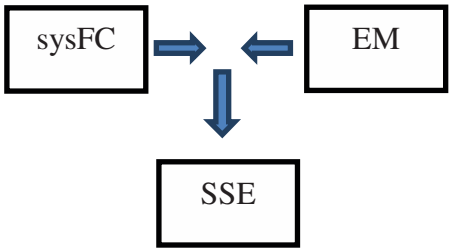	The secondary source recovers the kinetic energy of braking and also receives power from the fuel cell system.
Stop	$P_{EM} = 0$ $P_{sysFC} = 0$ $P_{SSE} = 0$	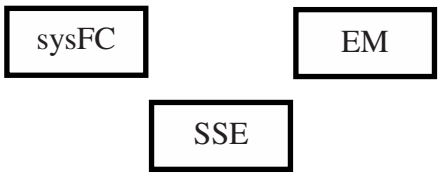	No energy flow.
	$P_{EM} = 0$ $P_{sysFC} > 0$ $P_{SSE} < 0$	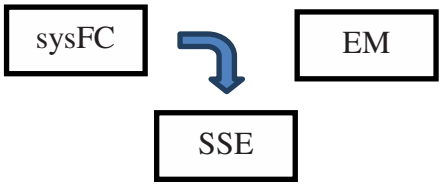	The fuel cell system recharges the secondary source.

sysFC: system FC
SSE: Secondary Source of Energy
EM: Electric Machine

Tab3. Energy flows within the power-train.

Creative Commons Attribution-NonCommercial-NoDerivatives 4.0 International License (CC BY-NC-ND)

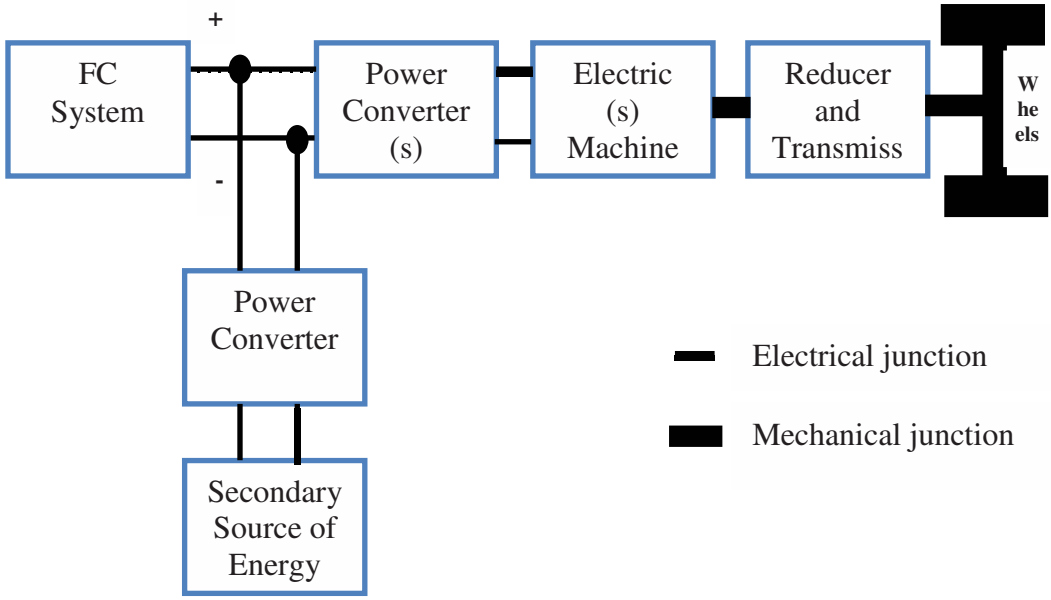

Fig14. Example for Hybrid Fuel Cell Vehicle Architecture

c. The secondary source of energy:

The main characteristic of the secondary source of energy is that it is reversible in power. The secondary source can be recharged by kinetic energy recovery or by the fuel cell system (**Table 3**).

In a hybrid fuel cell vehicle, two technologies are generally retained to form the secondary source of energy: ***batteries and super-capacitors***.

A battery is an electrochemical energy converter that stores energy in a chemical way. In the case of hybrid vehicles, the main technologies used are lead-acid batteries, Nickel Metal Hydride (Ni- MH) batteries and Lithium-ion (Li-ion) batteries **[37]**. Ni-MH technology is the most popular because it offers good performance in terms of capacity, life and cost. Li-ion technology has a higher specific power (W / kg) and a better specific capacity (Wh / kg), but improvements are still necessary concerning the cost, the safety of operation, the service life and performance at low temperatures. Lead technology suffers from a low specific capacity due to the high weight of the batteries; however, it is a robust technology available at low cost and still benefiting from developments **[38]**.

A super-capacitor (or double-layer capacitor) stores the energy electro-statically by polarizing an electrolytic solution. There is no chemical reaction involved, resulting in high lifetimes (a super-capacitor can be charged and discharged hundreds of thousands of times). Les super-capacitors have an extremely low specific capacity but have a significant specific power. In addition, their efficiency in charge and discharge is high. In a hybrid application, super-capacitors are intended to satisfy the strong power peaks **[39]**.

A fuel cell, a battery and a super-capacitor have extremely different electrical characteristics. The Ragone plan (**Figure 15**) illustrates the differences in terms of specific

Creative Commons Attribution-NonCommercial-NoDerivatives 4.0 International License (CC BY-NC-ND)

powers and specific capacities of different power sources **[40]**.The fuel cell and hydrogen have the highest specific ***capacity***, followed by batteries and then super-capacitors. In contrast, super-capacitors have the highest specific ***power***, followed by batteries and fuel cells.

One of the challenges in the design of a fuel cell hybrid vehicle is to determine an ideal combination of the fuel cell system and the secondary energy source to satisfy the dynamic performance of the vehicle while ensuring sufficient autonomy.

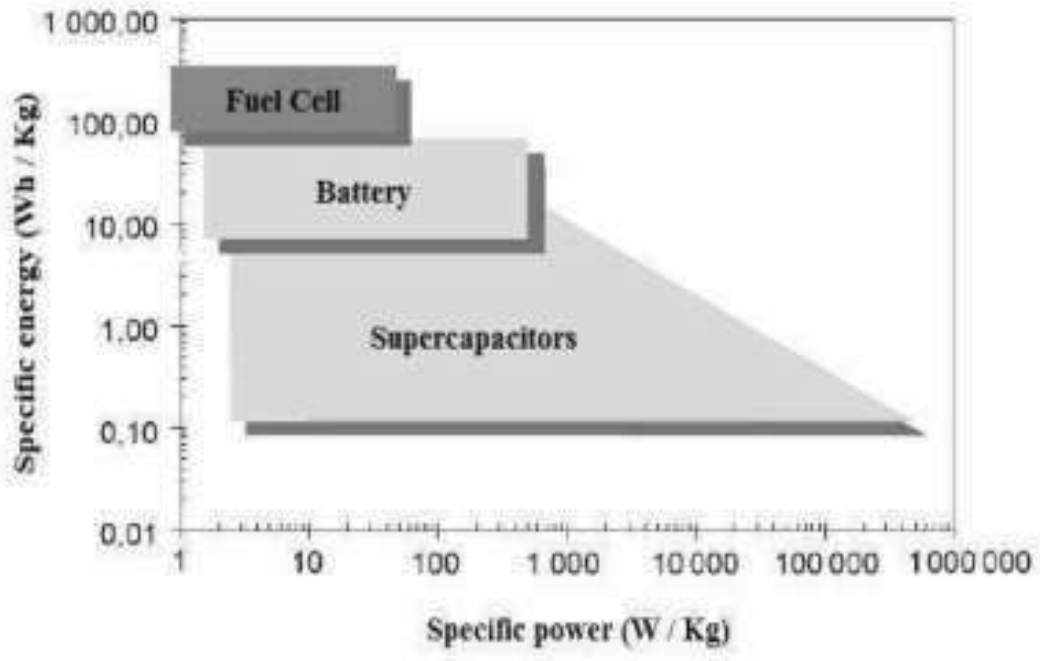

Fig15. Plan of Ragone [40]

3.1.4. Dimensioning and control strategy:

a. Dimensioning of the hybrid power source:

The sizing of the power source (fuel cell system and secondary energy source) has an essential impact on both the dynamic performance of the vehicle (driving pleasure) and the hydrogen consumption (vehicle range).It is obviously a function of a specification related to the application. The solutions obtained for this specification can be many and varied (choice of secondary source for example).In this case, to make a choice, one must be sure to have a control strategy that makes the best use of energy exchanges. The choice of components and the control strategy are therefore intimately linked for sizing. Sizing must take into account several aspects:

- **Driving situations and dimensioning:**

It is not possible to take into account all possible driving situations. The specifications therefore impose minimum performance for "characteristic" driving conditions. For the special cases of constant speed and constant acceleration of the vehicle (**Figure 16**),

Creative Commons Attribution-NonCommercial-NoDerivatives 4.0 International License (CC BY-NC-ND)

minimum limits can easily be calculated for the energy and power of the secondary energy source:

- Case of the constant speed of the vehicle:

  The vehicle must be able to drive at a constant speed V_{const} for an extended period of time (typically on the highway for several tens of minutes), which equates to a constant power demand P_{speed_const} of the engine.

  Since the secondary power source has a limited amount of power, it cannot provide extended power assistance to the fuel cell system. The fuel cell system must therefore have a maximum power sufficient $P_{sysFCmax}$to maintain the speed of the vehicle **[41][42][43][28]**.

- Case of acceleration of the vehicle:

  The acceleration of the vehicle is characterized by power peaks P_{accel} of limited duration of the engine (a few seconds).The fuel cell system is not always able to ensure the acceleration of the vehicle alone either because its dynamics is limited or because it's maximum power $P_{sysFCmax}$ is limited.

  The missing power P_{accel}- $P_{sysFCmax}$is then supplied by the secondary energy source **[28][42]**.The hybrid configuration is also particularly interesting to overcome the limit dynamics of the fuel cell system **[22][44]**.

Creative Commons Attribution-NonCommercial-NoDerivatives 4.0 International License (CC BY-NC-ND)

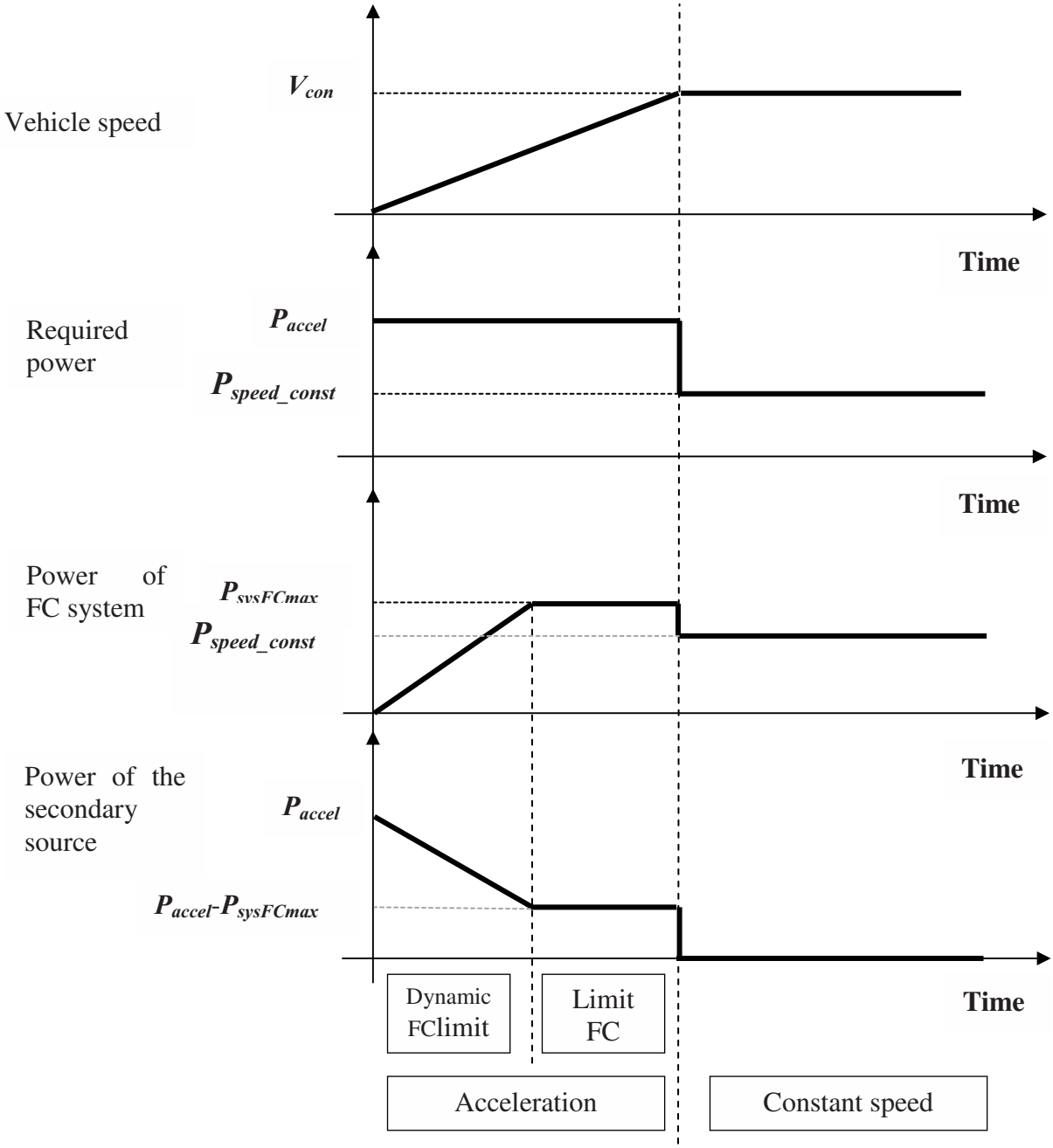

Fig16. Example of the powers involved in accelerating and maintaining the speed of the vehicle.

- **Energy criteria and sizing:**

An important part of hydrogen saving is obtained by kinetic energy recovery **[45][42][46]**. The sizing of the secondary source must therefore make it possible to recover as much as possible the braking energy **[47] [41] [48]**.However, the kinetic energy recoverable and the power demand of the motorization depend on the envisaged use of the vehicle (urban, periurban or highway, mixed...).As a result, the sizing of the power source is specific to a particular application **[49] [50] [42]**.

Creative Commons Attribution-NonCommercial-NoDerivatives 4.0 International License (CC BY-NC-ND)

- **Vehicle mass problem:**

Hydrogen consumption is influenced by the mass of the vehicle. The mass of the power source (fuel cell system + secondary energy source) is therefore an important factor in the design process **[49][51][46]**. At the limit, the overweight introduced can go as far as canceling the benefits obtained thanks to the secondary source.

Due to the additional weight introduced by the secondary source of energy as well as the increase in the complexity of the powertrain, can be considered the use of a single fuel cell which naturally has a high efficiency over a wide range of use **[52]**.

- **Energy vs. Power: Battery or Super-capacitor?**

It is difficult to advocate the use of battery or super-capacitor, the two technologies having very different characteristics. Some authors favor the use of super-capacitors **[41][50]** because of their energy efficiency and specific power, but their low capacity can be a handicap. Conversely, batteries are able to store a large amount of energy but are penalized by their specific power. One solution is to couple batteries and super-capacitors to combine their advantages (power and energy) **[53][41][50]**, but this inevitably increases the complexity and ***cost*** of the secondary energy source.

In summary, in the context of automotive use, if there is consensus on the interest of a hybrid fuel cell system, the choice of secondary source technology remains open. In addition, there does not appear to be a trend among automakers to use super-capacitors or precise battery technology (**Table 2**).

Life-time constraints **[53]** or cost criteria **[54]** are also involved in the sizing process.

Creative Commons Attribution-NonCommercial-NoDerivatives 4.0 International License (CC BY-NC-ND)

Conclusion:

With the growth of environmental problems and the expected shortage of energy sources for the next decades, it is important to find other more efficient and clean forms of energy, the overall oil reserves are only sufficient for about 40 years. However, the global economy is growing rapidly with a subsequent increase in oil consumption, CO2 emission has grown enormously in this period. In addition to contributing to the reduction of the greenhouse effect, vehicles powered by a fuel cell, more commonly called zero emission vehicles (ZEV), allow the improvement of the quality of urban life thanks to their low noise pollution. However, the prospects for commercial development have never been better as a result of the combined efforts of various research institutes worldwide, several large industrial groups and car manufacturers. Performance, reliability, durability, cost, fuel availability, public satisfaction, and performance during transients [19] are essential factors in developing fuel cell electric vehicles that can compete with the ICE vehicles that are monopolizing the streets. Thus, automotive manufacturers started to produce fuel cell vehicles.

Creative Commons Attribution-NonCommercial-NoDerivatives 4.0 International License (CC BY-NC-ND)

References:

https://fr.wikipedia.org/wiki/Norme_europ%C3%A9enne_d%27%C3%A9mission

A. Fonseca (2000), Comparaison de machines à aimants permanents pour la traction de véhicules électriques et hybrids, Thèse de doctorat INPG Génie électrique, septembre.

D.Benedittis (2002), Etude et modèle électromagnétique de machine asynchrone pour alternateur démarreur, Thèse de doctorat INPG Génie électrique.

R. Joumard (25 et 26 juin 2002), INRETS Les enjeux de la pollution de l'air des transports 5ème Colloque C-VELEC – Grenoble.

Association Française de l'hydrogène, Le programme DaimlerChrysler, Mémento de l'hydrogène, Fiche 9.1.1, September 2016
http://www.afhypac.org/documents/toutsavoir/Fiche%209.1.1%20%20Daimler%20rev.sept%20%202016%20Th.pdf

Thierry Alleau (25 et 26 juin 2002), Association française de l'hydrogène L'hydrogène; vecteur d'énergie du futur? 5ème Colloque C-VELEC – Grenoble.

Scott Hardman, Gil Tal (13 September 2018), Who are the early adopters of fuel cell vehicles?, Institute of Transportation Studies, University of California, Davis, USA, International Journal of Hydrogen Energy Volume 43, Issue 37, Pages 17857-17866.

EV Volumes, EV data center (2018), http://www.ev-volumes.com/

Fuel Cell Today, news site on the fuel cell, http://www.fuelcelltoday.com/

SAE (Society of automotive Engineer), History of Fuel Cells, https://www.sae.org/

K.A. Burke (17–21 August 2003), Fuel Cells for Space Science Applications, First International Energy Conversion Engineering Conference, Virginia.

K.B. Prater (Janvier 1992), Solid polymer fuel cell developments at Ballard, Journal of Power Sources, Volume 37 (1-2), pages 181-188.

https://fr.wikipedia.org/wiki/Pile_%C3%A0_combustible#/media/File:Fuel_cell_NASA_p48600ac.jpg

CEA (Commissariat à l'Énergie Atomique) (hiver 2004/2005), L'hydrogène-Les nouvelles technologies de l'énergie, Clefs CEA, Magazine numéros 50/51.

Société Axane, Typology of fuel cells, 2005, http://www.axane.net/

J. Lachaize (2004), Etude des stratégies et des structures de commande pour le pilotage des systèmes énergétiques à Pile à Combustible (PAC) destinés à la traction, Thèse de doctorat, Laboratoire d'Électrotechnique et d'Électronique Industrielle, Institut National Polytechnique de Toulouse.

A. Emadi, K. Rajashekara, S. Williamson, S. Lukic (Mai 2005), Topological Overview of Hybrid Electric and Fuel Cell Vehicular Power System Architectures and Configurations, IEEE Transaction on Vehicular Technology, Vol.54 (3).

Creative Commons Attribution-NonCommercial-NoDerivatives 4.0 International License (CC BY-NC-ND)

D.D. Boettner, G. Paganelli, Y.G. Guezennec, G. Rizzoni, M.J. Moran (March 2002), ''Proton Exchange Membrane (PEM) fuel cell system for automotive vehicle simulation and control'', Journal of Energy Resources Technology (Transactions of the ASME), Vol. 124 (1), pp. 20-27.

M.D. Ruge (2003), Entwicklungeinesflüssigkeitsgekühlten Polymer-Elektrolyt-Membran-BrennstoffzellenstapelsmiteinerLeistung von 6,5 kW, Thèse de doctorat, ETH Zürich.

Dupont, Nafion membrane manufacturing company,http://www.dupont.com/.

P. Rodatz (2003), Dynamics of the Polymer Electrolyte Fuel Cell: experiments and model-based analysis, doctoral thesis, ETH Zürich.

Y. Guezennec, T.Y Choi, G. Paganelli, G. Rizzoni (June 2003), Supervisory control of fuel cell vehicles and its link to overall system efficiency and low-level control requirements, Proceedings ofthe American Control Conference 2003, Vol. 3, pages 2055-2061.

A. Züttel (September 2003), Materials for hydrogen storage, Materials Today, Vol. 6 (9), pages 24-33.

V. Ananthachar, J.J. Duffy (May 2005), Efficiencies of hydrogen storage systemsonboard fuel cellvehicles, Journal of Solar Energy, Vol. 78 (5), pp. 687-694.

L. Zhou (August 2005), Progress and problems in hydrogen storage methods, Renewable and Sustainable Energy Reviews, Vol. 9 (4), pp. 395-408.

P. Guay, L. Barry, L. Stansfield, A. Rochefort (2004), On the control of carbon nanostructures for hydrogen storage applications, Carbon, Vol. 42 (11), pp. 2187-2193.

S. Rogg, M. Höglinger, E. Zwittig, C. Pfender, W. Kaiser, T. Heckenberger (2003), Cooling Modules for Vehicles with a Fuel Cell Drive, Fuel Cells, Willey Interscience, Vol. 3 (3) , pp. 153-158.

T. Markel , M. Zolot , K.B. Wipke , A.A. Pesaram (June 2003), Energy storage requirements for hybrid fuel cell vehicles, Advanced Automotive Battery Conference, Nice, France.

Honda, Honda Fuel Cell Vehicle, http://world.honda.com/FuelCell/.

Toyota, Toyota's Fuel-Cell Hybrid Vehicles (FCHV), https://www.toyota.com/

Nissan, Fuel CellVehicle X-Trail FCV, Notes techniques (2006), https://www.nissan-global.com

General Motors, Technical Data of HydroGen3, Donnée techniques (2004), https://www.gmheritagecenter.com/featured/Fuel_Cell_Vehicles.html

PSA, La pile à combustible - une énergie d'avenir, Communiqué de presse 2006, https://www.groupe-psa.com/fr/, https://www.actu-environnement.com/ae/news/1471.php4

Michelin, Hy-Light, Le concept car Michelin de la mobilité propre, https://www.michelin.com/fre/presse/Presse-et-actualites/actualite-michelin/Innovation/Concept-Vision-MICHELIN

F.N. Büchi, G. Paganelli, P. Dietrich, D. Laurent, A. Tsukada, P. Varenne, A. Delfino, R. Kötz, S.A. Freunberger, P.A. Magne, D. Walser, D. Olsommer (2007), Consumption and Efficiencyof a Passenger Car with a Hydrogen/Oxygen PEFC based Hybrid Electric Drivetrain, Fuel Cells, Vol.7, pp. 329-335.

K.S. Jeong, B.S. Oh (2002), Fuel economy and life-cost analysis of a fuel cell hybrid vehicle, Journal of Power Source, Vol. 105, pp. 58-65.

R. Spotnitz (September 2005), Advanced EV and HEV Batteries, IEEE Vehicle and Power Propulsion Conference, Chicago.

Creative Commons Attribution-NonCommercial-NoDerivatives 4.0 International License (CC BY-NC-ND)

M.L. Soria, F. Trinidada, J.M. Lacadenaa, A. Sáncheza, J. Valencianoa, ''Advanced valveregulated lead-acid batteries for hybrid vehicle applications'', Journal of Power Sources,Vol. 168 (1), pp. 12-21 May 2007.

P. Barrade, A. Rufer (October 2004), The use of super-capacitors for energy storage in traction systems, IEEE Vehicle Power and Propulsion Conference, Paris.

A. Schneuwly, M. Bärtschi, V. Hermann, G. Sartorelli, R. Gallay, R. Koetz (February 2002), BOOSTCAPDouble-Layer Capacitors for Peak Power Automotive Applications, International AdvanceAutomotive battery conference (AABC), Las Vegas.

W. Gao (May 2005), Performance Comparison of a fuel cell battery hybrid powertrain and a fuel cell ultra-capacitor hybrid powertrain, IEEE Transaction On Vehicular Technology, Vol. 54 (3).

R.K. Ahluwalia, X. Wang, A. Rousseau (2005), Fuel economy of hybrid fuel-cell vehicles, Journal of Power Sources, Vol. 152, pp. 233-244.

D.D. Boettner, G. Paganelli, Y.G. Guezennec, G. Rizzoni, M.J. Moran (November 2001), Component power sizing and limits of operation for proton exchange membrane (PEM) fuel cell/battery hybrid automotive applications, Proceedings of ASME International Mechanical EngineeringCongress and Exposition , New York.

K.W. Suh, A.G. Stefanopoulou (April 2006), Effects of Control Strategy and Calibration on Hybridization Level and Fuel Economy in Fuel Cell Hybrid Electric Vehicle, SAE World Congress &Exhibition, Detroit.

K.S. Jeong, B.S. Oh (2002), Fuel economy and life-cost analysis of a fuel cell hybrid vehicle, Journalof Power Source, Vol. 105, pp. 58-65.

O. Sundström, A. Stefanopoulou (May 2007), Optimum Battery Size for Fuel Cell Hybrid Electric Vehicle With Transient Loading Consideration-Part II, Journal of Fuel Cell Science and Technology, Vol. 4 (2), pp. 176-184.

M. Zolot, T. Markel, A.A. Pesaran (June 2004), Analysis of fuel cell vehicle hybridization andimplications for energy storage devices, Advanced Automotive Battery Conference, San Francisco.

M.J. Kim, H. Peng (2007), Power management and design optimization of fuel cell/battery hybridvehicles, Journal of Power Source, Vol. 165, pp. 819-832.

K.B Wipke, T. Markel, D. Nelson (2001), Optimizing energy management strategy and degree ofhybridization for a hydrogen fuel cell SUV, Electric Vehicle Symposium EVS 18, Berlin.

G. Pede, A. Iacobazzi, S. Passerini, A. Bobbio, G. Botto (2004), FC vehicle hybridisation: anaffordable solution for an energy-efficient FC powered drive train, Journal of Power Sources,Vol. 125, pp. 280-291.

O. Sundström, A. Stefanopoulou (May 2007), ''Optimum Battery Size for Fuel Cell Hybrid ElectricVehicle-Part I'', Journal of Fuel Cell Science and Technology, Vol. 4 (2), pp. 167-175.

D.J. Friedman (1999), Maximizing direct-hydrogen fuel cell vehicle efficiency - Is hybridizationNecessary?, SAE Paper Number.1999-01-0539, Society of Automotive Engineers.

N. Schoffield, H.T. Yap, C.M. Bingham (September 2005), Hybrid energy sources for electric and fuel cellvehicle propulsion, IEEE Vehicle Power and Propulsion Conference, Chicago.

Y. Wu, H. Gao, R. Sharma (October 2004), Optimal design for fuel cell and super-capacitor hybrid electric vehicle, IEEE Vehicle Power and Propulsion Conference, Paris.

Creative Commons Attribution-NonCommercial-NoDerivatives 4.0 International License (CC BY-NC-ND)

Algerian Journal of Engineering Architecture and Urbanism Vol. 5 Nr. 3 2021
ISSN: 2588-1760

TREATMENT OF OILY WATER FROM THE API-CINA HMD UNIT
TRAITEMENT DES EAUX HUILEUSES DE L'UNITE API-CINA HMD

ALLEM Mohamed Nazim (mastérant)
Institut de Maintenance et de Sécurité Industrielle / Université Oran 2-Mohamed Ben Ahmed
nazim.allem@gmail.com

HEBBAR Chafika (Professeur)
Laboratoire d'Ingénierie en Sécurité Industrielle et Développement Durable/Institut de Maintenance et de Sécurité Industrielle / Université Oran 2-Mohamed Ben Ahmed
hebbar.chafika@univ-oran2.dz

KHEMSINE Yanis (mastérant)
Institut de Maintenance et de Sécurité Industrielle / Université Oran 2-Mohamed Ben Ahmed

Résumé :
La pollution de l'environnement, problème majeur et urgent de ce temps, est liée principalement aux rejets industriels. La pollution générée par l'industrie des hydrocarbures constitue une menace permanente pour la dégradation de cet environnement.
L'objectif de notre travail consiste à évaluer la performance de l'unité de déshuilage « API » de la station CINA-API par l'analyse de la qualité de ses eaux huileuses.
Les résultats des analyses des eaux de rejet de la station de déshuilage « API » obtenus ont montré que l'efficacité de traitement est démontrée pour l'abattement des valeurs des différents paramètres (pH, Matières en suspension, Hydrocarbures) à des valeurs respectant la norme nationale.

Mots clefs : Eaux huileuses, pollution, Unité de déshuilage API.

Abstract:
Environmental pollution, a major and urgent problem of the time, is mainly linked to industrial discharges. The pollution generated by the hydrocarbon industry constitutes a permanent threat to the degradation of this environment.
The objective of our work is to assess the performance of the "API" de-oiling unit of the CINA-API station by analyzing the quality of its oily water.
The results of the analyses of the discharge water from the "API" de-oiling station showed that the treatment efficiency is demonstrated for the abatement of the values of the various parameters (pH, Suspended solids, Hydrocarbons) values that meet the national standard.
Key words: Oily water, pollution, API de-oiling unit.

Creative Commons Attribution-NonCommercial-NoDerivatives 4.0 International License (CC BY-NC-ND)

Introduction :

Un approvisionnement adéquat en eau de bonne qualité est essentiel au développement continu de n'importe quelle société industrielle. Dans toute activité industrielle, l'eau entre en contact avec des gaz, des solides et des liquides, qu'elle dissout ou entraîne sous forme de matières en suspension ou émulsion plus ou moins finement dispersées. Les lubrifiants dérivés de la pétrochimie présentent des risques pour les écosystèmes et donc pour les ressources naturelles (**Bartz**, **1997**).

Les puits producteurs de pétrole du champ de Hassi-Messaoud (HMD), produisent quotidiennement de grandes quantités d'eaux contaminées par des hydrocarbures, dites eaux huileuses. Le traitement des eaux résiduaires huileuses est d'une grande importance dans la gestion des rejets industriels usagés. Les hydrocarbures sont considérés comme des déchets dangereux pouvant avoir un important impact négatif sur l'environnement. Toutefois, l'hydrocarbure ou l'huile peuvent être valorisés, récupérés ou recyclés à condition qu'ils soient séparés de l'eau (**Gousmi et Bensadok, 2016)**.

La protection de l'Environnement et la remédiation des problèmes environnementaux sont des défis majeurs pour une amélioration effective de la qualité de vie et pour un développement durable.

Problematique :

L'unité de traitement des eaux huileuses du complexe CINA a été conçue pour produire une eau traitée avec des spécifications suivantes (**Gouvernement Algerien**, **2006**). Après sa mise en service, l'unité d'exploitation a constaté plusieurs problèmes qui empêchaient la production d'une eau traitée conforme aux spécifications exigées, parmi lesquels nous pouvons citer : le dégazage de la charge à l'entrée du bassin surtout dans la période d'été, un dysfonctionnement fréquent du système de régulation et un impact sur l'environnement suite à l'arrêt de la dite unité.

Quatre types de coagulants (C1, C2, C3 et C4) sont utilisés pour étudier leur concentration optimale. Les résultats ont montré que pour chaque préparation, l'efficacité du traitement est dépendante de la dose du coagulant utilisé et préparé par l'addition 4ml de silicate de sodium et 0.45ml d'acide sulfurique.

Matériél et méthodes:

Zone d'étude :

Le complexe industriel CINA, situé au nord du champ, mis en service depuis 1958 est l'un des premiers complexes au niveau du champ de Hassi-Messaoud qui reçoit la production totale en huile et gaz des zones nord qui provient essentiellement des unités satellites et des séparateurs sur champ, d'une part, et directement des puits en LDHP (ligne directe haute pression), et en LDMP (ligne directe moyenne pression), d'autre part.

Creative Commons Attribution-NonCommercial-NoDerivatives 4.0 International License (CC BY-NC-ND)

La réalisation de la station de déshuilage du CIS était dans le cadre de la mise en application de la politique de l'entreprise relative à la préservation de l'environnement visant l'élimination ou la réduction des impacts environnementaux liés à ses activités. Elle a été mise en service afin de traiter les eaux de production (eaux huileuses), dans le but de les réinjecter pour maintenir la pression du gisement. L'effluent à la sortie de la station doit donc répondre aux normes exigées par la réglementation (**Bourekia & Kerkoub, 2016**).

La station de déshuilage CINA (fig. 1) est conçue pour :

• la collecte des eaux huileuses sur les différents sites (les champs satellites et les différentes unités du centre industriel) pour une capacité de traitement maximale de 6000 m^3/j.

• le traitement physico-chimique des eaux huileuses et la récupération d'huiles.

• l'expédition des eaux traitées vers la station satellite OMP53.

Fig. 1. Station de déshuilage API- CINA (Vue externe).

Le traitement des eaux industrielles se réalise selon trois voies :

Traitement physique : La séparation physique joue sur la différence des densités entre les différentes phases (fig. 2). L'eau arrivant au séparateur triphasique se débarrasse de la majorité de MES dans le compartiment d'admission à l'aide de la plaque inclinée permettant :

-la sédimentation des particules solides les plus lourdes.

-l'accumulation et la chute des particules solides les moins lourdes le long de la plaque inclinée.

-la tranquillisation de l'écoulement de l'eau huileuse.

-l'échappement du gaz vers le haut du séparateur profitant de l'écoulement ascendant de l'eau.

-la formation de la première couche d'huile libre à la surface de l'eau.

Le bassin API est un pré-déshuileur assurant l'extraction de la totalité de l'huile libre et la réduction de la teneur des particules solides.

Creative Commons Attribution-NonCommercial-NoDerivatives 4.0 International License (CC BY-NC-ND)

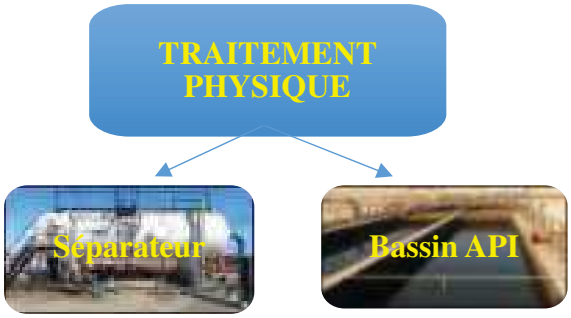

Fig. 2. Traitement physique des eaux industrielles.

Traitement chimique : La séparation par voie chimique permet de modifier les caractéristiques de la couche externe des particules (huileuses et solides) existantes dans l'eau afin de faciliter son élimination. Les skids d'injection de produits chimiques permettent d'éliminer les traces des bactéries existantes dans l'eau et inhiber l'activité corrosive de l'oxygène dissous dans l'eau afin de protéger les installations mises en service. Le séparateur DGF fonctionne à une pression moyenne variant entre 0,5 à 1 bar. L'huile et les matières en suspension sont récupérées au niveau des cellules de flottation est acheminées vers un compartiment de stockage à l'intérieur du séparateur DGF (fig. 3).

Fig.3. Traitement chimique des eaux industrielles.

Filtration : En sortant du séparateur IGF ou DGF, l'eau sera acheminée vers un filtre à poches afin de procéder la dernière étape de traitement, Les matières et les solides colloïdaux qui peuvent s'échapper du séparateur à gaz seront collectés dans des poches filtrantes (fig. 4).

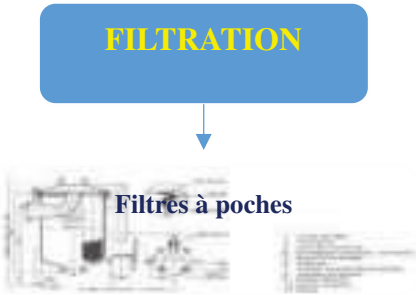

Fig.4. Filtration des eaux industrielles.

Creative Commons Attribution-NonCommercial-NoDerivatives 4.0 International License (CC BY-NC-ND)

La station API-CINA a utilisé deux méthodes pour la préparation de la silice activée. Une première méthode manuelle adoptée en 2012 où l'opérateur extérieur qui prépare le mélange avec le dosage requis, et une autre automatique appliquée en 2016 où on s'aperçoit l'absence du manipulateur, il intervient seulement dans la salle de commandes. Cette dernière méthode a montré des résultats positifs améliorés (concernant l'analyse de certains paramètres physicochimiques à savoir : pH, MES, HC qui restent toujours inférieures aux normes régies par la réglementation algérienne.

Echantillonnage :

Les échantillons d'eau proviennent de deux points de prélèvement :

-L'échantillon 1 est prélevé à la sortie du ballon triphasique de l'unité de traitement des eaux huileuses CINA.

-L'échantillon 2 est prélevé à la sortie DGF / IGF après traitement final par l'unité CINA.

Les paramètres recherchés sont : le pH, les MES, teneurs en hydrocarbures et détermination de la concentration optimale de coagulant (silice activée) par le jar-test.

Le jar-test vise à déterminer l'efficacité comparée d'un coagulant en fonction des doses injectées sur un échantillon donné. Nous en déduirons la dose optimale nécessaire au traitement et le pH auquel son action est la plus efficace. Nous déterminons quels sont les couples quantités de réactifs /vitesse et temps d'agitation qui permettent d'obtenir l'eau la plus limpide, les flocs les plus gros et les mieux décantés.

La préparation de 04 coagulants à base de silicate de sodium et d'acide sulfurique (fig. 5) est réalisée en vue d'améliorer le processus de traitement appliqué au niveau de l'unité de traitement des eaux huileuses CINA – HMD. La coagulation nécessite une vitesse d'agitation plutôt rapide 150 rpm (rotation par minute) pendant 1 minute (afin de bien mélanger l'eau et que les colloïdes et les cations métalliques se rencontrent et se neutralisent). En revanche, la floculation nécessite une vitesse relativement lente 30 rpm pendant 20 minutes (afin de favoriser la rencontre et l'agrégation des colloïdes mais sans détruire les flocs déjà formés). Ensuite un temps de sédimentation des flocs de 45 minutes avant de déterminer par analyses les teneurs en HC, MES et turbidité.

Fig.5. Influence de la concentration de la silice activée sur les eaux huileuses.

Creative Commons Attribution-NonCommercial-NoDerivatives 4.0 International License (CC BY-NC-ND)

Resultats et discussion:

Comparaison des paramètres physicochimiques obtenus selon les deux méthodes (manuelle et automatique) :

Les résultats d'analyse des trois paramètres (pH, MES et HC) par la méthode manuelle montre que l'eau à la sortie de l'unité contient toujours des traces d'hydrocarbures qui dépassent les normes de réinjection, des concentrations de matières en suspension plus grandes et une légère variation à l'entrée et à la sortie de l'unité API. Cette méthode a été annulée car elle se basait sur la manipulation de l'opérateur qui donnait un dosage erroné ce qui va influencer sur le traitement.

Un nouveau système du dosage automatique basé sur un système de régulation qui intervient sur les quantités voulues du dosage ainsi que sur l'ouverture et la fermeture des vannes est lancé. Les résultats obtenus ont enregistré des valeurs de pH à l'entrée de l'unité comprises entre 4,2 et 5,95 tandis qu'à la sortie de l'unité, le pH varie entre 5,8 et 6,35 avec une tendance vers la neutralisation.

Les teneurs en hydrocarbures à l'entrée de l'unité ont atteint des valeurs de 873,4 ppm qui sont largement supérieures à la norme requise (10 ppm). A la sortie de l'unité, ces concentrations sont réduites jusqu'à 5,2 ppm.

Les concentrations de matières en suspension à l'entrée de l'unité se situent entre 107 et 271 ppm, tandis qu'à la sortie elles sont diminuées jusqu'à 16 ppm et par conséquent répondent à la norme requise (30 ppm).

Nous remarquons que le taux de traitement de MES par la méthode de dosage manuel est de 73,9% tandis que dans la méthode de dosage automatique est de 81,1%. Une augmentation d'un ordre de 5% entre les taux de traitement des hydrocarbures dans le dosage manuel et automatique qui sont 91,7% et 96,9% respectivement. Le taux de traitement de pH dans le dosage avec la méthode automatique est important par rapport à la méthode manuelle avec 10,6%.

Les travaux de **Mekhalif** (**2009**) ont montré que la coagulation-floculation est l'étape principale du processus de dépollution des eaux résiduaires industrielles et la plus efficace avec le sulfate d'aluminium, dont la concentration de ce dernier influe sur le pH et la turbidité ainsi que les autres paramètres analysés ; ceci assure une bonne clarification avec un moindre coût.

Nos résultats obtenus sont similaires aux résultats des différents paramètres physicochimiques des eaux usées à l'entrée et à la sortie de la station de déshuilage HBK enregistrés et sont inférieures aux normes algériennes et confirment le bon fonctionnement de la station (**Benguettane** et **Hadbouli, 2016**).

Creative Commons Attribution-NonCommercial-NoDerivatives 4.0 International License (CC BY-NC-ND)

Le but des travaux de **Bourekia et Kerkoub (2016)** était de déterminer les doses de coagulant et floculant nécessaires à la réduction du taux des matières en suspension, des hydrocarbures, de la DCO et de la DBO5 dans l'eau huileuse issue du traitement physique de la station de déshuilage du CIS jusqu'à atteindre la norme (MES < 35 mg/l, HC < 10 mg/l, DCO < 120 mg/l et DBO5 <40mg/l). Le protocole suivi ne permet qu'une détermination grossière de la quantité optimale des coagulant et floculant à injecter. En effet, les résultats doivent être affinés sur site (injection des doses dans le ballon DGF).

Les résultats des travaux de **Bouziane** et **Sache** (**2017**) ont montré que la méthode la plus rentable de traitement des eaux usées pétrolières de la station « Haoud Berkaoui : HBK » est la Décantation par gravité – Adsorption par Charbon actif.

Les travaux de **Braik** (**2017**) ont évalué l'étude de la faisabilité d'application du traitement par photocatalyse hétérogène solaire sur les eaux huileuses de la station de déshuilage « Hassi R'mel » surtout que cette activité s'inscrit dans le cadre de développement durable utilisant le soleil comme source d'énergie renouvelable.

Influence de la dose optimale du coagulant sur les MES, HC et pH

Quatre types de coagulants (C1, C2, C3 et C4) sont utilisés pour étudier leur concentration optimale. Les résultats ont montré que pour chaque préparation, l'efficacité du traitement est dépendante de la dose du coagulant (tab. 1).

Pour le coagulant C1, une dose de 20 ppm a permis l'élimination des hydrocarbures et la diminution de leur concentration de 295 ppm à 15,2 ppm. Pour la même dose, une valeur de 37 mg/l de MES proche de la norme (30 mg/l) a été enregistrée. L'addition de 8 ml de coagulant C1 a provoqué l'augmentation de pH de 5.27 à 6.04.

Pour le coagulant C2, pour une dose de 5 ppm, la teneur enregistrée en hydrocarbures est 290 ppm ; elle passe à une teneur de 7,4 ppm pour une dose de 30 ppm de coagulant. Le pH est passé de 5,2 à 5,78. La même dose du coagulant C2 génère une réduction du taux de MES de 146 à 57 mg/l, mais reste supérieure à la norme (30mg/l).

L'addition du coagulant C3 a provoqué l'augmentation du pH de 6,1 à 6,48 qui tend à la neutralisation. En effet, à une dose de 20 ppm du coagulant, la teneur en hydrocarbures a diminué et atteint 9,2 ppm répondant à la norme de réinjection. Il y a eu aussi une réduction du taux de MES de 417 à 19,1 mg/l conformément à la norme (30 mg/l).

A une dose de 5ppm du coagulant C4, les teneurs enregistrées du pH, d'hydrocarbures et de MES sont respectives à 5.06 ; 261 ppm et 162 ppm. L'addition du coagulant C4 de dose de 40 ppm, a provoqué une augmentation de pH de 5,06 à 5,68, une élimination d'hydrocarbures à 4.2ppm et une réduction de la teneur en MES à 4.2ppm.

Les meilleurs résultats de traitement s'obtiennent à une dose optimale de 20 ppm lors de l'emploi du coagulant C3 préparé par : 4ml de silicate de sodium et 0.45ml d'acide sulfurique. Les caractéristiques de l'eau traitée avec 20 ppm du coagulant **C3** montre que les

Creative Commons Attribution-NonCommercial-NoDerivatives 4.0 International License (CC BY-NC-ND)

exigences environnementales imposées par l'entreprise sont atteintes pour tous les paramètres. Ainsi cette eau pourra être employée comme eau de réinjection (tab.1).

	C1 20ppm	C2 30ppm	C3 20ppm	C4 40ppm
pH	6.04	5.78	6.48	5.68
MES (mg/l)	37	57	19.1	63
HC (ppm)	15.2	7.4	9.2	4.2

Tableau 1. Détermination de la concentration optimale des 4 coagulants (C1, C2, C3, C4).

Conclusion:

Les effluents industriels sont multiples, les normes de rejets, de plus en plus strictes et la réduction des empreintes environnementales, est devenue une priorité pour la réglementation algérienne. Les eaux usées de l'industrie pétrolière influencent négativement sur l'environnement vu la toxicité des éléments hydrocarbures qu'elles contiennent, leur traitement s'avère très important.

Afin d'exploiter l'unité en toute sécurité, de produire une eau conforme et de protéger l'environnement, l'unité de traitement des eaux huileuses « CINA » a été rénovée par la direction régionale de Hassi-Messaoud (HMD).

Pour assurer plus un bon rendement de l'unité de traitement des eaux huileuses du complexe CINA et produire une eau traitée, nous projetons plusieurs recommandations :

-Vérification continue de la préparation et de l'injection de la silice activée.

-Vérification continue de la préparation et de l'injection de kurifix.

-Suivi instantané des eaux huileuses à l'entrée de la station.

-Vérification et nettoyage des pompes et des circuits d'injection des produits chimiques.

-Drainage du ballon DGF ou IGF.

Références :

Bartz W.J, (1997), *Lubricants and the environment*. New Dir Tribol, Plenary Invited Pap World TribolCongr. 103-19.

Benguettane H., Hadbouli Kh, (2016), *Analyse des eaux industrielles de la station déshuilage de la zone HBK.* Mémoire de Master 2. Université Kasdi Merbah Ouargla. 41p.

Bourekia I., Kerkoub M.H, (2016), *Optimisation des paramètres physico-chimique dans le processus du traitement des eaux huileuses (Cas des eaux huileuses du complexe CIS de HMD).* Mémoire de Master. Université Abderrahmane Mira de Bejaia. 104p.

Bouziane A., Sache D, (2017), *Choix d'une méthode de traitement des eaux usées de l'industrie pétrolière cas station de déshuilage HBK Ouargla.* Mémoire de Master. Université M'hamed Bougara de Boumerdes. 48p.

Braik M, (2016), *Analyse de la performance du traitement de l'unité de déshuilage de Hassi R'mel et application du traitement par photocatalyse hétérogène solaire aux eaux huileuses*. Mémoire de Master. Université M'hamed Bougara – Boumerdès. 76p.

Gousmi N., Bensadok K, (2016), *Etude de l'applicabilité du procédé d'électrocoagulation pour le traitement de rejets pétroliers*. Third International Conference on Energy, Materials, *Applied Energetics and Pollution*. ICEMAEP2016, October 30-31, 2016, Constantine, Algeria.

Creative Commons Attribution-NonCommercial-NoDerivatives 4.0 International License (CC BY-NC-ND)

Gouvernement Algerien (2006), *Décret exécutif n° 06-141 du 20 Rabie El Aouel 1427 correspondant au 19 avril 2006 définissant les valeurs limites des rejets d'effluents liquides industriels.* Journal Officiel de la République Algérienne Démocratique et Populaire.
Mekhalif F, (2009), *Réutilisation des eaux résiduaires industrielles épurées comme eau d'appoint dans un circuit de refroidissement.* Mémoire de Magister. Université du 1 Août 1955 Skikda. 133p.

Creative Commons Attribution-NonCommercial-NoDerivatives 4.0 International License (CC BY-NC-ND)

Algerian Journal of Engineering Architecture and Urbanism Vol. 5 Nr. 3 2021
ISSN: 2588-1760

TECHNICAL STUDY AND SIMULATION OF THE WASTE WATER TREATMENT

Nour el houda Herarsi
First author, PhD student, Manufacturing Engineering Laboratory of Tlemcen (MELT), Electrical and Electronics Department, Faculty of Technology
Abou-Bekr Belkaid University, Tlemcen, Algeria,
nourelhouda.herarsi@univ-tlemcen.dz
Ahmed Hassam
Second author, scientific title (PhD), Manufacturing Engineering Laboratory of Tlemcen (MELT), Electrical and Electronics Department, Faculty of Technology
Abou-Bekr Belkaid University, Tlemcen, Algeria,
Ahmed.hassam@univ-tlemcen.dz
Mohammed el amin Mkedder
Third author, scientific title (Senior Research Engineer), Manufacturing Engineering Laboratory of Tlemcen (MELT), Electrical and Electronics Department, Faculty of Technology
Abou-Bekr Belkaid University, Tlemcen, Algeria,
Mohammedelamin.mkedder@univ-tlemcen.dz

Abstract:
The work that we will present concerns the technical study and the simulation of the production system of the residual STEP of the complex of the Maïserie de Maghnia, the latter is located in the industrial zone of Maghnia. , its main products are starch and glucose syrup. . First of all, we expose the specifications of the different basins and stations, then we will and stations, then we will model in graphic form using the language of modeling automated systems modeling language GRAFCET then we present the programs written in S7- GRAPH language. written in S7-GRAPH language of the software STEP7 SIMATIC Manager of Siemens in order to automate to automate the STEP.
Considering the complexity of the system and the large number of GRAFCET models, we will only present the GRFCET modeling and the programming in S7-GRAPH language of the V7 oxidation basin.

Key words: Wastewater treatment plant STEP, Grafcet, S7-GRAPH, STEP 7 from Siemens, PLC.

Introduction:

Aujourd'hui les systèmes de production automatisés (SPA) ne cessent de croître en Complexité, suite à de large bande d'exigences du marché industriel, de concurrence interne, de qualité ainsi que de densité et de diversité des produits qu'ils traitent. Pour cela les systèmes complexes utilisés dans les industries modernes sont commandés via des Automates Programmables Industriels (API) au lieu de l'ancienne technologie basée sur la logique des relais câblés. Les automates programmables industriels (API) sont des dispositifs électroniques comprenant un processeur, des mémoires internes et externes (sous forme de carte mémoire), des interfaces d'entrées numériques pour se relier avec les capteurs numériques et des interfaces d'entrées analogiques pour les capteurs analogiques, des

Creative Commons Attribution-NonCommercial-NoDerivatives 4.0 International License (CC BY-NC-ND)

interfaces de sortie numériques et analogique pour la liaison avec les pré-actionneurs numériques et analogiques respectivement, ils contiennent aussi des blocs d'alimentation ainsi que des interfaces de communication pour créer des réseaux industriels utilisant des protocoles de communications tel que : Profibus, Profinet, AS-i, ModBus, entre autres. Cela nous amène à les considérer comme des micro-ordinateurs dédiés à l'industrie.

L'utilisation des Automates Programmables Industriels (API) est devenue une nécessité pour la gestion des systèmes et des ateliers moderne de production dans plusieurs disciplines. Beaucoup d'études et de recherches sont faites dans ce domaine. Dans le contrôle et la commande des systèmes de gestion d'électricité afin de rendre ces stations et ces centraux de distribution plus performants et plus fiables ainsi pour faire la distribution du réseaux électriques **[Picoronea A.A.M, De Oliveirab T.R, Sampaio-Neto R, Khosravy M, Ribeiro M.V**(2020)**][Ioannides M.G** (2014)**][Alphonsus E.R, Abdullah M.O** (2016)**]**. Les API sont très utilisés dans toutes les industries modernes tel que l'industrie automobile, l'industrie agroalimentaire, l'industrie pharmaceutique, l'industrie électronique entre autres **[Hu W, Starr A.G, Leung A.Y.T** (2003)**][Bührer U.T, Legat C, Vogel-Heuser B**,(2015)**]**. On voit aussi une grande utilisation des API dans les industries du pétrole et du gaz car ces dernières doivent assurer une production continue

Toutes en garantissant un niveau de sécurité très élevé ce qui oblige l'introduction de systèmes de supervision et de surveillance en temps réel qui utilise des automates programmables **[Srivastavaa A, Gupta J.P,** (2010)**][Prati T. J, Farines J. M, De Queiroz M. H,** (2015)**][Redutskiy Y**,(2016)**]**. Les automates programmables sont aussi utilisés dans la nouvelle génération d'industrie qui est l'industrie 4.0 surtout avec l'informatisation de l'industrie et l'utilisation du big data, des internet des objets et des systèmes cyber-physique [**Legat C, Vogel-Heuser B, (**2017)][**Chen J.Y, Tai K.C, Chen G.C,** (2017)][**Langmann R, Stiller M,** (2019)].

Les stations de dessalement et d'épuration de l'eau modernes utilise aussi les API comme moyen de contrôle et de commande de leurs systèmes [**Bayindir R, Cetinceviz Y,** (2011)][**Manesis S.A, Sapidisb D.J, King R.E**, (1998)][**Fantozzia M, Popescub I, Farnhamc T, Archettid F, Mogree P, Tsouchnikae E**, (2014)].

Dans cet article nous allons justement faire l'étude d'une station d'épuration d'eau, où nous allons étudier la station, puis modélisé sont fonctionnement avec GRAFCET et enfin programmé les modèles avec le langage graphique S7-GRAPH de Siemens.

Description et fonctionnement général de la station d'épuration STEP :

Dans cette section nous allons présenter le fonctionnement général de la station D'épuration STEP sous forme d'un schéma illustré dans la figure suivante (Fig. 1)

Creative Commons Attribution-NonCommercial-NoDerivatives 4.0 International License (CC BY-NC-ND)

Algerian Journal of Engineering Architecture and Urbanism Vol. 5 Nr. 3 2021
ISSN: 2588-1760

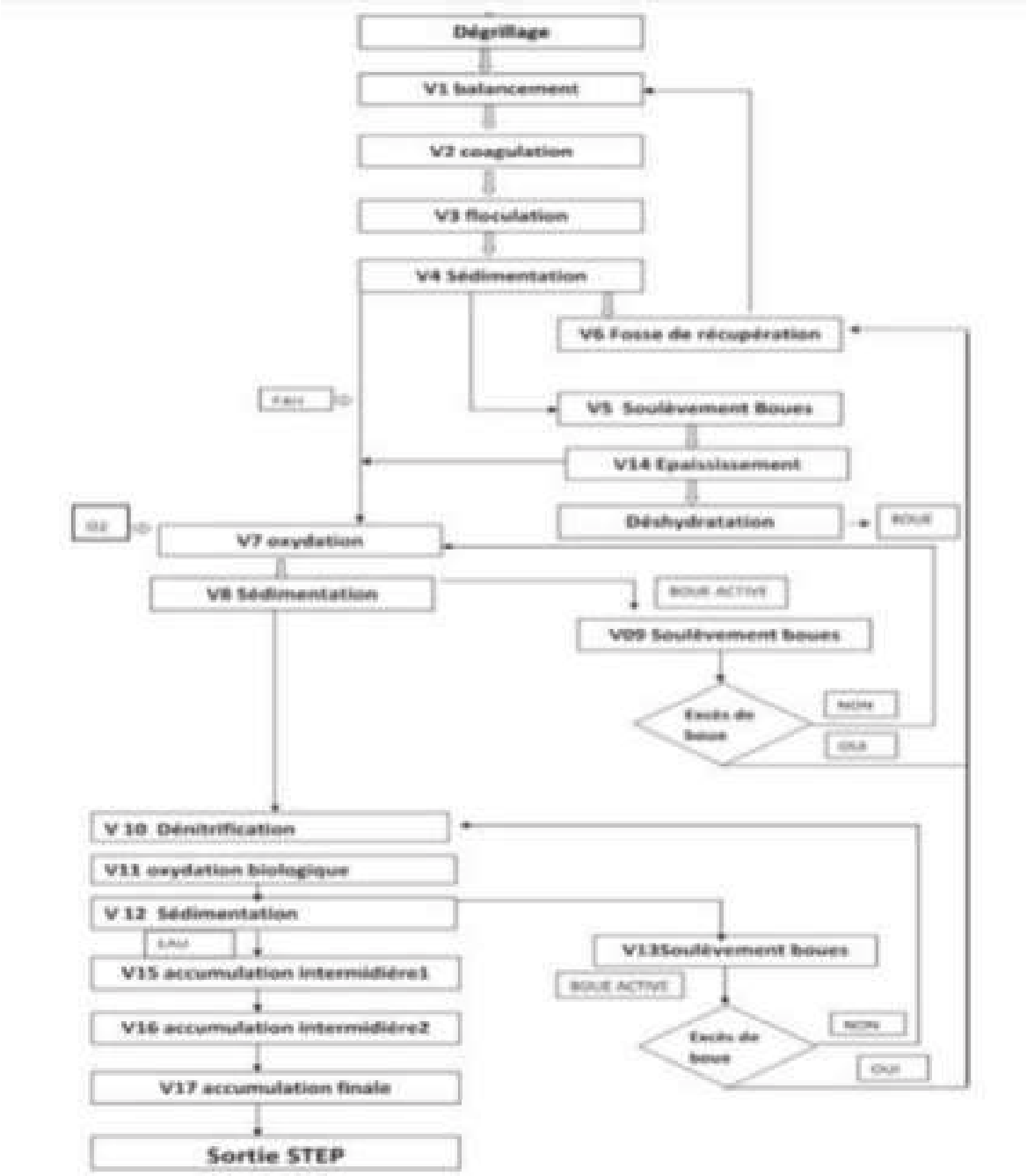

Fig1. Description et fonctionnement générale de la STEP

Dans la station d'épuration on a 16 bassins de traitement d'eau, en amont du bassin de balancement V1, un canal de grillage CG1 est réalisé qui traverse la grille GA1 pour la séparation éventuelle des corps solide grossiers présents dans les rejets ayants des dimensions caractéristiques supérieur à l'espace entre les barres de la grille. Après le dégrillage, les impuretés découlent par la gravité dans le bassin de balancement V1 où se produit l'égalisation hydraulique et l'homogénéisation des caractéristiques du rejet en utilisant deux mélangeurs submersibles MX1 et MX2 pour éviter la sédimentation sur le fond.

Creative Commons Attribution-NonCommercial-NoDerivatives 4.0 International License (CC BY-NC-ND)

Un régulateur de niveau à pression LP1 est installé pour détecter le niveau minimum. Un régulateur de niveau à flotteur LV1 donne un signal d'alarme pour le déchargement de l'excès dans le canal de dérivation V17, Un mesureur de débit MP1 et une soupape motorisée VM1 ont été installé pour stabiliser le débit en entrée au traitement chimio-physique. C'est les pompes P1 et P2 qui envoient le rejet dans le bassin V2 fonctionnent en continu et en alterné, elles ne s'arrêtent que si le niveau minimum LP1 est atteint.

La station d'épuration STEP est constituée des composantes qui suit :

- **Groupe de dosage produit anti-mousse (CH4/F3)** : Le produit anti-mousse (CH4/F3) est Dosé dans le bassin V1, le dosage sera établi pendant le démarrage de la station et devra Être modifié en fonction de la présence d'écumes.
- **Bassin de neutralisation/coagulation (V2)** :

À l'intérieur du bassin de neutralisation/coagulation V2 est installé un agitateur lent AG1 (58 rpm). L'eau en entrée est conditionnée avec le lait du chaux (CH1), dont le dosage est Effectué en automatique, sur la base de la valeur remarquée du pH-mètre PH1. Il est Fondamental donc de maintenir l'instrument fonctionnel.

- **Groupe de dosage de la chaux (CH1)** :

La chaux est préparée dans le bassin CH1 à travers l'afflux d'eau du réseau, le mélange est Exercé par deux agitateurs AG3 et AG8 qui fonctionnent en continu et s'arrêtent avec le Niveau minimum du bloc LU1, Le lait du chaux (CH1) arrive au bassin V2 en mode Continu et avec un débit constant à travers la valve à manchon EV1 normalement ouverte Commandé par PH1.

- **Bassin de floculation (V3)** :

L'eau en entrée est conditionnée avec un poly-électrolyte anionique arrivant en mode continue ce qui permet la coagulation et la floculation des flocons de boue en formation.

- **Groupe de dosage poly-électrolyte anionique (CH2) :**

Le groupe de préparation du poly-électrolyte est constitué de deux bassins de réaction fonctionnant en série. Le poly-électrolyte produite à concentration contrôlée est prélevée par les pompes P6 et P7 fonctionnant en continu et en alterné.

- **Bassin de relevage boues (V5) :**

Les pompes P8 et P9 aspirent la boue de la fosse centrale du sédimentateur et l'envoient dans le bassin V14. Les pompes fonctionnent en continuent et en alternées et s'arrêtent au niveau minimum de sécurité LV2 du bloc.

- **Fosse de récupération mousse (V6)** :

Le puisard ramasse les boues des vidanges du bassin V9 et du bassin V13 et les rejets s'écoule dans bassin V1 à travers un collecteur.

- **Bassin d'oxydation (V7)** :

L'eau dans le bassin V7 est soumise à l'oxydation à travers cent quinze (115) pentes simples chacune d'elle aliment huit (8) diffuseurs tubulaires et est réglée d'une soupape manuelle.

- **Sédimentateur V8** :

L'eau par gravité dans le sédimentateur V8 où la boue s'accumule sur le fond et les râteaux du pont roulant CP2 la trainent dans le puisard central d'évacuation.

- **Bassin de relevage des boues V9** :

Les pompes P10 et P11 aspirent la boue du puisard central du sédimentateur et l'envoient au bassin V7.

Creative Commons Attribution-NonCommercial-NoDerivatives 4.0 International License (CC BY-NC-ND)

• **Bassin de dénitrifications (V10)** :
L'eau arrive par gravité du sédimentateur V8 rentre dans le bassin V10 où la présence de bactéries dénitrifiant, l'absence d'air et l'agitation exercée des deux mélangeurs submersibles MX4 et MX5 permettent l'éloignement sous forme gazeuse de l'azote présent dans les nitrates et les nitrites.
• **Bassin d'oxydation de deuxième phase (V11)** :
L'eau en bassin V11 est soumise à une oxydation à travers soixante-neuf (69) pentes simples chacune d'elle alimente huit (8) diffuseurs tubulaires.
• **Sédimentateur dynamique (V12)** :
L'eau arrive par gravité dans le sédimentateur V12 où la boue s'accumule sur le fond et les râteaux du pont roulant CP3 l'envoient dans le puisard central d'évacuation. L'eau clarifiée s'écoule au bassin V15 à travers un collecteur en AISI 304 DN 200. Le collecteur est installé avec une pente 0,3% pour éviter la stagnation du rejet sur le fond et maintenir le nettoyage de la section d'écoulement.
• **Bassin de relevage des boues (V13)** :
Les pompes P14 et P15 aspirent la boue du puisard central du sédimentateur et ils l'envoient au bassin V10 et V11, la portée est partielle grâce à deux soupapes manuelles z245 et z246.
• **Bassin d'accumulation intermédiaire (V15)** :
Le bassin alimente le filtre FQ1. Les pompes de relevage P21 et P22 fonctionnent en mode alternée, ils se mettent en fonction lorsque le niveau du bassin arrive à LV8 et ils s'arrêtent à LV9.
• **Filtration sur quartz (FQ1)** :
L'eau entre à travers la soupape EV5 et après avoir été filtrée par la couche de grenaille sort à travers la soupape EV6 et est cumulée en bassin V16.
• **Bassin d'accumulation final (V16)** :
Le bassin alimente le contre-lavage du filtre FQ1 et le lavage de la presse a ruban NP1. Les pompes de relevage P25 et P26, comme les pompes P23 et P24, fonctionnent en alternanceet s'arrêtent à LV12.
• **Epaississement (V14)** :
La boue provenant du bassin V5 au moyen des pompes P8 et P9 sont épaissies et cumulées sur le fond, où des râteaux du pont roulant CP4 l'envoient dans le puisard central pour l'évacuation.
• **Déshydratation (NP1)** :
La boue conditionnée entre dans le blutoir B1 où il subit un mélange plus intense et une première déshydratation partielle, ensuite elle arrive sur les rubans de la NP1 qui en exerçant une pression, réduisent le pourcentage d'eau présent. La boue déshydratée est stockée dans des caissons pour l'évacuation.

Bassin d'oxydation (V7) :

Fonctionnement du bassin d'oxydation (V7) :

Le fonctionnement du bassin d'oxydation (V7) est présenté dans ce qui suit :

• L'eau en bassin V7 est soumise à l'oxydation à travers cent quinze (115) pentes simples chacune d'elle alimente huit (8) diffuseurs tubulaires et est réglée d'une soupape manuelle.
• Le mélangeur MX3 favorise le flux de l'eau à l'intérieur du bassin
• Les blocs de niveau minimum ne sont pas prévus.
• OD1 un mesureur d'oxygène dissous.
• La concentration de l'oxygène dissous en bassin devra être d'environ 2 mg/l
• Il sera établi un seuil à PLC qui règle le fonctionnement des soufflantes SF3, SF4 et SF5

Creative Commons Attribution-NonCommercial-NoDerivatives 4.0 International License (CC BY-NC-ND)

• Par sécurité, il est prévu une éventuelle activation manuelle de la soufflante SF6 avec réglage manuel du débit.
• Un point d'eau du réseau de service z168 (Nettoyage sonde d'oxygène).
• Il est prévu quatre lignes en entrée du bassin :
▪ Entrée de l'eau de séparation de la boue épaissie en V14.
▪ Entrée de l'eau de séparation de la boue pressée en NP1.
▪ Entrée de la boue de circulation du bassin V9.
▪ Entrée du dosage de la chaux au moyen d'une ligne indépendante à réglage manuelle z294 (Le dosage doit être effectué dans le cas où le pH dans le bassin d'oxydation descend en dessous de 8 ou 9 unités pH).
• La concentration de la boue présente dans le mélange aéré devra être d'environ 4 gr/l, la mesure des boues en bassin sera effectuée à travers un cône.

Tableau des variables (entrées / sorties) avec descriptions (tables des mnémoniques) :

Dans cette section nous présentons sous forme de tableau l'ensemble des variables d'entrées et de sorties, avec la description de chaque variable ainsi que l'adresse de chaque variable dans le programme de l'automate programmable industriel.

Variable	opérande	Description
Ssf4	E 127.1	Section de SF4 ouvert Capteur
Mixer MX3 en marche	E 23.2	Capteur détecte MX3 en marche Capteur
Ssf3	E 127.0	Section de SF3 ouvert capteur
Mesure PH1 , OD1,OD2 active	E 124.6	Ligne de mesure PH(ph mètre),ligne de mesure d'oxygène sonde à immersion électrode Capteur
Senseur thermique MX3	E 11.6	Capteur permet de démarrer MX3
Ssf5	E 127.2	Section de SF5 OUVERT CAPTEUR
Extracteur VN1 en marche	E 30.2	Capteur détecte VN1 ventilateurs1 en marche Capteur
Extracteur VN2 en marche	E 30.4	Capteur détecte VN2 ventilateurs1 en marche Capteur
Déclenchement de protection VN1	E 30.5	Pas de déclenchement de protection VN1 pour démarrer VN1 Capteur
Déclenchement de la protection MX3	E 23.3	Pas de Déclenchement de la protection MX3pour démarrer mx3 capteur
Mx3.ox1	A 36.6	Mélangeur 3 actionneur
Estrac VN1	A 39.4	Ventilateur 1 actionneur
Estrac VN2	A 39.5	Ventilateur 2 actionneur
MX3.OX1	A 36.6	Mélangeur 3 actionneur

Creative Commons Attribution-NonCommercial-NoDerivatives 4.0 International License (CC BY-NC-ND)

SF3	A 33.7	Soufflante 3 actionneur
SF4	A 34.7	Soufflante 4 actionneur
SF5	A 20.0	Soufflante 5 actionneur
SF6	A20.1	Soufflante 6 actionneur
DV8	A 43.3	Déchargement ou vidange en V8

Table 1. Table des mnémoniques du bassin V7

Grafcet du bassin S7 et des soufflantes :

Cette partie sera consacrée à la présentation des GRAFCET qui décrivent le fonctionnement du bassin V7 (Fig. 2), puis (Fig. 3) nous présentons le GRAFCET des soufflantes et on termine par la présentation du GRAFCET de fonctionnement de chaque soufflante qui est représenté (Fig. 4)

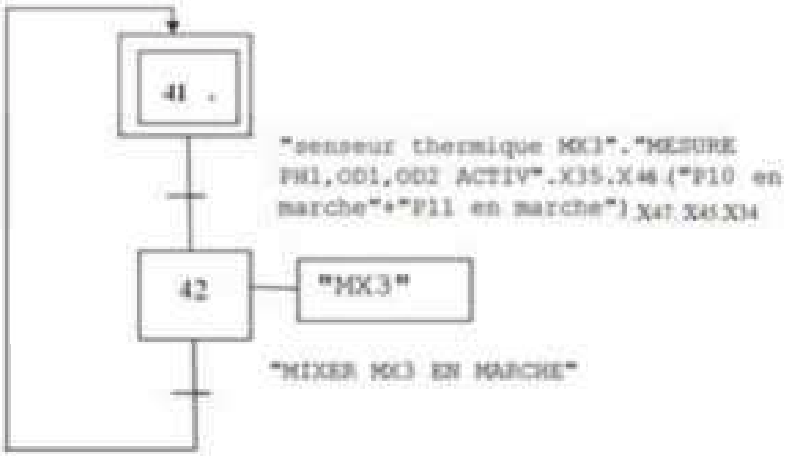

Fig2. Grafcet du bassin V7.

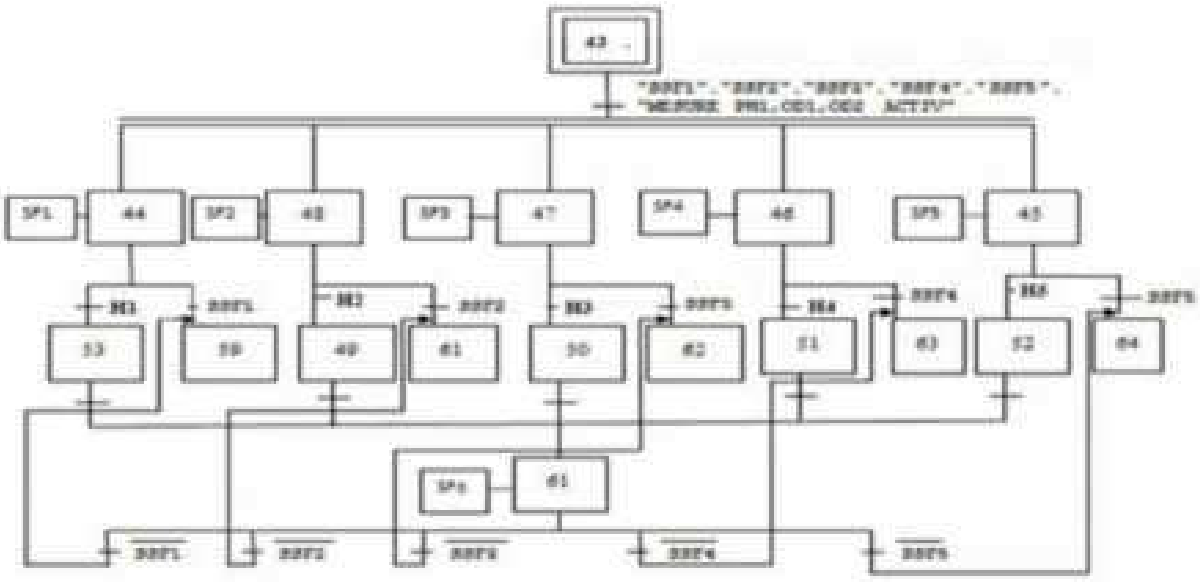

Fig3. Grafcet des soufflantes.

Creative Commons Attribution-NonCommercial-NoDerivatives 4.0 International License (CC BY-NC-ND)

H1 : $\overline{ssf1}$.ssf2 .ssf3 .ssf4 .ssf5
H2 : ssf1.$\overline{ssf2}$.ssf3.ssf4.ssf5
H3 : ssf1. ssf2. $\overline{ssf3}$ .ssf4. ssf5
H4 : ssf1. ssf2. ssf3. $\overline{ssf4}$. ssf5
H5 : ssf1. ssf2. ssf3. ssf4.$\overline{ssf5}$

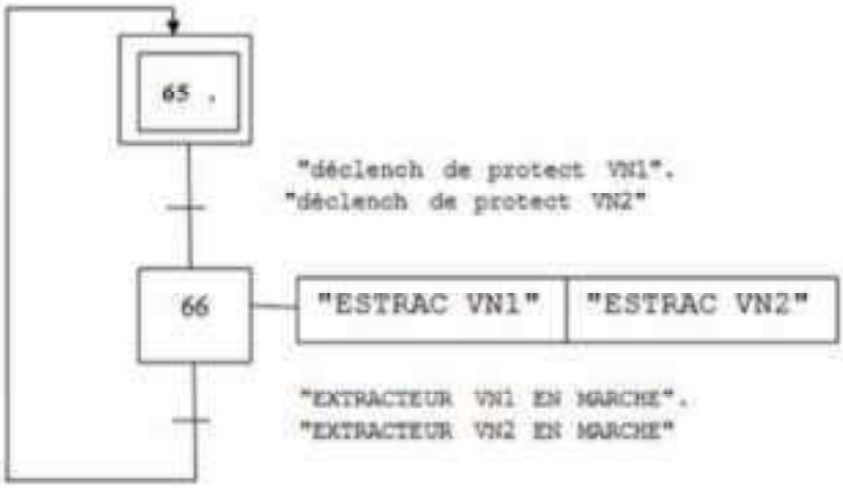

Fig4. Grafcet de fonctionnement de chaque soufflante.

Programme S7-GRAPH du bassin et des soufflantes :

Dans la partie qui suit nous allons présenter les programmes S7-GRAPH que nous avons écrit sur SIMATIC Manager STEP 7, le premier programme représente le fonctionnement du bassin V7 (Fig5), le second programme illustré sur (Fig6) décrit le fonctionnement des soufflantes et la dernière illustration (Fig7) représente le programme S7-GRAPH de chaque soufflante.

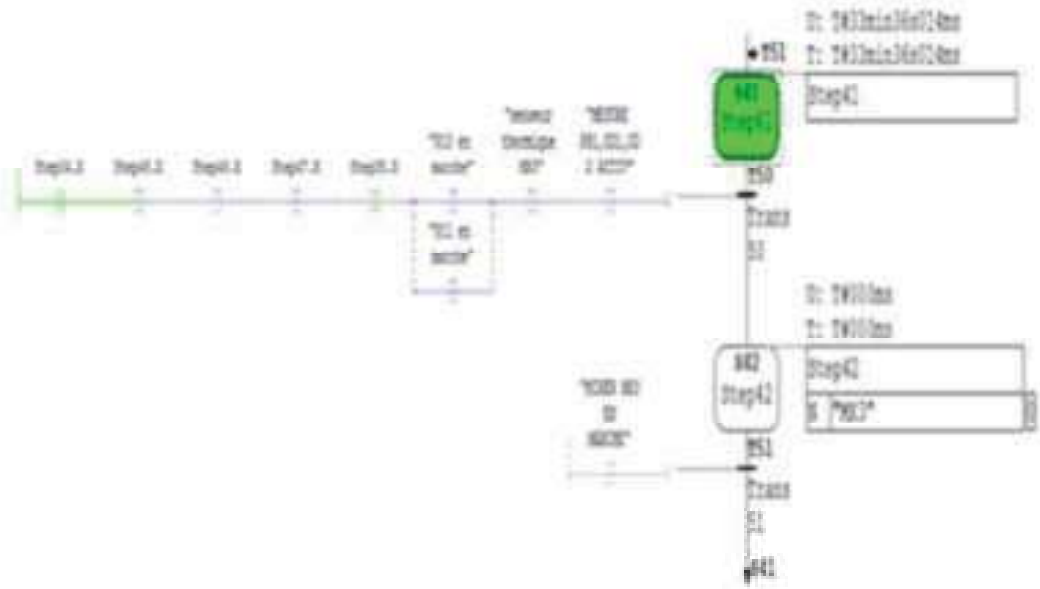

Fig5. Programme S7-GRAPH du bassin V7.

Creative Commons Attribution-NonCommercial-NoDerivatives 4.0 International License (CC BY-NC-ND)

Algerian Journal of Engineering Architecture and Urbanism Vol. 5 Nr. 3 2021
ISSN: 2588-1760

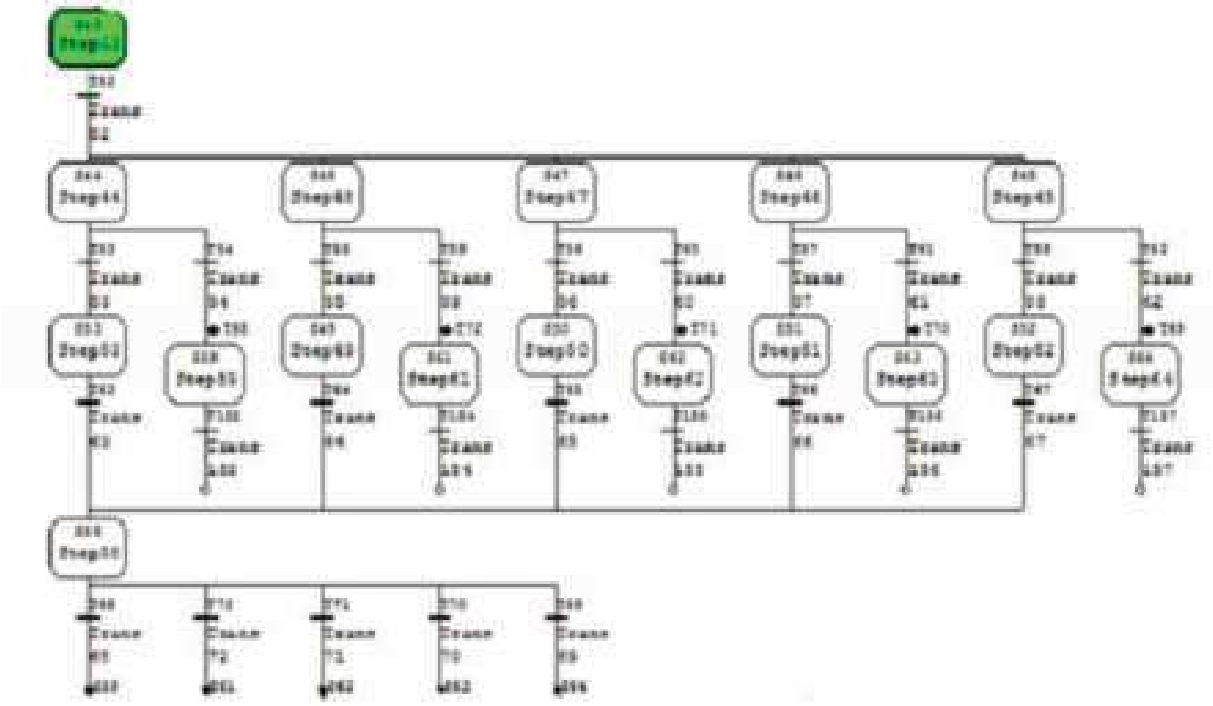

Fig6. Programme S7-GRAPH des soufflantes.

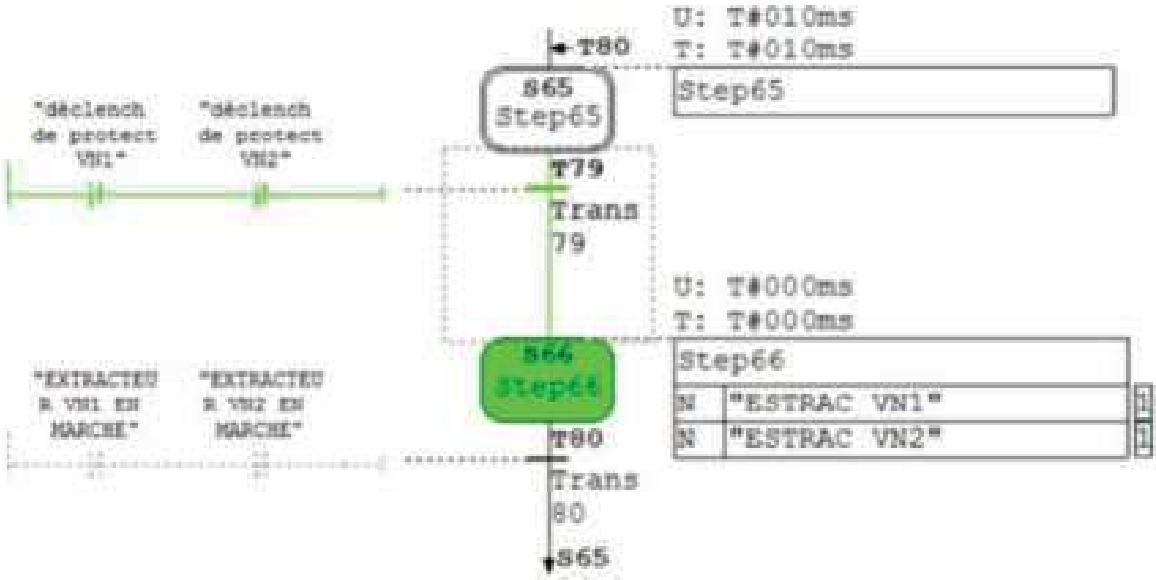

Fig7. Programme S7-GRAPH de fonctionnement de chaque soufflante.

Conclusion:

Tous les programmes développés ont été programmés puis simulés sur STEP7 SIMATIC MANAGER et ont fonctionné avec succès et sans erreurs.

Creative Commons Attribution-NonCommercial-NoDerivatives 4.0 International License (CC BY-NC-ND)

Dans ce travail nous nous sommes intéressés à l'étude, la programmation et la simulation du système automatisé de la station d'épuration STEP de la maïserie TAFNA de Maghnia. Tous d'abord nous avons donné l'architecture générale de la station d'épuration STEP, puis on a expliqué brièvement le rôle de chaque composante de cette station. On suite, et cause du nombre très importants des bassins et des composantes de la station STEP, nous n'avons présenté que le fonctionnement, la modélisation et la programmation du bassin d'oxydation V7.

Dans cette partie on a commencé par présenter le fonctionnement du bassin d'oxydation V7, puis on a abordé la partie modélisation GRAFCET où nous avons présenté trois modèles, un modèle pour le fonctionnement du bassin V7, un deuxième modèle pour le fonctionnement de toutes les soufflantes et un troisième modèle qui représente le fonctionnement de chaque soufflante. La dernière partie de cette section a été consacrée à la présentation des programmes en langage graphique S7-GRAPH des trois modèles Grafcet présenté précédemment. Cette étude nous a permis d'analyser de modéliser et de programmer le fonctionnement des différentes composantes de la station d'épuration STEP, ces programmes ont été tous simulés avec le logiciel SIMATIC Manager Step 7 et ont donné un fonctionnement correct du système.

References:

Alphonsus E.R, Abdullah M.O. (2016), "A review on the applications of programmable logic controllers (PLCs)", Renewable and Sustainable Energy Reviews 60 (2016) 1185–1205.

Bayindir R, Cetinceviz Y. (2011), "A water pumping control system with a programmable logic controller (PLC) and industrial wireless modules for industrial plants—An experimental setup", ISA Transactions 50- 321–328.

Bührer U.T, Legat C, Vogel-Heuser B. (2015), "Changeability of Manufacturing Automation Systems using an Orchestration Engine for Programmable Logic Controllers", IFAC-Papers On Line 48-3 (2015) 1573–1579.

Chen J.Y, Tai K.C, Chen G.C. (2017), "Application of Programmable Logic Controller to Build-up an Intelligent Industry 4.0 Platform", Procedia CIRP 63 150 – 155.

Fantozzia M, Popescub I, Farnhamc T, Archettid F, Mogree P, Tsouchnikae E. (2014), "ICT for Efficient Water Resources Management: The ICeWater Energy Management and Control Approach", Procedia Engineering 70 633 – 640.

Hu W, Starr A.G, Leung A.Y.T. (2003), "Operational fault diagnosis of manufacturing systems", Journal of Materials Processing Technology 133 (2003) 108-117.

Ioannides M.G. (2014), VOL. 19, NO. 3, September 2004. "Design and Implementation of PLC BasedMonitoring Control System for Induction Motor", IEEE transactions on energy conversion**.**

Langmann R, Stiller M. (2019), **"**The PLC as a Smart Service in Industry 4.0 Production Systems", Appl. Sci. 2019, 9, 3815; doi:10.3390/app9183815**.**

Legat C, Vogel-Heuser B. (2017), "A configurable partial-order planning approach for field level operation strategies of PLC-based industry 4.0 automated manufacturing systems", Engineering Applications of Artificial Intelligence 66 128–144.

Manesis S.A, Sapidisb D.J, King R.E. (1998), "Intelligent control of wastewater treatment plants", Artificial Intelligence in Engineering 12- 275-281**.**

Picoronea A.A.M, De Oliveirab T.R, Sampaio-Neto R, Khosravy M, Ribeiro M.V. (2020), "Channel characterization of low voltage electric power distribution networks for PLC applications based on measurement campaign", Electrical Power and Energy Systems 116 (2020) 105554.

Prati T. J, Farines J. M, De Queiroz M. H. (2015), "Automatic test of safety specifications for PLC programs in the Oil and Gas Industry", IFAC-Papers On Line 48-6 (2015) 027–032.

Redutskiy Y. (2016), Number 1, March 2017 "Optimization of safety instrumented system design and maintenance frequency for oil and gas industry processes", Volume 8, , pp. 46–59**.**

Srivastavaa A, Gupta J.P. (2010), "New methodologies for security risk assessment of oil and gas industry", Process Safety and Environmental Protection 88 (2010) 407–412.

Creative Commons Attribution-NonCommercial-NoDerivatives 4.0 International License (CC BY-NC-ND)

Algerian Journal of Engineering Architecture and Urbanism Vol. 5 Nr. 3 2021
ISSN: 2588-1760

STUDY AND SUPERVISION OF A MPS SYSTEM VIA WINCC FLEXIBLE SOFTWARE

Nour el houda Herarsi
First author, PhD student, Manufacturing Engineering Laboratory of Tlemcen (MELT), Electrical and Electronics Department, Faculty of Technology
Abou-Bekr Belkaid University, Tlemcen, Algeria,
nourelhouda.herarsi@univ-tlemcen.dz
Ahmed Hassam
Second author, scientific title (PhD), Manufacturing Engineering Laboratory of Tlemcen (MELT), Electrical and Electronics Department, Faculty of Technology
Abou-Bekr Belkaid University, Tlemcen, Algeria,
Ahmed.hassam@univ-tlemcen.dz
Mohammed el amin Mkedder
Third author, scientific title (Senior Research Engineer), Manufacturing Engineering Laboratory of Tlemcen (MELT), Electrical and Electronics Department, Faculty of Technology
Abou-Bekr Belkaid University, Tlemcen, Algeria,
Mohammedelamin.mkedder@univ-tlemcen.dz

Abstract:
Supervisory systems are very important for industrial control and safety, in this article we will present an approach for the design of supervisory systems applied to industrial processes via HMI, using the WinCC Flexible tool. We will expose a complete method to build a HMI of supervision of the MPS system through WinCC Flexible software, starting from the study, the modifications of the set of programs that are in each sub-station and then the simulation in then the simulation using the two simulators PLCsim of STEP 7 for the programming part and Runtime of WinCC Flexible for the supervision part.

Key words: FESTO MPS 500, PLCsim, Runtime, SCADA, WinCC Flexible, STEP 7.

Introduction:

La sécurité industrielle est une partie très importante de l'automatisation des systèmes et inséparable de la partie commande des systèmes industriels, car on ne peut pas envisager une implémentation des équipements industriels sans aucune preuve qui assure la sécurité. Par conséquent, l'absence ou la négligence de la sécurité dans les systèmes modernes peut provoquer des dégâts matériels et humains. Pour cela la sécurité industriel garantis la continuation et la stabilité de la production, comme elle assure la survie des installations Industriels. Aujourd'hui, un autre défi est relevé, il s'agit de l'automatisation de la supervision des processus en utilisant des systèmes intelligents sous formes d'IHM qui offrent à l'industrie d'intervenir sur les systèmes automatisés à distance. Ces derniers Fournissent à l'utilisateur une aide dans la gestion de ses tâches d'alarmes urgentes dans le but d'augmenter la fiabilité et la sûreté de fonctionnement des différents processus industriels.

Creative Commons Attribution-NonCommercial-NoDerivatives 4.0 International License (CC BY-NC-ND)

L'état de l'art:

Aujourd'hui, l'intervention sur les systèmes de production devient de plus en plus complexe. WinCC en général et avec ses options est considéré comme un moyen de supervision très puissant qui permet de concevoir plus facilement plusieurs types d'éléments de systèmes, tels que les capteurs et les actionneurs, il est très efficace pour concevoir des interfaces IHM contenant un système de contrôle, de commande et de supervision plus proches de l'utilisateur et très loin des systèmes de production. Ces interfaces sont implémentées par via des moyens de communication adéquat afin de gérer le fonctionnement du système en temps réel.

D'autre part Step7 est un outil très performant pour la programmation des automates ainsi que pour la simulation des systèmes de production

Dans le but d'enrichir notre travail qui est la réalisation d'une IHM pour le système MPS de type FMS on est articulée sur plusieurs travaux de chercheur dans le domaine de la supervision qui sont utilisés dans le monde entier pour diverses applications, allant de l'industrie des traitements des eaux ABC PEPSI "à ROUIBA", un travail réalisé par le chercheur [Guendoul, A., & Abdi, R. (2017)] sur l'automate programmable de Siemens S7-300 qui a développé une automatisation complète d'une station de traitement des eaux et a réalisé une plateforme IHM pour la supervision de cette station via le logiciel de supervision WinCC Professionnel de TIA PORTAL V13, dans le but de faciliter la tâche de contrôle et de commande de la station pour l'opérateur[1]. Aussi dans l'industrie de fabrication de margarine un travail a été réalisé par les chercheurs [Cherchour, H., Chahboune, M. L., &Mendil, B. (2015)] qui appliquent une méthodologie générale sur l'automatisation et la supervision d'un système industriel, où ils ont fait une étude détaillée sur la chaine de pilotage pour la fabrication de la margarine. Dans ce travail les chercheurs ont élaboré un programme API via le logiciel STEP7 qu'il l'ont injecté au niveau de l'automate S7-300 afin d'automatisé le fonctionnement de la station. D'autre part une interface homme-machine a été créée sur le logiciel WinCC flexible. L'intégration de ces deux logiciels Step7 et Wincc Flexible a permis entre autres, la récupération et l'affichage en ligne des variables qui caractérise le processus. Dans le travail de [Aberkane,A. (2012)] dans l'entreprise de fritte, le chercheur a utilisé le logiciel STEP7 en repérant les variables les plus pertinentes pour qu'ils puissent aboutir à la création d'une plateforme de supervision SCADA au sein de l'entreprise Engobes et Emauxde Khemis Khechna. Ce travail a permis au chercheur de Réaliser à l'aide d'intégration des deux logiciels Step7 et WIN CC une plateforme de supervision SCADA qui prend en charge tous les ateliers grâce à un réseau local PROFIBUS DP configuré en "maitre – esclave intelligent ", cette plate-forme prend en charge la gestion des alarmes afin de détecter un éventuel comportement anormal des installations, et faciliter ainsi la mission de surveillance et de supervision [Aberkane,A. (2012)]. Le secteur des hydrocarbures est aussi un des secteurs touchés par l'automatisation où on est obligé a utilisé les technologies tel que les automates programmables et bien sûr l'acquisition et la supervision des données. Comme exemple on peut citer le travail de Attou, M. et Al qui se résume dans la mise en œuvre de l'automatisation et la supervision du système de stockage du dépôt de carburant de la société METALENG, via un API S7-300 de Siemens et l'utilisation du logiciel TIA-Portal V13, afin de réaliser la simulation puis le contrôle et la supervision du système [Attou, M., & Mahdi, I. (2017)]. Dans le même domaine on peut parler aussi de l'article présenté par [YAN, W. J., & MAO, X. Z. (2005)] sur un système de surveillance et de contrôle automatique à distance de barrage en caoutchouc d'une petite centrale Hydroélectrique, basé sur l'automate série S7-200 et une IHM développée par l'outil WinCC.

Creative Commons Attribution-NonCommercial-NoDerivatives 4.0 International License (CC BY-NC-ND)

Description du système MPS500:

Le système MPS FMS 500 (Modular Production System flexible manufacturing system) est un SPA (système de production automatisé) et le chiffre 500 signifie la disposition des stations à l'alentour du convoyeur. Ce système est installé actuellement au sein du laboratoire de recherche en productique MELT de l'université de Tlemcen. C'est le système sur le quel on va entamer notre étude de supervision

Fig1. Configuration MPS 500 3D.

En configuration maximale, la pièce à usiner est transmise, isolée, de la station de distribution à la station de contrôle (entrée des marchandises). La station de contrôle vérifie les caractéristiques des pièces à usiner, exclut les mauvaises pièces le cas échéant et transmet les bonnes pièces à la station du système de transport. L'entrée des marchandises s'effectue ainsi à partir de la station de distribution au système. Si aucune station de distribution n'est présente dans le système, la pièce à usiner peut-être déposée à un endroit quelconque sur un porte-pièces. Il convient de s'assurer qu'aucun porte-pièces ne soit retiré du système.

La station d'usinage est alimentée à l'aide d'une station de manipulation. La pièce à usiner est usinée puis contrôlée. La station de manipulation retourne la pièce à usiner au système de transport.

A la station d'assurance qualité, la pièce à usiner est contrôlée par rapport à la tolérance dimensionnelle. La station de robotique monte un vérin modèle à partir du corps de base. La station de stockage peut stocker des pièces à usiner et les remettre au système en cas de besoin.

A la station de tri/regroupement (sortie des marchandises), les pièces à usiner peuvent être retirées du système. A l'aide de la station de manipulation, les pièces à usiner sont transférées de la station du système de transport à la station de tri pour y être triées par couleur et sont ensuite prêtes pour la sortie des marchandises. La station de regroupement en trie pas les pièces à usiner par couleur, mais prélève une certaine quantité, à savoir 18 pièces. Les trois glissières supérieures sont réservées aux pièces à usiner, la quatrième glissière sert au dépôt des pièces pendant le processus de mise en référence.

Creative Commons Attribution-NonCommercial-NoDerivatives 4.0 International License (CC BY-NC-ND)

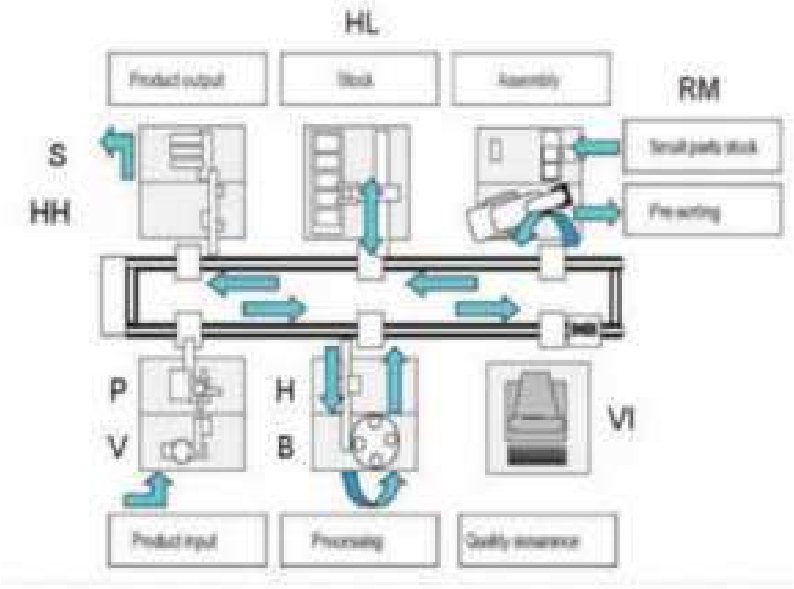

Fig2. Configuration MPS 500.

- H station de manipulation.
- B : Station d'usinage.
- VI : Station de visualisation.
- RM : station d'assemblage robotisé.
- HL : station du magasin central automatisé.
- HH : station de manipulation.
- S : station de tri.

Ce système est composé de Six (6) Stations plus un convoyeur principal qui peut gérer la Circulation du flux de production entre ces stations à l'aide des palettes bien orienté. Les Station sont les suivants :

- Station de Distribution.
- Station de Production.
- Station de Qualité (La Caméra).
- Station d'assemblage.
- Station de Stockage et déstockage.
- Station de Trie ou Bien de Livraison.

Le système est contrôlé par des automates programmable Industriel de Type Siemens commandé par Logiciel Step7 et un Cerveau Industriel (Régulateur Industriel) dédie au reboot Mitsubishi dans la station d'assemblage.

On peut trouver dans ce système des Capteurs qui font le transfert de l'information. Parmi les capteurs

Implémentés c'est les capteurs Optique dans les trois type (à barrage, à réflex, à proximité), les Capteurs Inductifs à Proximité, les capteurs Capacitifs à proximité, les capteurs fins de course (ex : Capteur électromagnétique, électromécanique), un capteur de qualité (la caméra). Comme on peut trouver des actionneur (ex : Moteurs), des effectuer qui ont relation directe avec le produit (ex : la Table dial de la station de production), des pré actionneurs pneumatique et électrique, des pupitres de commande.

Creative Commons Attribution-NonCommercial-NoDerivatives 4.0 International License (CC BY-NC-ND)

Les moyens de communication entre les différentes stations et les automates se font par des câbles profibus, des Câbles syslink, des câbles ASI (actuator sensor interface), CAN-Open (Contrôler area network).

- La conception de l'interface de supervision sera aboutie après l'acquisition des données concernant le système à partir du logiciel CIROS Automation suite(Advanced Mechatronic) du constructeur FESTO, puis on va faire une étude des différentes stations et sous stations de MPS 500 (Dans ce travail six sous stations) afin de réaliser l'IHM du système de production MPS via le logiciel Wincc flexible qui est la suite de supervision du logiciel de programmation des automates STEP 7 tous les deux de Siemens. L'essai de cette réalisation de l'IHM se fait en mode simulation sur le simulateur PLCsim de STEP7 pour chaque sous station puis se refait sur le système MPS en temps réel. ce travail va donner un saut et un aide pour toute personne qui veut entamer des recherches dans ce matériel.
  - Les sous stations à étudier sont :
    - La sous station du Magasin + le Module de transfère.
    - La sous station de contrôle.
    - La sous station de Production (Usinage).
    - La sous station de Manipulation partie Production.
- La partie Simulation avec le simulateur PLC Sim de STEP7 en premier temps, puis on va faire une exécution du système MPS 500 via le Runtime du Logiciel WinCC Flexible SP2 à partir de l'interface IHM réalisé. Dans nos interfaces on a utilisé des cercles, des rectangles et des carrés pour représenter les différentes capteurs et actionneurs qu'on a dans les Stations traités.

- La représentation des cercles avec une couleur Jaune dans la bordure plus un texte explicatif en jaune signifier que : le Capteur est alimenté mais à l'état 0. (Ne détecte rien)
- La représentation des cercles avec une couleur Verte dans la surface plus un texte explicatif en jaune signifier que : le Capteur est alimenté mais à l'état 1. (Avec détection).
- La représentation des cercles avec une couleur Verte dans la bordure plus un texte explicatif en Bleu signifie que : l'actionneur à l'état 0 (en arrêt).
- La représentation des cercles avec une couleur Verte dans la surface plus un texte explicatif en Bleu signifie que : l'actionneur à l'état 1 (en marche).
-Les carrés ou des rectangles représentent des capteurs à l'état 0 quand la surface est transparente. Et à l'état 1 quand la surface est colorée en rouge ou bien Orange.
-Le choix des rectangles ou des carrés ou cercles c'était à cause de la non-disponibilité de tous les capteurs et les actionneurs dans la bibliothèque de notre logiciel WinCC Flexible SP2.

Objectif de travail:

Dans ce Travail on s'intéresse à la supervision de trois stations, sachant que chaque station contient deux sous stations et nos interfaces de supervision se font dans chaque sous station indépendamment à l'autre c'est-à-dire chaque sous station a une interface IHM séparément à la deuxième sous station.

La conception de l'interface de supervision sera aboutie après l'acquisition des données concernant le système à partir du logiciel CIROS Automation suite(Advanced Mechatronic) du constructeur FESTO, puis on va faire une étude des différentes stations et sous stations de MPS 500 (Dans ce travail six sous stations) afin de réaliser l'IHM du système de production

Creative Commons Attribution-NonCommercial-NoDerivatives 4.0 International License (CC BY-NC-ND)

MPS via le logiciel Wincc flexible qui est la suite de supervision du logiciel de programmation des automates STEP 7 tous les deux de Siemens. L'essai de cette réalisation de l'IHM se fait en mode simulation sur le simulateur PLCsim de STEP7 pour chaque sous station puis se refait sur le système MPS en temps réel. ce travail va donner un saut et un aide pour toute personne qui veut entamer des recherches dans ce matériel.

Les sous stations à étudier sont :

- La sous station du Magasin + le Module de transfère.
- La sous station de contrôle.
- La sous station de Production (Usinage).
- La sous station de Manipulation partie Production.

La partie Simulation avec le simulateur PLC Sim de STEP7 en premier temps, puis on va faire une exécution du système MPS 500 via le Runtime du Logiciel WinCC Flexible SP2 à partir de l'interface IHM réalisé.

Dans nos interfaces on a utilisé des cercles, des rectangles et des carrés pour représenter les différentes capteurs et actionneurs qu'on a dans les Stations traités.

- La représentation des cercle avec une couleur Jaune dans la bordure plus un texte explicatif en jaune signifier que : le Capteur est alimenté mais à l'état 0.(ne détecte rien)
- La représentation des cercles avec une couleur Verte dans la surface plus un texte explicatif en jaune signifier que : le Capteur est alimenté mais à l'état 1. (avec détection).
- La représentation des cercles avec une couleur Verte dans la bordure plus un texte explicatif en Bleu signifie que : l'actionneur à l'état 0 (en arrêt).
- La représentation des cercles avec une couleur Verte dans la surface plus un texte explicatif en Bleu signifie que : l'actionneur à l'état 1 (en marche).

-Les carrés ou des rectangles représentent des capteurs à l'état 0 quand la surface est transparente. Et à l'état 1 quand la surface est colorée en rouge ou bien Orange.

-Le choix des rectangles ou des carrés ou cercles c'était à cause de la non disponibilité de tous les capteurs et les actionneurs dans la bibliothèque de notre logiciel WinCC Flexible SP2.

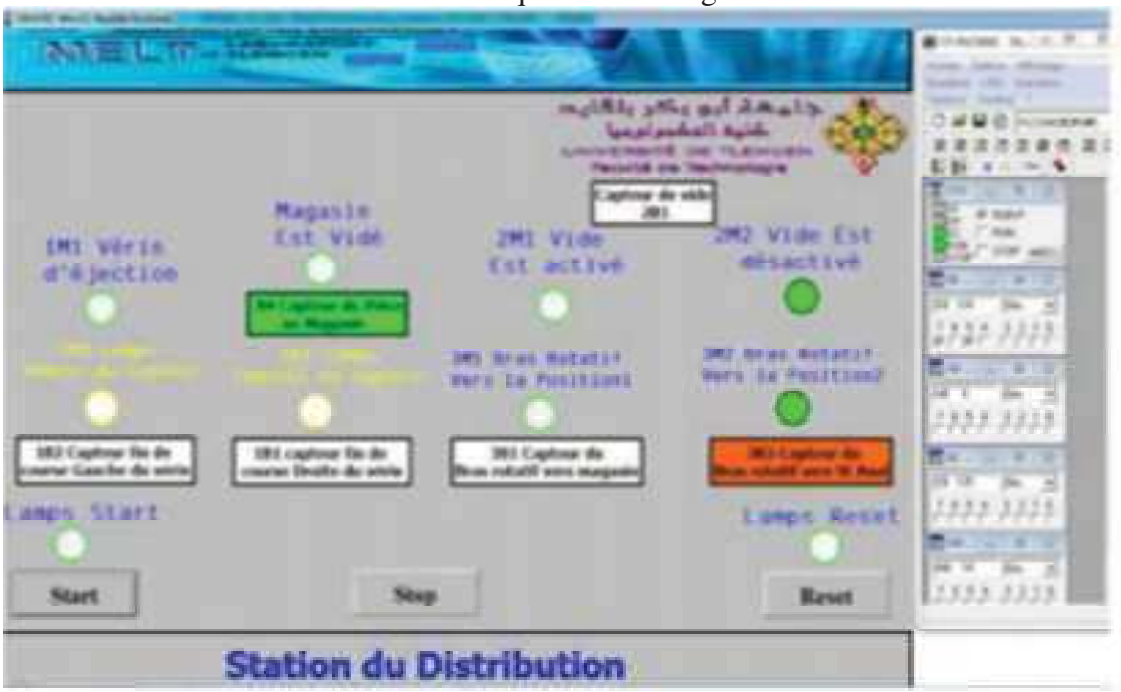

Fig1. Station distribution en exécution sous simulation.

Creative Commons Attribution-NonCommercial-NoDerivatives 4.0 International License (CC BY-NC-ND)

Cette figure représente une IHM de la station distribution en mode simulateur Runtime de WinCC Flexible sans pris en considération le Simulateur PLC Sim de STEP 7. On remarque très bien que tous les capteurs et actionneurs sont alimenté et leurs états de bit est à 0 mise à part le capteur du Magasin B4 qui est aussi alimenté est au niveau de bit 1.

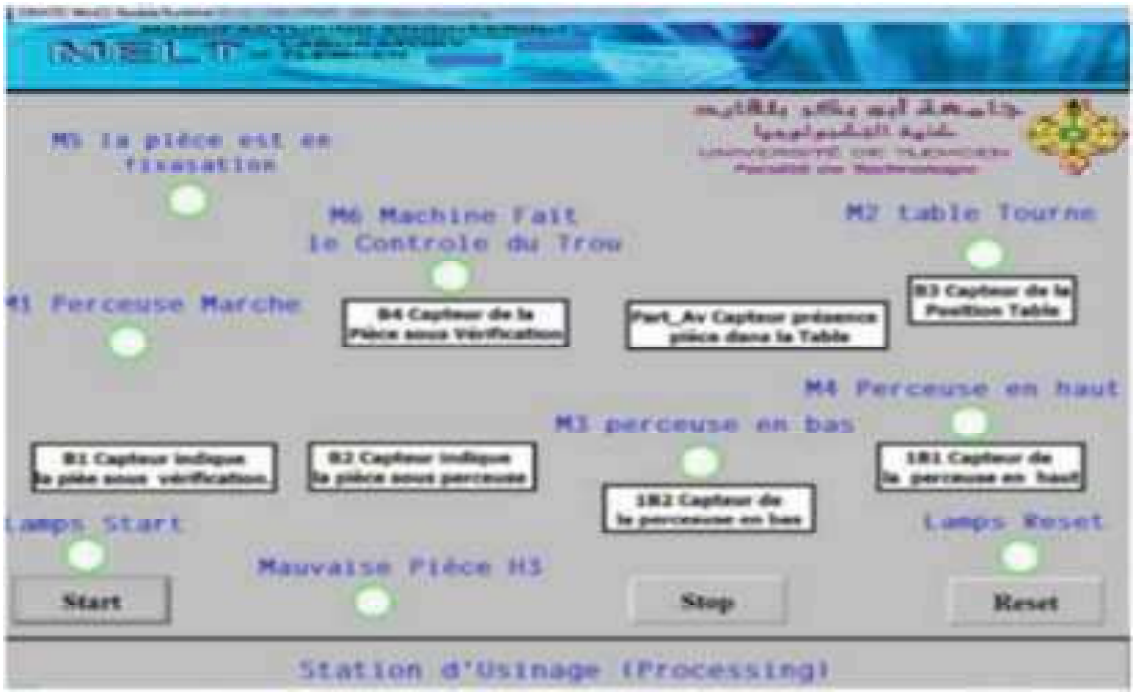

Fig4. La Station d'usinage en Mode Runtime

La figure 4 représente une IHM de la station d'usinage en mode simulateur Runtime de WinCC Flexible sans pris en considération le Simulateur PLC Sim de Step7. On remarque très bien que tous les capteurs et actionneurs sont alimenté et leurs états de bit est à 0.

Creative Commons Attribution-NonCommercial-NoDerivatives 4.0 International License (CC BY-NC-ND)

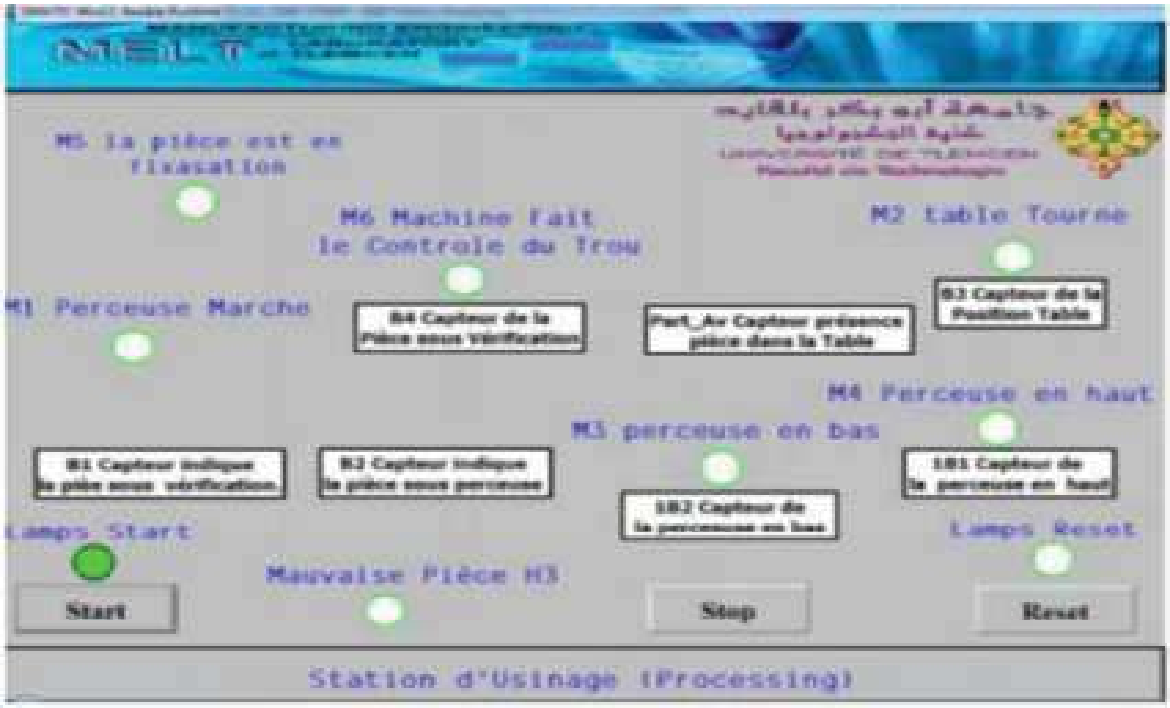

Fig5. La Station d'usinage en attente de Start.

La figure 5 représente une IHM de la station d'usinage en mode simulateur Runtime de WinCC Flexible et mode Simulateur PLC Sim de Step7. On remarque très bien après l'activation du simulateur PLC Sim (PLC Sim en mode Run) et l'initialisation de la station à partir de l'interface on a obtenu au niveau de notre interface l'allumage du lampe Start qui nous informe elle-même que le Bouton Start est prêt à l'appuyer afin de lancer la station.

Conclusion:

Dans cet article nous avons exposé une méthode complète pour construire une IHM de supervision du système MPS via logiciel WinCC Flexible, allant de l'étude et les modifications de l'ensemble des programmes qui se trouvent dans chaque sous station ciblé en passant par la simulation au niveau des deux simulateurs PLC Sim pour les programmes en STEP7 et Runtime pour la partie supervision afin de visualiser les modèles obtenus en mode Simulation.

Ce travail a été finalisé par la Réalisation des interfaces homme machine (IHM) des sous stations automatisées du système MPS afin d'implémenter les résultats obtenus dans un environnement SCADA qui nous permet lui-même de superviser ces derniers à distance et en temps réel.

Enfin, nous avons procédé à la validation des résultats obtenus de la réalisation et la simulation en faisant intervenir une phase de d'expérimentation sur le modèle.

References:

Aberkane, A. (2012). Centralisation des plateformes de supervision des chaines de productions automatisées (Doctoral dissertation).

Attou, M., Mahdi, I. (2017). Automatisation et supervision d'un système de stockage et de distribution de dépôts carburant de" Ain Mlila" (Doctoral dissertation).

Cherchour, H., Chahboune, M. L., Mendil, B. (2015). Commande et supervision d'un processus de margarine via un automate programmable chaine pilote (Doctoral dissertation, Université Abderrahmane mira Bejaia).

Creative Commons Attribution-NonCommercial-NoDerivatives 4.0 International License (CC BY-NC-ND)

Guendoul, A., Abdi, R. (2017). Automatisation et supervision d'une station de traitement des eaux à l'aide d'un automate Siemens S7-300 (Doctoral dissertation).
YAN, W. J., MAO, X. Z. (2005). Power Station Automatic Remote Monitor System Design Based on PLC and WinCC J. Mechanical & Electrical Engineering Magazine,3.

Creative Commons Attribution-NonCommercial-NoDerivatives 4.0 International License (CC BY-NC-ND)

Algerian Journal of Engineering Architecture and Urbanism Vol. 5 Nr. 3 2021
ISSN: 2588-1760

The Flow Analysis of Electrical Charges deposited by Corona Discharge on Polyethylene Terephthalate (PET) Plates

Karima SMILI
Doctor, Higher School of Industrial Technologies, Annaba, Algeria; Laboratory of Electromechanical Engineering, Algeria, Karimasmili@yahoo.fr

Lazhar HEROUS
Professor, Laboratory of Electromechanical Engineering, Algeria, lherous@yahoo.fr

Azzedine DEKHANE
Doctor, Higher School of Industrial Technologies, Annaba, Algeria,
a.dekhane@esti-annaba.dz

Abstract:
Polymer aging issue is a major industrial concern. Electrical, chemical or mechanical constraints indicate that the aging issue depends on several factors and according to the material's characteristics. The present work tackles the flow analysis of charges (negative ions) deposited on the surface by the corona effect, on polyethylene terephthalate (PET) samples; with a thickness of 1 mm by measuring the surface potential decay (SPD), according to the initial voltage -900V to 1600V, and the charge deposition time 5 and 20 seconds. The experimental tests were conducted in a climatic chamber to allow controlling the temperature and relative humidity. As for the negative charge deposition, we used a tip / plane geometry powered by a high voltage source. The measurement is made, without contact, utilizing an electrostatic voltmeter. All these operations are controlled and piloted by a computer. The findings revealed that the evolution of the charging process, at the surface of PET, can be the result of three phenomena combination: charge injection, surface conduction, and polarization.

Key words: surface potential decay, corona discharge, PET, charge injection, polarization.

Introduction:

Les matériaux isolants tiennent une place de plus en plus importante dans le domaine des applications industrielles où un signal électrique est présent. Ils peuvent être obtenus à partir du règne végétal (bois, coton, etc.…) ou du règne minéral (pétrole : quasi-totalité des matières plastiques). Les diélectriques issus du pétrole ont un coût de fabrication bien plus faible et des caractéristiques plus intéressantes.

Le nom d'un polymère est généralement constitué du préfixe poly qui signifie plusieurs suivi du nom chimique du matériau qui peut être soit le monomère dans le cas où le polymère résulte d'une simple polymérisation, soit du motif structural unitaire du polymère lorsque ce dernier résulte d'une polyaddition de plusieurs monomères.

Le problème du vieillissement des polymères est aujourd'hui un enjeu industriel important. Les contraintes électriques chimiques ou mécaniques font que le problème de vieillissement dépend de plusieurs facteurs et selon les caractéristiques du matériau, il n'est jamais fonction

Creative Commons Attribution-NonCommercial-NoDerivatives 4.0 International License (CC BY-NC-ND)

d'un unique paramètre. Dans le domaine du génie électrique, les contraintes dues aux phénomènes électrostatiques peuvent entraîner non seulement des accidents par des simples chocs électriques à des explosions pouvant engendrer des pertes humaines. Les charges électrostatiques entraînent aussi un vieillissement prématuré du matériau pouvant altérer les propriétés isolantes. La compréhension de l'évolution de ce processus permettra de développer des matériaux pour des tenues en tensions plus élevées. En d'autres termes, il est important de pouvoir analyser le mode d'écoulement de charges électriques présentées sur la surface et dans le volume de l'isolant.

Les défaillances constatées concernent généralement les propriétés fonctionnelles, liées à l'aspect, à la tenue mécanique, aux propriétés électrique, à l'étanchéité, la perméabilité, etc.

Comme exemple d'évolution de l'aspect. La figure 1 montre deux plaques de polymère injecté utilisées pour fabriquer des boucliers de voiture (Dubois, 2004).

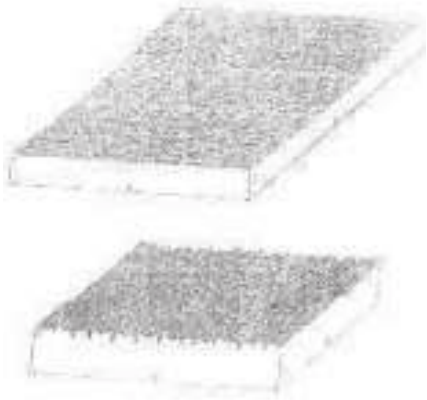

Fig. 1. Echantillon en polymère (Dubois, 2004)

On observe la surface du matériau à l'état initial et ce qu'elle devient après quelques centaines d'heures d'exposition en milieu accélérant le vieillissement.

On voit apparaître des fissures qui vont se traduire par une diminution du brillant et un blanchiment de la surface.

Historiquement, les études de potentiel de surface ont été menées principalement en lien avec trois domaines de recherche appliquée : l'étude des électrets et des propriétés de stockage stable de la charge dans un matériau (utilisées en particulier dans la fabrication de microphones), le développement des dispositifs de reprographie utilisant l'activation photoélectrique de la conduction et l'étude de propriétés isolantes du polyéthylène pour son utilisation dans les câbles de transport d'énergie électrique (Anton, 2000), (Pinelet, 2000) , (Duboix,2002).

Par ailleurs, l'électricité statique se présente fréquemment sur les matériaux isolants selon des mécanismes différents. On peut citer le frottement d'un corps isolant contre un autre, le simple contact d'un corps isolé avec un corps chargé, l'approche d'un corps initialement neutre au voisinage d'un corps électrisé, le dépôt superficiel de charges sur un isolant lorsque celui-ci se trouve ou traverse une zone fortement ionisée.

Ces mécanismes de chargement sont généralement cumulatifs dans le temps. Certain dégâts sont latents et le système peut ne plus fonctionner pour une contrainte faible.

Creative Commons Attribution-NonCommercial-NoDerivatives 4.0 International License (CC BY-NC-ND)

La première conséquence de la présence de charges électriques sur un objet isolé est la création d'un champ électrique. Il peut poser l'effet de l'attraction ou de répulsion liée à des forces électrostatiques. De plus, lorsque le champ électrique créé par une densité superficielle ou volumique de charges dépasse la rigidité diélectrique du milieu environnant, une décharge se produit dans ce milieu. Les nuisances liées à l'accumulation de l'électricité statique peuvent aller du simple désagrément ressenti en approchant la main jusqu'à de très graves risques d'explosion.

Notre travail consiste à essayer de comprendre l'évolution des charges déposées sur la surface du polyéthylène-téréphtalate (PET) par décharge couronne. En effet, les résultats nous permettrons de définir le mécanisme de vieillissement pouvant entraîner la perte des caractéristiques du matériau. La compréhension de ce phénomène permettra aux industriels d'améliorer par des procédés de polymérisation la tenue de ce matériau face à ces contraintes et d'améliorer la durée de vie.

Mode expérimental :

Description des échantillons:

Les échantillons utilisés dans cette étude sont en polyéthylène téréphtalate (PET) est un thermoplastique appartenant à la famille des polyesters. Il est largement connu sous le nom commercial mylar, mélinex ou hostaplan. Le PET est souvent utilisé comme diélectrique dans les condensateurs, câbles électriques et l'isolation de bobinage des moteurs électriques. Il peut présenter des morphologies différentes (amorphe ou avec différents taux de cristallinité).

Ils sont fabriqués par polycondensation d'acide téréphtalique : (nHOOCC6H4COOH) et d'éthylène glycol : NHOCH2CH2OH.

Acide téréphtalique

Ethylène glycol

La structure chimique du monomère sera comme suit :

Creative Commons Attribution-NonCommercial-NoDerivatives 4.0 International License (CC BY-NC-ND)

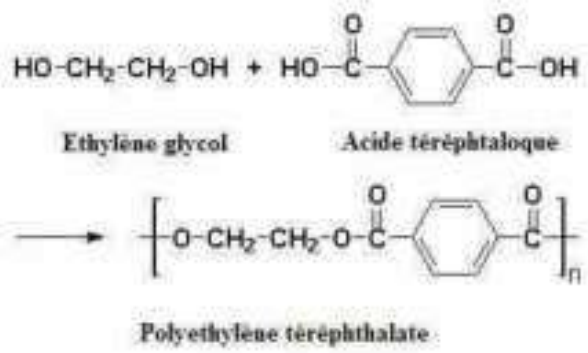

Les échantillons utilisés à cette expérience ont une forme rectangulaire 7cm X 7cm avec une épaisseur de 1mm dont la face arrière est métallisée avec la laque d'argent (contre-électrode), (Fig. 2).

Fig. 2. Echantillon de polyéthylène téréphtalate 7*cm* x 7*cm*

Dispositif de mesure de DPS:

Le principe de la technique du déclin de potentiel en surface (DPS) est de suivre en fonction du temps l'évolution du potentiel de surface d'un échantillon préalablement chargé par décharge couronne. La mesure du potentiel en surface de l'échantillon au cours du temps à partir d'une sonde électrostatique à condensateur vibrant de type TREK (Fig. 3.) permet de fournir des informations sur le mode d'écoulement (surfacique et / ou volumique) des charges déposées et sur la mobilité de ces charges.

La technique du déclin du potentiel en surface comprend pour son fonctionnement deux phases, une phase de charge par décharge couronne, en utilisant une configuration pointe-plan et l'autre de mesure de potentiel en surface sans avoir aucun contact avec le matériau. Le dispositif expérimental est constitué d'un plateau circulaire tournant. Il comporte un porte-échantillon en cuivre permettant d'assurer un bon contact entre la face arrière de l'échantillon et la terre. L'ensemble de dispositif est installé dans une enceinte fermée (Fig. 3.).

Creative Commons Attribution-NonCommercial-NoDerivatives 4.0 International License (CC BY-NC-ND)

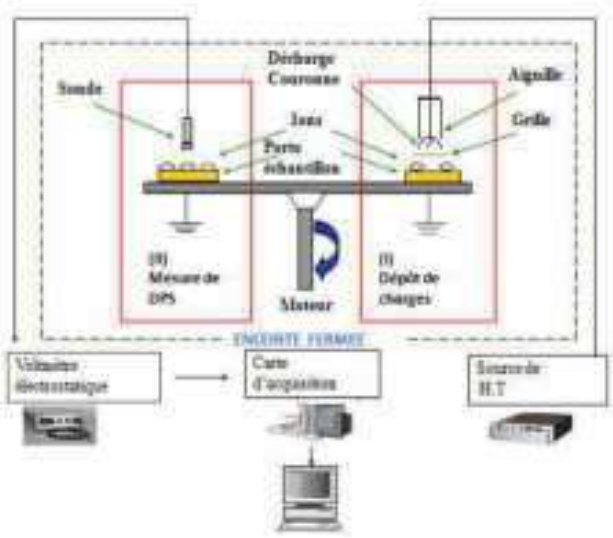

Fig. 3. Dispositif expérimental de mesure du déclin de potentiel de surface

L'échantillon à étudier, se trouve initialement sous le poste de mesure. Un moteur pas à pas fait tourner le porte-échantillon jusqu'à l'amener au poste de charge, une décharge couronne se produit afin de charger le matériau en surface. L'échantillon revient de nouveau au poste de mesure (3s) pour mesurer le potentiel de surface. Une grille métallique en filet fin positionnée entre l'aiguille et la surface de l'échantillon a pour rôle de répartir uniformément les ions sur la surface de l'échantillon. Dans le cadre de cette étude, nous avons appliqué des décharges couronnes continues négatives haute tension de courte durée (5s : 20s). Des décharges de -2 KV à -7 KV ont permis de mesurer des potentiels de surface initiaux de -900V à -1600V respectivement. Toutes les expériences ont été réalisées à l'air ambiant. L'humidité relative de l'atmosphère varie entre 55 % et 80%. La température de l'échantillon est un paramètre important, sa valeur est proche de 28°C

Résultats expérimentaux:

Influence de la polarite :

La figure 4 Présente les résultats de la mesure de DPS en polarités positive et négative.

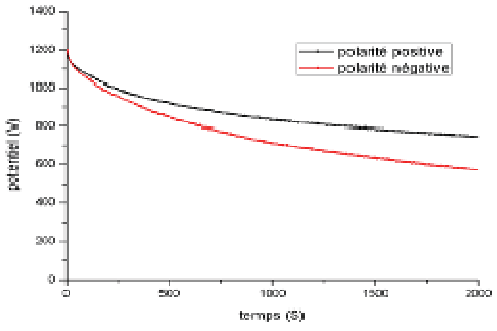

Fig. 4. Déclin de potentiel de surface en double polarité

Creative Commons Attribution-NonCommercial-NoDerivatives 4.0 International License (CC BY-NC-ND)

Ce résultat montre que le déclin en polarité négative est plus rapide qu'en polarité positive, cette différence peut être attribuée aux espèces neutres excitées qui assistent l'injection en polarité négative contrairement à la polarité positive (Rouagdia, 2015).

Effet de la tension de dépôt :

Dans cette partie, nous avons étudié l'effet de la densité de charges sur le comportement du déclin de potentiel en surface du PP.

Les mesures sont reportées sur la figure 5 On observe une évolution temporaire du DPS pour différentes valeurs du potentiel de dépôt.

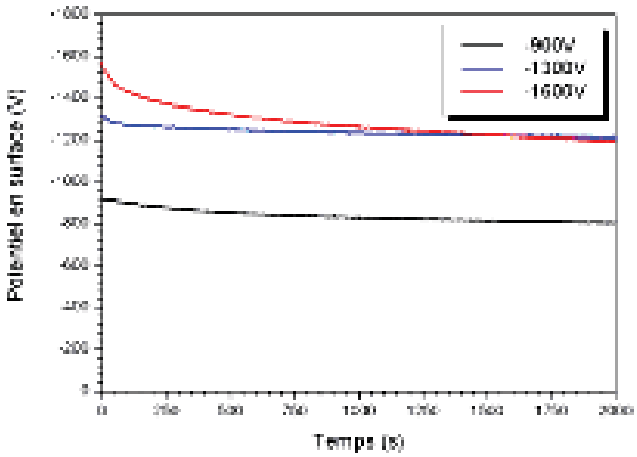

Fig. 5. Effet de la tension de dépôt

Nous avons noté une dépendance avec ce paramètre. Cette étude a par ailleurs mis en évidence l'existence du phénomène de « cross-over ». On observe nettement un croisement de courbes montrant qu'au bout du même temps de mesure, la déclinaison de l'échantillon chargé à –1600V est plus rapide que celle chargé à –1300V. Cet effet suppose selon plusieurs auteurs (Molinié, 1995) ; (Llovera, 2002); (Sessler, 1989); (Moreno, 1976) que le mécanisme qui gouverne l'évolution des charges est l'injection dans le volume du matériau. De plus on observe une évolution du DPS plus rapide aux premiers instants de mesure et que la charge sur la surface des matériaux n'est pas totalement évacuée. Une partie de la charge reste sur la surface de l'isolant qu'on peut appeler charge résiduelle. Pour les potentiels moins importants, le DPS est moins important pour ne pas dire insignifiant. Ceci peut être expliqué par l'effet du champ qui est a notre avis très faible pour pouvoir agir sur les porteurs de charges. Il est clair aussi que l'allure des courbes obtenues n'est pas exponentielle d'où l'absence d'une conduction volumique ou d'une conduction surfacique. Ces résultats nous orientent déjà vers le mécanisme d'une injection partielle dans le volume du matériau, les charges qui restent sont piégées sur la surface de l'isolant à cause du manque d'énergie. Les charges qui s'injectent son animées par une grande énergie et peuvent dériver sous leur propre champs dans le volume du matériau vers l'autre face du matériau isolant.

Effet de temps de dépôt :

L'influence du temps de dépôt tp sur le déclin de potentiel de surface est donnée par les courbes de la figure 6. La tension de dépôt de charge est égale à -1600 V, l'humidité relative

Creative Commons Attribution-NonCommercial-NoDerivatives 4.0 International License (CC BY-NC-ND)

et la température sont respectivement égales à 60% et 28°C. L'épaisseur de l'échantillon du PET est égale à 1mm. La durée de dépôt de charges est égale à 5s et 20s.

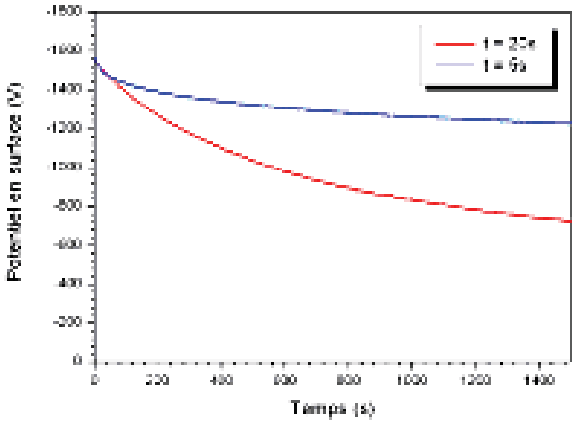

Fig. 6. Effet de la tension de dépôt

Nous avons noté une dépendance avec ce paramètre, on observe un déclin plus significatif particulièrement dans les temps courts lorsqu'on augmente la durée du temps de dépôt. Dans les temps longs, on observe une tendance d'un déclin pratiquement la même. On observe ainsi un taux de décroissance initial élevé suivi par une valeur quasi stationnaire du potentiel.

Effet du champ Electrique :

Pour voir l'influence du potentiel déposé sur la surface de l'échantillon, nous avons représenté les courbes normalisées par rapport au potentiel initial V_0, LogV(t)/Vo=f(t) sur la figure 7.

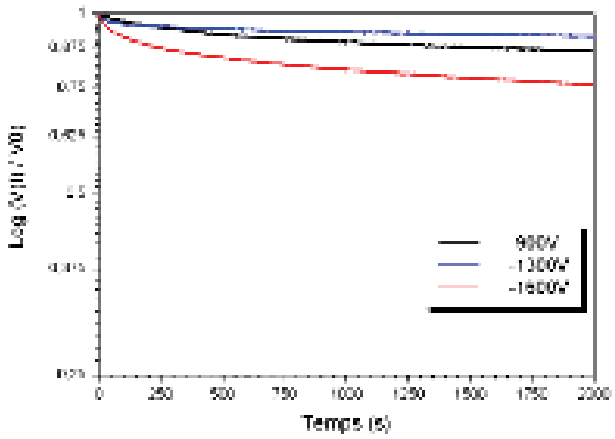

Fig. 7. Effet du champ électrique

Ce résultat peut expliquer l'existence d'un effet de champ sur le matériau on observe que les courbes ne se superposent pas. Il est par conséquent intéressant de supposer que les phénomènes liés à la mobilité électronique (dépiégeage – accélération – repiégeage) seront plus dépendants du champ (Moreno, 1976); (Molinie, 2000); (Pouilles, 1995) ; (Sigmond, 1982); (Batra, 1970). Un électron sautant d'un niveau de piège de surface à un niveau de

Creative Commons Attribution-NonCommercial-NoDerivatives 4.0 International License (CC BY-NC-ND)

volume est une injection de charge dépendante du champ qui peut assister le saut et ensuite l'accélérer dans le matériau (Rouagdia, 2018); (Mellouki, 2018); (Rouagdia, 2015) ; (Smili, 2019).

Conclusion :

Le matériau utilisé est le polyéthylène téréphtalate (PET) ; il est utilisé généralement dans l'isolation des moteurs électriques, l'isolation des câbles et comme diélectrique dans les condensateurs. Le dépôt de charges est réalisé à partir d'une décharge couronne par une géométrie pointe/plan.

Les résultats obtenus nous ont prouvé que l'hypothèse la plus probable de l'évolution des charges sur la surface du PET est l'injection de charge à l'intérieur du matériau isolant.

L'analyse des résultats expérimentaux en fonction des différents paramètres, nous a permis de démontrer que l'évolution du processus de charge à la surface du PET peut être le résultat d'une association de trois phénomènes : l'injection de charge, la conduction surfacique et le phénomène de polarisation. Nous pouvons dès lors confirmer que ces résultats peuvent être d'une grande utilité pour la caractérisation des matériaux isolants et la mise en évidence d'un probable processus de vieillissement ou la modification des propriétés diélectriques des polymères.

Enfin, il devient important aux constructeurs de matériaux isolants et en particulier le polyéthylène téréphtalate (PET) de se pencher sur ce constat et d'essayer d'y remédier en essayant d'améliorer les propriétés du phénomène d'injection afin d'éviter ce mode de vieillissement.

References:

Dubois J.C. (2004), *Dielectic properties of polymers*, Technical engineering, electrical treated. E1850.

Anton A. (2000) , *Solid insulating materials electrical characteristics*, Technical engineering, electrical treated, D 2315.

Pinelet B, Duchateau F. (2000) , *Insulation function in dielectric materials*, Technical engineering, D 2 302.

Duboix J.C. (2002), *Dielectic properties of polymers,* Technical engineering, E 1850.

Rouagdia K., Herous L., Nemamcha M., Dascalescu L., Fatihou A., Tabti B., (2015), *Experimental modeling of the electric potential decay at the surface of polypropylene films (PP)*, Journal of Electrostatics, vol.76, pp. 262-267.

Molinié P. (1995). *Surface potential decay on corona-charged epoxy samples due to polarisation processes*. Journal of Physics D: Applied Physics, 28, pp. 1601-1610.

Llovera P., Molinié P. (2002). *Charge injection dynamics on thin films: Limited by surface detrapping or by charge drift mobility? A new contribution using surface potential measurements*. 3rd Conference of French Society of Electrostatics, Toulouse, France.

Sessler G.M, (1989), *Charge Storage in Dielectrics*. IEEE Transactions on Electrical Insulation,24(3), pp. 394–402.

Moreno R.A., Gross B. (1976), *Measurement of potential buildup and decay, surface charge density, and charging currents of corona-charged polymer foil electrets*. Journal of Applied Physics, 47(8), pp. 3397–3402.

Molinie P, Llovora P. (2000), *Surface potential measurements : implementation and interpretation,* 8th, Int conf DMMA. Edinburgh.

Pouilles V. (1995), *Surface potentiel measurement : A tool complex permittivity determination in the very low frequency range*, IEEE 5th Interna. Conf. On. Conduc. And . Break in Solid Dielec.

Sigmond R.S ., Goldman M. (1982), *Corona discharges physics and applications*, Electrical breakdown and discharges: phenomen Press, pp1-64.

Creative Commons Attribution-NonCommercial-NoDerivatives 4.0 International License (CC BY-NC-ND)

Batra I.P., Kanazawa K.d., Seki H. (1970), *Discharge charateristics of photoconducting insulators*, J. Appl. Phys, Vol. 41, pp. 3416-3422.
Rouagdia K., Nemamcha M., Herous L., Dascalescu L. (2018), *Robust design of neutralization process of the residual electric charge on the surface of PP-films*, IEEE Trans. On. Dielec. V .25. Issue .2.
Mellouki H., Herous L., Neagoe B., Prawatya Y., Zeghloul T., Dascalescu L. (2018), *Experimental modeling of the conformal-contact tribocharging of polymers*, IEEE Trans. On. Dielec. V 25. Issue. 1.
Rouagdia K., Herous L., Nemamcha M., Fatihou A., Tabti B., Dascalescu L. (2015), *Experimental modeling of the electric potential decay at the surface of polypropylene films (PP)*, J. Of .Electrostatics, Vol. 76, pp. 262-267.
Smili K., Herous L. (2019), *Corona charging and charge decay on polyethylene terephthalate films*. Electrotehnică, Electronică, Automatică Journal, 67(3), pp. 82-90.

Creative Commons Attribution-NonCommercial-NoDerivatives 4.0 International License (CC BY-NC-ND)

Algerian Journal of Engineering Architecture and Urbanism Vol. 5 Nr. 3 2021
ISSN: 2588-1760

DIRECT DETERMINATION OF IRON(III) IN WATER BY UV-VISIBLE SPETROPHOTOMETRY APPLICATION TO WATERS LOADED WITH METALLIC CATIONS

Rayane Nadjet Fassi
(PhD student), Laboratory of pollution and water treatment, University Mentouri Brothers Constantine1, Algeria.
e-mail: fassirayane@yahoo.com

Chahrazed Boukhalfa –Djebbar
(Pr), Laboratory of pollution and water treatment, University Mentouri Brothers Constantine1, Algeria.
e-mail: chahrazed_boukhalfa@yahoo.com

Abstract:
The aim of this study is the optimization of the direct determination of Fe(III) in water by UV-Visible spectrophotometry in the absence and in the presence of metallic cations (Cu(II), Co(II), Ni(II), Mn(II), Cd(II) and Zn(II)). A calibration curve was established, the detection limit was determined and the stability of the iron solutions was evaluated as a function of time. Then, the effects of the presence of metallic ions were evaluated.
The obtained results show that Fe(III) determination can be realized in the absence of an acid. Linear calibration curve is obtained in the concentration range: 1-10 $mg.mL^{-1}$. The measured absorbance remains stable for 40 minutes. The detection limit is 0,1mg/L. Among the metallic ions studied, only Cu(II) ions has a significant effect on the analysis of Fe(III) ions. The presence of Co(II), Ni(II), Mn(II), Cd(II) and Zn(II) with a concentration five times higher than that of Fe(III) ions, has no effect.

Key words: UV-Visible spectrophotometry; Fe(III); metallic ions; water analysis.

Introduction:

Dans la croûte terrestre, le fer est le quatrième élément le plus abondant et le deuxième métal après l'aluminium**.** Il ne se trouve pas en tant que métal libre dans la nature; il a tendance à se lier avec des ligands organiques et inorganiques pour former un grand nombre de minéraux (***Ilbert. M, 2013)*****.** Le fer est l'un des éléments essentiels les plus importants (***Balcerzak .M, 2008)*****.** Il participe aux processus physiologiques vitaux, assurant une croissance et un développement normaux des plantes (***Becana.M, 1998)*****.** Il est nécessaire à toute vie humaine et animale, notamment en assurant le transport de l'oxygène dans le sang. On le trouve aussi dans les cytochromes qui transportent les électrons dans les chaînes respiratoires et dans certaines enzymes (***Brissot.P ,2006)*****.** Sa carence ou sa surcharge peut entraîner des problèmes de santé (***Balcerzak .M, 2008)*****.** L'excès de fer se dépose dans les tissus de l'ensemble de l'organisme. Des symptômes et des complications peuvent apparaître si le fer s'accumule dans les organes endocriniens, en particulier le pancréas et l'hypophyse, ainsi que dans le foie

Creative Commons Attribution-NonCommercial-NoDerivatives 4.0 International License (CC BY-NC-ND)

et le cœur ***(James Peter Hamilto.M., 2019)*.** De fortes concentrations en fer dans le sol peuvent conduire à des symptômes de toxicité, tel que le stress oxydatif. En plus de brunir les feuilles, d'assombrir l'apex des racines et de générer une flaccidité et une inhibition de la croissance des racines ***(Snowden, R., 1995,et Schmidt. W, 1998)*** **,** il produit des espèces réactives de l'oxygène, modifiant l'intégrité des structures cellulaires ***(Vansuyt, G.,1997)***

Le fer est largement appliquée sous forme d'acier dans la construction, et dans l'industrie technologique sous forme de fer métallique et d'oxydes**.** Ses ions sont souvent présents dans les rejets des eaux industrielles. En milieu aqueux, il se trouve sous deux états d'oxydation: Fe(II) et Fe(III). En milieu oxygéné, les ions Fe(II) s'oxydent en ions Fe(III). La présence du fer rend l'eau dure, parce qu'une fois exposé à l'air, il rouille. Il est donc fondamental d'exercer un contrôle de la concentration des ions Fe(III) dans l'eau.

L'objectif de la présente étude est l'optimisation du dosage direct des ions Fe(III) par spectrophotométrie UV-Visible et l'évaluation de son application dans les eaux chargées en métaux.

Problématique:

Il est d'usage de distinguer deux catégories de méthodes d'analyse. Le choix peut se faire entre des méthodes chimiques proprement dites, entraînant une réaction spécifique du composé qu'on veut doser et des techniques physiques utilisant ses propriétés physico-chimiques. Ces dernières méthodes ont supplanté les méthodes traditionnelles. Elles se sont fortement développées ces dernières décennies en relation avec la numérisation des données (***Francis.R, 2016)*.**

En raison de l'importance des métaux dans notre vie, les chercheurs scientifiques ont développé au fil du temps de nombreuses méthodes pour les doser dans les différents échantillons que nous utilisons. Les méthodes physico-chimiques utilisées pour le dosage des métaux sont les méthodes électrochimiques (voltampérométrie et polarographie) ***(Christopher.M, 1993)*,** et les méthodes spectrométriques (spectrométrie d'absorption atomique, spectrophotométrie d'émission de flamme, spectrophotométrie à plasma inductif, spectrophotométrie UV-Visible) **(*Douglas. A, 2003)***. Certaines de ces méthodes ne sont pas disponibles dans tous les laboratoires à cause de leur coût. Dans la présente étude, nous nous intéressons à la spectrophotométrie UV-Visible, qui est une méthode de dosage relativement plus accessible que les autres. Cependant, le dosage des cations métalliques par cette méthode nécessite l'utilisation de plusieurs réactions et réactifs chimiques comme c'est le cas lors du dosage des ions Fe(III) qui doivent être réduits en ions Fe(II) ***(Charlot.G,Masson, 1974)*** L'objectif de la présente étude est d'optimiser le dosage direct des ions Fe(III) dans les effluents chargés en métaux.

Matériel et méthodes:

Creative Commons Attribution-NonCommercial-NoDerivatives 4.0 International License (CC BY-NC-ND)

Nous avons initialement procédé à l'optimisation du dosage direct des ions Fe(III) en absence des métaux. Nous avons procédé à l'établissement de la droite d'étalonnage. Dans l'application de la loi de Beer-Lambert, la méthode de dosage avec une gamme d'étalonnage permet de vérifier les conditions de validité de la loi à travers la linéarité de la fonction A=f(C). Elle consiste à préparer une gamme de dilutions d'une solution étalon "mère", à mesurer l'absorbance de chacune de ces solutions étalons "filles", puis à tracer la courbe d'étalonnage A = f(C). Afin d'établir la droite d'étalonnage du dosage direct des ions Fe(III), nous avons réalisé le dosage à différentes concentrations des ions Fe(III) dans la gamme de concentration 1-10mg/L. Nous avons aussi vérifié la stabilité de la solutions en fonction du temps et déterminer la limite de détection. Une solution mère de Fe(III) à la concentration de 100 mg/L. a été préparée à partir du sel $FeCl_3$, $6H_2O$.

Dans un deuxième temps; nous avons evalué l'effet des cations métalliques: Cr(III), Mn(II) Co(II), Ni(II), Cu(II), Zn(II) et Cd(II). Les solutions mères de ces ions ont été préparées en utilisant les sels CrN_3O_9, $9H_2O$. $MnCl_2$, $4H_2O$, $CoCl_2$,$6H_2O$, $NiCl_2$,$6H_2O$, ZnN_2O_6,$6H_2O$ et CdN_2O_6,$6H_2O$ respectivement.

Le dosage a été réalisé à l'aide d'un spectrophotomètre UV-Visible Schimadzu 1650.

Résultats et discussions:

Caractérisation spectrophotométrique d'une solution de Fer(III)

Selon le diagramme de spéciation, les ions Fe(III) en solution aqueuse s'hydrolysent pour former des complexes hydroxyles (Figure 1). A pH< 4, les ions Fe(III) ($Fe(H_2O)_6^{3+}$) et $FeOH^{2+}$ ($Fe(H_2O)_5OH^{2+}$) prédominent.

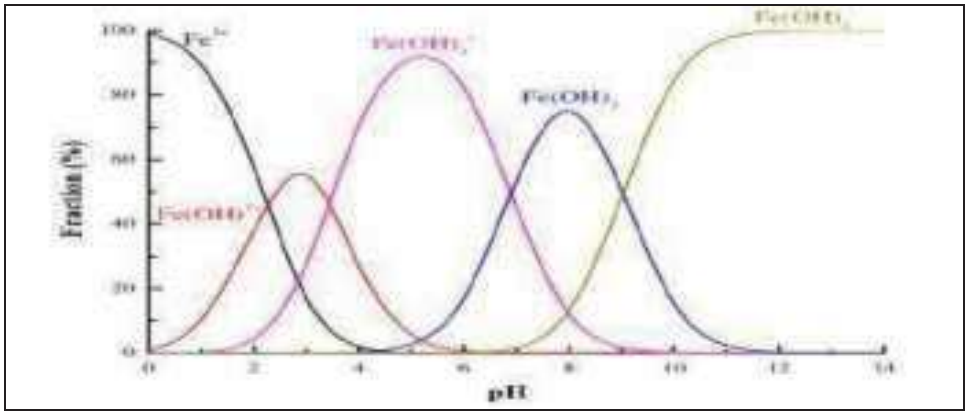

Figure 1. Diagramme de spéciation des ions Fe(III) dans l'eau

Une solution aqueuse de $Fe(H_2O)_6^{3+}$ est rouge brique, la couleur absorbée est le bleu-vert, le complexe apparaît avec la couleur complémentaire. La transition d-d consiste au passage d'un électron du niveau t_{2g}^3-e_g^2 au niveau t_{2g}^2-e_g^3.

En absence d'acide, le spectre UV-Visible d'une solution de Fer(III) (Figure 2), présente une bande d'absorption dans le domaine de l'ultraviolet à 293,8 nm, qui est due au complexe $FeOH^{2+}$ ***(Stefansson.A, 2008 et Ishibashi, M. 1956)***. En présence de HCl, une bande vers 224,4nm est observée; elle est attribuée aux ions Fe^{3+} qui prédominent à pH très acide (pH<2).

Creative Commons Attribution-NonCommercial-NoDerivatives 4.0 International License (CC BY-NC-ND)

Algerian Journal of Engineering Architecture and Urbanism Vol. 5 Nr. 3 2021
ISSN: 2588-1760

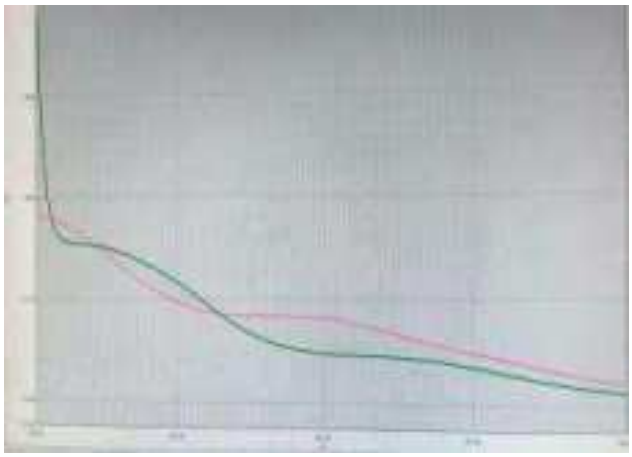

Figure 1. Spectres UV-Visible d'une solution de Fe(III) en absence et en présence de HCl (1M)
(– en absence d'acide; – en présence d'acide)

Etablissement de la droite d'étalonnage

Dans le but de proposer une gamme d'étalonnage, nous avons essayé de déterminer les conditions optimales pour le dosage, en evaluant en premier l'effet de la présence de l'acide HCl**.** L'évolution de l'absorbance des solutions de Fer(III) à différentes concentrations, montre que la loi de Beer-Lambert est bien vérifiée pour le domaine de concentration 1-10mg/L en absence de l'acide (Figure 3).

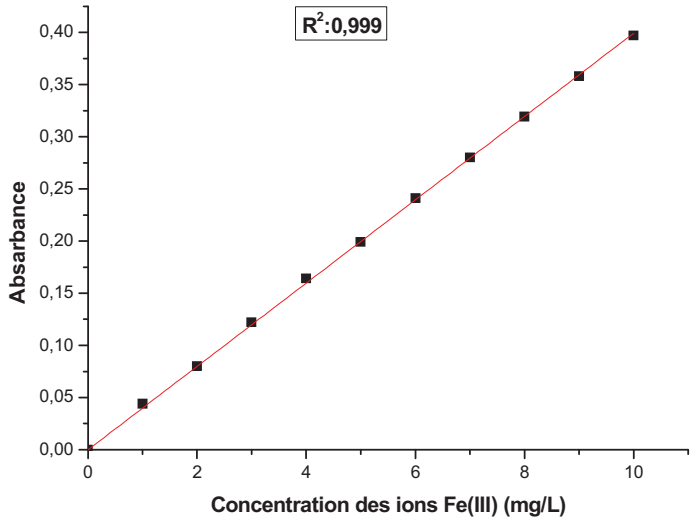

Figure 3. Droite d'étalonnage du dosage direct des ions Fe(III) (λ=293,8nm)

En présence de HCl à différentes concentrations, les absorbances mesurées ne montrent pas un parfaite linéarité (Figure 4). Dans la suite du travail, le dosage des ions Fe(III) est réalisé en absence d'acide.

Creative Commons Attribution-NonCommercial-NoDerivatives 4.0 International License (CC BY-NC-ND)

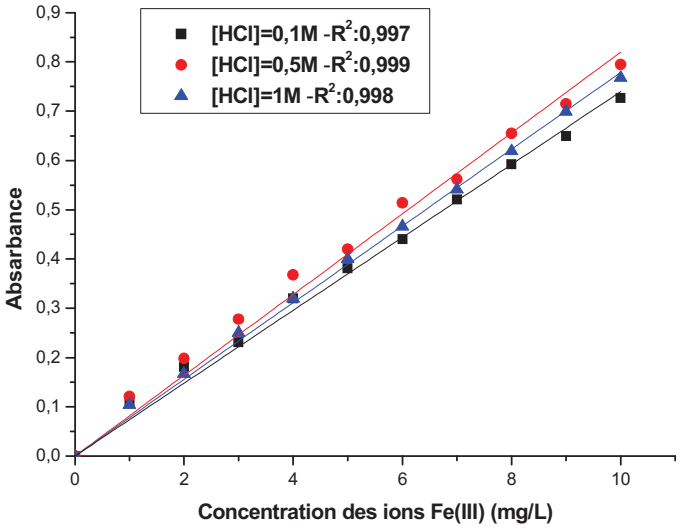

Figure 4. Droite d'étalonnage du dosage direct des ions Fe(III) en présence de HCl (λ=224,43nm)

Evaluation de la stabilité des solutions de Fe(III) en fonction du temps

La stabilité des solutions de Fe(III) avec le temps est évaluée à travers le suivi de l'évolution de l'absorbance pour différentes concentrations de Fe(III) en fonction du temps de repos avant dosage. Les résultats obtenus (**Tableau 1**), montrent qu'après 4à minutes de repos, la solution reste stable.

Tableau 1. Effet du temps sur la stabilité des solutions de Fe(III)

Concentration de Fe(III) (mg/L)	Concentration de Fe(III) (M)	Temps avant dosage (min)	Absorbance (293,8nm)
5	**$8{,}9.10^{-5}$**	10	0,189
		15	0,189
		40	0,188
10	**$1{,}8.10^{-4}$**	10	0,341
		40	0,341

Creative Commons Attribution-NonCommercial-NoDerivatives 4.0 International License (CC BY-NC-ND)

Détermination de la limite de détection

Pour déterminer la limite de détection, nous avons suivi l'évolution de l'absorbance à 293,8nm avec la diminution de la concentration des ions Fe(III). Les résultats obtenus (**Tableau 2**), indiquent que dans les conditions optimisées, la limite de détection du dosage direct des ions Fe^{3+} est 0,1 mg/L. Dans ce domaine, une bonne sensibilité est obtenue.

Tableau 2. Evolution de l'absorbance des solutions de Fe(III) (C≤1mg/L)

$C_{Fe(III)}$ (mg/L)	1	0,5	0,25	0,1	0,05	0,01	0,05
$C_{Fe(III)}$ (mol/L)	$1,8.10^{-5}$	$8,9.10^{-6}$	$4,5.10^{-6}$	$1,8.10^{-6}$	$8,9.10^{-7}$	$1,8.10^{-7}$	$8,9.10^{-8}$
Absorbance (λ=293,8nm)	0,040 ±0,002	0,020 ±0,003	0,009 ±0,001	0,005 ±0,001	0,005 ±0,001	0,005 ±0,001	0,005 ±0,001

Application aux eaux chargées en métaux

Les effets des cations métalliques Cr(III), Mn(II), Co(II), Ni(II), Cu(II), Zn(II) et Cd(II) ont été évalués. Des mesures d'absorbance ont été effectuées pour les solutions contenant 10 mg/L de Fe(III) en présence des quantités appropriées de chaque cation. Les résultats sont présentés dans la Figure 5. On constate que seuls les ions Cu(II) ont un effet significatif sur le dosage des ions Fe(III). Une augmentation de la valeur de l'absorbance est enregistrée. Cet effet augmente avec l'augmentation de leur concentration. La présence des ions Cr(III), Mn(II) Co(II), Ni(II), Cd(II) et Zn(II) avec une concentration cinq fois supérieure à celle des ions Fe(III), n'a aucun effet.

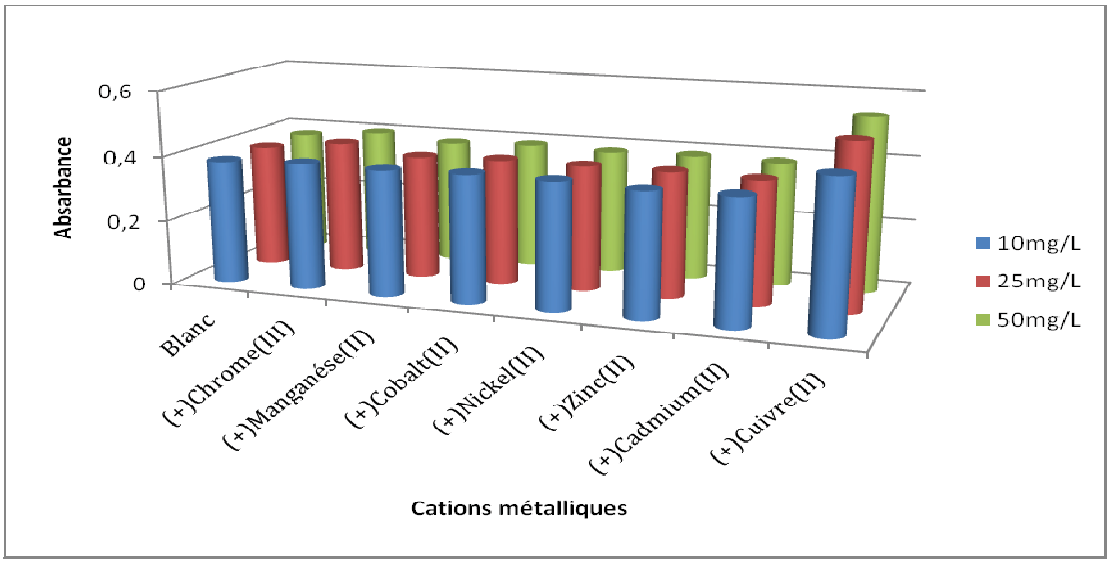

Figure 5. Effets des cations métalliques sur le dosage des ions Fe(III)

Conclusion

Creative Commons Attribution-NonCommercial-NoDerivatives 4.0 International License (CC BY-NC-ND)

- Le dosage direct des ions Fe(III) par spectrophotométrie UV-Visible peut être réalisé avec une limite de détection de l'ordre de 0,1mg/L.
- Une droite d'étalonnage selon la loi de Beer-Lambert, peut être établie dans le domaine de concentration: 1-10mg/L.
- La présence des ions Cr(III), Mn(II), Co(II), Ni(II), Zn(II) et Cd(II) avec une concentration cinq fois supérieure à celle des ions Fe(III), n'a aucun effet.
- Les ions Cu(II) ont un effet important sur le dosage des ions Fe(III).

Références

Balcerzak .M, Tyburska. A, *(2008), Selective determination of Fe(III) in Fe(II) samples by UV-spectrophotometry with the aid of quercetin and morin. Department of Analytical Chemistry Warsaw University of Technology 00-664 Warsaw, Poland.*

Becana, M, Moran, J.F, Iturbe-Ormaetxe. I, *(1998). Iron-dependent oxygen free radical generation in plants subjected to environmental stress: toxicity and antioxidant protection. Plant Soil 201, 137–14.*

Brissot.P Olivier. l *(2006) . Métabolisme du fer . La Revue du Praticien 56(19);2111-7.*

Charlot.G,Masson. *(1974).Chimie analytique quantitative: Méthodes sélectionnées d'analyse chimique des éléments.6éme éditions, VIIIp.-p.327-571-XXIV p.*

Christopher.M, Brett.A, Ana.M et Brett.O, *(1993). Electrochemistry Principles Methods And Applications, 1ére Edition, Oxford Science Publications, Royaume-Uni.*

Douglas A. Skoog ،F. James Holler ،Timothy A. Niema ,*(2003). Principes d'analyse instrumentale.5éme editions de boeck universté.*

Francis. R, Annick .R, Arnaud. M, *(2016).Analyse chimique Méthodes et techniques instrumentales. Dunod .9éme édition,Malakoff.*

James Peter Hamilto.M., Hopkins.J, *(2019). surcharge en fer, University School of Medicine.*

Ishibashi, M., Shigematsu, T., Yamamoto, Y., Tabushi, M., & Kitagawa, T. *(1956). Ultraviolet Spectrophotometric Determination of Iron. Bulletin of the Chemical Society of Japan, 29(1), 57–60.*

Ilbert. M, Bonnefoy. V, *(2013). Insight into the evolution of the iron oxidation pathways. Biochimica et Biophysica Acta (BBA) - Bioenergetics, 1827(2), 161–175.*

Schmidt, W. Fuhner, C, *(1998). Sensitivity to and requirement for iron in ¨ Plantago species. New Phytol. 138, 639–651.*

Snowden, R.E., Wheeler, B.D, *(1995). Chemical changes in selected wetland plant species with increasing Fe supply, with specific reference to root precipitates and Fe tolerance. New Phytol. 131, 503–520.*

Stefánsson, A., & Seward, T. M*. (2008). A spectrophotometric study of iron(III) hydrolysis in aqueous solutions to 200 °C. Chemical Geology, 249(1-2), 227–235.*

Vansuyt, G., Lopez, F., Inze, D. Briat, J.F., Fourcroy, P, *(1997). Iron triggers a rapid induction of ascorbate peroxidase gene expression in Brassica napus. FEBS Lett. 410, 195–200.*

Creative Commons Attribution-NonCommercial-NoDerivatives 4.0 International License (CC BY-NC-ND)

Algerian Journal of Engineering Architecture and Urbanism Vol. 5 Nr. 3 2021
ISSN: 2588-1760

Performance evaluation of FSO-OF-VLC

Mohammed Larbi TAYEBI
MCB, Telecommunications, Telecommunications and Digital Signal Processing Laboratory, University of Djillali Liabes, Sidi Bel Abbes, Algeria, e-mail: tayebi_med@hotmail.com

Amina DJIR
PhD student, Telecommunications, Telecommunications and Digital Signal Processing Laboratory, University of Djillali Liabes, Sidi Bel Abbes, Algeria, e-mail: djir_amina@yahoo.com

Abstract:
Optical communication offers a very wide bandwidth, much more than radio frequency communication can offer. In this article, we have proposed a hybrid system based on Free space optical, Communication through Optical Fiber and Visible light communications (FSO-OF-VLC). This system uses the SAC OCDMA spectral amplitude optical code division access technique. The most variable propagation channel in this research is the FSO channel due to the constantly changing weather conditions (rain, snow and fog), resulting in a significant degradation of performance. Optical fiber connects the signal from the FSO to the user using the VLC. The FSO-OF-VLC system will constitute an "all-optical" communication between the transmitter and the receiver. The very wide bandwidth allows an increase in the number of users. This system was simulated with Optisystem v17.0 simulation software and the performance analysis was evaluated in terms of Q factor, and eye diagram.

Key words: FSO, OF, VLC, SAC OCDMA.

Introduction:

The study of optical communications is expanding rapidly due to its high bandwidth and various techniques such as fiber optic and free space communication (FSO and VLC) **(Y. L. Yu et al., 2015)**. FSO is a wireless communication technology that requires direct alignment between emission source and destination; it uses light to transmit data between two fixed points **(Singh, 2017).** The optical link has a low cost and it is robust against electromagnetic interference. Its installation is quick and simplified **(Kaushal and Kaddoum, 2017).** Due to its various advantages, the FSO link can be used in several fields like communications between large towers **(Willebrand and Ghuman, 2001)**, space communication **(Son and Mao, 2016)**, military applications **(Shaulov et al., *2005)***, medical services **(Sharma and Kaler, 2012)** and many more others (**Farooq et al.**, 2018). However, the FSO is sensitive to weather conditions (**Khalighi et al.**, **2014**)**.** and more particularly to fog (**Kumar and Sohal**, **2014**) , which degrades the performance of the system and therefore affects the availability of the optical link between the transmitter and the receiver (**Ijaz *et al.***, **2013**), By introducing new designs, the quality of free space optical link communications systems can be improved in order to overcome the distance limitation problem. In (**Tayebi et al.,2020**), An FSO-FSO link has been studied and simulated, the proposed solution shows that the range between the transmitter and the receiver is doubled under the same atmospheric conditions. The design proposed in (**Mesri and Djebbari**, **2018**). Also shows that the performance of the SAC-

Creative Commons Attribution-NonCommercial-NoDerivatives 4.0 International License (CC BY-NC-ND)

OCDMA-FSO system using ZCC (Zero Cross Correlation) codes is improved in terms of range for different types of fog (dense fog, moderate fog, haze and on a clear day). Fiber optic access systems have now become a very important solution to support next generation Fiber To The X (FTTx) applications (**Grobe and Elbers**, **2008**), FTTx is a solution based on a fiber-optic-based network architecture commonly known as passive optical networks (PON). They are supposed to provide a large capacity due to the very large bandwidth **(Banerjee et al., 2005**). Many architectures have proposed an upgrade of a PON network based on an increased number of channels using wavelength division multiplexing (WDM) techniques commonly referred to as a wavelength-multiplexed passive optical network. This system uses multiple wavelengths in a single optical fiber (**De Andrade et al., 2013**). We need to assign each user a permanent wavelength, which requires two pairs of transmitter and receiver to form point-to-point communication **(Zhang et al., 2010**). Among the existing techniques adopted to PON networks is the OCDMA technique (**Nowshin et al**, **2012**). This technique allows users to access the same optical network by sharing optical bandwidth to build optical codes (**Kandouci and Djebbari, 2016**).

In this present work we have proposed a system based on the OCDMA multiplexing technique which allows encoding operations to be carried out; we therefore speak of SAC OCDMA (Spectral Amplitude Coding optical code division multiple access) (**Kalos et al., 2012)**. This technique is used to reduce the problem of multiple access interference (MAI) in optical CDMA systems (**Driz and Djebbari, 2019)**. The encoding and decoding process with the SAC OCDMA technique is done with WDM multiplexing / demultiplexing, which allows each user to be assigned a spectral code in order to build their spectral signature (**Djellab et al., 2018)**. WDM multi-channel modulation is one of the most promising techniques in FSO systems **(Malik and Singh, 2014)**. WDM is an optical technology where many channels are multiplexed with each other, (**Majumdar, 2014)**. The system proposed in (**Singh, 2018)** provides an efficient solution to increase the capacity of the channel. Here, (**Robinson and Jasmine, 2016)** reports an analysis of an FSO link based on the WDM multiplexing technique in order to increase the capacity of the system under various adverse weather conditions. In (**Dayal et al., 2017)**, a hybrid configuration of optical amplifiers in a WDM-based FSO link is demonstrated. The results presented in (**Grover et al., 2018)** show that using the multi-beam FSO-WDM system, link performance is improved in different weather conditions.

Visible light communication (VLC) has emerged to cater for multiple users and thus provide a reliable link in fiber-based passive optical networks (**Kaur et al., 2019)**. Primarily, this communication technique is intended for indoor applications to create last-meter connections. VLC is a new area of research that uses LEDs to transmit information from one point to another (**Wang et al., 2017)**. It combines lighting with communication techniques (**Chi, 2018)**. Its advantages are broad spectrum, high energy efficiency and easy handling. Its cost is low and its lifespan is long.

In this work, we have proposed a hybrid FSO-OF-VLC system. The FSO link is used to achieve the outdoor connectivity between buildings. The received signal is distributed to the various offices via fiber optic based connections to create the passive optical network. Finally, VLC technology is made to connect the different users inside the building. The proposed system is designed to guarantee "all optical" communication in order not to lose speed. This work was carried out using the OPTISYSTEM 17.0 simulation software. The performance analysis was done in terms of Q factor and eye diagram. The rest of this article is structured as follows: In section 2, the theoretical model is proposed. Section 3 studies and discusses the different simulations and a conclusion is given in Section 4.

Creative Commons Attribution-NonCommercial-NoDerivatives 4.0 International License (CC BY-NC-ND)

Problematic:
Wireless transmissions based on visible light and infrared provide a bandwidth not yet matched with radiofrequency techniques. In this work, we wanted to communicate two remote users who are not in line of sight. In order not to reduce the bandwidth of the transmission channel, and therefore to be able to increase the number of users, we have decided to use only optical techniques. For the transmission in free space, we used lasers. Indoor transmission is provided by an optical fiber and VLC visible light communication provides a mobile link.

II. Theoretical model

In this section we will study the different channel models used in our system, namely the FSO channel, the optical fiber and the VLC channel.

FSO link

FSO transmission is similar to the conventional fiber optic system. Both links use light to transport information. FSO is however sensitive to atmospheric attenuations caused by changes in environmental conditions. This attenuation phenomenon is the main challenge affecting the performance of outdoor wireless optical communications (**Alnajjar et al., 2019**). The signal attenuation is calculated on reception. It varies depending on atmospheric conditions according to the Beer-Lambert law. The attenuation of an optical beam during its propagation in air is defined by the ratio between the power received and the power transmitted. It can be calculated using the following equation:

$$A_{ATM} = \frac{P_R}{P_T} = e^{-\alpha L} \tag{1}$$

Where α is the attenuation coefficient and L is the distance from the link (in km). The determination of the values of the atmospheric attenuation coefficients α is possible using a rough estimate based on the visibility and the wavelength. It is given by the following relation (**Kim et al., 2001**):

$$\alpha = \frac{3.912}{V}\left(\frac{\lambda}{550(nm)}\right)^{-q} \tag{2}$$

Where α denotes the attenuation coefficient, V, λ and q respectively represent the visibility vector in km, the wavelength in nm and the scattering particle size distribution coefficient. The coefficient q could be defined from the models of KIM, KRUSE and AL NABOULSI. The values of q can be obtained from the KRUSE model (**Kruse et al., 1962**)

$$q = \begin{cases} 1.6 & for\ V > 50 \\ 1.3 & for\ 6 < V < 50 \\ 0.585.V^{\frac{1}{3}} & for\ V < 6 \end{cases} \tag{3}$$

Parameter q has the following values according to the KIM model (**Kim et al., 2001**)

Creative Commons Attribution-NonCommercial-NoDerivatives 4.0 International License (CC BY-NC-ND)

$$q = \begin{cases} 1.6 \ \ for \ V > 50 \\ 1.3 \ for \ \ 6 < V < 50 \\ 0.16V + 0.34 \ for \ 1 < V < 6 \\ V - 0.5 \ \ for \ \ 0.5 < V < 1 \\ 0 \ \ for \ V < 0.5 \end{cases} \quad (4)$$

Several studies have shown that fog is the most critical effect for free-space optical communication systems and can cause fatal degradation in performance. Optical attenuation can reach up to 340 dB / km in fog with visibility of 50 m. In this regard, an approximation of the attenuation for two types of fog on wavelengths varying between 0.69 and 1.55 µm and a visibility between 50 and 1000 m, was developed by Al Naboulsi and can be put in the following form (**Al Naboulsi et al., 2004**):

$$\sigma_{Adv} = \frac{0.11478\,\lambda + 3.8367}{V} \quad (5)$$

$$\sigma_{Rad} = \frac{0.18126\,\lambda^2 + 0.13709\,\lambda + 3.7502}{V} \quad (6)$$

Optical fiber

Recently we have seen a change in access networks. It is well known that conventional access networks based on traditional means such as copper have quite limited bandwidth capacity, so they cannot meet current needs. A new transmission technology has gradually replaced these technologies and supports bandwidth and throughput requirements. This growth is driven by new services such as high definition television (HDTV) and video services (**Lee et al., 2006**). For long distance and broadband systems, FTTx are generally used to realize next generation fiber optic access networks (**Rajalakshmi et al., 2012**). Optical fibers have many advantages such as low cost, high bandwidth, low attenuation and finally they are purely dielectric waveguides, so they are insensitive to electromagnetic interference (**Kumar and Deen**, **2014**).Passive optical networks have become one of the new solutions that have grown enormously in recent years to implement next generation FTTx applications (**Garg and Janyani, 2015**). The optical fiber is used to carry the optical signal from the FSO to the VLC system. Optical fiber is characterized by very low attenuation, in the order of 0.2 dB / km. In our case, this attenuation is insignificant and certainly does not depend on weather conditions as is the case with the FSO system.

VLC channel model

Recent advances in wireless services have created a new optical transmission technology based on visible radiation to eliminate the problem of the unavailability of the radio frequency spectrum. In addition, it constitutes a method of high-speed wireless optical transmission. The idea of this type of communication is to transfer data in a path that uses light as a signal that carries information (**Matheus et al., 2019**). In VLC (**Anwar et al., 2019**), emitters are generally diodes, they can be light emitting diodes (LEDs) or laser diodes (LD). Photodiodes (PD) are used as receivers. Usually, light-emitting diodes are the most feasible components in VLC not only because of their low costs but also the absence of electromagnetic disturbance despite the wide band available between the color blue at 380nm and the color red at 760nm. This communication technology is now becoming a method that meets today's needs such as communication and lighting **(Saadi et al., 2013)**. This technology is primarily intended for

Creative Commons Attribution-NonCommercial-NoDerivatives 4.0 International License (CC BY-NC-ND)

indoor applications to provide last-meter access networks. Two types of links are used in VLC transmission configurations depending on the absence (NLOS) or presence (LOS) of a direct path between sender and receiver. In the LOS link the transmitter must send a narrow beam and the receiver must be in line of sight of the transmitter. Whereas in the NLOS circling link the transmitter has to send a wider beam with a wide FOV (**Djordjevic**, **2018).**
In general, when it comes to indoor VLC systems, the requested mechanism is based on a direct LOS link, as shown in Figure 1, where the receiver must be within sight of the transmitter (FOV Field of view)

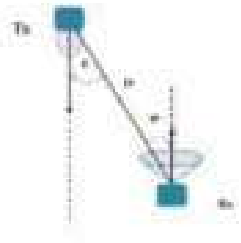

Fig 1. LOS channel model (Lambertian source) (**Djordjevic**, **2018)**

The transceiver link in VLC can be modeled as Lambertian sources. This principle is generally used to study the intensity radiated from the LED lamp through the channels of the line of sight (LOS). It is characterized by its Lambertian order (m) and the angle between the emitter and the axis normal from the same transmitter $\boldsymbol{\varphi}$. Lambertian radiant intensity is defined as **(Zhang et al., 2019)**:

$$R_0(\varphi) = \frac{m+1}{2\pi}\cos^m \varphi \tag{7}$$

Where $R_0(\varphi)$ the angular distribution of the radiated intensity of a Lambertian emitter and m the generalized Lambertian order of the emitter given by:

$$m = -\frac{ln(2)}{ln(\cos(\varphi_{1/2}))} \tag{8}$$

The Lambertian order m depends on a characteristic called the half-power angle of the source noted $(\varphi_{(1/2)})$ It corresponds to half of the optical power received.

Simulation design
Figure 2 shows the complete diagram of the FSO-OF-VLC hybrid optical transmission chain. The transmitter consists of a data generator, a non-return-to-zero (NRZ) pulse generator, a laser diode and a Mach-Zehnder modulator. The receiver is composed of a photodiode and a set of filters. As for the transmission channel, it is composed of an FSO channel, an optical fiber and a VLC system. The FSO links two distant points using free space as a propagation channel. Fiber optic links the FSO to the end user and the VLC system allows the end user to enjoy room-level mobility. The simulations were carried out for different attenuations (10dB / km up to 100dB / km).

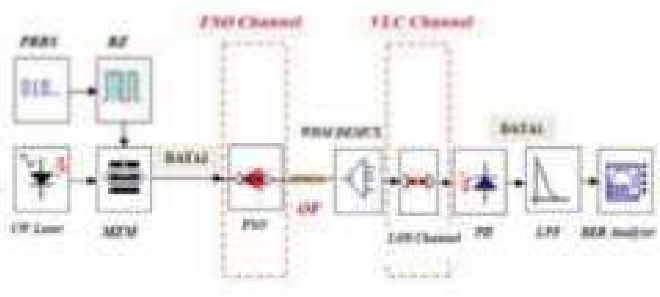

Fig 2. Block diagram of FSO-OF-VLC link.

The parameters used in the simulation are listed in table 3.

Operating parameters	Value
FSO wavelength	1550 nm
Transmission rate	10 Gbps
Transmission power	875 mw
Distance	100-800 m
Attenuation	10-100dB/km
lens diameter (emitter)	5 cm
lens diameter (receiver)	20 cm
Optical fiber length	0.25 km

Table1. Simulations parameters.

Figure 3 shows schematically the proposed model.

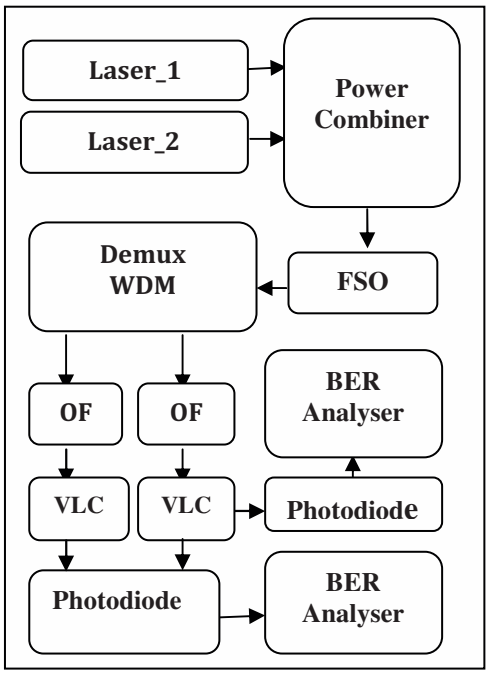

Fig 3. Diagram of the system proposed to increase the number of users

The modulated signals from the two users are injected into a power combiner. The signal thus formed is transmitted through the FSO channel. The WDM Demultiplexer separates the two signals. So we have two signals with two identical transmission channels, each composed of an optical fiber and a VLC system.

Results and discussions

Creative Commons Attribution-NonCommercial-NoDerivatives 4.0 International License (CC BY-NC-ND)

In this article, an FSO-OF-VLC link was studied and simulated using the optisystem 17.0 simulation software for different attenuations. The proposed system is designed to operate at the wavelength of 1550 nm and for a link distance varying from 100 m up to 800 m. The performance of the proposed system was analyzed and compared on the basis of the Q factor. Figure 4 shows the evolution of the Q factor as a function of the length of the FSO channel for 3 values of the attenuation which represents meteorological conditions. The results obtained using the BER analyzer clearly shows that for different attenuations; the distance severely affects the performance of the system.

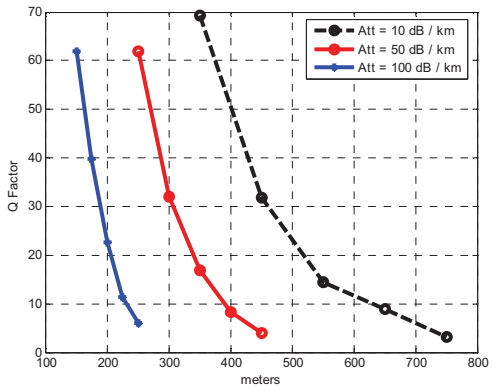

Fig 4. Evolution of the Q factor as a function of distance.

We notice that if the length of the FSO channel is long then the signal quality deteriorates. This deterioration is more accentuated if the attenuation due to weather conditions is great. Indeed, for an attenuation of 10 dB / km and for a distance which varies from 350 meters to 750 meters, the quality factor goes from 70 to 5. While for an attenuation of 100 dB / km, the quality factor Q varies from 62 to 5 for a variation distance of only 150 to 250 meters. In this analysis, we see that the performance degradation results from the increased attenuation due to weather conditions and the link distance between the transmitter and receiver in free space.
Figure 5 shows the change in the Q factor as a function of the attenuation due to weather conditions for 3 values of the length of the FSO channel. Indeed, the performance for a distance of 750 meters deteriorates when the attenuation reaches 25dB / km while for a distance of 250 meters, the deterioration in performance is felt from 90dB / km. We notice that if the attenuation is great then the signal quality deteriorates. This deterioration is more accentuated if the length of the FSO channel is long. Indeed, for a distance of 250 meters, and for an attenuation of 50 dB / km, the quality factor is equal to 55. Whereas, for a distance of 750 meters, the quality factor is equal to 48 for an attenuation equal to 5 dB/km. This quality factor deteriorates rapidly as attenuation increases.

Creative Commons Attribution-NonCommercial-NoDerivatives 4.0 International License (CC BY-NC-ND)

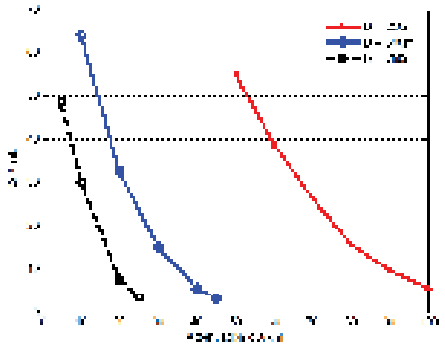

Fig 5. Evolution of the Q factor as a function of the attenuation.

Figure 6 (a) shows the eye diagram for attenuation = 100 dB / km and distance of 250 meters. The quality factor Q is equal to 6.3 and Figure 8(b) shows the eye diagram for attenuation = 10 dB / km and a distance of 750 meters. The quality factor Q is equal to 27.7.

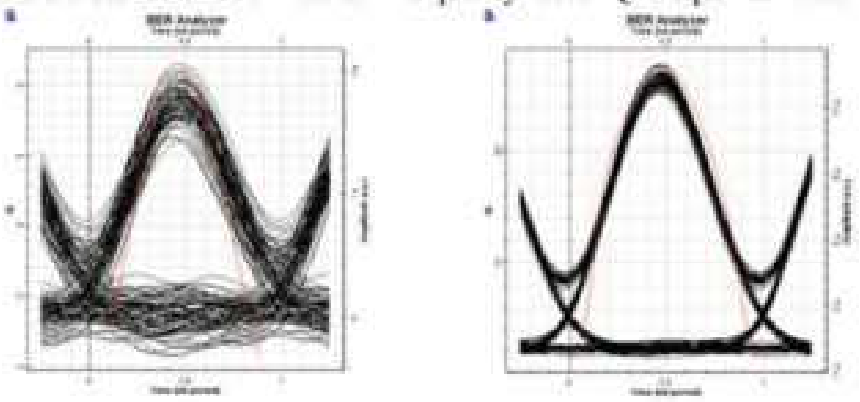

(a) (b)

Fig 6. Eye diagram for (a) a distance d = 250 meters and attenuation = 100 dB / km (b) a distance of 750 meters and attenuation = 10 dB / km

Figure 7 shows a two-user FSO-OF-VLC link. The signals from the two modulators are fed into a power combiner. At the receiver, a bidirectional WDM demodulator is used to separate the two signals. Each signal is routed to end users who are equipped with a VLC system to activate a wireless link. At the transmitter level, the transmitted signal may consist of a single wavelength, but may also consist of a set of wavelengths formed by the optical code of the OCDMA modulation.

Creative Commons Attribution-NonCommercial-No Derivatives 4.0 International License (CC BY-NC-ND)

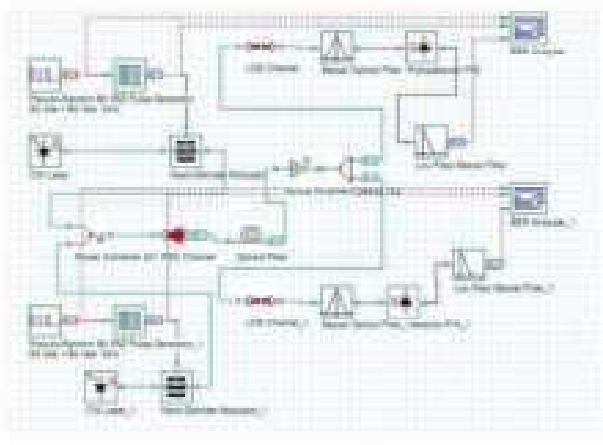

Fig 7. FSO-OF-VLC transmission chain for two users

Conclusion:

In this work, an FSO-OF-VLC link was simulated under different weather conditions and with different distances. This technique has allowed us to achieve 'all-optical transmission' from the transmitter to the receiver. By using SAC-OCDMA modulation and using the very wide bandwidth available for optical transmissions, we can increase the number of users. The proposed solution is designed to achieve both internal connectivity in the access networks of the last meter for the purpose of sharing the received data to end users and external connectivity in last mile access networks. The optical fiber is used to connect the signal from the FSO to the different rooms where the different users are located.

References:

Y. L. Yu, S. K. Liaw, H. H. Chou, H. Le-Minh, and Z. Ghassemlooy, 2015,'A Hybrid Optical Fiber and FSO System for Bidirectional Communications Used in Bridges,' *IEEE Photonics J.*, vol. 7, no. 6, pp. 1–9.

M. Singh, 2017 "Mitigating the Effects of Fog Attenuation in FSO Communication Link Using Multiple Transceivers and EDFA," *J. Opt. Commun.*, vol. 38, no. 2, pp. 169–174.

H. Kaushal and G. Kaddoum, 2017 "Optical Communication in Space: Challenges and Mitigation Techniques," *IEEE Commun. Surv. Tutorials*, vol. 19, no. 1, pp. 57–96.

A. Sharma and R. S. Kaler, 2012 "Designing of high speed inter building connectivity by free space optical link with radio frequency backup," *IET Commun.*, vol. 6, no. 16, pp. 2568–2574.

H. A. Willebrand and B. S. Ghuman, 2001 "Fiber Optic Without Fiber Light Pointe Communicattens," *Spectrum, IEEE*, vol. 38, no. 8, pp. 40–45.

I. K. Son and S. Mao, 2016 "Author ' s Accepted Manuscript A Survey of Free Space Optical Networks Reference : To appear in : Digital Communications and Networks," *Digit. Commun. Networks*.

G. Shanlev, J. Patel, B. Whitlock, P. Mena, and R. Scarmozzino, 2005,'Simulation-assisted design of free space optical transmission systems,' in *MILCOM 2005 2005 IEEE Military Communications Conference*, pp. 918–922: IEEE.

Creative Commons Attribution-NonCommercial-No Derivatives 4.0 International License (CC BY-NC-ND)

A. Sharma and R. S. Kaler, 2012 "Designing of high-speed inter-building connectivity by free space optical link with radio frequency backup," *IET Commun.*, vol. 6, no. 16, pp. 2568–2574.

E. Farooq, A. Sahu, and S. K. Gupta, 2018 "Survey on FSO Communication system—limitations and enhancement techniques," *Lect. Notes Electr. Eng.*, vol. 472, pp. 255–264.

M. A. Khalighi, M. Uysal, C. Marseille, and E. Engineering, 2014 "Survey on Free Space Optical Communication : A Communication Theory Perspective," no. c, pp. 1–29.

N. Kumar and H. Sohal, 2014 "Impact of Various Weather Condition on the Performance of Free Space Optical Communication System," vol. 35, no. 1, pp. 45–49.

M. Ijaz *et al.*, 2013 "Experimental validation of fog models for FSO under laboratory controlled conditions," in *2013 IEEE 24th Annual International Symposium on Personal, Indoor, and Mobile Radio Communications (PIMRC)*, pp. 19-23: IEEE.

M. L. Tayebi, A. Djir, and F. Meskine, 2020 "Performance evaluation of a multiple optical link FSO–FSO," *J. Opt. Commun.*, vol. 1.

L. Mesri and A. Djebbari, 2018 "Performance Limits of FSO Based SAC-OCDMA System under Weather Conditions," J. Opt. Commun., pp. 1–8.

K. Grobe and J.-P. Elbers, , 2008 "PON in adolescence: from TDMA to WDM-PON," *IEEE Communications Magazine,* vol. 46, no. 1, pp. 26-34.

J. Prat, , 2008"Next-generation FTTH passive optical networks," *Springer Science+ Business Media BV*.

A. K. Garg and V. Janyani, , 2015"Analysis of OOK Upstream Signal Remodulation for Different Data Rates in WDM PON Network," *International Journal of Signal Processing Systems,* vol. 3, no. 2, pp. 134-138.

A. Banerjee *et al* 2005, "Wavelength-division-multiplexed passive optical network (WDM-PON) technologies for broadband access: a review," *Journal of optical networking,* vol. 4, no. 11, pp. 737-758.

M. De Andrade, M. Tornatore, and A. Pattavina, 2013 "Optimization scheme for WDM-based transmission technology selection in future passive optical networks," *Journal of Optical Communications and Networking,* vol. 5, no. 9, pp. 1010-1020.

F. Zhang, S. Fu, J. Wu, K. Xu, J. Lin, and P. Shum, 2010 "A wavelength-division-multiplexed passive optical network with simultaneous centralized light source and broadcast capability," *IEEE Photonics Journal,* vol. 2, no. 3, pp. 445-453.

F. Effenberger *et al.* 2007, "An introduction to PON technologies [Topics in Optical Communications]," *IEEE Communications Magazine,* vol. 45, no. 3, pp. S17-S25.

N. Nowshin, A. K. M. Arifuzzman, M. Tarique, and S. Member, 2012 "System for Next-Generation Fiber Optic Communication," pp. 573–577.

C. Kandouci and A. Djebbari, 2016 "Design of new hybrid Wavelength Hopping/Time Spreading codes for Optical CDMA by combining OCC and BIBD ZCC codes," *Opt. - Int. J. Light Electron Opt.*.

R. Kalos *et al.*, 2012 "Performance of SAC OCDMA-FSO communication systems," *Opt. - Int. J. Light Electron Opt.*, pp. 9–11.

S. Driz and A. Djebbari, 2019 "Performance Evaluation of Sub-carrier Multiplexed SAC-OCDMA System Using Optimal Modulation Index," J. Opt. Commun., vol. 40, no. 1, pp. 83–92.

Creative Commons Attribution-NonCommercial-NoDerivatives 4.0 International License (CC BY-NC-ND)

H. Djellab, N. Doghmane, A. Bouarfa, and M. Kandouci, 2018 "Study of the Different Optical Filters in SAC-OCDMA System," *Journal of Optical Communications,* vol. 39, no. 4, pp. 381-386.

Aditi Malik and Preeti Singh, 2014 "Comparative Analysis of Point to Point FSO System Under Clear and Haze Weather Conditions," *Wirel. Pers. Commun.*, vol. 80, no. 2, pp. 483–492.

A. K. Majumdar, 2014 *Advanced free space optics (FSO): A systems approach*. Springer.

M. Singh, 2018 "Performance analysis of WDM-FSO system under adverse weather conditions," *Photonic Netw. Commun.*

S. Robinson and S. Jasmine, 2016 "Performance Analysis of Hybrid WDM-FSO System under Various Weather Conditions," pp. 1–9.

N. Dayal, P. Singh, and P. Kaur, 2017 "Long Range Cost-Effective WDM-FSO System Using Hybrid Optical Amplifiers Long Range Cost-Effective WDM-FSO System Using," *Wirel. Pers. Commun.*, no. August, ,

M. Grover, P. Singh, and P. Kaur, 2018 "Performance Analysis of Multibeam WDM-FSO System in Clear and Hazy Performance Analysis of Multibeam WDM-FSO System in Clear and Hazy Weather Conditions,".

S. Kaur, M. Kumar, and A. Verma, 2019"An Integrated High-Speed Full Duplex Coherent OFDM-PON and Visible-Light Communication System," *Journal of Optical Communications,* vol. 1, no. ahead-of-print,.

Z. Wang, Q. Wang, W. Huang, and Z. Xu, 2017 *Visible light communications: modulation and signal processing*. John Wiley & Sons.

N. Chi, 2018 LED-based visible light Communications. Springer.

S. H. Alnajjar, M. H. Ali, and A. Abass, 2019 "Enhancing Performance of Hybrid FSO/Fiber Optic Communication Link Utilizing Multi-Channel Configuration," Journal of Optical Communications, vol. 1, no. ahead-of-print.

Kim I.I., McArthur B., Korevaar; 2001 "Comparison of laser beam propagation at 785 nm and 1550 nm in fog and haze for optical wireless communications", Proc. SPIE, 4214, 26-37.

Kruse P.W. and al. 1962; "Elements of infrared technology: Generation, transmission and detection", J. Wiley and sons, New York.

M. C. Al Naboulsi, H. Sizun, and F. de Fornel, 2004"Fog attenuation prediction for optical and infrared waves," *Optical Engineering,* vol. 43, no. 2, pp. 319-330.

C.-H. Lee, W. V. Sorin, and B. Y. Kim, 2006 "Fiber to the home using a PON infrastructure," *Journal of lightwave technology,* vol. 24, no. 12, pp. 4568-4583,

S. Rajalakshmi, A. Srivastava, and A. Pandey, 2012"Performance analysis of receivers in WDM for extended reach passive optical networks," *International Journal of Computer Science (IJCSI),* vol. 9, no. 2, pp. 217-222.

S. Kumar and M. J. Deen, **2014** *Fiber optic communications: fundamentals and applications*. John Wiley & Sons.

A**. K. Garg and V. Janyani, 2015**"Analysis of OOK Upstream Signal Remodulation for Different Data Rates in WDM PON Network," *International Journal of Signal Processing Systems,* vol. 3, no. 2, pp. 134-138,.

Creative Commons Attribution-NonCommercial-NoDerivatives 4.0 International License (CC BY-NC-ND)

S. Mostafa, A. E. N. A. Mohamed, F. E. A. El-Samie, and A. N. Z. Rashed, 2017, "Performance Evaluation of SAC-OCDMA System in Free Space Optics and Optical Fiber System Based on Different Types of Codes," *Wirel. Pers. Commun.*, vol. 96, no. 2, pp. 2843–2861.

L. E. M. Matheus, A. B. Vieira, L. F. M. Vieira, M. A. M. Vieira, and O. Gnawali, **2019** "Visible Light Communication: Concepts, Applications and Challenges," *IEEE Commun. Surv. Tutorials*, vol. 21, no. 4, pp. 3204–3237.

D. N. Anwar, A. Srivastava, and V. A. Bohara, **2019** "Adaptive channel estimation in VLC for dynamic indoor environment," *Int. Conf. Transparent Opt. Networks*, vol. 2019-July, no. 0, pp. 1–5.

M. Saadi, L. Wattisuttikulkij, Y. Zhao, and P. Sangwongngam, **2013** "Visible Light Communication : Opportunities , Challenges and Channel Models," *Int. J. Electron. Informatics*, vol. 2, no. 1, pp. 1–11.

I**. B. Djordjevic**, **2018** *Advanced optical and wireless communications systems*. Springer.

S. Zhang, P. Du, C. Chen, W. De Zhong, and A. Alphones, 2019 "Robust 3D Indoor VLP System Based on ANN Using Hybrid RSS/PDOA," *IEEE Access*, vol. 7, pp. 47769–47780.

Creative Commons Attribution-NonCommercial-NoDerivatives 4.0 International License (CC BY-NC-ND)

Algerian Journal of Engineering Architecture and Urbanism Vol. 5 Nr. 3 2021
ISSN: 2588-1760

SEGMENTATION FOR DIFFERENT IMAGE MODALITY

Dr. Lalaoui Lahouaoui
Dept electronics, Laboratory LGE department electronics University of M'sila 28000 City Ichbilia M'sila, Algeria,
e-mail: lahouaoui.lalaoui@univ-msila.dz
djaalab abdelhak
Dept electronics, Laboratory LGE department electronics University of M'sila 28000 City Ichbilia M'sila, Algeria,
e-mail: abdelhak.djaalab@univ-msila.dz
Dib Fouad
Dept electronics, Laboratory LGE department electronics University of M'sila 28000 City Ichbilia M'sila, Algeria,
e-mail: fouad.dib@univ-msila.dz

Abstract:
In this paper, we presented comparative methods for image segmentation. There are several existing techniques, which used for image segmentation. These all techniques have their own importance. These all techniques can be approached from two basic approaches of segmentation i.e. region based or edge based approaches. Every technique can applied on different images to perform required segmentation. These all techniques also can classified into three categories The Segmentation of different modality images is an important step in forming realistic tissue models. Current segmentation approaches reviewed with an emphasis placed on revealing the advantages and disadvantages of these methods for medical imaging applications. To assist in classifying the relevant literature, there many methods for image segmentation image, we used a method witch based region segmentation. Segmentation of medical images is an important step in forming realistic tissue models. Segmentation of the image is an image processing operation, particularly in the medical field. Diagnostic imaging is an invaluable tool in medicine today. Magnetic resonance imaging (MRI), computed tomography (CT), digital mammography, and other imaging modalities provide an effective means for noninvasively mapping the anatomy of a subject. The segmentation of medical images is of paramount importance in the diagnosis and detection of various pathologies. We present in this paper a comparative study of segmentation methods by region such Fuzzy C-Means, K-Means, Meanshift and EM, where the results obtained are evaluated by three criteria: IntraInter_LN, Intra_LN, CritAtt, we used medical images base and x-ray image image Ultra Sound. The diversity of segmentation methods offers us several ways to segment the image. Always look for the EM method to get good results.
Key words: Image segmentation, modality of image, criteria for evaluation

Introduction:

Digital image processing is the use of computer algorithms to perform image processing on digital images. Image segmentation is an important and challenging process of image processing. Image segmentation technique is used to partition an image into meaningful parts having similar features and properties.

Image processing is an invaluable tool in domain different such as medicine, military etc... Magnetic resonance imaging (MRI), computed tomography (CT), digital mammography, and other imaging modalities provide an effective means for noninvasively mapping the anatomy of a subject. These technologies have greatly increased knowledge of normal and diseased

Creative Commons Attribution-NonCommercial-NoDerivatives 4.0 International License (CC BY-NC-ND)

anatomy for medical research and are a critical component in diagnosis and treatment planning. X-ray segmentation methods have received a considerable amount of attention recently. X-ray segmentation is challenging as X-ray images have a complex nature. .

In this paper, we used the approach in which an image is segmented into regions based on discontinuity. The edge detection based segmentation falls in this category in which edges formed due to intensity discontinuity y are detected and linked to form boundaries of regions

Several segmentation techniques have been developed and reported in the literature. The aim of segmentation of MRI Brain images is to Study anatomical structure, Identify region of interest: locate tumor, others abnormalities, measure tissue size (to follow the evolution of tumor) and help in treatment planning prior to radiation therapy (radiation dose calculation). However, the segmentation of MRI Brain images has remained a challenge in image segmentation. In addition, this is due to partial volume effects, motion (patient movement, blood circulation and respiration), the existence of image noise, the presence of smoothly varying intensity in-homogeneity, the fact that different anatomical structures may share the same tissue contrast and large amounts of data to be processed. For these and others many approaches have been studied, including Methods based edge [Kalavathi, 2013][Cheng, Chen, 2007][Karras and Mertzios, 2003], methods based region [Lisowski, et all, 2011], Methods based on thresholding [Tohka, et all, 2010][Sharma, et all, 2008], methods based artificial neural networks [Stella and Mackiewich, 2009], data fusion methods [Anami, and Unki, 2013], and hybrid Methods [Dempster, Laird, and Rubin, 1997].

This paper is organized as follows. In Section 2, common terminology and issues associated with the segmentation of different modality images are defined and discussed. In Section 3, we briefly describe methodologies used in common segmentation approaches. In Section 4, we review the ways in which segmentation methods have recently been applied in different imaging modalities. Finally, in Section 5, important issues relating to the future of medical image segmentation are discussed.

Materials and methods:

The simple approaches to segment an image based on the intensity levels and called as threshold-based approach. Threshold based techniques classifies the image into two classes and works on the postulate that pixels belonging to certain range of intensity values represents one class and the rest of the pixels in the image represents the other class. There are several existing techniques, which used for image segmentation. These all techniques have their own importance. These all techniques can be approached from two basic approaches of segmentation i.e. region based or edge based approaches.

Every technique can be applied on different images to perform required segmentation. These all techniques also can classified into three categories. The goal this works is present a comparative study for based image segmentation applied for different modality of image. Image segmentation is an important step perform in image analysis, image processing is a research theme located between computer science and signal processing. In this paper, we presented the results of the different tests on the different images databases. We use the MATLAB to program the segmentation methods by region that we studied on the medical images, then the analysis of the results. We have proposed three criteria to evaluate the

Creative Commons Attribution-NonCommercial-NoDerivatives 4.0 International License (CC BY-NC-ND)

results, this objective as well as subjective criteria allow us to make a decision on the change of image. In this works, I want to present the based image segmentation algorithms.

II.1 A. K-MEANS

This algorithm clusters the point nearest to the centroid. The centroid is the average of all the points in that cluster and has coordinate as the arithmetic mean over all points in the cluster, separately for each dimension.

K-Means algorithm is an unsupervised clustering algorithm that classifies the input data points into multiple classes based on their inherent distance from each other. Macqueen first proposed the iterative K-Means clustering algorithm. The algorithm aims at partitioning the data set, consisting of ℓ expression patterns {x1,..., xℓ} in an n dimensional space, into k disjoint clusters , such that the expression patterns in each cluster are more similar to each other than to the expression patterns in other clusters. There are two popular partitioned clustering strategies: square error and mixture modeling. The sum of the squared Euclidian distances between the samples in a cluster and the cluster center called within-cluster variation. K-Means are widely used in many applications such as data extraction and image segmentation. The K-Means method is an iterative algorithm that minimizes the sum of distances between each object and its cluster centroid.

Steps in K-Means algorithm:

1. Choose the number of clusters K.
2. Select at random K points, the centroids (not necessarily from your dataset).
3. Assign each data point to the closest centroid → that forms K clusters.
4. Compute and place the new centroid of each cluster.
5. Reassign each data point to the new closest centroid. If any reassignment. Took place, go to step 4, otherwise, the model is ready.

II.2 FUZZY C-MEANS (FCM)

In this algorithm, the test pixel allowed to be member of two or more clusters with different membership coefficient. FCM algorithm is iterative in nature, generate fuzzy partition matrix, and requires cluster center along with objective function. The FCM is an unsupervised fuzzy clustering algorithm. Excerpted from the algorithm of C-means, it introduces the concept of fuzzy set in the definition of classes; each point in the data set belongs to each cluster with a certain degree, and all clusters characterized by their center of gravity. The FCM clustering algorithm was first suggested by Dunn and latter improved by Bezdek. The FCM method proposes a fuzzy membership that assigns a degree of membership for each class by iteratively updating the cluster centers and the membership degrees for each data point. The cluster that has an associated pixel is one whose membership degree is highest. A novel approach called enhanced possibility Fuzzy C-Means clustering proposed for segmenting MR brain image into different tissue types on both normal and tumor affected pathological brain images. FCM methods has proposed for the segmentation of MR Images and for the

Creative Commons Attribution-NonCommercial-NoDerivatives 4.0 International License (CC BY-NC-ND)

segmentation of major tissues in litteratury and possible tumor on T1-weighted volumes. The FCM often used in medical image segmentation. Chen et al. have proposed an algorithm based on FCM for the correction of intensity in homogeneity and for segmentation of MRI images. Improved and enhanced FCM clustering algorithms by Tolias, Y. A. and Panas, S. M.(1998) and a Gaussian kernel-based fuzzy c-means algorithm with a spatial bias correction by M.-S. Yang and H.-S. Tsai(2008) have been used to accelerate the image segmentation process and to correct the intensity inhomogeneity during segmentation. FCM is the most effective algorithm for data clustering. FCM was proposed by Dunn and later on it was modified by Bezdek(1980). The standard FCM objective function for partitioning the data into C clusters is given as:

$$J_{\mathrm{FCM}} = (U, V) = \sum_{i=1}^{c} \sum_{k=1}^{N} \mu_{ik}^{p} \left\| x_k - v_i \right\|^2 , \tag{1}$$

II.3 MEAN SHIFT ALGORITHM

Gradient-based methods of feature space analysis use gradients of the probability density function to find the maxima. Such methods are complex because, among other things, of the need for an estimate of the probability of density. The gradient-based methods first calculate the gradient and then the kernel is shifted by a specific length vector in the direction of a maximum increase of density.

The magnitude is the step size which has to be chosen appropriately. The task is how to choose a suitable step size because a small step size will slow down the convergence.

The mean shift algorithm solves the main problem of gradient methods. The main idea of the mean shift is to treat the points in D-dimensional feature space as an empirical probability density function where dense regions correspond to the local maxima of the underlying distribution. Gradient ascent is performed in the feature space on the local density estimation until convergence. After the procedure, stationary points correspond to the modes of the distribution, and the same stationary points are considered members of the same cluster.

The step size of the mean shift is adaptive and depends on the gradient of the density of probability. The gradient is not calculated, instead, a more efficient mean shift vector is calculated. The mean shift vector points in the same direction as the gradient in gradient-based methods.

In contrast to the well known K-means clustering approach, mean shift does not need assumptions on the number of clusters and the shape of the distribution, but its performance relies on the selection of scale parameters. Bandwidth is the only parameter to tune, so for the one-dimensional case this is a relatively simple procedure, but in a multidimensional case, it can be difficult. Mean shift might not work well in higher dimensions.

The mean shift procedure consists of two steps:

1. Construction of probability density in some feature space,
2. The mapping of each point to the maximum (mode) of the density, which is closest to it.

Each data point is shifted to the weighted average of the data set. The mean shift algorithm tries to find stationary points of an estimated Probability Density Function (PDF).

II. 4. Expectation-Maximization (EM) algorithm

Creative Commons Attribution-NonCommercial-NoDerivatives 4.0 International License (CC BY-NC-ND)

K-means algorithm is simple. However, it is easy to get stuck in local optimal. The EM algorithm tends to get stuck less than K-means algorithm. The idea is to assign data points partially to different clusters instead of assigning to only one cluster. To do this partial assignment, we model each cluster using a probabilistic distribution.
So a data point associates with a cluster with certain probability and it belongs to the cluster with the highest probability in the final assignment.
We can use mixture of Gaussian distributions to model this. The mixture model is a weighted sum of K Gaussian distributions. The weights sum up to 1. Let the parameter of jth distribution be θj and its weight be wj , the probability of a data point xi given this model is

$$p(x_i|\Theta) = \sum_{j=1}^{K} w_j p_j(x_i|\theta_j),$$

where $\theta = (w1,\ldots,w_K, \theta_1,\ldots, \theta_k)$.
To do clustering, we want to determine the probability of the cluster Cyi for each data point xi given θ, that is, .

III. Results and discussions:

III.1 Information image IRM

The image below (Fig.1), presents a medical image MRI, a normal cranium, the size of this image 256 × 256 pixel (original, untreated), encoded on 8 bits. In this part, we applied the different methods of segmentation based on regions. In the figures and tables below, we applied four different segmentation methods and three evaluation criteria for the MRI image.

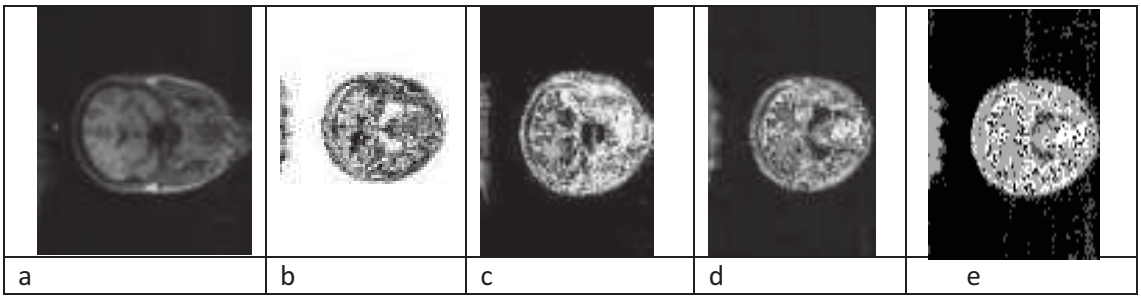

Fig 1 : IRM image segmentation results, a) original image, b) fuzzy C-medium method (FCM), c) k-means method, d) Mean Shifte method, e) Expectation Maximization (EM) method.
Table 1. Segmentation Evaluation Results in Fig.2 for an MRI Image

Criteria and Methods	FCM	KMeans	MeanShift	EM
IntraInter_LN	0.6013	0.6019	0.5836	0.5986
Intra_LN	0.0798	0.0803	0.0179	0.1224
CritAtt	0.1849	0.0255	0.0213	0.0018

III.2 Image information X-ray

In this part, we applied the different methods of segmentation based on regions. In the figures and tables below, we applied four different method of segmentation and three evaluation criteria for the x-ray image. The image below (Fig.2), presents a medical image X-ray, of a normal cranium, the size of this image 256 × 256 pixel, encoded on 8 bits. We found by the site: http: //www.aylward.org/notes/Open-access-medical-image-repositories in the Internet library.

Creative Commons Attribution-NonCommercial-NoDerivatives 4.0 International License (CC BY-NC-ND)

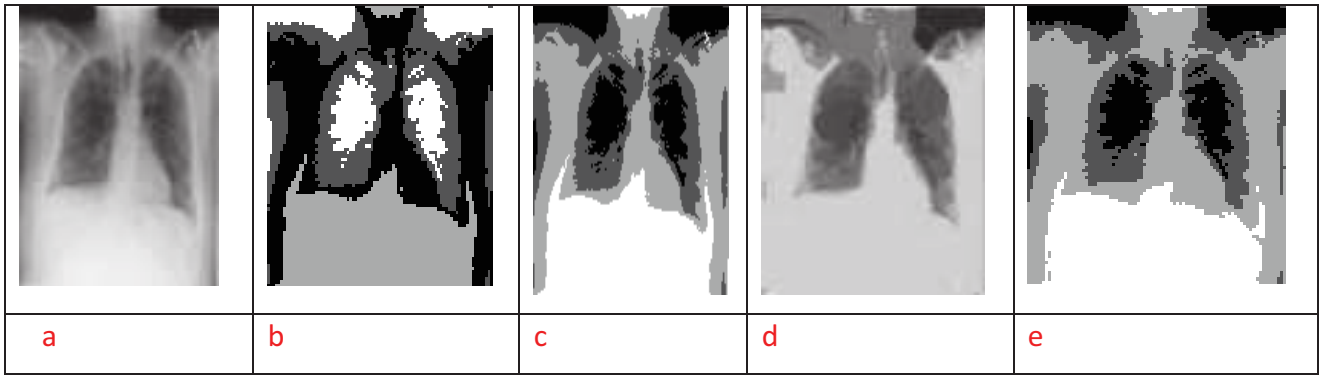

Fig.2: X-ray image segmentation results, a) original image, b) fuzzy C-Means method (FCM), c) k-means method, d) Mean Shift method, e) Expectation Maximization (EM) method

Table 2. Segmentation Evaluation Results in Fig.2 for an X-ray Image

Methods and criteria	FCM	K-means	Mean shift	EM
IntraInter_LN	0.5875	0.5865	0.5741	0.5896
Intra_LN	0.0805	0.0806	0.6648	0.0815
CritAtt	0.2087	0.2971	0 .2322	0.2261

III.3 INFORMATIONS ABOUT ULTRA SOUND

In this part, we applied the different methods of segmentation based on regions. In the figures and tables below, we applied four different methodologies of segmentation and three evaluation criteria for the image Ultra Sound. The image below (Fig.3), presents a medical image Ultra Sound, a normal skull, the size of this 256 × 256 pixel image encoded on 8 bits. We found by the site: http: //www.splab.cz/en/download/databaze/ultrasound in the Internet library.

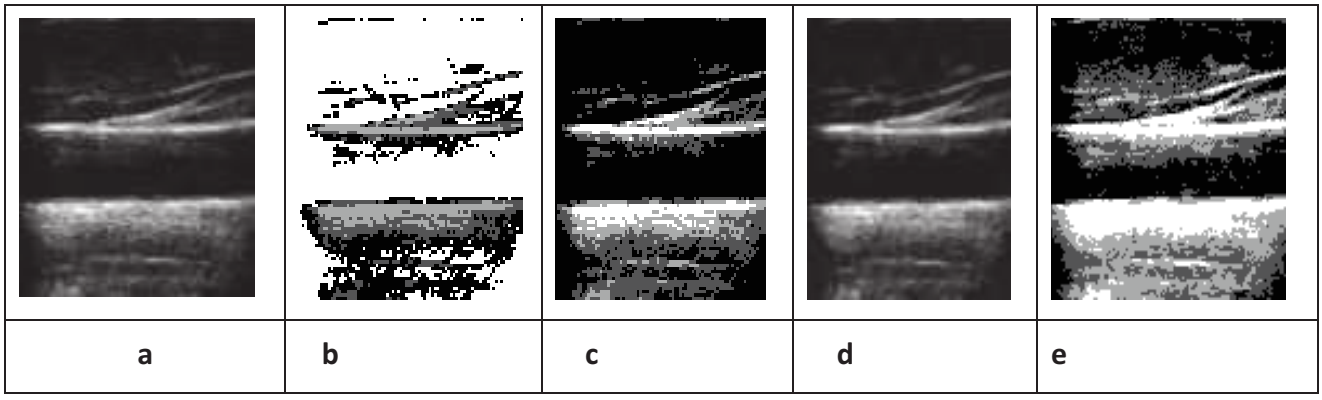

Creative Commons Attribution-NonCommercial-NoDerivatives 4.0 International License (CC BY-NC-ND)

Fig.3 : Ultra sound image segmentation results, a) original image, b) fuzzy C-medium method (FCM), c) k-means method, d) Mean Shifte method, e) Expectation Maximization (EM) method.

Table 3. Segmentation Evaluation Results in Fig.3 for an Ultra Sound Image

Methods and criteria	FCM	K-means	Mean shift	EM
IntraInter_LN	0.5839	0.5845	0.5825	0.5561
Intra_LN	0.0868	0.0852	0.0580	0.1282
CritAtt	0.0502	0.0119	0.0032	0.0014

VI. Conclusion and discussion

We applied four methods of image segmentation by region (FCM, K-Means, Mean Shift, EM) are presented in the previous chapter to segment three sub-bases of images (MRI image, X-ray image, Ultra image Sound.) In addition, the values of the criteria (IntraInter_LN, Intra_LN, CritAtt) and a table is made for each result, this table presents the values of some evaluation criteria without truth in the field.

The segmentation process can be divided into various category based on the parameter selected for segmentation like pixel intensity, homogeneity, discontinuity, cluster data, topology etc. From the previous tables and figures, we noticed that: The results demonstrated that the K-Means segmentation method is the best compared to other magnetic resonance imaging (MRI) segmentation techniques.

The second image x-ray results demonstrated that the segmentation method (EM) is the best. The latest Ultra Sound image demonstrated results that the K-Means segmentation method is the best.

V. Conclusion

The purpose of our study is to compare a set of segmentation methods by region to segment medical images. The unsupervised criteria for evaluating segmentation that are used in this chapter are IntraInter_LN, Intra_LN, CritAtt. The application of these criteria is shown in the above tables that the best values of the criteria are varied. When a value is near to one reflects a very good segmentation result.

The results obtained show that the K-Means method is the best in both types of magnetic resonance images (MRI) and Ultra Sound. Moreover, the method (EM) is the best in the x-ray image.

References:

Kalavathi P. (2013), “Brain Tissue Segmentation in MR Brain Images using Multiple Otsu's Thresholding Technique”. The 8th International Conference on Computer Science & Education (ICCSE) April 26- 28, 2013. Colombo, Sri Lanka.

Cheng C., Chen Y., Lin T. (2007)“FCM Based Automatic Thresholding Algorithm to Segment the Brain MR Image” Machine Learning Machine Learning and Cybernetics, 2007 International Conference on Volume: 3 **Digital** Object IdentifieR;

D.A Karras and B.G. Mertzios.(2003) “On Edge Detection in Mri Using the Wavelet Transform and Unsupervised Neural Networks”, EC-VIP-MC. 4th EURASIP Conference focused on Video I Image Processing and Multimedia Communications, 2-5 July 2003, Zagreb, Croatia

Creative Commons Attribution-NonCommercial-NoDerivatives 4.0 International License (CC BY-NC-ND)

L.**Gui, R. Lisowski, T. Faundez, P.S. Huppi, F. Lazeyras and M. Kocher**.(2011) "Automatic Segmentation of Newborn Brain Mri Using Mathematical morphology". 978-1-4244-4128-0/11/$25.00 IEEE.

J. Tohka, I. D. Dinov, D.W. Shattuck, A.W. Toga. (2010)"Brain MRI tissue classification based on local Markov random fields" Magnetic Resonance Imaging, Volume 28, Issue 4, May, pp 557-573

N. Sharma, A. Ray, S. Sharma, K. Shukla, S. Pradhan and L.(2008)Aggarwal, "Segmentation and Classification of Medical Images using TexturePrimitive Features: Application of BAM-type Artificial Neural Network", Medical Physicists, vol. 33, pp. 119-126.

M. Stella and B. Mackiewich, (2009)"Fully Automated Hybrid Segmentation of Brain, " Handbook of Medical Imaging: Processing and Analysis Management, I. Bankman, Ed,.

B.S. Anami, P.H. Unki.(2013) "A combined fuzzy and level sets based approach for brain MRI image segmentation" Computer Vision, Pattern Recognition, Image Processing and Graphics (NCVPRIPG), 2013 Fourth National Conference on Digital Object Identifier: 10.1109/NCVPRIPG.2013.6776216. pp 1 – 4.

Dempster, A. P., Laird, N. M. and Rubin, D. B. (1997), Maximum likelihood from incomplete data via the EM algorithm. Journal of the Royal Statistical Society. 1977, Vol. 39, 1, pp. 138.

Tolias, Y. A. and Panas, S. M.(1998), "Image segmentation by a fuzzy clustering algorithm using adaptive spatially constrained membership functions," IEEE Transactions on Systems, Man, and Cybernetics—Part A: Systems and Humans., vol. 28, no. 3, pp. 359–369.

Yang, M.-S. and Tsai, H.S.(2008), "A Gaussian kernel-based fuzzy c-means algorithm with a spatial bias correction," Pattern Recognition Letters, vol. 29, no. 12, pp. 1713–1725.

Bezdek, J. C.(1980), "A convergence theorem for the fuzzy ISODATA clustering algorithms," IEEE Transaction on Pattern Analysis and Machine Intelligence, vol. 2, no. 1, pp. 1–8.

Creative Commons Attribution-NonCommercial-NoDerivatives 4.0 International License (CC BY-NC-ND)

Algerian Journal of Engineering Architecture and Urbanism Vol. 5 Nr. 3 2021
ISSN: 2588-1760

POWER QUALITY IMPROVEMENT USING FUZZY LOGIC CONTROL FOR PWM RECTIFIER

Aziz Boukadoum
Labget laboratory, Department of Electrical Engineering, University of Tebessa, Algeria
E-mail: azizboukadoum@yahoo.fr
Tahar Bahi
Department of Electrical Engineering, University of Annaba, Algeria
Abla Bouguerne
Department of Electrical Engineering, University of Tebessa, Algeria

Abstract:
Power electronic equipment constructor family of rectifiers, cause more and more problem in electrical networks, because, which are a nonlinear time varying load topology. They have many problems as following: harmonics pollution and reactive power consumption into the grid because of current waveform distortion. In this paper, to improve the power quality in the grid, and to suppressing harmonics pollution, fuzzy logic controller based PWM rectifier is new technologies to improving the power factor quality and harmonic suppression is presented.
Keywords: Nonlinear load, Harmonics, Fuzzy logic controller, PWM rectifier, Power quality

Introduction

At present, the use of the active power filters (APF) and PWM converters are two typical examples to suppressing harmonic pollution and reactive power compensation. The active power filter and PWM converter named three phase PWM rectifier have basically the same circuit configuration and can operate based on the same control principle.
The PWM converter made a six power transistors (Mosfet) with anti-parallel diodes. These diodes are mainly used to carry out the PWM generation as well as the power bidirectional conversion. The converter is supplied by three-phase source in series with coupling input filter (Malinowski et al., 2001; Marian et al., 1998). This converter have some important advantages: does not produce harmonic distortion in line current, bi-directional power flow, regulation the power factor to unity, adjustment and stabilization of DC voltage and reduced the size of DC filter capacitor (Dixon Juan et al., 1998; Hong, et al., 2001; WEN et al., 2013). In particular, several standards have introduced important and stringent limits on harmonics that can be injected into the power supply (IEEE 519, 1993, International Standard).
In recent years different strategies have been proposed for controlling PWM AC/DC converter. In this paper, fuzzy logic control is proposed to control the three-phase PWM converter. The performances of the converter are evaluated using Matlab/Simulink. The basic structure of the PWM converter is shown in Figure 1.

Creative Commons Attribution-NonCommercial-NoDerivatives 4.0 International License (CC BY-NC-ND)

Algerian Journal of Engineering Architecture and Urbanism Vol. 5 Nr. 3 2021
ISSN: 2588-1760

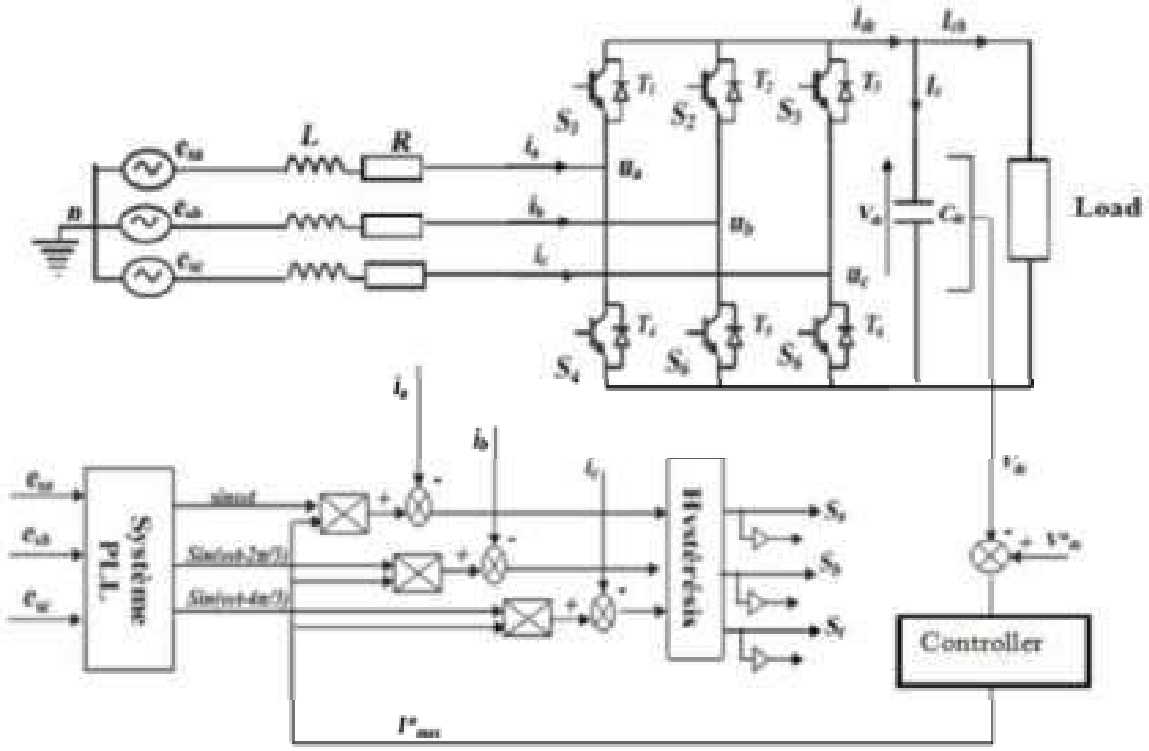

Fig. 1 Strucure of a three-phase PWM AC/DC converter

2 Analytical model of three-phase PWM AC/DC Convert

Three phase voltage source fed AC/DC PWM converter and the lines current are given by :

$$\begin{cases} e_{sa}(t) = E_{\max}\sin(\omega t) \\ e_{sb}(t) = E_{\max}\sin(\omega t - \frac{2\pi}{3}) \\ e_{sc}(t) = E_{\max}\sin(\omega t - \frac{4\pi}{3}) \end{cases} \quad (1)$$

$$\begin{cases} i_a(t) = I_{\max}\sin(\omega t + \varphi) \\ i_b(t) = I_{\max}\sin(\omega t - \frac{2\pi}{3} + \varphi) \\ i_c(t) = I_{\max}\sin(\omega t - \frac{4\pi}{3} + \varphi) \end{cases} \quad (2)$$

Where

E_{max} is the peak value of the input phase voltage and I_{max} is the peak value of the input currents.

With assumption:

$$i_a(t) + i_b(t) + i_c(t) = 0 \quad (3)$$

In α, β stationary system, the equations (1) can be expressed by:

$$\begin{cases} e_{s\alpha}(t) = \frac{\sqrt{3}}{2}E_{\max}\sin(\omega t) \\ e_{s\beta}(t) = \frac{\sqrt{3}}{2}E_{\max}\cos(\omega t) \end{cases} \quad (4)$$

Creative Commons Attribution-NonCommercial-NoDerivatives 4.0 International License (CC BY-NC-ND)

Algerian Journal of Engineering Architecture and Urbanism Vol. 5 Nr. 3 2021
ISSN: 2588-1760

Similarly, the input voltages in the synchronous d-q coordinates are expressed by (Mariusz Cichowlas,. 2004) :

$$\begin{cases} e_{sd}(t) = \dfrac{\sqrt{3}}{2} E_{\max} = \sqrt{e^2 sd + e^2 sq} \\ e_{sq}(t) = 0 \end{cases} \tag{5}$$

Line to line input voltages of PWM AC/DC converter can be described as:

$$\begin{cases} u_{ab} = (S_a - S_b) * V_{dc} \\ u_{bc} = (S_b - S_a) * V_{dc} \\ u_{ca} = (S_c - S_a) * V_{dc} \end{cases} \tag{6}$$

And phase voltages are equal:

$$\begin{cases} v_{sa} = f_a * V_{dc} \\ v_{sb} = f_b * V_{dc} \\ v_{sc} = f_c * V_{dc} \end{cases} \tag{7}$$

Where the switching states of the PWM rectifier are:

$$\begin{bmatrix} f_a \\ f_b \\ f_c \end{bmatrix} = \frac{1}{3} \begin{bmatrix} 2 & -1 & -1 \\ -1 & 2 & -1 \\ -1 & -1 & 2 \end{bmatrix} \begin{bmatrix} S_a \\ S_b \\ S_b \end{bmatrix} \tag{8}$$

The voltage equations for balanced three-phase system without the neutral connection can be written as:

$$\begin{cases} e_{sa} = v_a + Ri_a + L\dfrac{di_a}{dt} \\ e_{sb} = v_b + Ri_b + L\dfrac{di_b}{dt} \\ e_{sc} = v_c + Ri_c + L\dfrac{di_c}{dt} \end{cases} \tag{9}$$

And, additionally for currents is:

$$C\frac{dv_{dc}}{dt} = S_a i_a + S_b i_b + S_c i_c - i_{dc} \tag{10}$$

3 Control Fuzzy logic conroller

The two input quantities are discredited with a sampling period of Ts and normalized by means of normalization gains, (e(k) for the error and Δe(k) for the variation of the error). They are defined by the following expressions, Kessal et al (2012), Konghirun (2007), Panigrahi et al (2014), figure 2.

The DC bus voltage adjustment error is defined by the deviation:

$$e(k) = v^*_{dc}(k) - v_{dc}(k) \tag{11}$$

The incremental variation of the adjustment error is defined by:

$$\Delta e(k) = e(k) - e(k-1) \tag{12}$$

Creative Commons Attribution-NonCommercial-NoDerivatives 4.0 International License (CC BY-NC-ND)

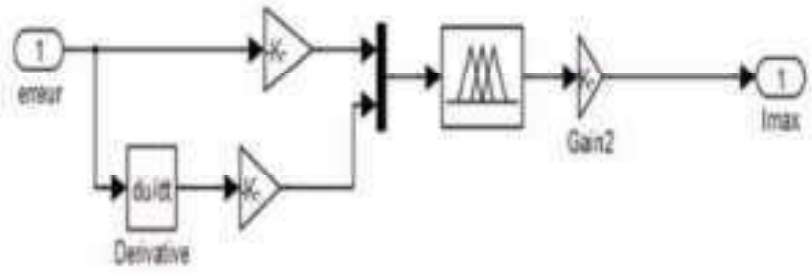

Fig. 2 Internal structure of fuzzy controller

3 Simulation results

To validate the effectiveness of fuzzy logic controller based PWM converter, numerical simulation of the proposed system was carried out using Matlab/Simulink. All spectrums analysis harmonic figures are under the levels imposed by international standards recommendation IEEE 519-1992, in terms of total distortion harmonic (THD).
In the normal condition, the three-phase input voltage waveforms are shown in Figure 3, that the supply voltage generating pure sinusoidal waveforms.

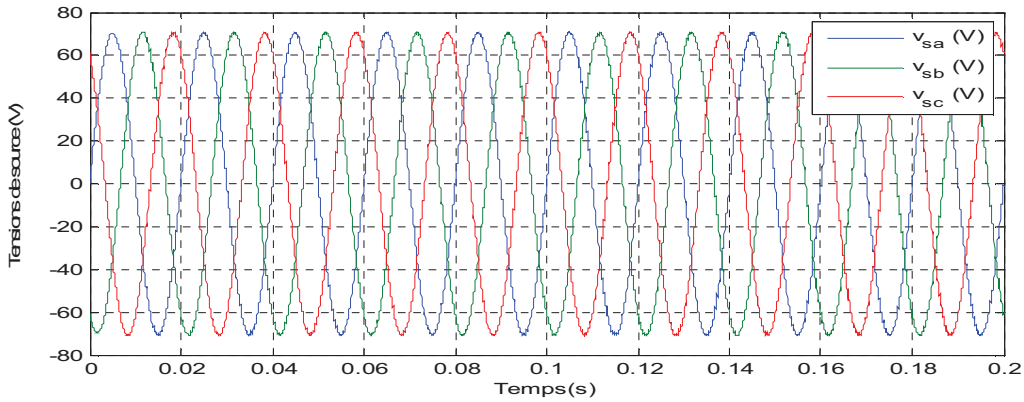

Fig. 3 Input voltages

Figure 4 shows the line currents. In the presence of PWM rectifier, it can be seen that theses currents are sinusoidal.

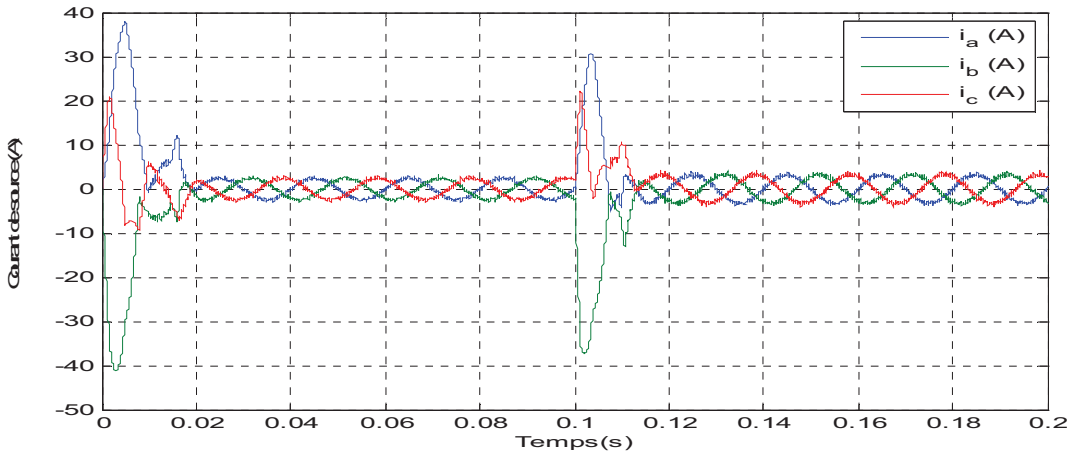

Fig. 4 Input Currents

Creative Commons Attribution-NonCommercial-NoDerivatives 4.0 International License (CC BY-NC-ND)

Figure 5 shows the line current and the input voltage superposition, it's clearly see that the line current is sinusoidal and nearly in-shape with the respective phase voltages.

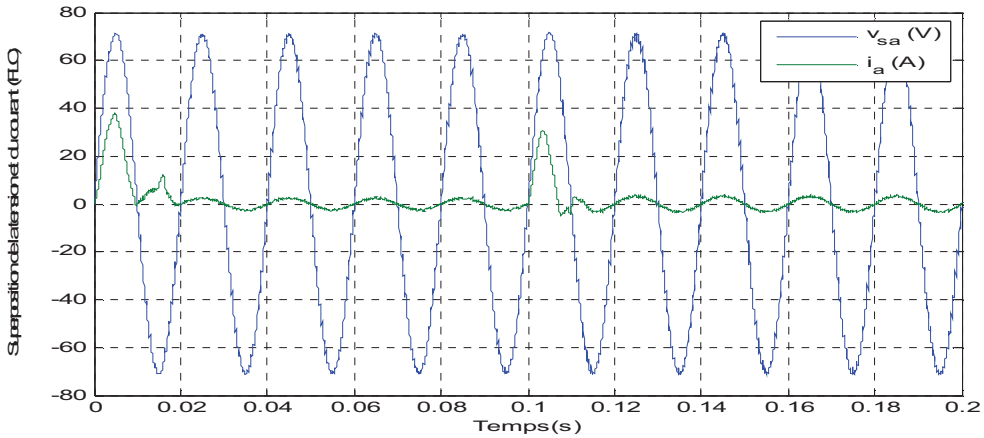

Fig. 5 Superposition between input current and voltage

To test the robustness an effectiveness of fuzzy logic controller, the DC capacitor voltage (V_{dc}) is sensed and compared with the reference value from 140V. We can observe that its value flows up to there, that is the objective of fuzzy logic controller, the reference value have been changed to 160V at t= 0.1s, the DC voltage keeps tracking the reference with good dynamic performance, as shown in Figure 6.

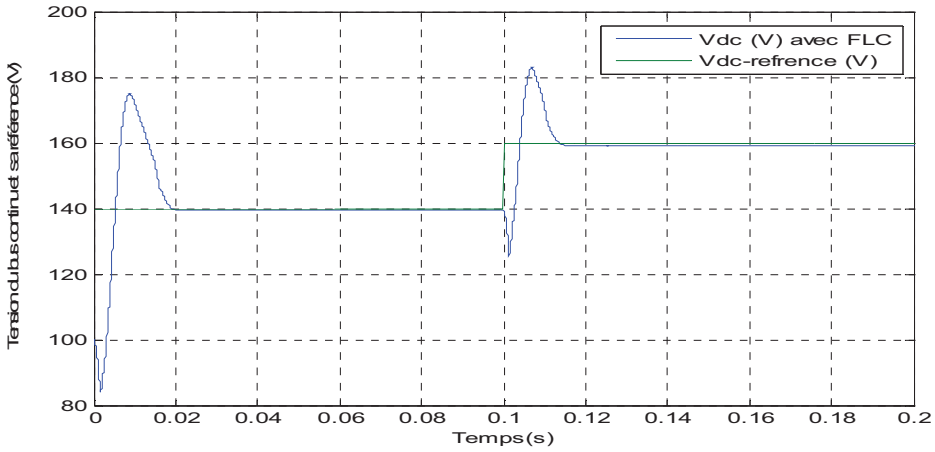

Fig. 6 DC voltage (AC/DC PWM converter)

The active and reactive powers are presented in Figure.7, in this case the reactive power flow is zero consumption, which is very favorable for the system performances and so the power-factor is almost equal to unity, as shown in Figure.8.

Creative Commons Attribution-NonCommercial-NoDerivatives 4.0 International License (CC BY-NC-ND)

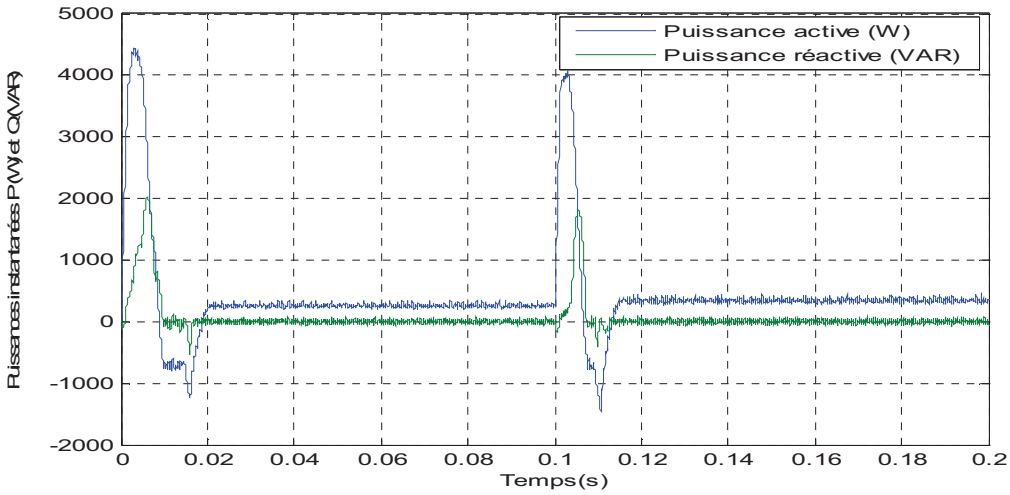

Fig. 7 Instantaneous active and reactive power grid

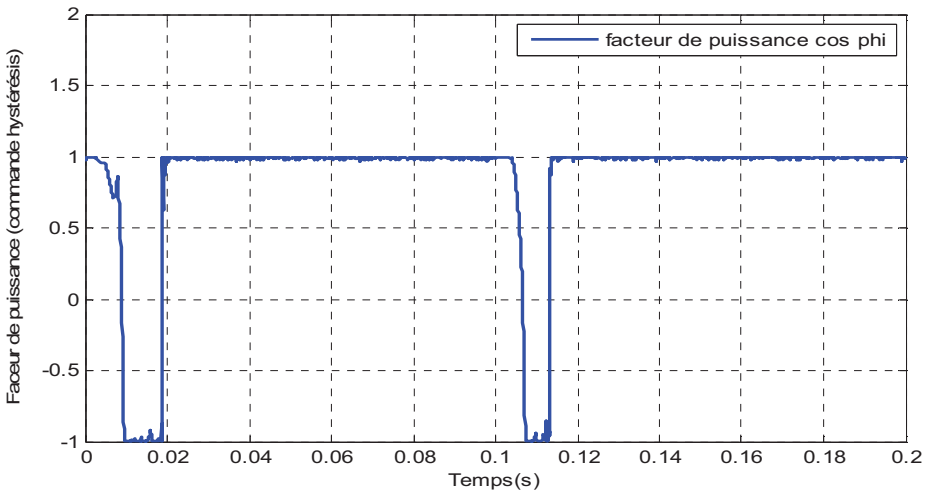

Fig; 8 Power factor

4 Conclusion :

In this paper, we have presented a new improved control structure for PWM converter. It depends on the use of the fuzzy logic controller. The simulation results prove that this control strategy improves the system performances. It illustrates the system response on stabilizing DC voltage, the control of the line sinusoidal currents and unity power factor with perfectly suppressing harmonics. The fuzzy logic controller has an extremely simple and robust structure and provides the excellent dynamic performances. Its gives a PWM converter as a dependable accost effective and solution to power quality.

References:

Malinowski, M., Kaźmierkowski, M.P., Hansen, S., Blaabjerg, F., Marques, G. D., (2001), Virtual flux based Direct Power Control of three-phase PWM rectifier», IEEE Trans. on Ind. Applications, vol. 37, no. 4, pp. 1019-1027.

Creative Commons Attribution-NonCommercial-NoDerivatives 4.0 International License (CC BY-NC-ND)

Marian P. Kazmierkowski and Malesani, L., (1998) , Current Control Techniques for Three-Phase Voltage-Source PWM Converters: A Survey, IEEE Transactions on Industrial Electronics, Vol. 45, No. 5, pp 691-703.

Dixon Juan W, ooi Boon Teck. (1998), Indirect current control of a unity power factor sinusoidal current boost type three- phase rectifier". IEEE Trans. I nd.Electron,35 (4), pp 508-515.

Hong, M., Zhaolin, Wu,. (2001), Study on the Sensorless Current Control Strategy of Three-Phase Voltage-Source PWM Rectifier". Transactions of China Electrotechnical Society, 16(2), pp 56-60.

WEN, Q., ZHU, L., FU, C., (2013), Research on deadbeat Current Control Strategy of Three-Phase PWM Voltage Source Rectifier ' Proceedings of the 2nd International Conference on Computer Science and Electronics Engineering, pp 1769 1772.

Kessal, A., Rahmani, L., Mostefai, M., (2012), Power Factor Correction based on Fuzzy Logic Controller with Fixed Switching Frequency», Electronics and Electrical Engineering, ISSN 1392 – 1215, No.2(118), , pp, 67-72.

Konghirun. M., (2007), A Three-Phase Space-Vector Based PWM Rectifier with Power Factor Control '1-4244-0844-X/07/$20.00 ©2007 IEEE. pp 57-61.

Panigrahi, R.., Subudhi, B., Chandra Panda, P., (2014), A comparative assessment of hysteresis and dead beat controllers for performances of three phase shunt active power filtering', Journal of Power Technologies 94 (4), pp 286–295.

Creative Commons Attribution-NonCommercial-NoDerivatives 4.0 International License (CC BY-NC-ND)

Algerian Journal of Engineering Architecture and Urbanism Vol. 5 Nr. 3 2021
ISSN: 2588-1760

Conception d'observateur proportionnel intégral à entrée inconnue (PI-UIO) pour l'estimation simultanée d'état et de défaut

INES Righi

Faculté des Sciences et de Technologies, Univ. Souk Ahras-LEER- BP 1553
Souk-Ahras, 41000. Algérie, e-mail: **i.righi@univ-soukahras.dz**

Résumé :

Dans ce travail le problème d'estimation d'état et de défaut affectant les systèmes non linéaire de type Takagi-Sugeno (T-S) à variable de décision mesurable (VDM) est traité, une synthèse d'observateur proportionnel intégral à entrée inconnue (PI-UIO) est conçu, et est exactement donnée et prouvée avec précision. Il est important de noter que le défaut de l'actionneur peut se produire fréquemment, ce qui peut avoir des conséquences désastreuses pour les systèmes de commande moderne. Pour cette raison, l'observateur PI-UIO est proposé, et est étudié plus en détail pour reconstruire l'état et le défaut de l'actionneur simultanément. La théorie de Lyapunov est utilisée pour développer les conditions de stabilité de cet observateur, l'analyse de la stabilité est démontrée à l'aide de la fonction candidate non quadratique du Lyapunov, les gains de l'observateur sont calculés au travers la résolution des inégalités matricielles linéaire (LMIs), l'approche descripteur est envisagée pour réduire le conservatisme. Enfin, un exemple de simulation d'un disque roulant est adopté pour montrer l'applicabilité des stratégies de conception réalisées.

Mots-clés : estimation simultanée d'état et de défaut ; variable de décision mesurable (VDM) ; observateur proportionnel intégral à entrée inconnue (PI-UIO) ; modèle floue singulier de type Takagi-Sugeno (T-S).

I. Introduction :

Les systèmes physiques sont souvent complexes, et l'étude de ces systèmes fait appel aux modèles non linéaires pour décrire le comportement dynamique des systèmes réels **(Orjuela et al., 2006)**. Ce type de modèle est difficilement exploitable, notamment pour la commande, le diagnostic et l'estimation, une hypothèse communément faite est la linéarité des systèmes, car les techniques d'analyse des modèles linéaires, ont été largement développées dans la littérature. Cependant, l'hypothèse de linéarité n'est vérifiée que dans une plage de fonctionnement restreinte autour d'un point de fonctionnement donné, et les performances du modèle se dégradent quand on éloigne de ce point **(Akhenak. A., 2004),** donc les méthodes de commande, d'estimation développé à base des modèles linéaires donnent des résultats insatisfaisants dès qu'on s'éloigne de ce point de fonctionnement **(Ichalal 2009).**

Afin d'améliorer les performances des systèmes, il est impératif de prendre en considération les non-linéarités dans la phase de modélisation. Cela permet de décrire le comportement d'un système réel non linéaire sur une large plage de fonctionnement, avec une meilleure précision comparée à celle obtenue avec des modèles linéaires.

Une nouvelle approche pour représenter un système non linéaire par des multiples modèles, autour de différents points de fonctionnement dite « *multi-modèles* », ou représentation « *poly-topique* ». Cette représentation consiste en une collection de systèmes linéaires (polytopes) interconnectés par des fonctions non linéaires scalaires. Plusieurs catégories de multi-modèles existent dans la littérature, notamment les systèmes linéaires à

Creative Commons Attribution-NonCommercial-NoDerivatives 4.0 International License (CC BY-NC-ND)

paramètres variant dans le temps (LPV), ou encore appelés systèmes Takagi-Sugeno (T-S) **(T. Takagi et M. Sugeno., 1985).** Récemment, les systèmes non linéaires décrits par les modèles T-S ont été fortement considérés et spécialement dans les domaines de l'estimation d'état et de défaut des systèmes non linéaires. Sur un autre front de recherche, il y a eu un intérêt considérable pour la conception d'observateurs pour toutes sortes de systèmes en raison de leur importance particulière dans la commande basé sur les observateurs et la reconstruction des défauts.

Malheureusement, la plupart des résultats concernent la synthèse d'observateurs avec des entrées connues, ce qui est relativement conservateur. Des perturbations externes et des mesures bruitées, qui peuvent être considérées comme des entrées inconnues, apparaîtront inévitablement dans le processus commandé, et conduiront en outre à de mauvaises performances de modélisation **(Chakrabarty, A et al., 2019).** Dans cette situation, il semble important de développer des observateurs capables de résister à des entrées inconnues. Plusieurs approches ont proposé des observateurs pour les systèmes conventionnels ou ordinaires. Les chercheurs par exemple, sur la base de concepts géométriques, l'observateur de type P-UIO a été présenté pour la première fois dans **(Basile, G et al.,1969)** pour les systèmes linéaires**.** De manière similaire à la théorie linéaire, le problème de la synthèse d'un observateur pour les systèmes singuliers T-S (non linéaire) a été traité par des nombreux auteurs, des approches sont notamment basées sur la construction d'observateur P-UIO pour les systèmes non linéaires, voir **(Mu, Zhang et al., 2020)** et **(Zhang, Chadli et al., 2019)**, et d'autre type d'observateurs considérés, comme l'observateur proportionnel inégral à entrée inconnue PI-UIO et l'observateur proportionnel multi-inégral à entrée inconnue PMI-UIO, qui sont traités simultanément par **(Djeddi,et al., 2020)**, d'autres approches développent le concept de la décomposition en valeurs singulières et de la matrice inverse généralisée, qui a été initié depuis les travaux de **(H. Muller et al.,1999),** afin de reconstruire le vecteur d'état pour cette classe des systèmes**,** aussi les auteurs ont étudiés le problème d'observation des états des systèmes singuliers linéaires à paramètres variant, et étendu au cas des systèmes non linéaire, veuillez consulter les références **(Do, Koenig et al. 2020)** et **(Oliveira et al., 2020)**, ces type d'observateurs aussi ont été appliqués pour l'estimation et le diagnostic **(Hassanabadi, et al.,2017)** . En ce qui concerne les systèmes non linéaires, et sur la base des systèmes singulière d'ordre fractionnaire non linéaires, ce travail a été abordé dans **(Komachali., et al, 2019).**

En outre, une autre type de PI-UIO a été proposée pour les systèmes linéaire à paramètres variables (LPV) dans **(Hamdi, et al., 2012),** pour la détection et l'isolation de défaut. De plus, des problèmes similaires ont également été résolus où une fonction de Lyapunov floue a été utilisée lors de l'analyse de convergence. Dans **(Li, et al., 2019),** les auteurs ont ainsi développés des techniques utilisant des observateurs à mode glissant et observateur par perturbation dans **(Ning, et al.,2017)**. Cependant, peu de travaux ont été effectués pour la synthèse d'observateurs pour les systèmes singuliers non linéaires, tout en y effectuant un diagnostic de défaut, mais la synthèse de cet observateur peut devenir très délicate voire impossible en fonction de la complexité (comportement non linéaire), ainsi que le type du modèle employé, d'ou l'importance de la modélisation mathématique du système qui doit en même temps être simple et au plus proche du système. L'approche Multi-modèles est donc la technique la plus performante pour la modélisation des systèmes non linéaires singuliers de type T-S; elle est notamment un bon compromis entre la précision du modèle et sa complexité **(ichalal 2009)**. Les multi-modèles sont connus par leur capacité de prise en compte des changements de points de fonctionnement du système, et leur habilité de reproduire la dynamique de celui-ci, avec précision sur une large plage de fonctionnement. De plus, leurs

Creative Commons Attribution-NonCommercial-NoDerivatives 4.0 International License (CC BY-NC-ND)

propriétés mathématiques sont très appréciables lors de la synthèse d'observateurs. Ces propriétés tiennent en particulier dans le fait que l'on utilise des techniques linéaires qui sont utilisées pour traiter des systèmes non linéaires. La représentation multi-modèles à été généralisée et utilisée dans de nombreux problèmes d'automatique, Néanmoins, la plupart des résultats susmentionnés se concentrent uniquement sur les systèmes à temps continu, ce qui est inutile pour la contrepartie à temps discret. En fait, les techniques de conception de PI-UIO à temps discret doivent être explorées en profondeur.

Motivé par les discussions ci-dessus, en utilisant la méthode des systèmes singuliers, un PI-UIO a été adressé dans **(Li, X., et al 2017)**, pour réaliser l'estimation des défauts, ce travail donc est étendu, afin d'avoir une estimation d'état ainsi que des défauts actionneurs pour un système non linéaire modélisé par l'approche multi-modèle, dans le domaine à temps discret. L'idée primordiale, est la synthèse d'un observateur PI-UIO à entrées inconnues. Pour cela, il faut tout d'abord obtenir une représentation du système non linéaire sous une forme multi-modèle. Ensuite, l'observateur PI-UIO est développé pour l'estimation simultanée du vecteur d'état et les défauts affectant l'actionneur.
L'existence et les conditions de stabilité de cet observateur sont efficacement synthétisées pour le système considéré. Voici quelques contributions de ce travail :

- Pour réduire le conservatisme, une fonction de Lyapunov non quadratique floue est utilisée pour présenter des critères suffisamment relaxés, pour la convergence de l'observateur conçu dans ce travail, ainsi l'approche descripteur (système singulière) est envisagée.
- De manière significative, l'observateur PI-UIO est étudié plus avant pour reconstruire le défaut de l'actionneur dans le cas de défaut existant, ce qui est avantageux pour les extensions potentielles de la commande tolérante aux pannes.

Le papier est organisé comme suit : dans la section **II**, la présentation du problème est exposée sur l'aspect modélisation du système ainsi que les diverses hypothèses nécessaires. Dans la section **III**, nous présentons la synthèse du multi-observateur PI-UIO. La structure et la synthèse des différentes matrices et les conditions d'existence de cet observateur sont établies. Finalement, la section **IV** représente un exemple pratique illustratif qui détermine l'efficacité de la méthode développée.

II. Conception d'observateur PI-UIO :

II.1. Notations: Tout au long de cet article, les notations suivantes sont adoptées pour représenter commodément les différentes expressions, étant donné un ensemble de fonctions non linéaires: $\mu_i(.); i \in \{1,\dots,r\}$, sont les fonctions d'activation scalaires satisfait la propriété de somme convexe. Ce travail se concentre uniquement sur les variables de prémisse mesurables regroupées dans le vecteur des variables de décision $\xi(k)$, dont les mesures peuvent être obtenues à partir de la sortie $y(k)$, ou à partir da construction d'un observateur. Ces notations abrégée seront utilisées dans la suite pour représenter la propriété de somme convexe des expressions de matrices variant en temps discret: $Y_\mu = Y_\mu(\xi(k)) = \sum_{i=1}^{r} \mu_i(\xi(k)) Y_i$, pour une somme convexe simple ; $Y_{\mu-} = Y_{\mu-}(\xi(k)) = (\sum_{i=1}^{r} \mu_i(\xi(k)) Y_i)^{-1}$ pour une somme convexe inverse; et $Y_{\mu\mu} = Y_{\mu\mu}(\xi(k)) = \sum_{i=1}^{r}\sum_{j=1}^{r} \mu_i(\xi(k))\mu_j(\xi(k)) Y_{ij}$ pour une somme convexe double et relaxé. Pour un vecteur x et ξ, x_k désigne $x(k)$, ξ_k définit la notation $\xi(k)$ et x_{k+} par $x(k+1)$. I_r

Creative Commons Attribution-NonCommercial-NoDerivatives 4.0 International License (CC BY-NC-ND)

designe l'ensemble $\{1, 2, \cdots, r\}$, $\mathfrak{N}^+$ représente l'ensemble des entiers positives réelle. $\mathcal{H}(A) = A + A^T$ est la matrice hermitienne de A. $A^\dagger = (A^T A)^{-1} A^T$ représente la matrice pseudo-inverse de A. $\mathbb{Z} + (*)$ désigne $\mathbb{Z} + \mathbb{Z}^T$. I est la matrice identité. Un astérisque * symbolise des blocks symétrique d'une matrice.

II.2. Cas de variable de décision mesurable :

Dans ce cas les variables de décision sont mesurable càd :$\{ \mu_k = \hat{\mu}_k \}$ et $\{ \mu_i(\xi_k) = \mu_i(\hat{\xi}_k) \}$.
Soit le système singulier de type Takagi Sugeno à variable de décison mesurable soumis au défaut actionneur et à la perturbation externe :

$$\begin{cases} E\dot{x}(k+1) = \sum_{i=1}^{r} \mu_i(\xi_{ik})(A_i x_k + B_i u_k + D_f f_a(k)) + B_\omega \omega_k \\ y_k = C x_k \end{cases} \quad (1)$$

Ou : $x_k \in \mathfrak{N}^{n_x}$, $u_k \in \mathfrak{N}^{n_u}$, $y_k \in \mathfrak{N}^{n_y}$, $f_a(k) \in \mathfrak{N}^{n_f}$ et $\omega_k \in \mathfrak{N}^{n_\omega}$, sont respectivement le vecteur d'etat, le vecteur d'entrée de commande connue, la sortie le défaut affectant l'actionneur et la perturbation externe affectant le système.

Dans le reste du papier, on note :$\mathfrak{S}_\mu = \sum_{i=1}^{r} \mu_i(\xi_{ik})\, \mathfrak{S}_i$ pour simplifier l'écriture. Les fonctions d'activation vérifient la propriété de somme convexe :

$$\begin{cases} \sum_{i=1}^{r} \mu_i(\xi_{ik}) = 1 \\ 0 \leq \mu_i(\xi_{ik}) \leq 1 \end{cases} \quad (2)$$

Les variables de décision ξ_{ik} sont supposées accesssible à la mesure en temps réel, dépendant de l'entrée de commande ou des sorties.

II.3. Obtention du modèle T-S par approche multi-modèle :

Considérons le modèle non linéaire :

$$\begin{cases} E\dot{x}(k+1) = f(x_k, u_k) \\ y(k) = h(x_k, u_k) \end{cases} \quad (3)$$

Soit **k** le nombre de fonctions non linéaires présentés dans le système (1). On les note : $f^i, i = 1, \ldots, k$. Supposons qu'il existe un compact $\mathbb{C}$ des variables ξ_{ik} où les non-linéarités sont bornées :

$$f^i(\xi_{ik}) = f^i_{min} w^i_0(\xi_{ik}) + f^i_{max} w^i_1(\xi_{ik}) \quad (4)$$

$$f^i \in [f^i_{min}, f^i_{max}], i = 1, \ldots, k \quad (5)$$

Les non-linéarités f^i peuvent alors s'écrire de la manière suivante **(Ichalal 2009)** :

$$\begin{cases} w^i_0 = \frac{f^i_{max} - f^i(\xi_{ik})}{f^i_{max} - f^i_{min}} \\ w^i_1 = \frac{f^i(\xi_{ik}) - f^i_{min}}{f^i_{max} - f^i_{min}} \end{cases} \quad (6)$$

Les fonctions d'activation $\mu_i(\xi_{ik}), i = 1, \ldots r$ sont obtenues à partir des fonctions w^i_0 et w^i_1. Le nombre de sous-modèles r est égale à 2^k.

Creative Commons Attribution-NonCommercial-NoDerivatives 4.0 International License (CC BY-NC-ND)

Avant d'expliciter les principaux résultats, nous allons faire les hypothèses suivant, dont les matrices E, A_i, B_i et C sont des matrices connu de dimensions appropriées. D_f est une matrice colonne d'influences de défauts de rang plein.Généralement $rang(E) = n_E < n_x$ càd E est singulière.

Soit le triplet (E, A_i, C), les conditions suivantes sont vérifiées simultanément :
H 1 :

$$rang\begin{pmatrix} E \\ C \end{pmatrix} = n_x \tag{7}$$

C : est une matrice de rang plein ligne.

H 2 : le triplet (E, A_i, C) est D_f-observable càd :

$$rang\begin{pmatrix} sE - A_i \\ C \end{pmatrix} = n_x, \qquad \forall s \in \mathcal{C}\ |s| > 1 \tag{8}$$

$\mathcal{C}$: est l'ensemble des nombres complexe.
La D_f-observabilité caractérise la capacité de reconstruire l'état de la partie dynamique.

H 3 **:** les termes impulse du système (1) sont observable, (le triplet (E, A_i, C) est impulse-observable), $\forall i = 1,2,\ldots..r$,i.e.,

$$\begin{cases} rang\begin{bmatrix} E & A_i \\ 0 & E \\ 0 & C \end{bmatrix} = n_x + rang(E) \\ U_3 E + U_4 C = I_{n_x} \end{cases} \tag{9}$$

Avec : U_3 et U_4 sont deux matricces non singulières.
L'hypothèse (3) est equivalent à l'hypothèse (1).
L'observabilité impulsive garantit la capacité d'estimer l'état de la partie statique.

H 4 : Tout au long de cette section, les défauts sont supposée constatnts, i.e. :

$$f_a(k+1) \approx f_a(k) \tag{10}$$

Remarque 1 : *L'hypothèse (10) est classiquement utlisée pour la démonstration théorique de la convergence de l'observateur PI-UIO, bien qu'en pratique, on constatera qu'on peut s'affranchir en augmentant les gains de l'observateurs afin d'élargir sa bande passante , permettant ainsi la prise en compte des dynamiques négligées.Cela provoque cependant une augmentation de la sensibilité aux bruits. Le choix des gains de l'observateur est alors déterminé par la satisfaction d'un compromis entre la robustesse et les performances de l'obseravteurs.*

Lemme 1 : Pour deux matrices Φ et ψ de dimension appropriées, si la condition (7) est vérifiées, alors :

$$rang\begin{pmatrix} \Phi \\ \psi \end{pmatrix} = rang(\Phi) \tag{11.a}$$

$[U_3 \quad U_4]\Phi = \psi$, a une solution. Alors la solution générale peut étre exprimées par :

$$[U_3 \quad U_4] = \psi\Phi^{+} + Y(I - \Phi\Phi^{+}) \tag{11.b}$$

Creative Commons Attribution-NonCommercial-NoDerivatives 4.0 International License (CC BY-NC-ND)

Ou : Υ est une matrice arbitraire de dimension appropriées.

Finsler's lemma : soit $x_k \in \Re^{n_x}, Q = Q^T \in \Re^{n_x \times n_x}$ et $\mathcal{R} \in \Re^{n_x}$ tel que: $rank(\mathcal{R}) \leq n_x$; les expressions suivants sont équivaut :

$$\begin{cases} a)\ x_k^T Q x_k < 0 \quad : \quad \{\forall x_k \in \Re^{n_x}; x_k \neq 0 ; \mathcal{R} x_k = 0\} \\ b)\ \exists\ \mathcal{M} \in \Re^{n_x} : \quad \{Q + \mathcal{M}\mathcal{R} + \mathcal{R}^T \mathcal{M}^T < 0\} \end{cases} \tag{12}$$

Complément de schur : soit trois matrices $P_{22} = P_{22}^T, P_{11} < P_{11}^T$ et P_{12} de dimensions appropriées, si la matrice P_{22} est inversible, alors les LMIs suivantes sont équivalentes:

1. $\begin{bmatrix} P_{11} & P_{12}^T \\ P_{12} & P_{22} \end{bmatrix} > 0$ (13.a)
2. $P_{22} > 0, P_{11} - P_{12}^T P_{22}^{-1} P_{12} < 0.$ (13.b)
3. $P_{11} > 0, P_{22} - P_{12} P_{22}^{-1} P_{12}^T < 0.$ (13.c)

Lemme 2 : (Congruence) soit deux matrices $\mathbb{P}$ et $\mathbb{Q}$, si $\mathbb{P}$ est une matrice définie positive et $\mathbb{Q}$ une matrice colonne de rang plein, alors la matrice $\mathbb{Q}\mathbb{P}\mathbb{Q}^T$ est définie positive.

Lemme 3 : soit $\mathbb{U} = \mathbb{U}^T > 0$ et $\mathbb{V}$ matrices de dimensions appropriées, la propriété suivante est vérifiée :

$$(\mathbb{V} - \mathbb{U})\mathbb{U}^{-1}(\mathbb{V} - \mathbb{U}) \geq 0 \leftrightarrow \mathbb{V}^T \mathbb{U}^{-1} \mathbb{V} \geq \mathbb{V} + \mathbb{V}^T - \mathbb{U} \tag{14}$$

Lemme de relaxation : soit T_{ij} une matrice symétrique de dimensions appropriées, et $\mu_i(\xi_{ik})$, $i \in I_r$ toutes familles de fonctions satisfaisant la propriété de somme convexe.

La condition: $\sum_{i=1}^{r} \sum_{j=1}^{r} \mu_i \mu_j T_{ij} < 0$, est vérifiée si :

$$\begin{cases} T_{ij} < 0 \\ \frac{2}{r-1} T_{ii} + T_{ij} + T_{ji} < 0 \end{cases} \qquad (i,j) \in I_r \times I_r,\ i \neq j \tag{15}$$

Remarque 2: *Pour synthétiser l 'observateur PI-UIO exactement, c'est nécessaire de déterminer les matrices U_2 et U_4, tel que relations (11.a) et (11.b) sont vérifiées simultanément.*

Pour garantir l'hypothèse 1 et à partir du lemme 1 les matrices U_2 et U_4 sont définies par :

$$\begin{cases} U_2 = D_2 + \Upsilon \mathcal{J}_2 \\ U_4 = D_4 + \Upsilon \mathcal{J}_4 \end{cases} \tag{16}$$

Avec :

$$\begin{cases} D_2 = \begin{bmatrix} E \\ C \end{bmatrix}^{\dagger} \begin{bmatrix} I_{n_x} \\ 0 \end{bmatrix} \\ D_4 = \begin{bmatrix} E \\ C \end{bmatrix}^{\dagger} \begin{bmatrix} 0 \\ I_{n_y} \end{bmatrix} \end{cases} \tag{17}$$

$$\begin{cases} \mathcal{J}_2 = (I_{n_x+n_y} - \begin{bmatrix} E \\ C \end{bmatrix} \begin{bmatrix} E \\ C \end{bmatrix}^{\dagger}) \begin{bmatrix} I_{n_x} \\ 0 \end{bmatrix} \\ \mathcal{J}_4 = (I_{n_x+n_y} - \begin{bmatrix} E \\ C \end{bmatrix} \begin{bmatrix} E \\ C \end{bmatrix}^{\dagger}) \begin{bmatrix} 0 \\ I_{n_y} \end{bmatrix} \end{cases} \tag{18}$$

Creative Commons Attribution-NonCommercial-NoDerivatives 4.0 International License (CC BY-NC-ND)

Algerian Journal of Engineering Architecture and Urbanism Vol. 5 Nr. 3 2021
ISSN: 2588-1760

III.Synthèse d'observateur PI-UIO :

La synthèse de l'observateur PI-UIO est basée sur le concept du découplage des défauts. L'estimation globale des états est une combinaison non linéaire des différentes sorties des observateurs locaux. L'observateur global sera alors une somme pondérée des différents observateurs linéaires. La structure du multi-observateur proposé pour le système (1) est décrit par :

$$\begin{cases} \eta_{k+} = \sum_{i=1}^{r} \mu_i(\xi_k)\left(M_i\eta_k + S_i u_k + L_P^i y_k + U_3 D_f \hat{f}_a(k)\right) \\ \hat{x}_k = \eta_k + U_4 y_k \\ \hat{f}_a(k+1) = f_a(k) - \sum_{i=1}^{r} \mu_i(\xi_k) L_I^i (y_k - \hat{y}_k) \\ \hat{y}_k = C\hat{x}_k \end{cases} \tag{19}$$

Les gains de l'observateur PI-UIO: M_i, S_i , L_P^i et L_I^i sont à déterminer tel que :
L_P^i représente le gain propotionnel pour l'estimation de l'état.
L_I^i représente le gain intégral pour estimation du défaut actionneur.

L'objectif de la synthèse, est de déterminer les gains matriciels afin que l'état estimé $\hat{x}_k$ converge vers l'état réel x_k du système.

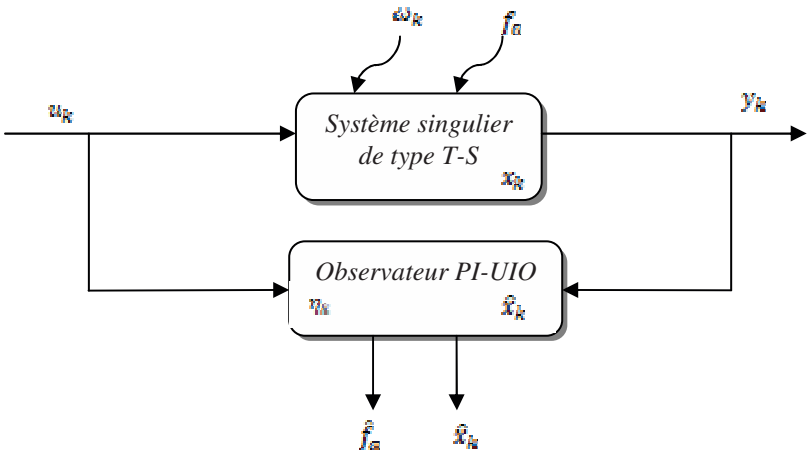

Fig.1 : architecture d'estimation avec un observateur PI-UIO.

Remarque 3: *L'observateur PI-UIO présenté donne alors une estimation asymptotique à la fois du vecteur d'état du système et aussi l'estimation des défauts actionneurs.*

Définition 1 : Les équations (19) définissent l'observateur PI-UIO pour le système (1), pour des conditions initiales arbitraires $x(0)$, $\eta(0)$ et une entrée arbitraire u_k, les relations suivantes sont vraies :

$$\lim_{k\to\infty}(x_k - \hat{x}_k) = 0 \tag{20}$$
$$\lim_{k\to\infty}(f_a(k) - \hat{f}_a(k)) = 0 \tag{21}$$

On définit l'erreur d'estimation d'état par : $e_0(k) = x_k - \hat{x}_k$, en utilisant (19) et l'égalité $y_k = Cx_k$, on obtient :

$$e_0(k) = x_k - \eta_k - U_4 y_k = U_3 E x_k - \eta_k \tag{22}$$

D'après le critère d'impulse-observabilité (9), il existe une matrice réelle $U_3 \in \mathfrak{M}^{n_x \times n_u}$ telle que :

Creative Commons Attribution-NonCommercial-NoDerivatives 4.0 International License (CC BY-NC-ND)

$U_3E = I_{n_x} - U_4C$.

Sa dynamique devient alors:

$$e_0(k+1) = U_3Ex_{k+} - \eta_{k+} = M_\mu e_0(k) + (U_3A_\mu - L_p^iC + M_\mu U_4C - M_\mu)x_k + (U_3B_\mu - S_\mu)u_k + U_3D_f e_{f_a}(k)) + U_3B_\omega\omega_k$$

(23)

La dynamique de l'erreur d'estimation d'état se simplifie à :

$$e_0(k+1) = M_\mu e_0(k) + U_3D_f e_{f_a}(k) + U_3B_\omega\omega_k \quad (24)$$

avec les contrainte :

$$\begin{cases} U_3A_\mu - L_p^iC + M_\mu U_4C - M_\mu = 0 \\ U_3B_\mu - S_\mu = 0 \end{cases} \quad (25)$$

Les gains de l'observateur sont définit par :

$$\begin{cases} N_\mu = M_\mu U_4 - L_p^i \\ M_\mu = U_3A_\mu + N_\mu C \\ L_p^i = M_\mu U_4 - N_\mu \end{cases} \quad (26)$$

La dynamique de l'erreur d'estimation est équivalent à :

$$e_0(k+1) = (U_3A_\mu + N_\mu C)e_0(k) + U_3D_f e_{f_a}(k) + U_3B_\omega\omega_k \quad (27)$$

Remarque 4 : *Si l'équation dynamique de l'erreur d'estimation ci-dessus est asymptotiquement stable, l'état estimé tend asymptotiquement vers l'état réel c'est-à-dire :* $\hat{x}_k \to x_k$. *Cela signifie que le multi-observateur (19) est un multi-observateur proportionnel à entrées inconnues stable pour le système singulier (1). La synthèse d'un tel multi-observateur revient à résoudre les équations (26, tout en garantissant la stabilité de toutes les matrices* M_i *(*M_i *des matrices de Hurwitz).*

L'erreur de défaut est défini par :

$$e_{f_a}(k) = f_a(k) - \hat{f}_a(k) \quad (28)$$

En considérant l'hypothèse 4 ou : $f_a(k+1) \approx f_a(k)$. alors sa dynamique est défini par :

$$e_{f_a}(k+1) = f_a(k+1) - \hat{f}_a(k+1) = f_a(k) - \hat{f}_a(k+1) = f_a(k) - f_a(k) + \sum_{i=1}^{r}\sum_{j=1}^{r}\mu_i(\xi_k)\mu_j(\xi_k)L_i^i(y_k - \hat{y}_k) = \sum_{i=1}^{r}\sum_{j=1}^{r}\mu_i(\xi_k)\mu_j(\xi_k)(L_i^iCe_0(k))$$

(29)

L'idéee pricipale à vérifier maintenant ; est de découplé le défaut de l'erreur d'estimation d'état, alors on pose le vecteur d'erreur augmentée suivant :

$$e_a^T(k) = [e_0^T(k) \quad e_{f_a}^T(k)] \quad (30)$$

Creative Commons Attribution-NonCommercial-NoDerivatives 4.0 International License (CC BY-NC-ND)

Algerian Journal of Engineering Architecture and Urbanism Vol. 5 Nr. 3 2021
ISSN: 2588-1760

$$\begin{bmatrix} e_0(k+1) \\ e_f(k+1) \end{bmatrix} = \begin{bmatrix} M_\mu & U_2 D_f \\ L_i^i C & 0 \end{bmatrix} \begin{bmatrix} e_0(k) \\ e_{f_a}(k) \end{bmatrix} + \begin{bmatrix} U_2 B_\omega \\ 0 \end{bmatrix} \omega_k \leftrightarrow e_a(k+1) = \mathcal{T}_\mu e_a(k) + \mathcal{B}_\omega \omega_k \tag{31}$$

Le système (31) peut se ré-écrire comme suit :

$$\mathcal{T}_\mu = \begin{bmatrix} M_\mu & U_2 D_f \\ L_i^i C & 0 \end{bmatrix} = \begin{bmatrix} U_2 A_\mu + N_\mu C & U_2 D_f \\ L_i^i C & 0 \end{bmatrix} = \begin{bmatrix} U_2 A_\mu & U_2 D_f \\ 0 & I_{n_{f_a}} \end{bmatrix} + \begin{bmatrix} N_\mu \\ L_i^i \end{bmatrix} [C \quad 0]$$

$$\mathcal{T}_\mu = \mathcal{A}_\mu + \mathcal{K}_\mu \mathbb{C}$$

avec :

$$\begin{cases} \mathcal{A}_\mu = \begin{bmatrix} U_2 A_\mu & U_2 D_f \\ 0 & 0 \end{bmatrix} \\ \mathcal{K}_\mu = \begin{bmatrix} N_\mu \\ L_i^i \end{bmatrix} \\ \mathbb{C} = [C \quad 0] \end{cases} \tag{32}$$

III.1. Observateur $\mathcal{L}_2$ gain :

Dans cette section, nous traitons le problème de rejet de perturbations en considérant le critère $\mathcal{L}_2$, dont l'ojectif d'atténuer l'effet de ω_k sur l'erreur d'estimation augmentée $e_a(k)$; on utilisera l'approche $\mathcal{L}_2$ extension directe de la norme $\mathcal{L}_\infty$ **(Ichalal 2009)**. On cherche à guarantir :

$$\frac{\|e_a(k)\|_2^2}{\|\omega_k\|_2^2} \leq \gamma^2 \tag{33}$$

Avant d'entamer la procédure de résolution, on donne les conditions suffisantes d'existences de l'observateur envisagé.

Les conditions d'existence du Multi-Observateur Proportionnel Intégral (19) à entrées inconnues existent, si et seulement si les paires (A_i, C) sont détectables, $\forall i = 1, \ldots, r$. Le Théorème suivant résume ces conditions :

Théorème 1 : L'observateur PI-UIO du système singulièr converge asymptotiquement vers zéro, si et seulement si la condition suivante est vérifiée :

$$rang\left(\begin{bmatrix} sE - A_i & D_f \\ 0 & sI_{n_f} \\ C & 0 \end{bmatrix}\right) = n_x + n_f \text{ et } Re(s) \geq 0 \tag{34}$$

Avec : $rang\left(\begin{bmatrix} E \\ C \end{bmatrix}\right) = n_x$

Preuve : étant donné que :

$$\begin{cases} [U_3 \quad U_4] \begin{bmatrix} E \\ C \end{bmatrix} = I_{n_x} \\ rang([U_3 \quad U_4]) = rang\left(\begin{bmatrix} E \\ C \end{bmatrix}^\dagger\right) \end{cases} \tag{35}$$

Alors quelque soit s complexes, on a :

$$rang\left(\begin{bmatrix} U_3 & 0 & U_4 & 0 \\ 0 & I & 0 & 0 \\ 0 & 0 & I & -sI \\ 0 & 0 & 0 & I \end{bmatrix} \begin{bmatrix} sE - A_i & D_f \\ 0 & sI_{n_f} \\ sC & 0 \\ C & 0 \end{bmatrix}\right) = rang\left(\begin{bmatrix} sE - A_i & D_f \\ 0 & sI_{n_f} \\ C & 0 \end{bmatrix}\right) \tag{36}$$

Creative Commons Attribution-NonCommercial-NoDerivatives 4.0 International License (CC BY-NC-ND)

$$rang\left(\begin{bmatrix} sI - U_3A_i & U_3D_f \\ 0 & sI_{n_f} \\ C & 0 \end{bmatrix}\right) = rang\left(\begin{bmatrix} sE - A_i & U_3D_f \\ 0 & sI_{n_f} \\ C & 0 \end{bmatrix}\right) \quad (37)$$

Théorème 2 : l'observateur PI-UIO est asymptotiquement stable, s'il existe une matrice symétrique définie positive $X_i = X_i^T$, avec : $X_i = P_i^{-1}$, et un scalaire $\bar{\gamma} = \sqrt{\gamma^2}$, satisfaisant la condition (15), remplissant les conditions LMI suivante (système augmenté) :

$$\min_{P_i>0} \gamma \quad (38)$$

$$\begin{bmatrix} -X_i - 2\alpha X_i + I & * & * \\ 0 & -\gamma^2 I & * \\ X_i\mathcal{A}_i + \Xi_i\mathfrak{C} & X_iB_\omega & -X_i \end{bmatrix} < 0 \quad (39)$$

Remarque 5: *afin de déterminer les gains Ξ_i telle que l'erreur d'estimation converge asymptotiquement vers zéro, aussi, afin de déterminer ces gains, il faut s'assurer de la détectabilité des paires $(\mathcal{A}_i, \mathfrak{C})$, $\forall\, i = 1,2,\dots r$.*

Preuve : analyse de stabilité
Soit la fonction candidate non quadtratique du Lyapunov proposée suivante :

$$V(e_a(k)) = e_a^T(k)P_\mu^{-1}e_a(k) \quad (40)$$

Avec : $P_\mu = P_\mu^T > 0$.

La dérivée de $V(e_a(k))$ le long de trajectoire de $e_a(k)$ est donné par :

$$\Delta V(e_a(k)) = e_a^T(k+1)P_\mu^{-1}e_a(k+1) - e_a^T(k)P_\mu^{-1}e_a(k) = e_a^T(k)(\mathcal{T}_\mu^T P_\mu^{-1}\mathcal{T}_\mu - P_\mu^{-1})e_a(k) < 0 \quad (41)$$

Le système générant l'erreur d'estimation est stable et le gain $\mathcal{L}_2$ noté γ du transfert de ω_k vers $e_a(k)$ est borné, si :

$$\Delta V(e_a(k)) + e_a^T(k)\,e_a(k) - \gamma^2\omega_k^T\omega_k < 0 \quad (42)$$

III.2. α – stabilité:

L' α – stabilité est une technique très simple utilisée pour l'ammélioration des performances d'un système dans le domaine temporel (continue/discret). A partir d'une condition initiale x_0 (pour $k = 0$), l'idée est d'imposer un critère afin que la trajctoire en boucle fermée converge le plus rapidement possible vers le point d'équilibre.

Remarque 6: *Le but principale de la technique α – stabilité est d'augmenter la qualité de l'estimation, on définit une surface S à gauche du plan complexe, délimitée par une droite d'abscisse $(-\alpha)$ où $\alpha \in \Re^+$ .Cette surface assure une certaine bornitude de la partie imaginaire des valeurs propres des matrices du système générant l'erreur d'estimation d'état de façon à éviter les comportements oscillatoires, et assurer un bon amortissement de cette erreur d'estimation.*

Définition 2 : les systèmes (1) et (19) sont dit α – stable, s'il existe $\alpha > 0$ tel que la dérivée de la fonction de Lyapunov $\Delta V(e_a(k))$ satisfati l'inégalité suivante :

Creative Commons Attribution-NonCommercial-NoDerivatives 4.0 International License (CC BY-NC-ND)

$$\Delta V(e_a(k)) \leq 2\alpha V(e_a(k)), \forall\ e_a(k) \in \Re^{n_x \times n_f}$$

Alors, afin d'assurer une vitesse de convergence de l'erreur d'estimation rapide, on peut définir une surface S à gauche du plan complexe délimitée par une droite d'abscisse $(-\alpha)$ ou $\alpha \in \Re^+$. Les LMIs (42) sont alors remplacées par les LMIs suivantes :

$$\Delta V(e_a(k)) - 2\alpha V(e_a(k)) + e_a^T(k)e_a(k) - \gamma^2\omega_k^T\omega_k < 0\ ;\ \forall i \in \{1,\dots,r\} \tag{43}$$

Remplaçant (40) dans (43) :

$$e_a^T(k)\left(\mathcal{J}_\mu^T\mathcal{P}_\mu^{-1}\mathcal{J}_\mu - \mathcal{P}_\mu^{-1} + I - 2\alpha\mathcal{P}_\mu^{-1}\right)e_a(k) + e_a^T(k)\left(\mathcal{J}_\mu^T\mathcal{P}_\mu^{-1}\mathcal{B}_\varphi\right)\varphi_k + \varphi_k^T\left(\mathcal{B}_\varphi^T\mathcal{P}_\mu^{-1}\mathcal{J}_\mu\right)e_a(k) + \varphi_k^T\left(\mathcal{B}_\varphi^T\mathcal{P}_\mu^{-1}\mathcal{B}_\varphi - \gamma^2 I\right)\varphi_k < 0 \tag{44}$$

L'inégalité (44) est simplifié sous forme matricielle suivante :

$$\begin{bmatrix} e_a(k) \\ \varphi_k \end{bmatrix}^T \begin{bmatrix} \left(\mathcal{J}_\mu^T\mathcal{P}_\mu^{-1}\mathcal{J}_\mu - \mathcal{P}_\mu^{-1} + I - 2\alpha\mathcal{P}_\mu^{-1}\right) & \mathcal{J}_\mu^T\mathcal{P}_\mu^{-1}\mathcal{B}_\varphi \\ \mathcal{B}_\varphi^T\mathcal{P}_\mu^{-1}\mathcal{J}_\mu & \mathcal{B}_\varphi^T\mathcal{P}_\mu^{-1}\mathcal{B}_\varphi - \gamma^2 I \end{bmatrix} \begin{bmatrix} e_a(k) \\ \varphi_k \end{bmatrix} < 0 \tag{45}$$

Appliquant le complément de Schur ,on arrive à :

$$\begin{bmatrix} \left(\mathcal{J}_\mu^T\mathcal{P}_\mu^{-1}\mathcal{J}_\mu - \mathcal{P}_\mu^{-1} + I - 2\alpha\mathcal{P}_\mu^{-1}\right) & \mathcal{J}_\mu^T\mathcal{P}_\mu^{-1}\mathcal{B}_\varphi \\ \mathcal{B}_\varphi^T\mathcal{P}_\mu^{-1}\mathcal{J}_\mu & \mathcal{B}_\varphi^T\mathcal{P}_\mu^{-1}\mathcal{B}_\varphi - \gamma^2 I \end{bmatrix} \leftrightarrow \begin{bmatrix} -\mathcal{P}_\mu^{-1} + I - 2\alpha\mathcal{P}_\mu^{-1} & 0 \\ 0 & -\gamma^2 I \end{bmatrix} + \begin{bmatrix} \mathcal{J}_\mu^T \\ \mathcal{B}_\varphi^T \end{bmatrix} \mathcal{P}_\mu^{-1} \begin{bmatrix} \mathcal{J}_\mu & \mathcal{B}_\varphi \end{bmatrix}$$
$$= \begin{bmatrix} -\mathcal{P}_\mu^{-1} + I - 2\alpha\mathcal{P}_\mu^{-1} & * & * \\ 0 & -\gamma^2 I & * \\ \mathcal{J}_\mu & \mathcal{B}_\varphi & -\mathcal{P}_\mu \end{bmatrix}$$

Avec le lemme de congruence : $diag\left[I \quad I \quad \mathcal{P}_\mu^{-1}\right]$, avec le changement de variable : $\mathcal{X}_\mu = \mathcal{P}_\mu^{-1}$; LMI (39) est vérifié, la preuve est terminée.

- ***Procédure de synthèse d'observateur PI-UIO :***

Initialement, la méthode consiste à approximer un système singulier non linéaire par un multi-modèle de la forme (1), et on suppose que les hypothèses ***H1, H2*** et ***H3*** sont vérifiées. Le PI-UIO est donné par (19). Il y a plusieurs paramètres à déterminer pour la synthèse de l'observateur proposé, notamment deux gains matriciels qui sont : le gain proportionnel L_P^i et le gain intégral L_I^i . Ces deux gains assurent la stabilité de l'erreur d'estimation et l'erreur de défaut. Les paramètres sont calculés de la façon suivante :

Etape1 : confirmation que les matrices satisfaites les hypothèses 1,2 et 3 ou non, si oui on passe à l'étape 2 sinon la synthèse d'observateur PI-UIO est faux.

Etape 2 : résoudre le problème d'optimisation des LMIs (38), (39) pour obtenir les variables: $\mathcal{P}_i$, L_I^i et N_i à partir du vecteur $\mathcal{K}_i = [N_i \quad L_I^i]^T$ ou : $\mathcal{K}_i = \mathcal{X}_i^{-1}\Xi_i = \mathcal{P}_i\Xi_i$.

Etape 3 : obtenir S_i à l'aide de la contrainte (25) : $\{U_2B_i - S_i = 0\}$.

Creative Commons Attribution-NonCommercial-NoDerivatives 4.0 International License (CC BY-NC-ND)

Algerian Journal of Engineering Architecture and Urbanism Vol. 5 Nr. 3 2021
ISSN: 2588-1760

Etape 4 : si N_i est disponible, alors M_i et L_p^i sont résolu à l'aide de l'équation mentionné dans (26).

Alors l'observateur proportionnel à entrée inconnue PI-UIO est synthétisé correctement.

IV. Exemple illustrative :

Soit le système singulier perturbé de type Takagi Sugeno d'un disque roulant, soumis au défaut actionneur, représentée par la figure suivante :

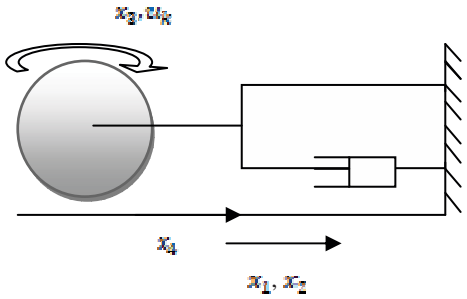

Fig.2 : Disque roulant.

On désigne les états par :
x_{1k} : la position du centre du disque.
x_{2k} : la vitesse de translation du disque.
x_{3k} : la vitesse angulaire du disque.
x_{4k} : la force de frottement entre le disque et le sol.
u_k : désigne l'entrée de commande qui est un moment de rotation appliqué au centre du disque.

Les paramètres sont donnés dans le tableau suivant :

Coefficient du ressort du disque roulant.	K	$100[N.m^{-1}]$
Coefficient d'humidité du disque roulant.	b	30
La masse du disque.	m	$40[Kg]$
Le rayon du disque.	r	$0.4[m]$

Table 1 : les paramètres physique du disque roulant.

Les non-linéarités du système sont choisit par: $\xi_{1k} = \frac{K}{m(1+x_{1k}^2)}$ et $\xi_{2k} = \frac{K}{m(1+x_{3k}^2)}$.

Creative Commons Attribution-NonCommercial-NoDerivatives 4.0 International License (CC BY-NC-ND)

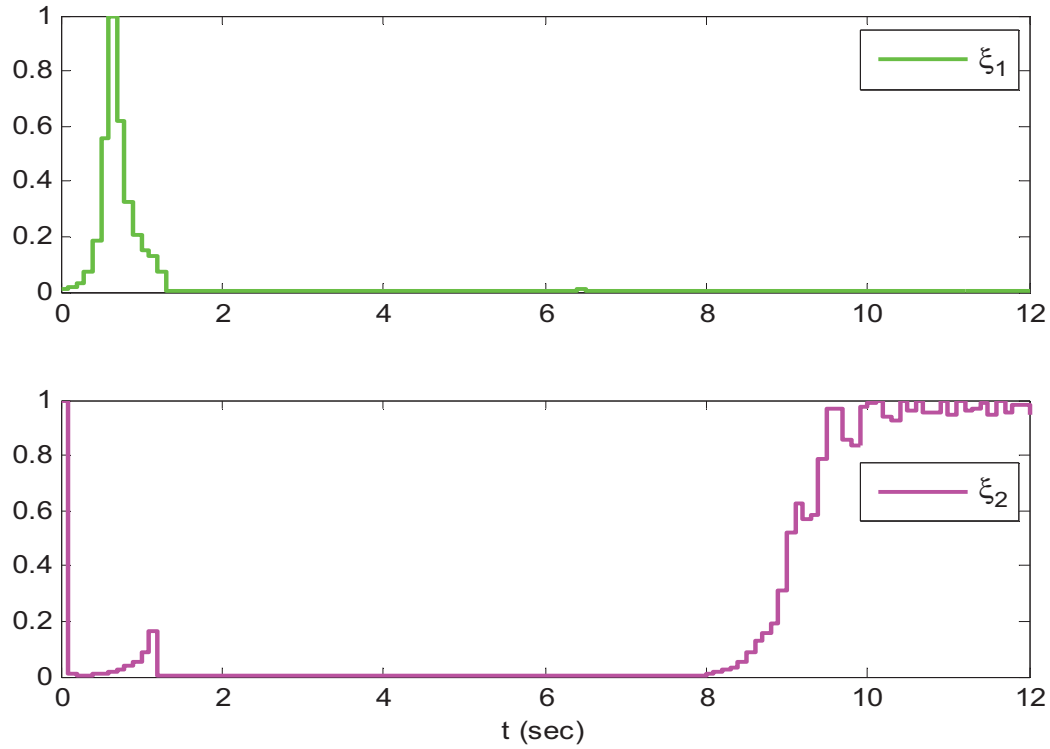

Fig 3: Les nonlinéaritées.

Les fonctions d'activations dépendent des variables de prémisse ξ_{1k} et ξ_{2k} qui sont définie comme suit :

$$\begin{cases} \mu_1(\xi_{1k},\xi_{1k}) = \left(\frac{\xi_{1k}-\xi_{1min}}{\xi_{1max}-\xi_{1min}}\right)\left(\frac{\xi_{2k}-\xi_{2min}}{\xi_{2max}-\xi_{2min}}\right) \\ \mu_2(\xi_{1k},\xi_{2k}) = \left(\frac{\xi_{1k}-\xi_{1min}}{\xi_{1max}-\xi_{1min}}\right)\left(\frac{\xi_{2min}-\xi_{2k}}{\xi_{2max}-\xi_{2min}}\right) \\ \mu_3(\xi_{1k},\xi_{2k}) = \left(\frac{\xi_{1min}-\xi_{1k}}{\xi_{1max}-\xi_{1min}}\right)\left(\frac{\xi_{2k}-\xi_{2min}}{\xi_{2max}-\xi_{2min}}\right) \\ \mu_4(\xi_{1k},\xi_{2k}) = \left(\frac{\xi_{1min}-\xi_{1k}}{\xi_{1max}-\xi_{1min}}\right)\left(\frac{\xi_{2min}-\xi_{2k}}{\xi_{2max}-\xi_{2min}}\right) \end{cases}$$

Vérifient la propriété de somme convexe :

$$\mu_1(\xi_{1k},\xi_{2k}) + \mu_2(\xi_{1k},\xi_{2k}) + \mu_3(\xi_{1k},\xi_{2k}) + \mu_4(\xi_{1k},\xi_{2k}) = 1 \quad \text{Et} \quad \begin{cases} 0 \le \mu_1(\xi_{1k},\xi_{2k}) \le 1 \\ 0 \le \mu_2(\xi_{1k},\xi_{2k}) \le 1 \\ 0 \le \mu_3(\xi_{1k},\xi_{2k}) \le 1 \\ 0 \le \mu_4(\xi_{1k},\xi_{2k}) \le 1 \end{cases}$$

Creative Commons Attribution-NonCommercial-NoDerivatives 4.0 International License (CC BY-NC-ND)

Algerian Journal of Engineering Architecture and Urbanism Vol. 5 Nr. 3 2021
ISSN: 2588-1760

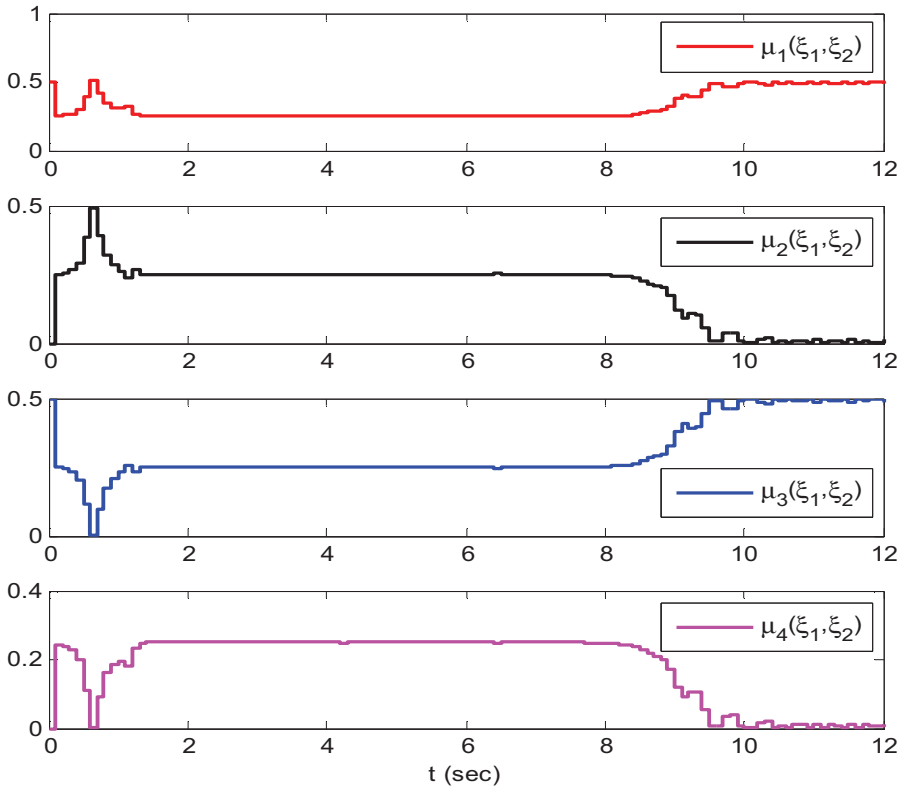

Fig. 4 : les fonctions d'activation.

Le défaut affectant l'actionneur et l'entrée de commande sont définis par :

$$f_a(k) = \begin{cases} 50 * t & ; \ si \quad 1 \leq t \leq 3 \\ -25 * t & ; \ si \quad 4 \leq t \leq 6 \\ 0 & ; \ ailleurs \end{cases} \qquad u_k = \begin{cases} 50 & ; \ si \quad 1 \leq t \leq 2 \\ -50 & ; \ si \quad 4 \leq t \leq 6 \\ 0 & ; \ ailleurs \end{cases}$$

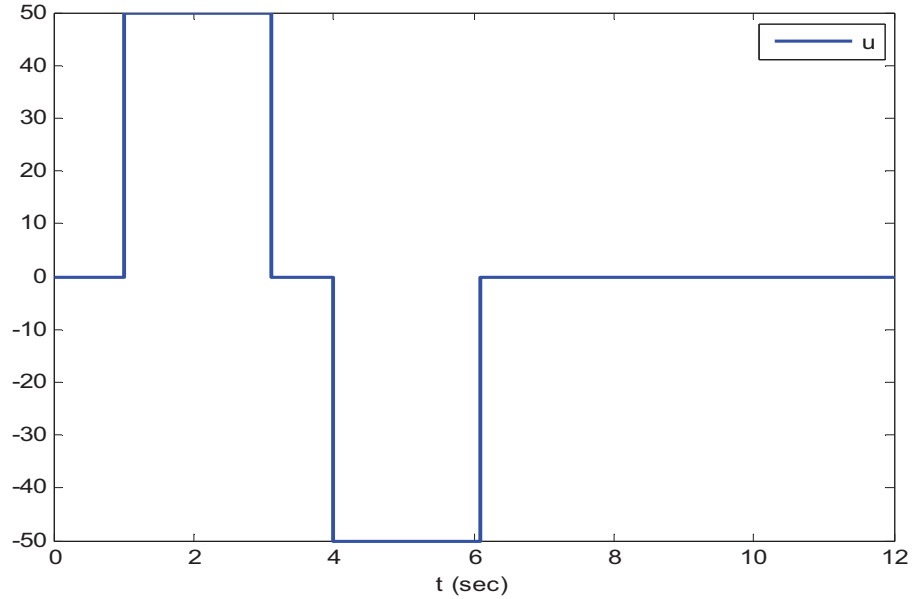

Fig. 5 : la commande d'entrée.

Creative Commons Attribution-NonCommercial-NoDerivatives 4.0 International License (CC BY-NC-ND)

La perturbation externe persistante est exprimée par : $\omega_k = 10 * sin(t + 0.7)$.

Avec conditions initiale :

$x(0) = [10 \quad -10 * \pi/3 \quad 0 \quad 0]$; $\hat{x}(0) = [10 \quad 20 * \pi/3 \quad 0 \quad 0]$ et $\eta(0) = [10 \quad -10 * \pi/3 \quad 0 \quad 0]$.

Le but général de cet exemple est de comparer les résultats présentés par rapport à ceux donnés dans la littérature. Pour montrer la validité de notre approche, nous résolvons d'abord le problème d'optimisation du théorème 2, en résolvant les conditions de LMI. Tous les calculs sont effectués sous le logiciel MATLAB avec le solveur LMI de la boîte à outils de contrôle robuste, aboutissant à des solutions réalisables. Les gains matriciels suivant sont obtenues :

$$U_3 = \begin{bmatrix} 0.6667 & 0 & 0 & 0 \\ 0 & 1 & 0 & 0 \\ -0.3333 & 0 & 0 & 0 \\ 0 & -1 & 0 & 0 \end{bmatrix} \; ; \; U_4 = \begin{bmatrix} 0.3333 & -0.333 & 0 \\ 0 & 0 & 0 \\ 0.3333 & 0.6667 & 0 \\ 0 & 0 & 1 \end{bmatrix}.$$

$$\mathcal{P}_1 = \mathcal{P}_2 = \mathcal{P}_3 = \mathcal{P}_4 = \begin{bmatrix} 2.1800 & -0.0143 & 0.0009 & -0.0602 & 0.0067 \\ -0.0143 & 4.0490 & 0.0039 & -0.5222 & 0.6511 \\ 0.0009 & 0.0039 & 2.1378 & 0.0374 & 0.0114 \\ -0.0602 & -0.5222 & 0.0374 & 2.0284 & 0.1597 \\ 0.0067 & 0.6511 & 0.0114 & 0.1597 & 2.4162 \end{bmatrix}.$$

$$M_1 = M_2 = M_3 = M_4 = \begin{bmatrix} -0.0040 & 0.0592 & 0.0045 & -0.1075 \\ -0.2847 & -0.2128 & 0.0386 & -1.0191 \\ 0.0384 & -0.00212 & -0.0029 & 0.0621 \\ 0.3013 & -0.2029 & -0.0234 & 0.6034 \end{bmatrix}$$

$$N_1 = N_2 = N_3 = N_4 = \begin{bmatrix} -0.6707 & 0.6752 & -0.1075 \\ -0.0347 & 0.0733 & 0.0621 \\ 0.3717 & -0.3746 & 0.0621 \\ 0.0513 & -0.0747 & 0.696 \end{bmatrix}$$

$$L_i^1 = L_i^2 = L_i^3 = L_i^4 = [-0.0046 \quad 0.0072 \quad -0.0767];$$

$$L_P^1 = L_P^2 = L_P^3 = L_P^4 = \begin{bmatrix} 0.6709 & -0.6709 & 0 \\ -0.0473 & 0.0473 & 0.0063 \\ -0.3699 & 0.3599 & 0 \\ 0.0413 & -0.0413 & -0.0062 \end{bmatrix} \quad ; \quad S_1 = S_2 = S_3 = S_4 = \begin{bmatrix} 0 \\ 0.25 \\ 0 \\ -0.25 \end{bmatrix}.$$

Creative Commons Attribution-NonCommercial-NoDerivatives 4.0 International License (CC BY-NC-ND)

Algerian Journal of Engineering Architecture and Urbanism Vol. 5 Nr. 3 2021
ISSN: 2588-1760

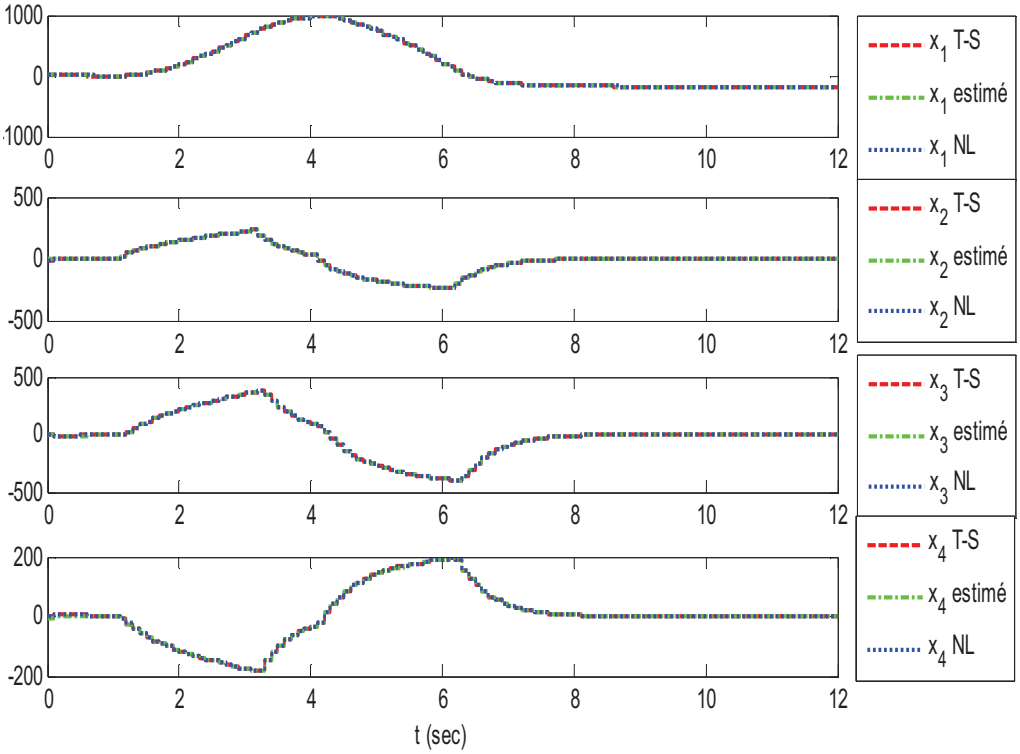

Fig.6 : Les variables d'état et leurs estimés.

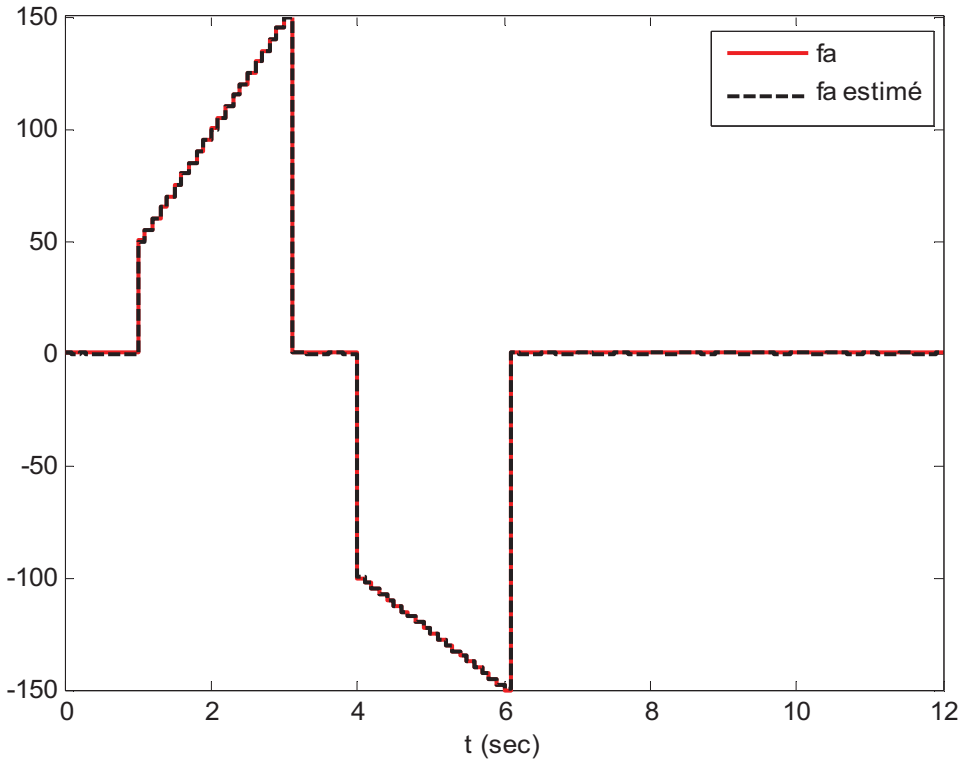

Fig.7 : le défaut actionneur et leur estimation.

Creative Commons Attribution-NonCommercial-NoDerivatives 4.0 International License (CC BY-NC-ND)

Algerian Journal of Engineering Architecture and Urbanism Vol. 5 Nr. 3 2021
ISSN: 2588-1760

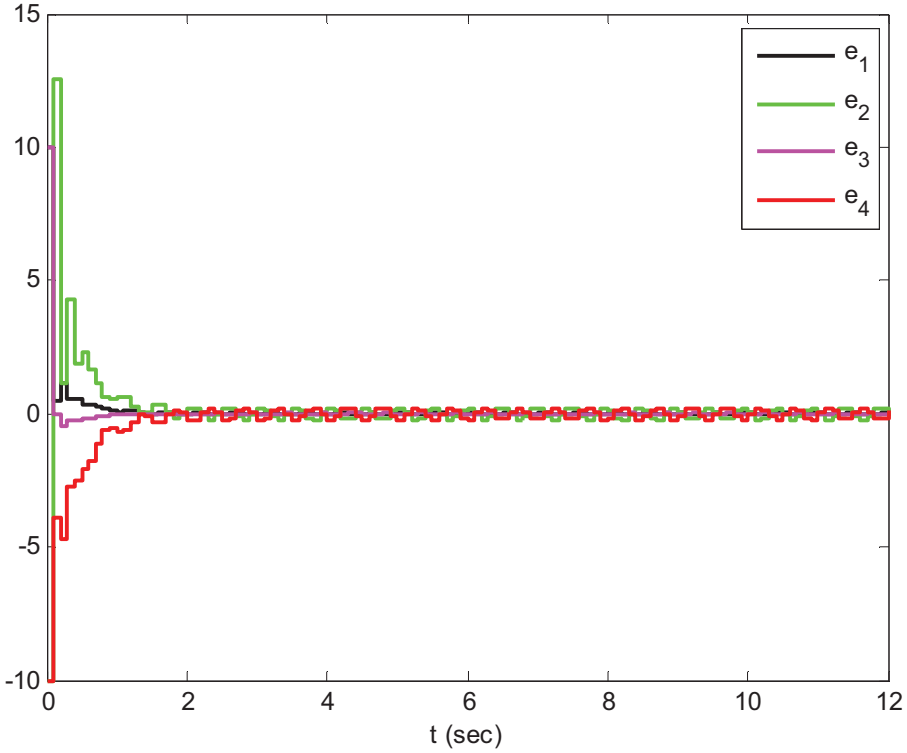

Fig.8 : Les erreurs d'estimations d'état.

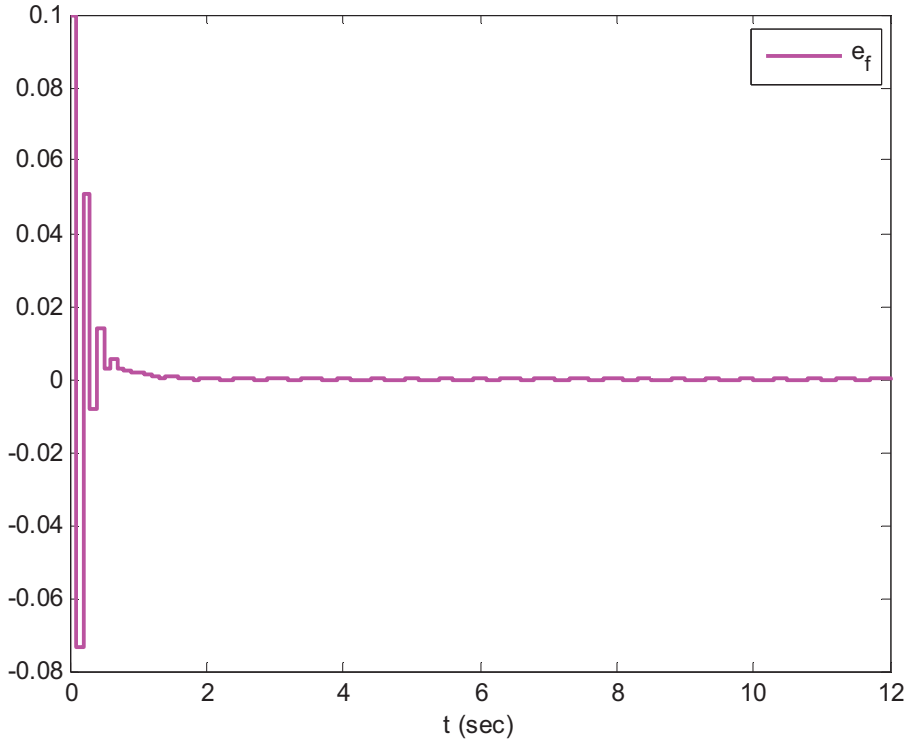

Fig.9 : L'erreur de défaut.

Creative Commons Attribution-NonCommercial-NoDerivatives 4.0 International License (CC BY-NC-ND)

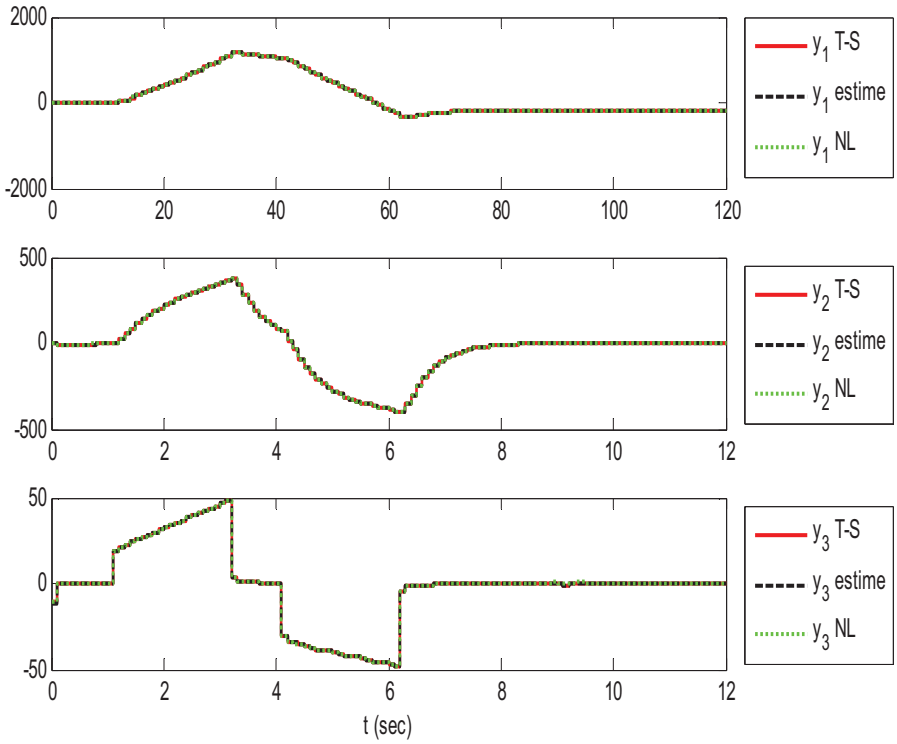

Fig 10: Les sorties mesurée.

Discussion :

La figures (6), (7) et aussi (10) représentent les estimations des états et de défaut du système singulier de type T-S : on peut voir que les estimations sont tout à fait correctes. D'autre part, dans la figure (8) et (9) les erreurs d'estimation d'état et l'erreur de défaut respectivement convergent asymptotiquement vers zéro avec un taux de convergence : $\alpha = 0.15$.

On peut voir clairement d'après les figures que l'observateur synthétisé estime non seulement correctement les états du système, mais aussi qu'il produit une estimation de bonne qualité de défaut.

Conclusion :

Dans cet article, l'approximation des systèmes singuliers non linéaires par une représentation multi-modèle à été considérée. Les méthodes de modélisation utilisées telles que l'approche floue de type Takagi-Sugeno (T-S), nécessitent la présence d'un modèle explicite sur lequel s'effectue la transformation polytopique convexe. Nous avons ainsi traité dans cet article, la synthèse d'observateur à temps discret pour les systèmes non linéaires parfaitement représentés par des multi-modèles. L'application de cette approche sur un système non linéaire singulier a produit de bons résultats mettant en évidence l'efficacité et la capacité double de cet observateur en estimant correctement les états du système non linéaire mais aussi en estimant très correctement le défaut sur un tel système, malgré la présence de perturbation externe avec un bon rejet de perturbation. La stabilité de l'erreur d'estimation ainsi que la synthèse des gains de cet observateur est assurée par la résolution des LMIs.

Creative Commons Attribution-NonCommercial-NoDerivatives 4.0 International License (CC BY-NC-ND)

Référence :

Bergsten, P., R. Palm, et al. *(2001). Fuzzy observers. 10th IEEE International Conference on Fuzzy Systems.(Cat. No. 01CH37297), IEEE.*

Bergsten, P., R. Palm, et al. *(2002). "Observers for Takagi-Sugeno fuzzy systems." IEEE Transactions on Systems, Man, and Cybernetics, Part B (Cybernetics)* ***32****(1): 114-121.*

Chadli, M. and P. Borne *(2012). Multiple models approach in automation: Takagi-Sugeno fuzzy systems, John Wiley & Sons.*

Guzman, J., F.-R. López-Estrada, et al. *(2021). "Actuator fault estimation based on a proportional-integral observer with nonquadratic Lyapunov functions." International Journal of Systems Science: 1-14.*

Liu, X., Z. Gao, et al. *(2017). "Takagi–Sugeno fuzzy model based fault estimation and signal compensation with application to wind turbines." IEEE Transactions on Industrial Electronics* ***64****(7): 5678-5689.*

Ouzaz, M., A. El Assoudi, et al*. (2020). Design of State and Fault Observer Based on the Euler discretization for Takagi-Sugeno Implicit Models with Lipschitz constraints. 2020 Fourth International Conference On Intelligent Computing in Data Sciences (ICDS), IEEE.*

T. Takagi and M. Sugeno*. (1985). Fuzzy identification of systems and its applications to modeling and control. IEEE Transactions on Systems, Man, and Cybernetics, 15 :116–132.*

K. Tanaka and H.O. Wang*, (2001).Fuzzy Control Systems Design and Analysis : A Linear Matrix Inequality Approach. John Wiley and Sons.*

A. Morales and J. Alvarez-Ramirez*,(2002). A PI observer for a class of nonlinear oscillators, Physics Letters A 297 205-209, Elsevier Science.*

H. Hamdi, M. Rodrigues, C. Mechmeche, D. Theilliol and N. BenHadj Braiek*, (2009).State Estimation for Polytopic LPV Descriptor Systems : Application to Fault Diagnosis, the 7th IFAC Symposium on Fault Detection, Supervision and Safety of Technical Processes, Barcelona, Spain, June 30 - July 3,pp 438-443.*

H. Muller, P. C. Muller*, J nuary(1999).Observer Design for Descriptor Systems, EEE transactions on automatic control, vol. 44, No. 1.*

Akhenak, A*.(2004). Conception d'observateurs non linéaire par approche multi-modèle: application au diagnostic. Thèse de doctorat, Institut National Polytechnique de Lorraine Nancy France.*

Djeddi, A., Y. Soufi, et al. *(2020). "Synthesis of unknown Inputs PI and PMI Observers for Takagi-Sugeno augmented Models applied on a Manipulator Arm." Electrotehnica, Electronica, Automatica* ***68****(1): 89-97.*

Do, M.-H., D. Koenig, et al. *(2020). "Robust H∞ proportional-integral observer-based controller for uncertain LPV system." Journal of the Franklin Institute* ***357****(4): 2099-2130.*

Hassanabadi, A. H., M. Shafiee, et al. *(2017). "Actuator fault diagnosis of singular delayed LPV systems with inexact measured parameters via PI unknown input observer." IET Control Theory & Applications* ***11****(12): 1894-1903.*

Ichalal, D. *(2009). Estimation et diagnostic de systèmes non linéaires décrits par un modèle de Takagi-Sugeno, Institut National Polytechnique de Lorraine.*

Mu, Y., H. Zhang, et al. *(2020). "Unknown input observer synthesis for discrete-time T–S fuzzy singular systems with application to actuator fault estimation." Nonlinear Dynamics* ***100****: 3399-3412.*

Ning, D., S. Sun, et al. *(2017). "Disturbance observer based Takagi-Sugeno fuzzy control for an active seat suspension." Mechanical Systems and Signal Processing* ***93****: 515-530.*

Orjuela, R., D. Maquin, et al. *(2006). Nonlinear system identification using uncoupled state multiple-model approach. Workshop on Advanced Control and Diagnosis, ACD'2006.*

Zhang, J., M. Chadli, et al. *(2019). "Finite-time observer design for singular systems subject to unknown inputs." IET Control Theory & Applications* ***13****(14): 2289-2299.*

Basile, G., Marro, G.*(1969)****.*** *On the observability of linear, time invariant systems with unknown inputs. J. Optim. Theory Appl. 3(6), 410–415.*

López-Estrada, F.R., Theilliol, D., Astorga-Zaragoza, C.M., Ponsart, J.C., Valencia-Palomo, G., Camas-Anzueto*(2019)****, J.:*** *Fault diagnosis observer for descriptor Takagi–Sugeno systems. Neurocomputing 331, 10–17.*

Li, X., Lu, D., Zeng, G., Liu, J., Zhang, W. *(2017)****:*** *Integrated fault estimation and non-fragile fault-tolerant control design for uncertain Takagi–Sugeno fuzzy systems with actuator fault and sensor fault. IET Control Theory Appl. 11(10), 1542– 1553.*

Creative Commons Attribution-NonCommercial-NoDerivatives 4.0 International License (CC BY-NC-ND)

Gao, Z., Breikin, T., Wang, H*.(2008)****:*** *Discrete-time proportional and integral observer and observer-based controller for systems with both unknown input and output disturbances. Optim. Control Appl. Methods 29(3), 171–189.*

Hamdi, H., Rodrigues, M., Mechmeche, C., Theilliol, D., Braiek, N.B*.(2012): Fault detection and isolation for linear parameter varying descriptor systems via proportional integral observer. Int. J. Adapt. Control Signal Process 26(3), 224– 240.*

Li, R., Zhang, X*.(2019): Adaptive sliding mode observer design for a class of T-S fuzzy descriptor fractional order systems. IEEE Trans. Fuzzy Syst. https://doi.org/10.1109/ TFUZZ.2019.292851.*

Komachali, F.P., Shafiee, M., Darouach, M. *(2019): Design of unknown input fractional order proportional–integral observer for fractional order singular systems with application to actuator fault diagnosis. IET Control Theory Appl. 13(14), 2163–2172.*

Chadli, M., Karimi, H.R*.(2013)****:*** *Robust observer design for unknown inputs Takagi–Sugeno models. IEEE Trans. Fuzzy Syst. 21(1), 158–164.*

Creative Commons Attribution-NonCommercial-NoDerivatives 4.0 International License (CC BY-NC-ND)

Algerian Journal of Engineering Architecture and Urbanism Vol. 5 Nr. 3 2021
ISSN: 2588-1760

Conception d'observateur proportionnel à entrée inconnue (P-UIO) pour les systèmes singuliers de type T-S

INES Righi

Faculté des Sciences et de Technologies, Univ. Souk Ahras-LEER- BP 1553
Souk-Ahras, 41000. Algérie, e-mail: **i.righi@univ-soukahras.dz**

Résumé

Ce papier traite l'estimation d'état et de l'entrée inconnue pour les systèmes descripteur singuliers de type Takagi-Sugeno (T-S) à variable de décision mesurable (VDM), au travers la synthèse d'un observateur proportionnel à entrée inconnue (P-UIO), les gains de l'observateur sont calculés à l'aide de la résolution d'inégalité matricielles linéaire (LMIs), via la fonction candidate non quadratique du Lyapunov. Un exemple de simulation illustrant la capacité de l'approche proposée pour estimer les états et les entrées inconnues est présenté, afin de monter la validité des résultats théoriques.

Mots-clés: système T-S singulier ; observateur proportionnel à entrée inconnue (P-UIO) ; variable de décision mesurable (VDM) ; estimation d'état et d'entrée inconnue.

I. Introduction:

Les systèmes technologiques actuels sont composés de nombreux composants en interactions. Ils ont de plus des comportements dynamiques différents suivant les conditions d'utilisation. Ces systèmes sont représentés par des modèles dynamiques non linéaires souvent complexes à manipuler. Afin de réduire la complexité de ces modèles, une technique reposant sur une décomposition en modèle plus simple, fréquemment linéaires, peuvent être utilisées en large partie de cette demande. La littérature présente ce type de modélisation sous diverses appellations que l'on peut regrouper sous le nom générique *l'approche multi-modèle*, qui se caractérise par une interpolation convexe des sous modèles linéaires avec des fonctions non linéaire appelé fonctions d'activation vérifiant la propriété de somme convexe **(Chadli and Borne 2012)** pour représenter de manière approchée ou exacte le comportement non linéaire du système, chaque modèle linéaire décrivant le comportement du système dans une zone de fonctionnement particulier.

Dans de nombreux travaux sur la commande des systèmes, le vecteur d'état est supposé accessible à la mesure. Or, d'un point de vue pratique, une telle hypothèse n'est pas toujours vérifiée. En effet, pour des raisons techniques et/ou économiques, il est difficile, voire impossible, de mesurer la totalité des variables d'état du système, d'où la nécessité d'estimer ces dernières à partir d'un jeu de données d'entrées-sorties. De façon générale, le besoin de connaître entièrement les variables d'état du système est souvent une nécessité dans les phases de modélisation ou d'identification, de diagnostic et de commande des systèmes, ce qui place le problème de la conception d'observateurs au cœur du problème général de contrôle des systèmes.

Il existe deux types de variables de décision qui interviennent dans les fonctions d'activation, mesurables dans le cas des variables d'entrées ou de sorties, ou non mesurables

Creative Commons Attribution-NonCommercial-NoDerivatives 4.0 International License (CC BY-NC-ND)

dans le cas des variables d'état indisponibles. Ils ont été montré dans **(Ichalal 2009)**, si la variable d'état est utilisée comme variable de décision. Il est donc intéressant d'exploiter cette approche dans la synthèse des observateurs pour l'estimation d'état, le diagnostic et le contrôle des systèmes de type T-S. L'étude de la stabilité et de la stabilisation est étroitement liée à l'estimation d'état des modèles flous T-S. Par conséquent, la convergence des erreurs d'estimation est développée par la théorie de Lyapunov, et est formulée sous les contraintes d'inégalité linéaire matricielles (LMIs). Cependant, dans tous ces travaux, les auteurs supposent que la variable de décision (notée $\xi(k)$ dans 1) est mesurable (i.e $\xi(k) = u(k)$ ou $\xi(k) = y(k)$). Dans le problème du diagnostic, cette hypothèse oblige à concevoir des bancs d'observateurs à base de multi-modèles dont les fonctions d'activation dépendent de l'entrée $u(t)$, pour la détection et la localisation des défauts actionneurs, ou de la sortie $y(k)$ pour la détection et la localisation des défauts capteurs. Ceci nécessite l'élaboration de deux multi-modèles différents représentant le même système, selon que l'on veut détecter et localiser des défauts capteurs ou des défauts actionneurs. Pour éliminer ce problème, il est intéressant de considérer le cas où les fonctions d'activation dépendent de l'état du système. Parmi les rares travaux publiés dans ce contexte, on peut citer par exemple **(Palm and Bergsten 2000)**,**(Bergsten, Palm et al. 2001)** et **(Bergsten, Palm et al. 2002** qui, sous l'hypothèse de fonctions d'activation $\mu_i(x_k)$ lipschitziennes, ont proposé un observateur de type Luenberger. Les conditions de stabilité de ce dernier sont formulées sous forme d'inégalités linéaires matricielles (LMI) ce qui en rend la synthèse facile. Dans **(Palm and Bergsten 2000)**,**(Bergsten, Palm et al. 2001)**, se basant sur les résultats obtenus dans **(Palm and Bergsten 2000)** et **(Bergsten, Palm et al. 2002)**un observateur à mode glissant est proposé pour compenser les termes inconnus du système. Dans **(Ichalal, Marx et al. 2007)**, une autre approche a été proposée pour permettre de réduire le conservatisme inhérent aux méthodes précédentes et d'élargir le domaine des solutions. Il a été montré dans la littérature que les modèles T-S à variables de décision non mesurables (VDNM), permettent une représentation d'une classe de système plus large et de manière exacte dans un compact de l'espace d'état. De plus, dans le contexte du diagnostic, contrairement aux modèle T-S à variables de décision mesurables (entrées ou sorties du système), un seul modèle T-S suffit pour la construction de bancs d'observateurs destinés à la détection et la localisation de défauts de capteurs et d'actionneurs d'un système. Cependant, l'étude de cette classe de modèles T-S à variables de décision non mesurables est souvent complexe et constitue un champ de recherche intéressant. Pourtant les résultats obtenus, dans la littérature, sur l'estimation d'état et la commande utilisant les modèles T-S sont basés sur l'hypothèse de mesurabilité des variables de prémisses ou variables de décision intervenant dans les fonctions d'activation du modèle T-S. Or, ces fonctions d'activation peuvent dépendre partiellement ou entièrement du vecteur d'état qui peut ne pas être mesurable. Ce type de problème est très souvent rencontré dans la modélisation T-S issue des transformations par secteurs non linéaires **(T. Takagi and M. Sugeno, 1985).**

L'observateur P-UIO permet l'estimation des états et des entrées inconnue par découplage càd permet de découpler complètement les entrées inconnues pour que l'erreur d'estimation devienne insensible à ces entrées. On peut citer par exemple les travaux de **(Liu, Gao et al. 2017)** pour des variables de décision mesurables et **(Ouzaz, El Assoudi et al. 2020)**, **(Guzman, López-Estrada et al. 2021)** pour les variables de décision non mesurables. En comparaison avec les études précédentes, on note que cet observateur estime simultanément les états et les entrées inconnues. De plus, l'introduction d'un système descripteur permet de réduire les résultats de conservatisme car il constitue un degré de liberté supplémentaire à déterminer.

Creative Commons Attribution-NonCommercial-NoDerivatives 4.0 International License (CC BY-NC-ND)

L'objectif de ce travail est de traiter simultanément le problème d'estimation d'état et d'entrée inconnue d'un système singulière de type Takagi-Sugeno à VDM, l'approche proposé développe le concept de la décomposition en valeurs singulières, leur synthèse repose sur la résolution d'inégalités linéaire matricielle LMIs.
Le papier est organisé comme suit : dans la section **II**, quelques notations et la présentation du problème est exposée sur l'aspect modélisation du système ainsi que les diverses hypothèses nécessaires. Dans la section **III**, nous présentons la synthèse du multi-observateur Proportionnel à entrées inconnues. La structure, la synthèse des différentes matrices et les conditions d'existence de cet observateur sont établies, la section **IV** propose une méthode de synthèse de cet observateur et un exemple illustratif qui expose l'efficacité de la méthode développée dans la section **V**.

II. Notation et position du problème :

II.1. Notations: Tout au long de cet article, les notations suivantes sont adoptées pour représenter commodément les différentes expressions, étant donné un ensemble de fonctions non linéaires: $\mu_i(.); i \in \{1 \dots .r\}$, sont les fonctions d'activation scalaires satisfaites la propriété de somme convexe. Ce travail se concentre uniquement sur les variables de prémisse mesurables regroupées dans le vecteur des variables de décision $\xi(k)$, dont les mesures peuvent être obtenues à partir de la sortie $y(k)$, ou à partir de la construction d'un observateur.
Ces notations abrégée seront utilisées dans la suite pour représenter la propriété de somme convexe, les expressions de matrices variant en temps discret: $Y_\mu = Y_\mu(\xi(k)) = \sum_{i=1}^{r} \mu_i\left(\xi(k)\right) Y_i$, pour une somme convexe simple; $Y_{\mu-} = Y_{\mu-}(\xi(k)) = (\sum_{i=1}^{r} \mu_i(z(k)) Y_i)^{-1}$ pour une somme convexe inverse; and $Y_{\mu\mu} = Y_{\mu\mu}\left(\xi(k)\right) = \sum_{i=1}^{r}\sum_{j=1}^{r} \mu_i\left(\xi(k)\right)\mu_j\left(\xi(k)\right) Y_{ij}$ pour une somme convexe double et relaxé. Pour un vecteur x et ξ, x_k désigne $x(k)$, ξ_k définit par la notation $\xi(k)$ et x_{k+} par $x(k+1)$. I_r designe l'ensemble $\{1, 2, \cdots, r\}$, $\mathfrak{N}^+$ représente l'ensemble des entiers positives réelle. $\mathcal{H}(A) = A + A^T$ est la matrice hermitienne de A. $A^\dagger = (A^T A)^{-1} A^T$ représente la matrice pseudo-inverse de A. $\mathbb{Z} + (*)$ désigne $\mathbb{Z} + \mathbb{Z}^T$. I est la matrice identité. Un astérisque * symbolise des blocks symétrique d'une matrice.

Soit le système descripteur singulier à temps discret non linéaire suivant :

$$\begin{cases} E\, x_{k+} = f(x_k, u_k, d_k) \\ y_k = g(x_k, d_k) \end{cases} \tag{1}$$

Ou : $x_k \in \mathfrak{N}^{n_x}$, $u_k \in \mathfrak{N}^{n_u}$, $y_k \in \mathfrak{N}^{n_y}$, $d_k \in \mathfrak{N}^{n_d}$ sont respectivement le vecteur d'etat, le vecteur d'entrée de commande connue, la sortie et l' entrée inconnu affecte le système.

Dans le reste du papier, on note : $\mathfrak{S}_\mu = \sum_{i=1}^{r} \mu_i(z_k) \mathfrak{S}_i$ pour simplifier l'écriture, $\mathfrak{S}_i$ une matrice quelconque.

<u>Cas des variables de décision mesurable (VDM)</u>: $\{\, \xi_k = \hat{\xi}_k \,\}$ *et* $\{\, \mu_i(\xi_k) = \mu_i(\hat{\xi}_k) \,\}$

Soit le système non linéaire singulier (descripteur) à temps discret décrit sous forme Takagi-Sugeno obtenu par la transformation du secteur non linéaire **(T. Takagi and M. Sugeno, 1985)**:

Creative Commons Attribution-NonCommercial-NoDerivatives 4.0 International License (CC BY-NC-ND)

$$\begin{cases} E x_{k+} = \sum_{i=1}^{r} \mu_i(\xi_k)(A_i x_k + B_i u_k + H_i d_k) \\ y_k = C x_k + R d_k \end{cases} \quad (2)$$

$\xi_k = [\xi_{1k}\ \xi_{2k} \dots \xi_{rk}]^T$représente le vecteur des variables de décisions .$\mathcal{F}_{il}$ $(i \in \mathcal{T}, l \in \vartheta)$ sont des ensembles floues caractérisée par des fonctions d'activation avec : $\mathcal{T} = \{1,2, \dots n\}, \vartheta = \{1,2, \dots r\}$, avec : r est le nombre de sous-modèle floue et n est le nombre de vecteur de décision.
$n = r$ pour système T-S.
$n \neq r$ pour système singulier.

Ces fonctions d'activation vérifient la propriété de somme convexe, c'est-à-dire :

$$\begin{cases} \sum_{i=1}^{r} \mu_i(\xi_k) = 1 \\ 0 \leq \mu_i(\xi_k) \leq 1 \end{cases} \quad (3)$$

Les matrices E, A_i, B_i et C sont des matrices connu de dimensions appropriées.$H_i$et R sont des matrices colonne d'influences des entrées inconnues de rang plein. Généralement $rang\,(E) = n_E \leq n_x$, ce qui implique que E est singulière.

Les variables de décision ξ_k sont supposées accesssible à la mesure en temps réel, dépendant de l'entrée de commande ou des sorties.

Avant d'expliciter les principaux résultats, nous allons faire les hypothèses suivant :

Soit le triplet (A_i, B_i, C), les conditions suivantes siont vérifiées simultanément :

H 1 :

$$rang \begin{pmatrix} E \\ C \end{pmatrix} = n_x \quad (4.a)$$

C: est une matrice de rang plein ligne.

H 2 :

$$rang \begin{pmatrix} sE - A_i \\ C \end{pmatrix} = n_x, \forall\, s \in \mathcal{C}\ |s| > 1 \quad (4.b)$$

$\mathcal{C}$: est l'ensemble des nombres complexe.

H 3 :

$$rang \begin{bmatrix} E & 0 \\ C & R \\ I_{n_x} & 0 \end{bmatrix} = rang \begin{bmatrix} E & 0 \\ C & R \end{bmatrix} = n_x + rang(R) \quad (4.c)$$

Lemme 1 : Pour deux matrices Φ et ψ de dimension appropriées, si la condition (4.c) est vérifiées, alors :

$$rang \begin{pmatrix} \Phi \\ \psi \end{pmatrix} = rang(\Phi) \quad (5)$$

$[U_1 \quad U_2]\Phi = \psi$, a une solution. Alors la solution générale peut étre exprimées par :

$$[U_1 \quad U_2] = \psi \Phi^{+} + W(I - \Phi \Phi^{+}) \quad (6)$$

Ou : W est une matrice arbitraire de dimension appropriées.

Lemme de Finsler's : soit $x_k \in \mathfrak{R}^{n_x}, Q = Q^T \in \mathfrak{R}^{n_x \times n_x}$ et $\mathcal{R} \in \mathfrak{R}^{n_x}$ tel que: $rank(\mathcal{R}) \leq n_x$; les expressions suivantes sont équivalents :

Creative Commons Attribution-NonCommercial-NoDerivatives 4.0 International License (CC BY-NC-ND)

$$\begin{cases} a)\ \xi_k^T Q \xi_k < 0 \quad : \quad \{\forall\, x_k \in \mathfrak{R}^{n_x}; x_k \neq 0\,; \mathcal{R} x_k = 0\} \\ b)\ \exists\ \mathcal{M} \in \mathfrak{R}^{n_x} : \quad \{Q + \mathcal{M}\mathcal{R} + \mathcal{R}^T \mathcal{M}^T < 0\} \end{cases} \tag{7}$$

Complément de Schur : soit trois matrices $P_{22} = P_{22}^T, P_{11} < P_{11}^T$ et P_{12} de dimensions appropriées, les LMIs suivantes sont équivalentes :

Si la matrice P_{22} est inversible, alors les LMIs suivantes sont équivalentes:

1. $\begin{bmatrix} P_{11} & P_{12}^T \\ P_{12} & P_{22} \end{bmatrix} > 0$ (8.a)
2. $P_{22} > 0, P_{11} - P_{12}^T P_{22}^{-1} P_{12} < 0,$ (8.b)
3. $P_{11} > 0, P_{22} - P_{12} P_{22}^{-1} P_{12}^T < 0,$ (8.c)

Lemme 2 (Congruence) : soit deux matrices *P* et *Q* de dimensions appropriées, si *P* est une matrice définie positive et *Q* une matrice colonne de rang plein, alors le produit QPQ^T est définie positive.

Lemme 3 : soit $U = U^T > 0$ et V deux matrices de dimensions appropriées, la propriété suivante est vérifiée :

$$(V - U)U^{-1}(V - U) \geq 0 \leftrightarrow V^T U^{-1} V \geq V + V^T - U \tag{9}$$

Hypothèses :

***H 4* :** soit le couple (E, A_i) est régulier, i.e :

$$det(sE - A_i) = 0, \forall\, s \in \mathcal{C} \tag{10}$$

H 5 : Tous sous modèles (2) sont impulse-observable et détectable.

Afin d'obtenir des conditions de stabilisation moins conservatrices, nous introduisons des matrices libres pour réduire le conservatisme des conditions exprimées à partir de sommes doubles. Dans ce travail, nous avons opté pour le lemme de relaxation, qui constitue un bon compromis entre complexité et réduction du conservatisme, ce schéma de relaxation se présente comme suit:

Lemme de relaxation :

Soit T_{ij} une matrice symétrique de dimensions appropriées, et $\mu_i(\xi_k),\ i \in I_r$ toutes familles de fonctions satisfaisant la propriété de somme convexe.

La condition: $\sum_{i=1}^{r} \sum_{j=1}^{r} \sum_{i=1}^{r_s} \mu_i \mu_j T_{ij} < 0$, est vérifiée si:

$$\begin{cases} T_{ij} < 0 \\ \dfrac{2}{r-1} T_{ii} + T_{ij} + T_{ji} < 0 \end{cases} \qquad (i,j) \in I_r \times I_r,\ \ i \neq j \tag{11}$$

Creative Commons Attribution-NonCommercial-NoDerivatives 4.0 International License (CC BY-NC-ND)

III. Proposition d'observateur proportionel à entrée inconnue (P-UIO) :

Le but est de proposer un observateur proportionnel à entrée inconnue pour l'estimation simultanée de l'état et de l'entrée inconnue, cet observateur est pris sous la forme suivante :

$$\begin{cases} \eta(k+1) = \sum_{i=1}^{r} \mu_i(\xi_k)(M_i\eta_k + S_i u_k + L_i y_k) \\ \hat{x}_k = \eta_k + U_2 y_k \\ \hat{y}_k = C\hat{x}_k + R\hat{d}_k \end{cases} \quad (12)$$

η_k , $\hat{x}_k$: sont respectivement l'etat de l'observateur et l'estimé de l'état du système.
M_i, S_i et L_i : sont l'ensemble des gains matricielle à déterminer.

Définition 1 : Le système (12) définissant l'observateur proportionnel intégral à entrée inconnnue (P-UIO) pour le système (2), avec des conditions iniriales $x(0)$ et une entrée arbitraire u_k, les relations suivantes sont vraies :

$$\lim_{k\to\infty}(x_k - \hat{x}_k) = 0 \quad (13)$$

Représente l'erreur d'observation:

$$\lim_{k\to\infty}(d_k - \hat{d}_k) = 0 \quad (14)$$

Représente l'erreur d'entrée inconnue.

Remarque 1: *Pour la technique de conception de l'observateur P-UIO par découplage, les termes d_k et d_{k+} , n'apparaissent pas dans la dynamique de l'erreur, en effet l'avantage de ce type d'observateur,est de permet de découpler complètement les entrées inconnues pour que l'erreur d'estimation devient insensible à ces entrées.*

L'erreur d'estimation d'état est donné par :

$$e_0(k) = x_k - \hat{x}_k = x_k - \eta_k - U_2 y_k = U_1 E x_k - \eta_k - U_2 R d_k \quad (15)$$

Sa dynamique est définit par :

$$e_0(k+1) = U_1 E x_{k+} - \eta_{k+} - U_2 R d_{k+} = U_1 \sum_{i=1}^{r} \mu_i(\xi_k)\left((A_i x_k + B_i u_k + H_i d_k) - (M_i\eta_k + S_i u_k + L_i C x_k + L_i R d_k)\right) - U_2 R d_{k+}$$

(16)

Après réorganisation des termes de la partie droite de la dynamique de l'erreur d'estimation d'état, et en utilisant les définitions de y_k et de η_k.

$$e_0(k+1) = \sum_{i=1}^{r}\mu_i(\xi_k)\left((M_i e_0(k) + (U_1 A_i - M_i + M_i U_2 C - L_i C)x_k + (U_1 B_i - S_i)u_k + (U_1 H_i + M_i U_2 R - L_i R)\right)d_k - U_2 R d_{k+}$$

(17)

Avec : $\sum_{i=1}^{r}\mu_i(\xi_k) N_i = \sum_{i=1}^{r}\mu_i(\xi_k)(M_i U_2 - L_i)$ (18)

Creative Commons Attribution-NonCommercial-NoDerivatives 4.0 International License (CC BY-NC-ND)

Si les conditions de contraintes suivantes sont vérifiée :

$$\begin{cases} U_1 A_i - M_i + M_i U_2 C - L_i C \\ U_1 B_i - S_i \\ U_1 H_i + M_i U_2 R - L_i R = 0 \\ U_2 R = 0 \end{cases} \quad (19)$$

Alors, la dynamique de l'erreur d'estimation est simplifiée par :

$$e_0(k+1) = \sum_{i=1}^{r} \mu_i(\xi_k) M_i e_0(k) \quad (20)$$

Pour résoudre les gains de l'observateur, soit :

$$\begin{cases} M_i = U_1 A_i + N_i C \\ U_1 H_i + N_i R = 0 \\ N_i = M_i U_2 - L_i \end{cases} \quad (21)$$

La dynamique de l'erreur est equivalent à :

$$e_0(k+1) = \sum_{i=1}^{r} \mu_i(\xi_k) (U_1 A_i + N_i C) e_0(k) \quad (22)$$

Remarque 2: *Pour synthétiser l 'observateur P-UIO exactement, c'est nécessaire de déterminer les matrices* U_1 *et* U_2 *tel que relations (5) et (6) sont vérifiées simultanément.*

Pour garantir l'hypothèse 3 et à partir du lemme 1 les matrices non singulières U_1 et U_2 sont définies par :

$$\begin{cases} U_1 = D_1 + W \mathcal{J}_1 \\ U_2 = D_2 + W \mathcal{J}_2 \end{cases} \quad (23)$$

Avec :

$$\begin{cases} D_1 = [I_{n_x} \quad 0] \begin{bmatrix} E & 0 \\ C & R \end{bmatrix}^{\dagger} \begin{bmatrix} I_{n_x} \\ 0 \end{bmatrix} \\ D_1 = [I_{n_x} \quad 0] \begin{bmatrix} E & 0 \\ C & R \end{bmatrix}^{\dagger} \begin{bmatrix} 0 \\ I_{n_y} \end{bmatrix} \end{cases} \quad (24)$$

$$\begin{cases} \mathcal{J}_1 = (I_{n_x+n_y} - \begin{bmatrix} E & 0 \\ C & R \end{bmatrix} \begin{bmatrix} E & 0 \\ C & R \end{bmatrix}^{\dagger}) \begin{bmatrix} I_{n_x} \\ 0 \end{bmatrix} \\ \mathcal{J}_2 = (I_{n_x+n_y} - \begin{bmatrix} E & 0 \\ C & R \end{bmatrix} \begin{bmatrix} E & 0 \\ C & R \end{bmatrix}^{\dagger}) \begin{bmatrix} 0 \\ I_{n_y} \end{bmatrix} \end{cases} \quad (25)$$

$$U_1 = [I_{n_x} \quad 0] \begin{bmatrix} E & 0 \\ C & R \end{bmatrix}^{\dagger} \begin{bmatrix} I_{n_x} \\ 0 \end{bmatrix} + W (I_{n_x+n_y} - \begin{bmatrix} E & 0 \\ C & R \end{bmatrix} \begin{bmatrix} E & 0 \\ C & R \end{bmatrix}^{\dagger}) \begin{bmatrix} I_{n_x} \\ 0 \end{bmatrix} \quad (26)$$

$$U_2 = [I_{n_x} \quad 0] \begin{bmatrix} E & 0 \\ C & R \end{bmatrix}^{\dagger} \begin{bmatrix} 0 \\ I_{n_y} \end{bmatrix} + W (I_{n_x+n_y} - \begin{bmatrix} E & 0 \\ C & R \end{bmatrix} \begin{bmatrix} E & 0 \\ C & R \end{bmatrix}^{\dagger}) \begin{bmatrix} 0 \\ I_{n_y} \end{bmatrix} \quad (27)$$

Théorème 1 : l'observateur P-UIO est globalement asymptotiquement stable, s'il existe une matrice symétrique et définie positive $\mathcal{Y}_i = \mathcal{Y}_i^T$ avec $\mathcal{Y}_i = P_i^{-1}$ et des matrices $\mathcal{V}, \mathcal{Z}_i$ remplissant les conditions LMI suivantes :

$$\begin{bmatrix} -\mathcal{Y}_i + 2\alpha \mathcal{Y}_i & * \\ \mathcal{X} D_1 A_i + \mathcal{V} \mathcal{J}_1 A_i + \mathcal{Z}_i C & -\mathcal{Y}_i^T - \mathcal{X} - \mathcal{X}^T \end{bmatrix} < 0 \quad (28)$$

Creative Commons Attribution-NonCommercial-NoDerivatives 4.0 International License (CC BY-NC-ND)

$$\begin{bmatrix} -\delta I & * \\ (\mathcal{X}D_1H_i + \mathcal{V}J_1H_i + \mathcal{Z}_iR)^T & -I_{n_x} \end{bmatrix} < 0 \quad (29)$$

Analyse de stabilité : soit la fonction candidate non qudratique du Lyapunov suivante :

$$V(e_0(k)) = e_0^T(k)P_\mu^{-1}e_0(k) \quad (30)$$

avec $P_\mu = P_\mu^T > 0$

***α − stabilité*:**

L' **α − stabilité** est une technique très simple, utilisée pour l'ammélioration des performances d'un système dans le domaine temporel. A partir d'une condition initiale x_0 pour $k = 0$, l'idée est d'imposer un critère afin que la trajctoire en boucle fermée converge le plus rapidement possible vers le point d'équilibre.

Définition 2 : les systèmes (2) et (12) sont dit **α − stable**, s'il existe $\alpha > 0$ tel que la dérivée de la fonction de Lyapunov $\Delta V(e_0(k))$ satisfait l'inégalité suivante :

$$\Delta V(e_0(k)) \leq 2\alpha V(e_0(k)), \forall\ e_0(k) \in \mathfrak{R}^{n_x}$$

Alors, afin d'assurer une vitesse de convergence de l'erreur d'estimation, on peut définir une surface S à gauche du plan complexe délimitée par une droite d'abscisse $(-\alpha)$ ou $\alpha \in \mathfrak{R}^+$.

$$\Delta V(e_0(k)) = e_0^T(k+1)P_\mu^{-1}e_0(k+1) - e_0^T(k)P_\mu^{-1}e_0(k) + 2\alpha e_0^T(k)P_\mu^{-1}e_0(k) < 0 \quad (31)$$

$$\begin{bmatrix} e_0(k) \\ e_0(k+1) \end{bmatrix}^T \sum_{i=1}^r \mu_i(\xi_k) \left(\begin{bmatrix} -P_i^{-1} + 2\alpha P_i^{-1} & 0 \\ 0 & P_i^{-1} \end{bmatrix} \right) \begin{bmatrix} e_0(k) \\ e_0(k+1) \end{bmatrix} < 0 \quad (32)$$

De (20) : $-e_0(k+1) + \sum_{i=1}^r \mu_i(\xi_k) M_i e_0(k) = 0 \rightarrow [\sum_{i=1}^r \mu_i(\xi_k) M_i \quad -I_{n_x}] \begin{bmatrix} e_0(k) \\ e_0(k+1) \end{bmatrix} = 0$ (33)

Par l'utilisation du lemme de Finsler's ,et on pose : $\mathcal{M} = \begin{bmatrix} 0 \\ \mathcal{X} \end{bmatrix}$ ($\mathcal{X}$ est une matrice auxiliaire)

$$\sum_{i=1}^r \mu_i(\xi_k) \left(\begin{bmatrix} -P_i^{-1} + 2\alpha P_i^{-1} & 0 \\ 0 & P_i^{-1} \end{bmatrix} + \begin{bmatrix} 0 \\ \mathcal{X} \end{bmatrix} [M_i \quad -I_{n_x}] + (*) \right) < 0 \quad (34)$$

(34) donne :

$$\begin{bmatrix} -P_i^{-1} + 2\alpha P_i^{-1} & * \\ \mathcal{X}M_i & -P_i^{-1} - \mathcal{X} - \mathcal{X}^T \end{bmatrix} < 0 \quad (35)$$

On remplace M_i par son équation définit dans (21), ensuite U_1 par son expression dans (23), on obtient :

$$\mathcal{X}M_i = \mathcal{X}D_1A_i + \mathcal{X}W J_1A_i + \mathcal{X}N_iC \quad (36)$$

Avec le changement de variable bijectif : $\mathcal{Z}_i = \mathcal{X}N_i$ et $\mathcal{V} = \mathcal{X}W$, alors (36) devient :

$$\mathcal{X}M_i = \mathcal{X}D_1A_i + \mathcal{V}J_1A_i + \mathcal{Z}_iC \quad (37)$$

Creative Commons Attribution-NonCommercial-NoDerivatives 4.0 International License (CC BY-NC-ND)

A partir de : $U_1H_i + N_iR = 0$, on remplace U_1 par sa formule, on obtient : $D_1H_i + WJ_1H_i + N_iR = 0$, et on multiplie cette dernière par X:

$$XD_1H_i + XWJ_1H_i + XN_iR = 0 \tag{38}$$

(38) devient : $XD_1H_i + VJ_1H_i + Z_iR = 0$ (39)

L'égalité qui apparait dans les critères de stabilité, n'est pas facile à résoudre via l'outil LMI toolbox, un petit scalaire $\delta > 0$, peut étre choisi tel que LMI (39) est formulé par :

$$(XD_1H_i + VJ_1H_i + Z_iR)^T(XD_1H_i + V_iJ_1H_i + Z_iR) < -\delta I$$

qui représente LMI (29) .

IV. Procédure de synthèse d'observateur P-UIO :

Etape1 **:** confirmer que les matrices satisfaites les hypothèses 1,2 et 3 ou non, si oui on passe à l'étape 2 sinon la synthèse d'observateur P-UIO est faux.

Etape 2 **:** résoudre le problème d'optimisation des LMIs (28) et (29) pour obtenir les variables, à son tour $X^{-1}Z_i = N_i$ et $X^{-1}V = W$ sont déterminée.

Etape 3 **:** obtenir les matrices U_1 et U_2 à l'aide de la condition (23)-(27) et obtenir S_i à l'aide de l'équation (14).

Etape 4 **:** si N_i est disponible, alors M_i et L_i sont résolu à l'aide de des égalités mentionnée dans (21).

Alors l'observateur proportionnel à entrée inconnue (P-UIO) est synthétisé correctement.

Estimation d'entrée inconnue :

Après l'estimation de l'état, en découplant complètement ou partiellement l'influence de l'entrée inconnue de l'erreur d'estimation d'état, il est possible alors d'estimer l'entrée inconnue à partir de l'estimation de vecteur d'état.

Plusieurs étude concernant l'estimation de l'entrée inconnue pour les systèmes non linéaire dynamique sont prise en compte. La méthode utilisée la plus performante est basé sur la meilleurs estimation de l'etat.

En effet si les conditions de convergence asymptotique sont vérifiées dans l'état régulier, l'erreur d'estimation d'état converge vers zéro, donc on peut remplacer x_k par $\hat{x}_k$ dans l'equation de multi-modèle (2) :

$$\begin{cases} E\hat{x}_{k+} = \sum_{i=1}^{r} \mu_i(\xi_k)(A_i\hat{x}_k + B_iu_k + H_i\hat{d}_k) \\ \hat{y}_k = C\hat{x}_k + R\hat{d}_k \end{cases} \tag{40}$$

$\hat{d}_k$: est seulement la variable inconnue, l'equation (40) se ré-écrit par l'expression suivante :

Creative Commons Attribution-NonCommercial-NoDerivatives 4.0 International License (CC BY-NC-ND)

$$\begin{bmatrix} E\hat{x}_{k+} \\ \hat{y}_k \end{bmatrix} = \begin{bmatrix} \sum_{i=1}^{r} \mu_i(\xi_k)\,(A_i\hat{x}_k + B_i u_k) \\ C\hat{x}_k \end{bmatrix} + W\hat{d}_k \tag{41}$$

Pour estimer l'entrée inconnue, il faut que le rang de la matrice W vérifie à chaque instant k la condition :

$$Rang(W) = n_d \tag{42}$$

n_d: etant la dimension de d_k, si cette condition est vérfiée, West de plein rang colonne et sa pseudo inverse à gauche est définie par :

$$W^{+} = (W^{T}W)^{-1}W^{T} \tag{43}$$

Avec : $W = \begin{bmatrix} \sum_{i=1}^{r} \mu_i(\xi_k) H_i \\ R \end{bmatrix}$. W est une matrice colonne de rang plein, la variable $\hat{d}_k$ est obtenu par la matrice pseudo-inverse de W.

1ère possibilté : L'entrée inconnue peut alors se calculer de la façons suivante:

$$\hat{d}_k = (W^{T}W)^{-1}W^{T}\begin{bmatrix} E\hat{x}_{k+} - \sum_{i=1}^{r} \mu_i(\xi_k)\,(A_i\hat{x}_k + B_i u_k) \\ y_k - C\hat{x}_k \end{bmatrix} \tag{44}$$

Et l'erreur de l'entrée inconnue :

$$e_d(k) = d_k - \hat{d}_k = d_k - W^{+}\begin{bmatrix} E\hat{x}_{k+} - \sum_{i=1}^{r} \mu_i(\xi_k)\,(A_i\hat{x}_k + B_i u_k) \\ y_k - C\hat{x}_k \end{bmatrix} \tag{45}$$

Autres possibiltée d'obtenir l'erreur d'entrée iconnue :

2ème possibilité : A partir de la dynamique du système, l'entré inconnue est définit par :

$$\hat{d}_k = \sum_{i=1}^{r} \mu_i(\xi_k)\, H_i^{\dagger}[E\hat{x}_{k+} - \sum_{i=1}^{r} \mu_i(\xi_k)\,(A_i\hat{x}_k + B_i u_k)] \tag{46}$$

L'erreur d'entrée inconnue est défini par :

$$e_d(k) = d_k - \hat{d}_k = d_k - \sum_{i=1}^{r} \mu_i(\xi_k)\, H_i^{\dagger}[E\hat{x}_{k+} - \sum_{i=1}^{r} \mu_i(\xi_k)\,(A_i\hat{x}_k + B_i u_k)] \tag{47}$$

3ème possibilté **:** La matrice R est supposé de rang plein, à partir de l'quation de mesure, l'estimation de l'entrée inconnue peut se fait en utilisant l'equation suivante :

$$\hat{d}_k = R^{\dagger}[(y_k - C\hat{x}_k)] \tag{48}$$

L'erreur d'entrée inconnue est définit par : $e_d(k) = d_k - \hat{d}_k = d_k - R^{\dagger}[(y_k - C\hat{x}_k)])$ (49)

Remarque 3: *La convergence asymptotique de* $\hat{x}_k \to x_k$ *entraine la convergence asymptotique de* $\hat{d}_k \to d_k$.

V. Exemple de simulation :

Creative Commons Attribution-NonCommercial-NoDerivatives 4.0 International License (CC BY-NC-ND)

Soit un système singulier non linéaire donné par l'ensemble des équations algébro-différentielles représenté par le système 2 :

Les valeurs numériques de ces matrices sont les suivantes :

$$E=\begin{bmatrix}1&0&0\\0&1&0\\0&0&0\end{bmatrix};A_1=\begin{bmatrix}-0.4&0.2&0.3\\0.3&-0.6&0.3\\0.4&0.2&0.6\end{bmatrix};A_2=\begin{bmatrix}-0.45&0.375&0.375\\0.15&-0.45&0\\0.75&0.75&-0.45\end{bmatrix};B_1=\begin{bmatrix}1\\0\\-0.5\end{bmatrix};B_2=\begin{bmatrix}0.5\\1\\0\end{bmatrix}$$

$$H_1=\begin{bmatrix}0.1\\-0.2\\0.1\end{bmatrix};H_2=\begin{bmatrix}0.1\\0.1\\-0.2\end{bmatrix};C=\begin{bmatrix}1&0&0\\0&1&1\end{bmatrix};R=\begin{bmatrix}1\\1.2\end{bmatrix}.$$

Les fonctions d'activations dépend de l'état x_{1k} sont définie comme suit :

$$\begin{cases}\mu_1(x_{1k})=(1+\sin(x_{1k}))/2\\ \mu_2(x_{1k})=1-\mu_1(x_{1k})\end{cases}$$

Vérifient la propriété de somme convexe :

$$\mu_1(x_{1k})+\mu_2(x_{1k})=1 \quad \text{et} \quad \begin{cases}0\le\mu_1(x_{1k})\le 1\\ 0\le\mu_2(x_{1k})\le 1\end{cases}$$

d_k est une entrée inconnue persistante appliquée dans toute l'intervalle définit par :

$$d_k=8*e^{(-0.15*k)}*\sin(2*k).$$

Avec conditions initiale : $x(0)=[5\quad -0.5\quad 0.5]$ et $\hat{x}(0)=[0\quad 0\quad 0.1]$.

Le but de cet exemple est de comparer les résultats présentés par rapport à ceux donnés dans **(Blandeau et al .2017).** Pour montrer la validité de notre approche, nous résolvons d'abord le problème d'optimisation du théorème 1, en résolvant les conditions de LMI. Tous les calculs sont effectués sous le logiciel MATLAB avec le solveur LMI de la boîte à outils de contrôle robuste, aboutissant à des solutions réalisables. Les gains matriciels suivant sont obtenues :

$$S_1=\begin{bmatrix}1.0000\\0.1173\\1.0827\end{bmatrix};S_2=\begin{bmatrix}0.5000\\1.0000\\-0.4000\end{bmatrix};L_1=\begin{bmatrix}-0.2600&0.3000\\-0.2755&0.1592\\-0.2565&0.2008\end{bmatrix};L_2=\begin{bmatrix}-0.3500&0.3750\\-0.2111&0.1056\\-0.4289&0.3444\end{bmatrix};$$

$$M_1=\begin{bmatrix}-0.1612&-0.0824&0.0176\\0.5368&-0.8522&-0.0460\\-0.6229&0.8472&0.1611\end{bmatrix};M_2=\begin{bmatrix}-0.2112&0.0927&0.0927\\0.3073&-0.8334&-0.1019\\-0.4504&1.0360&0.3044\end{bmatrix};$$

$$U_1=\begin{bmatrix}1.0000&0.0000&0.00000\\0.0000&1.0000&-0.2346\\1.2000&-1.0000&0.2346\end{bmatrix};U_2=\begin{bmatrix}0.0000&0.0000\\0.0000&0.0000\\-1.2000&1.0000\end{bmatrix};N_1=\begin{bmatrix}0.2388&-0.2824\\0.3307&-0.2052\\0.0633&-0.0397\end{bmatrix}\text{ et}$$

$$N_2=\begin{bmatrix}0.2388&-0.2823\\0.3333&-0.2074\\0.0636&-0.0400\end{bmatrix}.$$

Creative Commons Attribution-NonCommercial-NoDerivatives 4.0 International License (CC BY-NC-ND)

Algerian Journal of Engineering Architecture and Urbanism Vol. 5 Nr. 3 2021
ISSN: 2588-1760

Afin d'évaluer les performances du P-UIO pour l'estimation des états et des entrées inconnues, les résultats de simulation sont présentés avec les mêmes fonctions d'activation que le multi-modèles (2) .

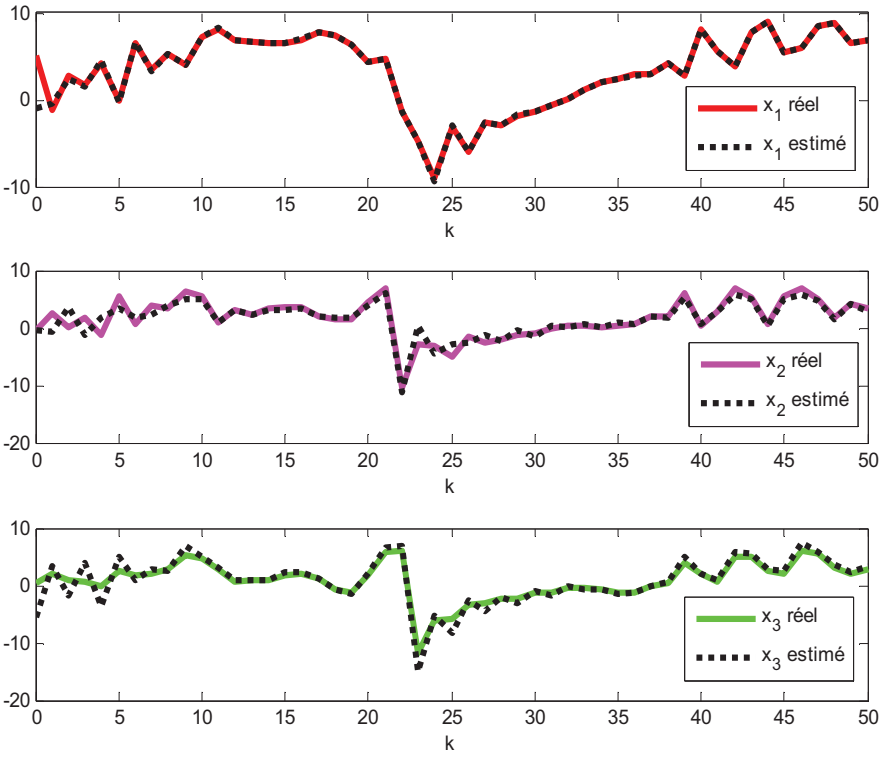

Fig1. Les variables d'état et leur estimés.

Creative Commons Attribution-NonCommercial-NoDerivatives 4.0 International License (CC BY-NC-ND)

Algerian Journal of Engineering Architecture and Urbanism Vol. 5 Nr. 3 2021
ISSN: 2588-1760

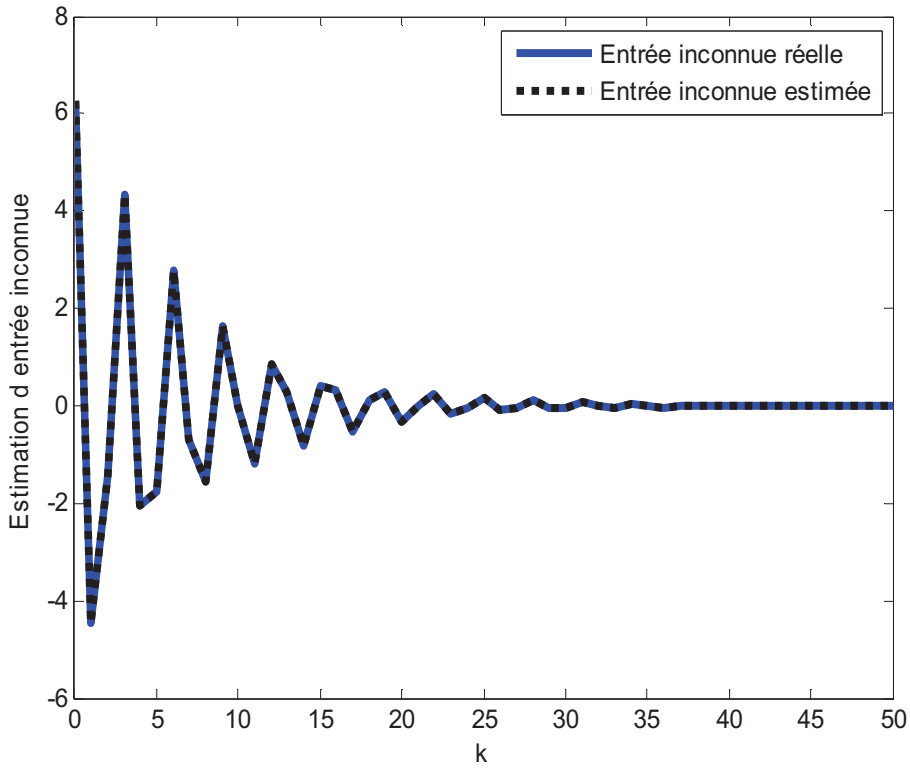

Fig.2 : l'entrée inconnue et leur estimation.

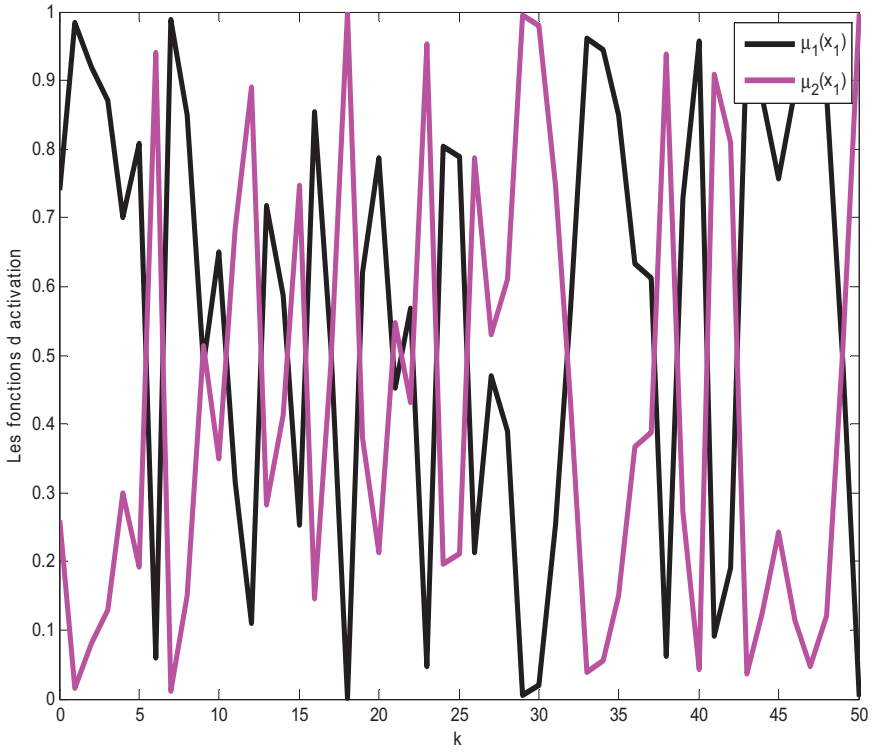

Fig. 3 : les fonctions d'activation.

Creative Commons Attribution-NonCommercial-NoDerivatives 4.0 International License (CC BY-NC-ND)

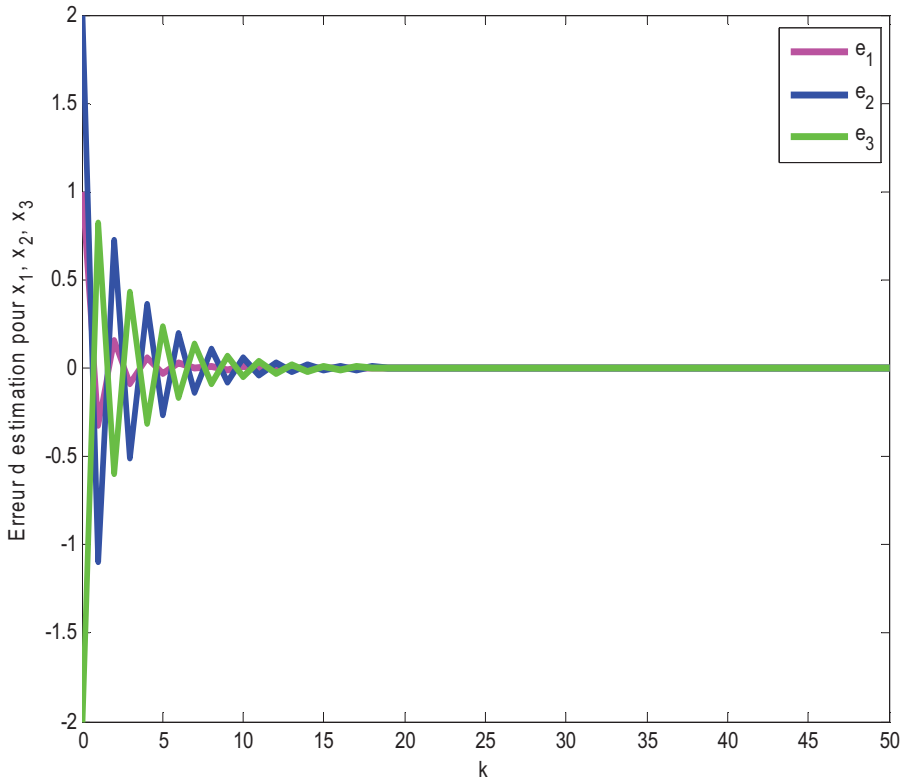

Fig.4 : Les erreurs d'estimations d'état.

Discussion :

La figures (1) représentent les estimations des états du système singulier de type T-S : on peut voir que les estimations sont tout à fait correctes. D'autre part, la figure (2) montre l'entrée inconnue ainsi que son estimation provenant du P-UIO.

On peut voir clairement d'après cette figure, que l'observateur synthétisé estime non seulement correctement les états du système, mais aussi qu'il produit une estimation de bonne qualité de l'entrée inconnue.

V. Conclusion :

Dans ce papier, une attention particulière a été portée au multi-modèle couplé appelé aussi multi-modèle de Takagi-Sugeno qui est le plus utilisé, la synthèse des multi-observateurs à temps discret pour les systèmes non linéaires parfaitement représentés par des multi-modèles est traitée. Un type de multi-observateur des systèmes singuliers à entrées inconnues a été développé et est appelé : un multi-observateur proportionnel. Les conditions d'existence de ce type de multi-observateurs ont été établies, Elles sont exprimées en termes d'inégalités matricielles linéaires LMIs. Une étude comparative au niveau de la conception et des performances des estimateurs d'état et des entrées inconnues a été proposée. En effet il a été montré à travers l'étude de l'observation du multi-modèle, que le multi observateur amélioré parvient à une estimation performante des états du système et du signal d'entrée inconnue affectant le système étudié.

Creative Commons Attribution-NonCommercial-NoDerivatives 4.0 International License (CC BY-NC-ND)

Référence:

Bergsten, P., R. Palm, et al. *(2001). Fuzzy observers. 10th IEEE International Conference on Fuzzy Systems.(Cat. No. 01CH37297), IEEE.*

Bergsten, P., R. Palm, et al. *(2002). "Observers for Takagi-Sugeno fuzzy systems." IEEE Transactions on Systems, Man, and Cybernetics, Part B (Cybernetics)* ***32****(1): 114-121.*

Chadli, M. and P. Borne *(2012). Multiple models approach in automation: Takagi-Sugeno fuzzy systems, John Wiley & Sons.*

Guzman, J., F.-R. López-Estrada, et al. *(2021). "Actuator fault estimation based on a proportional-integral observer with nonquadratic Lyapunov functions." International Journal of Systems Science: 1-14.*

Ichalal, D. *(2009). Estimation et diagnostic de systèmes non linéaires décrits par un modèle de Takagi-Sugeno, Institut National Polytechnique de Lorraine.*

Ichalal, D., B. Marx, et al. *(2007). Conception d'observateurs pour un modèle de Takagi-Sugeno à variables de décision non mesurables. 8ème conférence internationale des Sciences et Techniques de l'Automatique, STA'2007.*

Liu, X., Z. Gao, et al. (2017). *"Takagi–Sugeno fuzzy model based fault estimation and signal compensation with application to wind turbines." IEEE Transactions on Industrial Electronics* ***64****(7): 5678-5689.*

Ouzaz, M., A. El Assoudi, et al*. (2020). Design of State and Fault Observer Based on the Euler discretization for Takagi-Sugeno Implicit Models with Lipschitz constraints. 2020 Fourth International Conference On Intelligent Computing in Data Sciences (ICDS), IEEE.*

Palm, R. and P. Bergsten (2000). *Sliding mode observer for a Takagi Sugeno fuzzy system. Ninth IEEE International Conference on Fuzzy Systems. FUZZ-IEEE 2000 (Cat. No. 00CH37063), IEEE.*

Valencia-Palomo, G., F.-R. López-Estrada, et al*. (2020). Optimization for Control, Observation and Safety, MDPI.*

Chang, J. L. *(2006). Applying discrete-time proportional integral observers for state and disturbance estimations. IEEE Transactions on Automatic Control, 51(5), 814–818*

Ahmadizadeh, S., Zarei, J., & Karimi, H. R. *(2014). Robust unknown input observer design for linear uncertain time delay systems with application to fault detection. Asian Journal of Control, 16(4), 1006–1019.*

Zhou, M., Wang, Z., & Shen, Y. *(2017). Fault detection and isolation method based on H−/H∞ unknown input observer design in finite frequency domain. Asian Journal of Control, 19(5), 1777–1790.*

T. Takagi and M. Sugeno*. Fuzzy identification of systems and its applications to modeling and control. IEEE Transactions on Systems, Man, and Cybernetics, 15 :116–132, 1985.*

K. Tanaka and H.O. Wang*. Fuzzy Control Systems Design and Analysis : A Linear Matrix Inequality Approach. John Wiley and Sons, 2001.*

Blandeau, M., Guerra, T. M., Estrada-Manzo, V., Pudlo, P., & Gabrielli, F. *(2017). Unknown input observer based on discrete-time nonlinear descriptor model for understanding sitting control. IFAC-PapersOnLine, 50(1), 820-825.*

Creative Commons Attribution-NonCommercial-NoDerivatives 4.0 International License (CC BY-NC-ND)

Algerian Journal of Engineering Architecture and Urbanism Vol. 5 Nr. 3 2021
ISSN: 2588-1760

ELABORATION AND CHARACTERIZATION OF CU-W OBTAINED BY SINTERING AND COLD ROLLING.

Nor-el-houda BERRAMDAN
PhD student, Laboratory of Mining, Metallurgy and Materials "L3M",
National School of Mining and Metallurgy "ENSMM"Amar LASKRI
Annaba, Algeria.
nor-el-houda.berramdane@ensmm-annaba.dz

Samia LEMBOUB
PhD, Laboratory of Metallurgy and Materials Engineering "LMGM"
University of Badji Mokhtar Annaba, Algeria.
National School of Mining and Metallurgy "ENSMM" Amar LASKRI
Annaba, Algeria.
samia.lemboub@ensmm-annaba.dz

Said BOUDEBANE
Professor, Laboratory of Metallurgy and Materials Engineering "LMGM"
University of Badji Mokhtar Annaba, Algeria.
bkam_23@yahoo.fr

Abstract :
Cu-W alloys were fabricated to fix the effect of W addition in improving the properties of Cu. Composite preforms of (0 to 20% W) were prepared from elemental copper and tungsten powders using the powder metallurgy method. The samples were sintered at 800°C then cold-rolled to obtain a better density. The microstructural characteristics of the Cu-W composite were studied. Experimental results showed that the microhardness of the finished Cu–W composite increased with increasing W content, whereas electrical conductivity decreased with increasing tungsten compared to pure copper. On the other hand, the incorporation of tungsten into the copper also leads to a hardening of the copper matrix.

Keywords: Composites, sintering, electrical resistivity, Microstructure, Microhardness.

Introduction :

Un matériau composite est une combinaison de deux ou plusieurs matériaux ayant des caractéristiques différentes avec des phases et des propriétés supérieures aux matériaux de base. Les matériaux composites sont produits par Méthodes de coulée et de métallurgie des poudres [1,2].

Les composites à base de cuivre semblent être un matériau prometteur pour les applications d'ingénierie pour les raisons suivantes leurs excellentes propriétés thermo-physiques associées à des propriétés mécaniques à haute température par rapport au cuivre pur et aux alliages de cuivre. Ces composites sont choisis pour des applications essentielles, une bonne résistance à l'usure et sans perte de conductivité électrique de la matrice est la considération première [3].

Les matériaux composites cuivre-tungstène (Cu-W) sont développés pour des applications telles que les contacts électriques, les électrodes à résistance et les pointes de contact dans les pistolets à souder ainsi que pour les pièces nécessitant une plus grande résistance à l'usure [4]. En plus du Cu-W, d'autres matériaux potentiels pour des applications similaires sont Cu-Mo, Cu-Al_2O_3, Ag-Mo, Ag-Mo, Ag-W et Ag-CdO [4], ont rapporté que, parmi divers renforts, le tungstène est bien connu pour sa très faible solubilité et sa bonne mouillabilité avec le cuivre due à son très haut point de fusion [4, 5].

Une revue de la littérature existante indique que peu d'attention a été accordée au pressage uniaxiale, bien qu'il s'agisse de la technique de production la plus économique [6] Les matériaux fabriquer par métallurgie de poudre étant toujours poreux, l'existence de pores internes diminue les propriétés mécaniques des matériaux frittés [6,7]. Cependant, un écrouissage peut donner de meilleures propriétés mécaniques [8].

Problématique :
Cette étude a été entreprise dans le but d'améliorer la durée de vie des électrodes de soudage par points, en usage dans les entreprises de fabrication des treillis soudés. Le tungstène, élément réfractaire, est introduit dans la matrice en cuivre pour maintenir une dureté acceptable au cours de l'exploitation, sans altérer la conductibilité électrique du matériau.

Matériaux et techniques :
Des poudres de cuivre et de tungstène, avec une pureté de 99,5% et 99,00% respectivement ont été utilisées pour élaborer les alliages composites Cu-W. Les granulométries moyennes des poudres de cuivre et de tungstène sont respectivement 5-10 µm et 10-15 µm. Les mélanges de départ sont confectionnés selon des proportions (5%, 10%,15% et 20% W). Les masses de poudres entrant dans la constitution des alliages sont données par le tableau 1.

Echantillon	Compositions (g)	
	Cu	W
1	2,85	0,15
2	2,70	0,30
3	2,55	0,45
étudi4	2,40	0,60

Table 1. Composition des mélanges de poudres étudiés

Une fois la pesée des poudres réalisée, on procède à l'opération du mélange pour assurer une distribution homogène des particules de cuivre et de tungstène, et cela dans à un mélangeur à billes métalliques, pendant une durée d'une heure.
Après homogénéisation du mélange, on procède au compactage des poudres par compression uniaxiale à froid afin d'assurer une cohésion suffisante, pouvant garantir une densité a vert de l'ordre de 45-50%, permettant la manipulation des échantillons comprimés sans effritement.

Par cette opération, on vise aussi la mise en contact des particules et la création des interfaces particule – particule nécessaires au bon déroulement des mécanismes de frittage. Pratiquement, le compactage à froid a été réalisé dans une matrice cylindrique en carbure de tungstène (diamètre 13mm), sous une charge de 528 MPa.

Les comprimés ont été ensuite frittés dans un four tubulaire sous vide primaire. Le régime de traitement thermique appliqué consiste à un chauffage des échantillons jusqu'à la température de 800°C suivi d'un maintien isotherme de 3 heures puis d'un refroidissement dans le four jusqu'à la température ambiante.

Les échantillons préalablement frittés ont été consolidés par laminage à froid afin d'étudier l'influence des particules de tungstène sur la capacité de la matrice en cuivre de maintenir un écrouissage, L'opération a été réalisée sur un laminoir à froid de laboratoire.

La densité relative des frittés a été appréciée grâce à la détermination de la masse volumique réelle des échantillons après élaboration. Le calcul de la densité relative a permis de mettre en évidence l'évolution de la porosité des différentes compositions Cu-W, après frittage.

La préparation de surface des échantillons a été entreprise afin de pouvoir réaliser les techniques de caractérisation de notre matériau. A cet effet, les échantillons frittés et laminés ont été découpés à froid, enrobés à chaud, polis et attaqués chimiquement afin de rendre possible l'examen microscopique de l'alliage étudié.

Après le polissage, les observations métallographiques de l'échantillon, en microscopies optique à balayage ont été effectuées sur un microscope optique de type (Nikon industrial Microscope ECLIPSE LV150 NL) et sur microscope à balayage de type Quanta 250, avec analyse par spectroscopie à rayons X à dispersion d'énergie (EDXS).

Les mesures de dureté ont été réalisées au moyen d'un Microduromètre du type (Innnovatest Europe BV) à l'aide d'un pénétrateur pyramidal en diamant sous une charge de 50 gf.
La mesure de la résistivité électrique a été effectuée selon la méthode des quatre pointes.

Résultats et discussion

- **La densité relative**

La figure 1 montre la variation de la densité relative des échantillons frittés avec différentes teneurs en tungstène

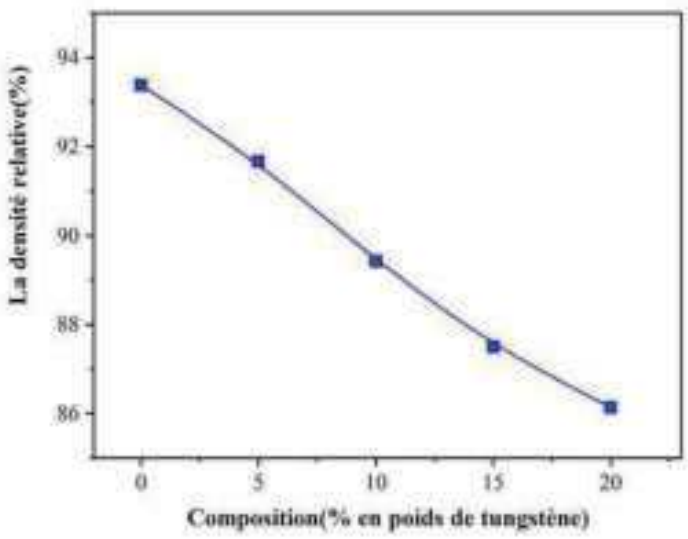

Fig 1. Variation de la densité relative des échantillons frittés en fonction de la teneur en tungstène.

On peut constater que la densité relative du composite Cu-X% W diminue progressivement avec l'augmentation de la teneur en tungstène. Il faut noter que la valeur de la densité du cuivre sans ajout de W est de l'ordre de 93%. L'évolution de la courbe de la densification du mélange Cu+W, en fonction de la teneur en W pourrait s'expliquer par l'altération de la compressibilité du mélange, suite à l'introduction du W, métal réfractaire à haute limite d'élasticité mais avec une aptitude à la déformation plastique relativement plus faible.
A premier abord, nos résultats sont en accord avec les résultats de travaux antérieurs [1] où il est signifié que la densité relative enregistrée est de l'ordre de 90%, après frittage et extrusion à froid.

- **Evolution microstructurale**

Les résultats des analyses métallographiques sur microscope optique des alliages de Cu-W frittés et après attaque chimique sont présentés par la figure 1.

Deux phases différentes ont été clairement mises en évidence dans la structure des alliages Cu-W, en l'occurence les particules de tungstènequi de couleur bleue assez vive et la matrice en cuivre relativemenrt plus claire. Les grains qui sont beaucoup plus foncé sont ceux de Cu_2O.
L'analyse révèle la morphologie du renfort, sous d'amas de particules de tungstène, répartis d'une manière aléatoire, dans la matrice métallique. L'existence de pores et des particules de cuivre légèrement oxydées (Cu_2O) a été également confirmée

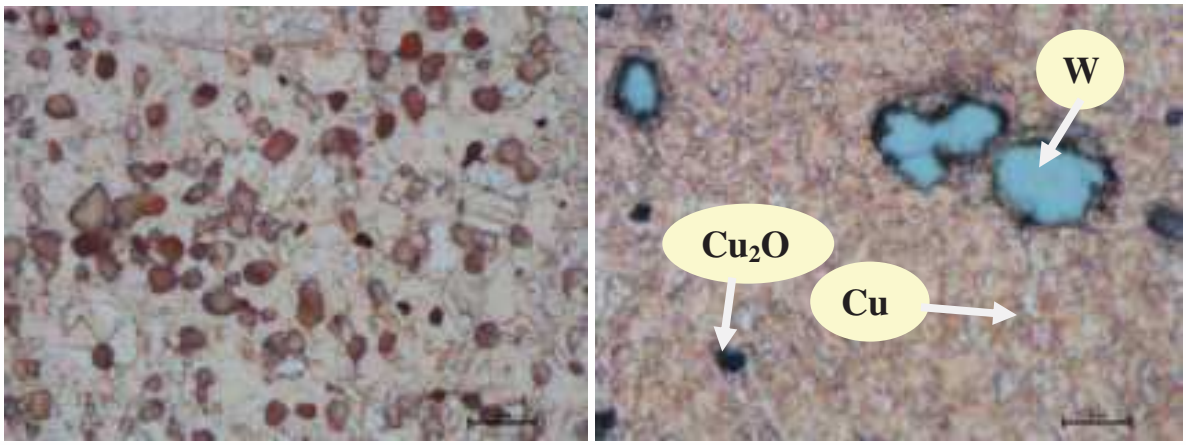

a) Brut

b) Cu - 5% W

c) Cu-10% W

d) Cu–15 % W

e) Cu – 20% W

Fig 2. Micrographies optiques des composites Cu + W frittés après attaque chimique.

- **Analyse par spectroscopie dispersive d'énergie**

La spectroscopie à dispersion d'énergie (EDXS) a été utilisée pour confirmer les éléments présents dans le matériau composite en question.

La figure 3 (a-b) montre le profil EDXS du cuivre pur et du composite Cu-15W après le frittage. La Figure 3(a)montre le spectre EDXS obtenu sur la matrice de Cu. Outre le pic du cuivre, élément prédominant, on note la présence de pics de l'oxygène. Il provient probablement des molécules d'air adsorbées à la surface des particules de cuivre. Lors du stockage de la poudre les traces de C sont dues aux résidus de graphite provenant de la réduction sous vide de la réduction de La figure 3(b) représentant le spectre EDXS du Cu-15%W montre l'apparition des éléments suivants : Cu, W, C et O.

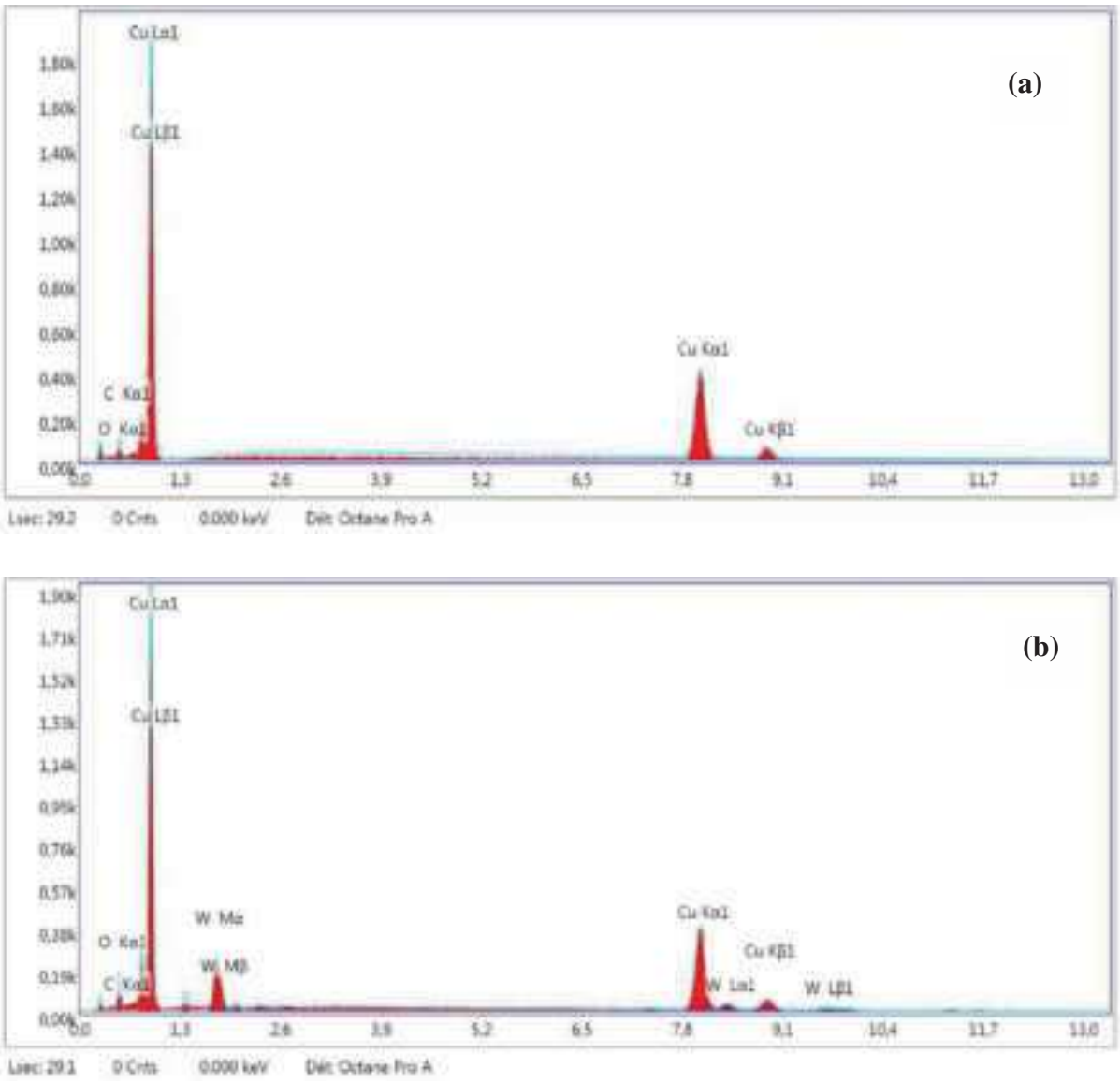

Fig 3. EDXS d'un échantillon après frittage (a) Cu pur (b) Composite Cu-15W.

- **La microdureté**

Les mesures de dureté ont été réalisées au moyen d'un Microduromètre (Innovatest Europe BV) à l'aide d'un pénétrateur pyramidal en diamant sous une charge de **50 gf**. Nous avons effectué des mesures avant et après laminage à froid, les valeurs moyennes sont présentées par les courbes ci-dessous.(Figure 4)

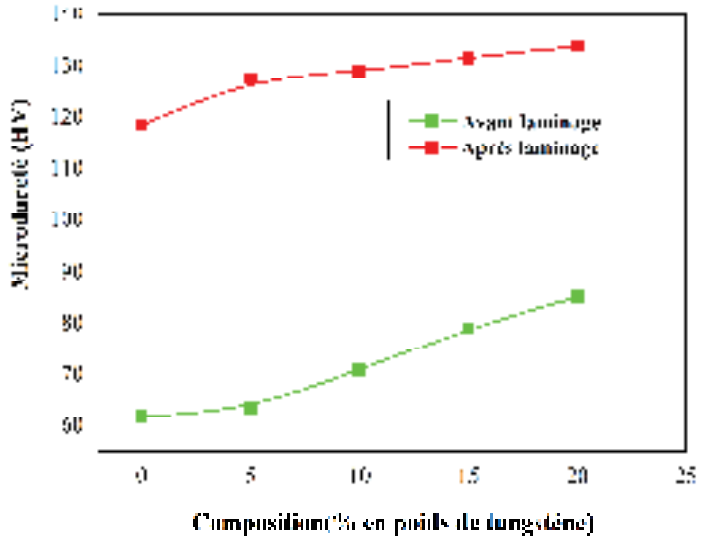

Fig 4. Evolution de la microdureté en fonction de la teneur en W des composites Cu-W après frittage, et après frittage-laminage.

La Figure 4 révèle bien que la microdureté du matériau augmente avec l'augmentation de la teneur en tungstène introduite dans le mélange de départ. Il ressort également que l'écrouissage introduit par laminage conduit à une augmentation importante de la dureté du composite de l'ordre de 50%. Ces constatations restent valables quel que soit le pourcentage de tungstène introduit.

- **La résistivité électrique**

Le cuivre a une meilleure conductivité électrique que ses alliages [5]. De ce fait, l'augmentation de la teneur en W engendre un accroissement rapide de la résistivité dans l'intervalle (0-10%W), au-delà de 10%W, la résistivité du composite reste constante.

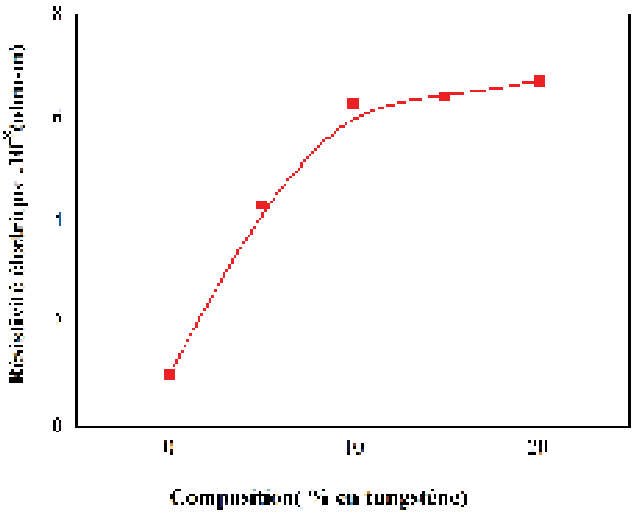

Fig 5. Résistivité électrique de divers composites Cu-W.

La figure 5 montre la résistivité électrique de Cu pur et des échantillons des composites élaborés par frittage à 800˚C. La valeur expérimentale de la résistivité électrique du cuivre pur est de 0,98× 10^{-8} Ω-m. Cependant, l'augmentation du pourcentage de W dans le Cu, conduit à une chute de la conductivité électrique, en raison de la quantité de renfort, de la taille et du volume des pores. Cependant, c'est l'ajout des éléments d'alliage dans un métal pur, qui se révèle prépondérant quant à l'augmentation de la résistivité électrique. Ceci est confirmé par les valeurs de la résistivité du cuivre pur qui est de l'ordre de 0,98 ×10^{-8}Ω-m et qui atteint la valeur de 6,7.10^{-8}Ω-m pour l'alliage Cu-20%W.

Conclusion :

Les principaux résultats de ce travail, portant sur l'élaboration du composite Cu-W par frittage en phase solide sont les suivants :

1- Les ajouts de W diminuent la compressibilité du mélange Cu-W d'où une moindre densification. La porosité résiduelle augmente avec l'augmentation du taux de W.

2- La structure du fritté se présente sous forme d'une matrice en Cu renforcée par des colonies de particules de W, en présence d'une porosité résiduelle.

3- L'augmentation de la teneur en W conduit à un durcissement sensible de la matrice en Cu.

4- Un laminage post-frittage améliore la dureté du composite d'au moins deux fois.

6- La résistivité du Cu est très sensible aux ajouts de W. Une nette augmentation de la résistivité a été enregistrée pour des ajouts de 5 à 10% de W, au-delà, les valeurs de la résistivité se stabilisent

Références :

S.C.Vettivel, N.Selvakumar and P.V.Ponraj (2012), *Mechanical behaviour of sintered Cu-5% W nano powder composite*, Procedia engineering, 38, 2874-2880.

L.Yang,L. Ran and M.Yi (2011),*Carbon fiber knitted fabric reinforced copper composite for sliding contact material*, Materials & Design, 32(4), 2365-2369.

N.Selvakumar, S.C.Vettivel (2013), *Thermal, electrical and wear behavior of sintered Cu–W nanocomposite*,Materials & Design, 46, 16-25.

Maji, P., Dube, R. K., & Basu, B. (2009). Enhancement of wear resistance of copper with tungsten addition (≤ 20 wt%) by powder metallurgy route. Journal of tribology, 131(4).

Gautam, R. K., Ray, S., Jain, S. C., & Sharma, S. C. (2008). Tribological behavior of Cu–Cr–SiCp in situ composite. Wear, 265(5-6), 902-912.

Selvakumar, N., Raj, A. M., & Narayanasamy, R. (2012). Experimental investigation on workability and strain hardening behaviour of Fe–C–0.5 Mn sintered composites. Materials & Design, 41, 349-357.

Bedir, F. (2007). Characteristic properties of Al–Cu–SiCp and Al–Cu–B4Cp composites produced by hot pressing method under nitrogen atmosphere. Materials & design, 28(4), 1238-1244.

Mordike, B. L., Kaczmar, J., Kielbinski, M., & Kainer, K. U. (1991). Effect of tungsten content on the properties and structure of cold extruded Cu-W composite materials. PMI. Powder metallurgy international, 23(2), 91-95.

Algerian Journal of Engineering Architecture and Urbanism Vol. 5 Nr. 3 2021
ISSN: 2588-1760

Preparation and physical state characterization of metformin in PLA microparticles

Sihem BOURICHE

Doctorante, laboratoire des Materiaux Organiques (LMO), Faculté de Technologie, Departement de Génie des Procédés, Université de Bejaia, 06000, Bejaia, e-mail:Bs-sihem@hotmail.fr

Farouk REZGUI

Professeur, laboratoire des Matériaux Organiques (LMO), Faculté de Technologie, Département de Génie des Procedés, Université de Bejaia, 06000, Bejaia, e-mail: rezgui-farouk@neteourrier.com

Abstract

Metformin is a drug that is commonly used in the treatment of type 2 diabetes. This drug has a half-life (1.5-1.6 h) and a low bioavailability, so it needs to be given in a repeated dose to be effective. The daily dose used is 1.5- 3 g, with the incidence of side effects such as diarrhoea, nausea, anorexia, vomiting, weight loss, and taste disturbance. Therefore, microencapsulation of the drug in biodegradable polymer is a suitable approach to overcome the above limitations. The aim of this paper was to prepare microparticles from poly (lactic acid) (PLA) as coating material by double emulsion solvent evaporation method. The prepared microcapsules were evaluated for encapsulation efficiency, drug loading capacity and morphological properties by using UV spectrophotometer and scanning electron microscope (SEM). The physical state of metformin in microparticles was conducted by X-Ray powder diffractometry (XRD) and differential scanning calorimetry (DSC). Metformin encapsulated PLA microparticles were spherical in shape with high encapsulation efficiency. The obtained Results from XRD and DSC analysis indicate the change of polymer and metformin crystallinity during the encapsulation process.

Keywords

Poly (lactic acid), metformin, microparticles, X-Ray diffractometry, differential scanning calorimetry.

Introduction

For several decades, microparticles prepared from biodegradable and biocompatible polymers have been used in oral drug delivery systems (Jana et al., 2020; Molavi et al., 2020). Microparticles can improve the efficacy and safety of drug administration by controlling the rate, time, and place of drug release (Siepmann and Siepmann, 2006). Biodegradable polyesters such as poly (lactide-co-glycolide) (PLGA) and poly lacticacid (PLA) have been widely investigated for this purpose because of their

Creative Commons Attribution-NonCommercial-NoDerivatives 4.0 International License (CC BY-NC-ND)

biodegradability and biocompatibility. They are extensively used to encapsulate various types of drug either hydrophilic or hydrophobic (Varde et al., 2004).

Microparticles encapsulating hydrophilic drugs have been widely made by the water-in-oil-in-water (W/O/W) double emulsion method (Nihant et al., 1994; Iqbal et al., 2015). In this method, the drug dissolved in the aqueous phase of de-ionized water (W1) is added to the organic phase (O) which consists of a polymer solution in an appropriate organic solvent. The two phases are mixed under vigorous stirring until a primary water in oil emulsion is obtained (W1/O). In the next step, the forming emulsion was then dispersed in a second aqueous phase (W2) containing a surfactant to form the double emulsion (W1/O/W2). After solvent evaporation, the microparticles were recovered by centrifugation (Naviendri et al., 2016). Several studies report that changes in the properties of the polymer take place during particles formulation by emulsion solvent evaporation methods which affect its degradation rates and thus the drug release (Mendoza-muñoz et al.,2016). The encapsulated drug also undergoes structural modification especially the crystalline molecules. Determination of these structural changes is important, and can be carried out by examining the microparticles samples by DSC method and X-rays analysis (Annasya et al., 2016).

One of the drugs commonly used in oral administration is metformin. Metformin is a highly hydrophilic drug, that is used in the treatment of type 2 diabetes. This drug has a short half-life (1.5-1.6 h) and a low bioavailability, so it needs to be given in a repeated dose to be effective (1.5-3 g/ day). The problems observed are the adverse effects of metformin involving the gastrointestinal tract with high doses (Nayak et al., 2014). Thus, their reduction through the use of controlled oral release microparticles is desirable. Several studies have attempted to overcome the above drawbacks, by encapsulating metformin in diverse polymers such as the chitosan (Nander et al., 2013), or polymethacrylic (Hasan et al., 2013)…etc.

In this work, metformin as a drug model and PLA as the carrier were chosen for the preparation of microparticles. The prepared microcapsules were evaluated for encapsulation efficiency and drug loading capacity by using a UV spectrophotometer. Scanning electron microscopy (SEM), powder X-ray diffraction (P-XRD), and differential scanning calorimetry (DSC) were performed for the physical characterization of the microparticles.

Creative Commons Attribution-NonCommercial-NoDerivatives 4.0 International License (CC BY-NC-ND)

2. Materials and methods

2.1 Materials

Poly (lactic acid) PLA (Average MW 150 000 g/mol) was obtained from Cargill-Dow. Metformin hydrochloride (Mw 165.6 g /mol, 99.6%) was obtained from Granules INDIA (Madhapur, INDIA). Poly (vinyl alcohol) 95 % hydrolyzed (PVA, M_w = 85 000-124 000), methylcellulose, methylene chloride (CH_2Cl_2) were purchased from Biochem, Chemopharm (Quebec, Canada).

2.2 Methods

Preparation of microspheres

The microparticles were produced by the double emulsion solvent evaporation technique, as described elsewhere (Peres et al., 2016). Approximately 200 mg PLA was dissolved in 10 mL methylene chloride (DCM, Organic phase: O). 1mL of aqueous solution (W_1) containing metformin 150 mg) was drooped to the organic phase and emulsified by means of magnetic stirring for 3 min. The resulting water-in-oil (W/O) emulsion was further emulsified with 40 mL of PVA solution (0.1%, w/v) by stirring for 15 min (400 rpm), giving rise to the water-in-oil-in-water emulsion (W/O/W). After DCM evaporation at room temperature, microparticles were collected by centrifugation (3000 rpm for 15 min), washed with distilled water to remove the surfactant, dried, and stored in a desiccator under vacuum conditions.

Encapsulation efficiency and Drug loading capacity

The supernatant recovered after centrifugation was analyzed by a UV visible spectrophotometer at the maximum wavelength of metformin with distilled water as a blank. To determine the amount of non encapsulated metformin (m_n), the supernatant was diluted to be within the 2-12 mg/l concentration range. The encapsulation efficiency (EE) and percentage drug loading capacity were calculated by using the following formula:

$$EE(\%) = \frac{Metformin\ weight\ in\ mgs}{Initial\ weight\ of\ metformin} \times 100 \ldots\ldots\ldots\ldots (1)$$

$$\%\ DL = \frac{Metformin\ weight\ in\ mgs}{weight\ of\ microparticles} \times 100 \ldots\ldots\ldots\ldots (2)$$

Creative Commons Attribution-NonCommercial-NoDerivatives 4.0 International License (CC BY-NC-ND)

Morphology

The shape and surface morphology of metformin loaded PLA microparticles were observed using scanning electron microscopy (SEM) (Quanta 200 system, FEI. Hillsboro, OR). Microparticles were spread on a stub, and the micrographs were recorded at 10 kV.

Differential Scanning Calorimetry

The DSC analysis of pure drug, pure PLA, and microparticles was carried out using a Setaram DSC 131 calorimeter to evaluate the physical state of metformin after encapsulation. Samples (~10 mg) were accurately weighed and heated in sealed aluminum pans at a rate of 20°C/min from 30 to 300°C temperature range.

Powder X-ray Diffractometry

PXRD study of raw materials and microparticles was performed on PANalytical X Pert PRO diffractometer using Cu radiation (λ = 0.154 nm) at 40 kV voltage and 30 mA current. The scanning speed employed was 5°/min over the range 2θ from 5 to 40°.

3. Results and discussion

Surface Morphology, encapsulation efficiency, and drug loading

In this study, a double emulsion solvent evaporation method was used to encapsulate metformin within PLA microparticles. This preparation technique is commonly used for the microencapsulation of water-soluble drugs in hydrophobic polymeric systems (Iqbal et al., 2015). PLA microparticles showed metformin encapsulation efficiency higher than 90 % and drug loading of 21 %, indicating their efficacy in the encapsulation of the hydrophilic drug, metformin.

As shown in Fig.1, which reports the PLA microparticles loaded with metformin recorded at two magnifications x 400 (A) and x 3000 (B), the particles were spherical in shape and very irregular surface.

Creative Commons Attribution-NonCommercial-NoDerivatives 4.0 International License (CC BY-NC-ND)

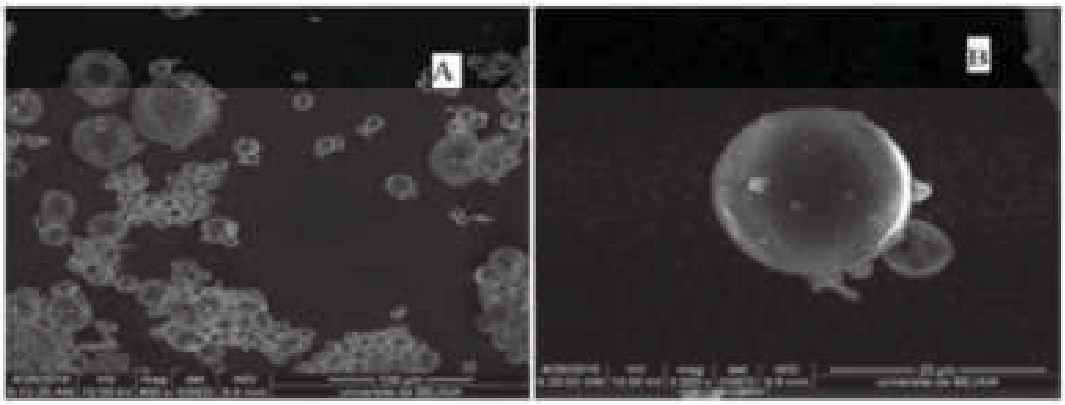

Fig. 1. SEM micrographs of metformin-loaded PLA microparticles

X-ray diffraction (XRD)

The XRD curves of metformin, PLA, and metformin-loaded PLA microparticles (e) are shown in Fig. 2. XRD curve of metformin (Fig. 2a) exhibited a crystalline diffraction pattern with well-defined peaks at angles 2θ: 13.18°, 17.67°, 24.47°, 37.08° and 39.34° characteristic of its crystalline nature (Vaingankar and Amin, 2017). XRD curve of PLA (Fig. 2b) shows two very intense peaks at 16.67° and 18.96° characteristic of its semi-crystalline structure (Selukar et al., 2012). The XRD curve of metformin-loaded PLA microparticles evidences the absence of diffraction peaks characteristic of the crystalline structure of metformin, indicating its amorphous nature into microparticles.

Creative Commons Attribution-NonCommercial-NoDerivatives 4.0 International License (CC BY-NC-ND)

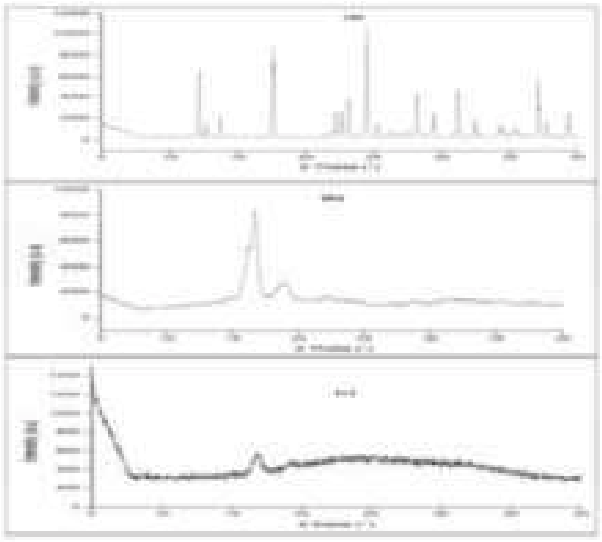

Fig. 2. XRD pattern of metformin (a), PLA (b), and metformin-loaded PLA microparticles (c).

Differential scanning calorimetry (DSC)

Fig. 3 shows the DSC curves of metformin (a), PLA (b), and metformin-loaded PLA microparticles (c). DSC curve of metformin exhibits a sharp endothermic peak at 232°C associated with the compound melting point (Nayak et al., 2011). DSC curve of PLA shows an endothermic peak at 176.32 °C related to its crystalline melting temperature (Tm). In the DSC curve of metformin loaded PLA microparticles, the endothermic peak of PLA was found with a shift in Tm value. But metformin's endothermic melting peak disappeared, indicates a change in the crystalline state of metformin after microencapsulation, suggesting that the metformin in microparticles is present in an amorphous state (Nayak et al., 2011). This result is in good agreement with XRD finding.

Creative Commons Attribution-NonCommercial-NoDerivatives 4.0 International License (CC BY-NC-ND)

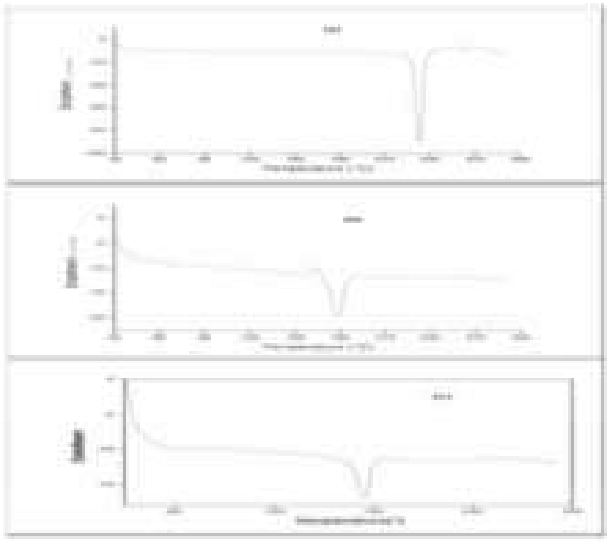

Fig. 3. DSC curves of metformin (a), PLA (b), and metformin-loaded PLA microparticles (c).

CONCLUSION

In this research, microparticles of PLA were prepared by double emulsion solvent evaporation technique. These microparticles were characterized by a spherical shape and high encapsulation efficiency. DSC and X-ray diffraction techniques were used for the characterization of the crystalline state of drug and polymer before and after microencapsulation. Comparing the XRD pattern of metformin loaded microcapsules and pure metformin, it was found that all characteristic peaks of metformin were disappeared thus indicating changes in crystalline structure to the amorphous state. DSC results demonstrated also that drug loaded microcapsules is in the amorphous state.

References:

Arıdoğan G., Boşdiki C., Aksu B., Tunçel N. (2016). *Quality by design case study-I: Design of 5-fluorouracil loaded lipid nanoparticles by the W/O/W double emulsion - Solvent evaporation method.* European Journal of Pharmaceutical Sciences 84: 92-102.

Hasan I., Pal S., Akhter S., Ayon N. J., Rizvi M. S. (2015). *Evaluation and optimization of influence of permeability property and concentration of polymethacrylic polymers on microspheres of metformin HCl.* Dhaka University Journal of Pharmaceutical Sciences 12(2): 151-157.

Iqbal M., Zafar N., Fessi H., Elaissari A. (2015). *Double emulsion solvent evaporation techniques used for drug encapsulation.* International journal of pharmaceutics 496(2): 173-190.

Jana P., Shyam M., Singh S., Jayaprakash V., Dev A. (2020). *Biodegradable Polymers in Drug Delivery and Oral Vaccination.* European Polymer Journal: 110155.

Mendoza-Muñoz N., Alcalá-Alcalá S., Quintanar-Guerrero D. (2016). *Preparation of polymer nanoparticles by the emulsification-solvent evaporation method: from vanderhoff's pioneer approach to recent adaptations.* In: Polymer Nanoparticles for Nanomedicines. Springer, Cham: 87-121.

Molavi F., Barzegar-Jalali M., Hamishehkar H. (2020). *Polymer based polymeric nano and microparticles for pharmaceutical purposes: A review on formulation approaches.* Journal of Controlled Release 320: 265-282.

Nayak A., Jain S.K., Pandey R. S. (2011). *Controlling release of metformin HCl through microparticulate wax matrix based floating alginate beads.* Molecular pharmaceutics 8(6): 2273-2281.

Nayak A.K., Pal D., Santra K. (2014). *Interpolymer mucoadhesive beads of Metformin HCl: development by response surface methodology.* Carbohydrate Polymers 107: 41-50.

Niharika N., Selvagens C., Grandfils C., Jerome R., Teyssié P. (1994). *Polylactide microparticles prepared by double emulsion/evaporation technique. I. Effect of primary emulsion stability.* Pharmaceutical research 11(10): 1479-1484.

Creative Commons Attribution-NonCommercial-NoDerivatives 4.0 International License (CC BY-NC-ND)

Novendra D., Jaswir I., Taher M., Mohamed F., Salleh H. M., Noorbatcha I. A., Abdullah A. (2016). *Fabrication of paracetamol-loaded nanoparticles (F-LM) by two steps double-emulsion solvent evaporation method and characterization of paracetamol release and lipase interaction.* Journal of oleo science 65(8): 641-653.

Peres L. B., Peres L. B , de Araújo P. H. H., Sayer C. (2016). *Solid lipid nanoparticles for encapsulation of hydrophobic drugs by an organic solvent free double emulsion technique.* Colloids and Surfaces B: Biointerfaces 140: 317-323.

Sander C., Madsen K. D., Hyrup B., Nielsen H. M., Rantanen J., Jacobsen J. (2013). *Characterization of spray dried bioadhesive mesoporous microparticles for pulmonary administration.* European journal of pharmaceutics and biopharmaceutics 85(3): 687-698.

Selukar B.S., Parwe S.P., Mohite K.K., Garnaik B. (2012). *Synthesis and characterization of linear polylactic acid based urethanes using Tungstophosphoric solid acid/silica-108 catalyst.* Advanced Materials Letters 3(2): 161-171.

Siepmann J., Siepmann F. (2006). *Microparticles used as drug delivery systems. In: Smart colloidal materials.* Springer, Berlin, Heidelberg 15-21.

Vairagkar P., Amin P. (2007). *Continuous melt granulation to develop high drug loaded sustained release tablet of Ibuprofen IP.* Asian journal of pharmaceutical sciences 2 (1): 27-30.

Vasdekis N. K., Pack D. W. (2009). *Microspheres for controlled release drug delivery.* Expert opinion on biological therapy 9(1): 15-31.

Creative Commons Attribution-NonCommercial-NoDerivatives 4.0 International License (CC BY-NC-ND)

Algerian Journal of Engineering Architecture and Urbanism Vol. 5 Nr. 3 2021
ISSN: 2588-1760

ELECTROCHEMICAL NUCLEATION AND GROWTH OF NICKEL IN THE PRESENCE OF SURFACTANTS

Ilhem DJAGHOUT
PhD
Laboratoire d'Analyses Industrielles et Génie des Matériaux, Université 8 Mai 1945 Guelma,
Département de Génie des Procédés, Université Mohamed Chérif Messaadia, Souk Ahras,
i.djaghout@univ-soukahras.dz

Rabah KSOURI
Laboratoire de chimie appliquée, Département de Génie des Procédés, Université 8 Mai 1945 Guelma,
ksourira@hotmail.com

Fatima KESRI
Laboratoire d'Analyses Industrielles et Génie des Matériaux, Université 8 Mai 1945 Guelma,
fatima.kesri@gmail.com

Abed Mohamed AFFOUNE
Laboratoire d'Analyses Industrielles et Génie des Matériaux, Département de Génie des Procédés,
Université 8 Mai 1945 Guelma,
affoune2@yahoo.fr

Abstract:
This paper deals with the effect of sodium dodecyl sulfate (SDS) and polyvinylpyrrolidone (PVP) on the kinetics and electrochemical nucleation of nickel from Watts bath using the electrochemical methods (cyclic voltammetry and chronoamperometry). Cyclic voltammetry and chronoamperommetric measurements revealed that cathodic process was inhibited by both SDS and PVP and the effect was more pronounced for PVP. Analysis of transient currents using a theoretical model of Bewick and Scharifker-Hills indicated that the nucleation mechanism of Watts bath and Watts containing SDS followed three-dimensional instantaneous nucleation mechanism and the process was disturbed by concurrent protons reduction. Whereas the mechanism for the bath containing PVP approaches toward 3D progressive nucleation and hydrogen coevolution has been decreased. The mathematical model proposed by Palomar-Pardavé confirmed the result of the considered system. Also, the roughness and corrosion current density of nickel deposits were examined for different temperatures.
Key words: Electrodeposition, Nickel, PVP, SDS, Nucleation

Introduction:

The nickel electrodeposition is an important process in industry, it is driven by numerous actual and potential applications, such as mechanical strength, corrosion resistance and heat resistance (Z. Yiyuan, 2017, H. Zargarnezhad, 2017). Various baths are used for obtaining uniform electrodeposits with required quality and morphology. The Watts bath is widely applied for nickel electrodeposition, and its impact on the development of modern nickel electroplating technology cannot be overestimated (J. K Dennis, 1993, L. Biao, 2015). It is also well known that the addition of special organic compounds in small amounts results in significant changes in the properties and morphology of the deposit (Di Bari, 2010, N. P. Wasekar, 2016), these additives serve a variety of purposes by acting as surfactants, refiners, brighteners, and levelling agents.

Creative Commons Attribution-NonCommercial-NoDerivatives 4.0 International License (CC BY-NC-ND)

The metal electrodeposition is often accompanied by hydrogen reduction. In general, this concurrently reaction is not desired and unavoidable. The reduction of hydrogen ion not only decreases the cathode current efficiency, but also degrades the morphology of nickel surface (M. Palomar-Pardave, 2005). This can be resolved by addition of surfactants (L. Jing, 2010, G. Chao, 2008).

In the past few years, sodium dodecyl sulfate (SDS) has become the most important surfactant used to ameliorate the performances of nickel electrodeposits (U.S. Mohanty, 2009) . Furthermore, this additive affects other coatings properties such as the electrochemical properties of zinc (G. Robab Khayat, 2006) and the stress of electroplated copper (S. Kim, 2007). However, the effect of this additive on the nucleation and growth of nickel deposits has not been studied yet.

Polyvinylpyrrolidone (PVP) is a famous macromolecule surfactant that has many benefits (W. Peng, 2013). Up to now, PVP has brought substantial interest and has been widely used in different fields such as anticorrosion (M.M. Khaled, 2001, A.A. Gurten, 2005), chemical deposition (L. Qi, 2010, B. Ezgi, 2013, L. Dayong, 2008, X. Liu, 2008) and electrodeposition (C. Zhigang, 2006, G. Shahram, 2007). PVP was used as a wetting agent and a refiner in plating baths of ZnO (C. Zhigang, 2006) and PbO_2 (G. Shahram, 2007). However, there are no researches focused on the effect of PVP as surfactant in nickel electrodeposition.

Problematic:

In our previous study, we have found that PVP enhances the brightness of nickel electrodeposits better than SDS (I. Djaghout, 2015). The brightness is determined by the degree to which structural components of the surface are in the same plane. Moreover, a production of small grains is another important matter to obtain high brightness (D. S. Stoychev, 1978, S. Esma, 2012). Thus, the present paper investigates the effect of SDS and PVP on the kinetic and nucleation of nickel electroplating from Watts baths.

Materials and methods:

Nickel coatings were prepared by direct-current galvanostatic deposition onto copper substrate (20 mm × 10 mm), from a conventional Watts bath composed of 250 gL^{-1} $NiSO_4.6H_2O$, 45 gL^{-1} $NiCl_2.6H_2O$, and 40 gL^{-1} H_3BO_3. An appropriated amount of sodium dodecyl sulfate ($NaC_{12}H_{25}SO_4$) and polyvinylpyrrolidone $(C_6H_9NO)_n$ with an a molecular weight of 40000 was added to the electrolytic bath (Table 1). All solutions were prepared with analytical grade chemicals and ultrapure water. Prior to nickel electrodeposition the substrate surface was subjected to mechanical treatment with metallurgical papers of 800, 1200 and 2000 grits, then cleaned with HCl (0.1 M) and rinsed by ultrapure water. All the electrodeposition experiments were conducted for 120 s by applying current from an AX 501 METRIX regulated power supplier (0–30 V/2.5 A). After electrolysis, the samples were removed from the cell and thoroughly washed with ultrapure water and dried.

Creative Commons Attribution-NonCommercial-NoDerivatives 4.0 International License (CC BY-NC-ND)

Cyclic voltammetry experiments were carried out in a conventional three-electrode glass cell using an EG & G Princeton Applied Research potentiostat/galvanostat model 273A controlled by Power Suite software. A copper substrate and platinum wire of 0.5 mm diameter were used as working and auxiliary electrodes respectively, saturated calomel electrode (SCE) served as reference electrode. Voltammograms were obtained in the potential range between −1200 mV and +50 mV, with a scan rate of 20 mVs^{-1}. The corrosion resistance of the nickel coatings was studied in 3.5 % NaCl. Prior to experiments, samples were immersed in solution for 30 min, at room temperature. The polarization curves were performed from − 500 to 0 mV at scan rate of 5 mVs^{-1}, using an EG & G Princeton Applied Research potentiostat/galvanostat model VersaSTAT 3 controlled by VersaStudio software. Instantaneous roughness criteria measurements (arithmetic mean roughness, Ra) of nickel deposits are obtained by means of a Mitutoyo Surftest 201 roughness meter. The length examined was 2.4 mm with a basic span of 3. The measurements were repeated three times and the result is an average of these values.

Table 1 Chemical composition of plating baths

N° baths	Watts bath (gL^{-1})			Surfactants (gL^{-1})	
	$NiSO_46H_2O$	$NiCl_26H_2O$	H_3BO_3	$NaC_{12}H_{25}SO_4$	$(C_6H_9NO)_n$
1	250	45	40		
2	250	45	40	1	
3	250	45	40		1

Results and discussions:

Cyclic voltammetry:

Fig. 1 shows cyclic voltammograms obtained onto copper substrate during nickel electrodeposition from three different plating baths (table 1). Typical voltammogram related to Watts bath is presented in Fig. 1. The potential scanning was started from -150 mV, during the forward scan towards more cathodic potential, no significant currents were recorded until the potential reaches – 600 mV. Then the current increases sharply once nucleation has begun, followed by a further increase in the current since deposition of nickel is accompanied by hydrogen coevolution. The potential was reversed at -1200 mV and finally stopped at the initial voltage, during reverse scan two characteristic crossovers between the branches for the negative and positive sweeps indicating the feature of nucleation process (R. Ewa, 2012). The current became anodic at a potential of approximately − 390 mV where the electrooxydation of metallic nickel starts and a pronounced peak is developed. The influence of SDS and PVP on the polarization curve of nickel electrodeposition was also illustrated in Fig. 1. The extent

Creative Commons Attribution-NonCommercial-NoDerivatives 4.0 International License (CC BY-NC-ND)

of the polarization increased with the addition of both surfactants in the initial stage of electrodeposition. Therefore, the presence of surfactants in the electrolyte obviously inhibited the reduction process and the polarization by PVP was greater than that of SDS as soon as the reduction began. The inhibition induced par SDS is close to that reported by (L. Jing, 2010, U.S. Mohanty, 2009) in nickel sulfate solution. Thus the tendency observed here can be attributed to the decreasing number of active sites as the surfactants were adsorbed to the working electrode surface and the availability of PVP to adsorb exceeds that of SDS.

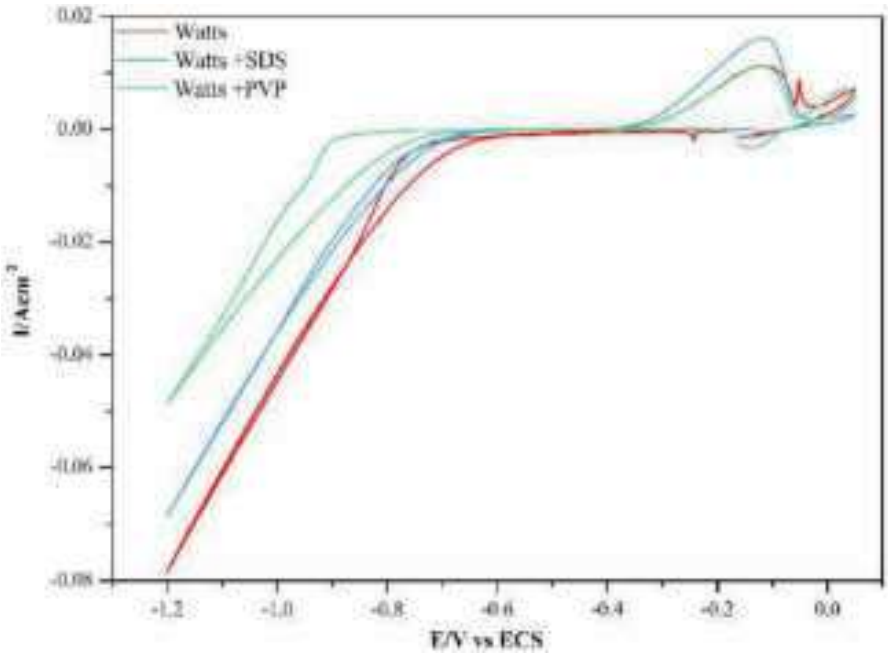

Fig1. CYCLIC VOLTAMMOGRAMS RECORDED FOR THE COPPER ELECTRODE IN DIFFERENT NICKEL PLATING SOLUTIONS, AT THE SCAN RATE V= 20 mVs^{-1}.

Chronoamperometry

Fig. 2 shows potentiostatic transient curves recorded for various nickel baths composition at deposition potential of -1.1 V in order to study the reduction of Ni^{+2} and the hydrogen evolution reaction (HER). The reduction of Ni^{+2} ions occurs before the potential of HER. According to reference (A. Sahari, 2008), HER start at -1 V. We believe that at -1.1 V, the rate of HER remains significant despite the addition of surfactants as confirmed by our obtained results. It is of considerable interest to investigate the mechanism of the nucleation and crystal growth of nickel deposition with hydrogen evolution reaction (HER).

The transients having relatively similar behavior are characterized by gradual increase of cathodic current up to a maximum that corresponds to the birth of the individual isolated nickel nuclei and/or the increase of the number of nuclei, followed by a decrease of the current until a limit which is imposed by the diffusion of the electroactive species through the solution towards the surface of the electrode (A. Sahari, 2008, Y. Messaoudi, 2013). The maximum of the current transient decreases with the addition of surfactants, such observation corroborates the trends mentioned in the cyclic voltammetry. On the other hand, the current

Creative Commons Attribution-NonCommercial-NoDerivatives 4.0 International License (CC BY-NC-ND)

density in the diffusion part does not drop wholly but approaches a relatively stable value (X. Huang, 2013), this situation may be attributed to the concurrent reduction of hydrogen, which became less intense from PVP-containing bath.

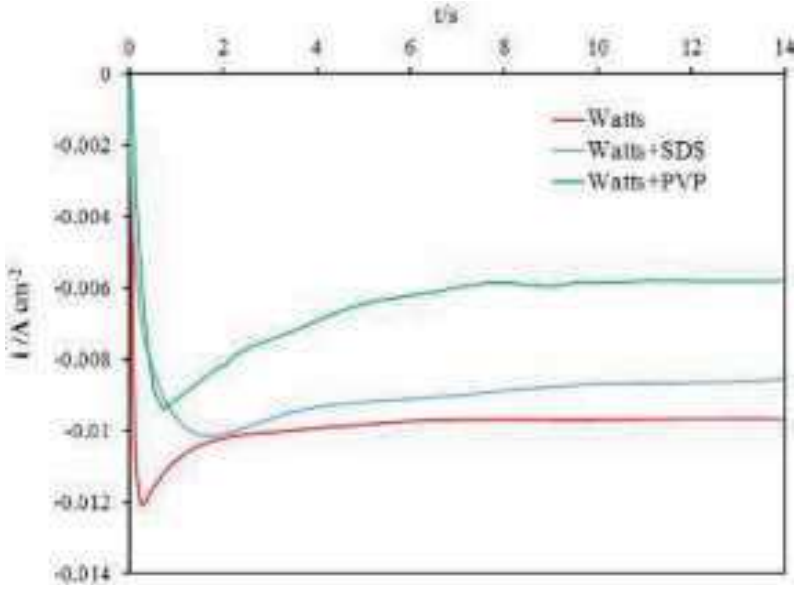

Fig2. CHRONOAMPEROMETRIC TRANSIENTS OF NICKEL PLATING BATHS AT DEPOSITION POTENTIAL OF -1.1V.

The nucleation mechanism involved here was determined by comparing the experimental potentiostatic transients in non-dimensional form with theoretical nucleation models developed by Bewick for 2D Growth (A. Bewick, 1992) and Sharifker-Hills for 3D Growth (B. Scharifker, 1983) :

For 2D instantaneous model: $$\left(\frac{i}{i_{\max}}\right)=\left(\frac{t}{t_{\max}}\right)\exp\left[-1/2\left(\left(\frac{t}{t_{\max}}\right)^{2}-1\right)\right] \quad (1)$$

For 2D progressive model: $$\left(\frac{i}{i_{\max}}\right)=\left(\frac{t}{t_{\max}}\right)^{2}\exp\left[-2/3\left(\left(\frac{t}{t_{\max}}\right)^{3}-1\right)\right] \quad (2)$$

For 3D instantaneous model: $$\left(\frac{i}{i_{\max}}\right)^{2}=\frac{1.9542}{t/t_{\max}}\left[1-\exp\left(-1.2564\frac{t}{t_{\max}}\right)\right]^{2} \quad (3)$$

For 3D progressive model: $$\left(\frac{i}{i_{\max}}\right)^{2}=\frac{1.2254}{t/t_{\max}}\left[1-\exp\left(-2.3364\left(\frac{t}{t_{\max}}\right)^{2}\right)\right]^{2} \quad (4)$$

Where $i_{\max}$ and $t_{\max}$ are the maximum values of the current transient and corresponding deposition time, respectively.

Creative Commons Attribution-NonCommercial-NoDerivatives 4.0 International License (CC BY-NC-ND)

Figs. 3a and 3b show the comparison between the experimental plots and theoretical nucleation models. It is clear that the experimental nickel nucleation curves are consistent with 3D Scharifker-Hills model. Experimental curve plotted by 3D growth show also that the rising part of experimental curves of Watts bath and Watts containing SDS follow the instantaneous nucleation, whereas in the case of Watts containing PVP, the curve lie between the two limiting nucleation exhibiting an intermediate behavior. At $(t/t_{max}) \succ 1$ the curves of Watts bath and Watts containing SDS show large deviation from the theoretical nucleation, especially at $(t/t_{max}) \succ 2$, this deviation is most likely related to reduction of hydrogen ions and hydrogen evolution. While in the curve of Watts containing PVP, the nucleation keeps an intermediate mechanism and the deviation has been decreased. We can explain the nucleation mechanism in the case of bath containing PVP by decreasing the rate of nucleation because the surface is partially covered by PVP.

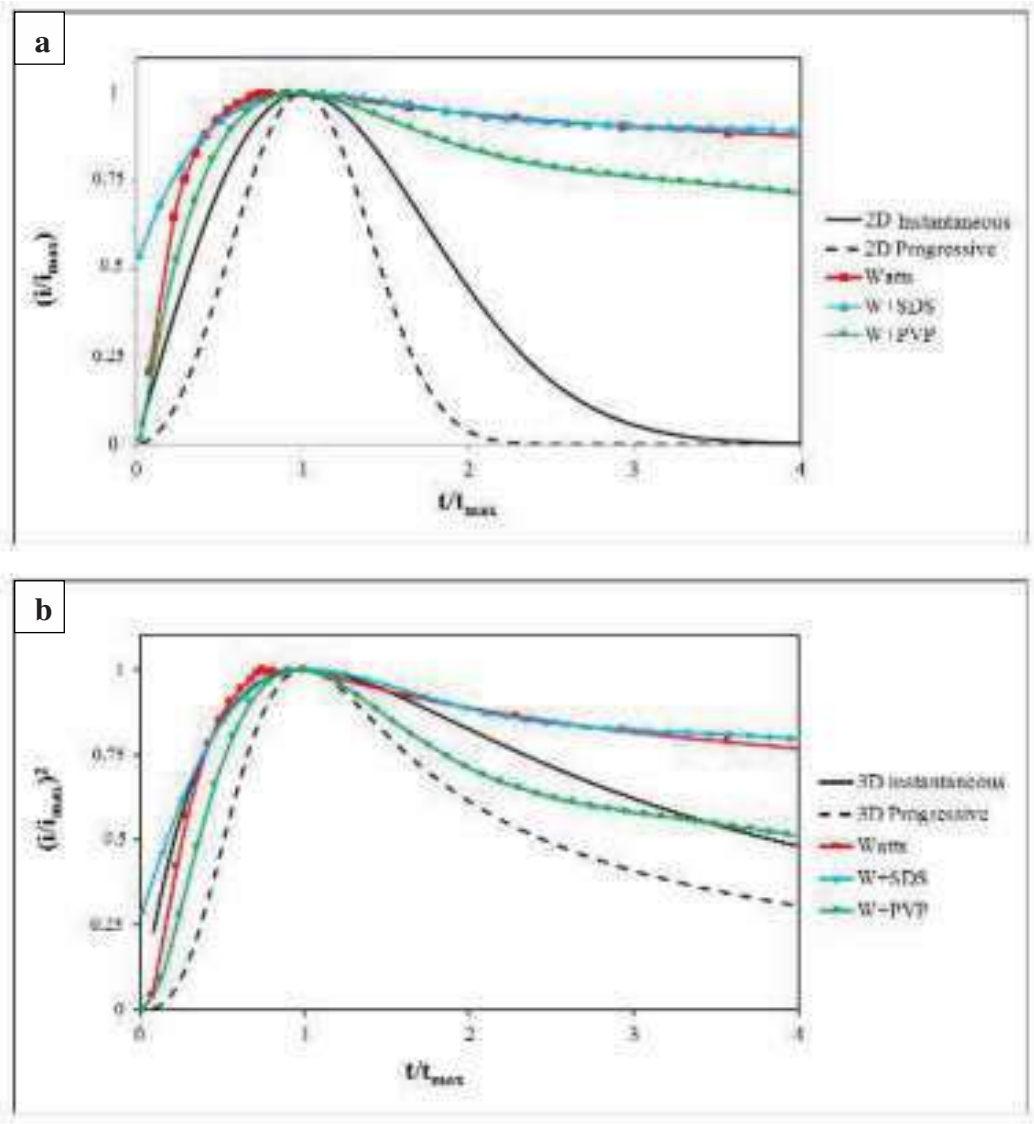

Creative Commons Attribution-NonCommercial-NoDerivatives 4.0 International License (CC BY-NC-ND)

Fig3. COMPARISON BETWEEN NON-DIMENSIONAL 2D AND 3D THEORETICAL PLOTS FOR INSTANTANEOUS (FULL LINE) AND PROGRESSIVE NUCLEATION (DASHED LINE) AND EXPERIMENTAL PLOTS FOR DIFFERENT NICKEL PLATING BATHS.

Hence Scharifker–Hills model cannot adequately describe the nickel electrodeposition process, the deviation that the experimental current follows are most likely related to the proton reduction. The latter was taken into account by (Palomar-Pardave *et al,* 2005). who proposed a mathematical model for metal electrocrystallization which takes into consideration the contribution of parallel hydrogen reaction. The model that allows obtaining partial current of nickel deposition and hydrogen evolution contributions is given by:

$$i_{total} = \left(P_1^* + P_4 t^{-0.5}\right)\left(1 - \exp\left\{-P_2\left[t - \frac{1-\exp\left(-P_3 t\right)}{P_3}\right]\right\}\right) \quad (5)$$

$$P_1^* = Z_{PR} F k_{PR}\left(\frac{2Mc}{\pi\rho}\right)^{0.5} \quad (6)$$

$$P_2 = D\pi N_0\left(\frac{8\pi c}{\rho}\right)^{0.5} \quad (7)$$

$$P_3 = A \quad (8)$$

$$P_4 = 2Fc\left(\frac{D}{\pi}\right)^{0.5} \quad (9)$$

Where Z_{PR} is the number of electrons transferred during elementary reaction of hydrogen ions reduction, F the Faraday constant, k_{PR} the rate constant of the proton reduction, M the molar mass of deposited metal, c the concentration of metal ions in the bulk of the solution, ρ the density of deposited metal, D the diffusion coefficient, N_0 the density of nucleation sites and A is the rate of nucleation.

P_1^*, P_2, P_3 and P_4 parameters are determined by iterative fitting of equation (5) to the experimental chronoamperograms of Fig. 2, and are listed in Table 2. According to obtained values, the kinetic parameters such as N_0, A and k_{PR} can be calculated.

The comparison between the experimental chronoamperograms and the fitted transients that were generated by non-linear Marquardt–Levenberg algorithm is presented in Fig. 4. As it has found that there is a competition between nickel reduction and hydrogen evolution. The current of proton reduction is higher than that of the nickel ions reduction in Watts bath. From Watts containing SDS bath, the current of nickel reduction increases little and current of proton reduction decreases also slightly, while from Watts containing PVP, the current of nickel reduction exceeds that of the proton coevolution. Such phenomenon can be ascribed to the ability of surfactants, especially PVP, to remove evolved hydrogen. These results could corroborate with those reported by (Dayong Liu *et al*., 2008) and Xiaodan LIU *et al*., 2008). They reported the effect of PVP on the morphology of nickel nanoparticles deposited by

Creative Commons Attribution-NonCommercial-NoDerivatives 4.0 International License (CC BY-NC-ND)

chemical reduction. The authors claimed that PVP could control the nucleation and the growth processes of nickel nanoparticles synthesis.

According to table 2, both A and N_0 decrease with the addition of surfactants, especially PVP, this is also the confirmation that the surfactants are adsorbed on the cathode surface as it has discussed in cyclic voltammetry and chronoaperommetry studies. The values of N_0 are in the same order of magnitude as that determined for nickel deposition from ammoniacal alkaline solutions (L. Dayong, 2006), while A are higher than that of the same reference. The rate constant of hydrogen ion reduction (k_{PR}) were also estimated. The values of 10^{-6} mol/cm^{2}s were found from Watts bath, such value was in good agreement with published results in similar bath onto different substrate (R. Ewa, 2012), whereas k_{PR} value of Watts containing PVP is lower than that mentioned in the same reference from Watts bath containing gluconate as additive.

Table 2 Kinetic parameters determined from the fitted transients

Bath	P_1^* (A cm^{-2})	P_2 (s^{-1})	P_3 = A (s^{-1})	P_4 (A cm^{-2} s$^{0.5}$)	N_0 (cm^{-2})	k_{PR} (mol cm^{-2} s^{-1})
Watts	9.18×10^{-3}	14.16	45.67	1.65×10^{-3}	$7.16\times10^{+10}$	1.28×10^{-6}
W+SDS	7.70×10^{-3}	2.38	9.43	3.34×10^{-3}	$0.29\times10^{+10}$	1.08×10^{-6}
W+PVP	3.90×10^{-3}	3.89	5.32	5.55×10^{-3}	$0.17\times10^{+10}$	0.546×10^{-6}

Creative Commons Attribution-NonCommercial-NoDerivatives 4.0 International License (CC BY-NC-ND)

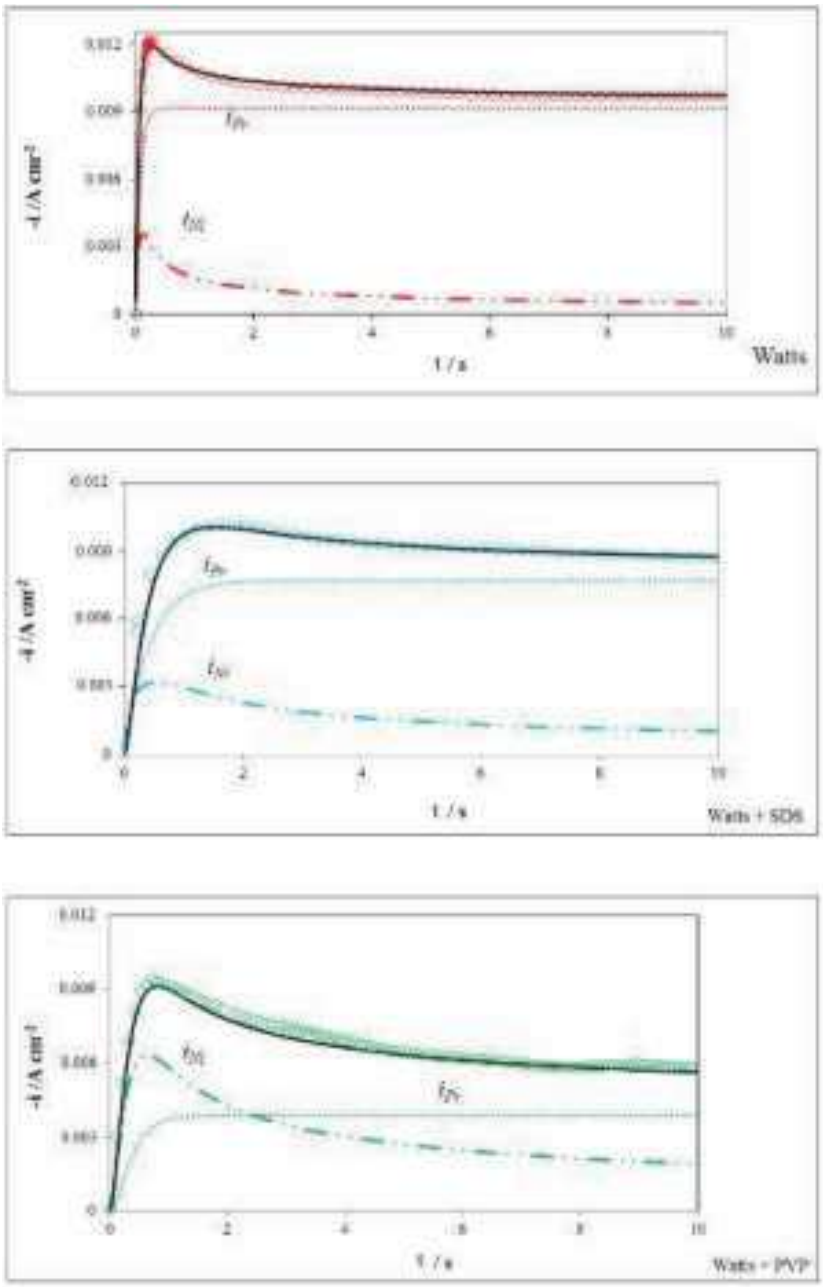

Fig4. COMPARISON BETWEEN THE EXPERIMENTAL CHRONOAMPEROGRAMS (SYMBOLS) AND THE THEORETICAL CURRENT TRANSIENTS OBTAINED AFTER NON-LINEAR FITTING OF EQ (5) TO THE EXPERIMENTAL DATA (SOLID LINES).

Nickel deposits properties

The effect of surfactants on the roughness and corrosion current density of nickel electrodeposits at three different temperatures is shown in Fig 5. The results of surface roughness indicate that a more uniform surface with lower roughness was obtained using PVP. Furthermore, it appears that PVP play major role in improving the corrosion resistance

Creative Commons Attribution-NonCommercial-NoDerivatives 4.0 International License (CC BY-NC-ND)

of the coatings. The adsorption of PVP could fill the pores and micro-holes of hydrogen bubble and decreased the tendency of the coatings to corrosion.

The roughness and the corrosion current were obviously decreased in the presence of surfactants, while the temperature affects the roughness and corrosion current of deposits obtained from Watts bath strongly than those obtained from Watts free surfactants. Hence Watts bath is more sensitive to the change in the temperature.

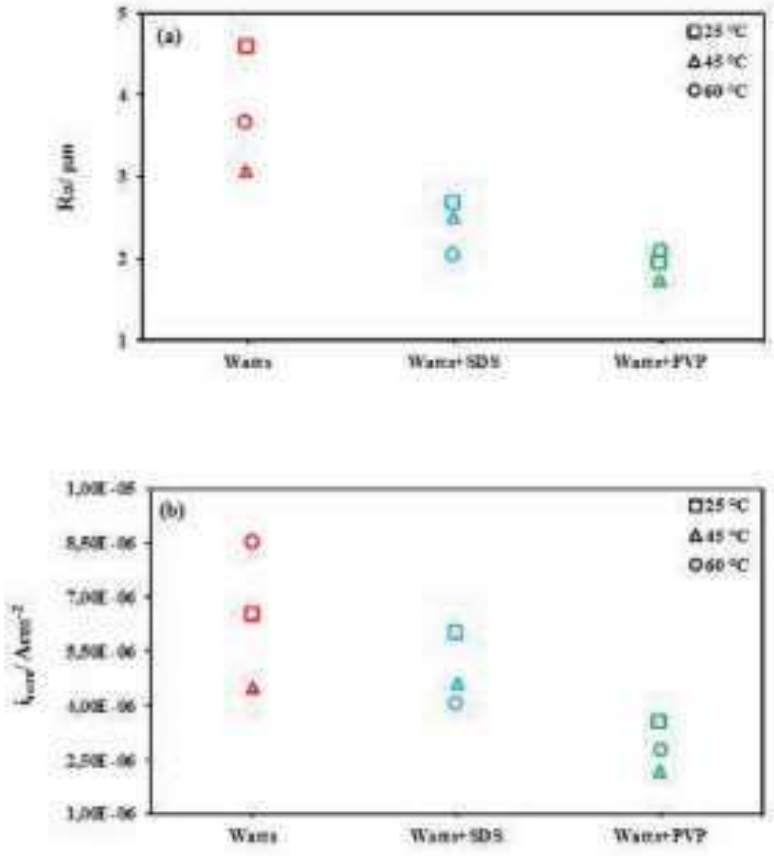

Fig5. (a) SURFACE ROUGHNESS AND (B) CORROSION CURRENT DENSITY OF NICKEL DEPOSITS OBTAINED FROM DIFFERENT PLATING BATHS

Conclusion:

Nickel electrodeposition on copper substrate from Watts bath with and without surfactants has been investigated using cyclic voltammetry and chronoamperometry methods. The voltammetric results revealed an inhibitive effect exerted by both SDS and PVP, the degree of inhibition is higher with bath containing PVP. Chronoamperometric study indicates that the initial stage of nickel reduction is controlled by diffusion and follows three-dimensional (3D) growth. The theoretical model of Scharifker-Hills was used to analyze the current transients, it revealed that the nucleation of nickel from Watts bath or Watts containing SDS follows (3D) instantaneous mechanism and the nickel growth is accompanied by concurrent hydrogen reduction. Whereas the curve of bath containing PVP approaches towards progressive nucleation since the surface was partially covered by PVP.

Creative Commons Attribution-NonCommercial-NoDerivatives 4.0 International License (CC BY-NC-ND)

Mathematical model proposed by Palomar-Pardavé shows that the current of nickel reduction in the presence of PVP, and unlike SDS, is higher than that of proton reduction. Furthermore, the lowest values of roughness and corrosion current density of nickel deposits were obtained in the presence of this additive at temperature of 45 °C.

Hence these specific properties classify PVP as very promising additive for future industrial applications in nickel electroplating.

References:

Yiyuan Z. (2017), *The effect of valine on the process of nickel electrocrystallization on glassy carbon electrode*, Journal of Electroanalytical Chemistry **796(): ** 43-48.

Zargarnezhad H., Dolati A. (2017), *3D Continuum-Kinetic Monte Carlo simulation Study of Early Stages of Nucleation and Growth in Ni Electrodeposition*, Electrochimica Acta **236(): ** 1-9.

Dennis J. K, (1993), *Nickel and chromium plating*, 3rd ed, Cambridge: Woodhead Lts.

Biao L., Zhenfeng H., Xiaohe W., Binshi X. (2015), *Electrodeposition of nanocrystalline nickel assisted by flexible friction from an additive-free Watts bath*, Surface & Coatings Technology **270 (): ** 123-131

Di Bari GA. (2010), In: *Electrodeposition of nickel*. Schlesinger M, Paunovic M, editors. New Jersey: Wiley and Sons, Inc, 55.

Wasekar N. P., Haridoss P., Seshadri S.K., Sundararajan G. (2016), *Influence of mode of electrodeposition, current density and saccharin on the microstructure and hardness of electrodeposited nanocrystalline nickel coatings*, Surface & Coatings Technology **291():**130 -140.

Palomar-Pardave M., Scharifker B.R., Arce E.M., M. Romero-Romo(2005*), Nucleation and diffusion-controlled growth of electroactive centers Reduction of protons during cobalt electrodeposition*, Electrochimica Acta **50()**: 4736-4745.

Mohanty U.S., Tripathy B.C., Das S.C., Singh P., Misra V.N. (2009)*, Effect of sodium lauryl sulphate (SLS) on nickel electrowinning from acidic sulphate solutions*, Hydrometallurgy **100():** pp 60-64.

Jing L., YANG Q., ZHANG Z. (2010), *Effects of additives on nickel electrowinning from sulfate system*, Transactions of Nonferrous Metals Society of China **20()**: 97- 101.

Robab Khayat G., Zahra R. (2006), *Performance improvements of alkaline batteries by studying the effects of different kinds of surfactant and different derivatives of benzene on the electrochemical properties of electrolytic zinc*, Journal of Power Sources **162():** 893-899.

Kim S., Jang J.H., Lee J.S. 2007, *Stress behavior of electrodeposited copper films as mechanical supporters for light emitting diodes*", Electrochemical Acta **52():** 5258-5265.

Peng W., Tian G., Jianfeng Z., Jing L., Shenghui Z. (2013), *Polyvinylpyrrolidone-enhanced electrochemical oxidation and detection of acyclovir*, Journal of Molecular Liquids 177(): 129-132.

Khaled M.M. (2001), *The effect of molecular weight on the corrosion protection properties of polyvinylpyrrolidone polymers on stainless steel*, The Arabian Journal for Science and Engineering 35() 29-39.

Gurten A.A., Erbil M., Kayakırılmaz K. (2005), *Effect of polyvinylpyrrolidone on the corrosion resistance of steel*, Cement & Concrete Composites 27(): 802-808.

Qi L., Guo-Zhen Z., Wei-Feng Z., Guo-Hua C. (2010), *Preparation and characterization of nickel-coated graphite nanosheets*, Synthetic Metals**160()**: 200-202.

Ezgi B., Tuba Gürkaynak A., Ali Faruk Öksüzömer M. (2013), *Effects of PVP on the preparation of nanosized Al_2O_3 supported Ni catalysts by polyol method for catalytic partial oxidation of methane*, Fuel Processing Technology **110():** 167-175.

Zhigang C., Yiwen T., Lisha Z., Lijuan L. (2006), *Electrodeposited nanoporous ZnO films exhibiting enhanced performance in dye-sensitized solar cells*, Electrochimica Acta **51():** 5870-5875.

Shahram G., Mir Fazllolah M., Mojtaba S. 2007, *Electrochemical deposition of lead dioxide in the presence of polyvinylpyrrolidone A morphological study*, Electrochimica Acta **53():** 459-467.

Creative Commons Attribution-NonCommercial-NoDerivatives 4.0 International License (CC BY-NC-ND)

Djaghout I., Affoune A.M., Chelaghmia M.L. and Bendjaballah M. (2015), *Experimental Investigation of Nickel Electrodeposits Brightness in the Presence of Surfactants: Modeling, Optimization and Polarization Studies*, Portugaliae Electrochimica Acta **33(): ** 209-222.

Stoychev D. S., Tomov I., Vitanova I. and Rashkov S.T. (1978), *Determination of the size of the crystallites that form bright galvanic copper coating*, Surface Technology **7(): ** 433-441.

S. Esma, U. Belkıs, Ramazan K. (2012), *Effects of a N,N-dimethyl-N-2-propenyl-2-propene-1-ammonium chloride-2-propenamide copolymer on bright nickel plating*, Surface & Coatings Technology **213(): ** 253-263.

Ewa R., Marek W., Grzegorz W. (2012), *Effect of gluconate addition on the electrodeposition of nickel from acidic baths,* Surface & Coatings Technology **207(): ** 375-388.

Sahari A., Azizi A., Schmerber G., Dinia A. (2008), *Nucleation, growth, and morphological properties of electrodeposited nickel films from different baths*, Surface Review and Letters**15(): ** 717-725.

Messaoudi Y., Azizi A., Fenineche N., Schmerber G., and Dinia A. (2013), *Electrochemical Production of Magnetic Co–Mo Alloys*, Thin Films**11(): ** 1622-1626.

Huang X., Chen Y., Zhou J., Zhang Z., Zhang J. (2013), *Electrochemical nucleation and growth of Sn onto double reduction steel substrate from a stannous fluoborate acid bath*, Journal of Electroanalytical Chemistry **709(): ** 83-92.

Bewick A., Thirsk H. R., Fleischmann M. (1992), *Kinetics of the electrocristallization of thin films of calomel*, Transaction of the faraday society **58(): ** 2200-2216.

Scharifker B. 1983, *Theoretical and experimental studies of multiple nucleation*, Electrochemica acta **28(): ** B79-89.

Darko G., Batric P. (2006), *Electrochemical and AFM study of nickel nucleation mechanisms on vitreous carbon from ammonium sulfate solutions*, Electrochimica Acta **51(): ** 2678-2690

Creative Commons Attribution-NonCommercial-NoDerivatives 4.0 International License (CC BY-NC-ND)

Algerian Journal of Engineering Architecture and Urbanism Vol. 5 Nr. 3 2021
ISSN: 2588-1760

MODELING AND DYNAMIC SIMULATION OF A ROBOT USING THE SOLIDWORKS MOTION TOOL

Billel LOUNICI
PhD student, Mec, Structures Research Laboratory, Department of Mechanics, Saad DAHLAB University of Blida 1, Lounici.billel@etu.univ-blida.dz

Mohammed OUALI
Prof, Mec, Structures Research Laboratory, Department of Mechanics, Saad DAHLAB University of Blida 1, Oualimohammed@yahoo.fr

El Hadi OSMANI
MAB, Mec, Structures Research Laboratory, Department of Mechanics, Saad DAHLAB University of Blida 1, Osmani-acts@live.fr

Abstract:
Robotizing manufacturing systems is becoming more and more the ideal solution, especially during the COVID pandemic, where workers in almost all sectors have been quarantined. The teleoperation control of many tasks requires special features to be satisfied, which implies very important costs for the realization of the command online.

In this paper, we propose to create a dynamic simulator based on the analysis of the robot motion during a specific task using the SolidWorks motion tool of SolidWorks software.

The simulation of the robot on the suggested tool could be performed using as input the solution of one of the robot models: the geometric model, the kinematic model and the dynamic model. We use the MATLAB software to establish the computational code for these models. In order to evaluate the validity of our solution, a comparison between the results of the proposed tool and those of the code generated on MATLAB will be made.

Key words: Robotic modeling, dynamic simulation, SolidWorks motion

Introduction:

The term robotics refers to all the fields that works on improving robots of different types, from design to control and use, through modeling. All of these fields make sure that the robot in question is best suited for the task it is assigned to. Robot can be as simple as those in children's games, or as complex as surgical or space robots.

The industrial robot is a very popular type of robot because of its versatility. No matter the industry, an industrial robot for a specific task already exists. It can easily be adapted for a specific task, handling, welding, painting or other. The manufacturers of industrial robots make sure to optimize a range for each type of industry.

Creative Commons Attribution-NonCommercial-NoDerivatives 4.0 International License (CC BY-NC-ND)

Problematic:

The adaptation of industrial robots to carrying out operations requiring a high degree of precision is the subject of recent research, particularly in the welding of electronic components, the handling of fragile objects, and painting work. Generally, the achievements of robotic tasks is given in terms of the trajectory followed, generated in the articular space of the robot, or Cartesian space. More precisely, it is about generating the movement of the final effector in the space of the task.

Precise trajectory planning requires the establishment of algorithms and programs based on mathematical models widely used in robotics. They allow to obtain positions, speeds, accelerations and torques corresponding to the desired trajectory.

The mathematical expressions of these models are implicit, complex in term of programming and requires a lot of time to be established. Some of the mathematical equalities and expressions do not take into account of:

- the external geometry of the robot bodies;
- stops, and joint limits;
- obstacles in the space of the task;
- trajectory constraints during robot operation.

To eliminate or minimize some drawbacks of these mathematical models, robot manufacturers use specialized software for design, programming and control. This makes it possible to model, simulate and inspect robotic systems in a way that is closer to reality.

It is for this reason that it is important to predict the behavior of the said robot, in order to be able to program, plan and optimize its trajectory (Ionescu, 2000).

Simulations are proving to be very beneficial in robotics. They also save time and avoid the need for physical prototyping (Ionescu, 2002), as well as detect and fix problems before they occur (Žlajpah, 2008).

In this work, we propose to develop a simulation tool based on the SolidWorks software, more precisely on the SolidWorks motion tool. The proposed solution is not only a versatile tool, but it also allows:

- implementation assessment, feasibility studies, animated presentations and offline programming;
- avoid singularities as well as obstacles during movement;
- to determine with precision the optimal trajectory during operation
- To be used for all existing robot models, unlike software that are specific to each robot manufacturer.

In order to verify the validity of our contribution, a robot with two degrees of freedom of rotoïd joint used for a tracing operation will be designed and developed using Matlab software. The objective is to establish the different models of the robot and to obtain

Creative Commons Attribution-NonCommercial-NoDerivatives 4.0 International License (CC BY-NC-ND)

numerical results in graphic form. These will be compared with those obtained by the proposed simulation tool.

Materials and methods:

Programming in Matlab facilitates the symbolic calculation of the mathematical models necessary for the design and control of robots such as:

- the geometric model, for calculating the positions necessary to perform the desired task,
- the kinematic model, to find the speeds and accelerations corresponding to each joint following the desired operational condition (parameters),
- and finally the calculation of the joint torques for the dynamic model, by introducing the interaction efforts of the tool with its environment.

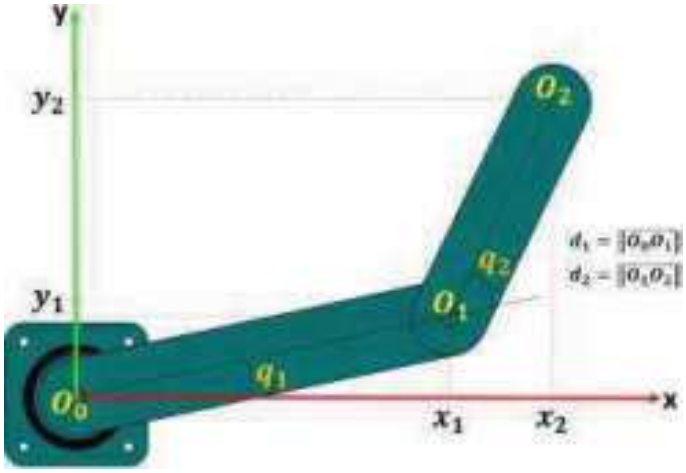

Fig 1. ROBOT WITH TWO DEGREES OF FREEDOM

Robot modeling:

The robot presented in this study is a SCARA type with two degrees of freedom. The end effector equipped with a scribing tool mounted at the end of the second axis and its axis of rotation is perpendicular to the plane (*x*, *y*). The geometric parameters of the robot (Corke, 2017) are presented (Table 1).

j	σ	α_j(rad)	$d_j(m)$	$r_j(m)$	q_j(rad)
1	0	0	$d_1 = 0.4$	0	q_1
2	0	0	$d_2 = 0.25$	0	q_2

Table 1. ROBOT GEOMETRICAL PARAMETERS

The articular position (*q*1*; q*2) is related to the desired position (*x*2, *y*2) of tracer TCP (Fig. 1) by the geometric model of the robot defined by (1).

$$\begin{cases} q_2 = cos^{-1}\left(\frac{(x_2)^2+(y_2)^2-(d_1)^2-(d_2)^2}{2*d_1*d_1}\right) \\ q_1 = sin^{-1}\left(\frac{A.y_2-B.x_2}{A^2+B^2}\right) \end{cases} \quad (1)$$

Creative Commons Attribution-NonCommercial-NoDerivatives 4.0 International License (CC BY-NC-ND)

We note that: : $A = d_1 + d_2.cosq_2$; $B = d_2.sinq_2$.

Obtaining a kinematic model of the robot also requires the knowledge of the Jacobian matrix ***J***, such as:

$$J(q) = \begin{bmatrix} -d_1 sin(q_1) - d_2 sin(q_1 + q_2) & -d_2 sin(q_1 + q_2) \\ d_1 cos(q_1) + d_2 cos(q_1 + q_2) & d_2 cos(q_1 + q_2) \end{bmatrix} \quad (2)$$

The relationship between joint speed and the desired speed of the task is given by:

$$\begin{pmatrix} \dot{q_1} \\ \dot{q_2} \end{pmatrix} = J(q)^{-1}.\begin{pmatrix} \dot{x_2} \\ \dot{y_2} \end{pmatrix} \quad (3)$$

The calculation of joint accelerations is done by deriving equation (3):

$$\begin{pmatrix} \ddot{q_2} \\ \ddot{q_2} \end{pmatrix} = J(q)^{-1}.\left(\begin{pmatrix} \ddot{x_2} \\ \ddot{y_2} \end{pmatrix} - \dot{J}(q)\begin{pmatrix} \dot{q_1} \\ \dot{q_2} \end{pmatrix}\right) \quad (4)$$

In this work, it is assumed that the robot's bodies are rigid. And we note that:
- each body is modeled by its mass *mi*,
- the position of its center of gravity is *Gi* and its inertia matrix [*Mii*] is assumed to be diagonal,
- the robot only performs movements in the plane, so only the element *I*11 is involved in the modeling, and
- the tool is modeled by a mass m placed at the point O_2.

Applying Lagrange's equations, gives the joint couples (Khalil, 2004):

$$\Gamma = M(q)\ddot{q} + C(q,\dot{q})q + G(q) + F_v\dot{q} + F_s sign(\dot{q}) \quad (5)$$

With: **M** the robot's inertia matrix, **C** the vector of centrifugal and Coriolis forces, **G** gravity, **Fv** and **Fs** are respectively the viscous and dry friction coefficients of the joints. The details of these elements are taken from (Yao, 1999).

Proposed solution Description:

The goal is to facilitate the understanding and make the offline programming of industrial robots more profitable. The proposed solution is simple and based on the understanding of the SolidWorks motion tool whose remarkable advantages are:
- program trajectories and modify some robot parameters to obtain optimal, reliable and realistic solutions,
- minimizing in one hand, the computation time by comparing with the important resolution time during programming when using the above mentioned mathematical models,
- and on the other hand, minimize the maintenance cost compared to direct tests on industrial robots.

Creative Commons Attribution-NonCommercial-NoDerivatives 4.0 International License (CC BY-NC-ND)

Algerian Journal of Engineering Architecture and Urbanism Vol. 5 Nr. 3 2021
ISSN: 2588-1760

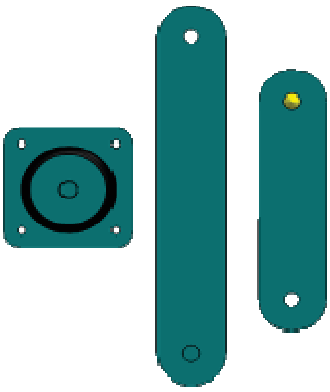

Fig 2. ROBOT PARTS

Fig 3. MOTOR CHOICE

In this section, we summarize the necessary steps to use our proposal easily:

- **Assembly parts**
  The step concerns the assembly of the robot parts (Fig. 2) taking into account the constraints necessary to ensure the proper functioning of the simulator.
- **SolidWorks motion**
  In this step, the activation of the SolidWorks motion tool is necessary for the simulation to work on the "motion analysis" type.
- **Motors add**
  It allows to move a component as if it was activated by a motor. SolidWorks provides three types of motors (Fig. 3): circular, linear (actuator) and the third type that we have chosen for our study is a motor with constraint (Fig. 4). We consider the tracing trajectory as a constraint and the feed rate as an input data.

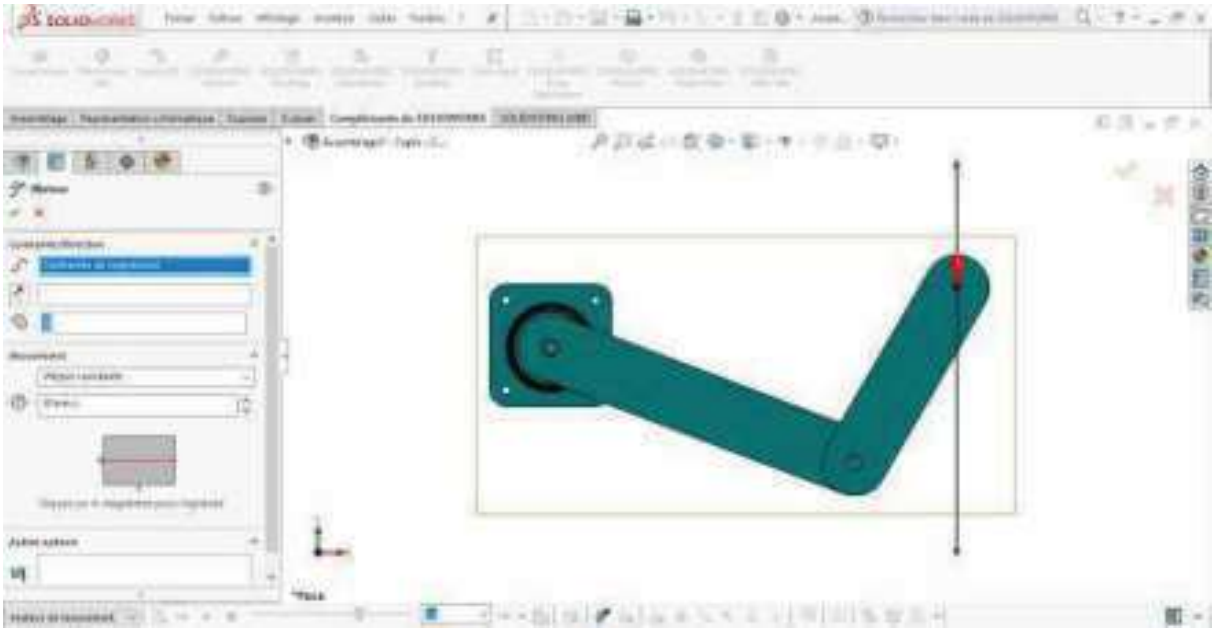

Fig 4. SELECTED MOTOR LOCATION

Creative Commons Attribution-NonCommercial-NoDerivatives 4.0 International License (CC BY-NC-ND)

- **Calculator**

  The step that allows at the same time to launch the necessary calculations and to dynamically simulate the robot according to the assembly or motion constraints (Fig. 5).

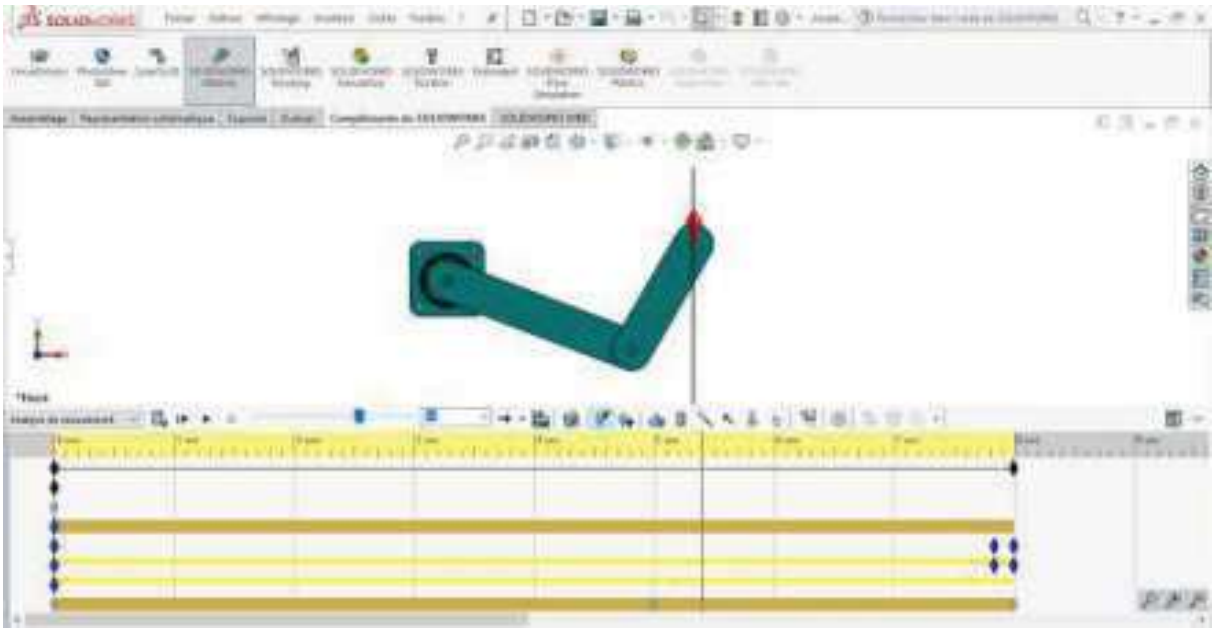

Fig 5. ROBOT CALCULATION AND DYNAMIC SIMULATION

- **Results and graphs**

  The proposed tool provides about ten results associated with the calculated motion study.

Results and discussions:

The use of a robot is necessary in the tracing operation to guide the tool fixed on its terminal organ, along a rectilinear trajectory at a speed that increases to reach the desired feed speed and keep it constant until the end of the trajectory. The end member keeps a fixed orientation with respect to the horizontal plane (x_0, y_0). The robotic tracing parameters are shown (Table 2).

Parameters	Values	Units
Trajectory type	straight path	/
Starting position (P_0)	[0.5;-0.25]	m
Feed rate (V_a)	0.06	m/s
end time (T_f)	8	s

Table 2. TRACING APPLICATION DESIRED PARAMETERS

Creative Commons Attribution-NonCommercial-NoDerivatives 4.0 International License (CC BY-NC-ND)

Algerian Journal of Engineering Architecture and Urbanism Vol. 5 Nr. 3 2021
ISSN: 2588-1760

The results section focuses on the graphical presentation of the results of the previous modeling in Matlab, such as: positions (Fig. 6), velocities (Fig. 7) and joint accelerations of the robot (Fig. 8) required performing the desired operation.

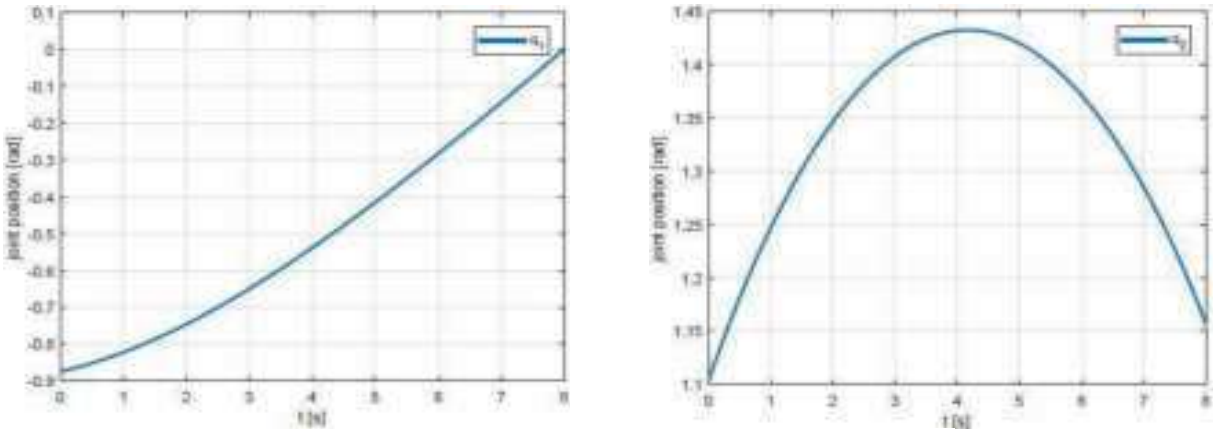

Fig 6. MATLAB CALCULATED JOINT POSITION

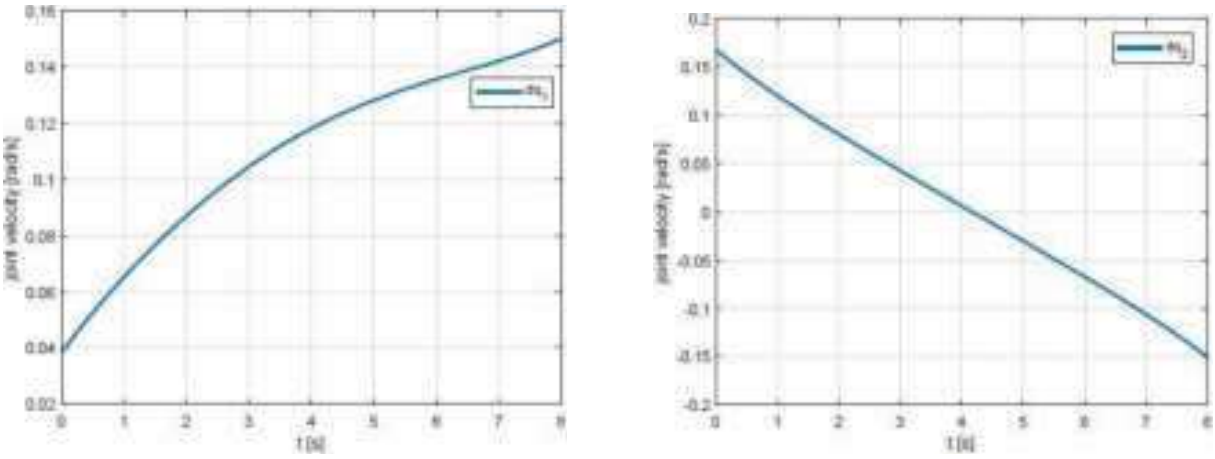

Fig 7. MATLAB CALCULATED JOINT VELOCITY

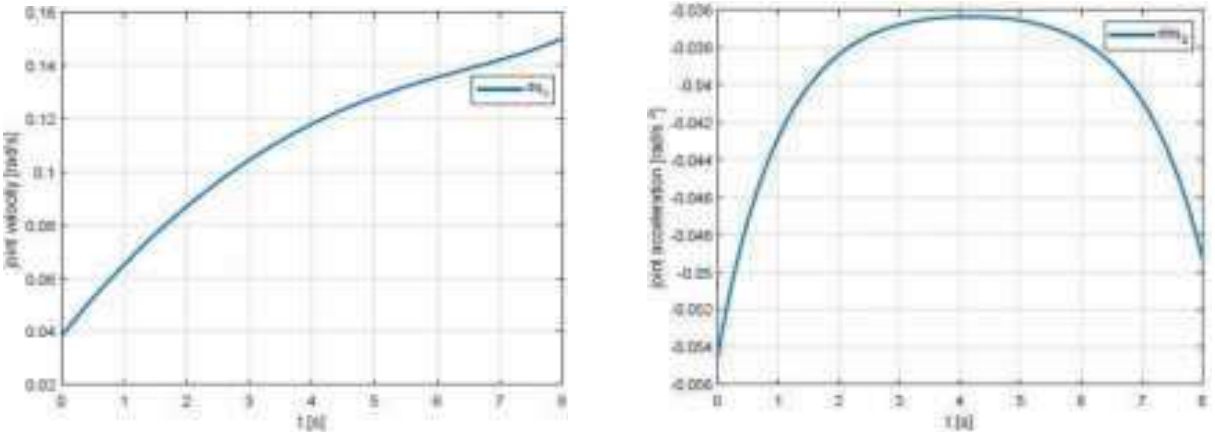

Fig 8. MATLAB CALCULATED JOINT ACCELERATION

Creative Commons Attribution-NonCommercial-NoDerivatives 4.0 International License (CC BY-NC-ND)

The same conditions in Table 2 are applied to the simulator, in order to compare the simulated results with the results obtained by Matlab in sight illustrate the industrial interest of the simulator.

Figures (Fig. 9, Fig. 10, and Fig. 11), respectively, represent the simulated positions, velocities, and joint accelerations.

We notice that the results are identical to those of Matlab. We can say that the proposed simulation tool is accurate and shows the reality with a good reliability.

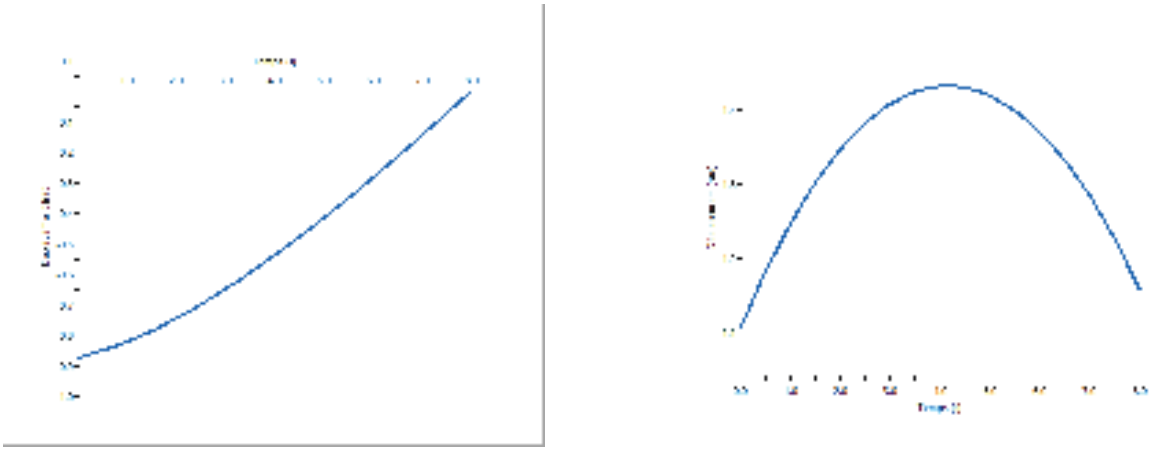

Fig 9. SOLIDWORKS SIMULATED JOINT POSITION

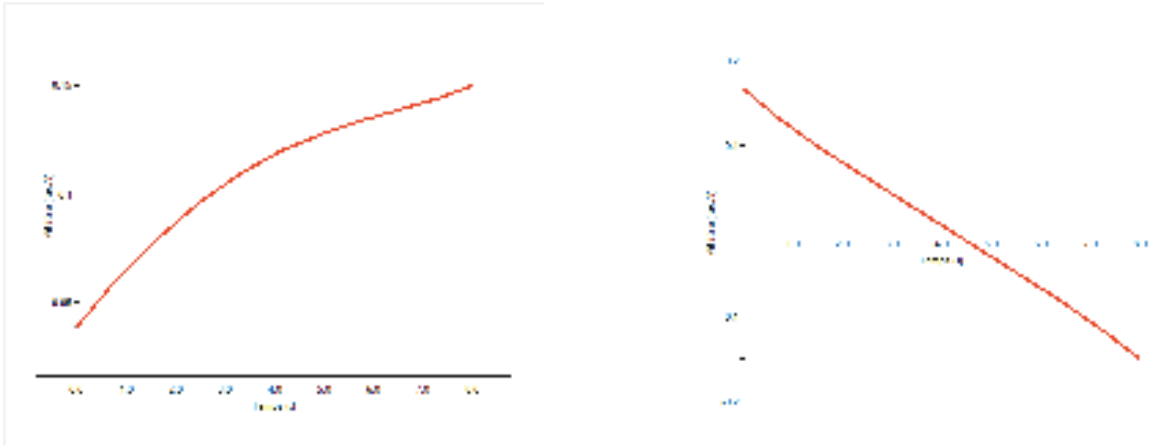

Fig 10. SOLIDWORKS SIMULATED JOINT VELOCITY

Creative Commons Attribution-NonCommercial-NoDerivatives 4.0 International License (CC BY-NC-ND)

Fig 11. SOLIDWORKS SIMULATED JOINT ACCELERATION

Conclusion:

On the one hand, this article presented the calculation by the classical method used in robotics for obtaining the joint variables such as: positions, speeds and accelerations necessary for a specific task, using the Matlab software. On the other hand, a general presentation of the proposed simulator implementation this fact.

A tracing application on a two degree of freedom robot has been presented. A comparison between the Matlab results and the proposed simulator proved the reliability of the simulator. The proposed solution is not only a versatile tool but also enables:

- To use, for layout assessment, feasibility studies and offline programming;
- Generate 3D animations of multi-body systems;
- Avoid singularities and obstacles during movement;
- Accurately prediction robot position and optimal end effector trajectory in real time.

Following the results obtained in the present work and as a perspective, we set a study that consists in the consideration of geometric defects, structural or articular deformations of the robot during the execution of tasks that require an important contact with the environment. The objective is to improve the offline programming.

References :

[1] **Ionescu, F., Chojnowski, F., & Constantin, G**. (2002). *Virtual reality in mechanical engineering, modelling and simulation with solid dynamics.* ARA Journal, 2000(25-27), 150-157.

[2] **Ionescu, F., & Stefanoiu, D.** (2002). *HYPAS-A Modular Structured Model Design, Simulation and Control Programming Environment.* Proceed. of the IASTED Intern. Confer. On Artificial and Computational Intelligence, Sept, 25-27.

[3] **Žlajpah, L.** (2008). Simulation in robotics. *Mathematics and Computers in Simulation*, *79*(4), 879-897.

[4] **Corke, P.** (2017). *Robotics, vision and control: fundamental algorithms in MATLAB® second, completely revised* (Vol. 118). Springer.

Creative Commons Attribution-NonCommercial-NoDerivatives 4.0 International License (CC BY-NC-ND)

[5] **Khalil, W., & Dombre, E.** (2004). *Modeling, identification and control of robots*. Butterworth-Heinemann.
[6] **Yao, Y. L., & Cheng, W. Y.** (1999). *Model-based motion planning for robotic assembly of non-cylindrical parts*. The International Journal of Advanced Manufacturing Technology, 15(9), 683-691.

Creative Commons Attribution-NonCommercial-NoDerivatives 4.0 International License (CC BY-NC-ND)

Algerian Journal of Engineering Architecture and Urbanism Vol. 5 Nr. 3 2021
ISSN: 2588-1760

FINITE ELEMENT ANALYSIS OF HIERARCHICAL HONEYCOMB STRUCTURES UNDER IMPACT LOADING

Ilyas BENSALEM
PhD student, Mechanics of Structures and Materials Laboratory, University of Batna 2, Algeria, e-mail: i.bensalem@univ-batna2.dz
Abdennour BENHIZIA
Dr, Mechanics of Structures and Materials Laboratory, University of Batna 2, Algeria, e-mail: a.benhizia@univ-batna2.dz

Abstract:
This paper describes a computational investigation on the response and energy absorption of hierarchical honeycomb structures under dynamic compression loading. In order to determine the ideal absorber structure, different wall thicknesses have been studied and compared in terms of deformation, force history, and energy absorption capabilities. The structures were constructed by replacing every three-edge vertex of a regular hexagonal lattice with a smaller hexagon. The dynamic compression loading is simulated by Abaqus software. Detailed deformation features and energy absorption characteristics during the crushing process were presented. The numerical results showed that the wall thickness has more effect on energy absorption comparing to core geometrical parameters. The thin wall thickness cause bending collapse mode during the crushing process and led to a lower energy absorption capability. This deformation instability is disappeared by increasing the thickness. Starting from 27mm face thickness value, the axial collapse mode is observed and ensure the maximum energy absorption.

Key words: Impact; Plastic collapse; Hierarchical honeycomb; Bending; Energy absorption

Introduction:

Shock absorbers are the responsible part to dissipate the kinetic energy and minimize the damage during an impact (Huang, 2021).The energy absorbers performance is usually evaluated through a crush test, by calculating the amount of absorbed energy during the impact (Huang, 2021. Zhao, 2017) . An ideal shock absorber is one that has a long constant stress plateau during the crush test.

Due to its excellent energy absorption capacity, honeycomb structures have been used to protect passengers and structures in different industrial sectors as an example aeronautics (Lamb, 2011), automotive (Surdjadi, 2019) and machine tools (Song, 2019).

The crashworthiness of honeycomb structures have been widely investigated using theoretical (Zhang, 2015), experimental (Wang, 2019. Mertani, 2019), and numerical simulation methods (Du Bois, 2004).

The investigations have focused on honeycombs topologies, where the structural hierarchy have been introduced into conventional honeycombs, replacing the cell walls of regular honeycombs by hexagonal, kagome and triangular lattices (Chen, 2018. Tao, 2017). The compressive performance of these structures shows that hierarchical honeycombs can be stiffer than ordinary honeycombs up to 2.0 - 3.5 times at the same mass (Wang, 2019. Tao, 2017).

In this paper, the response and the energy absorption of hierarchical hexagonal lattice honeycomb structure have been investigated numerically under dynamic compression loading, using the Abaqus software.

During a dynamic compression loading, tow response modes can be observed:

- Bending collapse mode;

Creative Commons Attribution-NonCommercial-NoDerivatives 4.0 International License (CC BY-NC-ND)

- Axial collapse mode;

The effect of wall thickness on the response mode have been studied. Detailed deformation features and energy absorption characteristics during the crushing process were presented.

The paper is organized as follows:

- The description of the proposed hierarchical honeycombs structure and the finite element modeling are presented in section 2.
- The dynamic compression results are presented and discussed in section 3.
-The concluding remarks are given in section 4.

Hierarchical honeycombs modeling:

Model description

The second order hierarchical honeycomb topology described in this work is made by replacing the cell walls of regular honeycombs with hexagonal lattices as shown in Fig. 1.

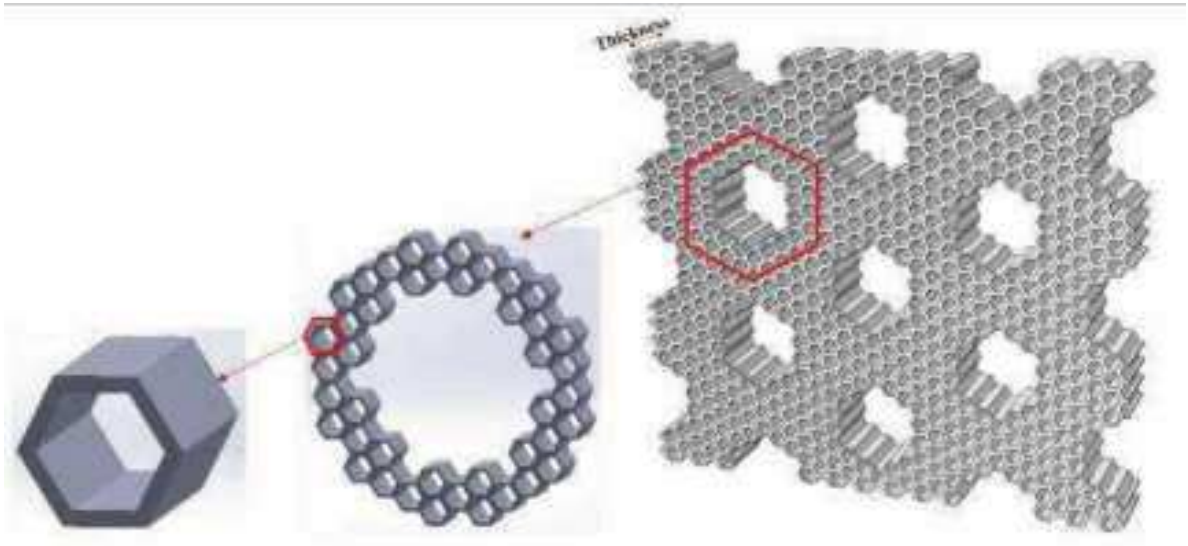

a *b* *c*

Fig.1. Geometrical illustrations of the proposed second order hierarchical honeycomb. (a) Regular honeycomb cell wall, (b) A substructure composed of a hexagonal lattice, (b) Second order Hierarchical honeycomb structure.

Finite element analysis

To investigate the axial crushing performance of the proposed hierarchical honeycomb, the finite element (FE) models were developed in commercial code ABAQUS/ Explicit as shown in Fig. 2. The structure was supported by a rigid fixed lower platen and loaded by a rigid moving upper platen at a constant velocity of 15.2 m/s (Tarlochan, 2013).

Creative Commons Attribution-NonCommercial-NoDerivatives 4.0 International License (CC BY-NC-ND)

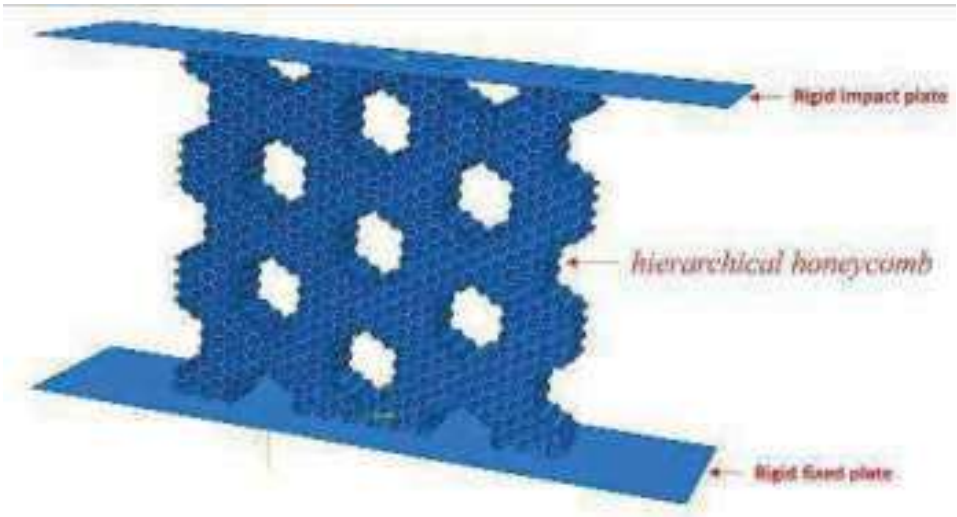

Fig.2. Numerical model of hierarchical honeycomb structure and initial boundary conditions.

The hierarchical honeycomb structure is discretized using hexahedral elements, while the remaining two plates are meshed with shell elements as shown in Fig 3.

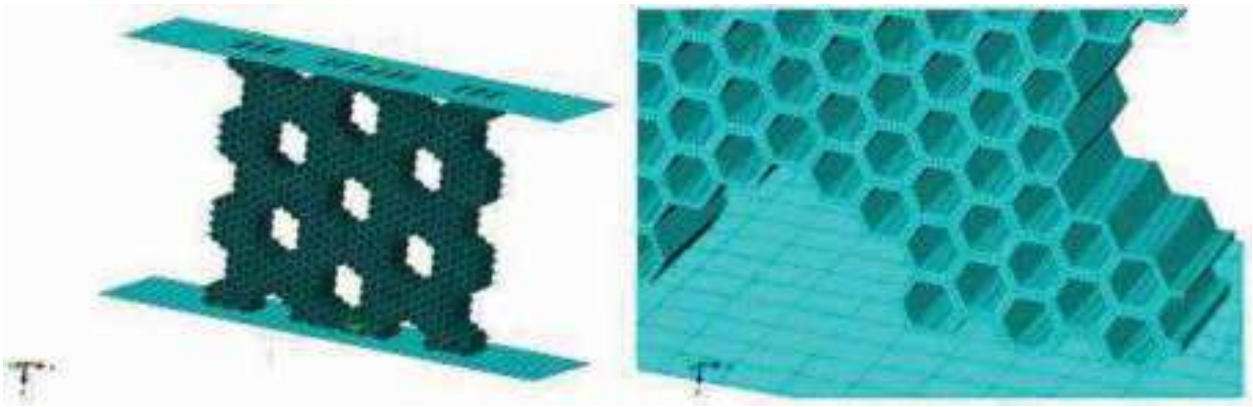

Fig.3. 3D FE assembly model and zoom in meshed geometry.

The hierarchical honeycombs are made of aluminum. The mechanical properties of Aluminum employed to represent the cell wall material, are listed in Table 1.

Density (tonne/mm3)	$2.71*10^{-9}$
Poisson's ratio	0.3
Young's modulus (GPa)	68.2
Yield-stress (N/mm2)	80
Plastic-stress (MPa)	**Plastic-strain**
80	0
115	0.024
139	0.049
150	0.079
158	0.099
167	0.124
171	0.149
173	0.174

Table 1. Material properties of Aluminum used in FE study (Du Bois, 2004).

Creative Commons Attribution-NonCommercial-NoDerivatives 4.0 International License (CC BY-NC-ND)

In order to determine the ideal hierarchical honeycomb absorber structure, different wall thicknesses have been studied and compared.

Numerical results:

Mechanical response and Von Misses stress *evolution*

The results of the numerical simulations presented below show the evolution of the Von Misses stress for the different studied wall thicknesses, after an impact of 0.008s and 0.012s respectively.

- *After an impact of 0.008s*

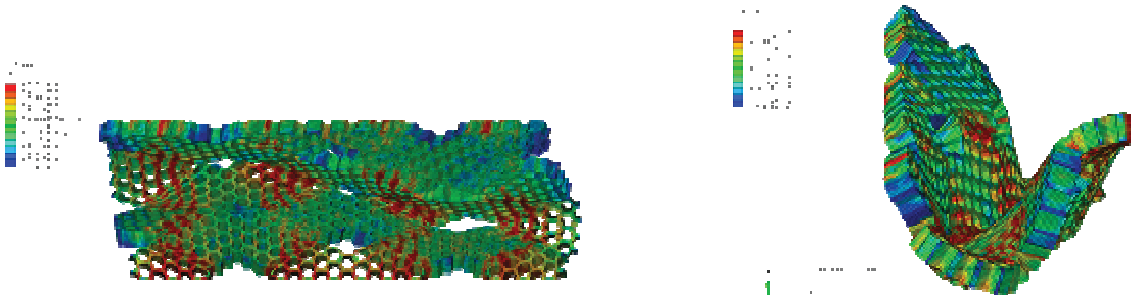

(a)Wall thickness = 10 mm

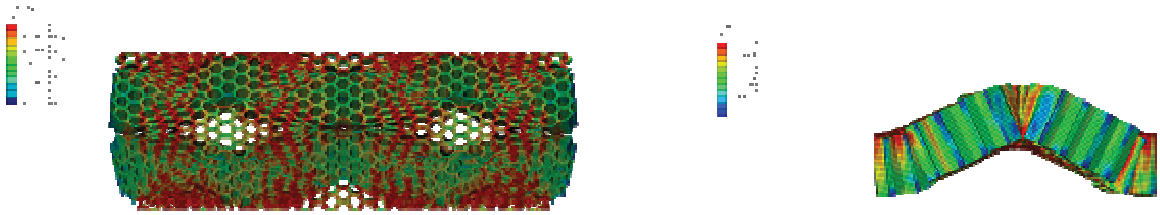

(b)Wall thickness=20mm

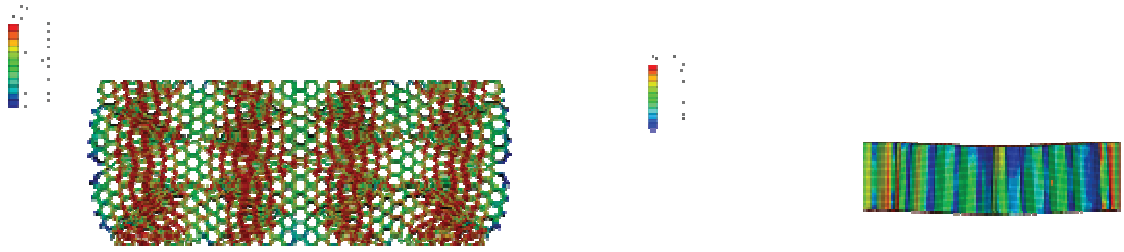

(c) Wall thickness=25mm

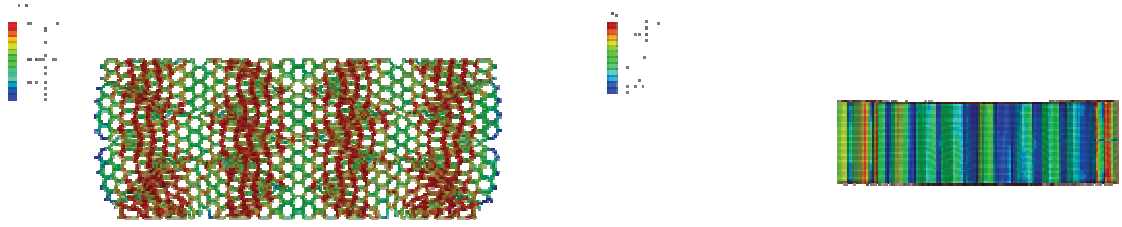

(d) Wall thickness=27.5mm

Creative Commons Attribution-NonCommercial-NoDerivatives 4.0 International License (CC BY-NC-ND)

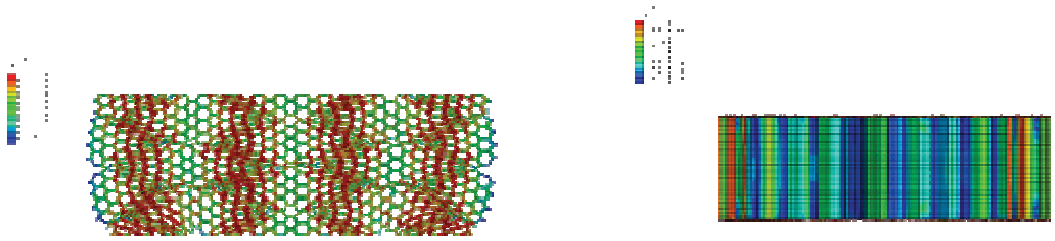

(e) Wall thickness=30 mm

Fig.4. Comparison of deformation mode and Von Misses stress obtained of hierarchical honeycomb structure with different wall thicknesses, after impact of 0.008s.

- *After an impact of 0.012s*

Creative Commons Attribution-NonCommercial-NoDerivatives 4.0 International License (CC BY-NC-ND)

Algerian Journal of Engineering Architecture and Urbanism Vol. 5 Nr. 3 2021
ISSN: 2588-1760

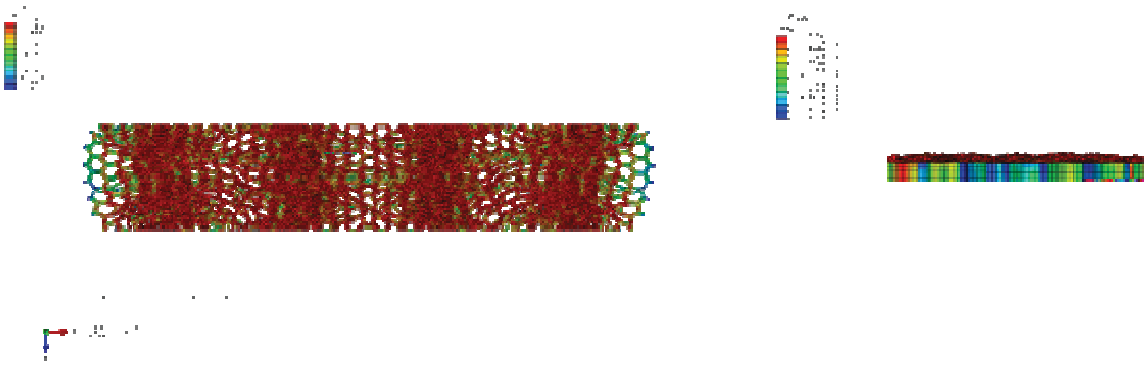

Creative Commons Attribution-NonCommercial-NoDerivatives 4.0 International License (CC BY-NC-ND)

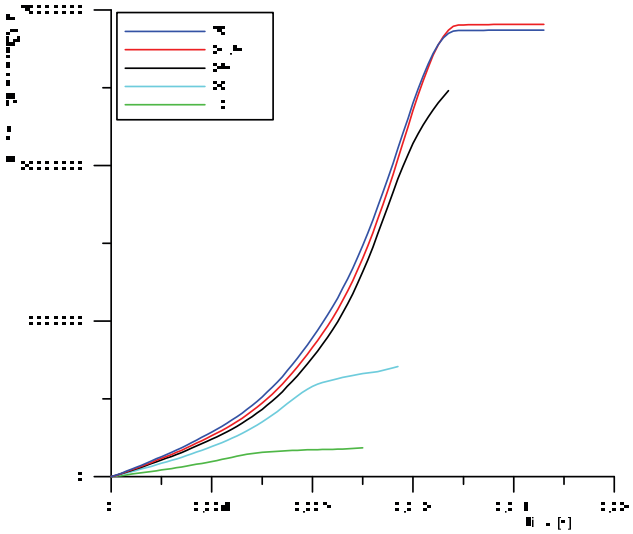

(c)

Fig.6. Comparison curves for different wall thicknesses during impact: (a) Force-crush distance; (b) kinetic and (c) Plastic dissipation energy.

From the numerical results of the crushing samples, it was shown that:

- The mechanical response of the hierarchical honeycomb in compression can be divided into three stages: elastic deformation, stress plateau and densification stage.
- At the end of analysis, the total kinetic energy of the model was completely dissipated in form of plastic deformation (see Figure 6.b thicknesses 27.5mm and 30mm).

Conclusion:

In order to improve the dynamic compression loading and energy absorption capacities of hexagonal honeycombs, one kind of hierarchical architectures topology is proposed by replacing the cell walls of regular honeycombs with hexagonal lattices. The dynamic compression loading is simulated by Abaqus software. The numerical results showed that:

- Adding hierarchy into hexagonal honeycombs caused a variation of local stress evolution during the dynamic crushing.
- The wall thickness has more effect on energy absorption comparing to the core geometrical parameters.
- The thin wall thickness cause a bending collapse mode during the crushing process and led to a lower energy absorption capability. This deformation instability is disappeared by increasing the thickness. Starting from 27mm face thickness value, the axial collapse mode is observed and ensure the maximum energy absorption.

The presented numerical simulations provided some useful guide, and give more explanation on the dynamic response and energy absorption capacity of hierarchical cellular structures.

References:

Chen Y. , Li T. , Jia Z. , Scarpa F. , Yao C.W. , Wang L. (2018), *3D printed hierarchical honeycombs with shape integrity under large compressive deformations.* Materials and Design.

Du Bois P. , Chou C.C. , Fileta B.B. , Khalil T.B., King A.I. , Mahmood H.F. , Metz H.I. , Wismans J. (2004), *Vehicle crashworthiness and occupant protection.* American Iron and Steel Institute.

Creative Commons Attribution-NonCommercial-NoDerivatives 4.0 International License (CC BY-NC-ND)

Huang Z. , Li Y. , Zhang X. , Chen W. , Fang D. (2021), *A comparative study on the energy absorption mechanism of aluminum/CFRP hybrid beams under quasi-static and dynamic bending*. Thin-walled structures vol.163, 107772

Lamb A. J. , Pickett A.K. , Chaudoye F. (2011), *Experimental characterization and numerical modelling of hexagonal honeycomb cellular solids under multi-axial loading*, Strain. 47

Mertani B. , Keskes B. , Tarfaoui M. (2019), *Numerical study on the compressive behavior of an aluminum honeycomb core* , Materiali in Tehnologije .

Song J. , Zhou W. , Wang, R.Fan, Y.Wang, J.Chena, Y.Lu, L.Li (2019), *Octet-truss cellular materials for improved mechanical properties and specific energy absorption* , Materials and Design.

Surjadi J.U. , Gao L. , Du H. , Li X. , Xiong X. , Fang N.X. ,et al. (2019),*Mechanical metamaterials and their engineering applications*, Adv. Eng. Mater. 1 .

Tarlochan F. , Samer F. , Hamouda A.M.S. , Ramesh S. , Khalid K. (2013), *Design of thin wall structures for energy absorption applications: Enhancement of crashworthiness due to axial and oblique impact forces.* Thin-Walled Structures;; 717–17.

Tao Y. , Duan S.Y. , Wen W.B. , Pei Y.M. , Fang D.N. (2017), *Enhanced out-of-plane crushing strength and energy absorption of in-plane graded honeycombs.* Compos B Eng;118:33–40.

Tao Y. , Li W. , Wei K. , Duan S. , Wen W., Chen L. , Pei Y. , Fang D. (2019), *Mechanical properties and energy absorption of 3D printed square hierarchical honeycombs under in-plane axial compression.* Composites Part B 176-107219.

Pashchanka M. (2020), *Multilevel self-organization on anodized aluminum: discovering hierarchical honeycombs from nanometer to sub-millimeter scale*. Physical Chemistry Chemical Physics .

Wang ZG. (2019),*Recent advances in novel metallic honeycomb structure.* Compos B Eng;166:731–41.

Zhang Q.C. , Yang X.H. , Li P. , Huang G.Y. , Feng S.S. , Shen C. , Han B. , Zhang X.H. , Jin F. , Xu F. , Lu T.J. (2015). *Bioinspired engineering of honeycomb structure–Using nature to inspire human innovation.* Prog Mater Sci ;74:332–400.

Zhao W. , Xie Z. , Li X. , Yue X. , Sun J. (2017), *Compression after impact behavior of titanium honeycomb sandwich structures*, Journal of Sandwich Structures & Materials.

Creative Commons Attribution-NonCommercial-NoDerivatives 4.0 International License (CC BY-NC-ND)

Algerian Journal of Engineering Architecture and Urbanism Vol. X Nr. Y 201Z
ISSN:
title (no more than two lines)
F1. Last1, F2. Last2

HYBRID FUZZY-VECTOR CONTROL OF A DOUBLY FED INDUCTION MACHINE

Abdelghafour HERIZI
Dr, Mohamed Boudiaf M'sila University, Faculty of Technology, Department of Electrical Engineering, email: abdelghafour.herizi@univ-msila.dz

Riyadh ROUABHI
Dr, Mohamed Boudiaf M'sila University, Faculty of Technology, Department of Electrical Engineering, email: riyadh.rouabhi@univ-msila.dz

Kaisse TOUMIAT & Abdelmonim ZANAT
Master student, Mohamed Boudiaf M'sila University, Faculty of Technology, Department of Electrical Engineering

Abstract:
In this article we present the vector control of the doubly fed induction machine (DFIM) fed by a PWM inverter. The oriented stator flux vector control is efficient because of the simplicity of design and implementation and allows a natural decoupling between flows and currents. The application of this strategy is achieved by using Proportional Integral (PI) Controllers. The parameters of these controllers are calculated directly from the parameters of the machine using conventional analytical methods, which require careful calculation and a good knowledge of all machine parameters. The aim of our study is to try to replace the controller (PI) for speed and flux by a fuzzy logic controller type 1. Robustness tests of the control vis-à-vis the parametric variations of the machine will be made.

Key words: DFIM; Vector Control; Stator Flux Oriented; PI Controller; Fuzzy Logic

Introduction:

Les machines asynchrones sont les plus utilisées dans les secteurs industriels en raison liée au faible coût, à la masse réduit, à la robustesse, à la construction simple et à un minimum d'entretien, bien que celles-ci imposent des structures internes et des stratégies de commande plus complexes [1-3].

De nos jours, plusieurs travaux ont été orientés vers l'étude de la machine asynchrone à double alimentation "MADA", qui est une machine asynchrone triphasée à rotor bobiné alimentée par deux sources de tension l'un au stator et l'autre au rotor [4]. Cette dernière et grâce au développement des équipements de l'électronique de puissance et l'apparition des techniques de commande modernes présentent une solution idéale pour les entraînements à hautes puissances et à vitesse variable. L'intérêt de telles machines est qu'elles assurent un fonctionnement à très basse vitesse. L'application potentielle de la MADA a été un sujet de recherche le long de la dernière décennie. L'association des machines asynchrones à double alimentation à des convertisseurs statiques permet de donner différentes stratégies de commande et présente un autre avantage d'utilisation de ces machines [5-7].

Creative Commons Attribution-NonCommercial-NoDerivatives 4.0 International License (CC BY-NC-ND)

Problématique

La commande de cette machine est une opération délicate à cause ce moteur caractérise par une dynamique multivariable, non linéaire, à paramètres variants dans le temps et avec un fort couplage entre le comportement magnétique (flux) et la partie mécanique (vitesse et couple). De plus, le problème des variables inaccessibles à la mesure directe, telle que : le flux rotorique où l'utilisation des capteurs physiques ne présente pas une solution parfaite. Il existe aussi le problème de la variation paramétrique, en particulier, les résistances rotorique et statorique (chose qui est due à l'effet thermique) [8-12]. À cet effet, pendant longtemps, des efforts importants ont été déployés pour développer des commandes performantes permettant de maîtriser le comportement dynamique de moteur asynchrone à double alimentation.

L'histoire de la commande des machines asynchrones a commencé en Allemagne au début des années soixante-dix avec la proposition de la théorie d'orientation du champ par Blaschke [13]. Cette théorie a permis de résoudre le problème du découplage, par conséquent, il est devenu possible de commander séparément le flux et la vitesse (couple) [14-18]. Toutefois, malgré l'amélioration apportée par cette commande, certains inconvénients ont limité son utilisation dans les applications de hautes performances. En effet, elle ne peut réaliser qu'un découplage asymptotique autour d'un flux constant [19]. En plus, l'établissement de cette commande utilise des régulateurs PI qui nécessitent une parfaite connaissance du modèle du système à régler et qui présentent une grande sensibilité aux variations paramétriques, notamment à la variation de la résistance rotorique qui a une relation directe avec l'angle d'orientation du flux.

De tels inconvénients ont poussé les chercheurs vers le développement des techniques de commande non linéaire, un important développement a été enregistré pendant les deux dernières décennies. En effet, l'apparition de nouvelles techniques, telles que : la logique floue, les réseaux de neurones, les algorithmes génétiques et d'autres, a permis de former une nouvelle discipline appelée intelligence artificielle. Les techniques d'intelligence artificielle ont permis, non seulement, d'améliorer la commande des systèmes et de surmonter les inconvénients des techniques classiques mais, également, de changer entièrement les concepts utilisés dans l'étude et la réalisation des systèmes de commandes. L'avantage essentiel des techniques suscitées, consiste dans le fait qu'elles s'orientent plus vers l'approximation des systèmes que vers la recherche de leurs modèles précis [6, 20, 21].

La logique floue est l'une des branches importantes de l'intelligence artificielle. Les bases théoriques de cette logique ont été établies en 1965 par le professeur Lotfi Zadeh à l'université de Berekley en Californie, qui introduit la notion de l'ensemble flou [22, 23]. Celle-ci permet d'obtenir une loi de réglage souvent très efficace sans devoir faire des modélisations approfondies. Par opposition à un régulateur standard ou à un régulateur à contre-réaction d'état, le régulateur par logique floue ne traite pas une relation mathématique bien définie, mais utilise des inférences avec plusieurs règles, se basant sur des variables linguistiques. Ainsi, il est possible de tenir compte des expériences acquises par les opérateurs d'un processus technique. La logique floue d'être l'un des moyens les plus utilisés pour l'amélioration de la robustesse de la commande vis-à-vis de la variation paramétrique et non paramétrique [24-27].

Creative Commons Attribution-NonCommercial-NoDerivatives 4.0 International License (CC BY-NC-ND)

À la lumière de ce qui a été dit, nous proposons dans ce travail une association combinant la logique floue avec la commande la commande vectorielle à flux statorique orienté de la MADA. Cette association sera exploitée pour établir une nouvelle commande robuste, à base de la logique floue, en vue d'améliorer les réponses dynamiques du moteur.

Modélisation de la MADA:

La machine utilisée est supposée à distribution sinusoïdale, symétrique et non saturée. Elle est alimentée en tension à travers un onduleur MLI. Dans un repère lié au champ tournant (d, q), on peut écrire les équations électriques de la MADA sous la forme [7, 20, 21]:

$$\begin{cases} V_{sd} = R_s I_{sd} + \frac{d\varphi_{sd}}{dt} - \omega_s \varphi_{sq} \\ V_{sq} = R_s I_{sq} + \frac{d\varphi_{sq}}{dt} + \omega_s \varphi_{sd} \\ V_{rd} = R_r I_{rd} + \frac{d\varphi_{rd}}{dt} - (\omega_s - \omega_r)\varphi_{rq} \\ V_{rq} = R_r I_{rq} + \frac{d\varphi_{rq}}{dt} + (\omega_s - \omega_r)\varphi_{rd} \end{cases} . \quad (1)$$

Les équations magnétiques de la MADA peuvent s'écrire:

$$\begin{cases} \varphi_{sd} = L_s I_{sd} + M.I_{rd} \\ \varphi_{sq} = L_s I_{sq} + M.I_{rq} \\ \varphi_{rd} = L_r I_{rd} + M.I_{sd} \\ \varphi_{rq} = L_r I_{rq} + M.I_{sq} \end{cases} \quad (2)$$

Avec:

$\omega_r = \omega_s - P.\Omega$;

$L_s = l_s - M_s$, $L_r = l_r - M_r$: inductances cycliques d'une phase statorique et rotorique ;

$[l_s]$, $[l_r]$: inductances propres d'une phase statorique et rotorique ;

M_s, M_r: inductances mutuelles entre deux phases respectivement statorique et rotorique ;

M: maximum d'inductance mutuelle entre une phase statorique et rotorique (les axes des deux phases coïncident).

L'expression du couple électromagnétique de la MADA en fonction des flux et courants statoriques s'écrit comme suit:

$$C_{em} = P\frac{M}{L_s}\left(\varphi_{sq} I_{rd} - \varphi_{sd} I_{rq}\right) \quad (3)$$

Avec P: nombre de paires de pôles de la MADA.

Le modèle de la machine asynchrone à double alimentation peut être écrit sous la forme matricielle comme suit [7, 28]:

$$\dot{X} = AX + BU \quad (4)$$

Avec :

$X = [\varphi_{sd} \quad \varphi_{sq} \quad I_{rd} \quad I_{rq}]^T$ et $U = [V_{sd} \quad V_{sq} \quad V_{rd} \quad V_{rq}]^T$

$$[A] = \begin{bmatrix} -\frac{1}{T_s} & \omega_s & \frac{M}{T_s} & 0 \\ -\omega_s & -\frac{1}{T_s} & 0 & \frac{M}{T_s} \\ \alpha & -\beta\omega & -\delta & (\omega_s - \omega) \\ \beta\omega & \alpha & -(\omega_s - \omega) & -\delta \end{bmatrix}; [B] = \begin{bmatrix} 1 & 0 & 0 & 0 \\ 0 & 1 & 0 & 0 \\ -\frac{M}{\sigma L_s L_r} & 0 & \frac{1}{\sigma L_r} & 0 \\ 0 & -\frac{M}{\sigma L_s L_r} & 0 & \frac{1}{\sigma L_r} \end{bmatrix}$$

Creative Commons Attribution-NonCommercial-NoDerivatives 4.0 International License (CC BY-NC-ND)

Où :

$\alpha = \frac{M}{\sigma L_r L_s T_s}$; $\beta = \frac{M}{\sigma L_r L_s}$; $\delta = \frac{1}{\sigma}\left(\frac{1}{T_r} + \frac{M^2}{L_s T_s L_r}\right)$; $\sigma = 1 - \frac{M^2}{L_r L_s}$; $T_r = \frac{L_r}{R_r}$; $T_s = \frac{L_s}{R_s}$

L'équation mécanique est de la forme suivant :

$$J\frac{d\Omega}{dt} = C_{em} - C_r - f\Omega \quad (5)$$

Avec:

C_{em} et C_r : le couple électromagnétique et le couple résistant (la charge mécanique) ;

f et J : coifficient de frottement et moment d'enertie de l'arbre de rotor.

Commande vectorielle de la MADA:

Dans notre étude, la fréquence et la tension sont constantes. On peut constater, d'après la relation (3), le fort couplage entre les flux et les courants. En effet, le couple électromagnétique est le produit croisé entre les flux et les courants statoriques, ce qui rend la commande de la MADA particulièrement difficile. Afin de simplifier la commande, nous approximons son modèle à celui de la machine à courant continu qui a l'avantage d'avoir un découplage naturel entre les flux et les courants.

Pour cela, nous appliquons la commande par orientation du flux qui consiste à aligner le flux statorique φ_s suivant l'axe d du référentiel tournant, (Figure 1), [28]. On a donc: $\varphi_{sd} = \varphi_s$ et par suite $\varphi_{sq} = 0$.

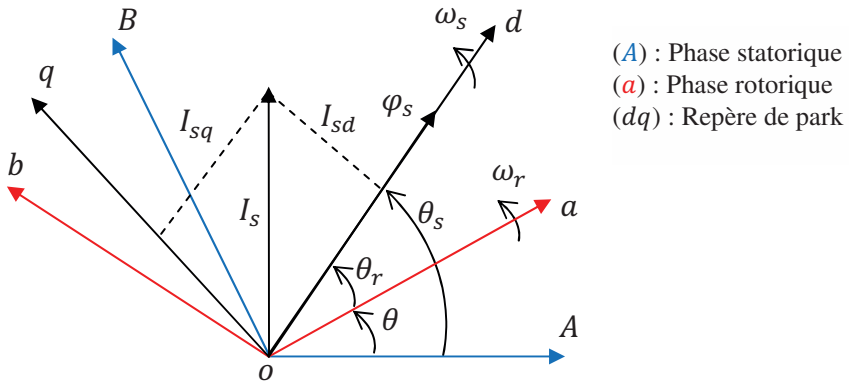

Fig 1. Principe de l'orientation du flux statorique.

Le couple électromagnétique de l'équation (3) s'écrit alors:

$$C_{em} = -P\frac{M}{L_s}\varphi_{sd} I_{rq} \quad (6)$$

et l'équation (2) des flux devient:

$$\begin{cases}\varphi_{sd} = \varphi_s = L_s I_{sd} + M.I_{rd} \\ \varphi_{sq} = 0 = L_s I_{sq} + M.I_{rq}\end{cases} \Leftrightarrow \begin{cases} I_{sd} = \frac{1}{L_s}(\varphi_s - M I_{rd}) \\ I_{sq} = -\frac{1}{L_s} M I_{rq}\end{cases} \quad (7)$$

Si l'on prendre le courant statorique dans l'axe d nul, $I_{sd} = 0$, hypothèse réaliste pour les machines de forte puissance, le courant et la tension dans cet axe sont alors en phase $V_s = V_{sq}$ et $I_s = I_{sq}$.

Dans ce cas, nous obtenons:

Creative Commons Attribution-NonCommercial-NoDerivatives 4.0 International License (CC BY-NC-ND)

$$\begin{cases} I_{rd} = \frac{\varphi_s}{M} \\ I_{rq} = -\frac{L_s}{PM\varphi_s} C_{em} \end{cases} \quad (8)$$

Avec l'hypothèse du flux statorique constant, on obtient les équations électriques sous la forme:

$$\begin{cases} V_{sd} = R_s I_{sd} \\ V_{sq} = R_s I_{sq} + \omega_s \varphi_{sd} \\ V_{rd} = R_r I_{rd} - (\omega_s - \omega_r)\varphi_{rq} \\ V_{rq} = R_r I_{rq} + (\omega_s - \omega_r)\varphi_{rd} \end{cases} \quad (9)$$

Dans le principe de l'orientation du champ statorique $(\varphi_{sq} = 0)$, le modèle de la machine MADA s'écrive:

$$\begin{cases} \frac{d\varphi_{sd}}{dt} = \frac{M}{T_s} I_{rd} - \frac{1}{T_s}\varphi_{sd} + V_{sd} \\ \frac{d\varphi_{sq}}{dt} = \frac{M}{T_s} I_{rq} - \omega_s \varphi_{sd} + V_{sq} \\ \frac{dI_{rd}}{dt} = -\delta I_{rd} + (\omega_s - \omega) I_{rq} + \alpha \varphi_{sd} - \frac{M}{\sigma L_s L_r} V_{sd} + \frac{1}{\sigma L_r} V_{rd} \\ \frac{dI_{rq}}{dt} = -(\omega_s - \omega) I_{rd} - \delta I_{rq} + \beta \omega \varphi_{sd} - \frac{M}{\sigma L_s L_r} V_{sq} + \frac{1}{\sigma L_r} V_{rq} \end{cases} \quad (10)$$

L'équation mécanique s'écrit:

$$\frac{d\Omega}{dt} = -\frac{1}{J}\left(P\frac{M}{L_s}\varphi_{sd} I_{rq} + f\Omega + C_r\right) \quad (11)$$

D'après l'équation (10), on trouve les tensions de la commande comme suit:

$$V_{rd} = R_r I_{rd} + \sigma L_r \frac{dI_{rd}}{dt} + \frac{M}{L_s} V_{sd} - (\omega_s - \omega)\sigma L_r I_{rq} \quad (12)$$

$$V_{rq} = \left(R_r + \frac{M^2}{L_s T_S}\right) I_{rq} + \sigma L_r \frac{dI_{rq}}{dt} + \frac{M}{L_s} V_{sq} - \frac{M}{L_s}\omega \varphi_{sd} + (\omega_s - \omega)\sigma L_r I_{rd} \quad (13)$$

Commande par la logique floue:

Un système flou peut être vu comme un système expert fonctionnant à partir d'une représentation de connaissance basée sur la théorie des ensembles. Un système flou est composé d'une base de données qui comptent l'ensemble des renseignements que nous possédons sur le processus ce qui nous permet de définir les fonctions d'appartenance et les règles floues de ce système flou, d'une base de règles floues qui est une collection de règle IF-THEN, d'une interface numérique-symbolique ou fuzzification de type singleton et d'une interface symbolique-numérique ou défuzzification par la méthode des centres pondérés qui revient à faire une somme pondérées des centres des ensembles flous inférés multipliés par les degrés d'appartenances correspondant [21-23].

$$y = \sum_{j=1}^{M} w_j b_j / \sum_{j=1}^{M} w_j \quad (14)$$

Avec:

w_j est le degré d'activation de la j^{th} règle flou.

$b_{j,i}$ $i = 1,2, \ldots n$ sont les coefficients de la j^{th} conséquence linéaire.

y^i la sortie numérique de la j^{th} règle flou où $j \in [1, M]$.

M: le nombre total des règles d'inférence.

Creative Commons Attribution-NonCommercial-NoDerivatives 4.0 International License (CC BY-NC-ND)

1. Principe d'une commande floue:

La structure d'une commande floue, présentée dans la figure 2, peut être décomposée en trois grands modules.

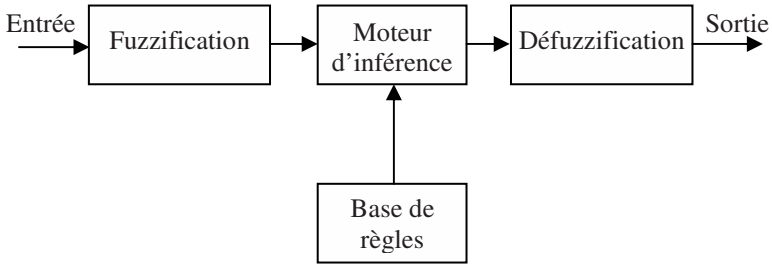

Fig 2. Structure générale d'une commande floue

Le premier de ces modules traite les entrées du système: c'est la fuzzification. Il permet d'associer à chacune des entrées réelles, par le biais de fonctions d'appartenances, un degré d'appartenance pour chacun des sous-ensembles flous définis sur l'ensemble du discours.

Le deuxième module est constitué du moteur d'inférence et de la base de règles. Celle-ci est constituée de règles de type: "Si..., Alors..." et va permettre de passer des degrés d'appartenance des grandeurs d'entrées aux degrés d'appartenance aux sous-ensembles flous de la grandeur de commande. Le moteur d'inférence, lui, va permettre de générer une conclusion à partir des entrées et des règles actives. Il calcule alors les degrés d'appartenance aux sous-ensembles flous correspondant à la commande du système.

Enfin, le dernier module, l'interface de défuzzification, va permettre de transformer les degrés d'appartenance des sous-ensembles flous de commande en grandeur numérique. C'est la transformation inverse du module de fuzzification.

À partir de cette structure, différents types de correcteurs flous vont alors pouvoir être définis. La section suivante présente plus particulièrement la structure que nous avons utilisée pendant nos travaux.

2. Régulateur PI-flou:

Généralement, la conception d'un régulateur flou pour la commande des entrainements électrique exige les choix des paramètres suivants: les variables linguistiques, les fonctions d'appartenance, la méthode d'inférence et la stratégie de défuzzification.

Pour les systèmes mono-variables simples, les entrées du contrôleur flou sont généralement l'erreur et sa variation. La majorité des contrôleurs développés utilisent le schéma simple proposé par Mamdani, comme le montre dans la figure suivante [21, 28]:

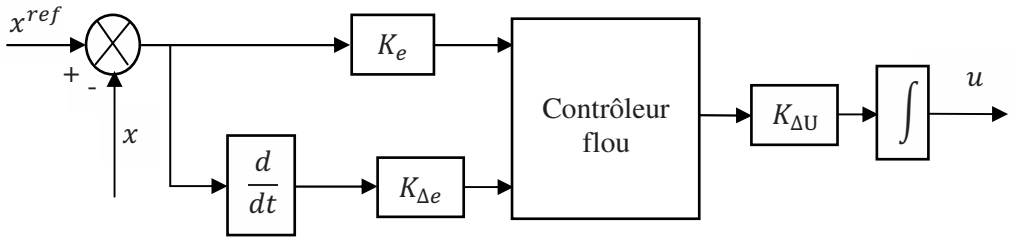

Fig 3. Schéma synoptique d'un régulateur PI-flou.

Creative Commons Attribution-NonCommercial-NoDerivatives 4.0 International License (CC BY-NC-ND)

La sortie du régulateur correspond à la variation de la commande. K_e, $K_{\Delta e}$ et $K_{\Delta u}$ sont des gains de normalisation qui peuvent être constants (ou même variables). Le système de régulation floue se compose essentiellement:

- Bloc de calcul de la variation de l'erreur au cours du temps.
- Facteurs d'échelle K_e, $K_{\Delta e}$ et $K_{\Delta u}$: qui sont des gains de normalisation et dénormalisation. Le choix adéquat de ces derniers permet de garantir la stabilité et l'amélioration des performances dynamiques et statiques ciblées du système à régler.
- Bloc de fuzzification de l'erreur et de sa variation. Pour le choix de la forme des fonctions d'appartenances, nous avons opté pour les formes triangulaire et trapézoïdale comme indiquée dans la figure suivante.

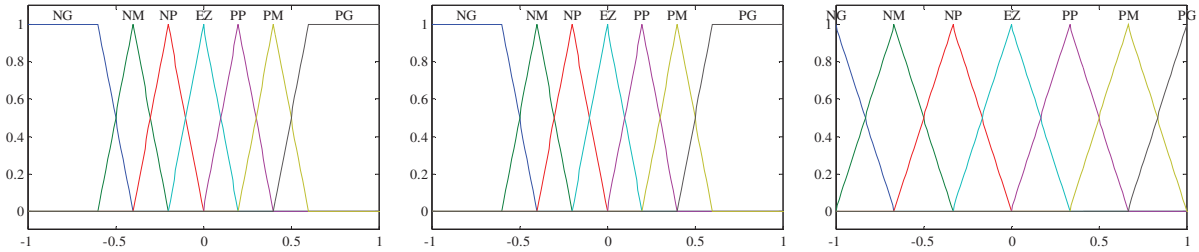

Erreur e Dérivée d'erreur Δe La commande

Fig 4. Fonctions d'appartenances utilisées.

- Le choix des variables linguistiques sont représentées par: Négatif grand noté NG, Moyen Négatif noté NM, Négatif petit noté NP, Environ de zéro noté EZ, Positif petit noté PP, Positif Moyen noté PM, Positif grand noté PG.
- Les règles d'inférences permettant de déterminer la variable de sortie pour le réglage des courants regroupés dans le tableau ci-dessous. La méthode d'inférence utilisée est la méthode « min-max » de Mamdani.

La commande		Erreur						
		NG	NM	NP	EZ	PP	PM	PG
Dérivé de l'erreur	NG	NG	NG	NG	NG	EZ	EZ	EZ
	NM	NG	NG	NM	NM	EZ	EZ	EZ
	NP	NG	NG	NP	NP	PP	PP	PM
	EZ	NG	NM	NP	EZ	PP	PM	PG
	PP	NM	NP	NP	PP	PP	PG	PG
	PM	EZ	EZ	EZ	PM	PM	PG	PG
	PG	EZ	EZ	EZ	PG	PG	PG	PG

Table 1. Les règles d'inférences.

- Bloc de défuzzifîcation de la variation de la commande. Les sorties du mécanisme d'inférence qui sont des variables floues doivent être reconverties en des grandeurs réelles de sorties pour que le système puisse les utiliser. Dans cette étape, une valeur réelle de la variable de sortie est obtenue en employant la méthode du centre de gravité.

La commande par la logique floue de la MADA est représentée dans la figure 5. Il contient deux régulateurs de type PI-floue pour la vitesse et le flux et deux régulateurs classiques.

Creative Commons Attribution-NonCommercial-NoDerivatives 4.0 International License (CC BY-NC-ND)

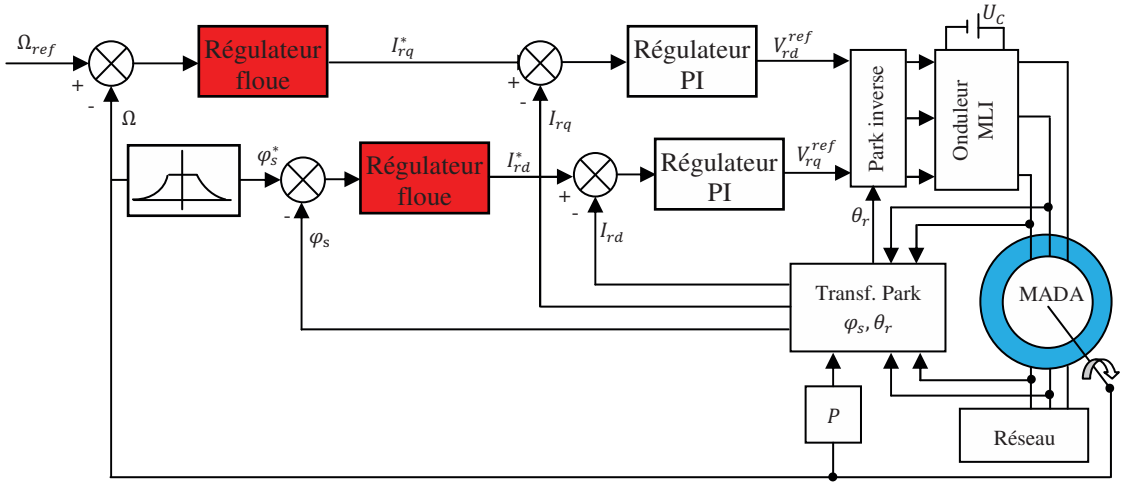

Fig 5. Principe de la commande par la logique floue de la MADA.

Résultats et discussions:

L'objectif de cette étape est de contrôler la MADA par la commande de la logique floue. Différents tests seront appliqués pour montrer les performances de cette commande.

1. Fonctionnement de la machine lors de la variation de charge:

Dans ces conditions, la machine tourne à sa vitesse nominale sous une charge ($C_r = 15N.m$) entre les instants t = 1.5s et t = 2.5s. Les résultats de simulation correspondante sont regroupés dans la figure 6. Nous constatons que le couple électromagnétique suit parfaitement sa consigne. On peut noter également que la variation de charge influée légèrement sur les grandeurs de vitesse, de flux et des courants de commande, ainsi le découplage entre flux et couple est toujours réalisé.

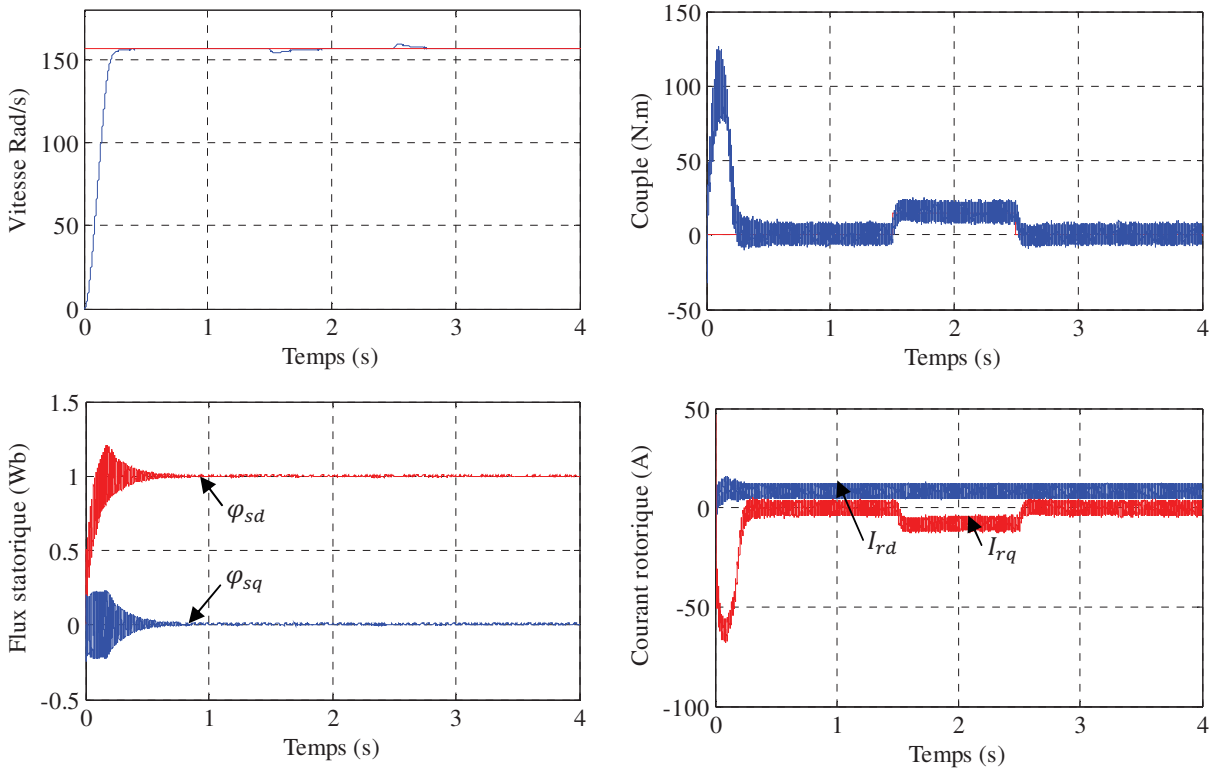

Fig 6. Résultats de simulation lors de la variation de la charge.

Creative Commons Attribution-NonCommercial-NoDerivatives 4.0 International License (CC BY-NC-ND)

2. Fonctionnement de la machine lors de la variation de la vitesse:

La machine est initialement tourne à la vitesse nominale de 157 rad/s. À l'instant t = 1.5s on inverse le sens de rotation de la machine de (-157rad/s) et à l'instant t = 3s, la machine tourne à une faible vitesse de 50 rad/s. On applique aussi une charge de valeur $(C_r = 15N.m)$ entre les instants t = 1.5s et t = 2.5s.

On peut signaler la bonne poursuite de la vitesse vers sa nouvelle référence présentant une erreur presque nulle avec un pic lors du passage d'un état à un autre. De même le flux statorique présentant un découplage parfait avec le couple $(\varphi_{sq} = 0Wb)$. Le flux subi une faible variation lors du changement de la vitesse au moment de la variation.

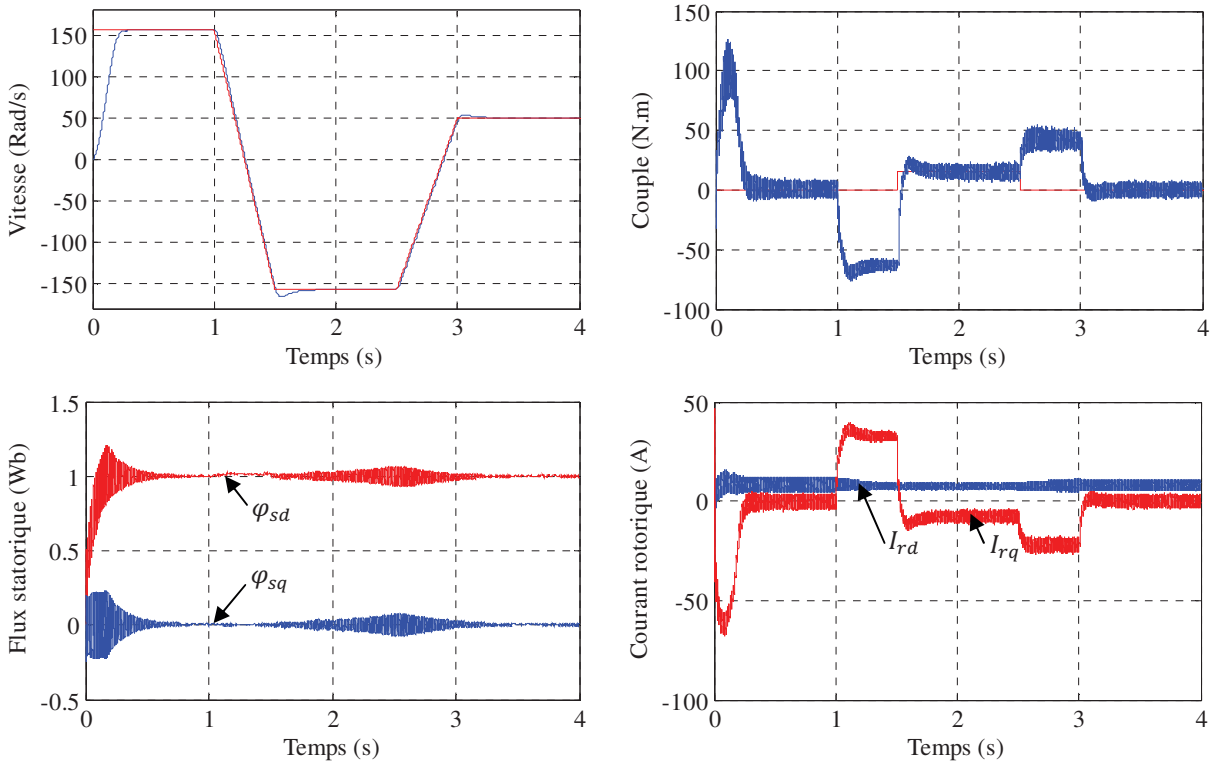

Fig 7. Résultats de simulation lors de la variation de la vitesse.

3. Fonctionnement de la machine lors de la variation de la résistance rotorique:

La variation de la résistance rotorique de +100% de sa valeur nominale sera appliquée entre les instants t = 1.5s et t = 2.5s avec une charge de valeur $(C_r = 15N.m)$ entre les mêmes instants.

D'après les résultats obtenus, on peut constater que la variation du R_r n'influer pas sur toutes les réponses dynamiques. Le flux présente une légère variation de son module alors que le découplage est toujours maintenu. Les courants en phase présentent une forme sinusoïdale qui augmente avec l'augmentation de la résistance et la charge.

Creative Commons Attribution-NonCommercial-NoDerivatives 4.0 International License (CC BY-NC-ND)

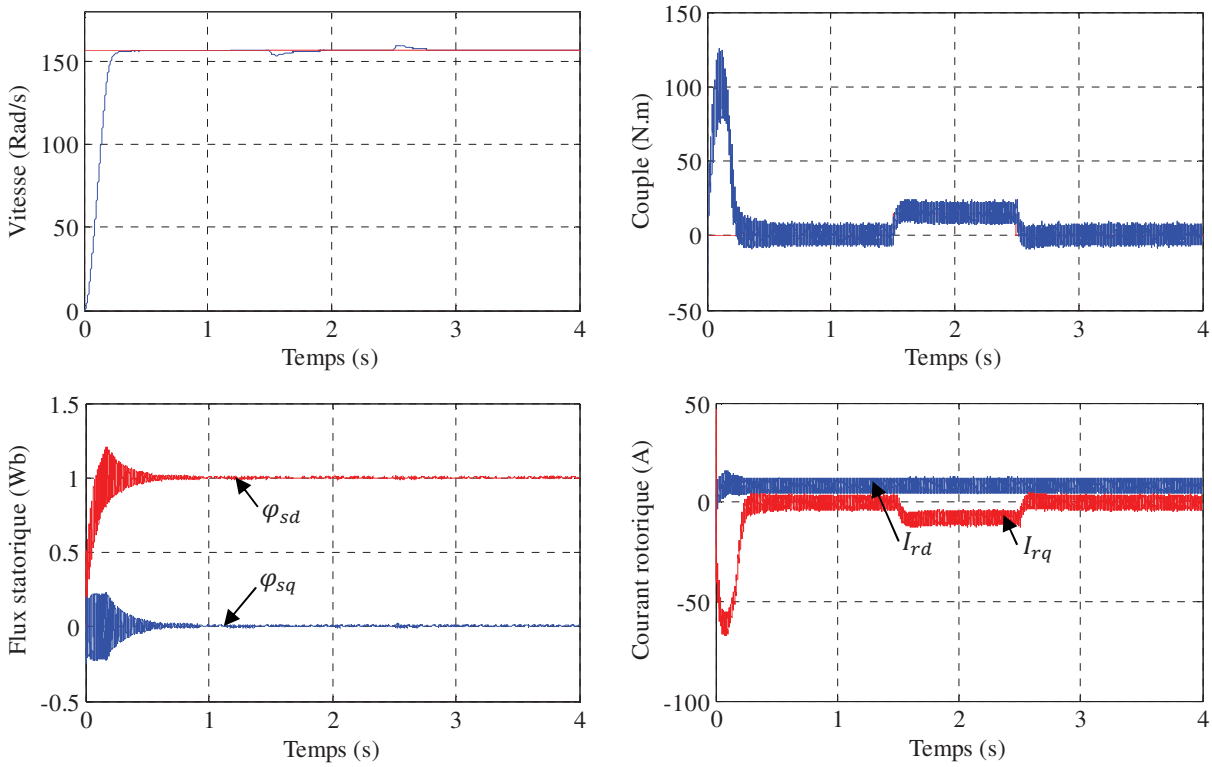

Fig 8. Résultats de simulation lors de la variation de la résistance rotorique.

Conclusion:

Les résultats obtenus montrent que le contrôleur flou utilisé donne meilleurs résultats par rapport à la commande vectorielle, non seulement en poursuite mais aussi en régulation, avec un très bon suivi de la vitesse de référence, une erreur statique presque nulle. Ceci se traduit par une erreur de poursuite bien inférieure à celle obtenue à l'aide de le régulateur PI, ceci montrant la parfaite du réglage floue à la commande. On remarque également que l'orientation du flux statorique est parfaitement assurée.

Donc, les résultats montrent un comportement satisfaisant de l'approche floue en régulation et en poursuite par rapport au contrôleur conventionnel du type PI a été mise en évidence par l'amélioration de la dynamique, un meilleur résultat contre la variation paramétrique.

References:

[01] *M. S. Vicatos & A. J. Tegopoulos, "A doubly-fed induction machine differential drive model for automobiles", IEEE Transactions on Energy Conversion, vol. 18, no. 2, pp. 225-230, 2003.*

[02] *L. Holdsworth, X. G. Wu, J. B. Ekanayake & N. Jenkins, "Comparison of fixed speed and doubly fed induction wind turbines during power system disturbances", IEE Proc. - Generation, Transmission and Distribution, vol. 150, no. 3, pp. 343-352, 2003.*

[03] *S. Drid, "Contribution à la modélisation et à la commande robuste d'une machine à induction double alimentée à flux orienté avec optimisation de la structure d'alimentation: théorie et expérimentation", Thèse de doctorat, Université Hadj Lakhdar, Batna, Algérie, 2005.*

[04] *P.E. Vidal, "Commande non-linéaire d'une machine asynchrone à double alimentation", Thèse de doctorat, Institut National Polytechnique, Toulouse, France, 2004.*

Creative Commons Attribution-NonCommercial-NoDerivatives 4.0 International License (CC BY-NC-ND)

[05] *F. Poitiers, "Etude et commande des génératrices asynchrone pour l'utilisation de l'énergie éolienne: machine asynchrone à cage autonome et machine asynchrone à double alimentation reliée au réseau", Thèse de doctorat, Ecole Polytechnique de l'Université de Nantes, France, 2003.*

[06] *A. Chaiba, "Commande de la machine asynchrone à double alimentation par des techniques de l'intelligence artificielle", Thèse de doctorat, Université Hadj Lakhdar, Batna, Algérie, 2010.*

[07] *R. Rouabhi, "Contrôle des puissances générées par un système éolien à vitesse variable basé sur une machine asynchrone double alimentée", Thèse de doctorat, Université Hadj Lakhdar, Batna, Algérie, 2016.*

[08] *W. Leonhard, "Control of electrical drives", 2nd edition, Springer-Verlag Berlin Heidelberg, New York, 1996.*

[09] *W. Leonhard, "Control of electrical drives", 3rd edition, Springer-Verlag Berlin Heidelberg, New York, 2001.*

[10] *M. Bodson & J. Chiasson, "Differential-geometric methods for control of electric motor", International Journal of Robust and Nonlinear Control, vol. 8, no. 11, pp. 923-954, 1998.*

[11] *M. Pinard, "La commande électronique des machines", Dunod, Paris, 2013.*

[12] *J. Pyrhonen, V. Hrabovcova & R. S. Semken, "Electrical machine drives control: an introduction", First edition, John Wiley & Sons Ltd, 2016.*

[13] *F. Blaschke, "The principle of field orientation as applied to the new transvector closed-loop system for rotating-field machines", Siemens Review, vol. 34, no. 3, pp. 217-220, 1972.*

[14] *S. K. El khil, "Commande vectorielle d'une machine asynchrone doublement alimentée (MADA)", Thèse de doctorat, Institut National Polytechnique, Toulouse, France, 2006.*

[15] *A. M. Trzynadlowski, "The field orientation principle in control of induction motors", Springer Science+Business Media, New York, 1994.*

[16] *N. P. Quang & J. A. Dittrich, "Vector control of three-phase AC machines: system development in the practice", Second edition, Springer-Verlag Berlin Heidelberg, New York, 2015.*

[17] *S. Chaouch, "Commande vectorielle robuste d'une machine a induction sans capteur de vitesse", Thèse de doctorat, Université Hadj Lakhdar, Batna, Algérie, 2005.*

[18] *A. Boukhelifa, "Les éléments d'optimisation du pilotage d'une machine asynchrone en vue d'un contrôle vectoriel", Thèse de doctorat, École Nationale Polytechnique, Alger, Algérie, 2007.*

[19] *R. Marino, S. Peresada & P. Valigi, "Adaptive input-output linearizing control of induction motors", IEEE Transactions on Automatic Control, vol. 38, no. 2, pp. 208-221, 1993.*

[20] *A. Zemmit, "Contribution à la commande de la machine asynchrone à double alimentation (MADA) par les techniques intelligentes", Thèse de doctorat, Université Mohamed Boudiaf, M'sila, Algérie, 2017.*

[21] *K. Loukal, "Commande robuste des machines asynchrones à double alimentation à base des systèmes flous type deux", Thèse de doctorat, Université Mohamed Boudiaf, M'sila, Algérie, 2017.*

[22] *C. Dualibe, M. Verleysen & P. G. A. Jespers, "Design of analog fuzzy logic controllers in CMOS technologies", Kluwer Academic Publishers, New York, 2003.*

[23] *R. Lowen & A. Verschoren, "Foundations of generic optimization, Volume 2: applications of fuzzy control, genetic algorithms and neural networks", Springer, 2008.*

[24] *K. Loukal & L. Benalia, "Type-2 fuzzy logic control of a doubly-fed induction machine (DFIM)", IAES International Journal of Artificial Intelligence (IJ-AI), vol. 4, no. 4, pp. 139-152, 2015.*

[25] *D. Ben Attous & Y. Bekakra, "Speed control of a doubly fed induction motor using fuzzy logic techniques", International Journal on Electrical Engineering and Informatics, vol 2, no. 3, pp 179-191, 2010.*

[26] *N. Bounar, A. Boulkroune & F. Boudjema, "Adaptive fuzzy control of doubly-fed induction machine", Journal of Control Engineering and Applied Informatics, vol. 16, no. 2, pp. 98-110, 2014.*

[27] *N. Bounar, A. Boulkroune, F. Boudjema, M. M'Saad & M. Farza, "Adaptive fuzzy vector control for a doubly-fed induction motor", Neurocomputing, vol. 151, no. 2, pp. 756-769, 2014.*

[28] *Herizi A., Bouguerra A., Zeghlache S., Rouabhi R., "Backstepping control of a doubly-fed induction machine based on fuzzy controller", European Journal of Electrical Engineering, vol. 20, no. (5-6), pp. 647-657, December 2018.*

Creative Commons Attribution-NonCommercial-NoDerivatives 4.0 International License (CC BY-NC-ND)

Algerian Journal of Engineering Architecture and Urbanism Vol. 5 Nr. 3 2021
ISSN: 2588-1760

NATURAL AND MIXED CONVECTION HEAT TRANSFER IN 'T' LID-DRIVEN CAVITY

Messaoud HAMDI
Laboratoire de physique théorique, Faculté de Technologie, Université de Bejaia, 06000 Bejaia, Algérie, messaoud.hamdi@univ-bejaia.com

Bachir MEZIANI
Laboratoire de physique théorique, Faculté des sciences exactes, Université de Bejaia, 06000 Bejaia, Algérie, bachir.meziani@univ-bejaia.dz

Aimad KOULALI
Laboratoire de physique théorique, Faculté de Technologie, Université de Bejaia, 06000 Bejaia, Algérie, koumaimad06@gmail.com

Djamel SADAOUI
Laboratoire de mécanique, matériaux et énergétique, Faculté de Technologie, Université de Bejaia, 06000 Bejaia, Algérie, sadaouidjamel@yahoo.fr

Abstract:
Numerical investigation of mixed and natural convection in a rectangular cavity with rectangular alveolus is analyzed using the finite volume method. The cavity is subject to vertical gradient temperature while its top sidewalls remain thermally insulated. The top wall is subject to a sinusoidal temperature and the bottom shaped wall is at a fixed warm temperature. Numerical simulations are discussed in terms of streamlines, isotherms, Nusselt number along the moving lid for several parameters. The results revel that the flow field is significantly affected by the Reynolds, Grashof and Prandtl numbers such as the aspect ratio (C). Further, increasing the Prandtl number improves the heat transfer rate which is much more important when buoyant forces are combined to shear forces due to lid motion. In mixed convection, it's noted that at constant Gr, the variation of *Re* causes significant changes in the mean Nusselt compared to the case where *Re*=100 and $10^3<Gr<10^5$. This is particularly verified for largest *Pr* (0.7 and 7.2), for low *Pr* (0.026) the change is imperceptible.

Key words: Natural convection - Mixed convection - 'T' lid-driven cavity - Finite volume method.

Introduction:

Convection heat transfer in enclosures has received considerable attention during the last three decades owing to its importance in many practical applications. A literature survey related to this topic revealed that considerable amounts of work have been done both experimentally and numerically and are substantially orientated toward the description of phenomena governing natural convection in cavities with flat walled geometries. In this field, benchmark solution of De Vahl Davis [1] has been widely considered as a reference by many authors. The interest has now shifted to

Creative Commons Attribution-NonCommercial-NoDerivatives 4.0 International License (CC BY-NC-ND)

complex enclosures therefore; irregular surfaces are suitable techniques to improve the thermal performance of heat transfer devices. References [2–6] give some ideas about fluid flow and thermal characteristics inside cavities with different boundary conditions. In the light of the above literature, it is pointed out that the enclosure area as well as the inclination has an importance on its performance. Several correlations of the average Nusselt number were proposed as a function of Rayleigh number and geometric ratios.

The fundamental problem of mixed convection in closed cavities has has attracted the interest of many scientists and industrialists over the past few decades in view of the numerous potential applications such as solar collectors, heat exchangers, local ventilation and electronic cooling devices, as well as in many other applications. The physical phenomena associated with fluid flow and heat transfer in lid-driven cavities is one of the most widely considered problems in thermofluids areas. The modeling and simulation for such a problem are performed for various combinations of temperature gradients and cavity configurations. I this context, Migeon et al.[7] analyzed experimentally the effects of lid-driven cavity shape on the flow establishment for square, rectangular and semi-circular cavities. While Cheng et al. [8–9] in a series of papers, studied experimentally and numerically the effects of buoyancy and convective heat transfer on the flow pattern inside an arc-shape cavity. For a similar geometry, the effects of arc angle ratio, on the formation of vortical structures, as well as on the existence of periodic solutions are discussed by Mercan et al. [10] up to Re=8000. Recently, M. Bhattacharya et al. [11] analyzed flow structures during mixed convection within a lid-driven trapezoidal enclosure subjected to a constant gradient temperature.

Numerous other studies were also carried out to understand the combined effects of the buoyancy and shear forces in cavities on the flow behavior. Khanafer et al. [12] performed a numerical study in cavities, investigating the effect of the sliding top plate, submitted to a sinusoidal horizontal oscillation. Luo et al. [13] considered multiple fluid flow and heat transfer mechanisms during mixed convection occurring in a square enclosure with oppositely moving horizontal walls. Later, Basak et al. [14] investigated the effect of various thermal boundary conditions on mixed convection heat transfer within a square cavity in presence of adiabatic moving top wall an uniform and non-uniform heating. Dos Santos et al. [15] used large eddy simulation of mixed convection in transient, two-dimensional laminar and turbulent flows in cavities for different Reynolds and Richardson numbers. While, Wahba [16], adopted a stream function–vorticity formulation to show that steady flow simulations are, in fact, computable up to Re = 35000. More recently, Roy [17] examined mixed convection in closed cavities induced by the motion of the horizontal or vertical walls for various fluids, Prandtl and Reynolds numbers. In summary, it is namely revealed that the core flow is highly influenced by the mechanical motion of the walls which in turn affect significantly the heat transfer.

Moreover, the effects of inclined cavities on the resulting convection processes are also reported in the literature. It is worth to outline that the enclosure inclination has importance on its performance due to the change in the total net acceleration of gravitational. In this regard, Sharif [18] investigated laminar mixed convection in inclined shallow rectangular cavities at different Richardson numbers. Oztop et al. [19] performed a numerical study to obtain combined convection field in inclined porous lid-driven enclosures with a non-uniformly heater. The mixed convection in an inclined square cavity was studied by Ogut [20] using the

Creative Commons Attribution-NonCommercial-NoDerivatives 4.0 International License (CC BY-NC-ND)

differential quadrature method. Cheng et al. [21] analyzed numerically the effects of inclination angle, Richardson number, and aspect ratio on the flow structures and heat transfer in a air-filled 2D cavity.
Further, wavy surfaces are suitable techniques to improve the thermal performance of heat transfer devices. Al-Amiri et al. [22], considered the effect of sinusoidal wavy bottom surface on mixed convection heat transfer in a lid-driven cavity. Nasrin [23] examined mixed convection in a horizontal lid driven enclosure with the wavy bottom wall for various cavity aspect ratios. While, the work of Muthtamilselvan [24] concerned the 2D steady state mixed convection in a lid-driven square cavity filled with Cu–water nanofluid in the presence of internal heat generation. The hydrodynamic and thermal transport of Cu-H_2O nanofluid in a differentially heated lid-driven square enclosure in the presence of a rotating circular cylinder is investigated numerically by Chatterjee et al. [25].
Furthermore, the combination effects of inclination angle and a wavy wall have also been investigated until recently. Thus, Alinia et al. [26] and Cho et al. [27] investigated mixed convection heat transfer in an inclined square cavity with curved side walls filled with the nanofluid involving horizontally moving side walls. Mekroussi [28], presented a numerical study on the mixed convection in an inclined lid-driven cavity with a sinusoidal wavy surface. The foregoing review revealed that the heat transfer rates and the flow field inside the enclosure depend strongly upon the tilt angle and the boundary conditions as well as the sliding walls. It was also observed that the effect of inclination angle is more pronounced at high Richardson numbers due to domination of natural convection. The average Nusselt number at the heated surface increases with an increase of the number of undulations as well as the angle of inclination. Other results indicate that the average Nusselt number increases mildly with increasing cavity inclination for dominating forced convection while it is much steeper in dominating natural convection.
It's worthy of note that there are other interesting works on this subject with various other applications. An overview of this topic can be found in the publications of Moraga [29], Prasad [30], Aminossadati [31], Allegrini [32], Al-Salem [33], Cheng [34], Muthtamilselvan [35] and Kefayati [36].

Under this circumstance, it is of great importance to investigate heat transfer and fluid flow in a shaped enclosure with a moving lid subjected to a sinusoidal temperature. Attention is also paid to examine the influence of several parameters such as *Re*, *Gr* (*Ri*), *Pr* and N.

Description and Formulation of the problem:

The physical problem considered in this study is the 2D flow heat fields in a concave shaped enclosure filled with different fluids (Fig. 1). It consists in a lid driven cavity with two vertical and thermally insulated sides and two horizontal active surfaces. The upper wall subjected to a cold sinusoidal temperature (T_c) moves from left to right with a constant velocity u_o while the shaped bottom wall is assumed to be isothermal at a warm temperature T_h. In these figures, H_1, L_1 and H_2, L_2 shows the height and the length of the enclosure and the micro-cavity (alveolus), respectively. For commodity, these parameters are defined in terms of geometric ratios such as: $a = H_1/L_2=0.25$; $b = L_1/L_2=1.5$ and $C= L_2/H_2$. Knowing that each value of C (4, 2, 1 and ¾), correspond to a configuration with a specific number of alveoli (N=1, 2, 3 and 4). The sinusoidal temperature is expressed as follow: $T =T_c+(T_h-T_c)\ \sin(\pi x/L_o)= T_c+(T_h-T_c)\ \sin(\pi X)$

Creative Commons Attribution-NonCommercial-NoDerivatives 4.0 International License (CC BY-NC-ND)

Algerian Journal of Engineering Architecture and Urbanism Vol. 5 Nr. 3 2021
ISSN: 2588-1760

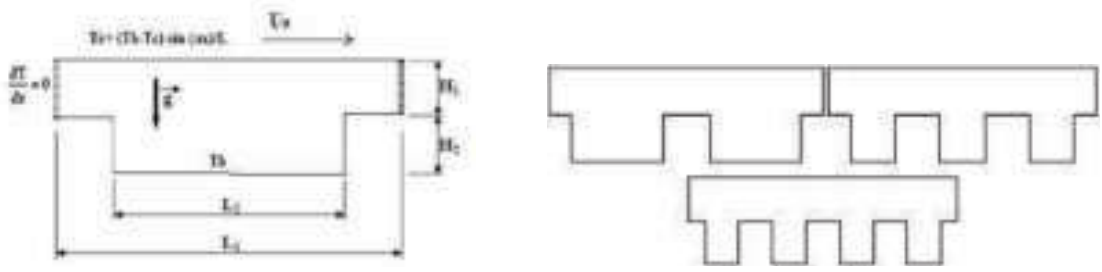

Fig1. Physical domain

The numerical model for heat transfer and fluid flow in the partitioned square enclosure was developed under some assumptions as steady state, laminar and incompressible Newtonian fluid. Viscous dissipation and compressibility effects are neglected. Also, the fluid properties are assumed constant except the density in the buoyancy term of the momentum equations, which can be approximated by the standard Boussinesq model. The mathematical formulation governing the two dimensional fluid flow and heat transfer can be written on dimensionless form in Cartesian coordinates (X, Y) as follow:

$$\left(\frac{\partial U}{\partial X}+\frac{\partial V}{\partial Y}\right)=0 \tag{1}$$

$$\left(U\frac{\partial U}{\partial X}+V\frac{\partial U}{\partial Y}\right)=-\frac{\partial p}{\partial X}+\frac{1}{Re}\left(\frac{\partial^2 U}{\partial X^2}+\frac{\partial^2 U}{\partial Y^2}\right) \tag{2}$$

$$\left(U\frac{\partial V}{\partial X}+V\frac{\partial V}{\partial Y}\right)=-\frac{\partial p}{\partial Y}+\frac{1}{Re}\left(\frac{\partial^2 V}{\partial X^2}+\frac{\partial^2 V}{\partial Y^2}\right)+\frac{Gr}{Re^2}\theta \tag{3}$$

$$\left(U\frac{\partial \theta}{\partial X}+V\frac{\partial \theta}{\partial Y}\right)=\frac{1}{Pr\,Re}\left(\frac{\partial^2 \theta}{\partial X^2}+\frac{\partial^2 \theta}{\partial Y^2}\right) \tag{4}$$

Assuming the non-slip flow, the relevant dimensionless boundary conditions can be written as follows:

$$\begin{array}{lll} \theta=\sin(\pi X) & U=1, & V=0 \quad \text{(moving lid : top wall)} \\ \partial\theta/\partial X=0 & U=V=0 & \text{(upper side walls)} \\ \theta=1, & U=V=0 & \text{(bottom wall)} \end{array} \tag{5}$$

The dimensionless quantities appearing in Eqs (1)-(4) are the Grashof, Prandtl and Reynolds numbers respectively, defined as : $Gr=g\beta(T_h-T_c)L_o^3/(\nu^2)$, $Re=u_o\ L_o/\nu$ and $Pr=\nu/\alpha$. Further, one can also define a dimensionless quantity so called Richardson number as follows $Ri=Gr/Re^2$. In the above equations, P, θ are the dimensionless pressure and temperature, while (X, Y) and (U, V) are the dimensionless Cartesians coordinates and corresponding velocity components, respectively.

Numerical approach:

The mass, momentum and energy balance equations (1)-(4) subjected to the specified boundary conditions Eqs. (5) are solved numerically using a developed solver based on a control-volume method under non-uniform grid system in x and y directions. The described solver uses a pressure correction based on iterative SIMPLER algorithm (for more details, see

Creative Commons Attribution-NonCommercial-NoDerivatives 4.0 International License (CC BY-NC-ND)

[37]). To check the convergence of the sequential iterative solution, the normalized residual is calculated for the mass, momentum and energy equations. The convergence is obtained when the residual becomes smaller than 10^{-7}.

Grid dependency and validation

A curvilinear grid was generated to solve the problem treated. Reliable results have been obtained with various grid combinations (60×60 to 160×160). As shown in Fig.2 small elements which are not visible on this figure, are used to resolve the laminar boundary layers near the walls where the most important gradients are located. The presence of at least 4 thin elements with relative sizes was necessary to ensure the convergence of the results. For each grid size, average Nusselt number is calculated and summarized in Table 1 for $Gr=10^4$ and $Re=100$. Throughout this investigation, *Nu* remains almost the same for grids finer than 100x100 witch satisfies the grid dependency. Hence, considering both the accuracy and the computational costs, most computations reported in the current work were performed with a multiple grid system of 120x120.

The computational procedure is validated against the basic model of Chen [6] corresponding to natural convection in concave partitioned enclosure ($a=1/4$; $b=3/2$ and $Gr=10^4 - 2x10^5$). The comparison is made with the averaged Nusselt number, as shown in Table 2.
Furthermore, extensive validations of the developed code for mixed convection in an air-filled square driven cavity have been also done. The mean Nusselt number numerically deduced are compared to those obtained by Ögüt [20] for various Richardson numbers. As listed in Table 2; the comparisons are in good agreements with the benchmark cases.

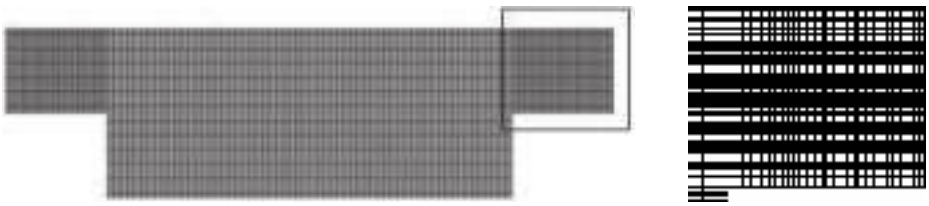

Fig2. Detail of the computational grid

Grid	60x60	80x80	100x100	120x120	140x140	160x160
Average *Nu*	2.288	2.299	2.303	2.308	2.310	2.311

Table 1. Grid independence study for $Gr=10^4$, $Re=100$

Natural convection				**Mixed convection**			
Gr	Ref. [6]	Current		***Ri***	Ref. [20]	Current	
10^4	11.132	11.034	(0.880)	0,1	3.850	3.890	(1.038)
$5x10^4$	13.914	13.811	(0.740)	1	2.602	2.631	(1.114)
10^5	15.582	15.438	(0.924)	10	2.139	2.163	(1.122)
$2x10^5$	17.704	17.978	(1.548)	100	1.884	1.906	(1.167)

Note. The values in ( ) are the absolute difference in %.

Table 2. Average Nusselt number: comparison with refs. [20] and [5]

Results and Discussion:

In this section, simulations have been carried out for fluids with different *Pr* (0.026; 0.7 and 7.2). Further, two cases have been considered, firstly for natural convection the

Creative Commons Attribution-NonCommercial-NoDerivatives 4.0 International License (CC BY-NC-ND)

Grashof number *Gr* varies from 10^4 to 10^7. Secondly for mixed convection, the Grashof and Reynolds numbers varies in the range (10^3 - 10^5) and (10 – 100), respectively. The Richardson number is used to differentiate between the natural, forced and mixed convection dominance (*Ri* = 0.1 to10).

Natural Convection:

Flow and thermal fields:

Effect of Gr and number of alveolus

Discussion of these numerical results can be emphasized by the study of the streamlines and velocity contours in the cavity. The Figs 3–4, illustrate the effect of Grashof number and aspect ratio ''C'' on the flow pattern and temperature contours in the enclosure. The force circulation of the flow within the cavity takes place by virtue of thermal buoyancy which is represented by the Grashof number *Gr*. The symmetric boundary conditions in the vertical direction produce a symmetric behaviour with respect to the vertical axis.

For small values of *Gr* ($\leq 10^5$), the fluid motion involves two symmetric major recirculating vortices of relatively weak velocity extending throughout the cavity with clockwise and counter clockwise rotations (C=1).

As the number of alveolus (N) increases, the minor cells with lower intensity are formed in each micro-cavity. Moreover, with the increase of the number of alveoli (N), the core of the main circulation stretches and shifts upward. Further, the secondary circulations grow in size and intensity in the case of high Grashof numbers ($Gr=10^6$ and 10^7) as shown in Figs 3 and 4.

Isothermal lines extending between the cold surface and the adiabatic surfaces are normal to the insulated walls in accordance with the literature without surface radiation. For relatively low Grashof numbers, the isotherms plots are smooth curves indicating that the conduction is the dominant heat transfer mechanism. The distributions of isotherms are almost invariant. However, the increase in the Grashof number ($\geq 10^6$) caused by the increased buoyancy forces alters the flow pattern so the isotherms are distorted indicating that, the convective heat transfer is the dominant mode. Consequently, the heat convection is weakened significantly when *Gr* is highest.

More interesting results are given by the study of the effect of the Prandtl number on the flow field for two Grashof numbers as shown in Fig.4. As can be seen, *Pr* affects the streamlines and the temperature distribution only at highest *Gr*. Indeed, the plots remain invariant at lowest *Gr* (10^4).

Analysis of the streamlines for $Gr=10^7$ exhibits the changes observed in the flow and temperature distribution. As observed, the presentation exhibits a multi cell structure. The minor cells grow and consequently, the convective major cells shift from the bottom to the top and stretch horizontally to occupy the entire upper part of the cavity located above the alveoli. An increase of the Prandtl number affects noticeably the flow behavior and distorts significantly the isotherm pattern. The convection currents are greater which indicates the dominance of convection mode heat transfer. Hence, results highlights that the rise of *Pr* promotes the convection process.

Creative Commons Attribution-NonCommercial-NoDerivatives 4.0 International License (CC BY-NC-ND)

Algerian Journal of Engineering Architecture and Urbanism Vol. 5 Nr. 3 2021
ISSN: 2588-1760

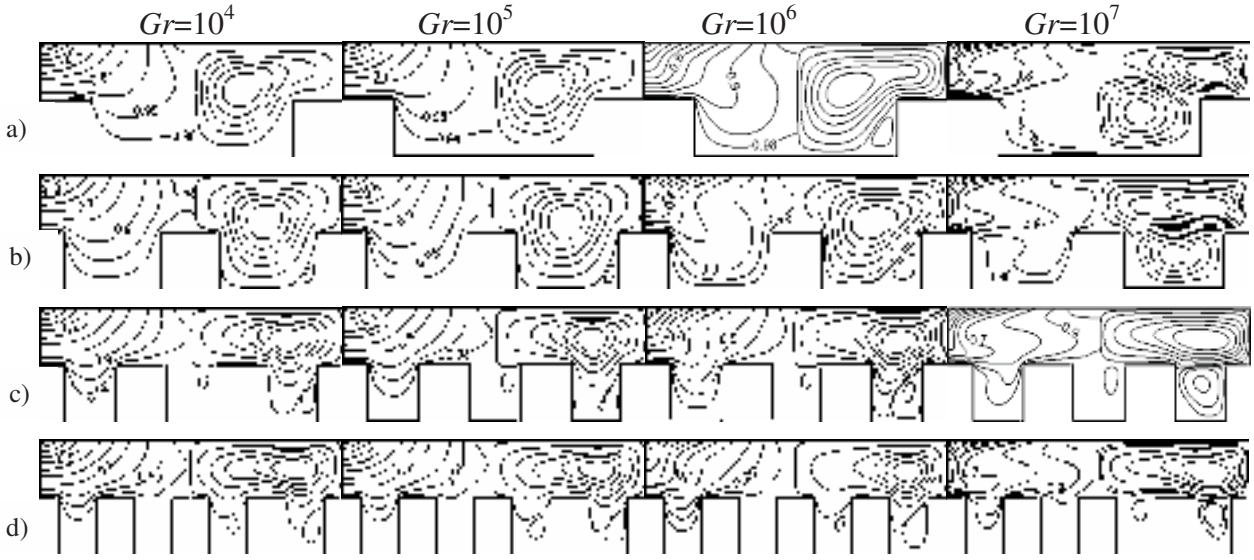

Fig3. Isotherms and streamlines for *Pr*=0,7
a) C=1 b) C=2 c) C=3 d) C=4

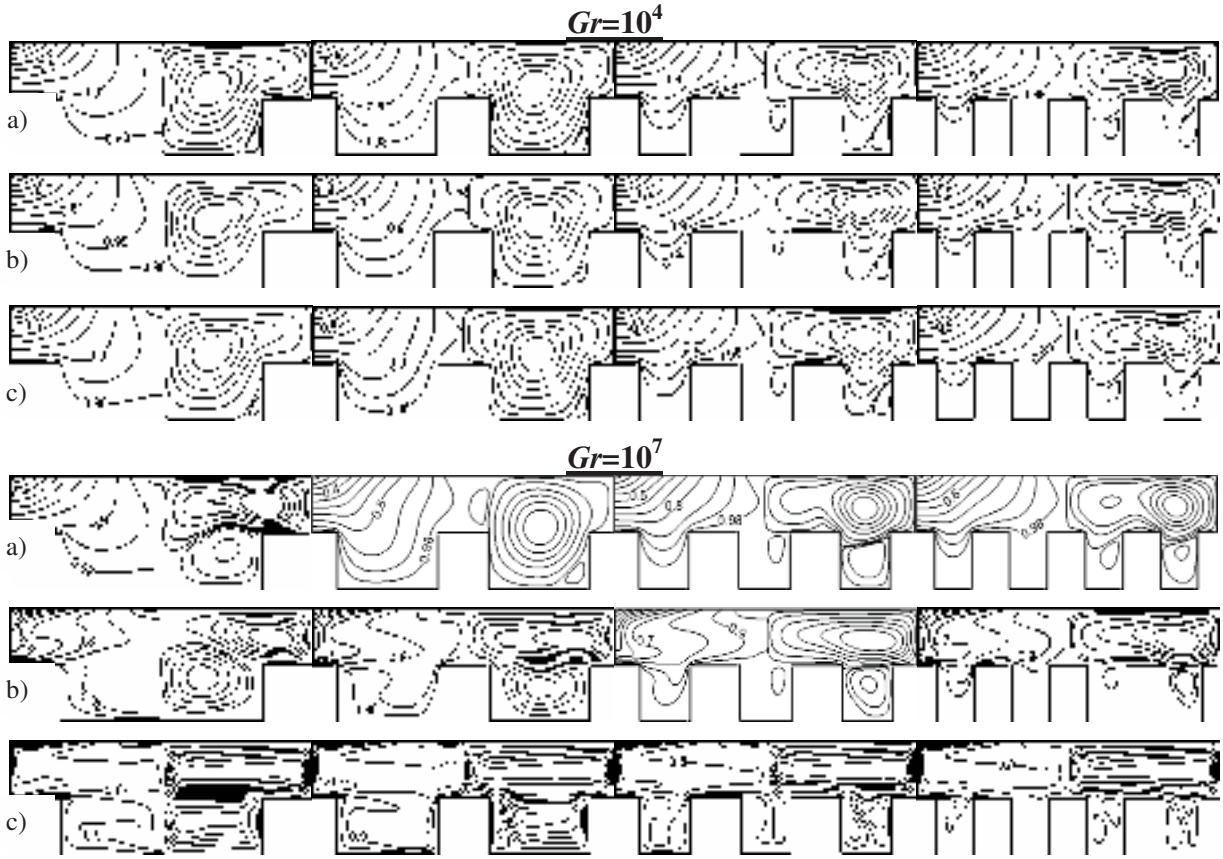

Fig4. Isotherms and streamlines for
a) *Pr*=0,026 b) *Pr*=0,7 c) *Pr*=7,2

Creative Commons Attribution-NonCommercial-NoDerivatives 4.0 International License (CC BY-NC-ND)

Algerian Journal of Engineering Architecture and Urbanism Vol. 5 Nr. 3 2021
ISSN: 2588-1760

Heat Transfer:

The analysis of the intensity of heat exchange within the cavity is made through a dimensionless average (*Nu*) Nusselt number through the hot bottom wall, deduced from the integration of the local quantity (*Nu*x):

$$\overline{Nu} = \int_0^L Nu_X \, dX \qquad Nu_X = -\frac{\partial \theta}{\partial Y}$$

The derivative in the local Nusselt number is calculated according to the difference formula by using the temperature obtained on the first ring of elements around the wall. An accurate calculus of the integral is obtained by linear interpolation according to the step size at each node of the required elements.

Fig. 5 depicts the effect of number of alveolus on the average Nusselt number along the lid wall at various Grashof and Prandtl numbers ($Gr = 10^3 - 10^7$; Pr=0.026 – 7.2).

When the heat transfer is only due to conduction, the Grashof number does not entail any significant change and the mean Nusselt number remains unchanged whether increasing Gr. Also, when the heat transfer is partly or mainly due to convection, the mean Nusselt is found to be affected significantly by the Grashof Number. Indeed, increasing *Gr* produces the higher buoyancy-induced flow within the enclosure, consequently the higher convective *Nu*.
Furthermore, as expected the heat transfer rate depends closely on the Prandtl number especially when the convection prevails in the entire cavity. In fact, the increase in *Pr* promotes significantly the convective Nusselt number. However, decreasing the Prandtl number damps the flow field and greatly weakens the convection, leading to reduce considerably the Nusselt values and lengthens the conduction mode. It's also noted that the heat transfer is not susceptible to changes of parameter C, i.e. the number of alveolus.

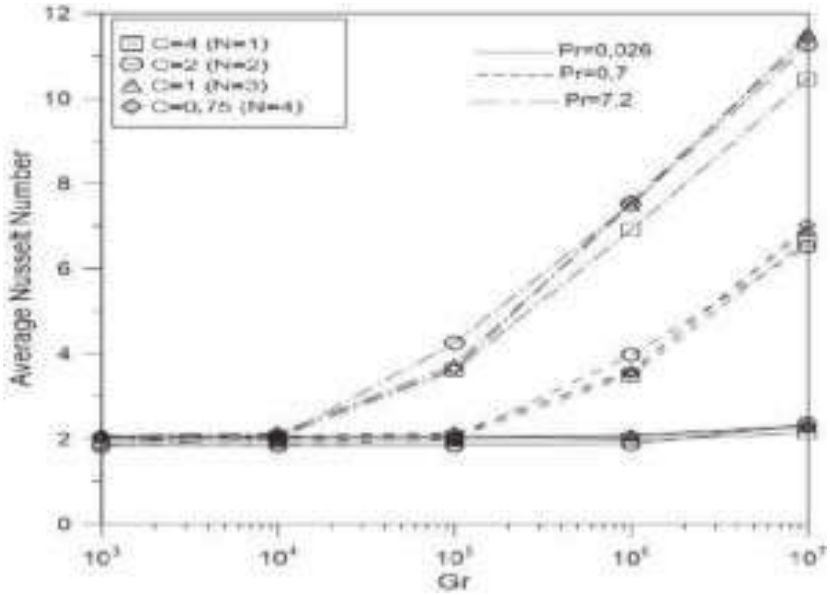

Fig5. Effect of *Pr* and *Gr* numbers on the average Nusselt number

Creative Commons Attribution-NonCommercial-NoDerivatives 4.0 International License (CC BY-NC-ND)

Mixed Convection:

Mixed convection, the Richardson number is used to distinguish between flow pattern where either the forced convection is dominant ($Ri<<1$) or the natural convection is dominant $Ri>>1$). For $Ri=1$, the two heat transfer modes occur simultaneously, both the buoyancy force and moving lid contribute to the resultant flow.

Streamlines and Isotherms:

Figs 6 and 7 display the effects of Richardson and Prandtl numbers on the flow structure and heat transfer occurring in the cavity through the streamlines and isotherms.

At low Grashof number; the considered Richardson leading to low Reynolds numbers (not larger than 100), a symmetrical behaviour is observed in the streamlines for all Prandtl values. The fluid flow is characterized by a single-cell structure extending over the whole cavity with one and two cores for N=1 and N=2, respectively. For largest N (>2), besides the primary vortex located in the upper part of the cavity, secondary cells appear in the alveoli (bottom part of the cavity). The corresponding isotherm plot indicates that their development is substantially independent of lid's motion. This remark is even more verified that Prandtl values are small (Pr=0.026 and 0.7).

In contrast, at high Gr ($Gr=10^6$), the flow structure is not symmetric due to the high lid velocity (Re>316). However, due to the moving cold lid from left to right, the core of the main upper cell (driven by the shear force) is pulled in the sense of motion towards the vertical left side of the cavity. The tiny circulation cell formed in each microcavity (alveolus) rotates counter clockwise while the major cell turns clockwise.

As Ri decreases Ri=10; 1; 0.1 (Re increase), the secondary recirculation formed in the bottom right corner of the microcavity (induced by the buoyancy force) grows pushing the main cell out. When the Re approaches Re = 3162 (Ri=0.1) the dominant modes of heat transfer is the forced convection, the two recirculation (major and minor) intensity becomes almost equivalent. Further, at highest Ri, the buoyancy force plays the dominant role which promotes the natural convection this is accompanied by significant changes in the flow structure and the thermal field as can be seen. However, at Ri=1, mixed convection occurs.

For low Pr value (Pr=0.026) isotherms distribution are almost invariant and emphasize the conduction dominance so that minor changes in the flow and thermal fields can be noted by varying Ri. As the Prandtl number increase (Pr=0.7 and 7.2) the thermal fields are more affected and the isotherms are distorted significantly indicating that, the convective heat transfer is dominant inside the entire cavity.
Pr=0.026

Creative Commons Attribution-NonCommercial-NoDerivatives 4.0 International License (CC BY-NC-ND)

Algerian Journal of Engineering Architecture and Urbanism Vol. 5 Nr. 3 2021
ISSN: 2588-1760

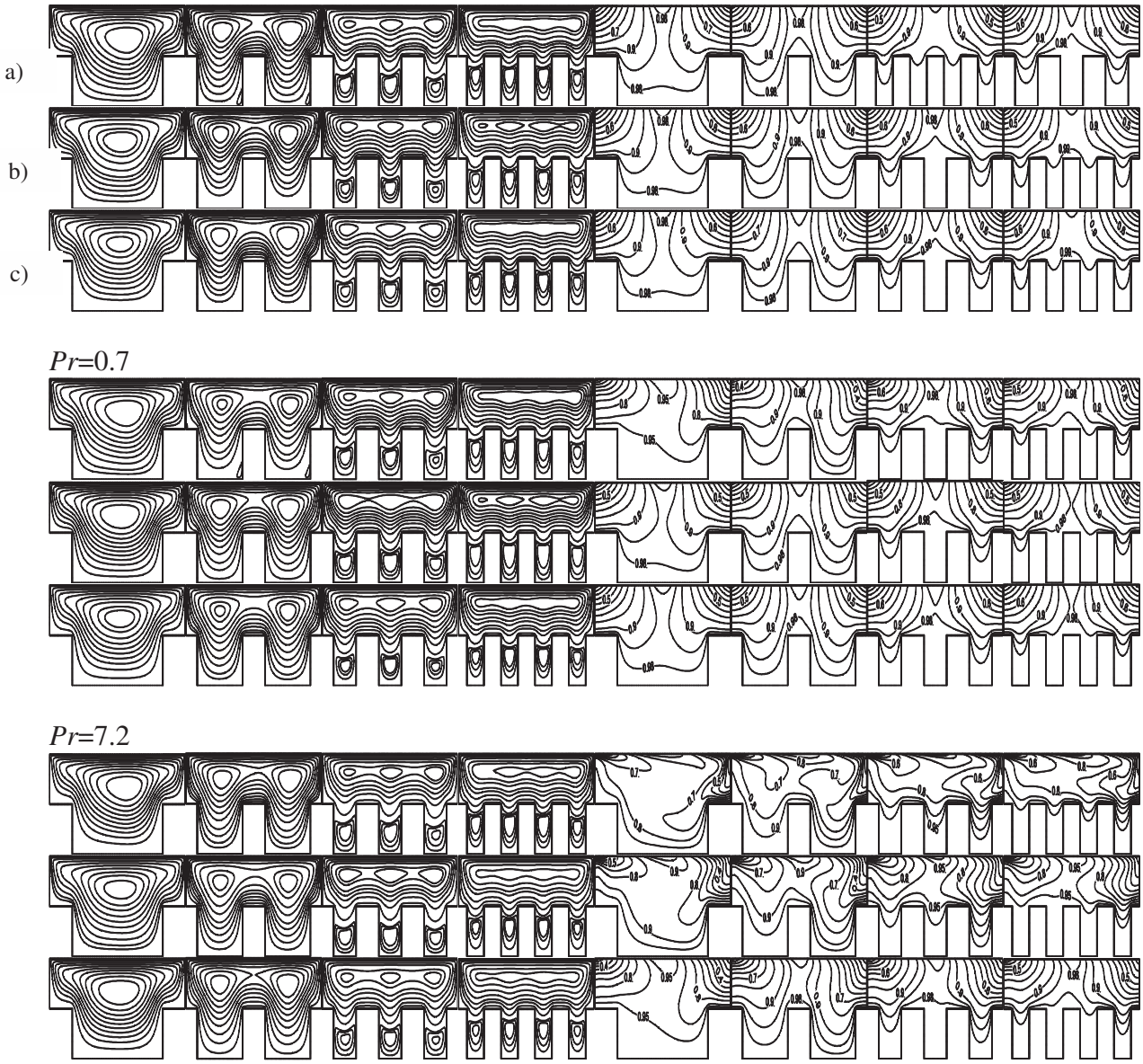

Fig6. Effect of Pr and Ri on streamlines and isotherms for $Gr=10^3$:
a) $Ri=0.1$ b) $Ri=1$ c) $Ri=10$

Creative Commons Attribution-NonCommercial-NoDerivatives 4.0 International License (CC BY-NC-ND)

Algerian Journal of Engineering Architecture and Urbanism Vol. 5 Nr. 3 2021
ISSN: 2588-1760

Pr=0.026

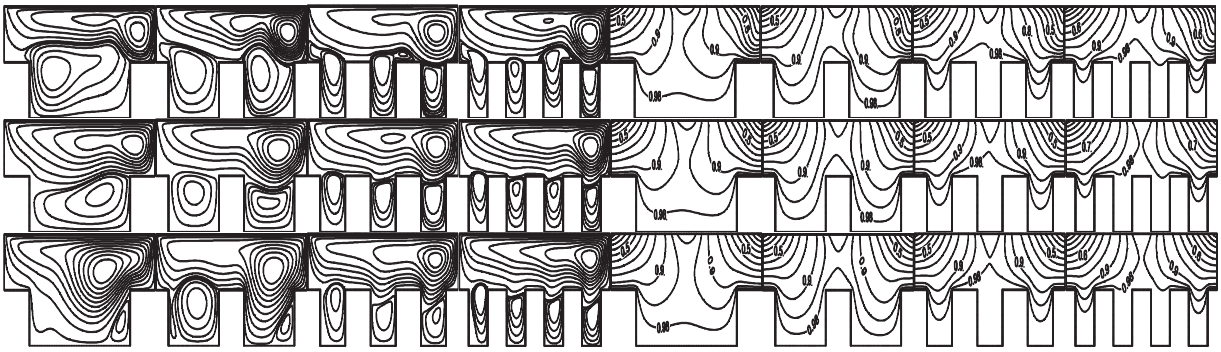

Pr=0.7

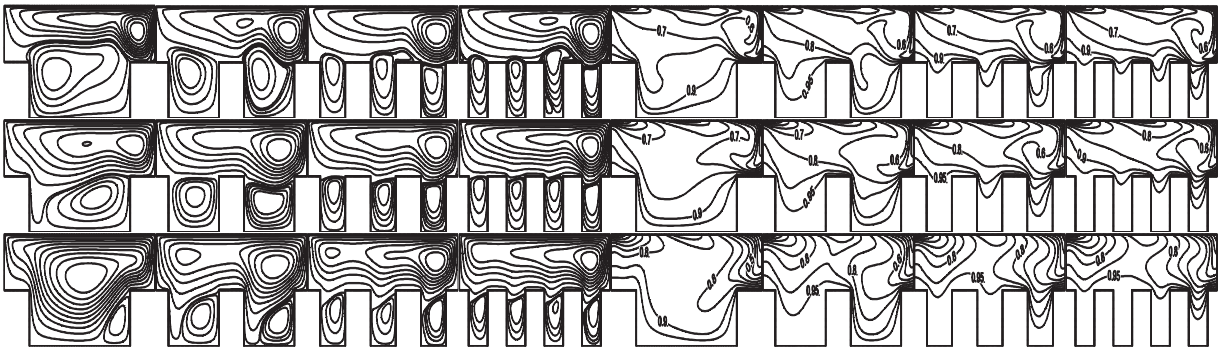

Pr=7.2

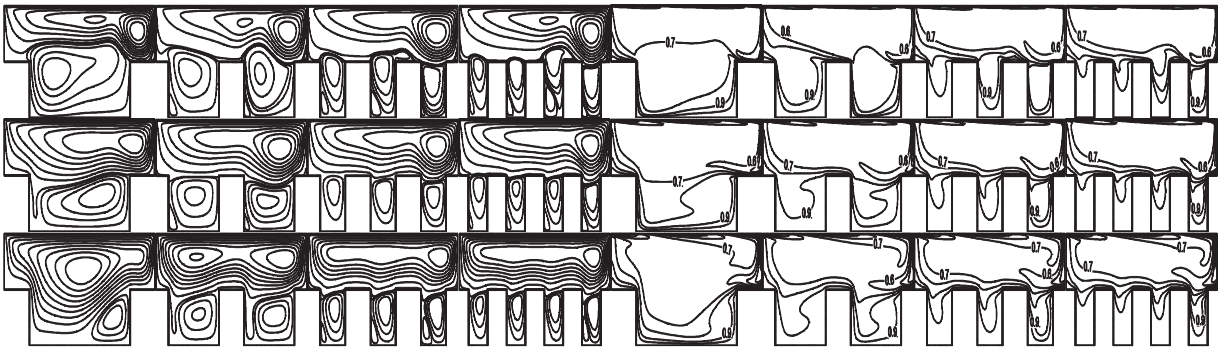

Fig7. Effect of *Pr* and *Ri* on streamlines and isotherms for $Gr=10^6$:
a) *Ri*=0.1 b) *Ri*=1 c) *Ri*=10

Heat Transfer

The variation of the mean Nusselt number of the hot bottom wall with Ri for different *Pr* and C is shown in Figs. 8a and b. In fig.8a the Grashof number is set equal to 2 while the *Re* varies between 10^3 and 10^5. As can be seen, the mean Nusselt remain invariant for all cases ($10^2 \leq Re \leq 10^3$) at low Prandtl number (*Pr*=0.026) indicating the conduction dominance (conduction is the dominant heat transfer mechanism). However, the heat transfer is highly influenced by the nature of the fluid in this regard, if the Prandtl number is further increased the heat transfer in all situations (*Re*=100 to 1000) is significantly improved.

Creative Commons Attribution-NonCommercial-NoDerivatives 4.0 International License (CC BY-NC-ND)

Algerian Journal of Engineering Architecture and Urbanism Vol. 5 Nr. 3 2021
ISSN: 2588-1760

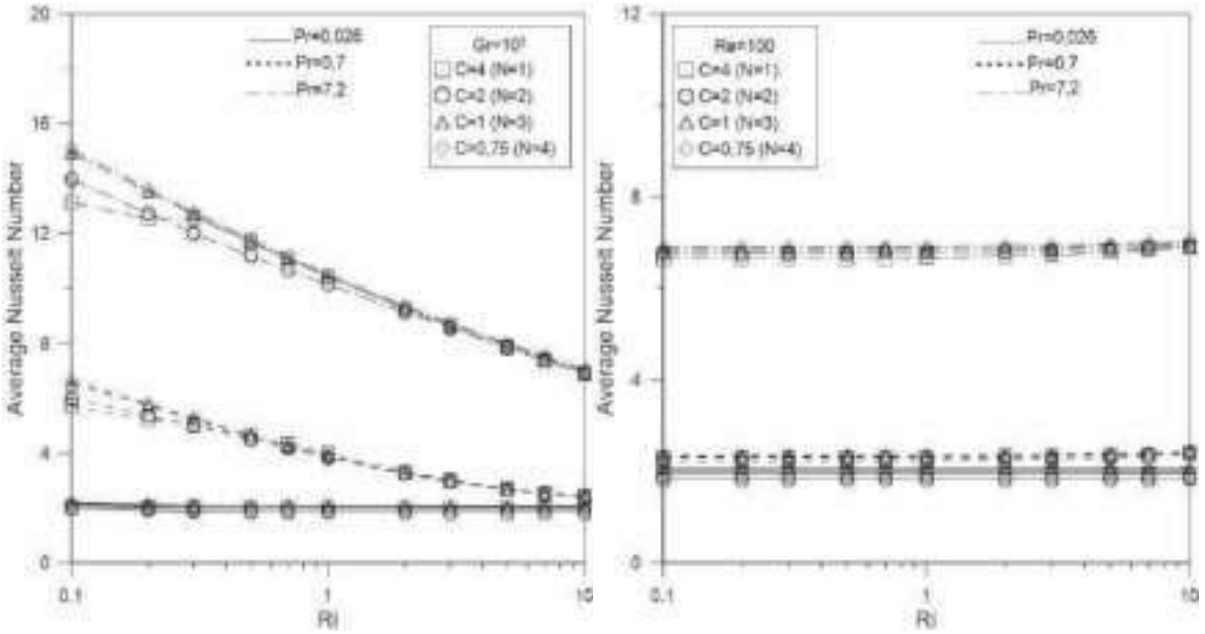

Fig 8. Averaged Nusselt for different *Ri*; *Pr* and alveolus numbers (N)
a) $Gr=10^5$ ($10^2 \leq Re \leq 10^3$) b) $Re=100$ ($10^3 \leq Gr \leq 10^5$).

For higher *Ri* corresponding to low lid speed ($Re=100$) with highest buoyancy force ($Gr=10^5$), the natural convection dominates the thermal transport causing reduction in the heat transfer rate. Increasing *Re* due to high lid speed, the convective transport grows, which lead to better mixing of the fluid, and consequently the higher heat transfer rate from the cover. The mixed convection plays the dominant role over the free convection. Further interesting results; indicate that the mean Nusselt is almost independent of aspect parameter C (number of alveolus) for low *Ri*. Hence, subsequent increase in N (number of alveolus) decreases the mean Nusselt number this is due to the reduction of convection currents in the alveolus.

Furthermore, the buoyant forces (*Gr*) for a constant lid speed ($Re=100$) as illustrated in fig.8b, have slight impact on heat transfer rate when varying *Ri* whatever the number of alveolus. In parallel, as pointed before, the Prandtl number has a major effect on the Nusselt number. Hence, the heat transfer is highest at greatest *Pr* than for lowest ones.

For considered situations (pure free convection or mixed convection), increasing the Prandtl number improves the heat transfer rate but in different manner. Indeed, the heat transfer is much more important when buoyant forces are combined to shear forces due to the lid motion.
In mixed convection case, at a constant $Gr=10^5$, the variation of *Re* causes significant changes in the Nusselt number compared to the case where $Re=100$ and $10^3<Gr<10^5$. This is particularly verified for largest *Pr* (0.7 and 7.2), for low *Pr* (0.026) the change is imperceptible.

Conclusion:

The numerical study has emphasized the conditions of the enhancement of heat transfer in a concave shaped cavity with a moving lid subjected to sinusoidal cold temperature. The study of Boussinesq model shows the variations of the mean Nusselt numbers for certain

Creative Commons Attribution-NonCommercial-NoDerivatives 4.0 International License (CC BY-NC-ND)

range of the Reynolds, Grashof and Prandtl numbers. The analysis of the streamlines and isotherms, has given some valuable information concerning the flow field in the cavity.

The numerical analysis leads to the following conclusions:

- For natural convection, streamlines and isotherms are symmetrical with respect to the vertical axis of the cavity. Due to buoyancy force dominance, the flow intensity increase with the Grashof number. For mixed convection, as the Richardson number decreases, inertial force caused by the lid-driven wall alters the symmetry.
- The increase of the number of alveolus (N) at the heated bottom wall causes small vortices appear at alveolus in addition to the large vortices occupying the whole cavity and the isotherms back slightly at the lower part of the cavity.
- The Prandtl number affects greatly the heat transfer and fluid flow especially Pr=7.2.
- The average Nusselt number does not change substantially with number of micro-cavities (N) for free convection case.
- For large Pr and small values of Ri (when forced convection dominates) the mean Nusselt number increases with the number of micro-cavities (N).
- The average Nusselt number increases when Ri number decreases and Gr number increases.

References:

[1] G. de V. Davis, Natural convection of air in square cavity: a benchmark numerical solution. Int. J. Numerical Methods Fluids Vol.3, pp. 249-264, 1983.

[2] I.E. Sarris, I. Lekakis, and N.S. and Vlachos, Natural convection in a 2D enclosure with sinusoidal upper wall temperature. Num. Heat Transfer, Part A, Vol. 42, pp.513-530, 2002.

[3] A. Dalal and M. K. Das, Laminar natural convection in an inclined complicated cavity with spatially variable wall temperature. Int. J. Heat Mass Transfer, 48 (18) (2005) 3833-3854.

[4] M. Hasnaoui, M. Bakkas and A. Amahmid, Natural convective flows in a horizontal channel provided with heating isothermal blocks: Effect of the inter blocks spacing. Ene. Conv. and Management, Vol. 51, pp. 296–304, 2010.

[5] H. Singh, and P.C. Eames, A review of natural convective heat transfer correlations in rectangular cross-section cavities and their potential applications to compound parabolic concentrating (CPC) solar collector cavities. App. Ther. Engineering, Vol. 31, pp. 2186-2196, 2011.

[6] C.L. Chen, and C.H. Cheng, Predictions of buoyancy-induced flow in various across-shape concave enclosures. Int. Comm. Heat and Mass Transfer, Vol. 38, pp. 442–448, 2011.

[7] C. Migeon, A. Texier, G. Pineau, Effects of lid-driven cavity shape on the flow establishment phase. J. of fluids and structures, volume 14, issue 4, may 2000, 469-488.

[8] C.H. Cheng, C.L. Chen, Numerical study of effects of inclination on buoyancy induced flow oscillation in a lid-driven arc-shaped cavity. Num. Heat Transfer A 4 8 (2005) 77–97.

[9] C.H. Cheng, C.L. Chen, Buoyancy-induced periodic flow and heat transfer in lid driven cavities with different cross-sectional shapes. Int. Comm. Heat Mass 32 (2005) 483–490.

[10] H. Mercan, K. Atalık, Vortex formation in lid-driven arc-shape cavity flows at high Reynolds numbers. Eur. J. of Mech.- B/Fluids 28 61–71 (2009).

[11] M. Bhattacharya, T. Basak, H.F. Oztop, Y.Varol, Mixed convection and role of multiple solutions in lid-driven trapezoidal enclosures. Int. J. Heat and Mass Transfer 63 366–388 (2013).

Creative Commons Attribution-NonCommercial-NoDerivatives 4.0 International License (CC BY-NC-ND)

[12] K.M. Khanafer, A.M. Al-Amiri, I. Pop, Numerical simulation of unsteady mixed convection in a driven cavity, using an externally excited sliding lid. Eur. J. Mech. – B/Fluids 26 (2007) 669–687
[13] W.J. Luo, R.J. Yang, Multiple fluid flow and heat transfer solutions in a two sided lid-driven cavity. Int. J. Heat Mass Transfer 50 (2007) 2394–2405.
[14] T. Basak, S. Roy and P.K. Sharma, Analysis of mixed convection flows within a square cavity with uniform and non-uniform heating of bottom wall. Int. J. of Ther. Sciences, Vol. 48, pp. 891–912, 2009.
[15] E.D. Dos Santos, G.L. Piccoli, F.H.R. França, A.P. Petry, Analysis of mixed convection in transient laminar and turbulent flows in driven cavities. Int. J. Heat Mass Transfer 54 4585–4595 (2011).
[16] E.M. Wahba, Steady flow simulations inside a driven cavity up to Reynolds number 35,000. Computers & Fluids 66 85–97 (2012).
[17] M. Roy, S. Roy, T. Basak, Role of various moving walls on energy transfer rates via heat flow visualization during mixed convection in square cavities. Energy 82 1–22 (2015).
[18] M. A. R. Sharif, Laminar mixed convection in shallow inclined driven cavities with hot moving lid on top and cooled from bottom. App. Ther. Engineering, 27 (2007) 1036-1042.
[19] H. Oztop and A. Varol, Combined convection in inclined porous lid-driven enclosures with sinusoidal thermal boundary condition on one wall. Prog. in Comp. Fluid Dynamics, 9 (2009) 127-131.
[20] Öğüt, E. B., Mixed convection in an inclined lid-driven enclosure with a constant flux heater using differential quadrature (dq) method. Int. J. Physical Sciences, Vol. 5, no. 15, pp. 2287–2303, 2010.
[21] T.S. Cheng, W.-H. Liu, Effects of cavity inclination on mixed convection heat transfer in lid-driven cavity flows. Computers & Fluids 100 108–122 (2014).
[22] A. Al-Amiri, K. Khanafer, J. Bull and Pop. Ioan, Effect of sinusoidal wavy bottom surface on mixed convection heat transfer in a lid-driven cavity. Intl. J. Heat Mass Transfer, (50) (2007) 1771-1780.
[23] R. Nasrin, Influences of physical parameters on mixed convection in a horizontal lid-driven cavity with an undulating base surface. Num. Heat Trans A-Appl 2012;61:306-21.
[24] M. Muthtamilselvan, D. H. Doh, Mixed convection of heat generating nanofluid in a lid-driven cavity with uniform and non-uniform heating of bottom wall. App. Mathematical Modelling 38 3164–3174 (2014).
[25] D. Chatterjee, S. K. Gupta, B. Mondal, Mixed convective transport in a lid-driven cavity containing a nanofluid and a rotating circular cylinder at the center. Int. Comm. in Heat and Mass Transfer 56 (2014) 71–78
[26] M. Alinia, D.D. Ganji, M. Gorji-Bandpy, Numerical study of mixed convection in an inclined two sided lid driven cavity filled with nanofluid using two-phase mixture model. Int. Comm. Heat Mass Transfer 2011;38:1428–35.
[27] C.C.Cho, C.L. Chen, C.K. Chen, Mixed convection heat transfer performance of water-based nano fluids in lid-driven cavity with wavy surfaces. Int. J. Therm. Sci. (2013);68:181-90
[28] S. Mekroussi, D. Nehari, M. Bouzit and N.E. Sad Chemloul, Analysis of mixed convection in an inclined lid-driven cavity with a wavy wall. J. of Mechanical Science and Technology 27 (7) (2013) 2181-2190
[29] N. Moraga and S. López, Numerical simulation of three dimensional mixed convection in an air-cooled cavity. Num. Heat Transfer, Part A, 45 (8) (2004) 811-824.

Creative Commons Attribution-NonCommercial-NoDerivatives 4.0 International License (CC BY-NC-ND)

[30] Y.S. Prasad, M.K. Das, bifurcation in mixed convection flow inside a rectangular cavity. Int. J. Heat Mass Transfer 2007;50:3583–98.

[31] S.M. Aminossadati and B. Ghasemi, A numerical study of mixed convection in a horizontal channel with a discrete heat source in an open cavity. Eur. J. of Mech.- B/Fluids, Vol. 28, pp. 590–598, 2009.

[32] J. Allegrini, V. Dorer, T. Defraeye and J. Carmeliet, An adaptive temperature wall function for mixed convective flows at exterior surfaces of buildings in street canyons. Building and Environment, Vol. 49, pp. 55-66, 2012.

[33] K. Al-Salem, H.F. Oztop, I. Pop, Y. Varol, Effects of moving lid direction on MHD mixed convection in a linearly heated cavity. Int. J. Heat and Mass Transfer 55 1103–1112 (2012).

[34] T.S. Cheng, and W.H. Liu, Effect of temperature gradient orientation on the characteristics of mixed convection flow in a lid-driven square cavity, Computers and Fluids, Vol.39, pp.965–978, 2010.

[35] M. Muthtamilselvan, Forced convection in a two-sided lid-driven cavity filled with volumetrically heat-generating porous medium, *Int. J. of Appl. Math. and Mech.* **7**(13): 1-16 (2011).

[36] GH.R. Kefayati, Magnetic field effect on heat and mass transfer of mixed convection of shear-thinning fluids in a lid-driven enclosure with non-uniform boundary conditions. J. of the Taiwan Institute of Chemical Engineers 000 1–14 (2015).

[37] S.V. Patankar, Numerical Heat Transfer and Fluid Flow. Hemisphere, McGraw- Hill, Washington DC, 1980.

Creative Commons Attribution-NonCommercial-NoDerivatives 4.0 International License (CC BY-NC-ND)

Algerian Journal of Engineering Architecture and Urbanism Vol. 5 Nr. 3 2021
ISSN: 2588-1760

STUDY OF THE MAGNETIC INDUCTION OF AN ELECTROMAGNETIC SOLENOID APPLIED TO PLASMA ARC TORCHES.

Abderrahmane HALIS
Lecturer, Dr, QUERE "Quality of Energy in Electrical Networks" Research Laboratory, Department of Electrical Engineering, Faculty of Technology, Ferhat ABBAS University of Setif 1, 19000 Setif, Algeria
E-mail: halis_abd@yahoo.fr

Abstract:
This study aims to assist in the design of suitable magnetic coils for a good functioning of plasma arc torches. We present an analysis of the distribution of the axial component B_z of the flux density inside a solenoid. The aim of the main analysis and calculation is obtaining the profile of the axial component of the magnetic field induced in each point of the interior of the coil. Calculation is based on the Biot Savart law. An analytical expression of the axial component B_z expressed by simple trigonometrically functions is found. This expression is in good agreement with that which is written using elliptic integrals. The results presented show that the value of B_z for a short solenoid is maximum in the median plane, close to its winding and not in the center of the coil. It is confirmed that the number of the solenoid turns affects the value of B_z and that the distribution of the magnetic field is function of the coil length.

Key words: Calculation; Magnetic fields; Coil design; Plasma arc torches.

Introduction:

We developed a torch with tubular electrodes to obtain an air plasma jet of low power. This torch is stabilized by magnetic fields (fig.1) (Abderrahmane Halis et al, 2011). One method of reducing electrode erosion in plasma arc heaters is to use an axial magnetic field to rotate the arc over the electrode surface as quickly as possible, thereby minimizing the arc residence time, and thus minimizing heating of the electrode surface (P. Fauchais et al, 1996), (J. Aubreton et al, 1981). It is shown by (J.Lawton, 1970), (J.F. Brilhac et al, 1994), (J.F. Brilhac et al, 1995), (D. Rigot et al, 2003) that, strong control of the arc position and rotation can be obtained with even simplest field geometry such as a constant axial magnetic field. Experimental results indicate that the arc plasma moves towards the cathode bottom as the magnetic field strength increases, while a higher arc current facilitates the cathode arc root to move to the cathode terminus (C. Wang et al, 2020). The use of magnetic field has been explored in plasma torches as a means of:

- Stabilization of the arc and control of its position.
- Uniformly heating gases to high temperatures by rotation of the arc at right angles to the gas stream.

Thus the British patent (George A.P. et al, 1976), propose that the current of the magnetic field coil oscillates at a frequency between 0.5 Hz and 10-4 Hz. This patent postulates that it is the movement of oscillation of the arc root, rather than local rotation on the interior surface of the electrode in a fixed axial position which is effective. (Mingdong Li et al, 2004) show that the lifetime of the tubular cathode electrode of arc plasma torches can be prolonged

Creative Commons Attribution-NonCommercial-NoDerivatives 4.0 International License (CC BY-NC-ND)

considerably by application of a double magnetic field to alternating frequencies. The rotation of cathode spot may be induced by the radial component of the magnetic field (Cheng Wang et al, 2019)

This study is aimed to help to design a suitable magnetic field coil for plasma arc heaters.

It is of use to name solenoid a coil, of tubular form, conceived to produce a magnetic field. We shall consider a tubular solenoid, uniformly wound. For a given solenoid which is wound by different wires the profile of the field has been calculated.

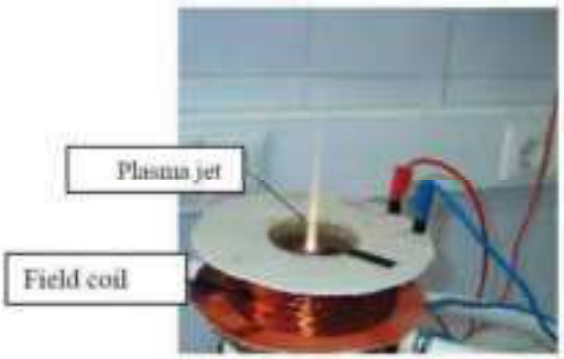

Fig.1. Plasma jet of the Torch

Theory:

Magnetic fields are produced by electric current. The basic relation for the magnetic flux density at a point P as produced by a current carrying element is given by the Biot-Savart relation:

$$dB = k\frac{Idl\sin\theta}{r^2} \qquad (1)$$

Where dB = infinitesimal flux density at point P

k = constant of proportionality

I = current in element

dl = length of element

θ = angle between current direction and radius vector to P

r = distant from element to P

The quantity k is a constant of proportionality given by:

$$k = \frac{\mu}{4\pi}$$

Where μ = permeability of the medium. The permeability of vacuum is designated μ0 and has a value of $4\pi \times 10^{-7}\, henry/meter$

It is assumed in (1) that the medium has a uniform permeability. In effect this limits us to nonferrous media, for which μ is nearly equal to μ_0.

Introducing the value for k in (1), we obtain:

$$dB = \frac{\mu Idl\sin\theta}{4\pi r^2} \qquad (2)$$

Creative Commons Attribution-NonCommercial-NoDerivatives 4.0 International License (CC BY-NC-ND)

The direction of dB is normal to the element of length dl.

The flux density due to one current loop of the solenoid in the z direction:

Let the solenoid consist of N turns of thin wire (diameter w) carrying a current I. The solenoid has a length L and inside diameter 2a (Fig.2).

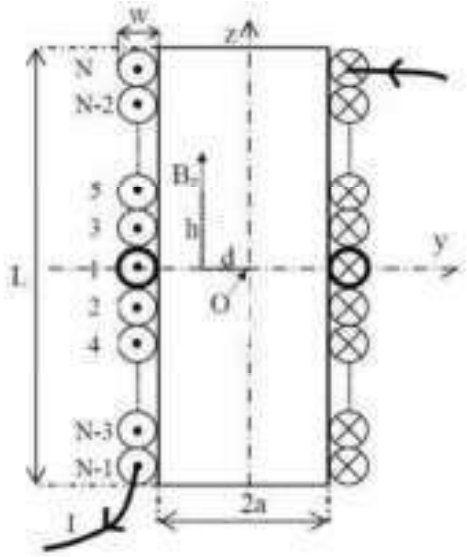

Fig.2. A cross section through the solenoid.

Let a current loop located in the xoy plan and which has as a center O (the origin) as shown in Fig.3 (Halis et al, 2004). The axis of the loop coincides with that of the z axis.

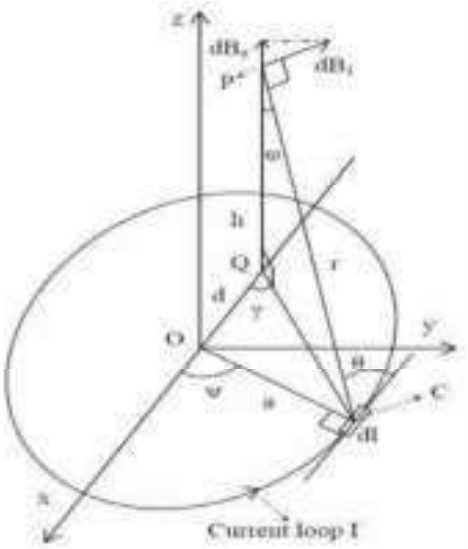

Fig.3. Construction to find the magnetic flux density at P on an axis different from that of the loop.

The loop of diameter 2a is traversed by a current I. According to the Biot and Savart law at the point P the local flux density dB1 produced by a small element length dl of the loop is:

Creative Commons Attribution-NonCommercial-NoDerivatives 4.0 International License (CC BY-NC-ND)

$$dB_1 = \frac{\mu I\, dl \sin\theta}{4\pi r^2} \quad (3)$$

The loop is immersed in a medium of permeability μ. The flux density dB1 in the plan QCP is in the normal direction with PC which has a length of r (fig.3)
The component dB1 of dBz in the direction of Z axis is such as:

$$dB_z = dB_1 \cos(\frac{\pi}{2} - \varphi) = dB_1 \sin\varphi \quad (4)$$

Thus :

$$dB_z = \frac{\mu I dl \sin\theta \sin\varphi}{4\pi r^2} \quad (5)$$

according to (Halis et al, 2004) :

$$\sin\theta = \sqrt{1 - \frac{d^2\Omega^2}{a^2(\Omega^2+1)}} \quad (6)$$

$$\Omega = \frac{a\ sin\psi}{d + a\ cos\psi} \quad (7)$$

$$\sin\varphi = \sqrt{\frac{a^2 sin^2\Psi(\Omega^2+1)}{\Omega^2 h^2 + a^2 sin^2\Psi(\Omega^2+1)}} \quad (8)$$

One has (fig.3):

$$r = \sqrt{h^2 + a^2 + d^2 + 2ad\ cos\psi} \quad (9)$$

From equations (6) and (7):

$$sin\theta = \frac{dcos\psi + a}{\sqrt{a^2+d^2+2ad\ cos\psi}} \quad (10)$$

From equations (7) and (8):

$$sin\varphi = \frac{\sqrt{a^2+d^2+2ad\ cos\psi}}{\sqrt{h^2+a^2+d^2+2ad\ cos\psi}} \quad (11)$$

One has

$$dl = a\ d\psi \quad (12)$$

And from (5), (9) and (12):

Creative Commons Attribution-NonCommercial-NoDerivatives 4.0 International License (CC BY-NC-ND)

Algerian Journal of Engineering Architecture and Urbanism Vol. 5 Nr. 3 2021
ISSN: 2588-1760

$$dB_z = \frac{\mu a I \sin\theta \sin\varphi}{4\pi(h^2+a^2+d^2+2ad\,cos\psi)} d\Psi \qquad (13)$$

In the vacuum the flux density of B_z due to a loop of the coil in direction z, for a point distant d of the axis of the coil and h of its median plan is:

$$B_z = \int_0^{2\pi} dB_z = \int_0^{2\pi} \frac{10^{-7}\, a\, I\, sin\theta\, sin\varphi}{(h^2+a^2+d^2+2ad\,cos\psi)}\, d\Psi$$

The symmetry of fig.3 makes it possible to write:

$$B_z = 2\int_0^{\pi} \frac{10^{-7}\, a\, I\, sin\theta\, sin\varphi}{(h^2+a^2+d^2+2ad\,cos\psi)}\, d\Psi \qquad (14)$$

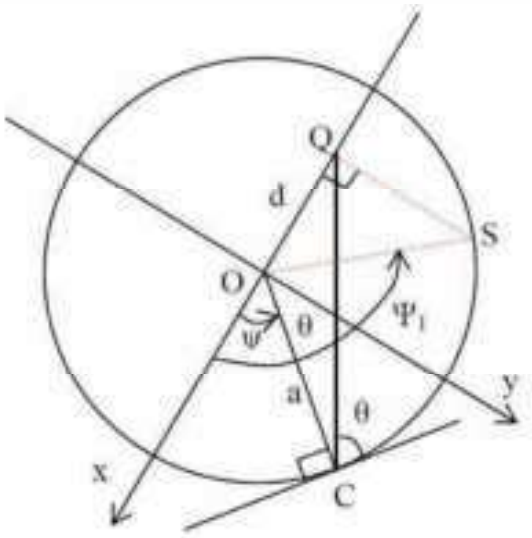

Fig.4. Plan x-y of the current loop.

The average values of sin θ and cos φ in the intervals $0 \le \Psi < \frac{\pi}{2}$, $\frac{\pi}{2} \le \Psi < \Psi_1$ and $\Psi_1 \le \Psi < \pi$ (Fig.4) are respectively$(\sin\theta)_{m1}$, $(\sin\theta)_{m2}$ and $(\sin\theta)_{m3}$, and the average values of cos φ are $(\sin\varphi)_{m1}$, $(\sin\varphi)_{m2}$ et $(\sin\varphi)_{m3}$ tel que:

$$\Psi_1 = \pi - arc\,cos\left(\frac{d}{a}\right) = arc\,cos(-\frac{d}{a})$$

In the interval: $0 \le \Psi < \frac{\pi}{2}$:

$$(sin\theta)_{m1} = \frac{sin\theta\ (pour\ \Psi = 0) + sin\theta\ \left(pour\ \Psi = \frac{\pi}{2}\right)}{2} = 1 + \frac{a}{\sqrt{(a+d)^2}} \qquad (15)$$

$$(sin\varphi)_{m1} = \frac{sin\varphi\ (pour\ \Psi = 0) + sin\varphi\ \left(pour\ \Psi = \frac{\pi}{2}\right)}{2} = \frac{1}{2}\left(\frac{a+d}{\sqrt{h^2+(a+d)^2}} + \frac{\sqrt{a^2+d^2}}{\sqrt{h^2+a^2+d^2}}\right) \qquad (16)$$

Creative Commons Attribution-NonCommercial-NoDerivatives 4.0 International License (CC BY-NC-ND)

In the interval: $\frac{\pi}{2} \leq \Psi < \Psi_1$:

$$(sin\theta)_{m2} = \frac{sin\theta\ \left(pour\ \Psi = \frac{\pi}{2}\right) + \ sin\theta\ (pour\ \Psi = \Psi_1)}{2}$$
$$= \frac{1}{2}\left(\frac{a}{\sqrt{a^2+d^2}} + \frac{\sqrt{a^2-d^2}}{a}\right) \quad (17)$$

$$(sin\varphi)_{m2} = \frac{sin\varphi\ \left(pour\ \Psi = \frac{\pi}{2}\right) + \ sin\varphi\ (pour\ \Psi = \Psi_1)}{2}$$
$$= \frac{1}{2}\left(\frac{\sqrt{a^2+d^2}}{\sqrt{h^2+a^2+d^2}} + \frac{\sqrt{a^2-d^2}}{\sqrt{h^2+a^2-d^2}}\right) \quad (18)$$

In the interval: $\Psi_1 \leq \Psi < \pi$:

$$(sin\theta)_{m3} = \frac{sin\theta\ (pour\ \Psi=\Psi_1) + sin\theta\ (pour\ \Psi=\pi)}{2}$$
$$= \frac{1}{2}\left(\frac{\sqrt{a^2-d^2}}{a} + 1\right) \quad (19)$$

$$(sin\varphi)_{m3} = \frac{sin\varphi\ (pour\ \Psi=\Psi_1) + sin\varphi\ (pour\ \Psi=\pi)}{2}$$
$$= \frac{1}{2}\left(\frac{\sqrt{a^2-d^2}}{\sqrt{h^2+a^2-d^2}} + \frac{a-d}{\sqrt{h^2+(a+d)^2}}\right) \quad (20)$$

By replacing the values of sin θ and cos φ by their average values in the equation 14, one finds:

$$B_z = 2\int_0^{\frac{\pi}{2}} \frac{10^{-7}\ a\ I\ (\sin\theta)_{m1}\ (\sin\varphi)_{m1}}{(h^2+a^2+d^2+2ad\ \cos\psi)}\ d\Psi + 2\int_{\frac{\pi}{2}}^{\Psi_1} \frac{10^{-7}\ a\ I\ (sin\theta)_{m2}\ (sin\varphi)_{m2}}{(h^2+a^2+d^2+2ad\ cos\psi)}\ d\Psi + 2\int_{\Psi_1}^{\pi} \frac{10^{-7}\ a\ I\ (sin\theta)_{m3}\ (sin\varphi)_{m3}}{(h^2+a^2+d^2+2ad\ cos\psi)}\ d\Psi \quad (21)$$

Let us pose:

$$\tan\frac{\Psi}{2} = t \ \text{ thus } \ d\Psi = \frac{2dt}{1+t^2} \text{ and } cos\psi = \frac{1-t^2}{1+t^2}$$

What makes it possible to write:

$$\int \frac{d\Psi}{h^2+a^2+d^2+2ad\ cos\psi} = \int \frac{dt}{A+B\ t^2}$$
$$= \frac{arc\ tg\left[\frac{\sqrt{A}}{\sqrt{B}}t\right]}{\sqrt{A}\sqrt{B}} \quad (22)$$

Such as:

$$A = \frac{h^2 + a^2 + d^2 + 2ad}{2}$$
$$B = \frac{h^2 + a^2 + d^2 - 2ad}{2}$$

Creative Commons Attribution-NonCommercial-NoDerivatives 4.0 International License (CC BY-NC-ND)

Thus:

$$\boldsymbol{B_z} = \boldsymbol{2\,X\,10^{-7}\,a\,I}\left((\boldsymbol{sin\theta})_{m1}\,(\boldsymbol{sin\varphi})_{m1}\left[\frac{arc\,tg[\frac{\sqrt{A}}{\sqrt{B}}t]}{\sqrt{A}\sqrt{B}}\right]_0^1 + (\boldsymbol{sin\theta})_{m2}\,(\boldsymbol{sin\varphi})_{m2}\left[\frac{arc\,tg[\frac{\sqrt{A}}{\sqrt{B}}t]}{\sqrt{A}\sqrt{B}}\right]_1^{t_1} + (\boldsymbol{sin\theta})_{m2}\,(\boldsymbol{sin\varphi})_{m2}\left[\frac{arc\,tg[\frac{\sqrt{A}}{\sqrt{B}}t]}{\sqrt{A}\sqrt{B}}\right]_{t_1}^{\infty}\right) \quad (23)$$

Such as:

$$t_1 = \tan\frac{arc\,cos(-\frac{d}{a})}{2} = \cot\frac{arc\,cos(\frac{d}{a})}{2}$$

Thus

$$B_z = \frac{2\,X\,10^{-7}\,a\,I}{\sqrt{A}\sqrt{B}}\Big((sin\theta)_{m1}\,(sin\varphi)_{m1}arc\,tg\left[\frac{\sqrt{A}}{\sqrt{B}}\right]\Big) + (sin\theta)_{m2}\,(sin\varphi)_{m2}\left[arc\,tg\left[\frac{\sqrt{A}}{\sqrt{B}}t_1\right] - arc\,tg\left[\frac{\sqrt{A}}{\sqrt{B}}\right]\right] + (sin\theta)_{m3}\,(sin\varphi)_{m3}\left[\frac{\pi}{2} - arc\,tg[\frac{\sqrt{A}}{\sqrt{B}}t_1]\right] \quad (24)$$

Comparative study:

There are several methods of resolution of system of equations which describe the electromagnetic problems. Among these methods, the analytical methods, and the numerical methods are to which one has recourse as soon as the nature of the problem becomes complicated. The axial component B_z in any point in the space of a loop can be calculated from the vector potential A. induction B is given by the relation $B = \nabla \times B$ and consequently we can write (Joseph V. Stewart, 2001):

$$B_z = \frac{\mu_0 I}{2\pi}\frac{1}{\sqrt{(a+d)^2+z^2}}\left[\left(\frac{a^2-d^2-z^2}{(a-d)^2+z^2}\right)E(k) + K(k)\right] \quad (25)$$

Where:

$$K(k) = \int_0^{\frac{\pi}{2}} \frac{d\theta}{\sqrt{1-k^2\,(\sin\theta)^2}}$$

is known as complete elliptic integral function, first order, and,

$$E(k) = \int_0^{\frac{\pi}{2}} \sqrt{1-k^2\,(\sin\theta)^2}\,d\theta$$

is the complete elliptic integral function, second-order.

In these expressions K is defined like:

$$k = \sqrt{\frac{4ad}{(a+d)^2+z^2}}$$

To check the solution, the variation of B_z as a function of h is calculated for a loop of radius a=10 mm and a=100 mm supplied with a current of 1A in a wires of standard gauge SWG(19) diameter (1.02 mm). Fig.5 represents the variation of B_z according to h for the three methods. The geometrical method is founded on the calculation of the integral of the equation (14)

Creative Commons Attribution-NonCommercial-NoDerivatives 4.0 International License (CC BY-NC-ND)

numerically, the analytical method is represented according to the equation (24) and the method of the elliptic functions is clarified by the equation (25).

To compare the numerical and analytical results, the error between the numerical and analytical results is calculated, according to the following relation:

$$\varepsilon = \frac{B_{numérique} - B_{analytique}}{B_{numérique}} \times 100$$

The results of the geometrical method are identical to those of the elliptic functions method. The maximum of variation between the numerical and analytical method reaches 4.97%

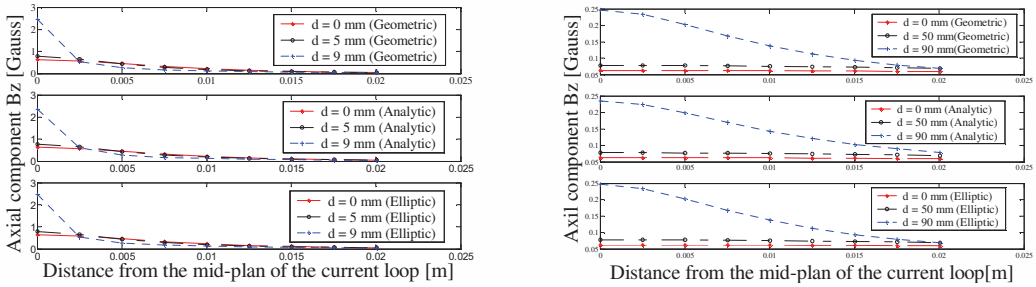

a. the radius of the loop a = 10 mm b. the radius of the loop a = 100 mm

Fig.5- The variation of B_z according to h for the three methods

Study of the axial magnetic profile for a current loop:

The field produced by a current of 1 A passing through different loops has been investigated. Two examples of the field distribution has been selected, one for a = 10 mm and another for a = 100 mm. The result of computation is plotted in Fig.6.

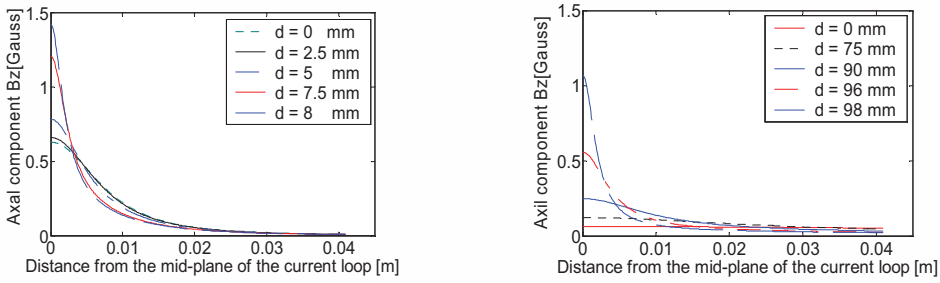

a. The loop radius a = 10 mm b. The loop radius a = 100 mm

Fig.6- B_z as a function of the distance from the mid-plane of the current loop

The flux density at the mid-plane of the solenoid and the effect of the number of turns:

The field produced at each point on the mid-plane of a solenoid formed by different wires has been investigated. Four wires of standard gauge has been used, SWG (14), SWG(19), SWG (25), SWG (42). The value of B_z is evaluated by taking into account the influence of each field loop of the coil. Each loop has its own field distribution. The field at each point inside the solenoid is the result of the superposition of all the fields produced by the whole loops of the coil.

Creative Commons Attribution-NonCommercial-NoDerivatives 4.0 International License (CC BY-NC-ND)

Algerian Journal of Engineering Architecture and Urbanism Vol. 5 Nr. 3 2021
ISSN: 2588-1760

The field at a point on an axis j produced by the loop N°: i is designated by B_{jzi}. The value of B_z at the mid-plane of the solenoid as a function of the number of loops is computed on the basis of the following steps:

1 loop : $B_z = B_{jz1}$

3 loops : $B_z = B_{jz1} + 2B_{jz2}$

(since by symmetry $B_{jz2} = B_{jz3}$)

5 loops : $B_z = B_{jz1} + 2B_{jz2} + 2B_{jz4}$

(since by symmetry $B_{jz4} = B_{jz5}$)

…

…

…

(N-2) spires $B_z = B_{jz1} + 2(B_{jz2} + B_{jz4} + \ldots + B_{jz(N-3)})$

(N) spires $B_z = B_{jz1} + 2(B_{jz2} + B_{jz4} + \ldots + B_{jz(N-1)})$

The result of the calculation is shown in Fig.7.

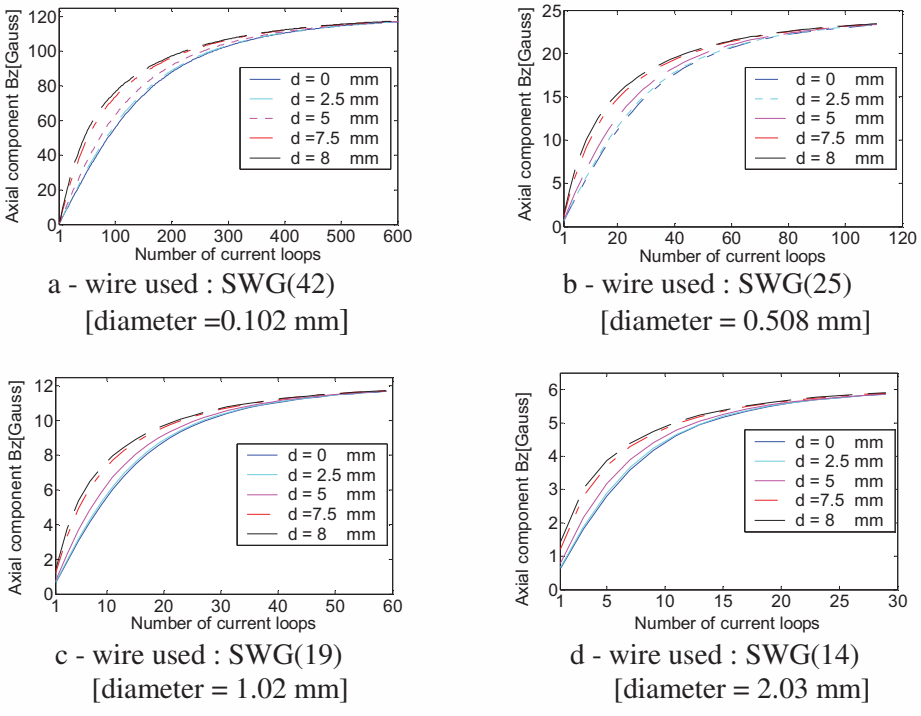

a - wire used : SWG(42) [diameter =0.102 mm]

b - wire used : SWG(25) [diameter = 0.508 mm]

c - wire used : SWG(19) [diameter = 1.02 mm]

d - wire used : SWG(14) [diameter = 2.03 mm]

Fig.7- B_z as a function of number of current loops.

Discussion:

From fig.6, we can say that the maximum value of the axial component B_z is in the mid-plane of the loop and close to the wire. The radius of the loop has an effect on the field distribution. At the centre of the loop and for large radius, B_z is negligible compared to its value at the inner border of the loop. For a = 100 mm, B_z = 0.06284 G at the centre (d=0) and B_z= 1.069 G at the inner edge of the loop (d = 98 mm).

Creative Commons Attribution-NonCommercial-NoDerivatives 4.0 International License (CC BY-NC-ND)

One may remark that for long solenoid the field is constant inside the coil and depend on the cross section of the wire. The flux density B at the centre of the solenoid is equal to,

$$B = \frac{\mu NI}{\sqrt{4a^2 + l^2}} \qquad (26)$$

Where l = length of solenoid

If the length of the solenoid is much greater than its radius (l » a), (26) reduces to

$$B = \frac{\mu NI}{l} \qquad (27)$$

In our case the length of the solenoid is equal to l=Nw. Therefore B_z at the centre of the solenoid for different cross section of the wire and for a current of 1 A is shown in table 1:

Table.1: The flux density B at the centre of the solenoid as a function of different wires.

w [mm]	0.102	0.508	1.02	2.03
B.[Gauss]	123.2	24.737	12.32	6.1903

These values of the flux density are approximately equal to those obtained by calculation. We can say also that for long solenoid, B_z is uniform at its mid-plane On the other hand, for short solenoid the field is maximum close to its inner winding. From Fig.7, we may state that the solenoid is long if its length is equal more than five times the radius of the solenoid or to change its profile.

Conclusion:

An analytical expression of B_z is presented in this work. It is in good agreement with that calculated by the elliptic integrals and that resulting from the numerical approximations. The analytical expression is useful to calculate B_z without use of numerical calculation on the computer or computation charts.

The method used allows the plotting of the axial magnetic component profile inside any solenoid. It has been concluded that the magnetic field shape at the mid-plane of the solenoid depends on the length of the coil. For each cross section of the wire there is a maximum value of B_z. This maximum will be reached when a specific number of turns is attained. At this specific number of turns it will not be useful to use further loops to increase the field intensity.

References:

Abderrahmane Halis, Bernard Pateyron, Mohammed El Ganaoui (2011), *Dimensionnement et réalisation d'un générateur à plasma d'arc à air de faible puissance (2 kW), AFM, EDP Sciences 2011, Mécanique & Industries 12, 325–330.*

C. Wang, Q. Sun, Z. Zhang & W. Xia (2020), *Experimental Observation and Numerical Analysis of the Arc Plasma Axial Motion in a Magnetically Rotating Arc Plasma Generator, Plasma Physics Reports volume 46, pages 617–626.*

Creative Commons Attribution-NonCommercial-NoDerivatives 4.0 International License (CC BY-NC-ND)

Cheng Wang, Jianqiao Li, Zelong Zhang, Lei Ye, Weiluo Xia & Weidong Xia (2019), *An Experimental Investigation of Cathode Spot Motion in a Magnetically Rotating Arc Plasma Generator at Atmospheric Pressure, Plasma Chemistry and Plasma Processing volume 39, pages 259–276.*

D. Rigot, G. Delluc, B. Pateyron, J.F. Coudert, P. Fauchais, J. Wigren (2003), *Transient evolution and shifts of signals emitted by a DC plasma gun (type PTF4), High Temp. Mat. Processes, 2, 175-185.*

George A.P., Richardson C.J and Holmer H (1976), *British Patent No: 1, 520, 365, (1976).*

Halis A, Zehar K, Benarioua Y, Bouzit N (2004), *Calculation of the axial component Bz at any point inside a magnetic field coil for plasma torches. WSEAS Transactions On Circuits And Systems, Issue 2, Vol.3, 203-206.*

J. Aubreton, B. Pateyron, P. Fauchais (1981), *Les fours à Plasma. Rev. Int. Hautes Temp. et Réfract., 18, 293.*

J.F. Brilhac, B. Pateyron, J.F. Coudert, P. Fauchais, A. Bouvier (1995), *Study of the dynamic and static behavior of DC vortex plasma torches : Part 2 : Well-type cathode, Plasma chemistry and plasma processing, 15 (1), p 231-255.*

J.F. Brilhac, B. Pateyron, P. Fauchais (1994), *Investigation of the thermal characteristics of d.c. vortex plasma torches, High Temp. Chem. Processes, 3, p 419-425.*

J.Lawton (1970), *ECRC/M307.*

Joseph V. Stewart (2001), *Intermediate electromagnetic theory, Science.*

Mingdong Li, Weiwei Deng, Yousan Fan, Jiyuan Yang, and Xiaolei Liu (2004), *Study on Arc Movement in Hollow Electrode, Plasma Generators with Impressed Double Magnetic Fields, Plasma Chemistry and Plasma Processing, Vol. 24, No. 1, 73-84*

P. Fauchais, J.F. Coudert, B. Pateyron (1996), *La production de plasmas thermiques. Revue Générale de Thermique, 35(416), p 543-560.*

Creative Commons Attribution-NonCommercial-NoDerivatives 4.0 International License (CC BY-NC-ND)

Algerian Journal of Engineering Architecture and Urbanism Vol. 5 Nr. 3 2021
ISSN: 2588-1760

NUMERICAL ANALYSIS OF CONVECTION HEAT TRANSFER OF NANOFLUIDS

Djamila BENYOUCEF
LMD ST Department, Faculty of Engineering Sciences
University of Batna 2, Algeria, e-mail: d.benyoucef@univ-batna2.dz

Afaf DJARAOUI
LMD ST Department, Faculty of Engineering Sciences
University of Batna 2, Algeria, e-mail: a.djaraoui@univ-batna2.dz

Samira NOUI
Department of Physics, Faculty of Sciences
University of Batna 1, Algeria, e-mail: samira.demagh@gmail.com

Abstract:
The nanofluids laminar flow and natural convection heat transfer characteristics in square cavities using the single-phase are numerically investigated. Results are compared to the literature-published papers to validate the geometric model used for the nanofluids, from the experimental and numerical standpoint. The simulation has been carried out for a significant number of pertinent parameters, such as the Rayleigh number ($10^3 \leq Ra \leq 10^6$), the volume concentration of nanoparticles ($0\% \leq \phi \leq 20\%$) and various values of heat source length and location ($0.2 \leq B \leq 0.8$ and $0.2 \leq D \leq 0.5$, respectively). Their effect on the heat transfer and fluid flow are discussed. Velocity profile results between nanofluid and water for various Rayleigh numbers and volume concentrations of nanofluids are plotted and compared. In addition, both dynamic and thermal maps are analyzed. Noteworthy results exist in the CFD simulated model and the literature-published data on the heat transfer rate relation (Nusselt number) and Rayleigh number. Moreover, the nanoparticle dispersion into the base fluid can significantly enhance the fluid flow and the convection heat transfer.

Key words: CFD, Heat transfer, Nanofluids, Natural convection, Single-phase mode.

Introduction:

Nanosciences and nanotechnologies constitute an important set of achievements. These terms, which have become common in recent years, remain complex in spite of everything. On the other hand, nanoparticles today represent a major technological and economic challenge. They allow very promising innovations in many fundamental areas such as health, energy and industry. The term nanofluid was introduced by Choi (1995) for thermal applications and remains commonly used to designate this type of suspension.

Natural convection and fluid flow in the confined cavity have received considerable attention for their ability to solve many industrial applications. Through publications, it has been found that natural convection in cavities filled by nanofluids has received much attention thus far (Wang (1999), Wang (2003), Kim (2004), Wen (2005)). Ho (2008) carried out a numerical study on natural convection within a differentially heated square cavity, filled with a water-Al_2O_3 nanofluid. For the range $10^3 \leq Ra \leq 10^6$ and $0 \leq \phi \leq 0.40$; it's noted that the effective dynamic viscosity model selected for nanofluid is the parameter in order to simulate cases close-

Creative Commons Attribution-NonCommercial-NoDerivatives 4.0 International License (CC BY-NC-ND)

reality. Aminossadati (2011) studied numerically the natural convection in a square cavity filled with nanofluid (CuO-water) with a volume concentration up to 4%, for two considered cases. They found that case 1 provides a higher heat transfer rate than case 2 where the streamlines and isotherms are symmetrical. Also revealed that in both cases, the rate of heat transfer increases with increasing Rayleigh number and nanofluid concentration. Fattahi (2012) studied the nanoparticles type effect (Cu and Al_2O_3) on dynamic and thermal characteristics of the heat transfer flow within a square cavity with differentially heated. Heat transfer rate results show an increase as a function of the Rayleigh number and the volume nanoparticle concentration. In addition, the use of nanoparticles has made it possible to optimize the heat exchange in the enclosure.

The goal of the numerical study is to examine the natural convective of nanofluid in a square cavity under boundary conditions using the nanofluid models proposed. Different nanofluids have verified the thermal and dynamic performance. The validation is obtained, the effect of the control parameters on fluid flow and thermal fields are researched.

Problematic:

Fig.1 shows the two-dimensional physical model considered, with the important geometric parameters. It consists of a square L-dimension cavity, the bottom wall has an embedded symmetrical heat source with a constant heat flow (q) of length *l*, sited at a distance d for the left wall. The vertical and the horizontal upper walls of the enclosure are maintained at a constant temperature T_C. The remaining boundary portions of the enclosure are adiabatic. The nanofluids used in the analysis are assumed to be Newtonian, incompressible and laminar. The base fluid (water) and the solid spherical nanoparticles (Cu, Ag, Al_2O_3 and TiO_2) are in thermal equilibrium.

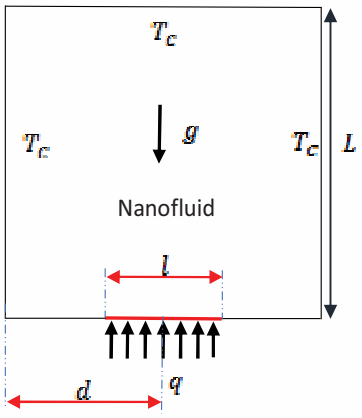

Fig1. Discretization physical model.

The thermophysical properties of the base fluid and of the nanoparticles are given in Table 1.

	ρ (Kg.m^{-3})	C_P (J.kg^{-1}. K^{-1})	k (W. m^{-1}. K^{-1})	β x 10^{-5}(K^{-1})
Water (Pr =6.2)	997.1	4179	0.613	21
Cu	8933	385	401	1.67
Ag	10500	235	429	1.89
Al_2O_3	3970	765	40	0.85
TiO_2	4250	686.2	8.9538	0.9

Table 1. Thermophysical properties of base fluid and nanoparticles.

The steady-state governing equations of the problem are based on the laws of mass, momentum, energy and thermo-physical models of nanofluids. The buoyancy forces are taken into account applying the Boussinesq approximation. According to the literature assumptions, these equations are written in a dimensional form as (Varol (2008)):

Creative Commons Attribution-NonCommercial-NoDerivatives 4.0 International License (CC BY-NC-ND)

Algerian Journal of Engineering Architecture and Urbanism Vol. 5 Nr. 3 2021
ISSN: 2588-1760

Conservation of mass equation

$$\frac{\partial u}{\partial x}+\frac{\partial v}{\partial y}=0 \quad (1)$$

Conservation of x-momentum equation

x-direction:

$$\rho\left(u\frac{\partial u}{\partial x}+v\frac{\partial u}{\partial y}\right)=-\frac{\partial p}{\partial x}+\mu\left(\frac{\partial^2 u}{\partial x^2}+\frac{\partial^2 u}{\partial y^2}\right) \quad (2)$$

y-direction:

$$\rho\left(u\frac{\partial v}{\partial x}+v\frac{\partial v}{\partial y}\right)=-\frac{\partial p}{\partial y}+\mu\left(\frac{\partial^2 v}{\partial x^2}+\frac{\partial^2 v}{\partial y^2}\right)-g\beta(T-T_C) \quad (3)$$

Conservation of energy equation

$$\rho C_p\left(u\frac{\partial T}{\partial x}+v\frac{\partial T}{\partial y}\right)=k\left(\frac{\partial^2 T}{\partial x^2}+\frac{\partial^2 T}{\partial x^2}\right) \quad (4)$$

The thermo-physical models

Density:

$$\rho_{nf}=(1-\phi)\rho_f+\phi\rho_s \quad (5)$$

Thermal Conductivity:

$$k_{nf}=\frac{k_s+2k_f+2\phi(k_s-k_f)}{k_s+k_f-\phi(k_s-k_f)}k_f \quad (6)$$

heat capacity

$$(\rho C_p)_{nf}=(1-\phi)(\rho C_p)_f+\phi(\rho C_p)_s \quad (7)$$

Thermal expansion coefficient

$$(\rho\beta)_{nf}=(1-\phi)(\rho\beta)_f+\phi(\rho\beta)_s \quad (8)$$

Viscosity

$$\mu_{nf}=\frac{\mu_f}{(1-\varphi)^{2.5}} \quad (9)$$

Thermal diffusivity

$$\alpha_{nf}=\frac{k_{nf}}{(\rho C_p)_{nf}} \quad (10)$$

The studied phenomenon is subject to the boundaries listed below as:

$$u=v=0 \text{ et } T=T_C \text{ for } x=0;\ x=L;\ 0\le y\le L \quad (11)$$

$$u=v=0 \text{ et } T=T_C \text{ for } y=L;\ 0\le x\le L \quad (12)$$

$$u=v=0 \text{ et } q=\frac{\partial T}{\partial y} \text{ for } y=0;\ (d-0.5b)<x<(d+0.5b) \quad (14)$$

$$u=v=0 \text{ et } \frac{\partial T}{\partial y}=0 \text{ for } y=0;\ 0\le x<(d-0.5b);\ (d+0.5b)<x\le L \quad (15)$$

The dimensionless formulation are:

$$X=\frac{x}{L},Y=\frac{y}{L},B=\frac{l}{L},D=\frac{d}{L},U=\frac{uL}{\alpha_f},V=\frac{vL}{\alpha_f},\theta=\frac{T-T_C}{\Delta T},\Delta T=\frac{qL}{k_f},Ra=\frac{\beta g\Delta T L^3}{\nu_f\alpha_f},Pr=\frac{\nu_f}{\alpha_f}$$

Where X, Y and x, y are the dimensioneless and dimension coordinates, respectively. B is the dimensionless length of heat source, D is the dimensionless distance of heat source from the left wall. U, V and u, v are dimensionless ad dimension velocity components in x, y directions, respectively. ν, κ, β and α are kinematic viscosity, thermal conductivity, thermal expansion coefficient and thermal diffusivity, respectively. g is the gravitational acceleration and ΔT is the temperature difference.

The local Nusselt number on the heat source can be defined as:

$$Nu_s=\frac{hL}{k_{fb}} \text{ With } h=\frac{q}{T_s-T_C} \quad (16)$$

The mean Nusselt number (Nu_m) is determined by integrating Nu_s along the hot wall.

$$Nu_m=\frac{1}{b}\int_{d-0.5b}^{d+0.5b}Nu_s(x) \quad (17)$$

Materials and methods:

The governing equations along with the boundary conditions were numerically discretized using a finite volume formulation given by Patankar (1980). Pressure-velocity coupling dissolved by SIMPLE algorithm and the convective terms of discretized equations were treated with a Second Order-Upwind scheme. The convergence criterion for the solution

Creative Commons Attribution-NonCommercial-NoDerivatives 4.0 International License (CC BY-NC-ND)

procedure 10^{-6}. The numerical study was implemented in a CFD code. The effect of grid resolution was examined in order to select the appropriate grid density. Uniform grid sizes were used.

Table 2. displays the grid independence results on the average Nusselt number in the heat source for the different meshes. Based on the uniform grid (60×60) which meets the grid independence. The grid-independent values are chosen and the obtained results (CFD code) are compared to the reference Aminossadati (2009) (FORTRAN program). All values show that the difference between the two results is less than (0.1%).

Ra	10^5				
Grid	20x20	40x40	60x60	80x80	100x100
	7.191	7.184	7.183	7.183	7.183

Table 2. Grid independency results (Cu-Water, B=0.4, D=0.5, $\phi = 0.1$, Ra = 10^5).

Results and discussions:

After the numerical modeling and the choice of the mesh, one presents in this chapter the results of the numerical simulation obtained and their interpretations, to analyze the thermal and dynamic behavior inside the two-dimensional square cavity filled with selected nanofluids. Velocity, temperature profiles, local and average Nusselt number as a function of dimensionless quantities variation are plotted using Origin software.

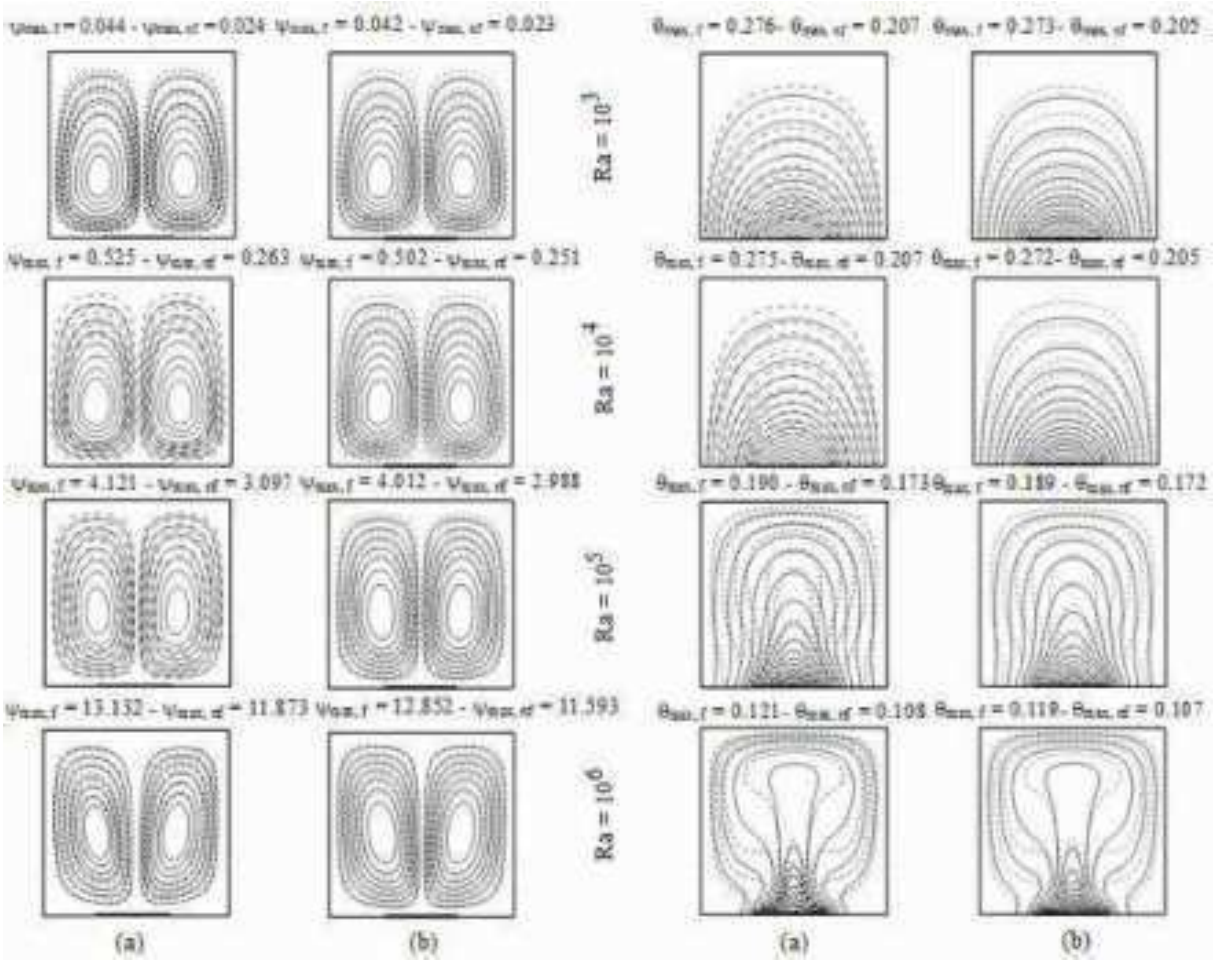

Creative Commons Attribution-NonCommercial-NoDerivatives 4.0 International License (CC BY-NC-ND)

Fig2. Streamlines (left) and isotherms (right) for the cavity filled with nanofluid (Cu-water; $\phi = 0.10$, solid lines) and water (dashed lines) at different Rayleigh number (B = 0.4, D = 0.5). (a) Present work and (b) Aminossadati (2009).

Volume nanoparticle concentration

Fig2. posters the streamlines and isotherms at different Rayleigh numbers ((a): present results; (b): Aminossadati (2009) results) for the nanofluid (Water-Cu, $\phi = 0.1$, Solid line) and pure water (dotted lines). Two counter-rotating symmetrical rolls are observed for all Rayleigh values. In fact, the temperature gradient generates the buoyancy forces that cause an ascending flow in the middle and descending near the sides of the cavity. Isotherms, also have symmetrical patterns. It swings between a conduction heat transfer (dominate for low Rayleigh numbers) and a convection heat transfer (dominate for upper Rayleigh numbers) where the flow becomes more intensive and distinguished. In order to get more precise results, the results obtained are compared and displayed for the four types of the used nanofluids, a considerable range of the Rayleigh number and the different solid volume fraction.

Fig. 3 (a and b) shows the variation of the maximum heat source temperature and the local Nusselt number with the volume nanoparticule concentration and a range of Rayleight number ($10^3 \leq Ra \leq 10^6$). Fig3. (a) shows that the maximum heat source temperature is reduced as the volume nanoparticle concentration increases. This reduction is less apparent because the heat transfer mechanism inside the cavity changes from conduction (low Ra) to convection (high Ra). At this point, for all volume nanoparticule concentration and Ra = 10^5, the local Nusselt number for the nanofluid (Cu-water) is minimal in the middle of the heat source (Fig3. (b)). Thus, we note that the local Nusselt number increases in the middle and decreases at the border of the heat source with the increase of the volumetric fraction.

Creative Commons Attribution-NonCommercial-NoDerivatives 4.0 International License (CC BY-NC-ND)

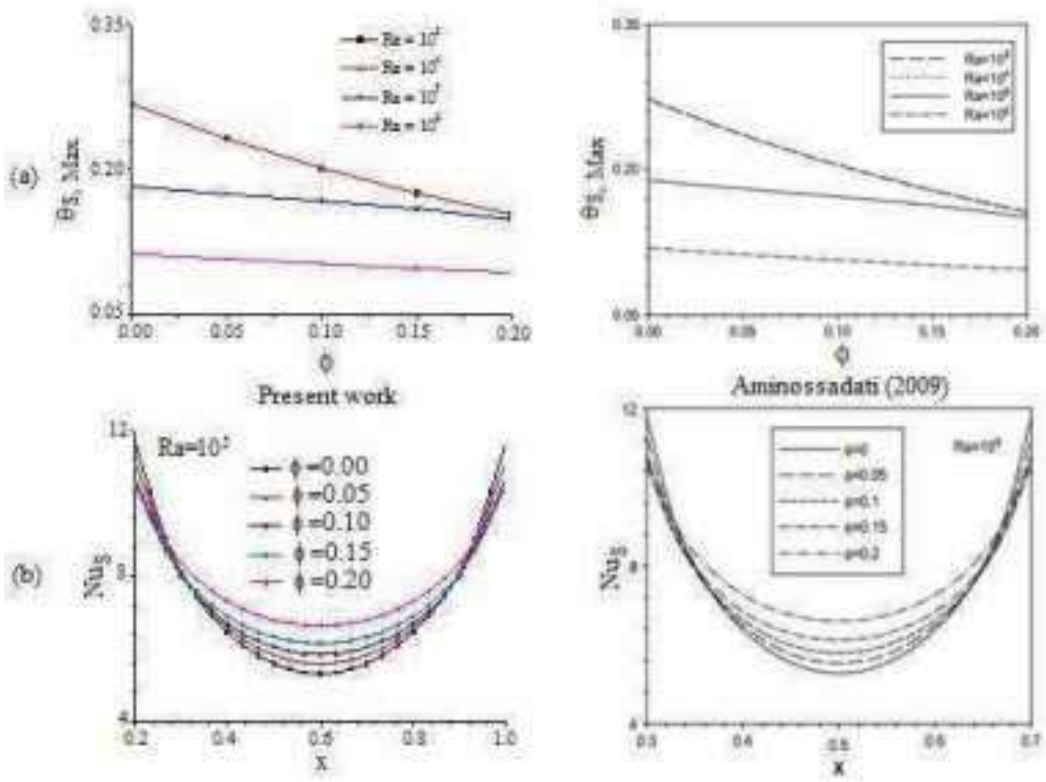

Fig3. (a): Maximum heat source temperature variation with the volume nanoparticle concentration at different Rayleigh numbers, (b): Local Nusselt number of the heat source as a function to volume nanoparticle concentration and Ra = 10^5 (Cu-water, B = 0.4, D = 0.5).

To validate the simulation procedure using CFD. The results obtained are compared to those of Aminossadati (2009) (Table 3). A good agreement can be observed.

	Present results				Aminossadati (2009)			
Ra	10^3	10^4	10^5	10^6	10^3	10^4	10^5	10^6
Nu_m	5.447	5.471	7.183	13.956	5.451	5.474	7.121	13.864
$\theta_{S,\,\mathrm{Max}}$	0.202	0.202	0.169	0.104	0.205	0.205	0.172	0.107

Table 3. Comparison of the present numerical results.

Length and location of the heat source

Creative Commons Attribution-NonCommercial-NoDerivatives 4.0 International License (CC BY-NC-ND)

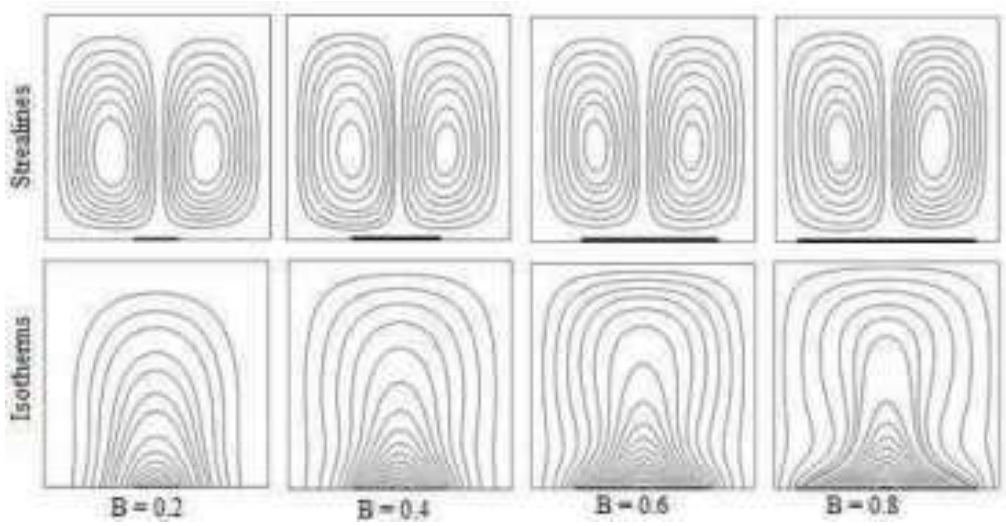

Fig4. Streamlines (upper) and isotherms (lower) for the Cu-water nanofluid filled-cavity (ϕ=0.1) at diverse heat source length (Ra = 10^5, D = 0.5).

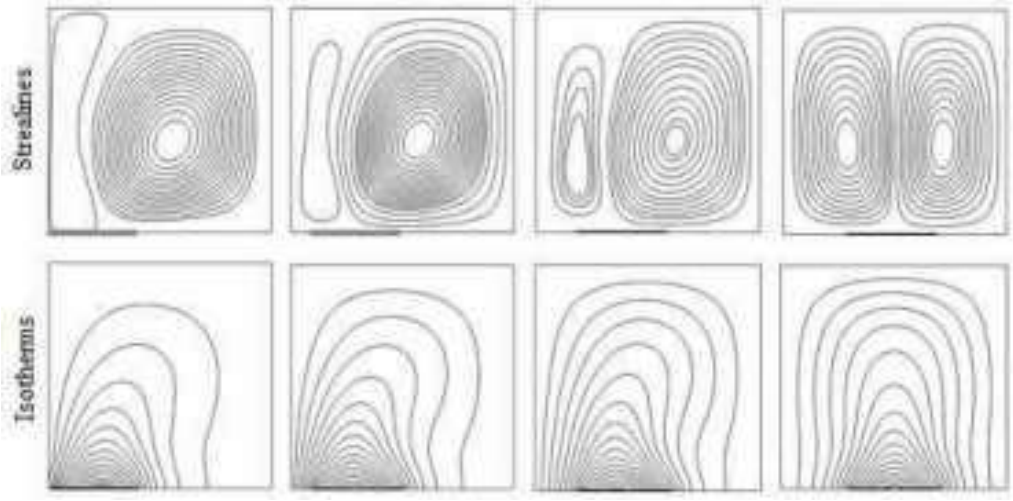

Fig5. Streamlines (upper) and isotherms (lower) for the Cu-water nanofluid filled-cavity (ϕ=0.1) at diverse heat source location (Ra = 10^5, B = 0.4).

Fig4. and Fig5. display the effect of heat source length and its location on streamlines (upper) and isotherms (lower) for Ra = 10^5, respectively. The results illustrate that the flow intensity is directly proportional to the heat source length and higher temperature patterns are observed. This can be explained by the higher heat generation rate created by the increased heat source length associating to the stronger buoyancy forces. The cells are symmetrical regardless of the heat source length. While, the second figure (Fig5.) shows asymmetric flow near the left wall and becomes symmetric in the middle with same strength, as it moves away from the left wall. Isotherms show that the maximum flow temperature grows up when the heat source moves away to the cavity middle. Isotherms show that the maximum flow temperature grows up when the heat source moves to the middle of the cavity, it is clear that it follows the heat source motion and their extension becomes evidently in the cavity. This can be expounded by the distance must travel in the single-cell to exchange heat.

Creative Commons Attribution-NonCommercial-NoDerivatives 4.0 International License (CC BY-NC-ND)

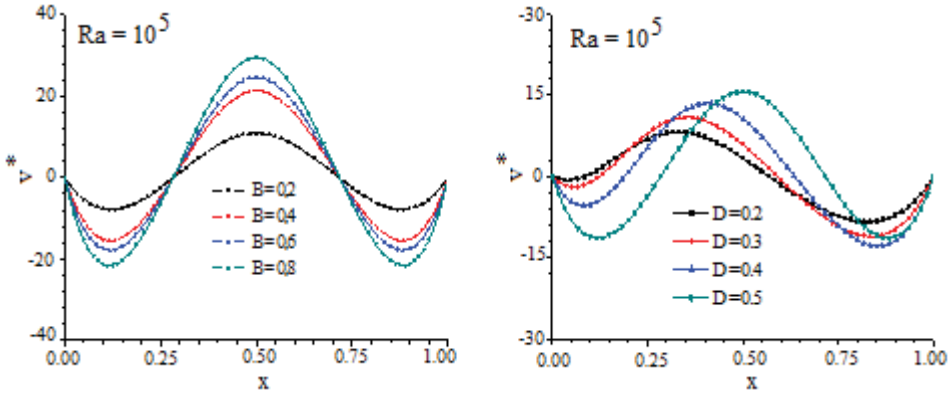

Fig6. (left): Horizontal velocity profiles along the mid-section cavity at diverse heat source length (D = 0.5), (right): Horizontal velocity profiles along the mid-section cavity at diverse location heat source (B = 0.4), (ϕ = 0.1, Ra = 10^5).

The vertical velocity profiles along the mid-section of the cavity have a better explanation of the flow behavior. Fig6. clarifying, the symmetric and asymmetric form in the vertical velocity plots which indicate the rotation direction of the flow in the enclosure. It is also clear that the absolute magnitude of the profiles increases with the length heat source increase, due to a stronger floating flow (left). While The results prove the existence of two contrarotating circulation cells for all the different locations of the heat source (right). In addition, the maximum speed increases as the heat source length increase or move towards the middle.

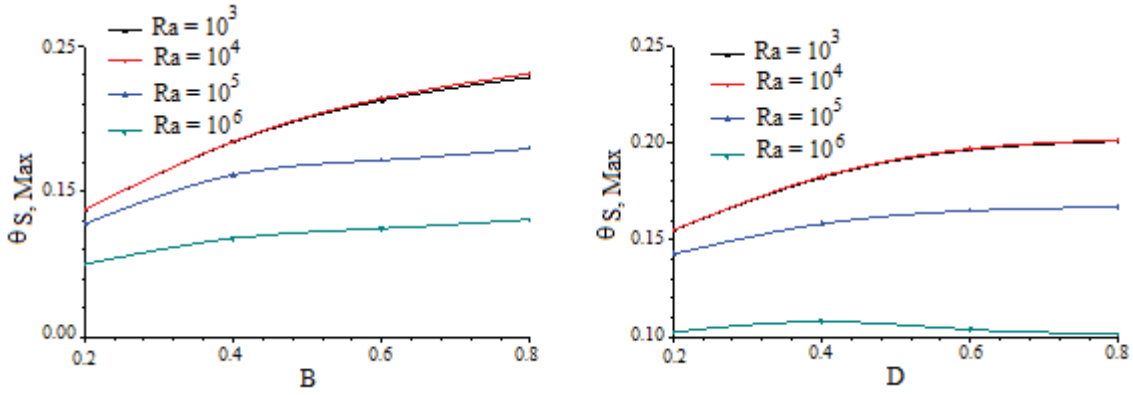

Fig7. (a): Temperature profiles of the heat source at diverse length (ϕ = 0.1 and D = 0.5), (b): Temperature profiles of the heat source at diverse location (ϕ = 0.1 and B = 0.4), at differnt Rayleigh.

Fig7. explain the effect of heat source length and its location on flow performance, by plotting the maximum heat source temperature for a range of Rayleigh numbers. In the convection dominant flow regime, the maximum temperature decreases as the Rayleigh number increases due to stronger buoyancy forces. As the length of the heat source increases, the maximum temperature continuously increases due to the higher heat flux generated by the heat source. While the maximum temperature increases with the Rayleigh number increase, due to the moving of the heat source away from the cold wall. At high Rayleigh numbers (Ra = 10^6), the heat source temperature reaches a maximum at D = 0.3. This behavior may be related to floating flows stronger at this Rayleigh number.

Nanofluids type

Creative Commons Attribution-NonCommercial-NoDerivatives 4.0 International License (CC BY-NC-ND)

Fig8. plots the average Nusselt number variation as a function to volume nanoparticle concentration. It shows that at low Rayleigh numbers (Ra = 10^4) the mean Nusselt number increases almost slightly with the phi for all nanofluids. At Ra = 10^5, the mean Nusselt number also increases with a lower gradient than that for Ra = 10^4. At Ra = 10^6, a slight increase is observed for the Cu and Ag nanoparticles, while for Al_2O_3 and TiO_2, optimal values can be found for the volume fraction. Moreover, Table 4. presents some benchmark results on the steady-state natural convection. In this Table, the values of $\theta_{s,\,max}$ and Nu_m are presented for heat source length equal to 0.4 in the middle of the bottom wall and $\phi = 0.1$. The results confirm that as Ra increases, the buoyant flows become stronger. This in turn results in higher values for Nu_m and lower values for $\theta_{s,\,max}$.

Ra	Nanoparticule	Nu_m	$\theta_{S,\,Max}$
10^3	Cu	5.447	0.201
	Ag	5.471	0.201
	Al_2O_3	5.378	0.207
	TiO_2	5.187	0.211
10^4	Cu	5.471	0.202
	Ag	5.471	0.201
	Al_2O_3	5.409	0.208
	TiO_2	5.211	0.212
10^5	Cu	7.183	0.167
	Ag	7.180	0.167
	Al_2O_3	7.017	0.170
	TiO_2	6.902	0.174
10^6	Cu	13.956	0.102
	Ag	13.902	0.107
	Al_2O_3	13.759	0.103
	TiO_2	13.510	0.105

Table 4. Benchmark results for the base case (ϕ = 0.1, D = 0.5 and B = 0.4).

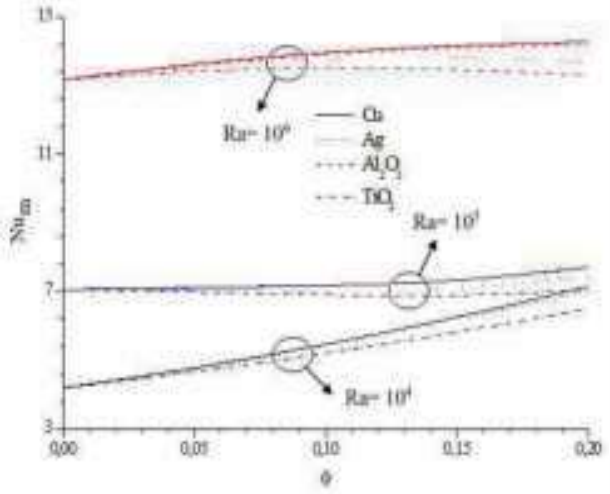

Fig8. Variation of the average Nusselt number with volume nanoparticle concentration at various Rayleigh numbers for different nanofluids (D = 0.5, B = 0.4)

Conclusion:

The numerical investigation of the natural convection in a square cavity heated from below and filled with four nanofluids types. The effects on the thermal and the flow performance by the control parameters are studied. The important remarks are :

- ✓ The Rayleigh number increases the strength of the natural convection, which decreases the temperature heat source.
- ✓ Nanoparticle concentration decreases the heat source temperature, especially for weak Rayleigh numbers where conduction is the mechanism of heat transfer.
- ✓ Increasing the heat source length increases the heat source temperature, so rises heat dissipation by strength natural convection. While, the heat source position has a linear influence on $\theta_{S,\,max}$ and Nu_m inversely depending on Rayleigh Number.
- ✓ Cu and Ag are proven to have the highest performance in reducing $\theta_{S,\,Max}$. While the influence of (Al_2O_3 and TiO_2) isn't important.

References:

Creative Commons Attribution-NonCommercial-NoDerivatives 4.0 International License (CC BY-NC-ND)

Aminossadati, S., Ghasemi, B. (2009). *Natural convection cooling of a localised heat source at the bottom of a nanofluid-filled enclosure*. European Journal of Mechanics-B/Fluids **28**, 630–640.

Aminossadati S.M., Ghasemi B. (2011). *Natural convection of water-CuO nanofluid in a cavity with two pairs of heat source-sink*, Int. Commun. Heat Mass Transfer. 38. 672-678.

Choi, S.U., Eastman, J.A. (1995). *Enhancing thermal conductivity of fluids with nanoparticles*. Technical Report.

Fattahi, E., Farhadi, M., Sedighi, K., Nemati, H. (2012). *Lattice Boltzmann simulation of natural convection heat transfer in nanofluids*. International Journal of Thermal Sciences, **52**, 137-144.

Ho C.J., Chen M.W., Li Z.W. (2008). *Numerical simulation of natural convection of nanofluid in a square enclosure: Effects due to uncertainties of viscosity and thermal conductivity*. Int. J. of heat and Mass Transfer, **51**, 4506-4516.

Kim J., Kang Y.T., Choi C.K. (2004). *Analysis of convective instability and heat transfer characteristics of nanofluids*. Physics of Fluids, **16(7)**: 2395-2401.

Patankar S.V. (1980), *Numerical Heat Transfer and Fluid Flow*, Hemisphere Publishing Corporation, Taylor and Francis Group, New York.

Varol, Y., Oztop, H.F. (2008). *A comparative numerical study on natural convection in inclined wavy and flat-plate solar collectors*. Building and environment **43**, 1535–1544.

Wang X., Xu X., Choi S.U.S. (1999). *Thermal Conductivity of Nanoparticle-Fluid Mixture*, J. Thermophysics and Heat Transfer. 474-480.

Wang B.X., Zhou L.P., Peng and X.F. (2003). *A fractal model for predicting the effective thermal conductivity of liquid with suspension of nanoparticles*. International Journal of Heat and Mass Transfer, **46(14)**: 2665-2672.

Wen D., Ding Y. (2005). *Formulation of nanofluids for natural convective heat transfer applications*. Int. J. Heat Fluid Flow, **26**: 855-864.

Creative Commons Attribution-NonCommercial-NoDerivatives 4.0 International License (CC BY-NC-ND)

Algerian Journal of Engineering Architecture and Urbanism Vol. 5 Nr. 3
2021
ISSN: 2588-1760

NUMERICAL INVESTIGATION OF HEAT TRANSFER WITH PHASE CHANGE IN Al- 7wt% Si

Afaf DJARAOUI
LMD ST Department, Faculty of Engineering Sciences
University of Batna 2, Algeria, 16000, e-mail: a.djaraoui@univ-batna2.dz

Djamila BENYOUCEF
LMD ST Department, Faculty of Engineering Sciences
University of Batna 2, Algeria, 16000, e-mail: d.benyoucef@univ-batna2.dz

Samira NOUI
Department of Physics, Faculty of Sciences
University of Batna 1, Algeria, 16000, e-mail: abdou.demagh@gmail.com

Abstract:

The objective of our study is the 2D numerical simulation of a heat transfer problem with phase change, of an Al-7wt% Si binary alloy, in a square and closed cavity. We consider two adiabatic walls while the others are kept isothermal: one at a hot temperature above the alloy liquidus temperature and the other at a cold temperature below the alloy solidus temperature.
In order to test the effect of natural convection and gravity, we assume two cases known in the fluid mechanics theory (differently heated and the Rayleigh Bernard problems). The numerical study is done using ANSYS Fluent 19.1.
The results obtained illustrate the importance of the enthalpy method which ensures the determination of the liquid / solid interface with a minimum computational in terms of calculation time, hence the interest of the ANSYS Fluent. The convective regime gains importance over the conductive regime. Consideration of gravity affects the shape and number of flow fields, isotherms, and the liquid / solid interface.

Key words: Heat transfer, Natural convection, phase change, ANSYS Fluent, Binary alloy.

Introduction:

Heat transfer is a process of great importance in industry and technology. Heat transfer with phase change by solidification and/or melting has been the subject of several experimental and numerical studies because of its interest among scientists due to its technological importance in crystal preparation. There are several experimental and numerical studies on the subject. We can note some of theme and for mor details, the reader can refer to Mergui (1997), Calcagni (2005), Younsi (2017), Bouarab (2017), Sheikholeslami (2019),

Creative Commons Attribution-NonCommercial-NoDerivatives 4.0 International License (CC BY-NC-ND)

Algerian Journal of Engineering Architecture and Urbanism Vol. 5 Nr. 3
2021
ISSN: 2588-1760

the analysis of heat transfer with phase change problem allowed us to observe the presence of natural convection in most cases Djaraoui (2018). The diffuculties which govern the study, above all, in the case of multidimensional problems is the determination of the shape and the position of the liquid/solid interface given the influence of the various parameters that govern the process. This is why we felt that it would be useful to approach the mechanism to make a contribution to the physical phenomena responsible for the different behaviors that occur during the solid and liquid phases transition.
In the present paper, we attend to study the evolution of the heat transfer with phase change of a fluid with a low Prandlt number in a square cavity, based on the commercial computer code ANSYS Fluent 19.1.

Problematic:

The physical problem is shown schematically in figure 1. It is a two-dimensional enclosure filled with an Al-7pd% Si binary alloy. The alloy is initially at a temperature T_0. To get a general idea of the behavior of our alloy under the influence of the thermal gradient, natural convection and gravity, we considered two cases known in the theory of heat transfer with phase change: the differentially heated problem where the horizontal walls are adiabatic while the two left and right vertical walls are maintained isothermal at constant temperatures T_c (cold) and T_h (hot), respectively. The second case is the Rayleigh-Bénard problem where the vertical walls are adiabatic while the two up and bottom vertical walls are maintained isothermal at the constant temperatures T_C and T_H, respectively. Note that $T_c<T_{sol}$ and $T_h>T_{liqu}$ where the T_{sol} and T_{liq} are the solidus and liquidus temperatures, respectively. We assume, for the two cases, a no-slip condition for the liquid velocity to all the walls

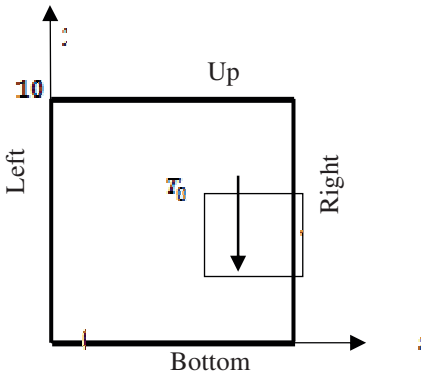

Fig1. physical problem considered

ANSYS Fluent uses an enthalpy formulation to simulate the process of heat transfer with phase change. The physical domain is divided into three regions liquid, solid and mushy zone. According to this method, the mushy zone is calculated through the liquid fraction which is calculated at each iteration, based on an enthalpy approach. Assuming that the fluid is a continuous medium, we can use the classical conservation laws ANSYS Fluent (2018).
The energy equation used in the heat transfer calculation, is expressed in equation (1) :

$$h = h_{ref} + \int_{T_{ref}}^{T} C_p dT \qquad (1)$$

Creative Commons Attribution-NonCommercial-NoDerivatives 4.0 International License (CC BY-NC-ND)

Algerian Journal of Engineering Architecture and Urbanism Vol. 5 Nr. 3
2021
ISSN: 2588-1760

Where h_{ref} is the reference enthalpy, T_{ref} is the reference temperature and c_P is the specific heat capacity at constant pressure.
The liquid fraction, f_L, can be defined as :

$$f_l = \begin{cases} 1, & T > T_{liq} \\ \frac{T - T_{sol}}{T_{liq} - T_{sol}}, & T_{liq} > T > T_{sol} \\ 0, & T < T_{sol} \end{cases} \quad (2)$$

Where T is the mushy zone temperature.
Equation (2) is referred to as the lever rule. The phase change takes place on the range of temperatures between T_{liq} and T_{sol}.
For the phase change problem, the energy conservation equation is written as :

$$\frac{\partial}{\partial t}(\rho h + \rho f_l L) + \nabla(\rho \vec{v} h) = K\Delta T + S \quad (3)$$

Where h is the enthalpy, ρ is the density, $\vec{v}$ is the fluid velocity, L_v is the latent heat of fusion and K is the thermal conductivity.
The solution for temperature is essentially an iteration between the energy equation (eq.3) and the liquid fraction equation (eq.2). The conservation equations of mass and momentum are decoupled from the one of thermal energy.

Materials and methods:

The fluid (Al- 7wt% Si melting alloy) contained in the enclosure is assumed to be viscous, incompressible and Newtonian. Its flow is two-dimensional, laminar and steady without viscous dissipation or radiative heat transfer. Also, the liquid motion induced by volumetric variation during melting is supposed to be neglected. Initially, the fluid is assumed to be maintained at a constant temperature T_0=860K. This equilibrium is upset by imposing the thermal boundary conditions on the walls of the enclosure.

The temperatures difference results a density difference in the cavity which includes, in each calculation cases in a convective fluid flow which also leads to a heat transfer with a phase change.
The physical properties are constant except for the density variation which obeys the Boussinesq approximation in the buoyancy term. The latent heat of the solvent Engineering ToolBox (2008) as well as the physical and thermal properties of the liquid alloy used, taken at a temperature 15K above the temperature of the liquidus Willers (2008). are given in Table 1. The liquidus temperature is calculated using the equation $T_l = T_m + Cm$ with $T_m = 933.5\ K$ Willers (2008) is the melting temperature, $C = 0.07$ is the alloy concentration and $m = -662.7\ K$ Willers (2008) is the liquidus slope.

Property	Symbol	Unit	Value
Density	ρ	$Kg.m^{-3}$	2390
Spesific heat	c_P	$J.Kg^{-1}.K^{-1}$	958
Thermal conductivity	K	$W.K^{-1}.m^{-1}$	70

Creative Commons Attribution-NonCommercial-NoDerivatives 4.0 International License (CC BY-NC-ND)

Algerian Journal of Engineering Architecture and Urbanism Vol. 5 Nr. 3
2021
ISSN: 2588-1760

Viscosity	μ	$Kg.m^{-1}.s^{-1}$	$1{,}146.10^{-3}$
Thermal expansion coefficient	β_T	K^{-1}	$1{,}1.10^{-4}$
Solvant latent heat	L	J.Kg	396.10^{+3}
Solidus temperature	T_{sol}	K	850
Liquidus temperature	T_{liq}	K	887

Table 1. Thermophysical properties of the Al- 7wt% Si

The boundary conditions associated with this problem are summarized for each case in Tables 2-3.

Position	Thermal conditions	Kenetic conditions
$x = 0m$ et $0 \leq y \leq 0.1m$	$T = T_c$	$u = v = 0$
$x = 0{,}1\text{m}$ et $0 \leq y \leq 0.1\text{m}$	$T = T_f$	$u = v = 0$
$y = 0m$ et $0 \leq x \leq 0.1m$	$\frac{\partial T}{\partial x} = 0$	$u = v = 0$
$y = 0{,}1\text{m}$ et $0 \leq x \leq 0.1\text{m}$	$\frac{\partial T}{\partial x} = 0$	$u = v = 0$

Table 2. Boundary conditions applied to the walls of the first case.

Position	Thermal conditions	Kenetic conditions
$x = 0m$ et $0 \leq y \leq 0.1m$	$\frac{\partial T}{\partial y} = 0$	$u = v = 0$
$x = 0{,}1\text{m}$ et $0 \leq y \leq 0.1\text{m}$	$\frac{\partial T}{\partial y} = 0$	$u = v = 0$
$y = 0m$ et $0 \leq x \leq 0.1m$	$T = T_c$	$u = v = 0$
$y = 0{,}1\text{m}$ et $0 \leq x \leq 0.1\text{m}$	$T = T_f$	$u = v = 0$

Table 3. Boundary conditions applied to the walls of the second case.

The present numerical model rests on a finite volume method based on the pressure-velocity coupling according to the SIMPEL algorithm Patankar (1980). The second order-upwind scheme was used for the discretization of the momentum and energy equations. The domain was meshed with uniform size. In order to minimize the mesh influence on the solution, we carried out several tests considering the 1st case. A preliminary calculation of the temperature and velocity field for the dimensionless horizontal position (Y = 0.5) undertaking four meshes, of 40 ×.40, 60 × 60, 80 × 80 and 100 × 100 divisions in X and Y directions. As exposed in figure2, the results obtained were identical for all the meshes for the temperature profiles and almost identical for the velocity profiles.

Creative Commons Attribution-NonCommercial-NoDerivatives 4.0 International License (CC BY-NC-ND)

Algerian Journal of Engineering Architecture and Urbanism Vol. 5 Nr. 3
2021
ISSN: 2588-1760

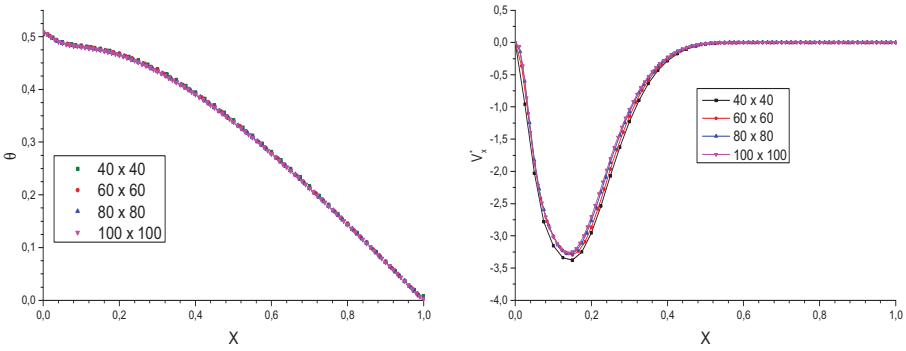

(a) Temperature profiles (b) velocity Profiles

Fig2. Grid independense study analysis.

Results and discussions:

In this section, we present, using the ANSYS Fluent 19.1 code, the results obtained from the numerical study for the chosen mesh (60 × 60 divisions) of the stationary problem of heat transfer with phase change of the binary alloy Al-7pd% Si content inside a square cavity of 10 cm × 10 cm. Also, we examine the influence of the physical parameters on the observed phenomenon.

Fluid flow

Figure 3 illustrates the fluid flow due to natural convection, resulting from temperature differences existing in the cavity plane and causing the flow of the current lines. Vortices can be observed in the fluid held between two isothermally active walls having hot and cold temperatures. This is a natural convection problem: the fluid heated near the hot wall expands, rises and orients towards the cold wall where it cools and returns to the hot wall. The difference in the shape of the vortices is well observed following the choice of adiabatic walls. The fluid particles always search for following the longest path during its path by looking for equilibrium (phase change).

For the first case (fig 3-a), the gravity effect is neglected. The field is unicellular and rotates clockwise around a point representing the vortex center. This field is present in the left part of the enclosure, which proves that the existing phase in this part is liquid and in the right part of the cavity the phase is solid and immobile. On the other hand (fig 3-b), once the gravity is considered the phenomenon changes. We can distinguish longitudinal rollers, parallel and almost symmetrical with respect to the vertical axis, in the lower part of the enclosure. indicating that the phase is liquid. At the top, the absence of these vortices indicates that the phase is solid and immobile.

Creative Commons Attribution-NonCommercial-NoDerivatives 4.0 International License (CC BY-NC-ND)

Algerian Journal of Engineering Architecture and Urbanism Vol. 5 Nr. 3
2021
ISSN: 2588-1760

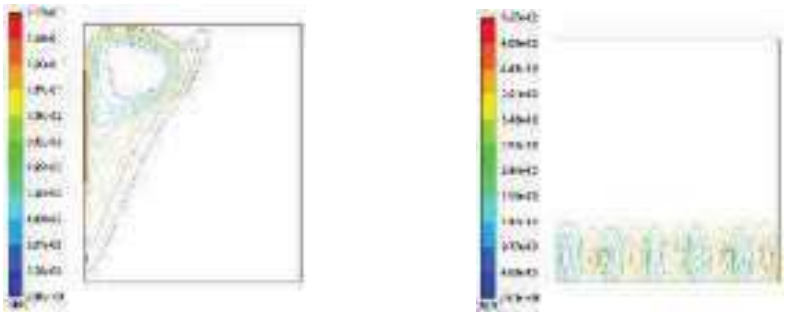

a b

Fig3. Streamlines for (a) – first case and (b) – second case.

For more details, to examine the physical phenomena that occur in the liquid medium of the cavity for the different cases studied, we can show, in figures 4 and 5, the direction and magnitude of the flow using the profiles variation of the horizontal component velocity u (x, y) as a y function in several x positions and of the vertical component velocity v (x, y) as x function in several y positions.

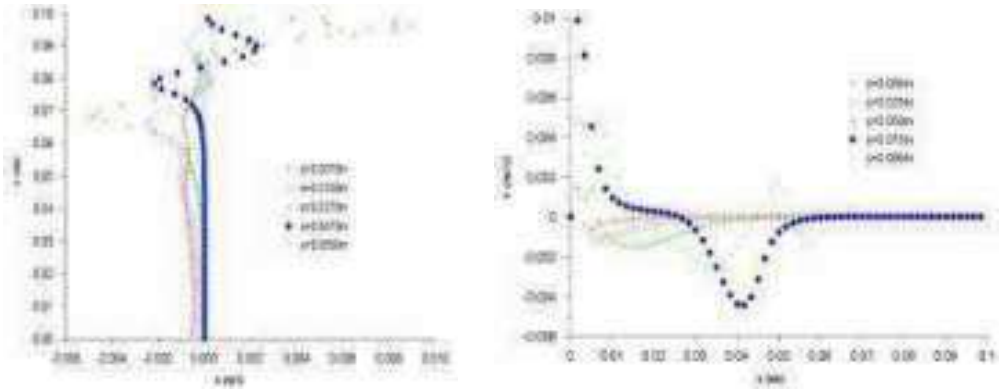

a b

Fig4. Velocity profiles in the first case: (a) variation of the component *u* as a *y* function at different *x* positions and (b) - variation of the component *v* as a *x* function of at different *y* positions.

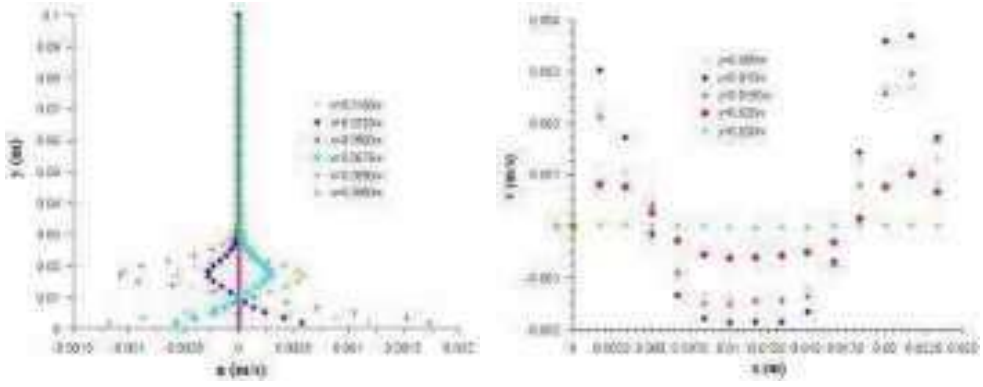

a b

Creative Commons Attribution-NonCommercial-NoDerivatives 4.0 International License (CC BY-NC-ND)

Algerian Journal of Engineering Architecture and Urbanism Vol. 5 Nr. 3
2021
ISSN: 2588-1760

Fig5. Velocity profiles in the second case: (a) variation of the component *u* as a *y* function at different *x* positions, (b) - variation of the component *v* as a *x* function of at different *y* positions.

Temperature field

The temperature field variation in the cavity, for the two cases studied, is shown in figure 6. There is a progression of the variation in the fluid temperature in the enclosure from the cold wall to the hot one. This variation is greater within the liquid, which proves that the heat transport toward this region is greater due to the presence of natural convection. The heat transport by conduction, in the solid part (close to the cold wall), is illustrated and it is more evident in the 2nd case where the isotherms are formed by straight lines and parallel to the cold wall.

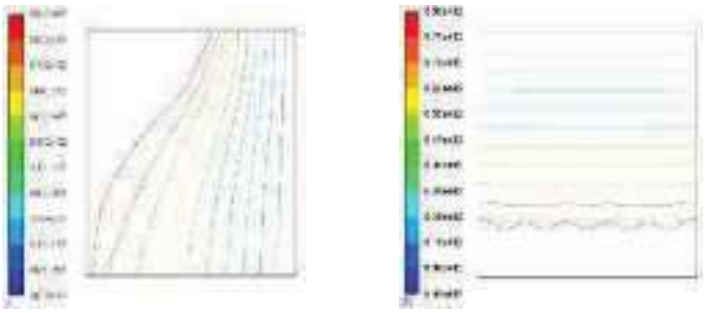

a b

Fig6. Isotherms for each case studied: (a) - first case, (b) - second case

A curvature of the isotherms at the liquid/solid interface is especially noted in the 2nd case, thus noting the gravity effect and natural convection. Consideration of the gravity existence increased the isotherms deformation at the liquid/solid interface. Another evident observation is the adiabatic condition effect imposed in each studied case of our physical problem. The isotherms intersect the adiabatic wall at right angles.

The liquid/solid interface and the liquid fraction

The interface is the boundary separating the two liquid and solid phases. It can be followed in an interval of liquid fraction variation f_l (or the solid fraction $f_s = 1 - f_l$). The interface is limited by $f_l = 0$ (for solid) and $f_l = 1$ (for liquid).

The observation of figure 7 shows us the variation of the liquid fraction lines in a small interval (between 0 and 1). The choice of the boundary conditions (the adiabatic condition) controls the convective fluid motion which affects the interface shape and the liquid fraction contours orientation.

Creative Commons Attribution-NonCommercial-NoDerivatives 4.0 International License (CC BY-NC-ND)

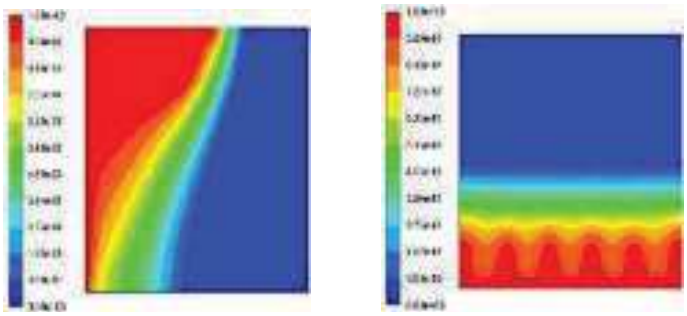

a b

Fig7. The liquid fraction lines for each case studied:
(a) - first case and (b) - second case.

Due to the weak natural convection effect, the liquid/solid interface shape is characterized by straight lines near the cold wall having a deviation towards the adiabatic wall near the cold one. This characteristic proves that the heat transfer in these regions is dominated by conduction.
In regions close to the liquid, a curvature of the liquid fraction contours is visible, this is a convective regime characteristic. In particular, the convective regime, in the second case, strongly influences the shape of the liquid fraction contours and therefore the interface shape leading to an apparent deformation in the lower region of the cavity.

Conclusion:

In this work, we presented a numerical study of heat transfer with phase change in a square cavity filled with a binary Al-7pd% Si melting alloy using the ANSYS Fluent 19.1. Two of the enclosure walls are adiabatic and the other walls are isothermal maintained at hot and cold temperatures, the hot temperature is higher than the temperature of the liquidus of our alloy considered and the cold temperature is lower than the temperature of the solidus of the same alloy. Two cases were considered: the first case corresponds to differentially heated natural convection; the horizontal walls are adiabatic and the vertical walls are thermally active. The second case corresponds to the Rayleigh Bénard problem. In this case, the vertical walls are adiabatic and the horizontal walls are isothermal. These conditions are taken into account to ensure a thermodynamic equilibrium of the liquid and solid phases separated by an interface to be determined.

The ANSYS Fluent commercial code models by the finite volume method used for the discretization of the partial differential equations of the mathematical model. This method allows an efficient conservative discretization of the conservation equations and the iterative solution of the equations of the mathematical model.
The results obtained indicate that the temperature difference in the cavity causes natural convection in the liquid phase illustrated by a fluid movement in circulations form. In the second case, gravity also controls the intensity of the flow. The thermal field shows little variation in the parts close to the cold wall due to the conductive regime. A progression of this

Creative Commons Attribution-NonCommercial-NoDerivatives 4.0 International License (CC BY-NC-ND)

variation is remarkable while moving towards the hot wall where the mode is convective because of the natural convection. The curvature of the isotherms observed in the liquid part and the straight and parallel lines in the solid part of the second case is due to the effect of the buoyancy forces due to the presence of gravity and natural convection.

The same behavior is observed by examining the liquid fraction lines. Gravity, in addition to natural convection, controls the shape and orientation of the liquid fraction contours and thus the liquid/solid interface.

References:

ANSYS Fluent 19.1 (2018), user's Guide.

Bouarab S., Mokhtari F., Kaddeche S., Hamrani A., Merah A., & Haddad F. (2017), *Résolution d'un problème de convection naturelle en 2D et 3D par la méthode spectrale,* In *Congrès français de mécanique*. AFM, Association Française de Mécanique.

Calcagni B., Marsili F., Paroncini M. (2005), *Natural convective heat transfer in square enclosures heated from below*, Applied thermal engineering, 25(16): 2522-2531.

Djaraoui A., Nebti S., Noui S. (2009), *ANALYSIS OF NON-STEADY STATE STAGE DURING RAPID SOLIDIFICATION OF AN Al-Mg ALLOY*, Congrès Algérien de Mécanique « CAM2009 », Biskra.

Djaraoui A., Nebti S. (2018), *Solidification Behavior Study of Al-8 wt% Mg Alloy*, In Proceedings of the 1st International Conference of Computer Science and Renewable Energies (ICCSRE 2018), pages 238-243, Maroc, ISBN: 978-989-758-431-2

Engineering ToolBox (2008), *Metals Latent Heat of Fusion*, [online] Available at: https://www.engineeringtoolbox.com/fusion-heat-metals-d_1266.html.

Mergui S., Penot F. (1997),. *Analyse des vitesses et température de l'air en convection naturelle dans une cavité carrée différentiellement chauffée à Ra= 1.69× 109,* International journal of heat and mass transfer, 40(14): 3427-3441.

Sheikholeslami M., Zareei A., Jafaryar M., Shafee A., Li Z., Smida A., Tlili I. (2019), *Heat transfer simulation during charging of nanoparticle enhanced PCM within a channel*, Physica A: Statistical Mechanics and its Applications, 525: 557-565.

Patankar S.V. (1980), *Numerical Heat Transfer and Fluid Flow*, Hemisphere Publishing Corporation, Taylor and Francis Group, New York.

Willers B., Eckert S., Nikrityuk P. A., Räbiger D., Dong J., Eckert K., Gerbeth G. (2008). *Efficient melt stirring using pulse sequences of a rotating magnetic field: Part II, Application to solidification of Al-Si alloys*, Metallurgical and Materials Transactions B, 39(2): 304-316.

Younsi Z., Naji H. (2017), *A numerical investigation of melting phase change process via the enthalpy-porosity approach: application to hydrated salts*, International Communications in Heat and Mass Transfer, 86: 12-24.

Creative Commons Attribution-NonCommercial-NoDerivatives 4.0 International License (CC BY-NC-ND)

Algerian Journal of Engineering Architecture and Urbanism Vol. 5 Nr. 3 2021
ISSN: 2588-1760

SPEED CONTROL OF ULTRASONIC MOTOR USING FUZZY PI CONTROLLER

Fatima Zohra Kebbab,
Laboratoire DAC HR , Ferhat Abbas University Setif I
fatimazohra.kebbab@univ-setif.dz
Louarem sabah ,
Ferhat Abbas University Setif I ,slouarem@univ-setif.dz
Djamel eddine chouaib belkhiat
Laboratoire DAC HR , Ferhat Abbas University Setif I,djamel.belkhiat@univ-setif.dz,

Abstract:
Time-varying nonlinearity of ultrasonic motor makes it harder to control. an online adaptive correction of PI control parameters based on fuzzy logic is presented. The special nature of ultrasonic motor's speed control is fully taken into account in designing fuzzy rules. The frequency of driving voltage is used as the control parameter to realize the control method. In order to validate the performance of the proposed controller, simulation result has been obtained and analyzed for varying load

Key words: Nonlinear control; fuzzy logic controller; Daimler–Benz AWM90-X.

1. Introduction:

Ultrasonic motor is a kind of new type-driving device in recent years; It has more characteristics than electromagnetic motor, such as low speed and high torque, light weight, micro-displacement, no noise, no electromagnetic effect and self-locking power [1]- [2]- [3]. Driving principles of the ultrasonic motor (USM) are based on the ultrasonic vibration force of piezoelectric elements and mechanical frictional force. Therefore, the dynamic model of the USM is very complicated. And the motor parameters are nonlinear and difficult to obtain. Moreover, the control characteristics of the USM are complicated and highly nonlinear [4]-[5]. In addition, the motor parameters are time varying due to the increase in temperature and changes in motor drive operating conditions, such as driving frequency, source voltage, and load. .

Application of ultrasonic motor can not be achieved without driving and control, whose technology decides the output performance of ultrasonic motor directly and affects its application and promotion. Recently, many researchers have carried on a great deal of research on drive control technique of ultrasonic motors [6], which are a combination of control strategies and also bring their advantages into full play. The speed/position of the USM was controlled using the driving voltage frequency, phase shift, and dual control by combined the two control signals [7]- [8]- [9].

PI control is rather a common and mature way of control during the industrial processes. However, traditional PI [6].. controller can't meet the need of time-varying and nonlinear controlled member. Fuzzy control can deal with nonlinear controlled member under the circumstances that has loose input, which can not depend on USM mathematical model [10]. Furthermore, fuzzy control can not reach the higher effectiveness of the control scheme, thus,

Creative Commons Attribution-NonCommercial-NoDerivatives 4.0 International License (CC BY-NC-ND)

the design of controllers is adopted for a combination of the fuzzy control and other control methods, such as fuzzy PID control, fuzzy neutral net. Yu Cheng et al proposed Auto-Tuning Fuzzy PI Control that The controller can compensate the property uncertainties of the motors by optimizing the fuzzy control rules, which determine the proportional gain and integral gain of the PI controller, by means of the on-lineauto-tuning factors [11]. Tomonobu Senjyu et all proposed a speed control system for ultrasonic motors by PI (proportional and integral) control which has auto-tuning structure based on fuzzy reasoning realized by neural network [12] kanaya et all presented a PI control method adjusted by a genetic algorithm (GA) for an ultrasonic motor (USM) [13]. In the proposed method, proportional and integral gains are adjusted using a GA in order to compensate the characteristic variations of the plant .Aiming at Daimler–Benz AWM90-X type ultrasonic motors as the object of study, a fuzzy PI compound control is proposed to drive the speed of the Daimler–Benz AWM90-X motor.

2. Design of Fuzzy PI Speed Controller:

In this paper, the traveling wave ultrasonic motor speed fuzzy PI control system structure is shown in Figure 1 [14]. Speed closed loop control achieved by the PI controller, fuzzy regulator is used for online correcting parameters of PI controller to improve the control performance.

For achieving effective control of ultrasonic motor speed, the controlled variable can choose plus drive voltage amplitude, frequency or phase difference of motor . In this paper, we use the driving frequency as the controlled variable, that is the controlled variable of the output of the PI controller is the driving frequency of set value f . The input of fuzzy regulator is the ultrasonic motor speed error e and error variation Δe and the output is the incremental ΔKp, ΔKi.

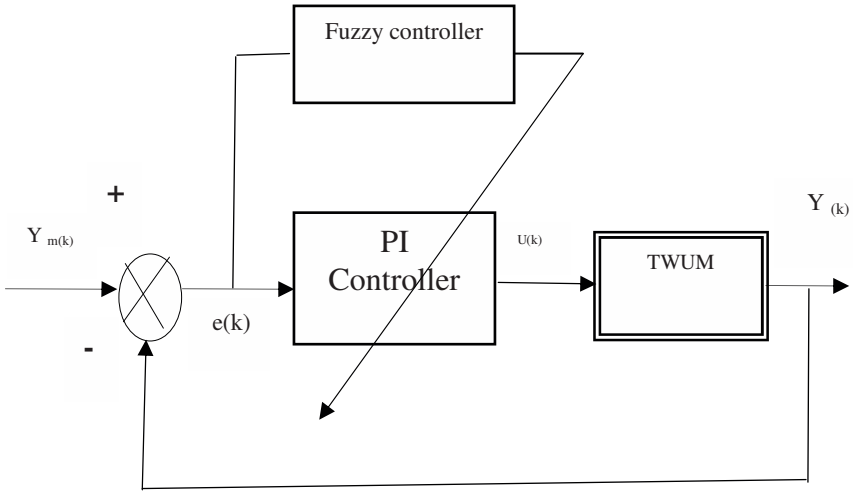

Fig. 1. Speed control system using fuzzy PI controller .

where $y_m(k)$ is commanded speed, $y(k)$ is rotor speed, $e(k)$ is speed error, and $u(k)$ is control signal (driving frequency).

The control input for the PI controller is determined by:

$$u(k) = K_P e(k) + T_s K_I \sum_{n=0}^{k} e(n) \qquad (1)$$

Creative Commons Attribution-NonCommercial-NoDerivatives 4.0 International License (CC BY-NC-ND)

K_P and K_I are proportional and integral gains in the PI controller and T_S denotes sampling period.

✓ Fuzzy Online Adjustment of PI Control Parameters :

As mentioned above, the input of fuzzy regulator is the speed error *e* and error variation **Δe** and the output is the incremental *ΔKp, ΔKi,* of PI control parameters *Kp, Ki,*. All of the fuzzy language value of five input and output variables is taken as 5: NB (negative big), NM (negative Medium), Z (zero), PM (positive Medium) and PB (positive big). Membership function is selected trapezoidal function, and each of variables membership function defined in the unit domain of discourse distribution are shown in Figure 2, Figure 3, respectively. The fuzzy inference method of the fuzzy regulator is MAX-MIN method, and the defuzzification method is centroid method

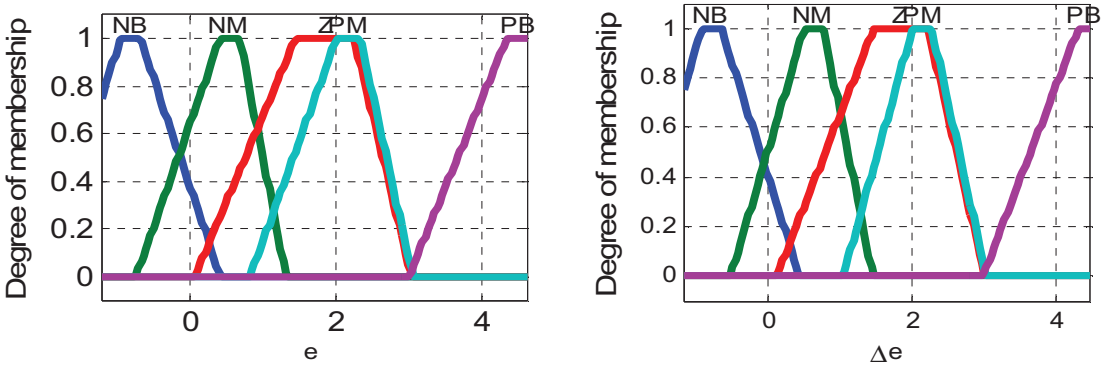

Fig .2. Membership Function Distribution of *e* and **Δe**

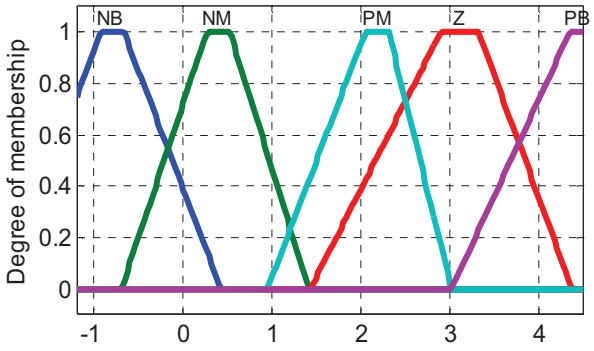

Fig 3. Membership Function Distribution of Δkp, Δki,

3. Simulation Results And Discussion

Speed response for loaded motor is analyzed for the considered TWUSM, type Daimler–Benz AWM90-X.
Simulation results of speed response are presented to validate the effectiveness of the proposed Fuzzy-PI for no load condition and loaded motor conditions.
The Parameters of piezoelectric motor are as follows.

- $570 volt$ is excitation voltages amplitude
- $\pi/2 rad$ is the shift between the two excitations.

Creative Commons Attribution-NonCommercial-NoDerivatives 4.0 International License (CC BY-NC-ND)

Algerian Journal of Engineering Architecture and Urbanism Vol. 5 Nr. 3 2021
ISSN: 2588-1760

The parameters values of the motor used for the simulation are presented in [15]-[16]. Result has been obtained by keeping the reference speed equals to $45.4\,rpm$.

- No loaded motor conditions

The speed response characteristics of motor without load is presented in Fig.4

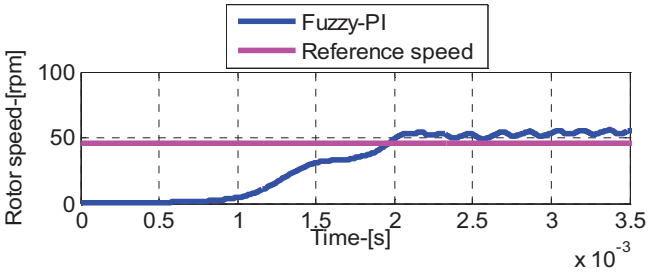

Fig. 4. Rotor speed without load

From the results obtained, shown in the fig 4, it can be clearly seen that the rotor speed follows the reference speed with a very small error . we note that a small oscillations of the rotor speed and of the driving torque can be caused by the non ideal traveling wave.

In the sequel, to validate the robustness of the proposed Fuzzy-PI, the motor was tested for different loads at $t = 2.5ms$.

- The load, 0.5Nm , 1Nm, 1.2Nm,1.6Nm

From the response plots shown in the Fig.5 (a) (b) (c), the proposed Fuzzy-PI drive the TWUSM to track the reference speed.

To validate the efficiency of Fuzzy-PI, we are interested in the evaluation of the torque value which corresponds to the correct functioning of the controller; the motor has been loaded with 1.6Nm

From the fig 5(c) ,we note that the Fuzzy-PI regulator works well up to the value of torque 1.6Nm.

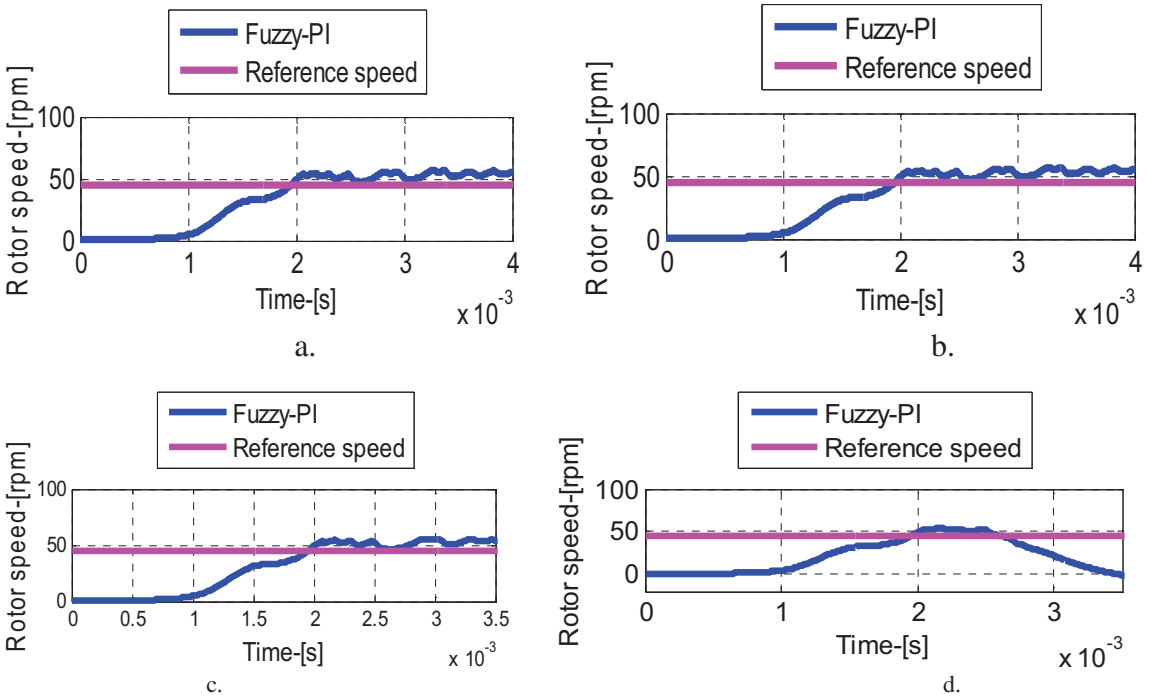

Fig. 5. Rotor speed, loaded motor a)0.5Nm , b)1NM,, c) 1.2Nm, d) 1.6Nm

Creative Commons Attribution-NonCommercial-NoDerivatives 4.0 International License (CC BY-NC-ND)

4. Conclusion

In this paper, the frequency speed control of the TWUSM, type Daimler Benz AWM90-X, has been studied. The design of the Fuzzy- PI controller has been presented and discussed. To illustrate the efficiency of the proposed controller to drive the TWUSM to track perfectly the reference speed, the motor was tested for different loads.

References :

[1] **Minghui Shi , Xuejiang Liu , Kai Feng , Kai Zhang (2021)** "Experimental and numerical investigation of a self-adapting non-contact ultrasonic motor" Tribology International volume 153 106624.

[2] **S. Wang, J. Xiu (2017),** "Piezoelectric parametric effects on wave vibration and contact mechanics of traveling wave ultrasonic motor", Ultrasonic*s*, volume 81, 2017, pp 118-126.

[3] **Shupeng Wang, Weibin Rong, Lefeng Wang, Zhichao Pei, Lining Sun (2017)** "A long range piezoelectric rotary motor with continuous output: Design, analysis and experimental performance" Sensors and Actuators , volume 263, 2017 , pp 179-187 .

[4] **Fazel BazrafshanBehnood Rasti, Hamed Mojallali (2010)"**Fuzzy Modeling and Position Control of a Traveling Wave Ultrasonic Motor" The 2nd International Conference on Computer and Automation Engineering (ICCAE) ,2010 , volume 5, pp 457 – 461, Singapore.

[5] **Yonfhong Tan, Ruili Dong ,Hui Chen (2017)** "Rotary speed control of ultrasonic motor with nonlinear estimator" 13th IEEE international conference on Control ,Automation (ICCA) , 2017 , pp7-11, Macedonia.

[6] **Sun Ligong1; Sun Xiangwen1 Zhang Juwei1; Liu Feng (2017)** "Position control of ultrasonic motor using fuzzy PID controller" Acta Technica 62 (2017), No. 6A, 47–58 c 2017 Institute of Thermomechanics CAS

[7] **Song Lu, Shi Jingzhuo , Zhou Ying (2020)** "Secant iterative learning control of ultrasonic motor" Volume 103, , pp 343-354

[8] **K. T. Chau, S. W. Chung, and C. C. Chanb(2003)** " Neuro-Fuzzy Speed Tracking Control of Traveling-Wave Ultrasonic Motor Drives Using Direct Pulse width Modulation", IEEE Transactions on industry applications, volume. 39, NO. 4, 2003, pp 1061 – 1069.

[9] **Altan Gencer (2015)** "A Comparative Speed/Position Control Technique Based Fuzzy Logic Control for Travelling Wave Ultrasonic Motor" 7th International Conference on Electronics, Computers and Artificial Intelligence (ECAI), 2015, pp SG-7 - SG-12, Bucharest, Romania

[10] **J.-M. Allenbach (2001)** "Asservissements par logique floue" N° 129R Volume 5 R Edition 2001.

[11] **Yu Cheng, Fu-Rong Lei, Wen-Li Xu and Yi-Sheng Zhong(2002)"**Speed Control of Ultrasonic Motors by Auto-Tuning Fuzzy PI Control" Proceedings of the 4th World Congress on Intelligent

Creative Commons Attribution-NonCommercial-NoDerivatives 4.0 International License (CC BY-NC-ND)

Control and Automation (Cat. No.02EX527) ,2002 , volume: 3 , pp 1882 - 1886 , Shanghai, China, China.

[12] **Tomonobu Senjyu , Satoru Yokoda (1996)** "Speed Control of Ultrasonic Motors Using Fuzzy Neural Network" Proceedings of the IEEE IECON. 22nd International Conference on Industrial Electronics, Control, and Instrumentation , 1996 , volume 2 ,pp 887 – 892, Taipei, Taiwan.

[13] **Kanya Tanaka, Yuji Wakasa, Takuya Akashi, Masato Oka (2009)** "PI Control Adjusted by GA for Ultrasonic Motor" Electrical Engineering in Japan, volume. 169, No. 1, 2009.

[14] **Zhen-Yu Zhao, Masayoshi Tomizuka, Satoru Isaka, (1993)** " Fuzzy Gain Scheduling of PID Controllers" **IEEE** transactions on systems, man, and cybernetics. vol. 23, no. 5. septemberioctober 1993

[15] **F. Z. Kebbab, D. E. C. Belkhiat, D. Jabri, S. Belkhiat (2018)** "Frequency Speed Control of Rotary Travelling Wave Ultrasonic Motor Using Fuzzy Controller" Engineering Technology & Applied Science Research ,volume . 8, No. 4, 2018, pp 3276-3281

[16] **Z. Boumous , S.Belkhiat, F.Z Kebbab (2009)** "Effect of shearing deformation on the transient response of a traveling wave ultrasonic motor". Sensors and Actuators A, volume 150 , 2009, pp 243–250.

Creative Commons Attribution-NonCommercial-NoDerivatives 4.0 International License (CC BY-NC-ND)

Algerian Journal of Engineering Architecture and Urbanism Vol. 5 Nr. 3 2021
ISSN: 2588-1760

UNE NOUVELLE MAPPE DE QUALITÉ POUR LE DÉROULEMENT DE PHASE DE L'INSAR

Tarek Bentahar
Laboratoire LABGET, Université de Larbi Tébessi-Tébessa-Algérie
tarek.bentahar@univ-tebessa.dz

Atef Bentahar
Laboratoire LAMIS, Université de Larbi Tébessi-Tébessa-Algérie
atef.bentahar@univ-tebessa.dz

Riad Saidi
Laboratoire LABGET, Université de Larbi Tébessi-Tébessa-Algérie
riad.saidi@univ-tebessa.dz

Résumé :
Dans cet article, une nouvelle mappe de qualité basée sur une modification de la mappe de la variance de la dérivée de la phase est proposée. Comme cette mappe proposée fournit plus détails sur les variations locales de l'interférogramme notamment pour les franges et les bords, le déroulement de phase pourrait être plus précis et fiable. L'influence de telle mappe de qualité se manifeste substantiellement sur les régions de forte densité des résidus. Pour prouver l'efficacité de notre proposition, le test a été réalisé sur des données satellitaires réelles et la comparaison a été faite selon plusieurs métriques pertinentes.

Mots-clés : Interférogramme InSAR, Déroulement de phase, Mappe de qualité.

1- Introduction

Depuis plusieurs décennies, les chercheurs ont porté; et portent encore, un grand intérêt à la surveillance et à l'acquisition d'informations sur la surface terrestre. Cet axe est considéré comme l'une des applications radar les plus importantes [1]. Par rapport au système d'imagerie optique, l'imagerie radar est un système actif grâce à sa propre source d'illumination qui est l'onde électromagnétique. Cette propriété permet au système de fonctionner le jour comme la nuit et dans toutes les conditions météorologiques. Parmi les systèmes d'imagerie radar, le radar à ouverture synthétique interférométrique (inSAR en Anglais) a la capacité d'exploiter les informations de phase en utilisant la technique d'interférométrie. Son principe de fonctionnement est basé sur une double acquisition du signal rétrodiffusé à l'aide soit de deux antennes séparées par une ligne de base en un seul passage (appelé mode un mono-passe), soit d'une antenne et deux passes (appelé mode multi-passes) [2]. L'image de phase résultante est précisément dite l'image de phase interférométrique ou plus couramment « interférogramme ». En mode multi-passes, la dé-corrélation temporelle générée est exploitée pour les applications de détection des changements ou des déformations de la surface [3,4]. Alors que la dé-corrélation spatiale est exploitée dans le mode mono-passe, ce qui le rend appropriée pour la cartographie terrestre et la génération des modèles numériques du terrain (DEM en Anglais) [5,6].

Creative Commons Attribution-NonCommercial-NoDerivatives 4.0 International License (CC BY-NC-ND)

La matière brute (Interférogramme) n'est pas directement exploitable le fait que toutes les phases sont déroulées dans l'intervalle $(-\pi,+\pi]$. Pour calculer la phase réelle qui interprète correctement l'élévation du point imagé le processus de déroulement de phase doit être exécuté. Sans résidus, l'interférogramme est facilement déroulé par une accumulation (somme) des gradients roulés. Malheureusement, les interférogrammes sont inévitablement bruités par les résidus. Dans ce cas, l'utilisation du processus de base sans tenir en compte la présence des résidus est inutile parce que le décalage de phase créé par un résidu se propagera le long du parcours choisi. Donc, le déroulement de phase doit tenir en compte le problème des résidus. Durant plus de quatre décennies, plusieurs algorithmes de déroulement de phase ont été proposés [7]. Parmi ces algorithmes nous trouvons la classe de « Guidée par la Qualité » « *Quality-Guided Phase Unwrapping* »(QGPU) [8-15]. Dans cette classe d'algorithmes, le parcours d'intégration optimal est choisi en fonction de la qualité des pixels impliqués pour le calcul de la phase réelle. Pour ce but, une autre information supplémentaire doit être utilisée qui est généralement une mappe dite la mappe de qualité [16]. Parmi ces mappes nous trouvons : la cohérence ou encore les coefficients de corrélation (CC) qui est systématiquement fournie par le système InSAR, le gradient conventionnel, la variance de la dérivée de la phase (PDV) [17], la pseudo-corrélation (PC) [18], la cooccurrence du niveau de gris [19], une mappe basée les régions connectées [20] et le maximum gradient MG [21].

Dans ce travail, nous proposons une nouvelle mappe de qualité déduite d'une nouvelle stratégie de calcul de la variance des dérivées. La modification concerne le sens (direction) et le nombre des dérivées calculées dans une fenêtre 3x3. Le reste de l'article est organisé comme suivant : Section 2 est pour donner une généralité sur le système InSAR et ses images en particulier les intergérogrammes. Dans la section 3, l'entité des résidus et la propagation de leurs erreurs sont expliqués. Dans la section 4, quelques techniques pionnières de déroulement de phase sont présentées ; en particulier, celles de la classe QG. La section 5 est consacrée à expliquer la mappe proposée et à révéler la différence entre elle et la PDV ordinaire. Dans la section 6, nous présentons l'implémentation de la mappe proposée et autres mappes largement répandues et nous discutons les résultats obtenus. Finalement, la section 7 conclue l'article en révélant les principaux points déduits.

2- Généralité sur l'imagerie InSAR.

SAR et InSAR sont deux systèmes d'imagerie radar capables de fournir l'image d'amplitude. La différence entre SAR et InSAR est dans la double acquisition du signal rétrodiffusé sous deux angles différents. Les deux acquisitions sont séparées par une petite distance appelée ligne de base. Alors, deux manières sont possibles : une seule antenne et deux passages ou deux antennes et un passage. Dans la première, la dé-corrélation temporelle est engendrée ce qui rend ce mode pertinent pour les applications de détection de changement. Alors que la seconde engendre la dé-corrélation spatiale et par conséquent les applications de topographie sont les plus pertinentes. Le fait que le signal est auto-interféré, toutes les phases seront soustraites sauf la différence de la phase du trajet. Cette différence trajectoire de la phase est dite interférométrique et l'image correspondante est dite interférogramme. La figure 1 montre un exemple d'image d'amplitude, l'interférogramme et l'image de cohérence. L'image d'amplitude est une image d'intensité de la rétrodiffusion, elle dépend de la nature et l'orientation du point imagé. La cohérence est une image qui mesure le degré de corrélation entre les deux signaux reçus, elle est considérée comme une mappe de qualité de mesure. L'image d'interférogramme est l'image de différence de phase interférométrique, elle dépend du trajet et donc géométriquement elle peut interpréter l'élévation du point image. Toutes les

Creative Commons Attribution-NonCommercial-NoDerivatives 4.0 International License (CC BY-NC-ND)

Algerian Journal of Engineering Architecture and Urbanism Vol. 5 Nr. 3 2021
ISSN: 2588-1760

phases dans un interférogramme sont roulées dans l'intervalle (–π,+π]. L'opération de roulement n'est pas le modulo, le modulo donne des valeurs entre 0 et 2π. Cependant, il y a relation entre ces deux opérateurs comme il est montré par l'équation 1.

$$\phi^{W} = \mathrm{Wrap}(\phi^{r}) = \mathrm{Mod}_{2\pi}(\phi^{r} + \pi) - \pi \quad (1)$$

Avec ϕ^{r} et ϕ^{w} sont respectivement la phase réelle et la phase roulée.

En tant donné que les phases sont limitées dans l'intervalle (–π,+π], la forme des franges caractérise les interférogrammes (voir figure 1). Les pixels noirs et blancs correspondent respectivement à –π et +π, et les autres pixels sont graduellement gris selon la valeur de la phase. Les franges ne sont pas stationnaires et leurs fréquences sont variables. En plus, les régions incohérentes à cause de fort bruit possèdent des franges ambigües.

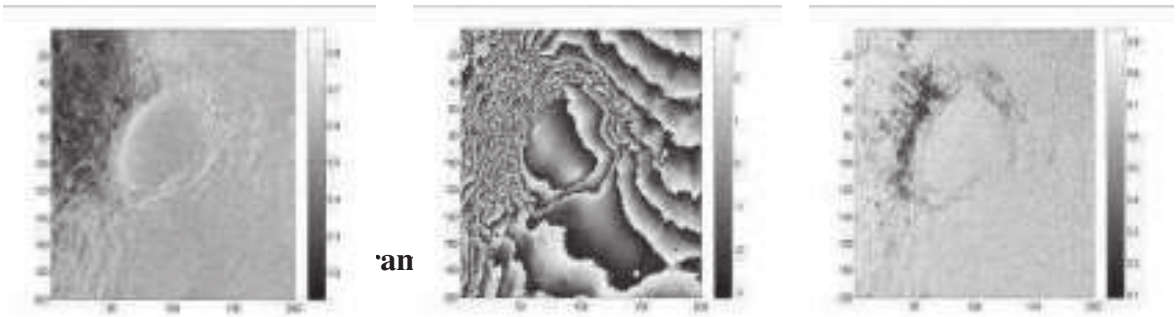

(a) (b) (c)

Figure 1. Exemple d'images InSAR : (a) Amplitude, (b) Interférogramme, (c) Cohérence

Le bruit qui affecte les interférogrammes appelé résidus. Ils sont dû aux sauts de phase engendrés par les régions incohérente telles que les zones d'ombre, inversion, accumulation ou par les erreurs de système. La figure 2 (a) et (b) montre l'interférogramme précédent et sa mappe des résidus correspondante. Pour détecter un résidu dans un interférogramme, la somme des gradients roulés dans une boucle 2x2 doit être calculée. L'équation 2 montre ce propos.

$$R = \frac{1}{2\pi}\sum\left(\mathrm{Wrap}\left(\phi^{W}_{i+1,j} - \phi^{W}_{i,j}\right) + \mathrm{Wrap}\left(\phi^{W}_{i+1,j+1} - \phi^{W}_{i+1,j}\right) + \mathrm{Wrap}\left(\phi^{W}_{i,j+1} - \phi^{W}_{i+1,j+1}\right) + \mathrm{Wrap}\left(\phi^{W}_{i,j} - \phi^{W}_{i,j+1}\right)\right) \quad (2)$$

$$\phi^{W}_{i,j} = \phi^{W}_{n(i,j)} + Wrap\left(\phi^{W}_{i,j} - \phi^{W}_{n(i,j)}\right) \quad (3)$$

Le processus de base de déroulement de phase consiste à cumuler les gradients roulés dans un parcours comme il est montré par l'équation (3). Il est clair qu'à partir de n'importe quel pixel déjà déroulé on peut dérouler un pixel voisin. Mais, si ce processus traverse un résidu, un décalage (erreur) de phase se créera et cette erreur va se propager le long du parcours d'intégration choisi en calculant les pixels suivants. La figure 2(c) montre l'image de phase déroulée de même intérférogramme en utilisant le processus de base.

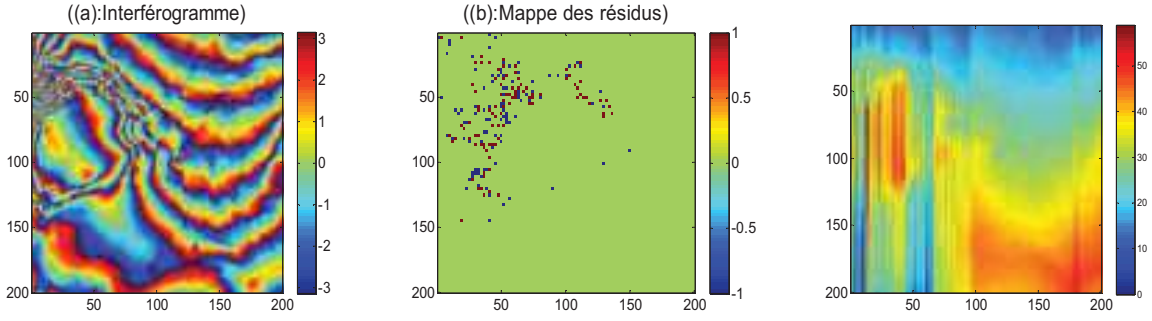

Figure 2, l'effet des résidus : a) Interférogramme, b) Mappe des résidus, c) Image déroulée par le processus de base.

4- Le déroulement de phase et mappes de qualité

Creative Commons Attribution-NonCommercial-NoDerivatives 4.0 International License (CC BY-NC-ND)

Pour que le déroulement soit immunisé aux résidus et le problème de la propagation d'erreur soit évité, le calcul de la phase doit tenir en compte la présence des résidus. Les algorithmes de déroulement adaptés aux résidus se catégorisent en trois grandes catégories I) Suivi du parcours, II) méthodes basées sur l'optimisation et III) dé-bruiter & dérouler [7]. La première catégorie se divise elle-même en deux sous-catégories : coupures en branches et déroulement guidé par la qualité. La deuxième est également divisée en deux sous-catégories : optimisation basée sur les statistiques et norme de minimisation. La figure 3 montre un diagramme de la catégorisation des méthodes de déroulement. La stratégie se diffère d'une catégorie à l'autre. Par exemple, les méthodes BC établissent des barrières appelées coupures des branches pour empêcher l'intégration à traverser les résidus. Ce processus (déroulement en évitant les branches) est dit Remplissage par Inondation ou encore par diffusion (*Flood-Fill*). Tandis que les méthodes QG guident le processus de base seulement dans les pixels de bonne qualité en utilisant une mappe de qualité comme référence. Les pixels de mauvaise qualité sont les derniers à dérouler. Les méthodes d'optimisation suivent une stratégie totalement différente qui est généralement un traitement global. L'objectif des méthodes d'optimisation est de minimiser la différence entre le gradient de la phase roulée et celui de la phase déroulée par le processus de base. Pour ce but, les méthodes statistiques changent la valeur de certaines phases en des fonctions statistiques pour estimer les valeurs convenables. Alors que les méthodes MN essayent de minimiser la différence en basant sur des techniques issues des méthodes numériques. Les méthodes dé-bruiter & dérouler ; comme leur nom indique, essayent de filtrer l'interférogramme définitivement des résidus puis les phases seront facilement déroulées.

Les mappes de qualité ne sont pas seulement utilisées dans les méthodes QG, certains algorithmes les utilisent pour concevoir un masque couvrant les résidus au lieu des branches [22]. Elles sont également utilisées dans certaines méthodes MN pour la pondération telle que [23] et certaines techniques de filtrage [24]. La figure 4 montre les mappes d'interférogramme susmentionné qui sont utilisées dans notre comparaison.

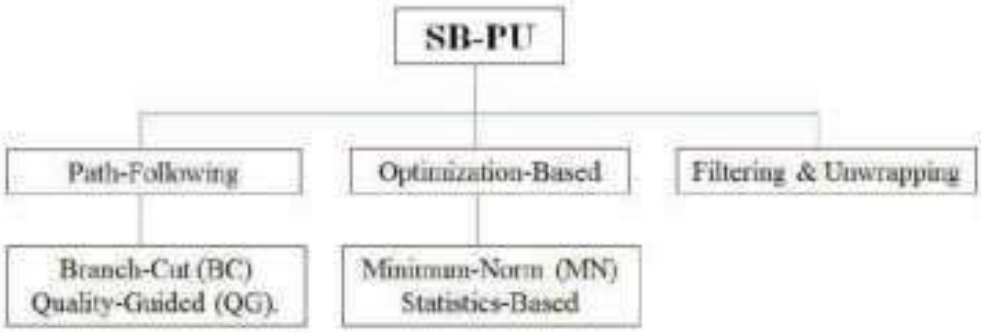

Figure 3 : les catégories de déroulement de phase à ligne de base unique.

Creative Commons Attribution-NonCommercial-NoDerivatives 4.0 International License (CC BY-NC-ND)

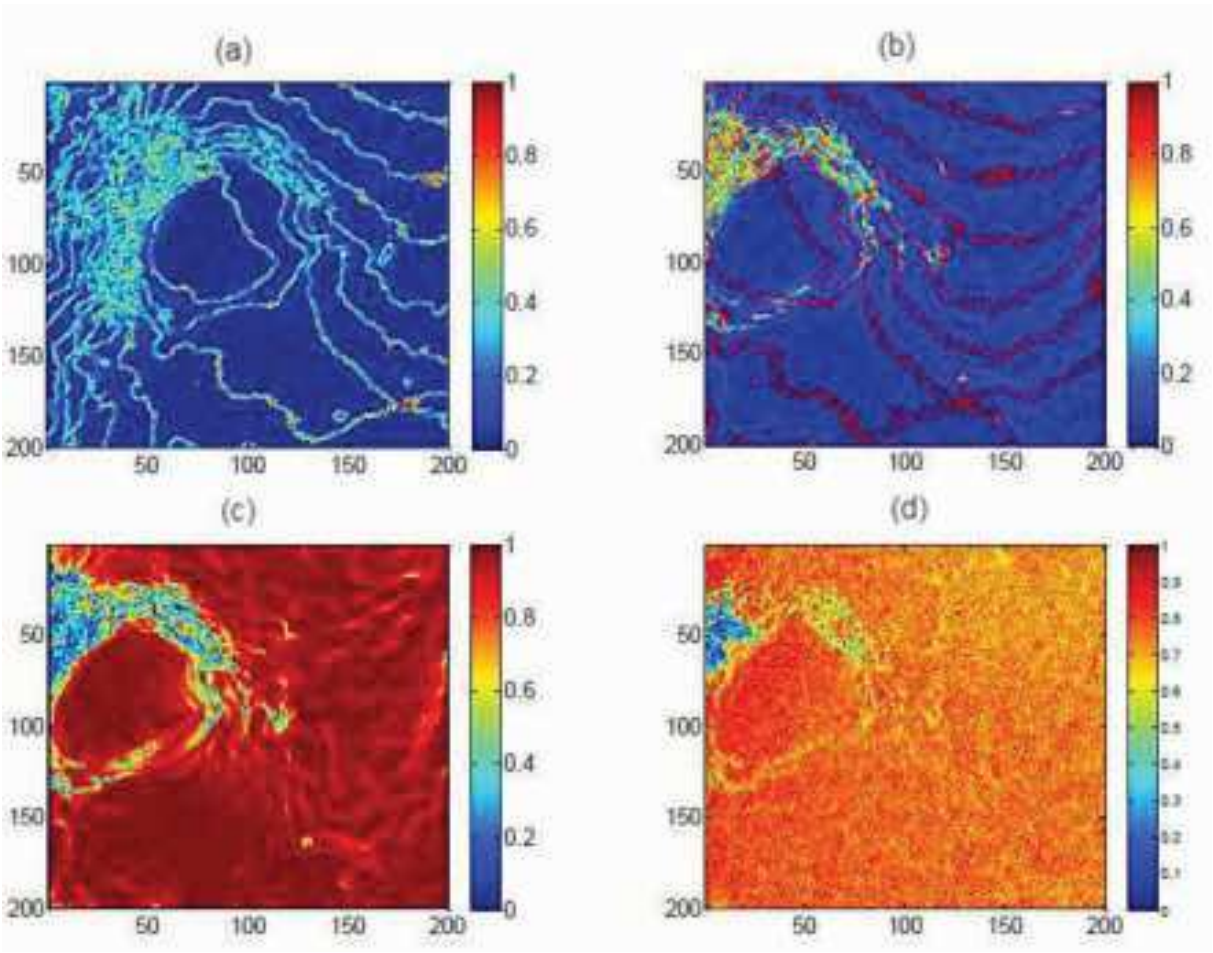

Figure 4, Mappe de qualité, a) PDV, b) MG, c) PC, d) CC.

5- La mappe proposée

La mappe PDV conventionnelle est calculée par la variance des dérivées locales (dans une fenêtre) selon deux sens (vertical et horizontal). En plus, les dérivées sont calculées par des différences successives c.-à-d. Le pixel courant moins le pixel précédent (voir équation 4 et figure 5a). Autrement dit, deux sens et quatre dérivées sont considérées dans la PDV conventionnelle. Notre proposition consiste à porter des modifications qui concernent le sens et le nombre des dérivées impliqués dans le calcul. Nous proposons de calculer les dérivées par rapport au pixel central au lieu les différences successives, car c'est le pixel central qui est référentiel et qui indiquera la qualité. Nous proposons de calculer huit dérivées au lieu quatre, car tous les huit pixels voisins de la fenêtre contribuent à attribuer la qualité au pixel central. Ce propos est montré dans la figure 5b.

Ces modifications peuvent donner plus de détails sur les variations locales critiques telles les franges. Effectivement, les franges dans la mappe proposée sont protubérantes comme il est montré dans la figure 6 par rapport à ce qu'il est dans la figure 4a.

$$PDV_{mn} = \frac{\sqrt{\sum(\Delta^x_{i,j} - \overline{\Delta^x_{m,n}})^2} + \sqrt{\sum(\Delta^y_{i,j} - \overline{\Delta^y_{m,n}})^2}}{k^2} \quad (4)$$

Creative Commons Attribution-NonCommercial-NoDerivatives 4.0 International License (CC BY-NC-ND)

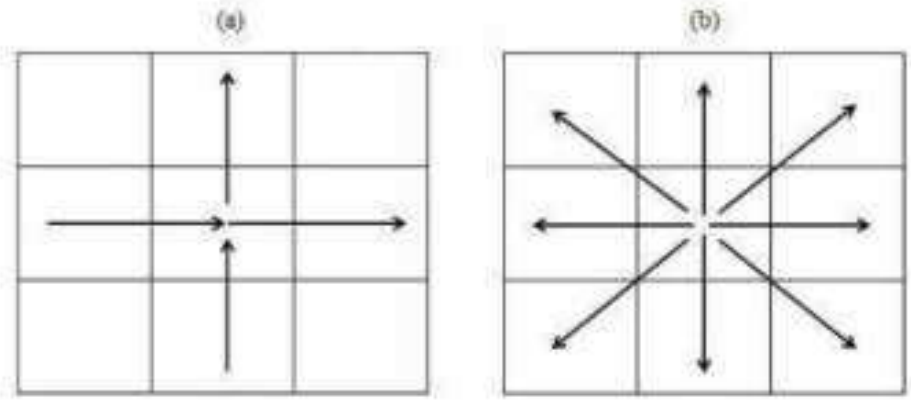

Figure 5 le sens et le nombre des dérivées dans :a) PDV conventionnelle, b) la mappe proposée.

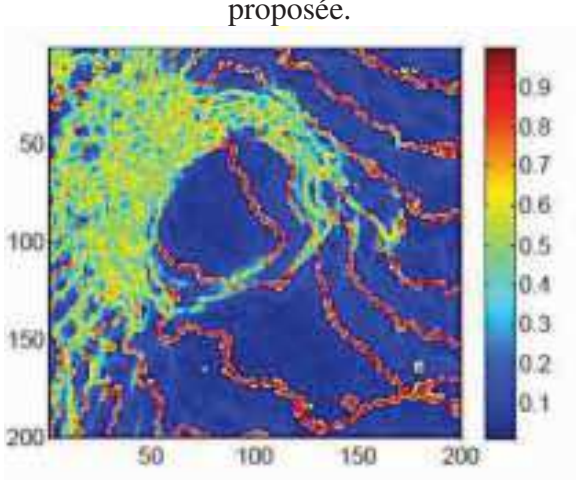

Figure 6, la mappe proposée.

6- Résultats et discussion

Le même interférogramme précédent est utilisé pour le test. Le déroulement de phase de la catégorie QG décrit dans [25] est implémenté avec les quatre mappes de qualité PDV, MG, PC, CC et ainsi que la mappe proposée. Visuellement, les images déroulées avec les cinq mappes ont une qualité visuelle (analyse informelle qualitative) proche. Pour cette raison, nous avons seulement illustré l'image déroulée en utilisant notre mappe proposée (figure 7). Pour une analyse quantitative, les métriques utilisées sont : MSE, SSIM, Points de discontinuité basée sur le gradient (ici noté DP-G)[26], Points de discontinuité basée sur la condition d'Itho (ici noté DP-I) , et ε [21]. Les deux premières sont très connues et répandues dans le domaine du traitement d'image en général, et les trois dernières sont typiquement pour le déroulement de phase. Sauf SSIM, plus la valeur de la métrique est petite, plus le déroulement est précis. Le tableau 1 résume les résultats obtenus en termes de ces métriques. Il s'est montré que le déroulement avec la mappe proposé a des valeurs satisfaisantes ; grand SSIM et petits DP-G, DP-I et ε.

Creative Commons Attribution-NonCommercial-NoDerivatives 4.0 International License (CC BY-NC-ND)

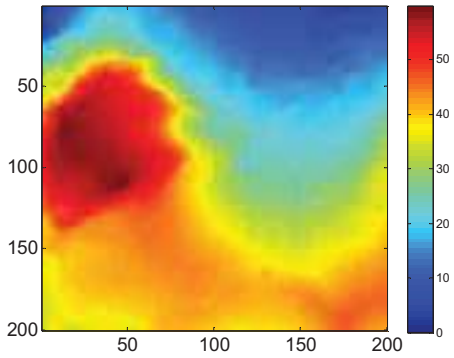

Figure 7, l'image déroulée par QG en utilisant la mappe proposée.

	PC	MG	PDV	CC	Mappe-Proposée
MSE	0.038	0.033	0.033	0.026	0.021
SSIM	0.864	0.897	0.917	0.922	0.927
DP-G (%)	0.743	0.706	0.655	0.392	0.171
DP-I (%)	0.235	0.177	0.097	0.046	0.032
ε	2.813	2.576	2.570	1.987	1.546

Tableau 1, les résultats obtenus en termes des métriques quantitatives.

7- Conclusion

Dans cet article, nous avons proposé une nouvelle mappe de qualité pour le déroulement de phase d'interférogramme inSAR. Notre proposition est dérivée de la mappe PDV conventionnelle avec des modifications dans le sens et le nombre des dérivées impliquées. Le test a été réalisé sur un interférogramme réel fourni par ESA ERS-1 et la comparaison a été faite avec quatre autres mappes largement utilisées. Les métriques adoptées sont aussi variés et pertinentes. Notre proposition a donné des résultats satisfaisants selon les cinq métriques utilisées.

8- Références

[1] Raney, K. (2014). Radar, Altimeters. In Encyclopedia of Remote Sensing (pp. 525–532). Springer New York.
[2] Moreira, A., Prats-Iraola, P., Younis, M., Krieger, G., Hajnsek, I., & Papathanassiou, K. P. (2013). A tutorial on synthetic aperture radar. IEEE Geoscience and Remote Sensing Magazine, 1(1), 6–43.
[3] Osmanoğlu, B., Sunar, F., Wdowinski, S., & Cabral-Cano, E. (2016). Time series analysis of InSAR data: Methods and trends. ISPRS Journal of Photogrammetry and Remote Sensing, 115, 90–102.
[4] Monserrat, O., Crosetto, M., & Luzi, G. (2014). A review of ground-based SAR interferometry for deformation measurement. ISPRS Journal of Photogrammetry and Remote Sensing, 93, 40–48.
[5] Hoja, D., Reinartz, P., & Schroeder, M. (2007). Comparison of DEM generation and combination methods using high resolution optical stereo imagery and interferometric SAR data. Revue française de photogrammétrie et de télédétection, 2006(4), 89-94.
[6] Geymen, A. (2012). Digital elevation model (DEM) generation using the SAR interferometry technique. Arabian Journal of Geosciences, 7(2), 827–837.
[7] Yu, H., Lan, Y., Yuan, Z., Xu, J., & Lee, H. (2019). Phase Unwrapping in InSAR : A Review. IEEE Geoscience and Remote Sensing Magazine, 7(1), 40–58.
[8] Wei Xu, & Cumming, I. (1999). A region-growing algorithm for InSAR phase unwrapping. IEEE Transactions on Geoscience and Remote Sensing, 37(1), 124–134.
[9] Herráez, M. A., Burton, D. R., Lalor, M. J., & Gdeisat, M. A. (2002). Fast two-dimensional phase-unwrapping algorithm based on sorting by reliability following a noncontinuous path. Applied Optics, 41(35), 7437.

Creative Commons Attribution-NonCommercial-NoDerivatives 4.0 International License (CC BY-NC-ND)

[10] Abdul-Rahman, H. S., Gdeisat, M. A., Burton, D. R., Lalor, M. J., Lilley, F., & Moore, C. J. (2007). Fast and robust three-dimensional best path phase unwrapping algorithm. Applied Optics, 46(26), 6623.
[11] Zhong, H., Tang, J., Zhang, S., & Chen, M. (2011). An Improved Quality-Guided Phase-Unwrapping Algorithm Based on Priority Queue. IEEE Geoscience and Remote Sensing Letters, 8(2), 364–368.
[12] Dai, Z., & Zha, X. (2012). An Accurate Phase Unwrapping Algorithm Based on Reliability Sorting and Residue Mask. IEEE Geoscience and Remote Sensing Letters, 9(2), 219–223.
[13] Zhong, H., Tang, J., Zhang, S., & Zhang, X. (2014). A Quality-Guided and Local Minimum Discontinuity Based Phase Unwrapping Algorithm for InSAR/InSAS Interferograms. IEEE Geoscience and Remote Sensing Letters, 11(1), 215–219.
[14] Jian, G. (2016). Reliability-Map-Guided Phase Unwrapping Method. IEEE Geoscience and Remote Sensing Letters, 13(5), 716–720.
[15] Wang, H., Tong, L., Li, Y., & Xiao, F. (2019, July). Phase Unwrapping Algorithm Based on Improved Weighted Quality Graph. IGARSS 2019 - 2019 IEEE International Geoscience and Remote Sensing Symposium.
[16] Zhao, M., Huang, L., Zhang, Q., Su, X., Asundi, A., & Kemao, Q. (2011). Quality-guided phase unwrapping technique: comparison of quality maps and guiding strategies. Applied Optics, 50(33), 6214.
[17] Wang, Y., Huang, H., & Wu, M. (2014, May). A new phase unwrapping method for interferograms with discontinuities. 2014 IEEE Radar Conference.
[18] Xiao Feng, Wu Jicang, Zhang Lei, & Li Xiaoling. (2007). A new method about placement of the branch cut in two-dimensional phase unwrapping. 2007 1st Asian and Pacific Conference on Synthetic Aperture Radar.
[19] Liu, G., Wang, R., Deng, Y., Chen, R., Shao, Y., & Yuan, Z. (2014). A New Quality Map for 2-D Phase Unwrapping Based on Gray Level Co-Occurrence Matrix. IEEE Geoscience and Remote Sensing Letters, 11(2), 444–448.
[20] Zhang, T., Lv, X., & Hong, J. (2016, July). A novel interferogram quality assessment index based on connected area. 2016 IEEE International Geoscience and Remote Sensing Symposium (IGARSS).
[21] Man, Y., Goulin, L., & Huadong, H. (2010, December). Comparison among Quality Maps Applying in Phase Unwrapping for Different Terrain. 2010 International Conference on Computational and Information Sciences.
[22] Flynn, T. J. (n.d.). Consistent 2-D phase unwrapping guided by a quality map. IGARSS '96. 1996 International Geoscience and Remote Sensing Symposium
[23] Flynn, T. J. (1997). Two-dimensional phase unwrapping with minimum weighted discontinuity. Journal of the Optical Society of America A, 14(10), 2692.
[24] Bentahar, T., Benatia, D., & Boulila, M. (2016). De-noising interferogram inSAR using variance and absolute deviation functions. World Journal of Engineering, 13(2), 169–176.
[25] Ghiglia D. C. and Pritt M. D., Two-Dimensional Phase Unwrapping: Theory, Algorithms, and Software. New York: Wiley, 1998.
[26] Wang, H., Tong, L., Li, Y., & Xiao, F. (2019, July). Phase Unwrapping Algorithm Based on Improved Weighted Quality Graph. IGARSS 2019 - 2019 IEEE International Geoscience and Remote Sensing Symposium.

Creative Commons Attribution-NonCommercial-NoDerivatives 4.0 International License (CC BY-NC-ND)

Algerian Journal of Engineering Architecture and Urbanism Vol. 5 Nr. 3 2021
ISSN: 2588-1760

Analyze performances energetic of a diesel engine overfed by water injection in the channel of admission.

NEZLIOUI FERROUDJA
PhD student, Mech, Laboratory of Mechanics, Materials and Energetic (L2ME).Faculty of Technology, University of Bejaia, 06000 Bejaia, Algeria. **Email:** nezliouiferroudja27@hotmail.com.
BENSLIMANE ABDELHAKIM
Lecturer, Dr, Mech, Laboratory of Mechanics, Materials and Energetic (L2ME).Faculty of Technology, University of Bejaia, 06000 Bejaia, Algeria. **Email:** benslimane.ah@gmail.com.
HAMTACHE BRAHIM
Lecturer, Dr, Mech, Laboratory of Mechanics, Materials and Energetic (L2ME).Faculty of Technology, University of Bejaia, 06000 Bejaia, Algeria. **Email:** bhamtache@yahoo.fr.

Abstract: This work consisted in evaluating the energy performances of a diesel engine overfed D-245 by water injection in the channel of admission. They had aim was to compare its performances with those obtained during operation without water injection. On the basis of model of developed calculation, the parameters of the fresh load are given when water is provided until a flow of 6.8 kg/h. The results obtained, after the analysis and the comparison between the system injection without and with the water vapor show a reduction in the temperature of the fresh load has the value of 35C, and an increase light in the effective output at the point of flow 1 kg/h. another advantage of the system is had in work, is the growth of the mechanical output, which is due to the reduction in frictions in the cylinders.
Key words: Performances of the engine, injection of water in the channel of admission, parameters energy, diesel engine D-245.

Introduction

The water injection, by various ways (in the circuit of admission, directly in the combustion chamber with a separate injector or in emulsion with the fuel…) is a means used on the gas turbines and unquestionable diesel engine industrial, for example in marine propulsion, to reduce the NO_x emissions by fall in the temperature of combustion. The current tendency to the reduction of cubic capacity of the engines ("down-sizing") to reduce consumption leads to an increase in the average charge and it thus seems relevant to evaluate the potential of the water (Shah 2011). For that a theoretical study is made by modeling a model in order to determine the quantity of water to inject. Then, we will present the choice of the device used for the study, in order to show the influence of the injection with water on the various parameters thermodynamics of the driving cycle.

Problematic

The modern diesel engines become increasingly complex, and also severely subjected to international standards constantly updated in terms of consumption and respect of the environment. The least defect in these engines can generate a degradation of its performances as well as an increase in its pollutant emissions; from where the interest to develop a dynamic model, to analyze and include/understand the processes of degradation with an aim of improving the output. Later on with the scientific development, the water injection in the internal combustion engines is a technique is taken into account in the field of automobile and

Creative Commons Attribution-NonCommercial-NoDerivatives 4.0 International License (CC BY-NC-ND)

industrial research. Indeed it is regarded as one of the possible solutions technical, because it makes it possible to make Function the engine with higher compression ratios and stoechiometric combustions with strong load, which involves a fall of the specific fuel consumption on the general chart of the engine and the increase in the power of exit obtained. Thus, it allows the reduction in N_{ox} from an environmental point of view, can be interpreted as being the result of the temperature drop of combustion.

Materials and methods:

The method suggested in this system is to inject water, by using a pneumatic tube which is used to control the quantity of water provided by the feeding attachment, after the injection in the channel of admission water is pulverized with the compressed air. During the compression of the air in a turbo compressor part of heat of the load is consumed for the heating and evaporation of water in the air, which spirit a reduction in air and increases the density of the fresh load.

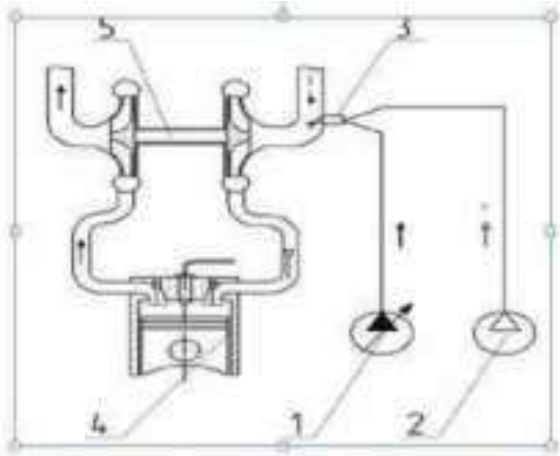

1- Water feeling attachement
2- Compressor
3- Pneumatic injector
4- Cylinder engine
5- Turbo compressor

Fig.1. System of water injection in an overfed diesel engine

Characteristics of the Engine: For this study, we have chooses the D-245 engine from where these characteristics are illustrated in the tables below

Parameters	Values
Numbers of cylinder	4
Piston stroke S (mm)	125
Cylinder bore D (mm)	110
The total cubic capacity of engine VI (l)	4.75
Compression ration E	19.1
Specific consumption of the fuel ge (g/kWh)	220
The Power Ne (kW)	77
Number of revolutions n (tr/min)	2200
The maximum couple N.m	381
Pressure of the compressed air Pk (MPA)	0.170
Coefficient of excess of air α	1.95

Table.1. Drive technical D 245 engine.

Temperature of the compressed air after water injection

The equation of the mixture of air with the water parameters can be expressed:

$$g_w h_w + g_a h_a = g_w h'_w + g_a h'_a.$$

Creative Commons Attribution-NonCommercial-NoDerivatives 4.0 International License (CC BY-NC-ND)

The difference in enthalpy of air before and after the mixture

$$h_a - h'_a = Cp_a\left(T_k - T'_k\right)$$

$$g_a\left(h_a - h'_a\right) = g_w\left(h'_w - h_w\right)$$

$$h_a - h'_a = \frac{g_w}{g_a}\left(h'_w - h_w\right)$$

While replacing h_a, h'_a by his expression, one obtains the temperature of cooling of the air.

$$\frac{g_w}{g_a}\left(h'_w - h_w\right) = Cp_a\left(T_k - T'_k\right)$$

$$T_k - T'_k = \frac{g_w}{g_a}\frac{1}{Cp_a}\left(h'_w - h_w\right)$$

$$T'_k = T_k - \frac{g_w}{g_a}\frac{1}{Cp_a}\left(h'_w - h_w\right)$$

Under the conditions of vaporization of water and the formation of the overheated vapor; the difference in enthalpy is expressed:

$$h'_w - h_w = Cp_w\left(T'_s - T_{inj}\right) + r + Cp'_w\left(T'_k - T'_s\right).$$

The analysis of the quoted formula enables us to conclude:

Cp_w , $Cp'_w \ll r$, Thus in an interval which is not also large (reasonable), the variations in temperature connecting the two heat-storage capacities can be neglected.

Into consequent the temperature of cooling of the air can be determined by the formula

$$T'_k = T_k - \frac{g_w}{g_a}\frac{1}{Cp_a}.r$$

$$T'_k = T_k - \frac{G_w}{G_a}\frac{1}{Cp_a}.r$$

$$G_a = \alpha G_T l_0$$

Parameters of gas and fuel

The air flow is calculated as follows, One calculates initially the time consumption of fuel G_T (kg/h):

$$G_T = N_e g_e.10^{-3}$$

Theoretical quantity of air necessary for the combustion of fuel 1kg

$$l_0 = \frac{1}{0.23}\left(\frac{8}{3}c + 8H - \mathrm{O}\right)$$

Into the case of the water vapor is not injected:

$$M_1 = \alpha L_0$$

In this case, it is necessary to take into account the presence of the water vapor in the load fresh (with the air). Where

$$M_1 = \alpha L_0 + \frac{G_w}{G_T \mu_w}$$

The total molar quantity of the products of combustion in the case, the vapor of water is not injected:

$$M_2 = \alpha L_0 + \frac{H}{4} + \frac{\mathrm{O}}{32}$$

Into the case, the water vapor is injected:

$$M_2 = \alpha L_0 + \frac{H}{4} + \frac{\mathrm{O}}{32} + \frac{G_w}{G_T \mu_w}$$

Creative Commons Attribution-NonCommercial-NoDerivatives 4.0 International License (CC BY-NC-ND)

The coefficient of the chemical molecular change of gas after combustion:

- Into the case vapor of water is not injected:

$$\beta_0 = \frac{M_2}{M_1}$$

- Into the case, the water vapor is injected:

$$\beta_{'0} = \frac{M_{'2}}{M_1}$$

Parameters of the atmospheric conditions and residual gases:

$p_k = (1.5 \ldots . 2.2)$ Average overfeeding

$$T_K = T_0 \left(\frac{p_k}{p_c} \right)^{\frac{n_2 - 1}{n_1}}$$

Process of admission

Density of the air to the admission

$$\rho_k = \frac{p_k.10^6}{\Gamma_k.T_k}$$

Pressure losses to the admission

$$\Delta P_a = \left(\beta^2 + \xi_a\right)\frac{wa^2}{2}\rho_k.10^{-6}$$

$$\Delta P_a = 3,25.\frac{75^2}{2}.1,76.10^{-6}$$

$$p_a = p_k - \Delta pa$$

The coefficient of résiduel gases

$$\gamma_r = \frac{T_K + \Delta T_K}{\sigma_r}.\frac{p_r}{\varepsilon p_a - p_r}$$

The temperature at the end of the admission

$$T_a = \frac{T_K + \Delta T + \gamma_r T_r}{1 + \gamma_r}$$

Compression

$$p_c = p_a \varepsilon^{n_1}$$

$$T_c = T_a \varepsilon^{n_1 - 1}$$

Heat-storage capacity of the load fresh at the end of compression

$$\mu C_{Vc} = \gamma_a \mu C_{Va} + \left(1 - \gamma_a\right)\mu C_{VW}$$

$$\mu C_{Va} = 20,16 + 1,74.10^{-3} T_C\,[KJ/Kg.k]$$

$$\mu C_{VW} = 28,75 + 6,25.10^{-3} T_C\,[KJ/Kg.k]$$

Combustion

Average molar heat-storage capacity of the products of combustion:

Creative Commons Attribution-NonCommercial-NoDerivatives 4.0 International License (CC BY-NC-ND)

$$\mu C_{pz} = 8,314 + \left(20,2 + \frac{0,92}{\alpha}\right) + \left(15,5 + \frac{13,8}{\alpha}\right).10^{-4} T_z$$

Molar quantity of the products of combustion

$$M_z = M_c + M_r$$

The coefficient of the change real molecular change of the mixture

$$\beta = \frac{M_z}{M_c}$$

Thermal output to gases

$$\Phi = \xi \Phi_M + 42.500(0.7 .....0.9)$$

The temperature at the end of combustion is determined starting from the equation

$$\beta \mu C_{pz} T_z = \frac{\xi \Phi_M}{M_C} + T_c\left(\mu C_{VC} + R\lambda\right)$$

While posing:

$$C = \frac{\xi \Phi_M}{M_C} + T_c\left(\mu C_{VC} + R\lambda\right)$$

Heat-storage capacity of the water vapor

$$\mu C_{Vw} = 28,75 + 6,25.10^{-3} T_C$$

That of the products of combustion

$$\mu C_{pz} = R + \left(20,2 + \frac{0,92}{\alpha}\right) + \left(15,5 + \frac{13,8}{\alpha}\right).10^{-4} T_z$$

Therefore, heat-storage capacity of the mixture of the products of combustion with the water vapor is:

$$\mu C_{pz} = r_w + 28,75 + \left(1 - r_w\right)\left(20,2 + \frac{0,92}{\alpha}\right) + R + \left[\left(r_w.6,25.10^{-3} + \left(1 - r_w\right)\left(15,5 + \frac{13,8}{\alpha}\right).10^{-4}\right]T_z\right.$$

Relaxation

The rate of posterior relaxation

$$\sigma = \frac{\varepsilon}{\rho}$$

The exhibitor polytrophic of relaxation

$$n_2 = 1,18 + \frac{130}{n}$$

$$p_b = \frac{p_z}{\sigma^{n_2}}$$

$$T_b = \frac{T_z}{\sigma^{n_2 - 1}}$$

RESULTS AND DISCUSSIONS

Temperature of the fresh load after water injection.

The figure2 illustrates the variation in the temperature of the fresh load according to the water flow.

Creative Commons Attribution-NonCommercial-NoDerivatives 4.0 International License (CC BY-NC-ND)

Algerian Journal of Engineering Architecture and Urbanism Vol. 5 Nr. 3 2021
ISSN: 2588-1760

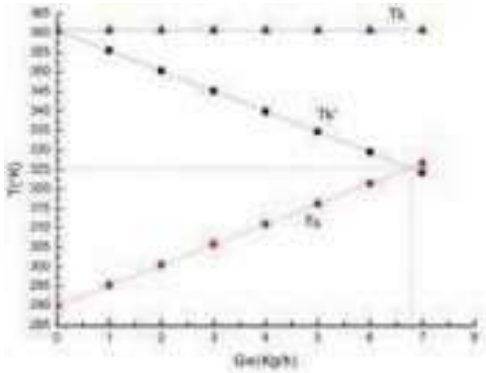

Fig.2. Variation in the temperature of the fresh lad a according to the water

According to the graph above, the point of intersection of the graphs of the temperatures of the fresh load Tk' and temperature of Ts' saturation determine the maximum quantity of water evaporated at the entry and the corresponding optimal reduction of the temperature of the air of overfeeding. According to the graph the temperature of the fresh load in the optimal point of the mixture is of 52C with a water flow of 6.8 kg/h.

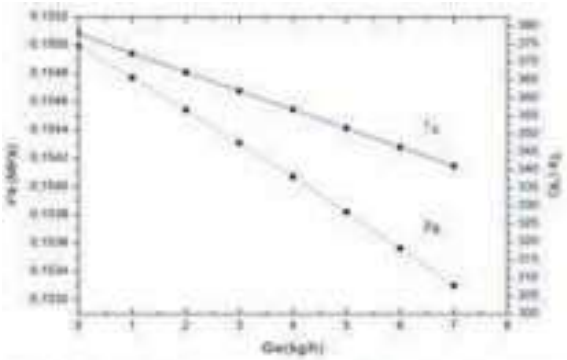

Fig.3. Variation in the temperature and the pressure with the admission according to the water flow

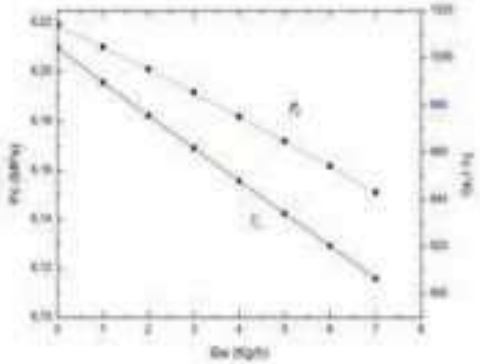

Fig.4. Variation in the temperature and the pressure at the end of compression

According to figure 3, we noticed that the temperature at the end of admission decreases proportionally with the water injection that is due to the transfer of heat between the airs towards the water vapor what involves the cooling of the mixture. One note that the pressure also at the end of admission decreases in inject water in the channel that with the increase in the pressure losses to the admission is caused by the packing of the fresh load.

Figure 4 shows us a pressure decrease and temperature at the end of compression according to the water vapor injected with the admission, that is due to the reduction in the parameters of admission pressure and temperature.

Creative Commons Attribution-NonCommercial-NoDerivatives 4.0 International License (CC BY-NC-ND)

Algerian Journal of Engineering Architecture and Urbanism Vol. 5 Nr. 3 2021
ISSN: 2588-1760

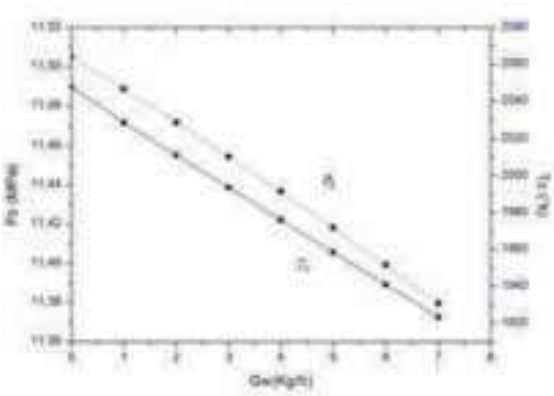

Fig.5. Variation in the temperature and the pressure at the end of combustion

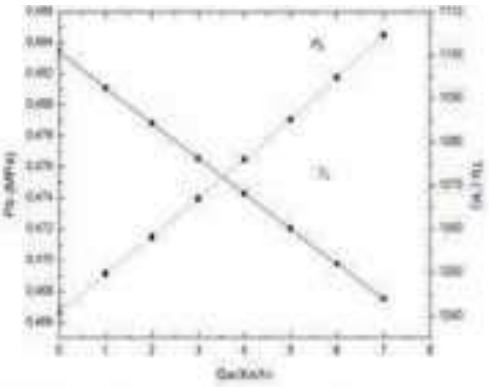

Fig.6. variation in the temperature and the pressure at the end of the relaxation

According to figure 5, we noticed a reduction in the temperature at the end of combustion that is due to the reduction in the temperature of compression. In the maximum point of the operation of this system, the temperature at the end of combustion decreases until $T_Z T_Z$= 1927.74°K, that is an advantage of this system seen that the temperatures higher involves considerable risks in the cylinder (detonation) and thus the increase in the polluting effects (NO_X).

The pressure at the end of combustion decreases proportionally with the water injection that is due to the pressure decrease at the end of compression.

According to figure 6, the temperature $T_b$decreases according to the water vapor, that is due to the reduction in the temperature at the end of combustionT_z.

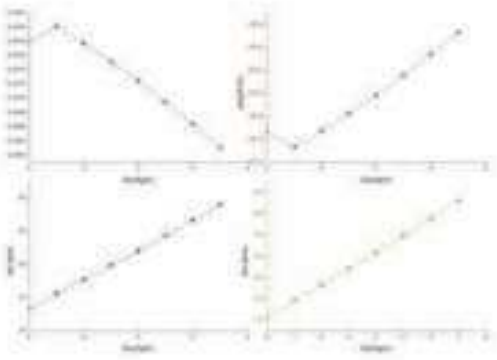

Fig7. Variation of the actual parameters according to the water flow.

Figure 7, shows us in a flow of 1 water Kg/h a light increase in the effective output, which is due to the excitation of fuel from where combustion is sharp, which entrained a light reduction in effective specific consumption. Starting from this flow we thus notice a reduction in the effective output, which is related to the reduction in the output indicated (formation of imbrues), that results the increase from effective specific consumption. Consequently, a considerable growth of the power and the couple manpower, since the system of water injection decreases the losses mechanics which makes the engine more powerful with the same nominal speed (number of revolutions).

Comparison of the parameters with and without water injection.

Quantity of total heat released by fuel in the engine

Creative Commons Attribution-NonCommercial-NoDerivatives 4.0 International License (CC BY-NC-ND)

$$Q_0 = Q_H . G_T [W]$$

$$G_T = g_e . N_e . 10^{-3}$$

Quantity of heat equivalent to effective work

$$Q_e = 1000 . N_e^I$$

Quantity of heat yielded of the system of cooling

$$Q_{ref} = C . i . D^{1+2m} . n^m . \frac{1}{\alpha}$$

C=0.45…..0.53, coefficient proportionality.

m=0.6…..0.70, index of power.

Quantity of heat carried by exhaust fumes.

$$Q_g = G_T [M_2 . \mu cp \Big|_0^{T_r} T_r - M_1 . \mu cp \Big|_0^{T_0}$$

Quantity of remaining heat.

$$Q_{rest} = Q_0 - (Q_e + Q_{ref} + Q_g)$$

The results without and with water vapor obtained of the heat balance are illustrated by the following table:

Parameters of the heat balance:	Results without water vapor [w]	Percentage: %	Results with the water vapor [w]	Percentage: %
Quantity of equivalent heat of effective work Q_e	77336.8	38.13	83584.3	38
Quantity of heat yielded of the system of cooling Q_{ref}	37935.2379	18.7	37935.2379	17.15
Quantity of heat carried by exhaust fumes Q_g	71437.2488	35.22	70467.57	32.1
Quantity of remaining heat Q_{rest}	16110.1583	7.9	27860.11	12.7
Quantity of total heat released by fuel Q_0	202819.44	100	219847.22	100

Table.2. Heat balance of the D 245 engine

Conclusion

The study undertaken in this work allowed us currently studies one of the existing solutions. Moreover the solution suggested is the water injection in the tubular one of admission which does not require significant modifications structural of the engine. For that one concluded that On the basis of model of developed calculation, the parameters of the fresh load are given when water is input until a flow of 6.8 Kg/h, there is an evaporation supplements beyond this flow the mixture becomes wet. The presence of the water vapor in the tubular one of admission, causes to decrease the temperature of the fresh load to the value of 35C, which is an advantage for combustion in order to decrease the temperature in the cylinder, which also made it possible to reduce the losses of heat to the walls; At the point of maximum operation of the system, the temperature at the end of combustion decreases by 6(%)and by using a model of calculation closely connected

Creative Commons Attribution-NonCommercial-NoDerivatives 4.0 International License (CC BY-NC-ND)

which taken into account the introduction of water, one obtains an increase in the effective power of 8 (٪) by injecting a flow of (6.8 kg/h).

Nomenclature

g_v et g_a h_v et h'_v T_v et T'_v	Mass portions of the vapor of water and air before the mixture. Water enthalpy before and after the mixture The temperature of the air of the load before and after the evaporation of water
T_{inj} et T'_s	The temperature of water injected and its temperature of saturation of the vapor in the load fresh.
r Cp_v ,Cp'_v	Latent heat of vaporization of water. Heat-storage capacities of water and its vapor with constant pressure In the preceding formula
$Cp_w(T'_s - T_{inj})$	Represent the quantity of heat spent by the heating of water injected.
$Cv'_{vp}(T'_s - T'_v)$	represent the quantity of heat for the heating of the water vapor
G_c	Time consumption of fuel in (kg/h)
G_a l_0 G_w	Mass throughput of air in (kg/h) Stoechiometric quantity of air necessary for the combustion of a 1kg of fuel Water rate per hour (kg/h)
μ_v	Mass molar water (kg/kmol)
γ_a $\gamma_w=(1-\gamma_a)$ ζ	The volumes portion of the air to the admission. Volumes fraction of the water vapor in the load fresh Load factor of heat transmitted to gases
g_e	The effective specific consumption of fuel (g/kWh)

REFERENCES

[1]. **S. Shah**. *Experimental study and Thermodynamical analysis of water injection in the intake manifold of an automotive Diesel Engine, for pollutant emission reduction. Reactive Fluid environment. Ecole Centrale Nantes, 2011. English.*

[2]. **Abdallah Bouam, Rabah Kadi, Slimane Aissani**. *Amélioration des performances des turbines à gaz par l'injection de la vapeur d'eau à l'amont de la chambre de combustion. JITH 2007, Au g 2007, Albi, France. 5p.*

[3]. **Professeur C.N. Devyanin**, *Augmentation de la capacité écologique du moteur Diesel en ajoutant de l'eau dans le Cylindre, université agricole de Moscou, 2006.*

[4]. **Heywood, J. B**, *"Internal Combustion Engine Fundamentals", McGraw-Hill Book Company, 1988.*

[5] **D. Zhao, Y. Ohno, T. Furuhata, H. Yamashita, N. Arai & Y. Hisazumi**, *Combustion technology in a novel gas turbine system with steam injection and two-stage combustion, J. Chemical Engineering of Japan, Volume 34, pp 1159-1164, 2001.*

[6] **Stefanie Falfari et al**, *Basics on Water Injection Process for Gasoline Engines, Energy Procedia 148 (2018) 50–57.*

[7] **Zahi Sabeh**, *Diagnostic à base de modèle : application à un moteur diesel suralimenté à injection directe, Institut National Polytechnique de Lorraine, 2006.*

[8] **Dan Scarpete,** *Diesel-Water emulsion, an alternative fuel to reduce diesel engine emissions, University "Dunarea de Jos" of Galati, Romania, 2013.*

Creative Commons Attribution-NonCommercial-NoDerivatives 4.0 International License (CC BY-NC-ND)

Algerian Journal of Engineering Architecture and Urbanism Vol. 5 Nr. 3 2021
ISSN: 2588-1760

INCORPORATION DES CENDRES DE BIOMASSE DANS UN BETONS AUTO-PLAÇANTS

GUERFI ROQIYA
Doctorante, LMGHU, Université 20 août1955 Skikda, BP 26, Route d'El Hadaiek- Skikda 21000, guerfi.rokaia@gmail.com

BOUDCHICHA Mohamed Redda
MCA, Ecole National Polytechnique de Constantine, Université Constantine 3, Ali Mendjli- Constantine 25000, boudred72@gmail.com

HEBHOUB Houria
LMGHU, Université 20 août1955 Skikda, BP 26, Route d'El Hadaiek- Skikda 21000, hebhoubhouria@yahoo.fr

Abstract:
L'objectif de cette étude est d'évaluer la faisabilité de l'incorporation de cendres de biomasse comme matériau de remplissage dans la production de béton autoplaçant (BAP). Les cendres de biomasse sont utilisées comme des fines de remplacement à des pourcentages variables de 0 %, 3 %, 9 %, 21 %. Des études expérimentales telles que la résistance à la compression, les mesures de résistance à la traction par flexion du béton auto-plaçant contenant un mélange de cendres de biomasse sont menées pour déterminer leurs propriétés mécaniques. L'ouvrabilité (slump flow, densité) sur l'enrobé correspondant permet également d'étudier les caractéristiques. Les résultats montrent que l'utilisation de déchets de cendres de biomasse a considérablement amélioré la maniabilité et augmenté la résistance à la compression des mélanges de BAP. De plus, tous les mélanges ont montré une performance acceptable en ce qui concerne le diamètre d'écoulement d'affaissement.

Key words: • Béton auto-plaçant, cendres de biomasse, caractérisation, résistance mécanique

Introduction:

Les bétons autobloquants (BAP) ont été initialement mis au point et développé en 1986 par les chercheurs Okamura, Ozawa et Maekawa de l'Université de Tokyo au Japon. Ces bétons autobloquants (BAP) représentent une nouvelle génération de béton, développés pour améliorer la qualité de la construction et aussi pour surmonter les problèmes de fabrication inadéquate **K. Ozawaet al**(1989). Ce sont des bétons innovants qui se mettent en œuvre sans vibration car ils sont caractérisés par une bonne ouvrabilité, une grande fluidité ainsi qu'une bonne homogénéité et une stabilité rhéologique performante. Ils s'adaptent ainsi à un bon nombre d'applications en génie civil et sont surtout demandés pour la réalisation de constructions complexes.

Cependant, la formulation des BAP est relativement coûteuse par rapport à un béton ordinaire en raison de leur demande, relativement élevée, en super plastifiant et en ajout minéraux. En effet, pour éviter la ségrégation des agrégats, le béton auto plaçant doit avoir une viscosité suffisante qui n'est permit que par l'augmentation en dosage des fines et par l'ajout d'adjuvants chimiques.

Creative Commons Attribution-NonCommercial-NoDerivatives 4.0 International License (CC BY-NC-ND)

Une des stratégies employées afin de pallier le problème du cout et de l'impact environnemental de cette classe de béton, est l'utilisation d'autres types d'ajouts ou de valoriser certains déchets tout en maintenant les caractéristique du BAP, tels que les pouzzolanes naturelles, la poudre de calcaire, les cendres volantes et le laitier de haut fourneau **F.A. Sabet et al** (2013), **M. Sahmaran et al** (2006)

L'utilisation de la cendre des déchets agricole en tant qu'ajout cimentaire alternatif a fait l'objet de plusieurs recherches depuis une quinzaine d'années **Ban CC et al** (2011), par exemple, les cendres de bois de palme (CBP) **N Ranjbar et al** (2014) et les cendres de l'écorce de riz (CER) **M.Jamil et al**(2016), **Ravinder KS et al(2017)**. Compte tenu de la teneur élevée en silice, le CER devient pozzolanique et agit efficacement comme matériau cimentaire de substitution (MCS) **Ravinder KS et al (2017)**. Aussi, la CBP a également montré un grand potentiel en tant que matériau de substitution du ciment pour la technologie du béton **N Ranjbar**(2014). D'autres cendres de déchets agricoles, telles que les cendres de canne à sucre (CCS) **Almir Sales Sofia** (2003), les cendres de maïs (CM) et CB, peuvent être utilisées comme substituant dans les matériaux à base de ciment **D.A.Adesanya** (1996), **M. Gori**(2013).

La cendre de bois CB, pour la plupart, comprend du bois d'anéantissement, des lits, des feuilles de fibres, des dépôts de l'industrie du bois, des traverses de chemins de fer, des arches, etc. il s'agit de la biomasse facile et peut également être connu comme un combustible inépuisable et de cette manière, il est extrêmement attrayant pour les usines d'allumage de biomasse à grande échelle. Cependant, utiliser CB en remplacement du ciment présente des limites. Bien que le remplacement partiel du ciment par CB améliore légèrement la résistance, une réduction peut se produire lorsque plus de 20% de remplacement est utilisé car le CB a une teneur en silice inférieure à celle du CER et du CBP. Par conséquent, des restrictions sont nécessaires pour utiliser la CB en remplacement du ciment **M. Safiuddin** (2011). De ce fait, il serait intéressant et prometteur d'élargir l'éventail d'utilisation de la CB en tant qu'ajout cimentaire en l'incorporant dans les BAP.

De nombreuses recherches ont été menées sur l'utilisation du CBP pour remplacer le ciment dans la production de BAP. **N. Ranjbar** (2016) ont été les premiers pionniers à mener une recherche sur le béton autoplaçant par ajout de CBP et sont toujours les plus fiables. Cependant, d'autres contributions respectées peuvent être trouvées de nos jours dans la littérature**N. Ranjbaret al** (2016), **B. Alsubari et al** (2018), **M.A. Salam et al**(2013).

Problematic:

L'utilisation de la cendre des déchets agricole en tant qu'ajout cimentaire alternatif a fait l'objet de plusieurs recherches[], dans l'objectif est de diminuer la consomation énergetique des industrie cimentaire, et aussi pour contribuer à limiter l'émission du CO2. Les cites ou les dechets de cendressin entreposés constitue eux aussi un problème majeur environementale et leur utilisation en tant que substitue de ciment pourait le résoudre.
Pour cela notre étude vise la valorisation des cendres de biomasse dans la composition des BAP.

Materials and methods:

Creative Commons Attribution-NonCommercial-NoDerivatives 4.0 International License (CC BY-NC-ND)

Dans le programme expérimental nous avons substitué une partie des ajouts dans un BAP par les cendres de biomasses avec un taux de 9 et 18% avec les paramètres fixes sont le dosage en ciment, le dosage en eau et le dosage en adjuvant.
Les essais réalisés sur le BAP a l'état frais son mesure de la densité et l'étalement, les essais réalisées sur BAP a l'état durci sont mesure de la résistance en compression et en traction par flexion a l'âge 28jours.

Results and discussions:

Etalement:

D'après la figure 1 on remarque que le remplacement des fillers par la cendre de biomass engendre une diminution de la fluidité. La réduction de la fluidité est environ 2%. La diminution de la fluidité peut s'expliquer par le besoin important en eau et à l'augmentation de SSB de notre cendre par rapport à les fillers.

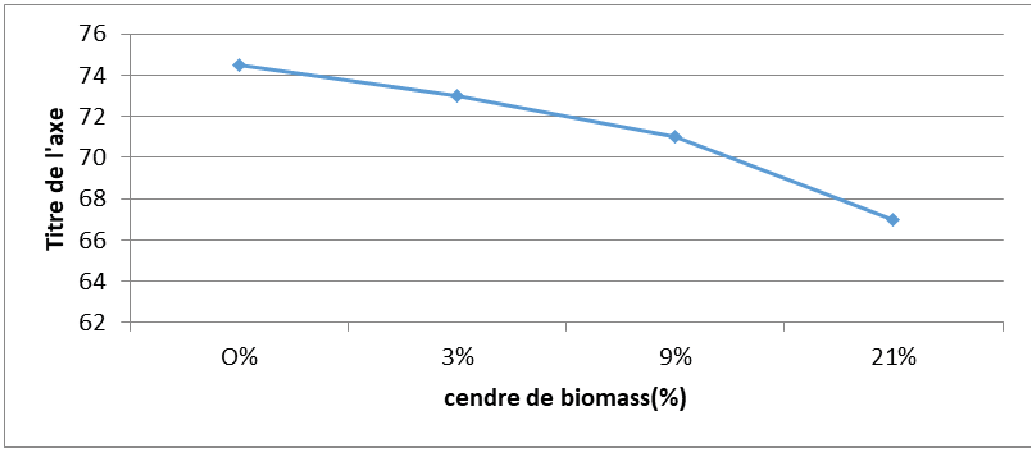

Fig. 1 Variation de l'étalement en fonction du taux de substitution

Densité à l'état frais :

On observe que la densité à l'état frais augmente lorsque la fraction volumique en cendre augmente jusqu'à 9% puis se stabilise à une valeur constante de 2.4g/cm^3 entre 9 et 21% en cendre (figure 2).

Creative Commons Attribution-NonCommercial-NoDerivatives 4.0 International License (CC BY-NC-ND)

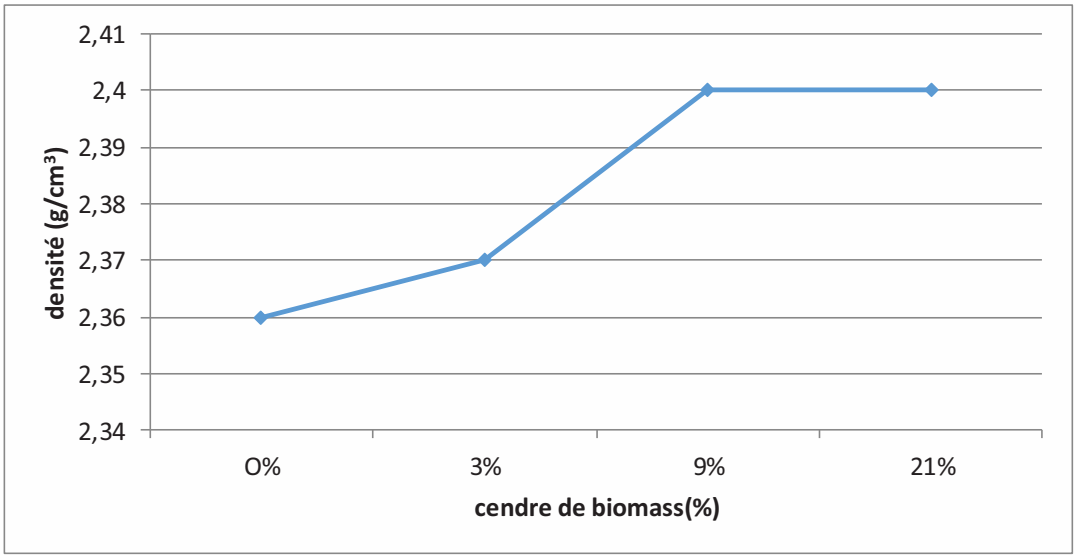

Fig.2. Variation de la densité en fonction du taux de substitution

La résistance à la compression:

Les performances des cendres de biomasse BAP en compression sont présentées dans la Fig. 3. Les comparaisons de la résistance du béton de cendres de biomasse avec celles du béton témoin (0%) des âges correspondants (28 jours) montrent que la résistance des cendres de biomasse SCC est généralement inférieurs à ceux du BAP ordinaire. Une explication possible de cette tendance est que la cendre de biomasse agit plus comme une charge dans la matrice que comme un liant.

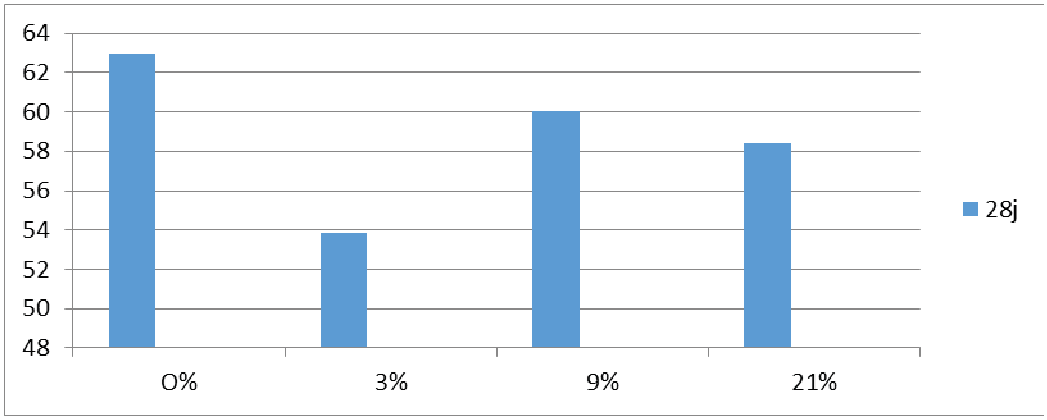

Fig.3. Influence du taux de substitution sur la résistance en compression

La résistance à la traction par flexion:

La résistance à la traction pour les échantillons testés en fractionnement à 28 jours est représentée sur la figure 4. Les résultats montrent qu'il n'y a pas eu d'amélioration dans les mélanges 9 ou 21 par rapport au témoin BAP. Au contraire, la résistance à la traction a

Creative Commons Attribution-NonCommercial-NoDerivatives 4.0 International License (CC BY-NC-ND)

diminué. On peut remarquer que le changement entre les valeurs de résistance à la traction des différents mélanges est faible et les valeurs étaient presque égales à celles du témoin BAP au même âge.

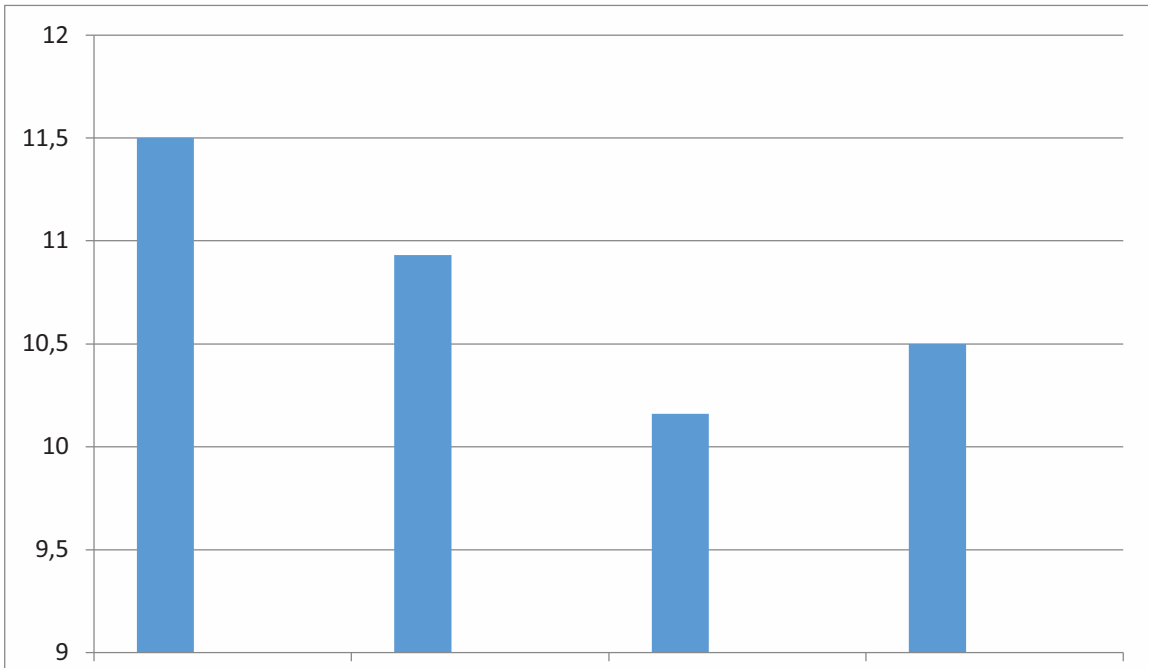

Fig.4. Influence du taux de substitution sur la résistance en traction par flexion

.

Conclusion:

Dans cette étude expérimentale, des déchets de cendre de biomasse ont été utilisés avec succès pour fabriquer du béton autoplaçant. L'utilisation de cendres de biomasse comme substitut du ciment dans le béton autoplaçant (BAP) peut réduire le coût de construction en raison de la diminution de la teneur en ciment et contribue également à résoudre les problèmes environnementaux et sociaux de santé. De cette étude, nous pouvons conclure:

-L'introduction de cendres de biomasse entraîne une diminution de la fluidité.

-La compacité augmente avec l'augmentation de la teneur en cendres.

-L'ajout de cendre de biomasse provoque une baisse des résistances à la traction.

Ce travail est une étude préliminaire, il nécessite d'autres types de tests pour mieux comprendre le comportement des BAP à base de cendre de biomasse

References:

K. Ozawa, K. Maekawa, M. Kunishima, H. Okamura (1989) *Development of high performance concrete based on the durability design of concrete structures*, Proceeding Second East - Asia Pacific Conf. Struct. Eng. Constr. (EASEC - 2). 445–450

Creative Commons Attribution-NonCommercial-NoDerivatives 4.0 International License (CC BY-NC-ND)

F.A. Sabet, N.A. Libre, M. Shekarchi (2013) *Mechanical and durability properties of self consolidating* , Constr. Build. Mater 44:175–184.

M. Sahmaran, H.A. Christianto, I.O. Yaman (2006) *The effect of chemical admixtures and mineral additives on the properties of self-compacting mortars,* Cem. Concr. Compos 28: 432–440.

Ban CC, Ramli M (2011) *The implementation of wood waste ash as a partial cement replacement material in the production of structural grade concrete and mortar: an overview*. Resour Conserv Recycl 55:669–85.

Rajamma R, Ball RJL, Tarelho AC, Allen G, Labrincha JA, Ferreira VM (2009) *Characterisation and use of biomass fly ash in cement-based materials*. J Hazard Mater 172:1049–60.

M.Jamil, M.N.N.Khan, M.R.Karim, A.B.M.A.Kaish, M.F.M.Zain (2016) *Physical and chemical* contributions of Rice Husk Ash on the properties of mortar, Constr Build Mater 128 (2016) 185-198

Ravinder KS, Rafat S (2017) *Influence of rice husk ash (RHA) on the properties of self-compacting concrete: A review*. Constr Build Mater 153: 751-764

N Ranjbar, M Mehrali, U.J.Alengaram, H. S. C.Metselaar, M. Z.Jumaat (2014) *Compressive strength and microstructural analysis of fly ash/palm oil fuel ash based geopolymer mortar under elevated temperatures*. Constr Build Mater 114-121

Almir Sales Sofia, Araújo Lima(2003) *Use of Brazilian sugarcane bagasse ash in concrete as sand replacement*. Cement and Concrete Composites 25, 7:737-749

D.A.Adesanya (1996) *Evaluation of blended cement mortar, concrete and stabilized earth made from ordinary Portland cement and corn cob ash.* Constr Build Mater 10:451-456

M. Gori, B. Bergfeldt, J. Reichelt, P. Sirini (2013) *Effect of natural ageing on volume stability of MSW* and *wood waste incineration residues* Waste Management 33, 4 : 850-857

M. Safiuddin, M.H. Isa, M.Z. Jumaat (2011) *Fresh properties of self-consolidating concrete incorporating palm oil fuel ash as a supplementary cementing material*, Chiang Mai J. Sci 38: 389–404.

N. Ranjbar, A. Behnia, B. Alsubari, P. Moradi Birgani, M.Z. Jumaat (2016) *Durability and mechanical properties of self-compacting concrete incorporating palm oil fuel ash.* J. Clean. Prod :112 723–730.

B. Alsubari, P. Shafigh, Z. Ibrahim, M.F. Alnahhal, M.Z. Jumaat (2018) *Properties of eco-friendly self-compacting concrete containing modified treated palm oil fuel ash.* Constr. Build. Mater 158 :742–754.

M.A. Salam, M. Safiuddin, M.Z. Jumaat (2013) *Microstructure of self-consolidating high strength concrete incorporating palm oil fuel ash*. Phys. Rev. Res. Int 3 :674–687.

B.H. Nagaratnam, M.A. Mannan, M.E. Rahman, A.K. Mirasa, A. Richardson, O. Nabinejad (2019) *Strength and microstructural characteristics of palm oil fuel ash and fly ash as binary and ternary blends in Self-Compacting concrete*, Constr. Build. Mater 202: 103–120.

Creative Commons Attribution-NonCommercial-NoDerivatives 4.0 International License (CC BY-NC-ND)

Algerian Journal of Engineering Architecture and Urbanism Vol. 5 Nr. 3 2021
ISSN: 2588-1760

Structural, electronic and magnetic properties of double perovskite $LaFeO_3$ using GGA and GGA+U

[1]W.Benosman
[1]Faculté des Sciences et de la Technologie, Université Abdelhamid Ibn Badis, Mostaganem.27000.
Email : w_physique@hotmail.fr

[2]N.Mehtougui
[2]Faculté des Sciences et de la Technologie, Université Abdelhamid Ibn Badis, Mostaganem.27000.
Email : meht_nabila@yahoo.fr

Abstract

The structural, electronic and magnetic properties of perovskite $LaFeO_3$, have been investigated by the full potential linearized augmented plane wave (FP-LAPW) method implemented in the Wien2k code. In order to determine these properties, we used the approximation of the generalized gradient (GGA) for the term of the exchange and correlation potential (XC).and GGA+U. the results given in this study are in good agreement with experimental. The Structural and electronic properties show that $LaFeO_3$ material is stable in the cubic phase which present a half-metallic character. The band gap value estimated by GGA+U approach was found to be 1.4 eV, which is very close to the reported experimental value (1.2 eV). contrary to the result given by GGA showing the metallic character of the material. The total magnetic moment is integer and it is mainly due to the magnetic moment of the transition metal. The energy-gap obtained by GGA+U calculations is a better than the GGA approximation.

Key words: DFT; Perovskite; Half metallic and GGA+U method.

1. Introduction:

In recent years, theoretical and experimental efforts have been performed in order to understand fundamental properties of mixed crystals type perovskites ABO3 depend upon the size of A or B-site ions, the electronic configuration of the transition-metal ions (usually B-site ions), and the nature of the covalent bonding between metal and oxygen ions.The ABO3 perovskite structure is composed of a three-dimensional chain of vertically branched BO6 octahedra while the cation A is surrounded by 12 oxygen atoms defined by Glazer [1], [2] **(Fig.1)** The cubic perovskites are a good baseline structure for determining suitable HM material candidates, because there are a variety of combinations for substituting the *A*-site or *B*-site elements. In order to find more potential HM materials. Half-metallic (HM) materials have received growing interest due to they can provide the conductive electrons with a 100% spin polarization and have great potential applications in many aspects [3] (eg. tunneling magneto-resistive, spin-injection and so on) [4]. This paper presents theoretical HM compound prediction on perovskites, we used the DFT, ab-initio methods [5] (Hohenberg, P., Kohn, W) implemented in the code Wien2k, The potential of Exchange and correlation is evaluated using the approximation (GGA) [6].

Creative Commons Attribution-NonCommercial-NoDerivatives 4.0 International License (CC BY-NC-ND)

Algerian Journal of Engineering Architecture and Urbanism Vol. 5 Nr. 3 2021
ISSN: 2588-1760

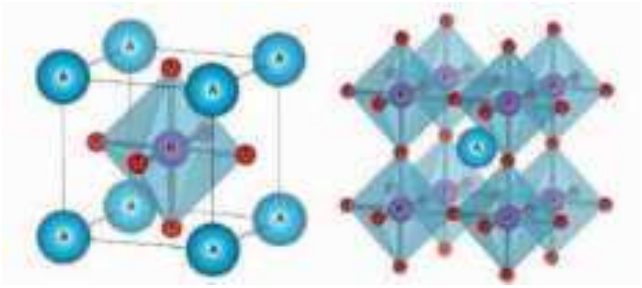

Fig 1. Crystal structure of LaFeO3.

2. Computational details:

The calculations of structural, electronic, magnetic properties of the perovskite LaFeO3 in tree structures: cubic, tetragonal and orthorhombic have been performed using Wien2k code [7] which is an implementation of the method. For the exchange and correlation potential, we have used the generalized gradient approximation (GGA) [8] and GGA+U [9], where U is the Hubbard on-site Coulomb interaction correction used for strongly correlated Fe (3d). The GGA + *U* calculations were performed with the rotationally invariant formulation of Dudarev et al. [10] with $U_{\text{eff}} = U - J$ (J = 0.91 eV represents Hund's rule exchange parameter) [11]. Different values of U_{eff} (4, 6, 8 eV) were obtained using the method of T. Lantri et al. [12], but only the results obtained for U_{eff} = 4 eV are presented in our work, since for the other values of U, the results were still similar.

Basis function, electron densities and potentials were expanded inside the muffin-tin (MT) spheres in combination with spherical harmonic function with cut-off I_{max} = 8, and in Fourier series in the interstitial region expanded charge density and potential was truncated at G_{max} =24. The total Brillouin zone was sampled with 1000 k-points to perform integration over the first Brillouin zone BZ, as in Monkhorst and Pack and to construct the charge density in each self-consistency step. The maximum angular momentum inside the muffin-tin sphere was confined to I_{max} = 10 which is the maximum value for partial waves inside the atomic sphere. The unit cell crystallizes in the cubic (space group Pm3m n° 121, a=b=c=3.850 [13]) the atomic distribution is as follows: La atom is located at cube corner position (0, 0, 0), Fe atom at body centre position (1/2, 1/2, 1/2), and three O atoms at face centered positions (1/2, 1/2, 0); (1/2 ,0, 1/2); (0, 1/2,1/2), tetragonal (space group P4mm n° 99, a=b=5.584, c=3.952 [14]) the atomic distribution is as follows: La (0.5,0.5,0.59), Fe (0,0,0.1), and three O (0.5,0,0.6) and orthorhombic (space group Pnma n° 62, a=5.565, b=7.854 et c=5.553 [15]) the atomic distribution is as follows: La (0.6548,0.2500,0.9849), Fe (0,0,0.5), and O1 (0.5265,0.7500,0.9059), O2 (0.9734 ,0.2500,0.4059) structure (see **Fig.2**) and the atomic positions (see Table.1). On the other hand the non-overlapping muffin-tin radii (RMT) were considered to be 2.5, 1.86, and 1.68 a.u (atomic units) for La, Fe and O atoms, respectively. We use a parameter $R_{\text{MT}}K_{max}$ = 8, which determines matrix size (energy convergence), where K_{max} is the plane wave cut-off and R_{MT} is the smallest of all the atomic sphere radii. The self-consistent calculation is assumed to have an energy convergence when it reaches 10^{-5} Ry.

Creative Commons Attribution-NonCommercial-NoDerivatives 4.0 International License (CC BY-NC-ND)

Algerian Journal of Engineering Architecture and Urbanism Vol. 5 Nr. 3 2021
ISSN: 2588-1760

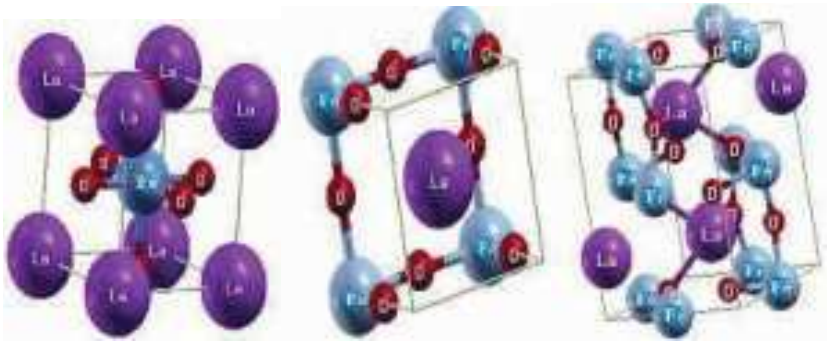

(a) (b) (c)

Fig 2. Crystal structure of LaFeO3 in: (a) Pm3m n° 121, (b) P4mm n° 99 and (c) Pnma n° 62.

3. Structural stability of LaFeO3 compound:

As a starting point we have carried out the structural details for perovskite LaFeO3 by the optimization of experimental lattice parameters and finding the stable magnetic structure. Birch-Murnaghan's equation of state has been used for geometry and structural optimization within cubic, tetragonal and orthorhombic phases by fitting energy as a function of cell volume (see equation 1). Cubic state was found to have minimum energy and hence a stable configuration as shown in **Figure 3** with GGA. The lattice constant (a), bulk modulus (B) and first-order pressure derivative of the bulk modulus (B′), cohesive energy are tabulated and compared in Table 1. The optimized ground state lattice constant parameter was found in close agreement with the already available experimental data [13]. The cohesive energies of the two alloys can be obtained from the equation:

$$E(V) = E_0(V) + \frac{9B_0V_0}{16}\left[\left\{\left(\frac{V_0}{V}\right)^{\frac{2}{3}} - 1\right\}^2 B'_0 + \left\{\left(\frac{V_0}{V}\right)^{\frac{2}{3}} - 1\right\}^2 \left\{6 - 4\left(\frac{V_0}{V}\right)^{\frac{2}{3}}\right\}\right]^2 \quad (1)$$

The cohesive energy (E_{coh}) measures the strength of the force that binds atoms together in the solid state and is correlated to the structural stability in the ground state. The cohesive energy is presented as:

$$E_{coh}^{LaFeO3} = E_{Tot}^{LaFeO3} - \left(E_{atome}^{La} + E_{atome}^{Fe} + 3E_{atome}^{O} \right) \quad (2)$$

Where E_{Tot}^{LaFeO3} is the total energy of the considered compound E_{atome}^{La}, E_{atome}^{Fe}, E_{atome}^{O} are the energies of isolated constituent atoms in each compound. In general, a negative value of cohesive energy (see Table 1) indicates the stability of the material. Based on the energy difference in Figure 3, the cubic state is the most stable magnetic phase. Therefore, we can confirm that the atoms of our compound LaFeO3 is exceptionally stable.

Creative Commons Attribution-NonCommercial-NoDerivatives 4.0 International License (CC BY-NC-ND)

Algerian Journal of Engineering Architecture and Urbanism Vol. 5 Nr. 3 2021
ISSN: 2588-1760

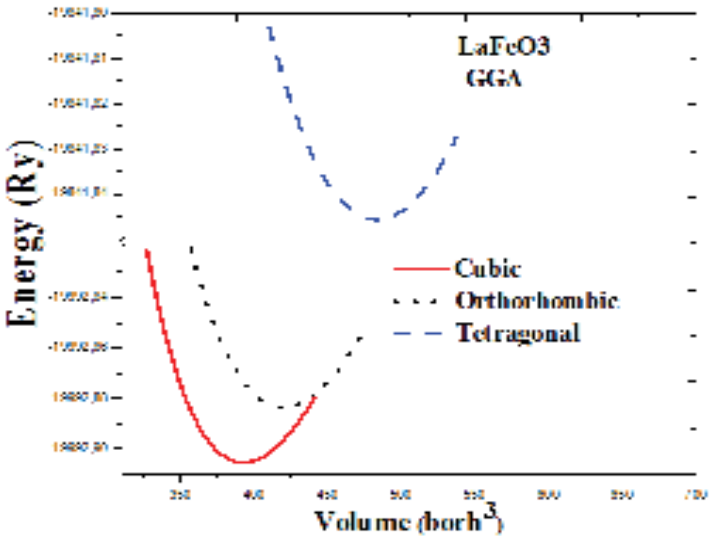

Fig.3 Calculated total energy versus volum in the tree structures of LaFeO3.

Table 1 Calculated equilibrium lattice parameters α (Å), bulk modulus B (GPa), its pressure derivative B' and cohesive energy (E_{coh}) of the cubic, orthorhombic and tetragonal perovskites LaFeO3, using GGA, in comparison to the available values in the literature.

Parameters	Cubic	Tetragonal	Orthorhombic
a(Å)	3.874 **3.850**[a]	5.390 **5.584**[b]	6.160 **5.565**[c]
b(Å)			7.860 **7.854**[c]
c(Å)		3.819 **3.952**[b]	5.645 **5.553**[c]
B(GPa)	156.55	158.34	152.16
B'	4.8	1.6	3.5
E_{coh}(Ry)	-2.39	30.45	-2.32

[a] Ref. [13], [b] Ref. [14], [c] Ref. [15].

Table 2 Calculated total (μ^{Cell}), interstitial (μ^{inst}) and magnetic moment of each atom for LaFeO3 (in μ_B) and energy gaps Eg(eV) of the LaFeO3 compound by the GGA-PBE and GGA+U for cubic state.

Compound	Methods	μ^{La}	μ^{Fe}	μ^{O}	μ^{int}	μ^{Cell}	Eg(eV)	Band gap
	GGA	-0.02	2.62	0.06	0.09	3.02	/	/
LaFeO3	*GGA+U*	-0.20	4.14	0.26	0.08	4.00	1.40	Indirect R→Γ

Creative Commons Attribution-NonCommercial-NoDerivatives 4.0 International License (CC BY-NC-ND)

	[a]1.20

[a]Ref[13].

4. Electronic band structure and density of states

The band structures and state densities of the compound LaFeO3 were calculated and plotted at its equilibrium lattice constant in the GGA-PBE and GGA + U configurations, as shown in Figs. 3-4. Standard DFT calculations, using (GGA) are shown that LaFeO3, is metallic in the both spin (spin-up) and (spin dn) channel. Where with GGA+U (we used for Fe (U = 6 eV)), while there is an energy gap around the Fermi level in the minority spin (spin-dn), that is to say, our compound exhibits HM characteristic. The energy gap (Eg) is listed in Table 2. The energy gap is the minimum energies between the lowest energy of minority spin conduction bands with respect to the Fermi level and the absolute values of the highest energy of the minority spin valence bands. In this compound the band-gap is indirect (R–Γ) around the Fermi level in the minority-spin channel, the energy gap is equal to 1.40 eV (GGA+U). These values indicate that this half-metal compound with 3D transition metals ensures a good application in spintronics, and agrees well with the experimental results. Therefore, the perovskite LaFeO3 has half-metallic character, and it could be applied in the thin films and magnetic tunnel junctions and can be used as electrodes in tunnel junctions No experimental or t theoretical data are available to compare with the obtained results.

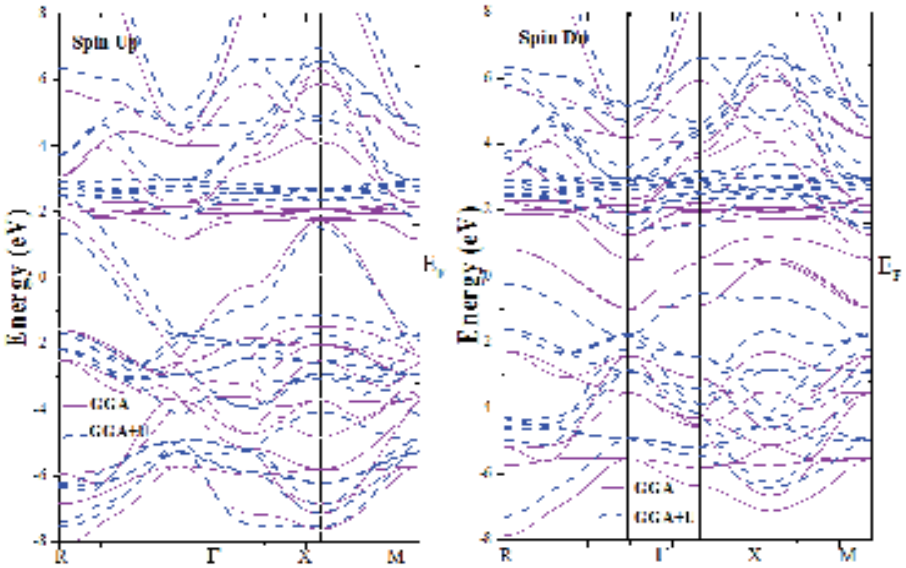

Fig. 3. Spin-up and spin-down band structures of LaFeO3 using GAA and GGA+U.

The total (TDOS) and partial density of states (PDOS) graph of LaFeO3 were calculated in the cubic state at the equilibrium lattice constant using GGA-PBE and GGA+U approximations to further reveal and understand the origin of the half-metallic character (see **Fig. 4**). The Fermi level E_F is represented by vertical dash line and set to 0 eV. As shown in Figure 4, it can easily be observed that the TDOS of LaFeO3 in the region between -5.0 and 5.0 eV as indicated by the band structures, shows the conductive nature for the both spin up and spin down in GGA approximation. From the (PDOS), it is clear that LaFeO3 exhibits a metallic character, because in the majority and minority spin, Fe-3d crosses the Fermi level using GGA, but with GGA+U (see **Fig.4**) for the minority spin direction, LaFeO3 compound have a band gap which exists between O (2p) occupied states and Fe (3d) unoccupied states. Furthermore, the top of the valence band between −2.00 eV to E_F, is composed of Fe (3d)

Creative Commons Attribution-NonCommercial-NoDerivatives 4.0 International License (CC BY-NC-ND)

states with small contribution of O (2p), whereas the minimum of the conduction band is principally composed of La (3d) and O (2p) states. Besides, the hybridization of La (3d) and O (2p) states is responsible for the conductivity in LaFeO3 perovskite. The half metallic character of the compound is in fact an excellent candidate for spintronics applications.

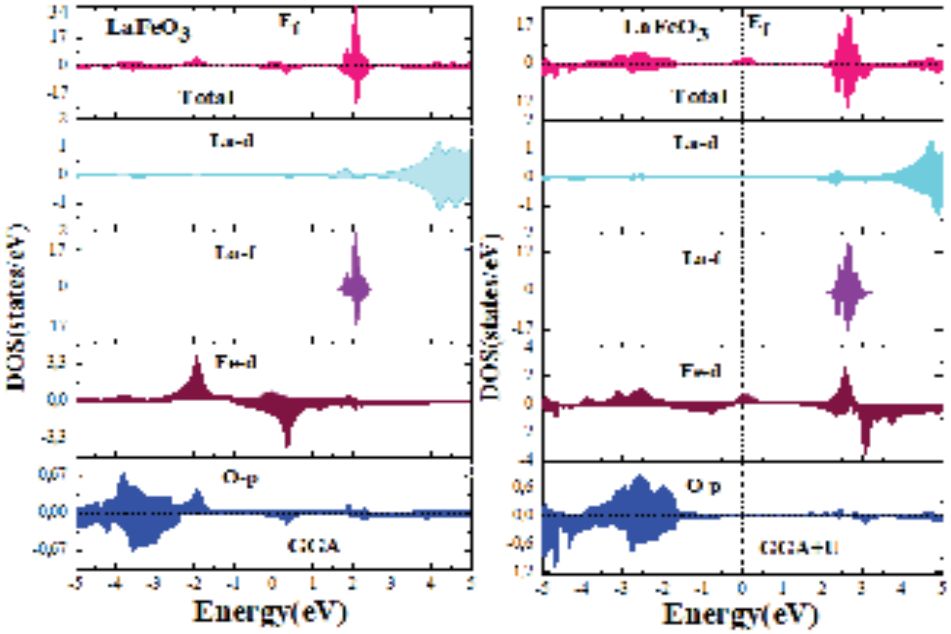

Fig. 4. Total and partial density of states of LaFeO3 using GGA and GGA + U.

5. Magnetic properties

The total, local and interstitial magnetic moments of LaFe03 compound calculated using GGA, GGA + U are listed in Table 2. We can be see that the positive values of the magnetic moments of the interstitial sites (for GGA, GGA+U) and of Fe atoms confirm that they are aligned anti parallel to the magnetic moments of La. The results show that the total magnetic moment is mainly due to the transition metal Fe, with a negligible contribution from the magnetic moment of La and O atoms and interstitial regions. The integer value (3μB) and (4μB) of the total magnetic moment for GGA and GGA + U means that the compound is half-metallic, which confirms the results obtained from the electronic properties. We can also notice from Table 2 that, the coulomb interaction may increase the localization of the related d orbitals and increase the local magnetic moments in the Fe sites, but decrease La and O local magnetic moment. These magnetic properties show that this compound can be used in several fields due to the ease of acquiring a magnetization directed in the same direction such as; computer memories, transformer cores and microwave components using magnetic polarization using artificial ferromagnetic elements.

6. Conclusion

In this paper, we have performed first-principles DFT calculations to investigate the structural, electronic and magnetic properties of half-metallic perovskite LaFeO3. Exchange and correlation effects are treated by PBE-GGA and GGA+U. From the structural properties, we found that the lattice parameter is in agreement with the experimental result and this compound is stable in the cubic phase for GGA approximation. The negative value of

Creative Commons Attribution-NonCommercial-NoDerivatives 4.0 International License (CC BY-NC-ND)

cohesive energy E_{coh} indicates that this compound can be synthesized experimentally. Also, we have calculated the electronic properties of the compound for the three approximations and we found that the LaFeO3 compound is half-metallic for GGA + U, it has indirect band gap in R-Γ direction for spin down direction and metallic character for spin up direction with an important integer magnetic moment of 4.00μB, where the Fe^{+3} have major contributions which means that our compound can be used in spintronic devices.

References:

[1] A.M. Glazer, ActaCrystallogr. B28 (1972)3384-3392
[2] R.H.Mitchell.Perovskites.Modern.and.ancient, ed., ed. AlmazPress. 2002.
[3] De Groot, R., Mueller, F., Van Engen, P., Buschow, K.(1983). New class of materials: half-metallic ferromagnets. Phys. Rev. Lett. 50, 2024.
[4] Birsan, A., Palade, P., Kuncser, V.(2013). Prediction of half metallic properties in Ti2CoSi Heusler alloy based on density functional theory. J. Magn. Magn. Mater. 331, 109–112.
[5] Hohenberg, P., Kohn, W.(1964). Inhomogeneous electron gas. Phys. Rev. 136, B864.
[6] Blaha, P., Schwarz, K., Sorantin, P., Tricky, S. (1990). First principle investigations on electronic, magnetic, thermodynamic, and transport properties of TlGdX2 (X= S, Se, Te). Comput Phys Commun 59, 399.
[7] F. Tran and P. Blaha, Phys. Rev. Lett. 102, 226401 (2009).
[8] W. Kohn and L. J. Sham, Phys. Rev. A 140, 1133 (1965).
[9] L. Bi, A.R. Taussig, H.Kim and L. Wang ; G.F. Dionne, D. Bono, K. Persson, Phys. Rev.B 78, 104106 (2008).
[10] Hua Wu, Phys. Rev. B 64 (2001) 125126
[11] Anisimov, V.I., Zaanen, J., Andersen, O.K.: Phys. Rev. B 943, 44 (1991)
[12] PHYSIQUE OF THE STATE Vol. 47 No. 11 2005
[13] https://materialsproject.org/materials/mp.
[14] Q. Huang, A. Santoro, J. W. Lynn, R. W. Erwin, J. A. Borchers, J. L. Peng, and R. L. Greene, Structure and magnetic order lanthanum manganite, Phys. Rev. B 55, 14987 (1997).
[15] H. J. Monkhorst and J. D. Pack, "Special points for Brillouin-zone integrations," Physical Review B, vol. 13, p. 5188, 1976.

Creative Commons Attribution-NonCommercial-NoDerivatives 4.0 International License (CC BY-NC-ND)

Algerian Journal of Engineering Architecture and Urbanism Vol. 5 Nr. 3 2021
ISSN: 2588-1760

EVOLUTION OF RADIUS OF PLASTIC ZONE WITH CRACK TIP-OPENING DISPLACEMENT

Mohamed Tahar HANNACHI[1]
[1] PhD (MCA), department of mechanical engineering ,university Larbi-Tébessi,Tébessa, Algéria e-mail: Mohamedtah334@gmail.com

Mohamed BRADJI[2]
[2] Third cycle-student, department of mechanical engineering ,university Larbi-Tébessi,Tébessa, Algéria e-mail: Mohamedbradji@gmail.com

Abstract:
In this study we tempted to describe and present the experiment mechanical properties of the steel S235JR. Then it was considered that this same is cracked, to see the relationship between the radius of plastic zone and the Crack tip-opening displacement, (abbreviation CTOD) simulated using finite element by the code CASTEM 2013.

Key words: plastic zone, crack, simulation, strain, radius.

Introduction:

The forming a bond between two pieces of metal results a serial deformations, however, a variety of defects is most often surface formed during in-service operation during fabrication (Eiber R. and Kiefner J. 1986). Structural components falling into this category made in field conditions for high pressure piping systems and steel. These configurations generally develop some stress in specimens (Donato G. 2008). The primary motivation to use tensile test of specimens in defect assessment procedures of pipes lies in stress and strain fields which drive the fracture process (Nyhus B. and Polanco M. 2003), (Cravero S. and Ruggieri C. 2005), (Silva L. et al. 2006). Our approach is based primarily on the study of the steel, which is an essential parameter, why it is necessary to select the appropriate mechanical properties of the material used (S235JR) and verify that this shade mechanical processing meets the conventional requirements (ductility properties and balanced properties of resistance). The tensile test was performed on test pieces.

Problematic:

Our approach is based primarily on the experimental determination of the mechanical properties of the considered steel (S235JR) and the study of relationship between the radius of plastic zone and the Crack tip-opening displacement (CTOD).

Materials and methods:

The material used is construction steel (S235JR), whose chemical composition is shown in table 1.

C %	Mn %	Si %	S %	P %	AL %

0.08-0.1	0.36	0.01	0.009	0.008	0.062

Table 1. CHEMICAL COMPOSITION OF STEEL (S235JR).

Materials and methods, Materials

Carbone (%)	Pearlite (%)	Ferrit (%)
0.08	10	90
0.09	11.25	88.75
0.1	12.5	87.5

Table 1. PERCENT OF THE FERRITIC AND PEARLITE PHASES OF STEEL.

According to specimens of tensile test, we consider a semi-infinite plate, subjected to a stress homogeneous, and having a crack length of side a. With Length of crack (20 mm), Width of specimen (40 mm), Length of specimen (80 mm) and thickness (7 mm).For this type of geometry, the stress intensity factor for pure opening mode (mode I), is:

$$K_I = 1{,}122.\sigma\sqrt{\pi a} \tag{1}$$

The theory of crack spacing (Crack-opening displacement, abbreviation CTOD.) was first formulated by Wells . The critical distance from the lips of a crack is considered a test of resistance to boot tears. This theory of the critical crack spacing is especially produces a blunting the crack tip whose surfaces differ at this level of δ, called CTOD (Crack Opening Displacement). The Calculations of *Burdekin and Stone 1966*, show that the crack spacing δ (at the bottom of the real crack) is given by the displacement in x ± a is: We whereas the first term only.

$$\delta = \frac{\pi a \sigma^2}{E\sigma_y} \tag{2}$$

Using the model proposed by Dugdale *(1960)* and Barenblatt *(1962*). we link the critical crack spacing and the fracture energy per unit area G_C.

The radius (rp) of a plasticized zone defined by Von Mises :

- case of plane deformations (Strains):

$$r_p = \frac{[1-2\nu]^2}{2\pi}\left(\frac{K_I}{\sigma_y}\right)^2 \tag{3}$$

- Case of plane stresses:

$$r_p = \frac{1}{2\pi}\left(\frac{K_I}{\sigma_y}\right)^2 \tag{4}$$

Algerian Journal of Engineering Architecture and Urbanism Vol. 5 Nr. 3 2021
ISSN: 2588-1760

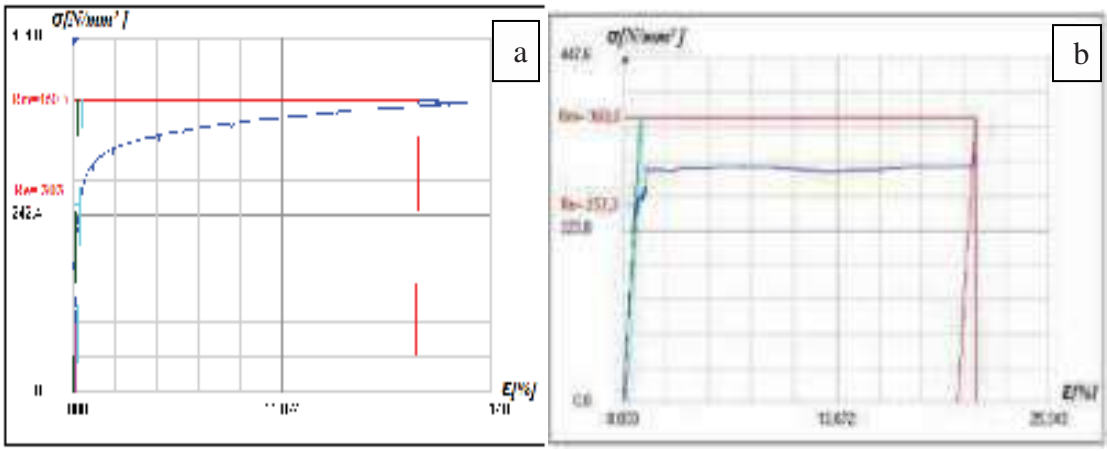

Fig. 1. THE STRESS-STRAIN CURVE OF THE FLAT
a) BEFORE ANNEALING ($\sigma_m = R_m$= 460.5 N / mm^2 and $\sigma_y = R_y$=303.0 N / mm^2).
b) AFTER ANNEALING ($\sigma_m = R_m$= 369.2 N / mm^2 and $\sigma_y = R_y$=257.3 N / mm^2)

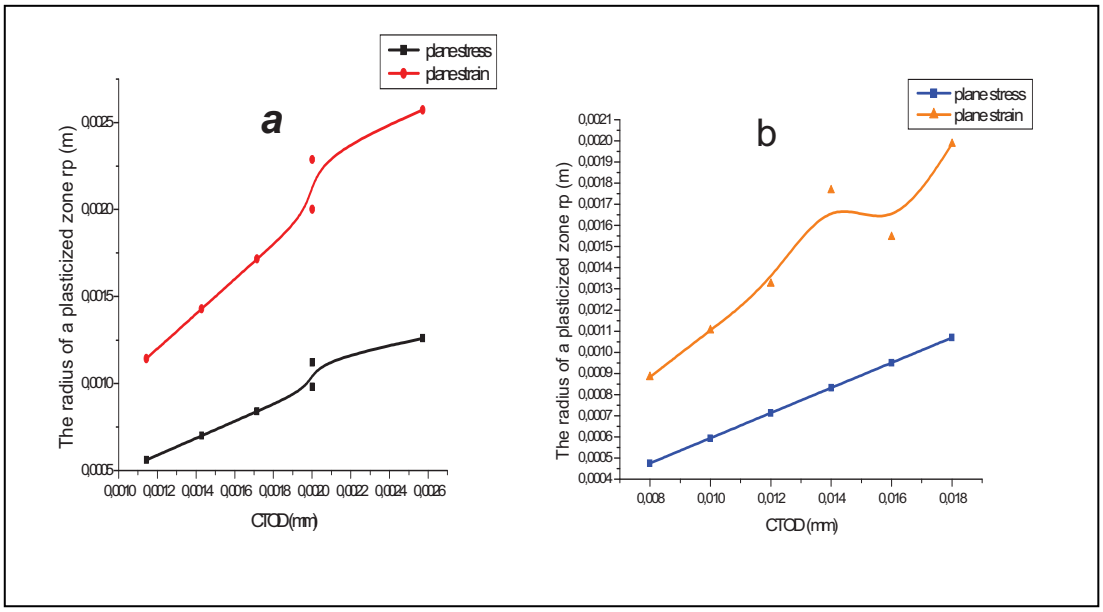

Fig.2 . THE RADIUS OF A PLASTICIZED ZONE DEFINED BY VON MISES, IN PLANES STRESSES AND STRAINS FOR TWO VALUES OF STRENGTH YIELDS : A) $\sigma_y = 257{,}3\ MPa$ and b) $\sigma_y = 303\ Mpa$.

Algerian Journal of Engineering Architecture and Urbanism Vol. 5 Nr. 3 2021
ISSN: 2588-1760

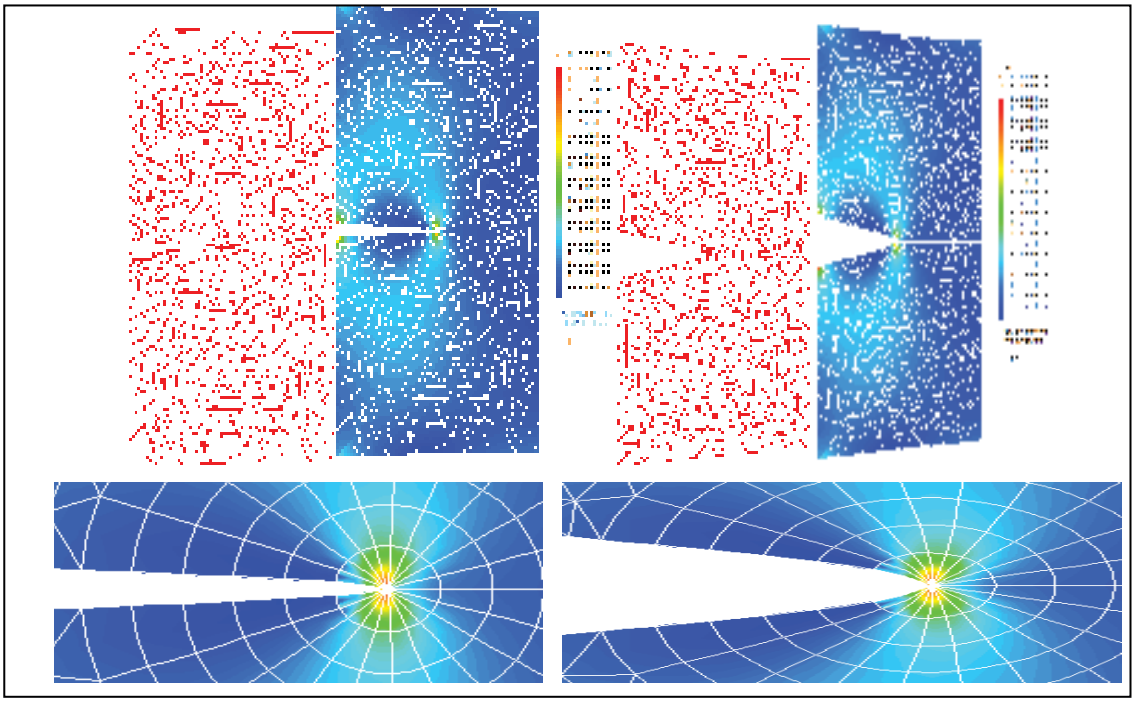

Fig. 3. DEFORMATION AND VON MISES STRESS AFTER 10 SEC AND 20 SEC.

Results and discussions:

Recently, Carboni *(2007)* and Newman *(2009)* used micro-strain gauges glued near the front of the crack locally to detect the small change of convenience for small cracks. In elastoplastic, the crack tip becomes blunt and some authors have proposed using the crack opening as a parameter of fracture mechanics. The CTOD, crack or gap δ has been defined from the displacement of the crack tip, measured at the intersection of the boundary of the plastic zone with the lips of the crack. Values of the crack opening (CTOD), during loading are shown in the eq.1. It is easy to evaluate the deformation locally by the metal locally measuring its thickness. There are many ways to calculate this distance δ. For example, Tracey has proposed to define this distance at the intersection of two lines passing at 45° to the axis and the lips of the crack. Nowell *(2004)* used the method of Moiré interferometry to measure the displacement of the lips of the crack to detect the closed position. Chang et al. *(2009)* proposed a technical for detecting acoustic emission to detect the closure of small cracks.

The results obtained about the mechanical behavior of the welded tubes, we provide in the following a comparative analysis:

In the case of the before annealing pieces are important and high, but a decrease in ductility properties**.** This is not the case for after annealing pieces (Fig. 1), where we can see an increase in ductility; this can be explained by the deformation process in the perpendicular These deformations have resulted in the hardening of the metal;- the effect of hardening increase the resistive properties (the yield strength, the tensile strength) and decrease the ductility properties (elongation and resilience). The ductile tearing process of specimen is similar to the standard specimen, including the initial crack blunting, crack initiation and propagation. The plastic zone size around the crack tip is closer to the real cracking. The maximum plastic strain (Fig. 2) in the crack plane during the initial crack blunting and increases with the radius of plastic zone. The increases of CTOD decrease the size of plastic zone with radius is governed by the laws of Von Mises (Fig. 2). After crack initiation, its overall propagation direction is perpendicular to the loading direction, roughly a straight, the deformations are recorded at different amplitudes in parallel induce Von Mises stresses in the same (Fig.3) and at the tip of the crack can clearly see the plasticized zone having residual stress due the gaps,. However, sometimes the crack is not straight in the local region. Such as, the zigzag pattern is observed in the initial stage of crack extension. The maximum plastic strain plane is one of preferred places for shear. Therefore, the plane at ±45 degree could be the first to the formation of crack initiation. However, the principal direction of crack propagation remains in its original plane in Mode I loading condition. As the load increases direction has the largest necking, which accelerates the crack tip, and leads to crack initiation. Therefore, the thinnest location is also one of crack propagation paths. According to the stress state, and often under plane strain condition, the stable plastic deformation and severe necking accelerate. However, free surfaces of the specimen are in the plane stress state with low stress triaxiality, which slows down crack formation.

Conclusion:

Conclusion To obtain the best compromise between different properties to use an alloy, it is necessary to understand the evolution of these properties in an integrated manner throughout the production process. The precision of the parts is related to the first

Creative Commons Attribution-NonCommercial-NoDerivatives 4.0 International License (CC BY-NC-ND)

functional tolerances tooling and a similar deformation or other validated in the case of plates subject of defects (cracks). To better improve the step of calculating, it has been a change in crack length, in order to determine the spacing (CTOD) and size of plastic. The behavior of the crack tip opening displacement (CTOD) his radius was increase with size of plastic zone. The geometric of CTOD and plastic zone have been widely used. The Simulation by finite element of single edge-crack of transverse weld joint specimen.

References:

BURDEKIN F. , STONE D. (1966), The crack opening displacement approach to fracture mechanics Yielding materials », Journal of strain Analysis 1-(2) :145 à153.

Carboni M. (2007), Strain gauge compliance measurement near the crack tip for crack closure evaluation: Application and accuracy. Engineering Fracture Mechanics ;74:563-577.

Chang H. , Han E. and Wang J. (2009), Acoustic emission study of fatigue crack closure of physical short and long cracks for aluminum alloy LY12CZ. International Journal of Fatigue; 31:403-407.

Cravero S. , Ruggieri C. (2005), Correlation of fracture behavior in high pressure pipelines with axial flaws using constraint designed test specimens – Part I: Plane-strain analyses. Engng Fract Mech 72:1344–60.

Donato G. (2008), Constraint effects and crack driving forces in surface cracked pipes subjected to reeling. In: ASME international conference on offshore mechanics and arctic engineering Lisbon (Portugal): American Society of Mechanical Engineers.

DUGDALE (1960), Yielding of steel sheets containing slits, J. Mech. Phys. Solids: 18 -100.

Eiber R. , Kiefner J. (1986), Failure of pipelines. Metals handbook, Failure Analysis and Prevention, 9th ed., vol. 11, American Society for Metals: 695–706p.

Naman Resch, (1995), rupture par fissuration des structures, édition Hermes (Paris 1995), pp.144-151.

Newman J. (2009), Crack under high load ratio condition for Inconel-718 near threshold behavior. Engineering Fracture Mechanics:76(209-220).

Nowell D. (2004), Crack closure measurements using Moiré interferometry with photoresist gratings. International Journal of Fatigue 26:1075-1082.

Nyhus B.; Polanco M. (2003), SENT specimens as an alternative to SENB specimens for fracture mechanics testing of pipelines. In: ASME international conference on offshore mechanics and arctic engineering, Cancun (Mexico): American Society of Mechanical Engineers.

Silva L., Cravero S. ,Ruggieri C. (2006), Correlation of fracture behavior in high pressure pipelines with axial flaws using constraint designed test specimens: 3-D effects on constraint. Eng. Fract. Mech 73: 2123–38.

Creative Commons Attribution-NonCommercial-NoDerivatives 4.0 International License (CC BY-NC-ND)